

Lecture Notes in Mechanical Engineering

Giampiero Mastinu · Francesco Braghin ·
Federico Cheli · Matteo Corno ·
Sergio M. Savaresi *Editors*

16th International Symposium on Advanced Vehicle Control

Proceedings of AVEC'24 – Society
of Automotive Engineers of Japan


OPEN ACCESS

 Springer

Lecture Notes in Mechanical Engineering

Series Editors


Fakher Chaari, *National School of Engineers, University of Sfax, Sfax, Tunisia*

Francesco Gherardini , *Dipartimento di Ingegneria “Enzo Ferrari”, Università di Modena e Reggio Emilia, Modena, Italy*

Vitalii Ivanov, *Department of Manufacturing Engineering, Machines and Tools, Sumy State University, Sumy, Ukraine*

Mohamed Haddar, *National School of Engineers of Sfax (ENIS), Sfax, Tunisia*

Editorial Board Members

Francisco Cavas-Martínez , *Departamento de Estructuras, Construcción y Expresión Gráfica Universidad Politécnica de Cartagena, Cartagena, Spain*

Francesca di Mare, *Institute of Energy Technology, Ruhr-Universität Bochum, Bochum, Germany*

Young W. Kwon, *Department of Manufacturing Engineering and Aerospace Engineering, Graduate School of Engineering and Applied Science, Monterey, USA*

Tullio A. M. Tolio, *Department of Mechanical Engineering, Politecnico di Milano, Milano, Italy*

Justyna Trojanowska, *Poznan University of Technology, Poznan, Poland*

Robert Schmitt, *RWTH Aachen University, Aachen, Germany*

Jinyang Xu, *School of Mechanical Engineering, Shanghai Jiao Tong University, Shanghai, China*

Lecture Notes in Mechanical Engineering (LNME) publishes the latest developments in Mechanical Engineering—quickly, informally and with high quality. Original research or contributions reported in proceedings and post-proceedings represents the core of LNME. Volumes published in LNME embrace all aspects, subfields and new challenges of mechanical engineering.

To submit a proposal or request further information, please contact the Springer Editor of your location:

Europe, USA, Africa: Leontina Di Cecco at Leontina.dicecco@springer.com

China: Ella Zhang at ella.zhang@cn.springernature.com

India, Rest of Asia, Australia, New Zealand: Swati Meherishi at swati.meherishi@springer.com

Topics in the series include:

- Engineering Design
- Machinery and Machine Elements
- Mechanical Structures and Stress Analysis
- Automotive Engineering
- Engine Technology
- Aerospace Technology and Astronautics
- Nanotechnology and Microengineering
- Control, Robotics, Mechatronics
- MEMS
- Theoretical and Applied Mechanics
- Dynamical Systems, Control
- Fluid Mechanics
- Engineering Thermodynamics, Heat and Mass Transfer
- Manufacturing Engineering and Smart Manufacturing
- Precision Engineering, Instrumentation, Measurement
- Materials Engineering
- Tribology and Surface Technology

Indexed by SCOPUS, EI Compendex, and INSPEC.

All books published in the series are evaluated by Web of Science for the Conference Proceedings Citation Index (CPCI).

To submit a proposal for a monograph, please check our Springer Tracts in Mechanical Engineering at <https://link.springer.com/bookseries/11693>.


Giampiero Mastinu · Francesco Braghin ·
Federico Cheli · Matteo Corno ·
Sergio M. Savaresi
Editors

16th International Symposium on Advanced Vehicle Control

Proceedings of AVEC'24 – Society
of Automotive Engineers of Japan

Editors

Giampiero Mastinu 
Department of Mechanical Engineering
Politecnico di Milano
Milano, Italy

Francesco Braghin 
Department of Mechanical Engineering
Politecnico di Milano
Milano, Italy

Federico Cheli 
Department of Mechanical Engineering
Politecnico di Milano
Milano, Italy

Matteo Corno 
Department of Electronics, Information
Technology and Bioengineering
Politecnico di Milano
Milano, Italy

Sergio M. Savaresi 
Department of Electronics, Information
Technology and Bioengineering
Politecnico di Milano
Milano, Italy



ISSN 2195-4356 ISSN 2195-4364 (electronic)
Lecture Notes in Mechanical Engineering
ISBN 978-3-031-70391-1 ISBN 978-3-031-70392-8 (eBook)
<https://doi.org/10.1007/978-3-031-70392-8>

© The Editor(s) (if applicable) and The Author(s) 2024. This book is an open access publication.

Open Access This book is licensed under the terms of the Creative Commons Attribution 4.0 International License (<http://creativecommons.org/licenses/by/4.0/>), which permits use, sharing, adaptation, distribution and reproduction in any medium or format, as long as you give appropriate credit to the original author(s) and the source, provide a link to the Creative Commons license and indicate if changes were made.

The images or other third party material in this book are included in the book's Creative Commons license, unless indicated otherwise in a credit line to the material. If material is not included in the book's Creative Commons license and your intended use is not permitted by statutory regulation or exceeds the permitted use, you will need to obtain permission directly from the copyright holder.

The use of general descriptive names, registered names, trademarks, service marks, etc. in this publication does not imply, even in the absence of a specific statement, that such names are exempt from the relevant protective laws and regulations and therefore free for general use.

The publisher, the authors and the editors are safe to assume that the advice and information in this book are believed to be true and accurate at the date of publication. Neither the publisher nor the authors or the editors give a warranty, expressed or implied, with respect to the material contained herein or for any errors or omissions that may have been made. The publisher remains neutral with regard to jurisdictional claims in published maps and institutional affiliations.

This Springer imprint is published by the registered company Springer Nature Switzerland AG
The registered company address is: Gewerbestrasse 11, 6330 Cham, Switzerland

If disposing of this product, please recycle the paper.

Preface

We are delighted to present the proceedings of the 16th International Symposium on Advanced Vehicle Control (AVEC'24), held from September 2–6, 2024, in Milan, Italy.

AVEC boasts a long and distinguished tradition dating back to 1992, when it was initiated by the Vehicle Dynamics Technical Committee of the Society of Automotive Engineers of Japan (JSAE). The symposium's founding vision was to bridge the gap between academia and industry, fostering a platform for leading international experts to exchange ideas and shape the future of vehicle control theory, design, and implementation.

This year's symposium once again provided a vibrant forum for the exchange of ideas on a broad range of topics critical to the future of vehicle dynamics and control. These topics are not only of significant academic interest but also hold immense relevance for the automotive industry and society.

The presented papers cover a wide spectrum of topics, including:

- **Vehicle Dynamics Theory:** Fundamental aspects of vehicle dynamics modeling and analysis form the bedrock for designing and optimizing control systems that ensure safe, stable, and predictable handling characteristics.
- **Steering, Brake, Tire, and Suspension:** Advancements in these core subsystems play a crucial role in enhancing vehicle responsiveness, maneuverability, and overall safety. Optimizing these elements leads to increased fuel efficiency, reduced wear and tear, and ultimately, a lower environmental impact.
- **Chassis Control & Powertrain:** Integration of powertrain and chassis control systems allows for the development of vehicles with superior handling, improved fuel economy, and smoother power delivery. This contributes to a more comfortable and efficient driving experience.
- **Electrified Vehicles:** Electric and hybrid vehicles become increasingly important as the automotive industry transitions towards more sustainable transportation solutions. New Powertrain management and efficient control systems are crucial for maximizing the range and performance of these vehicles, ultimately promoting wider adoption of electric mobility.
- **Active Safety Systems & ADAS:** The design and implementation of advanced driver-assistance systems (ADAS) are vital for enhancing vehicle safety and reducing the number of traffic accidents. These advancements directly contribute to saving lives and creating a safer driving environment for all road users.
- **Stability Enhancement Systems (ABS, TCS, ESC):** Continued development and optimization of stability control systems like ABS, TCS, and ESC play a critical role in preventing vehicle loss of control and mitigating the severity of accidents. This directly translates to a reduction in road fatalities and injuries.
- **Driver–Vehicle Systems:** Understanding the interaction between driver and vehicle is essential for designing the vehicle and active control systems, resulting in more intuitive and responsive vehicles, and providing the driver with a higher sense of

control. This leads to improved driver engagement and reduced fatigue, promoting safer and more enjoyable driving.

- **Automated Driving Systems:** Control strategies and technologies for autonomous vehicles represent the future of transportation. Advancements in this field hold the potential to revolutionize mobility, enhancing accessibility, safety, and efficiency on our roads.
- **Modeling:** Development and validation of accurate vehicle dynamics models are crucial for designing and testing vehicles and control systems in a virtual environment before real-world implementation. This translates to faster development cycles, reduced costs, and improved overall system performance.
- **Sensors and Actuators:** Advancements in sensor and actuator technologies are essential for enabling the development of increasingly sophisticated and responsive vehicles. These advancements are key to achieving the goals of enhanced vehicle safety, efficiency, and performance.
- **Testing and Validation:** Robust methodologies for evaluating the performance of vehicle control systems ensure their effectiveness and reliability in real-world driving conditions. This is critical for ensuring the safety and functionality of vehicles on the road.
- **Driving Simulator Dynamics and Control:** Driving simulators provide a valuable tool for testing and refining vehicle and control systems in a safe and controlled environment. This allows for a more efficient development process and contributes to the creation of robust and reliable control strategies.

The high quality of the submitted papers reflects the ongoing dynamic nature of the field of vehicle control. We are grateful to all the authors who contributed their research to AVEC'24 and to the reviewers who provided valuable feedback that ensured the scientific merit of the proceedings.

We extend our sincere appreciation to those who supported and helped to organize the conference. We would like to thank the authors who contributed to a very successful conference. We look forward to continuing this important dialogue at future AVEC conferences, building upon this 16-edition legacy of fostering collaboration and innovation in the field of vehicle control.

Giampiero Mastinu
Federico Cheli
Sergio M. Savaresi
Francesco Braghin
Matteo Corno

Organization

Program Committee Chairs

Gobbi, Massimiliano

Politecnico di Milano, Milan, Italia

Radrizzani, Stefano

Politecnico di Milano, Department of Electronics,
Information and Bioengineering, Milan, Italy

Vignati, Michele

Politecnico di Milano, Department of Mechanical
Engineering, Milan, Italy

Contents

Safe Control Allocation of Articulated Heavy Vehicles Using Machine Learning	1
<i>Sander van Dam, Lukas Wisell, Kartik Shingade, Mikael Kieu, Umur Erdinc, Maliheh Sadeghi Kati, Esteban Gelso, and Dhasarathy Parthasarathy</i>	
Trajectory Tracking for High-Performance Autonomous Vehicles with Real-Time Model Predictive Control	8
<i>Matteo Pierini, Paolo Fusco, Rodrigo Senofieni, Matteo Corno, Giulio Panzani, and Sergio Matteo Savaresi</i>	
Study on Linear Actuators for Intake and Exhaust Systems of Internal Combustion Engines (Analytical Consideration of Thrust Characteristics by Permanent Magnet Array)	15
<i>Jumpei Kuroda, Kaito Kimura, Ryutaro Ono, Ikkei Kobayashi, Daigo Uchino, Kazuki Ogawa, Keigo Ikeda, Ayato Endo, Hideaki Kato, and Takayoshi Narita</i>	
Drifting Maneuver Investigation via Phase Plane Analysis of Experimental Data	22
<i>Giovanni Righetti, Guido Napolitano dell'Annunziata, Flavio Farroni, Matteo Massaro, and Basilio Lenzo</i>	
Effects of External Tire Heating on Rolling Resistance Energy Consumption	29
<i>Mikael Askerdal, Fredrik Bruzelius, and Jonas Fredriksson</i>	
Bifurcation Analysis of a Nonlinear Vehicle Model on Banked Road	36
<i>Luca Zerbato, Enrico Galvagno, and Mauro Velardocchia</i>	
Regenerative Brake Blending in Electric Hypercars: Benchmarking and Implementation	43
<i>Rodrigo Senofieni, Federico Bassi, Matteo Corno, Sergio Matteo Savaresi, and Gianluca Savaia</i>	
A Method for Obtaining Reference Friction Values for Validation of Road Friction Estimation Algorithms	50
<i>Mattias Hjort, Fredrik Bruzelius, Sogol Kharrazi, and Derong Yang</i>	

Computing the Lateral Compliance of the Racing Line Using Trajectory Optimization	57
<i>R. K. Aggarwal and J. C. Gerdes</i>	
State Estimation and Sensorimotor Noise in a Driver Steering Model with a Gaussian Process Internal Model	64
<i>Harry Fieldhouse and David Cole</i>	
Energy Efficiency Oriented Robust Model Predictive Stability Control for Autonomous Electric Vehicles	71
<i>Ziang Tian, Huilong Yu, and Junqiang Xi</i>	
Profile Generation of Cooperative Driving in Urban Intersections for Energetic Evaluation	78
<i>Maximilian Flormann, Axel Sturm, Roman Henze, and Pongsathorn Raksincharoensak</i>	
Energetic Impact of Urban Cooperative Driving on the Example of Intersections	85
<i>Axel Sturm, Maximilian Flormann, Roman Henze, and Pongsathorn Raksincharoensak</i>	
Speed Control in the Presence of Road Obstacles: A Comparison of Model Predictive Control and Reinforcement Learning	91
<i>P. Mandl, F. Jaumann, M. Unterreiner, T. Gräber, F. Klinger, J. Edelmann, and M. Plöchl</i>	
A Geometric Electric Motor Model for Optimal Vehicle Family Design	98
<i>Maurizio Clemente, Olaf Borsboom, Mauro Salazar, and Theo Hofman</i>	
Road Friction Adaptive Lateral Control of Automated Vehicles with Differential Braking	109
<i>Jannes Iatropoulos, Tim Ahrenhold, Leon Salzwedel, and Roman Henze</i>	
Model-Free Automated Reversing of Articulated Heavy Goods Vehicles	116
<i>Shammi Rahman, Timothy Gordon, Leon Henderson, Yangyan Gao, Sonya Coleman, and Dermot Kerr</i>	
Nonlinear Dynamics of a Controlled Two-Wheeled Trailer	123
<i>Hanna Zsofia Horvath, Adam Balint Feher, and Denes Takacs</i>	
Yaw Stability Control of Vehicles Using a Slip Polytope Validated with Real Tests	130
<i>Umur Erdinc, Mats Jonasson, Maliheh Sadeghi Kati, Leo Laine, Bengt Jacobson, and Jonas Fredriksson</i>	

Study on Accident-Avoidance Mechanism in Driver-Vehicle System When Activating Level-2 ADAS	137
<i>Norika Arai, Jinnosuke Kamimura, Yohei Fujinami, Xingguo Zhang, Pongsathorn Raksincharoensak, Masaaki Uechi, Shintaro Inoue, Fumio Sugaya, Kazunori Nogi, Toshinori Okita, Hideaki Hayashi, and Keitaro Niki</i>	
Motion Control of a 6×4 Heavy Vehicle: Autonomous Collision Avoidance Using Integrated Chassis Control	144
<i>Aria Noori Asiabar, Timothy Gordon, Yangyan Gao, Leon Henderson, and Leo Laine</i>	
Investigating Characteristics and Opportunities for Rear-Wheel Steering	151
<i>Oskar Lind Jonsson, Arvind Balachandran, Jian Zhou, Björn Olofsson, and Lars Nielsen</i>	
Accuracy Requirements of Camera-Based Depth Estimation for Urban Automated Driving	158
<i>M. Westendorf, S. Thal, T. Ahrenhold, and R. Henze</i>	
STS-GAN: Spatial-Temporal Attention Guided Social GAN for Vehicle Trajectory Prediction	164
<i>Yanbo Chen, Huilong Yu, and Junqiang Xi</i>	
Automated Parking System for Tractor-Trailer Vehicle	171
<i>Jinwoo Kim and Seongjin Yim</i>	
Research on Jerk Reduction Route Planning Method for Autonomous Driving Using Vehicle Forward Information	178
<i>Takumi Komiya, Masato Abe, Yoshio Kano, Makoto Yamakado, Yu Sato, Ken-taro Ueno, and Yusuke Tanaka</i>	
Online Motion Planning for All-Wheel Drive Autonomous Race Cars	185
<i>Mischa Huisman and Erjen Lefeber</i>	
A Data-Driven Framework for Tire Force Estimation of Distributed Electric-Drive Vehicles	193
<i>Rujun Yan, Kun Jiang, Bowei Zhang, Jinyu Miao, and Diange Yang</i>	
Influence of the Front-Rear Torque Distribution on the Handling Characteristics and Stability Boundaries of an AWD-Vehicle	200
<i>Manuel Eberhart, Martin Arndt, Johannes Edelmann, and Manfred Plöchl</i>	

Determination of the Loss Behavior of Wheel Bearings Under Real Driving Conditions	207
<i>Lukas Hartmann, Leon Ohms, Ron Rebesberger, Gerrit Brandes, and Roman Henze</i>	
Prediction Based Cooperative Adaptive Cruise Control for Heterogeneous Platoons with Delays	214
<i>Redmer de Haan, Tom van der Sande, and Erjen Lefeber</i>	
Vertical Dynamics Control Using Active Tires and Preview	221
<i>Tom van der Sande and Nick te Kronnie</i>	
Time-Optimal Learning-Based LTV-MPC for Autonomous Racing	228
<i>Zijun Guo, Huilong Yu, and Junqiang Xi</i>	
Speed Profile Definition for GLOSA Implementation on Buses Based on Statistical Analysis of Experimental Data	235
<i>Daniele Vignarca, Stefano Arrigoni, Edoardo Sabbioni, and Federico Cheli</i>	
Longitudinal Control Concept for Automated Vehicles in Stop-and-Go Situations	244
<i>C. Pethe, M. Heinze, M. Flormann, and R. Henze</i>	
Inverse Approach to Vehicle Generalized Parameters for Individual Drives	251
<i>Vladimir Vantsevich, Jesse Paldan, David Gorsich, and Lee Moradi</i>	
Effect of Driving Force Control that Imitates the Function of Tire Lateral Force on Vehicle Dynamics	258
<i>Etsuo Katsuyama</i>	
Vibration Suppression of Automotive Drivetrains Based on Tire-Speed Observer and Backlash Compensation	265
<i>Kenta Maeda, Naoki Shinohara, Satoshi Kaneko, and Hiroki Sonoda</i>	
Robust Lane Keeping Control with Estimation of Cornering Stiffness and Model Uncertainty	272
<i>Junyeong Seong, Sungjun Park, and Kunsoo Huh</i>	
A Parametric Interpolation-Based Approach to Sideslip Angle Estimation	279
<i>Mariagrazia Tristano and Basilio Lenzo</i>	
Optimal Path Generator Embedded Model Predictive Control for Automated Vehicles	286
<i>Takashi Sago, Yoshihide Arai, Yuki Ueyama, and Masanori Harada</i>	

Development and Experimental Assessment of a Control Logic for Hydroplaning Prevention	293
<i>Edoardo Montini, Marco Salierno, Stefano Frigerio, and Stefano Melzi</i>	
Charging Stations for Electric Vehicles in SUMO Simulation Environment and Their Impact on the Traffic Flow	301
<i>Eva Spachtholz, Marvin Glomsda, Ingmar Kranefeld, Frédéric Etienne Kracht, and Dieter Schramm</i>	
Primary and Secondary Vehicle Lightweighting Achieved by Acting on the Battery Thermal Management System	308
<i>Giulia Sandrini, Daniel Chindamo, Marco Gadola, Andrea Candela, and Paolo Magri</i>	
A Propulsion Energy Estimator for Road Vehicles	315
<i>Carl Emvin, Fredrik Bruzelius, Luigi Romano, Bengt Jacobson, Pär Johannesson, and Rickard Andersson</i>	
Black Ice Detection Based on Tire Friction Coefficient Estimation of Vehicle Longitudinal Model	322
<i>Seung-Yong Lee, Ho-Jong Lee, and Gi-Woo Kim</i>	
Experimental Evaluation on Effects of Torque Vectoring Using Four In-Wheel Motor Independent Torque Control	329
<i>Yota Homma, Yoshihiro Yamakaji, Koji Kajitani, Richard Ford, and Yoshimi Furukawa</i>	
A Comprehensive Method for Computing Suspension Elasto-kinematics With Non-linear Compliance	336
<i>Paolo Magri, Marco Gadola, Daniel Chindamo, Giulia Sandrini, and Andrea Candela</i>	
A Novel Torque Vectoring Approach to Enhance Driving Experience	343
<i>Marco Papparone, Alessandro Pino, Filippo Giacomel, Giovanni Bussalai, Andrea Macaluso, Antoine Lamps, and Basileios Mavroudakos</i>	
Iterative Learning Trajectory Tracking Control of an Autonomous Bicycle	350
<i>Yixiao Wang, Fredrik Bruzelius, and Jonas Sjöberg</i>	
A General 3D Road Model for Motorcycle Racing	357
<i>Thomas Fork and Francesco Borrelli</i>	

Energy-Efficient Straight-Line Driving Torque Vectoring for Electric Vehicles with Disconnect Clutches and Unequal Front/Rear Motors	364
<i>Ivo Grđan, Branimir Škugor, and Joško Deur</i>	
Safety Filter for Lane-Keeping Control	371
<i>Chenhuan Jiang, Hanyu Gan, Illés Vörös, Dénes Takács, and Gábor Orosz</i>	
Neural Network Tire Force Modeling for Automated Drifting	378
<i>Nicholas Drake Broadbent, Trey Weber, Daiki Mori, and J. Christian Gerdes</i>	
Basic Study on the Effect of Driver Condition on Steering Burden	385
<i>Daigo Uchino, Ri Kintou, Ikkei Kobayashi, Jumpei Kuroda, Kazuki Ogawa, Keigo Ikeda, Taro Kato, Ayato Endo, Hideaki Kato, and Takayoshi Narita</i>	
YOLOgraphy: Image Processing Based Vehicle Position Recognition	392
<i>Ákos T. Köpeczi-Bócz, Tian Mi, Gábor Orosz, and Dénes Takács</i>	
Surrogate Modeling of Suspensions with High Stiffness Element for Real-Time Analysis Using Machine Learning	399
<i>Tojuro Hiraga and Taichi Shiiba</i>	
Data-Driven Risk Assessment with Scenario Classification for Collision Avoidance in Left/Right Turn Across Path Conflicts	406
<i>Wei Wang, Pongsathorn Raksincharoensak, and Roman Henze</i>	
Design and Analysis of Traction Control Strategies for Icy Road Conditions ...	413
<i>M. Mihalkov, C. Caponio, Z. Hankovszki, A. Sorniotti, U. Montanaro, and P. Gruber</i>	
Design and Verification of an Adaptive State-Tuned Power Management System for Series Hybrid Electric Tracked Vehicles	420
<i>Dersu Çeliksöz, İsmail Göçer, and Kerim Arda Gülseren</i>	
A Study on the Control of Handling and Stability of a Four Wheel Independent Steering Electric Vehicle	427
<i>Zhihao Wu, Ning Zhang, Pu Li, Zihong Li, and Jianrun Zhang</i>	
Using a Smartwatch to Evaluate Subjective Ratings of Driving Functions	434
<i>Panzer Anna, Lausch Hendryk, Iatropoulos Jannes, and Henze Roman</i>	

Speed Profile Generation for a Dual Motor Equipped Electrified Series Hybrid Tracked Vehicle Through Dynamic Programming Based Energy Optimization Procedure	440
<i>Ismail Gocer and S. Caglar Baslamisli</i>	
Energy and Time Optimal Control of Autonomous Vehicles by Using Frenet Frame Modelling and over-Actuation	447
<i>Wenliang Zhang, Lars Drugge, Mikael Nybacka, Jenny Jerrelind, Derong Yang, Rudolf Reiter, Jonathan Frey, and Annika Stensson Trigell</i>	
Robust 3D On-Road Object Detection and Distance Estimation for Active Vehicle Control Systems Based on Monocular Camera Image Data	454
<i>Xingguo Zhang, Daiki Ikami, and Pongsathorn Raksincharoensak</i>	
Occluded Area Detection Based on Sensor Fusion and Panoptic Segmentation	461
<i>Hiroshi Yoshitake, Jinyu Gu, and Motoki Shino</i>	
Temporal and Frequency Analysis with Empirical Mode Decomposition for Vehicle Vibration Signals	468
<i>Makoto Masuda and Taichi Shiiba</i>	
Dynamical Behaviours of the Nose Landing Gear with Freeplay and Stochastic Disturbance	474
<i>Xiaolei Du and Yong Xu</i>	
Tuning Time Delays to Improve the Performance of a Steering Controller	481
<i>Jialin Li, Denes Takacs, Jianwei Lu, Illes Voros, and Gabor Stepan</i>	
Vehicle Teleoperation: SRPT Approach Resilience to State Estimation Errors Through Simulation Insights	488
<i>Jai Prakash, Michele Vignati, and Edoardo Sabbioni</i>	
Advancing Autonomous Driving Safety Through LLM Enhanced Trajectory Prediction	496
<i>Qian Cheng, Xinyu Jiao, Mengmeng Yang, Mingliang Yang, Kun Jiang, and Diange Yang</i>	
Self-tuning of the Virtual-Bike Control for a Human-Powered Electric Bike with Series Architecture	503
<i>Stefano Radrizzani, Giulio Panzani, and Sergio Matteo Savaresi</i>	

Cooperative LiDAR-Aided Self-localization of CAVs in Real Urban Scenario	510
<i>Akif Adas, Luca Barbieri, Pietro Morri, Simone Mentasti, Satyesh Awasthi, Stefano Arrigoni, Edoardo Sabbioni, and Monica Nicoli</i>	
Subjective-Objective Assessment of Different Torque Vectoring Control Strategies	517
<i>Michele Asperti, Michele Vignati, and Edoardo Sabbioni</i>	
Retaining Cornering Performance and Reducing Energy Consumption with Torque Vectoring and Suspensions Tuning	525
<i>Michele Asperti, Michele Vignati, and Edoardo Sabbioni</i>	
Enhancing Steer-by-Wire Systems with an Integrated E-Motor and MR-Brake Actuator – Feedback Control Strategy	533
<i>Matthias Niegl, Johannes Hendewerk, Matthias Becker, Stefan Battlogg, and Peter Pfeiffer</i>	
A Rule-Defined Adaptive MPC Based Motion Planner for Autonomous Driving Applications	540
<i>Mohammed Irshadh Ismaaeel Sathyamangalam Imran, Satyesh Shanker Awasthi, Michael Khayyat, Stefano Arrigoni, and Francesco Braghin</i>	
Towards Friction Potential Estimation for Motorcycles	550
<i>Florian Klinger, Christoph Ott, Agnes Poks, Johannes Edelmann, and Manfred Plöchl</i>	
On the Stability of the Closed-Loop Teleoperated Vehicle and Teledriver System	557
<i>Ypti Hossain, Mathias Metzler, Johannes Edelmann, and Manfred Plöchl</i>	
Increasing Performance of Differential Braking as Steering Backup Using Combined Slip Effects	564
<i>Leon Salzwedel, Christian Frohn, Cedric Heise, Jannes Iatropoulos, and Roman Henze</i>	
Laboratory Abrasion Tester to Estimate Tyre Grip and Cornering Stiffness	571
<i>Francesco Colombo, Samuel Sonnino, Federico Mantovani, Andrea Ronchi, Luca Michielan, Michele Vignati, and Edoardo Sabbioni</i>	
Indoor Tyre Tread Wear Testing Driven by Outdoor Data Clustering	578
<i>Lorenzo Maglia, Davide Fantin, Stefano Pontoglio, Matteo Stella, and Edoardo Sabbioni</i>	

Trailer Reversing Supported by Steer-by-Wire	585
<i>Chang Liu, Jakob Roempe, Matthijs Klomp, and Lars Drugge</i>	
A Yaw Rate Based Stability Control Tuning via Virtual Methods	597
<i>Luca D'Avico, Fabio Carbone, Lucas Baudry, Fabrizio Forni, Pietro Caresia, and Gerardo Amato</i>	
Optimal Braking and Steering Control Under Split Friction on Curved Roads	604
<i>Ektor Karyotakis, Derong Yang, Mats Jonasson, and Jonas Sjöberg</i>	
A Fallback Approach for In-Lane Stop on Curved Roads Using Differential Braking	611
<i>Jihoon Sung, Seungwon Choi, and Kunsoo Huh</i>	
Steering Noise Cancelling for Drift Assist Control	618
<i>Yiwen Sun, Efsthathios Velenis, and Ajinkya Krishnakumar</i>	
A Decoupling Control Scheme for Path Tracking with Model Predictive Path Integral and Output Regulator	625
<i>Hang Wan, Hui Liu, Shida Nie, and Lijin Han</i>	
A Learning-Based Model Predictive Contouring Control for Vehicle Evasive Manoeuvres	632
<i>Alberto Bertipaglia, Mohsen Alirezaei, Riender Happee, and Barys Shyrokau</i>	
Predictive Braking on a Nonplanar Road	639
<i>Thomas Fork, Francesco Camozzi, Xiao-Yu Fu, and Francesco Borrelli</i>	
Variable-Step-Length Hybrid A* Based on Dichotomy Optimization for Path Planning of Autonomous Mining Trucks*	646
<i>Yichen Zhang, Yafei Wang, Mingyu Wu, and Ruoyao Li</i>	
Study on Continuous Road Friction Measurement Under Various Environmental Conditions	653
<i>Ichiro Kageyama, Atsushi Watanabe, Yukiyo Kuriyagawa, Tetsunori Haraguchi, Tetsuya Kaneko, and Minoru Nishio</i>	
Observer Design for Estimating Road Elevations at All Tire Contact Patches Using Only an Inertial Sensor	659
<i>Hosik Choi and Juhui Gim</i>	

Physics-Informed Neural Network for Mining Truck Suspension Parameters Identification	665
<i>Mingyu Wu, Yafei Wang, Yichen Zhang, and Zexing Li</i>	
Point Cloud Interpolation by RGB Image to Estimate Road Surface Profile for Preview Suspension Control	672
<i>Masato Inoue, Yosuke Kawasaki, Takuma Suzuki, Yuta Washimi, Tsutomu Tanimoto, and Masaki Takahashi</i>	
Gain-Scheduled Bicycle Balance Controller Based on System Identification ...	679
<i>Yixiao Wang, Fredrik Bruzelius, and Jonas Sjöberg</i>	
Investigating Reversing Motion of Truck-Semitrailer Along Clothoid Curve ...	686
<i>Levente Mihályi and Dénes Takács</i>	
A Way Beyond Drifting: Cornering at the Unexploited Region of Dynamics ...	693
<i>Hangyu Lu, Xiaodong Wu, and Liang Yan</i>	
Design and Implementation of a Slip Control for Electric Formula Student Vehicle Using Sliding Mode Control	700
<i>Ádám Alföldi, Dániel Fényes, and Péter Gáspár</i>	
Long Combination Vehicles Reverse Strategies Based on Articulation Angle Gradient	707
<i>Zhaohui Ge, Fredrik Bruzelius, and Bengt Jacobson</i>	
A Comparative Study of Discomfort Using Electrical and Friction Braking at Low Speed Driving	714
<i>Samira Deylaghian, Mats Jonasson, and Petri T. Piironen</i>	
Deriving Models from Field Test Data to Forecast Brake System Limits in Fuel Cell Heavy-Duty Trucks	721
<i>Seongjae Mun, Jinhui Park, Hongwoo Lee, and Changsun Ahn</i>	
Numerical Study on Vibration Characteristics of Non-pneumatic Tire Coupled with Quarter-Car Model	728
<i>Yuta Washimi, Takuma Suzuki, Toshihiko Okano, and Kensuke Sasaki</i>	
Study on the Effects of Long-Term Vibration and Visual Tasks on Visual Acuity in the Car	735
<i>Masateru Amano, Aya Kubota, Hiroyuki Yamaguchi, Yuji Muragishi, and Yoshikazu Hattori</i>	

Human-Centered Collaborative Decision-Making and Steering Control with Reinforcement Learning	742
<i>Liang Yan, Xiaodong Wu, and Hangyu Lu</i>	
A Study on Giant Magnetostrictive Actuator Used in Active Noise Control System for Ultra-compact Electric Vehicles (Analytical Consideration on Output Performance of the Actuator)	749
<i>Taro Kato, Ryusei Naganuma, Koki Bando, Ikkei Kobayashi, Junpei Kuroda, Daigo Uchino, Kazuki Ogawa, Keigo Ikeda, Ayato Endo, Xiaojun Liu, Hideaki Kato, Takayoshi Narita, and Mitsuaki Furui</i>	
Collision Prediction for a Mining Collision Avoidance System	756
<i>J. C. van Aswegen, H. A. Hamersma, and P. S. Els</i>	
Interactive and Robust Prevention of Lane Departure	763
<i>Syouma Edamoto, Shuuji Kimura, Tsutomu Tamura, Richard Gao, and Robert Fuchs</i>	
Effect of Control Laws for Torque-Vectoring Systems on Steady-State Cornering in Race Cars	770
<i>Ikkei Kobayashi, Fumiya Yoshida, Liting Fu, Yusuke Ebashi, Hayato Yamada, Junpei Kuroda, Daigo Uchino, Kazuki Ogawa, Keigo Ikeda, Taro Kato, Ayato Endo, Mohamad Heerwan Bin Peeie, Hideaki Kato, and Takayoshi Narita</i>	
Mapping and Localization Method for Autonomous Vehicles on Roads Using Environmental Magnetic Field	777
<i>Kyoya Ishii, Keisuke Shimono, Yoshihiro Suda, Takayuki Ando, Hirotaka Mukumoto, and Kazuo Urakawa</i>	
Consideration of Restoration in Yaw Resonance	784
<i>Hideki Sakai</i>	
Testing Urban Interaction Scenarios Between Automated Vehicles and Vulnerable Road Users Using a Vehicle-in-The-Loop Test Bench and a Motion Laboratory	791
<i>Michael Kaiser, Lisa Marie Otto, Steffen Müller, André Hartwecker, and Christian Schyr</i>	
Robust Inverse Vehicle Map Regression Based on Laplace Distribution	798
<i>Maxime Penet and Gaetan Le Gall</i>	

Energy-Efficient Optimal Torque Vectoring for a Four-Motor High-Performance Electric Vehicle 804
Mattéo Prost, Ivan Cvok, and Efstathios Velenis

A Lateral Control Based on Physics Informed Neural Networks for Autonomous Vehicles 812
Tamás Hegedűs, Dániel Fényes, Balázs Németh, Vu Van Tan, and Péter Gáspár

Enhancing Electric Vehicle Remaining Range Prediction Through Machine Learning 819
Byunggun Kim and Haeyoun Kim

Fuel Economy Assessment of MPC-ACC on Powertrain Testbed 826
Stefano Favelli, Luis M. Castellanos Molina, Alessandro Mancarella, Omar Mareello, Eugenio Tramacere, Raffaele Manca, Mario Silvagni, Andrea Tonoli, and Nicola Amati

MLIO: Multiple LiDARs and Inertial Odometry 833
Pragyan Dahal, Stefano Arrigoni, Mario Bijelic, and Francesco Braghin

Vehicle State Estimation Through Dynamics Modeled Factor Graph 843
Pragyan Dahal, Stefano Arrigoni, Mario Bijelic, and Francesco Braghin

Nonlinear Model Predictive Control for Enhanced Path Tracking and Autonomous Drifting Through Direct Yaw Moment Control and Rear-Wheel-Steering 854
Gaetano Tavolo, Pietro Stano, Davide Tavernini, Umberto Montanaro, Manuela Tufo, Giovanni Fiengo, Pietro Perlo, and Aldo Sorniotti

Powerslide Control with Deep Reinforcement Learning 862
Florian Jaumann, Tobias Schuster, Michael Unterreiner, Torben Gräber, Johannes Edelmann, and Manfred Plöchl

Simulating Effects of Suspension Damper Degradation on Common Sensor Signals for Diagnosis Models in the Context of Condition-Based Maintenance 869
Lorenz Ott, Torben Gräber, Michael Unterreiner, Johannes Edelmann, and Manfred Plöchl

Controllability of Steer-by-Wire Steering Angle Faults at the Limits of Driving Dynamics 876
Janick Birkemeyer, Lukas Borkowski, Ingo Wülfing, and Steffen Müller

An Automated Lane-Change System Based on Probabilistic Trajectory Prediction Network	883
<i>Yoonyong Ahn, Sangwon Han, Jihoon Sung, Jaeho Choi, and Kunsoo Huh</i>	
Development of Vehicle State Estimation Method for Dedicated Sensor-Less Semi-active Suspension Using AI Technology	890
<i>Yoshifumi Kawasaki, Akai Akihito, and Ryusuke Hirao</i>	
Validation of Control Method to Improve Posture Stability of Narrow Tilting Vehicles Using Real-Vehicle Dynamic Tests	897
<i>Keizo Araki, Jongseong Gwak, and Yoshihiro Suda</i>	
Gradient Correction for Asynchronous Stochastic Gradient Descent in Reinforcement Learning	904
<i>Jiaxin Gao, Yao Lyu, Wenxuan Wang, Yuming Yin, Fei Ma, and Shengbo Eben Li</i>	
Indoor Test-Rig to Measure the Lateral Characteristics of Bicycle Tyres	911
<i>Gabriele Dell'Orto and Giampiero Mastinu</i>	
Driver Behaviour Characterization Using an Instrumented Steering Wheel Conscious/Unconscious Muscle Activation	919
<i>Xabier Carrera Akutain, Francesco Comolli, Massimiliano Gobbi, Giampiero Mastinu, and Giovanni Radaelli</i>	
Interaction Between L4 AVs and Human Drivers in Italian Take-over Scenarios	926
<i>Linda Boscaro, Veronica De Guglielmo, Andrea Fossati, Andrea Galbiati, Massimiliano Gobbi, Gianpiero Mastinu, Giorgio Previati, Edoardo Sabbioni, Maria Gabriella Signorini, Antonella Somma, Luca Subitoni, and Lorenzo Uccello</i>	
A Moving Laboratory for Automotive Components Safety Testing (MoLAS)	933
<i>A. Biffi, F. Ballo, M. Gobbi, and G. Mastinu</i>	
Force Sensors for the Active Safety of Road Vehicles	940
<i>M. Milivinti, M. Amadini, F. Ballo, M. Gobbi, and G. Mastinu</i>	
Design of Explicit and Lateral-Longitudinal Integrated Motion Controller with Safety Guarantee for Autonomous Vehicles	947
<i>Haoyu Gao, Chang Liu, Yingxi Piao, Sen Yang, Beiyan Jiang, and Shengbo Eben Li</i>	

Towards Automated Driving: Findings and Comparison with ADAS	954
<i>Riccardo Donà, Konstantinos Mattas, Giovanni Albano, Sandor Váss, and Biagio Ciuffo</i>	
Stability Issues in Adaptive Cruise Control Systems and Traffic Implication	961
<i>Riccardo Donà, Konstantinos Mattas, Giovanni Albano, Sandor Váss, and Biagio Ciuffo</i>	
The Influence of Transient Tire Force Transmission on Sideslip Angle Estimation	968
<i>Dženana Puščul, Martin Schabauer, and Cornelia Lex</i>	
AI-Based Power Split Strategy for Hybrid Commercial Vehicle Applications	975
<i>Pratheesh Sivaraman Nair, Tomislav Bukic, Dominik Burnner, Georgios Koutroulis, and Milan Zivadinovic</i>	
Risk-Predictive Path Planning in Urban Autonomous Driving: A Geometric Approach to VRU Crossing	982
<i>Yohei Fujinami and Pongsathorn Raksincharoensak</i>	
Author Index	989



Safe Control Allocation of Articulated Heavy Vehicles Using Machine Learning

Sander van Dam^{1,2}, Lukas Wisell^{1,2}, Kartik Shingade^{1,2}, Mikael Kieu¹,
Umur Erdinc^{1,2}(✉), Maliheh Sadeghi Kati¹, Esteban Gelso¹,
and Dhasarathy Parthasarathy¹

¹ Volvo Group Trucks Technology, Gothenburg, Sweden
umur.erdinc@volvo.com

² Chalmers University of Technology, Gothenburg, Sweden

Abstract. As articulated heavy vehicles are over-actuated, achieving a safe control allocation is crucial to ensure stability. This study introduces a machine learning model developed to identify unsafe behaviours and modes, such as jack-knifing and trailer swing, enabling the control scheme to prioritize stability. High-fidelity simulations, focusing on high-risk scenarios, generate data for training the machine learning model. This model is integrated into the control scheme to predict safe braking allocations and prevent unsafe vehicle modes during real-time driving scenarios. Initial tests showed promising results regarding prediction accuracy and a safety margin that can be implemented to further ensure that safe vehicle motion is achieved.

Keywords: Control allocation · articulated heavy vehicles · machine learning · yaw instability

1 Introduction

Articulated heavy vehicles (AHVs) have proven to be excellent candidates for road transportation due to their significant positive impact on environmental and economic efficiency [1, 2]. However, concerns remain regarding their stability, including risks like jackknifing and trailer swing. The electrification of trucks introduced the concept of distributed propulsion across different vehicle units. To maximize power regeneration, braking with the propelled vehicle units and axles is preferred, which might cause instabilities such as jackknifing [3]. Distributed propulsion in AHVs adds another layer of complexity, impacting these vehicles which are already dynamically complex due to over-actuation and their articulation joints. Therefore, achieving a safe control allocation (CA) is crucial to ensure stability while maximizing the regenerated energy [4].

Using machine learning (ML) in the automotive industry is growing as a strong technique, bringing several benefits such as improved safety measures, enhanced vehicle efficiency, and better performance (e.g., [5–7]). To the best of our knowledge, there has been no work done to use ML in the control allocation

of forces in heavy vehicle applications. In this study, ML is applied to heavy vehicle applications to identify unsafe behaviours for a tractor-semitrailer vehicle combination, specifically yaw instabilities. This enables the control scheme to maintain the vehicle within safe operating conditions by requesting safe braking allocation, ensuring no unsafe modes will appear.

2 Machine Learning Model Development

To predict safe allocations, a high-fidelity vehicle model, referred to as Volvo Transport Model (VTM) [8], was used to perform simulations, collecting data on factors contributing to the unsafe behaviour of the tractor-semitrailer vehicle combination. Multiple simulations were performed focusing particularly on high-risk environmental and operational conditions such as low friction and high lateral acceleration on a circular track for different radii.

Approximately 25,000 uniformly random distributed simulations were performed for a range of brake-in-turn manoeuvres, varying parameters such as the initial velocity at which braking begins, friction, radius of the turn, load on the trailer, and braking allocations. The simulation was initialised during steady-state cornering of the vehicle, and data samples were collected until the vehicle either reached a standstill or an unsafe mode occurred. To differentiate between safe and unsafe modes, criteria were checked during the entire simulation on important vehicle states to monitor the state of the vehicle and classify the simulation as safe or unsafe. The criteria used were based on the value of the side-slip angle rate of the vehicle combination, as discussed in [9]. This metric captures whether the truck or trailer exhibits a fast change in yaw angle within a short amount of time, indicating unsafe behaviour in the form of either jack-knifing or trailer swing. The chosen thresholds to limit the side-slip angle rates of the tractor and trailer were set at 6 deg/s. This threshold value was validated with VTM and found to be effective in identifying yaw instabilities.

From these simulations, 20% were used for test data and 80% for training data. Each simulation yielded about 25 data points by sampling the vehicle state throughout the manoeuvre, resulting in around 625,000 data points overall. This extensive dataset was obtained with a total simulation time of about 275 h.

During each simulation, data was collected about the most informative states of the vehicle from a vehicle safety perspective. The selected states were used as features for the ML model, with labels classifying the state as feasible or infeasible. Using this labelled dataset, an ML model could be trained offline to be used as an online prediction tool within the control scheme. The chosen state vector as the features of the ML model included road friction, steering wheel angle, brake force of the tractor, brake force of the trailer, longitudinal velocity, side slip angle of each unit, side slip angle rate of each unit, articulation angle, articulation angle rate and axle loads of each axle, i.e. a total of 17 features. Considering the high dimensional inputs of the problem with these many features, it is too intricate to determine the safe allocation with simple boundaries and any analytical solution. Therefore, ML is a good tool to address this complexity.

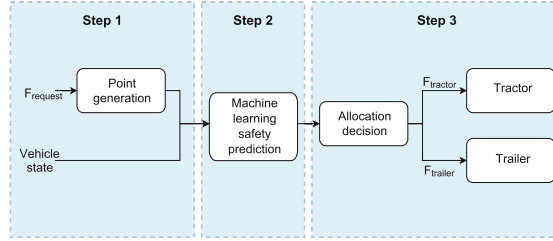


Fig. 1. Control scheme overview

Several ML models were evaluated on the dataset, including decision trees, random forest and neural networks. Among these, neural networks proved to be the most accurate with a training and validation accuracy of around 97%. The models were trained using the MATLAB classification learner app with default values for the hyperparameters not explicitly mentioned in this paper. The chosen model was a neural network consisting of three layers, each with 12 nodes. A higher cost was assigned to false positives since it is crucial for a safety critical system to accurately predict all unsafe points, even if it allows some error in predicting safe points.

3 Machine Learning Based Control Allocation Strategy

The control system is divided into a three-part process, as illustrated in Fig. 1. It begins by reading the vehicle state and brake request from the vehicle. This information is then used to calculate a set of potential braking allocations. The braking request, $F_{request}$, represents the total force request and is divided between the tractor and the trailer as $F_{request} = F_{tractor} + F_{trailer}$. From this set, 100 allocations are uniformly sampled that fulfil the total braking request, as illustrated by the points in Fig. 2a. All forces are normalised and therefore varying between 0 and -1 , where -1 corresponds to the maximum possible braking that each unit can achieve given the current friction, μ . This normalization is expressed as $F^* = F / (F_z \cdot \mu)$ for each unit, where F_z is the unit normal force. These points together with the vehicle state are then inputted to the ML model, which predicts the safety of each allocation, distinguishing between safe (green) and unsafe (red) points as in Fig. 2a. The predictions are performed assuming the driver input to the vehicle is kept constant until standstill. Lastly, a decision is made to select one of these safe allocations, as indicated by an orange circle in the last plot of Fig. 2a.

The decision of which allocation to choose provides considerable flexibility. As the ML model assigns labels to each point, this part becomes modular, allowing for an easily interchangeable strategy without affecting the overall design. This paper will not present any optimal solution to this, instead showing multiple viable options are possible, and that the safety prediction is reliable. For a given state, the predictions are similar to what can be seen in Fig. 2a (steps 2 and

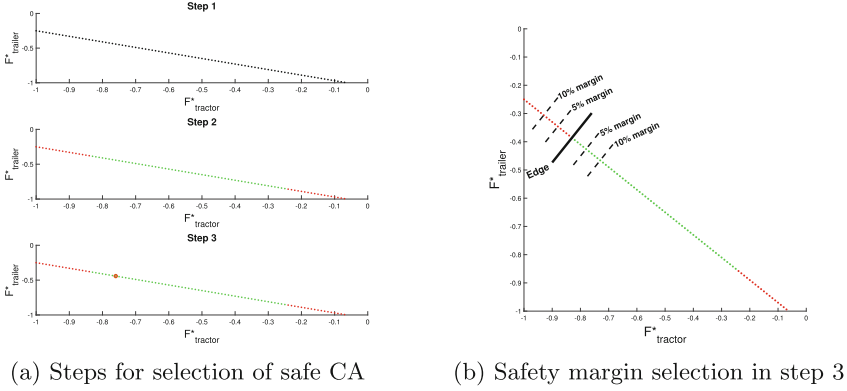


Fig. 2. Illustrations of the control allocation and the implemented safety margins.

3), demonstrating that extreme choices, braking only with the tractor or trailer, are the most unsafe, while intermediate options are safe. This is consistent with findings from previous research [3].

The proposed strategy was tested by picking an allocation that brakes as hard as predicatively possible with the tractor and with some safety margin. This corresponds to, for example, the orange circled point in “step 3” of Fig. 2a. However, when implementing this strategy, the edge can change rapidly due to the changing state of the vehicle. This is unwanted and could lead to unsafe behaviour of the vehicle combination. To accommodate this issue, a low-pass filter was added to the output of the CA. In Fig. 3a, the CA for the tractor is shown in one of these cases. The important observation here is that the CA varies rapidly and discretely. Figure 3a illustrates how the CA appears without a filter, while Fig. 3b shows the same scenario with the filter activated. It can be seen that the filter improves the allocation by eliminating these very fast changes in the CA.

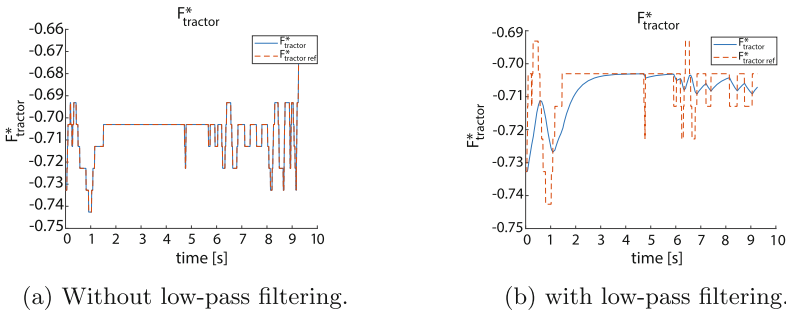


Fig. 3. Illustrations of force allocation for the tractor in the scenario with parameters: $v_x = 43 \text{ kph}$, $\mu = 0.3$, $R = 72 \text{ m}$, $F_{request}^* = -0.6$.

4 Validation of Proposed Control Allocation Strategy

Simulations were conducted to validate these predictions and ensure the controller functions as intended. During these simulations, a safety margin of 5 and 10% of the total amount of sampled allocations was applied around the prediction border, with simulations running on points from both safe and unsafe margins (see Fig. 2b). The safety margin addresses uncertainties and inaccuracies in vehicle parameters, modelling simplifications, etc. Ideally, selecting a safe point should result in a safe simulation, and choosing an allocation predicted as unsafe should lead to an unsafe outcome. Doing this verifies that the estimation of the prediction border is accurate. This was done for a number of test scenarios that were divided into edge and normal cases. Edge cases are defined as scenarios where the vehicle is in an initial state close to where the vehicle can no longer operate without showing unsafe behaviour. Normal cases are further from an unsafe initial state than edge cases which still contain control inputs that can result in unsafe modes.

The system was tested by running 26 cases, 13 normal and 13 edge cases, of the above mentioned cases. Table 1 illustrates the success rate (whether the prediction matches the simulated outcome) for different margins. Throughout the simulations, it was assumed that the tractor is electric with a conventional trailer, prioritizing tractor braking for enhancing energy regeneration. Besides testing with constant steering and perfect knowledge about the state (as during training), the system was also tested with disturbances. An active path-follower, emulating a driver trying to stay on the road (marked by “steering” in Table 1), was introduced. The system was also tested under “wrong friction” conditions, where friction measurement was intentionally increased to simulate a misestimation. During these tests, the steering input was kept constant. Additionally, all other parameters remained the same as the initial test case.

Table 1. Prediction accuracies for different cases (%)

Case	Unsafe 10%	Unsafe 5%	Safe 5%	Safe 10%	Safe 15%	Safe 20%
Normal	100	69.23	92.31	100	100	100
Edge	84.62	61.54	61.54	92.31	100	100
Steering normal	76.92	46.15	84.62	100	100	100
Steering edge	92.31	92.31	92.31	100	100	100
Wrong friction normal	100	100	7.69	53.85	84.62	100
Wrong friction edge	100	100	7.69	15.38	69.23	76.92

The controller accurately predicted safety and responded well, with high accuracy rates, particularly for the normal cases and a slight decrease for edge cases. A margin of 10% from the predicted edge gave results close to 100%, while a 5% margin resulted in accuracy ranging from 60–95%, depending on the cases. The controller and ML model performed well when a path controller was

active during braking, despite all training data being conducted under constant steering conditions.

5 Conclusion

This paper introduces a novel method of predicting the yaw instability in a tractor-semitrailer vehicle combination using machine learning. Additionally, it allocates the driver's brake request to individual vehicle units to avoid such yaw instability. To enhance the overall performance of the controller including ML, different ML models were tested and strategies were developed for allocation. The neural network classification model was found to outperform other models, even when integrated with the controller during random test manoeuvres in real time. The controller proved to be accurate at predicting the safety and responding accordingly. Accuracies were high, especially for the normal cases, but dropped somewhat for edge cases. The controller and ML model worked well when a path controller was active during braking, even though all training data was obtained with constant steering. This paper has shown that it is possible to predict safe allocations using a data-driven ML model, specifically a neural network model.

References

1. Bienkowski, B.N., Walton, C.M.: The economic efficiency of allowing longer combination vehicles in Texas. University of Texas at Austin. Center for Transportation Research, SWUTC/11/476660-00077-1 (2011)
2. Woodrooffe, J., Ash, L.: Economic efficiency of long combination transport vehicles in Alberta: final report. Technical report, Woodrooffe & Associates (2001)
3. Erdinc, U., Jonasson, M., Kati, M.S., Jacobson, B., Fredriksson, J., Laine, L.: Safe operating envelope based on a single-track model for yaw instability avoidance of articulated heavy vehicles. *Veh. Syst. Dyn.* **62**(8), 2138–2161 (2023)
4. Hansson, A., Andersson, E., Laine, L., Kati, M.S., Erdinc, U., Jonasson, M.: Safe operating envelope for limiting actuation of electric trailer in tractor-semitrailer combination. In: 2022 IEEE 25th International Conference on Intelligent Transportation Systems (ITSC), Macau, China, pp. 3886–3893 (2022)
5. Leoni, L., BahooToroody, A., Abaei, M.M., Cantini, A., BahooToroody, F., De Carlo, F.: Machine learning and deep learning for safety applications: investigating the intellectual structure and the temporal evolution. *Saf. Sci.* **170**, 106363 (2024). ISSN 0925-7535
6. Lattanzi, E., Freschi, V.: Machine learning techniques to identify unsafe driving behavior by means of in-vehicle sensor data. *Expert Syst. Appl.* **176**, 114818 (2021). ISSN 0957-4174
7. Norouzi, A., Heidarifar, H., Borhan, H., Shahbakhti, M., Koch, C.R.: Integrating machine learning and model predictive control for automotive applications: a review and future directions. *Eng. Appl. Artif. Intell.* **120**, 105878 (2023). ISSN 0952-1976
8. Fröjd, N.: Handling Analysis and Control Development of Commercial Trucks with Volvo Transport Models. MATLAB EXPO (2021). <https://www.mathworks.com/videos/handling-analysis-and-control-development-of-commercial-trucks-with-volvo-transport-models-1622035211192.html>

9. Fu, R., Zhang, H., Guo, Y., Yang, F., Lu, Y.: Real-time estimation and prediction of lateral stability of coaches: a hybrid approach based on EKF, BPNN, and online autoregressive integrated moving average algorithm. *IET Intell. Transp. Syst.* **14**, 1892–1902 (2020). <https://doi.org/10.1049/iet-its.2020.0385>

Open Access This chapter is licensed under the terms of the Creative Commons Attribution 4.0 International License (<http://creativecommons.org/licenses/by/4.0/>), which permits use, sharing, adaptation, distribution and reproduction in any medium or format, as long as you give appropriate credit to the original author(s) and the source, provide a link to the Creative Commons license and indicate if changes were made.

The images or other third party material in this chapter are included in the chapter's Creative Commons license, unless indicated otherwise in a credit line to the material. If material is not included in the chapter's Creative Commons license and your intended use is not permitted by statutory regulation or exceeds the permitted use, you will need to obtain permission directly from the copyright holder.





Trajectory Tracking for High-Performance Autonomous Vehicles with Real-Time Model Predictive Control

Matteo Pierini^(✉), Paolo Fusco, Rodrigo Senofieni, Matteo Corno, Giulio Panzani, and Sergio Matteo Savaresi

Dipartimento di Elettronica, Informazione e Bioingegneria, Politecnico di Milano,
Via Ponzio 34/5, 20133 Milan, Italy

{matteo.pierini,paolo.fusco,rodrigo.senofieni,matteo.corno,
giulio.panzani,sergio.savaresi}@polimi.it

Abstract. This work is the development of a Model Predictive Controller (MPC) for the integrated control of lateral and longitudinal dynamics of a high-performance autonomous car, which follows a given trajectory on a racetrack. The MPC model is based on an Affine-Force-Input single-track nonlinear bicycle model that accounts for actuation dynamics and delays. The MPC problem is formulated as a quadratic problem, enabling efficient real-time solution with a specific quadratic programming (QP) solver. The controller is implemented in C++ and tested in a real-time hardware-in-the-loop (HIL) simulator, showing excellent tracking performance up to 280 km/h.

Keywords: high-performance autonomous driving · real-time model predictive control · trajectory tracking · vehicle dynamics control

1 Introduction

In recent years, the field of autonomous vehicle technology has expanded into motorsport, with racing competitions like the Indy Autonomous Challenge and the Abu Dhabi Autonomous Racing League demonstrating the capabilities of these vehicles in extreme scenarios and serving as a challenging technology development platform. A critical aspect in the evolution of autonomous vehicles is the control of vehicle dynamics at the limit of handling, especially in high-speed and complex driving conditions that exceed the capabilities of average drivers.

Current literature in vehicle dynamics control predominantly focuses on lateral dynamics due to its significant impact on vehicle stability, particularly for commercial vehicles.

This study has been supported by MOST - Sustainable Mobility National Research Center and received funding from the European Union Next-GenerationEU (PIANO NAZIONALE DI RIPRESA E RESILIENZA (PNRR) - MISSIONE 4 COMPONENTE 2, INVESTIMENTO 1.4 - D.D. 1033 17/06/2022, CN00000023). This manuscript reflects only the authors' views and opinions, neither the European Union nor the European Commission can be considered responsible for them.

Most relevant works [1–3] focus on simple feedforward and feedback steering controllers, which guarantee the tracking of a reference path and the damping of yaw oscillations. For instance, in [1] feedback corrections are applied according to the slip of the wheels, while in [2] the feedback is computed as a desired front steering force and then converted to a steering angle through the inversion of the tire force model. A different approach is followed by [3], which is to impose the tangency of the vehicle sideslip to the reference trajectory.

More advanced lateral controllers are proposed in [4–6], mainly based on optimal control and Model Predictive Control (MPC), devoted to the stabilization of vehicle at the limit of handling and intended for collision avoidance and driver assistance systems. Control algorithms for combined lateral and longitudinal dynamics are presented in [7, 8], addressing the case of high-performance applications. These two studies present a hierarchical control structure with two optimization-based algorithms that addresses both the planning of the trajectory and the control of the vehicle. The higher-level controller computes the optimal path and speed profile, while a lower-level MPC optimizes the actual control actions online over a shorter horizon with a more complex vehicle model.

In this paper, an MPC controller for trajectory tracking of high-performance autonomous vehicles is presented. The algorithm is designed for controlling both the lateral and longitudinal dynamics of the vehicle on a racetrack, following a given path and speed profile. These are assumed to be provided by an external planner or available from a precomputed database. The controller is also able to manage actuation dynamics and delays. Finally, the algorithm is implemented in real time and its simulation results are briefly discussed in Sect. 4.

2 Control-Oriented Vehicle Model

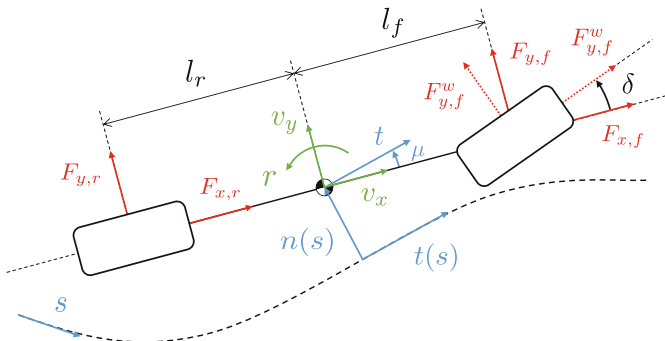


Fig. 1. Force-input bicycle model in Frenet frame.

The vehicle model implemented in the controller must achieve a delicate balance between accuracy and low complexity to ensure the feasibility of real-time solution of the MPC optimization problem.

The chosen model is based on an Affine-Force-Input (AFI) single-track nonlinear bicycle model, inspired by [9]. The inputs of the model (i.e. the outputs of the MPC optimization) are the forces at the wheels, which are used to compute the actual vehicle inputs, as explained in Sect. 3. This method removes the tire force nonlinearities from the vehicle model, thus reducing the complexity of the MPC optimization.

The position of the vehicle is expressed in a Frenet frame centered on the closest point of the reference path, while the velocities are expressed with respect to the vehicle local reference frame, as shown in Fig. 1. The inputs of the model are the longitudinal tire forces $F_{x,f}$, $F_{x,r}$ and the lateral force generated by the front tires $F_{y,f}$.

The final equations of the vehicle model read as

$$\begin{cases} \dot{s} = \frac{1}{1 - nk} [v_x \cos(\mu) - v_y \sin(\mu)], & (1a) \\ \dot{n} = v_x \sin(\mu) + v_y \cos(\mu), & (1b) \\ \dot{\mu} = r - \frac{k}{1 - nk} [v_x \cos(\mu) - v_y \sin(\mu)], & (1c) \\ \dot{v}_x = \frac{1}{M} (Mv_y r + F_{x,f} + F_{x,r} - F_{drag}), & (1d) \\ \dot{v}_y = \frac{1}{M} (-Mv_x r + F_{y,r} + F_{y,f}), & (1e) \\ \dot{r} = \frac{1}{J_z} (-l_r F_{y,r} + l_f F_{y,f}), & (1f) \end{cases}$$

where, the curvature of the path $k(s)$ is available from the knowledge of the reference trajectory. The lateral force on the rear tire $F_{y,r}$ is modeled using Pacejka's Magic Formula [10], while the drag force F_{drag} and the downforce are expressed as quadratic functions of the longitudinal speed.

3 MPC Implementation

The complete architecture of the controller consists of the following components:

- The *input interface* computes the initial conditions of the MPC problem, starting from the global position of the vehicle, the information on the reference trajectory and the last solution of the optimization problem.
- The *Model Predictive Controller* implements the vehicle model presented in Sect. 2, linearized around the operating point of the previous solution, and a first-order approximation of the actuators' dynamics. It computes the optimal inputs which minimize a given cost function, while satisfying a set of constraints.
- The *output interface* converts the optimal control actions computed by the MPC, which are expressed in terms of forces, into real vehicle inputs that can be actuated on the car, i.e. throttle, brake and steer commands. This is achieved by inverting the engine map, the brake characteristics and the nonlinear tire model, respectively.

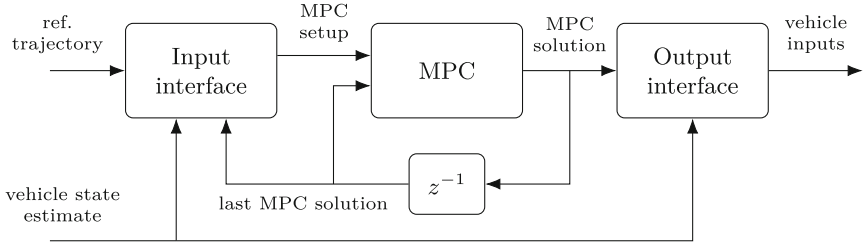


Fig. 2. Overall architecture of the controller.

3.1 Actuation Delays Compensation

The MPC implements a delay-free first-order approximation of the actuators' dynamics. However, the actuators may also present not negligible time delays. To account for them, a simple compensator is implemented as follows.

Let τ be the actuation time delay. At every iteration of the controller, instead of initializing the MPC problem with the measured state $x(t)$, the initial state is set to $\hat{x}(t + \tau)$, which is obtained with an open loop integration of the nonlinear model described by Eqs. (1a)–(1f), from the measured state $x(t)$. Hence, the first element of the resulting MPC optimal solution contains the actuator reference signals that compensate for time delays.

3.2 MPC Optimization Problem

The MPC optimization is formulated as a separable multistage quadratic problem, where the optimization variables are a set of N vectors, each one corresponding to a single time step in the prediction horizon.

$$\min_{z_1, \dots, z_N} \sum_{k=1}^N \frac{1}{2} z_k^T H_k z_k + f_k^T z_k \quad (2)$$

Each component of the sum involves quadratic penalties on the lateral error, the lateral error derivative and the control action variations, while a negative linear term maximizes the vehicle speed.

Maximum values for the lateral error and the input forces are imposed through lower and upper bound constraints. The adherence of the state variables to the model dynamics and the maximum absolute speed are represented by nonlinear constraints, which are linearized around the predicted operating points of the last MPC solution and implemented as linear inequalities.

4 Real-Time Simulation Results

The presented controller is implemented in C++, using OSQP [11] as the solver for the optimization problem, and tested within a real-time hardware-in-the-loop (HIL) simulator, conducting autonomous laps around various racetracks,

adhering to a predetermined racing line and speed profile. The simulated vehicle is a Dallara AV-21, a 470-horsepower autonomous racecar derived from the single-seater Dallara IL-15, designed for the Indy Lights championship. Its most relevant geometric parameters are reported in Table 1.

Table 1. AV-21 parameters.

Parameter	Symbol	Value
Total mass	M	780 kg
Yaw inertia	J_z	1170 kg m ²
Front axle distance from COG	l_f	1.65 m
Rear axle distance from COG	l_r	1.35 m

The real-time implementation of the algorithm enables its execution on a standard high-end Linux laptop with a 6-core 2.2 GHz CPU and 16 GB of RAM. The computation time during the simulations is always below 40 ms, allowing a prescribed execution rate of 25 Hz, with $N = 30$ steps in the prediction horizon. As in Fig. 3, the results of the simulations at the Monza Circuit show excellent tracking performance, achieving less than 0.6 m of lateral error, while reaching speeds up to 280 km/h and lateral accelerations up to 1.7 g.

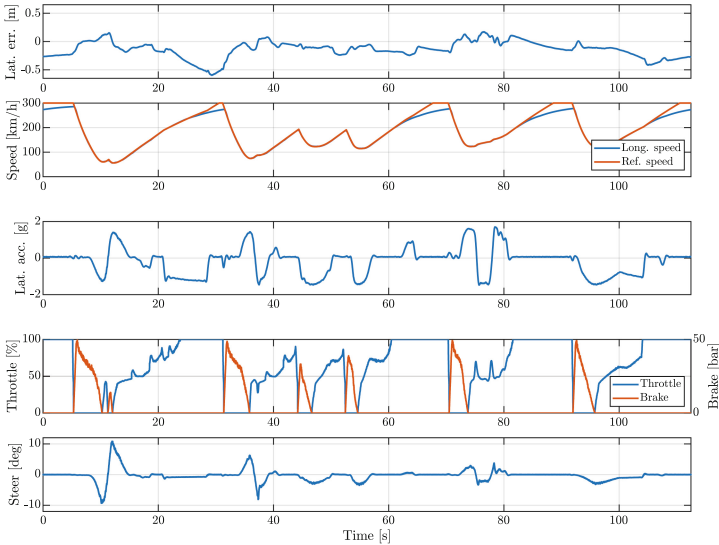


Fig. 3. Lateral and longitudinal tracking performance, lateral acceleration and actuators usage during a HIL simulation at the Monza Circuit.

5 Conclusions

This paper presents a MPC controller for the integrated control of lateral and longitudinal dynamics of a high-performance autonomous vehicle. The accuracy of the vehicle model allows to achieve excellent results in a realistic simulation environment, even in demanding scenarios such as driving at the limit of handling. Also, the feasibility of a real-time implementation is demonstrated by the low execution time of the algorithm on standard hardware. Future work will focus on the experimental validation of the controller on a real-world setup.

References

1. Kritayakirana, K., Christian Gerdes, J.: Autonomous vehicle control at the limits of handling. *Int. J. Veh. Auton. Syst.* **10**(4), 271–296 (2012)
2. Kritayakirana, K., Christian Gerdes, J.: Using the centre of percussion to design a steering controller for an autonomous race car. *Veh. Syst. Dyn.* **50**(Suppl. 1), 33–51 (2012)
3. Kapania, N.R., Christian Gerdes, J.: Design of a feedback-feedforward steering controller for accurate path tracking and stability at the limits of handling. *Veh. Syst. Dyn.* **53**(12), 1687–1704 (2015)
4. Beal, C.E., Christian Gerdes, J.: Model predictive control for vehicle stabilization at the limits of handling. *IEEE Trans. Control Syst. Technol.* **21**(4), 1258–1269 (2013)
5. Katriniok, A., Abel, D.: LTV-MPC approach for lateral vehicle guidance by front steering at the limits of vehicle dynamics. In: 2011 50th IEEE Conference on Decision and Control and European Control Conference, pp. 6828–6833 (2011)
6. Siampis, E., Velenis, E., Gariuolo, S., Longo, S.: A real-time nonlinear model predictive control strategy for stabilization of an electric vehicle at the limits of handling. *IEEE Trans. Control Syst. Technol.* **26**(6), 1982–1994 (2018)
7. Novi, T., Liniger, A., Capitani, R., Annicchiarico, C.: Real-time control for at-limit handling driving on a predefined path. *Veh. Syst. Dyn.* **58**(7), 1007–1036 (2019)
8. Vázquez, J., Brühlmeier, M., Liniger, A., Rupenyan, A., Lygeros, J.: Optimization-based hierarchical motion planning for autonomous racing. In: 2020 IEEE/RSJ International Conference on Intelligent Robots and Systems (IROS), pp. 2397–2403 (2020)
9. Beal, C.E., Christian Gerdes, J.: A method for incorporating nonlinear tire behavior into model predictive control for vehicle stability. In: *Dynamic Systems and Control Conference*, vol. 1, pp. 157–164 (2010)
10. Pacejka, H.: *Tire and Vehicle Dynamics*. Butterworth-Heinemann (2012)
11. Stellato, B., Banjac, G., Goulart, P., Bemporad, A., Boyd, S.: OSQP: an operator splitting solver for quadratic programs. *Math. Program. Comput.* **12**(4), 637–672 (2020)

Open Access This chapter is licensed under the terms of the Creative Commons Attribution 4.0 International License (<http://creativecommons.org/licenses/by/4.0/>), which permits use, sharing, adaptation, distribution and reproduction in any medium or format, as long as you give appropriate credit to the original author(s) and the source, provide a link to the Creative Commons license and indicate if changes were made.

The images or other third party material in this chapter are included in the chapter's Creative Commons license, unless indicated otherwise in a credit line to the material. If material is not included in the chapter's Creative Commons license and your intended use is not permitted by statutory regulation or exceeds the permitted use, you will need to obtain permission directly from the copyright holder.





Study on Linear Actuators for Intake and Exhaust Systems of Internal Combustion Engines (Analytical Consideration of Thrust Characteristics by Permanent Magnet Array)

Jumpei Kuroda^{1,2(✉)}, Kaito Kimura³, Ryutarō Ono³, Ikkei Kobayashi^{1,2}, Daigo Uchino⁴, Kazuki Ogawa⁵, Keigo Ikeda⁶, Ayato Endo⁷, Hideaki Kato⁸, and Takayoshi Narita⁸

¹ Course of Science and Technology, Tokai University, Kanagawa, Japan
3ctad006@mail.u-tokai.ac.jp

² Research Institute of Science and Technology, Tokai University, Kanagawa, Japan

³ Course of Mechanical Engineering, Tokai University, Kanagawa, Japan

⁴ Department of Mechanical Engineering, National Institute of Technology, Numazu College, Shizuoka, Japan

⁵ Department of Electronic Robotics, Aichi University of Technology, Aichi, Japan

⁶ Department of Mechanical Engineering, Hokkaido University of Science, Hokkaido, Japan

⁷ Department of Electrical Engineering, Fukuoka Institute of Technology, Fukuoka, Japan

⁸ Department of Mechanical System Engineering, Tokai University, Kanagawa, Japan
narita@tsc.u-tokai.ac.jp

Abstract. To enhance internal combustion engine performance, this study focuses on developing an electric valve drive system utilizing linear actuators for intake and exhaust valve control. The linear actuator, comprising a movable coil and a fixed permanent magnet, operates based on the principle of the Lorentz force. Unlike traditional magnetic circuits, this actuator employs five permanent magnets with different magnetization directions to concentrate the flux on the coil. In this study, multiple models with varying ratios of these permanent magnets were created and analyzed using finite element analysis conducted with the JMAG software to investigate the thrust characteristics during the reciprocating motion of the actuator. The vector plot of the magnetic flux density shows that the magnetic circuit is predominantly composed of permanent magnets. The average thrust at a 10 mm displacement was approximately 107 N in the largest model. Future studies will aim to design actuators with increased thrust capabilities.

Keywords: Linear Actuator · Lorentz Force · Magnetic Circuit · Engine · Intake and Exhaust System · Electromagnetic Field Analysis

1 Introduction

The electrification of automotive powertrains is actively promoted from the perspective of reducing environmental impact. Nevertheless, internal combustion engines are expected to continue to be used, including those utilizing biofuels or hydrogen, and

those incorporated in hybrid vehicles. Therefore, improvements in engine performance are necessary. Furthermore, to improve the aerodynamic performance of the entire vehicle, compactness of the powertrain is increasingly required. However, enhancing performance requires improving the combustion conditions of the engines. The combustion state of an engine is influenced by multiple parameters of the valve-train system. Engine valves operated by cam mechanisms can significantly affect fuel efficiency and power output depending on the operating conditions. To address this issue, variable valve mechanisms have been developed [1–3]. However, conventional variable valve mechanisms face technical challenges in achieving direct control at all engine speeds. Therefore, this study proposes an electromagnetic valve drive system. This system employs a linear actuator to drive the valve, allowing for continuous variations in valve lift and timing. Consequently, the valve control can be optimized according to the engine speed, thereby enhancing the environmental performance of the engine and suppressing backfire in the manifold of hydrogen engines. Other studies have proposed actuators for intake and exhaust systems. However, the seesaw-type electromagnetic valve drive proposed by Fuse et al. has significant issues such as the inclusion of large armatures and springs, leading to increased complexity and mass [4, 5]. Similarly, Okazaki et al. proposed a solenoid method that did not use permanent magnets. However, when coils are used in a stator, electrical resistance increases during high-speed motion, resulting in increased power requirements in high-speed engines [6]. Furthermore, the linear actuator proposed by Uchida et al. controls a valve with stator coils, making it disadvantageous for high-speed motion [7]. Thus, existing linear actuators face challenges related to their increased size, complex structure, and insufficient thrust. In light of these issues, we propose a voice coil motor-type linear actuator utilizing the Lorentz force [8–10]. This actuator simplifies the structure using a coil in the mover and achieves high responsiveness through operation at low AC frequencies. The voice coil motor type is particularly suitable for position control, enabling highly precise operation. The motion of the valve being a short reciprocating movement, the influence of the coil wiring on the movement of the mover is considered minimal. Moreover, a direct-drive system facilitates precise operation. This study focuses on the issues of actuator enlargement and the associated increases in volume and mass that arise when generating the thrust necessary for engine valve operation. Automotive engines face significant spatial constraints, necessitating the use of small actuators to drive the valves. To address this problem, we aimed to enhance the thrust per unit volume of the actuator at the foundational stage and prototype three models. These models vary the ratio of the permanent magnets within the actuator to examine their impact and evaluate the thrust characteristics through electromagnetic field analysis.

2 Enhancing Thrust Density with Dual Halbach Array

We applied a dual Halbach array to the linear actuator to enhance the thrust per unit volume. Figure 1 shows a schematic of the configuration of a dual Halbach array. This figure depicts the arrangement of the permanent magnets and coils, with the magnetization directions represented as N-S. By placing permanent magnets as shown, a magnetic circuit can be formed solely with permanent magnets, avoiding the generation of large

external magnetic fields. This configuration reduces the yoke volume required for the magnetic circuit formation, thereby decreasing the overall volume of the actuator. Previous studies conducted electromagnetic field analyses on models with dual Halbach arrays using three-dimensional computer-aided design software to investigate the magnetic field and thrust characteristics. The magnetic flux generated by the permanent magnets did not sufficiently intersect the coils orthogonally, resulting in a thrust of approximately 48.8 N, thereby limiting the performance of the actuator to low engine speed operations [11]. To address this, we developed three new models, maintaining the same external dimensions as the previous model (100 mm in diameter and 100 mm in height), but varying the ratio of the permanent magnets. Figure 2 shows a schematic of the newly prototype linear actuator. These actuators consist of permanent magnets and coils, with the coils serving as the mover and the permanent magnets serving as the stator. When electric current passes through the coils, the Lorentz force drives the coils in the axial direction, as indicated in the figure. Five permanent magnets magnetized in the same direction but with different orientations were arranged to concentrate the magnetic flux on the coils. Figure 3 shows a cross-sectional view of the actuator. As shown, the widths of the permanent magnets on either side of the coil (W_1) and the outermost permanent magnets (W_2) varied. W_2 was reduced from 10 mm to 0 mm in 5 mm increments, with a corresponding increase in W_1 's width. The dimensions for each model are: Model A with W_1 :9.5 mm, W_2 :10 mm; Model B with W_1 :12 mm, W_2 :5 mm; and Model C with W_1 :14.5 mm, W_2 :0 mm. The three models were compared and analyzed. The analytical conditions are listed in Table 1. We used a neodymium-sintered magnet, NMX-S52, for permanent magnets, and the temperature was set at 20 °C. The displacement of the coil (mover) was set to 10 mm, with a displacement of 1 mm every 0.1 s, resulting in one reciprocating motion over 2 s. The coil windings were set at 461 turns to maintain a fill factor below 45%, and the coil resistance was set to 1 Ω with a power supply voltage of 5 V, ensuring a current density below 10 A/mm². We applied 5 V from 0 to 1 s to measure the thrust during the upward movement from 0 to 10 mm, and -5 V from 1.1 to 2 s to evaluate the thrust during the downward movement from 10 to 0 mm. Based on these conditions, we conducted a transient response analysis using the finite element method. We used the electromagnetic field analysis software JMAG to investigate the thrust characteristics during the reciprocating motion of the mover.

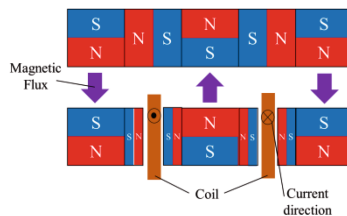


Fig. 1. Dual Halbach array applied to linear actuators.

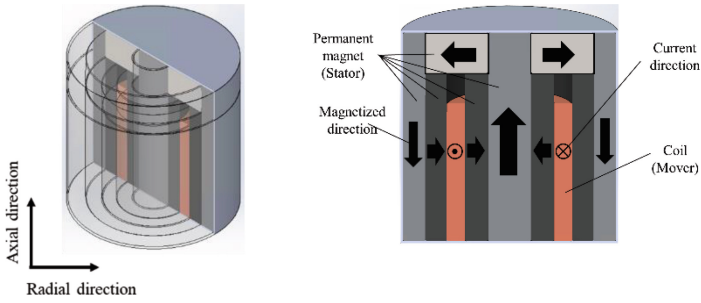


Fig. 2. Schematic of the linear actuator.

Table 1. Analysis conditions.

Parameters	Values
Voltage	5 V
Coil Resistance	1 Ω
Displacement per step	1 mm
Mover displacement	10 mm
Number of coil turns	461
Copper wire diameter	0.8 mm

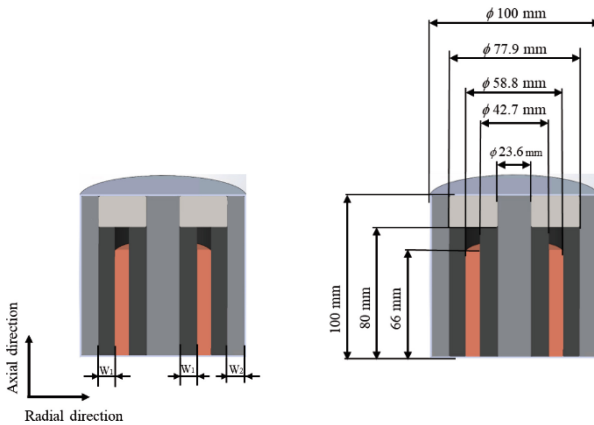


Fig. 3. Linear actuator dimensions

3 Lorentz Force Density and Thrust Analysis Results

The contour plot of the axial Lorentz force density acting on each model’s coil and the vector plot of the magnetic flux density over the entire actuator are shown in Fig. 4. The axial Lorentz force density on the coil increased from model A to model C. Comparing

the magnetic flux near the coil, model A exhibited a predominantly axial flux, whereas model C showed an increase in flux intersecting the coil vertically.

Consequently, the Lorentz force density reveals that while most of the coil in model A experiences a Lorentz force density of $0.5 \times 10^6 \text{ N/mm}^2$, regions indicating a $1.5 \times 10^6 \text{ N/mm}^2$ Lorentz force density increase in models B and C as the magnet ratios change. Figure 5 shows the average thrust of the moving coil for each model, with the vertical axis representing the average thrust and the horizontal axis denoting the model names. The coils, which are the movers in each model, ascend from the 0 mm point to the 10 mm point, stop at the 10 mm point, and then descend back to the 0 mm point. Figure 5 shows the average absolute values of each displacement point during this reciprocating motion. Notably, model A exhibited an average thrust of approximately 68.6 N, while models B and C yielded approximately 84.8 N and 107 N, respectively, indicating a difference of approximately 38.4 N between models A and C. This discrepancy is attributed to the flux density being perpendicular to the current flowing through the coil, resulting in a low Lorentz force density in Model A. By eliminating the permanent magnets at the ends of the dual-Halbach array (as shown in Fig. 1) and increasing the volume of the permanent magnets sandwiching the coil, we achieved an improved thrust per unit volume. At a cam actuation angle of 250° and a displacement of 10 mm, the engine rotational speeds corresponding to the thrust of models A, B, and C were approximately 5987, 6351, and 6838 rpm, respectively. Despite having the same volume, adjusting the permanent magnet ratios resulted in a maximum difference of 851 rpm in the engine rotational speeds each model could accommodate.

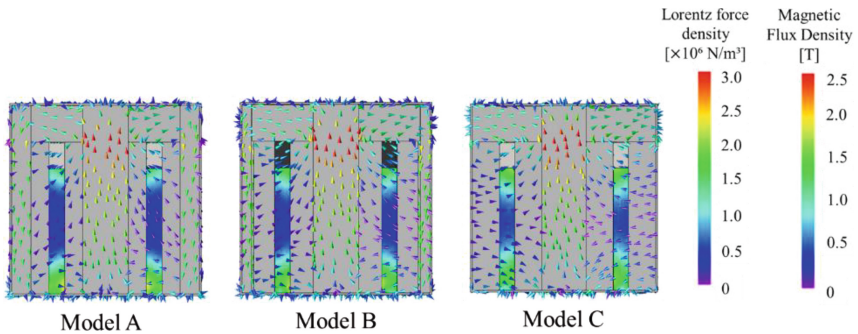


Fig. 4. Plot of Lorentz force density vs. magnetic flux density.

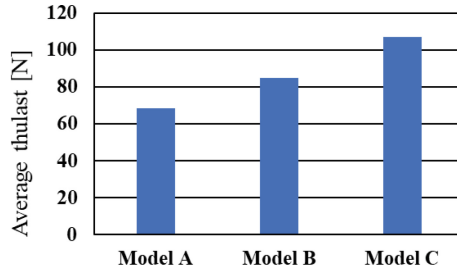


Fig. 5. Average thrust of each model.

4 Conclusion

In this study, we developed three linear actuator models with varying ratios of permanent magnets by applying a dual Halbach array to improve the thrust per unit volume. These models were compared and analyzed using electromagnetic field analysis. The results revealed that reducing the permanent magnets at both ends of the dual Halbach array and increasing the volume of the other permanent magnets effectively enhanced the thrust. Specifically, the maximum thrust was achieved by eliminating the permanent magnets at both ends and increasing the number of permanent magnets at the ends of the coil. Future investigations will focus on further enhancing the thrust by exploring different ratios of permanent magnets. When we are able to prototype a more efficient actuator, we plan to make a detailed comparison with standard valve and cam mechanisms to determine their performance and energy-saving advantages and limitations.

References

1. Fukunaga, S., Kobayashi, M., Murayama, T., Uchida, N.: The effect of variable valve control strategies using a heavy duty diesel engine equipped with 2-stage turbocharging system. *Trans. JSAE* **44**(2), 335–341 (2013)
2. Urata, Y., Kondo, T., Takabayashi, T.: Gasoline engine combustion technology in Honda. *J. Combust. Soc. Jpn.* **60**(191), 18–26 (2018)
3. Takatsuka, T., Hashimoto, M., et al.: Effects of intake valve closure timing on heavy-duty diesel engine performance. *Trans. JSAE* **53**(2), 308–313 (2022)
4. Fuse, H., Okada, Y., Matsuda, K., Konno, M.: Research on electromagnetic valve actuator. *Jpn. Soc. Mech. Eng.* 43–44 (2004)
5. Uno, M., Muraguchi, Y., et al.: Speed-up trial of electromagnetic engine valve. In: *The Proceedings of the Symposium on the Motion and Vibration Control*, vol. 7, no. 13, pp. 177–180 (2007)
6. Okazaki, A., Shibasaki, H., Ishihara, Y., Ogura, M.: Development of small size engine with electric magnetic driving valve for fuel competition vehicle. In: *The Proceedings of Conference of Kanto Branch*, pp. 465–466 (2011)
7. Uchida, M., et al.: Positioning control of linear motor via sliding mode servo control system with variable switching hyperplane. *IEEJ Trans. Electron. Inf. Syst.* **126**(9), 1112–1118 (2006)
8. Sato, Y., Narita, T., Kato, H., Uchida, H.T., Matsumura, Y.: Valve mechanism for gasoline engine with linear motor (fundamental consideration using electromagnetic field analysis). In: *Proceedings of the School of Engineering Tokai University, Series E*, pp. 35–39 (2019)

9. Majima, Y., Kuroda, J., et al.: Performance improvement of gasoline engines using a linear actuator: fundamental consideration of the heat effect on thrust characteristics. In: Proceedings of the School of Engineering Tokai University, Series E, pp. 37–42 (2021)
10. Kuroda, J., Majima, Y., et al.: Electromagnetic valve driven system using linear actuator (fundamental consideration on thrust characteristics). *J. JSAEM* **31**(3), 443–449 (2023)
11. Kuroda, J., et al.: A study on actuator for high-speed linear direct drive (fundamental consideration on concentration of magnetic flux to improve thrust) (2023). PB-1b-15-267297b

Open Access This chapter is licensed under the terms of the Creative Commons Attribution 4.0 International License (<http://creativecommons.org/licenses/by/4.0/>), which permits use, sharing, adaptation, distribution and reproduction in any medium or format, as long as you give appropriate credit to the original author(s) and the source, provide a link to the Creative Commons license and indicate if changes were made.

The images or other third party material in this chapter are included in the chapter's Creative Commons license, unless indicated otherwise in a credit line to the material. If material is not included in the chapter's Creative Commons license and your intended use is not permitted by statutory regulation or exceeds the permitted use, you will need to obtain permission directly from the copyright holder.





Drifting Maneuver Investigation via Phase Plane Analysis of Experimental Data

Giovanni Righetti, Guido Napolitano dell'Annunziata, Flavio Farroni, Matteo Massaro, and Basilio Lenzo^(✉)

Department of Industrial Engineering, University of Padova, Padua, Italy
`basilio.lenzo@unipd.it`

Abstract. This paper presents a comprehensive analysis of experimental data on drifting maneuvers, using vehicle data collected by Stanford University with a professional driver. Vehicle dynamics during drifting, characterised by high sideslip angles and countersteering, are examined. By using a nonlinear single track model with nonlinear tires, this study compares real-car data to simulated models within a phase-plane framework. It also explores the application of saddle-node bifurcation theory to understand the abrupt changes in vehicle behaviour during drifting.

Keywords: vehicle dynamics · drifting · phase-plane · experiments

1 Introduction

The study and analysis of drifting maneuvers gives relevant information about vehicle attitude when negotiating a turn in the nonlinear range of tyre characteristics. Drifting is commonly referred to as an unstable cornering condition, associated to large vehicle sideslip angles and countersteering [1]. Maintaining the control of the car in such situations is very challenging, so that only professional drivers are able to cope and even manage this vehicle behaviour. Among others, the saddle-node bifurcation theory - often applied in nonlinear dynamics and mathematics - is a useful tool to examine the sudden and abrupt changes in vehicle behavior during drifting maneuvers [2].

Several papers deal with vehicle drifting and focus on control strategies to stabilise it [3]. Voser et al. [4] propose a steering controller for autonomously performing high sideslip manoeuvres through a nonlinear single track model-based controller. Stanford University's vehicle dynamics group combines drifting control, path tracking and brake-based speed control [5]. Edelmann et al. [6] develop a driver model able to compute the necessary driver inputs to keep the vehicle in a large sideslip manoeuvre.

This work aims at giving a thorough and exhaustive analysis of experimental data concerning drifting manoeuvres, performed by professional driver Ken Gushi and collected by Stanford University, using the electric DeLorean prototype MARTY [7]. Real-car data are compared to a simple nonlinear single track model, by visualising vehicle states in a phase plane framework. Moreover, the relationship between drift and saddle-node bifurcation phenomenon is discussed.

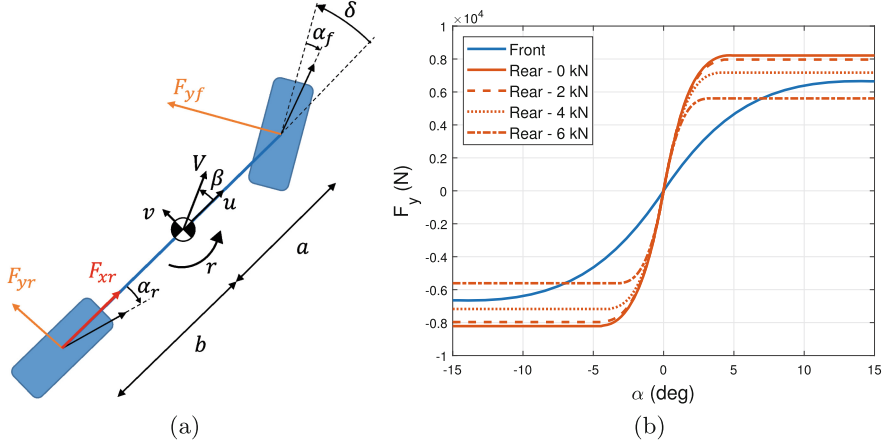


Fig. 1. (a) Schematic of the single track model. β is the vehicle sideslip angle. (b) Axle characteristics, with the rear one depicted for different values of F_{xr} .

Table 1. Main vehicle and tire parameters.

Parameter	Symbol	Value	Parameter	Symbol	Value
Mass	m	1700 kg	Front cornering stiff.	C_{α_f}	75 kN/rad
Yaw moment of inertia	I_{zz}	2385 kg m ²	Rear cornering stiff.	C_{α_r}	275 kN/rad
COG to front axle dist.	a	1.392 m	Front friction coeff.	μ_f	0.95
COG to rear axle dist.	b	1.008 m	Rear friction coeff.	μ_r	0.85

2 Vehicle and Tire Model

Figure 1a shows the used 3-degree-of-freedom (dof) single track model. The vehicle state includes longitudinal velocity, u , lateral velocity, v , yaw rate, r :

$$\dot{u} = \frac{1}{m} [-F_{yf} \sin(\delta) + F_{xr}] + vr \quad (1)$$

$$\dot{v} = \frac{1}{m} [F_{xf} \sin(\delta) + F_{yf} \cos(\delta) + F_{yr}] - ur \quad (2)$$

$$\dot{r} = \frac{1}{I_{zz}} [a(F_{xf} \sin(\delta) + F_{yf} \cos(\delta)) - bF_{yr}] \quad (3)$$

where F_{yf} and F_{yr} are the front and rear lateral forces, F_{xr} is the rear longitudinal force, δ is the steering angle at wheel. Since the experimental vehicle MARTY is rear wheel drive and the driver does not brake, the front longitudinal force $F_{xf} = 0$. Symbols and values of other relevant parameters are in Table 1.

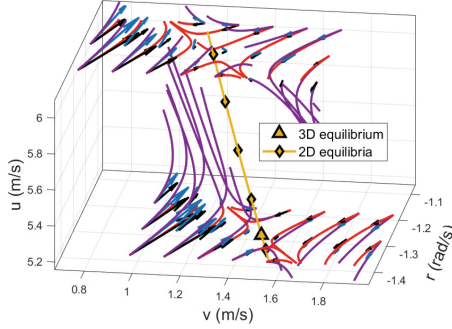


Fig. 2. v - r - u phase portrait. Purple and red curves are trajectories of the 3-dof and 2-dof systems, respectively. Blue and black arrows are vectors tangent to the trajectories of the 3-dof and 2-dof systems. Yellow diamonds are unstable equilibria for the 2-dof system, for various u . The yellow triangle is an unstable equilibrium of the 3-dof system.

Lateral forces are modelled using the slip Fiala tire model. For a generic tire:

$$\begin{cases} F_y = C_\alpha \tan \alpha - \frac{C_\alpha^2}{3F_{y,\max}} |\tan \alpha| \tan \alpha + \frac{C_\alpha^3}{27F_{y,\max}^2} \tan^3 \alpha, & |\alpha| \leq \alpha_s \\ F_y = F_{y,\max} \text{sgn}(\alpha), & \text{otherwise} \end{cases} \quad (4)$$

where C_α is the axle cornering stiffness and $F_{y,\max}$ is the maximum available axle lateral force, calculated using the friction circle theory:

$$F_{y,\max} = \sqrt{(\mu F_z)^2 - F_x^2} \quad (5)$$

where F_z is the vertical load and μ the friction coefficient. Kinematic equations define front and rear tire slip angles $\alpha_f = \delta - \arctan\left(\frac{v+ar}{u}\right)$, $\alpha_r = -\arctan\left(\frac{v-br}{u}\right)$, while α_s is the maximum slip angle beyond which the tire starts to slide: $\alpha_s = \arctan\left(\frac{3F_{y,\max}}{C_\alpha}\right)$. The axle characteristics are shown in Figure 1b.

3 Phase Plane and Space Representation

The dynamics of the vehicle model may be effectively represented via three-dimensional u - v - r phase portrait. The derivatives of the state variables are computed point-wise from equations of motion (1) (2) and (3). Hence, for each point (u_0, v_0, r_0) a vector \mathbf{t} composed by the three state derivatives is associated, $\mathbf{t} = \dot{v} \hat{\mathbf{v}} + \dot{r} \hat{\mathbf{r}} + \dot{u} \hat{\mathbf{u}}$, where $\hat{\mathbf{v}}$, $\hat{\mathbf{r}}$ and $\hat{\mathbf{u}}$ are the unit vectors of the three axes of the graph. \mathbf{t} defines the direction of vehicle state's time evolution. The same may be done for the 2-dof case, obtaining a 2-dimensional vector \mathbf{t}_2 defined by \dot{v} and \dot{r} for a given u . Since in both 2 and 3-dof systems \dot{v} and \dot{r} are computed by solving equations (2) and (3), the projections of 3D vectors \mathbf{t} on a $v-r$ plane coincide with the directions of 2D vectors \mathbf{t}_2 . This is in line with the results in [8]. In this work equilibrium *curves* may be distinguished in a $v-r-u$ phase

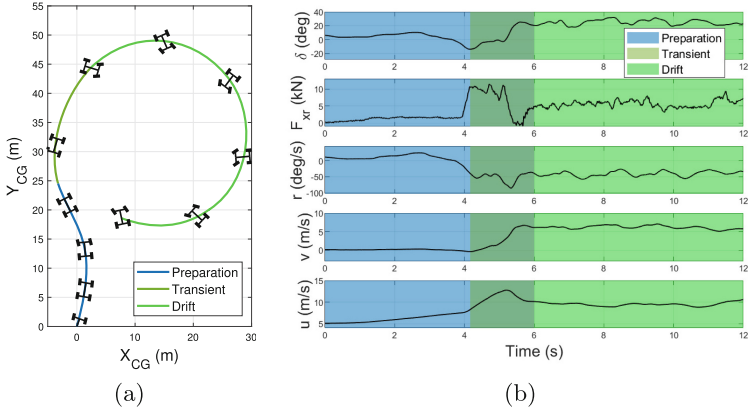


Fig. 3. (a) Trajectory and wheel orientation; (b) Time history.

space, Fig. 2, which are composed by the equilibrium *points* of $v-r$ phase planes computed at every vehicle speed (for fixed driver inputs). One relevant consequence is that equilibria of the 3-dof system are located on equilibrium curves, since they are constrained by the same lateral and yawing motion equations. Moreover, even if 2D equilibria cannot be classified as equilibria of the 3-dof system as well, \dot{v} and \dot{r} are zero in correspondence of equilibrium curves, and 2D and 3D trajectories behave similarly in their neighborhood.

On this basis, both 3D and 2D portraits are exploited for analysing experimental data and relate actual vehicle states to the studied vehicle model.

4 Experimental Data and Drift Phases

For space constraints, a single representative manoeuvre is analyzed. Figure 3 shows the vehicle path and the orientation of the wheels, along with relevant data. Graphs are split in 3 phases: *preparation*, *transient* and *drift*. As soon as the driver countersteers (end of the *preparation* phase) vehicle states evolve (*transient*) to reach the condition of a (quasi) steady-state manoeuvre (*drift*), with large β , steering angle oscillating around 25 deg and longitudinal force around 5.6 kN. It is interesting to note that: i) while the steering angle changes, the sign of the yaw rate does not; ii) both lateral velocity and yaw rate are kept almost constant by the driver, justifying the hypothesis of (quasi) steady-state; iii) the longitudinal velocity is also almost constant, even though, as discussed in previous section, that is not strictly required to drift.

5 Drift Equilibrium Analysis

Figure 4a presents the actual vehicle state in a 3D phase space fashion. It is compared to saddle equilibria of the 2D system, computed for steering angle

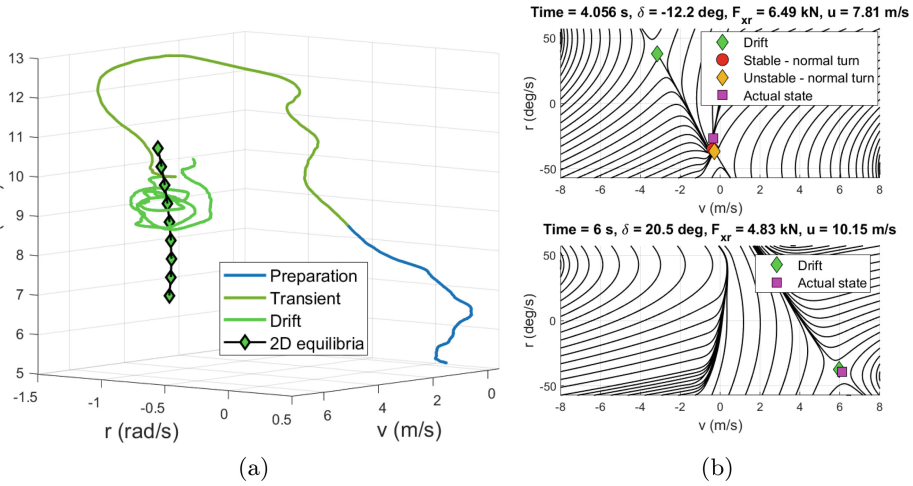


Fig. 4. (a) 3D portrait of the actual vehicle state evolution; (b) v - r phase plane (top) just before saddle-node bifurcation and (bottom) at the beginning of controlled drift.

and rear traction force equal to their mean values in the drift phase. It can be appreciated that the driver actively controls the vehicle stability and, in doing so, he keeps the vehicle in the neighborhood of the black curve. Figure 4b compares the phase plane of the system just before bifurcation [1] (4.056 s, three equilibria) and at the beginning of the controlled drift (6.000 s, only one equilibrium). The actual state of the vehicle is close to the stable-normal turn equilibrium [1] in the preparation phase, while it gradually moves toward drift after bifurcation.

Figure 5 shows that the time instant of bifurcation and the one the driver countersteers are very close, endorsing the goodness of the nonlinear single track model. When the steering rate changes sign (beginning of the transient), the driver has quickly brought rear traction to the limit, and he then maintains it for a while. This is probably done by the driver to maximise the yaw moment resulting on the vehicle, favouring the entrance in a drifting condition (with pretty much all the grip used longitudinally, equation (5) is ≈ 0). The procedure followed by the driver in the transient is then dictated by the need to stabilise the vehicle and it has a similar pattern to the one described in [9].

Another relevant insight is that yaw rate of the controlled drift is comparable to the one at the beginning of transient. Since it is a quasi-steady-state condition, the manoeuvre can be classified as an almost constant radius one. An important application of this would be autonomous drifting, where a vehicle is asked to carry out a turn of predetermined cornering radius, or the implementation of drift as a strategy to minimise lap-time (e.g. in Rally).

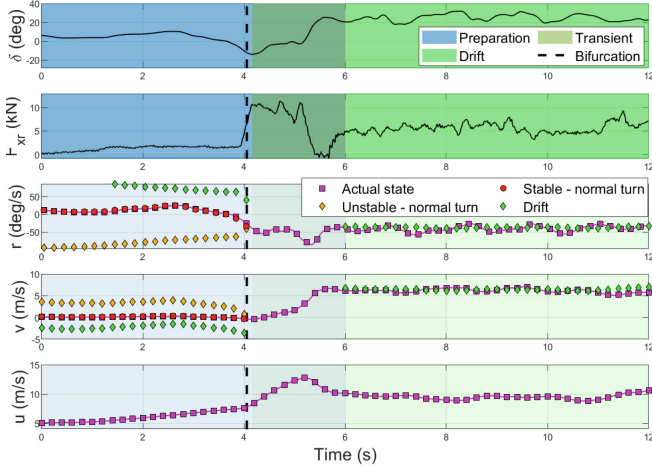


Fig. 5. Analysis of the drifting procedure. v and r are compared to 2D equilibria at each time instant with the nomenclature in [1], note the trends before/after bifurcation.

6 Conclusion

The paper provided a comprehensive understanding of the dynamics involved in vehicle drifting manoeuvres, emphasizing the critical role of saddle-node bifurcation theory in interpreting these complex scenarios. The proposed analysis, grounded in both experimental data and simple yet insightful models, highlights the intricate interplay between vehicle control, tire dynamics, and driver inputs during drifting. This could lead to innovations in vehicle safety and performance.

References

1. Righetti, G., Binetti, E., de Castro, R.P., Lot, R., Massaro, M., Lenzo, B.: On the investigation of car steady-state cornering equilibria and drifting. Technical report, SAE Technical Paper (2024)
2. Rossa, F.D., Mastinu, G., Piccardi, C.: Bifurcation analysis of an automobile model negotiating a curve. *Veh. Syst. Dyn.* **50**(10), 1539–1562 (2012)
3. Velenis, E., Frazzoli, E., Tsiotras, P.: On steady-state cornering equilibria for wheeled vehicles with drift. In: Proceedings of the 48th IEEE Conference on Decision and Control (CDC) held jointly with 2009 28th Chinese Control Conference, pp. 3545–3550. IEEE (2009)
4. Voser, C., Hindiyeh, R.Y., Gerdes, J.C.: Analysis and control of high sideslip manoeuvres. *Veh. Syst. Dyn.* **48**(S1), 317–336 (2010)
5. Goel, T.: In Complete Control Simultaneous Path Speed and Sideslip Angle Control of a Drifting Automobile. PhD thesis, Stanford University (2022)
6. Edelmann, J., Plöchl, M., Pfeffer, P.: Analysis of steady-state vehicle handling and driver behaviour at extreme driving conditions. na (2011)

7. Goh, J.Y., Gerdes, J.C.: Simultaneous stabilization and tracking of basic automobile drifting trajectories. In: 2016 IEEE Intelligent Vehicles Symposium (IV), pp. 597–602. IEEE (2016)
8. Beal, C.E., Boyd, C.: Coupled lateral-longitudinal vehicle dynamics and control design with three-dimensional state portraits. *Veh. Syst. Dyn.* **57**(2), 286–313 (2019)
9. Vignati, M., Sabbioni, E., Cheli, F.: A torque vectoring control for enhancing vehicle performance in drifting. *Electronics* **7**(12), 394 (2018)

Open Access This chapter is licensed under the terms of the Creative Commons Attribution 4.0 International License (<http://creativecommons.org/licenses/by/4.0/>), which permits use, sharing, adaptation, distribution and reproduction in any medium or format, as long as you give appropriate credit to the original author(s) and the source, provide a link to the Creative Commons license and indicate if changes were made.

The images or other third party material in this chapter are included in the chapter's Creative Commons license, unless indicated otherwise in a credit line to the material. If material is not included in the chapter's Creative Commons license and your intended use is not permitted by statutory regulation or exceeds the permitted use, you will need to obtain permission directly from the copyright holder.





Effects of External Tire Heating on Rolling Resistance Energy Consumption

Mikael Askerdal^{1,2} , Fredrik Bruzelius³ , and Jonas Fredriksson² 

¹ Department of Vehicle Motion and Thermal Management, AB Volvo, Gothenburg, Sweden

mikael.askerdal@volvo.com

² Department of Electrical Engineering, Chalmers University of Technology, Gothenburg, Sweden

³ Department of Mechanics and Maritime Sciences, Chalmers University of Technology, Gothenburg, Sweden

Abstract. It is known that the rolling resistance decreases with increasing tire temperature. If the tires could be heated to a high temperature, the rolling resistance's energy loss could be reduced. The question arises whether the reduced rolling resistance energy consumption overcomes the energy required to heat the tire.

This paper investigates the effects of external heating and improved tire insulation theoretically. The results indicate that external tire heating can be beneficial only if the heat used is waste heat, generated from a heat pump or similar with a coefficient of performance greater than one or taken from the grid.

Keywords: Rolling resistance · Tire temperature · Modeling

1 Introduction

Rolling resistance is impacted by the tire temperature mainly through the hysteresis losses that occur during the repeated compression-decompression of the rubber in a rolling tire. This loss energy will end up as heat in the tire. As the tire's temperature increases, the rolling resistance decreases. Rolling resistance is defined as the amount of mechanical energy converted into tire heat for a unit distance, according to [1]. From a tire perspective, this is a convenient definition since tire temperature can be measured and easily quantified. However, from a vehicle energy consumption perspective, this definition is not always adequate since there exist more energy losses related to a rolling vehicle, such as displacement of snow or water on the road, compression of soft road surfaces, and losses in suspension due to road unevenness.

This paper investigates the impact of tire temperature on rolling resistance in general and the potential energy consumption gains from external tire heating in

Supported by the Swedish FFI program in the project UFEEL ref. nr P2022-00948.

© The Author(s) 2024

G. Mastinu et al. (Eds.): AVEC 2024, LNME, pp. 29–35, 2024.

https://doi.org/10.1007/978-3-031-70392-8_5

particular. To analyze the effect on rolling resistance energy consumption from tire heating, a dynamic model is needed. Nielsen et al., [2], has developed such a model for the rolling resistance. This model uses a function of the tire temperature and a deviation between the current vehicle speed and a steady-state vehicle speed to determine the rolling resistance. The tire temperature is dynamically modeled, with the change rate being linear in the deviation between the current temperature and a steady-state temperature. From [2], it can be deduced that tire temperature is a key parameter for determining rolling resistance. Another interesting finding by [3] is that the shoulder temperature in steady state is close to the inflated air temperature within the tire. In [2], where their model is shown to perform well for tests a given truck in given conditions. This fact is used to motivate only one lumped state to describe the tire temperature. This radically simplifies the model. Furthermore, in [4, 5], a relation between rolling resistance and tire temperature is established. However, there are no attempts to investigate if external heating of tires would be beneficial.

The main scope of this paper is to use a simplified dynamic tire temperature and rolling resistance model to investigate the impact of external tire heating and if pre-heating of truck tires can be used to extend vehicle driving range. The rolling resistance models are based on the works of [2, 4], and the definition of rolling resistance from [1] is used.

2 Method

2.1 Effects from Tire Heating on Rolling Resistance

The hysteresis loss of a tire, the main contributor to rolling resistance, is highly dependent on the tire temperature. In [4], the rolling resistance coefficient, C_{rr} , is described as being an exponential function of the tire temperature, T_t . The dependency on the vehicle speed, v_v , is described as a shift in T_t while the dependencies on other parameters like tire pressure, P_t , road surface roughness, r_r , and tire wear, W_t , are not explicitly described. In our work, C_{rr} is modeled in the same way, i.e.:

$$C_{rr}(T_t) = c_0 + c_1 e^{-\frac{T_t + \Delta T_t(v_v)}{c_2}}, \quad (1)$$

where c_0, c_1 and c_2 are constant coefficients and

$$\Delta T_t(v) = T_h + (T_0 - T_h) \left(2 - \frac{2}{1 + e^{-c_3 v_v}} \right), \quad (2)$$

describes the shift in T_t as a function of v_v , where c_3 is a constant coefficient, T_h the tire temperature shift at infinite vehicle speed, and T_0 the tire temperature shift at zero vehicle speed.

With the chosen definition of rolling resistance, [1], the tire heat power generated by the rolling resistance, P_{rr} , at time t can be described by:

$$P_{rr}(t) = F_z C_{rr}(t) v_v(t), \quad (3)$$

where F_z is the total normal force of all tires, and v_v is the vehicle speed. Since this is the total tire heat generated from the rolling resistance, a dynamic temperature model (similar to [2]) can be developed according to:

$$\frac{dT_t}{dt} = \frac{P_{rr}(t) - P_{diss}(t) + P_{ext}(t)}{m_t c_t}, \quad (4)$$

where P_{diss} is the heat dissipation from the tire to the ambient air, road surface, and rim, m_t is the tire's mass, c_t the heat-specific capacity of the tire material, and P_{ext} is externally added heat power.

Assuming that the rim, the road surface, and the ambient air all have the same temperature, T_a , the heat dissipation can be described as:

$$P_{diss} = c_d(T_t(t) - T_a(t)), \quad (5)$$

where c_d is a coefficient determining the total heat dissipation of the tire.

2.2 Tire Temperature and Rolling Resistance Coefficient over Time

Equations (3), (4) and (5) can be used together with the current tire temperature, $T_t(0)$, to predict the tire temperature going forward, $T_t(t)$:

$$T_t(t) = T_t(0) + \int_0^t \frac{P_{rrh}(\tau) - P_{diss}(\tau) + P_{ext}(\tau)}{m_t c_t} d\tau \quad (6)$$

A possible way of solving (6) is to discretize the problem into N , sufficiently small steps, which gives:

$$T_{t,0} = T_t(0), \quad (7a)$$

$$T_{t,N} = T_t(t), \quad (7b)$$

$$t_s = \frac{t}{N}, \quad (7c)$$

$$T_{t,i+1} = T_{t,i} + t_s \frac{P_{rr}(T_{t,i}) - P_{diss}(T_{t,i}) + P_{ext}(\tau)}{m_t c_t}, \quad (7d)$$

$$T_{t,N} = T_{t,0} + \sum_{i=0}^N t_s \frac{P_{rr}(T_{t,i}) - P_{diss}(T_{t,i}) + P_{ext}(\tau)}{m_t c_t}. \quad (7e)$$

Equation (7) can now be used in a forward simulation to predict $T_t(t)$. By inserting $T_t(t)$ into (1), $C_{rr}(t)$ is given which is needed to compute the next value of $P_{rr}(T_{t,i})$. The parameter values used for the rolling resistance coefficients are taken from [4]. All parameter values are given in Table 1.

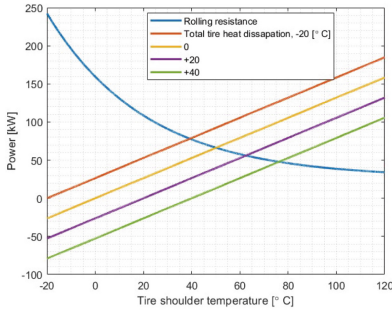
Table 1. Parameter values

Parameter	Value	Parameter	Value	Parameter	Value
c_0	3.09 [kg/ton]	c_1	15.21 [kg/ton]	c_2	0.0243 [$^{\circ}\text{C}^{-1}$]
c_3	0.0232 [h/km]	T_0	69.2 [$^{\circ}\text{C}$]	T_h	-25.7 [$^{\circ}\text{C}$]
m	40000 [kg]	g	9.81 [N/kg]	m_t	600 [kg]
c_t	1880 [$\text{J}/(\text{kg}^{\circ}\text{C})$]	c_d	1320 [$\text{W}/^{\circ}\text{C}$]		

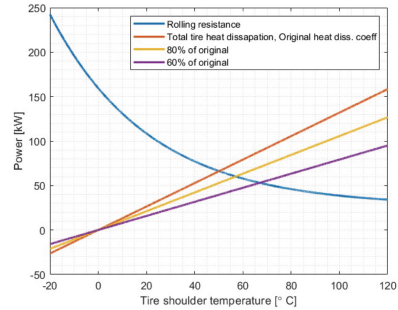
3 Results

In Fig. 1a, the rolling resistance power, $P_{rr}(T_t)$ is plotted towards T_t using Eq. 1 when running in 80 km/h together with heat dissipation power curves for four different ambient temperatures. The crossings between the P_{rr} curve and the heat dissipation curves give the steady-state rolling resistance power and steady-state T_t . This shows that one of the main reasons why rolling resistance tends to increase when the ambient temperature is decreased is that the tires will be colder.

In Fig. 1b, the effect on steady-state rolling resistance from different c_d is shown. It should be noted that a lower c_d gives lower steady-state rolling resistance. This means that running on road material with low heat conductivity, like packed snow, may give lower rolling resistance than running on road material with high heat conductivity. It also means that if tires can be heat insulated, it is likely to result in a significant reduction in P_{rr} .



(a) Rolling resistance and heat dissipation power in different ambient temperatures.



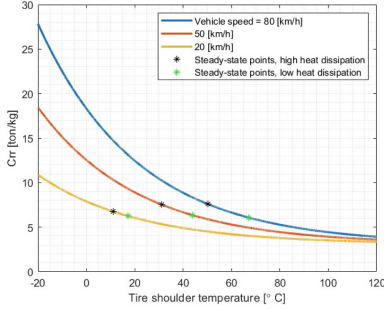
(b) Rolling resistance and heat dissipation power for different heat dissipation coefficients

Fig. 1. Rolling resistance and heat dissipation power.

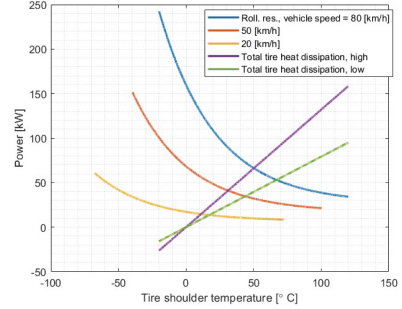
The vehicle speed dependency in the used model is described as a shift in tire temperature. Figure 2a illustrates how C_{rr} is changing with tire shoulder temperature for three different vehicle speeds. The black stars denote steady-state points when c_d is high, and the green stars do the same thing but when

c_d is low. The speed dependency of rolling resistance in steady-state seems to decrease with decreasing c_d .

In Fig. 2b, C_{rr} as function of T_t is plotted for three different values of v_v together with heat dissipation curves for high and low values of c_p . The dependency on T_t for P_{rr} is reduced with v_v which also means that the impact from c_d on steady-state rolling resistance increases with v_v .



(a) C_{rr} dependency on tire shoulder temperature and vehicle speed



(b) Rolling resistance power for different vehicle speeds

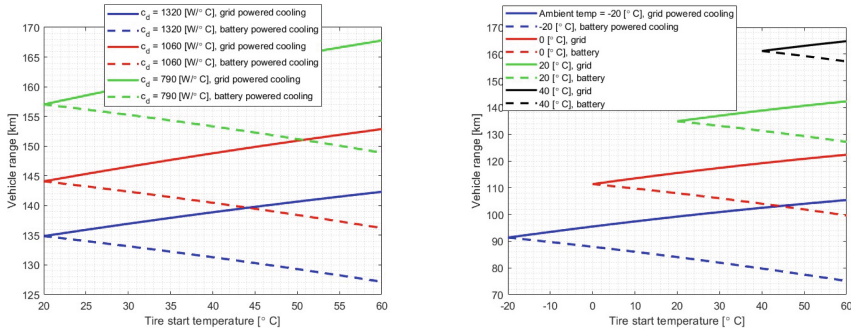
Fig. 2. C_{rr} and rolling resistance power at different vehicle speeds

The total vehicle range is affected by the tire temperature at the start of a trip. If assuming that the vehicle has a total of 100 kWh of battery capacity that is dedicated to rolling resistance energy consumption, the vehicle range can be computed from forward simulations of the rolling resistance energy consumption from (6). In Fig. 3a, the vehicle range for different initial tire temperatures are plotted for three different c_d at $T_a = 20^\circ\text{C}$. The solid lines denote the gross effect of tire heating, i.e., the range if the tires are pre-heated using grid energy. The dashed lines denote the net effect, i.e., if the tires are heated using battery energy of the vehicle. As can be seen, vehicle range is always benefiting from pre-heating from the grid. The effect is, however, not so large that it overcomes the loss in the range from using battery energy for the tire heating, which can be seen from the fact that the range for the net curves decreases with tire start temperature. This figure also shows that vehicle range is highly affected by c_d .

In Fig. 3b, the effect of tire heating at different ambient temperatures is illustrated. The lines are almost parallel, which means that tire pre-heating is likely to be as effective independently of ambient temperature. However, the curves are not completely linear. The vehicle range is growing slightly slower than linear in tire start temperature which means that tire pre-heating will be a little bit less effective for each degree T_t is increased.

4 Discussion and Conclusions

Overall, the benefit of adding external tire heat in terms of decreased rolling resistance energy will always be positive since rolling resistance energy con-



(a) Vehicle range with different heat dissipation coefficients and different initial tire temperatures. (b) Vehicle range in different ambient temperatures and different initial tire temperatures.

Fig. 3. Vehicle range dependency on initial tire temperature

sumption decreases monotonically with tire temperature. However, the gain in decreased rolling resistance energy consumption from external heating will always be smaller than the amount of external heat needed since some of the external heat will be dissipated to the surroundings. This means that external tire heating will never be beneficial unless the energy used comes from waste heat or is generated from a heat pump with a coefficient of performance greater than one. Tire pre-heating may still be a good idea when the vehicle is plugged into the grid utilizing cheap electricity or if vehicle range is vital to fulfill a transportation mission. To be able to avoid an extra charging stop is often more valuable than the cost of extra energy needed for tire heating. Note, though, that all computations are based on the assumption that the tires can be heated without any loss in energy, which is unrealistic. Hence, in reality, the dashed lines of Fig. 3 will be pointing even steeper downwards indicating higher total net energy loss.

Tire heating may be beneficial if there is a surplus in electric power, for example, when going downhill with a full battery, if waste heat can be utilized for heating the tires, or if using heat from a heat pump with a sufficiently high coefficient of performance.

References

- Schuring, D.J.: A new look at the definition of tire rolling loss. Tire Rolling Losses and Fuel Economy-An R&D Planning Workshop (1977)
- Nielsen, L., Sandberg T.: A new model for rolling resistance of pneumatic tires. SAE Trans. 1572–1579 (2002)
- Janssen, M.L., Hall, G.L.: Effect of ambient temperature on radial tire rolling resistance. SAE Trans. **89**, 576–580 (1980). <http://www.jstor.org/stable/44632443>
- Hyttinen, J., Ussner, M., Österlöf, R., Jerrelind, J., Drugge, L.: Truck tyre transient rolling resistance and temperature at varying vehicle velocities -Measurements and simulations. Polym. Test. **122** (2023)

5. Ydrefors, L., Hjort, M., Kharrazi, S., Jerrelind, J., Stensson, T.A.: Rolling resistance and its relation to operating conditions: A literature review. Proc. Inst. Mech. Eng., Part D: J. Autom. Eng. **235**(12), 2931–2948 (2021)
6. Mars, W.V., Luchini, J.R.: An analytical model for the transient rolling resistance behavior of tires. Tire Sci. Technol. **27**(3), 161–175 (1999)

Open Access This chapter is licensed under the terms of the Creative Commons Attribution 4.0 International License (<http://creativecommons.org/licenses/by/4.0/>), which permits use, sharing, adaptation, distribution and reproduction in any medium or format, as long as you give appropriate credit to the original author(s) and the source, provide a link to the Creative Commons license and indicate if changes were made.

The images or other third party material in this chapter are included in the chapter's Creative Commons license, unless indicated otherwise in a credit line to the material. If material is not included in the chapter's Creative Commons license and your intended use is not permitted by statutory regulation or exceeds the permitted use, you will need to obtain permission directly from the copyright holder.





Bifurcation Analysis of a Nonlinear Vehicle Model on Banked Road

Luca Zerbato^(✉), Enrico Galvagno, and Mauro Velardocchia

Department of Mechanical and Aerospace Engineering, Politecnico di Torino, Corso Duca degli
Abruzzi 24, 10129 Turin, Italy

{luca.zerbato, enrico.galvagno, mauro.velardocchia}@polito.it

Abstract. Towards the transition to automated driving, lateral stability of the vehicle represents a key requirement to guarantee the safety of passengers and vulnerable road users, especially during emergency operating conditions where nonlinearities arise. The present paper aims at investigating the effect of road banking angle on vehicle plane motion stability. To perform this analysis, a pure lateral nonlinear double track model is numerically derived for an oversteering vehicle. Lateral load transfer and its distribution among the axles are included for exploiting the tyre saturation region. The stability analysis is conducted by searching for the vehicle steady-state conditions and deriving the linearised equations around the equilibrium points. Moreover, the phase-plane plot is adopted to draw the states trajectories and to identify potential unstable regions. Finally, the bifurcation analysis as function of the road banking angle is investigated to highlight possible change of the phase portrait topology. The results show that a saddle-node bifurcation may occur when the vehicle is negotiating a certain level of bank road angle, affecting the vehicle yaw stability region.

Keywords: Stability analysis · nonlinear vehicle dynamics · bifurcation · phase-plane analysis

1 Introduction

Road safety represents a primarily concern when dealing with the standard and automated driving. Reducing dangerous situations for passengers and vulnerable road users is strictly related to understanding the vehicle limits and its stability, especially when the vehicle is engaged in an emergency manoeuvre. The analysis of vehicle stability under nonlinear operating conditions is a well-established topic: many authors have investigated the limit conditions due to different inputs (such as the vehicle speed, the steering wheel angle, the road friction) or vehicle parameters (such as the influence of the position of the centre of mass or the front/rear roll stiffness distribution) [1–3]. As shown in these works, the main cause of vehicle instability lies in the saturation of the rear axle cornering characteristics, which is a typical behaviour of oversteering vehicles. This condition leads to the presence of a couple of unstable equilibrium points, which can be clearly highlighted on a phase-plane plot. Most previous articles focus

their analysis on the vehicle alone, adopting the single- or double-track models, while the authors of [4, 5] extend the analysis including driver dynamics in the set of equations of motion governing vehicle dynamics. In particular, the authors demonstrated that, for an understeering vehicle, the coupling of vehicle and driver dynamics can result in a stable and unstable limit cycle above a critical speed. The attempt to extend the classic two-states phase-plane approach is performed by the authors of [6] where they proposed an enhanced three-state model which accounts for the longitudinal vehicle motion and the effect of the tyre slip combination on the system stability. The phase-plane plot is an effective tool, commonly used to investigate nonlinear systems, which allows possible unstable regions to be described through the phase-portrait. This approach makes it possible to determine the stability boundary of the vehicle, which can be proficiently used to set constraints for control purposes, as done by the authors of [7] where phase-plane analysis is used to define the boundary of stability, in terms of sideslip angle and sideslip velocity. Moreover, different phase-plane types have been used throughout the literature, as well-explained by the survey on lateral stability criterion presented in [8], where a classification of the different phase-plane types is presented and qualitatively evaluated in terms of measurability, relevance, sensibility, and controllability.

Nevertheless, the main literature studies are limited to bifurcation analysis on flat and horizontal road surfaces, whereas the effect of the banking of the road on stability is not deeply investigated. Thus, this paper aims at exploring the effects of the road banking angle in the nonlinear operative conditions, searching for possible stability limits and bifurcations through a classic phase-plane analysis on the yaw rate and sideslip angle plane. The paper is divided as follows. In Sect. 2 the vehicle model and the main hypothesis are presented. Moreover, the methodology to determine the presence of fixed points is discussed. Section 3 depicts the phase-portrait starting from a grid of initial conditions to the vehicle subject to different levels of bank angle. Finally, some conclusions of bifurcation analysis are derived in Sect. 4.

2 Model and Test Workflow

2.1 Vehicle Model

In this paper, a nonlinear vehicle model negotiating banked turns is under investigation. The model is a double-track vehicle (see Fig. 1) which is characterised by two degrees of freedom (lateral and yaw motion). The following assumptions are made:

- The vehicle body is assumed to be rigidly connected to the axles, thus roll and pitch motion are neglected.
- Vehicle velocity V is considered constant and the effect of tyre longitudinal forces on vehicle dynamics is neglected.
- Lateral load transfers, i.e. the variation of the vertical tyre forces while cornering, are modelled considering a constant distribution factor $k_{F/R}$ between the front and rear axle is assumed equal to 40:60.
- The wheels are always in contact with the ground; thus the rollover dynamics is neglected.

- The effect of road banking is modelled as a constant component of the weight force acting along the vehicle y -axis direction and applied to the centre of gravity. At the same time, the component of the weight force in the direction perpendicular to the road plane is reduced.
- The driver dynamics is not included in the set of equation of motion thus, the analysis is conducted at fixed steering angle.
- Tyre-contact forces are computed using the semi-empirical steady-state Pacejka Tyre Magic Formula [9]

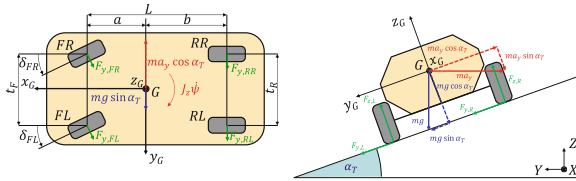


Fig. 1. Double-track nonlinear vehicle model scheme: on the left $x_G y_G$ plane, on the right YZ plane.

2.2 Equilibrium Points Search and Discussion

This section presents the method used to search for and discuss the presence of single or multiple steady-state conditions and the bifurcation analysis. From the theory of the nonlinear dynamics, a generic nonlinear system may exhibit more than one equilibrium point (or fixed point). In the specific case of vehicle plane motion (without considering the driver dynamics), the presence of more than one fixed point deals with oversteering vehicles [3].

Figure 2 synthesizes the adopted workflow to find and to discuss the model steady-state conditions. The procedure has been entirely developed in MATLAB/Simulink environment by exploiting the FSOLVE function, which has the objective of searching for the stationary solutions. A nonlinear vehicle Simulink model is set with the initial condition guess point $x_{0,start}$ and the input parameters (vehicle velocity V , steering wheel angle δ_{sw} , friction coefficient μ and bank angle α_T). The tyre lateral forces are gathered from the simulation results to a set of nonlinear equation of motion checking the presence of an equilibrium condition on lateral and yaw motion. If a solution $x_0 = [\beta_0, r_0]$ is found, the equations of motion are linearised around that equilibrium point, and, to assess stability in its neighbourhood, the trace and the determinant of the Jacobian matrix are computed. This procedure allows to classify the nature of the fixed point and to determine its stability.

The bifurcation analysis on road banking angle is performed by repeating the workflow on the following set of banking angles: $[-45^\circ, 45^\circ]$.

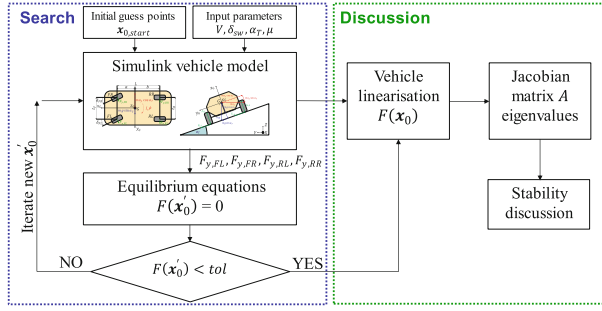


Fig. 2. Adopted workflow for the steady-state solutions and stability discussions.

3 Phase Plane Numerical Results

In this section the results from the bifurcation analysis and the numerical integration of the equation of motion of the model are presented. In this analysis an oversteering vehicle model is tested in all its operative working range, using the phase-plane ($\beta - r$) diagram. The states are represented by the vehicle sideslip angle β and the yaw rate r . The vehicle geometrical and inertial properties are listed in Table 1.

Table 1. Vehicle data

<i>Parameter</i>	<i>Value</i>
Mass [kg]	1600
Yaw moment of inertia [kgm ²]	2860
Wheelbase [m]	2.6
Front axle distance to CoG [m]	1.56
Rear axle distance to CoG [m]	1.04
Front and rear trackwidth [m]	1.54
Stiffness distribution factor k_F/R [-]	40:60

The model is numerically integrated to draw the phase-portrait at a set velocity V , steering wheel angle δ_{sw} and banking angle α_T . The proposed analysis investigates the steady-state solution when the vehicle is running on a banked road at 100 km/h with steering wheel angle null. The vehicle model is integrated by setting a grid of initial conditions (β_0, r_0) with a span of $5^\circ/s$ for the yaw rate and 5° for the sideslip angle respectively. In the following results the vertical load acting on each wheel is always higher than zero, thus rollover issues are not triggered.

Figure 3 depicts the phase-portrait obtained from the numerical simulation with three different levels of banking ($0^\circ, 20^\circ, 41^\circ$). The blue lines represent the states trajectories while the red circle, diamond and star are the three steady-states solutions obtained with the explained workflow. The circle is a stable focus, while diamond and star are two

saddle-points. It is worth noting that by increasing the road banking angle, the unstable node approaches the stable one: after 40° of lateral slope a saddle-node bifurcation occurs: beyond this value no more stable region is available.

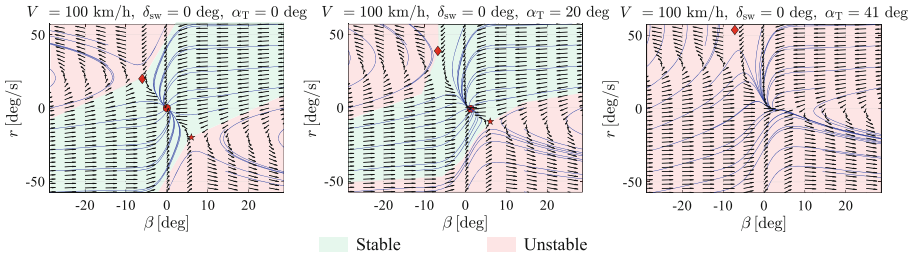


Fig. 3. Phase-portrait on $\beta - r$ plane of the nonlinear vehicle model running at 100 km/h with null steering wheel angle and three different level of banking angle (0° , 20° , 41°).

Figure 4 depicts the states trajectories obtained for a value of α_T equal to 20° in combination with a third axis represented by the Load Transfer Ratio (*LTR*), which is a quantity used to detect and predict the rollover risk [10]. *LTR* is defined as the relative vertical force on tyres between the right side ($F_{z,R}$) and left side ($F_{z,L}$) of a vehicle (Eq. 1):

$$LTR = \frac{F_{z,R} - F_{z,L}}{F_{z,L} + F_{z,R}} \quad (1)$$

Values lower than one indicates a normal force greater than zero for all the wheels. In this condition, tyres are always in contact with the ground.

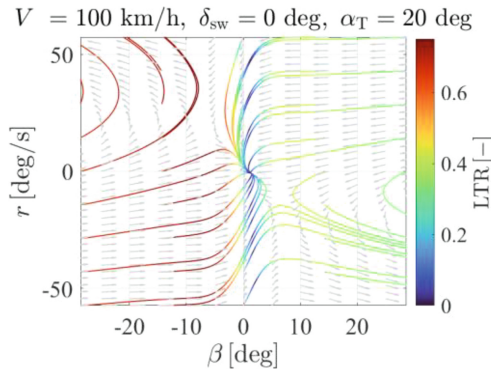


Fig. 4. Phase-plane using a third axis represented by the *LTR* values.

The numerical results show the presence of a clear bifurcation at a certain lateral slope value α_T .

It should be noted that the angle of banking that corresponds to the bifurcation is well above the common values encountered when a vehicle is travelling on normal roads.

However, looking at the distance between the stable equilibrium point (circle in Fig. 3) and the point closest to the stability boundary (star) in the phase plane graph, it can be seen that the progressive increase in transverse road inclination reduces the stability margin of the vehicle.

4 Conclusion

The conducted analysis of the vehicle stability in its nonlinear working points is crucial to define possible avoidable conditions, such as unstable steady state turning conditions. Albeit the bifurcation due to the steering angle and velocity is well established in the literature the analysis on lateral slope is not well investigated. To this aim, a nonlinear double track model has been developed and tested in different banked roads. The developed methodology revealed to be well suited to find the steady-state equilibrium conditions and, after the linearisation process, their stability discussion. A saddle-node bifurcation appears at certain level of lateral slope angle, since stable and unstable manifolds collides into a saddle-point. Further improvements will be devoted to the inclusion in the set of the equation the driver dynamics, roll dynamics and the wheel detachment dynamics.

References

1. Ono, E., Hosoe, S., Tuan, H.D., Doi, S.: Brief papers bifurcation in vehicle dynamics and robust front wheel steering control. *IEEE Trans. Control Syst. Technol.* **6**, 412–420 (1998)
2. Della Rossa, F., Mastinu, G., Piccardi, C.: Bifurcation analysis of an automobile model negotiating a curve. *Veh. Syst. Dyn.* **50**, 1539–1562 (2012). <https://doi.org/10.1080/00423114.2012.679621>
3. Farroni, F., Russo, M., Russo, R., Terzo, M., Timpone, F.: A combined use of phase plane and handling diagram method to study the influence of tyre and vehicle characteristics on stability. *Veh. Syst. Dyn.* **51**, 1265–1285 (2013). <https://doi.org/10.1080/00423114.2013.797590>
4. Della Rossa, F., Mastinu, G.: Straight ahead running of a nonlinear car and driver model—new nonlinear behaviours highlighted. *Veh. Syst. Dyn.* **56**, 753–768 (2018). <https://doi.org/10.1080/00423114.2017.1422526>
5. Mastinu, G.R.M., Previati, G., Della Rossa, F., Gobbi, M., Fainello, M.: How drivers lose control of the car. *SAE Int. J. Veh. Dyn. Stab. NVH* **8** (2024). <https://doi.org/10.4271/10-08-01-0007>
6. Beal, C.E., Boyd, C.: Coupled lateral-longitudinal vehicle dynamics and control design with three-dimensional state portraits. *Veh. Syst. Dyn.* **57**, 286–313 (2019). <https://doi.org/10.1080/00423114.2018.1467019>
7. Han, Z., Xu, N., Chen, H., Huang, Y., Zhao, B.: Energy-efficient control of electric vehicles based on linear quadratic regulator and phase plane analysis. *Appl. Energy* **213**, 639–657 (2018). <https://doi.org/10.1016/j.apenergy.2017.09.006>
8. Zhu, Z., Tang, X., Qin, Y., Huang, Y., Hashemi, E.: A survey of lateral stability criterion and control application for autonomous vehicles. *IEEE Trans. Intell. Transp. Syst.* **24**, 10382–10399 (2023). <https://doi.org/10.1109/TITS.2023.3280200>
9. Pacejka, H.: *Tire and Vehicle Dynamics*, 3rd edn. (2012). <https://doi.org/10.1016/C2010-0-68548-8>

10. Tota, A., Dimauro, L., Velardocchia, F., Paciullo, G., Velardocchia, M.: An intelligent predictive algorithm for the anti-rollover prevention of heavy vehicles for off-road applications. *Machines* **10** (2022). <https://doi.org/10.3390/machines10100835>

Open Access This chapter is licensed under the terms of the Creative Commons Attribution 4.0 International License (<http://creativecommons.org/licenses/by/4.0/>), which permits use, sharing, adaptation, distribution and reproduction in any medium or format, as long as you give appropriate credit to the original author(s) and the source, provide a link to the Creative Commons license and indicate if changes were made.

The images or other third party material in this chapter are included in the chapter's Creative Commons license, unless indicated otherwise in a credit line to the material. If material is not included in the chapter's Creative Commons license and your intended use is not permitted by statutory regulation or exceeds the permitted use, you will need to obtain permission directly from the copyright holder.





Regenerative Brake Blending in Electric Hypercars: Benchmarking and Implementation

Rodrigo Senofieni¹, Federico Bassi¹, Matteo Corno^{1(✉)},
Sergio Matteo Savaresi¹, and Gianluca Savaia²

¹ Politecnico di Milano, Piazza Leonardo da Vinci, 32, 20133 Milan, MI, Italy
{rodrigo.senofieni, federico.bassi, matteo.corno, sergio.savaresi}@polimi.it

² Rimac Technology, Ljubljanska ul. 7, 10431 Brezje, Croatia
gianluca.savaia@rimac-technology.com

Abstract. This paper presents a novel Regenerative Brake Blending (RBB) strategy for an electric hypercar, framing it as a multi-objective problem. These include thermal and lifespan management of various components plus maximizing energy recovery. We begin by mathematically modelling each subsystem of the RBB layout. Then, we define an acausal offline optimal control problem to establish a benchmark solution; subsequently we propose a causal real-time control strategy inspired by the Equivalent Consumption Minimization Strategy (ECMS). The proposed real-time strategy shows a performance loss of 1.6% compared to the benchmark underscoring the efficacy of the proposed RBB strategy in maximizing energy recuperation while considering for brake temperatures.

Keywords: Regenerative Brake Blending · Pontryagin's Minimum Principle · ECMS · Electric Vehicles

1 Introduction

Efficient energy management in electric vehicles (EVs) is essential for enhancing performance and extending range. Regenerative braking, which captures kinetic energy during deceleration and converts it into electrical energy, is a promising solution. This technology is especially critical for electric hypercars with large power outputs, requiring advanced strategies to manage energy recovery and optimize dynamical performance of the overall vehicle.

Regenerative Brake Blending (RBB) consists in the allocation of the braking force between electric motors and friction brakes. The allocation impacts several and conflicting aspects: energy recuperation, battery stress, and friction brakes temperature, to name the most important ones. RBB usually encompasses two primary allocation levels: first-level allocation, typically front/rear-based to comply with European ECE regulation 13H [1], and wheel-level allocation, aiming

to optimize energy, thermals, degradation considerations (for both brake and battery) in a blended strategy.

RBB at wheel level can be categorized into two main types: static and dynamic allocation methods. Static strategies, such as the serial blending strategy, rely on instantaneous efficiency maps of motor, inverter, battery and consist in instantaneously allocating all braking force to the electric motor (to maximize energy recuperation) and fulfilling the braking request (if necessary) with the friction brakes; these methods have been widely explored in literature and industrial applications [4, 7] and represent the state of the art. However, they are based on heuristic-driven approaches, often resulting in suboptimal outcomes.

In contrast, dynamic strategies incorporate predictive aspects and multi-objective functions, allowing for global optimality and the integration of constraints, system dynamics, and predictive features. Dynamic strategies have found application in the dual problem of optimizing power split between internal combustion engine and electric motors in hybrid vehicles [2, 6, 8]: acausal methods (like dynamic programming or Pontryagin’s Minimum Principle (PMP)) or casual ones like Equivalent Consumption Minimization Strategy (ECMS) have yet to be explored for RBB optimization in both literature and industrial practice.

Section 2 analyses the benchmark solution based on an acausal offline optimal control problem. Section 3 introduces a real-time implementation based on the ECMS principle and a comparative analysis with the acausal method and the baseline heuristic will be carried out. Finally, Sect. 4 draws conclusions about the aforementioned RBB strategy.

2 Benchmark Regenerative Brake Blending

This strategy is based on a control oriented model validated on real data. The model, schematically represented in Fig. 1, considers the main components of the powertrain: the battery, the power electronics, motor and friction brakes. The battery state of charge and thermal dynamics (T_{batt}) are modeled [10]. Friction brakes thermal dynamics are captured with a lumped model [3] which consists of two separate elements (disks - T_d - and pads - T_c -). Last, the electric motor and transmission have been included in the formulation via efficiency maps based on test bench data. Since the RBB strategy does not influence the longitudinal dynamics, the problem can be studied with the backward facing model approach [5].

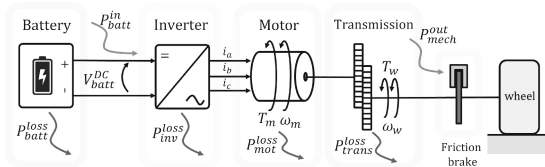


Fig. 1. Regenerative brake blending layout.

Given a predefined driving cycle, the brake blending problem can be framed as an constrained minimization problem of the following cost function:

$$J = \int_{t_0}^{t_f} (w_1(T_{batt}) + w_2(T_{\{c,d\},f}) + w_3(T_{\{c,d\}r}) + w_4(P_{reg})) dt \quad (1)$$

where the optimization variables are the four braking torques (electrical front and rear and friction front and rear). The constraints are summarized as follow:

$$\dot{x} = f(x(t), u(t), t), \quad (2)$$

$$x \in [X_{\min}, X_{\max}], \quad (3)$$

$$u \in [U_{\min}, U_{\max}], \quad (4)$$

$$T_{\text{req}}^{\text{front}} + T_{\text{req}}^{\text{rear}} = T_{\text{req}}^{\text{total}}, \quad (5)$$

$$T_{\text{req,EM}}^{\text{front}} \geq T_{\text{min,EM}}^{\text{front}}, T_{\text{req,EM}}^{\text{rear}} \geq T_{\text{min,EM}}^{\text{rear}}, \quad (6)$$

$$T_{\text{req,EM}}^{\text{front}} + T_{\text{req,FB}}^{\text{front}} = T_{\text{req}}^{\text{front}}, T_{\text{req,EM}}^{\text{rear}} + T_{\text{req,FB}}^{\text{rear}} = T_{\text{req}}^{\text{rear}}, \quad (7)$$

$$2T_{\text{req,EM}}^{\text{front}} \cdot \omega_{\text{mot}} \cdot \eta_{\text{front}} + 2T_{\text{req,EM}}^{\text{rear}} \cdot \omega_{\text{mot}} \cdot \eta_{\text{rear}} \geq P_{\text{min}}^{\text{batt}}(T_{\text{batt}}^{\text{c}}), \quad (8)$$

where (2) represents the system dynamics, (3) and (4) are the constraints on the states and control variables, equation (5) satisfy the total negative torque request (front plus rear), (6) limits the regenerative torque based on motors mechanical limits, (7) fullfill the brake request at wheel level (friction brake plus electric motor) and finally (8) limits the maximum regen torque based on battery derating.

In J (1), the weighting functions w are used to balance the conflicting objectives and to consider the nonlinear effect that temperature has on the life of the components. By changing the shape of the weights one can give priority to some aspects rather than others. Figure 2 shows the state trajectories for a state-of-the-art baseline (sequential blending) and two possible tunings of the weights: recovered energy optimization priority and battery temperature minimization. The optimal control strategy outperforms the baseline serial blending (black dotted), even when the request is to maximize energy recovery and minimize brake and battery temperatures. Note that regenerative braking has a low impact on battery temperature and that the main tradeoff is between harvested energy and brake temperatures. This information will be used to simplify the optimal control problem and make it implementable in real-time.

3 Real Time Implementation

The previous optimal problem formulation assumes a known driving cycle and is not therefore implementable on the vehicle. To address this, we took inspiration from the Equivalent Consumption Minimization Strategy (ECMS) [9]. ECMS transforms a dynamic constrained optimization problem into a static constrained optimization problem by introducing equivalence factors, which represent a trade-off between different energy sources.

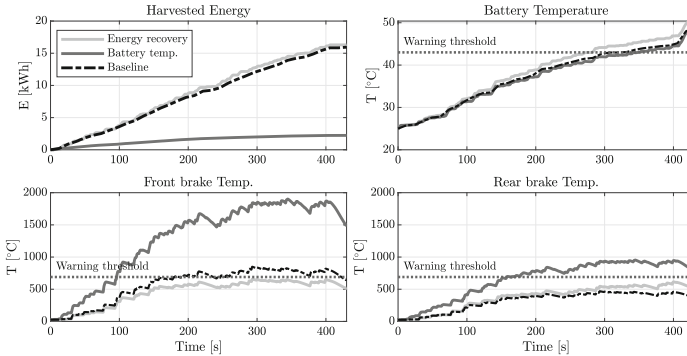


Fig. 2. State trajectories comparing the results of the offline optimal problem, for different weights, and the state-of-the-art sequential blending.

In the dual problem of power split (between internal combustion engine and electric motors) in hybrid vehicles, the generic formulation of ECMS involves minimizing a cost function that combines fuel consumption and electrical energy usage. The cost function is defined as:

$$J = m_f(t) + \sum_i s_i \cdot P_i(t) \quad (9)$$

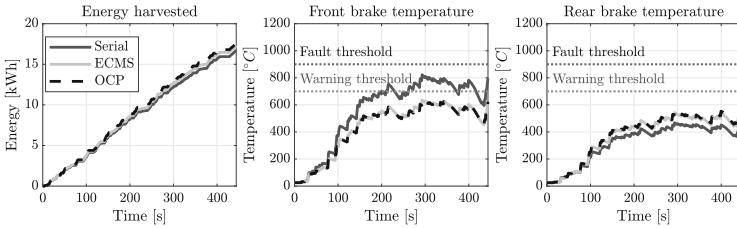
where $m_f(t)$ is the instantaneous fuel consumption, $P_i(t)$ are the electrical power demands, and s_i are the equivalence factors that convert electrical power into an equivalent fuel consumption. To make this approach implementable on a vehicle, we propose a method to tune the equivalence factors based on the co-states behavior in a Pontryagin's Minimum Principle (PMP) formulation [6]. By analyzing the behavior of the co-states, we can adjust the equivalence factors to ensure that the ECMS closely approximates the optimal solution given by the PMP. This tuning process allows the ECMS to dynamically adapt to varying driving conditions without requiring a pre-defined driving cycle, making it practical for real-world vehicle implementation.

Starting from the PMP insights, a formulation of the ECMS for the regenerative brake blending problem can be derived:

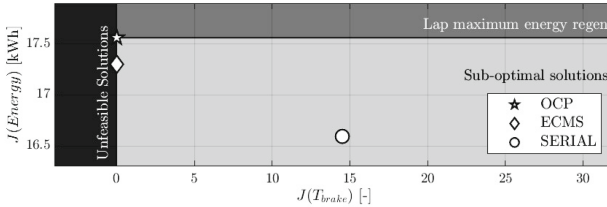
$$\begin{aligned} \min_u J = & -P_{regen}(x, u) + s_2 \cdot \dot{T}_{c,front}(x, u) + s_3 \cdot \dot{T}_{d,front}(x, u) \\ & + s_4 \cdot \dot{T}_{c,rear}(x, u) + s_5 \cdot \dot{T}_{d,rear}(x, u), \end{aligned} \quad (10)$$

subject to constraints (5, 6, 7, 8); u are the control variables (i.e., $T_{req,FB}^{front}$ and $T_{req,FB}^{rear}$) and s_i are the equivalence factors. The practical implication of the aforementioned ECMS formulation is that whenever the vehicle applies the friction brakes for slowing down, in subsequent instances, it will utilize the electric motors, and so the battery, to cool them instead and recharge the battery.

The qualitative results depicted in Fig. 3a show the ECMS can closely replicate the offline optimal solution. The dataset used consists in two flying laps of the Nordschleife circuit. In terms of harvested energy, the improvement with respect to the serial blending is just 1.6%. This is an expected outcome, since the sequential blending only aim is to maximize energy recovery. However, if we look at the brake thermal management, we can notice that the ECMS outperforms the state-of-the-art solution thanks to an optimal allocation of regenerative power between electric and friction brakes. This allows to maintain the front brakes (the most stressed ones) under the critical threshold of $750^\circ C$ even in two consecutive pushalaps of the Nordschleife. The pareto front illustrated in Fig. 3b shows the quantitative results of the aforementioned results.



(a) State trajectories comparing the results of the offline optimal problem (OCP), the state-of-the-art sequential blending (Serial) and the proposed acausal strategy (ECMS).



(b) Pareto plot.

Fig. 3. Real-time implementation performance assesment.

4 Conclusions

In this paper, we introduced a novel Regenerative Brake Blending (RBB) strategy for electric hypercars, framing it as a multi-objective problem. The acausal offline optimal control problem provided a benchmark solution, against which the proposed real-time strategy, based on the Equivalent Consumption Minimization Strategy (ECMS), was evaluated. Despite a minimal performance loss of only 1.6% compared to the benchmark, the real-time strategy demonstrated significant efficacy in maximizing energy recuperation while managing brake temperatures. This underscores the potential of advanced RBB strategies in enhancing energy efficiency and performance in high-performance electric vehicles.

Acknowledgments. We would like to thank Gianluca Savaia for his technical contributions and Rimac Technology for providing the data used in this research.

References

1. UN Regulation No 13-H: Uniform provisions concerning the approval of passenger cars with regard to braking [2023/401]. Commission Regulation (EU), <https://eur-lex.europa.eu/legal-content/EN/TXT/PDF/?uri=CELEX:42023X0401>
2. Ebbesen, S., Salazar, M., Elbert, P., Bussi, C., Onder, C.H.: Time-optimal control strategies for a hybrid electric race car. *IEEE Trans. Control Syst. Technol.* **26**(1), 233–247 (2018). <https://doi.org/10.1109/TCST.2017.2661824>
3. Göltz, S., Sawodny, O.: Simplified disc brake modeling, identification, and validation focusing on temperature influences. In: *IECON 2020 The 46th Annual Conference of the IEEE Industrial Electronics Society*, pp. 2063–2068 (2020). <https://doi.org/10.1109/IECON43393.2020.9254389>
4. Heydari, S., Fajri, P., Rasheduzzaman, M., Sabzehgar, R.: Maximizing regenerative braking energy recovery of electric vehicles through dynamic low-speed cutoff point detection. *IEEE Trans. Transp. Electrification* **5**(1), 262–270 (2019). <https://doi.org/10.1109/TTE.2019.2894942>
5. Mohan, G., Assadian, F., Longo, S.: Comparative analysis of forward-facing models vs backwardfacing models in powertrain component sizing. In: *IET Hybrid and Electric Vehicles Conference 2013 (HEVC 2013)*, pp. 1–6 (2013). <https://doi.org/10.1049/cp.2013.1920>
6. Onori, S., Serrao, L., Rizzoni, G.: *Hybrid electric vehicles energy management strategies*. Springer (2016)
7. Pennycott, A., De Novellis, L., Gruber, P., Sorniotti, A.: Optimal braking force allocation for a four-wheel drive fully electric vehicle. *Proc. Inst. Mech. Eng., Part I: J. Syst. Control Eng.* **228** (2014). <https://doi.org/10.1177/0959651814531124>
8. Pozzato, G., Formentin, S., Panzani, G., Savaresi, S.M.: Least costly energy management for extended-range electric vehicles: an economic optimization framework. *Eur. J. Control.* **56**, 218–230 (2020). <https://doi.org/10.1016/j.ejcon.2020.01.001>
9. Radrizzani, S., Brecciaroli, L., Panzani, G., Savaresi, S.M.: An efficiency based approach for the energy management in hev. *IFAC-PapersOnLine* **55**(24), 167–172 (2022). <https://doi.org/10.1016/j.ifacol.2022.10.279>, 10th IFAC Symposium on Advances in Automotive Control AAC 2022
10. Sabatini, S., Corno, M.: Battery aging management for fully electric vehicles. In: *2018 European Control Conference (ECC)*. pp. 231–236 (2018). <https://doi.org/10.23919/ECC.2018.8550592>

Open Access This chapter is licensed under the terms of the Creative Commons Attribution 4.0 International License (<http://creativecommons.org/licenses/by/4.0/>), which permits use, sharing, adaptation, distribution and reproduction in any medium or format, as long as you give appropriate credit to the original author(s) and the source, provide a link to the Creative Commons license and indicate if changes were made.

The images or other third party material in this chapter are included in the chapter's Creative Commons license, unless indicated otherwise in a credit line to the material. If material is not included in the chapter's Creative Commons license and your intended use is not permitted by statutory regulation or exceeds the permitted use, you will need to obtain permission directly from the copyright holder.





A Method for Obtaining Reference Friction Values for Validation of Road Friction Estimation Algorithms

Mattias Hjort¹ (✉), Fredrik Bruzelius², Sogol Kharrazi¹, and Derong Yang³

¹ VTI, Swedish National Road and Transport Research Institute, 581 95 Linköping, Sweden
mattias.hjort@vti.se

² Department of Mechanics and Maritime Sciences, Chalmers University of Technology,
41296 Gothenburg, Sweden

³ Department of Vehicle Motion and Control, Volvo Car Group, 418 78 Gothenburg, Sweden

Abstract. Data-driven development of friction estimators for passenger vehicles is becoming popular. They rely mainly on training data to obtain an accurate estimate of the current road conditions. However, reference or training data for natural conditions containing available friction is sparse. This limits the development of data-driven approaches for friction estimation. The current paper presents progress in a project devoted to developing a method to use standard equipment for road monitoring to acquire reference data for friction estimation, relevant to specific tyres and operating conditions. Results show how a mapping between existing test equipment readings and the real experienced coefficient of friction of a car tyre can be made.

Keywords: Tyre-to-road friction · friction measurement · friction reference value

1 Introduction

The available tyre-to-road friction limits the motion envelope of any road vehicle and is a hard constraint on all vehicle motion control functionality such as ABS, ESC, etc. For autonomous vehicles, this is even more pronounced and a correct prediction of friction ahead of the vehicle is a necessity to ensure safe operation. The current state-of-the-art friction estimation approaches use physical models. These approaches give correct estimates point-wise, and require special conditions to operate, leading to low data availability (see e.g. [1] and references therein). A current trend to solve the availability problem is to make use of data-driven approaches and machine learning. These types of approaches rely on available training data for all conditions the car is intended to operate. The availability of such data is currently very limited, which constrains the development of such algorithms and ultimately also the development of autonomous vehicles. A common problem is that there exists no good method to continuously measure a reference value of the tyre-road friction for a car. On test tracks, with large surfaces of uniform

friction, a full ABS brake test can be used for determining the friction. On real roads, however, where the surface conditions may be rapidly changing, such a measurement is in most cases impossible due to road curvature, and even more importantly, traffic safety.

Measuring the road surface is an ongoing activity for most road administrators. The main objective of such measurements is to monitor the conditions of road segments and to use this information for decision-making of road maintenance. Recently, the use of vehicles in a fleet as probes to a centralized cloud for this purpose has been investigated. However, the established method for these types of measurements is through dedicated devices attached to a vehicle. An example of such devices can be an extra tyre with a fixed slip ratio and a force sensor. A common aim with all these measurement techniques, including the cloud-based ones, is to monitor the road conditions. Hence, standard methods with special tyres are typically used.

In the current paper, the aim is to develop a measuring method for the vehicle industry that can provide them with the required reference friction data using the devices used typically by road administrators. The use of standardized methods with measurement devices cannot be applied directly to the problem that the vehicle industry is facing. The friction measurements need to reflect the friction level and conditions a car would experience to be relevant. Hence, translations between the readings from the device and the car friction level need to be developed through measurement campaigns. The purpose of this project has been to develop a method to derive this translation with a focus on minimizing the required measurements and additional sensors required.

2 Methodology

A commercial road friction measurement device that VCC has acquired (see Fig. 1a) was used via test track measurements to establish the correlation between friction values from this device and a few Volvo passenger cars on different road friction conditions. By driving in a caravan with a car, denoted the target vehicle, the continuously measured road friction values can then via the known correlation be transformed into reference friction values representative of the target vehicle. Wireless communication between the road friction device (RFD) and a target vehicle (TV) has been set up so that the reference friction can be logged synchronously together with other sensor data in the car.

The RFD is a trailer from the Norwegian producer ViaFriction, and this particular model is commonly used for routine friction assessment of winter roads in Sweden, carried out by the Swedish Transport Agency. It is equipped with two measurement wheels, one in each wheel track. Test tyres of type Trelleborg Unitester 520 were used, which is the standard test tyre to be used for winter road friction measurements according to the method description prescribed by the Swedish Transport Agency. The wheel load is set to 1000 N, and the measurement is supposed to be carried out at a fixed brake slip value of 20%. Commonly, road friction equipment of this type, measuring the longitudinal friction for a braked wheel, uses a mechanical gear system to provide a very stable wheel slip value regardless of the road friction. This particular RFD however, instead uses an electrical motor for each test wheel that continuously regulates the wheel slip. It was found that the wheel slip in many cases was unstable and care had to be taken to assure that obtained measurement data fulfilled the wheel slip requirement.

The available friction for a target vehicle equipped with specific tyres would most easily be determined from straight brake tests on a test track with a homogeneous surface. In this project there was an opportunity to also measure the available friction for a specific tyre by using VTI's tyre test equipment BV12. The BV12 (see Fig. 1b) is a mobile equipment for tyre friction characterization, which can measure both longitudinal and lateral friction slip curves of the tyres to determine the peak friction at various operating conditions. In theory, friction models based on slip curves measured at different wheel loads could be applied to different target vehicles which use the same tyre, thus expanding the use cases for a specific tyre mapping.

To limit the number of measurements it was decided to focus only on longitudinal brake friction. The BV12 brake slip curves are measured at constant speed, just as the RFD friction, while a brake test with a car will comprise a speed interval. Two week-long measurement campaigns were carried out on snow and ice tracks in Northern Sweden. The three equipment were driven consecutively, laterally displaced on the test tracks to avoid each other's wheel paths. Measurements carried out within a time frame of 5 min were considered to be pairwise comparable.

Three different winter tyres for the target vehicle, a Volvo XC60, were used: a European winter tyre, a Nordic winter tyre, and a studded winter tyre. The test tracks were prepared so that friction levels with the RFD were within 0.05–0.45. Measurements were carried out to allow for mappings at different vehicle speeds, wheel loads and inflation pressures. An optical sensor from Teconer [2] was also used for distinguishing between ice and snow surface in case this information would be necessary for the mapping.

The test tracks were rectangular, typically 20 m wide with a length of 600–1000 m. The Snow tracks were made available by the tyre manufacturer Pirelli, and were prepared according to their expertise to allow for repeatable tests. Tracks with different hardness of snow were used in the purpose of covering a range of available friction. Still, snow on these kind of tracks is generally much harder than conditions often found on the roads, and consequently exhibit quite high friction levels. The snow hardness was in the range of 82–90 CTI units (see ref [3] for a definition of snow hardness), and the ambient temperature ranged from +2 to –6 °C, with the snow temperature a few degrees colder. The RFD measured friction values varied between 0.28–0.44.



(a)



(b)

Fig. 1. The Volvo road friction device (a) and VTI BV12 tyre test equipment (b)

The ice tracks were divided into parallel corridors, 3 m wide and 300 m long, which could be prepared differently to allow for different preparation. A special ice-rugging trailer with 10 studded tyres rolling with large slip angles was constructed in order to transform a smooth ice with low friction, to rugged ice with different friction levels. In combination with large weather variations ice surfaces with RFD friction levels in the range of 0.05–0.45 were obtained.

3 Results

To obtain a functional translation of a brake slip curve on snow to the average friction obtained from full ABS braking with a passenger car, unprocessed data from a previous project [4] was analyzed. Brake tests on snow carried out with both BV12 and a passenger car for more than 40 different tyres indicate a close correlation between the slip curve peak friction and the average ABS retardation as shown in Fig. 2a. A linear fit suggests that the obtainable ABS friction is 85% of the peak friction of the brake slip curve on this type of hard packed snow surface. This relation was used in the analysis of the current study, and a generally good agreement between BV12 and XC60 results indicate that it works well, despite a different car and different snow tracks. Since slip curves on snow are quite flat, as shown in Fig. 2b, it is not surprising that the peak value is a good indicator of the attainable ABS brake friction. Slip curves on ice generally show a quite marked peak at low brake slip values, where the friction decreases significantly at higher slip. To estimate the ABS brake friction on ice, the integral of the slip curve within a fixed slip interval was used. As a starting point, the interval 5–55% was used, with the possibility to tune the interval according to comparisons with the XC60 results.

Data from the two campaigns is presented in Fig. 3, where the average RFD friction value of both wheel tracks is compared to the BV12 and the XC60 results.

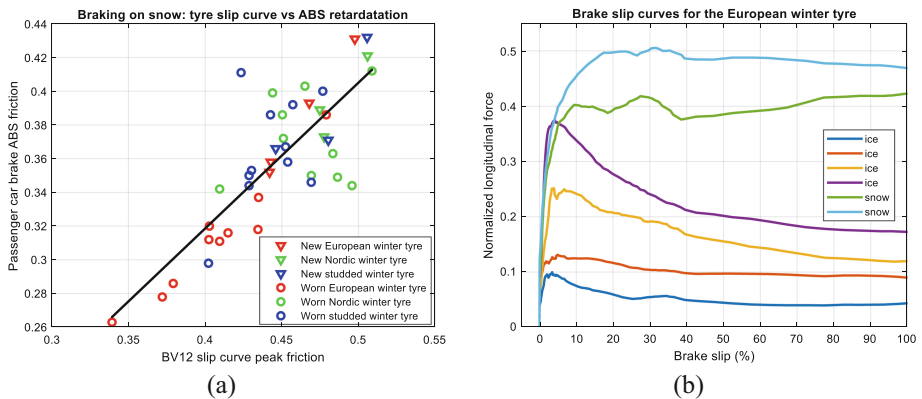


Fig. 2. Correlation between slip curve peak friction and ABS brake friction on snow (a) Typical brake slip curves on ice and snow for the European winter tyre (b)

Initial measurements were carried out at both 30 and 50 km/h, but since no clear difference was observed at these speeds, the majority of the measurements were then

done at 50 km/h. Most data was collected for the Nordic winter tyre, for which both BV12 and XC60 show a similar picture. The RFD underestimates the available friction at very slippery ice as well as for packed snow, while it provides a good estimate at intermediate ice friction levels. The data for the European winter tyre shows a similar behavior, but the European winter tyre has lower performance on slippery ice compared to the Nordic tyre, leading to a good correspondence with the RFD also at low friction.

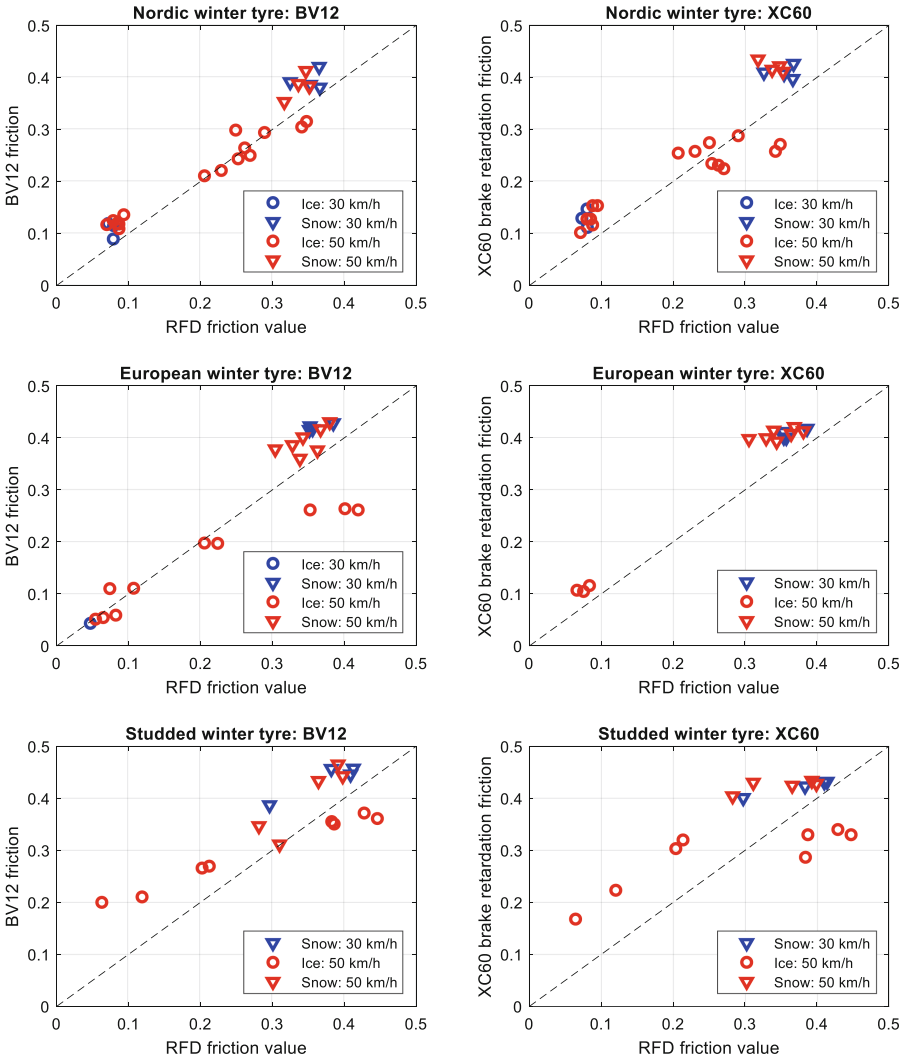


Fig. 3. RFD friction values compared to estimated brake friction from BV12 measurements and brake tests with the XC60.

An interesting anomaly for ice with very high friction is observed for the BV12 data. This particular ice track was covered with a layer of frost resulting in extremely high

RFD values, which clearly overestimated the brake friction for the European tyre. Unfortunately, the XC60 was not available for measurements with this tyre at this condition, but results for the studded tyres shows a similar behavior for both BV12 and XC60 on this high friction ice. As expected, the studded tyre generally provides increased ice grip level compared to the other tyres (as well as the RFD) on all other ice surfaces, while performing on par with the studless tyres on snow.

Two different mappings seem to be needed at RFD friction levels above 0.3 - one for snow and one for ice. Thus, information about the road conditions would be necessary. A technology using an optical sensor to discriminate between ice and snow has been tested in this project, and while the results on homogenous test tracks are promising, further testing is needed to conclude its effectiveness on real winter roads.

Measurements at different wheel loads ($\pm 50\%$) with the BV12 showed a very small effect on the brake friction. As did changes of the inflation pressure.

Comparison with the RFD driven straight and along a slalom pattern resulting in a lateral acceleration of 0.1 g indicated that the RFD friction value is decreased by 10% when measuring in a curve.

4 Conclusions

The results of elaborate field tests on ice and snow demonstrate that a dedicated road friction device can be a useful tool for continuously measuring available brake friction on winter roads for a specific vehicle and tyre, however the measured friction level by RFD should be adjusted for different tyre types. The data indicates that a model with piecewise linear mappings could be used, but additional information regarding the road surface conditions at RFD friction levels above 0.3 would be needed.

Acknowledgements. The authors would like to thank Sweden's innovation agency, Vinnova, for funding this project (grant number 2020-02910). The authors are also grateful to Pirelli for allowing us to use their snow and ice tracks for one of the measurements campaigns.

References

1. Albinsson, A.: Online and Offline Identification of Tyre Model Parameters. Ph.D. dissertation at Chalmers University of Technology, Gothenburg, Sweden (2018)
2. Surface condition and friction measurements - Teconer Oy. Accessed 12 Jan 2024
3. ASTM F-1805. Standard Test Method for Single Wheel Driving Traction in a Straight Line on Snow- and Ice-Covered Surfaces
4. Hjort, M., Eriksson, O., Bruzelius, F.: Comprehensive study of the performance of winter tires on ice, snow and asphalt roads: the influence of tire type and wear. *Tire Sci. Technol.* **45**(3), 175–199 (2017)

Open Access This chapter is licensed under the terms of the Creative Commons Attribution 4.0 International License (<http://creativecommons.org/licenses/by/4.0/>), which permits use, sharing, adaptation, distribution and reproduction in any medium or format, as long as you give appropriate credit to the original author(s) and the source, provide a link to the Creative Commons license and indicate if changes were made.

The images or other third party material in this chapter are included in the chapter's Creative Commons license, unless indicated otherwise in a credit line to the material. If material is not included in the chapter's Creative Commons license and your intended use is not permitted by statutory regulation or exceeds the permitted use, you will need to obtain permission directly from the copyright holder.





Computing the Lateral Compliance of the Racing Line Using Trajectory Optimization

R. K. Aggarwal^(✉) and J. C. Gerdes

Stanford University, Stanford, CA 94305, USA
{raggarw,gerdes}@stanford.edu

Abstract. While race car drivers speak often on racing lines, data reveals they do not follow consistent paths lap over lap. Furthermore, autonomous racing controllers designed to track optimal paths fail to keep pace with the best professional drivers. In this paper, we assess the importance of the racing line from an optimization perspective by evaluating its dynamic sensitivity to lateral perturbations. After applying the method to the Laguna Seca Raceway, we find that there is in fact a family of trajectories that are significantly different in path but similar in lap time. This finding is consistent with prior experimental work and indicates that extracting the peak dynamic performance from a vehicle may require reasoning through this whole family of solutions—instead of tracking a single line—to operate the vehicle at its true limits.

Keywords: vehicle racing · sensitivity analysis · human racing behavior

1 Introduction

The vehicle control community has long looked at human racing for inspiration in designing autonomous control for limit maneuvering to improve vehicle safety. One concept that emerges from this analysis is the notion of a racing line, which defines a minimum-time trajectory through the track. Researchers have leveraged this concept in formulating controllers for extreme maneuvering, largely due to its amenability with path-planning and tracking paradigms popular in control systems [2]. And indeed, recent work has confirmed the efficacy of this approach, with Kegelman *et al.* demonstrating that a racing line-based vehicle controller could beat a skilled amateur racecar driver on a closed course [5].

While these results present a major achievement, the authors importantly noted that their controller could not beat a professional human driver. And more recently, comparisons to human data by Hermansdorfer *et al.* reached a similar conclusion [4]. This difference between automated control and professional drivers indicates that state-of-the-art controllers may not be extracting all of the vehicle's dynamic potential; this observed performance gap has thus continued to motivate research.

In order to address this difference, additional literature has focused on studying the human racing *style*, instead of purely the performance, in more detail.

In a related study, Kegelman *et al.* instrumented human-driven racecars at the Laguna Seca Raceway and observed that human drivers, in actuality, do not track a static line when driving [6]. Instead, they appear to anchor their racing line on certain parts of the track, such as apexes, but drive more freely between. This statistical finding is consistent with some engineering handbooks on racing strategy (e.g. Smith [8]) and broaches whether a path planning and tracking paradigm is the most effective way to extract peak performance from a vehicle.

While this empirical compliance of the racing line has been observed and quantified, it has not yet, to the best of the authors' knowledge, been rationalized from an optimization point of view. In this paper, we assess the importance of the racing line by delineating the set of near-optimal solutions from a standard minimum-time trajectory optimization. We find, perhaps intuitively, that the basin of near-optimality is wide, indicating that there is a family of vehicle trajectories that are all competitive. This suggests that what might separate the best autonomous controllers from professional drivers is not a difference in ability to track a predefined trajectory, but rather an ability to constantly operate the vehicle at its limits in a meaningful way. These results have implications for more general vehicle control that demands extreme maneuvering capability, motivating the potential of alternate control paradigms that can better extract the most performance out of the vehicle.

The rest of this paper is structured as follows. First, we briefly review the phenomenon observed in Kegelman *et al.*; namely, human drivers' apparent consistency in lap time but variance in trajectory. We then set out to understand this phenomenon better using the language of trajectory optimization. In Sect. 3, we build a minimum-time trajectory optimization to find a racing line; then, in Sect. 4, we present a technique to compute the maneuvering time sensitivity to lateral variations. In Sect. 5, we analyze the results of this method when applied to the Laguna Seca Raceway, which shows consistency with the work presented in [6]. Lastly, we offer concluding thoughts in Sect. 6.

2 Observations from Human Driving

As mentioned previously, observations from human racing behavior indicate that humans do not place a uniform weight on tracking a predefined racing line. Kegelman *et al.* quantified this by instrumenting a racecar and collecting data from skilled human drivers [6]. As depicted in Fig. 1, the drivers exhibited significant path deviation lap-over-lap, on the order of one meter. This deviation was correlated to the track geometry, however, appearing tightest near the apexes and widest on the straight sectors. Remarkably, despite the variance in driven trajectories, the recorded mean lap times across drivers were extremely consistent—within 0.5%.

3 Minimum-Time Trajectory Optimization

To better comprehend this observation, we evaluate the compliance of a racing line from an optimization point of view. The first step in this process is to solve

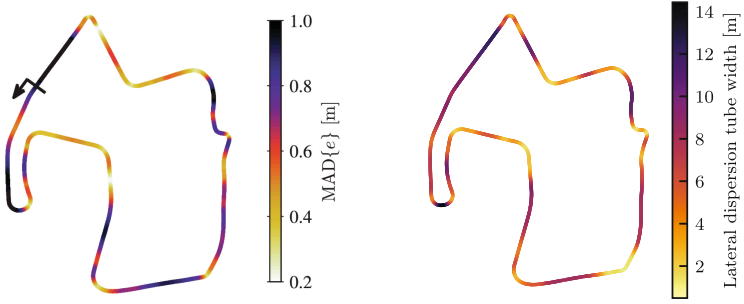


Fig. 1. Left: A visualization of the mean absolute dispersion in lateral position from the skilled human driver’s trajectories around the Laguna Seca Raceway studied in [6]. Right: The lap time sensitivity analysis proposed in this paper identifies a similar trend in lateral position compliance, suggesting that there is a tube of solutions that exhibits varying degrees of dispersion at different points along the track.

for a minimum-time line. In this section, we accomplish this using standard trajectory optimization techniques [9]. To simplify the analysis, we model the vehicle as a friction-limited point mass using parameters derived from the Grand Sport Corvette instrumented in [6].

The point mass’s state is characterized by its longitudinal velocity v_x , lateral velocity v_y , track centerline progress distance s , and lateral position to the centerline e . We assume direct force control over the point mass’s motion in the longitudinal and lateral directions (F_x and F_y). To facilitate straightforward slew rate constraints on the force inputs, we define the control vector as the force derivatives and the actual force inputs are appended to the state vector. The resulting state vector is thus defined as $\mathbf{x} := (v_x, v_y, s, e, F_x, F_y)$ with the control vector as $\mathbf{u} := (\dot{F}_x, \dot{F}_y)$. The state evolution is given by

$$\begin{aligned} \dot{v}_x &= (F_x - F_{d,x})/m + rv_y & \dot{s} &= v_x/(1 - \kappa e) & \dot{F}_x &= \dot{F}_x \\ \dot{v}_y &= (F_y - F_{d,y})/m - rv_x & \dot{e} &= v_y & \dot{F}_y &= \dot{F}_y, \end{aligned}$$

where m is the mass and κ is the local centerline curvature. The drag terms $F_{d,\{x,y\}}$ model the effects of aerodynamic resistance, and we assume a simplified model of drag which is quadratic in velocity.

In this derivation, we have added a notion of directionality to the point mass. This better facilitates encoding the difference between lateral force constraints (due to the friction circle) and longitudinal force constraints (due to the engine power limit and rear-wheel drive) in the trajectory optimization. The point mass’s xy -frame is here assumed to align with the local centerline’s se -frame; hence, the rotation rates r of these frames is given by $\kappa\dot{s}$.

The racing line optimization is now defined as

$$\underset{\mathbf{x}_{0:N}, \mathbf{u}_{0:N}}{\text{minimize}} \quad (t_N)^2 \quad (\text{Final time}) \quad (1a)$$

$$\text{subject to} \quad h_{\text{dyn}}(\mathbf{x}_i, \mathbf{u}_i, s_i, \mathbf{x}_{i+1}, \mathbf{u}_{i+1}, s_{i+1}) = 0 \quad (\text{Dynamics collocation}) \quad (1b)$$

$$|e_j| \leq (w/2) \quad (\text{Track width limits}) \quad (1c)$$

$$(F_{x_j})^2 + (F_{y_j})^2 \leq (\mu mg)^2 \quad (\text{Friction circle limit}) \quad (1d)$$

$$F_{x_j} v_{x_j} \leq P_{\text{eng}}^{\text{max}} \quad (\text{Power limit}) \quad (1e)$$

$$|\dot{F}_{x_j}|, |\dot{F}_{y_j}| \leq F_{\{x,y\}}^{\text{max}} \quad (\text{Force slew limit}) \quad (1f)$$

$$F_{x_j} \leq F_{x,\text{max}}^{\text{RWD}} \quad (\text{Rear axle force limit}), \quad (1g)$$

where $i = 0, \dots, N - 1$ and $j = 0, \dots, N$. The trajectory is discretized into $(N + 1)$ stages with the sole objective to minimize the total maneuvering time. We approximate the system's dynamics with a trapezoidal integration function h_{dyn} that uses a spatial reformulation of the dynamics as described in [9]. The final constraint imposes a drive traction limit on the F_x input, which incorporates the limits of the vehicle's rear-wheel drive and the effects of steady-state load transfer. This maximum traction force $F_{x,\text{max}}^{\text{RWD}}$ is defined as

$$F_{x,\text{max}}^{\text{RWD}} := \mu (F_{z,\text{r},\text{static}} + \Delta F_{z,\text{long}}) = \mu \left(\frac{a}{a+b} mg + \frac{F_x h_{\text{com}}}{a+b} \right).$$

4 Computing the Sensitivity of the Racing Line

Given a baseline racing line, we now investigate its lap time sensitivity to lateral perturbations. In principle, the solution gradients from Opt. 1 could be assembled to obtain a sensitivity at each position along the racing line. While these gradients generally provide useful information, in the context of a dynamical system, it is not immediately clear how to extract the absolute spread of trajectories from them. An impulse change in the lateral position e at one spatial index is nonphysical, as the vehicle's dynamics require time to develop and transition.

To address this, we explore a related method that is more dynamically consistent. The core idea is to construct optimization-based *subproblems* around the baseline solution, whose objectives are to delineate the boundary of the ϵ -suboptimal level set. Skaf and Boyd [7] provide an excellent discussion on this concept for the general optimization setting; below, we formulate an extension of this approach to the racing problem.

The main strategy is to convexify the original optimization problem around a solution and then batch solve for dispersion-maximizing subtrajectories subject to a time suboptimality constraint. For a given index-of-maximization k , the resulting subproblem is as below:

$$\begin{aligned}
& \underset{\delta \mathbf{x}_{0:N}, \delta \mathbf{u}_{0:N}}{\text{maximize}} && \pm (\delta e_k) && \text{(Path dispersion)} && (2a) \\
& \text{subject to} && h_{\text{dyn, lin}}(\delta \mathbf{x}_i, \delta \mathbf{u}_i, s_i, \\
& && \delta \mathbf{x}_{i+1}, \delta \mathbf{u}_{i+1}, s_{i+1}) = 0 && \text{(Dynamics collocation)} && (2b) \\
& && \text{Convexified con. (1c)-(1g)} && && (2c) \\
& && \delta t_N \leq \epsilon \cdot t_N^* && \text{(Time subopt).} && (2d)
\end{aligned}$$

The constraints are nearly identical to those in Opt. 1 apart from the added time suboptimality limit (2d). This subproblem relies on the linearized dynamics $h_{\text{dyn, lin}}$ about a solution from Opt. 1 using perturbational states $\delta \mathbf{x}$ and inputs $\delta \mathbf{u}$. The constraints (2c) are convexified versions of constraints (1c)-(1g) using these perturbational quantities. The resulting trajectories are hence locally dynamically feasible and better reflect the system’s dynamics than pointwise sensitivities.

5 Results for Laguna Seca and Human Data Comparison

After solving for a baseline racing line at Laguna Seca, we now solve the dispersion-maximizing subproblems at n_{sp} evenly spaced indices to produce a bundle of ϵ -suboptimal trajectories. The optimization problems are constructed and solved with the CasADi and CVXPY packages [1, 3]. Table 1 lists further parameters.

Figure 1 indicates that the lateral spread of suboptimal trajectories is not uniform across the whole track, appearing tightest in the corners and widest on the straights. This observation is consistent with the conclusion in [6] that driven trajectories “anchor” at the apexes and flow more freely in between. Figure 2 plots the lateral deviance against the path curvature showing that the basin of suboptimal solutions is narrowest at high curvature. These data suggest that the variability displayed by human drivers is not tracking error on an ideal line but instead may correspond to the selection of a nearly optimal solution most suited to the track and car conditions at that moment.

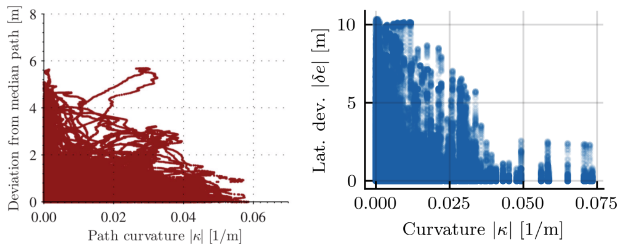


Fig. 2. Lateral path deviation plotted against the local curvature. Our analysis, right, reveals a similar inverse relationship as observed in the human data from [6], left.

Table 1. Vehicle and optimization parameters

Description	Variable	Value	Units
Vehicle mass	m	1014	kg
Center of mass (c.o.m.) height	h_{com}	0.5	m
Distance from c.o.m. to front, rear axle	a, b	1.20, 1.29	m
Drag coefficient	C_d	0.4	$\text{N}/(\text{m}/\text{s})^2$
Friction coefficient	μ	0.90	[-]
Maximum engine power	$P_{\text{eng}}^{\text{max}}$	361	kW
Maximum force slew rate	$\dot{F}_{\{x,y\}}^{\text{max}}$	10.	kN/s
No. of discretization steps, no. of subproblems	N, n_{sp}	1000, 1000	[-]
Time epsilon	ϵ	0.1	%

6 Conclusion

While the racing line’s compliance has been described qualitatively in handbooks on racing and quantified with analysis of instrumented race cars, in this paper we aimed to validate this phenomenon using mathematical optimization. Our results are consistent with prior observations and suggest that there is a tube of solutions that achieves the minimum-time objective. Automated vehicles tracking a fixed line have no guarantee that their closed-loop trajectory, inclusive of corrections, falls into this tube. This analysis motivates investigating control schemes that move beyond path-planning and tracking to consider optimality of the closed-loop trajectories.

References

1. Andersson, J.A.E., Gillis, J., Horn, G., Rawlings, J.B., Diehl, M.: CasADi: a software framework for nonlinear optimization and optimal control. *Math. Prog. Comp.* **11**(1), 1–36 (2019)
2. Betz, J., Zheng, H., Liniger, A., Rosolia, U., Karle, P., Behl, M., Krovi, V., Mangharam, R.: Autonomous vehicles on the edge: a survey on autonomous vehicle racing. *IEEE Open J. Intell. Transp. Syst.* **3**, 458–488 (2022)
3. Diamond, S., Boyd, S.: CVXPY: a Python-embedded modeling language for convex optimization. *JMLR* **17**(83), 1–5 (2016)
4. Hermansdorfer, L., Betz, J., Lienkamp, M.: Benchmarking of a software stack for autonomous racing against a professional human race driver. In: *Intl. Conf. on Eco. Veh. and Ren. Ener.*, pp. 1–8. IEEE, Monte-Carlo, Monaco (2020)
5. Kegelman, J.: Learning from professional race car drivers to make automated vehicles safer. PhD Dissertation, Stanford University (2018)
6. Kegelman, J.C., Harbott, L.K., Gerdes, J.C.: Insights into vehicle trajectories at the handling limits: analysing open data from race car drivers. *Veh. Syst. Dyn.* **55**(2), 191–207 (2017)
7. Skaf, J., Boyd, S.: Techniques for exploring the suboptimal set. *Optim. Eng.* **11**(2), 319–337 (2010)

8. Smith, C.: Drive to Win: The Essential Guide to Race Driving, 1st edn. Carroll Smith Consulting Inc., Rolling Hills Estates, California, USA (1996)
9. Subosits, J.K., Gerdes, J.C.: Impacts of model fidelity on trajectory optimization for autonomous vehicles in extreme maneuvers. IEEE Trans. Intell. Veh. **6**(3), 546–558 (2021)

Open Access This chapter is licensed under the terms of the Creative Commons Attribution 4.0 International License (<http://creativecommons.org/licenses/by/4.0/>), which permits use, sharing, adaptation, distribution and reproduction in any medium or format, as long as you give appropriate credit to the original author(s) and the source, provide a link to the Creative Commons license and indicate if changes were made.

The images or other third party material in this chapter are included in the chapter's Creative Commons license, unless indicated otherwise in a credit line to the material. If material is not included in the chapter's Creative Commons license and your intended use is not permitted by statutory regulation or exceeds the permitted use, you will need to obtain permission directly from the copyright holder.





State Estimation and Sensorimotor Noise in a Driver Steering Model with a Gaussian Process Internal Model

Harry Fieldhouse^(✉) and David Cole

Department of Engineering, University of Cambridge, Cambridge CB2 1PZ, UK
hamf2@cam.ac.uk

Abstract. Refinements to a mathematical model of human drivers' steering control incorporating driver learning are reported. State estimation and realistic sensorimotor noise sources are introduced to the driver model to better represent neural processes. It is found that the driver model exhibits the expected learning behaviour in terms of estimation and control performance. Further work is planned to validate the model experimentally.

Keywords: Driver Modelling · Human Learning · State Estimation · Gaussian Process · Model Predictive Control

1 Introduction

Realistic mathematical driver steering control models are useful tools for developing driver assistance systems such as stability control and lane-keeping assistance. Driver models allow the vehicle design space to be explored safely and at low cost.

State of the art driver models typically use optimisation-based predictive control algorithms. These require a prediction model, which in a human context is known as the internal model, and represents the human understanding of the vehicle dynamics. The internal model is often assumed to be an accurate deterministic representation of the vehicle dynamics. However, it seems likely that in many cases a driver has an inaccurate and uncertain understanding of the vehicle dynamics, particularly in unfamiliar nonlinear regimes of operation.

Recently, a new approach has been taken by the authors, using Model Predictive Control (MPC) with a Gaussian Process (GP) providing a data-driven internal prediction model of the vehicle dynamics [4]. The motivation for using a GP is that it represents more closely the experience-based learning process and prediction uncertainty of the human driver. This approach was inspired by the

The work described in this paper is part of PhD research at Cambridge University Engineering Department, grant number G116038, funded by Toyota Motor Europe (TME). The industrial supervisor is Xabier Carrera Akutain of TME.

‘predictive processing’ hypothesis which has gained traction in several academic communities [2].

An example of a partially learnt GP model of nonlinear lateral-yaw vehicle dynamics is shown in Fig. 1, predicting the mean and variance of the vehicle lateral velocity state at the next time step given current vehicle states (here all zero) and steering angle input (on x-axis). The learning behaviour of the driver model is apparent in Fig. 2, which compares the RMS path error with RMS handwheel velocity (akin to control effort) over the course of twelve successive avoidance manoeuvres (elk or moose test).

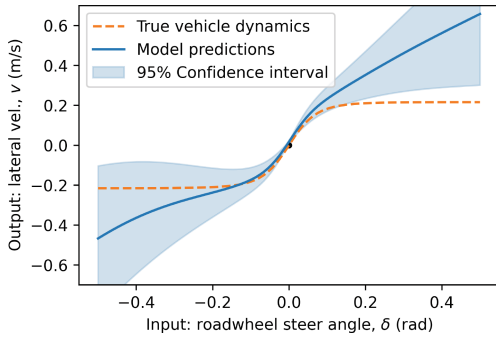


Fig. 1. Part-learnt GP model of nonlinear lateral-yaw vehicle dynamics [4]. Solid blue line is the mean prediction, light blue shaded area is the 95% confidence interval.

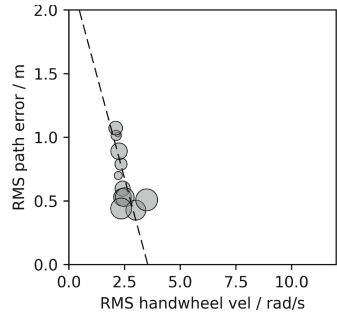


Fig. 2. RMS path error against RMS handwheel velocity for a simulated driver performing twelve successive avoidance manoeuvres. The smallest circle is the first manoeuvre and the largest is the twelfth. The dashed line is a diagonal regression.[4].

It is reported in [4] that the simulated learning behaviour seen in Fig. 2 is similar to that measured in some of the human test subjects that performed the manoeuvres in a real vehicle on a test track. The behaviour can be described as ‘cautious’, where control activity increases and path error decreases with successive manoeuvres. Some other drivers in the experiment displayed ‘adventurous’ behaviour, characterised by control activity and path error decreasing with successive manoeuvres.

The MPC+GP driver model architecture described in [4] is shown in Fig. 3, with additional elements introduced in the present work shown in orange and grey to be described in the next sections. The model includes additive memory data noise but no sensory measurement noise. The GP internal model generates predictions. Control actions are optimised to minimise a cost function that penalises predicted lateral and yaw deviations from a previewed target path, together with other penalties on GP internal model prediction variance and the

first and second derivatives of steering angle with respect to time. Cautious and adventurous steering behaviours are generated by adjusting the penalty on GP internal model prediction variance [4].

The aim of the work in this paper is to improve the MPC+GP driver steering model by sensory noise and state estimation. Based on experimental observations in the field of computational neuroscience, it is believed that human sensory measurement noise is signal-dependent, where the noise is proportional to the signal being measured [7]. In human control, there is evidence that state estimation is performed by the brain in a probabilistically optimal, Bayesian manner [3, 5], using internal model predictions to improve the accuracy of the state determination and mitigate effects of sensory noise. In the present paper the existing MPC+GP driver model is extended to include realistic sensorimotor noise and a state estimator that uses the GP for the state prediction step. The performance of the model is then investigated.

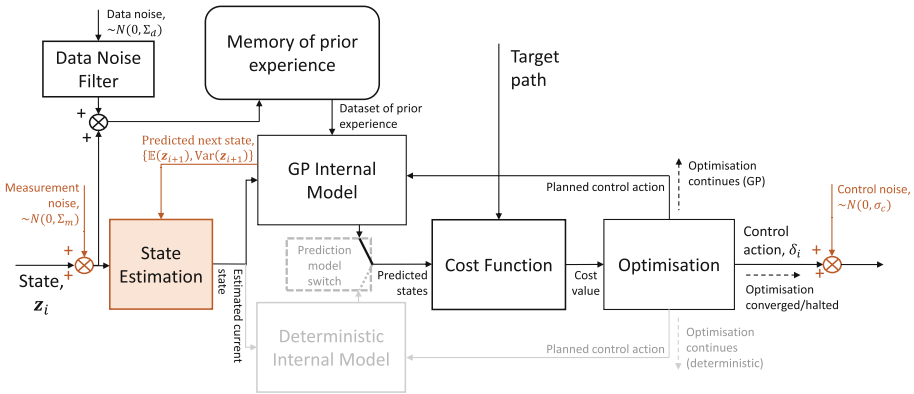


Fig. 3. Driver model architecture from [4] with new elements shown in orange and elements used solely for analysis shown in grey.

2 Noise Model and State Estimation

Signal-dependent noise sources are added to represent measurement noise and control (or process) noise, as shown in orange in Fig. 3. The noise is modelled as shown in Fig. 4, with constant signal to noise ratio (SNR) and a noise floor to represent sensory perception threshold.

With reference to the variables in Fig. 3, measurement variance is diagonal, with $(\Sigma_m)_{k,k} = \max((z_{i,j})_k^2 (s_m)_k^{-1}, (n_m)_k)$, and control variance, $\sigma_c = \max(\delta_i^2 s_c^{-1}, n_c)$. Here $z_{i,j}$ is the state vector at the i^{th} timestep of the j^{th} manoeuvre, s_m is the measurement SNR for each state dimension, n_m is the measurement noise floor, δ_i is the planned control action for the i^{th} timestep, s_c and n_c are the control SNR and noise floor.

Physiologically plausible values for SNRs and noise floors can be ascertained from the literature on sensory thresholds and just noticeable differences (JNDs), for example [3, 6, 7]. SNRs are typically in the region of unity; a value of 1.6 is used for the results in the present paper.

The *State Estimation* block (Fig. 3) is implemented as a Kalman Filter. The state estimation process uses the *GP Internal Model* to predict the next state of the vehicle given the current state and control input. From this, with the predicted state, the measured state and the variances of each, Kalman Filtering is used to update the state estimate probabilistically. This state estimate is then used as the believed current state from which to predict future states when optimising the control action. The equations for the Kalman Filter prediction and update are implemented as follows, based on [1]:

$$\begin{aligned}
 \text{Prediction Step: } \hat{\mathbf{x}}_{k|k-1} &= \text{GP Prediction}(\hat{\mathbf{x}}_{k-1|k-1}, u_{k-1}P_{k-1|k-1}) \\
 P_{k|k-1} &= \text{GP Variance}(\hat{\mathbf{x}}_{k-1|k-1}, u_{k-1}, P_{k-1|k-1}) \\
 \text{Update Step: } K_k &= P_{k|k-1}H^T(H P_{k|k-1}H^T + R_k)^{-1} \\
 \hat{\mathbf{x}}_{k|k} &= \hat{\mathbf{x}}_{k|k-1} + K_k(\mathbf{y}_k - H\hat{\mathbf{x}}_{k|k-1}) \\
 P_{k|k} &= (I - K_kH)P_{k|k-1}
 \end{aligned}$$

where $\hat{\mathbf{x}}_{k|k-1}$ and $P_{k|k-1}$ are the GP model predicted current state mean and covariance, $\hat{\mathbf{x}}_{k-1|k-1}$ and $P_{k-1|k-1}$ are the previous state estimate mean and covariance and u_{k-1} is the previous control input.

The Kalman filtered state estimates are not used in the memory dataset for training the GP internal model. This is because the Kalman filtering introduces a bias to the data towards the errors in the learnt model, so the use of this filtered data significantly reduces the learning rate. Instead, the GP internal model is trained on the raw measured data, and the Kalman Filter is used only for state estimation during the control optimisation process. As the GP internal model improves and the state estimate becomes more accurate, better predictions of future states can be made leading to better control performance.

3 Simulation Results and Discussion

In this section simulations were performed with the control noise in Fig. 3 set to zero. The measurement noise was set to give an SNR of 1.6. Simulations were initially performed with the *Deterministic Internal Model* block shown in grey in Fig. 3 switched in and data noise set to zero. This enabled the effect of GP learning on state estimation to be investigated separately from the GP’s effect on control optimisation. The GP was initialised with fifty data points randomly

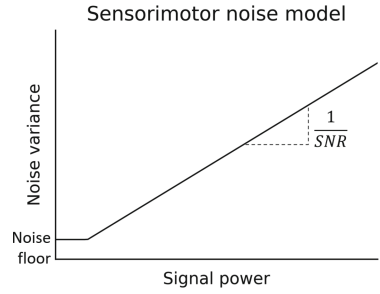


Fig. 4. Measurement variance relation to signal power for approximation used [6].

distributed within the vehicle’s operating envelope. The driver steering model was then run to perform twelve successive elk avoidance manoeuvres, with the memory dataset and the GP updated after each of the twelve manoeuvres. For the purpose of determining statistically reliable results, the sequence of twelve manoeuvres was repeated one hundred times, each time with different uncorrelated noise signals.

The performance of the state estimator in each of the twelve manoeuvres was quantified by calculating the ratio of the variance of the true state to the variance of the state estimation error. This ratio is also denoted as a SNR. However, to avoid the calculated SNR being dependent on the performance of the controller in each manoeuvre, the vehicle states during each manoeuvre were not used in calculating the estimator’s SNR. Instead, a set of 2000 independent randomly generated starting states with measurement noise of SNR=1.6 was used to evaluate the performance of the state estimator, using the GP internal model from each of the twelve manoeuvres. The SNR of the estimator was also calculated for multiple timesteps beyond the starting state.

It can be seen in Fig. 5 that the SNR of the estimate of lateral velocity improves over the course of the twelve manoeuvres as the GP internal model learns the vehicle dynamics. The SNR reduces as more timesteps are advanced, converging to an SNR of around 3 for the first manoeuvre and 10 for the final manoeuvre, which is significantly improved from the measurement SNR of 1.6 and confirms the effectiveness of the estimator.

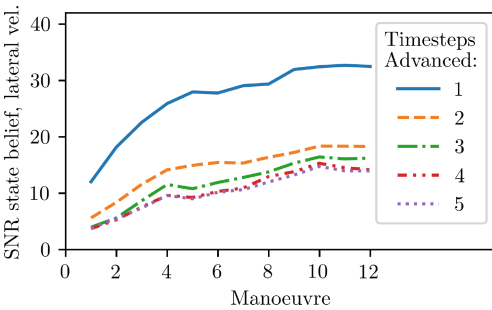


Fig. 5. Plot of the median SNR of state estimates to true states against manoeuvre number. The SNR is calculated over one hundred repeats of twelve elk test manoeuvres on a test set of 2000 randomly generated starting states. Different lines are plotted for additional timesteps advanced from the starting states.

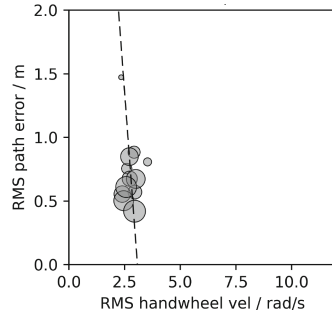


Fig. 6. Conflict plot showing RMS path error against RMS handwheel velocity for the MPC+GP driver model with sensory noise and state estimation.

Another simulation was run with the *prediction model switch* (Fig. 3) set to use the GP internal model for control optimisation as well as for state estimation. Figure 6 shows the RMS path error against RMS handwheel velocity over twelve

elk avoidance manoeuvres. The control performance and learning behaviour of the new model are similar to that of the earlier model seen in Fig. 2, and therefore similar to the measured behaviour of human test subjects reported in [4].

The work reported in this paper contributes increased realism of driver models for use in virtual vehicle development. Work is planned to add visual and vestibular sensory dynamics to the driver steering model, and to validate further the model against experiments with human test subjects.

4 Conclusion

- There is a need for realistic mathematical driver steering control models that represent human learning behaviour.
- Recent work by the authors has combined MPC with a GP internal model.
- The present work adds signal-dependent sensorimotor noise and state estimation to the MPC+GP driver model.
- Simulation results show that the state estimator with a GP internal model exhibits the expected improvement in estimation accuracy with successive manoeuvres.
- The results also show that control performance and learning behaviour are similar to measured human behaviour reported recently.
- Further work is planned to extend the model to include visual and vestibular sensory dynamics, and to perform more experimental validation.

References

1. Chui, C.K., Chen, G.: Kalman Filtering. Springer, Cham (2017)
2. Ciria, A., Schillaci, G., Pezzulo, G., Hafner, V.V., Lara, B.: Predictive processing in cognitive robotics: a review. *Neural Comput.* **33**, 1402–1432 (2021)
3. Faisal, A.A., Selen, L.P., Wolpert, D.M.: Noise in the nervous system. *Nat. Rev. Neurosci.* **9**, 292–303 (2008)
4. Fieldhouse, H., Keen, S., Cole, D.: Measurement and modelling of driver learning of steering control during successive obstacle avoidance manoeuvres. Apollo - University of Cambridge Repository. Submitted to *Vehicle System Dynamics* (2024). <https://doi.org/10.17863/CAM.109315>
5. Körding, K.P., Wolpert, D.M.: Bayesian integration in sensorimotor learning. *Nature* **427**, 244–247 (2004)
6. Nash, C.J.: Measurement and modelling of human sensory feedback in car driving. Ph.D. thesis, Department of Engineering, University of Cambridge (2018)
7. Todorov, E.: Stochastic optimal control and estimation methods adapted to the noise characteristics of the sensorimotor system. *Neural Comput.* **17**, 1084–1108 (2005)




Open Access This chapter is licensed under the terms of the Creative Commons Attribution 4.0 International License (<http://creativecommons.org/licenses/by/4.0/>), which permits use, sharing, adaptation, distribution and reproduction in any medium or format, as long as you give appropriate credit to the original author(s) and the source, provide a link to the Creative Commons license and indicate if changes were made.

The images or other third party material in this chapter are included in the chapter's Creative Commons license, unless indicated otherwise in a credit line to the material. If material is not included in the chapter's Creative Commons license and your intended use is not permitted by statutory regulation or exceeds the permitted use, you will need to obtain permission directly from the copyright holder.





Energy Efficiency Oriented Robust Model Predictive Stability Control for Autonomous Electric Vehicles

Ziang Tian , Huilong Yu ^(✉) , and Junqiang Xi 

School of Mechanical Engineering, Beijing Institute of Technology, Beijing, China
huilong.yu@bit.edu.cn

Abstract. The four-wheel independent steering and drive autonomous vehicle is a typical over-actuated system. The complexity of controlling it is increasing with the number of actuators. Since the model-based approach can solve the constrained multiple output problem, it is mostly utilized in the existing works. However, they usually investigate a single objective optimization, while employing simplified prediction models to relieve computational burdens. In this case, the robustness of the controller will inevitably suffer from model mismatch, which makes it hard to fulfill the various demands of autonomous driving. This work proposes a multi-objective control framework, which optimizes stability and energy efficiency simultaneously. Furthermore, robust model predictive control is introduced to address the model mismatch. Compared with the state-of-the-art, the effectiveness of the proposed approach has been validated by hardware-in-the-loop tests. Under the double lane change Maneuver, the longitudinal speed is maintained 1.7% higher. The vehicle stability is enhanced, while the motor energy loss and tire slip energy are reduced by 23.3% and 8.3%, respectively.

Keywords: multi-objective optimization · tube-based robust model predictive control · stability · energy efficiency

1 Introduction

With the development of automotive intelligence and electrification, the requirements for autonomous electric vehicles (AEVs) are expanded from safety to energy efficiency. Four-wheel independent steering and drive (4WIS-4WID) technologies are the current hotspots. Their prominent advantage is flexible control, which can further enhance stability when reasonably allocating torque vectoring and steering [1]. However, improper allocation may result in tire wear and additional energy consumption, thus reducing stability and energy efficiency.

In existing works, MPC has shown remarkable superiority in solving AEV stability control problems with multiple constraints [2]. However, it is always affected by discrepancies between actual vehicles and models, which always appear in practice and impact vehicle safety [3]. To address this issue, Tube-based RMPC is proposed to satisfy the original constraints under the worst conditions

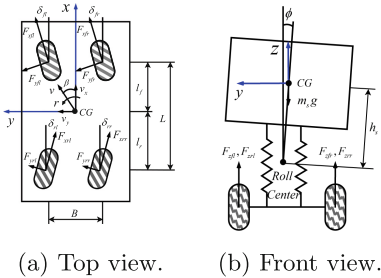
and shows outstanding robustness [4]. Besides stability, EVs also have a critical issue of energy efficiency. Reducing motor energy consumption and tire energy dissipation are the main approaches [5]. The UniTire model is widely applied to calculate tire slip power because of its accuracy and simplicity. To optimize energy efficiency while enhancing stability simultaneously, hierarchical control is a common approach [6]. The stability is ensured in the upper layer, and the lower layer controls actuators while reducing energy consumption. However, objectives are not optimized together in these works, causing suboptimal results.

Reviewing the state-of-the-art, the impacts of excessive tire slippage on stability and energy consumption are rarely considered while designing a path tracking strategy. In addition, most hierarchical approaches construct single-objective optimization problems in each layer, which may lead to underperformance. To reduce the computational burden, simplified models are typically used to predict vehicle states, inevitably leading to model mismatches that affect the robustness of the MPC controller. To address the problems above, we propose an RMPC-based multi-objective path tracking strategy in this work. The original contributions are: 1) An integrated path tracking framework is proposed, which realizes steering and torque vectoring while simultaneously considering stabilization, motor power loss, and tire slip power. 2) To ensure performance despite model deviations, an RMPC-based controller is designed to address the tire stiffness error of the model.

The rest of this paper is organized as follows. In the second section, the models built for multi-objective control are introduced. The RMPC-based integrated path tracking framework is proposed in the third section. Additionally, the performance of the proposed strategy is verified in the fourth section by hardware-in-the-loop (HIL) tests. Finally, conclusions are presented in the fifth section.

2 System Modeling

The 4-degree-of-freedom (4DOF) vehicle dynamic model is shown in Fig. 1. Its lateral, longitudinal, yaw, and roll dynamics equations are given as (1), where m_s represent the sprung mass, respectively, h_s represents the height of the sprung



(a) Top view.

(b) Front view.

$$m(\dot{V}_x - V_x \beta r) + F_a = \sum F_x, \quad (1a)$$

$$mV_x(\dot{\beta} + r) + m_s h_s \ddot{\phi} = \sum F_y, \quad (1b)$$

$$I_z \dot{r} - I_{xz} \ddot{\phi} = \sum M_z, \quad (1c)$$

$$I_x \ddot{\phi} - I_{xz} \dot{r} = \sum M_x. \quad (1d)$$

Fig. 1. 4DOF dynamics model.

mass, I_z , I_x and I_{xz} represent the moment and product of inertia, respectively. β is the sideslip angle, r is the yaw rate, ϕ is the roll angle. F_a donates the air resistance, ΣM_z , and ΣM_x donate the combined moments, respectively.

The tire model utilized in this work is linear. Its rotational dynamics equation is derived as:

$$J_w \dot{\omega}_i = T_{m,i} - T_{r,i} - T_{b,i} - R_w F_{x,i}, \quad (2)$$

where J_w and R_w donate the wheel rotational inertia and effective radius, respectively. ω_i represents the rotational speed. $T_{m,i}$ and $T_{b,i}$ are the driving and braking torques, $T_{r,i}$ is the rolling resistance torque, and $F_{x,i}$ is the longitudinal driving force, where $i = \{fl, fr, rl, rr\}$ represents the wheel location.

A UniTire semi-empirical model is employed to accurately calculate the tire slip power, which calculates slip force and velocity by analyzing forces between slip regions and adhesion in the tire contact patch as follows:

$$V_{s,j,i} = -\frac{s_{j,i}}{1 - s_{j,i}} \cdot V_{j,i} \cdot \cos \alpha_i, F_{s,j,i} = F_{s,i} \cdot \frac{s_{j,i}}{\sqrt{s_{j,i}^2 + s_{j,i}^2}}, \quad (3)$$

where $F_{s,i}$ is the resultant slip force, $j = \{x, y\}$ is the direction of force.

The power of tire slip $P_{s,t}$ is given as follows:

$$P_{s,t} = \sum_{i=fl,fr,rl,rr} F_{sx,i} V_{sx,i} + F_{sy,i} V_{sy,i}. \quad (4)$$

The power loss generated by the in-wheel motor $P_{ml,t}$ can be fitted by a cubic polynomial:

$$P_{ml,t} = \sum_{i=fl,fr,rl,rr} a(n_i) T_{m,i}^3 + b(n_i) T_{m,i}^2 + c(n_i) T_{m,i} + d(n_i), \quad (5)$$

where a , b , c , and d are fitted coefficients determined by motor speed n_i .

Applying the Taylor expansion and zero-order hold (ZOH) methods to linearize and discretize the dynamics equation as follows:

$$\begin{cases} x(k+1) &= \bar{A}_k x(k) + \bar{B}_{k1} u(k) + \bar{B}_{k2} w(k) + d_{t1} \\ y(k) &= C_t x(k) + D_t u(k) + d_{t2} \end{cases}, \quad (6)$$

where the state vector $x = [V_x, Y, \beta, r, \varphi, \dot{\phi}, \ddot{\phi}, s_{x,fl}, s_{x,fr}, s_{x,rl}, s_{x,rr}]^T$, the control vector $u = [T_{m,fl}, T_{m,fr}, T_{m,rl}, T_{m,rr}, \delta_{f,l}, \delta_{f,r}, \delta_{r,l}, \delta_{r,r}]^T$, the output vector $y = [V_x, Y, \beta, \varphi, r, P_{ml,t}, P_{s,t}]^T$, and $w = [C_{x,f}, C_{x,r}, C_{\alpha,f}, C_{\alpha,r}]^T$ represents the bounded disturbance.

3 Controller Design

As shown in Fig. 2, a multi-objective controller framework is proposed. To handle multiple objectives in a single layer, an integrated tube-based RMPC is designed, which includes contractive constraints and multi-objective cost functions. The motion states constraints are set to ensure vehicle stability. However, under

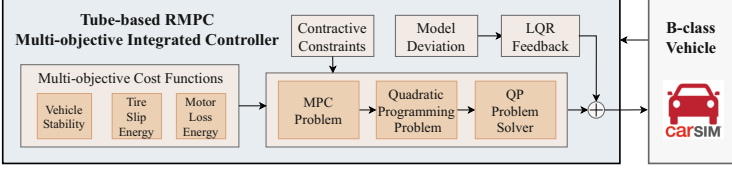


Fig. 2. Framework of the multi-objective integrated path tracking controller.

aggressive driving scenarios, changes in cornering or longitudinal stiffness will cause bounded disturbances to the system.

Equation (6) can be rewritten as a nominal system without disturbance in the actual system. The state variable is denoted by z and satisfies $z(0) = x(0)$, while the control variable is represented by v and the output by $\eta = y$. Therefore, the state error between the actual system and the nominal system is calculated as $e(k) = x(k) - z(k)$. The RMPC introduces a linear state feedback for $e(k)$ to compute the control $u(k) = v(k) + Ke(k)$, where the feedback gain K is designed to satisfy $|\text{eig}(\bar{A}_t - \bar{B}_{t1}K)| < 1$, thus $A_K = \bar{A}_t - \bar{B}_{t1}K$ is Hurwitz.

Since the disturbance $w \in \mathbb{W}$ is bounded, it is proven to exist a robust positively invariant set $A_K\Gamma \oplus \mathbb{W} \subset \Gamma$, where \oplus is Minkowski sum. Therefore, contractive constraints of the state and control for the nominal system are given as $\mathbb{Z} \in \mathbb{X} \ominus \Gamma, \mathbb{V} \in \mathbb{U} \ominus K\Gamma$, where \ominus is Pontryagin difference, \mathbb{X} and \mathbb{U} are the polyhedron of the state and control constraints. The cost function of the multi-objective optimization problem is given as:

$$J_{MPC} = \sum_{i=1}^{N_p} \|\eta(i) - \eta_{zref}(i)\|_w^2 + \|z(N_p) - z_{ref}(N_p)\|_P^2 + \sum_{i=0}^{N_c-1} \Delta v(i)_R^2 \quad (7)$$

where, N_p and N_c donate the prediction and control horizon. w , P , and R represent weight matrices. Therefore, the nominal MPC problem is designed as:

$$\min_{\Delta u} J_{MPC}, \quad (8a)$$

$$\text{s.t. } z(k+1) = A_t(k)z(k) + B_{t1}(k)v(k) + d_{t1}, \quad (8b)$$

$$|\Delta v| \leq \Delta v_{\max}, \quad (8c)$$

$$z_i \in \mathbb{Z}, \quad \forall i \in [0, N_p - 1], \quad (8d)$$

$$v_i \in \mathbb{V}, \quad \forall i \in [0, N_p - 1], \quad (8e)$$

$$z_{N_p} \in \mathbb{Z}_f, \quad (8f)$$

where \mathbb{Z}_f is set to ensure asymptotic stability and recursive feasibility. A quadratic programming problem (QP) is built, while the active set method is utilized to generate the real control input $u^* = v^* + K(x - z^*)$.

4 HIL Test Results

Considering driving safety under high-speed conditions and the reliability of the steer-by-wire system (SBW), HIL tests are employed to evaluate the performance of the proposed strategy. A double lane change (DLC) case is designed. The friction coefficient of the road is 0.85, the target speed is 100 km/h. Optimization objectives include vehicle stability (VS), tire slip energy (TSE), and motor energy loss (MEL). The state-of-the-art approaches are compared to show the advantages of the proposed method: 1) Hierarchical MPC (HMPC), a hierarchical control strategy introduced in [7]; 2) Single-layer MPC (SMPC), a strategy that employs a single layer instead of a hierarchical structure; 3) Single-layer robust MPC (SRMPC), the strategy proposed in this work.

Fig. 3-5 shows the inputs and outputs. Under aggressive maneuvers, the HMPC tends to input higher torques and track the reference path better. However, its speed-holding ability and energy efficiency are underperformed. In contrast, the single-layer strategies input smaller torques due to the optimization of multiple objectives and reduce more energy consumption. Additionally, the approach proposed in this work shows the best performance. Compared with the other strategies, it maintains longitudinal speed 2.8% and 1.7% higher, reduces 43.3% and 23.3% motor energy loss, 12.4% and 8.3% tire slip energy dissipation. Meanwhile, as shown in Fig. 5(b)–(d), the vehicle applying the proposed method has the best stability. This is achieved by effectively addressing the model mismatch shown in Fig. 5(g)–(h).

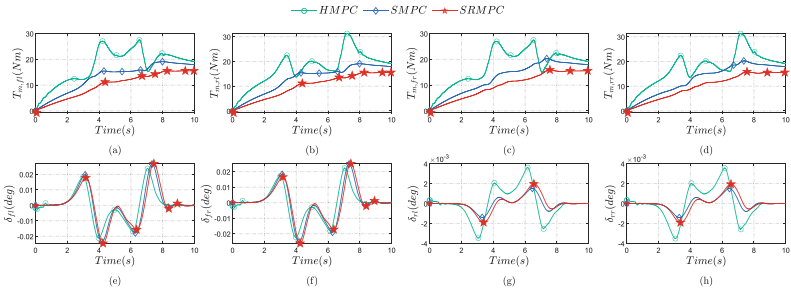


Fig. 3. Comparison of torques and steering angles under DLC case. (a)–(d) each wheel torque; (e)–(h) each wheel steering angle.

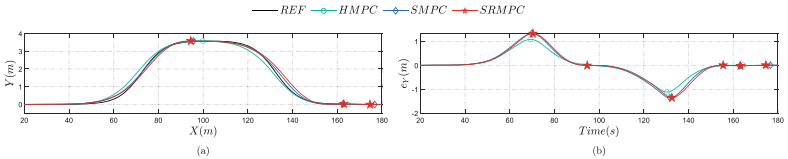


Fig. 4. Comparison of reference path tracking errors under DLC case.

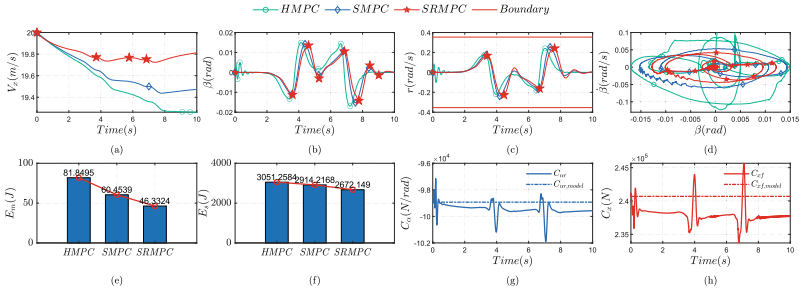


Fig. 5. Comparison of the results under DLC case. (a) longitudinal speed; (b) side slip angle; (c) yaw rate; (d) sideslip angle rate - sideslip angle phase diagram; (e)–(f) energy consumption; (g)–(h) tire stiffness changes.

5 Conclusion

In this work, an RMPC-based integrated multi-objective path tracking framework is devised and validated in HIL. Experiment results demonstrate that the proposed strategy can effectively enhance vehicle stability while improving energy efficiency. Compared with the state-of-the-art, the longitudinal speed is maintained 1.7% higher, while the motor energy loss and tire slip energy are reduced by 23.3% and 8.3% under the DLC case, respectively. HIL test shows that the designed RMPC-based controller can address the model mismatch well and further enhance vehicle performance. In the future, the proposed strategy will be verified under more complex maneuvers.

References

1. Jing, H., Jia, F., Liu, Z.: Multi-objective optimal control allocation for an over-actuated electric vehicle. *IEEE Access* **6**, 4824–4833 (2018)
2. Li, S., Wang, G., Zhang, B., Yu, Z., Cui, G.: Vehicle yaw stability control at the handling limits based on model predictive control. *Int. J. Automot. Technol.* **21**, 361–370 (2020)
3. Hu, K., Cheng, K.: Robust tube-based model predictive control for autonomous vehicle path tracking. *IEEE Access* **10**, 134389–134403 (2022)
4. Mayne, D.Q.: Model predictive control: recent developments and future promise. *Automatica* **50**(12), 2967–2986 (2014)
5. Zhao, B., Xu, N., Chen, H., Guo, K., Huang, Y.: Design and experimental evaluations on energy-efficient control for 4wimd-evs considering tire slip energy. *IEEE Trans. Veh. Technol.* **69**(12), 14631–14644 (2020)
6. De Filippis, G., Lenzo, B., Sorniotti, A., Gruber, P., De Nijs, W.: Energy-efficient torque-vectoring control of electric vehicles with multiple drivetrains. *IEEE Trans. Veh. Technol.* **67**(6), 4702–4715 (2018)
7. Zhao, B., Xu, N., Chen, H., Guo, K., Huang, Y.: Stability control of electric vehicles with in-wheel motors by considering tire slip energy. *Mech. Syst. Signal Process.* **118**, 340–359 (2019)

Open Access This chapter is licensed under the terms of the Creative Commons Attribution 4.0 International License (<http://creativecommons.org/licenses/by/4.0/>), which permits use, sharing, adaptation, distribution and reproduction in any medium or format, as long as you give appropriate credit to the original author(s) and the source, provide a link to the Creative Commons license and indicate if changes were made.

The images or other third party material in this chapter are included in the chapter's Creative Commons license, unless indicated otherwise in a credit line to the material. If material is not included in the chapter's Creative Commons license and your intended use is not permitted by statutory regulation or exceeds the permitted use, you will need to obtain permission directly from the copyright holder.





Profile Generation of Cooperative Driving in Urban Intersections for Energetic Evaluation

Maximilian Flormann¹ (✉) , Axel Sturm¹ , Roman Henze¹,
and Pongsathorn Raksincharoensak² 

¹ Institut für Fahrzeugtechnik, Technische Universität Braunschweig, 38106 Braunschweig, Germany

m.flormann@tu-braunschweig.de

² Department of Mechanical Systems Engineering, Tokyo University of Agriculture and Technology, Fuchu, Japan

Abstract. In the context of urban smart mobility, automated vehicles communicating with each other, surrounding infrastructure, and other traffic participants yield the use for cooperative driving in urban environments. This, alongside an increase in safety and comfort, can help to reduce fuel and energy consumption individually and with regard to the cooperative vehicle cluster. In this paper we are addressing the impact urban cooperative driving has on the energy consumption of electric vehicles and further investigate the impact on drive systems and their layout, as well as the impact different control strategies of the cooperative network and scenarios with varying vehicles densities have. In order to evaluate the impact, defined driving profiles from a graph based optimization for cooperation networks are evaluated with regard to their energy consumption. Based upon the results the overall energetic impact of different intersection approaching strategies as well as the drive system impact are discussed.

Keywords: Automated driving · electric drive systems · energy consumption reduction · cooperative driving · drive system optimization · graph optimization

1 Introduction

In the context of urban smart mobility networks, it is essential for vehicles to establish communication links with one another, the surrounding infrastructure, and fellow traffic participants. Through the implementation of Vehicle2X (V2X) communication, the exchange of crucial data such as the vehicles' positions, driving dynamics and intentions becomes feasible and yield the extension of the complexity of automated driving functions, such as cooperative driving in complex urban scenarios [1]. This paper utilizes a methodology for the cooperative driving of automated vehicles in mixed traffic scenarios. This methodology applies V2X-communication and a graph-based cooperation algorithm to optimize urban cooperative intersection scenarios with regard to overall time and energy efficiency [2]. The resulting vehicle-individual trajectories can be further utilized by optimizing dedicated battery electric vehicles (BEV) drive systems with

consideration of the automated driving system [3]. The impact of automated driving systems on the layout of drive systems and fuel and energy consumption was analyzed previously [4, 5]. Within this paper, the impact of connected driving on the dimensioning of the drivetrain and the energy consumption is analyzed in comparison to customer operation.

2 Methodology and Approach

The urban traffic scenarios analyzed in this paper are representative excerpts from an urban traffic simulation applied to the research intersection in Braunschweig. These scenarios are derived from real world measurements by a test vehicle equipped with LIDARs. The scenarios involve various (BEV) vehicles in a complex urban environment, as shown in Fig. 1.

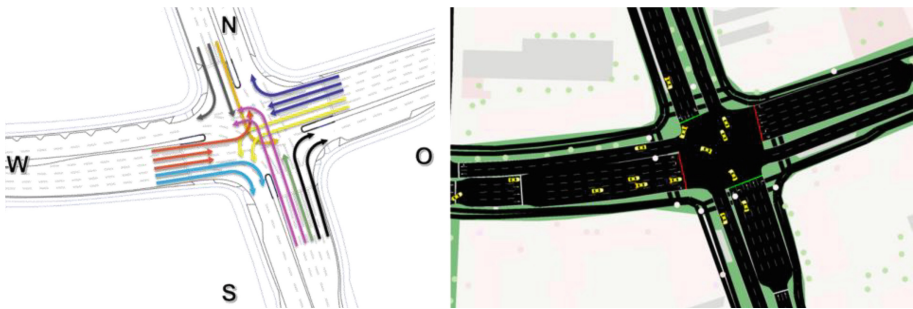


Fig. 1. Research intersection in Braunschweig with marked traffic rules and the resulting SUMO Simulation

These vehicles form a cooperative network with each other. The trivial approach of solving the conflicts inherent in such a network are traffic lights with fixed time control. Alternatively, in the absence of traffic lights, a trivial “first come first serve” approach, where every vehicle is driving in the order it arrived at the intersection is applied. Both these approaches can be optimized with regard to overall time and energy efficiency by taking advantage of the possibility to communicate within this network. Therefore, the real world traffic scenarios are transferred to a graph based structure in order to optimize the cooperative network. Hereby, the graph is defined by a fixed set of rules:

Rule 1: Every traffic participant is a node in the graph.

Rule 2: Every traffic participant has a characteristic driving maneuver after whose execution the traffic participant is no longer relevant for the situation and vice-versa.

Rule 3: Every traffic participant’s characteristic maneuver may block and may be blocked by another traffic participant. The execution time after which participant A clears the path for traffic participant B is the weight of the directed edge connecting the two corresponding nodes.

Rule 4: If a traffic participant’s characteristic maneuver does not block another traffic participant, the weight of the connecting edge is 0.

These rules can be applied to any traffic scenario, resulting in a graph with a corresponding adjacency matrix, as shown exemplarily in Fig. 2. By formalizing the cooperative networks in a graph structure, it is possible to optimize the driving order of the vehicles by interpreting it as a traveling salesman problem. By visiting every node of the graph exactly once, a unique optimized driving order is calculated. Additionally, it is possible to define a set of prioritization rules, granting right of way to public transport, goods transportation or emergency vehicles by visiting these nodes first. According to the driving order calculated by this methodology, the vehicles adapt the speed curve of their individual trajectories according to a pre-defined safety distance of 2 s. Even though this approach can be calculated decentralized, this paper focuses on the calculation by a centralized cooperation infrastructure.

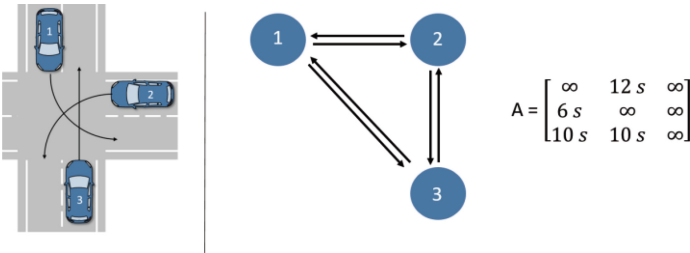


Fig. 2. Transfer of driving scenario to graph structure and adjacency matrix

By comparing the trajectories of cooperative networks with different vehicle densities in both conventional fixed time traffic light control and the cooperation optimization algorithms, the impact of the control algorithm on the energy consumption is estimated. As shown in Fig. 3, the resulting trajectories are optimized towards the energy consumption and drivetrain topologies of the connected vehicles, further optimizing the overall network regarding its efficiency. The methodology is explained in detail in another AVEC paper.

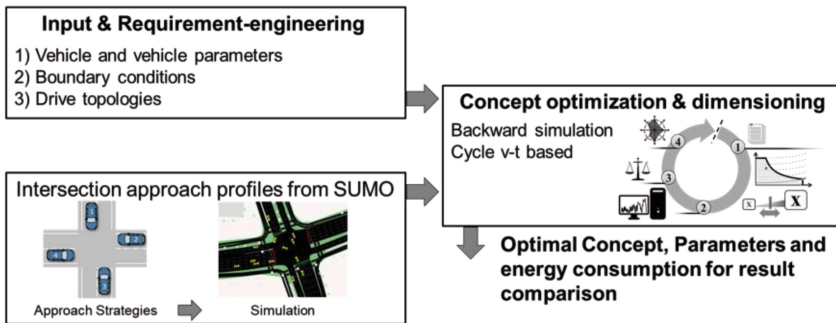


Fig. 3. Overall methodology with scenario generation & optimization, requirement engineering and drivetrain optimization

The simulated scenarios contain 6 D-segment vehicles with the trajectories and vehicle parameters shown in Fig. 4. For the V2X-hardware and auxiliary components, an additional consumption of 15 W and mass of 2 kg is assumed for each vehicle. In total, these vehicles are applied to 7 scenarios in 3 groups. First and second, the fixed time traffic light control (FTTL) and the “first come, first serve” approach, each with safety distances of 0, 1 and 2 s. Third, the cooperative algorithm by graph based optimization described beforehand. In both the FCFS scenarios and the cooperative scenario, the vehicles are connected with each other and the intersection via V2X.

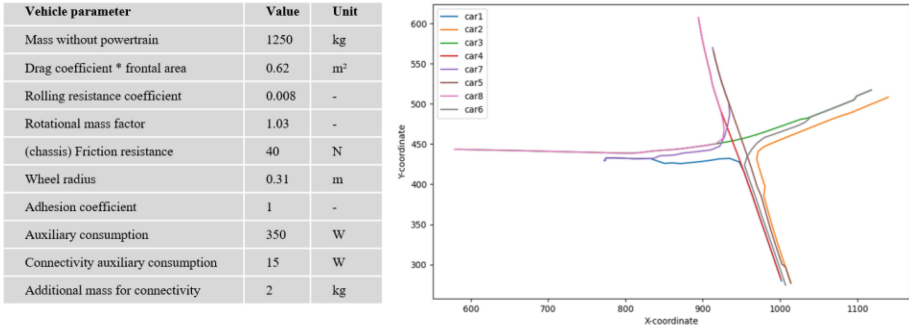


Fig. 4. Vehicle parameters and trajectories in the simulated scenarios

3 Result Discussion and Outlook

The results of the simulation toolchain are compared regarding their overall improvement towards time and energy consumption in an average traffic scenario with 6 vehicles. Hereby, the cooperative driving algorithm with a safety distance of 2 s between the vehicles is compared to a fixed time traffic control (FTTL) and the trivial “first come first serve” (FCFS) approach, each with safety distances of 2, 1 and 0 s. A safety distance of 0 s means, that there is no safety distance at all, the vehicles are driving immediately after each other. The metric to evaluate the overall time efficiency of the cooperative driving maneuver is the overall execution time, which is the sum of the times each vehicle takes to finish the scenario. The results shown in Fig. 5 indicate, that there is only slight to no gain in time efficiency when decreasing the safety distances for either fixed time traffic control and “first come first serve”, with the latter being slightly more efficient overall. The cooperative algorithm increases the overall time efficiency, as previously shown in [2]. When applied to these urban scenarios, the cooperation algorithm optimizes the overall execution time of the scenario by 38% compared to the conventional fixed time traffic light control and by 15% compared to the “first come first serve” approach, while simultaneously keeping the same safety distance between the vehicles.

When analyzing the optimized trajectory and drivetrain adaption with regard to the resulting overall energetic optimization, Fig. 6 shows the gain in efficiency when comparing two different drivetrain topologies (1 & 2 speed transmission BEV) in each

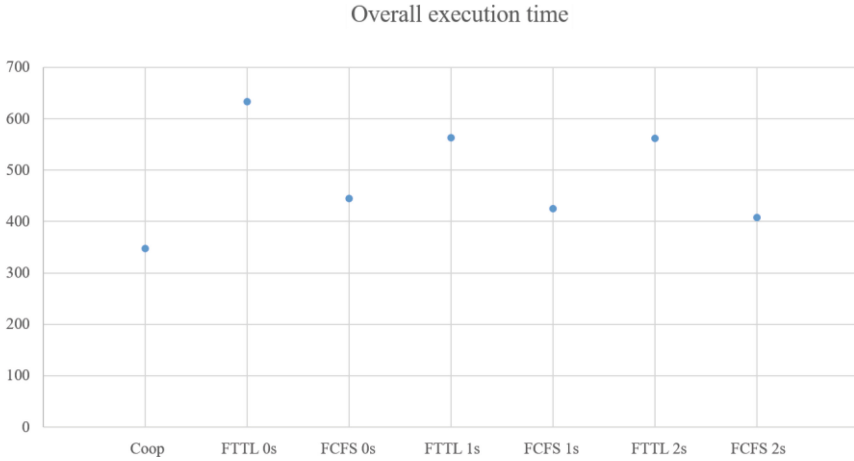


Fig. 5. Summed overall execution time of each scenario

driving scenario. Hereby, the drive system topology has no significant impact on the energy demand, mainly due to the short scenarios and the low velocity profiles with a high share of acceleration operations. Aside from the drivetrain topology, the overall energy consumption decreases as the total scenario execution time decreases, mainly because of the reduced energy consumption of the auxiliary consumers and the reduced conversion losses in the drivetrain due to fewer driving operations. This results in a reduction in energy demand of 14% when comparing fixed time traffic light control with the cooperation algorithm and 7% in comparison to the “first come first serve” approach while keeping the same safety distances. Figure 6 shows, that in order to be comparable to the cooperation algorithm with regard to overall energy consumption, FTTL would need to be applied with no safety distances at all, thus making it impractical in real traffic applications.

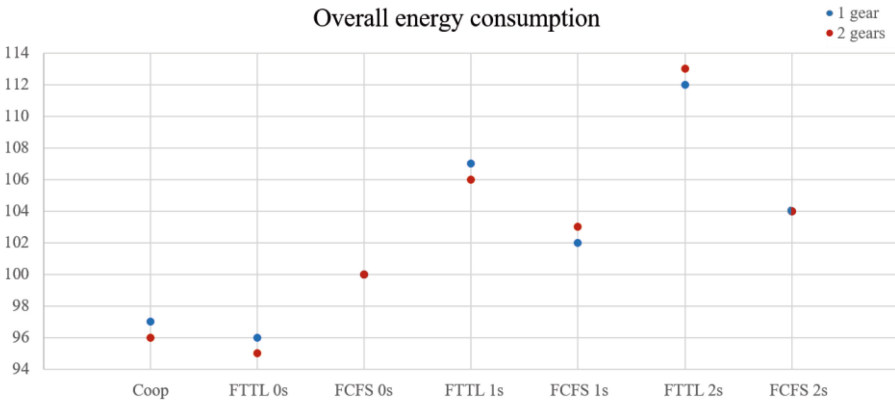


Fig. 6. Overall energy consumption of each scenario with optimized drivetrains, each with 1 and 2 speed transmissions (1 gear/2 gear)

4 Conclusion and Outlook

Within this paper, we investigated the impact of cooperative driving on the example of urban intersections with regard to the overall time and energy efficiency. Therefore, based on measurements in real world traffic, seven different intersection scenarios were generated, ranging from fixed time traffic light control, the original measurements were based on, to varying complexities of cooperative algorithms. Based on the resulting swarm trajectories, a drive system simulation of 1 and 2 speed transmission BEV concepts was applied. Hereby, the drive system topology has no significant impact on the energy demand, mainly due to the short scenarios and the low velocity profiles with a high share of continuous accelerations. When looking at the overall energy consumption, this investigation showed, that cooperative functions enable energy consumption reduction of up to 14% in such urban scenarios, while simultaneously optimizing the overall time efficiency up to 38%.

For future research, there are various potentials to optimize the energy and time efficiency of such multi vehicle systems further. By applying multi-criteria optimization, the overall scenario can be optimized with regard to both overall execution and time and energy efficiency. Furthermore, expanding the scenarios to a larger inner-urban scale and optimizing the drive systems within each scenario in order to identify the optimal drive system parameters for the overall lowest energy consumption are future expansions of the presented method to investigate additional potentials.

References

1. Schmidt, R.K., Leinmüller, T., Böddeker, B.: V2X-Kommunikation. In: Proceedings of 17th Aachener Kolloquium (2008)
2. Flormann, M.: Kooperative Fahrstrategien für automatisierte Fahrzeuge im Mischverkehr. Dissertation, TU Braunschweig, Institut für Fahrzeugtechnik (2022)
3. Sturm, A., Küçükay, F., Henze, R.: Electrified Drives for Automated Vehicles. Technical Paper 2023-01-1679. In: SAE International (Hg.): Energy & Propulsion Conference & Exhibition. SAE International (2023)
4. Dvorkin, W., King, J., Gray, M., Jao, S.: Determining the Greenhouse Gas Emissions Benefit of an Adaptive Cruise Control System Using Real-World Driving Data. In: SAE Technical Paper 2019-01-0310 (2019). <https://doi.org/10.4271/2019-01-0310>
5. Plum, T.: Einfluss moderner Antriebsstränge auf den Energiebedarf automatisierter Fahrzeuge. Dissertation. RWTH Aachen. Institut für Verbrennungskraftmaschinen (2019)

Open Access This chapter is licensed under the terms of the Creative Commons Attribution 4.0 International License (<http://creativecommons.org/licenses/by/4.0/>), which permits use, sharing, adaptation, distribution and reproduction in any medium or format, as long as you give appropriate credit to the original author(s) and the source, provide a link to the Creative Commons license and indicate if changes were made.

The images or other third party material in this chapter are included in the chapter's Creative Commons license, unless indicated otherwise in a credit line to the material. If material is not included in the chapter's Creative Commons license and your intended use is not permitted by statutory regulation or exceeds the permitted use, you will need to obtain permission directly from the copyright holder.





Energetic Impact of Urban Cooperative Driving on the Example of Intersections

Axel Sturm¹ , Maximilian Flormann¹ , Roman Henze¹,
and Pongsathorn Raksincharoensak² 

¹ Institut für Fahrzeugtechnik, Technische Universität Braunschweig, 38106 Braunschweig, Germany

a.sturm@tu-braunschweig.de

² Department of Mechanical Systems Engineering, Tokyo University of Agriculture and Technology, Tokyo 183-8538, Japan

Abstract. The use of automated driving and connectivity can be an additional lever to reduce fuel and energy consumption in real driving and has an impact on the drive system and its dimensioning as well. In this paper we are addressing the impact urban cooperative driving on the energy consumption of electric vehicles and investigate further the impact of the drive system and their layout. To this end, a concept study is being conducted for a D-segment vehicle and two battery electric powertrains. In order to evaluate the impact, defined driving profiles from a connected intersection are used for simulation. Based upon the results the overall energetic impact of different intersection approaching strategies as well as the drive system impact are discussed. It showed that a cooperative intersection scenario leads to an energy reduction of 14% and first come first serve scenarios to an energy reduction of 7%.

Keywords: Automated driving · electric drive systems · energy consumption reduction · cooperative driving · drive system optimization

1 Introduction

Vehicle development is currently driven and influenced by the topics of electrification, digitalization, automated driving and mobile services. These trends influence each other and impact all aspects of the vehicle and especially the drive system. Drive system electrification is the biggest lever for fuel and energy reduction, especially considering battery electric vehicles (BEV). The savings potentials depend on the drive system layout itself, the operation strategy and also the optimization regarding driving operations. In particular changed driving profiles due to automated and connected driving require a different drive layout, compared to customer driving. Especially cooperative adaptive cruise control (CACC) and adaptive cruise control (ACC) [1–3] are subject of many studies and research projects regarding their impact on fuel consumption and improved traffic flow. In a previous investigation [4] the impact of automated driving on the drive system dimensioning and fuel and energy consumption especially for a highway pilot was analyzed. Within this paper we want to elaborate on the impact of connected driving on the drive system and the energetic impact in comparison to customer operation.

© The Author(s) 2024

G. Mastinu et al. (Eds.): AVEC 2024, LNME, pp. 85–90, 2024.

https://doi.org/10.1007/978-3-031-70392-8_13

2 Methodology and Approach

The overall approach is a connected approach and is shown in Fig. 1. For the concept tool one input is the relevant vehicle and drive data and underlying boundary conditions. By means of an urban traffic simulation representative driving profiles are generated for different approach strategies of an intersection, which are the second input to the tool. Those profiles are the basis for the drive simulation with the developed concept optimization process. The concept optimization process consists in itself of four different modules and is explained in detail in [4]. The processes are a drive dimensioning, where the drives are dimensioned according to the underlying requirements. Furthermore, this module parametrizes the subsequent backwards simulation. The results of the simulation are the performances and efficiencies of each drive system with the corresponding aggregate operation points at each timestep of the cycle. Those results are the input for the evaluation module, where all concepts are assessed in detail. Furthermore, multi-criteria optimizations can be carried out as well.

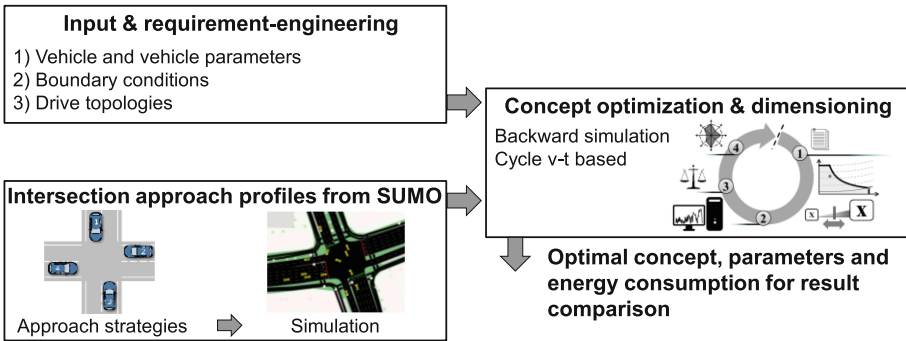


Fig. 1. Cooperative approach for drive system and energy consumption analysis, divided into the inputs to the concept optimization, the cooperative intersection simulation and the input data and requirement-engineering

The investigation is carried out for a D-segment vehicle, with the corresponding vehicle parameters in Table 1. For the additional connectivity elements an additional auxiliary consumption of 15 W and mass of 2 kg is assumed for each vehicle.

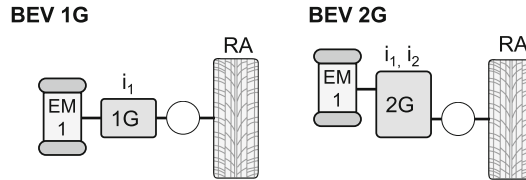
The investigated drive systems are a one-speed transmission (1G) and a two-speed transmission (2G). The drive layouts are displayed in Fig. 2. The 1G concept has a fixed transmission ratio $i_1 = 7$ and an electric machine (EM) power $P_{EM} = 220$ kW. The 2G concept has the ratios $i_1 = 9$ and $i_2 = 4$ and an EM power $P_{EM} = 180$ kW. Both variants are requirement sufficient and allow a maximum velocity $v_{max} = 180$ km/h and an acceleration time $t_{0-100,el}$. Below 6 s.

3 Result Discussion

In total seven different intersection scenarios are investigated. Three scenarios are fixed time traffic light control (FTTL) with vehicle safety distances of 2 s, 1 s and 0 s. Three other scenarios are a first come first serve (FCFS) with safety distances of 2 s, 1 s and 0 s.

Table 1. Vehicle parameters of the investigated D-segment vehicle

Vehicle parameter	Value	Unit
Mass without powertrain	1250	kg
Drag coefficient * frontal area	0.62	m ²
Rolling resistance coefficient	0.008	-
Rotational mass factor	1.03	-
(chassis) Friction resistance	40	N
Wheel radius	0.31	m
Adhesion coefficient	1	-
Auxiliary consumption	350	W
Connectivity auxiliary consumption	15	W
Additional mass for connectivity	2	kg

**Fig. 2.** Drive system layout for one-speed transmission BEV 1G on the left side and two-speed transmission BEV 2G on the right side, both concepts are rear wheel drives (RA)

The seventh scenario is a cooperative scenario (Coop), where the traffic flow is optimized while having a safety distance of 2 s. In all FCFS scenarios and the cooperative scenario the vehicles are connected to the intersection via Vehicle2X (V2X). For each intersection scenario the trajectories of a total of eight vehicles are simulated. Figure 3 shows the range of energy consumption of the battery E_{Battery} of all eight vehicles with 1G and 2G concept for each investigated scenario.

When assessing the total energy consumption for each scenario, it is clear that the crossing strategies lead to different energy consumption. In particular, the consumption range of all vehicles differs significantly between the scenarios. The differences between the 1G and 2G concepts are small and do not show a significant impact on the energy consumption. Especially due to the low speeds and short distances, the transmission losses in the 1G concept are high and comparable to the 2G concept.

The average energy consumption for each scenario is shown in Fig. 4 for each scenario in dependency of the overall scenario execution time. As the total scenario execution time decreases, the energy consumption decreases. This is mainly due to the reduced energy consumption of the auxiliary consumers and also due to the reduced conversion losses especially in the EM from fewer driving operations.

The FTTL scenario with a safety distance 0s is an exception in terms of execution time, due to the fact, that one vehicle is stopping. The energy reduction potential caused

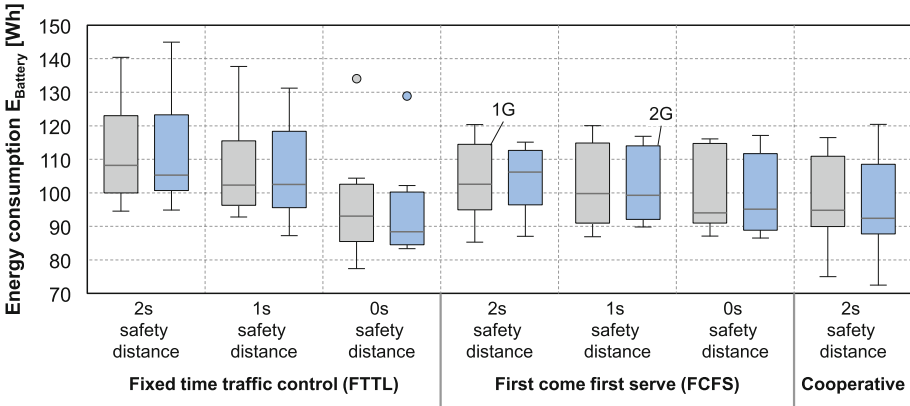


Fig. 3. Energy consumption of the Battery E_{Battery} for the investigated scenarios for the 1G and the 2G concept

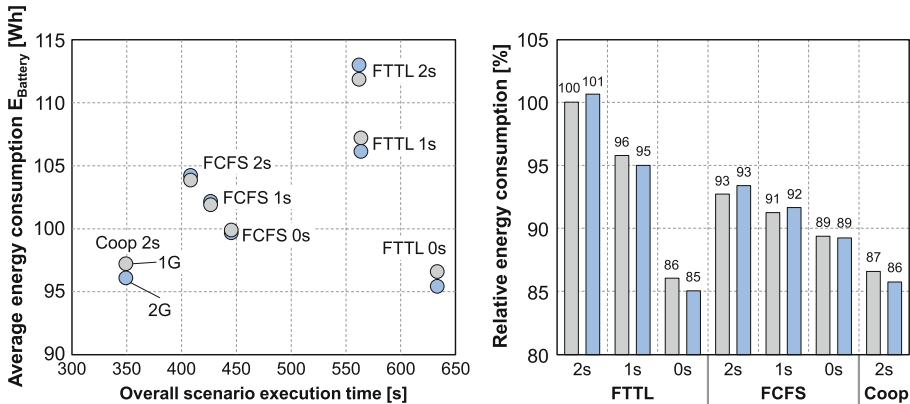


Fig. 4. Average energy consumption of each scenario in dependency of the overall scenario execution time for the 1G concept, grey, and the 2G concept, blue, on the left-hand side, right-hand side relative energy consumption of the 1G and 2G concept in the different scenarios (Color figure online)

by the optimized driving profiles result in lower total absolute driving resistances and thus to lower overall drive system energy consumption. The additional energy required to operate the V2X functionality for the cooperative and FCFS scenarios is overcompensated by the reduction of the driving operation and thus also conversion losses. The cooperative scenario allows a 14% reduction in energy consumption compared to a FTTL with the same safety distance of 2 s, while the FCFS scenario leads to a 7% reduction in energy consumption with the same safety distance. The Coop scenario with a safety distance of 2 s achieves a similar consumption to the FTTL scenario with a safety distance of 0 s.

Figure 5 shows the vehicle energy demand and losses for each vehicle in three different scenarios for the 1G concept. The energy demand and losses are divided into driving

resistances, transmission losses, EM losses and other energy losses and consumers. These include wheel slip losses, mechanical brake losses, auxiliary energy demand as well as drag and inertia losses. The highest energy demand is caused by the driving resistances. The sum of driving resistance energy demand does not change significantly throughout the different scenarios, although the scenario and driving operations are significantly longer. The energy demand displays the sum of driving resistances, whereby the deceleration phases reduce the overall driving resistances. The higher driving operations lead to increased conversion losses of the EM and also to increased mechanical brakes losses, due to the reached recuperation criterion of a minimum speed of 7 km/h. Vehicle 5 highlights this behavior.

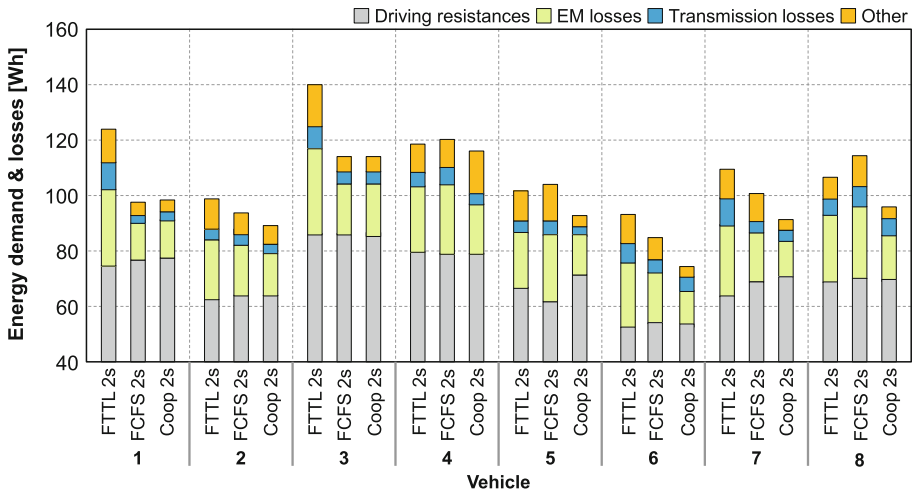


Fig. 5. Energy demand for 1G concept from driving resistances, EM losses, transmission losses and other energy losses during the scenarios FTTL 2s, FCFS 2s and Coop 2s for each of the eight simulated vehicles in each scenario

Another major share make up the EM losses, which differ significantly between the different scenarios, mainly caused by the extended driving operation and multiple energy conversion, also during recuperation. The transmission losses of all scenarios are mostly similar for each vehicle and scenario. Only in some instances (e.g. vehicle 1) the transmission losses are significantly higher caused by multiple starting maneuvers from standstill. The differences for the remaining losses are mainly attributed to braking losses during deceleration maneuvers and are secondarily attributed to minor changes in wheel slip losses.

4 Conclusion and Outlook

Within this paper we investigated the energetic impact of cooperative driving on the example of intersections. Therefore, seven different intersection scenarios were generated and the resulting profiles were the basis for drive system simulation of a 1G BEV

concept and a 2G BEV concept. The assessment of the results showed, that the drive system topology has no significant impact on the energy demand, mainly due to the short scenarios and the low velocity profiles with a high share of acceleration operation. When looking at the overall energy consumption, this investigation showed, that cooperative functions enable an energy consumption reduction of up to 14% in a cooperative scenario and an energy consumption reduction of up to 7% for first come first serve scenarios with a safety distance of 2 s.

In further investigations we want to emphasize two aspects. On the one hand, we want to optimize the drive systems within each scenario in order to identify the optimal drive system parameters for the overall lowest energy consumption. Furthermore, the vehicle individual optimal drive system, thus the lowest overall energy consumption for each scenario would be interesting. On the other hand, further investigations will focus on the scenario definition and expanding the scope of the scenario across the intersection. The definition of a fixed range before the intersection will also allow further scenario investigations when considering the profiles of each vehicle within the defined investigation window.

References

1. Dvorkin, W., King, J., Gray, M., Jao, S.: Determining the greenhouse gas emissions benefit of an adaptive cruise control system using real-world driving data. In: SAE Technical Paper 2019-01-0310 (2019). <https://doi.org/10.4271/2019-01-0310>
2. Plum, T.: Einfluss moderner Antriebsstränge auf den Energiebedarf automatisierter Fahrzeuge. Dissertation. RWTH Aachen. Institut für Verbrennungskraftmaschinen (2019)
3. Tate, L., Hochgreb, S., Hall, J., Bassett, M.: Energy efficiency of autonomous car powertrain. In: SAE Technical Paper Series. WCX World Congress Experience, SAE International (SAE Technical Paper Series) (2018)
4. Sturm, A., Küçükay, F., Henze, R.: Electrified Drives for Automated Vehicles. Technical Paper 2023-01-1679. In: SAE International (Hg.): Energy & Propulsion Conference & Exhibition, 2023-10-31. SAE International (2023)

Open Access This chapter is licensed under the terms of the Creative Commons Attribution 4.0 International License (<http://creativecommons.org/licenses/by/4.0/>), which permits use, sharing, adaptation, distribution and reproduction in any medium or format, as long as you give appropriate credit to the original author(s) and the source, provide a link to the Creative Commons license and indicate if changes were made.

The images or other third party material in this chapter are included in the chapter's Creative Commons license, unless indicated otherwise in a credit line to the material. If material is not included in the chapter's Creative Commons license and your intended use is not permitted by statutory regulation or exceeds the permitted use, you will need to obtain permission directly from the copyright holder.





Speed Control in the Presence of Road Obstacles: A Comparison of Model Predictive Control and Reinforcement Learning

P. Mandl¹(✉), F. Jaumann^{1,2}, M. Unterreiner², T. Gräber², F. Klinger¹,
J. Edelmann¹, and M. Plöchl¹

¹ TU Wien, Institute of Mechanics and Mechatronics, Vienna, Austria
philipp.mandl@tuwien.ac.at

² CARIAD SE, Vehicle Motion & Energy, Wolfsburg, Germany
<https://www.mec.tuwien.ac.at/vsd>, <https://cariad.technology/>

Abstract. The paper compares two optimal control methods — Reinforcement Learning and Model Predictive Control — for adaptive speed control in the presence of road obstacles to enhance ride comfort. Both methods use a model for training or prediction and a reward or cost function to achieve a desired control objective. Using the same quarter-car model and objective function for both methods, differences in planned speed profiles, optimality of the control objective, and differences in computational time are analysed through simulations over a series of cosine-shaped road bumps.

Keywords: Model Predictive Control · Reinforcement Learning · Longitudinal Control · Ride Comfort

1 Introduction

The automotive industry is moving towards fully self-driving vehicles by automating both lateral and longitudinal driving tasks. To achieve this, vehicles have to respond to road obstacles using preceding road information. Two key methods for the control task are Reinforcement Learning (RL) and Model Predictive Control (MPC). RL has gained significant interest for its ability to learn optimal policies directly from environmental interactions, enabling robust control of complex systems. Although training is computationally expensive, evaluating the trained models is fast. MPC is an established optimal control method that, like RL, uses model information to predict future system behaviour and optimise actions over a defined horizon. While MPC is fast to deploy, its online computational requirements increase significantly with system complexity [1].

This paper presents a comparative study of RL and MPC on a novel control problem. It introduces a speed planner for the coupled problem of vertical and longitudinal dynamics when traversing road obstacles to improve ride comfort, specifically road bumps by controlling the vehicle's longitudinal motion. Improving ride comfort through suspension control using classical control methods [2]

© The Author(s) 2024

G. Mastinu et al. (Eds.): AVEC 2024, LNME, pp. 91–97, 2024.

https://doi.org/10.1007/978-3-031-70392-8_14

and RL [3, 4] has been extensively studied in the literature. However, optimising ride comfort via speed planning is an emerging topic [5].

2 Problem Description and Methods

To maximise ride comfort over a given road segment within the preview distance l_{prev} , it is crucial to select the optimal vehicle speed v . This decision takes into account the current vehicle state \mathbf{x} , the speed limits v_{max} and lower v_{min} , and the acceleration limits a_{max} and a_{min} . The control architecture is illustrated in Fig. 1a, while the quarter-car model is shown in Fig. 1b.

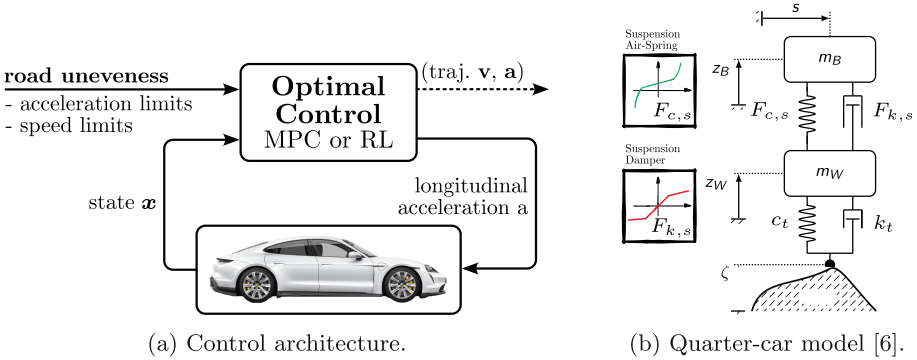


Fig. 1. Optimal longitudinal motion control using either MPC or RL on the left. Both methods are based on the quarter-car model shown on the right.

2.1 Vehicle Model

RL and MPC share similarities in their approach, utilising the same quarter-car model in Fig. 1b for prediction or training. The governing equations of motion are taken from [6]. The spring force $F_{c,s}$ is modelled by an air suspension model based on [7]. The damper force $F_{k,s}$ is represented by piecewise linear damper characteristics with distinct high and low-speed damping for compression and rebound. Additional end-stops for rebound and compression are included. The tyre load is modelled by a linear spring c_t and damping coefficient k_t . The quarter-car state is $\mathbf{x} = [\zeta - z_W, \dot{z}_W, z_W - z_B, \dot{z}_B, v]^T$ with road elevation ζ , wheel travel z_W , sprung-mass travel z_B and vehicle speed $v = \dot{s}$. The nonlinear continuous-time equations are transformed into the space domain, similar to [6].

2.2 Model Predictive Control

The Optimal Control Problem (OCP) for the MPC is formulated as a nonlinear static optimisation with CasADi¹ and solved with IPOPT². The continuous-space dynamics are discretised using an implicit Euler integration scheme. The

¹ web.casadi.org.

² github.com/coin-or/Ipopt.

road is represented by the change in road elevation $\zeta' = \frac{d\zeta}{ds}$ at discrete points along $l_{\text{prev}} = 40$ m with step size $\Delta s = 5$ cm. The OCP is expressed as the following multishooting problem:

$$\min_{\mathbf{X}, \mathbf{a}} \sum_{k=1}^N \underbrace{Q_{\ddot{z}_B} \left(\frac{\ddot{z}_{B,k}}{g} \right)^2 + Q_{\ddot{z}_W} \left(\frac{\ddot{z}_{W,k}}{g} \right)^2}_{J_{\text{heave},k}} + \underbrace{Q_a \left(\frac{a_k}{g} \right)^2}_{J_{\text{long},k}} + \underbrace{Q_v \left| \frac{v_k - v_{\text{ref}}}{v_{\text{ref}}} \right|}_{J_{\text{speed},k}} \quad (1a)$$

$$\text{s.t.} \quad \mathbf{x}_{k+1} = \mathbf{x}_k + \mathbf{f}_{\text{quarter-car}}(\mathbf{x}_{k+1}, a_k, \zeta'_k), \quad \mathbf{x}_1 = \mathbf{x}(t), \quad (1b)$$

$$v_{\min} \leq v_k \leq v_{\max}, \quad a_{\min} \leq a_k \leq a_{\max}, \quad (1c)$$

where $k \in \{1, 2, \dots, N\}$ with $N = \frac{l_{\text{prev}}}{\Delta s}$. $J_{\text{heave},k}$ compromises ride comfort through $\ddot{z}_{B,k}$ and dynamic wheel load through $\ddot{z}_{W,k}$. The sprung mass m_B is 567 kg. The unsprung mass m_W is 60 kg. Longitudinal comfort and control input a_k are considered via $J_{\text{long},k}$. Reference speed v_{ref} tracking is managed by $J_{\text{speed},k}$. By suitably weighing these criteria through $Q_v = 1$, $Q_a = 1$, $Q_{\ddot{z}_B} = 50$ and $Q_{\ddot{z}_W} = 0.5$, the ride comfort is improved while maintaining swift passage of the obstacle. g is the gravitational acceleration.

2.3 Reinforcement Learning

Assuming a Markov decision process (MDP) that, starting from an initial state \mathbf{x}_0 , forms a trajectory τ of states, actions and rewards. RL aims for the optimal control policy $\pi^*(a|\mathbf{x})$ that solves the optimization problem

$$\pi^* = \arg \max_{\pi_\theta} \mathbb{E}_{\tau \sim \pi} \left[- \sum_{k=0}^{\infty} \gamma^k R_k(\mathbf{o}_k) \right] \quad (2)$$

with discount factor $\gamma \in [0, 1)$, step reward R_k and observations \mathbf{o}_k .

Observation Space and Action Space. The list of observations visible to the agent comprises the necessary information to learn an optimal policy and pose a subset of the vehicle state and road. The observation space \mathbf{o}_k is defined by

$$\mathbf{o}_k = [v_k, a_k, \ddot{z}_{B,k}, \ddot{z}_{W,k}, z_{W,k} - z_{B,k}, d_{\text{sb},k}, h_{\text{sb},k}, l_{\text{sb},k}, v_{\text{ref},k}]^T. \quad (3)$$

While v_k , a_k describe the longitudinal motion of the vehicle, the vertical movement is observed by $\ddot{z}_{B,k}$, $\ddot{z}_{W,k}$ and $z_{W,k} - z_{B,k}$. The agent sees the upcoming road obstacle via the longitudinal distance between the current vehicle position and the peak position of the obstacle $d_{\text{sb},k}$, the obstacle's maximum height $h_{\text{sb},k}$, and the obstacle length $l_{\text{sb},k}$. With v_{ref} , the agent is aware of the current reference speed. The agent controls the longitudinal motion of the vehicle by setting a_k . The choice of the interval of possible acceleration values is motivated by the system limitations of a real-world adaptive cruise control system.

Reward Function. The reward function encourages or punishes an agent's behaviour by defining favourable environment states. To ensure comparability, the step reward function R_{step} is based on (1a):

$$R_k = J_{\text{heave},k} + J_{\text{long},k} + J_{\text{speed},k} + J_{v_{\text{min}},k} + J_{\text{step},k}. \quad (4)$$

To enforce the lower speed limit, an additional speed cost $J_{v_{\text{min}},k}$ is added when the agent drops below v_{min} . For numerical reasons, a step reward $J_{\text{step},k} = -0.05$ is added to encourage progress along the road. Additionally, to penalise premature termination of an episode, such as when the vehicle speed drops below 1 km/h, a large cost of $J_{\text{termination}} = 5000$ is added.

Training and Network Architecture. The RL agent is trained using Stable Baselines3’s implementation of the Proximal Policy Optimization (PPO) algorithm³. It utilises a multilayer perceptron (MLP) with two hidden layers of 128 neurons each and is optimised with the Adam optimiser using a learning rate of 3×10^{-4} and a discount factor of 0.999. Each training episode begins with a randomly initialised road, with all training roads having a length of 100 m. The obstacle’s dimensions and position vary for each road, with the obstacle height h_{sb} and length l_{sb} ranging between [0.03 m, 0.08 m] and [0.65 m, 2 m], respectively. The obstacle is positioned between [40 m, 80 m]. The vehicle’s initial v_0 and reference speeds v_{ref} are set between [10 km/h, 50 km/h] and [25 km/h, 50 km/h], respectively. During training, all values are sampled from a uniform distribution within specified bounds. To ensure robust training, there is a ten percent chance that no obstacle will be present, which enforces the training of reference speed tracking. Each training episode consists of 10,000 steps. The policy is evaluated based on a predefined set of roads and velocities.

3 Comparison Between MPC and RL

Both approaches are compared by simulation when crossing over three consecutive cosine-shaped bumps of varying heights and lengths. The first bump is at 50 m with a length of 1 m and height of 5 cm, the second bump at 90 m with a length of 0.75 m and height of 3.5 cm, and the third bump at 100 m with a length of 0.65 m and height of 7.5 cm. The preview distance l_{prev} for both methods is 40 m. The admissible speed range is 5 to 50 km/h, with a reference speed of v_{ref} of 50 km/h. The longitudinal acceleration limits are $a_{\text{max}} = 2.5 \text{ m/s}^2$ and $a_{\text{min}} = -3.7 \text{ m/s}^2$. Note, that this scenario exceeds the training dataset of the RL agent.

Planned Speed and Acceleration Profile. Figure 2 illustrates the planned speed and acceleration profiles for both MPC and RL. RL is represented in red, while MPC in blue. For the first bump, the MPC reduces the speed to approximately 20 km/h, whereas the RL slows down to about 6 km/h. As bump heights increase and length decreases, the MPC approaches the lower speed limit as well. Acceleration profiles show the MPC with a linear increase in braking and acceleration, while the RL prefers constant braking and acceleration. The MPC utilizes the entire available acceleration band, while the RL only uses the maximum acceleration. Reference speed tracking is achieved at the start and end for both methods.

³ stable-baselines3.readthedocs.io.

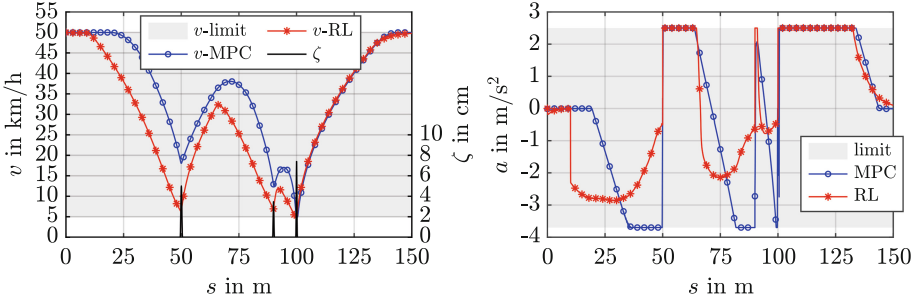


Fig. 2. Speed profiles v for MPC and RL running over consecutive cosine-shaped bumps with road elevation ζ on the left. Longitudinal acceleration a on the right.

Optimality. Figure 3 provides a detailed breakdown of the planned speed profiles' differences. The top row displays J_{heave} for each bump, followed by the speed cost J_{speed} in the second row, and the longitudinal cost J_{long} in the last row. When observing J_{heave} for the three bumps in the top row, it becomes evident that the RL approach enhances the ride comfort criterion more notably on the first and second bump due to its lower transition speed than the MPC. This improvement comes with the drawback of occurring larger costs in J_{speed} . Overall, the total cost is primarily influenced by J_{speed} . While the RL approach significantly outperforms the MPC w.r.t J_{heave} , its cumulative cost or optimality w.r.t. the cost function is worse, with a score of 7045 for the RL approach compared to 5762 for the MPC.

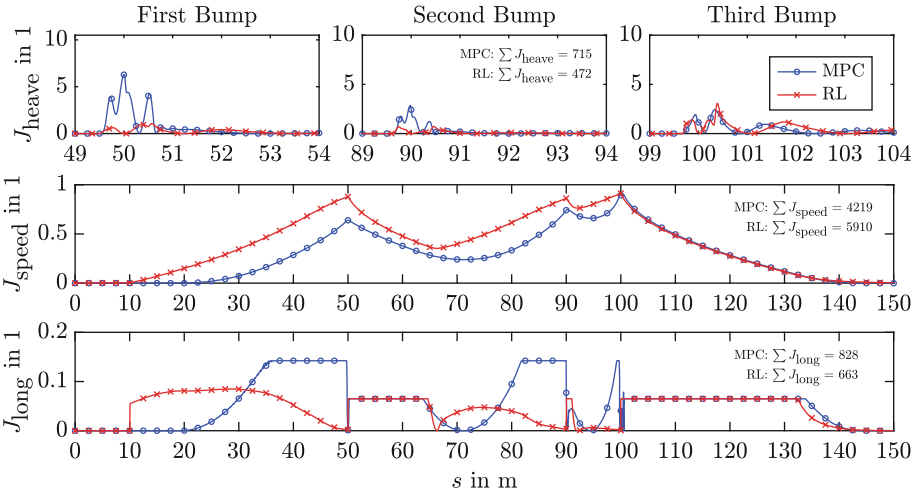


Fig. 3. Cost terms for the simulation running over three consecutive cosine-shape bumps. Total accumulated cost: $J_{\text{MPC}} = 5762$, $J_{\text{RL}} = 7045$.

Computational Demand. The calculations were performed on consumer-grade laptops, with several runs averaged. The average computation time for the MPC was around 380 ms, with peaks of 1700 ms, compared to an average time of 0.15 ms with peaks of less than 1 ms for the RL approach.

4 Summary and Outlook

This study compared RL and MPC in speed control to improve ride comfort when crossing road obstacles. Both methods utilised the same quarter-car model and cost function for control decisions. While RL learnt optimal policies directly from interactions, MPC used model-based predictions to optimise upcoming behaviour. Through simulations of running over cosine-shape road bumps, the study compared their performance in planned speed profiles, optimality, and computational efficiency. Results showed that the RL outperformed the MPC regarding improved ride comfort, albeit with increased speed costs, resulting in a less optimal solution. The computational demands varied significantly, raising concerns about MPC's suitability for vehicle application in this case. RL demonstrated potential in chassis control application, particularly in planning tasks, but further exploration is needed. Future research should focus on optimising hyperparameters and exploring alternative learning algorithms. The road embedding method used in this study should be extended to a more generic approach. For MPC, computational efficiency can be enhanced by adopting a different road embedding method and employing variable space discretisation to reduce the number of free variables in the OCP.

References

1. D. P. Bertsekas. Reinforcement learning and optimal control. Belmont, Massachusetts: Athena Scientific, 2019. isbn: 978-1-886529-39-7
2. Tseng, H.E., Hrovat, D.: State of the art survey: active and semi-active suspension control. In: Vehicle System Dynamics (2015)
3. Dridi, I., Hamza, A., Ben Yahia, N.: A new approach to controlling an active suspension system based on reinforcement learning. Adv. Mech. Eng. (2023)
4. Ming, L. et al.: Semi-active suspension control based on deep reinforcement learning. In: IEEE Access (2020)
5. Wu, J. et al.: Ride comfort optimization via speed planning and preview semi-active suspension control for autonomous vehicles on uneven roads. In: IEEE Trans. Vehic. Technol. (2020)
6. Mandl, P.: Predictive driver model for speed control in the presence of road obstacles. MA thesis. Vienna, Austria: TU Wien (2021)
7. Savaresi, S.M. et al.: CHAPTER 2 - Semi-active suspension technologies and models. In: semi-active suspension control design for vehicles. Ed. by S. M. Savaresi et al. Boston: Butterworth-Heinemann, isbn: 978- 0-08-096678-6 (2010)

Open Access This chapter is licensed under the terms of the Creative Commons Attribution 4.0 International License (<http://creativecommons.org/licenses/by/4.0/>), which permits use, sharing, adaptation, distribution and reproduction in any medium or format, as long as you give appropriate credit to the original author(s) and the source, provide a link to the Creative Commons license and indicate if changes were made.

The images or other third party material in this chapter are included in the chapter's Creative Commons license, unless indicated otherwise in a credit line to the material. If material is not included in the chapter's Creative Commons license and your intended use is not permitted by statutory regulation or exceeds the permitted use, you will need to obtain permission directly from the copyright holder.





A Geometric Electric Motor Model for Optimal Vehicle Family Design

Maurizio Clemente^(✉) , Olaf Borsboom , Mauro Salazar ,
and Theo Hofman 

Eindhoven University of Technology, 5612 AZ Eindhoven, The Netherlands
{m.clemente,o.j.t.borsboom,m.r.u.salazar,t.hofman}@tue.nl

Abstract. This paper presents a design optimization framework that jointly optimizes battery size with the geometric dimensions of the electric motor for a family of battery electric vehicles, with global optimality guarantees. As opposed to conventional models, we devise a quasi-static model of the motor internal losses as a function of both its geometry and operating points, using a convex surrogate modeling approach. Specifically, we implement a low-level motor scaling, capturing the impact on performance and losses of changing the motor geometry in axial and radial directions. Hence, we leverage the framework to solve a concurrent optimization problem and identify the optimal module sizing for a family of electric vehicles. Finally, we test our framework on a benchmark problem where we jointly design motor and battery for three different types of vehicles (a city car, a compact car, and a cross over), whereby the prediction efficiency is in line with the high-fidelity modeling software.

Keywords: Electric powertrain design · Electric Motor Modeling · Concurrent Design Optimization · Surrogate Modeling · Convex Optimization

1 Introduction

In the last decade, the passenger vehicle market has witnessed a significant increase in its share of electrified variants. However, widespread adoption is still hindered by the relatively high price and short range of these vehicles, compared to their conventional, fossil-fuel-powered counterparts [1]. A few researchers have addressed this problem by developing holistic and system-level optimization methodologies to lower the electric vehicles' price while preserving performance [2, 3]. Although these approaches appear intriguing, their main limitation is that the optimal design is inherently influenced by the accuracy of the models employed in the framework, causing unreliable results and a lower fidelity in the design. In this paper, we overcome the shortcomings owing to the motor model

This publication is part of the project NEON with project number 17628 of the research program Crossover which is (partly) financed by the Dutch Research Council (NWO). The first two authors contributed equally to this work.

presented in a previous paper [4], where we considered the motor peak power to stretch the efficiency map linearly. Against this backdrop, we devise a low-scale, quasi-static state model of the electric motor as a function of its geometry and operations, leveraging a convex surrogate modeling approach. Ultimately, we leverage our framework to jointly design battery size and motor low-scale dimensions for three different vehicle types: a city car, a compact car, and a cross over.

Related Literature The topic of this paper relates to the design optimization of electric vehicle powertrains. An overview of system-level perspectives of this problem can be found in [5], where authors generally choose simplified models for components, together with derivative-free [6] or convex optimization [7–9] algorithms. Relevant advances have been made in powertrain design using more detailed component models, for instance in [10] and [11]. However, the former does not guarantee global optimality, whereas the latter makes assumptions to pre-compute the required mechanical electric motor power. Therefore, we deem the powertrain models used in these optimization frameworks to date unsuitable to represent the system behavior for different geometrical scalings and operations.

Statement of Contributions In this paper, we present a concurrent design optimization framework that jointly optimizes the size of the battery with the geometric dimensions of the electric motor for a family of electric vehicles, with global optimality guarantees. Specifically, we developed an electric motor model to estimate with a high degree of fidelity the motor’s internal power losses as a function of its dimensions (axial and radial scaling factors, k_{ax} and k_{rad} respectively), and the vehicle’s operations (motor power P_m and speed ω_m), using a surrogate modeling approach. Finally, compared to our previous work in [4], this framework makes it possible to consider a transmission, in this case a Fixed Gear Transmission FGT, thanks to the novel Electric Motor EM model and central drive/axle motors. In conclusion, here we contribute by jointly optimizing the design of the powertrain of a fleet of electric vehicles with global optimality guarantees, whilst including the transmission ratio and accounting for the low-scale design of the electric motor.

Organization This paper is organized as follows: Sect. 2 presents the framework’s methodology, including vehicle and powertrain component models and the optimization problem. In Sect. 3, we showcase the optimization framework with a numerical study on designing a fleet of electric vehicles. The conclusions are drawn in Sect. 4, together with an outlook on future research.

2 Methodology

This section presents a convex optimization framework to design a family of Battery Electric Vehicles BEVs, with particular attention to low-level motor

geometry effects on performance and losses. First, we describe the set of equations constituting the vehicle model, then we frame the optimization problem. We finalize this section with a discussion of the assumptions and limitations of the approach.

2.1 Longitudinal Vehicle Dynamics

For every vehicle i out of N we aim to co-design, we can compute the required power at the wheels $P_{v,i}(t)$ as

$$P_{v,i}(t) = v(t) \left(m_i a(t) + \frac{1}{2} \rho c_{d,i} A_{f,i} v(t)^2 + m_i g (\sin \alpha(t) + c_{r,i} \cos \alpha(t)) \right), \quad (1)$$

where $v(t)$, $a(t)$, and $\alpha(t)$ are the velocity, acceleration and road inclination given by the selected drive cycle as a function of the time t , respectively; m_i , $c_{d,i}$, and $A_{f,i}$ are the total mass, the aerodynamic drag coefficient, and the frontal area of vehicle i , respectively. Moreover, ρ is the density of air, g is the gravitational constant, and $c_{r,i}$ is the rolling resistance coefficient. From this point onward, we will drop the time dependence on the variables whenever it is clear from the context.

2.2 Mass

We consider the effect of weight introduced by powertrain components' sizing in the vehicle mass m_i equation. Therefore, we account for the glider mass $m_{g,i}$, the driver mass m_d , the payload mass $m_{pl,i}$, the total mass of the $N_{m,i}$ motors $m_{m,i}$, and the $N_{b,i}$ battery packs m_b

$$m_i = m_{g,i} + m_d + m_{pl,i} + m_{m,i} + m_{b,i}. \quad (2)$$

2.3 Transmission

We model the FGT as an efficiency η_{gb} , in line with common practice in the field [12]. Hence, we write the output mechanical power of each motor $P_{m,i}$ following the convex relaxation introduced by [13]

$$P_{m,i} \geq P_{v,i} \frac{1}{\eta_{gb} N_{m,i}}, \quad (3)$$

$$P_{m,i} \geq P_{v,i} \eta_{gb} \frac{r_{b,i}}{N_{m,i}}, \quad (4)$$

where $r_{b,i}$ is the regenerative braking fraction, depending on whether vehicle i is equipped with a front-wheel or all-wheel drive. Hereby we assume that both motors mounted on each axle in an all-wheel drive configuration are operated identically. The transmission has a fixed ratio γ , such that

$$\omega_{m,i} = \gamma \frac{v}{r_{w,i}}, \quad (5)$$

where $\omega_{m,i}$ is the mechanical speed of the motor and $r_{w,i}$ is the radius of the wheels.

2.4 Electric Motor

We devise a model of the electric motor as a function of its dimensions and operating point, whereby we take inspiration from the surrogate modeling approach in [11] and the scaling in [14]. The design variables are the scaling factors, which uniformly scale all inner and outer dimensions of the motor in axial and radial direction, increasing the supplied current but keeping the voltage equal. Assuming a constant density of the motor, the mass of the motor $m_{m,i}$ is then given by

$$m_{m,i} = m_{m,o} k_{ax} k_{rad}^2,$$

where $m_{m,o}$ is the mass of the reference motor and $k_{ax} \in [\underline{k}_{ax}, \bar{k}_{ax}]$ and $k_{rad} \in [\underline{k}_{rad}, \bar{k}_{rad}]$ are the axial and radial scaling factors, respectively. In order to maintain convexity, we rewrite this expression as

$$m_{m,i} k_{sh} \geq m_{m,o} k_{rad}^2, \quad (6)$$

where $k_{sh} = \frac{1}{k_{ax}}$ is defined as the motor *shortness* scaling factor or, in other words, the reciprocal of the axial scaling factor. Hence, the mass relation in Eq. (6) can be rewritten as a convex second-order conic constraint [15]. In this framework, we conduct a Latin Hypercube experimental design with the electric motor design software Motor-CAD [16]. For a given transmission ratio we can pre-compute the motor speed through Eq. (5). Then, similarly to [11,17], we create a model of the power losses $P_{m,loss,i}$ for multiple levels of motor speed j , which is equal to

$$P_{m,loss,i} \geq x_{m,i}^\top Q_{m,j}(t) x_{m,i} + q_{m,j}(t) x_{m,i} + q_{m0,j}(t) \quad \forall j \in \{1, \dots, N_\omega\}, \quad (7)$$

where N_ω is the number of motor speed fitting levels, and $x_{m,i}$ is a vector consisting of convex functions of the model inputs

$$x_{m,i} = [|P_{m,i}|, P_{m,i}^2, P_{m,i}^4, k_{sh}, k_{sh}^2, k_{sh}^4, k_{rad}, k_{rad}^2, k_{rad}^4]^\top.$$

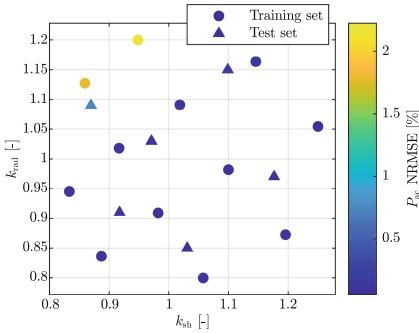


Fig. 1. The EM AC power NRMSE values of each sample in the design space, for both the training and test set.

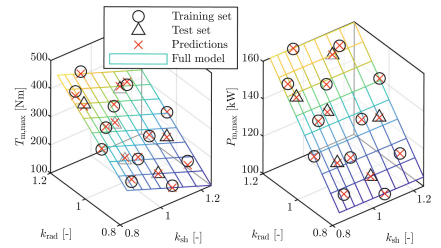


Fig. 2. The training and testing data and predictions, along with the model over the full design space.

The fitting parameters $Q_{m,j}(t)$, $q_{m,j}(t)$, and $q_{m0,j}(t)$ are pre-computed at each time step, whereby we linearly interpolate the fitting parameters between sampled speed levels. We ensure that the motor model is convex by imposing the following conditions on the coefficients: every $Q_{m,j}$ is positive semi-definite, and the elements of all $q_{m,j}$ and $q_{m0,j}$ should be non-negative [18, 19]. To the end of retaining the problem's convexity, we relax Eq. (7) to

$$P_{m,\text{loss},i} \geq x_{m,i}^{+\top} Q_{m,j}(t) x_{m,i}^+ + q_{m,j}(t) x_{m,i}^+ + q_{m0,j}(t) \quad \forall j \in \{1, \dots, N_\omega\}, \quad (8)$$

$$P_{m,\text{loss},i} \geq x_{m,i}^{-\top} Q_{m,j}(t) x_{m,i}^- + q_{m,j}(t) x_{m,i}^- + q_{m0,j}(t) \quad \forall j \in \{1, \dots, N_\omega\}, \quad (9)$$

where

$$x_{m,i}^+ = [P_{m,i}, P_{m,i}^2, P_{m,i}^4, k_{\text{sh}}, k_{\text{sh}}^2, k_{\text{sh}}^4, k_{\text{rad}}, k_{\text{rad}}^2, k_{\text{rad}}^4]^\top, \quad (10)$$

$$x_{m,i}^- = [(-P_{m,i}), (-P_{m,i})^2, (-P_{m,i})^4, k_{\text{sh}}, k_{\text{sh}}^2, k_{\text{sh}}^4, k_{\text{rad}}, k_{\text{rad}}^2, k_{\text{rad}}^4]^\top, \quad (11)$$

following a lossless epigraphic relaxation of the constraint [18]. Due to the particular problem structure, the constraint will always hold with equality for the optimal solution. In fact, assuming any value higher than the strict necessary would be sub-optimal as it entails a higher energy consumption. The electrical input power $P_{\text{ac},i}$ is given by

$$P_{\text{ac},i} = P_{m,i} + P_{m,\text{loss},i}. \quad (12)$$

As shown in Figs. 1 and 2, we train our models on a training set and evaluate the quality of our models on a test set, which is also synthesized using a Latin Hypercube design of experiments. We obtain a $P_{\text{ac},i}$ normalized root-mean-squared error (NRMSE) of 0.19% and an adjusted $R^2 = 0.92$ for the full test set. Finally, we display the efficiency maps of the test set alongside the model's predictions in Fig. 3.

To approximate the torque and power limits, $\bar{T}_{m,i}$ and $\bar{P}_{m,i}$, respectively, we use linear regression models that are equal to

$$P_{m,i} \leq \beta_{p,0} + \beta_{p,1} k_{\text{sh}} + \beta_{p,2} k_{\text{rad}}, \quad (13)$$

$$P_{m,i} \geq -(\beta_{p,0} + \beta_{p,1} k_{\text{sh}} + \beta_{p,2} k_{\text{rad}}), \quad (14)$$

$$P_{m,i} \leq \omega_{m,i} (\beta_{t,0} + \beta_{t,1} k_{\text{sh}} + \beta_{t,2} k_{\text{rad}}), \quad (15)$$

$$P_{m,i} \geq -\omega_{m,i} (\beta_{t,0} + \beta_{t,1} k_{\text{sh}} + \beta_{t,2} k_{\text{rad}}), \quad (16)$$

where all $\beta_{\{\cdot\}}$ are fitting parameters. Finally, we pose performance constraints on the electric motor, so that all vehicles are able to drive at a certain maximum velocity \bar{v} , to launch from standstill at a certain road inclination $\bar{\alpha}$, and to drive at a constant velocity v_α at the same road inclination. These constraints are written as

$$\bar{P}_{m,i} \eta_{\text{gb}} \geq \frac{1}{2} \rho c_{d,i} A_{f,i} \bar{v}^3, \quad (17)$$

$$\bar{T}_{m,i} \eta_{\text{gb}} \geq m_i g \sin \bar{\alpha} \frac{r_{w,i}}{\gamma_i}, \quad (18)$$

$$\bar{P}_{m,i} \eta_{\text{gb}} \geq m_i g \sin \bar{\alpha} v_\alpha. \quad (19)$$

2.5 Battery

In order to compute the battery output power $P_{b,i}$, we consider a fixed inverter efficiency η_{inv} and constant auxiliary power P_{aux} , such that

$$P_{b,i} \geq P_{ac,i} \frac{N_{m,i}}{N_{b,i} \eta_{inv}} + P_{aux}, \quad (20)$$

$$P_{b,i} \geq P_{ac,i} \frac{N_{m,i} \eta_{inv}}{N_{b,i}} + P_{aux}, \quad (21)$$

after convex relaxations similar as in [13]. We find the internal battery power $P_{i,i}$ using the the short-circuit power $P_{sc,i}$, representing a variable efficiency depending on the losses, approximated with a piece-wise affine model [4]

$$P_{i,i} \geq P_{b,i} + \frac{1}{P_{sc,i}} P_{i,i}^2, \quad (22)$$

The energy dynamic of the battery is influenced by $P_{i,i}$ through

$$\frac{d}{dt} E_{b,i} = -P_{i,i}. \quad (23)$$

Hence, the energy capacity limit of the full battery pack $\bar{E}_{b,i}$ scales with the size S_b and number $N_{b,i}$ of battery modules respect to the reference battery energy capacity $\bar{E}_{b,o}$ as

$$\bar{E}_{b,i} = \bar{E}_{b,o} S_b N_{b,i}. \quad (24)$$

We set limits on the State-of-Charge SOC ξ by

$$E_{b,i} \in [\underline{\xi} \bar{E}_{b,i}, \bar{\xi} \bar{E}_{b,i}], \quad (25)$$

where $E_{b,i}$ is the battery State-of-Charge SOE, $\underline{\xi}$ and $\bar{\xi}$ are the minimum and maximum SOC levels, respectively. The mass of the full battery pack is equal to

$$m_{b,i} = m_{b,o} S_b N_{b,i}, \quad (26)$$

where $m_{b,o}$ is the mass of the reference battery. Since we consider a variable efficiency of the battery through $P_{sc,i}$, we include a constraint to ensure that the operations are conducted around the half-capacity level of the battery by averaging the maximum capacity at the start and the minimum capacity at the end of the driving cycle

$$E_{b,i}(0) + E_{b,i}(T) = S_b (\bar{\xi} + \underline{\xi}) \bar{E}_{b,o} N_{b,i}, \quad (27)$$

where T is the total duration of the drive cycle. Additionally, we require that the range d of the vehicle is larger than the minimum requirement $\underline{d}_{r,i}$ on one fully-charged battery by

$$\Delta E_{b,i} \leq (\bar{\xi} - \underline{\xi}) \bar{E}_{b,i} \frac{d}{\underline{d}_{r,i}}. \quad (28)$$

Finally, we write the objective function of the optimization problem as

$$J_o = \sum_{i=1}^N (E_{b,i}(0) - E_{b,i}(T)),$$

where J_o is the family energy consumption during the driving cycle.

2.6 Optimization Problem for a Family of Vehicles

Summarizing, to obtain the optimal powertrain component sizing for a family of electric vehicles minimizing energy consumption, we solve a convex optimal design problem, considering given γ_i , $N_{m,i}$, $N_{b,i}$, and $r_{b,i}$. The design variables of the modules, shared by the whole family, are $p = \{k_{sh}, k_{rad}, S_b\}$, whereas the only state variable is $x = E_{b,i}$, which is different for every vehicle.

Problem 1 (*Electric Vehicle Family Design*): *The optimal powertrain design for a family of electric vehicles to minimize the total energy consumption is the solution of*

$$\begin{aligned} \min_{x,p} \quad & J_o \\ \text{s.t.} \quad & (1) - (6), (11) - (28), \\ & (9), (9), \\ & p = \{k_{sh}, k_{rad}, S_b\}. \end{aligned} \quad \begin{aligned} & \forall i \in \{1, \dots, N\}, \\ & \forall i \in \{1, \dots, N\} \quad \forall j \in \{1, \dots, N_\omega\}, \end{aligned}$$

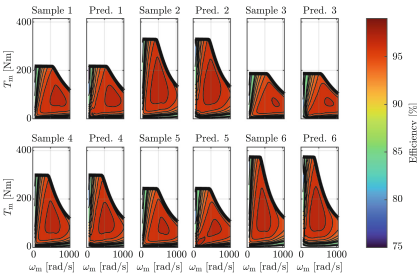


Fig. 3. The efficiency maps of the test set, both from Motor-CAD, denoted with “Sample”, and the predictions, denoted with “Pred.”

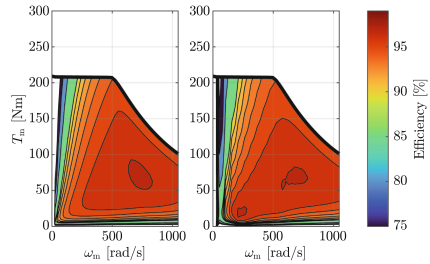


Fig. 4. The efficiency maps of the optimized motor obtained with the high fidelity tool Motor-CAD [16] (left) alongside the model predictions (right).

Since the constraint set and the cost function are convex, we ensured that our problem is fully convex and therefore we can compute the globally optimal solution [18] with standard nonlinear programming methods.

2.7 Discussion

A few comments are in order. First, the electric motor model has been trained on samples for design variables in a range of $\pm 20\%$ with respect to the reference motor. Outside this interval, we cannot ensure an accurate representation of the losses. Second, while the identification process has been based on an interior permanent magnet synchronous machine, the methodology can be readily adapted to other technologies. Third, we do not consider any thermal effects, as they have little influence on the motor operations of conventional vehicles [20]. Moreover, we scale the battery size only by acting on the number of cells in parallel, thus changing its energy without altering the battery voltage. Concerning the numerical solution of Problem 1, we use standard nonlinear programming methods, even though the problem is a semi-definite program (convex) due to the fact that standard convex solvers are not able to work with the higher-order input functions of our electric motor model. Finally, it is important to underline that, in our framework, only scaling factors are optimization variables, whilst the modules' multiplicities are given parameters. This limitation could be readily overcome by solving a sequence of problems in a combinatorial manner, yet this is beyond the scope of the present paper.

3 Results

In this section, we showcase our framework on the simultaneous design of a city car, a compact car, and a cross over. The general parameters are reported in Table 1, while the vehicle-specific parameters are given in Table 2. In our case study, we consider the Class 3 Worldwide harmonized Light-duty vehicles Test Procedure (WLTP), discretizing with a sampling time of 1 s and the forward Euler method. Finally, we solve the problem using the nonlinear solver IPOPT [22] in 120s after parsing it with CasADi [23] in 58s. The results of our case study show the design of single-sized components able to serve a diverse family of vehicles. We can observe the optimization output and the vehicles' performance in Table 3. In Fig. 4, we compare the efficiency maps of the motor with optimized axial and radial geometrical dimension obtained through the high-fidelity modeling software Motor-CAD [16] (left) and our model's predictions (right). In this specific case, the motor map of the optimal geometrical design presents two high-efficiency regions, virtually introducing higher efficiencies in the low-torque low-speed region. Since this region contains operating points common to all the vehicles, a map of this type is favored in the simultaneous design over the ones with a single high-efficiency region located in the middle shown in Fig. 3. However, this behavior could be avoided by adding regularization terms in the identification of the fitting parameters $Q_{m,j}(t)$, $q_{m,j}(t)$, and $q_{m0,j}(t)$ at the cost of a slight reduction in overall accuracy. Compared to the high-fidelity software, the NRMSE for the motor losses $P_{m,\text{loss}}$ is 5.7%, while it equals 0.33% for the overall electrical power $P_{ac,i}$.

Table 1. General Parameters.

Parameter	Value
$\bar{E}_{b,o}$	84.53 MJ
ρ	1.25 kg/m ³
$\bar{k}_{\{ax,rad\}}$	1.2
$\underline{k}_{\{ax,rad\}}$	0.8
v_α	15 km/h
$\bar{\alpha}$	25 %
$\bar{\xi}$	0.8
$\underline{\xi}$	0.2
$m_{b,o}$	138.6 kg
η_{inv}	96 %
η_{gb}	98 %
$m_{m,o}$	50.7 kg
m_d	80 kg
g	9.81 m/s ²
$\underline{d}_{r,i}$	300 km
\bar{v}	130 km/h

Table 2. Vehicle Parameters [21].

Parameter	City Car	Compact Car	Cross Over
$A_{f,i}c_{d,i}$ (m ²)	0.69	0.5589	1.1997
$c_{r,i}$	0.01	0.008	0.02
$N_{m,i}$	2	2	2
$N_{b,i}$	1	1	2
$r_{w,i}$ (m)	0.3498	0.3594	0.3630
$m_{g,i}$ (kg)	850	1250	2000
γ	8	8	8

Table 3. Optimization results for the concurrent design.

Vehicle	F_v (Wh/km)	k_{sh}	k_{rad}	S_b	M_i (kg)	d (km)	P_m (kW)	E_b (kWh)
City Car	191.86	0.93	0.85	3.171439	310	224	74	
Compact Car	188.93	0.93	0.85	3.171839	315	224	74	
Cross Over	396.99	0.93	0.85	3.173028	300	224	148	

4 Conclusions

This paper presented a design optimization framework featuring a geometric model of the EM that allows for joint design of the EM low-scale dimensions and battery sizing with global optimality guarantees, for a family of battery electric vehicles. We identified the fitting parameters with an average normalized root mean squared error of 0.19% and an adjusted R^2 value of 0.92 for the full test set. Finally, we determined the optimal joint design of the motor and battery from the perspective of using the components on every vehicle in the family, composed of a city car, a compact car and a cross over. The results display a normalized root mean squared error of 0.33% for the motor power in the motor map of the optimal geometrical design found.

Future Work: This work opens the field for the following extensions: We aim to sophisticate the model by incorporating the gear ratio and powertrain topology (layout of components) among the design variables, and jointly optimizing the multiplicity of components within each vehicle.

Acknowledgment. We thank Ir. J. van Kampen, Ir. L. Pedroso, Dr. D. Herceg, and Dr. I. New for proofreading this paper.

References

1. IEA, “Global EV outlook 2020,” International Energy Agency, Tech. Rep. (2020)
2. Anselma, P.: Electric powertrain sizing for vehicle fleets of car makers considering total ownership costs and CO_2 emission legislation scenario. *Appl. Energy* **1**(314), 118902 (2022)
3. Guanetti, J., Formentin, S., Corno, M., Savaresi, S.M.: Optimal energy management in series hybrid electric bicycles. In: *Proc. IEEE Conf. on Decision and Control* (2015)
4. Clemente, M., Salazar, M., Hofman, T.: Concurrent powertrain design for a family of electric vehicles. In *10th Advances in Automotive Control* (2022)
5. Silvas, E., Hofman, T., Murgovski, N., Etman, P., Steinbuch, M.: Review of optimization strategies for system-level design in hybrid electric vehicles. *IEEE Trans. Vehicular Tech.* **66**(1), 57–70 (2016)
6. Kim, K., et al.: A component-sizing methodology for a hybrid electric vehicle using an optimization algorithm. *Energies* **14**(3147), 1–15 (2021)
7. Borsboom, O., Fahdzyana, C.A., Hofman, T., Salazar, M.: A convex optimization framework for minimum lap time design and control of electric race cars. *IEEE Trans. Vehic. Tech.* **70**(9), 8478–8489 (2021)
8. Murgovski, N., Johannesson, L., Sjöberg, J., Egardt, B.: Component sizing of a plug-in hybrid electric powertrain via convex optimization. *Mechatronics* **22**(1), 106–120 (2012)
9. Clemente, M., Salazar, M., Hofman, T.: Concurrent design optimization of powertrain component modules in a family of electric vehicles. *Applied Energy*, (2024), under review. Available online at <https://arxiv.org/pdf/2311.03167>
10. Krüger, B., Keinprecht, G., Filomeno, G., Dennin, D., Tenberge, P.: Design and optimisation of single motor electric powertrains considering different transmission topologies. *Mech. Mach. Theory* **168**, 104578 (2022)
11. Borsboom, O., Salazar, M., Hofman, T.: Electric motor design optimization: a convex surrogate modeling approach”. *Symp. Adv. Autom. Control* **55**(24), 373 (2022)
12. Guzzella, L., Sciarretta, A.: *Vehicle Propulsion Systems: Introduction to Modeling and Optimization*, 2nd edn. Springer, Berlin Heidelberg (2007)
13. Verbruggen, F.J.R., Salazar, M., Pavone, M., Hofman, T.: Joint design and control of electric vehicle propulsion systems. In *European Control Conference*, 2020
14. Stipetic, S., Zarko, D., Popescu, M.: Ultra-fast axial and radial scaling of synchronous permanent magnet machines. *IET Electr. Power Appl.* **10**(7), 658–666 (2016)
15. Ebbesen, S., Salazar, M., Elbert, P., Bussi, C., Onder, C.H.: Time-optimal control strategies for a hybrid electric race car. *IEEE Trans. Control Syst. Tech.* **26**(1), 233–247 (2018)
16. Ansys Motor-CAD. ANSYS, Inc. Available at <https://www.ansys.com/products/electronics/ansys-motor-cad>
17. Korzilius, O., Borsboom, O., Hofman, T., Salazar, M.: Optimal design of electric micromobility vehicles. In *Proceedings of IEEE International Conference on Intelligent Transportation Systems*, (2021) In Press. Extended version available at <https://arxiv.org/abs/2104.10155>
18. Boyd, S.P., Wegbreit, B.: Fast computation of optimal contact forces. *IEEE Transactions on Robotics* (2007)

19. Parrilo, P.A.: Sum of squares programs and polynomial inequalities. *SIAG/OPT Views News* **15**(2), 7–15 (2004)
20. Konda, M., Hofman, T., Salazar, M.: Energy-optimal design and control of electric powertrains under motor thermal constraints. In *European Control Conference*, (2022) In Press. Available online at <https://arxiv.org/abs/2111.07711>
21. WheelSize. Tire and wheel application fitment data. (2023) Online. Wheel-size.com. <https://www.wheel-size.com/>
22. Wachter, A., Biegler, L.T.: On the implementation of an interior-point filter line-search algorithm for large-scale nonlinear programming. *Math. Progr.* **106**(1), 25–57 (2006)
23. Andersson, J.A.E., Gillis, J., Horn, G., Rawlings, J.B., Diehl, M.: Casadi-a software framework for nonlinear optimization and optimal control. *Math. Progr. Comput.* **11**(1), 1–36 (2019)

Open Access This chapter is licensed under the terms of the Creative Commons Attribution 4.0 International License (<http://creativecommons.org/licenses/by/4.0/>), which permits use, sharing, adaptation, distribution and reproduction in any medium or format, as long as you give appropriate credit to the original author(s) and the source, provide a link to the Creative Commons license and indicate if changes were made.

The images or other third party material in this chapter are included in the chapter's Creative Commons license, unless indicated otherwise in a credit line to the material. If material is not included in the chapter's Creative Commons license and your intended use is not permitted by statutory regulation or exceeds the permitted use, you will need to obtain permission directly from the copyright holder.





Road Friction Adaptive Lateral Control of Automated Vehicles with Differential Braking

Jannes Iatropoulos¹ (✉), Tim Ahrenhold², Leon Salzwedel³, and Roman Henze¹

¹ Institute of Automotive Engineering, Technische Universität Braunschweig,
Hans-Sommer-Straße 4, 38106 Braunschweig, Germany
j.iatropoulos@tu-braunschweig.de

² IAV GmbH, Rockwellstraße 3, 38518 Gifhorn, Germany

³ Volkswagen AG, Berliner Ring 2, 38436 Wolfsburg, Germany

Abstract. Differential braking offers a promising approach to ensure lateral control of automated vehicles in the event of steering actuator failure. Braking interventions induce longitudinal forces on the wheel, which influence the vehicle's yaw motion and thus enable lateral control along a given trajectory. Within the scope of this paper, a road friction adaptive system for lateral vehicle control by differential braking on a dry, wet, snow- and ice-covered road is derived simulatively. The investigated friction coefficient adaption is implemented by a variable path planning and calculated on the basis of an estimated road friction coefficient. The driving situation considered is based on the severe lane-change maneuver according to ISO 3888-2 for the investigation of vehicle dynamics and road-holding ability. The limitation of the trajectory results from the maximum yaw rate and expands the trajectory's length for the different road friction coefficients.

Keywords: differential braking · lateral vehicle control · road friction · fallback level

1 Introduction

After the steering system, the use of braking systems offer a high potential for the lateral control of a vehicle [1]. In the event of a failure in the steering system (e.g. Steer-by-Wire system) official standards describe potential redundancies [2]. With the help of a functional redundancy in form of the brake system already present in the vehicle, a fallback level can be created. This allows actuators already installed in the vehicle to be used and saves costs in the manufacturing process. Wheel-specific braking interventions generate longitudinal forces that influence the yaw moment of the vehicle and thus influence lateral control of an automated vehicle along a given trajectory (Steer-by-Brake, SbB). In order to continue to ensure driving safety in road traffic despite a potential steering failure, the functionality of such a SbB system can be used. In critical situations the fallback system could just function like an automated emergency brake. But if the collision-avoiding braking distance exceeds the last possible avoidance distance, there is only the possibility to steer the vehicle to take evasive action along a calculated trajectory.

© The Author(s) 2024

G. Mastinu et al. (Eds.): AVEC 2024, LNME, pp. 109–115, 2024.

https://doi.org/10.1007/978-3-031-70392-8_16

Under these conditions, a collision could potentially be avoided. The potential of braking interventions for lateral control of automated vehicles has already been discussed in several publications. The majority of the investigations have taken place in simulative environments studies [3], but some publications also validate their results experimentally using real driving tests [4, 5]. The investigations in [5] have shown, that the road friction coefficient is a relevant influencing variable. In order to continue to ensure driving safety in road traffic despite a potential steering failure, the functionality of such a SbB system can be adapted to the road friction coefficient. The focus of the investigations in this paper is not on the possibilities of measuring or estimating the road friction coefficient, but rather on the effects of the SbB function being able to calculate and adapt to the road friction coefficient.

2 Method

The used methodology takes into account the true road friction coefficient μ_R and an estimated value μ_E of the road friction coefficient which are integrated into the SbB function. This method is already used in [6] to investigate the road friction coefficient sensitivity and adaption of automatic emergency braking (AEB) [7] and lane keeping assist (LKA). In this paper, the road friction sensitivity and the friction coefficient adaption for the four classes of a dry, wet, snow- and ice-covered road are simulatively investigated. The four classes of road friction are assigned to four representative characteristic parameters (Table 1).

Table 1. Representative road friction coefficients.

Road condition class	Dry	Wet	Snow	Ice
Road friction coefficient	1.0	0.6	0.3	0.15

3 Function

The trajectory used by the SbB function is calculated depending on two input parameters: the lateral offset y_e which should be achieved and the predefined maximum yaw rate $\dot{\psi}_{max}$. With these two parameters an optimizer is minimizing the best fitting trajectory, so that it achieves the lateral offset and is not exceeding the maximum yaw rate during the maneuver. The y-coordinates $y(x)$ of the trajectory are calculated by a polynomial of the seventh degree [8], the lateral offset y_e which should be achieved and the evasive trajectory length x_e .

$$y(x) = y_e \left[-20 \left(\frac{x}{x_e} \right)^7 + 70 \left(\frac{x}{x_e} \right)^6 - 84 \left(\frac{x}{x_e} \right)^5 + 35 \left(\frac{x}{x_e} \right)^4 \right] \quad (1)$$

The curvature of the trajectory is determined by the first and second derivatives of the coordinates x and $y(x)$ in relation to the arc length s .

$$\kappa(s) = \frac{\dot{x}(s) \cdot \ddot{y}(s) - \ddot{x}(s) \cdot \dot{y}(s)}{(\dot{x}(s)^2 + \dot{y}(s)^2)^{3/2}} \quad (2)$$

The yaw rate $\dot{\psi}(s)$ of the trajectory is calculated by the curvature $\kappa(s)$ and the initial driving speed v_0 .

$$\dot{\psi}(s) = \kappa(s) \cdot v_0 \quad (3)$$

The maximum yaw rate $\dot{\psi}_{max}$ of the evasive trajectory is derived by the context from the kamm's circle, which in this paper is based on the assumption that at the friction limit the same amount of force can be applied in the lateral direction as in the longitudinal direction. As a result, the maximum possible yaw rate $\dot{\psi}_{max}$ of the trajectory is calculated depending on the acceleration of gravity g , the constant road friction coefficient μ_R , a scaling factor k , which describes the ellipse of the kamm's circle and takes the value 0.9 in this investigation and the initial driving speed v_0 [9].

$$\dot{\psi}_{max} = \sqrt{(\mu_R \cdot g)^2 - \frac{(\mu_R \cdot g)^2}{2 \cdot k^2}} / v_0 \quad (4)$$

4 Driving Maneuver

The driving maneuver under investigation (Fig. 1) corresponds to an evasive maneuver with a safety distance of 2.5 m between the vehicles center of gravity (CoG). In this case, a stationary vehicle is approached at initial driving speed v_0 of 80 km/h. Compared to the evasive test according to the standard [10], the lateral safety distance is chosen to be smaller in order to investigate an emergency avoidance maneuver. The test is performed with a non-functioning steering system and the driver does not apply any steering torque during the test procedure. In the beginning the initial lane is driven through a constant driving speed and then changed to a second lane with an offset which is achieved exclusively via differential braking.

Two characteristic parameters are used to investigate the road friction coefficient sensitivity (Fig. 1). The first parameter describes the lateral offset d_Y that is reached at the end of the evasive trajectory, while the second parameter describes the additional distance Δd_E if the vehicle moves out too early due to an incorrectly estimated road friction coefficient μ_E .

The road friction sensitivity and adaption are simulated using a validated dual-track model. In the dual-track model there is a validated steering-model and a Magic Formula tire model of Version 5.2 with the measured parameters of a current winter tire.

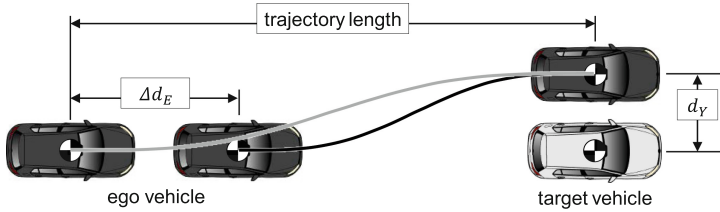


Fig. 1. Driving maneuver of an emergency evasion with differential braking and associated characteristic parameters.

5 Road Friction Coefficient Sensitivity

To find out the sensitivity of differential braking, the road friction coefficient between the selected classes (Table 1) is reduced step by step and the selected characteristic parameter of the lateral offset d_Y is calculated. At the beginning, an SbB function without friction coefficient adaption is examined. This is calculated by the friction coefficient of a dry road surface. It can be seen that the evasive trajectory on the dry road with a road friction coefficient of 1.0 can be driven on with the SbB function, but if the road friction coefficient is now reduced, the evasive action is taken too late on the wet, snow- and ice-covered road and the required lateral offset d_Y can no longer be maintained. Table 2 contains the characteristic parameters of the road friction coefficient sensitivity. It can be seen that the SbB function can only generate the required lateral offset on a dry road, in all other cases it leads to a collision with the target vehicle due to non-compliance with the lateral offset $d_Y = 2.5$ m. The analyses show that the SbB function is very sensitively influenced by the road friction coefficient. In order to nevertheless ensure vehicle safety, the SbB function is to be implemented in a friction-adaptive manner in the further course.

Table 2. Characteristic parameters for road friction coefficient sensitivity of a SbB function.

Road condition class	Dry	Wet	Snow	Ice
Road friction coefficient	1.0	0.6	0.3	0.15
Lateral offset d_Y	2.5 m	2.0 m	1.2 m	0.7 m

6 Road Friction Coefficient Adaption

The road friction coefficient adaption replaces the previously constant parameter of the road friction coefficient μ_R in the calculation of the maximum possible yaw rate $\dot{\psi}_{max}$ of the evasive trajectory with the estimated value μ_E . This estimated value can take the road friction coefficient of a dry, wet, snow- or ice-covered road. The maximum yaw rates to be maintained are now calculated for the evasive trajectories on the various road

friction coefficients according to the following correlation.

$$\dot{\psi}_{max} = \sqrt{(\mu_E \cdot g)^2 - \frac{(\mu_E \cdot g)^2}{2 \cdot k^2}} / v_0 \quad (5)$$

Figure 2 shows four different evasive trajectories that are calculated with the estimated value of a dry, wet, snow-covered or ice-covered road. It can be seen that all calculated trajectories achieve the desired lateral offset $d_Y = 2.5$ m. To guarantee this, the evasive trajectories are lengthened as the estimated value decreases, so that the SbB function evades at comparatively large relative distances to the target vehicle.

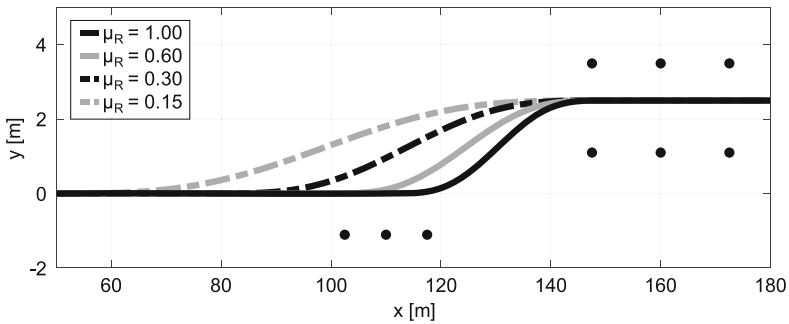


Fig. 2. Evasive trajectories of the SbB function for the road friction coefficients of a dry, wet, snow- and ice-covered road for a vehicle with winter tires.

Due to the correlations, the evasive trajectory of the dry road has the largest and the trajectory of the ice-covered road has the smallest maximum yaw rate $\dot{\psi}_{max}$ that the vehicle must withstand in order to negotiate this path. In the following, the described friction coefficient adaption is examined for an initial driving speed v_0 of 80 km/h. For this purpose, the selected driving maneuver is repeated for the friction coefficients of a dry, wet, snow- or ice-covered road as well as for the estimated values of these classes. The characteristic parameters of the friction coefficient adaption of each individual combination are then calculated and shown in Table 3. It can be seen that the characteristic parameters of the first row correspond to the characteristic parameters of the road friction coefficient sensitivity. For the characteristic parameters of the other rows, the distances of the evasive maneuver were adapted to the estimated values of a wet, snow- or ice-covered road. If the estimated value μ_E corresponds to the true road friction coefficient μ_R , the required lateral offset d_Y can always be maintained. The same applies if the estimated value μ_E is smaller than the true road friction coefficient μ_R . Although the lateral offset can be achieved in this case, the SbB function deviates too early by the distance Δd_E . If the estimated value μ_E is greater than the true road friction coefficient, the required lateral offset $d_Y = 2.5$ m is not reached.

Table 3. Characteristic parameters for road friction coefficient adaption of a SbB function.

		Road friction coefficient μ_R			
		1.0	0.6	0.3	0.15
Estimated road friction coefficient μ_E	1.0	$d_Y = 2.5$ m	$d_Y = 2.0$ m	$d_Y = 1.2$ m	$d_Y = 0.7$ m
	0.6	$\Delta d_E = 11.78$ m	$d_Y = 2.5$ m	$d_Y = 1.6$ m	$d_Y = 1.1$ m
	0.3	$\Delta d_E = 32.94$ m	$\Delta d_E = 21.16$ m	$d_Y = 2.5$ m	$d_Y = 1.7$ m
	0.15	$\Delta d_E = 62.78$ m	$\Delta d_E = 51$ m	$\Delta d_E = 29.83$ m	$d_Y = 2.5$ m

7 Conclusion

The simulation results show, that the evasion test can be passed even on snow- or ice-covered roads. The prerequisite for this is an adaption of the SbB system with regard to an estimated road friction coefficient μ_E . With this method, the required accuracy of the friction value estimation can be determined and also information regarding the driving strategy (e.g. limitation of the maximum speed) can be generated in the event of a steering failure. It can also be seen that a mistake from wet to dry road does not lead to the required lateral offset $d_Y = 2.5$ m, but to a lateral offset of 2 m. This means that the safety distance of 0.5 m between the target and the ego vehicle can no longer be maintained, but a collision with the target vehicle is basically avoided. If the SbB function is compared with that of an AEB, it can be seen that in the event of a steering error on a dry road, the triggering of an AEB is sufficient. However, if the road friction coefficient is reduced, the strengths of the SbB function come into play. In this case, the length of the avoidance distance is shorter than the required braking distance of an AEB, so that potential collisions due to faults in the steering system can be avoided.

References

- Isermann, R. (ed.): *Fahrdynamik-Regelung: Modellbildung, Fahrerassistenzsysteme*, Mechatronik; mit 28 Tabellen, 1st edn. Vieweg, Wiesbaden (2006)
- Kraftfahrzeuge - Anforderungen an ein. Steer-by-Wire (SbW)-System, DIN 70065: 2023-07. Deutsches Institut für Normung, Berlin (2023)
- Kissai, M., Mouton, X., Monsuez, B.: EPAS fail-safe control using differential braking. *Transp. Res. Procedia* **52**, 300–306 (2021). <https://doi.org/10.1016/j.trpro.2021.01.035>
- Salzwedel, L., Iatropoulos, J., Henze, R.: Potential of differential braking as backup system for steering actuators. In: *32th Aachen Colloquium Sustainable Mobility* (2023)
- Jonasson, M., Thor, M.: Steering redundancy for self-driving vehicles using differential braking. *Veh. Syst. Dyn.* **56**(5), 791–809 (2018). <https://doi.org/10.1080/00423114.2017.1356929>
- Anforderungen an die Güte, Verfügbarkeit und Vorausschau einer Reibwertschätzung aus Funktionssicht. *FAT-Schriftenreihe*, no. 355 (2022)
- Ahrenhold, T., Iatropoulos, J., Pethe, C., Henze, R., Küçükay, F.: Accuracy requirements for the road friction estimation of a friction-adaptive Automatic Emergency Brake (AEB). In: *30th Aachen Colloquium Sustainable Mobility* (2021)

8. Tigges, F., Krauns, F., Hafner, A., Henze, R., Küçükay, F.: Controller concept for automated lateral control. In: Pfeffer, P.P.E. (ed.) Proceedings, 8th International Munich Chassis Symposium 2017, pp. 465–481. Springer Fachmedien Wiesbaden, Wiesbaden (2017). https://doi.org/10.1007/978-3-658-18459-9_30
9. Winner, H., Hakuli, S., Lotz, F., Singer, C.: Handbuch Fahrerassistenzsysteme, 3rd edn. Springer Fachmedien Wiesbaden, Wiesbaden (2015). <https://doi.org/10.1007/978-3-658-05734-3>
10. Passenger cars – test track for a severe lanechange manoeuvre – part 2: Obstacle avoidance. ISO 3888-2, International Organization for Standardization, Geneva (2002)

Open Access This chapter is licensed under the terms of the Creative Commons Attribution 4.0 International License (<http://creativecommons.org/licenses/by/4.0/>), which permits use, sharing, adaptation, distribution and reproduction in any medium or format, as long as you give appropriate credit to the original author(s) and the source, provide a link to the Creative Commons license and indicate if changes were made.

The images or other third party material in this chapter are included in the chapter's Creative Commons license, unless indicated otherwise in a credit line to the material. If material is not included in the chapter's Creative Commons license and your intended use is not permitted by statutory regulation or exceeds the permitted use, you will need to obtain permission directly from the copyright holder.





Model-Free Automated Reversing of Articulated Heavy Goods Vehicles

Shammi Rahman^{1,2}(✉) , Timothy Gordon² , Leon Henderson³ ,
Yangyan Gao⁴ , Sonya Coleman¹ , and Dermot Kerr¹ 

¹ Ulster University, Magee Campus, Northland Road, Londonderry BT48 7J, UK
srahman@lincoln.ac.uk

² University of Lincoln, Brayford Way, Lincoln LN6 7TS, UK

³ Chalmers University of Technology, Gothenburg 412 96, Sweden

⁴ Volvo Group North America LLC, Greensboro, NC 27409, USA

Abstract. This paper presents a technique for automated reversing control of articulated vehicles. Reversing articulated Heavy Goods Vehicles (HGVs) can be a challenging and time consuming task for a human driver, sometimes requiring multiple forward and backward motions to reduce errors. Here, the aim is to automate the task to provide high levels of precision using Artificial Flow Guidance (AFG). AFG uses simple geometry to define a spatially distributed motion reference, requiring only short-range error corrections and possessing global convergence properties. AFG has previously been applied to rigid and articulated vehicles in forward motion, with demonstrable benefits in terms of tracking precision and robustness. Here results focus on the tractor-semitrailer, but the AFG approach is equally applicable to the reversing of longer combination vehicles.

Keywords: Automated Reversing · Articulated Vehicles

1 Introduction

Efficient goods transportation is vital to smart manufacturing, industrial automation and commerce in general. HGVs, which are popularly used for goods transportation [11] can however pose stability issues, especially when docking or reversing as the open-loop system is unstable [2,3]. The problem is three-fold: (i) the system is unstable and require the driver feedback to stabilise the vehicle [2] (ii) the trailer moves in the opposite direction to the steering applied at the lead vehicle unit and [5] (iii) the driver cannot always see the rear end of the vehicle, which makes it harder to track the vehicle state as it reaches its control limit [5].

Thus, automated reversing control of articulated vehicles is an active field of research. Notable publications include [2,3,12,13] among others. In [12] a state

The authors would also like to acknowledge the support of the University of Lincoln, Volvo Group Trucks and Innovate UK. This work is supported by the Smart Manufacturing Data Hub project (contract no. 10017032) www.smdh.uk.

© The Author(s) 2024

G. Mastinu et al. (Eds.): AVEC 2024, LNME, pp. 116–122, 2024.

https://doi.org/10.1007/978-3-031-70392-8_17

feedback controller was designed based on a linear dynamic model. The controller was seen to provide good path-tracking performance for vehicles formed of one to three trailers. Altafini et al. [2] also used linear state feedback, a switching logic was applied to allow the multi-unit vehicle to drive forward when at the risk of jackknifing. Yue et al. [13] used a kinematic model to form a Model Predictive Control (MPC) which provides path tracking for both forward and backward direction. In [3] Pure Pursuit was combined with a hitch angle compensator to provide stable reversing on tractor-semitrailers. Again a kinematic model was used. While several other methods have also been successful in providing motion control for reversing, this reliance on vehicle modelling is a common feature. Moreover, prior research have often used optimal or predictive control, which increases design complexity and the number of tuning parameters.

Artificial Flow Guidance (AFG) is a general motion planning method that uses a spatial distribution of desired motion vectors in place of an explicit target path [7, 10]. AFG has minimal tuning parameters and does not rely on detailed vehicle modelling [11]. The method has previously been used for path-tracking in forward motion for a conventional car [7], 4-wheel-steering car [6] and multi-axle steered articulated HGVs [10, 11]. In [9] experimental tests were carried out on a full-size articulated HGV. This showed that AFG can provide precise path-tracking and is feasible for real-time applications [9].

While previous research have demonstrated a number of advantages for AFG in forwards motion, it has not been applied to the reversing of articulated vehicles. Here, for simplicity, we focus on designing a reversing controller for a tractor-semitrailer combination.

2 Artificial Flow Guidance

Individual 2D vectors in the AFG field are calculated using simple geometry and a reference path – see Eq. 1 and Fig. 1(a) respectively. Here, R is a tracking point on the vehicle intended to follow the flow vectors and hence converge to the target path. P is a preview point and Q is the nearest point to R on the desired path. Unit vectors \hat{t}_1 and \hat{t}_2 are tangents at points Q and P , respectively, and \hat{t}_3 is a unit vector at R which points towards P ; 2θ is the angle between tangents \hat{t}_1 and \hat{t}_2 [11]:

$$w = \begin{cases} \hat{t}_3 + \frac{\hat{t}_1 - \hat{t}_2}{2 \cos \theta}, & \text{if } |S_y| \geq S_{y_0} \\ [\cos \Gamma \quad \sin \Gamma]^T, & \text{otherwise} \end{cases} \quad (1)$$

$$\Gamma = \Gamma_0 + \left(\frac{|S_y|}{S_{y_0}} \right) \Gamma_b \quad (2)$$

The flow is modified in the immediate vicinity of the target path in the form of a ‘boundary layer’, where flow angle Γ is interpolated from the exterior flow Γ_b at the boundary – see Fig. 1(b). S_y is the lateral distance between points R and Q , and S_{y_0} is half of the width of the boundary layer. This boundary layer

improves the uniformity of the flow in the presence of sharp curvature changes [11]. Also, imposing a constant magnitude for Γ_b , global convergence is assured provided local tracking errors are bounded [11].

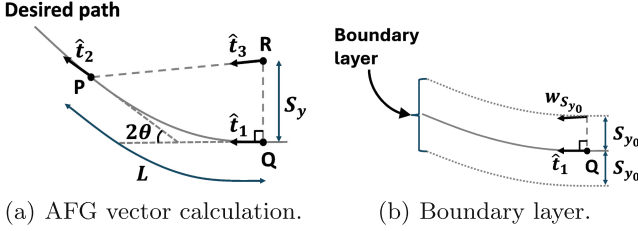


Fig. 1. The AFG vector w is calculated based on the path geometry. A 0.1 m boundary is imposed around the desired path to improve the tracking performance.

The distance between Q and P is the preview distance, L :

$$L = \bar{v} \sqrt{\frac{|S_y|}{2a}} \quad (3)$$

where \bar{v} is the vehicle speed. There are just two tuning parameters: $a = 0.2 \text{ m/s}^2$ is a flow acceleration parameter, and the boundary-layer half-width $S_{y_0} = 0.05 \text{ m}$.

3 Controller Design

We chose the rear end of the semitrailer as the tracking point, for which the AFG vector is found from Eqs. 1–3. The longitudinal component of all velocity vectors on the trailer centre-line are equal, and normalized to unity for interpolation. The AFG vector is also normalised to give \hat{w}_T as the reference (see Fig. 2a).

For low-speed motion we assume zero-sideslip at the 2nd axle on the trailer. In terms of the trailer yaw angle ψ_2 , its normalized velocity is $\hat{v}_z = [\cos \psi_2 \quad \sin \psi_2]^T$. From this and \hat{w}_T , the interpolated velocity at the hitch is found:

$$V_H^d = -\frac{x_T}{L_2} \hat{w}_T + \left(1 + \frac{x_T}{L_2}\right) \hat{v}_z \quad (4)$$

Here, x_T is the distance between the 2nd axle on the trailer and the tracking point, and, L_2 is the trailer wheelbase as shown in Fig. 2(a). The lower-level controller (shown in Fig. 2b) converts this to a yaw rate motion reference using the following:

$$r_1^{ref} = -K(\psi_1 - \phi) + r_2^{ref} \quad (5)$$

Here, ϕ is the angle of the velocity reference at the hitch point with respect to the global X-axis and r_2^{ref} is the reference yaw rate for the trailer, calculated

by considering the desired lateral velocity at the tracking point V_T using $r_2^{ref} = V_T/x_T$. We assume that the hitch point coincides with the zero-sideslip point on the tractor. This means, lateral velocity at the hitch point cannot be controlled directly, and the tractor must be aligned with ϕ to give the correct directional motion. Thus the feedback control aims match the tractor yaw angle ψ_1 to ϕ . $K = 10$ is a proportional gain.

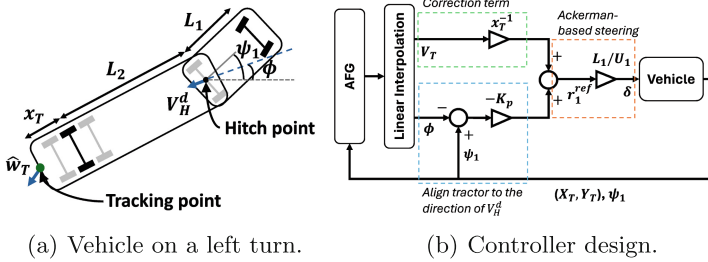


Fig. 2. The lower-level controller uses vehicle kinematics to align the tractor to the direction of the desired velocity vector at the hitch point.

This method also works for cases where the hitch point may be in front of the zero-sideslip point (such as in a 2-axle tractor) but this introduces some tracking error. Finally, the steering angle at the front axle δ is calculated using Ackermann as shown in Eq. 6. Here, U_1 and L_1 are the longitudinal velocity and the effective wheelbase of the tractor, respectively.

$$r_1^{ref} = \frac{U_1 \tan \delta}{L_1} \quad (6)$$

Furthermore, the steering angle is saturated within $-\pi/4 \leq \delta \leq \pi/4$. This also limits the articulation angle to prevent jackknifing [8].

4 Results and Discussion

All simulations were carried out in TruckMaker, which is a commercial simulation software with a library of high-fidelity models. Here, a 6x4 tractor and a 3-axle semitrailer are chosen. The performance of the controller is tested using two maneuvers: (i) a 450° roundabout of radius 20 m and (ii) a 20 m lane change formed using a cosine (equivalent radius is 250 m). The longitudinal velocity is kept constant at -1 m/s for both cases – note that this method also works for variable speeds provided slip angles at the tyres remain small. Figures 3 and 4 shows the results. Here, offtracking is defined as the lateral offset from the desired path.

For the roundabout maneuver shown in Fig. 3, maximum offtracking at the tracking point is 10 cm. This occurs when the vehicle is exiting the roundabout

due to the large change in curvature experienced. With a single steered axle, AFG can only control a single point – this is the rear end of the trailer. The rest of the vehicle follows this point passively.

Figure 4 shows the lane change, maximum offtracking is only 1 cm at the tracking point. For both cases, the vehicle remains stable throughout with the articulation angle staying within 21.2° for the roundabout and 1.7° for the lane change.

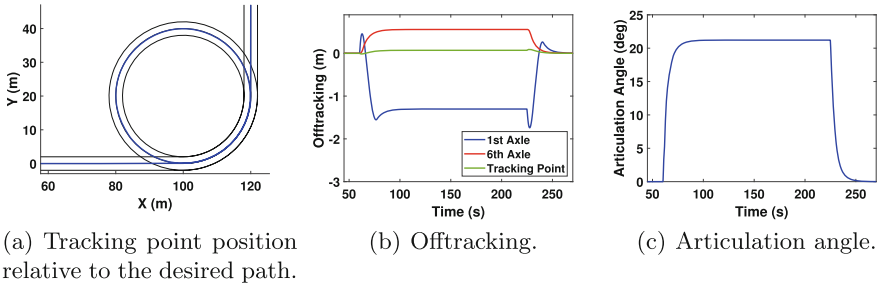


Fig. 3. Simulation results for the roundabout maneuver. Here, 1st axle is the front axle on the tractor and the 6th axle is the rearmost axle on the trailer.

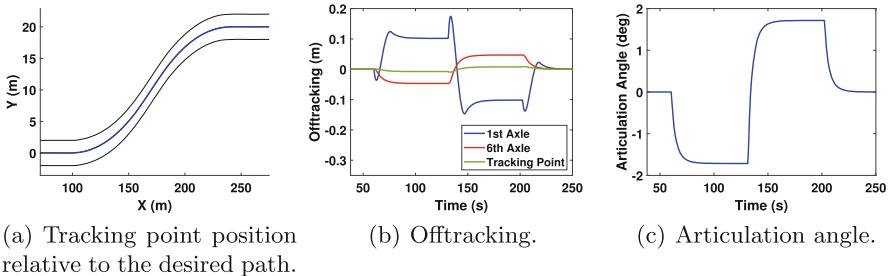


Fig. 4. Simulation results for the lane change maneuver. Here, 1st axle is the front axle on the tractor and the 6th axle is the rearmost axle on the trailer.

5 Conclusion

Reversing HGVs can be a time consuming and challenging task for the human driver. Automating this process can improve supply chain efficiency and contribute positively towards smart manufacturing. AFG was used to design a controller for automated reversing control on tractor-semitrailers. A simple lower-level controller is used to convert the velocity reference at the rear end of the trailer to a yaw rate reference at the fifth wheel.

Simulations rendered in TruckMaker show good tracking performance at the rear end of the semitrailer. For the maneuvers tested, the rear end of the trailer stays within 10 cm of the desired path, even during large changes in path curvature. These results are comparable, if not better than recent publications on reversing control of tractor-semitrailers [1, 4]. This, combined with the simplicity of the control method makes this an attractive solution to the reversing problem.

References

1. Aldughaiyem, A., Bin Salamah, Y., Ahmad, I.: Control design and assessment for a reversing tractor-trailer system using a cascade controller. *Appl. Sci.* **11**(22), 10634 (2021)
2. Altafini, C., Speranzon, A., Wahlberg, B.: A feedback control scheme for reversing a truck and trailer vehicle. *IEEE Trans. Robot. Autom.* **17**(6), 915–922 (2001)
3. Hamaguchi, Y., Raksincharoensak, P.: Automated steering control system for reverse parking maneuver of semi-trailer vehicles considering motion planning by simulation of feedback control system. *J. Robot. Mechatr.* **32**(3), 561–570 (2020)
4. Jing, J., Maroli, J.M., Salamah, Y.B., Hejase, M., Fiorentini, L., Özgüner, Ü.: Control method designs and comparisons for tractor-trailer vehicle backward path tracking. In: 2019 American Control Conference (ACC). pp. 5531–5537. IEEE (2019)
5. Kageyama, I., Saito, Y.: On the backward maneuverability of articulated vehicles. *Veh. Syst. Dyn.* **15**(sup1), 222–232 (1986)
6. Liu, Q., Gordon, T., Rahman, S.: Model-free autonomous control of four-wheel steering using artificial flow guidance. *Vehicle System Dynamics* pp. 1–22 (2023)
7. Liu, Q., Gordon, T., Rahman, S., Yu, F.: A novel lateral control approach for path tracking of automated vehicles based on flow guidance. In: International Conference on Computing, Control and Industrial Engineering. Springer, pp. 100–109. (2021)
8. Morales, J., Martínez, J.L., Mandow, A., García-Cerezo, A.J.: Steering the last trailer as a virtual tractor for reversing vehicles with passive on-and off-axle hitches. *IEEE Trans. Ind. Electron.* **60**(12), 5729–5736 (2013)
9. Rahman, S., Gordon, T., Gao, Y., Henderson, L., Liu, Q., Laine, L.: Automated steering control for precise path tracking and improved stability of articulated heavy goods vehicles. (Submitted)
10. Rahman, S., Gordon, T., Liu, Q., Gao, Y., Henderson, L., Laine, L.: Improved lateral performance of a long combination vehicle based on artificial flow guidance. In: The IAVSD International Symposium on Dynamics of Vehicles on Roads and Tracks. Springer, pp. 726–735 (2021)
11. Rahman, S., Gordon, T., Liu, Q., Gao, Y., Henderson, L., Laine, L.: Artificial flow guidance method for combined off-tracking and stability improvement for automated articulated vehicles. *J. Dyn. Syst. Measur. Control* **146**(3), 1 (2024)
12. Rimmer, A.J., Cebon, D.: Theory and practice of reversing control on multiply-articulated vehicles. *Proc. Inst. Mechan. Eng. Part D. J. Autom. Eng.* **230**(7), 899–913 (2016)
13. Yue, M., Wu, X., Guo, L., Gao, J.: Quintic polynomial-based obstacle avoidance trajectory planning and tracking control framework for tractor-trailer system. *Int. J. Control Autom. Syst.* **17**, 2634–2646 (2019)

Open Access This chapter is licensed under the terms of the Creative Commons Attribution 4.0 International License (<http://creativecommons.org/licenses/by/4.0/>), which permits use, sharing, adaptation, distribution and reproduction in any medium or format, as long as you give appropriate credit to the original author(s) and the source, provide a link to the Creative Commons license and indicate if changes were made.

The images or other third party material in this chapter are included in the chapter's Creative Commons license, unless indicated otherwise in a credit line to the material. If material is not included in the chapter's Creative Commons license and your intended use is not permitted by statutory regulation or exceeds the permitted use, you will need to obtain permission directly from the copyright holder.





Nonlinear Dynamics of a Controlled Two-Wheeled Trailer

Hanna Zsofia Horvath^{1(✉)}, Adam Balint Feher¹, and Denes Takacs^{1,2}

¹ Budapest University of Technology and Economics, Faculty of Mechanical Engineering, Department of Applied Mechanics, Budapest, Hungary

hanna.horvath@mm.bme.hu

² HUN-REN-BME Dynamics of Machines Research Group, Budapest, Hungary

Abstract. The nonlinear dynamics of towed two-wheeled trailers is investigated using a spatial, 4-DoF model. Namely, the yaw, pitch, and roll motions are all taken into account. Geometrical nonlinearities and the non-smooth characteristics of the tire forces are considered. A linear state feedback controller with feedback delay is designed to enhance the stability performance of the trailer. Numerical bifurcation analysis is performed to investigate the large amplitude vibrations and unsafe (bistable) zones, where the stable rectilinear motion and the stable limit cycle coexist with each other. The effects of the control gain and the feedback delay of the controller are presented on bifurcation diagrams. It is shown, that with appropriately chosen control gains, the size of the bistable region can be limited.

Keywords: towed two-wheeled trailer · stability control · nonlinear analysis · feedback delay

1 Introduction

Vehicle handling and stability are critical factors in road transportation; hence, they became relevant research topics a long time ago, see e.g. [1–4]. Unfortunately, several road accidents happen due to the not appropriately chosen amount of payload or payload position, which easily leads to the so-called snaking and rocking motions of trailers. Most of the previous studies are limited to linear stability analysis and are based on single-track (in-plane) models. In this study, we focus on the nonlinear dynamics of two-wheeled trailers, using a spatial mechanical model.

2 Mechanical Model and Control Design

The applied spatial, 4-DoF mechanical model is shown in Fig. 1(a). The trailer is towed with constant towing speed v . For the sake of simplicity, the towing car is imitated by a lateral spring and damper at the kingpin A. The motion of

the system can be described with the yaw angle ψ , the pitch angle ϑ , the roll angle φ , and the lateral displacement of the king pin u . Details of the derivation of the governing equations can be found in [5]. Here, we only present the different sources of the relevant nonlinearities and non-smoothness.

Figure 1(b) shows the non-smooth characteristics of the suspension forces. A piecewise smooth formula is introduced for the right $F_R = F_s(d_R)$ and the left $F_L = F_s(d_L)$ suspension forces, where d_R is the distance measured between the points R and R', and d_L is the distance measured between points L and L', see panel (a) of Fig. 1. We take into account that the right or left tire can detach from the ground, and the related vertical load N_R or N_L becomes zero. We neglect the effect of the unsprung mass by considering zero masses for the wheels. Hence, zero normal load corresponds to zero suspension forces in our model. In Fig. 1(b), L_{\max} relates to the maximal length of the suspension, i.e., where the suspension is fully expanded. In addition, for $d < L_{\min}$, we consider higher stiffness and damping for the full compression case.

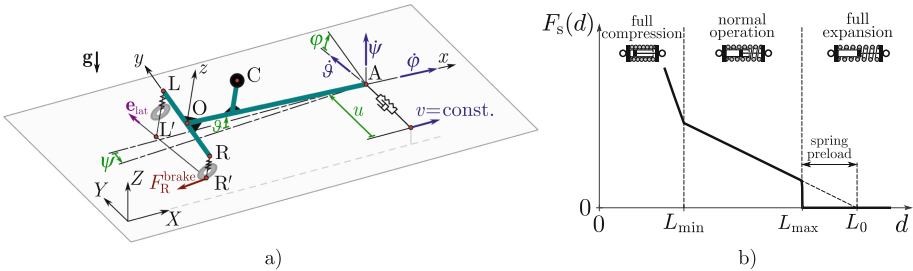


Fig. 1. (a) The towed two-wheeled trailer with the braking force at the right wheel, (b) the schematic non-smooth characteristic of the suspension forces

The effect of the tires is taken into account by means of the lateral tire forces only, which are calculated based on Pacejka's Magic Formula [6]:

$$\mu(\alpha) = D \sin (C \arctan (B \alpha - E (B \alpha - \arctan (B \alpha)))) , \quad (1)$$

where B , C , D and E are semi-empirical factors, and α is the side slip angle of the right (α_R) and the left (α_L) wheel. With these, the tire forces are

$$F_R^{\text{tire}} = N_R \mu(\alpha_R), \quad F_L^{\text{tire}} = N_L \mu(\alpha_L). \quad (2)$$

Namely, we assume that the lateral tire forces depend linearly on the vertical loads. In addition, we neglect the dependencies of the factors of the Magic Formula on the static and dynamic coefficients of friction, the temperature, and the camber angle.

To control the snaking motion of the trailer, we design a linear state feedback controller, which operates with the braking forces applied to the right and the left wheels, see Fig. 1(a). We consider braking forces proportional to the yaw

rate $\dot{\psi}$ and take into account the deadzone $2\dot{\psi}_0$ of the controller, where no braking force is actuated. Furthermore, we consider the feedback delay τ of the controller. Thus, the non-smooth characteristics of the right and left braking forces can be formulated as

$$F_R^{\text{brake}} = \begin{cases} D(\dot{\psi}(t - \tau) - \dot{\psi}_0), & \text{if } \dot{\psi}(t - \tau) > \dot{\psi}_0, \\ 0, & \text{if } \dot{\psi}(t - \tau) < \dot{\psi}_0, \end{cases} \quad (3)$$

$$F_L^{\text{brake}} = \begin{cases} -D(\dot{\psi}(t - \tau) + \dot{\psi}_0), & \text{if } \dot{\psi}(t - \tau) < -\dot{\psi}_0, \\ 0, & \text{if } \dot{\psi}(t - \tau) > -\dot{\psi}_0, \end{cases} \quad (4)$$

where D is the control gain. The non-smooth characteristics of the tire forces and the braking forces are handled by a smoothed Heaviside-function in our numerical investigation, see, e.g. [5]. Since we investigate the straight running of the two-wheeled trailer, the reference yaw rate is set to zero in this study.

For the sake of simplicity, we do not implement the combined slip in the model. However, we pay attention to the relation between the longitudinal forces (i.e., the braking forces), the lateral tire forces, and the vertical loads. Namely, we define the required coefficients of friction $\mu_{\text{req,R}}$ and $\mu_{\text{req,L}}$ as

$$\mu_{\text{req,R}} = \frac{\sqrt{(F_R^{\text{brake}})^2 + (F_R^{\text{tire}})^2}}{N_R}, \quad \mu_{\text{req,L}} = \frac{\sqrt{(F_L^{\text{brake}})^2 + (F_L^{\text{tire}})^2}}{N_L}. \quad (5)$$

3 Nonlinear Stability Analysis

Nonlinear bifurcation analysis is carried out with *DDE-BIFTOOL* [7]. The stable and unstable periodic solutions are depicted in bifurcation diagrams, in the plane of the towing speed v and the maximum amplitudes of the yaw angle ψ , the pitch angle ϑ , the roll angle φ , and the lateral displacement of the king pin u , see Fig. 2. Based on the continuation, one can observe that the pitch motion is asymmetric. Thus, both the max/min values of the periodic solutions are illustrated for ϑ . The results are shown for parameter values described in [5], but for vertical payload position of $h = 0.27$ m. The half-width of the deadzone was $\dot{\psi}_0 = 0.1$ rad/s in this study.

In the bifurcation diagrams, dashed red lines and solid blue lines refer to unstable and stable motions, respectively. For every branch point of the periodic solutions, the required coefficients of friction of Eq. (5) are calculated. During the continuation of the bifurcation branch, if $\mu_{\text{req,R}}$ and/or $\mu_{\text{req,L}}$ reaches the pre-defined threshold $\mu_{\text{cr}} = 1$, we define the corresponding branch point as the limit of validity. The remaining segment of the bifurcation branch is plotted thin and gray, namely, we consider it invalid.

The bifurcation diagrams in Fig. 2 are constructed for the delay-free case (i.e., $\tau = 0$) for different control gains. For the uncontrolled case (i.e., $D = 0$), a relatively wide bistable region is present, where the stable rectilinear motion coexists with unstable and stable periodic solutions. It is considered an unsafe

zone since the global stability of the rectilinear motion is not ensured in this linearly stable towing speed range, and large enough perturbations may lead to unwanted large amplitude vibrations of the trailer. By increasing the control gain, the width of the unsafe zone and the amplitudes of the vibrations are decreased.

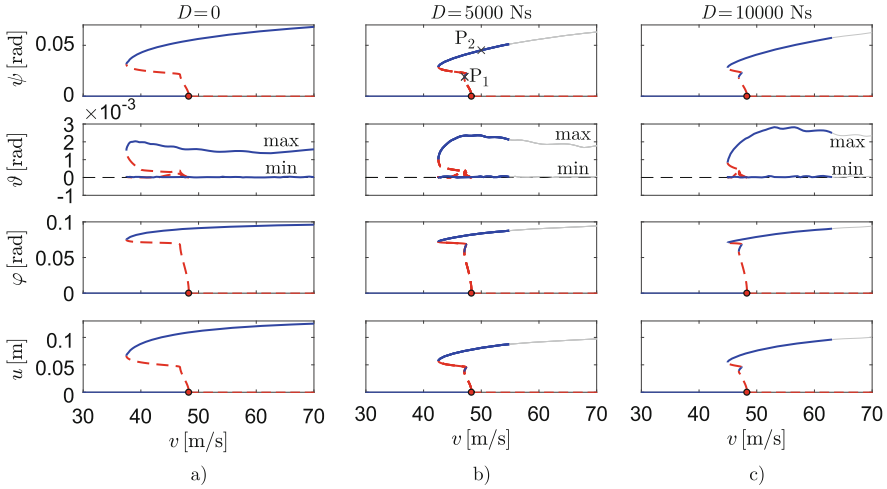


Fig. 2. Bifurcation diagrams with respect to the towing speed v for the delay-free controller ($\tau = 0$) and for different control gains: a) $D = 0$, b) $D = 5000 \text{ Ns}$, c) $D = 10000 \text{ Ns}$

In Fig. 3, numerical results are presented for points P_1 and P_2 of Fig. 2(b). Namely, the periodic solutions for the normal loads, the tire forces, the braking forces, and three of the generalized coordinates (ψ , φ , and u) are plotted for one period T of the oscillation. Point P_1 corresponds to the point of the stable branch with smaller amplitudes and towing speed of $v = 47.22 \text{ m/s}$. As can be observed in Fig. 3(a), no loss of contact of tires happens for this point, i.e., no rocking motion occurs. In addition, the tire forces, the braking forces, and the amplitudes of the vibrations remain moderate. Point P_2 corresponds to the point of the stable branch with larger amplitudes and towing speed of $v = 50.35 \text{ m/s}$. Both full compression and full expansion of the wheel suspension happen, and loss of contact of tires also occurs, see Fig. 3(b). Furthermore, the tire forces, the braking forces, and the amplitudes of the vibrations are remarkably larger.

The effect of the feedback delay τ is shown in the bifurcation diagrams of Fig. 4 for a fixed value of the control gain $D = 5000 \text{ Ns}$. As shown, it significantly affects the nonlinear stability properties. The unsafe zone is narrower, and the amplitudes of the corresponding periodic solutions are smaller for larger feedback delay values. This is a counterintuitive result since it suggests that the feedback delay can be beneficial. Of course, a very large delay (i.e., $\tau \geq 0.2 \text{ s}$) degrades the performance of the controller.

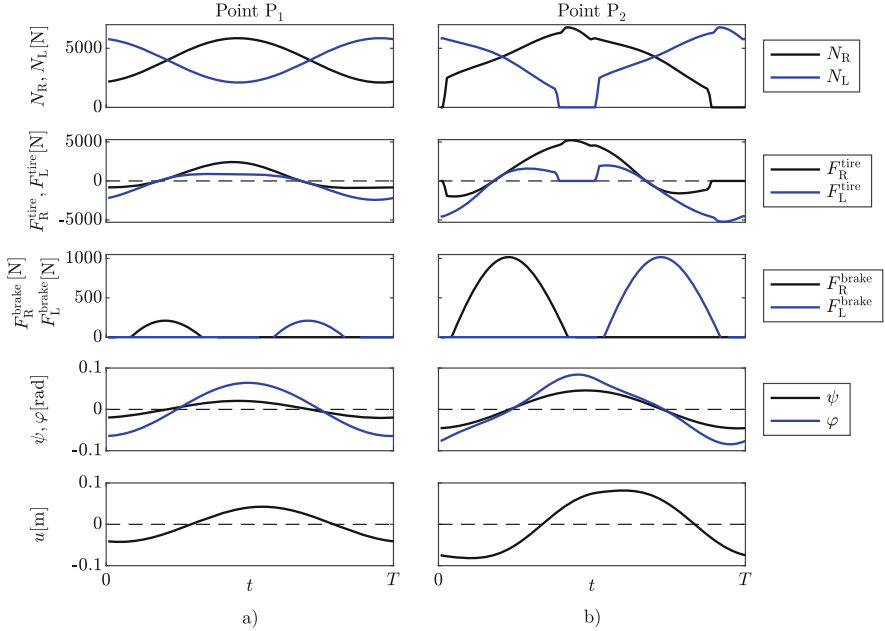


Fig. 3. Numerically determined time histories of the normal loads, the tire forces, the braking forces and the generalized coordinates ψ , φ , and u , for control gain $D = 5000$ Ns and feedback delay $\tau = 0$. Panels refer to the points marked in Fig. 2(b).

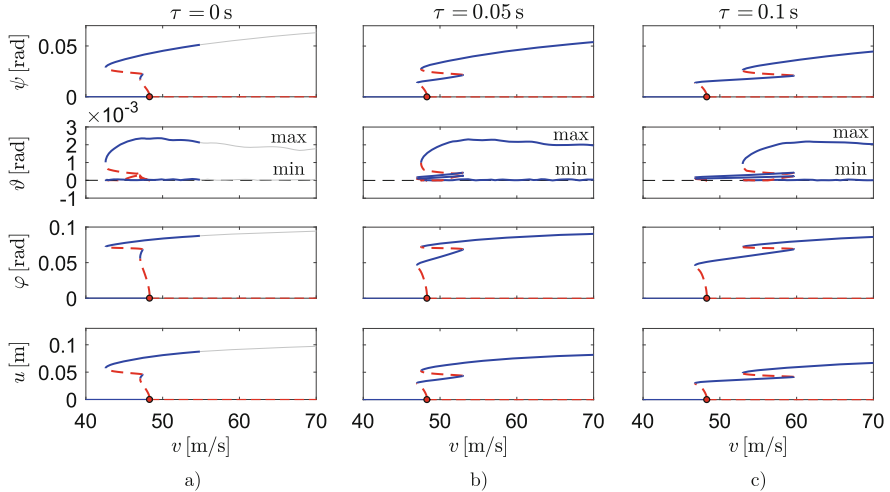


Fig. 4. Bifurcation diagrams with respect to the towing speed v for fixed control gain ($D = 5000$ Ns) and for different feedback delays: a) $\tau = 0$ s, b) $\tau = 0.05$ s, c) $\tau = 0.1$ s

4 Conclusions

In this study, we performed nonlinear stability analysis of the spatial mechanical model of towed two-wheeled trailers. A linear state feedback controller with feedback delay was designed to reduce the unwanted vibrations of snaking trailers. The deadzone and the feedback delay of the controller were taken into account. For the uncontrolled case, a considerably wide unsafe zone (a so-called bistable region) can be observed. It was shown that this unsafe zone can be reduced by applying braking forces to the wheels. In addition, some feedback delays may have some beneficial effects on global stability.

Acknowledgements. The research is supported by the National Research, Development and Innovation Office under grant no. NKFI-146201, 2020-1.2.4-TET-IPARI-2021-00012 and partly supported by the Janos Bolyai Research Scholarship of the Hungarian Academy of Sciences. Supported by the UNKP-23-5-BME-299, UNKP-23-3-II-BME-137 New National Excellence Program of the Ministry for Innovation and Technology from the source of the National Research, Development and Innovation Fund. This project has received funding from the HUN-REN Hungarian Research Network. The research is partly supported by the Foundation for Mechanical Engineering Education.

References

1. Darling, J., Tilley, D., Gao, B.: An experimental investigation of car-trailer high-speed stability. *Proc. Inst. Mech. Eng. Part D. J. Autom. Eng.* **223**(4), 471–484 (2009). <https://doi.org/10.1243/09544070JAUTO981>
2. Sharp, R.S., Fernandez, M.A.A.: Car-caravan snaking - part 1: the influence of pintle pin friction. *Proc. Inst. Mech. Eng. Part C J. Mech. Eng. Sci.* **216**(7), 707–722 (2002). <https://doi.org/10.1243/09544060260128760>
3. Troger, H., Zeman, K.: A nonlinear-analysis of the generic types of loss of stability of the steady-state motion of a tractor-semitrailer. *Vehicle Syst. Dyn.* **13**(4), 161–172 (1984). <https://doi.org/10.1080/00423118408968773>
4. Kang, X., Deng, W.: Parametric study on vehicle-trailer dynamics for stability control. *SAE Technical Paper Series* (2003). <https://doi.org/10.4271/2003-01-1321>
5. Horvath, H.Z., Takacs, D.: Stability and local bifurcation analyses of two-wheeled trailers considering the nonlinear coupling between lateral and vertical motions. *Nonlinear Dyn.* **107**, 2115–2132 (2022). <https://doi.org/10.1007/s11071-021-07120-9>
6. Pacejka, H.B.: *Tyre and Vehicle Dynamics*. Elsevier Butterworth-Heinemann (2002)
7. Engelborghs, K., Luzyanina, T., Samaey, G.: *DDE-BIFTOOL v. 2.00: a Matlab package for bifurcation analysis of delay differential equations*. Department of Computer Science, K.U. Leuven (2001)

Open Access This chapter is licensed under the terms of the Creative Commons Attribution 4.0 International License (<http://creativecommons.org/licenses/by/4.0/>), which permits use, sharing, adaptation, distribution and reproduction in any medium or format, as long as you give appropriate credit to the original author(s) and the source, provide a link to the Creative Commons license and indicate if changes were made.

The images or other third party material in this chapter are included in the chapter's Creative Commons license, unless indicated otherwise in a credit line to the material. If material is not included in the chapter's Creative Commons license and your intended use is not permitted by statutory regulation or exceeds the permitted use, you will need to obtain permission directly from the copyright holder.





Yaw Stability Control of Vehicles Using a Slip Polytope Validated with Real Tests

Umur Erdinc^{1,2}(✉), Mats Jonasson², Maliheh Sadeghi Kati¹, Leo Laine^{1,2}, Bengt Jacobson², and Jonas Fredriksson²

¹ Volvo Group Trucks Technology, Gothenburg, Sweden
umur.erdinc@volvo.com

² Chalmers University of Technology, Gothenburg, Sweden

Abstract. Articulated heavy vehicles (AHVs) face yaw instabilities, especially under extensive propulsion or regenerative braking force on the driven axles, risking their directional stability and potentially leading to jackknifing. Hence, safe operating envelopes (SOEs) are essential for allocating propulsion and braking forces among different units. This study proposes a novel approach to ensure yaw stability by reducing longitudinal slip limits of the electric motors (EMs) based on side-slip, enhancing stability and acceleration performance. Validation through simulations and real vehicle tests shows promising results.

Keywords: Safe Operating Envelope · Slip Polytope · Jackknifing · Articulated Heavy Vehicles · Slip Controller · Yaw Stability

1 Introduction

Electrification affects both trucks and trailing units like trailers and dollies. With multiple units propelled, AHVs face increased risk of yaw instabilities. Regenerative braking by tractor's EMs without braking semitrailer can cause jackknifing, while braking only semitrailer's EMs with an unbraked tractor can lead to trailer swing [1]. The same problems may also occur during propulsion. Hence, safe motion control of AHVs is crucial while maintaining the highest energy efficiency. While previous research defines SOEs in wheel force domain [1, 2], side-slip angle vs. side-slip angle rate [3], lateral velocity vs. yaw rate [4] or side-slip angle vs. yaw rate [5], this study forms a SOE in the longitudinal slip vs. side-slip angle domain. Advanced EMs in modern AHVs offer new opportunities for ensuring yaw stability. While slip controllers usually have rather constant longitudinal slip limits, it is a well-known fact in vehicle dynamics that high longitudinal slip reduces lateral force generation for a given lateral slip [6]. Thus, an advanced slip control strategy, rather than fixed slip limits, is needed to ensure yaw stability.

This study investigates an electric tractor and conventional semitrailer combination, introducing a new slip control strategy. Longitudinal slip limits of EMs vary based on side-slip angle deviation from an estimated reference value at the driven axle. This approach ensures adequate lateral force capability and yaw stability, tested first through

simulations, and then validated with a real test vehicle on a circular snow/ice test track, at Colmis Proving ground in Northern Sweden.

2 Reference Side-Slip Angle Estimation

A reference side-slip angle for the vehicle is obtained with an estimator incorporating a single-track vehicle model. The free-body diagram of the tractor is shown in Fig. 1. The lateral force and the yaw moment equilibria around the center of gravity (CoG) for the tractor are expressed as:

$$\begin{aligned} m_1 \cdot (\dot{v}_{1y} + \omega_{1z} \cdot v_{1x}) &= \cos(\delta_f) \cdot F_{1f_{yw}} + F_{1r_y} + P_{1c_y} \\ J_1 \cdot \dot{\omega}_{1z} &= F_{1f_{y'}} \cdot l_{1CoG} - F_{1r_y} \cdot (L_1 - l_{1CoG}) - P_{1c_y} \cdot (l_{1c} - l_{1CoG}) \end{aligned} \quad (1)$$

The compatibility equations are derived as:

$$\begin{aligned} v_{1f_y} &= v_{1y} + \omega_{1z} \cdot l_{1CoG}, & v_{1f_{xw}} &= v_{1x} \cdot \cos(\delta_f) + v_{1f_y} \cdot \sin(\delta_f) \\ v_{1r_y} &= v_{1y} - \omega_{1z} \cdot (L_1 - l_{1CoG}), & v_{1f_{yw}} &= -v_{1x} \cdot \sin(\delta_f) + v_{1f_y} \cdot \cos(\delta_f) \end{aligned} \quad (2)$$

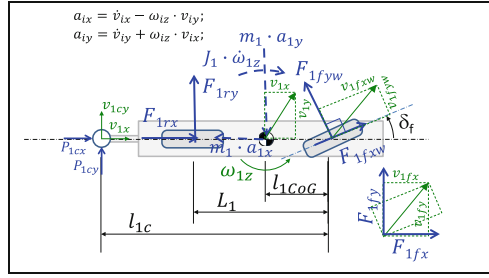


Fig. 1. Free body diagram of the tractor

The lateral axle slips and the lateral tire forces are defined as:

$$s_{1f_y} = \frac{v_{1f_{yw}}}{|v_{1f_{xw}}|}, \quad s_{1r_y} = \frac{v_{1r_y}}{|v_{1x}|} \quad (3)$$

$$F_{1f_{yw}} = -C_{1f} \cdot s_{1f_y} \cdot F_{1f_z}, \quad F_{1r_y} = -C_{1r} \cdot s_{1r_y} \cdot F_{1r_z} \quad (4)$$

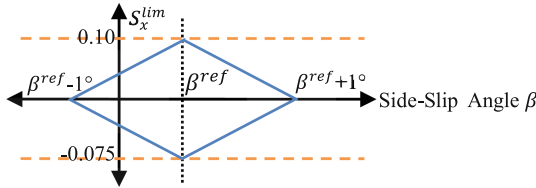
Here, the tractor yaw acceleration, $\dot{\omega}_{1z}$, is assumed to be zero for model simplicity. As longitudinal speeds are always positive, the absolute signs in (3) are omitted. All longitudinal wheel forces are set to zero, meaning the reference side-slip angle is calculated for a quasi steady-state turning maneuver without braking or propelling. The longitudinal vehicle speed, v_{1x} , and the steering angle, δ_f , are known inputs to the estimator. Furthermore, the lateral coupling force, P_{1y} , is considered known, simplifying the estimator and avoiding the semitrailer equations. A total of 10 equations can be solved for 10 unknowns: ω_{1z} , $F_{1f_{yw}}$, F_{1r_y} , s_{1f_y} , s_{1r_y} , $v_{1f_{yw}}$, v_{1r_y} , $v_{1f_{xw}}$, v_{1f_y} , v_{1y} . The vehicle parameters are given in Table 1. This open-loop estimator calculates the reference lateral axle slip, s_{1r_y} , as a side-slip angle (β^{ref}) at the tractor drive axle. Its accuracy, validated against VTM (Volvo Transport Model) high-fidelity model [7] simulations, reaches approximately $\pm 0.1^\circ$ for various maneuvers.

Table 1. Tractor vehicle parameters for reference side-slip angle estimation

Parameter	Explanation	Value	Unit
F_{1fz}, F_{1rz}	Front and rear axle normal loads	67689, 91741	N
C_{1f}, C_{1r}	Normalized front and rear axle cornering stiffnesses	6	N/N/rad
L_1	Tractor wheelbase	3.8	m
l_{1CoG}, l_{1c}	Tractor CoG and coupling distance to the front axle	1.351, 3.225	m
m_1	Tractor mass	9000	kg

3 Simulation Tests

In this section, the performance of two slip controllers are compared: one with a fixed longitudinal slip limit and another one with an adaptive longitudinal slip limit based on the side-slip angle, using the VTM. In the first controller, S_x^{lim} is set at +10% for propulsion and -7.5% braking. In the second controller, S_x^{lim} decreases for any deviation from β^{ref} (estimated via the estimator explained in Sect. 2), on the tractor drive axle, as shown in Fig. 2. S_x^{lim} is linearly decreased and set as 0 for $\pm 1^\circ$ deviation from β^{ref} . This would provide more lateral force capability for the tires to maintain yaw stability at high side-slip angles and high lateral accelerations. The resultant shape of the slip limits is a 2-dimensional polytope.

**Fig. 2.** Tractor EM slip limit. Case a: fixed (orange), Case b: adaptive (blue).

β^{ref} is estimated using the estimator for a quasi-steady-state maneuver as explained in Sect. 2. Inputs to the estimator, (v_{1x} , δ_f , and P_{1y}), are extracted from the VTM model. Figure 3 illustrates a propel-in-turn maneuver performed on ice (with 0.1 friction coefficient, μ) on a reference path with a 115 m turning radius. The vehicle combination accelerates to 25 km/h with a rather low, 40% friction utilization (3670 N axle force). Here, the friction utilization is defined as $F_x/(\mu F_z)$, where the F_x and F_z are the longitudinal and normal forces on the wheels. When the vehicle reaches 25 km/h (indicated by a black vertical line), the tractor drive axle propulsion forces are increased from 3670 N to 9170 N, reaching full (100%) friction utilization. Slip controllers control wheel slips, with one EM equipped with a slip controller per driven wheel. A simple PID controller for path-following steers the vehicle. The vehicle equipped with a fixed slip limit controller (case a) experiences jackknifing, with the speed, V_x reaching a maximum of 26.3 km/h. The vehicle equipped with more advanced slip controller with an adaptive S_x^{lim} (case b),

on the other hand, can accelerate smoothly and stably up to 34 km/h. During maneuver b, longitudinal slip, S_x ; side-slip angle, β ; and steering wheel angle, δ , are kept at reasonable values.

In Table 2, simulation results for four maneuvers are presented, comparing constant and adaptive slip limits. Previous results are related to maneuver 1. Two friction coefficients are tested: $\mu = 0.1$ for ice, and $\mu = 0.3$ for snow. Four turning radii, R , with various initial speeds, $V_{initial}$, and target speeds, V_{target} , are examined. $V_{initial}$ is the speed at which the longitudinal force corresponding to full friction utilization is applied, indicated by solid vertical lines in Fig. 3. In Table 2, additionally, normalized lateral acceleration values, $\frac{V_{target}^2/R}{\mu \cdot g}$, for the given friction coefficients and turning radii, are included. These values, ranging between 0.7 and 0.8 for all maneuvers, signify the aim for high lateral accelerations by the end of the maneuvers.

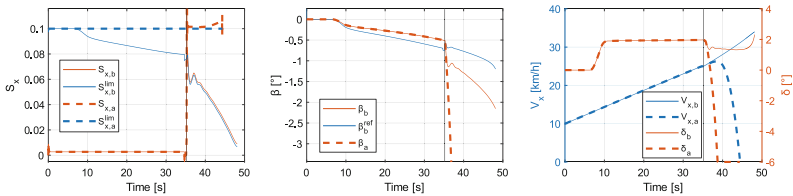


Fig. 3. Simulated test state plots for constant (a) and adaptive (b) slip limits

Table 2. Simulation test results

Maneuver	μ	R [m]	$V_{initial}$ [km/h]	V_{target} [km/h]	$\frac{V_{target}^2/R}{\mu \cdot g}$	a: Constant S_x^{lim}		b: Adaptive S_x^{lim}	
						V_{max} [km/h]	Jack-knifing	V_{max} [km/h]	Jack-knifing
1	0.1	115	25	34	0.79	26.3	Yes	34.0	No
2	0.1	160	30	40	0.79	31.1	Yes	40.0	No
3	0.3	70	35	44	0.73	37.5	Yes	44.0	No
4	0.3	137.5	50	61	0.71	52.0	Yes	61.0	No

All maneuvers employing slip controllers with fixed slip limits result in jackknifing, with the vehicle's maximum reachable speed, V_{max} , only a few km/h higher than $V_{initial}$. This indicates that applying a high propulsion force with a fixed slip limit on the slip controller leads to instability and jackknifing, as shown in the path plots in Fig. 4. Conversely, the vehicle equipped with slip controllers with adaptive slip limits can reach V_{target} , without encountering stability problems.

4 Real Vehicle Tests

The test vehicle accelerates from 25 km/h to 40 km/h on an ice surface ($\mu \approx 0.1$) along a circular track with a radius of 115 m, with a high propulsion force corresponding to full friction utilization. The slip controller for the tractor's EM is activated, while the electronic stability controllers are turned off. Side-slip angles are accurately measured using a global navigation satellite system/inertial navigation system.

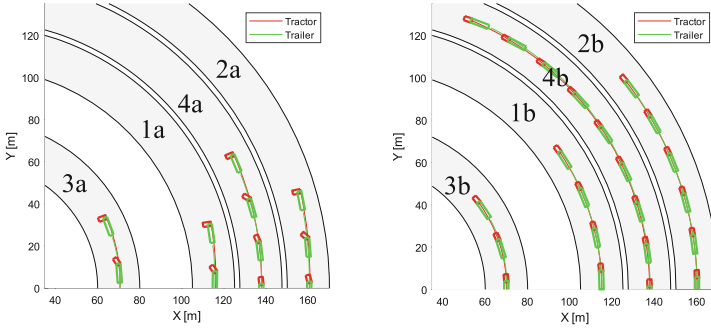


Fig. 4. Path plots of the maneuvers

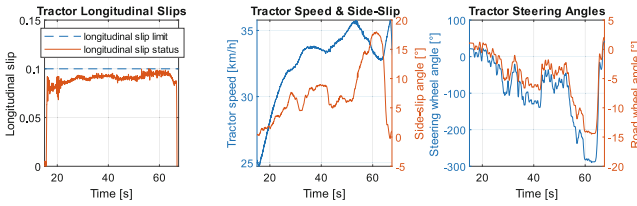


Fig. 5. State plots for real vehicle test with default slip controller

With the default slip controller (constant 10% slip limit), depicted in Figs. 5 and 7, the longitudinal slips remain under 10%. However, despite significant counter-steering effort by the driver (up to -15° road wheel angle), the side-slip angle grows to significant values (up to 18°). The vehicle fails to accelerate up to 40 km/h even in 53 s. The vehicle motion is quite unstable and always has large yaw dynamics.

The test results with the adaptive slip limit are shown in Figs. 6 and 7. β^{ref} is set at $+1^\circ$, which represents the observed quasi-steady-state β for the maneuver, without using the β^{ref} estimator as in the simulated tests. However, the side-slip angle margin remains at $\pm 1^\circ$, consistent with the simulated tests. With this strategy, the vehicle reaches a speed of 40 km/h in just 17 s, as shown in Fig. 6. Moreover, this is achieved with minimal side-slip angles (always below 2°) and without requiring additional driver counter-steering effort from the driver. The driver can easily follow the lane with a very reasonable (approximately) 1.5° road wheel angle.

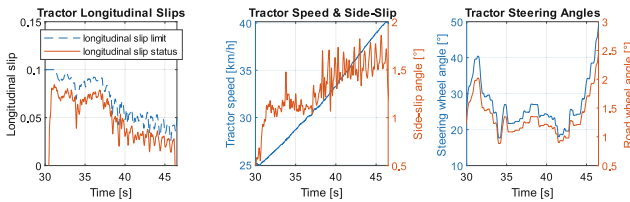


Fig. 6. State plots for real vehicle test with slip controller with adaptive slip limits

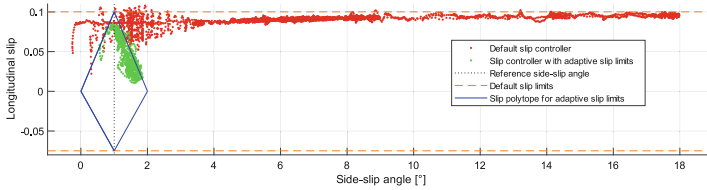


Fig. 7. Longitudinal slip vs. side-slip angle scatter plot for two types of controllers

5 Conclusion

This study introduces a side-slip angle estimator and a slip controller incorporating an adaptive longitudinal slip limit based on lateral slip and compares it against the default slip controller through both simulations and real vehicle tests. Simulation results demonstrate the superior performance of adaptive slip limits over fixed slip limits for various maneuvers on ice and snow, and for different turning radii. In real tests, the superior performance of the adaptive slip limits is validated when the driver is in the loop. The study shows that adaptive slip limits not only ensure yaw stability but also improve acceleration performance. The slip polytope used in this study is two-dimensional, constraining longitudinal slip as a function of the tractor's side-slip angle. However, it is envisioned that the polytope can have more dimensions, such as side-slip angles of the trailing units, and yaw rates. A reference side-slip angle estimator for a well-performing quasi-steady-state turning maneuver is presented. Additionally, this estimator can also estimate the reference yaw rate, which can be employed in the safety polytope. A significant advantage of this method is that friction estimation is not required although it could improve the reference side-slip angle estimator. Even though this paper focuses on a tractor and a semitrailer combination, the adaptive slip limits are applicable to passenger cars and single unit heavy vehicles as well.

References

1. Erdinc, U., Jonasson, M., Kati, M.S., et al.: Safe operating envelope based on a single-track model for yaw instability avoidance of articulated heavy vehicles. *Veh. Syst. Dyn.* (2023). <https://doi.org/10.1080/00423114.2023.2276767>
2. Erdinc, U., Jonasson, M., Kati, M.S., et al.: Validation of high-fidelity simulation-based safe operating envelopes for articulated heavy vehicles using real test data. *Veh. Syst. Dyn.* (2024). <https://doi.org/10.1080/00423114.2023.2296595>
3. Fu, R., Zhang, H., Guo, Y., et al.: Real-time estimation and prediction of lateral stability of coaches: a hybrid approach based on EKF, BPNN, and online autoregressive integrated moving average algorithm. *IET Intell. Transp. Syst.* **14**(13), 1892–1902 (2020). <https://doi.org/10.1049/iet-its.2020.0385>
4. Funke, J., Brown, M., Erlien, S.M., et al.: Collision avoidance and stabilization for autonomous vehicles in emergency scenarios. *IEEE Trans. Control Syst. Technol.* **25**(4), 1204–1216 (2017). <https://doi.org/10.1109/TCST.2016.2599783>
5. Erlien, S.M., Fujita, S., Gerdes, J.C.: Shared steering control using safe envelopes for obstacle avoidance and vehicle stability. *IEEE Trans. Intell. Transp. Syst.* **17**(2), 441–451 (2016). <https://doi.org/10.1109/TITS.2015.2453404>

6. Jacobson, B.J.H.: Vehicle Dynamics Compendium. Chalmers University of Technology, Gothenburg (Sweden) (2020)
7. Fröjd N. Handling analysis and control development of commercial trucks with Volvo Transport Models. Material presented at: MATLAB EXPO 2021; 2021 May 4–5. Available from: <https://se.mathworks.com/videos/handling-analysis-and-control-development-of-commercial-trucks-with-volvo-transport-models-1622035211192.html>

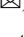
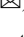





Open Access This chapter is licensed under the terms of the Creative Commons Attribution 4.0 International License (<http://creativecommons.org/licenses/by/4.0/>), which permits use, sharing, adaptation, distribution and reproduction in any medium or format, as long as you give appropriate credit to the original author(s) and the source, provide a link to the Creative Commons license and indicate if changes were made.

The images or other third party material in this chapter are included in the chapter's Creative Commons license, unless indicated otherwise in a credit line to the material. If material is not included in the chapter's Creative Commons license and your intended use is not permitted by statutory regulation or exceeds the permitted use, you will need to obtain permission directly from the copyright holder.





Study on Accident-Avoidance Mechanism in Driver-Vehicle System When Activating Level-2 ADAS

Norika Arai¹  , Jinnosuke Kamimura¹ , Yohei Fujinami¹ , Xingguo Zhang¹ ,
Pongsathorn Raksincharensak¹ , Masaaki Uechi², Shintaro Inoue²,
Fumio Sugaya² , Kazunori Nogi², Toshinori Okita², Hideaki Hayashi²,
and Keitaro Niki²

¹ Tokyo University of Agriculture and Technology, Tokyo, Japan
arai@st.go.tuat.ac.jp

² Toyota Motor Corporation Higashi-Fuji Technical Center, Shizuoka, Japan

Abstract. Advanced Driver Assistance Systems (ADAS) in passenger cars, such as Adaptive Cruise Control (ACC) and Lane Keeping Assist (LKA), have recently been widely deployed. However, these systems are not designed for high-risk situations, yet some drivers over trust the system and engage in secondary tasks. These behaviours may lead to serious accidents. On the other hand, it has been reported that the use of ACC reduced approximately half of the collision rate on highways based on public road data. This study aims to clarify the mechanism how ADAS affects driver behaviour and enhances accident prevention performance. Specifically, the focus is on the forward collision risk and the driver's brake operating behaviour. Through the analysis using a driving simulator, this study compared driver behaviour in high collision risk situations in the case with and without ACC. The analysis of subject drivers' internal parameters confirmed the driver behaviour that avoided a collision by using ADAS to take over control and brake earlier.

Keywords: Adaptive Cruise Control · Driving simulator · Driver-vehicle system · Distracted driving · Highway safety

1 Introduction

Advanced Driver Assistance Systems (ADAS), such as Adaptive Cruise Control (ACC) and Lane Keeping Assist (LKA), have recently become widespread. These systems are designed to reduce the driver's workload. Consequently, these systems cannot handle high accident risk situations. However, some drivers over trust ADAS and this results in distracted driving. Several serious accidents have occurred when using ADAS due to driver overconfidently trusting the system and sometimes lead to fatal accidents [1, 2]. On the other hand, Otsuki et al. reported that the ratio of collisions on highways is reduced to less than half with the use of ACC [3]. These facts indicate that although ADAS alone do not have high accident-avoidance performance, ADAS can avoid accidents by influencing on driver before the accident risk increases. The accident reduction mechanism has not been quantitatively clarified yet.

This research aims to quantitatively clarify the mechanism by which ADAS influences driver behavior and enhances accident-avoidance performance before accident risk increases. To clarify driver behavior when using ADAS, experiments with subject drivers were conducted using a driving simulator. Two experiments, gaze movement during distracted driving and driver collision avoidance behavior, were examined respectively under two conditions, with and without ADAS. This analysis was based on the hypothesis that active deceleration intervention and warning of ADAS hasten the driver's perception of forward risk even though ADAS induce forward inattention. This paper focuses on acceleration and deceleration support in the front and rear directions and verifies the hypothesis using the situation where the preceding vehicle suddenly brakes in distracted driving.

2 Driving Simulator Experiment

2.1 Experiment Overview

Two experiments were conducted for monitoring eye movement and driver risk-avoidance behavior respectively. A motion-based driving simulator with four electric actuators, which conduct motion cueing in the pitch and roll directions, was used. The main task of the subject driver during the experiment was to follow a preceding vehicle traveling at varying speeds of 80–100 km/h on the highway. In addition, as a subtask to replicate distracted driving, the participants were instructed to answer simple questions on a fixed smartphone within designated sections. This task was designed to imitate operating a car navigation system. The subtask sections appeared several times on the driving course. The driving simulator was also equipped with ACC and LKA to mimic the commercial Level-2 ADAS. Before starting the test, the experiment participants agreed to give informed consent and practiced using the driving simulator to familiarize themselves with the simulator environment. These experiments were approved by the Ethical Review Committee of the Tokyo University of Agriculture and Technology.

2.2 Gaze Movement

In order to quantify the forward inattention state during doing the subtask, all participants put on glasses-type eye tracker, Tobii pro Glasses 2. The setting of the experiment is shown in Fig. 1. These test runs were conducted for each subject under two conditions: ACC ON and ACC OFF, with LKA always activated to reduce the driving burden. The order of testing was changed for each half to account for order effects. 24 subjects who hold driving licenses participated in the experiment. Their average age was 26.1 years (range: 21–54). To guarantee uniformity in the risk perception for the preceding vehicle even without the activation of ACC, zones indicating the recommended maximum and minimum headway distances were displayed in the driving sections without secondary task execution.

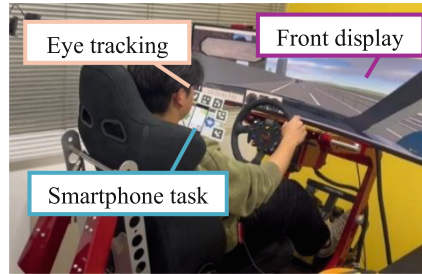


Fig. 1. The setting of driving simulator experiment using eye tracker.

2.3 Driver Risk-Avoidance Behavior

In order to evaluate the collision risk and quantify the driver's brake stepping behavior, the preceding vehicle suddenly braked at the end of the final subtask section. This emergency scenario could not be avoided solely by relying on ACC and the drivers were not informed about it before the test. These test runs were conducted for each subject under two conditions: ADAS ON (ACC and LKA were activated) and ADAS OFF (manual driving). 7 subjects who hold driving licenses participated in the experiment. Their average age was 29.7 years (range:21–49). Considering the physical workload experienced by the participants and the impact of familiarity to the driving scenario, every trial was carried out with a gap of more than one week between each trial.

3 Driver Behavior Analysis

3.1 Gaze Movement Analysis

To ascertain whether the driver's visual focus was on the preceding vehicle or not, a bounding box was assigned to the preceding vehicle on the front display, followed by the computation of the distance to the viewpoint coordinates. If the calculated distance was smaller than the threshold value, the viewpoint was considered to be close to the preceding vehicle and the driver was considered to be gazing at the preceding vehicle. Although there are various definitions for the size of the visible range, an effective field of view (within approx. 15 deg to the left and right, 8 deg above and 12 deg below) [4] was defined as the range within which the behavior of the preceding vehicle was visible in this experiment, where information could be gazed at using only eye movements and information was instantly visible. If this range is applied to the simulator environment, it corresponds to a range of approximately 11 m to the left and right of the preceding vehicle, and a size of 300 pixels of the front display. Thus, the threshold of the distance between the preceding vehicle and the gaze point was defined as 300 pixels, which defined the state of gazing at the preceding vehicle in this experiment. An example of the range of the preceding vehicle's viewable area on the front display is shown in Fig. 2. The preceding vehicle's bounding box is a yellow frame, and if the gaze coordinates are within a blue range of 300 pix from its boundary, it was judged that the driver is in the state of gazing at the preceding vehicle.

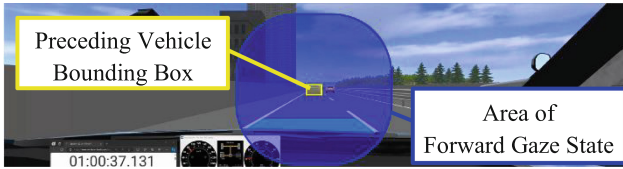


Fig. 2. Example of possible surroundings for preceding vehicle on front display.

As the set Time Headway (T_{hw}) of ACC was 1.8 s, each forward gaze duration (eye point is within the blue area) and looking away duration (eye point is out of the blue area) were calculated for the subtask section where the average T_{hw} was within 1.8 ± 0.3 s, respectively. When using ACC, the average forward gaze duration is a little shorter than when not using ACC as shown in Fig. 3-a. Moreover, when using ACC, the average looking away duration is quite longer than when not using ACC and there is a significant difference ($*p < 0.05$) as shown in Fig. 3-b. These results indicate that drivers who are using ACC tend to overtrust the system and fall into an inattentive state when doing distracted driving.

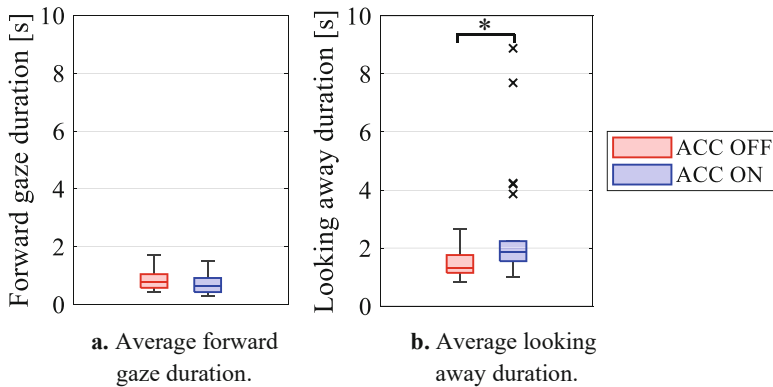


Fig. 3. Average duration time of each subject compared between ACC ON and ACC OFF.

3.2 Collision Risk

The collision risk in the scene of the preceding vehicle’s sudden braking was quantified using $iTTC$ [s^{-1}], which is defined as the inverse of the Time-To-Collision (TTC). This $iTTC$ indicates a higher collision risk for larger values and a lower collision risk for smaller values. Figure 4 shows an example of a collision risk reduction result when using ADAS. In the case of ADAS OFF, this driver did not step on the brake pedal in time for a collision, while the risk of collision increased. On the other hand, in the case of ADAS ON, the increased risk of collision was reduced, thus avoiding a collision.

In summary, in the experiment, 4 out of 7 participants had a smaller maximum $iTTC$ in ADAS ON than in ADAS OFF, reducing the collision risk as shown in this example.

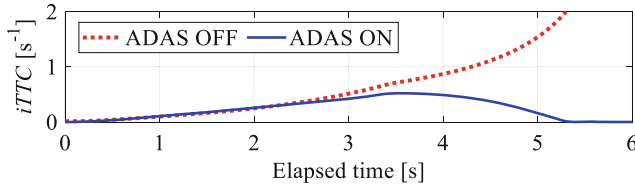


Fig. 4. Time history of inverted Time-To-Collision $iTTC$ from the time instant that the preceding vehicle started sudden braking.

3.3 Brake Pedal Operation Behavior

To find out why the collision risk became lower when using ADAS, the driver brake pedal operation behavior was modeled by considering the driver reaction delay from the sudden braking initiation of the preceding vehicle as the dead time, and the driver brake pedal stroke as the first-order delay system. Figure 5 shows the block diagram of brake stepping behavior. In the case of ADAS ON, ACC deceleration control was activated, and the driver can easily perceive forward risk through the posture change by deceleration and the alert. Three parameters, Reaction delay τ [s], Time constant T_b [s], and Gain H_b [-], after the sudden braking of the preceding vehicle were identified for each participant and compared depending on with or without ADAS.

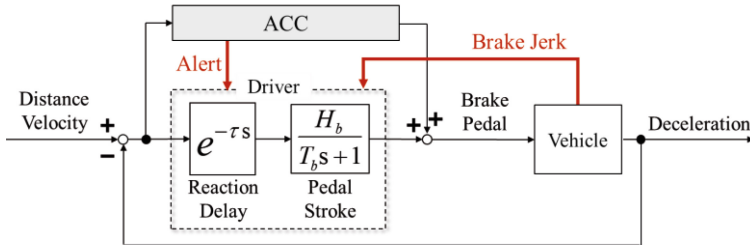


Fig. 5. Block diagram of driver-vehicle braking behavior model.

Figure 6 shows the relationship between the amount of brake pedal stroke and each parameter. The vertical axis shows the amount of driver's brake pedal stroke, which was calculated by defining the time from the start of emergency braking by the preceding vehicle until the driver started to brake as the reaction dead time τ , the maximum amount of brake operation by the driver as the gain H_b , and the time from the start of driver braking until the value of 63.2% ($= 1 - e^{-1}$) of gain H_b was reached as the time constant T_b was defined and calculated.

The result was that all 4 participants, who reduced the collision risk in ADAS ON compared to ADAS OFF, had a shorter reaction delay when using ADAS. Furthermore, these 4 participants braked after ACC deceleration had started but before the collision alert sounded. Thus, when the preceding vehicle conducted sudden braking, it was confirmed that the use of ADAS with ACC deceleration enabled the driver to avoid the risk of collision by bringing the driver back to primary driving task more quickly than without ADAS, even though ADAS alone could not avoid the risk.

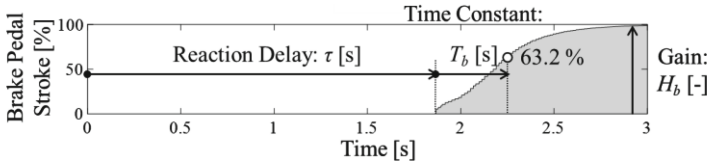


Fig. 6. Relationships of braking behavior parameters

4 Conclusion

This paper conducted quantitative analyses of the change in driver's eye movement and driver's behavior in the high collision risk situation, depending on whether ADAS was used or not. The following two findings were identified.

- A) When using ADAS, drivers tend to overconfidently trust the system and lose focus on the risk ahead when they are distracted while driving.
- B) The use of ADAS with active deceleration intervention enabled drivers, who tend to be more distracted, to bring the drivers back to primary driving task more quickly and improved their performance in avoiding critical accidents.

The subsequent stage involves the clarification of how drivers perceive ACC deceleration and its impact on collision avoidance actions. The findings from experimental study will contribute to the design of next-generation ADAS to enhance safety for unsafe drivers who tend to drive while distracted.

References

1. National Transportation Safety Board, Collision between a car operating with automated vehicle control systems and a tractor-semitrailer truck. Highway Accident Report, PB2017-102600 (2017)
2. National Transportation Safety Board, Collision between vehicle controlled by developmental automated driving system and pedestrian. Highway Accident Report, PB2019-101402 (2019)
3. Otsuki, M., Shimizu, T., Ikedo, Y.: Accident reduction effect analysis of driving load reduction system based on market data. *Trans. Soc. Autom. Eng. Jpn.* **54**(2), 284-287 (2023). (in Japanese)
4. Japan Society of Automotive Engineering: *Automotive Ergonomics Technology*, Automotive Engineering Series 8, p.10, ISBN: 4-254-23648-4 (1998) (in Japanese)


Open Access This chapter is licensed under the terms of the Creative Commons Attribution 4.0 International License (<http://creativecommons.org/licenses/by/4.0/>), which permits use, sharing, adaptation, distribution and reproduction in any medium or format, as long as you give appropriate credit to the original author(s) and the source, provide a link to the Creative Commons license and indicate if changes were made.

The images or other third party material in this chapter are included in the chapter's Creative Commons license, unless indicated otherwise in a credit line to the material. If material is not included in the chapter's Creative Commons license and your intended use is not permitted by statutory regulation or exceeds the permitted use, you will need to obtain permission directly from the copyright holder.





Motion Control of a 6×4 Heavy Vehicle: Autonomous Collision Avoidance Using Integrated Chassis Control

Aria Noori Asiabar¹ , Timothy Gordon¹, Yangyan Gao²,
Leon Henderson^{3,4}, and Leo Laine^{3,4}

¹ University of Lincoln, Brayford Way, Lincoln LN6 7TS, UK
anoori@lincoln.ac.uk

² Volvo Trucks North America, 7900 National Service Rd,
Greensboro, NC 27409, USA

³ Volvo Group Trucks Technology, SE-405 08 Gothenburg, Sweden

⁴ Chalmers University of Technology, Chalmersplatsen 4,
412 96 Gothenburg, Sweden

Abstract. This paper considers the coordinated chassis control of a 6×4 HGV tractor unit using a multivariable nonlinear controller for a transient handling manoeuvre under friction-limited conditions. The controller's performance is evaluated through simulation. It receives Centre of Gravity (CG) longitudinal and lateral acceleration targets, corresponding to curvature and longitudinal acceleration requests, and aims for the CG to track the target accelerations. It employs the Modified Hamiltonian Algorithm (MHA) to generate steering and braking commands for the tractor. A combined-slip Magic Formula tyre model used within the algorithm allows for simultaneous stability control and path tracking, even in scenarios where the vehicle is operating at the limits of tyre adhesion. The manoeuvre is an autonomous obstacle avoidance on a packed snow. Results show the advantages and possible limitations of tracking acceleration targets for integrated chassis control.

Keywords: Vehicle Control · Handling Limits · Autonomous Obstacle Avoidance

1 Introduction

Heavy goods vehicles (HGVs) are an essential part of modern society for the transportation of goods. Despite their widespread and long-established use, heavy vehicles contribute significantly to severe accidents, necessitating a continuing focus on safety enhancement [1].

Future vehicle advancements and increasing availability of actuators such as independent wheel braking control and steer-by-wire can improve vehicle safety.

Supported by Volvo Trucks and University of Lincoln.

© The Author(s) 2024

G. Mastinu et al. (Eds.): AVEC 2024, LNME, pp. 144–150, 2024.

https://doi.org/10.1007/978-3-031-70392-8_21

Various chassis control algorithms - including optimization-based control allocation algorithms, such as Model Predictive Control (MPC), and Nonlinear MPC (NMPC), have been explored in the literature to realize these improvements [2]. These approaches typically reference a suitable desired motion path, which can be undesirable when reaching the limits of adhesion. The selected path may be too conservative or not achievable, as this depends on the details of the vehicle dynamics, the control actuators and the road surface. In other approaches, a CG acceleration reference is determined [3,4] (e.g. using a simple particle model). Assuming the acceleration target has been appropriately defined, e.g., to follow a collision-free path within the capabilities of the vehicle and the road surface, the key question is the vehicle's performance in tracking that reference. Acceleration magnitude will be set according to the adhesion limits of individual tyres, so the vehicle will normally be in a condition where it needs to maximize the available CG acceleration in the desired direction.

The main focus of this paper is on maximising the available CG acceleration in a direction that is computed by the algorithm. The general approach, as well as the use of acceleration targets, was developed from the more formal optimal control-based method of QLOC [3] while avoiding any significant optimization or nonlinear simulation within the control loop.

MHA has previously been shown to be a robust motion control methodology for light vehicles, operating effectively up to the friction limits [4], and the present paper makes a contribution towards its development as a control method for HGVs. It includes a high-level reference generator, as well as a low-level control allocator. Indeed MHA splits the motion control problem into parallel sub-problems, to be solved locally for each wheel. This is achieved based on Pontryagin's minimum principle [5], with control signals being obtained by minimization of a linear Hamiltonian function. The general control architecture is shown in Fig. 1.

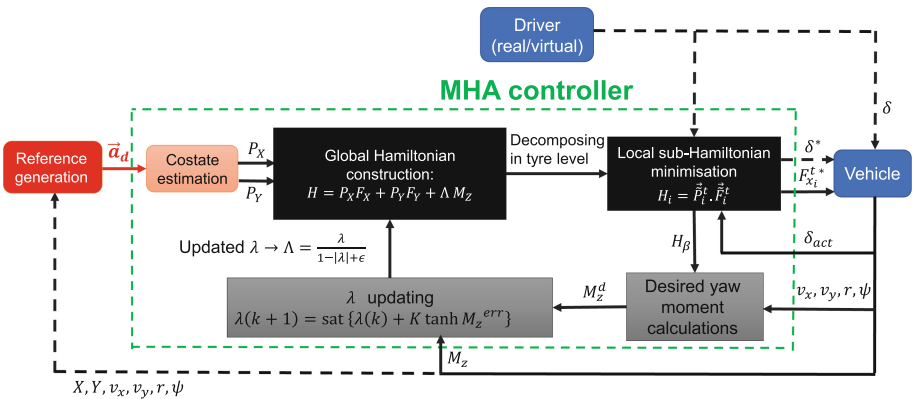


Fig. 1. MHA controller structure.

We consider an emergency lane-change scenario from two perspectives. In the first case, the acceleration request is pre-computed and does not change during the manoeuvre (open-loop). The second case uses an updating reference (closed-loop) obtained from a particle subject to sliding mode control - see [3, 7, 8] for details. Furthermore, in the MHA algorithm, the tracking performance is strongly influenced by the lambda adaptation gain, K , [4] with larger values of K being beneficial during severe transient demands. we will investigate this through simulation results for an open-loop case.

2 Scenarios

This section examines both open-loop and closed-loop scenarios for an evasive lane change, with control performance evaluated in simulation. It makes use of a high-fidelity truck model (Volvo Transport Models - VTM [9]) for a 6×4 Volvo FH tractor. In all cases a low-friction surface is assumed, representing packed snow and with $\mu = 0.3$.

2.1 Scenario 1 - Simulated Open-Loop Evasive Lane-Change

The chosen manoeuvre assumes a desired lateral acceleration of 2.5 m/s^2 occurring from 5 to 6.5s, followed by a rightward desired lateral acceleration of -3 m/s^2 from 6.5 to 9.5s.

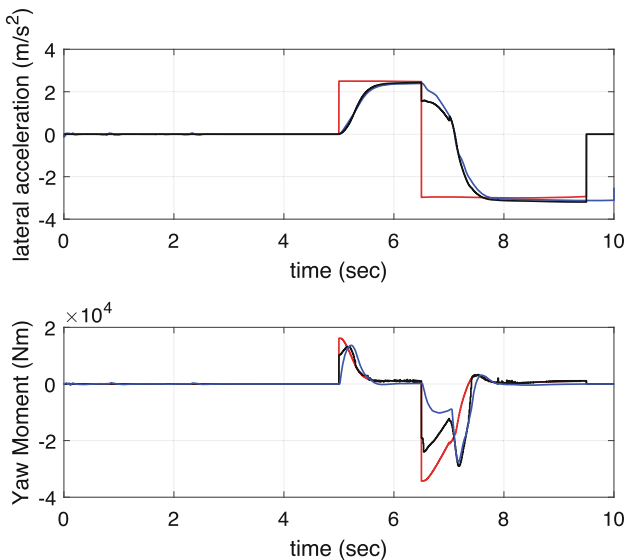


Fig. 2. Top: lateral acceleration tracking performance in vehicle coordinates. Bottom: yaw moment performance diagnostics. Red: desired Blue: from simulation Black: MHA internal estimation

The initial speed is set at 80 km/h, and a PID speed controller is used to maintain this speed before the manoeuvre begins, while it is deactivated during and after the manoeuvre. This open-loop desired acceleration vector roughly emulates an obstacle avoidance lane change. The lateral acceleration tracking performance in vehicle coordinates is shown in Fig. 2. It is seen that lateral acceleration targets are tracked well, though with some delay due to the yaw dynamics being required to establish slip angles at the rear tyres. The yaw moment plot is to confirm that MHA drives the yaw dynamics in a suitable way. This provides a diagnostic check on the algorithm, in which precise tracking of M_z is neither expected nor required.

2.2 Scenario 2 - Simulated Closed-Loop Evasive Lane-Change

Here, a closed-loop lane change is executed, with a target window of three seconds, where a Sliding Mode Controller approach is used to provide a lateral acceleration reference based on a predefined path [7]. Pure Pursuit is employed before and after the lane change manoeuvre as a steering controller [8]. The reference speed is 50 km/h and again the speed control is disconnected at the start of the manoeuvre. Figure 3 shows time histories for the vehicle speed, lateral acceleration tracking, vehicle sideslip angle and CG lateral offset.

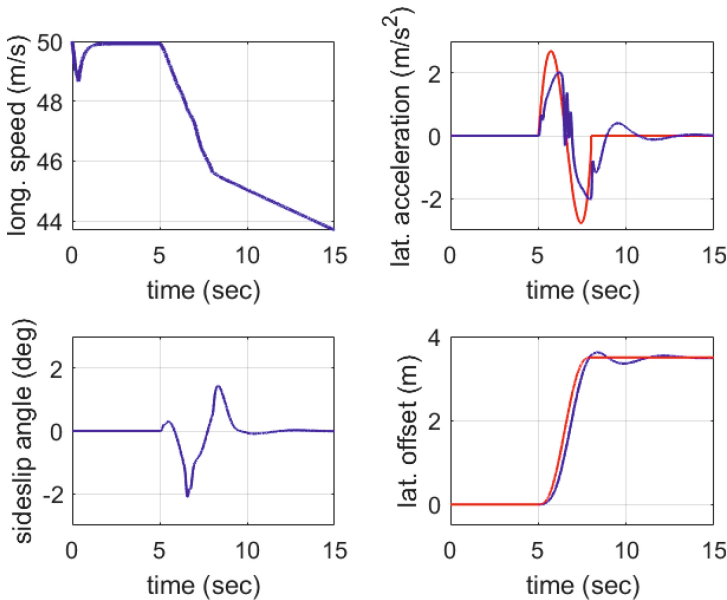


Fig. 3. Lateral acceleration and vehicle motion variables. Red: desired blue: from simulation

Even though the target acceleration request is purely lateral, the vehicle speed is seen to reduce due to the use of differential braking for yaw control.

Note that MHA effectively controls the rear lateral tyre forces via yaw moments and body sideslip corrections.

3 Impact of λ Updating Gain (K) on MHA Performance

Referring to Fig. 1, parameter lambda is adjusted in real-time to control the yaw dynamics, while parameter K controls the speed of response of this parameter. Here we briefly investigate the effect of K on acceleration tracking, and for simplicity, the open-loop manoeuvre of scenario 1 is used. Results are shown in Fig. 4.

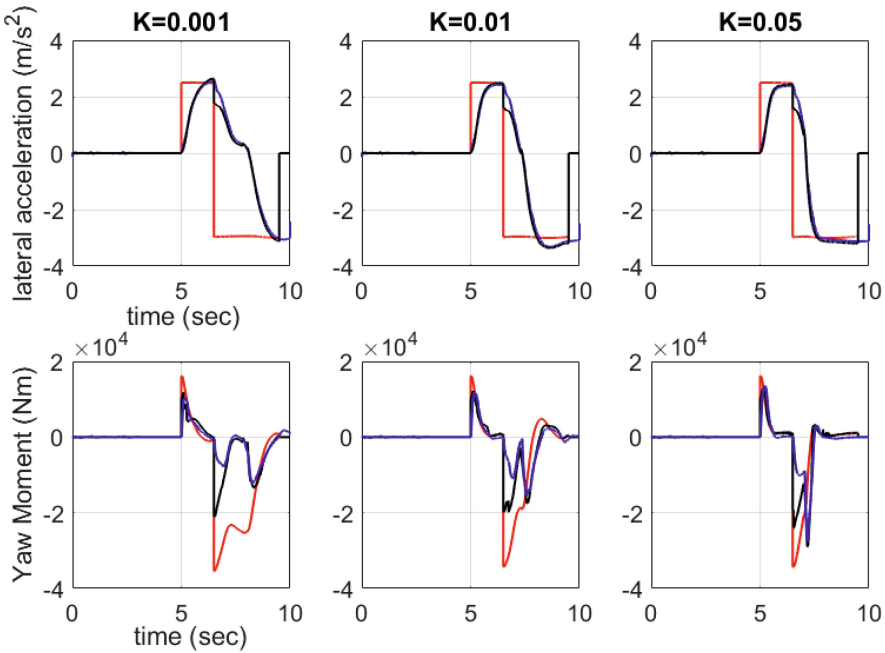


Fig. 4. Lateral acceleration in vehicle coordinate and yaw moment diagnostic plots. Blue: from simulation Black: MHA internal estimation Red: desired

It is seen that the larger value of K is required to achieve the speed of response necessary for tracking highly transient lateral acceleration demands. Moreover, the yaw moment diagnostic curves are more convergent in the case where K is larger, indicating the overall satisfactory performance of the algorithm. Further increases in K is however not desirable because of a tendency towards high-frequency chattering in the actuator commands.

4 Conclusion

This paper considered the coordinated chassis control of a 6×4 HGV tractor using MHA to control transient manoeuvres under friction-limited conditions. It is understood that the control of lateral acceleration is crucial in these kinds of scenarios, with the speed of its tracking response being equally vital during evasive lane change manoeuvres. By examining the MHA internal diagnostic plots, we could assess the controller's performance and how it was realized from the vehicle's perspective. We also found that while MHA is effective for integrated chassis control, the parameter K needs to be adjusted and tuned. Additional experimental results, obtained using a lower K value, closely matched the simulation results; however, due to space constraints, these details were not included in this paper. Although MHA was applied to a three-axle HGV tractor, it can be easily adapted for use in two- or four-axle vehicles and deals with such changes in a straightforward manner.

References

1. Woodrooffe, J., Blower, D.F., Gordon, T., Green, P.E., Liu, B., Sweatman, P.: Safety Benefits of Stability Control Systems for Tractor-Semitrailers. National Highway Traffic Safety Administration, Washington (2009)
2. Sinigaglia, A., Tagesson, K., Falcone, P., Jacobson, B.: Coordination of motion actuators in heavy vehicles using model predictive control allocation. In: 2016 IEEE Intelligent Vehicles Symposium (IV), pp. 590–596 (2016)
3. Yang, D., Gordon, T.J., Jacobson, B., Jonasson, M.: Quasi-linear optimal path controller applied to post impact vehicle dynamics. *IEEE Trans. Intell. Transp. Syst.* **13**, 1586–1598 (2012)
4. Gao, Y., Lidberg, M., Gordon, T.: Modified Hamiltonian algorithm for optimal lane change with application to collision avoidance. *MM Sci. J.*, 576–584 (2015)
5. Kirk, D.E.: *Optimal Control Theory: an Introduction*. Courier Corporation, Chelmsford (2004)
6. Noori Asiabar, A., Gordon, T., Gao, Y., Henderson, L., Laine, L.: On the control allocation performance of longer combination vehicles. In: *The IAVSD International Symposium on Dynamics of Vehicles on Roads and Tracks*, pp. 757–766. Springer, (2021)
7. Noori Asiabar, A., Gordon, T., Gao, Y., Henderson, L., Laine, L.: Coordinated chassis control of a tractor-semitrailer combination operating at its handling limits using the MHA methodology. *Veh. Syst. Dyn.* 1–26 (2024). <https://doi.org/10.1080/00423114.2024.2367612>
8. Noori Asiabar, A., Gordon, T., Gao, Y., Henderson, L., Laine, P.J.: Integrated motion control of heavy goods vehicles using multiple actuators. In: *Advances in Dynamics of Vehicles on Roads and Tracks II: Proceedings of the 28th Symposium of the International Association of Vehicle System Dynamics, IAVSD 2023, August 21–25, Ottawa, Canada* (2023)
9. Model, V.T.: Simulink Library Developed at Volvo Group Trucks Technology. Department BF72991 (2014)

Open Access This chapter is licensed under the terms of the Creative Commons Attribution 4.0 International License (<http://creativecommons.org/licenses/by/4.0/>), which permits use, sharing, adaptation, distribution and reproduction in any medium or format, as long as you give appropriate credit to the original author(s) and the source, provide a link to the Creative Commons license and indicate if changes were made.

The images or other third party material in this chapter are included in the chapter's Creative Commons license, unless indicated otherwise in a credit line to the material. If material is not included in the chapter's Creative Commons license and your intended use is not permitted by statutory regulation or exceeds the permitted use, you will need to obtain permission directly from the copyright holder.





Investigating Characteristics and Opportunities for Rear-Wheel Steering

Oskar Lind Jonsson¹(✉), Arvind Balachandran¹, Jian Zhou¹, Björn Olofsson^{1,2},
and Lars Nielsen¹

¹ Department of Electrical Engineering, Linköping University, Linköping, Sweden
`oskar.lind.jonsson@liu.se`

² Department of Automatic Control, Lund University, Lund, Sweden

Abstract. The potential of additional steering possibilities (like rear-wheel or all-wheel steering) is analyzed for critical situations to investigate possible safety improvements. For this purpose, a dynamic optimization problem is formulated to find the best possible maneuver. The optimization criterion is to maximize the entry speed into a constant radius 90° -curve. The optimization problem is solved for different steering topologies, and the results quantify the increase in maximum entry speed, highlighting the potential for safety improvements. Further, the optimal steering strategies are determined, and they show interesting characteristics like initial diagonal driving or, in other cases, a transition from initial out-of-phase steering to in-phase steering.

Keywords: Optimal maneuvers · Safety-critical handling · Dynamics

1 Introduction

Rear-wheel steering is available and has demonstrated improved performance in maneuverability at low speeds and driving stability at higher speeds [1, 2]. Further, even more rear-wheel steering capability has been introduced, e.g., in vehicles such as the GMC Hummer or the Hyundai Ioniq 5 with diagonal driving. These new developments in rear-wheel steering may also be used for increased safety, and the potential for this is the research question of this paper.

Dynamic optimization has been used to study critical vehicle maneuvers in at-the-limit driving to find control principles and devise control schemes [3–5]. To specifically study safety, recent articles have used the optimization criterion of maximum entry speed into a scenario (e.g., a constant radius 90° -curve) [6, 7]. By definition, this computation gives the maximum speed that can still be handled when entering a situation. Furthermore, it has been used to analyze safety potential using data from crashes [8], and for developing control principles and schemes [7]. This paper uses this methodology to investigate the characteristics and opportunities of adding rear-wheel steering capabilities.

The funding from the Knut and Alice Wallenberg Foundation (KAW), Sweden, and from the ELLIIT Strategic Area for ICT Research, supported by the Swedish government, is gratefully acknowledged.

© The Author(s) 2024

G. Mastinu et al. (Eds.): AVEC 2024, LNME, pp. 151–157, 2024.

https://doi.org/10.1007/978-3-031-70392-8_22

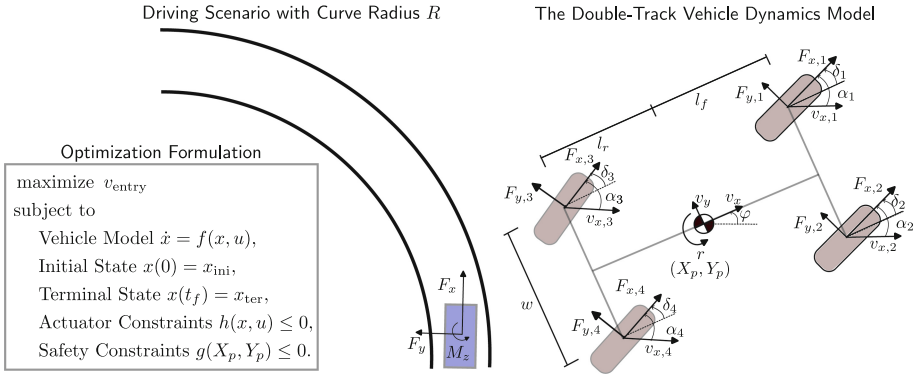


Fig. 1. The studied driving scenario, the optimization formulation, and the vehicle dynamics model for the scenario, [5].

2 Steering Topologies, Scenarios, and Optimization

Here, critical cornering at the limit of friction is studied for different steering topologies with varying amounts of steering capability and different curve radii. The vehicle is described by a double-track dynamics model as depicted in Fig. 1. The dynamic equations and parameters are the same as in [5], with fixed distribution between rear and front braking based on the proportional weight on each axle, hence one control input for the total amount of braking. The steering topologies studied are the traditional front-wheel steering (FWS), rear-wheel steering (RWS), all-wheel steering (AWS), and individual-wheel steering (IWS). The difference between the two latter is that in AWS, wheels on the same axle have the same steering angle, whereas in IWS, the steering angle is individually controlled for each wheel. The front-wheel steering angle is, for all cases, limited to a standard $\pm 30^\circ$. However, the study varies the rear-wheel steering capability by examining maximum rear steering angles with 0, 1, 3, 5, 7, 10, 15, 20, 30, 40, and 50° , respectively. Also, [9] studied different steering architectures in combination with differential braking for a lane-change maneuver. The scenarios here, all consist of a constant radius 90° -curve as shown in Fig. 1, and it is studied for the curve radii 10, 20, 30, 50, and 70 m. The maximum entry speed that can be managed for these vehicles and scenarios is computed. This computation is based on dynamic optimization as shown in Fig. 1, where the optimization formulation, the modeling used, and the numerical solution principles follow the methods described in [5–7].

3 Results

It turns out that the most interesting results from this research are about the initial driving strategy to avoid going off-road. Therefore, for Figs. 2, 3 and 4, the focus is on the first part of the constant radius 90° -curve.

3.1 FWS, RWS, AWS, and IWS

For the same case as in Fig. 1, i.e., a curve with a radius of 30 m, the first part of the optimal solutions are presented in Fig. 2 for the four steering topologies FWS, RWS, AWS, and IWS. The first part of the curve is shown in the top left plot. The lane's width indicates the allowed area for the vehicle's CoG, and the box's width indicates the vehicle's track width (tire-to-tire). The angle of the vehicle box shows the vehicle's orientation.

It is seen that for this scenario and these parameters (with a maximum rear steering angle of 5°), the rear wheels change δ_3, δ_4 from negative to positive, which means that the optimal strategy for both AWS and IWS is to change from out-of-phase steering to in-phase diagonal driving. This will be studied in more detail in Sect. 3.2. Another major conclusion from Fig. 2, and in other performed computations, is that the difference between AWS and IWS is minor. Thus, the following will only present detailed results for AWS.

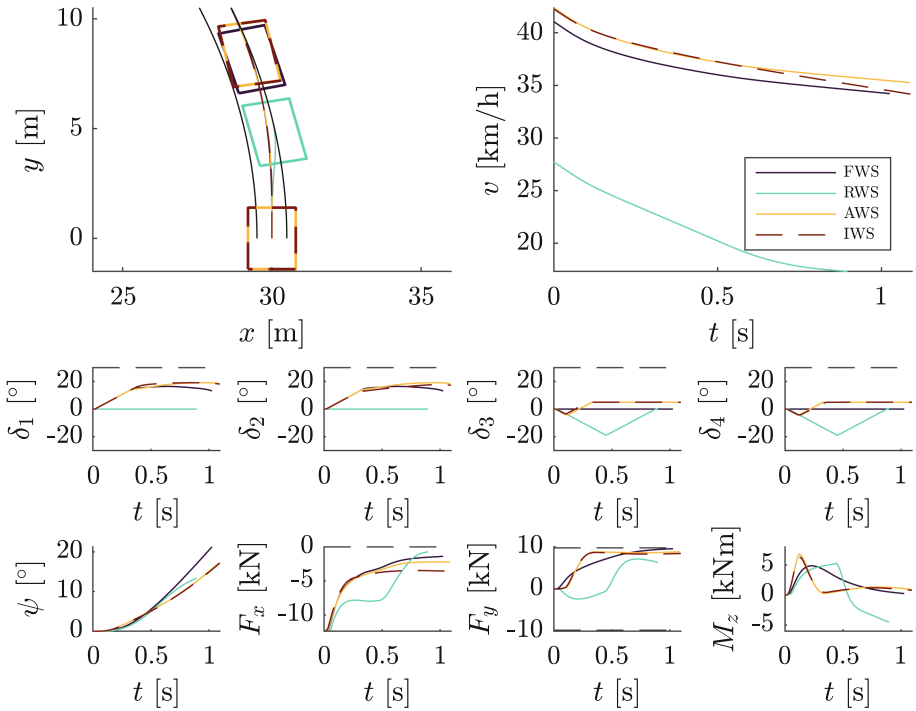


Fig. 2. Optimal solutions for FWS, RWS, AWS, and IWS. The first row shows initial paths (left) and velocities (right). The second row shows the individual steering angles, the third row the heading, the total longitudinal and lateral forces on the vehicle, and the total moment acted on the vehicle. All variables are presented in the vehicle coordinate system, referring to the notation in Fig. 1.

3.2 Characteristics for Different δ_{\max} and R

For AWS, wheels on the same axle have the same steering angle, so $\delta_1 = \delta_2$ with maximum $\pm 30^\circ$ and $\delta_3 = \delta_4$ with maximum denoted δ_{\max} . As pointed out in Fig. 2, there is a shift from out-of-phase steering (where δ_1, δ_3 have different signs) to in-phase diagonal driving (where δ_1, δ_3 have the same sign). It can also be seen (top left) from the vehicle orientation that AWS prioritizes diagonal driving compared to FWS. To study these aspects more in detail, Fig. 3 presents the optimal solutions for $R = 30$ m and for maximum rear-wheel steering capability $\delta_{\max} = 0, 1, 3, 5, 7, 10, 15, 20, 30, 40,$ and 50° . As before, the case of $\delta_{\max} = 5^\circ$ leads to a shifting strategy in the rear-wheel steering, whereas for $\delta_{\max} = 30^\circ$, the strategy is diagonal driving during the whole start of the maneuver. Thus, it seems advantageous to start rotating the vehicle for less steering capability of the rear wheels. Still, for larger steering capability, it seems better to move sideways directly and then rotate in the turn when the critical part is cleared. This is manifested in the top left part of Fig. 3, where it can be seen that 10 m into the curve, the vehicle rotates less when δ_{\max} is increased, and thus, has focused more on diagonal driving than rotation. Concerning the shifting in steering strategy, Fig. 4 shows the rear-wheel steering solutions for the curve radii $R = 10, 20, 30,$ and 50 m. The sharper the curve, i.e., the smaller the R is, it is natural that there is more out-of-phase steering on the rear wheels to get the vehicle to rotate. The switching point from out-of-phase steering ($\delta_3 < 0^\circ$) to in-phase steering ($\delta_3 > 0^\circ$) depends on the curve radius. For $R = 10$ m, the switching point comes earlier with smaller δ_{\max} . On the other hand, for $R \geq 20$ m, the switching point comes later with smaller δ_{\max} .

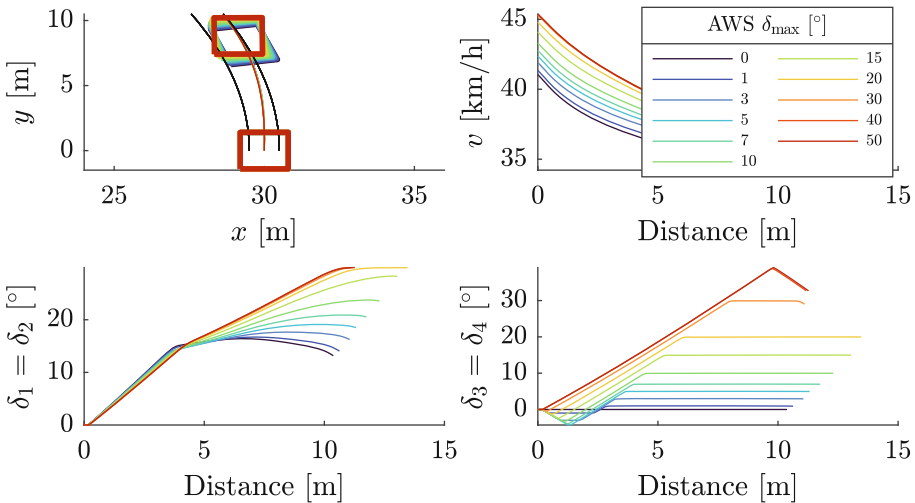


Fig. 3. Initial paths, velocities, and steering angles for AWS (for $R = 30$ m) with different maximum rear steering angles, δ_{\max} . FWS corresponds to $\delta_{\max} = 0^\circ$.

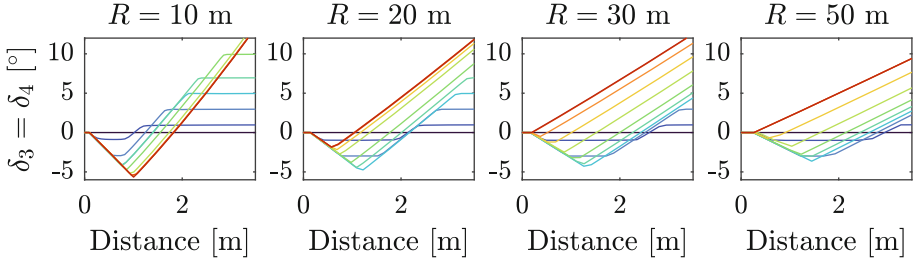


Fig. 4. Rear steering angle for FWS and AWS for different radii R . The color coding for δ_{\max} is the same as in Fig. 3.

3.3 Improved Safety

Having observed interesting steering behaviors in the previous subsection, the next question is what crash avoidance or mitigation could mean regarding saved lives and reduced injury for increased traffic safety. As seen in the top right of Fig. 2, higher entry speeds can be handled when using rear-axle steering in AWS or IWS, which is an indicator of improved safety. To provide more details, the left plot in Fig. 5 shows the maximum entry speed as a function of δ_{\max} and R . Recall that $\delta_{\max} = 0^\circ$ corresponds to the regular FWS, so the curves in the left plot show the improvement in maximum entry speed compared with FWS as an evaluation of safety. When it comes to saved lives and mitigated injuries, a full analysis of crash databases could be made [8]. However, a simple way to get a first estimate is to compare the kinetic energy, which is made in the right plot of Fig. 5, where the relative improvement in terms of kinetic energy, $\Delta v^2/v^2$, is plotted. Compared to regular FWS, being the origin, the improvement is almost linear when adding just some steering capability in terms of δ_{\max} for the rear wheels, but then it flattens out. Using this simple way would indicate a safety improvement in the order

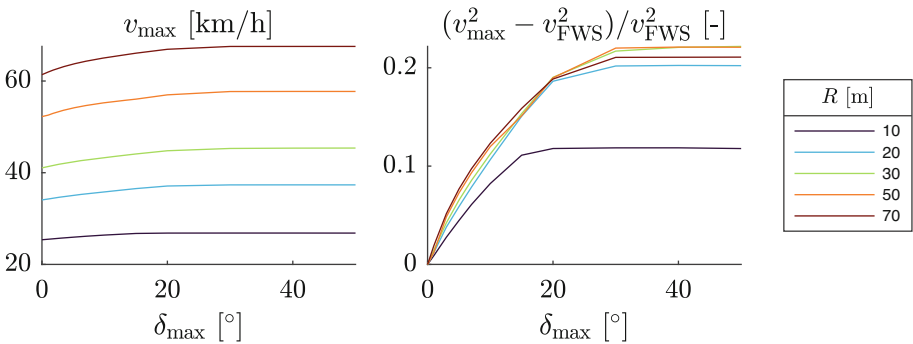


Fig. 5. Left: Maximum entry speed for different maximum allowed rear-steering angles and curve radii. Right: The relative difference in kinetic energy for different maximum allowed rear-steering angles and curve radii.

of 10 % already for $\delta_{\max} = 7^\circ$, and then it starts to flatten out at $\delta_{\max} = 20^\circ$ to eventually reach about 20 %. Another observation that was not foreseen is that all curves in the right plot of Fig. 5 are so similar, except for $R = 10$ m.

4 Conclusions

The steering capabilities of the rear wheels are introduced mainly to improve maneuvering or stability. Still, here, they are investigated in terms of improved handling of critical situations even at the limit of friction. The main takeaways are as follows. It was shown that already small steering capabilities on the rear wheels could give significant safety improvements, e.g., for seven degrees as the maximum rear-wheel steering angle it provides in the order of approximately 10 %, and for additional steering capability, it gives approximately double. Interestingly, the initial steering strategy for avoiding going off-road depends on the steering and scenario parameters and varies from initial out-of-phase steering (to achieve vehicle rotation) to initial in-phase steering (parallel driving) to get the vehicle away from the critical road border.

References

1. Park, K., Joa, E., Yi, K., Yoon, Y.: Rear-wheel steering control for enhanced steady-state and transient vehicle handling characteristics. *IEEE Access* **8**, 149282–149300 (2020)
2. Nagai, M., Hirano, Y., Yamanaka, S.: Integrated control of active rear wheel steering and direct yaw moment control. *Veh. Syst. Dyn.* **27**(5–6), 357–370 (1997)
3. Gao, Y., Gordon, T.: Optimal control of vehicle dynamics for the prevention of road departure on curved roads. *IEEE Trans. Veh. Technol.* **68**(10), 9370–9384 (2019)
4. Subosits, J.K., Gerdes, J.C.: From the racetrack to the road: Real-time trajectory replanning for autonomous driving. *IEEE Trans. Intell. Veh.* **4**(2), 309–320 (2019)
5. Berntorp, K., Olofsson, B., Lundahl, K., Nielsen, L.: Models and methodology for optimal trajectory generation in safety-critical road-vehicle manoeuvres. *Veh. Syst. Dyn.* **52**(10), 1304–1332 (2014)
6. Fors, V., Olofsson, B., Nielsen, L.: Formulation and interpretation of optimal braking and steering patterns towards autonomous safety-critical manoeuvres. *Veh. Syst. Dyn.* **57**(8), 1206–1223 (2019)
7. Fors, V., Olofsson, B., Nielsen, L.: Models for Optimization of Vehicle Maneuvers, 1st edn. Linköping University, Linköping (2023)
8. Olofsson, B., Nielsen, L.: Using crash databases to predict effectiveness of new autonomous vehicle maneuvers for lane-departure injury reduction. *IEEE Trans. Intell. Transp. Syst.* **22**(6), 3479–3490 (2021)
9. Andreasson, J.: Enhancing active safety by extending controllability – How much can be gained? In: Proceedings of IEEE Intelligent Vehicles Symposium, Xi’an, Shaanxi, China, pp. 658–662 (2009)

Open Access This chapter is licensed under the terms of the Creative Commons Attribution 4.0 International License (<http://creativecommons.org/licenses/by/4.0/>), which permits use, sharing, adaptation, distribution and reproduction in any medium or format, as long as you give appropriate credit to the original author(s) and the source, provide a link to the Creative Commons license and indicate if changes were made.

The images or other third party material in this chapter are included in the chapter's Creative Commons license, unless indicated otherwise in a credit line to the material. If material is not included in the chapter's Creative Commons license and your intended use is not permitted by statutory regulation or exceeds the permitted use, you will need to obtain permission directly from the copyright holder.





Accuracy Requirements of Camera-Based Depth Estimation for Urban Automated Driving

M. Westendorf^(✉), S. Thal, T. Ahrenhold, and R. Henze

Institute of Automotive Engineering, Technische Universität Braunschweig,
Hans-Sommer-Str. 4, 38106 Braunschweig, Lower Saxony, Germany
m.westendorf@tu-braunschweig.de
<https://www.tu-braunschweig.de/iffzg>

Abstract. For autonomous driving in urban areas higher accuracy requirements for localization of surrounding traffic participants become apparent. The use of cost-efficient camera sensors shows potential for a performant depth estimation and can supplement perception systems to achieve redundancy. Current research focuses on improving the algorithms towards better performance whereas the application-oriented analysis of present estimation errors in relation to urban traffic scenarios is often neglected. Based on stereo and mono camera images, a benchmark analysis of rule- and deep learning-based depth estimation approaches is conducted in this work. The error-prone estimation results are then analyzed against braking distances of urban traffic scenarios simulated by a two-track model to analyze the criticality of different depth estimation approaches. The application-oriented evaluation shows that current approaches could already be used in real automated driving systems and enable the definition of requirements.

Keywords: Automated Driving Systems · Sensors and Actuators · Identification and Estimation

1 Introduction and Framework

In this work, the focus is set on depth estimation of binocular and monocular camera systems for autonomous driving in urban areas. For monocular systems with a single input image the issue persists that depth estimation leads to ambiguous results. To overcome this issue predictive models can be used to learn the relationship between images and depth [5]. In stereo vision, two rectified input images provide a remedy for the issue as epipolar geometry can be used to generate disparity maps. The disparity map can then be transferred into depth maps by the given geometric camera relation. Predictive models are capable of learning the stereo matching in an end-to-end fashion while increasing accuracy [6]. Two predictive models define key points of this work. Monodepth2 [5] represents the mono camera-based model whereas 2D-MobileStereoNet (2D-MSNet) [6] is the chosen model for stereo matching.

© The Author(s) 2024

G. Mastinu et al. (Eds.): AVEC 2024, LNME, pp. 158–163, 2024.

https://doi.org/10.1007/978-3-031-70392-8_23

Both models are characterized by low hardware requirements and are therefore suitable for vehicle-related application. The baseline of the analysis is a geometric approach which uses camera extrinsics and inverse projection to determine metric object depth [3]. For all depth estimation approaches we use a Python Framework, the original algorithm repositories and the Kitti tracking multi-object dataset [4] as image source. The 2D object detection information is taken from the dataset and used to locate and classify a filtered object class subset consisting of vehicles, pedestrians and bicycles.

2 Methodology

To infer metric object depth, any lens distortion must be removed from input images. Afterwards the image is processed by the stated depth estimation algorithms in Sect. 1. As an evaluation basis, we use trained models. For Monodepth2 the model “mono+stereo 640 × 192” is selected and for 2D-MSNet the model “SF + DS + KITTI2015”. The resulting disparity maps from the deep-learning models are converted to metric depth maps by scaling known from the camera setup. The given ground truth object detection results are used in parallel to generate a list of reference points and bounding box properties per image. Using these object reference points as index for depth maps results in metric depth per object. Figure 1 visualizes exemplary inference output for both deep-learning based approaches and details the the different referent points chosen. The lower reference point is only used for the rule-based inverse perspective mapping (IPM) since the used algorithm projects the pixel coordinates into the camera reference frame. The assumption that each reference point is located on the road plane solves the ambiguity of the inverse projection. Since the rule-based distance estimation is affected by the vehicles dynamics, we use the given pitch and roll angles by the dataset to compensate vehicle movement [3]. After depth estimation for each of the 21 data splits, we filter truncated and occluded objects and calculate the absolute error based on ground truth LiDAR depth maps per chosen distance intervals.

The simulated braking distances represent an automatic emergency brake (AEB) in Euro NCAP Car-to-Pedestrian Nearside Adult (CPNA) [2] and Car-to-Car Rear stationary (CCRs) [1] test scenarios with a maximum velocity of 50 [km/h]. The simulation is based on a two-track model of the institute of Automotive Engineering which is statistically validated with real driving data. A Magic Formula tire model of Version 5.2 with parameters of current summer and winter tires and road friction coefficients of $\mu_R = 0.3, 0.6, 1$ for snow, wet and dry road conditions are considered. The trigger distance is set to the braking distance to fulfill the collision unavoidable criteria [7]. Both the performance measures of the depth estimation and the results of the two-track model form the basis for the evaluation. Whereas current publications focus strongly on optimization, the outlined methodology closes the gap between the algorithmic evaluation on depth metrics and real applications like autonomous driving in urban scenarios. The results enable the definition of accuracy requirements and the impact assessment of estimation errors.



Fig. 1. Depth map samples for image number 150 of split 20 in the Kitti Tracking dataset [4]. Above the depth map of the Monodepth2 inference is shown, below the results of the 2D-MSNet. A ground truth bounding box is highlighted with both reference points (center: Monodepth2 and 2D-MSNet, center bottom: IPM). In both color variations, darker colors represent distance. Lighter colors emphasize proximity.

3 Evaluation

For the full training dataset and the object classes car, van, cyclist and pedestrian mean absolute error values of the metric depth are given per ground truth distance intervals of 10 m in Fig. 2. Exemplary objects evaluated with the IPM algorithm have a mean abs. error of 14.96 [m] for the interval which spans from 40 [m] to 50 [m]. The corresponding number of estimations (images \times objects) is detailed on the right. As the distance towards the objects increases, the number of objects decreases which reflects the extra urban and urban environments of the data set. In summary the 2D-MSNet shows the lowest error values across all data, as the image data from the left and right cameras are used to solve the correspondence problem. Both monocular-camera-based approaches have comparable error values up to 30 [m]. Whereas the error value of the IPM approach stagnates from a distance interval of 50 [m] at approx. 15 [m] under the conditions used, the error values of Monodepth2 continue to increase.

In regards to the application of autonomous driving, depth underestimation leads to an earlier braking event, overestimation means a late event. The former can cause self-inflicted rear-end collisions, the latter is safety-critical for front collisions. Considering the collision unavoidable criteria for autonomous emergency braking, full braking triggers when the metric object depth corresponds to the required braking distance [8]. Hence absolute error statistics must be added to braking distances and lead to a collision with a simulated collision velocity $v_{Collision}$. Figure 3 shows the simulated velocity profile over the braking distance s_B for a road friction coefficient of $\mu_R = 0.3$ and winter tires. The braking distance shifted by the 75% error quantile $s_B + \epsilon_{s_B, 0.75}$ is detailed for the Monodepth2 algorithm. The quantile is calculated based on a narrower distance interval which spans over the simulated braking distance of 35.9 [m] with a tol-

erance ± 1 [m]. The added error leads to a simulated collision velocity $v_{Collision}$ of 23.55 [km/h]. Based on the ISO/DIS 26262-3 standard and severity levels of an automotive safety integrity level classification, this qualifies as a severity level $S2$ (< 40 [km/h], severe injuries). Furthermore, the given speed limits of the standard can be used to calculate the required error reduction $\Delta_{s_B,S}$ for the next lower severity level depending on the tire type and the road friction coefficient. For the parameters of Fig. 3 the severity level can be reduced to $S1$ ($v_{Severity} = 20$ [km/h]) if the $\epsilon_{s_B,q_{0.75}}$ is reduced by $\Delta_{s_B,S} = 2.22$ [m]. The simulated braking distance with applied error reduction $s_B + \epsilon_{s_B,q_{0.75}} - \Delta_{s_B,S}$ is visualized with a dashed line. Since the standard does not detail the collision velocity for a severity level $S0$, the level is only achievable if a crash is prevented. So the required error reduction equals the quantile $\epsilon_{s_B,0.75}$ for $S0$.

Table 1 summarizes simulations results for all parameter combinations and algorithms as well as the requirements for error reduction. The lower error values of the 2D-MSNet over the entire data set are reflected in the resulting severity classes.

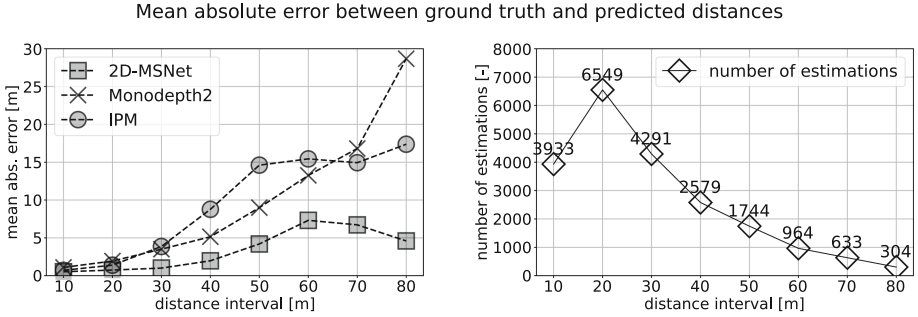


Fig. 2. Mean absolute error per distance interval is shown on the left side. On the right number of estimation per distance interval is shown.

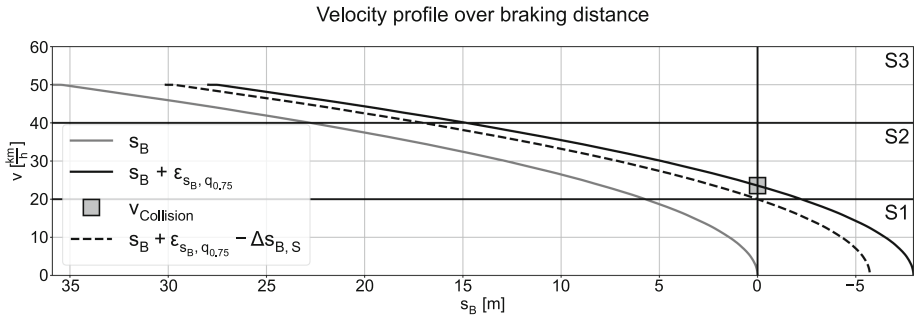


Fig. 3. Simulated velocity profile over braking distance s_B and braking distance shifted by error quantile $s_B + \epsilon_{s_B,q_{0.75}}$ for winter tires and a road friction coefficient of $\mu_R = 0.3$ (condition class: snow). The 75% quantile is based on the Monodepth2 algorithm. Collision velocity borders per severity level are indicated by horizontal lines.

Table 1. Accuracy requirements formulated as $\Delta_{s_B,S}$ for the resulting severity class for selected depth estimation algorithms. Lowest absolute error quantiles and delta values given in bold over all algorithms per tire type.

	2D-MSNet					Monodepth2						
	summer tires			winter tires		summer tires			winter tires			
μ_R [-]	0.3	0.6	1	0.3	0.6	1	0.3	0.6	1	0.3	0.6	1
s_B [m]	53.78	18.25	9.4	35.9	17.9	11.2	53.78	18.25	9.4	35.9	17.9	11.2
$\epsilon_{s_B, q_{0.75}}$ [m]	10.39	1.33	1.35	4.85	1.30	1.29	20.56	2.93	1.67	7.94	2.84	1.72
$v_{Collision}$ [$\frac{km}{h}$]	16.66	16.64	18.31	18.41	12.81	15.49	28.14	20.07	20.59	23.55	19.64	18.2
Severity [-]	1	1	1	1	1	1	2	2	2	2	1	1
$vSeverity$ [$\frac{km}{h}$]	0	0	0	0	0	0	20	20	20	20	0	0
$\Delta_{s_B,S}$ [m]	10.39	1.33	1.35	4.85	1.30	1.29	7.95	0.17	0.85	2.22	2.84	1.72

	IPM					
	summer tires			winter tires		
μ_R [-]	0.3	0.6	1	0.3	0.6	1
s_B [m]	53.78	18.25	9.4	35.9	17.9	11.2
$\epsilon_{s_B, q_{0.75}}$ [m]	18.92	2.76	1.29	10.29	2.53	1.40
$v_{Collision}$ [$\frac{km}{h}$]	26.76	19.41	17.93	26.86	18.44	16.26
Severity [-]	2	1	1	2	1	1
$vSeverity$ [$\frac{km}{h}$]	20	0	0	20	0	0
$\Delta_{s_B,S}$ [m]	6.32	2.76	1.29	4.57	2.53	1.40

4 Conclusion and Future Work

The proposed evaluation method of depth estimation algorithms as a function of real applications shows based on low severity levels that depth estimation of the 2D-MSNet algorithm can already be used in real driving scenarios. The IPM results motivate further usage for the road condition classes “dry” and “wet”. Moreover accuracy requirements for achieving a lower severity level can be formulated based on collision velocity limits given by standards as shown in Table 1. These detail an application-based foundation for further algorithm optimization and self-trained neural networks. A decisive factor of the proposed methodology is the assumption that a braking event is triggered as soon as a collision can no longer be prevented. Future analysis will target the impact on comfort-oriented braking systems. Since the used training dataset does not incorporate the weather conditions of the simulated braking distance and chosen road friction coefficients in image data, future work will take into account the impact of weather conditions on the depth estimation and object detection.

Acknowledgement. The research presented in this paper is supported by the Federal Ministry for Economic Affairs and Climate Action of the Federal Republic of Germany as part of the SUE (Self- Driving Urban E-Shuttle) project.

References

1. European New Car Assessment Programme: Test protocol – aeb car-to-car systems: Implementation 2023 (2022). <https://cdn.euroncap.com/media/67887/euro-ncap-aeb-c2c-test-protocol-v40.pdf>
2. European New Car Assessment Programme: Test protocol – aeb/lss vru systems: Implementation 2023 (2022). <https://cdn.euroncap.com/media/70313/euro-ncap-aeb-lss-vru-test-protocol-v42.pdf>
3. Fermi, T., Singh, M., Theers, M.: Algorithms for Automated Driving (2023). <https://doi.org/10.5281/zenodo.7887756>. <https://thomasfermi.github.io/Algorithms-for-Automated-Driving/Introduction/intro.html>
4. Geiger, A., Lenz, P., Urtasun, R.: Are we ready for autonomous driving? The kitti vision benchmark suite. In: 2012 IEEE Conference on Computer Vision and Pattern Recognition, pp. 3354–3361. IEEE (2012). <https://doi.org/10.1109/CVPR.2012.6248074>
5. Godard, C., Mac Aodha, O., Firman, M., Brostow, G.: Digging into Self-supervised Monocular Depth Estimation. <https://doi.org/10.48550/arXiv.1806.01260>
6. Shamsafar, F., Woerz, S., Rahim, R., Zell, A.: Mobilestereonet: Towards Lightweight Deep Networks for Stereo Matching. <http://arxiv.org/pdf/2108.09770v1>
7. Ahrenhold, T., Iatropoulos, J., Pethe, C., Henze, R., Küçükay, F.: Accuracy requirements for the road friction estimation of a friction-adaptive automatic emergency brake (AEB). In: 30th Aachen Colloquium Sustainable Mobility (2021)
8. Winner, H., Hakuli, S., Lotz, F., Singer, C.: Handbuch Fahrerassistenzsysteme. Springer Fachmedien Wiesbaden, Wiesbaden (2015). <https://doi.org/10.1007/978-3-658-05734-3>

Open Access This chapter is licensed under the terms of the Creative Commons Attribution 4.0 International License (<http://creativecommons.org/licenses/by/4.0/>), which permits use, sharing, adaptation, distribution and reproduction in any medium or format, as long as you give appropriate credit to the original author(s) and the source, provide a link to the Creative Commons license and indicate if changes were made.

The images or other third party material in this chapter are included in the chapter's Creative Commons license, unless indicated otherwise in a credit line to the material. If material is not included in the chapter's Creative Commons license and your intended use is not permitted by statutory regulation or exceeds the permitted use, you will need to obtain permission directly from the copyright holder.





STS-GAN: Spatial-Temporal Attention Guided Social GAN for Vehicle Trajectory Prediction

Yanbo Chen, Huilong Yu^(✉), and Junqiang Xi

School of Mechanical Engineering, Beijing Institute of Technology, Beijing, China
huilong.yu@bit.edu.cn

Abstract. Accurately predicting the trajectories of other vehicles is crucial for autonomous driving to ensure driving safety and efficiency. Recently, deep learning techniques have been extensively employed for trajectory prediction, resulting in significant advancements in predictive accuracy. However, existing studies often fail to explicitly distinguish the impact of historical inputs at different time steps and the influence of surrounding vehicles at distinct locations. Moreover, deep learning-based approaches generally lack model interpretation. To overcome the issues, we propose the Spatial-Temporal Attention Guided Social GAN (STS-GAN). In the generator, we proposed a spatial-temporal attention mechanism to guide the utilization of trajectory features and interaction of the target vehicle with its surrounding vehicles. The spatial attention mechanism evaluates the importance of surrounding vehicles for predictions of the target vehicle, while the temporal attention mechanism learns the significance of historical trajectory information at different historical time steps, thereby enhancing the model interpretation. A convolutional social pooling module is employed to capture interaction features from surrounding vehicles, which are subsequently fused with the attributes of the target vehicle. Experimental results demonstrate that our model achieves competitive performance compared with state-of-the-art methods on publicly available datasets.

Keywords: autonomous driving · trajectory prediction · spatial-temporal attention mechanism

1 Introduction

Recently, vehicle trajectory prediction has garnered significant attention due to its critical applications in autonomous driving [1, 2]. However, predicting the trajectories of social vehicles is not trivial due to the inherent uncertainty variability in the motion patterns of objects [3].

Benefiting from the potent deep learning, pioneering work in vehicle trajectory prediction has addressed some of the above challenges. Variational Autoencoders (VAE) [4], Generative Adversarial Networks (GAN) [5], and Graph Neural

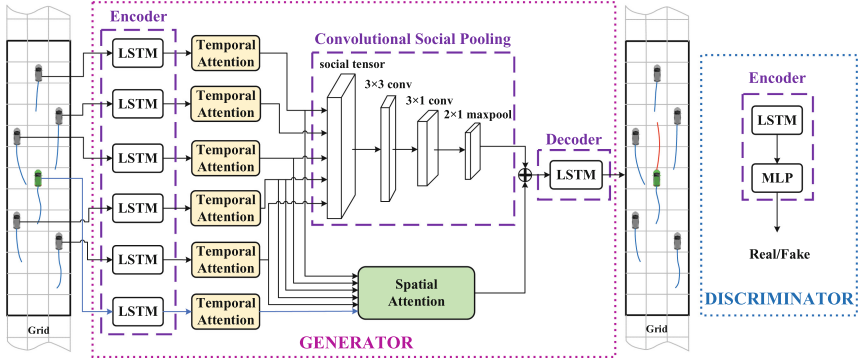


Fig. 1. Overview of proposed STS-GAN.

Networks (GNN) [6] have been utilized to learn trajectory representations and generate multiple possible trajectory samples, effectively capturing multimodal features. These techniques model the complex relationships between vehicles and capture social interactions, leading to more accurate trajectory predictions.

Despite significant progress, existing vehicle trajectory prediction methods struggle with interpretability, especially concerning long-term historical data and nearby vehicle information. Questions about which parts of historical trajectories or nearby vehicle positions influence future motion and how to quantify this influence remain unanswered. To address this, we introduce a spatial-temporal attention mechanism in our STS-GAN model. This approach matches the prediction accuracy of state-of-the-art techniques and enhances interpretability by highlighting the influence of historical trajectories and nearby vehicles through attention weights. Our main contributions are:

- 1) Proposing a spatial-temporal attention-guided social GAN model for vehicle trajectory prediction;
- 2) Developing a temporal attention mechanism to identify the importance of historical trajectories at different times for predicting future behavior;
- 3) Designing a spatial attention mechanism to quantify the influence of nearby vehicles on the trajectory prediction of the target vehicle.

2 Methods

The overall network architecture is shown in Fig. 1. To better understand the importance of different vehicle locations for prediction, similar to research [7], we define a 3×13 spatial grid around the predicted vehicles (Fig. 1).

LSTM Encoder. We first use a single-layer fully connected (FC) network to embed the position of each vehicle x_t^i , obtaining the vector $e_t^{e,i}$. Then, the LSTM encoder processes these embedding vectors for each vehicle i over time steps $t = 1, \dots, h$.

Temporal Attention. The hidden states of vehicle v in the LSTM encoder are denoted as $H_t^{e,v} = \{h_{t-h}^{e,v}, \dots, h_j^{e,v}, \dots, h_t^{e,v}\}$. Subsequently, the temporal attention weights are computed as follows:

$$A_t^v = \text{softmax}(\text{tanh}(W_\alpha H_t^{e,v})). \quad (1)$$

Next, the hidden states $H_t^{e,v}$ and temporal attention A_t^v are combined through a weighted processing, resulting in:

$$\mathcal{H}_t^v = H_t^{e,v} (A_t^v)^\top = \sum_{j=t-h}^t \alpha_j^v h_j^{e,v}. \quad (2)$$

Spatial Attention. Each cell on the grid is denoted as $G_t = \{G_t^1, \dots, G_t^N\}$. N is the total number of grid cells, which can be calculated as follows

$$G_t^n = \begin{cases} \mathcal{H}_t^v, & \text{if any vehicle } v \text{ locates at grid cell } n \\ \mathbf{0} \in \mathbb{R}^{d \times 1}, & \text{otherwise} \end{cases} \quad (3)$$

The spatial attention weights for all vehicles at time step t , denoted as $B_t = \{\beta_t^1, \dots, \beta_t^n, \dots, \beta_t^N\}$, are calculated as follows:

$$B_t = \text{softmax}(\text{tanh}(W_\beta G_t)), \quad (4)$$

where W_β is learnable weights matrix. Finally, we combine all of the historical information from its surrounding vehicles as follows:

$$V_t = G_t (B_t)^\top = \sum_{n=1}^N \beta_t^n G_t^n. \quad (5)$$

LSTM Decoder. After concatenating the nearby vehicles' spatial-temporal feature vectors, and their social context vectors, we use an LSTM layer followed by a FC layer to predict the future trajectory.

Discriminator. The discriminator evaluates the accuracy of the predicted and actual trajectories

$$h_{t+1}^{D,i} = \text{LSTM}(h_t^{D,i}, x_t^{D,i}; W_{D, \text{encoder}}), \quad (6)$$

$$s_{t+1}^{D,i} = \text{Sigmoid}(\text{FC}(h_{t+1}^{D,i}; W_D)). \quad (7)$$

3 Datasets and Experiments Setup

STS-GAN is trained and evaluated using the Next Generation Simulation (NGSIM) ([8]) US-101 and I-80 datasets, each containing 45-min vehicle trajectories split into six 15-min segments. These segments are further divided into training, validation, and test datasets in a 0.7 : 0.1 : 0.2 ratio, resulting in 5,922,867 training entries, 859,769 validation entries, and 1,505,756 test entries.

Table 1. Performance Metrics (ADE/FDE) Comparison with Other Methods

Models	Prediction Horizons				
	1s	2s	3s	4s	5s
CS-LSTM	0.339/0.579	0.632/1.267	1.065/2.107	1.599/3.181	1.922/4.512
STA-LSTM	0.296/0.456	0.526/0.969	0.797/1.605	1.114/2.396	1.485/3.379
ST-GAN	0.286/0.445	0.513/0.953	0.782/1.581	1.095/2.360	1.463/3.339
SS-GAN	0.286/0.452	0.517/0.957	0.783/1.571	1.092/2.345	1.455/3.309
TS-GAN	0.273/0.439	0.500/0.931	0.761/1.536	1.065/2.293	1.422/3.248
STS-GAN	0.264/0.423	0.493/0.926	0.754/1.531	1.059/2.289	1.414/3.221

The Average Displace Error (ADE) and the Final Displacement Error (FDE) are employed as the performance metrics to evaluate the prediction accuracy, defined as:

$$\text{ADE} = \frac{\sum_{i=1}^n \sum_{T=t+1}^{t+p} \|x_T^i - \hat{x}_T^i\|}{np}, \quad (8)$$

$$\text{FDE} = \frac{\sum_{i=1}^n \|x_{t+h}^i - \hat{x}_{t+h}^i\|}{n},$$

where n represents the number of predicted samples. \hat{x}^i and x^i are the predicted and true trajectories of group i data, respectively. The batch size is set to 128, the optimiser used is Adam with a learning rate of 0.001, and the number of training epochs is 10.

To verify the effectiveness of STS-GAN in vehicle trajectory prediction, we compare several state-of-the-art methods. Additionally, to validate the effectiveness of the network structure and the proposed spatial-temporal attention mechanism, we also design ablation experiments. Specifically, we evaluate: 1) **CS-LSTM** [7], an LSTM encoder-decoder model using a convolutional pooling layer; 2) **STA-LSTM** [9], a trajectory prediction model that incorporates spatial-temporal attention mechanisms in LSTM networks; 3) **ST-GAN**, a GAN-based network for spatial-temporal attention mechanisms, but without the introduction of convolutional social pooling; 4) **SS-GAN**, a GAN-based network that incorporates convolutional social pooling and spatial attention mechanisms, but without temporal attention mechanisms; and 5) **TS-GAN**, a GAN-based network that incorporates convolutional social pooling and temporal attention mechanisms, but without spatial attention mechanisms.

4 Results and Analysis

Table 1 compares the ADE/FDE of different models over prediction horizons from 1 to 5 s. STS-GAN outperforms other models across short-term, and long-term predictions, showcasing its superior predictive capabilities. Specifically, CS-LSTM performs the worst due to the absence of attention mechanisms, resulting in higher errors. STA-LSTM, despite incorporating spatial-temporal

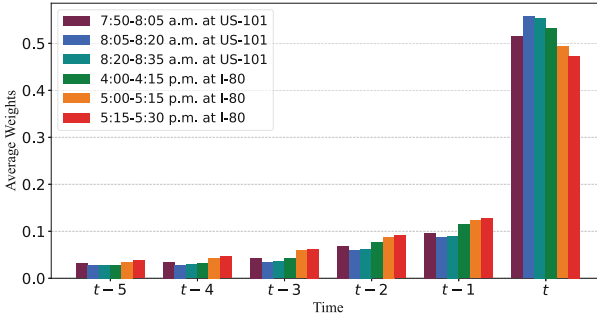


Fig. 2. The average weights of the six adjacent time steps calculated using the six subsets of data, with weights for moments before $t - 5$ ignored.

attention mechanisms, lacks social pooling and generative adversarial mechanisms, leading to lower predictive accuracy. ST-GAN, an ablation study without social pooling, exhibits decreased accuracy compared to STS-GAN, emphasizing the importance of considering social interactions. SS-GAN, focusing on temporal attention, shows slightly lower accuracy than STS-GAN, suggesting limited improvement from the temporal attention mechanism. TS-GAN, concentrating on spatial attention, also demonstrates slightly lower accuracy than STS-GAN but still outperforms models lacking spatial attention.

We calculate the average weights for the last 15 time steps (from $t - 14$ to t) within each interval. Figure 2 displays these weights from time $t - 5$ to t due to smaller weights before $t - 5$. The results reveal that the weight is highest at the current time step t , indicating that the future trajectory of the target vehicle is primarily influenced by its recent trajectory and those of nearby vehicles. This finding aligns with human cognition.

We further analyze the spatial attention mechanism and observe that the spatial attention weights of the predicted vehicle are highest within the grid space. Combined with the earlier analysis of temporal attention, this suggests that the future trajectory of the predicted vehicle is largely influenced by its own driving state. To illustrate the distribution of attention weights of nearby vehicles, we select two typical scenarios. We then normalize and plot the remaining attention weights on a 3×13 grid, excluding those of the predicted vehicle. In Fig. 3(a), we depict a common driving scenario where the predicted vehicle primarily focuses on the vehicle ahead in the same lane, with relatively high weights (e.g., 28.4%, 16.3%, 17.9%), while the weights in other grids are relatively low. Notably, the weight of the grid directly in front of the predicted vehicle is low, possibly due to the typically large following distance for driving safety, resulting in the grid directly ahead often being unoccupied. Figure 3(b) illustrates the spatial weight distribution in a left lane-changing scenario. Unlike the common driving scenario, the predicted vehicle does not focus as much on the vehicle ahead in the same lane but instead pays more attention to vehicles in the target lane, both in front and behind. This observation aligns with human driving experience, where

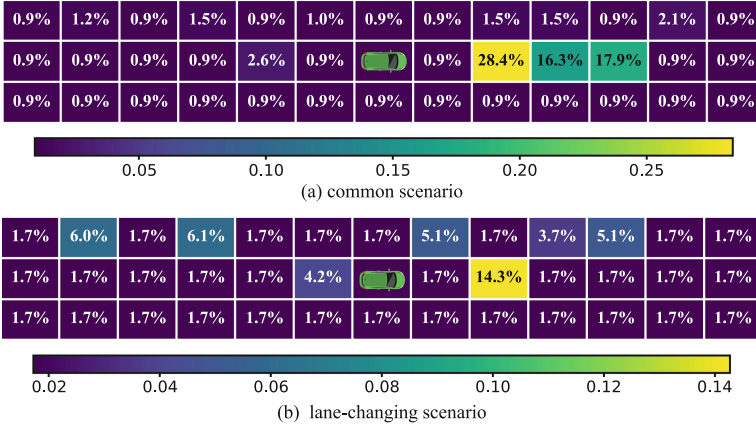


Fig. 3. The distributions of spatial attention weights in two driving scenarios.

drivers assess lane change opportunities by observing the behavior of vehicles in the target lane.

5 Conclusions

This paper presents STS-GAN, a spatial-temporal attention guided social GAN model for vehicle trajectory prediction. The temporal attention mechanism highlights significant time points in historical trajectories, while the spatial attention mechanism measures the influence of nearby vehicles. Key findings from ablation experiments and comparisons with state-of-the-art models include: 1) STS-GAN achieves state-of-the-art prediction accuracy, 2) recent historical trajectory segments are sufficient for accurate predictions, and 3) although the accuracy of STS-GAN is similar to that of ST-GAN and SS-GAN, it offers better interpretability through its spatial-temporal attention weights.

References

1. Carvalho, A., Gao, Y., Lefevre, S., Borrelli, F.: Stochastic predictive control of autonomous vehicles in uncertain environments. In: 12th International Symposium on Advanced Vehicle Control, vol. 9 (2014)
2. Kapania, N.R., Gerdes, J.C.: An autonomous lanekeeping system for vehicle path tracking and stability at the limits of handling. In: Proceedings of the 12th International Symposium on Advanced Vehicle Control (AVEC), pp. 720–725 (2014)
3. Benrachou, D.E., Glaser, S., Elhenawy, M., Rakotonirainy, A.: Use of social interaction and intention to improve motion prediction within automated vehicle framework: a review. *IEEE Trans. Intell. Transp. Syst.* **23**(12), 22807–22837 (2022)
4. Zhu, W., Lü, C., Chen, X.: A crash occurrence risk prediction model based on variational autoencoder and generative adversarial network. *Transportmetrica B Transp. Dyn.* **12**(1), 2358211 (2024)

5. Guo, L., Ge, P., Shi, Z.: Multi-object trajectory prediction based on lane information and generative adversarial network. *Sensors* **24**(4), 1280 (2024)
6. Yin, Y.H., Lü, X., Li, S.K., Yang, L.X., Gao, Z.Y.: Graph representation learning in the its: Car-following informed spatiotemporal network for vehicle trajectory predictions. In: *IEEE Transactions on Intelligent Vehicles* (2024)
7. Deo, N., Trivedi, M.M.: Convolutional social pooling for vehicle trajectory prediction. In: *Proceedings of the IEEE Conference on Computer Vision and Pattern Recognition Workshops*, pp. 1468–1476 (2018)
8. SIMulation, G.: US Highway 101 Dataset (2007)
9. Lin, L., Li, W., Bi, H., Qin, L.: Vehicle trajectory prediction using lstms with spatial-temporal attention mechanisms. *IEEE Intell. Transp. Syst. Mag.* **14**(2), 197–208 (2021)

Open Access This chapter is licensed under the terms of the Creative Commons Attribution 4.0 International License (<http://creativecommons.org/licenses/by/4.0/>), which permits use, sharing, adaptation, distribution and reproduction in any medium or format, as long as you give appropriate credit to the original author(s) and the source, provide a link to the Creative Commons license and indicate if changes were made.

The images or other third party material in this chapter are included in the chapter's Creative Commons license, unless indicated otherwise in a credit line to the material. If material is not included in the chapter's Creative Commons license and your intended use is not permitted by statutory regulation or exceeds the permitted use, you will need to obtain permission directly from the copyright holder.





Automated Parking System for Tractor-Trailer Vehicle

Jinwoo Kim  and Seongjin Yim  

Seoul National University of Science and Technology, Seoul 01811, Republic of Korea
acebtif@seoultech.ac.kr

Abstract. By virtue of recent development in automated parking system, there has been growing interest in tractor-trailer automated parking application (TTAPA). However, there are two major obstacles when developing TTAPA. The one is low maneuverability of reversing a tractor-trailer vehicle (TTV), caused by hitch angle steering characteristic, and the other is heavy computational cost from non-linearity of model. This paper considers an autonomous parking system (APS) for a TTV. To achieve successful autonomous parking under various circumstances, this system adopts nonlinear model predictive control and LQR as path planner and path tracking controller, respectively. To validate the proposed APS for TTV, the system is implemented and evaluated in MATLAB/Simulink and TruckSim co-simulation environment. From simulation results, it is shown that the proposed APS can achieve parking scenario goal with good performance for a TTV.

Keywords: Tractor-trailer vehicle · Path tracking control · Automated parking system · Path planning

1 Introduction

Parking a tractor-trailer vehicle (TTV) is different from parking a single tractor or a single vehicle in that a trailer is steered via hitch angle when driving backward. For the reason, reverse driving of a TTV heavily depends on the driver's skill level and an unskilled driver has a hard time parking a TTV [1]. To solve the problem, various path planning and path tracking algorithms for automatic parking of TTVs have been proposed to date [2–4]. In addition to hitch angle steering characteristics, reversing control of a TTV has various difficulties such as high nonlinearity of the system, constraint on control input and state resulting from mechanical factors [5].

To cope with the difficulties, several methods such as adaptive neuro-fuzzy inference system (ANFIS) [6] or model predictive control (MPC) [7–9] have been applied to date. However, those methods require a large amount of computation time and, as a result, are hard to be implemented in a real TTV [10]. For the reason, it is necessary to develop a system for the purpose of reducing excessive computational cost and conducting path planning and path tracking control that matches with actual parking scenarios for a TTV. For the purpose, nonlinear model predictive control (NMPC) and linear quadratic regulator (LQR) are adopted as a path planner and path tracking controller or path tracker, respectively, in this paper. To validate the proposed system, simulation via MATLAB/Simulink and TruckSim is conducted.

2 Design of Automated Parking System

2.1 Kinematic Model for Tractor-Trailer Vehicle

Figure 1 shows the kinematic model of a TTV [11]. The angle α denotes front steering angle for the tractor and the angles β and θ denote the global yaw angles of the tractor and trailer, respectively. Because parking scenarios for a TTV are usually conducted in low speed, under the assumption that there are no tire slips, the kinematic model for a TTV can be obtained as Eq. (1), where v is the longitudinal velocity.

$$\begin{bmatrix} \dot{x} \\ \dot{y} \\ \dot{\theta} \\ \dot{\beta} \end{bmatrix} = \begin{bmatrix} v \cos \beta \left(1 - \frac{h}{b} \cdot \tan \beta \tan \alpha \right) \cos \theta \\ v \cos \beta \left(1 - \frac{h}{a} \cdot \tan \beta \tan \alpha \right) \sin \theta \\ v \left(\frac{1}{b} \cdot \sin \beta + \frac{h}{ab} \cdot \cos \beta \tan \alpha \right) \\ v \left(\frac{1}{a} \cdot \tan \alpha - \frac{1}{b} \sin \beta - \frac{h}{ab} \cdot \cos \beta \tan \alpha \right) \end{bmatrix} \quad (1)$$

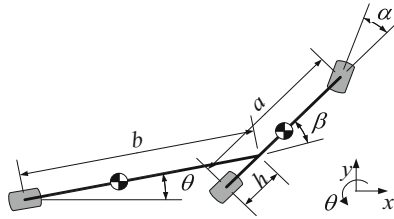


Fig. 1. Kinematic model of tractor-trailer vehicle

2.2 Design of Path Planner with NMPC

In this paper, the path planner is designed with NMPC [12]. With the kinematic model given in Eq. (1), NMPC solves a trajectory optimization problem. The longitudinal velocity, v , and steering angle, θ , are set to be both control inputs and regulated output at the same time. To consider the restrictions on states and regulated outputs, several constraints are derived from a geometry of a TTV and collision avoidance objective.

In the previous work, MPC has been widely adopted as a path tracker [13]. However, it requires a large amount of computation time. For the reason, it is not easy to implement MPC in a real TTV. Instead of MPC, LQR is adopted as a path tracker to reduce the computation time for real-time application [14]. For LQR in path tracking stage, additional considerations are required in planning stage. More specifically, additional strict constraint on hitch angle is applied in NMPC in order to minimize the possibility of jackknifing and cost function, which is needed to reduce transition of driving direction.

To define a parking scenario, initial and target states of TTV and global positions of obstacles are required. By applying NMPC in a constrained circumstance, an optimal state sequence, i.e., optimized path and pose from initial state to final state, is obtained as a result.

2.3 Design of Path Tracker with LQR

By setting the lateral error e , the trailer yaw error θ_e , and the hitch angle error β_e as the error state from the kinematic model Eq. (1), the error dynamics is derived as Eq. (2), where κ_{ref} is the curvature of the reference path and β_{ref} is the reference hitch angle. In Eq. (2), the steering angle α is the control input.

$$\begin{bmatrix} \dot{e} \\ \dot{\theta}_e \\ \dot{\beta}_e \end{bmatrix} = \begin{bmatrix} v \cos \beta \left(1 - \frac{h}{a} \cdot \tan \beta \tan \alpha\right) \sin \theta_e \\ v \left(\frac{1}{b} \cdot \sin \beta + \frac{h}{ab} \cdot \cos \beta \tan \alpha - \kappa_{ref} \cos \theta_e / (1 - \dot{e} \kappa_{ref})\right) \\ v \left(\frac{1}{a} \cdot \tan \alpha - \frac{1}{b} \cdot \sin \beta - \frac{h}{ab} \cdot \cos \beta \tan \alpha\right) - \dot{\beta}_{ref} \end{bmatrix} \quad (2)$$

Under constant speed assumption and small-angle approximation, the error model Eq. (2) is linearized around an equilibrium point or an origin. With the linearized model, LQR path tracker is designed [15].

The LQ cost function J is defined as Eq. (3) with the weights ρ_i , which are determined by Bryson's rule [16]. In Eq. (3), the maximum allowable values on each error state were selected by considering the fact that hitch angle tracking performance is critical for preventing jackknife. Afterwards, with the selected weights and linearized model, the controller gain K_{LQR} was calculated by solving a corresponding Riccati equation.

$$J = \int_0^{\infty} \left(\rho_1 e^2 + \rho_2 \theta_e^2 + \rho_3 \beta_e^2 + \rho_4 \alpha^2 \right) dt \quad (3)$$

2.4 Design of Path Tracker with NMPC

As a baseline, NMPC path tracker is designed to compare with the proposed LQR one in terms of the performance and computation time. The designed NMPC path tracker has identical constraint and cost function from NMPC path planner.

3 Simulation of Automated Parking System

3.1 Simulation Environment

To validate the proposed APS, simulation was conducted in a co-simulation environment with MATLAB/Simulink and TruckSim. Both of path planner and trackers were implemented on MATLAB/Simulink. As a plant model, 2-axle tractor 1-axle trailer model with fifth wheel hitching was selected from TruckSim. The vehicle speed was set to 18 km/h in both of forward and backward directions. The tire-road friction coefficient was set to 0.85, which means dry asphalt road surface.

3.2 Result of NMPC Path Planner

Figure 2a shows the initial and final states of the parking scenario for NMPC. From these states, optimal state sequence is obtained from NMPC path planner. As shown in Fig. 2b, optimal state sequence was obtained without jackknifing.

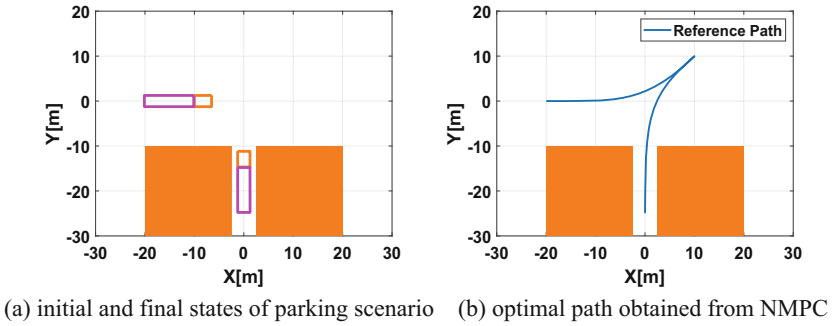


Fig. 2. Initial and final states for NMPC and optimal path from NMPC

3.3 Results of NMPC and LQR Path Trackers

Simulation results of NMPC and LQR path trackers are shown in Fig. 3. As shown in Fig. 3, NMPC path tracker shows satisfactory performance without obstacle collision within 0.37 m of lateral offset, 0.6° of trailer yaw error and 1.4° of hitch angle error. LQR path tracker shows also satisfactory performance within 0.12 m of lateral offset, 1.1° of trailer yaw error and 1.6° of hitch angle error.

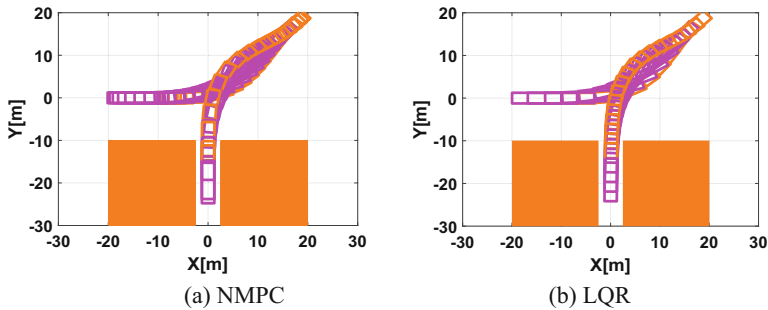


Fig. 3. Trajectories of TTV from NMPC and LQR path trackers

The lateral offset, the trailer yaw and hitch errors are given in Fig. 4. As shown in Fig. 4, LQR path tracker followed the reference path with smaller lateral offset but larger yaw and hitch errors compared to NMPC path tracker. This is caused by the fact that the plant model used for designing LQR path tracker is linearized at the equilibrium point, i.e., the origin. On the contrary, NMPC path tracker linearizes the given plant model at each sequence.

3.4 Comparison of Computation Time Between NMPC and LQR

To compare the computation times of the LQR and NMPC path trackers, the computation time per simulation loop was logged during the simulation. From the simulation results, the computation time of NMPC path tracker is much larger than that of LQR path tracker.

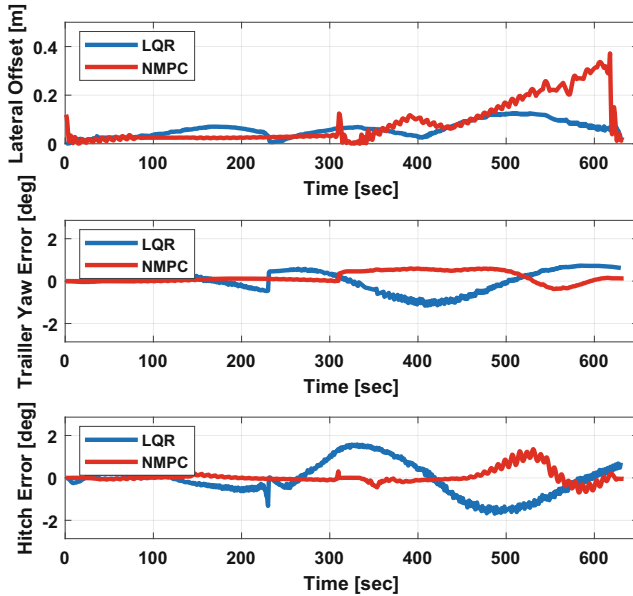


Fig. 4. Simulation results of NMPC and LQR path trackers.

For instance, NMPC path tracker requires 93 ms on average per 1 ms simulation loop calculation (SLC). On the contrary, LQR path tracker requires 0.12 ms on average per 1 ms SLC. From these results, it was shown that LQR path tracker is much faster than NMPC one. For the reason, LQR is recommended as a path tracker for a TTV, instead of MPC or NMPC.

4 Conclusion

In this paper, the automatic parking system for a tractor-trailer vehicle was proposed with NMPC path planner and LQR path tracker. The kinetic model was selected as a vehicle one for a tractor-trailer vehicle. To validate the proposed APS, simulation on MATLAB/Simulink and TruckSim was conducted. The performance and computation time of LQR and NMPC path trackers was compared. From the simulation results, it was shown that NMPC and LQR path trackers show equivalent performance and that the proposed APS with LQR path tracker can park the tractor-trailer vehicle with smaller error and much smaller computational cost, compared to NMPC.

Acknowledgement. This work was supported by the Ministry of Education through the National Research Foundation of Korea (NRF) under Basic Science Research Program (NRF-2019R1A6A1A03032119).

References

1. Berg, U., Wojke, P., Zöbel, D.: Driver training simulator for backing up commercial vehicles with trailers. *J. Mech. Syst. Transp. Logist.* **1**(2), 181–191 (2008)
2. Manav, A.C., Lazoglu, I.: A novel cascade path planning algorithm for autonomous truck-trailer parking. *IEEE Trans. Intell. Transp. Syst.* **23**(7), 6821–6835 (2021)
3. Hamaguchi, Y., Raksincharoensak, P.: Automated steering control system for reverse parking maneuver of semi-trailer vehicles considering motion planning by simulation of feedback control system. *J. Robot. Mechatron.* **32**(3), 561–570 (2020)
4. Sudhakaran, A.: Autonomous Parallel Parking of a Scaled Tractor Semi-trailer. Master thesis, Eindhoven University of Technology (2018)
5. Latif, A., Chalhoub, N., Pilipchuk, V.: Control of the nonlinear dynamics of a truck and trailer combination. *Nonlinear Dyn.* **99**(4), 2505–2526 (2020)
6. Azadi, S. H., Nedamani, H. R., Kazemi, R.: Automatic parking of an articulated vehicle using ANFIS. *Glob. J. Sci. Eng. Technol.*, 93–104 (2013)
7. Bin, Y., Shim, T.: Constrained model predictive control for backing-up tractor-trailer system. In: Proceedings of the 10th World Congress on Intelligent Control and Automation, pp. 2165–2170 (2012)
8. Hejase, M., Jing, J., Maroli, J. M., Salamah, Y. B., Fiorentini, L., Özgüner, Ü.: Constrained backward path tracking control using a plug-in jackknife prevention system for autonomous tractor-trailers. In: 2018 21st International Conference on Intelligent Transportation Systems (ITSC), pp. 2012–2017 (2018)
9. Qiu, D., Qiu, D., Wu, B., Gu, M., Zhu, M.: Hierarchical control of trajectory planning and trajectory tracking for autonomous parallel parking. *IEEE Access* **9**, 94845–94861 (2021)
10. Kayacan, E., Saeys, W., Ramon, H., Belta, C., Peschel, J.M.: Experimental validation of linear and nonlinear MPC on an articulated unmanned ground vehicle. *IEEE/ASME Trans. Mechatron.* **23**(5), 2023–2030 (2018)
11. Altafini, C.: The general n-trailer problem: conversion into chained form. In: Proceedings of the 37th IEEE Conference on Decision and Control (1998)
12. Bos, M., Vandewal, B., Decré, W., Swevers, J.: MPC-based motion planning for autonomous truck-trailer maneuvering. *IFAC-PapersOnLine* **56**(2), 4877–4882 (2023)
13. Fan, M., Yue, M., Zhang, H., Liu, Z.: Anti-jackknife reverse perpendicular parking control of tractor-trailer vehicle via MPC technique. In: 2019 IEEE 9th Annual International Conference on Cyber Technology in Automation, Control, and Intelligent Systems, (2019)
14. Vivek, K., Sheta, M. A., Gumtapure, V.: A comparative study of stanley, LQR and MPC controllers for path tracking application (ADAS/AD). In: 2019 IEEE International Conference on Intelligent Systems and Green Technology (ICISGT) (2019)
15. Hamaguchi, Y., Raksincharoensak, P.: Study on path planning and tracking algorithm for autonomous parking system of semi-trailers. *Mech. Eng. J.* **10**(3), 22–00361 (2023)
16. Bryson, A.E., Ho, Y.C.: Applied Optimal Control. Hemisphere, New York (1975)

Open Access This chapter is licensed under the terms of the Creative Commons Attribution 4.0 International License (<http://creativecommons.org/licenses/by/4.0/>), which permits use, sharing, adaptation, distribution and reproduction in any medium or format, as long as you give appropriate credit to the original author(s) and the source, provide a link to the Creative Commons license and indicate if changes were made.

The images or other third party material in this chapter are included in the chapter's Creative Commons license, unless indicated otherwise in a credit line to the material. If material is not included in the chapter's Creative Commons license and your intended use is not permitted by statutory regulation or exceeds the permitted use, you will need to obtain permission directly from the copyright holder.





Research on Jerk Reduction Route Planning Method for Autonomous Driving Using Vehicle Forward Information

Takumi Komiya¹, Masato Abe¹, Yoshio Kano¹, Makoto Yamakado¹(✉), Yu Sato², Ken-taro Ueno², and Yusuke Tanaka³

¹ Kanagawa Institute of Technology, 1030 Shimo-Ogino, Atsugi-shi 243-0292, Japan
yamakado@cco.kanagawa-it.ac.jp

² Hitachi Astemo, Ltd., 4-7-1 Onnna, Atsugi-chi 243-8510, Japan

³ Isuzu Motors, Ltd., 8 Tsuchidana, Fujisawa-shi 252-0881, Kanagawa, Japan

Abstract. We propose a forward-gazing model for path planning (Preview Path-Planning model) as the most basic model that provides insight to people who share the paradigm of human-like path-planning modeling. The basic concept is to apply a low-pass filter to changes in forward curvature. In addition, the phase delay due to the low-pass filter is compensated by forward gaze. We also report the results of determining the longitudinal motion by applying the GVC technology to the situation in which the vehicle could run perfectly along the path.

Keywords: Vehicle Dynamics · Driver Model · Motion Control · Jerk · G-Vectoring Control

1 Introduction

To determine lateral motion, both “path planning” and “path following” are necessary. The most fundamental model for human “path following” is Kondo’s forward-looking model (Preview path-following model) [1]. Defining a fundamental model for human “path planning” remains a challenge, with existing methods lacking intuitive clarity.

The paper introduces a foundational model aligned with human-like “path planning” the Preview path-planning model. It aims to provide insights for those modeling human-like path planning. Additionally, the paper reports applying GVC technology [2] in scenarios where driving along the proposed path is achieved, showcasing the integration of lateral motion.

2 Information and Planning Guidelines for Path Planning

This chapter explores drivers’ considerations in path planning, assuming a target course centerline in the middle of the drivable area. Drivers aim to optimize their route, considering factors like shortcuts and avoiding abrupt curvature changes. The use of Tangent Points aids in understanding the target course centerline’s curvature. To control lateral

Table 1. Example of Waypoint data

i	X-Position x(i)	Y-Position y(i)	Curvature $\kappa_{org}(i)$	Direction $\theta(i)$
1	0	0	0	0
:	:	:	:	:
s_{ve}	$x(s_{ve})$	$y(s_{ve})$	$\kappa_o(s_{ve})$	$\theta(s_{ve})$
:	:	:	:	:
s_{pv}	$x(s_{pv})$	$y(s_{pv})$	$\kappa_o(s_{pv})$	$\theta(s_{pv})$
:	:	:	:	:
N	x(N)	y(N)	$\kappa_o(N)$	$\theta(N)$

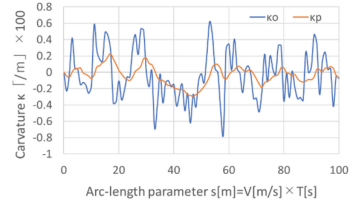


Fig. 1. Image of Curvature Smoothing

acceleration, the chapter proposes a path planning guideline: derive a smoothed curvature (κ_p) from the original curvature (κ_o) by reducing its maximum value and minimizing the time rate of change, ensuring it fits within the lane width.

3 Implementation of Path Planning Using Forward Info.

3.1 Reduction and Smoothing of Curvature Maximum

Considering the application of path planning guidelines from the previous chapter, Waypoint information for the centerline is crucial. If this data list, containing coordinates, curvature, and orientation information, is available, the vehicle’s current position (*ve*-th) and forward-looking point (*pv*-th) data can be referenced. An example Waypoint data table (Table 1) is introduced. The blue line in Fig. 1 represents the original curvature (κ_o) of the centerline. Applying the path planning guideline involves deriving a smoothed path (κ_p , orange line) to reduce the maximum curvature and its time variation, realizing a smoother path planning. The orange line (κ_p) is a result of applying a first-order low-pass filter to the original curvature (κ_o).

3.2 Phase Lag Compensation

To address phase lag introduced by the low-pass filter, the chapter incorporates forward-looking information and Taylor expansion. Anticipating future curvature based on current and forward-looking data compensates for phase lag, resulting in a simplified expression (Eq. (1)) for the smoothed path planning (κ_p).

$$\kappa_p(s_{ve}) = \kappa_o(s_{ve}) - C_\kappa (\kappa_o(s_{pv}) - \kappa_o(s_{ve}))V \tag{1}$$

3.3 Waypoint Offset Strategy for Path Planning

This section describes a specific method for path planning, which involves offsetting the X-Y coordinate information of the waypoints on the original centerline to create new

path planning waypoints. The waypoints are recorded for each unit arc length parameter s (Eq. (2)). The waypoint L meters ahead of the i -th waypoint is the $i + L$ -th waypoint.

$$\sqrt{(X_o(i) - X_o(i-1))^2 + (Y_o(i) - Y_o(i-1))^2} = 1 \quad (2)$$

For the i -th data point, the process is simplified as shown in Eq. (3).

$$\kappa_p(i) = \kappa_o(i) - \kappa_d(i) \quad (3)$$

Here, $\kappa_d(i)$ is redefined as follows:

$$\kappa_d(i) = C_\kappa(\kappa_o(i+L) - \kappa_o(i))V \quad (4)$$

Using Fig. 2, which shows continuous waypoints representing the centerline in the Cartesian coordinate system, the method for setting new path planning waypoints is illustrated. Let the coordinates of the $(i-1)$ -th waypoint on the centerline be $[X_o(i-1), Y_o(i-1)]$ with an orientation angle $\theta_o(i-1)$. Since the arc length parameter s is L , the angle changes when advancing by an arc length of 1 is $\kappa_o(i-1)$ (the lengths of the red and blue lines in the figure are 1).

$$\theta_o(i) = \theta_o(i-1) + \int_0^1 \kappa_o(i-1) ds = \theta_o(i-1) + \kappa_o(i-1) \quad (5)$$

Therefore, the orientation angle $\theta_p(i)$ of the new path planning waypoint () is:

$$\theta_p(i) = \theta_o(i) - \kappa_d(i-1) \quad (6)$$

The XY coordinates can be geometrically determined. Since the arc length parameter is 1, the distance from the coordinates of the (i) -th waypoint on the centerline (red) $[X_o(i), Y_o(i)]$ to the new path planning waypoint (blue) $[X_p(i), Y_p(i)]$ is approximately $\kappa_d(i-1)$ (green line). Using this relationship and the relationship with $\theta_o(i)$:

$$\begin{bmatrix} X_p(i) \\ Y_p(i) \end{bmatrix} = \begin{bmatrix} X_o(i) \\ Y_o(i) \end{bmatrix} + \begin{bmatrix} \sin \theta_o(i) \\ -\cos \theta_o(i) \end{bmatrix} \kappa_d(i-1) \quad (7)$$

This means the new path planning waypoint is offset from the centerline by a distance $\kappa_d(i-1)$ to the left or right, rather than altering the curvature. Reformulating it this way, the path planning strategy can be described as: "Path planning offsets the centerline to the left or right (outside or inside) by a value proportional to the gain C_κ , the current speed V , and the difference between the current curvature and the forward-looking curvature." This simple strategy allows easy management of how far the vehicle can move relative to the lane width using the gain C_κ in Eq. (4). Qualitatively, this strategy can be expressed as a straightforward driver behavior: "Path planning involves anticipating the amount of curvature ahead and adjusting the line to swell slightly to the opposite side. "This scenario is illustrated in Fig. 3. This model is referred to as the Preview Path-Planning Model (PPPM).

However, even if a path planning instructs the vehicle to move laterally by κ_d , the vehicle cannot move sideways. Therefore, when adopting the online PPPM for motion

control, it is necessary to calculate κ'_d for a forward distance of L' [m], generate a target path L' [m] ahead, and detect the lateral displacement of the vehicle and the deviation ε' from the target path after a time of L'/V , similar to Kondo's forward-looking path-following model [1]. Feedback control can then be implemented based on this deviation.

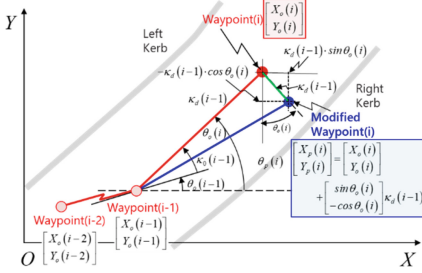


Fig. 2. Continuous Waypoints

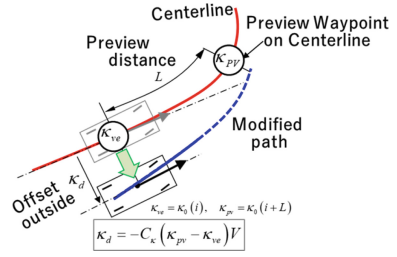


Fig. 3. Preview Path-Planning Model

4 Verification by Numerical Calculation

To purely verify the “validity of the target path” generated by the Preview Path-Planning Model (PPPM), any tracking error caused by the vehicle model or the path-following model may introduce noise. Therefore, we generated a path using the PPPM and evaluated the path followed perfectly by the vehicle’s center of gravity without any lateral slip (the velocity vector of the center of gravity always aligns with the tangent direction of the path). Specifically, we assessed the path, yaw rate (calculated from the velocity and curvature), lateral acceleration, jerk, and the integral of the squared jerk.

4.1 Verification by Pseudo Lane Change (Constant Speed)

As the simplest example, we created a crank (pseudo lane change) course as shown in Fig. 4. The vehicle’s center of gravity moved from left to right at a constant speed of 40 km/h. The approximate lane change width is 5.2 m, and the lane transition distance is about 40 m. For the PPPM, the forward-looking time was set to 1.8 s ($L = 20$ m) with a gain of $C_k = 20$.

As seen in Fig. 4, the PPPM generates a path offset from the center line (Normal) of the crank course. Moreover, before the Normal path curves to the right, it initially swells to the left (outside) and then exits the course in a straight line.

The initial outward swell in the opposite direction resembles a “counter-steering” maneuver. Assuming the vehicle follows such a path and aligns with the direction of travel, at the intersection point $[X, Y] = [25 \text{ m}, 0 \text{ m}]$ where the Normal and PPPM lines cross, the vehicle positions for both paths are identical. However, it should be noted that while the yaw angle is zero for the Normal line path, a yaw angle towards the direction of travel has already developed for the PPPM line. Figures 5 and 6 compare the yaw rate and lateral acceleration.

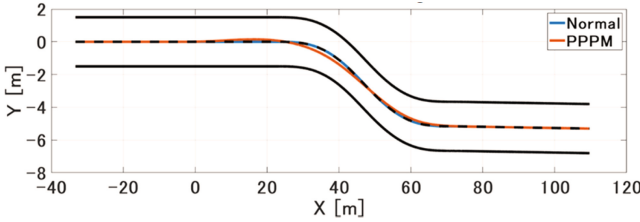


Fig. 4. Result of applying PPPM to a Lane-change-like course

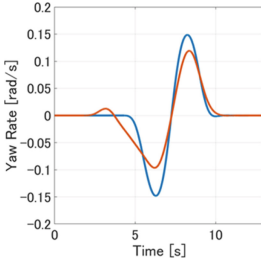


Fig. 5. Comparison of yaw rate

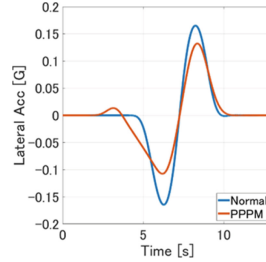


Fig. 6. Comparison of lateral acc.

4.2 Verification on a Complex Course (Speed Planning with GVC)

In addition to the path planning by PPPM, we applied GVC and demonstrated the results of moving the vehicle’s center of gravity based on the speed plan. When applying the G-Vectoring Control (GVC) associated with lateral motion, the longitudinal acceleration G_x of the vehicle can be expressed using the lateral acceleration G_y and gain C_{xy} , as shown in Eq. (8) (the sign function and first-order lag element [2] are omitted).

$$G_x = -C_{xy}\dot{G}_y \tag{8}$$

The vehicle’s center of gravity accelerates or decelerates solely based on the command of Eq. (8). Now, if the initial speed is V , and the speed changes by ΔV as the vehicle’s center of gravity moves along the path, this change integrates to the acceleration and deceleration commands, resulting in

$$\Delta V = \int_0^t G_x dt = -C_{xy} \int_0^t \dot{G}_y dt = -C_{xy}G_y \tag{9}$$

Therefore, by determining the initial speed and calculating ΔV at each computational step, we can determine the speed profile (speed design) [3]. Additionally, the longitudinal and lateral accelerations at that time will form an arc in the “g-g” diagram, exhibiting the unique longitudinal and lateral motion coupling characteristics of GVC.

Figure 7 depicts the paths of the set course’s center (Centerline: Normal) and PPPM, comparing scenarios with and without GVC application, each with deceleration gain of 0.03 and acceleration gain of 0.015, as in the previous section (initial speed 40 km/h, counterclockwise, preview time 1.8 s ($L = 20$ m), PPPM gain $C_k = 50$). Figures 8 and 9

compare longitudinal and lateral accelerations, while Figs. 10 and 11 illustrate the “g-g” diagram and the velocity of the center of gravity’s movement.

In Fig. 10, for both Normal and PPPM without GVC (blue and red lines), the longitudinal accelerations remain constant with speed, overlapping on the lateral acceleration axis. In contrast, with GVC applied (yellow and purple lines), longitudinal accelerations vary smoothly in conjunction with lateral acceleration, depicting a smooth arc-like change.

Observing Fig. 11, while the addition of GVC to the Normal line results in a slight reduction in speed compared to PPPM with GVC, the latter exhibits less speed reduction (moves faster). Nonetheless, despite this, the integration of the squared values of longitudinal and lateral jerk over one lap (cost function) as depicted in Fig. 12 and Fig. 13 shows that PPPM with GVC yields the smallest value. Thus, the effectiveness of the combined PPPM and GVC for autonomous driving route and speed planning is confirmed.

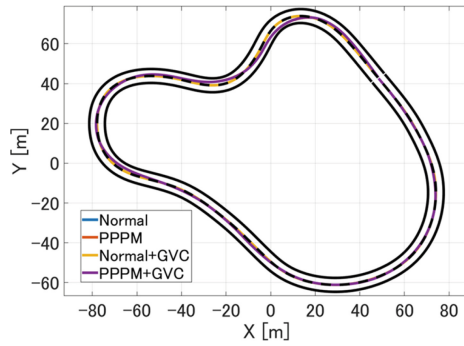


Fig. 7. Result of applying PPPM to a Combined course

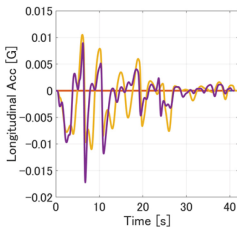


Fig. 8. Long. acc.

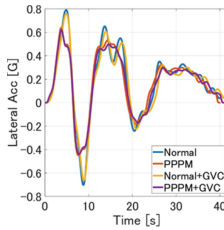


Fig. 9. Lateral acc.

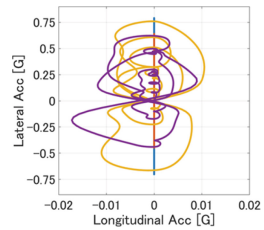


Fig. 10. “g-g” diagram

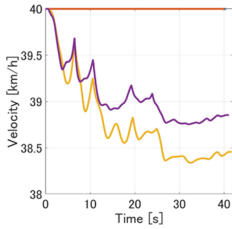


Fig. 11. Moving velocity

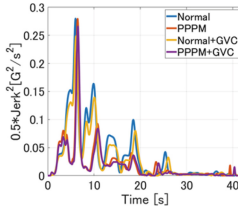


Fig. 12. $0.5 \times (J_x^2 + J_y^2)$

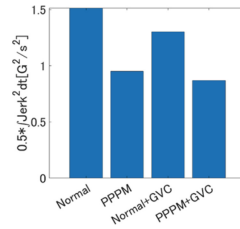


Fig. 13. $0.5 \times \int (J_x^2 + J_y^2) dt$

5 Conclusion

In this paper, a forward-looking model termed the Preview Path-Planning Model (PPPM) is formulated, capable of computing a route (X_p, Y_p) similar to that performed by humans based on the target course centerline (X_o, Y_o, θ_o) (where the forward-looking distance is denoted as L [m]).

$$\begin{bmatrix} X_p(i) \\ Y_p(i) \end{bmatrix} = \begin{bmatrix} X_o(i) \\ Y_o(i) \end{bmatrix} + \begin{bmatrix} \sin \theta_o(i) \\ -\cos \theta_o(i) \end{bmatrix} C_\kappa (\kappa_o(i + L) - \kappa_o(i)) V \quad (10)$$

Subsequently, the results of driving a lane-change course at a constant speed using PPPM and determining the speed with GVC applied to the planned route by integrating the squared values of jerk (cost function) are evaluated. The findings confirm that improved ride comfort can be achieved compared to driving along the target course centerline at a constant speed.

References

1. Kondo, M.: Fundamental relationships between steering and motion of automobiles. *Trans. Soc. Automot. Eng. Jpn.* (5), 40–43 (1958)
2. Yamakado, M., Takahashi, J., Saito, S., Yokoyama, A., Abe, M.: Improvement in vehicle agility and stability by G-vectoring control. *Veh. Syst. Dyn.* **48**, 231–254 (2010)
3. Yokoyama, A., Yamakado, M.: Energy regeneration effect of G-vectoring control using electric motors. *Trans. Soc. Automot. Eng. Jpn.* **44**(4), 1027–1032 (2013). (in Japanese)

Open Access This chapter is licensed under the terms of the Creative Commons Attribution 4.0 International License (<http://creativecommons.org/licenses/by/4.0/>), which permits use, sharing, adaptation, distribution and reproduction in any medium or format, as long as you give appropriate credit to the original author(s) and the source, provide a link to the Creative Commons license and indicate if changes were made.

The images or other third party material in this chapter are included in the chapter’s Creative Commons license, unless indicated otherwise in a credit line to the material. If material is not included in the chapter’s Creative Commons license and your intended use is not permitted by statutory regulation or exceeds the permitted use, you will need to obtain permission directly from the copyright holder.





Online Motion Planning for All-Wheel Drive Autonomous Race Cars

Mischa Huisman^(✉)  and Erjen Lefeber 

Eindhoven University of Technology, 5600MB Eindhoven, The Netherlands
{m.r.huisman,a.a.j.lefeber}@tue.nl
<https://research.tue.nl/en/persons/mischa-r-huisman>,
<https://www.tue.nl/en/research/researchers/erjen-lefeber>

Abstract. The advent of autonomous racing events, such as Formula Student Driverless Cup, requires online motion planning algorithms that push the vehicle to its limits while ensuring vehicle stability and preventing road departure. A popular method to find the optimal control input to drive at the limits of the car is Nonlinear Model Predictive Control (NMPC). However, when NMPC is used, often a trade-off has to be made between performance, accuracy, and computational complexity. In this manuscript, the principle of cascading different vehicle models is used to construct the prediction horizon. Initially, a two-track model optimizes steering and motor input, utilizing torque vectoring benefits. The horizon is then extended with a single-track model, and a lower fidelity point mass model, effectively reducing computational complexity. Furthermore, by adopting a curvilinear reference frame, a transformation towards the spatial domain is obtained, which allows us to use time as an optimization variable. A simulation study is performed for varying prediction horizon lengths which show the advantages of the cascaded vehicle model, achieving an 86% reduction in computation time with comparable lap times.

Keywords: Nonlinear Model Predictive Control · Motion Planning · Autonomous Racing

1 Introduction

To be the fastest on track, the car has to drive on the performance limits. In autonomous racing, this requires a combination of optimal path planning and motion control that also guarantees safe driving and vehicle stability. Nonlinear Model Predictive Control (NMPC) is a popular method for solving both path planning and motion control, where a trade-off has to be made between performance, accuracy, and computational complexity.

In [1], a hierarchical motion planning strategy combines offline path optimization and online reference tracking using NMPC. Consequently, [2] extends

The research leading to these results has received funding from the European Union's Horizon Europe programme under grant agreement No 101069748 - SELFY project.

© The Author(s) 2024

G. Mastinu et al. (Eds.): AVEC 2024, LNME, pp. 185–192, 2024.

https://doi.org/10.1007/978-3-031-70392-8_27

this work by integrating the low-level vehicle control for Torque Vectoring (TV). Good performance gains are obtained, however, path planning is computed offline due to computational complexity. Computational complexity can be reduced by exploiting Linear Parameter Varying (LPV) models. For example, in [3] an LPV model is used to implement a similar control strategy as [1], or in [4] where an LPV model is used to implement online path planning. However, using an LPV model requires linear tire dynamics, limiting the performance and accuracy. As an alternative to hierarchical methods, single-layer control structures are developed to prevent infeasible trajectories between different controllers at the cost of increasing model complexity. In [5] both online path planning and motion control are solved using a single-layer NMPC. The problem is solved using a cascaded vehicle model where a bicycle model’s prediction horizon, including nonlinear tire dynamics, is extended with a point mass. Using lower fidelity models reduces computational complexity, allowing for an increased prediction horizon therefore increasing performance. The controller concept is proven to work on a full-scale racing car, excluding TV.

In this manuscript, we want to exploit that race cars are equipped with four in-wheel motors, as seen in Formula Student Driverless cars, developed by student teams like University Racing Eindhoven [6]. Using a two-track model to solve the NMPC provides the performance gains from TV [1, 2], while using a cascaded vehicle model to reduce computational complexity [5].

2 Cascaded Prediction Horizon

In the single-layer NMPC for autonomous racing, there are two objectives; 1) motion control, and 2) path planning. The former requires a highly non-linear vehicle model to predict vehicle behavior, describing the longitudinal, stiff lateral, and stiff yaw dynamics. The latter requires a sufficiently long prediction horizon to determine an optimal path to avoid road departure and a safe velocity profile, which can be performed with a lower-fidelity vehicle model. As suggested

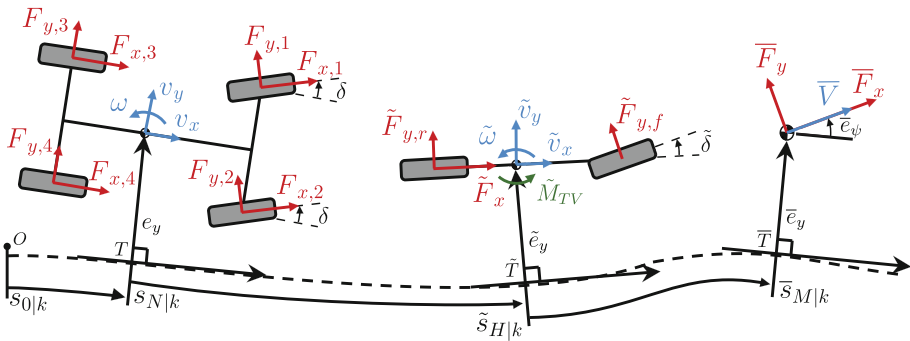


Fig. 1. Cascaded vehicle model horizon, consisting of a two-track model, single-track model, and a point-mass model.

in [5], these control objectives do not necessarily have a constant level of relevance or criticality throughout the prediction horizon. Therefore, the principle of cascaded vehicle models in a single planning horizon is introduced.

2.1 Vehicle Models

At first, a high-fidelity model is required to perform motion control. Therefore, we adopt a two-track model for the first part of the planning horizon to include TV in the NMPC, then extend the horizon with a single-track model. The two-track and single-track models, as depicted in Fig. 1, are characterized by the same states, namely; $v_{x,i|k}$, $v_{y,i|k}$, and $\omega_{i|k}$ represent the longitudinal, lateral, and yaw velocity, respectively, $\delta_{i|k}$ the steering angle, $e_{y,i|k}$ and $e_{\psi,i|k}$ represent the lateral and heading difference between the vehicle and the reference path, and $s_{i|k}$ the curvilinear coordinate along the reference path. We obtain the following two state-vectors $x_{i|k} = [v_{x,i|k}, v_{y,i|k}, \omega_{i|k}, \delta_{i|k}, e_{y,i|k}, e_{\psi,i|k}, s_{i|k}]^\top$, and $\tilde{x} = [\tilde{v}_{x,z|k}, \tilde{v}_{y,z|k}, \tilde{\omega}_{z|k}, \tilde{\delta}_{z|k}, \tilde{e}_{y,z|k}, \tilde{e}_{\psi,z|k}, \tilde{s}_{z|k}]^\top$, for the two-track and single-track model, respectively. Here $i \in \{0, 1, \dots, N\}$ and $z \in \{0, 1, \dots, H\}$ represent the prediction steps at iteration k with horizon length N and H .

The difference in the vehicle models is the required number of inputs, namely, the two-track model utilizes the four in-wheel motors by modeling the four longitudinal tire forces $F_{x,a,i|k}$, $a \in \{1, 2, 3, 4\}$, whereas the single track model only considers the total longitudinal force input $\tilde{F}_{x,z|k}$. To enhance TV, a TV moment $\tilde{M}_{TV,z|k}$ is considered an input in the single-track model. At last, the steering rates $\dot{\delta}_{in,i|k}$, and $\dot{\delta}_{in,z|k}$ are considered input.

Secondly, a low-fidelity model is used for path planning, namely a planar point-mass model as depicted in Fig. 1. Here $\bar{V}_{j|k}$ denotes the resulting velocity, $\bar{e}_{y,j|k}$ and $\bar{e}_{\psi,j|k}$ the lateral distance to the path and the heading difference between the velocity vector and the reference path, respectively, and $\bar{s}_{j|k}$ is the curvilinear coordinate along the reference path. We obtain the state vector $\bar{x} = [\bar{V}_{j|k}, \bar{e}_{y,j|k}, \bar{e}_{\psi,j|k}, \bar{s}_{j|k}]$, where $j \in \{0, 1, \dots, M\}$ represent the prediction steps, with horizon length M . As the point-mass model does not require a tire model, the total longitudinal force $\bar{F}_{x,j|k}$ and total lateral force $\bar{F}_{y,j|k}$ are considered inputs. Due to the low-dimensional model, excluding stiff dynamics, a larger look-ahead distance is obtained at a low computational cost.

The presented vehicle models combined form the cascaded vehicle model with horizon length $N + H + M$. Due to space restrictions, the reader is referred to [7, Section 2] for the corresponding dynamic models.

2.2 Mapping

The first step in serially cascading different vehicle models is carefully defining a mapping where the final state of one vehicle model propagates towards the initial state of the following vehicle model. Since the same states describe the two-track model and the single-track model, the two-track states at prediction

N define the initial state of the single-track model for $z = 0$, yielding

$$\tilde{v}_{x,0|k} = v_{x,N|k}, \quad \tilde{v}_{y,0|k} = v_{y,N|k}, \quad \tilde{\omega}_{0|k} = \omega_{N|k}, \quad \tilde{\delta}_{0|k} = \delta_{N|k} \quad (1a)$$

$$\tilde{e}_{y,0|k} = e_{y,N|k}, \quad \tilde{e}_{\psi,0|k} = e_{\psi,N|k}, \quad \tilde{s}_{0|k} = s_{N|k}. \quad (1b)$$

The mapping between the single track and point-mass model is defined differently, as the point-mass does not consider yaw dynamics and only a single velocity vector, and is adopted from [5]

$$\bar{V}_{0,k} = \sqrt{\tilde{v}_{x,H|k}^2 + \tilde{v}_{y,H|k}^2}, \quad \bar{e}_{y,0|k} = \tilde{e}_{y,H|k}, \quad (2a)$$

$$\bar{e}_{\psi,0|k} = \arctan\left(\frac{\tilde{v}_{y,H|k}}{\tilde{v}_{x,H|k}}\right) + \tilde{e}_{\psi,H|k}, \quad \bar{s}_{0|k} = \tilde{s}_{H|k}. \quad (2b)$$

Combining the mappings (1) and (2) with the corresponding dynamics provides the cascaded vehicle model, which can be used to predict the vehicle behavior.

3 Optimization Problem

The optimization problem formulation used in this manuscript is an extension of the work presented in [5], but then applied to a four-wheel drive vehicle. Therefore, due to the extensive expressions, only the changes and newly introduced objectives and constraints are discussed in this section. For the overall problem, the reader is referred to [7, Section 4.2].

3.1 Objective

The goal of the NMPC is to minimize the objective function,

$$\min_{X_k, U_k} \bar{t}_M + J_M + J_U + J_{\Delta U} + J_e + J_\alpha + J_\beta + J_{tr}, \quad (3)$$

which is the sum of seven different terms. At first, the primary objective is to minimize the lap time, hence minimizing the required time for the point-mass to reach the end of the planning horizon, denoted by \bar{t}_M . The cost J_M denotes the terminal cost, which controls the horizon to a safe terminal set. In path planning, the velocity, and lateral and heading deviation from the reference path define the safe terminal set and are penalized as such

$$J_M = W_{\bar{e}_y, M} \bar{e}_{y, M|k}^2 + W_{\bar{e}_\psi, M} \bar{e}_{\psi, M|k}^2 + W_{\bar{V}_M} \bar{V}_{M|k}^2, \quad (4a)$$

$$W_{\bar{V}_M} = \begin{cases} W_{\bar{V}_M}, & \text{if } \bar{V}_{M|k} \geq \bar{V}_{\text{safe}}, \\ 0, & \text{otherwise,} \end{cases} \quad (4b)$$

where $W_{\bar{e}_y, M}$ and $W_{\bar{e}_\psi, M}$ are static weights, and $W_{\bar{V}_M}$ is a dynamic weight only to penalize the horizon velocity when it exceeds a velocity that could result in road departure. In Formula Student, the track layout is unknown, however, the

smallest radius is defined beforehand. Therefore, a safe horizon velocity can be defined assuming steady-state cornering and using the tire characteristics

$$\bar{V}_{\text{safe}} = \sqrt{\frac{D_y R}{m}}, \quad (5)$$

with D_y the tire force peak factor according to a simplified Pacejka tire model [8] and R denotes the track radius. This cost forces the NMPC to slow down such that enough lateral grip is available to make the smallest turn.

In (3), J_U and $J_{\Delta U}$ represent a penalty on the input and change in input, respectively, J_e penalizes the lateral and heading deviations of the vehicle models. Furthermore, J_α and J_β represent a penalty on the tire slip and vehicle side slip angles. The former is already introduced in [5] to prevent excessive tire slip, whereas the latter is newly introduced. As the NMPC pushes the vehicle towards the limits, there is a chance the vehicle will start drifting. Since this is at the vehicle handling limit, any model mismatch can result in vehicle instability. Therefore, a penalty on excessive vehicle side slip angle β is applied at the point where gripping can not be guaranteed, yielding

$$J_\beta = W_{\beta_0} \sum_{i=0}^N \begin{cases} (|\beta_{i|k}| - \beta_{\max})^2, & \text{if } |\beta_{i|k}| \geq \beta_{\max} \\ 0, & \text{otherwise.} \end{cases} \quad (6)$$

$$+ W_{\beta_0} \sum_{z=0}^H \begin{cases} (|\tilde{\beta}_{z|k}| - \beta_{\max})^2, & \text{if } |\tilde{\beta}_{z|k}| \geq \beta_{\max} \\ 0, & \text{otherwise.} \end{cases},$$

where β_{\max} depends on many non-linear terms and usually is hard to predict, but the results in [9] indicate that it is between 5° and 7.5° .

Lastly, J_{tr} penalizes a non-smooth longitudinal and lateral forces transition, where $J_{tr} = J_{F|\bar{F}} + J_{\bar{F}|\bar{F}}$, $J_{F|\bar{F}}$ is the penalty on the transition between the two-track and single-track vehicle model, and $J_{\bar{F}|\bar{F}}$ the penalty on the transition between the single-track and point-mass model [7, Equation 4.28].

3.2 Constraints

The newly introduced TV moment \tilde{M}_{TV} should not exceed the maximum moment a two-track model can generate. Therefore, it is constrained by the resulting moment when all four wheels use their longitudinal peak force $D_{x,a}$, $a \in \{1, 2, 3, 4\}$ to rotate the vehicle, resulting in

$$|\tilde{M}_{TV}| \leq \frac{w_f}{2}(D_{x,1} + D_{x,2}) + \frac{w_r}{2}(D_{x,3} + D_{x,4}). \quad (7)$$

The two-track and single-track vehicle models use a simplified Pacejka tire model for the lateral tire forces and consider the longitudinal tire force as input. The tire friction ellipse is applied as a constraint to couple the lateral and longitudinal tire forces. Since the single-track model only considers a single longitudinal force, the distribution between the front and rear axles has to be defined. The grip of the axle scales with the vertical load acting on the axle, therefore, a fixed

longitudinal force distribution between the front and rear axle is defined by the weight distribution w_{dis} , providing the following constraints

$$\left(\frac{w_{\text{dis}}\bar{F}_x}{D_{x,f}}\right)^2 + \left(\frac{\bar{F}_{y,f}}{D_{y,f}}\right)^2 \leq 1, \quad \left(\frac{(1-w_{\text{dis}})\bar{F}_x}{D_{x,r}}\right)^2 + \left(\frac{\bar{F}_{y,r}}{D_{y,r}}\right)^2 \leq 1, \quad (8a)$$

$$\left(\frac{F_{x,a}}{D_{x,a}}\right)^2 + \left(\frac{F_{y,a}}{D_{y,a}}\right)^2 \leq 1, \quad \forall a \in \{1, 2, 3, 4\}. \quad (8b)$$

The point-mass force inputs \bar{F}_x and \bar{F}_y are also constrained via the friction ellipse, as described in [7, Equation 4.49]. The following section illustrates the advantages of a cascaded horizon via a simulation study.

4 Results

The influence of the cascaded vehicle model is evaluated through a simulation study comparing different horizon lengths. As baselines, the presented optimization problem is executed using a two-track and single-track model. The track layout, vehicle specifications, and cost weights are adopted from [7, Chapter 5].

In the left figure in Fig. 2, the lap times are compared with the average computation time of one iteration. Results from the single-track and two-track models are depicted in black and magenta, respectively. These results show the benefits of using TV, as the two-track model outperforms the single-track model by several seconds for every horizon length. However, the baselines also show a rapid increase in average computation time for longer prediction horizons.

It can be observed that the cascaded vehicle model not only improves lap time but also significantly reduces the average computation time. The point-mass model's non-stiff dynamics allow for a larger discretization step, which increases the look-ahead distance. Comparing the two-track model (with $N = 130$) to the cascaded vehicle model (with $N = 10$, $H = 10$, $M = 30$), both achieve a lap time of 22.8 s. However, the average computation time is reduced from 3.24 s to 0.46 s, marking an 86% reduction.

The GG-diagram in Fig. 2 shows that the use of TV results in faster cornering, evident from the increased lateral acceleration. The cascaded vehicle models obtain similar performance in terms of g-forces as the two-track baseline. Additionally, the single-track model does not push the vehicle to its full limits, as it underperforms in terms of g-forces.

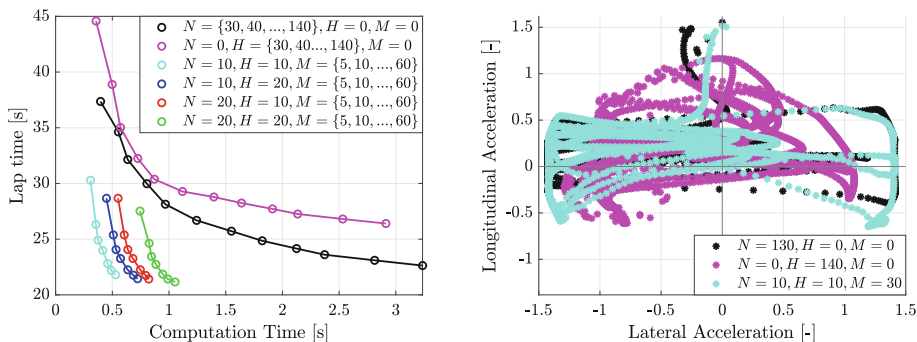


Fig. 2. Left) Computation time vs lap time. Right) GG-diagram.

5 Conclusion

A popular method to find the optimal control input to drive at the limits of the car is nonlinear model predictive control (NMPC). However, when NMPC is used, often a trade-off has to be made between performance, accuracy, and computational complexity. The results in this manuscript highlight the computational benefit that can be obtained by utilizing a cascaded vehicle model, reducing the trade-off between computational complexity and performance.

References

1. Vázquez, J., et al.: Optimization-based hierarchical motion planning for autonomous racing. In: International Conference on Intelligent Robots and Systems (IROS) (2020)
2. Srinivasan, S., et al.: Holistic motion planning and control solution to challenge a professional racecar driver. *IEEE Robot. Autom. Lett.* **6**, 7854 (2021)
3. Alcalá, E., et al.: Autonomous racing using linear parameter varying-model predictive control (LPV-MPC). *Control Eng. Pract.* **95**, 104270 (2020)
4. Alcalá, E., et al.: LPV-MP planning for autonomous racing vehicles considering obstacles. *Robot. Auton. Syst.* **124**, 103392 (2020)
5. Laurence, V., et al.: Long-horizon vehicle motion planning and control through serially cascaded model complexity. *IEEE Trans. Control Syst. Technol.* **30**, 166 (2022)
6. University Racing Eindhoven Homepage. <https://www.universityracing.nl/>. Accessed 17 Jan 2024
7. Huisman M., Lefeber E.: Online Motion Planning for All-Wheel Drive Autonomous Race Cars. <https://pure.tue.nl/ws/portalfiles/portal/251220895/0971152T>. Accessed 10 May 2024
8. Pacejka, H., Besselink, I.: *Tire and Vehicle Dynamics*. Elsevier BH, Amsterdam (2012)
9. Voser C., et al.: *Analysis and Control of High Sideslip Manoeuvres*. *Vehicle System Dynamics*, vol. 48 (2010)

Open Access This chapter is licensed under the terms of the Creative Commons Attribution 4.0 International License (<http://creativecommons.org/licenses/by/4.0/>), which permits use, sharing, adaptation, distribution and reproduction in any medium or format, as long as you give appropriate credit to the original author(s) and the source, provide a link to the Creative Commons license and indicate if changes were made.

The images or other third party material in this chapter are included in the chapter's Creative Commons license, unless indicated otherwise in a credit line to the material. If material is not included in the chapter's Creative Commons license and your intended use is not permitted by statutory regulation or exceeds the permitted use, you will need to obtain permission directly from the copyright holder.





A Data-Driven Framework for Tire Force Estimation of Distributed Electric-Drive Vehicles

Rujun Yan, Kun Jiang^(✉), Bowei Zhang, Jinyu Miao, and Diange Yang

School of Vehicle and Mobility, Tsinghua University, Beijing 100084, China
{yanrj20,zbw21,miaojy22}@mails.tsinghua.edu.cn,
{jiangkun,ydg}@mail.tsinghua.edu.cn

Abstract. In recent years, with the development of wheel-side motors and hub motors, distributed electric drive vehicles, gradually enter the electric vehicle market. Tire force are often derived from rule-based model in the past. However, distributed electric drive vehicles have a higher degree of freedom put forward new control requirements. This puts forward higher requirements for the accuracy of the tire force model. Rule-based model cannot meet the requirements quite well. Because of this, our study established a tire force residual correction framework for distributed electric drive vehicles. The framework consists of a neural network model (MLP, MLP-seq, and MLP-mixer) and a physical rule-based model. The framework was proved in the study to output a more accurate force estimation which will help dynamic modeling and control tasks.

Keywords: distributed electric drive vehicles · tire force estimation · neural network · residual correction framework

1 Introduction

With the development of electric motor technology, the power density of electric motors has increased sharply. This helps develop a new form of power drive vehicles: distributed-drive. Distributed electric drive vehicles have a high degree of freedom in control and a high complexity in the physical modeling of the vehicle.

Vehicle state estimation, a technique for inferring the dynamic state of a vehicle from sensor data and mathematical models, provides accurate information about the vehicle state, such as vehicle position and tire force [3]. The state estimation is the foundation of the vehicle control, which directly affects the accuracy of the downstream control tasks.

Most of the tire force state estimation methods that have been studied are based on physical rule models [4]. Under the trend of increasing control complexity and more complicated feasible working conditions in distributed electric drive vehicles, the accuracy of these traditional models seems limited [7]. Therefore, establishing a more accurate model for estimating the vehicle tire force state

is the starting point of this study. As the requirements for autonomous driving tasks become more complex, the limited capabilities of traditional rule models are being recognized by the industry. The attempts to use neural networks have started to increase gradually these years.

Some researchers employed a neural network for the modeling problem completely [5]. In 2019, an article published in *Science Robotics* used a pure neural network to achieve lateral trajectory tracking control of vehicles [8]. The other researchers did not abandon the original physical rule model. They combined the neural network model and rule-based model [1,6]. This kind of modeling idea is a kind of affirmation of the information processing and output ability of the rule model. It will reduce the training difficulty of the neural network model theoretically.

Some articles present a theory of building neural networks which incorporates Lagrange’s theorem [2,6]. A 2023 study used these ideas by proposing a neural network DNN. Combined with the tire magic formula, the DNN network was trained to estimate the parameters in the magic formula. After that, the tire force can be calculated [1].

The contributions of our study are as follows:

1) We proposed a combination of the two to build a tire force residual correction framework (TF-RCF) to improve the accuracy of vehicle tire force estimation.

2) In TF-RCF, we built the magic formula tire force model to have an initial estimation. The study used three neural networks, MLP, MLP-seq and MLP-mixer, to fit the residuals between the rule-based model outputs and the actual observations.

3) We tested the accuracy and the generalization ability of the TF-RCF. Results showed that the mean error is reduced from 134.9N to 21.2N. Meanwhile, the neural network had a good performance on the validation datasets.

2 Tire Force Residual Correct Framework

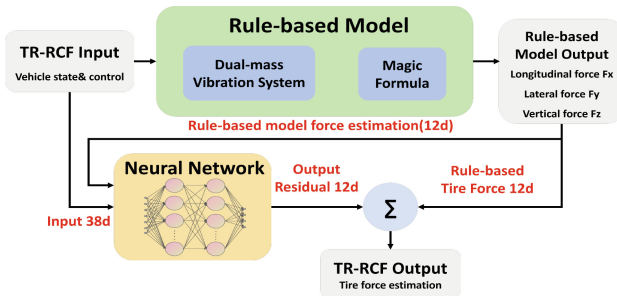


Fig. 1. Tire Force-Residual Correction Framework (TF-RCF)

2.1 Tire Force Residual Correction Framework (TF-RCF)

Our study built a residual correct framework for tire force estimation. As shown in Fig. 1, the framework is constructed mainly by a rule-based tire force model and a neural network model. The rule-based model consists of a dual-mass vibration system with a magic formula. The neural network is based on the MLP, MLP-seq and MLP-mixer model. We trained the neural network to learn the residual between the real forces (derived from Carsim) and the rule-based model output forces. Finally the trained neural network can output the residual to correct the rule-based output.

In the TF-RCF, we added the 12-dimensional tire force information output from the rule-based model as the neural network model input. The experiment shows that this can reduce the training difficulty of the neural network and improve the residual estimation accuracy of the neural network.

2.2 Tire Force Model Based on Magic Formula

H.B. Pacejke tire model (magic formula) [4], is based on a large number of data summarized by the empirical tire model. Because only a uniform set of formulas is needed for the expression of tire forces, the magic formula has been adopted by a large number of tire manufacturers.

The general expression for the tire magic formula is¹:

$$Y_x = D - \sin[C - \arctan(B - x - E(B - x - \arctan(B - x)))] \quad (1)$$

Y_x denotes the lateral force, longitudinal force, or backward correcting moment of the tire. The independent variable x is the lateral deflection angle or the longitudinal slip rate of the tire, respectively.

Our study used the two-mass vibration system for the wheels' vertical loads. The vertical motion of the body, tire and ground are represented by z , z_t and z_r . They satisfy the following differential equation:

$$m\ddot{z}_t = k_t(z_r - z_t) + k(z - z_t) + c(\dot{z} - \dot{z}_t) \quad (2)$$

2.3 Neural Network Model Based on MLP, MLP-seq and MLP-Mixer

MLP, MLP-seq and MLP-mixer are used as the neural network model [9, 10]. The detailed structure information of networks that used in the experiments is as follows: Input dimension: 26 and 38 (2 types). Output dimension: 12. Hidden dimensions: 1024. Hidden layers: 4. Sequence length: 3. MLP-mixer channels: 128. MLP-mixer layers: 4. The neural network was trained in Pytorch 1.12.1 and miniconda3. We used two loss functions: MAE (Mean Average Error) and variable weighted multi-task loss function. Adam is the optimizer. The learning

¹ The coefficients B, C, D are related to the vertical load and camber of the tire.

rates for the weights of network and multitask loss are 1e-3 and 1e-5, respectively. The training batch size is 4 and the maximum epoch is 256.

$$Multitaskloss = \sum_{i=1}^4 \sum_{j=x,y,z} \exp(-w_{i,j}) \cdot |\delta_{Fi,j} - \delta_{\hat{F}i,j}| + w_{i,j} \quad (3)$$

3 Experiments and Results

3.1 Experiment Setup

Our study used two methods to obtain data²:

- 1) Specific working conditions 1~6 (30000 sets): Design corresponding control sequences for different working conditions. These specific conditions are selected for the distributed electric drive vehicles, such as front and rear wheels rotating in the same direction and opposite directions.
- 2) Randomized control conditions 1~5 (21000 sets): Input random control sequences to the simulated vehicle. Our study set the random seed of the Gaussian random module for torque and angle control. The maximum frequency of the random control is 3Hz. In order to keep the vehicle stable, we set the front and rear wheels rotating in opposite direction.

We used two ways to divide the acquired data into training and validation datasets:

- 1) For data $[t, t - \Delta t, t - 2\Delta t]$, data $[t - \Delta t, t - 2\Delta t]$ is divided into the training set and the rest is divided into the validation set. The ratio of training and validation data is 2:1.
- 2) Classify the first 70% of the condition data as the training set and the last 30% as the validation set.

3.2 Performance Without Rule-Based Forces as Input

MLP, MLP-Seq and MLP-Mixer Performance. The mean loss value of the original Condition 1 data is 289.10 N. The best validation loss value for MLP (256 epochs), MLP-seq (256 epochs), MLP-mixer (128 epochs) is 3.3 N, 3.8 N, 1.3 N. The accuracy of the tire force prediction is significantly improved. Also, we found that network's performance for XYZ forces is different, which indicates the importance of using the variable weighted loss function.

We also obtained the original data of the carsim output. The network was also used to directly fit the original tire data. And the result show that the network trained with the residual dataset has better correction results than the original data in most cases. More specific results are shown in Table 1. In the Table 1, R means residual data and O means original data.

² Co-simulation of Carsim2020.0 and MATLAB2023b/Simulink

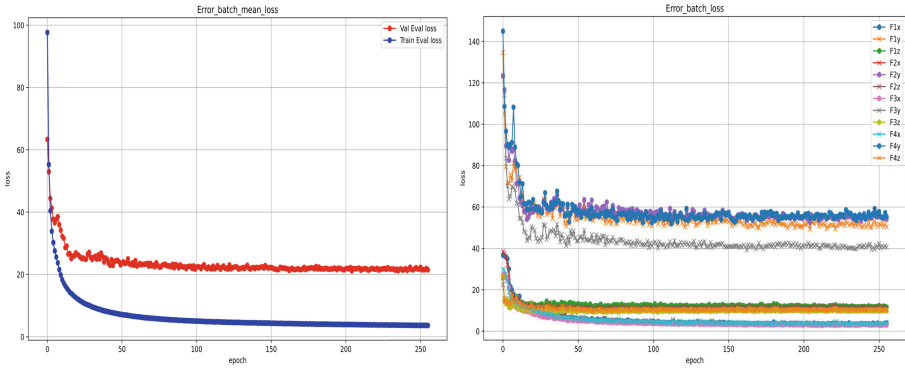
Performance with Rule-Based Forces as Input. During the experiments, we found that the MLP-mixer network is significantly overfitted in data of condition 1. To solve the overfitting problem of the network, we added the rule-based model output to the input of the neural network. Adding the rule forces to the network reduces the learning pressure of the network and the network’s difficulty in extracting the input information.

Our study set five comparison experiments for condition 1~5 (MLP-mixer): 1). 12d rule force+18d state+8d control, BAE: 4.3N 2). 12d rule force+8d control, BAE: 5.4N 3). 12d rule force+18d state, BAE: 7.2N 4). 12d rule force, BAE: 5.3N 5). 18d state+8d control, overfit. Results show that the neural network perform better after adding the rule force. There is no overfitting any more. Meanwhile, the comparison experiments further illustrate that the addition of rule forces as network inputs is responsible for the increase in the accuracy of the neural network.

Generalization Ability. Our study tested the generalization ability of network by random control data. Each the working condition data was divided into training and validation sets according to the first 70% and the last 30%. The sequence length was adjusted to 10. We applied the MLP-mixer network (38d). A dropout layer was also added to strengthen network’s stability. The dropout value is 0.3. Fig. 2a and 2b show the training and validation results of the network for random working conditions 1 to 5. The mean value of the original residual force in the validation set is 134.9N and the best MAE on the validation set is 21.2N. Due to the random control, the validation datasets are totally unseen for the network. The result can show a good generalization ability of the network.

Table 1. Detailed results for vehicle condition 1

Best Loss	F1x	F1y	F1z	F2x	F2y	F2z	F3x	F3y	F3z	F4x	F4y	F4z	mean
MLP (1-frame) R-256	0.807	4.127	5.068	0.436	3.965	4.186	0.763	4.672	5.499	0.683	5.304	4.931	3.3702
MLP-seq (3-frame) R-128	0.604	4.563	7.488	0.468	4.594	5.686	0.720	5.377	8.080	0.685	6.052	8.404	4.3933
MLP-seq (3-frame) O-128	7.283	23.629	14.12	9.802	33.28	7.853	7.993	19.999	9.596	9.726	24.31	8.041	14.6358
MLP-seq (3-frame) R-256	0.570	4.566	5.347	0.783	5.369	4.935	1.081	4.979	6.46	0.623	5.138	5.267	3.7598
MLP-mixer (3-frame) R-64	0.271	3.556	2.911	0.212	2.788	2.725	0.185	4.346	4.093	0.263	3.608	5.144	2.5086
MLP-mixer (3-frame) O-64	0.896	11.97	3.835	0.893	7.716	4.266	0.309	6.416	3.273	0.775	4.665	4.464	4.1236
MLP-mixer (3-frame) R-128	0.106	1.094	2.013	0.123	1.156	1.782	0.179	1.531	3.373	0.082	1.495	2.710	1.3036



(a) Random Control Condition 12345 70% train - 30% validate (Mean loss) (b) Random Control Condition 12345 70% train - 30% validate (Details)

Fig. 2. MLP-mixer Performance in Random Control Conditions

4 Conclusions

The study proposes a tire force residual correction framework (TF-RCF) consisting of a neural network model and a magic formula rule force model. The accurate tire force estimation can be used to build a more accurate dynamic model, which helps improve the accuracy in vehicle control scenarios. Our study has shortcomings: We haven't obtain real vehicle tire force data at present. So we lack strong evidence to prove the TF-RCF can fit the data from the real car. This is a continuing direction for our study. In the acquisition of datasets, the specific working conditions and random control conditions set by our study still lack some systemic and rationality. In the future, we will improve the network architecture and obtain datasets in a quicker and more reasonable way.

References

1. Chrosniak, J., Ning, J., Behl, M.: Deep Dynamics: Vehicle Dynamics Modeling with a Physics-Informed Neural Network for Autonomous Racing (2023). arXiv preprint [arXiv:2312.04374](https://arxiv.org/abs/2312.04374)
2. Cranmer, M., Greydanus, S., Hoyer, S., Battaglia, P., Spergel, D., Ho, S.: Lagrangian Neural Networks (2020). arXiv preprint [arXiv:2003.04630](https://arxiv.org/abs/2003.04630)
3. Guo, H., Cao, D., Chen, H., Lv, C., Wang, H., Yang, S.: Vehicle dynamic state estimation: state of the art schemes and perspectives. *IEEE/CAA J. Autom. Sin.* **5**(2), 418–431 (2018)
4. Pacejka, H.B., Bakker, E.: The magic formula tyre model. *Veh. Syst. Dyn.* **21**(S1), 1–18 (1992)
5. Punjani, A., Abbeel, P.: Deep learning helicopter dynamics models. In: 2015 IEEE International Conference on Robotics and Automation (ICRA), pp. 3223–3230. IEEE (2015)

6. Roehrl, M.A., Runkler, T.A., Brandstetter, V., Tokic, M., Obermayer, S.: Modeling system dynamics with physics-informed neural networks based on Lagrangian mechanics. *IFAC-PapersOnLine* **53**(2), 9195–9200 (2020)
7. Shim, T., Ghike, C.: Understanding the limitations of different vehicle models for roll dynamics studies. *Veh. Syst. Dyn.* **45**(3), 191–216 (2007)
8. Spielberg, N.A., Brown, M., Kapania, N.R., Kegelman, J.C., Gerdes, J.C.: Neural network vehicle models for high-performance automated driving. *Sci. Robot.* **4**(28), eaaw1975 (2019)
9. Taud, H., Mas, J.F.: Multilayer perceptron (MLP). IN: *Geomatic Approaches for Modeling Land Change Scenarios*, pp. 451–455 (2018)
10. Tolstikhin, I., Hounsby, N., Kolesnikov, A., Beyer, L., Zhai, X., Unterthiner, T., Yung, J., Steiner, A., Keysers, D., Uszkoreit, J., Heigold, G., Minderer, M., Dosovitskiy, A., Hounsby, N.: MLP-Mixer: An All-MLP Architecture for Vision (2021). arXiv preprint [arXiv:2105.01601](https://arxiv.org/abs/2105.01601)

Open Access This chapter is licensed under the terms of the Creative Commons Attribution 4.0 International License (<http://creativecommons.org/licenses/by/4.0/>), which permits use, sharing, adaptation, distribution and reproduction in any medium or format, as long as you give appropriate credit to the original author(s) and the source, provide a link to the Creative Commons license and indicate if changes were made.

The images or other third party material in this chapter are included in the chapter's Creative Commons license, unless indicated otherwise in a credit line to the material. If material is not included in the chapter's Creative Commons license and your intended use is not permitted by statutory regulation or exceeds the permitted use, you will need to obtain permission directly from the copyright holder.





Influence of the Front-Rear Torque Distribution on the Handling Characteristics and Stability Boundaries of an AWD-Vehicle

Manuel Eberhart¹(✉), Martin Arndt², Johannes Edelmann¹,
and Manfred Plöchl¹

¹ TU Wien, Institute of Mechanics and Mechatronics, Vienna, Austria

manuel.eberhart@tuwien.ac.at

² CARIAD SE, Vehicle Motion Energy, Wolfsburg, Germany

martin.arndt@cariad.technology

<https://www.mec.tuwien.ac.at/vsd>, <https://www.cariad.technology>

Abstract. The influence of the drive torque distribution of an AWD vehicle with individual motors at the front and rear axles on the handling and stability properties is investigated. By applying bifurcation analysis methods, different types of loss of stability at combined longitudinal and lateral acceleration are identified. The impact of the drive torque distribution on the stability boundaries in the GG diagram is examined, and the related stable acceleration envelope is compared to the envelope derived from applying optimisation methods. Representative corresponding handling characteristics are compared and discussed.

Keywords: Handling Characteristics · Stability · Bifurcation · Drive Torque Distribution · Optimisation · AWD Vehicle

1 Introduction

Drive train architectures of electric vehicles, often equipped with more than one electric motor, allow both to ‘stabilise’ and to make the vehicle’s motion ‘more responsive’ but also require a profound understanding of its influence on stability and handling to ensure safe operation. Depending on the longitudinal acceleration and drive train configuration, the handling behaviour and respective passive stability properties of the vehicle can significantly change [1, 5, 6]. To study these characteristic properties, a quasi-steady-state description is derived, where the state of a vehicle accelerated in longitudinal direction is transformed to a mechanically equivalent steady-state [1, 6].

Bifurcation analysis is frequently used to find stability boundaries [10]. In [3], Della Rossa et al. analyse the stability properties of a vehicle with different tyre configurations and demonstrate that various types of loss of stability may appear. Horiuchi et al. use a quasi-steady-state description to model transient states to investigate the loss of stability for a longitudinally accelerated vehicle

with fixed drive torque distribution in [5]. Lenzo et al. analyse the handling characteristics for different drive concepts and present the relation between yaw torque and understeer coefficient [7].

This paper investigates the impact of the drive torque distribution of an AWD vehicle with individual motors at the front and rear axles on the transient handling and stability properties. The vehicle state is transformed to a mechanically equivalent quasi-steady-state to apply linear stability theory and to utilise bifurcation and continuation algorithms. For various drive torque distributions, different types of bifurcations are found and discussed. The stable acceleration envelope is compared to the solution found by optimisation, and differences are discussed.

The paper is structured as follows: In the next Section, the vehicle and tyre models are addressed. In Sect. 3, the applied methods are briefly described. In the following Sect. 4, the impact of the longitudinal acceleration on the handling characteristics is shown. The stability boundary found with the bifurcation method is presented in the GG diagram and compared to the optimised acceleration envelope in Sect. 5.

2 Vehicle Model

A nonlinear four-wheel vehicle model with 10 degrees of freedom, as introduced and described in [4] and illustrated in Fig. 1, is considered in this study. The rigid vehicle body is modelled with 6 degrees of freedom, (longitudinal velocity v_{xB} , lateral velocity v_{yB} , vertical velocity v_{zB} , roll angle φ_B , pitch angle θ_B and yaw rate $\dot{\psi}_B$), and one rotational degree of freedom is considered for each wheel, ω_i ($i = 1, 2, 3, 4$). Input quantities are the drive torques at the individual wheels, $T_1 = T_2$ and $T_3 = T_4$, and the steering angle δ , where $\delta_1(\delta)$ and $\delta_2(\delta)$. The Magic Formula [9] is used to model the combined tyre force characteristics. In the subsequent figures, the vehicle states are represented in the x - y - z -coordinate frame depicted in red colour in Fig. 1.

For vehicle parameters, governing equations and tyre force characteristics, please refer to [4].

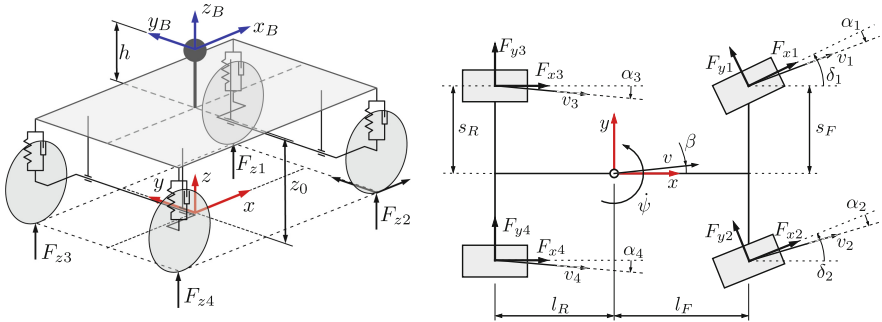


Fig. 1. Schematic illustration of the vehicle model

3 Methods

To apply continuation methods for the nonlinear stability analysis, the combined accelerated manoeuvre ($a_n \neq 0$ and $a_t \neq 0$) is transformed to a quasi-steady-state, mechanically equivalent state, which approximates the combined acceleration manoeuvre well [2, 5]. In this paper, similar to [5], an equivalent force in the direction of the velocity vector is applied at the centre of gravity of the vehicle. This system adaption considers both the load transfer and the mutual influence of the longitudinal and lateral tyre forces. Yaw acceleration $\dot{\psi}$, derivative of the vehicle sideslip angle $\dot{\beta}$, and the derivatives of the other states are set to zero to fulfil the steady-state condition.

Once equivalent equilibrium solutions are found, linear methods are applied to analyse stability properties. For that purpose, the equations of motion are linearised with respect to the equilibrium solutions, $\Delta \dot{\mathbf{x}} = \mathbf{A} \Delta \mathbf{x} + \mathbf{B} \Delta \mathbf{u}$. Lyapunov's first method implies that an equilibrium solution is stable if all eigenvalues λ_i from $(\mathbf{A} - \lambda_i \mathbf{I}) \mathbf{p}_i = \mathbf{0}$, with the right eigenvector \mathbf{p}_i , have negative real parts [10].

With the help of a path continuation algorithm [10], solution paths are found by varying parameters and inputs. A more detailed description of the used method is given in [4]. Moreover, optimisation techniques are applied to find the maximum possible acceleration envelope [8]. The result is compared to the stable acceleration envelope found with bifurcation analysis.

4 Handling Characteristics at Longitudinal Acceleration

The handling diagram for the considered vehicle with drive torque distribution $\gamma = 1$, i.e. rear-wheel-drive (RWD), and zero tangential acceleration shows understeer handling characteristics and limit understeer behaviour, see Fig. 2 (blue line). The respective vehicle configuration with $\gamma = 0$, i.e. front-wheel-drive (FWD), shows qualitatively the same characteristics and is not depicted.

Increasing the vehicle tangential acceleration, e.g. to $a_t = 4 \text{ m/s}^2$, results in a qualitative change to limit oversteer behaviour of the vehicle with $\gamma = 1$ (Fig. 2, orange line). In contrast, no qualitative change may be observed for $\gamma = 0$ (not depicted) and an all-wheel-drive (AWD) configuration with a certain portion of drive torque at the front axle (e.g. $\gamma = 0.7$, green line).

Evaluating the eigenvalues for $\gamma = 1$ at $a_t = 4 \text{ m/s}^2$ indicates a Hopf-type loss of stability (o in Fig. 2), characterised by a conjugate complex pair of eigenvalues with zero real part. For decreased parameter γ the Hopf point moves to higher normal accelerations a_n (black line) while the imaginary part of the Hopf eigenvalue λ_I decreases and finally results in two zero eigenvalues, Fig. 2 black x, called Takens–Bogdanov bifurcation. Further decrease of the drive torque distribution γ leads to limit understeer behaviour. The torque distribution at the Takens–Bogdanov point, $\gamma_{\text{TB}} \approx 0.86$ for a tangential acceleration of $a_t = 4 \text{ m/s}^2$, characterises the change from limit understeer to limit oversteer behaviour and vice versa. The Takens–Bogdanov solution for various γ and a_t is depicted in Fig. 2 (red line).

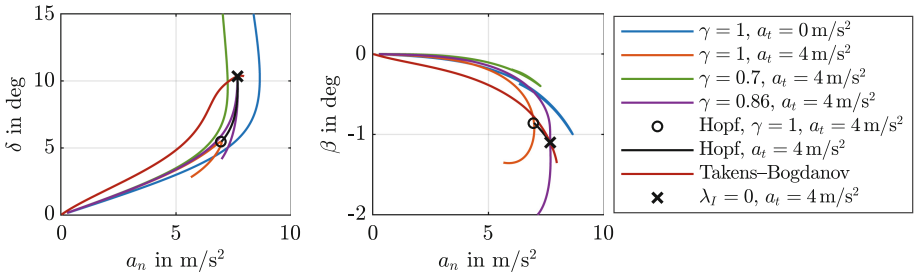


Fig. 2. Steering angle δ and vehicle sideslip angle β for different drive torque distributions γ at tangential acceleration a_t . Quasi-steady-state solutions for vehicle velocity $v = 20 \text{ m/s}^2$.

5 Takens–Bogdanov Point as Design Criteria

The corresponding a_x – a_y diagram (GG diagram) depicted in the left graph of Fig. 3 includes two coloured lines: the maximum lateral acceleration for the considered vehicle with $\gamma = 1$ (blue line) that shows limit understeer behaviour up to a longitudinal acceleration of $a_x = 2.6 \text{ m/s}^2$, followed by the Takens–Bogdanov solution for higher longitudinal accelerations (red line). In the right graph of Fig. 3 (red line), the respective torque distribution γ for the Takens–Bogdanov solution is plotted over the longitudinal acceleration a_x .

In addition, the numerically optimised GG diagram that represents the maximum acceleration envelope for the considered vehicle and the resulting optimisation parameter γ are plotted in Fig. 3 (black lines).

In the left graph, it can be seen that the solutions from bifurcation analysis and optimisation are almost equal. Nevertheless, at small longitudinal accelerations $a_x < 2.5 \text{ m/s}^2$ the maximum lateral accelerations a_y from the optimised drive torque distribution γ are slightly superior. Inspecting the respective drive torque distributions γ , right graph in Fig. 3, shows that an AWD configuration is beneficial in this regime.

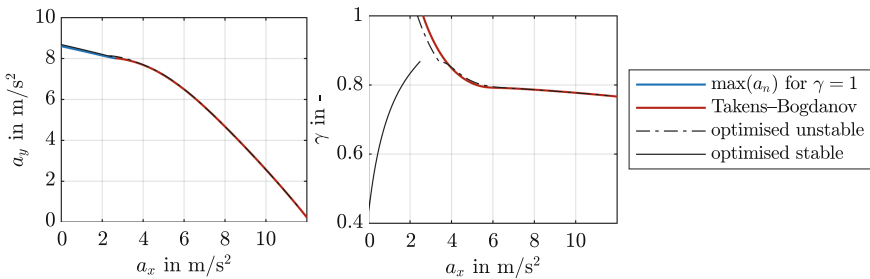


Fig. 3. Comparison of Takens–Bogdanov solution and optimised solution: Acceleration envelope a_x – a_y and drive torque distribution γ .

Considering the graph of the optimal drive torque distribution γ , at $a_x \approx 2.5$ m/s² a discontinuity can be noticed. Evaluating the stability properties of the steady-state solutions derived with the optimisation technique reveals a qualitative change from stable conditions (black solid line) to unstable conditions (black dashed-dotted line) at $a_x > 2.5$ m/s², whereas the Takens–Bogdanov solution characterises the stability boundary in the a_x – a_y -envelope. This can also be seen in Fig. 4 where handling curves for three constant tangential accelerations $a_t = 1, 3, 5$ m/s² are plotted for the respective optimal and Takens–Bogdanov quasi-steady-state solutions, and corresponding constant drive torque distributions γ_{opt} and γ_{TB} , respectively.

The handling curves for $a_t = 1$ m/s² show that the maximum normal acceleration a_n of the optimised solution is superior compared to the $\gamma = 1$ configuration. For $a_t = 3$ m/s² the optimal solution is found for $\gamma_{\text{opt}} < \gamma_{\text{TB}}$ after loss of stability (Fold bifurcation). The Fold bifurcation occurs after limit understeer behaviour and can be attributed to the saturation of the longitudinal tyre forces at the inner rear wheel ($i = 3$). The behaviour then changes to an unstable oversteer behaviour where the optimal solution is found.

At tangential acceleration $a_t = 5$ m/s² the torque distribution of the optimised solution is a little larger than the torque distribution of the Takens–Bogdanov point ($\gamma_{\text{opt}} > \gamma_{\text{TB}}$) and a slightly higher normal acceleration a_n is achieved. The optimised quasi-steady-state solution is again unstable following a Hopf bifurcation.

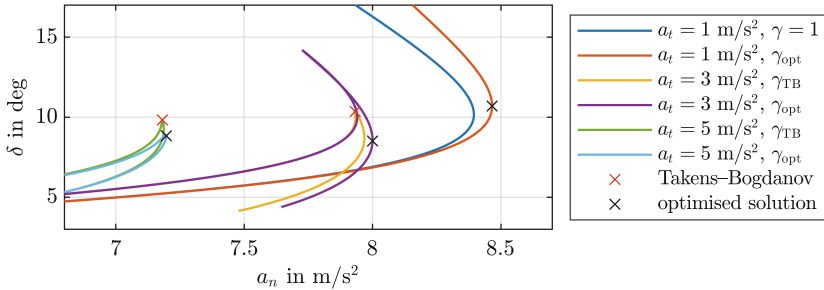


Fig. 4. Detail of handling diagram for different constant tangential accelerations a_t and drive torque distributions γ .

6 Conclusions

The transition between limit understeer and limit oversteer behaviour due to the change of the drive torque distribution at longitudinal acceleration in quasi-steady-state condition was investigated. It was shown that the Takens–Bogdanov solution characterises both the change from limit oversteer to limit understeer

behaviour and the change of the type of loss of stability from Hopf to Fold bifurcation.

A Takens–Bogdanov solution was identified by Della Rossa et al. in [3] by studying a pure lateral vehicle model with the same maximum friction potential of the tyres at the front and rear axles. In this study, it was shown that a similar behaviour may result from the mutual influence of longitudinal and lateral tyre forces at a vehicle accelerated in longitudinal direction.

The Takens–Bogdanov solution seems to be a reasonable design criterion for the drive torque distribution of an AWD vehicle since, for a given longitudinal acceleration (or an equivalent drive torque demand), almost the maximum normal acceleration may be achieved without ‘early’ limit understeer or oversteer behaviour. This may improve the vehicle’s safety and manoeuvrability during combined manoeuvres. In addition, the Takens–Bogdanov solution represents the acceleration envelope near the optimal (maximal) envelope. In contrast to the latter, which includes unstable solutions, the Takens–Bogdanov solution may be of more practical relevance, since the solutions are stable. However, potential practical implications have to be investigated thoroughly. The impact of relevant system parameters like tyre–road friction potential and different vehicle parameters have to be considered, and their influence on the shown method should be analysed.

Further investigations on the drive torque distribution to generate yaw torque to modify the handling behaviour and stability boundaries appear to be reasonable. This will be studied in more detail in a forthcoming paper.

References

1. Abe, M.: A theoretical analysis on vehicle cornering behaviors in acceleration and in braking. *Veh. Syst. Dyn.* **15**(1), 1–14 (1986). <https://doi.org/10.1080/00423118608969122>
2. De Novellis, L., Sorniotti, A., Gruber, P.: Optimal wheel torque distribution for a four-wheel-drive fully electric vehicle. *SAE Int. J. Passeng. Cars Mech. Syst.* **6**(1), 128–136 (2013). <https://doi.org/10.4271/2013-01-0673>
3. Della Rossa, F., Mastinu, G., Piccardi, C.: Bifurcation analysis of an automobile model negotiating a curve. *Veh. Syst. Dyn.* **50**(10), 1539–1562 (2012). <https://doi.org/10.1080/00423114.2012.679621>
4. Eberhart, M., Plöchl, M., Edelmann, J.: Stability boundaries and bifurcation analysis of an AWD vehicle with variable drive torque distribution. To be submitted to *Nonlinear Dynamics* (2024)
5. Horiuchi, S., Okada, K., Nohtomi, S.: Analysis of accelerating and braking stability using constrained bifurcation and continuation methods. *Veh. Syst. Dyn.* **46**(1), 585–597 (2008). <https://doi.org/10.1080/00423110802007779>
6. Klomp, M., Thomson, R.: Influence of front/rear drive force distribution on the lateral grip and understeer of all-wheel drive vehicles. *Int. J. Veh. Des.* **56**(1–4), 34–48 (2011). <https://doi.org/10.1504/IJVD.2011.043272>
7. Lenzo, B., Bucchi, F., Sorniotti, A., Frendo, F.: On the handling performance of a vehicle with different front-to-rear wheel torque distributions. *Veh. Syst. Dyn.* **57**(11), 1685–1704 (2019). <https://doi.org/10.1080/00423114.2018.1546013>

8. Massaro, M., Limebeer, D.J.N.: Minimum-lap-time optimisation and simulation. *Veh. Syst. Dyn.* **59**(7), 1069–1113 (2021). <https://doi.org/10.1080/00423114.2021.1910718>
9. Pacejka, H.: *Tire and Vehicle Dynamics*. Elsevier, Amsterdam (2005)
10. Seydel, R.: Practical bifurcation and stability analysis. In: *Interdisciplinary Applied Mathematics*, vol. 5. Springer, Cham (2009). <https://doi.org/10.1007/978-1-4419-1740-9>

Open Access This chapter is licensed under the terms of the Creative Commons Attribution 4.0 International License (<http://creativecommons.org/licenses/by/4.0/>), which permits use, sharing, adaptation, distribution and reproduction in any medium or format, as long as you give appropriate credit to the original author(s) and the source, provide a link to the Creative Commons license and indicate if changes were made.

The images or other third party material in this chapter are included in the chapter's Creative Commons license, unless indicated otherwise in a credit line to the material. If material is not included in the chapter's Creative Commons license and your intended use is not permitted by statutory regulation or exceeds the permitted use, you will need to obtain permission directly from the copyright holder.





Determination of the Loss Behavior of Wheel Bearings Under Real Driving Conditions

Lukas Hartmann^(✉), Leon Ohms, Ron Rebesberger, Gerrit Brandes,
and Roman Henze

Technische Universität Braunschweig, Institute of Automotive Engineering, Braunschweig,
Germany

l.hartmann@tu-braunschweig.de

Abstract. The characterization of component losses is typically conducted on dedicated test benches with the objective of enhancing component efficiency. Nevertheless, obtaining precise measurements of the actual loss contributions of components during real-world vehicle operations is often challenging. This challenge particularly pertains to wheel bearings, whose loss characteristics are efficiently delineated through the generation of efficiency maps on test benches at the Institute of Automotive Engineering. This submission presents a methodology for establishing these efficiency maps and introduces a developed methodology that enables the transfer of loss behavior from the component test into real-world driving conditions. Subsequently, the power losses are quantified across distinct driving domains, including *urban*, *rural*, and *highway* conditions. The outcomes of this methodology are contrasted with the losses observed on the test benches in order to identify potential avenues for reducing the losses of wheel bearings. Furthermore, the methodology is applied to homologation-relevant vehicle test benches with the objective of comparing the power losses under these conditions with real-world vehicle operations.

Keywords: Testing and Validation · Suspension · Powertrain · Energy losses

1 Introduction

1.1 Motivation

Increasingly stringent emission standards and the growing shift towards electric mobility are driving automotive manufacturers to focus on optimizing the efficiency of individual components within the powertrain. This also includes wheel bearings, crucial for supporting the rotational movement of wheels and transferring associated forces to the vehicle body. The resulting losses significantly affect the powertrain efficiency, leading to a reduction in overall efficiency [1, 2]. The presented methodology enables the determination of losses in real-world driving conditions and helps to identify deviations from homologation-relevant vehicle test benches. This is particularly important because analyzing the loss characteristics of wheel bearings in real-world vehicle operation is complex and expensive.

© The Author(s) 2024

G. Mastinu et al. (Eds.): AVEC 2024, LNME, pp. 207–213, 2024.

https://doi.org/10.1007/978-3-031-70392-8_30

1.2 Test Bench Setup

The schematic representation of the component test bench for determining friction losses of wheel bearings is depicted in Fig. 1. The bearing is mounted using two adapters within a climate chamber to maintain consistent ambient temperature conditions. An electric motor with dynamic control capabilities drives the bearing, while a load unit applies axial and radial loads. A sensor setup within the illustrated measurement unit captures the resulting friction losses of the measured bearing. Furthermore, various parameters, including ambient temperature, bearing temperature, and rotational speed, are recorded throughout the test.

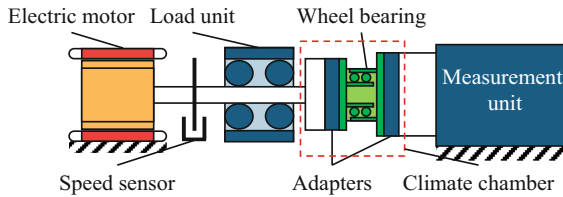


Fig. 1. Test bench setup to determine the friction losses of wheel bearings.

2 Methodology

The methodology aims to assess the losses experienced by wheel bearings under real-world driving conditions and identify deviations from homologation-relevant complete vehicle test benches. To achieve this, the methodology is divided into four distinct parts: acquiring real-world driving data, generating efficiency maps, validating the efficiency maps, and simulating and comparing the losses.

2.1 Measurement of Vehicle Data

To generate representative real-world driving data, a vehicle is equipped with measurement technology to record variables that affect friction losses, including wheel speed, ambient and bearing temperature. The static wheel loads, which influence the friction losses, are measured with wheel load scales [3, 4]. Figure 2 illustrates the measuring points using the example of the rear left wheel. The data is collected in *urban*, *rural* and *highway* environments in order to analyze diverse driving domains for identical driven bearings on the left side of an all-wheel-drive vehicle's front and rear axle.

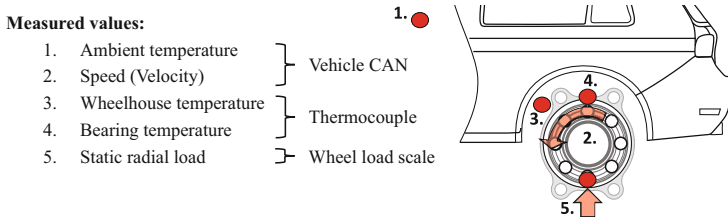


Fig. 2. Overview of the measuring positions of the test vehicle for the rear left wheel bearing.

2.2 Determination of the Efficiency Maps

The friction losses of the bearings are determined by means of measurements conducted on the friction torque test bench. A measurement cycle developed at the Institute of Automotive Engineering is employed to ascertain the losses occurring at the relevant operating points in accordance with the velocity and temperature for the front and rear left bearing of the test vehicle at different levels of radial wheel loads. The cycle effectively identifies the necessary operating points, thereby minimizing the time required for measurements. Figure 3 illustrates the efficiency maps for both bearings, which are dependent on the different applied radial wheel load levels.

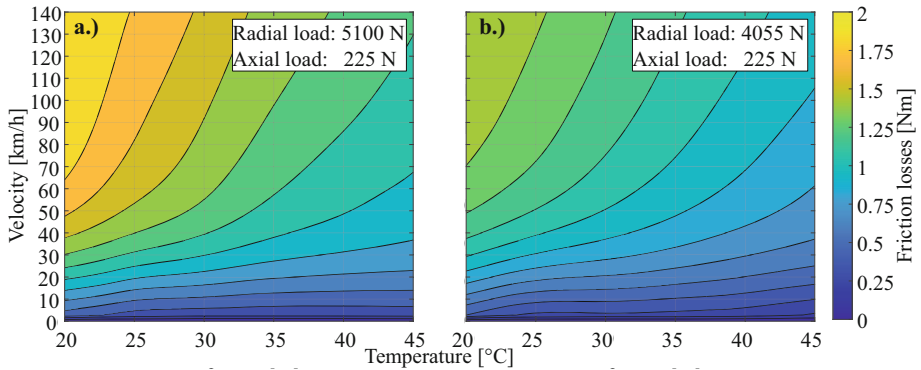


Fig. 3. Determined efficiency maps for the front left bearing a) and rear left bearing b) as a function of velocity, temperature, and radial wheel loads.

The analysis indicates that the bearings experience their most significant friction losses under conditions of low temperatures and high velocities. This is primarily due to the increased viscosity of the lubricant, which hinders the formation of a lubricating film and leads to increased friction losses, particularly at high rotational speeds. Furthermore, the material behavior at lower temperatures and the consistency of the lubricant affect the bearing rolling element’s mobility, contributing to higher losses [5, 6]. The front left bearing (Fig. 3a) also exhibits higher friction losses in comparison to the rear left bearing (Fig. 3b). This can be attributed to the higher applied radial loads during the measurements, which are a consequence of the differing levels of wheel loads of the

vehicle. To illustrate the influence of the radial load, Table 1 presents the maximum friction losses at the operating point at 20 °C and 140 km/h, as well as the arithmetic average losses over the total efficiency maps for both bearings.

Table 1. Maximum friction losses at the operating point at 20 °C and 140 km/h and the arithmetic average friction losses for the total efficiency map of the front and rear left bearing.

		Front left		Rear left	
		Maximum	Ø	Maximum	Ø
Losses	[W]	243.25	86.73	187.51	68.87
	[Nm]	1.98	1.25	1.52	0.99

The increased radial load intensifies the pressure on the contact surfaces between the rolling elements and the raceway. Furthermore, elevated loads induce elastic deformation, which alters the shape of the contact surfaces and reduces the thickness of the lubricating film. This results in an average increase in friction losses, as observed in the efficiency map of the front left bearing, which can be up to 20% depending on the lubrication, bearing geometry and sealing type [5, 6].

2.3 Validation of the Efficiency Maps

Additional measurements are performed on the friction torque test bench to verify the accuracy of the efficiency maps. During this process, the losses determined from the test bench are compared with the simulated losses. The velocity profile used for validation is based on two WLTC cycles and the measured bearing temperature, as shown in Fig. 4a. Figure 4b compares the losses measured on the test bench with those calculated for the front left bearing. Additionally, it illustrates the cumulative deviation of the friction energy between the measurement and the simulation.

The quantitative results of the friction losses determined using the efficiency map are in good agreement with the values measured on the test bench. However, a correlation analysis revealed an increasing qualitative discrepancy in losses, particularly at lower temperatures and velocities. This discrepancy arises because fewer operating points are available for modeling the efficiency maps at lower temperatures compared to higher temperatures. One reason for the reduced availability is that the bearings heat up rapidly during the efficiency map measurements at lower temperatures due to friction. Overall, the average friction losses per revolution for the complete cycle differ by 1.64%, and the cumulative deviation of the friction energy is 1.74 Wh.

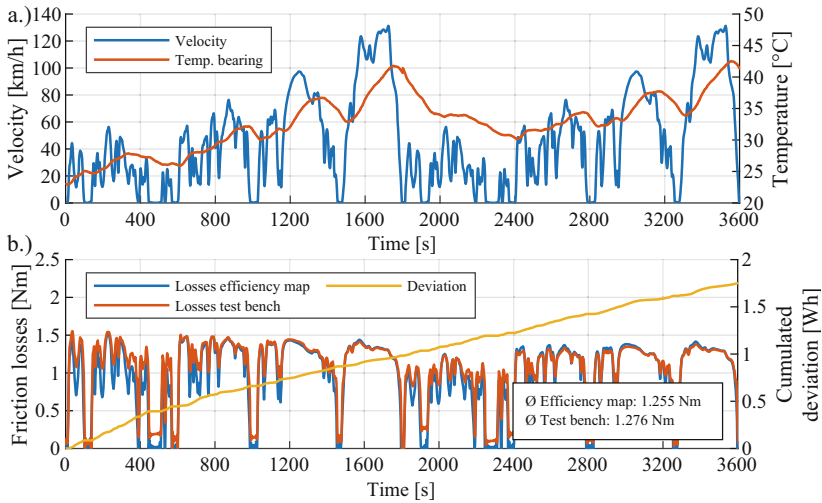


Fig. 4. Validation of the efficiency map depending on velocity and bearing temperature a) for the front left bearing with measurement on the test bench and simulating friction losses b).

2.4 Determination of the Friction Torque and Comparison

In the final step, the friction losses are simulated based on real-world driving operation data bearing temperatures and velocities, which were determined in Sect. 2.1 by using the test vehicle for *urban*, *rural*, and *highway* driving domains, to assess their contribution to drivetrain losses. Furthermore, the losses are calculated based on data recorded on a homologation-relevant vehicle dynamometer to illustrate differences between measurements on the dynamometer and real-world driving conditions. Figure 5a displays the velocity profile for real-world driving operation and dynamometer testing, bearing and wheel housing temperatures for the front left bearing for the rural driving domain. Figure 5b illustrates the friction losses simulated with the help of the recorded measurement data and using the efficiency map, to compare the conditions for real-world driving operations and dynamometer testing.

The temperature difference in the wheel housing between the data for real-world driving conditions and dynamometer testing is significant, mainly attributable to reduced airflow through the dynamometer’s air blower. This notably affects the heat convection of the bearings to the environment, especially at higher velocities. In this instance, a growing disparity in bearing temperature is evident from a time of 500 s due to this phenomenon. Consequently, the bearing experiences a greater temperature increase on the dynamometer, resulting in a reduction of friction losses. This results in a cumulative deviation of the friction energy over the *rural* cycle of 8.18 Wh. Figure 6 presents the average friction losses per revolution for all driving domains and both bearings in comparison between real-world driving and dynamometer conditions. The overview indicates that the front left bearing consistently experiences elevated friction losses across various driving domains, which is approximately 20% higher than for the rear left bearing. This is primarily attributed to the increased wheel load.

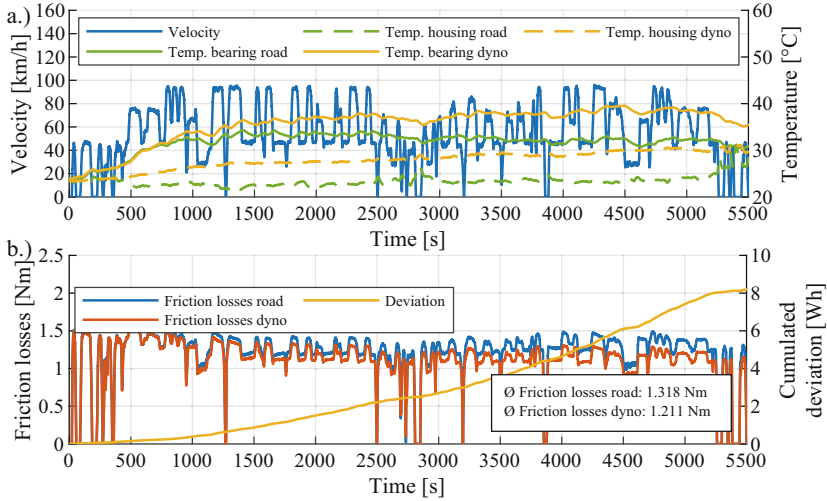


Fig. 5. Comparison of friction losses for the front left bearing b) for rural driving domain calculated with the efficiency map for real-world driving conditions and dynamometer testing a).

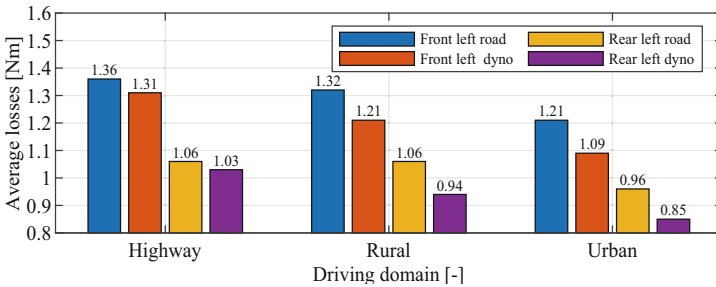


Fig. 6. Comparison of the average friction losses per revolution for the front and rear left wheel bearing between real-world driving operations and dynamometer testing data.

Furthermore, the varying friction losses resulting from declining average velocities across *highway*, *rural*, and *urban* driving domains are discernible. Additionally, discrepancies between real-world driving conditions and dynamometer testing data results are evident. In particular, real-world conditions indicates losses up to 12% higher due to improved heat dissipation from the airflow compared to the dynamometer.

3 Conclusion

The results presented in this study demonstrate the friction losses associated with the wheel bearings in the drivetrain across various driving domains and influencing parameters. They also illustrate the discrepancies between real-world driving operations and dynamometer testing due to varying temperature conditions, which can present challenges in conducting real driving emissions cycle measurements. Furthermore, analyzing

the differences in wheel loads between real-world driving operations and dynamometer testing in the future would be beneficial for further investigating these variances. This approach can be applied to other components, allowing for the evaluation of component behavior in real-world vehicle operations.

References

1. Küçükay, F.: Grundlagen der Fahrzeugtechnik. Springer, Wiesbaden (2022)
2. Brähler, S., Preiß, H.: Optimierung der gesamtreibung in einem radlager der 3. Generation. In: Experten-Forum Powertrain: Reibung in Antrieb und Fahrzeug 2020. Springer, Wiesbaden (2020)
3. Jurkschat, T., Otto, M., Lohner, T., Stahl, K.: Bestimmung des verlustverhaltens und der wärmebilanz von wälzlagern. Forsch. Ingenieurwes. **82**, 149 (2018)
4. Wang, D.: Berechnung der Wälzlagerreibung Aufgrund Weiterentwickelter Rheologischer Fluidmodelle. Dissertation, Gottfried Wilhelm-Leibniz-Universität Hannover, Fakultät für Maschinenbau, Hannover (2015)
5. Hamrock, B., Schmid, S., Jacobson, B.: Fundamentals of Fluid Film Lubrication. Dekker, New York (2004)
6. Spura, C., Fleischer, B., Wittel, H., Jannasch, D.: Roloff/Matek Maschinenelemente. Springer, Wiesbaden (2023)

Open Access This chapter is licensed under the terms of the Creative Commons Attribution 4.0 International License (<http://creativecommons.org/licenses/by/4.0/>), which permits use, sharing, adaptation, distribution and reproduction in any medium or format, as long as you give appropriate credit to the original author(s) and the source, provide a link to the Creative Commons license and indicate if changes were made.

The images or other third party material in this chapter are included in the chapter's Creative Commons license, unless indicated otherwise in a credit line to the material. If material is not included in the chapter's Creative Commons license and your intended use is not permitted by statutory regulation or exceeds the permitted use, you will need to obtain permission directly from the copyright holder.





Prediction Based Cooperative Adaptive Cruise Control for Heterogeneous Platoons with Delays

Redmer de Haan^(✉), Tom van der Sande, and Erjen Lefeber

Eindhoven University of Technology, Eindhoven, The Netherlands
{r.d.haan,t.p.j.v.sande,a.a.j.lefeber}@tue.nl

Abstract. We present a prediction based controller for heterogeneous platoons with actuation delay. By using a prediction of the ego vehicle's acceleration and compensating the ego vehicle's influence on the error dynamics, we obtain a controller that achieves input-to-state stability (ISS) with respect to the preceding vehicle's acceleration. The result is a controller that does not require driveline information of the preceding vehicle, which enables platooning in a heterogeneous setting. An analysis is presented of the string stability properties of the system with both actuation and communication delays. The effectiveness of the controller is shown in simulation.

Keywords: Cooperative Adaptive Cruise Control · Delay · Prediction

1 Introduction

Cooperative Adaptive Cruise Control (CACC) utilizes vehicle-to-vehicle (V2V) communication and on-board sensors like a radar to maintain a desired headway to the preceding vehicle. CACC's ability to maintain short following distances while attenuating disturbances through the vehicle string (string stability) can enhance traffic flow and safety [5]. To enable adoption of the technology, the controller should be able to deal with heterogeneities in the platoon. Furthermore, actuation delays of the ego vehicle can be detrimental to the performance of controllers that are designed without taking into account this delay [2].

In this paper, we present a prediction based control approach to enable control of heterogeneous platoons where the ego vehicle experiences a delay in the driveline. We use a prediction of the (effects) of the ego vehicle's acceleration (on the error dynamics) to obtain a controller that is ISS with respect to the preceding vehicle's acceleration.

The outline of the paper is as follows. The controller design is presented in Sect. 2. An analysis of the string stability of the system, taking into account actuation and communication delays, is presented in Sect. 3. To validate the controller, simulations of a platoon employing the controller are presented in Sect. 4. Finally, the conclusions and recommendation for future research are presented in Sect. 5.

2 Controller Design

Consider a heterogeneous string of n vehicles as depicted in Fig. 1, where each vehicle's dynamics are described by

$$\begin{aligned} \dot{q}_i(t) &= v_i(t) \\ \dot{v}_i(t) &= a_i(t) \\ \dot{a}_i(t) &= -\frac{1}{\tau_i} a_i(t) + \frac{1}{\tau_i} u_i(t - \phi_i). \end{aligned} \quad i = 1, 2, \dots, n \quad (1)$$

Here, q_i , v_i , a_i denote the position, velocity and acceleration of vehicle i respectively, for the platoon of length $n \in \mathbb{N}^+$ vehicles. The desired acceleration u_i is considered the input to the system, and $\tau_i > 0$ and $\phi_i \geq 0$ are a time constant and actuation delay associated with the driveline of vehicle i respectively.

The vehicle-following objective, i.e. follow the predecessor at constant headway $h_i > 0$, can be captured in the error definition

$$e_i(t) = q_{i-1}(t) - q_i(t) - h_i v_i(t) - r_i - L_i, \quad (2)$$

where $r_i \geq 0$ is a constant to account for a certain distance at standstill, and L_i is the length of vehicle i .

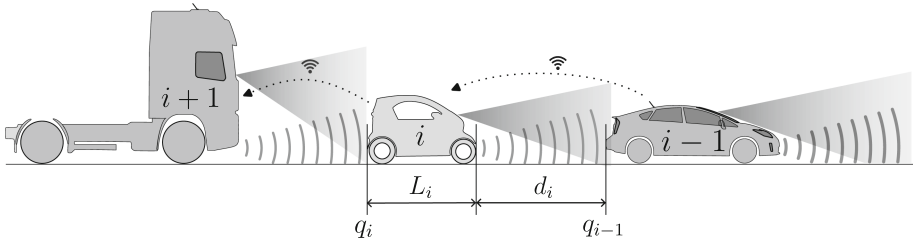


Fig. 1. Heterogeneous string of vehicles equipped with CACC.

2.1 Controller Design

Defining the coordinate transformation along the lines of [3]

$$\begin{aligned} x_1(t) &= e_i(t) = q_{i-1}(t) - q_i(t) - h_i v_i(t) - r_i - L_i \\ x_2(t) &= \dot{e}_i(t) = v_{i-1}(t) - v_i(t) - h_i a_i(t) \\ x_3(t) &= v_{i-1}(t) - v_i(t), \end{aligned} \quad (3)$$

the error (2) and its dynamics are given by

$$\begin{aligned} \dot{x}_1(t) &= x_2(t) \\ \dot{x}_2(t) &= a_{i-1}(t) - \frac{h_i - \tau_i}{h_i \tau_i} [x_2(t) - x_3(t)] - \frac{h_i}{\tau_i} u_i(t - \phi_i) \\ \dot{x}_3(t) &= \frac{1}{h_i} x_2(t) - \frac{1}{h_i} x_3(t) + a_{i-1}(t). \end{aligned} \quad (4)$$

We propose a prediction based control law for vehicle i , given by

$$u_i(t) = \left[1 - \frac{\tau_i}{h_i}\right] \hat{a}_i^{\phi_i}(t) + \frac{\tau_i}{h_i} a_{i-1}(t) - \frac{\tau_i}{h_i} \bar{u}_i(t), \quad (5a)$$

$$\text{with } \hat{a}_i^{\phi_i}(t) = \exp\left(-\frac{\phi_i}{\tau_i}\right) a_i(t) + \int_{t-\phi_i}^t \frac{1}{\tau_i} \exp\left(-\frac{t-\sigma}{\tau_i}\right) u_i(\sigma) d\sigma \quad (5b)$$

$$\text{and } \bar{u}_i(t) = -[k_p \ k_d] \left(\begin{bmatrix} 1 & \phi_i \\ 0 & 1 \end{bmatrix} \begin{bmatrix} x_1(t) \\ x_2(t) \end{bmatrix} + \int_{t-\phi_i}^t \begin{bmatrix} t-\sigma \\ 1 \end{bmatrix} \bar{u}_i(\sigma) d\sigma \right), \quad (5c)$$

where k_p and k_d are controller gains. To compensate for the delay ϕ_i , the inputs u_i and feedback-control actions \bar{u}_i over the past ϕ_i seconds are used to construct a prediction $\hat{a}_i^{\phi_i}$ of the acceleration a_i and evolution of the system (4). Applying the prediction based controller (5) on the system (4), results in closed-loop dynamics

$$\dot{x}(t) = \begin{bmatrix} \dot{x}_1(t) \\ \dot{x}_2(t) \\ \dot{x}_3(t) \end{bmatrix} = \begin{bmatrix} 0 & 1 & 0 \\ -k_p & -k_d & 0 \\ 0 & \frac{1}{h_i} & -\frac{1}{h_i} \end{bmatrix} \begin{bmatrix} x_1(t) \\ x_2(t) \\ x_3(t) \end{bmatrix} + \begin{bmatrix} 0 \\ w(t) \\ a_{i-1}(t) \end{bmatrix}, \quad (6)$$

where

$$\begin{aligned} w(t) = & a_{i-1}(t) - a_{i-1}(t - \phi_i) - k_p \int_0^{\phi_i} \sigma [a_{i-1}(t - \sigma) - a_{i-1}(t - \phi_i - \sigma)] d\sigma \\ & - k_d \int_0^{\phi_i} [a_{i-1}(t - \sigma) - a_{i-1}(t - \phi_i - \sigma)] d\sigma. \end{aligned}$$

The closed loop system (6) is input to state stable (ISS) with respect to the predecessors acceleration $a_{i-1}(t)$ for $k_p > 0$, $k_d > 0$. That is, $x(t)$ remains bounded for bounded $a_{i-1}(t)$, and $x(t)$ converges to zero when $a_{i-1}(t)$ converges to zero. It is worth to note that including the preceding vehicle's future acceleration, $a_{i-1}(t + \phi_i)$, in the control action (5a) instead of the current acceleration, $a_{i-1}(t)$, would eliminate the disturbance $w(t)$. However, the future acceleration of the preceding vehicle is generally not available. Instead, a prediction of the preceding vehicle's future acceleration $\hat{a}_{i-1}(t + \phi_i)$ could be used to improve performance. Constructing such a prediction is considered outside the scope of this paper and left for future research.

3 String Stability

The attenuation of disturbances through the vehicle string is an important design objective of vehicle platoons. To analyze the string stability of the system employing controller (5) we adopt the notion of \mathcal{L}_2 string stability [4]. To this end, we define the transfer function relating the velocity of (a preceding) vehicle k to the velocity of vehicle $i > k$, referred to as the String Stability Complementary Sensitivity (SSCS), as $\Gamma_i^k = \frac{v_i(s)}{v_k(s)}$, where $v_i(s)$ is the Laplace transform of $v_i(t)$. The platoon is \mathcal{L}_2 string stable if [4]

$$\|\Gamma_i^k(s)\|_{\mathcal{H}_\infty} = \sup_{\omega \in \mathbb{R}} |\Gamma_i^k(j\omega)| \leq 1, \quad (7)$$

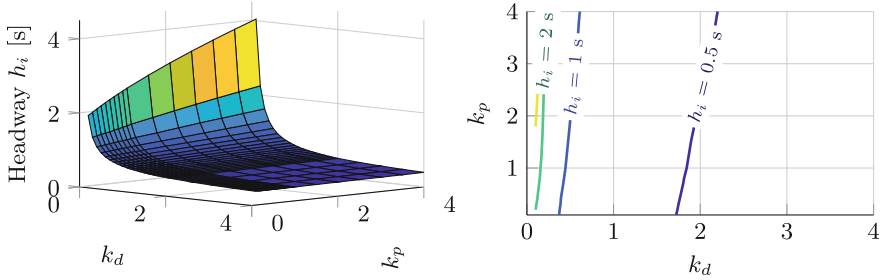


Fig. 2. Minimum required headway h_i for (9) to satisfy (7) given k_p , k_d with $\phi_i = 0.15$ s, $\theta_i = 0.02$ s.

where $\|\cdot\|_{\mathcal{H}_\infty}$ denotes the \mathcal{H}_∞ norm. Note that the SSCS for the string of vehicles starting at index k and ending with index i is equal to the product of the SSCS of the individual vehicles with respect to their direct predecessor: $\Gamma_i^k = \prod_{j=k+1}^i \Gamma_j^{j-1}$. Consequently, if each individual vehicle i satisfies condition (7) with respect to its direct predecessor $i-1$, it implies (7) is satisfied for the entire platoon. Therefore, we focus the analysis of string stability on an individual vehicle with its direct predecessor, for which condition (7) should hold.

3.1 String Stability with Communication Delays

The control action (5) requires the preceding vehicle's acceleration a_{i-1} , which cannot be directly measured with sensors on-board of vehicle i . This means that in practice V2V communication is used to obtain this information. Including a communication delay $\theta_i \geq 0$ in the control action (5a) gives

$$u_i(t) = \left[1 - \frac{\tau_i}{h_i}\right] \hat{a}_i^{\phi_i}(t) + \frac{\tau_i}{h_i} a_{i-1}(t - \theta_i) - \frac{\tau_i}{h_i} \bar{u}_i(t). \quad (8)$$

The closed-loop system (6) employing (8) results in the SSCS as

$$\Gamma_i^{i-1}(s) = \frac{(s^2 + k_d s + k_p) e^{-\theta_i s} + [(k_d + k_p \phi_i) s + k_p] [1 - e^{-(\phi_i + \theta_i) s}]}{(h_i s + 1)(s^2 + k_d s + k_p)} e^{-\phi_i s}. \quad (9)$$

The SSCS (9) can be used to determine appropriate controller gains k_p and k_d to satisfy (7), given the actuation and communication delays, ϕ_i and θ_i respectively.

4 Tuning and Simulation

We experimentally validated the discrete time equivalent of the CACC controller with a platoon of two full-scale vehicles in [1]. There, we show that the closed-loop response of the vehicle employing controller (5) indeed behaves according to (6). In this section, we consider the tuning of the controller with respect to string stability and illustrate the results with time-domain simulations.

4.1 Tuning for String Stability

To determine an appropriate tuning for the controller that achieves string stability, given the characteristics of the experimental vehicle from [1] (time constant $\tau_i = 0.067$ seconds, actuation delay $\phi_i = 0.15$ seconds and a communication delay $\theta_i = 0.02$ seconds), we use a bi-section algorithm to numerically determine the minimum required headway h_i for which condition (7) is satisfied for (9) for a grid of k_p and k_d . The resulting Fig. 2 shows the minimum headway that can be achieved, greatly depends on the choice of controller gains. Especially k_d should be chosen sufficiently large to be able to employ small headways.

4.2 Simulation

To illustrate the effectiveness of the prediction based controller, we consider a heterogeneous platoon of $n = 6$ vehicles, with the parameters as listed in Table 1. Here, vehicle 2 and 3 have the characteristics of the experimental vehicles from [1] and [4] respectively. The leader vehicle is modeled without actuation delay, to illustrate the effectiveness of the controller in a setting where the preceding vehicle does not experience a delay. The communication delay $\theta_i = 0.02$ seconds is assumed to be identical for all vehicles. Furthermore, all vehicles use the same tuning of the feedback controller with $k_p = 1$ and $k_d = 4$. At the adopted headway $h_i = 0.5$ seconds, the string stability condition (7) is satisfied for each vehicle in the platoon, as can be seen in the magnitude plot of the SCS in Fig. 3a.

Table 1. Vehicle parameters of the platoon used in the simulation.

Vehicle index i	1	2	3	4	5	6
Driveline constant τ_i [s]	0.05	0.067	0.1	0.04	0.09	0.12
Actuation delay ϕ_i [s]	0	0.15	0.2	0.12	0.13	0.16

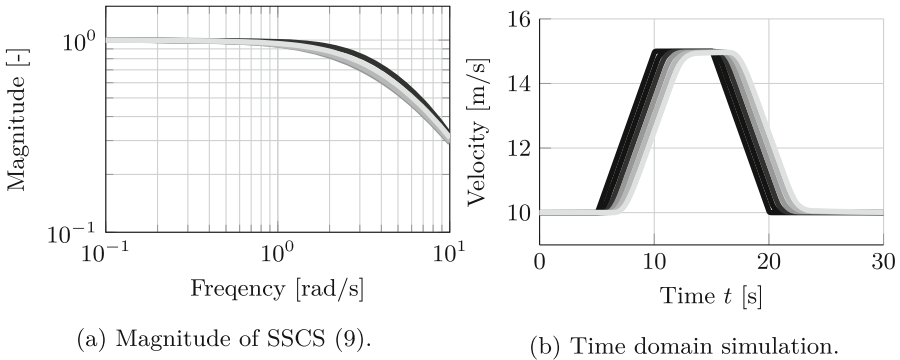


Fig. 3. Magnitude of SCS (9) and time domain velocity response of the platoon of six vehicles (black - light gray: $i = 1, 2, \dots, 6$) with distinct τ_i and ϕ_i as listed in Table 1, employing (5).

Figure 3b shows a time domain simulation of the platoon employing the discrete time equivalent of (5), obtained by discretizing system with ZOH at a sample time $T_s = 0.01$ seconds as described in [1]. The leader vehicle is prescribed an acceleration step of $u_1 = 1 \text{ m/s}^2$ for $t \in [5, 10]$, followed by a negative step $u_1 = -1 \text{ m/s}^2$ for $t \in [15, 20]$. No velocity overshoots are observed, indicating the platoon indeed exhibits string stable behavior.

5 Conclusion

In this paper, we present a prediction based control approach for platoons with actuation delay. The controller does not require any information of the driveline dynamics of the preceding vehicle, making it suitable for platoons that are heterogeneous with respect to both the driveline time constant and actuation delays. An analysis of the string stability properties considering both actuation and communication delays is presented, which shows the controller is able to achieve string stability at short headways (smaller than 0.5 seconds), given the properties of the experimental setup. A simulation confirms the effectiveness of the controller.

The presented prediction based controller only considers the predicted states of the ego vehicle and uses the current (communicated) state of the preceding vehicle. Consequently, a disturbance acts on the system which is a function of the preceding vehicle's acceleration. Although the system is ISS with respect to this disturbance regardless of the size of the actuation delay, a certain minimum headway time is required for string stability. Future research entails including the preceding vehicle's acceleration in a different manner in the control action to decrease or eliminate the minimum headway required for string stability. For instance, by predicting the preceding vehicle's future acceleration. Finally, in this paper only simulations are used to demonstrate the efficacy of the controller. For future research, we plan to conduct experiments with full-scale vehicles to validate the performance with respect to string stability.

References

1. de Haan, R., Redi, L., van der Sande, T., Lefeber, E.: Platooning of heterogeneous vehicles with actuation delays: theoretical and experimental results. arXiv (2024), <https://arxiv.org/abs/2404.15958>
2. de Haan, R., van der Sande, T., Lefeber, E.: Cooperative adaptive cruise control for heterogeneous platoons with actuator delay. IFAC-PapersOnLine **56**(2), 5579–5584 (2023)
3. Lefeber, E., Ploeg, J., Nijmeijer, H.: Cooperative adaptive cruise control of heterogeneous vehicle platoons. IFAC-PapersOnLine **53**(2), 15217–15222 (2020)
4. Ploeg, J., van de Wouw, N., Nijmeijer, H.: Lp string stability of cascaded systems: application to vehicle platooning. IEEE Trans. Control Syst. Technol. **22**(2), 786–793 (2014)
5. Rajamani, R., Shladover, S.: An experimental comparative study of autonomous and co-operative vehicle-follower control systems. Transp. Res. Part C Emerg. Technol. **9**(1), 15–31 (2001)

Open Access This chapter is licensed under the terms of the Creative Commons Attribution 4.0 International License (<http://creativecommons.org/licenses/by/4.0/>), which permits use, sharing, adaptation, distribution and reproduction in any medium or format, as long as you give appropriate credit to the original author(s) and the source, provide a link to the Creative Commons license and indicate if changes were made.

The images or other third party material in this chapter are included in the chapter's Creative Commons license, unless indicated otherwise in a credit line to the material. If material is not included in the chapter's Creative Commons license and your intended use is not permitted by statutory regulation or exceeds the permitted use, you will need to obtain permission directly from the copyright holder.





Vertical Dynamics Control Using Active Tires and Preview

Tom van der Sande^(✉) and Nick te Kronnie

Eindhoven University of Technology, Eindhoven, The Netherlands
t.p.j.v.d.sande@tue.nl

Abstract. In this paper, the effects of adding a tire actuator to a vehicle with active suspension and preview control are studied. For the controller, the LQR method is used. The dual actuator system with preview control is compared to other conventional systems to determine the performance gain. The results show a gain of 182.3% in comfort compared to the passive suspension. The dual actuator system with preview control outperforms systems with fewer actuators and is less affected by the trade-off between handling and comfort.

Keywords: Active vehicle suspension · Preview control · Active tires

1 Introduction

For an optimal experience and maximum safety while driving a vehicle, comfort and road holding are important factors. The suspension has a large impact on both comfort and road holding [2]. In a regular passenger car the suspension typically consists of a spring and a damper. By adding an actuator to the suspension (active suspension), comfort and road holding can be improved even further [5]. An active suspension typically acts upon the measured sprung acceleration and suspension travel and is therefore reactive [7]. To improve performance, a preview controller can be used that uses information about the road ahead.

Little research has been done on active tire control. D'Ambrosio [1] introduces Active Tire Pressure Control (ATPC), aimed at improving the fuel consumption, safety, and drivability of a car. However, the system is rather slow. Nandikolla [6] introduces a deformable smart tire with the use of SMA springs. By heating and cooling the SMA springs, the shape of the smart tire switches between two states: circular and square. Even though not a road vehicles, Maglev trains can be modeled in a similar way as a car. Maglev trains offer the opportunity to actively control the interaction between track and unsprung mass of the train, thereby adding the equivalent of a tire actuator. This leads to the open research question of determining the performance gain in terms of handling and comfort achievable with a dual actuator system with preview control over conventional and active suspension.

The outline of this paper is as follows, in Sect. 2 the quarter car model is introduced. Using this model, the controller is derived in Sect. 3. The effects of preview time and a comparison with existing controllers is shown in Sect. 4. Finally, conclusions are drawn in Sect. 5.

2 Vehicle Model

In this research the standard quarter car model [7], shown in Fig. 1, is used. Here m_s represents the sprung mass and m_u unsprung mass, which are connected via a spring (k_s) and damper (d_s). Furthermore, the tire is modeled as a spring with stiffness k_t . The actuator force between the sprung and unsprung mass is represented by F_s and the tire actuator by F_t . Finally, the preview time is indicated by t_p . The parameters of the quarter car model are given in Table 1. The equations of motion are given as

$$m_s \ddot{z}_s = -k_s(z_s - z_u) - d_s(\dot{z}_s - \dot{z}_u) - F_s \tag{1}$$

$$m_u \ddot{z}_u = k_s(z_s - z_u) + d_s(\dot{z}_s - \dot{z}_u) - k_t(z_u - z_r) + F_s - F_t. \tag{2}$$

For controller implementation, these equations of motion have been put into a linear state-space form

$$\dot{x} = \mathbf{A}x + \mathbf{B}_1 \mathbf{u}_1 + \mathbf{B}_2 z_r \tag{3}$$

$$y = \mathbf{C}x + \mathbf{D}_1 \mathbf{u}_1 + \mathbf{D}_2 z_r \tag{4}$$

with state space matrices \mathbf{A} , \mathbf{B}_1 , \mathbf{B}_2 , \mathbf{C} , \mathbf{D}_1 , and \mathbf{D}_2 denoting the state transition matrix, actuator force and disturbance input matrix, state to output matrix, force input to output matrix and disturbance to output matrix respectively.

The main purpose of a suspension is to provide comfort to the driver and keep the tires in contact with the road, which is important for vehicle handling. These objectives can be captured in the vertical acceleration of the sprung mass, \ddot{z}_s , which is a good measure of comfort, and in the dynamic tire compression, $z_u - z_r$, which is a good measure of handling [7]. For both quantities, the RMS value is used. In addition to that, suspension travel, $z_s - z_u$, is typically limited.

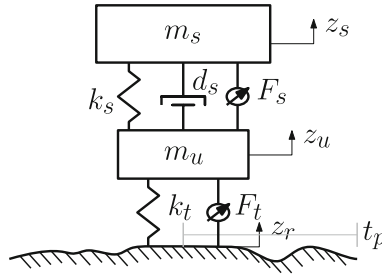


Fig. 1. Schematic representation of the quarter car model with suspension actuator, tire actuator, and preview control, adapted from [7]

3 Controller Design

Given the system dynamics with multiple control objectives and two actuators, a control method that can generate the optimal input for both the actuators

Table 1. System Parameters

Symbol	Value	Unit	Description
m_s	400	kg	sprung mass
m_u	40	kg	unsprung mass
k_s	25000	N/m	suspension stiffness
k_t	200000	N/m	tire stiffness
d_s	2000	Ns/m	damping coefficient

has to be designed. Assuming that the full state can be measured, an LQR is a suitable candidate. The cost function to be minimized is defined as

$$J = \frac{1}{2} \int_t^{t+t_p} (\mathbf{y}^T \mathbf{Q} \mathbf{y} + \mathbf{u}_1^T \mathbf{R} \mathbf{u}_1) d\tau; \quad (5)$$

$$\mathbf{Q} = \mathbf{Q}^T; \quad \mathbf{Q} \geq 0; \quad \mathbf{R} = \mathbf{R}^T; \quad \mathbf{R} > 0,$$

where \mathbf{Q} is a positive semidefinite weighting matrix on the output vector and \mathbf{R} is a positive definite matrix on the force inputs. They can both be chosen such that the aforementioned performance metrics can be individually emphasized (comfort or handling), while taking into account suspension travel and actuator load. The input \mathbf{u}_1 that minimizes J is determined as

$$\mathbf{u}_1 = -\mathbf{V}^{-1}(\mathbf{B}_1^T \mathbf{P} + \mathbf{D}_1^T \mathbf{Q} \mathbf{C}) \mathbf{x} + \mathbf{V}^{-1} \mathbf{B}_1^T \mathbf{r}, \quad (6)$$

which has both a state feedback part and a feedforward part based on the future response of the system \mathbf{r} . The matrix \mathbf{V} is defined as

$$\mathbf{V} = \mathbf{D}_1^T \mathbf{Q} \mathbf{D}_1 + \mathbf{R}; \quad \mathbf{V} = \mathbf{V}^T; \quad \mathbf{V} > 0, \quad (7)$$

and \mathbf{P} is the solution of the Algebraic Ricatti Equation (ARE) [4]

$$\mathbf{F}^T \mathbf{P} + \mathbf{P} \mathbf{F} + \mathbf{G} - \mathbf{P} \mathbf{H} \mathbf{P} = \mathbf{0}. \quad (8)$$

In the Ricatti equation, the following matrices are defined

$$\mathbf{F} = \mathbf{A} - \mathbf{B}_1 \mathbf{V}^{-1} \mathbf{D}_1^T \mathbf{Q} \mathbf{C}, \quad (9)$$

$$\mathbf{G} = \mathbf{C}^T (\mathbf{Q} - \mathbf{Q} \mathbf{D}_1 \mathbf{V}^{-1} \mathbf{D}_1^T \mathbf{Q}) \mathbf{C}, \quad (10)$$

$$\mathbf{H} = \mathbf{B}_1 \mathbf{V}^{-1} \mathbf{B}_1^T. \quad (11)$$

Road preview requires knowledge of the road disturbances up ahead. For now, it is assumed that this knowledge is available, either through, for example, detailed maps or a sensor on the vehicle that can measure the height of the road disturbance up ahead. In (6), the future response of the system, \mathbf{r} , was introduced. The upcoming section will discuss how the upcoming road disturbance is captured in \mathbf{r} .

First, the states of the system at the end of the preview time t_p , $\mathbf{x}(t + t_p)$, are determined, which will be used as a boundary condition in the next step. The calculation strategy for $\mathbf{x}(t + t_p)$ is suggested by Huisman [3]. Secondly, the response of the system over the preview distance is determined by backward integrating of

$$\dot{\mathbf{r}}(t^*) = -\mathbf{A}_g^T \mathbf{r}(t^*) + \mathbf{P}\mathbf{h}(t^*); \quad \mathbf{r}(t + t_p) = \mathbf{P}\mathbf{x}(t + t_p), \quad (12)$$

over the preview time t_p . Here $\mathbf{h}(t^*)$ defined as

$$\mathbf{h} = \mathbf{B}_2 \mathbf{u}_2, \quad (13)$$

and \mathbf{A}_g as

$$\mathbf{A}_g = \mathbf{F} - \mathbf{H}\mathbf{P}. \quad (14)$$

To perform the backwards integration, the approach of [4] is followed, where the substitution $\mathbf{r}(t) = \mathbf{s}(t + t_p - t^*)$ is made, such that

$$\dot{\mathbf{s}}(t) = \mathbf{A}_g^T \mathbf{s}(t) + \mathbf{P}\mathbf{B}_2 \mathbf{z}_r(t + t_p - t); \quad \mathbf{s}(0) = \mathbf{r}(t + t_p). \quad (15)$$

The states of the system, $\mathbf{x}(t)$, can be determined as

$$\dot{\mathbf{x}}(t) = \mathbf{A}_g \mathbf{x}(t) + \mathbf{H}\mathbf{r}(t) + \mathbf{h}(t); \quad \mathbf{x}(t) = \mathbf{x}(t - \Delta t). \quad (16)$$

Finally, the optimal input \mathbf{u}_1 over the interval $[t, t + t_p]$ can be determined by substituting $\mathbf{x}(t)$ and $\mathbf{r}(t)$ in (6).

4 Results

To achieve good comfort, the weighting matrices introduced in (5) have been chosen as

$$\mathbf{Q}_{comfort} = \begin{bmatrix} 22 & 0 & 0 \\ 0 & 1 & 0 \\ 0 & 0 & 1 \end{bmatrix}; \quad \mathbf{R}_{comfort} = \begin{bmatrix} 1 & 0 \\ 0 & 1 \end{bmatrix}, \quad (17)$$

thereby emphasizing the sprung acceleration, \ddot{z}_s , over the dynamic tire compression and suspension travel. Below, first the influence of preview time on the performance of the dual actuator system is shown. Secondly, the frequency response of the proposed controller will be compared to a one actuator system with and without preview as well as the two actuator case without preview.

4.1 Influence of Preview Time

In this section, the effect of preview time for the dual actuator system is investigated. As input a 0.05 m step input is used. The preview times shown range from 0.1 to 1 s, with a step of 0.1 s. In Fig. 2, the results of the look-ahead time for a comfort-oriented controller are shown. The handling-oriented controller results are not shown here but show similar results in terms of the influence of the

look-ahead time. From Fig. 2, it can be noted that the using road preview has the largest impact on the sprung acceleration and the suspension travel. Furthermore, the lines are converging with increasing preview times, which indicates the presence of an asymptote in performance. This is even more apparent from the fact that the controllers with larger preview time hardly show any movement of the suspension travel before 0.7 s. Changing the preview time shows little effect on the tire compression when the controller is tuned for comfort. In the next section the dual actuator controller is compared to other controllers, for this, a look-ahead time of 0.125 s will be used.

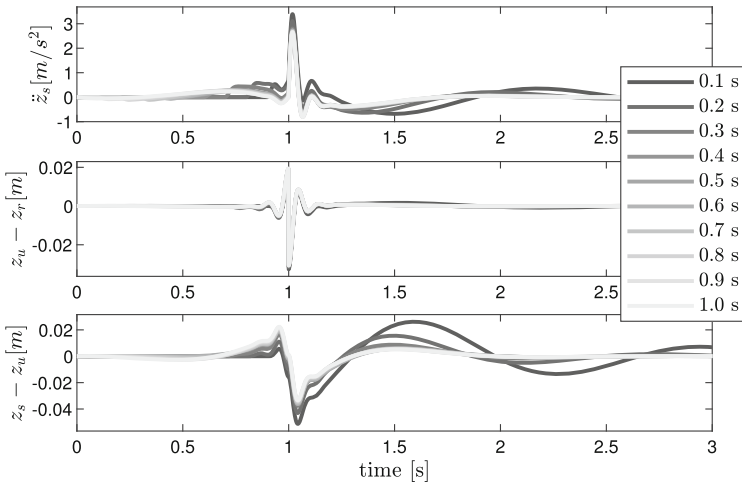


Fig. 2. Influence preview time on a dual actuator suspension with preview and comfort-oriented control with a step input of 0.05 m

4.2 Frequency Response

In this section, the frequency response of the two actuator controller with preview is compared with various other controllers. Figure 3 shows that the two actuator solution shows better comfort over the whole frequency range compared to the passive system and also the system with a single actuator (both with and without preview). In addition to that, it also shows that the two actuator solution with preview performs better than a dual actuator without preview. Both dual actuator systems also show that the comfort invariant point no longer exists for this setup.

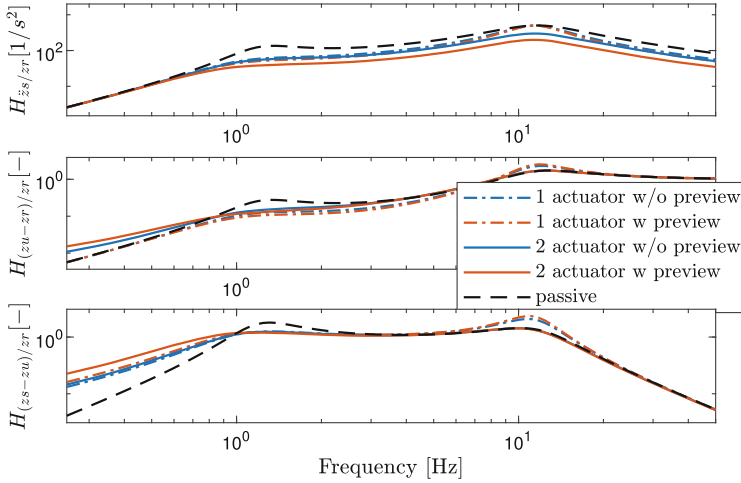


Fig. 3. Frequency response of systems with a comfort-oriented controller on a road disturbance

5 Conclusion

A quarter car model with an LQR and a preview strategy is developed to determine the comfort gain achievable with a dual actuator suspension with preview control. The performance gain is measured by three metrics: sprung acceleration, tire compression, and suspension travel. The weighting matrices are tuned so that maximum comfort or handling can be achieved within the limits of the constraints. The simulation results show that an improvement of 182.3% in sprung acceleration can be achieved on a 0.05 m step input.

References

1. D'Ambrosio, S., Vitolo, R., Salamone, N., Oliva, E.: Active tire pressure control (ATPC) for passenger cars: design, performance, and analysis of the potential fuel economy improvement. *SAE Int. J. Passenger Cars Mech. Syst.* **11**(5), 321–339 (2018)
2. Hac, A.: Optimal linear preview control of active vehicle suspension. *Proc. IEEE Conf. Decis. Control* **5**, 2779–2784 (1990)
3. Huisman, R.G.M., Veldpaus, F.E., Voets, H.J.M., Kok, J.J.: An optimal continuous time control strategy for active suspensions with preview. *Vehicle Syst. Dyn.* **22**(1), 43–55 (1993)
4. Huisman, R.G.M.: An investigation into the theoretical feasibility of active suspensions with preview. Master's thesis, Eindhoven University of Technology, Eindhoven (1992)
5. Huisman, R.G.M.: A controller and observer for active suspensions with preview. Ph.D. thesis, Eindhoven University of Technology, Eindhoven (1994)

6. Nandikolla, V.K., Costa, M., Boyd, N., Rosales, G.: Design of a deformable smart tire using soft actuator. In: Proceedings of the ASME 2019 International Mechanical Engineering Congress and Exposition (2019)
7. van der Sande, T.P.J., Besselink, I.J.M., Nijmeijer, H.: Rule-based control of a semi-active suspension for minimal sprung mass acceleration: design and measurement. *Veh. Syst. Dyn.* **54**(3), 281–300 (2016)





Open Access This chapter is licensed under the terms of the Creative Commons Attribution 4.0 International License (<http://creativecommons.org/licenses/by/4.0/>), which permits use, sharing, adaptation, distribution and reproduction in any medium or format, as long as you give appropriate credit to the original author(s) and the source, provide a link to the Creative Commons license and indicate if changes were made.

The images or other third party material in this chapter are included in the chapter's Creative Commons license, unless indicated otherwise in a credit line to the material. If material is not included in the chapter's Creative Commons license and your intended use is not permitted by statutory regulation or exceeds the permitted use, you will need to obtain permission directly from the copyright holder.





Time-Optimal Learning-Based LTV-MPC for Autonomous Racing

Zijun Guo , Huilong Yu  , and Junqiang Xi 

Beijing Institute of Technology, Beijing, China
huilong.yu@bit.edu.cn

Abstract. Autonomous racing is a time- and accuracy-critical application of vehicle motion planning and control techniques. Despite being promising for its ability to handle constraints, model predictive control (MPC) for autonomous racing is limited by the relatively low computational speed and the problem of model mismatch. In this work, we present a time-optimal linear-time-variant-MPC (LTV-MPC) that incorporates a min-time objective function, the friction ellipse constraint, and the successive linearization over the prediction horizon to improve computational speed and prediction accuracy. To tackle model mismatch, the proposed LTV-MPC is further combined with Gaussian process regression to learn the lateral tire force error. Compensation for the error is implemented over the prediction horizon and on the friction ellipse constraint. This work presents simulation validation on the racing track of Formula Student Autonomous China (FSAC) and experimental validation on a self-designed track. We show that compared with nonlinear MPC, the proposed LTV-MPC reduces the average computation time from 66 ms to 2.5 ms with a 0.6% increase in lap time. With learned tire force error, a 2% reduction in lap time can be achieved.

Keywords: Autonomous racing · Autonomous driving · Model predictive control · Gaussian process regression

1 Introduction

Model predictive control (MPC) is a suitable tool for autonomous racing due to its ability to handle constraints like vehicle dynamics and track boundaries. However, the time-optimal control problem for autonomous racing is nonlinear [5]. The direct use of nonlinear MPC (NMPC) leads to high computation time that is undesirable for racing [3], and the use of linear or adaptive MPC fails to accurately incorporate nonlinear objectives and constraints. Although linear-time-variant-MPC (LTV-MPC) can strike a balance between computational speed and accuracy, it is mainly used in trajectory tracking tasks and its application to autonomous racing is scarce in the literature.

Another limitation of MPC is model mismatch, which occurs when the control model differs from the actual plant, causing the degradation of control performance. Several techniques, e.g. error observers and Gaussian process regression

(GPR) [2], are adopted to tackle this issue. However, linear models like error observers omit the nonlinear portion of the error, and the learning-based method in [2] that learns the error of all state variables lacks interpretability and hinders further analysis of model mismatch.

To address the aforementioned problems, this work presents a time-optimal LTV-MPC with its min-time objective function and friction ellipse constraint successively linearized over the prediction horizon, and a GPR-based lateral tire force error model to adjust the control model and friction ellipse constraint.

2 Time-Optimal LTV-MPC Formulation

2.1 Vehicle Control Model

A 3-DOF single-track rear-wheel-drive vehicle dynamics model is adopted:

$$\dot{\mathbf{x}} = \begin{bmatrix} \dot{v}_x \\ \dot{v}_y \\ \dot{\psi} \\ \dot{s} \\ \dot{n} \\ \dot{\chi} \\ \dot{T} \\ \dot{\delta} \end{bmatrix} = \mathbf{f}(\mathbf{x}, \mathbf{u}) = \begin{bmatrix} (F_x - F_{y,f} \sin \delta) / m_t + \dot{\psi} v_y \\ (F_{y,f} \cos \delta + F_{y,r}) / m_t - \dot{\psi} v_x \\ (F_{y,f} l_f \cos \delta - F_{y,r} l_r) / I_z \\ \frac{v_x \cos \chi - v_y \sin \chi}{1 - n \kappa(s)} \\ v_x \sin \chi + v_y \cos \chi \\ \dot{\psi} - \kappa(s) \dot{s} \\ T_{\text{rate}} \\ \delta_{\text{rate}} \end{bmatrix}, \quad (1)$$

where there are eight state variables $\mathbf{x} = [v_x, v_y, \dot{\psi}, s, n, \chi, T, \delta]^\top$ and two control variables $\mathbf{u} = [T_{\text{rate}}, \delta_{\text{rate}}]^\top$, v_x, v_y , and $\dot{\psi}$ denote longitudinal velocity, lateral velocity, and yaw rate in vehicle coordinate frame, s, n , and χ denote vehicle pose in curvilinear coordinate frame, T and δ denote torque on the rear wheel and front-wheel steering angle. The above variables are depicted in Fig. 1.

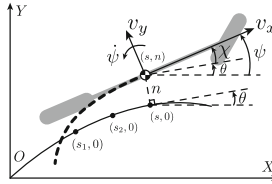


Fig. 1. 3-DOF single-track vehicle model in curvilinear coordinate frame.

In (1), $\kappa(s)$ is the road curvature at progress s , l_f and l_r denote the location of the center of gravity (CoG) behind the front axle and location of CoG in front of the rear axle, m_t and I_z are the total mass of the vehicle and the vehicle inertia about z axis, $F_x = T/R$ is the longitudinal force of the rear wheel, R is the tire radius, $F_{y,i}$, $i = \{f, r\}$ are the lateral forces of the front and rear wheels.

The longitudinal force of the front wheel is assumed to be zero. The lateral forces are calculated as

$$F_{y,i} = f_{\text{MF},i}(\alpha_i) = \mu_c F_{z,i} D_y \sin [C_y \text{atan} \{B_y \alpha_i - E_y (B_y \alpha_i - \text{atan}(B_y \alpha_i))\}], \quad (2)$$

where $F_{z,f} = m_t g l_r / l$, $F_{z,r} = m_t g l_f / l$, μ_c is the road adhesion coefficient of the control model, B_y , C_y , D_y , and E_y are parameters of the magic formula (MF) tire model, l is the wheelbase, $\alpha_f = \text{atan}((v_y + \dot{\psi} l_f) / v_x) - \delta$ and $\alpha_r = \text{atan}((v_y - \dot{\psi} l_r) / v_x)$ are the slip angles of the front and rear wheels.

2.2 Problem Formulation

The objective function of the time-optimal LTV-MPC is given as

$$\boldsymbol{\eta}_{\text{tr}} = \left[\frac{1 - n\kappa(s)}{v_x \cos \chi - v_y \sin \chi}, \dot{\psi} \right]^\top, \quad \boldsymbol{\eta}_{\text{ref}} = [0, 0]^\top, \quad (3)$$

where $\boldsymbol{\eta}_{\text{tr}}$ is the controlled output vector, $\boldsymbol{\eta}_{\text{ref}}$ contains the desired output values. The first element in $\boldsymbol{\eta}_{\text{tr}}$ equals $1/\dot{s}$, which means the time required to progress 1 m in curvilinear coordinate frame. Therefore, its 0 reference value serves the min-time purpose. The second element in $\boldsymbol{\eta}_{\text{tr}}$ serves to enhance vehicle stability.

The friction ellipse constraint is formulated as a hard constraint:

$$\boldsymbol{\eta}_{\text{c}} = \left[\frac{F_x}{\mu_c D_x F_{z,r}}^2 + \frac{F_{y,r}}{\mu_c D_y F_{z,r}}^2 \right]^\top, \quad (4)$$

where $\boldsymbol{\eta}_{\text{c}}$ is the hard constrained output vector, D_x is a parameter of the MF model. Due to the symmetry of the friction ellipse, the linearized hard constrained output is limited between -1 and 1.

The velocity and track constraints are formulated as soft constraints to prevent problem infeasibility when the constraints are temporarily violated by vehicle sensor noise. The soft constrained output vector is given as $\boldsymbol{\eta}_{\text{sc}} = [v_x, n]^\top$. Similar to the curvature κ , the upper and lower bounds for n are functions of s .

The final output vector is the concatenation of controlled, hard constrained, and soft constrained output vectors $\boldsymbol{\eta} = \mathbf{h}(\mathbf{x}) = [\boldsymbol{\eta}_{\text{tr}}, \boldsymbol{\eta}_{\text{c}}, \boldsymbol{\eta}_{\text{sc}}]^\top$. For the k -th ($k = 1, \dots, H$) discrete time step in the prediction horizon, the system equation $\dot{\mathbf{x}} = \mathbf{f}(\mathbf{x}, \mathbf{u})$ and output equation $\boldsymbol{\eta} = \mathbf{h}(\mathbf{x})$ are linearized at a reference point $[\hat{\mathbf{x}}^k, \hat{\mathbf{u}}^k]$. In this work, it is assumed that the difference between the solution of one control step and its subsequent (1/ f s later, where f is the control frequency) is small. Therefore, the solution of the last control step is used as the linearization reference point at the current step. After linearization, the system is discretized using the explicit fourth-order Runge-Kutta method. We refer the readers to [4] for further formulation of the LTV-MPC problem.

3 GPR-Based Lateral Tire Force Error Learning

GPR is a non-parametric machine learning method suited for small datasets. From the data collected when racing with LTV-MPC, the lateral forces $F_{y,i}$ can

be solved from two linear equations with two unknowns, extracted from (1):

$$\begin{cases} \dot{v}_y = (F_{y,f} \cos \delta + F_{y,r}) / m_t - \dot{\psi} v_x \\ \ddot{\psi} = (F_{y,f} l_f \cos \delta - F_{y,r} l_r) / I_z \end{cases}. \quad (5)$$

We choose to learn the dimensionless lateral tire force error with features $[|T|, |\alpha|]^\top \in \mathbb{R}^2$. The absolute value is taken to form a denser dataset. The corresponding dataset output is calculated as $[(|F_{y,r,\text{true}}| - |F_{y,r,\text{pred}}|) / F_{z,r}] \in \mathbb{R}^1$, where $F_{y,r,\text{true}}$ is solved based on vehicle states from sensors, $F_{y,r,\text{pred}}$ is solved based on predicted states from LTV-MPC. The predicted mean dimensionless error from GPR is denoted as g . The predicted variance is omitted. It is assumed that the characteristics of the front and rear tires are the same. Consequently, the error model learned from the rear tire is also applied to the front tire:

$$\begin{aligned} F_{y,f}^k &= f_{\text{MF},f}(\alpha_f^k) - F_{z,f} \frac{g(0, |\hat{\alpha}_f^k|)}{\hat{\alpha}_f^k} \alpha_f^k, \\ F_{y,r}^k &= f_{\text{MF},r}(\alpha_r^k) - F_{z,r} \frac{g(|\hat{T}^k|, |\hat{\alpha}_r^k|)}{\hat{\alpha}_r^k} \alpha_r^k, \end{aligned} \quad (6)$$

where \hat{T}^k and $\hat{\alpha}_f^k$ are reference points at which to evaluate error compensation at the k -th discrete time in the prediction horizon. Same as linearization, these reference points are calculated from the solution of the last control step. The slope of the learned dimensionless error is multiplied by the slip angle to establish a linear-time-variant relationship between error compensation and state variables. If the compensation is only added as a constant, its effect will be mitigated after linearization. For reference slip angle smaller than 0.0025, the error compensation is set to zero.

The friction ellipse constraint is adjusted in (7) based on the predicted dimensionless error at zero torque and maximum slip angle. Negative signs in (6) and (7) before g are because D_y has a negative value. For faster prediction, sparse GPR is adopted in this work. We refer the readers to [6] for more details.

$$\eta_c = \left[\frac{F_x}{\mu_c D_x F_{z,r}}^2 + \frac{F_{y,r}}{(\mu_c D_y - g(0, |\hat{\alpha}_{\text{max}}|)) F_{z,r}}^2 \right]^\top. \quad (7)$$

4 Algorithm Validation

4.1 Simulation and Experimental Setup

The simulation is performed on the racing track of Formula Student Autonomous China (FSAC) and executed on a laptop with an i7-12700H CPU and 32 GB RAM. We use a 7-DOF vehicle dynamics model [7] for simulation. The experiment is performed on a self-designed thin track with a steer-by-wire and drive-by-wire electric chassis and executed on a Jetson AGX Xavier with Carmel CPU. The directions of both tracks are clockwise. The following parameters are set to be the same for both the simulation and experiment: discretization step $\Delta t = 34$ ms, prediction horizon $H = 60$, and control horizon $H_c = 30$. Limited by the performance of Carmel CPU, the control frequency f is set to 100 Hz for simulation and 50 Hz for experiment.

4.2 Results

In the simulation, the proposed LTV-MPC is compared with an NMPC implemented using CasADi [1] with identical parameters. The NMPC also uses identical objectives and constraints (both nonlinear). The comparisons are plotted in Fig. 2, which shows the accuracy and improved computational speed of the proposed LTV-MPC. The lap time is 44.57 s for LTV-MPC and 44.29 s for NMPC (a slight increase of 0.6 %). The average computation time is 2.5 ms for LTV-MPC and 66 ms for NMPC (96 % reduction).

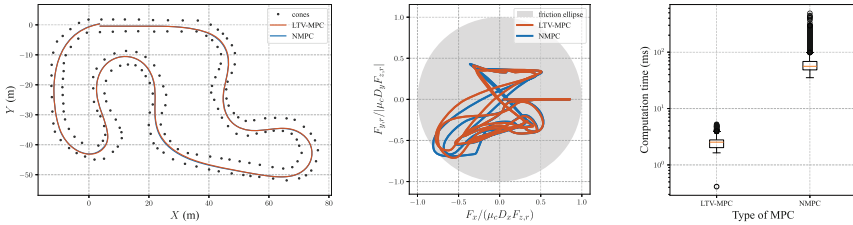


Fig. 2. Comparisons between the proposed LTV-MPC and NMPC on simulation trajectory, friction ellipse constraint violation, and computation time.

The robustness of the proposed LTV-MPC is validated in real-world experiments. The experiment data are exhibited in Fig. 3. The maximum velocity is set to 4 m/s and small adhesion coefficients are chosen for safety concerns.

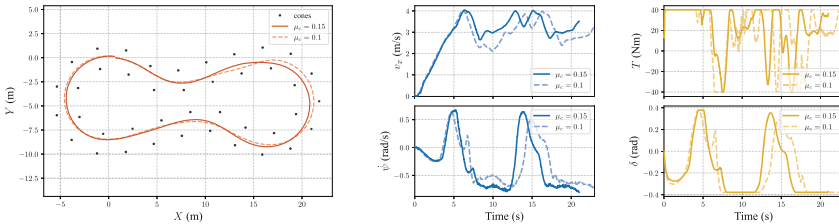


Fig. 3. Experimental trajectory and vehicle state plots with two different μ_c .

With μ_c set to 0.3, two simulation scenarios are used to validate the learning-based LTV-MPC: low adhesion (true adhesion coefficient is also 0.3 but with tire combined slip property not modeled in LTV-MPC) and higher adhesion (true adhesion coefficient is 0.7). The corresponding GP error models and the effects in mitigating model mismatch are shown in Fig. 4. The lap time in the low adhesion scenario is 44.57 s without GPR and 44.64 s with GPR (safer after learning the combined slip property). The lap time in the higher adhesion scenario is 44.16 s without GPR and 43.23 s with GPR (2% faster after learning).

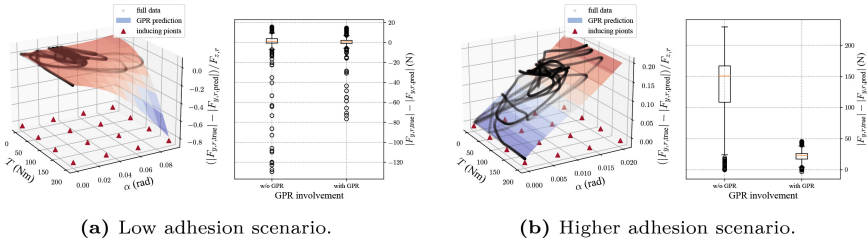


Fig. 4. GPR error models and the effects in mitigating model mismatch.

5 Conclusions

This work first presents a time-optimal LTV-MPC with min-time objective function and friction ellipse constraint. The proposed LTV-MPC is further combined with GPR to learn the lateral tire force error.

The efficiency, accuracy, and robustness of the proposed LTV-MPC are validated in simulation and experiment. The GPR error model successfully learns from the simulation data and improves the control performance. Experimental validation of the learning-based LTV-MPC will be performed in our future work.

References

- Andersson, J.A.E., Gillis, J., Horn, G., Rawlings, J.B., Diehl, M.: CasADi: a software framework for nonlinear optimization and optimal control. *Math. Progr. Comput.* **11**(1), 1–36 (2019). <https://doi.org/10.1007/s12532-018-0139-4>
- Kabzan, J., Hewing, L., Liniger, A., Zeilinger, M.N.: Learning-based model predictive control for autonomous racing. *IEEE Rob. Autom. Lett.* **4**(4), 3363–3370 (2019). <https://doi.org/10.1109/LRA.2019.2926677>
- Li, N., Goubault, E., Pautet, L., Putot, S.: A real-time NMPC controller for autonomous vehicle racing. In: 2022 6th International Conference on Automation, Control and Robots (ICACR). pp. 148–155 (Sep 2022). <https://doi.org/10.1109/ICACR55854.2022.9935523>
- Maciejowski, J.M.: Predictive Control: With Constraints. Prentice-Hall, Harlow, UK (2002)
- Scheffe, P., Henneken, T.M., Kloock, M., Alrifaaee, B.: Sequential convex programming methods for real-time optimal trajectory planning in autonomous vehicle racing. *IEEE Trans. Intell. Veh.* **8**(1), 661–672 (2023). <https://doi.org/10.1109/TIV.2022.3168130>
- Snelson, E.L.: Flexible and Efficient Gaussian Process Models for Machine Learning. University of London, London (UK) (2008)
- Yu, H., Castelli-Dezza, F., Cheli, F.: Optimal powertrain design and control of a 2-IWD electric race car. In: 2017 International Conference of Electrical and Electronic Technologies for Automotive. pp. 1–7 (Jun 2017). <https://doi.org/10.23919/EETA.2017.7993206>


Open Access This chapter is licensed under the terms of the Creative Commons Attribution 4.0 International License (<http://creativecommons.org/licenses/by/4.0/>), which permits use, sharing, adaptation, distribution and reproduction in any medium or format, as long as you give appropriate credit to the original author(s) and the source, provide a link to the Creative Commons license and indicate if changes were made.

The images or other third party material in this chapter are included in the chapter's Creative Commons license, unless indicated otherwise in a credit line to the material. If material is not included in the chapter's Creative Commons license and your intended use is not permitted by statutory regulation or exceeds the permitted use, you will need to obtain permission directly from the copyright holder.





Speed Profile Definition for GLOSA Implementation on Buses Based on Statistical Analysis of Experimental Data

Daniele Vignarca^(✉) , Stefano Arrigoni , Edoardo Sabbioni ,
and Federico Cheli 

Department of Mechanical Engineering, Politecnico di Milano,
Via La Masa 1, Milan 20156, Italy
daniele.vignarca@polimi.it

Abstract. The latest advancements in vehicle automation have revealed significant potential for enhancing traffic management via Advanced Driver Assist Systems (ADAS), benefiting both safety and environmental considerations. Green Light Optimal Speed Advisory (GLOSA) systems represent a significant application in the Cooperative-Intelligent Transportation System (C-ITS) field adopting Vehicle-to-Everything (V2X) communication technology. The literature nowadays addresses quite extensively the GLOSA, and C-ITS in general, for conventional vehicles like cars. At the same time, there is emerging research starting to involve also the public transportation vehicles within this framework. The focus for buses is typically posed either on the comfort and regularity of the service for passengers or on the energy consumption which is reduced by adopting suitable speed profiles for the vehicle, thus avoiding unnecessary stops. This work presents a statistical analysis based on experimental data collected in real-world urban scenarios over one entire year. The outcome of this analysis allows the design of speed profiles typical for a public transportation vehicle, accounting for features such as the bus stop station for getting passengers off and on.

Keywords: Bus · GLOSA · statistics · ITS · speed profile

1 Introduction

The latest advancements in vehicle automation have revealed significant potential for enhancing traffic management via Advanced Driver Assist Systems (ADAS), benefiting both safety and environmental considerations. Green Light

This work is part of the project “Joint Research Lab per la Mobilità urbana”. A particular acknowledgment goes to Azienda Trasporti Milanese S.p.A. and Comune di Milano for the possibility of performing the road testing campaign, as well as Vodafone Italia S.p.A. and Vodafone Automotive for the design and development of the communication architecture.

Optimal Speed Advisory (GLOSA) systems represent a significant application in the Cooperative-Intelligent Transportation System (C-ITS) field adopting Vehicle-to-Everything (V2X) communication technology [9]. Specifically, Green Light Optimal Speed Advisory (GLOSA) systems present an opportunity by providing real-time speed recommendations to vehicles, aiming to synchronize their movement with traffic light timings. This synchronization not only reduces fuel consumption, emissions, and travel time but also improves overall traffic flow [1, 8]. However, current GLOSA implementations predominantly target private vehicles, lacking the necessary customization to deal with urban bus peculiarities and its interaction with the infrastructure.

The literature nowadays addresses quite extensively the GLOSA, and C-ITS in general, for conventional vehicles like cars. At the same time, within this framework, there is emerging research starting to involve also the public transportation vehicles. The focus for buses is typically posed either on the comfort and regularity of the service for passengers [6] or on the energy consumption which is reduced by adopting suitable speed profiles for the vehicle, thus avoiding unnecessary stops [7]. [13] introduced an eco-driving strategy tailored for connected electric buses at signalized intersections, incorporating bus stops to underscore the advantages of multi-objective optimization in reducing energy consumption. In [3] energy-saving profile planning for connected and automated electric buses is addressed, leveraging non-linear programming techniques to optimize speed profiles while considering motor characteristics. Beyond adjusting vehicle speed via GLOSA systems, alternative approaches like Transit Signal Priority (TSP) systems aim to extend traffic light green times and reduce red times during bus intersection negotiations [11]. Additionally, the concept of Green Light Optimal Dwell Time Advisory (GLODTA) suggests increasing bus dwell time at stops [2]. Many studies advocate for a combined approach [5, 10, 14], aiming to harness the comprehensive benefits of multiple systems.

In terms of modeling bus trajectories, [7] distinguishes between the impact areas of bus stops and signalized intersections, ultimately formulating an optimization problem aimed at minimizing energy consumption through the use of the Dijkstra algorithm. The authors in [13] provide instead a comprehensive description of the bus stop negotiation process, taking into account the necessary time required for the vehicle to decelerate approaching the stop and to accelerate upon resuming its journey. All these studies showcase the increasing interest and progress in refining speed advisory systems for urban buses, highlighting the importance of customized strategies to enhance energy efficiency as well as passengers' comfort within public transportation networks.

This work presents a statistical analysis based on experimental data collected in real-world urban scenarios over one entire year. The outcome of this analysis allows the design of speed profiles typical for a public transportation vehicle, accounting for features such as the bus stop station for getting passengers off and on. The main contributions of the paper are the following:

- Report real-world statistical data in terms of dwell time at different bus stops for different clusters based on the day of the week and time of the day.

- Define a set of suitable speed profiles for GLOSA implementation on buses (B-GLOSA), based on real vehicle parameters such as acceleration/deceleration as well as dwell time available from the statistical analysis.

The remainder of the paper is organized as follows: after the description in Sect. 2 of the experimental setup used for the data acquisition during the regular service of the bus, the statistical analysis of the collected data is presented in Sect. 3. Section 4 is then devoted to proposing different possible speed profiles for GLOSA implementation as in [4] that can be designed based on the aforementioned statistical analysis. Finally, Sect. 5 concludes the work and indicates possible future developments.

2 Experimental Data Acquisition

This section presents the experimental setup for data acquisition during the vehicle's regular passenger service on the road. In particular, the vehicle shown in Fig. 1 is equipped with a Global Positioning System (GPS), an Inertia Measurement Unit (IMU), and the connection with the CAN-bus is established to read information coming from ECU such as vehicle speed and doors status. These data are used for vehicle localization presented in [12], as ego-vehicle position is then used to identify the bus stops present on the path. As far as the data acquisition is concerned, the following elements have been enclosed into a compact architecture: (a) a computational unit (Intel NUC Core i7 1165G7), operating on a soft real-time-based architecture using Robotic Operating System (ROS); (b) a 4 TB hard disk for data storage; (c) a 5G modem for internet connection; (d) a multi-port switch for the connection with sensors. All these devices, as well as the sensors, are powered by the 24 V battery module for auxiliaries existing on the vehicle.

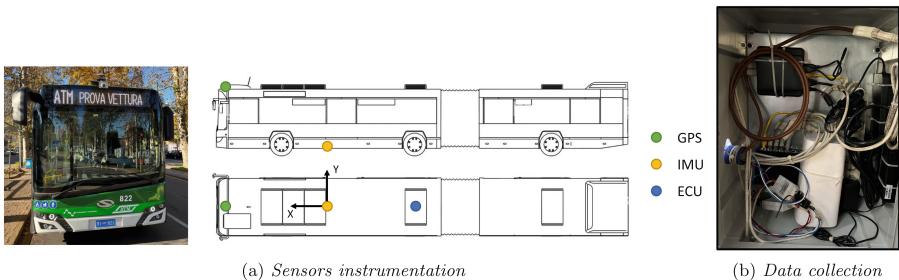


Fig. 1. Schematics of the sensor and data acquisition setup on the vehicle.

3 Statistical Analysis

The present section is intended to report the results of the statistical analysis conducted on the basis of the data collected throughout the whole year. Indeed, the focus is on the dwell time the vehicle spends in correspondence with the 16 bus stops along the considered route (i.e., a portion of the route followed by the circular trolley-bus line 90/91 which goes around the city of Milan). Thanks to vehicle localization and the date-time reconstruction from recorded timestamps, it was possible to identify the bus stops along the path and cluster the dwelling times. It is worth mentioning on the one hand that the stop condition is detected by the combined matching of the following three conditions: (1) vehicle position located in the ± 20 m around the bus stop position; (2) null vehicle speed and (3) opening of at least one of the four doors for passengers. On the other hand, samples associated with a stop duration shorter than 5 s and longer than 30 s are discarded, as they most likely are either not significant or affected by external factors.

As mentioned, the data are categorized according to the day of the week and the time of the day. In particular, the weekdays are divided into the following four clusters: (1) **h 7-10**; (2) **h 10-16**; (3) **h 16-19**; (4) **h 19-7**. These clusters are associated with different peak and off-peak hours for workers and students. During the weekend days, the day hours are divided just for the morning (i.e., **h 7-13**) and the afternoon (i.e., **h 13-19**), keeping the same cluster for the night hours (i.e., **h 19-7**). Each cluster is then fitted using a Generalized Extreme Value (GEV) distribution, described by a mean value μ and a standard deviation σ . As an example, Fig. 2 reports the distributions for each cluster of one of the most crowded stops along the path (i.e., in correspondence of the central railway station).

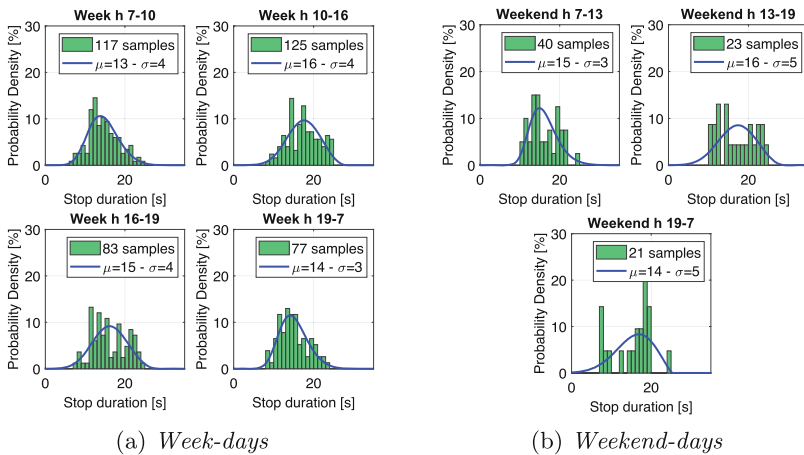


Fig. 2. GEV distribution fitting for different clusters at bus stop number 10 (i.e., central railway station).

Table 1 summarizes the results of the measured dwelling time for the clusters mentioned above, for all the 16 bus stops considered, reporting the mean of the dwelling time, as well as its standard deviation. It is worth specifying that for some bus stops, especially when dealing with the weekend clusters, the data are not reported as the number of significant samples was limited or badly distributed, making the GEV fitting unreliable. As can be observed from the statistical data, some trends with the time of the day can be barely inferred. Indeed, the central hours of the day (i.e., **h 10-16**) are characterized by a higher flow of passengers, making the dwelling time longer on average. On the other hand, there seems to be a not-so-evident difference between week-days and weekend-days, as the route is part of a quite busy portion of the city with a considerable amount of passengers throughout the whole day.

Table 1. Dwell time statistical data for different clusters.

	Week												Weekend											
	h 7-10			h 10-16			h 16-19			h 19-7			h 7-13			h 13-19			h 19-7					
	μ [s]	σ [s]	N	μ [s]	σ [s]	N	μ [s]	σ [s]	N	μ [s]	σ [s]	N	μ [s]	σ [s]	N	μ [s]	σ [s]	N	μ [s]	σ [s]	N			
Stop 1	12	4	97	13	4	175	14	3	121	13	3	105	14	4	61	14	4	46	13	4	28			
Stop 2	11	4	110	14	4	175	14	4	108	12	4	92	12	4	59	13	4	46	13	4	29			
Stop 3	14	4	92	14	4	135	13	3	98	12	3	96	12	3	57	12	3	44	13	4	29			
Stop 4	12	4	103	12	3	143	12	3	106	11	3	93	11	3	49	12	3	35	12	3	28			
Stop 5	14	5	95	16	4	159	16	4	104	15	4	94	17	4	50	-	-	34	15	5	27			
Stop 6	12	4	92	12	4	122	12	4	72	11	3	66	11	3	36	14	4	40	-	-	9			
Stop 7	14	4	119	15	4	190	13	3	117	13	4	96	15	4	42	16	5	36	14	4	21			
Stop 8	11	3	114	10	3	153	10	3	106	10	2	83	9	2	38	10	2	43	11	3	15			
Stop 9	12	3	98	14	4	154	12	4	103	11	3	97	11	3	46	13	4	52	11	3	26			
Stop 10	13	4	117	16	4	125	15	4	83	14	3	77	15	3	40	16	5	23	14	5	21			
Stop 11	11	3	104	13	3	175	12	4	102	11	3	82	13	4	46	13	4	32	13	3	25			
Stop 12	15	4	94	14	4	78	13	3	73	14	4	75	13	3	44	14	4	40	12	2	22			
Stop 13	11	3	99	12	3	152	11	3	113	10	3	92	10	3	47	11	3	47	10	2	17			
Stop 14	13	5	100	16	5	123	16	5	92	17	5	72	-	-	36	14	6	35	-	-	16			
Stop 15	11	3	108	10	2	157	10	2	111	9	2	91	9	2	43	10	2	47	10	2	24			
Stop 16	12	3	108	12	4	139	11	3	107	11	3	77	11	3	48	10	2	44	12	4	20			
Mean	12	4		13	4		13	3		12	3		12	3		13	4		12	3				

4 Speed Profile Definition

As reported in the previous section, the information about the dwell time for every bus stop as a function of the date-time opens the possibility of designing speed profiles suitable for GLOSA implementation of public transport vehicles such as buses (B-GLOSA). In this case, the vehicle motion optimization has to consider that it is going to stop for sure at a given known point. Moreover, common GLOSA algorithms typically look for an optimal speed allowing the vehicle to cross the upcoming intersection with the green light is on. Within this process, the dwelling time of the bus is an additional variable to be taken into account when dealing with B-GLOSA design. As a result, having on this

quantity a robust statistics to rely on, allows simplifying the modeling taking as a reasonable assumption a known constant dwelling time.

In this paper, four different possible speed profiles are proposed to address the B-GLOSA implementation. For the speed profile design, these quantities are assumed to be known: initial vehicle state (i.e., location along the path and speed), traffic light phases (i.e., minimum and maximum time available to reach the intersection with green light), bus stop location and corresponding dwell time (i.e., coming from statistics presented in Sect. 3), vehicle speed and acceleration limits (i.e., for both passengers safety and comfort issues). As far as the most suitable speed profile is concerned, it can be split into two sections: an initial one from the initial point to the bus stop and a final one from the bus stop up to the upcoming intersection. Each of these two sections is assumed to be either a simple uniformly accelerated motion or a uniformly accelerated motion followed by a constant speed motion. As a result, combining these options together, the four possible speed profiles shown in Fig. 3 are:

- **P1**: uniform acceleration - brake - dwell - uniform acceleration;
- **P2**: uniform acceleration - brake - dwell - uniform acceleration - constant speed;
- **P3**: uniform acceleration - constant speed - brake - dwell - uniform acceleration;
- **P4**: uniform acceleration - constant speed - brake - dwell - uniform acceleration - constant speed.

It is worth highlighting that, since the acceleration for the second section of the profile (i.e., from stop to intersection) is fixed, the whole section is constrained by the geometric characteristic of the path (i.e., the distance between stop and traffic light). As a consequence, depending on this information the chosen profile (in terms of final speed v_a) will either have a constant speed part (i.e., P2/P4) or not (i.e., P1/P3) as described in the flowchart in Fig. 4a, being the speed limit set to 40 km.h^{-1} for safety reasons.

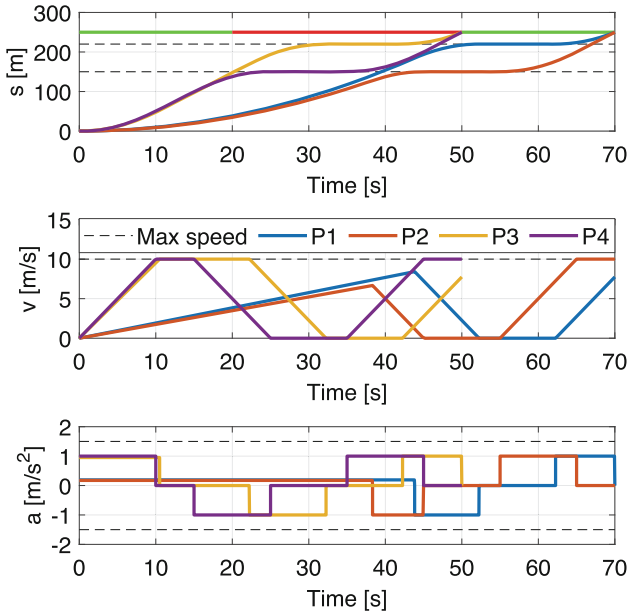


Fig. 3. Designed possible speed profiles.

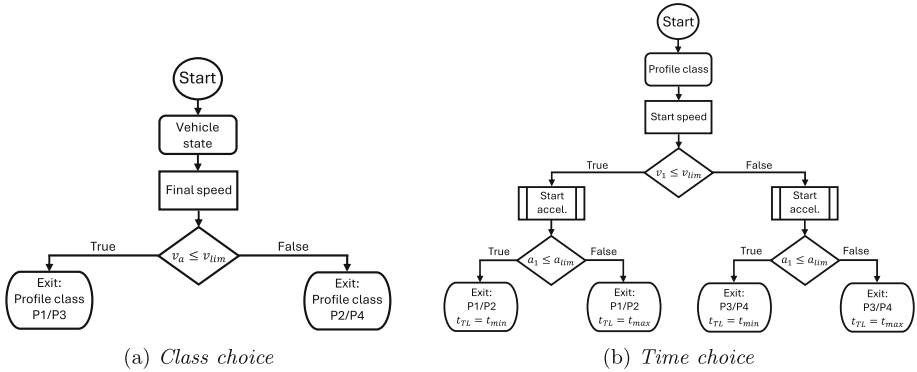


Fig. 4. Speed profile choice flowcharts.

Besides the topology of the route, the most affecting parameter is the time available to reach the intersection within the green light phase. In fact, to prioritize travel time reduction, the profile is designed so that the vehicle reaches the intersection at the switching time from red to green. The process followed for the timing choice is detailed in the flowchart reported in Fig. 4b, being constrained the deceleration (i.e., -1 m.s^{-2}) and the acceleration of the final section (i.e., -1 m.s^{-2}). As a consequence of these assumptions, the remaining free variable for the speed profile design is the acceleration a_1 in the initial stage from the

initial condition to the start of the braking manoeuvre. To calculate the start acceleration a_1 and the start speed v_1 reached in the first section of the profile, the set of equations related to the uniformly accelerated motion is solved. As a first step, to minimize the travel time the system is calculated with the minimum traffic light time available $t_{TL} = t_{min}$. Otherwise if the speed and acceleration limits are not respected the maximum time available is considered.

5 Conclusion

This research paper presented a robust statistical analysis based on real-world data collection throughout an entire year from an instrumented trolley bus during its regular passenger service. The outcome of these statistical results in terms of average dwelling time at the bus stop represented the basis for the speed profile definition when dealing with the implementation of a Green Light Optimal Speed Advisory system applied to local public transportation vehicles. In particular, four different speed profiles have been proposed leveraging topographic, vehicle performances, and timing constraints. The availability of such a great amount of data from a bus real service allows to perform further and deeper analysis of the data collected on the road, thus representing a straightforward future development for this activity. On the other hand, the implementation and testing, both numerical and experimental, of a GLOSA system based on the proposed speed profiles would give the possibility to assess them from a quantitative point of view.

References

1. Asadi, M., Fathy, M., Mahini, H., Rahmani, A.M.: A systematic literature review of vehicle speed assistance in intelligent transportation system. *IET Intell. Transp. Syst.* **15**, 973–986 (2021). <https://doi.org/10.1049/itr2.12077>
2. Gallo, F., Sacco, N.: On optimizing bus dwell times to reduce the probability of stopping for a red light at intersections. In: 2022 IEEE 25th International Conference on Intelligent Transportation Systems (ITSC). vol. 2022-October, pp. 1637–1644 (2022). <https://doi.org/10.1109/ITSC55140.2022.9922295>
3. Ji, J., Bie, Y., Shi, H., Wang, L.: Energy-saving speed profile planning for a connected and automated electric bus considering motor characteristic. *J. Cleaner Prod.* **448**, 141721 (2024). <https://doi.org/10.1016/j.jclepro.2024.141721>
4. Khayyat, M., Gabriele, A., Mancini, F., Arrigoni, S., Braghin, F.: Enhanced traffic light guidance for safe and energy-efficient driving: a study on multiple traffic light advisor (mtla) and 5g integration. *J. Intell. Robot. Syst.ms* **110**, 73 (2024). <https://doi.org/10.1007/s10846-024-02110-6>
5. Seredynski, M., Laskaris, G., Viti, F.: Analysis of cooperative bus priority at traffic signals. *IEEE Trans. Intell. Transp. Syst.* **21**, 1929–1940 (2020). <https://doi.org/10.1109/TITS.2019.2908521>
6. Seredynski, M., Ruiz, P., Szczypiorski, K., Khadraoui, D.: Improving bus ride comfort using glosa-based dynamic speed optimisation. In: 2014 IEEE International Parallel & Distributed Processing Symposium Workshops. pp. 457–463 (2014). <https://doi.org/10.1109/IPDPSW.2014.58>

7. Shan, X., Wan, C., Hao, P., Wu, G., Zhang, X.: Connected eco-driving for electric buses along signalized arterials with bus stops. *IET Intell. Transp. Syst.* **17**, 575–587 (2023). <https://doi.org/10.1049/itr2.12285>
8. Simchon, L., Rabinovici, R.: Real-time implementation of green light optimal speed advisory for electric vehicles. *Vehicles* **2**, 35–54 (2020). <https://doi.org/10.3390/vehicles2010003>
9. Stahlmann, R., Müller, M., Brauer, A., German, R., Eckhoff, D.: Exploring glosa systems in the field: Technical evaluation and results. *Computer Communications* **120**, 112–124 (5 2018). <https://doi.org/10.1016/j.comcom.2017.12.006>
10. Teng, K., Liu, H., Liu, Q., Lu, X.: A cooperative control method combining signal control and speed control for transit with connected vehicle environment. *IET Control Theory Appl.* (2023). <https://doi.org/10.1049/cth2.12608>
11. Truong, L.T., Currie, G., Wallace, M., Gruyter, C.D., An, K.: Coordinated transit signal priority model considering stochastic bus arrival time. *IEEE Trans. Intell. Transp. Syst.* **20**, 1269–1277 (2019). <https://doi.org/10.1109/TITS.2018.2844199>
12. Vignarca, D., Arrigoni, S., Sabbioni, E.: Vehicle localization kalman filtering for traffic light advisor application in urban scenarios. *Sensors* **23**(15), 6888 (2023). <https://doi.org/10.3390/s23156888>
13. Zhang, Y., Fu, R., Guo, Y., Yuan, W.: Eco-driving strategy for connected electric buses at the signalized intersection with a station. *Transp. Res. Part D Transp. Environ.* **128**, 104076 (2024). <https://doi.org/10.1016/j.trd.2024.104076>
14. Zimmermann, L., Coelho, L.C., Kraus, W., Carlson, R.C., Koehler, L.A.: Bus trajectory optimization with holding, speed and traffic signal actuation in controlled transit systems. *IEEE Access* **9**, 143284–143294 (2021). <https://doi.org/10.1109/ACCESS.2021.3122087>

Open Access This chapter is licensed under the terms of the Creative Commons Attribution 4.0 International License (<http://creativecommons.org/licenses/by/4.0/>), which permits use, sharing, adaptation, distribution and reproduction in any medium or format, as long as you give appropriate credit to the original author(s) and the source, provide a link to the Creative Commons license and indicate if changes were made.

The images or other third party material in this chapter are included in the chapter's Creative Commons license, unless indicated otherwise in a credit line to the material. If material is not included in the chapter's Creative Commons license and your intended use is not permitted by statutory regulation or exceeds the permitted use, you will need to obtain permission directly from the copyright holder.





Longitudinal Control Concept for Automated Vehicles in Stop-and-Go Situations

C. Pethe^(✉), M. Heinze, M. Flormann, and R. Henze

Institute of Automotive Engineering, TU Braunschweig, Braunschweig, Germany
c.pethe@tu-bs.de

Abstract. This paper presents a longitudinal control concept for automated vehicles in stop-and-go situations that enables the optimization of driving behavior in terms of occupant comfort and traffic efficiency. In a simulative validation based on real driving data, different variants are evaluated on the basis of objective criteria and an optimal functional behavior is derived.

Keywords: longitudinal control · stop-and-go · occupants comfort · traffic efficiency · adaptive cruise control · AD parametrization

1 Introduction

There has been great technical progress in automated driving. In terms of user acceptance, the question of optimum functional behavior is increasingly being raised, with the focus largely on occupant comfort [1, 2].

Using the example of stop-and-go situations, it is shown that the entire 3D parameter space [3] (driver, driven vehicle, driving environment) should be taken into account when designing automated driving behavior. Therefore, a follow-up driving controller is presented that can be optimized both in terms of occupant comfort and traffic efficiency in stop-and-go situations. Different variants of the controller are analyzed objectively and a recommendation for an optimal functional behavior is derived.

2 Stop-and-Go Follow-Up Control

The following vehicle controller is designed on the basis of findings from 20 h of real driving data in stop-and-go traffic and relates to the longitudinal control of an ego vehicle behind an object vehicle in front.

2.1 Follow-Up Concept

The basic idea behind the following distance control for automated vehicles in stop-and-go situations presented here is, to soften the conventional adaptive cruise control (ACC) follow-up concept with the aim of maintaining a constant time gap in favor of larger absolute distances, depending on the driving situation. These are used in the

further course of the journey to compensate higher object dynamics, by allowing the ego vehicle to approach a more decelerating object vehicle with less deceleration instead of also decelerating sharply immediately.

With further increasing distances or large relative velocity of the object vehicle, an increase in ego dynamics ensures that the absolute object distance does not exceed selectable limits, which benefits overall traffic efficiency [4].

2.2 Follow-Up Control Using MPC

The tracking controller is based on an MPC acceleration controller, that was parameterized very defensively with the help of auxiliary conditions that mainly concern a reduction of the longitudinal acceleration of the ego vehicle. The parameterization of the dynamic MPC model is based on [5] and is completely unchanged for different function variants.

With the relative speed Δv_x between object and ego vehicle and the distance error Δd , which describes the deviation between the current and desired distance based on safety distance and time gap (Eqs. 1, 2), the driving state under consideration is obtained according to Eq. (3).

$$\Delta v_x = v_{object} - v_{ego} \quad (1)$$

$$\Delta d = d - t_{gap} * v_{ego} + d_0 \quad (2)$$

$$\vec{x} = \begin{bmatrix} \Delta d \\ \Delta v_x \\ a_{ego} \\ v_{ego} \end{bmatrix} \quad (3)$$

Since the desired acceleration of the follow-up controller $a_{ego,MPC}$ does not affect the vehicle directly, the longitudinal dynamics are approximated by a first-order delay with the proportional factor K_L and the time constant T_L , so that the state equation is summarized according to Eqs. (4) and (5). For use in real-time simulation, the continuous-time state equation is discretized using Euler forward method [6].

$$\dot{\vec{x}}(t) = \begin{bmatrix} \Delta \dot{d}(t) \\ \Delta \dot{v}_x(t) \\ \dot{a}_{ego}(t) \\ \dot{v}_{ego}(t) \end{bmatrix} = \begin{bmatrix} 0 & 1 & -t_{gap} & 0 \\ 0 & 0 & -1 & 0 \\ 0 & 0 & -1/T_L & 0 \\ 0 & 0 & 1 & 0 \end{bmatrix} \begin{bmatrix} \Delta d(t) \\ \Delta v_x(t) \\ a_{ego}(t) \\ v_{ego}(t) \end{bmatrix} + \begin{bmatrix} 0 \\ 0 \\ K_L/T_L \\ 0 \end{bmatrix} a_{ego,MPC}(t) + \begin{bmatrix} 0 \\ 1 \\ 0 \\ 0 \end{bmatrix} a_{object}(t) \quad (4)$$

$$\vec{y}(t) = I_4 * \vec{x}(t) \quad (5)$$

2.3 Target Velocity Depending on Driving Status

The different driving behavior of various function variants is realized exclusively by the target speed setting; the MPC controller and the associated auxiliary conditions and factor weightings remain constant.

In contrast to conventional ACC, the target velocity is not selected by the driver but according to the driving situation (Fig. 1). The evaluation of 20 h of real stop-and-go situations on German highways, including the ego driving behavior as well as target object data, has shown that the average speed is less than 3.24 m/s in 75% of cases and less than 11.58 m/s in 90% of cases. On this basis, the maps shown in Fig. 1 were generated.

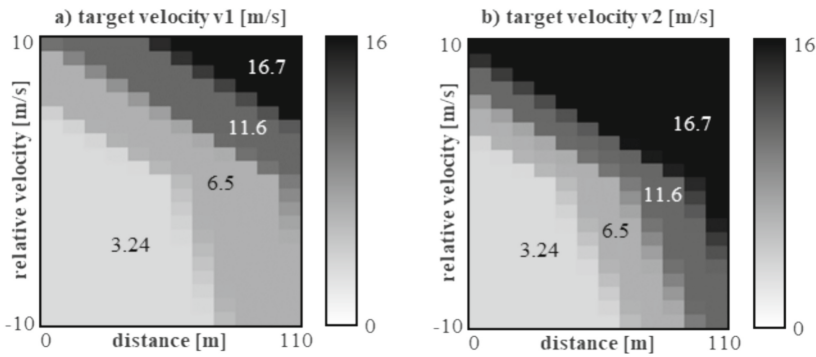


Fig. 1. Defensive (v1) and dynamic (v2) map for selecting target speed

The target velocity for the MPC longitudinal controller is selected depending on the distance and relative speed to the object vehicle in front. Figure 1 shows the limit curves between the target velocity ranges. These are mathematically formulated in such a way that different characteristic maps and thus different ego behavior can be achieved by adjusting five parameters. In principle, an increase in the ego dynamics requires a shift of the limit curves in the direction of smaller abscissa and/or ordinate values.

3 Validation

The longitudinal controller presented here is validated on the basis of several objective criteria for occupant comfort and traffic efficiency. The simulations are carried out on the basis of real measured object vehicle speeds in stop-and-go traffic.

Figure 2 shows an example of the simulated driving behavior for a defensive and a dynamic parameterization of the target speed map. It becomes clear that there is a trade-off between high comfort (low ego dynamics, v1) and high traffic efficiency (good following behavior, low object distances, v2).

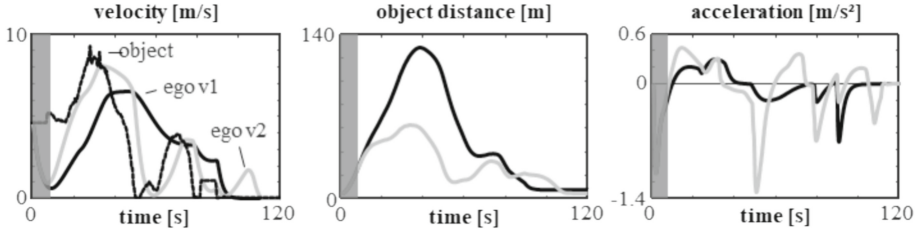


Fig. 2. Defensive (v1) and dynamic (v2) configuration of the longitudinal controller

3.1 Evaluation Criteria

Evaluation criteria are defined below for further objective analyses of the longitudinal controller. These are based on the longitudinal dynamics of the ego vehicle and the following behavior in relation to the object vehicle in front. This addresses occupant comfort and energy consumption of the ego vehicle on the one hand and traffic efficiency on the other, adding aspects from all areas of the 3D parameter space [3].

Based on the relationship between the longitudinal acceleration and the energy consumption of the ego vehicle [7], the parameter A_{ENERGY} is calculated as a measure of energy efficiency according to Eq. (6):

$$A_{ENERGY} = \frac{\int |a_{ego}| dt}{t_{SZENARIO}} \quad (6)$$

According to an internal evaluation of real driving data in the low speed range up to 60 km/h, the probability of incoming vehicles in the front area increases significantly if the distance to the object vehicle in front exceeds 45 m. An incoming vehicle in the front area leads to a deceleration of the ego vehicle and thus possibly to reduced driving comfort and reduced traffic efficiency [4, 8]. The integral of critical distances $D_{CUT IN}$ is therefore calculated according to Eq. 7:

$$D_{CUT IN} = \frac{\int (d \geq 45 m) dt}{t_{SZENARIO}} \quad (7)$$

For the objective analysis of driving comfort, critical [9, 10] accelerations and decelerations are integrated in $A_{COMFORT}$ (8) and the overall jerk of the ego vehicle in $J_{COMFORT}$ (9):

$$A_{COMFORT} = \frac{\int (a_{ego} \geq 0, 14 \frac{m}{s^2}) dt + \int (a_{ego} \leq -0, 25 \frac{m}{s^2}) dt}{t_{SZENARIO}} \quad (8)$$

$$J_{COMFORT} = \frac{\int |j_{ego}| dt}{t_{SZENARIO}} \quad (9)$$

3.2 Evaluation of Variants

For the objective evaluation of the functional variants presented, a representative scenario is derived from the 3D real driving data in the form of an acceleration curve of the object

vehicle in front, which was calculated from the relative velocity from the real driving data. The ego behavior in this scenario was then simulated.

For better comparability, the calculated parameters are normalized according to Eq. (10). By subtracting the normalized parameter value from 1, the normalized parameter x_{SCALED} is maximized for results to be evaluated as positive.

$$x_{SCALED} = 1 - \frac{x - x_{min}}{x_{max} - x_{min}} \tag{10}$$

The results are shown in Fig. 3. The subjective trade-off between high comfort and high traffic efficiency from Fig. 2 is also objectively significant. Three functional variants are compared with each other and with human driving behavior from the above-mentioned database. The human behavior represents a comparison option and is not necessarily representative of all drivers since it is a random sample. In addition to the parameters above, the driving behavior is evaluated with consideration of the maximum object distance (d_{MAX}) and the absolute number of stops (N_{STOPS}).

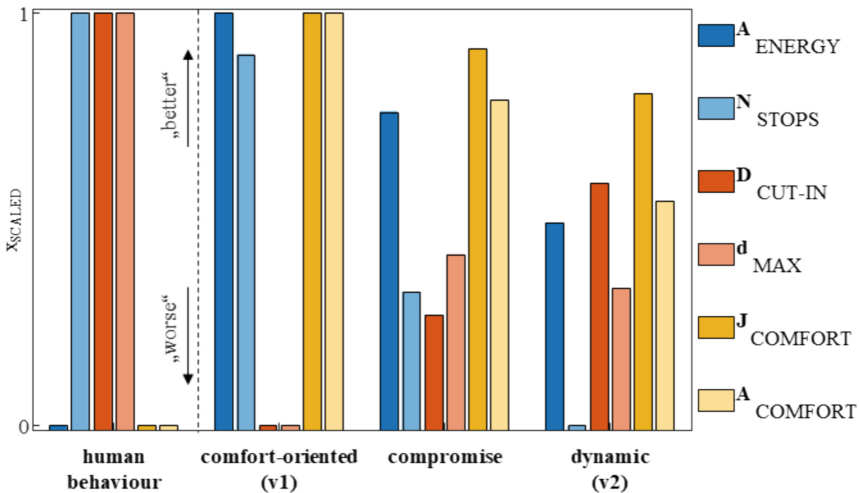


Fig. 3. Relative objective comparison of different function parameterizations

The human driving behavior shown has the worst energy efficiency and the lowest driving comfort. With regard to the number of stops and the object distance, the evaluation is best compared to the automated driving function.

Compared to the comfort-oriented variant of the automated driving function (v1), the dynamic variant (v2) shows a 21.2% reduction in jerk-related comfort and a 46.5% reduction in acceleration-related comfort. In contrast, the evaluation of the object distances is better with the dynamic variant. The maximum distance is 31.6% less and the time share of critical distances over 45 m is 61% less. The energy efficiency of the dynamic variant is 52.2% lower than that of the comfort-oriented driving strategy. Finally, it can also be observed that the dynamic driving strategy results in a higher number of standstills of the ego vehicle.

Overall, the ability of humans to only have to stop completely rarely even with small object distances is obvious. This is achieved by overall higher accelerations, which in turn result in poor energy efficiency. The automated driving strategy presented shows a trade-off between ego acceleration (comfort) and object distances (traffic efficiency). This can be adjusted with the help of the target speed maps presented, so that an (individually) good compromise is achieved. Furthermore, higher energy efficiency can be realized.

4 Conclusion

This paper presents the concept for a follow-up control system for automated vehicles in stop-and-go situations. The driving strategy is based on a defensively parameterized MPC acceleration controller. The desired speed, depending on the distance and relative velocity to a leading object vehicle, is used to parametrize different function variants. It is shown that objectively significant differences in the following behavior for automated vehicles in stop-and-go situations can be achieved with this strategy.

However, it must be taken into account that the available database of 20 h is not yet large enough to be considered fully representative, so that this publication focuses on the basic methodology as well as the controlling concept and further work in terms of parametrization is necessary.

In the further work on the controller shown, also the user acceptance for the function variants presented is recorded by subjective evaluations within a subject study.

References

1. Reuber, B.: Kundenorientierte systemapplikation eines autobahnpiloten. Diss., TU Braunschweig (2020)
2. Krauns, F.: Automatisiertes fahren an stadtkreuzungen. Diss., TU Braunschweig (2022)
3. Küçükay, F.: Grundlagen der Fahrzeugtechnik. Springer, Wiesbaden (2022)
4. Treiber, M.: Aggression im Straßenverkehr – wie menschliches Fahrverhalten die Stautenstehung beeinflusst. Heidelberg University Publishing, Campus Media (2018)
5. Li, S.: Model predictive multi-objective vehicular adaptive cruise control. In: IEEE Transactions on Control Systems Technology Bd, vol. 19, Nr. 3, pp. 556–566 (2011)
6. Burden, L.: Numerical Analysis. Cengage Learning, Brooks/Cole (2011)
7. Barth, M.: Impact of aggressive driving behavior on fuel consumption. Transportation Research Record: J. Trans. Res. Board (2009)
8. Festner, M.: Objektivierete Bewertung des Fahrstils auf Basis der Komfortwahrnehmung bei hochautomatisiertem Fahren in Abhängigkeit fahrfremder Tätigkeiten. Diss., TU München (2019)
9. Müller, T.A.: Ermittlung vestibulärer Wahrnehmungsschwellen zur zielgerichteten Gestaltung der Fahrzeug-Längsdynamik. Diss., TU München (2016)
10. Eberl, T.: Charakterisierung und Gestaltung des Fahr-Erlebens der Längsführung von Elektrofahrzeugen. Diss., TU München (2014)

Open Access This chapter is licensed under the terms of the Creative Commons Attribution 4.0 International License (<http://creativecommons.org/licenses/by/4.0/>), which permits use, sharing, adaptation, distribution and reproduction in any medium or format, as long as you give appropriate credit to the original author(s) and the source, provide a link to the Creative Commons license and indicate if changes were made.

The images or other third party material in this chapter are included in the chapter's Creative Commons license, unless indicated otherwise in a credit line to the material. If material is not included in the chapter's Creative Commons license and your intended use is not permitted by statutory regulation or exceeds the permitted use, you will need to obtain permission directly from the copyright holder.





Inverse Approach to Vehicle Generalized Parameters for Individual Drives

Vladimir Vantsevich¹, Jesse Paldan¹(✉), David Gorsich², and Lee Moradi¹

¹ Worcester Polytechnic Institute, Worcester, MA 01609, USA

j.paldan@wpi.edu

² US Army DEVCOM GVSC, Warren, MI 48397, USA

Abstract. In this paper, a method is presented to determine the individual tire slippages and wheel circumferential forces/torques for vehicles with individually-driven wheels. The method is based on a system of parameters of individual wheels mathematically linked to the vehicle generalized parameters. The paper demonstrates an inverse approach on how the generalized parameters can be used to determine individual wheel parameters when the vehicle generalized parameters are given for a single, generalized wheel, whose kinematics and dynamics are equivalent to those of the vehicle. The method can be applied to improve terrain mobility and energy efficiency of autonomous ground vehicles, including planet rovers whose guidance systems do not take into consideration that the tire slippages and circumferential forces are different or should be different by determining individual parameters of the e-motors to provide maximum mobility or energy efficiency in a straight line motion.

Keywords: Vehicle Dynamics · Individual Drives · Mobility

1 Introduction

The distribution of forces among the wheels of has a critical impact on the performance of multi-wheel drive vehicles, especially off-road where terrain conditions under the wheels may be very different. For vehicles with a mechanical driveline system, the configuration of the driveline determines the nature of the power split. In electric vehicles with individual wheel motors, the power split is determined by control of the wheel motors. Different methods have been studied for such control, based on factors such as stability, reducing battery usage, and utilizing most efficient regions of the motor [1–4].

However, navigation and guidance systems of autonomous vehicles (including planet rovers) usually do not take in consideration that the tire slippages and wheel circumferential forces are different or should be different and therefore treat a vehicle as a single wheel. For application to such systems, this paper’s approach is to consider that single wheel as the generalized wheel in a system of generalized parameters, and then splits the given generalized parameters into individual parameters of the wheels with e-motors to provide max mobility or energy efficiency. The method is designed to be applied as part of a two-step process in which a vehicle’s navigation system determines an assigned

velocity and the generalized parameters are used to determine an optimal split of wheel forces which provide the best mobility or energy efficiency while fulfilling the required vehicle straight line motion. Therefore, an inverse scenario is simulated where the vehicle velocity or acceleration is assigned, and the wheel forces and tire slippages need to be computed.

Generalized parameters represent a reduced set of parameters or time-variant states taking the place of and replacing those of individual wheels for a group of wheels or the entire vehicle [5]. The generalized parameters include various properties of the wheel dynamics such as tire slippage and rolling radii. Each driving wheel (i.e., a wheel loaded with torque) has a theoretical velocity V_i which is lower than its actual velocity V_x because of the tire slip s_δ :

$$V_x = V_i^{(')} \left(1 - s_{\delta i}^{(')}\right) \tag{1}$$

Here, ‘ and ‘’ indicate left and right wheels and i indicates a pair of left and right wheels ($i = 1, n$). The theoretical velocity for a wheel is determined from its angular velocity ω_w

$$V_i^{(')} = \omega_{wi}^{(')} r_{wi}^{0(')} \tag{2}$$

where r_w^0 is the tire rolling radius in the driven mode (at zero wheel torque) which depends on the tire inflation pressure and normal reaction, which can influence the theoretical velocities at different wheels of a vehicle. Slippages of different tires at the left and right wheels can be different due to the different terrain conditions and driveline system characteristics. However, as seen from Eq. (1), V_x in Eq. (1) is the same for all the wheels and known as the actual vehicle velocity. Similarly to the tire slippages, the vehicle generalized slippage $s_{\delta a}$ characterizes the velocity drop from the vehicle’s theoretical velocity, V_a , to V_x , which as mentioned earlier is the same for all wheels

$$V_x = V_a(1 - s_{\delta a}) = \omega_0 r_a^0(1 - s_{\delta a}) \tag{3}$$

where r_a^0 is rolling radius of a hypothetical/generalized wheel in the driven mode. The generalized wheel has actual linear velocity V_x and rotates with angular velocity ω_0 . A set of mathematical equations based on the vehicle’s driveline system outline can be derived to link the generalized parameters of the vehicle to their individual wheels. For example, for a 4×2 vehicle in straight line motion with a mechanical driveline using an open differential and without wheel hub gears, the generalized slippage of the drive axle can be derived from the following equations. Equations (1) and (2) can be re-written as

$$V_x = \omega_w'' r_w^{0''} \left(1 - s_\delta''\right) = \omega_w' r_w^{0'} \left(1 - s_\delta'\right) \tag{4}$$

which leads to

$$\frac{\omega_w'}{\omega_w''} = \frac{r_w^{0''} \left(1 - s_\delta''\right)}{r_w^{0'} \left(1 - s_\delta'\right)} \tag{5}$$

The relationship between angular velocities of the three links of the open differential is

$$\omega_0 = \frac{\omega'_w + \omega''_w}{2} \quad (6)$$

Here, ω_0 is the angular velocity of the differential's case that is the same as the rotational speed of the generalized wheel. Thus, the generalized wheel is reduced to the case of the axle's differential. Equations (5) and (6) result in

$$\omega''_w = 2\omega_0 \frac{r_w^{0'}(1 - s'_\delta)}{r_w^{0'}(1 - s'_\delta) + r_w^{0''}(1 - s''_\delta)} \quad (7)$$

Using Eqs. (3), (4) and (7), the axle generalized slippage is derived as

$$s_{\delta ai} = 1 - \frac{(r_w^{0''} + r_w^{0'}) (1 - s'_\delta) (1 - s''_\delta)}{r_w^{0'}(1 - s'_\delta) + r_w^{0''}(1 - s''_\delta)} \quad (8)$$

Similar analysis can be used to derive generalized slippage of the vehicle and generalized parameters for other driveline configurations. The generalized parameters mathematically link kinematics of the wheels through the generalized wheel to that of the vehicle. By combining the individual wheels-generalized wheel kinematics equations with vehicle dynamics equations, the wheel and vehicle dynamics can be studied by analyzing and optimizing driveline systems for vehicle mobility and energy efficiency.

This paper introduces generalized parameters for an electric vehicle with individual wheel motors and develops a method to split vehicle generalized parameters modeled for the overall vehicle into parameters of individual wheels. The generalized vehicle parameters are mathematically linked to the individual wheels through introduced distribution factors. The split of individual wheel parameters is based on criteria for maximizing mobility or energy efficiency which can then be applied as reference signals to control the wheel motors.

2 Generalized Parameters of Individual Drives

Slippage proportional factors γ are introduced in Eq. (9) to link the vehicle generalized slippage to individual tire slippages.

$$s'_{\delta i} = \gamma_i s_{\delta a} \quad (9)$$

Tire slippages are related to their circumferential forces F_x through Eq. (10) [6]

$$F'_{xi} = \mu'_{pxi} R'_{zi} \left\{ 1 - \left(s'_{\delta ci} / 2s'_{\delta i} \right) \left[1 - \exp \left(-2s'_{\delta i} / s'_{\delta ci} \right) \right] \right\} \quad (10)$$

where μ_{px} is the peak friction coefficient, $s_{\delta c}$ is a characteristic slippage past which the slippage becomes increasingly nonlinear, and R_z is the wheel normal reaction.

Circumferential forces F_x are produced by the wheel torques T_w and are related by Eq. (11).

$$T_{wi}^{('')} = F_{xi}^{('')} r_{wi}^{0('')} \tag{11}$$

The circumferential force distribution factor ν is introduced to characterize the distribution of the total circumferential force among the driving wheels.

$$F_{xi}^{('')} = \nu_i^{('')} F_{x\Sigma} = \nu_i^{('')} R_{m\Sigma} \tag{12}$$

$R_{m\Sigma}$ is the total resistance to motion which includes forces such as rolling resistance, grade resistance, inertia force, and air drag that impede vehicle motion. The sum of circumferential forces $F_{x\Sigma}$ must equal the sum of motion resistance $R_{m\Sigma}$ for the vehicle to maintain its assigned speed. Factor ν is introduced to connect the tires' rolling radii in the driven mode to the vehicle generalized rolling radius r_a^0 , derived by relating the sum of wheel torques to the overall resistance to motion multiplied by r_a^0 .

$$r_a^0 = \sum \nu_i^{('')} r_{wi}^{0('')} \tag{13}$$

Using the above-introduced equations, an inverse approach to vehicle simulation is considered in this paper. V_x is assigned and generalized slippage can be computed using the actual and theoretical velocities and ground conditions. In this paper, the generalized slippage is treated as a given input generated without individual wheel control. Figure 1 shows generalized slippage for a 5482 kg 4×4 vehicle moving on stochastically generated terrain in an offline simulation at a constant speed of 10 mph. The terrain is a sandy loam field with naturally packed soil after tilling with a moisture content of about 10% and is generated to fit the exponential function in Eq. (10). Left and right terrain conditions are the same while the front and rear differ due to soil compaction.

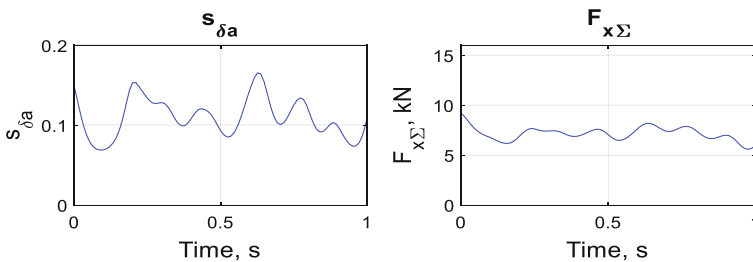


Fig. 1. Generalized slippage and total circumferential force on stochastic terrain.

Equations (9–13) split the generalized slippage into individual tire slippages which can be optimized for improved performance. Two optimal slippage configurations are considered in this paper, an optimal mobility case and optimal energy efficiency case. Slip energy efficiency is evaluated using Eq. (14); the slip efficiency of a 4×4 vehicle

was demonstrated to be maximum when the slips of the front and rear wheels are equal [5].

$$\eta_{\delta} = \frac{F_{x\Sigma}}{F_{x\Sigma} + \sum_{i=1}^n \left(\frac{F'_{xi} s'_{\delta i}}{1-s'_{\delta i}} + \frac{F''_{xi} s''_{\delta i}}{1-s''_{\delta i}} \right)} \quad (14)$$

The vehicle's mobility, considered as the conversion of the potential of the wheel loads into traction, occurs at a different combination of wheel traction forces than the maximum energy efficiency. Equation (15) is a Vehicle Mobility Performance index which was introduced to evaluate mobility relative to a hypothetical case where the complete potential of the wheel load can be converted into traction without any loss of velocity [7].

$$VMP = \frac{\sum_{i=1}^n F'_{xi} V_x + F''_{xi} V_x}{\sum_{i=1}^n R'_{zi} V'_{ti} + R''_{zi} V''_{ti}}, i = 1, 2 \quad (15)$$

Lagrangian optimization was used to determine the optimal slippages [7]. The optimal slippages and F_x forces with their corresponding circumferential forces are shown in Fig. 2. When the slippages are optimized for energy efficiency, it yields a different combination of circumferential forces than is needed for optimal mobility. Circumferential force distribution factors ν and slippage proportional factors γ from Eq. (9) and Eq. (12) needed for the optimal tire slippages are shown in Fig. 3.

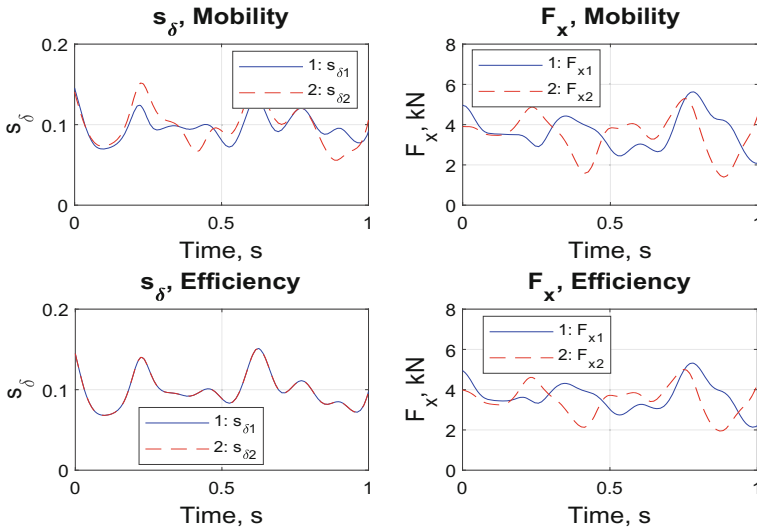


Fig. 2. Optimal slippages and circumferential forces for mobility and energy efficiency.

Compared to an equal torque split, the mobility-based power splits results in a mean VMP increase of 0.84% and the energy efficiency-based power split increases slip efficiency by 1.32% averaged over 10 simulation runs, which is a considerable improvement of mobility and energy efficiency.

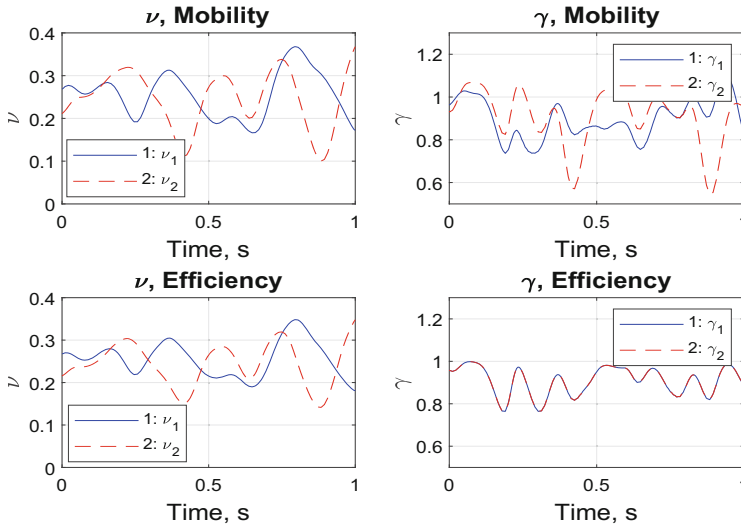


Fig. 3. Optimal ν and γ factors for mobility and energy efficiency.

3 Conclusion

In this paper, an inverse dynamics-based approach was presented which uses a system of generalized parameters to split a given generalized vehicle parameter into individual wheel parameters. The method is designed for optimizing the distribution of wheel forces when the vehicle motion is assigned without consideration of individual slippages (treating the vehicle as a single wheel). By applying conditions for optimal energy efficiency or mobility, the slippage proportional factors and circumferential force distribution factors can be computed which correspond to an optimized distribution of wheel forces and tire slippages that fulfils the assigned motion requirements of the vehicle. The generalized parameters for individual drives will be developed into reference signals for assigning e-motor wheel torques.

References

1. Zhang, B., Yu, Q., Wu, Y., Wang, C., Ma, S.: ISIGHT-based optimal analysis of torque distribution in the four-wheel drive system of electric vehicles. In: IEEE 6th Information Technology and Mechatronics Engineering Conference (ITOEC), pp. 2031–2035 (2022)
2. Lin, C., Liang, S., Chen, J., Gao, X.: A multi-objective optimal torque distribution strategy for four in-wheel-motor drive electric vehicles. *IEEE Access* **7**, 64627–64640 (2019)
3. Cao, K., Hu, M., Chen, L., Zhao, J., Xiao, Z.: Research on optimal economic dynamic torque distribution strategy for dual-motor four-wheel-drive considering voltage variation of power battery. *J. Energy Storage* **86**, 111006 (2024)
4. Xu, T., Zhao, Y., Deng, H., Guo, S., Li, D., Lin, F.: Integrated optimal control of distributed in-wheel motor drive electric vehicle in consideration of the stability and economy, In: *Energy*, vol. 282 (2023)

5. Andreev, A., Kabanau, V., Vantsevich, V.: Driveline Systems of Ground Vehicles. CRC Press, Boca Raton (2010)
6. Andreev, A., Vantsevich, V.: Tyre and Soil Contribution to Tyre Traction Characteristic. In: The Dynamics of Vehicles on Roads and Tracks. CRC Press, pp. 149–155 (2017)
7. Vantsevich, V., Gorsich, D., Paldan, J., Ghasemi, M., Moradi, L.: Terrain mobility performance optimization: Fundamentals for autonomous vehicle applications. Part I. New mobility indices: Optimization and analysis. *J. Terramech.* **104**, 31–47 (2022)

Open Access This chapter is licensed under the terms of the Creative Commons Attribution 4.0 International License (<http://creativecommons.org/licenses/by/4.0/>), which permits use, sharing, adaptation, distribution and reproduction in any medium or format, as long as you give appropriate credit to the original author(s) and the source, provide a link to the Creative Commons license and indicate if changes were made.

The images or other third party material in this chapter are included in the chapter's Creative Commons license, unless indicated otherwise in a credit line to the material. If material is not included in the chapter's Creative Commons license and your intended use is not permitted by statutory regulation or exceeds the permitted use, you will need to obtain permission directly from the copyright holder.





Effect of Driving Force Control that Imitates the Function of Tire Lateral Force on Vehicle Dynamics

Etsuo Katsuyama^(✉)

Toyota Motor Corporation, Shizuoka 410-1193, Japan
etsuo_katsuyama@mail.toyota.co.jp

Abstract. Various control methods have been proposed that aim to improve steering response, disturbance stability, and stabilize steering characteristics by distributing drive force to each wheel. Conventionally, controls have been constructed by combining those control methods and tuning gains for each control. However, such control design methods require a huge amount of man-hours, and besides, it is not clear which states are optimal. Therefore, in this paper, we first focused on the mechanism of tire lateral force. In general, vehicles can run stably against disturbances without implementing any feedback control. It was clarified that this is because the tire lateral force plays the role of a skyhook damper installed horizontally on the side of the vehicle. Therefore, we proposed a control method that brings out the maximum potential of tires based on the idea that tire longitudinal force should have the same function as tire lateral force.

Keywords: Vehicle Dynamics · Driving Force Control · Electric Vehicles · Tire workload

1 Background

Many researchers have been working on vehicle motion control by distributing driving force to each wheel for a long time. However, realizing the control requires a complex control device to distribute the driving force, so it has not yet become widely used for mass-produced vehicles. A movement that may change this situation is “electrification”, which is currently occurring. Unlike internal combustion engines, multiple electric motors can be installed in a vehicle, making it easier to implement driving force distribution control.

The driving force distribution controls that have been proposed so far have various aims, such as stabilizing steering characteristics, improving steering response, equalizing tire workloads, and improving disturbance stability [1–6]. All of those are important target characteristics, however there are still questions in control development, such as which combination of them is optimal, whether there are any that act redundantly, and whether the control gain has no choice but to rely on tuning. This paper discusses a method to uniquely derive the ideal driving force control logic.

2 Effect of Tire Lateral Force Restrained by Steering Angle

Focusing on vehicle motion control methods that use tire longitudinal forces, in most cases control commands are based on the yaw moment generated by the difference in driving force between the left and right wheels. In other words, control using tire longitudinal forces is generally performed by force (moment) control. On the other hand, tire lateral force is generally controlled not by force but by steering angle. In this chapter, in order to clarify the dynamic characteristics of the tire lateral motion, the function of lateral force is analyzed and discussed using equations of motion.

The lateral and yaw motion equations of a general bicycle model are shown in Eqs. (1) and (2), and the front and rear tire slip angles α_f, α_r are shown in Eqs. (3) and (4).

$$mV(r + \dot{\beta}) = -2K_f\alpha_f - 2K_r\alpha_r + F_{yd} \tag{1}$$

$$I_z\dot{r} = -2K_f\alpha_f l_f + 2K_r\alpha_r l_r \tag{2}$$

$$\alpha_f = \beta + \frac{l_f r}{V} - \delta_f \tag{3}$$

$$\alpha_r = \beta - \frac{l_r r}{V} - \delta_r \tag{4}$$

where, m is the vehicle mass, V is the vehicle speed, r is the raw rate, β is the slip angle at the CoG (center of gravity), K_f, K_r are the cornering stiffness of the front and rear tires, I_z is the yaw inertial moment, l_f, l_r are the distance from the CoG to front and rear axles, δ_f, δ_r are the front and rear steer angles, and F_{yd} is the lateral disturbance force.

Focusing on the lateral motion of the vehicle, the slip angle β for the steering input and lateral disturbance force is derived from the above equations. And it is expressed as Eq. (5), where, in order to roughly understand the principle, terms with high orders of s are deleted. This is also represented by the block diagram shown in Fig. 1.

$$\beta(s) \approx \frac{\frac{1}{2} - \frac{V^2}{lC_{rg}}}{\left(\frac{1+I_{zn}}{2}\right)\frac{V}{C_{ag}}s + 1 + AV^2} \delta_f + \frac{\frac{1}{2C_a}}{\left(\frac{1+I_{zn}}{2}\right)\frac{V}{C_{ag}}s + 1 + AV^2} \frac{F_{yd}}{mg} \tag{5}$$

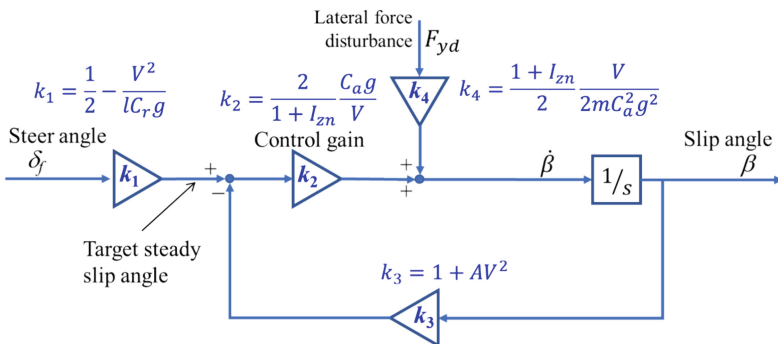


Fig. 1. Block diagram representing vehicle lateral motion.

where, l is the wheelbase, C_f , C_r are the normalized cornering stiffnesses, C_a is the reciprocal of the sum of reciprocals of C_f and C_r , I_{zn} is the normalized yaw inertial moment, A is the stability factor, g is the gravitational acceleration, and s is the Laplace operator.

This system uses tire cornering stiffness C_a as a control gain to reduce the error between the target steady slip angle and the actual slip angle due to steering angle input, while also compensating for external lateral disturbance force. It can be understood that it has the function of a skyhook damper installed on the lateral side of the vehicle. This is why it is effective in stabilizing the vehicle against disturbances without applying any feedback control.

3 Proposed Driving-Force-Control Method Acting as a Lateral Force

When a tire is moved laterally due to disturbance, lateral force is generated to resist it. However, such a reaction force does not occur in the tire longitudinal direction unless some kind of control is applied. This is because tires roll in the longitudinal direction. This is the reason why the right side of the equation of motion in Eqs. (1) and (2) consists only of the lateral-force elements of the tires.

Here, it is assumed that such geometric anisotropy in the longitudinal and lateral directions of the tire does not exist, and that force is generated in the longitudinal direction of the tire by the same mechanism as in the lateral direction. Then, the modified equations of motion are expressed as shown in Eqs. (6) and (7). The third and fourth terms on the right side of Eq. (7) are due to longitudinal force, and are defined to have the same structure as the first and second terms.

$$mV(r + \dot{\beta}) = -2K_f\alpha_f - 2K_r\alpha_r \quad (6)$$

$$I_z\dot{r} = -2K_f\alpha_f l_f + 2K_r\alpha_r l_r + 2K_{xl}s_{xl}\frac{t}{2} - 2K_{xr}s_{xr}\frac{t}{2} \quad (7)$$

where, K_{xl} , K_{xr} are the driving stiffnesses, s_{xl} , s_{xr} are the slip ratios at the left and right wheels, and they are defined by Eqs. (8) and (9) so that they have the same configuration as the slip angles in Eqs. (3) and (4).

$$s_{xl} = s_d - \frac{v_{wr} - v_{wl}}{2V} + \frac{t}{2} \frac{V}{l} \frac{1}{1 + AV^2} (\delta_f - \delta_r) \quad (8)$$

$$s_{xr} = s_d + \frac{v_{wr} - v_{wl}}{2V} - \frac{t}{2} \frac{V}{l} \frac{1}{1 + AV^2} (\delta_f - \delta_r) \quad (9)$$

The first term s_d is the slip ratio due to the driver's acceleration request, the second term is the slip ratio for the yaw rotation detected by the difference between the left and right wheel speeds v_{wl} and v_{wr} , and the third term is the slip ratio for the target yaw rate due to the driver's steering input. Here, if the slip ratio difference s_{xz} between the left and right wheels caused by yaw motion is defined by Eq. (10), Eq. (7), which is the

equation of motion for yaw, can be transformed into Eq. (11), and the third and fourth terms on the right side explains that the tire longitudinal force can be expressed in terms of translational slip and rotational slip.

$$s_{xz} \stackrel{\text{def}}{=} \frac{s_{xr} - s_{xl}}{2} = \frac{v_{wr} - v_{wl}}{V} - \frac{t}{V} \frac{V}{l} \frac{1}{1 + AV^2} (\delta_f - \delta_r) \quad (10)$$

$$I_z \dot{r} = -2K_f \alpha_f l_f + 2K_r \alpha_r l_r + 2(K_{xl} - K_{xr}) s_d \frac{t}{2} - 4K_x s_{xz} \frac{t}{2} \quad (11)$$

where, the K_x is the average value of left and right wheel driving stiffness K_{xl} and K_{xr} .

In order to further transform the equations, $2K_{xl}$ and $2K_{xr}$ are expressed as Eqs. (12) and (13).

$$2K_{xl} = C_x \left(\frac{mg}{2} - ma_y \frac{h}{t} \right) \quad (12)$$

$$2K_{xr} = C_x \left(\frac{mg}{2} + ma_y \frac{h}{t} \right) \quad (13)$$

where, the C_x is the normalized driving stiffness, a_y is the lateral acceleration, h is the CoG height, and t is the track at the front and rear. Here, we focus on the third term on the right side of Eq. (11). By substituting Eqs. (12) and (13) into the third term, it can be transformed into Eq. (14) by ignoring the driving resistance and assuming that $C_x s_d$ is equal to longitudinal acceleration a_x/g .

$$\begin{aligned} 2(K_{xl} - K_{xr}) s_d \frac{t}{2} &= -C_x m a_y h s_d \\ &= mgh \frac{a_x}{g} \frac{a_y}{g} \end{aligned} \quad (14)$$

The above equation is the yaw moment that occurs when the driving force is distributed in proportion to each wheel load. This is the so-called ideal driving force distribution. It is known that in the linear region of tires, the yaw moment theoretically cancels out changes in steering characteristics due to longitudinal load transfer during turns [7]. Here, Eq. (11) can be rearranged as Eq. (15).

$$I_z \dot{r} = -2K_f \alpha_f l_f + 2K_r \alpha_r l_r + mgh \frac{a_x}{g} \frac{a_y}{g} - 4K_x s_{xz} \frac{t}{2} \quad (15)$$

Considering the meaning of the derived longitudinal force term in the above equation, first, the third term on the right side means that the driver's required driving force is distributed in proportion to each wheel's load. Translating this into lateral motion, it corresponds to the generation of tire lateral force proportional to the load on each wheel during turns. As can be seen from Eq. (10), the fourth term plays the role of feedback compensation when an error occurs in the yaw rate estimated from the left and right wheel speed difference with respect to the target steady yaw rate determined from the driver's steering input. A schematic diagram of this is shown in Fig. 2, which shows that for yaw motion, skyhook dampers are applied in the direction of rotation.

This function attempts to maintain the left and right wheel speed difference at a certain target value in response to the driver’s steering input. Translating this into lateral motion, it corresponds to maintaining the steering angle difference between the front and rear wheels at a certain value in response to steering input. Since this control theory was derived by isotropicizing the longitudinal and lateral characteristics of tire, it is called as “Tire Isotropic Control (TIC)”.

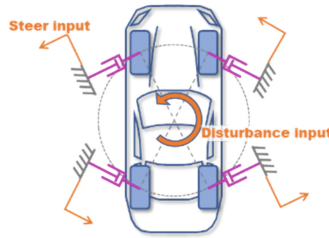


Fig. 2. Schematic diagram of Tire Isotropic Control (TIC).

4 Verification Using a Full Vehicle Simulation Model

The vehicle model has six degrees of freedom on its sprung mass, as well as degrees of freedom for each wheel to move up and down, rotate, and steer, and is equipped with suspension and tires with nonlinear characteristics. The yaw moment due to the tire longitudinal force shown in Eq. (15) is commanded by each wheel driving force.

Figure 3 shows the yaw rate, lateral acceleration, tire lateral and longitudinal forces, and tire workloads when a stepped steering is input at a speed of 80 km/h, and then a yaw moment disturbance is input. It can be confirmed that by applying longitudinal forces

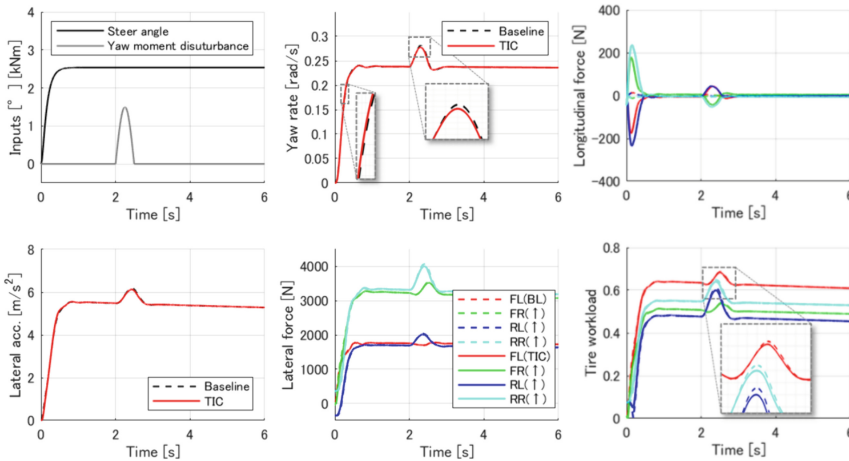


Fig. 3. Effect of TIC on steering response and yaw disturbance.

to each wheel appropriately, steering response and disturbance stability are improved while suppressing the tire workloads. This is the most efficient state in which the forces of each wheel do not cancel each other out, and it is possible to use the tire friction circles efficiently to the limit.

5 Conclusions

Conventionally, designing driving force distribution control has involved adjusting appropriate control gains through trial and error. In this paper, we proposed an original control method that generates longitudinal force that imitates tire lateral force, inspired by the mechanism of tire lateral force generation. As a result, it was shown that it is possible to use the tire friction circle without wasting it with a simple control law, and because the control gains are derived from the equation, the work of trial and error is freed. It was also clarified that this control method enables steering response and disturbance stability to be achieved as if the tire cornering stiffness has been increased.

In this paper, we focused on vehicles that can independently control the driving force of the four wheels, but in the actual market, few vehicles equipped with four motors are produced. In the future, we plan to study how to apply this control method to more realistic two-motor or three-motor vehicles, or vehicles equipped with brake actuators for each wheel.

References

1. Tomari, T., Moti, A., Shibahata, Y.: Development of SH-AWD based on DYC (Direct Yaw Control) concept. In: 8th International Symposium on Advanced Vehicle Control, Taipei (2006)
2. Sawase, K., Ushiroda, Y., Inoue, K.: Effect of the right-and-left torque vectoring system in various types of drivetrain. SAE Technical Paper, 2007-01-3645 (2007). <https://doi.org/10.4271/2007-01-3645>. Detroit
3. Sabbioni, E., Cheli, F., Vignati, M., Melzi, S.: Comparison of torque vectoring control strategies for a IWM vehicle. SAE J. Artic. 7(2), 565–572 (2014). Detroit
4. Fetrati, R.S., Teufel, S., Schramm, D.: Electrification of the torque-vectoring system to improve vehicle driving dynamics. 7th International Munich Chassis Symposium, pp. 307–321, Munich (2016)
5. Lenzo, B., Sorniotti, A., Gruber, P.: A single input single output formulation for yaw rate and sideslip angle control via torque-vectoring. In: 14th Symposium on Advanced Vehicle Control, Beijing (2018)
6. Takeuchi, T., Katsuyama, E.: Steering characteristics compensation by DYC considering combined tire slip. In: 15th Symposium on Advanced Vehicle Control, Kanagawa (2022)
7. Shibahata, Y., Shimada, K., Tomari, T.: The improvement of vehicle maneuverability by direct yaw moment control. In: 1st Symposium on Advanced Vehicle Control, Yokohama (1992)

Open Access This chapter is licensed under the terms of the Creative Commons Attribution 4.0 International License (<http://creativecommons.org/licenses/by/4.0/>), which permits use, sharing, adaptation, distribution and reproduction in any medium or format, as long as you give appropriate credit to the original author(s) and the source, provide a link to the Creative Commons license and indicate if changes were made.

The images or other third party material in this chapter are included in the chapter's Creative Commons license, unless indicated otherwise in a credit line to the material. If material is not included in the chapter's Creative Commons license and your intended use is not permitted by statutory regulation or exceeds the permitted use, you will need to obtain permission directly from the copyright holder.





Vibration Suppression of Automotive Drivetrains Based on Tire-Speed Observer and Backlash Compensation

Kenta Maeda¹(✉), Naoki Shinohara², Satoshi Kaneko², and Hiroki Sonoda²

¹ Hitachi, Ltd., Hitachinaka 312-0034, Ibaraki, Japan
kenta.maeda.ya@hitachi.com

² Hitachi Astemo, Ltd., Atsugi 243-8510, Kanagawa, Japan

Abstract. This paper proposes a novel vibration suppression control method, which suppresses the torsional resonance of the drive shaft caused by motor torque change in the general drivetrain structure of automobiles. For realizing the method in the simplest and most prospective way, the proposed method calculates the feedback torque from the difference between the motor speed and the tire speed multiplied by a proportional gain, with estimating the tire rotation speed by an observer. In addition, a backlash compensation method is developed to reduce noise and vibration in gear retightening in the backlash region. The method observes the fluctuation of the motor speed after the torque zero-crossing and determine the motor torque so that the motor rotation speed returns to the speed at the entrance of the backlash. The effectiveness of the proposed methods is verified by simulation and driving test on the experimental vehicle.

Keywords: xEVs · Torque Control · Drivetrain · Vibration · Backlash

1 Introduction

Due to the strong demand for decarbonization toward sustainable society, x-electric vehicles (xEVs) have been introduced to the global market. On the other hand, it is known that torsional resonance of the drive shaft caused by motor torque change in the general drivetrain structure of automobiles in which the drive source is connected to the left and right wheels via differential gear and drive shafts, as shown in Fig. 1. At the same time, because of the inevitable gear intervention, there is a dead zone called backlash, as shown in Fig. 2.

When implementing vibration suppression control in automobiles, it is often necessary to apply control methods that are within the scope of classical control and offer good visibility and performance. In the past, several vibration suppression control methods have been reported such as devising classical PI control [1], resonance ratio control using a disturbance observer [2], etc. These methods are based on the assumption that only the motor rotation speed is observable. Recently, however, a high vibration suppression effect by sensing the speed on the tire side has also been reported [3]. The simplest and

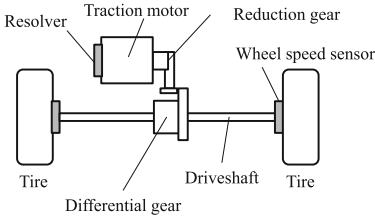


Fig. 1. Control target (drivetrain)

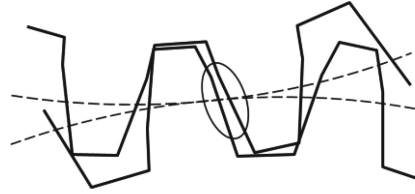


Fig. 2. An example of backlash of a gear.

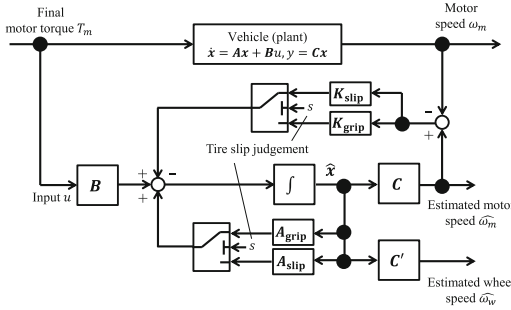


Fig. 3. Block diagram of wheel-speed observer.

most prospective method is to calculate feedback motor torque based on the difference between motor speed and tire speed multiplied by a proportional gain [4]. In this paper, therefore, an observer is introduced to estimate the tire rotation speed.

In addition, a backlash compensation method is developed to reduce noise and vibration in gear retightening in the backlash region. In backlash compensation, a method to set the torque to zero for a certain period of time at zero crossing has been reported [5]. This method has the problem that it takes time to pass through the backlash, which may lead to discomfort for the driver. This paper proposes a new torque compensation method that can solve this problem.

2 Vibration Suppression Control

2.1 Method

First, this section describes wheel-speed observer. The observer is configured as shown in Fig. 3 by equating a state equation ($\dot{x} = Ax + Bu, y = Cx$) from the motor torque to the rotation speed of the motor and tires. The load side changes depending on whether the tire is gripping or slipping, so the tire slip judgment s is included and the A and K matrices are switched ($A_{grip} \leftrightarrow A_{slip}, K_{grip} \leftrightarrow K_{slip}$). C and C' are the matrices that obtains observed output ω_m and ω_w respectively from the state vector x .

Figure 4 shows the block diagram of the vibration suppression control method. The method obtains estimated tire speed $\hat{\omega}_w$ from the observer and feed-backs motor torque by the difference from the motor speed ω_m . The observer parameters are switched by

the tire slip judgement s . The difference between the motor speed and the estimated tire speed is then calculated considering the reduction-gear ratio.

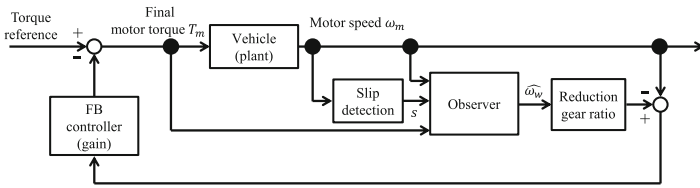
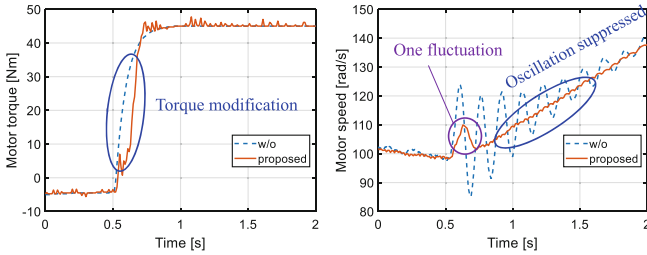


Fig. 4. Block diagram of speed difference feedback with observer.



(a) Motor torque.

(b) Motor speed.

Fig. 5. Experimental result of vibration suppression on high- μ road.

2.2 Experimental Validation

The effectiveness of the vibration suppression control is verified through driving tests on an experimental vehicle. In the driving test, acceleration was applied by an external step-shape acceleration command from the creep driving on high- μ surface. Figure 5(a) shows the motor torque, and acceleration started at the 0.5 s. Compared to the case without control (blue dot line), the proposed method (orange solid line) generates a torque modification to reduce vibrations in the motor rotation speed. The motor rotation speed at that time is shown in Fig. 5(b). While vibration occurs without control, the vibration is reduced by the proposed method. However, there is one fluctuation in the motor rotation speed right after 0.5 s, which is due to backlash.

Next, constant acceleration of 50 Nm was applied on low- μ (slippery) surface. Figure 6(a) shows the motor torque. Figure 6(b) shows the motor rotation speed, the tire rotation speed and observer output, which are converted to motor rotation shaft. In this test, the drive wheels started to slip at just before 1.8 s. When the tire slip started, there is an unexpected spike in the output of the observer (yellow solid line). To prevent the affect of this spike, the vibration suppression control was stopped for 0.2 s after the start of tire slip and restarted just before 2.0 s. Compared with the case without control (1.8–2.0 s), the vibration of motor speed is reduced after 2.2 s as shown in Fig. 6(b).

These results indicate a damping effect in both tire gripping and slipping conditions, and remaining issues with backlash-induced vibration and observer switching. The method for reducing vibration caused by backlash is presented in the next section.

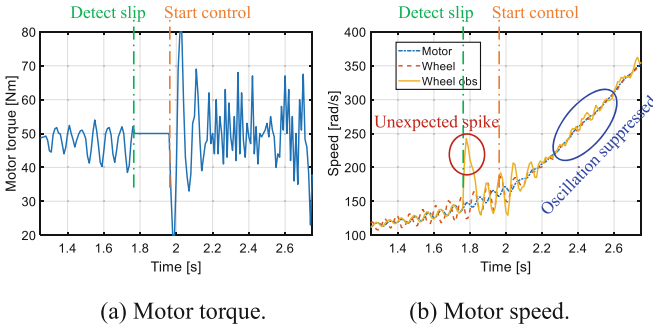


Fig. 6. Experimental result of vibration suppression when tire slips.

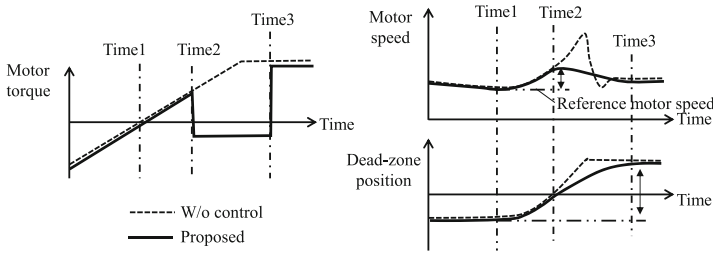


Fig. 7. Simulation result of backlash compensation method.

3 Backlash Compensation

3.1 Method

This section describes a backlash compensation method. Figure 7 illustrates the concept of the control method. In this figure, the torque command value from a driver’s gas-pedal operation (dashed line) changes from a negative value to a positive value (zero crossing) at time 1. The proposed method stores the value of the motor speed at time 1 as the reference motor speed. Then time 2 is defined as the time when the difference between the motor speed and the reference speed exceeds a predetermined value. At time 2, the compensation torque is calculated based on the backlash width that is known in advance, so that the motor speed at the exit of the backlash is the same as at time 1. After time 2, the torque command value is replaced by the compensation torque.

3.2 Simulation Analysis

First, the effectiveness of the proposed method is verified through simulation. The upper figure of Fig. 8 shows an example of motor speed fluctuation when passing through the backlash, and the lower figure shows the motor torque. The motor speeds were calculated by a vehicle plant model with the input of motor torque. The blue dot lines show the conventional method without torque compensation, while the orange solid lines show the results with the backlash compensation method. In this test, the vibration suppression control shown in the previous section was not combined to confirm the effectiveness of the backlash compensation method alone. The vibration (collision) at the end of the backlash occurs with an amplitude of 8.5 rad/s with the conventional method. On the other hand, the proposed method reduces the amplitude to 3.0 rad/s (about 65% of reduction compared with the conventional method), confirming the effectiveness of the proposed method.

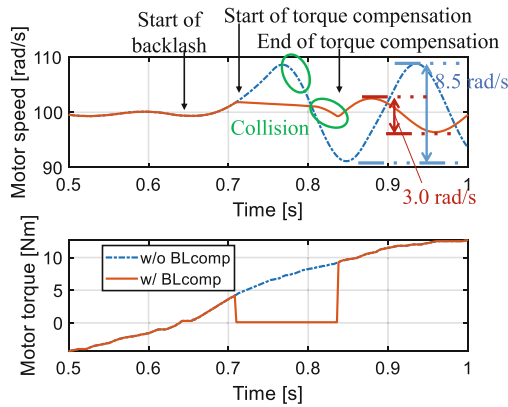
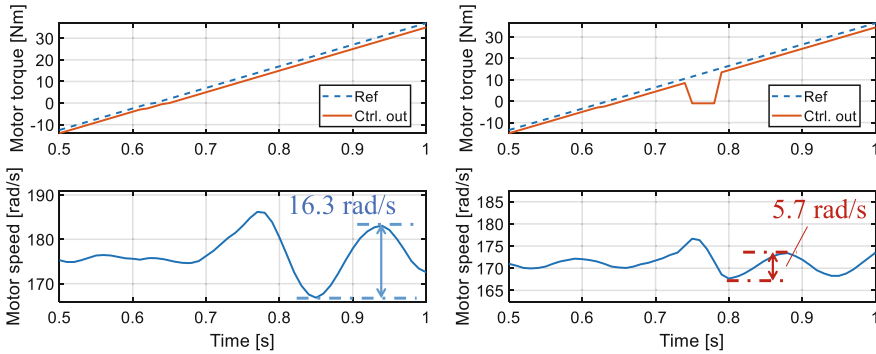


Fig. 8. Simulation result of backlash compensation method.

3.3 Experiment

Second, the effectiveness of the proposed method is also verified through driving tests on an experimental vehicle, with the same test procedure as simulation. In the driving test, acceleration was applied by an external ramp-shape acceleration command from the creep driving. The upper figures of Fig. 9 show the motor speed (dashed line as command value and solid line as actual value), and the lower figures show the motor torque. Figure 9(a) illustrates the result of conventional method without backlash compensation while Fig. 9(b) is the result of proposed method. In Fig. 9(a), there is no deviation between the dashed and solid lines except for a slight delay, while in Fig. 9(b), torque change due to the proposed method can be seen at 0.75 – 0.79 s. The vibration (collision) at the end of the backlash occurs with an amplitude of about 16.3 rad/s with the conventional method (Fig. 9(a)). On the other hand, the proposed method (Fig. 9(b)) reduces the amplitude to about 5.7 rad/s (about 65% of reduction compared with the conventional method), confirming the effectiveness of the proposed method.



(a) Without compensation.

(b) Proposed method.

Fig. 9. Experimental result of backlash compensation method.

4 Conclusion

This paper proposed a vibration suppression control that suppresses the torsional resonance of the drive shaft caused by motor torque change in the general drivetrain structure of automobiles. The proposed method calculates the feedback torque from the difference between the motor speed and the tire speed multiplied by a proportional gain, with estimating the tire rotation speed by an observer. The effectiveness of the proposed method was verified through driving tests, which confirmed a damping effect in both tire gripping and slipping conditions. This paper also proposed a backlash compensation method for reducing noise and vibration in gear retightening in the backlash region. The method observes the fluctuation of the motor speed after the torque zero-crossing and determine the motor torque so that the motor rotation speed returns to the speed at the entrance of the backlash. The effectiveness of the proposed method was verified through simulation and driving tests, which confirmed 65% reduction of vibration at the end of backlash. The future works will be to improve the accuracy of the observer behavior at the start of tire slip, and to combine the vibration suppression and the backlash compensation.

References

1. Szabat, K., et al.: Vibration suppression in a two-mass drive system using PI speed controller and additional feedbacks—Comparative study. *IEEE Trans. Ind. Electron.* **54**(2), 1193–1206 (2007)
2. Abeygunawardhana, P.K.W., et al.: Vibration suppression of two-wheel mobile manipulator using resonance-ratio-control-based null-space control. *IEEE Trans. Industr. Electron.* **57**(12), 4137–4146 (2010)
3. Emmei, T., et al.: Acceleration noise suppression for geared in-wheel-motor vehicles using double encoder. *IEEE J. Emerg. Sel. Top. Ind. Electron.* **2**(1), 53–60 (2021)

4. Tsuji, A., et al.: Mechanism analysis and counter measure study for electrified vehicles with drive line and chassis co-simulation. In: Proceedings of 2022 JSAE Annual Congress Autumn, p. 5. JSAE, Osaka (2022)
5. Ohno, S., et al.: Drive motor control method for suppressing drive shaft torsional vibration due to gear backlash. Nissan Tech. Rev. **82**, 23–30 (2018)

Open Access This chapter is licensed under the terms of the Creative Commons Attribution 4.0 International License (<http://creativecommons.org/licenses/by/4.0/>), which permits use, sharing, adaptation, distribution and reproduction in any medium or format, as long as you give appropriate credit to the original author(s) and the source, provide a link to the Creative Commons license and indicate if changes were made.

The images or other third party material in this chapter are included in the chapter's Creative Commons license, unless indicated otherwise in a credit line to the material. If material is not included in the chapter's Creative Commons license and your intended use is not permitted by statutory regulation or exceeds the permitted use, you will need to obtain permission directly from the copyright holder.





Robust Lane Keeping Control with Estimation of Cornering Stiffness and Model Uncertainty

Junyeong Seong¹(✉), Sungjun Park², and Kunsoo Huh³

¹ Department of Future Mobility, Hanyang University,
Seoul 04763, Republic of Korea
seongjy1@hanyang.ac.kr

² Department of Automotive Engineering (Automotive-Computer Convergence),
Hanyang University, Seoul 04763, Republic of Korea
sjpark1030@hanyang.ac.kr

³ Department of Automotive Engineering, Hanyang University,
Seoul 04763, Republic of Korea
khuh2@hanyang.ac.kr

Abstract. This paper introduces an adaptive lane-keeping control strategy that adapts to varying cornering stiffness while ensuring robustness against uncertainties. The system consists of three blocks: an Interacting Multiple Model (IMM) cornering stiffness estimator, a cornering stiffness uncertainty estimator, and a Robust Model Predictive Controller (RMPC). Improvements in estimation accuracy are achieved through a novel IMM probability derivation method, and the uncertainty estimator utilizes the IMM probability matrix to obtain reliable uncertainty boundaries. Real-time cornering stiffness estimations are integrated into the RMPC for adaptive model predictions. Uncertainty boundaries provide robustness against estimation error in the RMPC by constraint tightening and smoothing techniques. The performance of the estimator and controller is validated in simulations, where the overall control performance is compared to that of the Model Predictive Control (MPC) based on static cornering stiffness.

Keywords: Automated Driving Systems · Lane Keeping System · Cornering Stiffness Estimation · Parameter Uncertainty · Robust Model Predictive Control

1 Introduction

Vehicle automation and driver assistance systems are pivotal advancements in modern vehicles, overseeing safety, performance, and driver comfort. The Lane Keeping System (LKS), a fundamental technology for path tracking and lateral control, necessitates a robust control strategy as well as accurate knowledge of the vehicle's lateral dynamics characteristics.

Cornering stiffness, defining a tire's resistance to lateral deformation under lateral forces, is a critical parameter in vehicle lateral dynamics. Due to its significance and challenges in estimation, cornering stiffness estimation has been extensively studied. Multiple estimation techniques have been tested for cornering stiffness estimation [1, 2]. Notably, an estimator utilizing a KF-based IMM shows rapid responsiveness and smoothness in output [3] but is limited by model selection and computational load. This study builds upon this technique for a more robust and cost-effective estimation.

Aside from estimator inaccuracy, measurement signal errors contribute to estimation errors. While some studies propose estimation methods without using lateral speed, these techniques often lead to under-determined systems or limited usage due to extensive assumptions [4, 5]. In this study, a cornering stiffness uncertainty estimator is developed to compensate for such inevitable estimation errors. The obtained estimation uncertainty boundaries are coupled with an RMPC, utilizing real-time cornering stiffness estimations and uncertainty boundaries. The effectiveness of the RMPC under parametric uncertainty is demonstrated well in [6]. In summary, this paper presents an adaptive control algorithm resilient to estimation errors, contributing:

1. A novel probability calculation method in the IMM for reduced estimation bias.
2. Development of a cornering stiffness uncertainty boundary estimator.
3. A robust lane-keeping RMPC controller utilizing real-time cornering stiffness estimations and uncertainty boundaries.

2 Cornering Stiffness Estimation

2.1 Estimator Vehicle Model

This section outlines the vehicle dynamics model used in the IMM's Kalman Filters, based on a simplified 2-DOF bicycle model [7], assuming small slip angles and constant longitudinal speed.

$$m(\dot{v}_y + \gamma v_x) = C_f \alpha_f \cos \delta + C_r \alpha_r, \quad I_z \dot{\gamma} = l_f C_f \alpha_f \cos \delta - l_r C_r \alpha_r \quad (1)$$

$m, I_z, l_f, l_r, C_f, C_r$ are vehicle parameters; α_f and α_r are front and rear tire slip angles; γ denotes the yaw rate, with δ representing the front wheel steering angle. Front and rear tire slip angles are determined using vehicle geometry.

Cornering stiffness is represented by a modified linear tire model. The fluctuations and variations of the cornering stiffness C_f, C_r are denoted as a sum of its respective base values $C_{f,base}, C_{r,base}$ and candidate variance values $\Delta C_f, \Delta C_r$, allowing for estimations in the tire's nonlinear regions.

IMM accuracy is often linked with model selection. To enhance filter robustness and reduce reliance on model selection, a novel Approximate IMM (AIMM) is introduced in this study. As long as the cornering stiffness variance values encompass the potential range of cornering stiffness, the base and variance cornering stiffness values can be flexibly chosen.

2.2 Approximate IMM-KF

The IMM filter assesses multiple model filter estimations to derive probabilities for each model and a combined output. The IMM is selected for its rapid responsiveness, smooth output, and capability to integrate multiple vehicle models. For this study, 5 candidate cornering stiffness variance values of each front and rear tire are combined into a total of 25 filter models employed in the IMM.

Despite its advantages, the traditional method of probability calculation in the IMM is found to introduce estimation bias under certain conditions. Below are the modifications implemented in the IMM to mitigate bias and enhance consistency.

Min-Max Scaled Probability Calculation. In the traditional IMM, the range of probability distribution differs upon the excitation of the system. High excitation leads to large estimation errors and extreme probability gaps, while low excitation yields indistinct probability distributions. Min-max scaling is implemented in probability calculations to ensure that probability distributions are independent of system excitation and accurately represent model feasibility.

Approximate Probability Calculation. In IMM model filters comprising two or more varying parameter values, erroneous combinations of parameter values can lead to low estimation errors, thereby yielding falsely high probabilities. The approximate method calculates each parameter's probability individually, by fixing all other parameters as their approximate values. Subsequently, these calculated probabilities are combined to form the complete probability matrix for all model filters. In each subsequent cycle, previous approximations of each parameter are replaced with newly estimated parameter values, facilitating a gradual convergence toward the true value.

3 Cornering Stiffness Uncertainty Estimation

In this section, a novel strategy is introduced to isolate only the cornering stiffness uncertainty values from a basic disturbance observer. The proposed uncertainty estimator utilizes the probability distributions of each model from the AIMM to assess relative estimation certainty and determine upper and lower uncertainty proportions. A concentrated probability distribution indicates high estimation certainty, while a dispersed distribution suggests the opposite. The upper base uncertainty boundaries for each front and rear wheel are derived as the sum of products of positive cornering stiffness variance values and their corresponding probabilities, with similar construction for lower boundaries using negative variance values. Since the base uncertainty boundaries are proportional values, definitive uncertainty boundaries are expressed as the product of base uncertainty values $\Delta\tilde{C}_{f,base}$, $\Delta\tilde{C}_{r,base}$ and their respective weight factors ρ_1 , ρ_2 ,

Weight factors are determined through the integration of front and rear dynamics equations. The disturbance observer with the denotation of uncertainties is described below. Cornering stiffness uncertainty is denoted using base uncertainty values and weight factors, while lateral speed and force disturbances are denoted by k .

$$F_{yf}(1 + k_f) = \left(\delta - \frac{V_y(1+k_v)}{V_x} - \frac{l_f\gamma}{V_x} \right) (\hat{C}_f + \Delta\tilde{C}_{f,base} * \rho_1) \quad (2)$$

$$F_{yr}(1 + k_r) = \left(-\frac{V_y(1+k_v)}{V_x} - \frac{l_r\gamma}{V_x} \right) (\hat{C}_r + \Delta\tilde{C}_{r,base} * \rho_2) \quad (3)$$

Because the errors in F_{yf} and F_{yr} are caused mostly due to changes of vehicle mass, coefficients k_f and k_r can be assumed to be of equal size. Dividing Eq. 2 by Eq. 3 gives us:

$$\frac{F_{yf}}{F_{yr}} = \frac{(\alpha_f - \frac{V_y}{V_x}k_v)(\hat{C}_f + \Delta\tilde{C}_{f,base} * \rho_1)}{(\alpha_r - \frac{V_y}{V_x}k_v)(\hat{C}_r + \Delta\tilde{C}_{r,base} * \rho_2)} \quad (4)$$

because $|\alpha_f|, |\alpha_r| \gg \left| \frac{V_y}{V_x}k_v \right|$, the equation can be simplified to reveal the relationship between front and rear uncertainty boundaries. From where the weight factors and definitive uncertainty boundaries can be derived.

$$\frac{\hat{C}_f + \Delta\tilde{C}_{f,base} * \rho_1}{\hat{C}_r + \Delta\tilde{C}_{r,base} * \rho_2} = \frac{F_{yf}\alpha_r}{F_{yr}\alpha_f} \quad (5)$$

4 Controller

The proposed lane-keeping system is controlled through a robust model predictive controller (RMPC). The vehicle model used for model prediction is identical to the bicycle model used in the estimation phase. Estimated cornering stiffness is fed to the controller to update the vehicle model. The cornering stiffness uncertainty boundaries are implemented into the RMPC via constraint tightening and smoothing techniques. The cost function comprises the steering input derivation and lateral error with its respective weight factors for optimal control input.

5 Simulation

The CARMAKER software is used to validate estimator and controller performance. The vehicle is driven on a clothoid-shaped path with the turning radius decreasing from 50 m to 20 m, designed to induce decreasing cornering stiffness and test path tracking abilities.

5.1 Estimator Performance

The cornering stiffness estimation accuracy is tested by comparing it with the true value, while the uncertainty boundary’s capability to encapsulate error is evaluated. As depicted in Fig. 1, the cornering stiffness is estimated with an average error of 9.5% in the front and 13% in the rear tires. While the result shows reliable accuracy and tracking capabilities, some errors are evident. However, the uncertainty boundaries effectively encapsulate the true value even under these errors, expanding during periods of low certainty and contracting during high certainty.

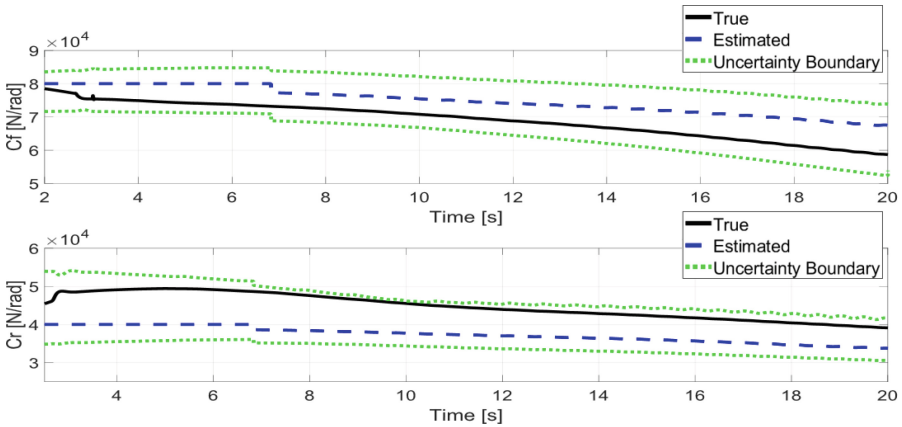


Fig. 1. Cornering stiffness estimation with uncertainty boundaries

5.2 Control Performance

The control performance of the proposed system’s RMPC is contrasted with that of a basic MPC lane-keeping system that shares the same vehicle model and cost function. However, the MPC model relies on a constant cornering stiffness value.

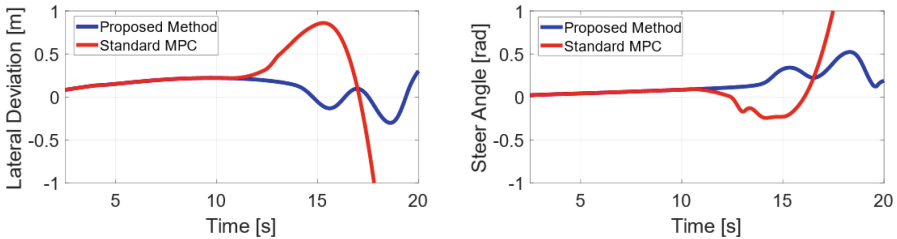


Fig. 2. LKS lateral deviation and steering angle

Figure 2 shows that the standard MPC deviates from the required curve at 12 seconds, while the RMPC maintains stability until 14 s due to accurate cornering stiffness updates. From 14 s onwards, the RMPC approaches the cornering stiffness uncertainty boundary constraints, prompting the generation of more aggressive control actions to sustain stability, as evidenced by the steering angle graph.

6 Conclusion

This paper presents the development of a robust Lane Keeping System (LKS) control system, integrating cornering stiffness estimation and uncertainty. The developed AIMM demonstrates reliable estimation capabilities, while the uncertainty estimator effectively compensates for potential estimation errors. Cornering stiffness values are utilized to update the vehicle model, while uncertainty boundaries serve as constraints in the RMPC, resulting in an adaptive and robust lane-keeping control system.

Simulation tests against a standard MPC underscore the proposed controller's ability to maintain stability in tight corners. The results show that combining the uncertainty estimator with RMPC forms an effective control framework, adept at handling parameter uncertainty and estimation errors. This suggests potential for future research to explore applying this framework in various vehicle control systems, enhancing robustness against diverse parameter uncertainties.

Acknowledgment. This work was supported by the Ministry of Trade, Industry, and Energy (MOTIE), South Korea, through the Technology Innovation Program (Development on Automated Driving with Perceptual Prediction Based on T-Car/Vehicle Parts to Intelligent Control/System Integration for Assessment) under Grant 20018101.

References

1. Baffet, G., Charara, A., Lechner, D.: Estimation of vehicle sideslip, tire force and wheel cornering stiffness. *Control. Eng. Pract.* **17**(11), 1255–1264 (2009)
2. Wang, Y., et al.: Estimation of sideslip angle and tire cornering stiffness using fuzzy adaptive robust cubature Kalman filter. *IEEE Trans. Syst., Man, Cybern.: Syst.* **52.3**, 1451–1462 (2020)
3. Joa, E., Yi, K., Hyun, Y.: Estimation of the tire slip angle under various road conditions without tire-road information for vehicle stability control. *Control. Eng. Pract.* **86**, 129–143 (2019)
4. Sierra, C., et al.: Cornering stiffness estimation based on vehicle lateral dynamics. *Veh. Syst. Dyn.* **44**(sup1), 24–38 (2006)
5. Han, K., Choi, M., Choi, S.B.: Estimation of the tire cornering stiffness as a road surface classification indicator using understeering characteristics. *IEEE Trans. Veh. Technol.* **67**(8), 6851–6860 (2018)

6. Han, S., et al.: Robust lane keeping control for tractor with multi-unit trailer under parametric uncertainty. *IEEE Trans. Intell. Veh.* (2023)
7. Rajamani, R.: *Vehicle dynamics and control*. Springer Science & Business Media (2011)

Open Access This chapter is licensed under the terms of the Creative Commons Attribution 4.0 International License (<http://creativecommons.org/licenses/by/4.0/>), which permits use, sharing, adaptation, distribution and reproduction in any medium or format, as long as you give appropriate credit to the original author(s) and the source, provide a link to the Creative Commons license and indicate if changes were made.

The images or other third party material in this chapter are included in the chapter's Creative Commons license, unless indicated otherwise in a credit line to the material. If material is not included in the chapter's Creative Commons license and your intended use is not permitted by statutory regulation or exceeds the permitted use, you will need to obtain permission directly from the copyright holder.





A Parametric Interpolation-Based Approach to Sideslip Angle Estimation

Mariagrazia Tristano^{1,2} and Basilio Lenzo¹(✉)

¹ Università degli Studi di Padova, Padova, Italy
{[mariagrazia.tristano](mailto:mariagrazia.tristano@unipd.it),[basilio.lenzo](mailto:basilio.lenzo@unipd.it)}@unipd.it
² Sheffield Hallam University, Sheffield, UK

Abstract. Vehicle sideslip angle has always been of interest for stability controls enhancing vehicle safety. As well-known, measuring sideslip is impractical and expensive, motivating techniques to estimate it using already-available vehicle sensors. This paper proposes a new methodology to estimate sideslip angle, separating kinematic and dynamic sideslip angle contributions with the idea that the former is straightforward and the latter may be obtained with a lateral-acceleration-based interpolation. The proposed approach is validated through experimental data on a passenger vehicle.

Keywords: vehicle dynamics · sideslip angle · estimation · dynamic sideslip angle · kinematic sideslip angle

1 Introduction

The rising interest in autonomous and semi-autonomous mobility has contributed to forging brand new research paths, aiming to improve vehicle handling and safety. When it comes to vehicle stability control, a key step is to identify meaningful vehicle states able to offer insight into the stability conditions of the vehicle. The existing literature on lateral stability controllers recurrently lists vehicle sideslip angle, β [1]. β is defined as the angle between the orientation of the centre-of-mass velocity vector and the longitudinal axis of the vehicle [2]. Despite knowledge of the sideslip angle being pivotal, it is a difficult quantity to monitor in real-time, as commercially available sensors are bulky and expensive. Alternatively, estimation techniques exist, which typically rely on model-based estimators, such as Kalman filters [3], or neural networks [4]. Such approaches have their own benefits and disadvantages and, to date, there is no “ultimate” solution.

This paper proposes a parametric estimation of the sideslip angle. The estimator features an interpolation-based formulation providing the dynamic sideslip angle component, while the kinematic component is provided as the result of kinematic steering. The entire strategy relies only on measurements coming from the vehicle Inertial Measurement Unit (IMU).

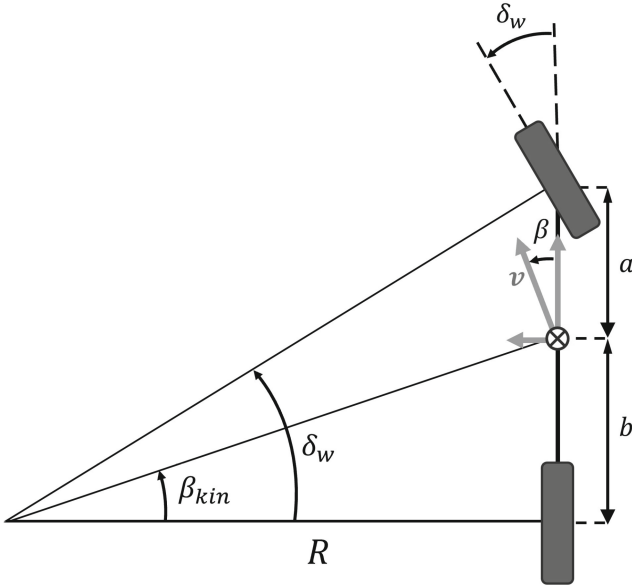


Fig. 1. Single-track model showing the kinematic sideslip angle.

2 Sideslip Angle Estimation

According to [5], β may be split into a kinematic component, β_{kin} , an intrinsic geometrical feature, and a dynamic component, β_{dyn} , arising as a result of tire slip:

$$\beta = \beta_{kin} + \beta_{dyn} \quad (1)$$

2.1 Kinematic Sideslip Angle Estimate

Remarks on kinematic phenomena within this paper all refer to the single-track model [6]. Looking at Fig. 1, in kinematic conditions:

$$\tan(\delta_w) = \frac{a+b}{R} \approx \delta_w, \tan(\beta_{kin}) = \frac{b}{R} \approx \beta_{kin} \quad (2)$$

where a and b are the front and rear semi-wheelbases and R the (kinematic) turning radius, δ_w the wheel steering angle. By eliminating R :

$$\beta_{kin} \approx \delta_w \frac{b}{a+b} \quad (3)$$

In actual driving conditions, this expression only approximates the kinematic sideslip angle [5], yet it is used in this paper as it does not require an estimation of vehicle longitudinal speed - e.g. through wheel speed sensors.

2.2 Dynamic Sideslip Angle Estimate

As seen above, the kinematic sideslip angle contribution at any point of the vehicle longitudinal axis depends on the distance between the rear axle and the point of interest - for the centre of mass, such distance is b .

Very interestingly, [5] shows that the dynamic sideslip angle contribution instead does not depend on the position along the vehicle longitudinal axis. The idea is then to find the dynamic sideslip angle contribution at the rear axle, which is easier, and that shall be the dynamic sideslip angle also at the vehicle centre of mass, to be used in Eq. 1.

The kinematic contribution at the rear axle is exactly 0. So, the overall sideslip angle at the rear axle is only made of the dynamic sideslip angle contribution - at least, for a non-rear-wheel steering vehicle. Since the rear steering angle is 0, the congruence equation [7] $\delta = \alpha + \beta$ reduces to $-\beta_R = \alpha_R$, where α denotes tire slip angle and the subscript R refers to the rear axle. And because at the rear axle there is no kinematic contribution, then

$$\beta_{\text{dyn}} = -\alpha_R \quad (4)$$

Below, a procedure is proposed to determine α_R based on lateral acceleration, a_y , which is readily available at the IMU of any passenger vehicle.

The key idea is that α_R depends on the rear axle lateral force, which in turn is a linear function of a_y [7]. So any constitutive relationship between lateral force and slip, such as the well-known Magic Formula, would approximate (only at steady-state the rear axle lateral force is just proportional to a_y) the relationship between a_y and $\alpha_R = -\beta_{\text{dyn}}$. This needs to be inverted, to provide $\alpha_R = -\beta_{\text{dyn}}$ as a function of a_y . Classical tire models are difficult to invert or piecewise defined. Here, we adopt the Root-Rational tire model [8], which is easy to invert, leading to:

$$\beta_{\text{dyn}} = \begin{cases} \frac{c_3 a_y}{c_1 - c_2 a_y} & \text{if } a_y < 0 \\ \frac{c_3 a_y}{c_1 + c_2 a_y} & \text{if } a_y \geq 0 \end{cases} \quad (5)$$

Interpolation coefficients c_1 , c_2 , c_3 are retrieved by solving a non-linear least squares problem on suitable vehicle data sets. Once both components are known, the full sideslip angle β is reconstructed using Eq. (1).

3 Results

Interpolation is performed using dataset groups [9,10], herein respectively referred to as D1 and D2. Coefficient values for both datasets are reported in Table 1, with Fig. 2 showing an overlap between original and interpolated data. The validity of the estimation strategy can be assessed by comparing its outcome against the measured signal: Fig. 3a–3b display the estimation outcome on a portion of data within D1 and D2 respectively.

Table 1. Interpolation parameters using dataset D1 and D2.

Dataset	c_1	c_2	c_3
D1	33901.36	1737.77	5580.54
D2	48585.36	2507.95	12949.62

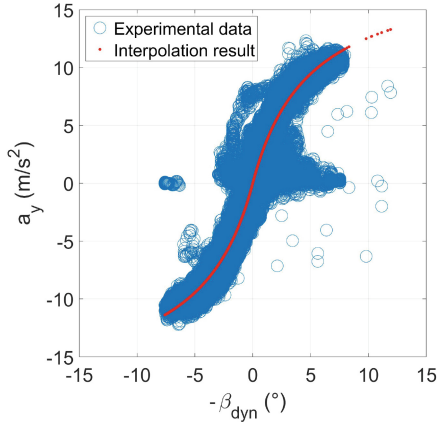


Fig. 2. Interpolation outcome on available datasets.

The numerical performance assessment is done through computing the Root-mean-square error (RMSE). The resulting validation RMSEs on four different runs belonging to datasets [9, 10] are listed in Table 2 and Table 3, with the RMSE generally around 0.5 deg.

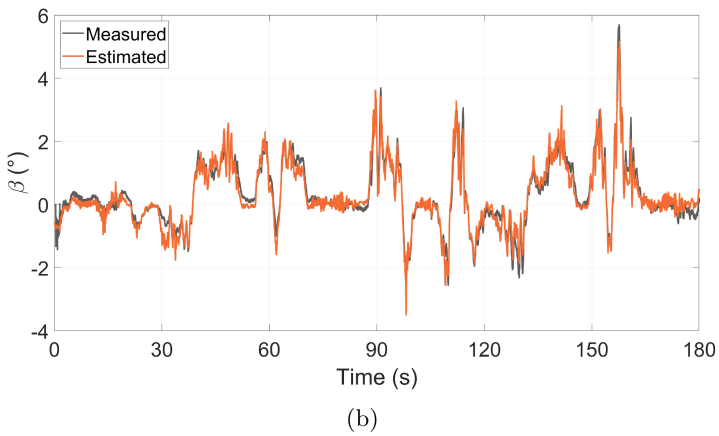
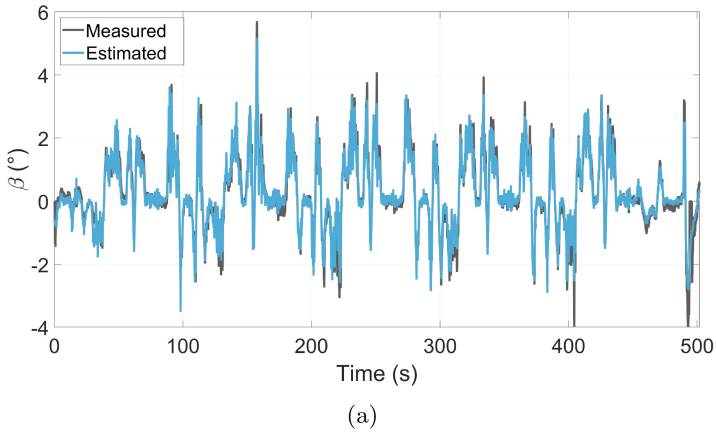


Fig. 3. Estimation outcomes from D1 (a) and D2 (b).

Table 2. Validation outcomes for four different datasets within D1.

Validation dataset	RMSE (°)
20130223_01_02_03_grandsport	0.415
20130222_01_01_03_grandsport	0.367
20130222_01_02_03_grandsport	0.342
20130222_02_01_03_grandsport	0.434

Table 3. Validation outcomes for four different datasets within D2.

Validation dataset	RMSE (°)
20140222_01_01_03_2501m	0.539
20140221_03_02_03_2501m	0.375
20140221_04_01_03_2501m	0.541
20140221_03_03_03_2501m	0.502

4 Conclusions

A parametric approach was proposed to tackle the challenge of estimating the vehicle sideslip angle. The estimation task was split in two sub-tasks, aiming to extract: i) the kinematic sideslip angle, as a result of kinematic steering; ii) the dynamic sideslip angle as a parametric approximation based on affinity with principles regulating tire models. Results both in terms of RMSE and normalised error distributions show there is little discrepancy with respect to the measured counterpart, hence encourage further studies.

Future work will include exploring this approach within larger sets of data and for different vehicles, and an on-vehicle implementation.

References

1. Huang, Y., Chen, Y.: Vehicle lateral stability control based on shiftable stability regions and dynamic margins. *IEEE Trans. Veh. Technol.* **69**(12), 14727–14738 (2020)
2. Lenzo, B.: Torque vectoring control for enhancing vehicle safety and energy efficiency. In: *Vehicle Dynamics: Fundamentals and Ultimate Trends*, pp. 193–233. Springer International Publishing, Cham (2022)
3. Naets, F., Aalst, S., Boulkroune, B., El Ghouti, N., Desmet, W.: Design and experimental validation of a stable two-stage estimator for automotive sideslip angle and tire parameters. *IEEE Trans. Veh. Technol.* **66**, 9727–9742 (2017)
4. Novi, T., Capitani, R., Annicchiarico, C.: An integrated artificial neural network-unscented Kalman filter vehicle sideslip angle estimation based on inertial measurement unit measurements. *Proc. Inst. Mech. Eng., Part D: J. Autom. Eng.* **233**, 1864–1878 (2019)
5. Lenzo, B., Sorniotti, A., Gruber, P., Sannen, K.: On the experimental analysis of single input single output control of yaw rate and sideslip angle. *Int. J. Automot. Technol.* **18**, 799–811 (2017)
6. Genta, G.: *Motor vehicle dynamics: modeling and simulation*. World scientific (1997)
7. Guiggiani, M.: Correction to: The Science of Vehicle Dynamics. In: *The Science of Vehicle Dynamics: Handling, Braking, and Ride of Road and Race Cars*, pp. C1–C1. Springer International Publishing, Cham (2023)
8. Tristano, M., Lenzo, B.: (under review) Analytical solution of vehicle phase plane equilibria through the Root-Rational tire model. *Vehicle System Dynamics*

9. Kegelman, J., Harbott, L., Gerdes, J.: Targa Sixty-Six. Stanford Digital Repository. (<http://purl.stanford.edu/yf219gg2055>, 2016) (2013)
10. Kegelman, J., Harbott, L., Gerdes, J.: Targa Sixty-Six. Stanford Digital Repository. (<http://purl.stanford.edu/hd122pw0365>,2016) (2014)

Open Access This chapter is licensed under the terms of the Creative Commons Attribution 4.0 International License (<http://creativecommons.org/licenses/by/4.0/>), which permits use, sharing, adaptation, distribution and reproduction in any medium or format, as long as you give appropriate credit to the original author(s) and the source, provide a link to the Creative Commons license and indicate if changes were made.

The images or other third party material in this chapter are included in the chapter's Creative Commons license, unless indicated otherwise in a credit line to the material. If material is not included in the chapter's Creative Commons license and your intended use is not permitted by statutory regulation or exceeds the permitted use, you will need to obtain permission directly from the copyright holder.





Optimal Path Generator Embedded Model Predictive Control for Automated Vehicles

Takashi Sago^(✉), Yoshihide Arai, Yuki Ueyama^(ID), and Masanori Harada

National Defense Academy of Japan, 1-10-20 Hashirimizu,
Yokosuka-shi, Kanagawa, Japan
ed22005@nda.ac.jp

Abstract. This paper investigates real-time optimal control for an automated vehicle. The model predictive control that generates the optimal trajectories has found wide applications in recent years due to increased computational performance. Numerical simulations of the full-vehicle model investigate the applicability of a path generator embedded model predictive control for the vehicle in the general shape road. The path generator is constructed by deep learning using the multiple open-loop optimal control problem solutions as the training dataset. Results demonstrate that the sequentially calculating optimal control command has the potential for real-time optimal control in the presence of the obstacle.

Keywords: Real-time optimal control · Trajectory generation · Full vehicle model · Deep-learning neural network

1 Introduction

Advanced safety technologies have become increasingly important with the realization of automated or unmanned vehicles. In such a requirement, a real-time optimal control (RTOC) system that can improve efficiency becomes available due to the increased computing power. A model predictive control (MPC) [1] is the most widely used RTOC algorithm that can optimize the cost value subject to constraints, including nonlinearity. The problem formulation is one of the crucial points for rapid convergence because the controller iteratively solves the optimal control problem. Thus, we have proposed the path generator embedded model predictive control (PG-MPC) approach, effectively reducing the computational burden [2]. However, the utility of the PG-MPC is not verified for the full-vehicle model environment.

This study applies the PG-MPC to the full-vehicle model simulation to evaluate its performance. The embedded path generator is constructed by deep learning [3] using the multiple open-loop optimal control problem solutions as the training dataset. The numerical simulation in the general layout course with the presence of the obstacle demonstrates the utility of the PG-MPC.

2 Vehicle Dynamics Model

A full-vehicle model is used for the numerical simulation, whereas an equivalent two-wheel model is used for the dynamics of each optimal control problem for open-loop optimal solutions and MPC to reduce the computational burden [4]. Equation (1) shows the equations of motion for the equivalent two-wheel model described in course coordinates with constant speed V . The vehicle state and control variables are $\mathbf{X} = [\beta \ r \ \psi \ x_s \ y_s \ \delta_f]^T$ and $\mathbf{U} = [\delta_{fc}]$.

$$\dot{\mathbf{X}} = \mathbf{f}(\mathbf{X}, \mathbf{U}) = \begin{bmatrix} -\frac{2(C_f + C_r)}{mV}\beta - \left(1 + \frac{2(C_f l_f - C_r l_r)}{mV^2}\right)r + \frac{2C_f}{mV}\delta_f \\ -\frac{2(C_f l_f - C_r l_r)}{I_z}\beta - \frac{2(C_f l_f^2 + C_r l_r^2)}{I_z V}r + \frac{2C_f l_f}{I_z}\delta_f \\ r \\ \frac{1}{1 - y_s \kappa} V \cos(\psi_v) \\ V \sin(\psi_v) \\ \frac{1}{T_d}(\delta_{fc} - \delta_f) \end{bmatrix} \quad (1)$$

Where β is the vehicle side slip angle; r is the yaw rate; ψ is the yaw angle; x_s and y_s are positions; δ_f and δ_{fc} are the front wheel steering angle and its command value; l_f and l_r are distance from the mass center and front and rear axel; C_f and C_r are the cornering power of the front and rear wheels; and I_z is the yaw moment of inertia. The relative yaw angles to the course center line are $\psi_s (= \psi - \theta)$ and $\psi_v (= \psi_s + \beta)$, where θ is the course tangent angle and κ is the curvature, which are functions of position x_s .

3 Optimal Path Generator Embedded MPC

3.1 Architecture of PG-MPC

The MPC architecture generally consists of the main frame and the optimization frame executed parallel during control, requiring information transfer between the frames. The optimization frame generates the optimal control input from the given information primarily through an iterative algorithm, which solves the optimal control problem in the optimization frame using the states and the reference path information from the main frame. However, generating the reference path while considering the target course and obstacle avoidance increases the computational burden of the main frame. Thus, in previous work, we proposed a PG-MPC algorithm in which the prescribed function provides the reference path directly during the iterative optimization computation.

Figure 1 shows the operation procedure of the PG-MPC for the vehicle in the course coordinate. The PG-MPC solves the nonlinear programming problem, which minimizes the cost function subject to the discretized dynamics, the initial conditions, and the path constraints. The prescribed function gives

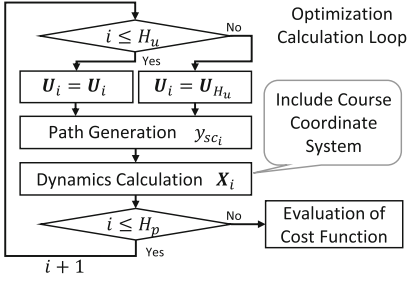


Fig. 1. Inner loop part of PG-MPC algorithm.

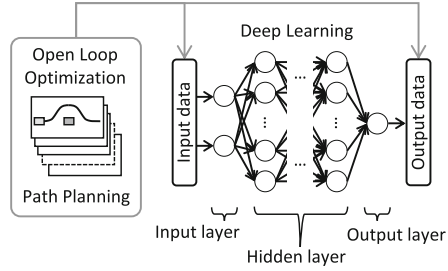


Fig. 2. Construction of optimal path generator using deep learning.

the reference value y_{sc_i} for each discrete point i , which works as the embedded path generator in the MPC algorithm, and its arguments use modest information from the main frame, which can reduce the computational burden of each frame. The primary key to this idea is to design an appropriate optimal path generator(OPG) function.

3.2 Construction of Optimal Path Generator

Figure 2 shows the construction of the OPG using the deep learning framework. Using a deep-learning neural network, we construct the nonlinear function that generates the optimal reference path. The multi-layer neural network function generated by the supervised deep learning algorithm approximates the nonlinear relationships of multiple open-loop optimal solutions, considering various situations, such as lateral displacement from the reference path and the relative position to the obstacles. The optimal solution is calculated numerically using an optimization method based on the pseudospectral (PS) method [5]. In addition, the time-axis folding method [6] is used to spread the dense discretization nodes around the obstacle. Optimal control solutions in the feasible region used for the training dataset are obtained by the following cost function, Eq. (2).

$$J = \int_{t_0}^{t_f} q_1 \Delta y_s^2 + q_2 \delta_f^2 + q_3 \ddot{y}_s^2 + q_4 (e^{-Wh(x_s(t), y_s(t))} - 1) dt \quad (2)$$

The first three terms in the Lagrange cost evaluate the position error($\Delta y_s = y_{s_{obs}} - y_{sc}$), the steering angular velocity(δ_f), and the lateral acceleration(\ddot{y}_s) respectively to follow the target course while moderating control input. The fourth term gives a risk potential value that increases the cost function J when the vehicle is close to the obstacle [7].

$$h(x_s(t), y_s(t)) = \left(\frac{x_s(t) - x_{s_{obs}}}{a} \right)^p + \left(\frac{y_s(t) - y_{s_{obs}}}{b} \right)^p - r^p \quad (3)$$

Where a, b, p, r, W determines the shape of the obstacle and x_{obs}, y_{obs} determines the position of the obstacle in the x_s and y_s axes.

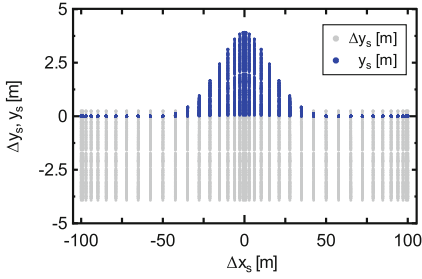


Fig. 3. Open-loop optimal trajectories used for a training dataset.

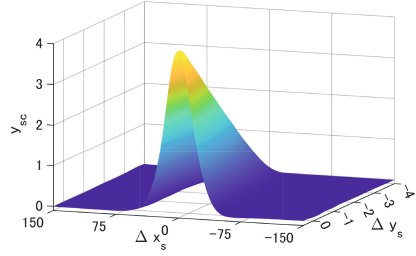


Fig. 4. Function value of OPG around obstacle.

Figure 3 shows the obtained discretization nodes of the open-loop optimal solution for the 220 cases used for the training dataset. The lateral distance increases to avoid the obstacle where the relative distance is near the obstacle; otherwise, the vehicle takes straight trajectories. By using this training dataset to obtain the OPG, several pairs of the number of hidden layers (HD) and the number of neurons (ND) were tried, and we found HD=4 and ND=14 minimize the average absolute error.

Figure 4 shows the function value of constructed OPG for domain around the obstacle. The reference command y_{sc} increases when the relative distance is close to the obstacle. The function is smooth, and there is no outlier value.

4 Numerical Simulation

This section demonstrates a numerical application of the PG-MPC developed in previous sections. The utility of the PG-MPC is evaluated by comparing it with the results of the standard MPC. A full-vehicle model of the middle-sized sedan runs in a general shape layout course consisting of straight and curved sections. Three obstacles on the course are assumed to be detected by sensors, and their relative position and speed can be used as information for controller inputs.

Table 1 shows the parameters of the numerical simulation. The cost function for both controllers is Eq. (2), but the standard MPC must consider the fourth term to avoid the obstacle, while the PG-MPC does not need this term because it only follows the reference path generated by the OPG. For this reason, the standard MPC requires large horizon parameters, H_p and H_u , to obtain a stable trajectory, which increases the computational burden.

Figure 5 shows the trajectories obtained by the full-vehicle model simulation, including the overall result and details around the obstacles. Both controllers successfully run around the overall course. However, the standard MPC takes inward avoidance trajectories at the obstacle $x_s = 950$, which runs off the course. Thus, an additional constraint is required to keep the vehicle inside the course.

Figure 6 shows the states variables, the G-G diagram, and computation time. It is clear that the PG-MPC runs a smoother trajectory and uses less G-force

Table 1. Parameters used for numerical simulation.

States	Standard MPC	PG-MPC
q_1, q_2, q_3, q_4	0.7, 0.001, 0.01, 5.0×10^4	1.0, 0.2, 0.05, 0.0
Horizon and Control Steps	$H_p = 40, H_u = 21$	$H_p = 10, H_u = 6$
Obstacle positions	$(x_{s_{obs1}}, x_{s_{obs2}}, x_{s_{obs3}}) = (450, 950, 1350), y_{s_{obs}} = 1.8$	

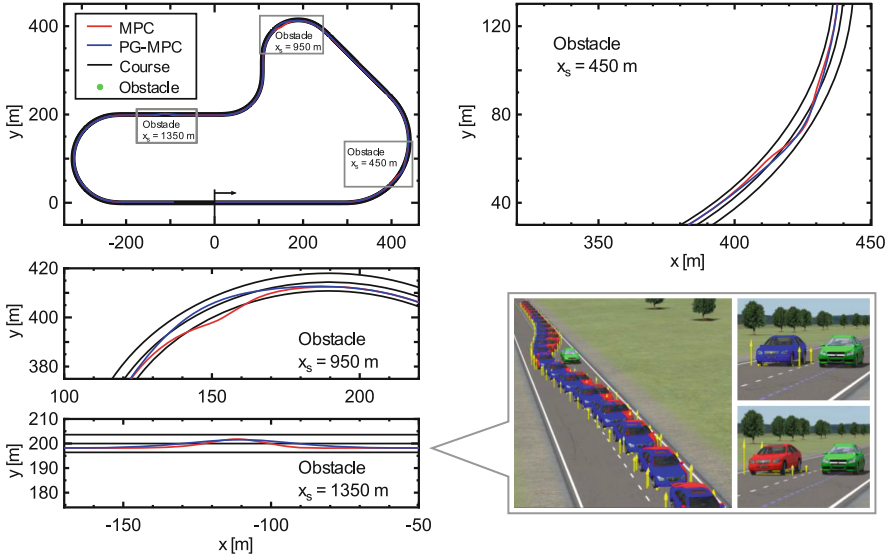


Fig. 5. Overall trajectory around the course, obstacle avoidance trajectory, and example scene.

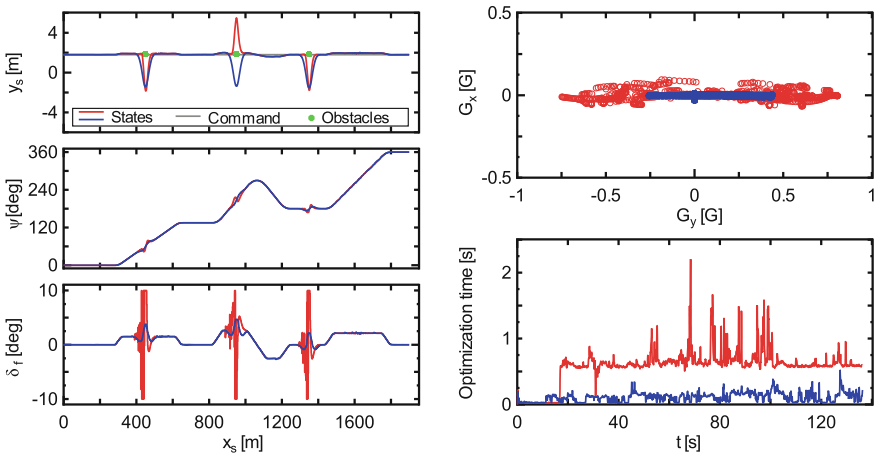


Fig. 6. States variables, G-G diagram, and computation time.

for comfortable driving. The computation time history shows that the appearance of the obstacle varies the evaluation character of the cost function, which increases the computational burden of the standard MPC. On the other hand, the PG-MPC has a level computation time because it follows the path generated by the OPG. Therefore, the PG-MPC can be applied to the full-vehicle model environment.

5 Conclusion

The model predictive control that sequentially generates the optimal trajectories has found wide applications in recent years. In previous studies, we have proposed the path generator embedded model predictive control approach, effectively increasing the performance. In this study, numerical simulations of the full-vehicle model investigate the applicability of the controller for the vehicle in the general shape road. The path generator is constructed by deep learning using the multiple open-loop optimal control problem solutions as the training dataset. Results demonstrate that the sequentially calculating optimal control command has the potential for real-time optimal control in the presence of the obstacle. Furthermore, the path generator embedded model predictive control has a level computation time because it only follows the smooth reference path.

References

1. Maciejowski, J.M.: Predictive control with constraints, pearson education limited, 2002 (Adachi, S., Kanno, M., trans., Predictive Control with Constraints), Tokyo Denki University Press (2005). (in Japanese)
2. Sago, T., Arai, Y., Ueyama, Y., Harada, M.: Obstacle avoidance maneuver using optimal path generator embedded model predictive control, transactions of japan society of mechanical engineers, Vol. 89, No. 926, pp. 23-00134 (2023). (in Japanese) <https://doi.org/10.1299/transjsme.23-00134>
3. Goodfellow, I., Bengio, Y., Courville, A.: Deep Learning, MIT Press (2016)
4. Sago, T., Arai, Y., Ueyama, Y., Harada, M.: Obstacle avoidance maneuver by optimal feedback control using deep learning neural networks. Trans. Soc. Autom. Eng. Japan. **54**, 6–2 (2023). (in Japanese) <https://doi.org/10.11351/jsaeronbun.54.1281>
5. Harada, M.: Direct trajectory optimization by a jacobi pseudospectral method with the weights of high-order gauss-lobatto formulae. Trans. Japan Soc. Mech. Eng., Series C **73**(728), 119–124 (2007). (in Japanese)
6. Kato, K.: Engineering Optimal Control, University of Tokyo Press (1988). (in Japanese)
7. Hurni, M.A., Sekhavat, P., Ross, I.M., Autonomous Trajectory Planning Using Real-Time Information Updates, AIAA Guidance, Navigation, and Control Conference, AIAA-2008-6305 (2008)

Open Access This chapter is licensed under the terms of the Creative Commons Attribution 4.0 International License (<http://creativecommons.org/licenses/by/4.0/>), which permits use, sharing, adaptation, distribution and reproduction in any medium or format, as long as you give appropriate credit to the original author(s) and the source, provide a link to the Creative Commons license and indicate if changes were made.

The images or other third party material in this chapter are included in the chapter's Creative Commons license, unless indicated otherwise in a credit line to the material. If material is not included in the chapter's Creative Commons license and your intended use is not permitted by statutory regulation or exceeds the permitted use, you will need to obtain permission directly from the copyright holder.





Development and Experimental Assessment of a Control Logic for Hydroplaning Prevention

Edoardo Montini^(✉), Marco Salierno, Stefano Frigerio, and Stefano Melzi

Mechanical Department, Politecnico di Milano, Milan, Italy

{edoardo.montini, marco.salierno, stefano.melzi}@polimi.it,
stefano11.frigerio@mail.polimi.it

Abstract. Hydroplaning plays a crucial role in road safety. The water layer wedged between the tires and the road reduces the capability of the vehicle to respond to the driver's inputs. Factors like vehicle speed, water layer thickness, tread pattern, and tire wear affect hydroplaning onset. Based on the technical literature and experimental tests, the research developed a tire model to simulate hydroplaning effects. Scaling factors were added to the MFTyre model to reproduce the changes in cornering stiffness, relaxation length, friction coefficient, and motion resistance. Then, a control logic to counteract hydroplaning was designed and implemented on a 14-dof vehicle model. As last, the effectiveness of the control logic was assessed through a series of indoor tests on a dynamic driving simulator.

Keywords: Hydroplaning · Tyre model · 14-dof model · Control Strategy · driving simulator

1 Introduction

Hydroplaning is a critical factor for road safety, as underscored by alarming statistics on road accidents. According to [1], adverse weather conditions contribute to 10% of fatal road accidents, with 3% occurring on icy or snow-covered roads and the remaining 7% on wet roads. The phenomenon's evolution was initially described by [2]. Tyre design, including tread grooves and sipes, plays a pivotal role in addressing hydroplaning by expelling water from the contact area and channeling it away. This design facilitates the tire's ability to maintain direct contact with the road surface, thereby minimizing the risk of hydroplaning.

According to the definition in [3], hydroplaning speed is the velocity corresponding to the contact patch detaching from the ground; it is determined by factors such as water film depth, tread pattern design, and tire wear. The research [4] emphasizes the adverse impact of hydroplaning on vehicle responsiveness, caused by the wedge of water formed between the tire and the road surface. Previous research, including studies by [5] and [6], investigated hydroplaning's effects on tire properties such as cornering stiffness, relaxation length, and friction coefficient. Road texture's influence has also been examined by [7] and [8].

© The Author(s) 2024

G. Mastinu et al. (Eds.): AVEC 2024, LNME, pp. 293–300, 2024.

https://doi.org/10.1007/978-3-031-70392-8_42

Furthermore, [9] explores how tread design affects a tire’s maximum volumetric flow rate, while [10] investigates the relationship between groove pattern and hydroplaning speed. The findings reported in [11] confirm that rear wheels develop tangential forces even when the front ones experience hydroplaning due to the *cleaning effect* of front tires.

Given the dangers associated with hydroplaning, various studies have sought to address it. The work [12] presents a control system based on a linear single-track model, while [13] suggests mitigating hydroplaning risk by using air streams to remove water ahead of the front tires. Detection of hydroplaning onset is crucial for activating control measures, as proposed by [14] through measurement devices and techniques.

Drawing from technical literature and experimental tests, researchers have developed a tyre model to simulate hydroplaning, incorporating scaling factors into the MFtyre model [15]. This model aims to replicate hydroplaning onset on a dynamic driving simulator [16] to evaluate a control logic designed to assist drivers in such hazardous situations.

2 Tyre Model Development

A tyre model able to simulate hydroplaning was developed. Based on technical data, four scaling factors were introduced in the MFtyre model [15] to adapt the nominal conditions to the wet environment. The scaling factors modify cornering stiffness, longitudinal stiffness, relaxation length, and friction coefficient. They are obtained from experimental data available in [5, 6] as a function of the speed, considering specific tire dimensions and a 5mm-deep water layer (Fig. 1a).

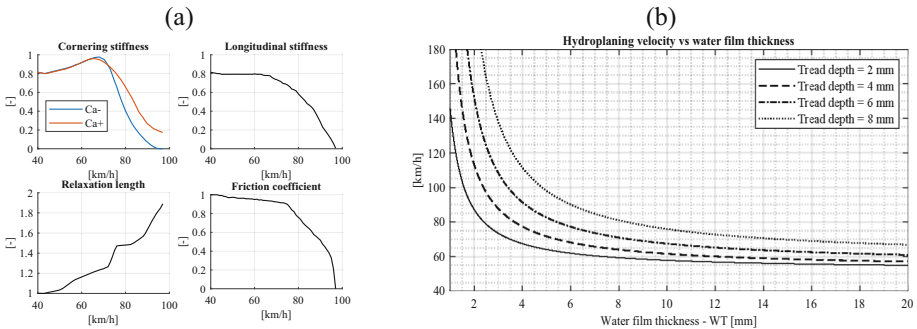


Fig. 1. Technical data used to modify the MF model: (a) scaling factor obtained from [5, 6], (b) hydroplaning speed vs tire characteristics obtained in [4]

To extend the range of possible scenarios, it is mandatory to relate the scaling factor with the maximum volumetric flow rate the tire can drain out. The research [3] provides the critical hydroplaning speed for different water layer depths and different tread tire characteristics (Fig. 1b). Thus, knowing the current tire and road condition and vehicle speed, it is possible to define an equivalent speed to be used in the experimental curves.

Moreover, the model includes the “cleaning effect” of the front tires: part of the water film is drained out by the front tires based on the maximum volumetric flow rate they can process. This phenomenon increases the critical hydroplaning speed for the rear axle. Research [11] relates the wedge of water under the front tires with the wedge of water under the rear tires, as a function of the speed. Knowing the speed, tire characteristics, and the amount of water, it is possible to scale the Pacejka’s curves also for the rear axle.

The proposed model was verified by comparing the outcomes of a sine sweep maneuver performed in [5]. Both sources exhibit similar trends in lateral forces. Figure 2 shows that the hydrodynamic interaction between the tyre and water leads to a more pronounced load shift asymmetry during turns, emphasizing the influence of the scaling factor on normalized cornering stiffness. The relaxation length significantly delays lateral force development, revealing a notable decrease in lateral force even at relatively low frequencies such as 2 Hz.

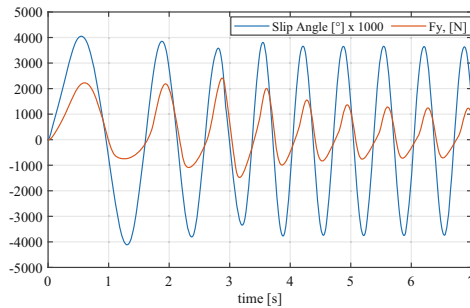


Fig. 2. Time histories of lateral force and slip angle during swept sine at 85 km/h.

3 Off-Line Development of Control Strategy

A control strategy, aimed at enhancing safety, has been developed to counteract the hydroplaning phenomenon. The working principle is based on the reduction of the vehicle’s speed below the critical threshold to restore contact between tires and the road. Therefore, taking advantage of the cleaning effect, braking torque is applied to the rear axle.

Concerning Fig. 3, the control logic activates independent braking of the rear tires taking advantage of the cleaning effect of the front ones; a yaw moment is generated, helping the driver to complete the manoeuvre. The yaw moment depends on the steering wheel angle δ required by the driver. If the absolute value of δ crosses a given threshold and the car is not turning, the logic applies a different braking torque at the rear wheels ($M_{br,l}$ and $M_{br,r}$). Lastly, activation of the logic is triggered assuming to use sensorized tires, able to detect hydroplaning onset.

The effectiveness of the logic was assessed through offline simulations and driving simulator tests. A double-lane-change manoeuvre was considered and developed. It is typical of highways when it is necessary to move on the adjacent lane and come back

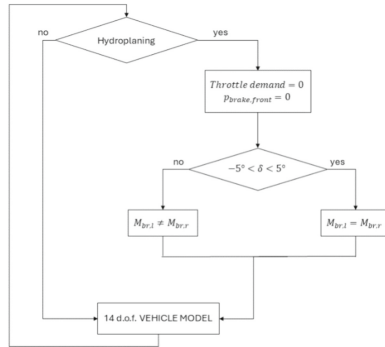


Fig. 3. ADAS logic scheme.

to the original one and it can become dangerous if water is present on the ground and the speeds are high. The scenario has been simulated according to the scheme of Fig. 4a: cones were distributed over an artificial pool of water. Many tests with different conditions of water and speed have been considered to tune and calibrate the logic gains. Therefore, firstly, offline simulation with the ideal driver has been tested. For seek of brevity, a test characterized by 8-mm water film depth and 90 km/h speed is reported, to emphasize the effect of hydroplaning and evaluate the effectiveness of the control logic in a critical scenario. Results show the power of the control logic; the ADAS helps the driver stay focused on obstacles without worrying about reducing speed, as the system handles it for him.

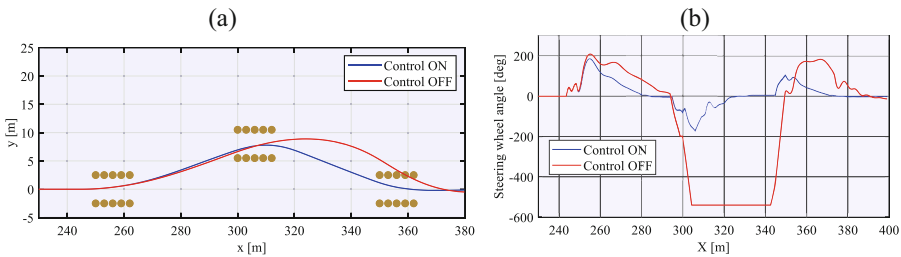


Fig. 4. Double-Lane-Change offline simulation, 90 km/h and 8-mm water depth: (a) comparison of the vehicle trajectories, (b) steering wheel angle asked by the ideal driver with ADAS on and off.

Figure 4a highlights the improvement in the vehicle’s trajectories when the ADAS is activated, while Fig. 4b shows the steering wheel angle asked by the ideal driver. With ADAS off, he saturates the maximum angle available.

Figure 5 shows the braking force on the rear axle, applied by the ADAS. First, the vehicle must turn to the left, thus a larger torque is applied to the rear left tire. In the second phase, the driver must turn to the right to avoid the second row of cones, coming back to the original lane. In this phase, a larger torque is applied by the logic to the rear right tire. Interesting to notice that the torque value starts oscillating; the vehicle speed

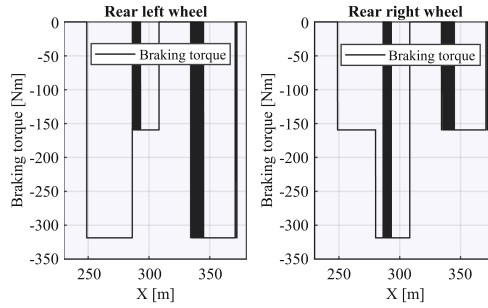


Fig. 5. Double-Lane-Change offline simulation, 90 km/h and 8-mm water depth: braking torque applied by the logic to complete the manoeuvre.

is across the critical hydroplaning one, leading to ON-OFF the logic depending if the speed is lower or larger than the critical one. Finally, the torque value on the rear left tire becomes once again larger, since the driver is turning on the left again to get the original lane straight line.

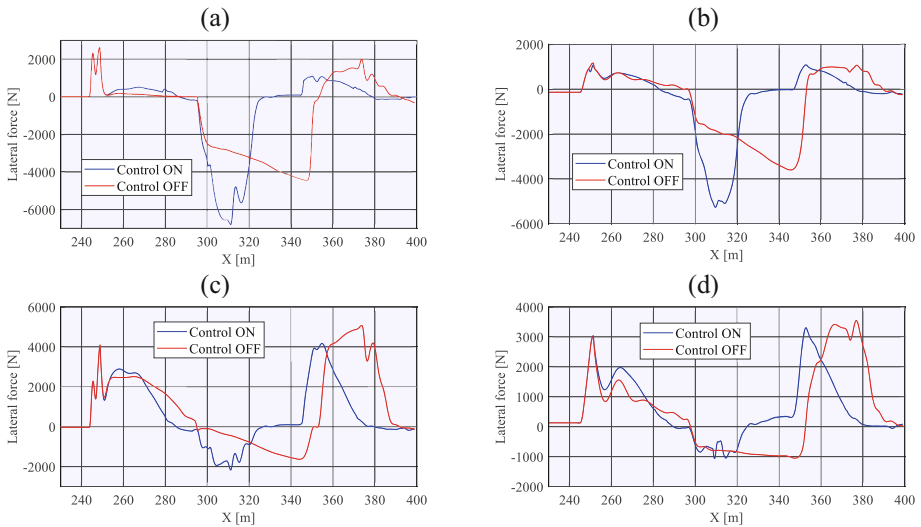


Fig. 6. Double-Lane-Change offline simulation, 90 km/h and 8-mm water depth, lateral forces: (a) front left tire, (b) front right tire, (c) rear left tire, (d) rear right tire.

Figure 6 shows the evolution of the lateral forces exchanged by the tires with the ground, on each corner. Without the control, front tires saturate the maximum lateral force exchangeable with the ground, colliding with the cones. Rear tires, thanks to the cleaning effect, can exchange larger amounts of force, but due to the presence of water and the loss of grip on the front axle, they undergo a delay, leading to a further decrease in the vehicle controllability.

4 On-Line Testing on the Driving Simulator

After completing the offline tuning, the model was implemented on the dynamic simulator of the Politecnico di Milano [6]. A panel of 37 volunteers (9 female and 28 male) was involved in an experimental campaign to assess the efficacy of the control logic. Users with different experiences, risk-taking attitudes, and genders had to drive the double lane change. This operating condition is rather typical when running on motorways. Tests were repeated changing the extension of the hydroplaning area, thus affecting the time of intervention of the control before the execution of the manoeuvre. Drivers were asked to control the vehicle with and without the assistance of the active control. The success rate in completing the manoeuvres determined the effectiveness of the proposed logic. The next figures compare the outcomes with and without the control logic. Figure 7 reports the average trajectory and the dispersion of trajectories ($\pm 1\sigma$) considering all the 37 drivers. Drivers were asked to maintain a speed of 120 km/h while approaching the pool of water. A 5-mm water depth was assumed.

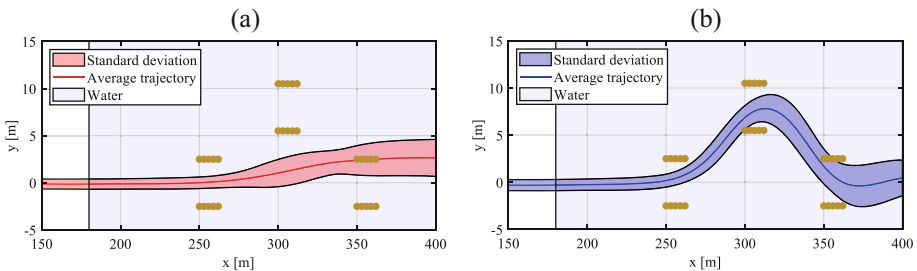


Fig. 7. Vehicle trajectories (average and dispersion) in double lane change at 120 km/h and 5-mm water layer: control logic OFF (a) and ON (b)

Figure 7 clearly shows that the logic improves the possibility of avoiding the cones. More specifically, the success rate can be summarized as follows: without the assistance of the ADAS, none of the drivers was able to close the manoeuvre without hitting the cones. With the assistance of the ADAS, 67% of the drivers were able to complete the manoeuvre without contacting the cones, 15% of the drivers failed the test on the first lane change, while 18% failed the test on the second lane change. These two percentages are mainly associated with the lack of confidence of the drivers, depending on whether they experienced hydroplaning firstly without the logic or with the logic active. Drivers who tested firstly without logic had a delay in applying the right steering wheel angle, leading to manage to steer, but touching the cones. Nevertheless, all of them were able to steer during hydroplaning conditions.

5 Conclusions

The research yielded intriguing insights into the behavior of everyday drivers encountering hydroplaning. An innovative tire model was developed and integrated with a 14-degree-of-freedom vehicle model to replicate hydroplaning effects. Additionally, an

ADAS system was designed to assist drivers in maintaining vehicle control. An offline simulation helped in tuning and calibrating the ADAS, and choosing the right gains. The results of the offline tests show that the developed system improves the vehicle's drivability, allowing the ideal driver to avoid obstacles without knocking over the cones. Finally, the effectiveness of this control logic was evaluated using the dynamic driving simulator at the Politecnico di Milano. A critical highway scenario involving a 5-mm water layer during an overtaking maneuver was designed and tested, revealing that most drivers struggled to maintain control without ADAS assistance. The findings demonstrated that such a control system could greatly enhance vehicle controllability. Finally, the potential of the driving simulator was highlighted; it allows for a deeper study of environmental phenomena like hydroplaning, aiding in the improvement of ADAS systems by examining tire behavior, and facilitates an in-depth analysis of human reactions to hazardous conditions in a controlled environment, essential for developing autonomous driving systems.

References

1. World Health Organization: Global Status Report on Road Safety (2019)
2. Albert, B.J.: Tyres and Hydroplaning, Automotive Engineering Congress and Exposition. SAE International (1968)
3. Plöchl, P., Pfeffer, P., Edelmann, J.: Advanced Vehicle Control. Taylor Francis Group (2017)
4. Malenska, M., Petry, F., Fehr, D., Schuhmann, W., Böhle, M.: Longitudinal hydroplaning performance of passenger car tyres. *Veh. Syst. Dyn.* (2021)
5. Melzi, S., Sbroisi, M., Sabbioni, E., d'Alessandro, V.: Experimental characterization of the lateral response of a tyre under hydroplaning condition. *SAE Int. J. Passeng.* (2012)
6. Fichtinger, A., Edelmann, J., Plochl, M., Holl, M.: Aquaplaning detection using effect-based methods: an approach based on a minimal set of sensors, electronic stability control, and drive torques. *IEEE Veh. Technol. Mag.* **16**(3), 20–28 (2021)
7. Mounce, J.M., Bartoskewitz, R.T.: Hydroplaning and roadway tort liability. *Transp. Res. Rec.* (1993)
8. Kienle, R., Ressel, W., Götz, T., Weise, M.: The influence of road surface texture on the skid resistance under wet conditions. *Proc. Inst. Mech. Eng.* (2020)
9. Bielse, F., Hermange, C., Todoroff, V., Le-Chenadec, Y.: Experimental investigation of the leading parameters influencing the hydroplaning phenomenon. *Veh. Syst. Dyn.* (2022)
10. Fwa, T., Srirangem, S., Anupam, K., Ong, G.: Effectiveness of tyre-tread patterns in reducing the risk of hydroplaning. *Transp. Res. Rec.: J. Transp. Res. Board* (2009)
11. Cerezo, V., Gothie, M., Menissier, M., Gibrat, T.: Hydroplaning speed and infra-structure characteristics. *Proc. Inst. Mech. Eng. Part J: J. Eng. Tribol.* **224**(9), 891–898 (2010)
12. Hartman, B., Klöster, A., Raste, T.: Hydroplaning avoidance – a holistic system approach (2019)
13. Jindřich, F., Motl, J., Mikulec, R., Moravcová, P., Bucsuházy, K.: Acquaplaning-preventing device based on blowing a wet road with a stream of air. *Transp. Res. Proc.* (2019)
14. Niskanen, A.J., Tuononen, A.J.: Accelerometer tyre to estimate the aquaplaning state of the tyre-road contact. In: *IEEE Intelligent Vehicles Symposium (IV)* (2015)
15. Pacejka, H.B.: Semi-empirical tyre models (chap. 4). In: *Tyre and Vehicle Dynamics*, pp. 176–182. Butterworth-Heinemann (2006)
16. Gobbi, M., et al.: A driving simulator for UN157 homologation activities. In: *Proceedings of the ASME International Design Engineering Technical Conferences and Computers and Information in Engineering Conference* (2022)

Open Access This chapter is licensed under the terms of the Creative Commons Attribution 4.0 International License (<http://creativecommons.org/licenses/by/4.0/>), which permits use, sharing, adaptation, distribution and reproduction in any medium or format, as long as you give appropriate credit to the original author(s) and the source, provide a link to the Creative Commons license and indicate if changes were made.

The images or other third party material in this chapter are included in the chapter's Creative Commons license, unless indicated otherwise in a credit line to the material. If material is not included in the chapter's Creative Commons license and your intended use is not permitted by statutory regulation or exceeds the permitted use, you will need to obtain permission directly from the copyright holder.





Charging Stations for Electric Vehicles in SUMO Simulation Environment and Their Impact on the Traffic Flow

Eva Spachtholz^(✉) , Marvin Glomsda , Ingmar Kranefeld ,
Frédéric Etienne Kracht , and Dieter Schramm 

Chair of Mechatronics, University of Duisburg-Essen, 47057 Duisburg, Germany
eva.spachtholz@uni-due.de

Abstract. Planning of charging stations is becoming increasingly prevalent. Consequently, it is of paramount importance to assess their impact on traffic flow and, subsequently, their optimal positioning. To identify these optimal positions, microscopic traffic flow simulations represent an efficacious tool. Different positions can be trialed until an optimal solution is identified. The open-source microscopic traffic flow simulation tool SUMO would be an optimal choice for this purpose, but does not yet offer the possibility of efficiently implementing charging stations in its traffic networks. As part of a current research project, a novel method for implementing charging stations at their real location within the SUMO environment is presented. Exemplary locations are selected in the German city of Essen.

Keywords: modeling · traffic flow simulation · electric vehicles · charging infrastructure

1 Introduction

Global warming is largely the result of carbon dioxide emissions, so minimizing emissions of this gas is a widely recognized goal. Transportation in particular is responsible for a large proportion of these emissions, and great effort is being put into reducing emissions further. Replacing internal combustion engine vehicles with electric vehicles (EVs) is currently being pursued as a way to reduce emissions. EVs do not produce local emissions and, depending on the production of electrical energy, lower global emissions in terms of CO₂ equivalents. However, they also present new challenges [1]. Conventional EVs typically store energy in batteries that need to be recharged. This can be done either at a private charging point, such as a wallbox, or at public charging stations. The use of a private wallbox is not a viable option in densely populated areas, nor are other forms of private charging points. Therefore, there are plans to expand the public charging infrastructure throughout Germany. The German government has set a target of one million public charging points by 2030 [2]. To implement a strategically appropriate expansion of the charging infrastructure, it is essential to consider the actual traffic flows. To realize that during the planning process, an approach is presented here

that integrates the charging infrastructure into a traffic flow simulation. This way, the impact on traffic flows can be determined and optimized in advance when planning a new charging station. However, before the simulated planning of new charging stations can begin, there must be a way to implement charging stations into the simulation environment. Therefore, this research paper presents the implementation of all existing public charging infrastructure of a given area into a traffic flow simulation. The traffic flow simulation software used is SUMO (Simulation of Urban MObility), developed by the German Aerospace Center (DLR), an open-source simulation software for large-scale microscopic traffic flow simulation [3]. To consider charging stations in the simulation scenario, an algorithm was developed to automatically import and position the charging stations within the simulation as close as possible to their real geographic coordinates. The fundamental principles of this import algorithm can also be used to import planned future charging stations, which are to be analyzed in a simulation environment first. This analysis allows urban and transport planners to assess the impact of the location of charging stations on traffic flow and their future use during the planning process for public charging infrastructure, thereby identifying the optimal location.

2 Database

Charging stations in public places in Germany can be found in the so-called charging station register (CSR) [4]. The charging stations of various operators are listed there, but this is not mandatory, so completeness is not always guaranteed. The register is freely available and serves as a database within this research paper. The data for each charging station includes the name of the charging station operator, the street, and house number where the charging station is located, as well as the postcode, city, and district. The longitude and latitude of the location, which are crucial for accurate placement within the simulation environment, are also provided for precise localization. Additionally, supplementary information regarding the charging capabilities is included. Furthermore, map data from OpenStreetMap (OSM) is used to describe the road network [5]. The map contains data on roads, railways, waterways, forests and buildings. These two databases are used to create the foundation of the traffic flow simulation. To complete the simulation, a description of the traffic demand is required, e.g. based on origin-destination (OD) matrices. Among others, a vehicle model for EVs is available that shows characteristic driving and charging behavior of common EV. Figure 1 shows a part of the German city of Essen, which is used here and serves as an exemplary region in the following. The area under consideration is the postcode area 45145 within the district of Frohnhausen with a size of around 3.6 km² and a population of around 33,200 [6]. The area under consideration in the figure has already been realized in SUMO and integrated into the appropriate image section of Google Maps [7] as an orientation.

3 Methodology

Currently, charging stations in SUMO are implemented as inductive loops embedded in road segments [8]. These inductive charging areas do not sufficiently reflect common charging options. The charging infrastructure mainly consists of charging stations with



Fig. 1. Area under consideration (45145, Germany), in sumo-gui and Google Maps©

multiple charging points. In reality, public charging stations are typically located in parking lots specifically designed for charging EVs. This behavior has to be mapped in SUMO. To represent this, a combination of inductive charging areas and parking lots can be used. An inductive charging area is placed on a lane, which is specified by the framework conditions in SUMO, and a parking lot is provided next to it on the roadside. In the simulation, the parking lot and the charging area are linked so that vehicles parked in the parking area can charge even though they are not placed directly on the inductive charging area. Even if the representation of the charging points deviates somewhat from reality due to this adjustment, the deviation between simulation and reality will be minimized when positioning the existing public charging stations correctly.

In order to import the public charging infrastructure into the simulation environment, an algorithm has been developed, which is visualized in Fig. 2. The first step is the user input. This includes OSM data of the road network to be simulated. The OSM-data serves as a fundamental component of the simulation, providing the road network (net-file) through an import process. The data required also includes the CSR. In order to import the charging stations from the CSR that are located in the area under consideration, it is necessary to specify the area to be simulated. This can be done either by the city name or by the postcode area. The input acts as a filter to identify the relevant charging stations. After all user inputs have been defined, the required information is extracted from the net-file and the CSR. Each individual edge, which represents a road section of the road network, is identified. The edges and their associated parameters are then stored. Of particular importance is the shape attribute of each edge, from which longitude and latitude of the edges can be determined.

The charging stations in the specified area are then selected from the CSR. Various information about the charging stations is taken into account, such as the geocoordinates, the provider, the charging power, and the number of charging points at the charging station. The power of the charging station and the number of charging points are used to calculate the power of each charging point. Once all the necessary information has been retrieved, the positioning of the charging stations begins. To do this, the nearest edge allowing car traffic (road edge) in the net-file must be found for each of the charging stations located in this area. For each station, the distance to all road edges is determined using geodetic distance. The charging station is placed at the edge with the shortest distance to it. It is important to note that only one corner of the edge is described by geocoordinates in the shape attribute of the edge. Therefore, the exact geocoordinate

of the charging station cannot be found, so the charging station is always placed at the beginning of the edge, resulting in a deviation between the positions from the CSR and the charging station in the simulation. A parking lot is placed next to each charging point as described above. All relevant parameters are determined for each charging point, such as the ID, the ID of the lane where the charging station is located, the available power, and the efficiency.

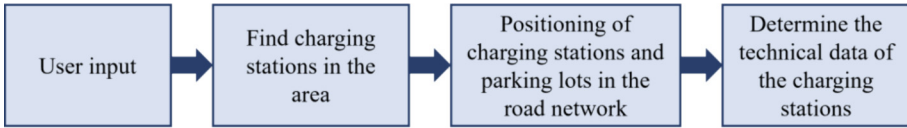


Fig. 2. Algorithm for the automated import of charging stations

4 Results

Once the algorithm has been executed, the charging stations are imported into the road network. An individual charging point always consists of an inductive charging area and a parking lot. The simulation software extracts all information from the data file to graphically represent the charging point and parking lot in the simulation environment, as shown in Fig. 3. As can be seen here, the orange-colored inductive charging area only affects the connected parking lot. The green outlined parking lot with the EV indicates that this parking lot is occupied and the charging process is currently in progress. To validate the algorithm, the area mentioned above was selected. The algorithm identifies six charging stations in this area, each with two charging points that need to be placed within the road network.

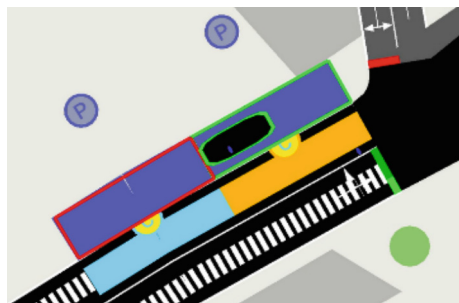


Fig. 3. Charging EV in a parking lot

The placement follows the procedure described above and is evaluated here. For the evaluation, the algorithm calculates the deviation between the real geocoordinates of the charging station taken from the CSR and the geocoordinates at which the charging station is to be placed in the simulation. The deviation is given in meters and is shown

in Table 1 for all six charging stations. The table shows that the maximum deviation is 90.71 m. The average deviation is 35.11 m. This deviation is inherent to the placement method used. Based on the available edge data, the charging stations are always placed at the start of the edge.

Table 1. Difference in location between real infrastructure and placement in simulation

charging station id	distance between actual and SUMO geocoordinates [m]
cs7270_Allego GmbH	7.58
cs7271_Allego GmbH	90.71
cs7272_Allego GmbH	15.66
cs7273_Allego GmbH	36.61
cs7274_Allego GmbH	23.06
cs7277_E.ON Drive Infrastructure	37.05

In reality, the charging station can be placed anywhere along the road. This can be seen in Fig. 4. In the simulation, the center of the road is the given geocoordinate. Therefore, the enlarged view in Fig. 4 shows, that the charging station was to be positioned in the center of the road.

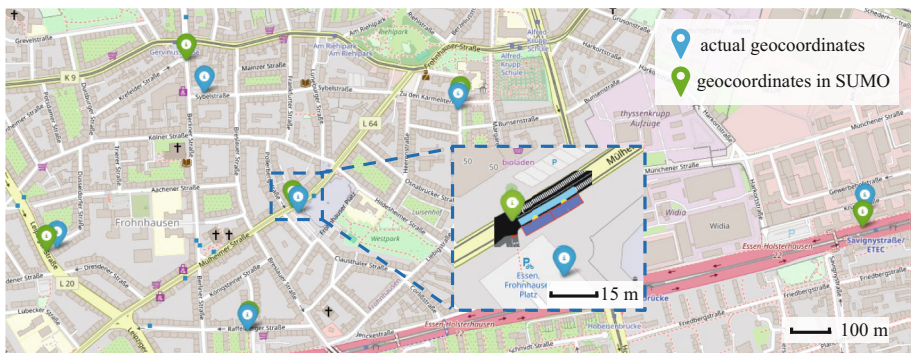


Fig. 4. Comparison of the actual geocoordinates and the geocoordinates in the simulation environment SUMO in the area under consideration of all six documented charging stations

The location of the charging station within the simulation differs from that of the intersection. Rather, it is situated at the beginning of the edge, with the parking lot situated adjacent to the edge. This configuration results in a smaller deviation of the final charging stations' locations than calculated above.

5 Conclusion

The algorithm for automatically importing charging stations into a traffic flow simulation in the SUMO simulation environment facilitates the configuration of a simulation with electric vehicles (EVs). The manual effort of placing charging points in the right locations is no longer necessary. In addition, the accuracy of the automated placement method is so high that no traffic impact is to be expected due to inaccuracy. To further increase the placement accuracy of the charging infrastructure, a logical next step could be to determine the geocoordinates over the entire length of the edges to enable more differentiated placement. In further steps the automated import routine can also be used to place additional charging points into a traffic flow simulation. The desired geocoordinates can be specified in a way that the algorithm can place the charging stations at desired locations. The placement could be derived from an analysis of the traffic flow in a simulation, for example on busy roads or avoiding them respectively. It would then be possible to evaluate how the additional charging points affect the traffic flow in the simulated area. Conclusively, the goal is to support urban planning by using simulative methods to place charging stations more efficiently for future construction projects and to reduce inner-city traffic overall.

Acknowledgement. Parts of the results of this paper have been developed within the STRALI project, which is funded by the German Federal Ministry for Digital and Transport (BMDV) and the mFund initiative under grant agreement no. 19F2260A.

References

1. Kathiresh, M., Kanagachidambaresan, G.R., Williamson, Sheldon S. (eds.): E-Mobility: A New Era in Automotive Technology. Springer International Publishing, Cham (2022)
2. F. G. o. Germany. So funktioniert der Ausbau der Ladeinfrastruktur. <https://www.bundesregierung.de/breg-de/aktuelles/ausbau-ladeinfrastruktur-2165204>. Last accessed 30 Apr 2024
3. Alvarez, P., et al.: Microscopic Traffic Simulation using SUMO. In: IEEE Intelligent Transportation Systems Conference (2018)
4. Bundesnetzagentur homepage: <https://www.bundesnetzagentur.de/DE/Fachthemen/ElektrizitaetundGas/E-Mobilitaet/start.html>. Last accessed 2 Jan 2024
5. OpenStreetMap homepage. <https://openstreetmap.de/faq/#was-ist-openstreetmap>. Last accessed 2 Jan 2024
6. Statistisches Bundesamt, Einwohner:innenzahl der Stadtteile in Essen im Jahr 2024 [Graph], Stadt Essen, 31. März, 2024. <https://de.statista.com/statistik/daten/studie/1234670/umfrage/einwohnerzahl-stadtteile-essen/>. Last accessed 5 May 2024
7. Google maps homepage: <https://www.google.de/maps/place/45145+Essen-Stadtbezirke+III>. Last accessed 5 May 2024
8. Kurczveil, T., López, P., Schnieder, E.: Implementation of an Energy Model and a Charging Infrastruktur in SUMO. In: Behrisch, M., et al. (eds.) SUMO 2013, pp. 33–43. Springer, Heidelberg (2014)

Open Access This chapter is licensed under the terms of the Creative Commons Attribution 4.0 International License (<http://creativecommons.org/licenses/by/4.0/>), which permits use, sharing, adaptation, distribution and reproduction in any medium or format, as long as you give appropriate credit to the original author(s) and the source, provide a link to the Creative Commons license and indicate if changes were made.

The images or other third party material in this chapter are included in the chapter's Creative Commons license, unless indicated otherwise in a credit line to the material. If material is not included in the chapter's Creative Commons license and your intended use is not permitted by statutory regulation or exceeds the permitted use, you will need to obtain permission directly from the copyright holder.





Primary and Secondary Vehicle Lightweighting Achieved by Acting on the Battery Thermal Management System

Giulia Sandrini^(✉), Daniel Chindamo, Marco Gadola, Andrea Candela, and Paolo Magri

Department of Mechanical and Industrial Engineering, University of Brescia, 25123 Brescia, Italy

giulia.sandrini@unibs.it

Abstract. Global warming and air pollution are the main factors influencing international, national, and local strategies for the transition towards clean technologies to reduce polluting and climate-altering emissions. A further reduction of the latter can be achieved, with the same powertrain technology, by reducing vehicle consumption. One technique is to lighten the vehicle. The goal of this feasibility study is to act on the battery thermal management system to achieve vehicle lightweighting. Specifically, a sedan car with active-cooled batteries was considered as a reference case, and primary lightweighting was achieved through the use of passive cooling methods, i.e., air and Phase Change Material (PCM) cooling systems, followed by secondary lightweighting to re-establish the target range of the reference vehicle by downsizing the batteries. The air-cooled system leads to greater lightweighting, but its field of application is limited to vehicles operating in fleets; this obstacle can be overcome by using a PCM.

Keywords: Vehicle Lightweighting · Secondary Lightweighting · Traction Battery Thermal Management System · Energy Consumption · Electric Vehicle; PCM (Phase Change Material)

1 Introduction

Today, the topic of environmental sustainability is very important, in fact the reduction of polluting and climate-altering emissions is the main factor influencing international, national, and local strategies for the transition towards clean technologies. In addition to adopting more sustainable powertrains, such as electric ones, a further emission reduction can be achieved, with the same powertrain technology, by reducing vehicle consumption. The reduction in consumption can be achieved in various ways, such as through appropriate regenerative braking logics [1, 2], through the improvement of the power management logics (in particular regarding hybrid electric vehicles [3–5]), but also through the lightweighting of the vehicle [6, 13].

The battery pack plays an important role regarding environmental sustainability [7]. Therefore, the study proposed here involves the analysis of different battery thermal

management strategies to achieve both primary lightweighting, which will lead to a reduction in consumption and a consequent increase in the vehicle's range, and secondary lightweighting by reducing the number of cells in the battery pack, and thus its capacity, to restore the initial range of the reference vehicle. This work consists of a feasibility analysis rather than a precise modelling of the thermal management system of the battery pack. For the study, an active cooling system (with a total weight of 88.84 kg and an average power consumption of 815.5 W) was compared with two passive cooling systems: air and PCM (Phase Change Material) cooling systems.

2 Materials and Methods

The SedanCar from VI-CarRealTime, a consolidated state-of-the-art vehicle dynamics simulation tool, was chosen as a basis for the reference vehicle: an all-wheel-drive, electric passenger car equipped with two electric motors, one for each axle, with a total mass of 1986.6 kg. For this reference vehicle, a total consumption of the auxiliaries of 1500 W was also considered, including consumption related to the battery active thermal management system. The latter and the battery pack are those considered in studies [8–10]. In particular the battery pack is made up of 5664 cells of the NCA-18650 type, in 96S59P configuration (96 cells in series and 59 in parallel), with a capacity of approximately 56 kWh (162 Ah), an optimal operating temperature of approximately 20 °C and a maximum operating temperature of 60 °C. The active cooling system considered has a total weight of 88.84 kg, an average power consumption of 815.5 W, and it is sized to maintain an average refrigerant temperature of approximately 20 °C. Through VI-CarRealTime simulations, the torque and angular velocity time histories of the electric motors were obtained on WLTC (class 3b) driving cycle, which is considered the reference cycle. These outputs were then used as inputs for the TEST (Target-speed EV, Electric Vehicles, Simulation Tool) model described in [11], customized for this purpose, enabling to obtain the power demand that the vehicle system requires from the battery pack. Finally, this power demand has been used as input for a Simulink model, that simulate the battery pack and its thermal management system performance [8, 9].

The thermally managed battery pack model is simplified, in fact the aim of the work is a feasibility study and not an accurate thermal management modelling. It contains the “Datasheet Battery” model of the Simulink “Library Browser” [12]. This model takes as input the battery current, temperature, number of cells in parallel and in series in the battery pack, the rated capacity of a single cell, the cell open circuit voltage as a function of the battery State of Charge (SOC), the cell internal resistance, and the initial battery capacity. The outputs are instead the following: battery voltage, battery SOC, battery power (and power loss), and cell energy. The following equations were used for the battery pack thermal management model, where Eq. (3) is valid only if $\sigma \leq 1$, and (4) is valid for $\sigma > 1$.

$$Q_{CP} = K_{CP} \cdot (T_{bat_prev} - T_{CP}) \quad (1)$$

$$T_{bat} = (Q_{bat} - Q_{CP}) \cdot dt / (\rho_{bat} \cdot v_{bat} \cdot c_{p, bat}) + T_{bat_prev} \quad (2)$$

$$C_h = (2.04 \cdot \sigma^2 + 2.79 \cdot \sigma) / 100 \quad (3)$$

$$C_h = (3.97 \cdot \ln \sigma + 4.83) / 100 \quad (4)$$

Q_{CP} is the cooling heating power of the cooling plate of the thermal management system, Q_{bat} is the heat generated by the batteries and it is calculated as C_h multiplied by the battery power, T_{bat} is the average battery pack temperature, T_{bat_prev} is the average battery temperature relative to the instant of calculation preceding the one considered, T_{CP} is the average temperature of the refrigerant flowing in the heat exchangers, K_{CP} is the heat conductance at the cooling plate, ρ_{bat} is the average battery density, $c_{p,bat}$ is the specific heat capacity of the battery, v_{bat} is the total volume of the batteries, and, finally σ is the ratio between the battery power (expressed in kW) multiplied by 1 h and the battery power storage (expressed in kWh). Q_{CP} is imposed equal to zero for passive air-cooling system. Null is also imposed for PCM cooling systems until the melting point temperature of the PCM is reached, after that, the battery pack temperature remains constant until the heat generated by the battery pack does not reach the maximum heat absorbable by the PCM during the change of state, then the batteries temperature starts to grow again as in the initial phase.

Different sets of simulations are performed, composed of the repetition of WLTC cycles (class 3b), starting from SOC equal to 100% until the SOC drops below 20%, considering a simulation sample time equal to 0.01 s. The simulation sets are repeated with different battery pack initial temperatures.

3 Results

The study led to the choice of two materials as PCM: glycerol ($C_3H_8O_3$), with a melting point at 26 °C; and stearyl alcohol ($C_{18}H_{38}O$, 1-octadecyl alcohol), with a melting point at 57 °C.

Figures 1, Fig. 2, and Fig. 3 show, in the top, the trend of the battery State of Charge (SOC) with the succession of repeated WLTC cycles, respectively for the vehicle with passive air-cooled battery pack, passive glycerol PCM, and passive stearyl alcohol PCM cooled battery pack, starting from different battery pack temperature. In particular, in each graph, the vertical red lines separate one WLTC cycle from the next, and the horizontal green line represents the 20% of SOC. Similarly, the bottom of the figures shows the trend of the average temperature of the battery pack, and, in each graph, the vertical red lines separate one WLTC cycle from the next, and the dotted horizontal red line represents the maximum temperature limit, equal to 60 °C. As can be seen from Fig. 1, for an initial temperature of the battery pack from -20 to approximately 30 °C the limiting aspect for the vehicle is the capacity of the battery pack, i.e. the achievement of the SOC equal to 20%. Starting from 40 °C, however, the limit temperature of 60 °C was reached, in these cases it is therefore not possible to use the entire SOC range consecutively, it will be necessary to take a pause for cooling. As can be seen from Fig. 2, the behaviour of the vehicle with a glycerol PCM-cooled battery pack is similar to that found for the vehicle with passively air-cooled batteries.

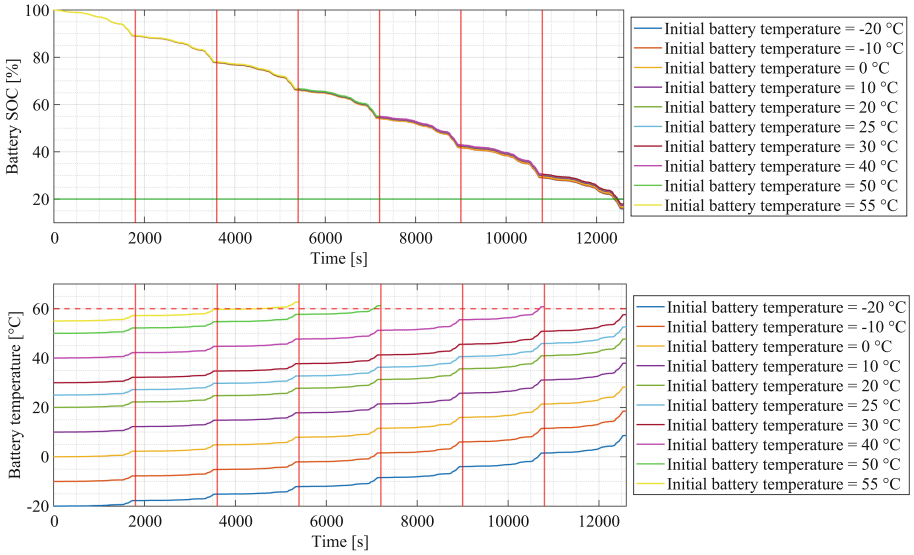


Fig. 1. Battery State of Charge (top), and battery pack average temperature (bottom). Passive air-cooled battery pack, in configuration 96S59P.

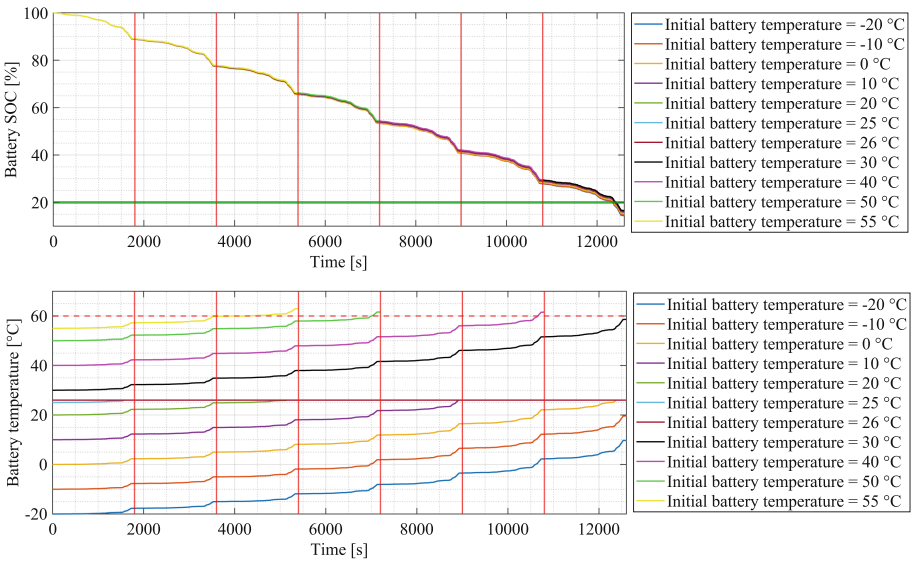


Fig. 2. Battery State of Charge (top), and battery pack average temperature (bottom). Passive glycerol PCM cooled battery pack, in configuration 96S59P.

Finally, as can be seen from Fig. 3, the stearyl alcohol PCM allows the vehicle to exploit the entire SOC range consecutively on the WLTC cycle, also starting from a battery pack temperature of 57 °C, the melting point temperature of this PCM.

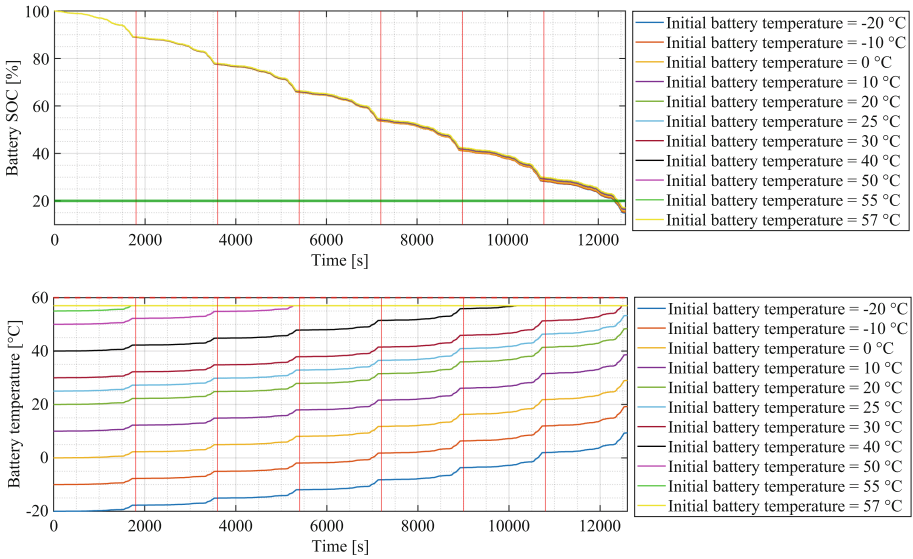


Fig. 3. Battery State of Charge (top), and battery pack average temperature (bottom). Passive stearyl alcohol PCM cooled battery pack, in configuration 96S59P.

As a secondary weight reduction measure, reducing the parallel cells of the battery pack from 59 to 54 was enough to achieve a range comparable to the one of the reference vehicle, for both air and PCMs cooled vehicles. This means removing from the battery pack 480 cells, for a total of 22.56 kg.

Table 1 resume the main results obtained in the study.

Table 1. Cooling system weight; primary and secondary lightweighting; and performance, in terms of energy consumption and vehicle range, on WLTC (class 3b) driving cycle.

System	Cooling system weight [kg]	Mass of cells removed [kg]	Primary lightweighting [kg]	Secondary lightweighting [kg]	Energy consumption [kWh/100km]	Range [km]
Active cooling	88.84	-	-	-	35.13	149.0
Air cooling	-	22.56	88.84	22.56	31.96	149.9
Glycerol	57.02	22.56	31.82	22.56	32.39	147.9
Stearyl alcohol	36.77	22.56	52.07	22.56	32.23	148.6

4 Conclusions

The air-cooled battery thermal management system is the simplest possible and leads to great potential for weight savings. However, it can be unsuitable for high starting temperatures of the battery pack. This issue also applies to the glycerol PCM-cooled system, which has however the added benefit of allowing the battery pack to operate near its optimal operating temperature for a longer time, thanks to its 26 °C melting point. Both systems suffer from the risk of excessive battery temperature rise but are suitable for vehicles operating in fleets with predefined and programmable missions. Finally, the stearyl alcohol PCM system is suitable for private use i.e. for less repetitive mission profiles and for varied driving styles, owing to its 57 °C melting point, although it sacrifices the ability to keep the batteries at an optimal operating temperature for longer periods.

References

1. Sandrini, G., Chindamo, D., Gadola, M.: Regenerative braking logic that maximizes energy recovery ensuring the vehicle stability. *Energies (Basel)* **15**, 5846 (2022). <https://doi.org/10.3390/en15165846>
2. Sandrini, G., Gadola, M., Chindamo, D., Magri, P.: Efficient regenerative braking strategy aimed at preserving vehicle stability by preventing wheel locking. *Transport. Res. Procedia* **70**, 28–35 (2023). <https://doi.org/10.1016/j.trpro.2023.10.005>
3. Zecchi, L., Sandrini, G., Gadola, M., Chindamo, D.: Modeling of a hybrid fuel cell powertrain with power split logic for onboard energy management using a longitudinal dynamics simulation tool. *Energies (Basel)* **15**, 6228 (2022). <https://doi.org/10.3390/en15176228>
4. Sandrini, G., Gadola, M., Chindamo, D., Zecchi, L.: Model of a hybrid electric vehicle equipped with solid oxide fuel cells powered by biomethane. *Energies (Basel)* **16**, 4918 (2023). <https://doi.org/10.3390/en16134918>
5. Sandrini, G., Gadola, M., Chindamo, D., Magri, P.: Application of solid oxide fuel cells on hybrid electric vehicles operating in fleet. *Transport. Res. Procedia* **70**, 20–27 (2023). <https://doi.org/10.1016/j.trpro.2023.10.004>
6. Sandrini, G., Gadola, M., Chindamo, D., Candela, A., Magri, P.: Exploring the impact of vehicle lightweighting in terms of energy consumption: analysis and simulation. *Energies (Basel)* **16**, 5157 (2023). <https://doi.org/10.3390/en16135157>
7. Sandrini, G., C6, B., Tomasoni, G., Gadola, M., Chindamo, D.: The environmental performance of traction batteries for electric vehicles from a life cycle perspective. *Env. Climate Technol.* **25**(1), 700–716 (2021). <https://doi.org/10.2478/rtuect-2021-0053>
8. Guo, J., Jiang, F.: A novel electric vehicle thermal management system based on cooling and heating of batteries by refrigerant. *Energy Convers. Manag.* **237**, 114145 (2021). <https://doi.org/10.1016/j.enconman.2021.114145>
9. Sreekanth, M., Feroskhan, M., Daniel, J., Gobinath, N.: Heat load estimation and thermodynamic analysis of the thermal management of an electric car. *Mater. Today Proc.* (2023). <https://doi.org/10.1016/j.matpr.2023.01.280>
10. Cao, W., Zhao, C., Wang, Y., et al.: Thermal modeling of full-size-scale cylindrical battery pack cooled by channeled liquid flow. *Int. J. Heat Mass Transf.* **138**, 1178–1187 (2019). <https://doi.org/10.1016/j.ijheatmasstransfer.2019.04.137>
11. Sandrini, G., Gadola, M., Chindamo, D.: Longitudinal dynamics simulation tool for hybrid apu and full electric vehicle. *Energies (Basel)* (2021). <https://doi.org/10.3390/en14041207>

12. MathWorks. Datasheet Battery. https://it.mathworks.com/help/autoblks/ref/datasheetbattery.html?searchHighlight=DATASHEET%20BATTERY&s_tid=srchtitle_support_results_1_DATASHEET%20BATTERY. Accessed 08 Apr 2024)
13. Candela, A., Sandrini, G., Gadola, M., Chindamo, D., Magri, P.: Lightweighting in the automotive industry as a measure for energy efficiency: review of the main materials and methods. *Heliyon* **10**, e29728 (2024). <https://doi.org/10.1016/j.heliyon.2024.e29728>

Open Access This chapter is licensed under the terms of the Creative Commons Attribution 4.0 International License (<http://creativecommons.org/licenses/by/4.0/>), which permits use, sharing, adaptation, distribution and reproduction in any medium or format, as long as you give appropriate credit to the original author(s) and the source, provide a link to the Creative Commons license and indicate if changes were made.

The images or other third party material in this chapter are included in the chapter's Creative Commons license, unless indicated otherwise in a credit line to the material. If material is not included in the chapter's Creative Commons license and your intended use is not permitted by statutory regulation or exceeds the permitted use, you will need to obtain permission directly from the copyright holder.





A Propulsion Energy Estimator for Road Vehicles

Carl Emvin¹(✉), Fredrik Bruzelius¹, Luigi Romano², Bengt Jacobson¹,
Pär Johannesson³, and Rickard Andersson⁴

¹ Chalmers University of Technology, Gothenburg, Sweden
`carl.emvin@chalmers.se`

² Linköping University, Linköping, Sweden

³ RISE, Gothenburg, Sweden

⁴ Volvo Group, Gothenburg, Sweden

Abstract. Residual range estimation plays a crucial role in route selection and the trust of electric vehicles (EVs). With inspiration from longitudinal vehicle dynamics, a simple and computationally efficient model for traction power is presented. Such a model has the advantage of being exclusively based on vehicle exogenous parameters. The model allows for insight into variations in power usage along a transport operation and separation of power losses originating from air drag, rolling resistance, hill climbing, and inertial forces. A model of this structure can handle regenerative braking and estimate service brake usage as an additional feature. Also, it treats the inherent truncation bias resulting from truncating a stochastic process. Evaluation of the performance is presented using Monte Carlo simulations, comparing the estimation error against a simple benchmark model and vehicle log data.

Keywords: Range estimation · Energy consumption · Truncation

1 Introduction

Electric vehicles (EVs) are an attractive medium of transportation, with excellent performance. The possibility of zero-emission fuel makes them a cornerstone in reaching the climate goals set by the European Commission. The vehicle industry's objective to meet climate goals typically translates into increasing sales of EVs. In 2023, the worldwide sales of electric cars almost reached 14 million and have seen an exponential increase in sold units over the recent year. However, the number of electric trucks sold remains small in 2023, resulting in about 54 thousand units sold [2].

In line with the sale numbers, electric trucks suffer from the lack of charging infrastructure, low power delivery at the connector, and yet small battery sizes. As a result, the feasibility of using an electric truck varies from operation to operation. The uncertainty the driver experiences posed by the variation is typically referred to as range anxiety, halting haulage from transitioning to electric

vehicles. Hence, a logistical effort targeting the variation in operations would benefit the rate of electrification. The foundation of such logistic effort is a good residual range estimate or energy prediction. The former is the distance until empty, and the latter is the energy consumed up to a distance ahead.

The vast literature covering residual range estimation can be divided into model-free approaches and model-based approaches. The model-free approach is generally based on the assumption that energy consumption is linearly increasing with traveled distance. The slope of the linear trend is the average specific energy consumption (SEC), typically calculated as a moving average of past driving, imposing similarities in future driving to that of the past. In [5], a model-free approach is presented, fitting SEC values to specific driving patterns. The model clusters regions of similar driving patterns based on average speed and average power and fits an SEC value to each cluster that matches the data. The model received an average relative error of 9 % when validated against log data from a BMW i3. However, the model is yet to be tested for heavy vehicles.

In [9], a semi-physical model, calculating the energy consumed over each road segment as the sum of energy losses due to road grade, air drag, change in kinetic energy, and a cruise penalty is presented. In this model, energy consumption is assumed to be constant over a road segment but allowed to vary from segment to segment, thus capturing the slow dynamics tied to the geometrical space, but not the fast dynamics and phenomena tied to other entities such as traffic. Also, the performance of the model is yet to be evaluated.

In a model-based approach, the main energy consumers are divided into the *auxiliary load* (air conditioner, displays, battery thermal management, and more) and *propulsion load* (energy consumed to propel the vehicle). In combination with a powertrain and an energy storage model, one can predict the total energy consumption of any vehicle, including *internal combustion engine vehicles* (ICEVs), and EVs. Hence, in the model-based approach, authors can make minor improvements to the whole model by studying the auxiliary or propulsion load in isolation. In this article, a traction force estimator derived from longitudinal vehicle dynamics is presented under Sect. 3. The model is complemented by a constrained Kalman filter state estimator, see Sect. 2, and a truncation bias correction method, see Sect. 4. In Sect. 5, the propulsion energy estimator is compared against vehicle log data and a simple benchmark model based on SEC.

2 State Estimation

A vehicle's longitudinal position, velocity, and acceleration, are integral parts to propulsion energy estimation. To estimate the states using a Kalman filter, a motion, and measurement model should be decided on. The measurement model uses vehicle wheel speed and odometer sensor measurements. To keep it simple, a kinematic motion model, namely the constant acceleration motion model (CA)

(CA)

$$\begin{aligned}
x_k &= \begin{bmatrix} 1 & T & \frac{1}{2}T^2 \\ 0 & 1 & T \\ 0 & 0 & 1 \end{bmatrix} x_{k-1} + q_{k-1}, \quad \text{with } q_{k-1} \sim \mathcal{N}(0, Q_{k-1}), \\
y_k &= [1 \ 1 \ 0] x_k + r_k, \quad \text{with } r_k \sim \mathcal{N}(0, \sigma_r^2),
\end{aligned} \tag{1}$$

is used. The process noise covariance matrix $Q_{k-1} = \int_0^T e^{\tilde{A}\tau} \tilde{Q} e^{\tilde{A}^\top \tau} d\tau$ is the analytical solution to the discretization of the continuous-time CA model with jerk modeled as a Gaussian white noise process. The measurement noise r_k is uniformly distributed around the CAN bus rounding error. To facilitate the assumption of normally distributed noise, the best approximation of the uniform distribution $\mathcal{U}(a, b)$ is the normal distribution $\mathcal{N}(\frac{a+b}{2}, \frac{(a-b)^2}{12})$. In addition, the speedometer cannot measure negative velocities, which excludes reversing maneuvers. The Kalman filter is hence modified to facilitate the inequality constraint $x_k(2) \leq 0$. The constrained solution to the Kalman filter is obtained by projecting the unconstrained *a posteriori* state estimate to the constrained space [6, 7]:

$$\begin{aligned}
&\text{minimize} && (x - \hat{x}_{k|k})^\top W_k^{-1} (x - \hat{x}_{k|k}), \\
&\text{subject to} && x(2) \geq 0.
\end{aligned} \tag{2}$$

A solution to the quadratic programming (QP) problem (2) is found by applying the active set method

$$\hat{x}_{k|k}^P = \hat{x}_{k|k} - \Upsilon(A\hat{x}_{k|k} - b), \quad \Upsilon = W_k^{-1} A^\top (AW_k^{-1} A^\top)^{-1}, \tag{3}$$

with weighting matrix W_k being the inverse of the covariance matrix, $A = [0, 1, 0]$, and $b = 0$. The same method is also applied for the *a priori* state estimate allowing the Kalman filter to do better predictions.

The yaw angle must also be estimated since it affects the air drag through the attack angle. Another kinematic motion model is used to estimate the yaw angle in the world frame, namely the coordinated turn (CT) motion model. Since the procedure is similar, no further explanation is provided.

3 Traction Force Estimation

At any time k , the total traction force $F_{t,k}$ for a road vehicle is a linear combination of five forces: rolling resistance force $F_{rr,k}$, air drag force $F_{ad,k}$, hill climbing force $F_{hc,k}$, translational inertial force $F_{it,k}$, and rotational inertial force $F_{ir,k}$,

$$F_{t,k} = F_{rr,k} + F_{ad,k} + F_{hc,k} + F_{it,k} + F_{ir,k}. \tag{4}$$

Rolling resistance force is the resistive force associated with a tire rolling under vertical load. In this paper, only the linear relationship between the nominal rolling resistance coefficient (C_r) and the vehicle's vertical load is modeled:

$$\hat{F}_{rr,k} = C_r m_k g \cos(\varphi_k) + e_{rr,k}, \tag{5}$$

where the error e_{rr} captures model inaccuracies coupled with using a simplified model that does not consider the temperature and pressure dependency of C_r . In [4], the mean relative error of a constant C_r over a certain driving cycle was found to be 12.9%. In this paper, the error is assumed to be normally distributed with zero mean and variance, $\sigma_{rr,k}^2 = (m_k g C_r \cdot 0.1)^2$.

Aerodynamic drag force is the resistive force acting on an object moving in air and in this paper, *model 1* [1] is used. The model is based on the state-of-art model:

$$\hat{F}_{ad,k} = \frac{1}{2} \rho C_D A_p(\theta_k) (v_{x,k} + v_{wx,k})^2 + e_{ad,k}, \quad (6)$$

in which the air density ρ and the drag coefficient C_D are constants. The relative longitudinal velocity experienced by the vehicle is the sum of the longitudinal vehicle $v_{x,k}$ and wind $v_{wx,k}$ speed. Additionally, the projected frontal area $A_p(\theta_k)$,

$$A_p(\theta_k) = A_f \cos(\theta_k) + A_{s,k} \sin(\theta_k), \quad \theta_k = \arctan \frac{|v_{wy,k}|}{v_{x,k}}, \quad (7)$$

is a function of the attack angle θ_k , a constant front area A_f , and a varying side area $A_{s,k}$, which is allowed to change between two discrete values representing with and without a trailer. The model has a root mean squared error $\text{RMS}(y_k - C_D A_p(\theta_k)) = 1.19$ when compared against CFD simulation results using a tractor with a semi-trailer. In this paper, the error is assumed to be normally distributed with zero mean, and variance, $\sigma_{ad,k}^2 = (1.2 \frac{1}{2} \rho (v_{x,k} + v_{wx,k})^2)^2$.

Hill climbing force is the gravitational force parallel to the road slope φ_k ,

$$F_{hc,k} = m_k g \sin(\varphi_k). \quad (8)$$

Inertial force consists of a translational and a rotational force. The translational inertial force is associated with longitudinal acceleration and the rotational with acceleration of the powertrain. They can be coupled by introducing the equivalent mass m^* :

$$\hat{F}_{it,k} + F_{ir,k} = m_k^* a_k + e_{i,k}, \quad m_k^* = m_k + I \frac{G_k^2}{\eta_g r^2}. \quad (9)$$

Here G is the gear ratio, I is the moment of inertia of the rotor, η_g is the gear efficiency, and r is the tire radius. Thus, a model for gear selection is required. A simple switch algorithm based on vehicle longitudinal speed is used.

The normally distributed acceleration estimation error propagates to the inertial force and hence, is the inertial force error $e_{i,k}$ normally distributed with zero mean, and variance, $\sigma_{i,k}^2 = (m^* \sigma_a)^2$.

4 Propulsion Power

The traction force F_t is the force applied at the wheel to propel and brake the vehicle. A negative traction force corresponds to braking, and a positive to propelling the vehicle. The propulsion power is thus:

$$P_{p,k} = \max(0, F_{t,k} v_{x,k}). \quad (10)$$

But since F_t is unknown, the traction force estimate \hat{F}_t has to be used. However, truncating a random variable will move the mean resulting in a truncation bias in the model. First, the traction force estimation error,

$$e_{t,k} = F_{t,k} - \hat{F}_{t,k}, \quad e_{t,k} = e_{rr,k} + e_{ad,k} + e_{i,k}, \quad (11)$$

is a linear combination of random normal distributed variables with zero mean. The error e_{ad} comes from simplifications in $A_{p,k}(\theta)C_d$, e_{rr} from simplifications in c_r , and $e_{i,k}$ from kalman filter uncertainties in the acceleration. Since none of the errors is a function of the same variable, one can claim independence resulting in a zero mean, normally distributed variable with variance, $\sigma_{t,k}^2 = \sigma_{rr,k}^2 + \sigma_{ad,k}^2 + \sigma_{i,k}^2$. The author acknowledges that the errors are likely auto-correlated, but are here regarded as time-independent. The traction power estimate $\hat{P}_{t,k}$ is thus also normally distributed with mean $\mu_k = F_{t,k} v_{x,k}$ and variance $\sigma_k^2 = v_{x,k}^2 \sigma_{t,k}^2$. Now, consider the truncated traction power estimate, i.e. the propulsion power estimate $\hat{P}_{p,k} = \max(0, \hat{P}_{t,k})$, corresponding to a lower-tail truncation at 0 with $\alpha = \frac{-\mu_k}{\sigma_k} = \frac{-F_{t,k}}{\sigma_{t,k}}$ and $\beta = \infty$. The probability density function and the cumulative distribution function evaluated in β are thus $\varphi(\beta) = 0$ and $\Phi(\beta) = 1$. The first moment of the propulsion power estimate can now be expressed as:

$$E(\hat{P}_{t,k} | \hat{P}_{t,k} > 0) = E(\hat{P}_{p,k}) = \mu_k + \sigma_k \frac{\varphi(\alpha)}{1 - \Phi(\alpha)} \quad (12)$$

5 Result

The model presented under Sect. 2, 3, and 4 is now to be evaluated under real operating conditions. That is, using vehicle log data from a single heavy vehicle operating all over Sweden, mainly transporting gravel. The vehicle log data is complimented with road [3] and weather [8] data from 3rd party data suppliers and the estimated propulsion power is compared against the on-board torque estimate, $P = T\omega$. The original validation data set is composed of 86 transport operations, typically 8–10 hours each, and after removing transport operations shorter than 10 km, the total number was now reduced to 59. As a reference, a primal history-based benchmark model is designed. It predicts today's (i) energy consumption E_i based on today's total travel distance d_i , and the previous transport operations' SEC value, f_{i-1} ,

$$E_i = f_{i-1} d_i. \quad (13)$$

The benchmark model, although simple, is built on the same postulate that was discussed in Sect. 1. That is, the near future is likely to be similar to the near past.

In Fig. 1, the x-axis represents the relative error $\frac{\hat{E}-E}{d}$ which has the same unit as SEC, kWh km⁻¹, and the y-axis, the represent the probability density

of a certain error. The figure has two histograms, the benchmark error (orange), representing the difference in SEC comparing transport mission k and $k - 1$, and the model error (blue). On top of the histograms, two normal distributions are drawn, the the model error pdf (green) has a mean $\mu_m = -0.01$ and standard deviation $\sigma_m = 0.40$, and the benchmark error pdf (red) has a mean $\mu_B = -0.02$ and standard deviation $\sigma_B = 0.52$. Hence, for each 100km driven, with 68% certainty, the benchmark error is smaller or equal to $[-54\ 50]$ kWh and the model error is smaller or equal to $[-41\ 39]$ kWh.

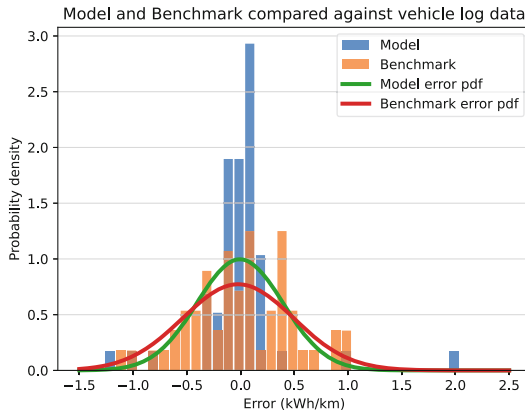


Fig. 1. The model (blue), and benchmark (orange) represent the relative error when compared against vehicle log data. Two normal distributions fitted using the model error (green), and benchmark error (red) are drawn on top. (Color figure online)

References

1. Askerdal, M., Fredriksson, J., Laine, L.: Development of simplified air drag models including crosswinds for commercial heavy vehicle combinations. *Veh. Syst. Dyn.* (2023). <https://doi.org/10.1080/00423114.2023.2213786>
2. European Parliament and Council: Regulation (EU) 2019/1242 of the European parliament and of the council of 20 June 2019 setting CO₂ emission performance standards for new heavy-duty vehicles and amending Regulations (EC) No 595/2009 and (EU) 2018/956 of the European Parl. *Off. J. Eur. Union* **198**(April), 202–240 (2019)
3. HERE Technologies: HERE Technologies. <https://www.here.com>
4. Hyttinen, J., Ussner, M., Österlöf, R., Jerrelind, J., Drugge, L.: Truck tyre transient rolling resistance and temperature at varying vehicle velocities - measurements and simulations. *Polym. Test.* **122**, 108004 (2023). <https://doi.org/10.1016/j.polymertesting.2023.108004>
5. Mao, L., Fotouhi, A., Shateri, N., Ewin, N.: A multi-mode electric vehicle range estimator based on driving pattern recognition. *J. Mech. Eng. Sci.* **236**(6), 2677–2697 (2022). <https://doi.org/10.1177/095440622111032994>

6. Nachi, G., Hauser, R.: Kalman Filtering with Equality and Inequality State Constraints. Technical report, Oxford Numerical Analysis Group (2008)
7. Sircoulomb, V., Hoblos, G., Chafouk, H., Ragot, J.: State estimation under non-linear state inequality constraints: a tracking application. In: 16th Mediterranean Conference on Control and Automation. IEEE, Ajaccio (2008). <https://doi.org/10.1109/MED.2008.4602024>
8. Swedish Meteorological and Hydrological Institute (SMHI): Swedish Meteorological and Hydrological Institute (SMHI). <https://www.smhi.se>
9. Zhang, Y., Wang, W., Kobayashi, Y., Shirai, K.: Remaining driving range estimation of electric vehicle. In: 2012 IEEE International Electric Vehicle Conference, pp. 1–7. IEEE (2012). <https://doi.org/10.1109/IEVC.2012.6183172>

Open Access This chapter is licensed under the terms of the Creative Commons Attribution 4.0 International License (<http://creativecommons.org/licenses/by/4.0/>), which permits use, sharing, adaptation, distribution and reproduction in any medium or format, as long as you give appropriate credit to the original author(s) and the source, provide a link to the Creative Commons license and indicate if changes were made.

The images or other third party material in this chapter are included in the chapter's Creative Commons license, unless indicated otherwise in a credit line to the material. If material is not included in the chapter's Creative Commons license and your intended use is not permitted by statutory regulation or exceeds the permitted use, you will need to obtain permission directly from the copyright holder.





Black Ice Detection Based on Tire Friction Coefficient Estimation of Vehicle Longitudinal Model

Seung-Yong Lee¹, Ho-Jong Lee², and Gi-Woo Kim¹ (✉) 

¹ Inha University, Incheon 22212, South Korea
gwkim@inha.ac.kr

² R&D Center, HanKook Tire and Technology Co., Daejeon, South Korea

Abstract. Black ice is a deadly hazard on the road because it is visually transparent and difficult to identify by driver's naked eye while driving. Because tire friction on a black icy road surface is obviously smaller than normal road, the braking distance significantly increases and leads to severe traffic accidents. Road hazard detection such as black ice has been actively attempted so far, usually focusing on methodology using intelligent vision systems (e. g., cameras). However, current image-based methods are prone to reduced low accuracy due to their susceptibility to vibrations transmitted from road surfaces to vehicles. In addition, incorporating cameras and light detection and ranging sensors increases the complexity and computational burden, especially when extending their functionality to include road surface classification. Therefore, we investigate the potential of new road surface classification based on vehicle longitudinal velocity and tire effective radius estimation from vehicle longitudinal model. This study explores a sensor-fusion type indirect road surface classification algorithm based on Kalman filtering.

Keywords: Black Ice Detection · Extended Kalman Filter · Vehicle Longitudinal Velocity · Tire Effective Radius · Wheel Slip Ratio

1 Introduction

Black ice is a deadly hazard on the road because it is visually transparent and difficult to identify by driver's naked eye while driving. The braking distance significantly increases and leads to severe traffic accidents because tire friction on a black icy road surface is obviously smaller than normal road [1]. Road hazard detection such as potholes and black ice has been actively attempted so far, usually focusing on methodology using intelligent vision systems (e. g., cameras). However, current image-based methods are prone to reduced low accuracy due to their susceptibility to vibrations transmitted from road surfaces to vehicles. In addition, incorporating cameras and light detection and ranging (LiDAR) sensors increases the complexity and computational burden, especially when extending their functionality to include road surface classification. The information of road conditions detected from smart tire sensors can be shared through a cloud server

when the first vehicle encounters the road hazards. This approach seems to be promising because subsequent vehicles can use this shared information to navigate and avoid road hazards such as potholes, potentially reducing computational demands and enhancing efficiency, as shown in Fig. 1. Considering that tires are the only components of the vehicle system in direct contact with the road surface, they inherently possess high potential for detecting road hazards such as black ice. The sensor fusion-based indirect method then can be effective supplement system to smart tire sensors or act as a fail-safe system where smart tire sensors may not function properly because sensor fusion-based indirect method through CAN bus is currently being effectively utilized in various real-time vehicle control systems with a relatively high sampling frequency (e. g., 1 kHz).

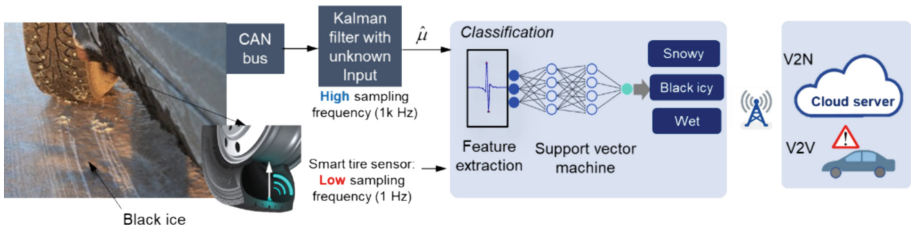


Fig. 1. Schematic overview of the proposed road surface classification both smart tire sensor built in pneumatic tires (direct, low sampling frequency) and sensor fusion based tire friction coefficient estimation (indirect, high sampling frequency) [2]

In this study, we explore new approach to achieve new cost-effective means of classifying road surface (i.e., tire friction coefficient) by measuring (or estimating) slip ratio and tire tractive force in real time, as shown in Fig. 2 This indirect sensor fusion method can compensate the accuracy of road surface classification in situations where smart tire sensors face limitations.

2 Slip Ratio and Vehicle Longitudinal Velocity Estimator

2.1 Vehicle Longitudinal Model

In this study, the wheel rotation dynamic model and vehicle longitudinal model of electric vehicles is used to estimate vehicle longitudinal velocity and the tire effective radius [3]. Assuming that the vehicle is driving on flat road ($\theta = 0$) and the braking force is inactive, the vehicle driving model in longitudinal direction can be governed by

$$I_{\omega}\dot{\omega} = T_m - RF_x - RC_{rr}mg \quad (1)$$

$$\gamma_m m \dot{v}_x = F_x - 0.5\rho C_d A_f v_x^2 - C_{rr}mg \quad (2)$$

where I_{ω} denotes the roll inertia, ω denotes the wheel angular velocity, T_m denotes the motor output torque, R denotes the tire effective radius, F_x denotes the tractive force, C_{rr} denotes the rolling resistance coefficient, m denotes the vehicle mass, γ_m represents the

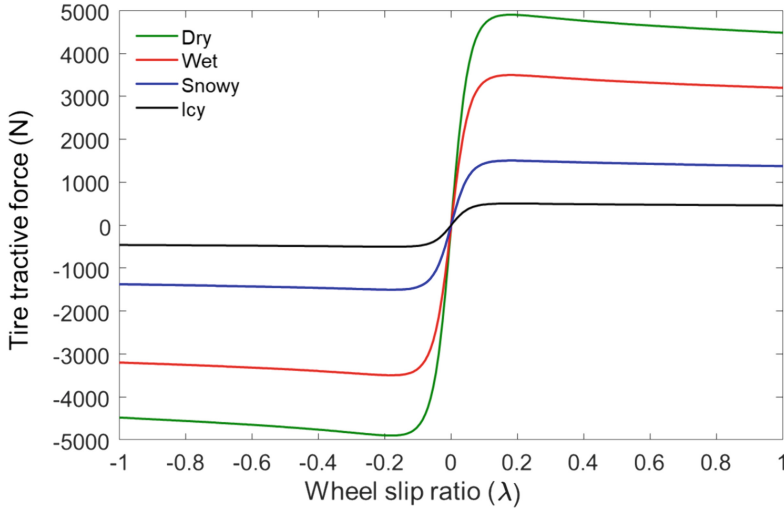


Fig. 2. Tire tractive force vs slip ratio showing road surface-dependent tire friction coefficient

mass factor, v_x denotes the vehicle longitudinal velocity, ρ denotes the air mass density, C_d represents the aerodynamic drag coefficient, and A_f represents the vehicle frontal area. Compared to conventional vehicles with internal combustion engines combined with multi-stepped automatic transmissions, the tractive force of electric vehicles can be easily determined by converting motor output torque as

$$F_x = \frac{T_m G \eta}{R} \tag{3}$$

where G denotes the reduction gear ratio, and η denotes the mechanical efficiency.

Introducing the additional assumption that the tire effective radius is in a quasi-static state ($\dot{R} \approx 0$), the state space equation can then be expressed as Eq. (4).

$$\dot{x} = f(x) = \begin{bmatrix} \dot{x}_1 \\ \dot{x}_2 \\ \dot{x}_3 \end{bmatrix} = \begin{bmatrix} \frac{T_m}{I_\omega} - \frac{T_m G \eta}{\gamma_m m R} - \frac{R C_{rr} m g}{I_\omega} \\ \frac{T_m G \eta}{\gamma_m m R} - \frac{I_\omega}{\rho C_d A_f v_x^2} - \frac{g C_{rr}}{\gamma_m} \\ 0 \end{bmatrix} \tag{4}$$

$$x = [x_1 \ x_2 \ x_3]^T = [\omega \ v_x \ R]^T, \ y = [\omega \ a_x]^T$$

Consequently, slip ratio λ is derived from the estimated v_x and R using Eq. (5) [4]

$$\lambda = \frac{v_w - v_x}{v_x} = \frac{R\omega}{v_x} - 1 \tag{5}$$

3 Design of Extended Kalman Filter

The nonlinear system model Eq. (4) is linearized using the Jacobian respect to the defined state variables and is discretized using Euler’s method for being applicable to the discrete-time extended Kalman filter (EKF). To design EKF, we discretized the continuous-time

state equation as follows [5]:

$$\begin{aligned} x_{k+1} &= f_k(x_k) + w_k \\ y_k &= h_k(x_k) + v_k \end{aligned} \quad (6)$$

where w_k is a system-noise vector and v_k is a measurement noise vector. The extended Kalman filter assumes the differentiability of the state-change function instead of the linearity of the model. The nonlinear system model was linearized using a Jacobian matrix as follows:

$$A_k = \left. \frac{\partial f_k}{\partial x} \right|_{x_{k-1}}, \quad H_k = \left. \frac{\partial h_k}{\partial x} \right|_{\hat{x}_k} \quad (7)$$

Matrices A and H of the system model were linearized using Eq. (7) are expressed as follows:

$$F_k = \frac{\partial f}{\partial x} = \begin{bmatrix} 0 & 0 & -\frac{C_{rr}mg}{I_\omega} \\ 0 & -\frac{\rho C_d A_f x_2}{\gamma_m m} & -\frac{T_m G \eta}{\gamma_m m x_3^2} \\ 0 & 0 & 0 \end{bmatrix}, \quad H_k = \frac{\partial h}{\partial x} = \begin{bmatrix} 1 & 0 & 0 \\ 0 & -\frac{\rho C_d A_f x_2}{\gamma_m m} & -\frac{T_m G \eta}{\gamma_m m x_3^2} \end{bmatrix} \quad (8)$$

The overall estimation process using the EKF algorithm represents as follow [5].

1) Initial estimation

$$\hat{x}_0 = E[x_0] \quad (9)$$

$$P_0 = E[(x_0 - \hat{x}_0)(x_0 - \hat{x}_0)^T] \quad (10)$$

2) Prediction

$$\hat{x}_k^- = f_{k-1}(\hat{x}_{k-1}) \quad (11)$$

$$P_k^- = AP_{k-1}A^T + Q \quad (12)$$

3) Kalman-gain calculation

$$K_k = P_k^- H^T (HP_k^- H^T + R)^{-1} \quad (13)$$

4) State correction

$$\hat{x}_k = \hat{x}_k^- + K_k(y_k - h(\hat{x}_k^-)) \quad (14)$$

$$P_k = P_k^- - K_k H P_k^- \quad (15)$$

4 Estimation of Tire Friction Coefficient

Based on two estimated variables (slip ratio and vehicle longitudinal velocity), tire friction coefficient was estimated. The simulation of the integrated vehicle model is performed assuming a scenario of a vehicle driving on four types of roads: icy, snowy, wet, dry. We assumed the tire friction coefficients for each type of road (icy, snowy, wet, dry) to be 0.1, 0.2, 0.4, and 0.8 respectively. The proposed estimation algorithm was implemented in MATLAB®. A classification algorithm is additionally required to classify road surface conditions based on the estimated vehicle longitudinal velocity and the tire effective radius. Deep learning model (e. g., support vector machine) is one of the methods to design the algorithm.

To evaluate the estimation performance, the simulation of the vehicle model was performed in a scenario that the vehicle accelerates from a standstill. The vehicle longitudinal velocity and the tire effective radius estimation results of performing the simulation are shown in Fig. 3 (a) and (b). It can be observed that the vehicle longitudinal velocity was correctly estimated compared to the measured values. A peak point in the tire effective radius is observed during the initial acceleration phase, and as the vehicle longitudinal stabilizes, the tire effective radius also remains constant. The same simulation was performed for each tire friction coefficient ($\mu = 0.1, 0.2, 0.4, 0.8$). With the assumption of motor output torque as the known input, tractive force is calculated by substituting the tire effective radius into Eq. (3). The estimated vehicle longitudinal

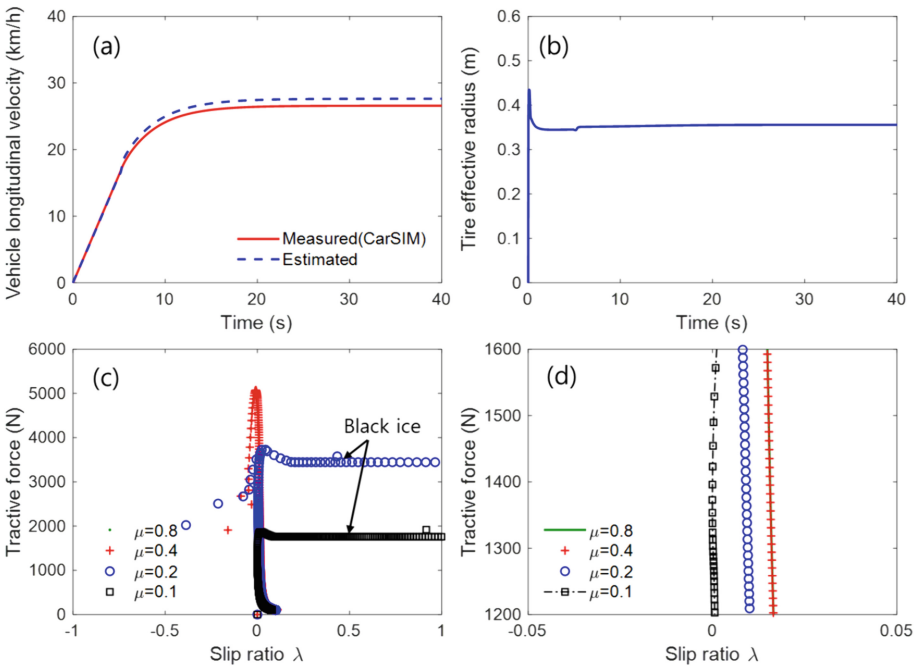


Fig. 3. Simulation result of estimation; (a) vehicle longitudinal velocity at $\mu = 0.1$, (b) Tire effective radius at $\mu = 0.1$, (c) Calculated tractive force vs estimated wheel slip ratio

velocity and the tire effective radius were substituted into Eq. (5) to calculate the slip ratio. The variations in tractive force concerning the variations in slip ratio for each tire friction coefficient are shown in Fig. 3 (c). It is observed that the shape of the graph varies for each tire friction coefficient. This variation can be used to classify the road surface conditions. However, in a range with a small slip ratio, it is challenging to classify wet and dry roads, as shown in Fig. 3 (d). Also, there are technical limitations to utilize such smart tire sensors capable of measuring the tire friction coefficients. Smart tire sensors typically have a low sampling frequency (e. g., 1 Hz) to save the life time. Given the vehicle's movement per second (e. g., at a speed of 50 km/h, driving 14 m per second), this low sampling frequency is not suitable for road surface classification. Moreover, high-frequency sensors based on smart tires, developed to address this issue, are facing challenges in commercialization due to battery life and durability concerns.

5 Conclusions

In this study, we proposed new method of estimating tire friction coefficient based on rigorous slip ration estimation enabled by tire effective radius and longitudinal vehicle velocity estimation using extended Kalman filtering. The estimated slip ratio and tractive force are used to estimate tire friction coefficient. The proposed method offers advantages in terms of cost and computational aspects compared to image-based methods. However, at a certain level of tire friction coefficient (e. g., $\mu = 0.4, 0.8$) the variations of the slip ratio versus tractive force are not clearly distinct. Additionally, this study did not reach the stage of designing classification algorithms. For future direction, we will design classification algorithm such as support vector machine (SVM).

Acknowledgements. This work was supported by Industrial Strategic Technology Development Program- Development of Smart Tire Technology for Automobiles with Integrated 1Hz Class Composite Sensor for Future Vehicle Safety and Functional Advancement (20024837) funded By the Ministry of Trade, Industry & Energy (Korea)

References

1. Harifi, A., et al.: Designing a sliding mode controller for slip control of antilock brake systems. *Transport. Res. Part C: Emerg. Technol.* **16**(6), 731–741 (2008). <https://doi.org/10.1016/j.trc.2008.02.003>
2. Lee, H.-B., Kim, G.-W.: Road pothole detection based on rack force estimation of electric power steering system. In: *Proceedings of the FISITA 2023 World Congress*, pp. 12–14 . FWC2023-SCA-028, Barcelona (2023)
3. Singh, K.B., Taheri, S.: Integrated state and parameter estimation for vehicle dynamics control. *Int. J. Veh. Perform.* **5**(4), 329–376 (2019)
4. Li, S., Kawabe, T.: Slip suppression of electric vehicles using sliding mode control method. *Intell. Control Autom.* **4**(3), 329 (2013)
5. Lee, D.-H., Yoon, D.-S., Kim, G.-W.: New indirect tire pressure monitoring system enabled by adaptive extended Kalman filtering of vehicle suspension systems. *Electronics* **10**(11), 1359 (2021)

Open Access This chapter is licensed under the terms of the Creative Commons Attribution 4.0 International License (<http://creativecommons.org/licenses/by/4.0/>), which permits use, sharing, adaptation, distribution and reproduction in any medium or format, as long as you give appropriate credit to the original author(s) and the source, provide a link to the Creative Commons license and indicate if changes were made.

The images or other third party material in this chapter are included in the chapter's Creative Commons license, unless indicated otherwise in a credit line to the material. If material is not included in the chapter's Creative Commons license and your intended use is not permitted by statutory regulation or exceeds the permitted use, you will need to obtain permission directly from the copyright holder.





Experimental Evaluation on Effects of Torque Vectoring Using Four In-Wheel Motor Independent Torque Control

Yota Homma¹✉, Yoshihiro Yamakaji¹, Koji Kajitani¹, Richard Ford², and Yoshimi Furukawa³

¹ EXEDY Corporation, 1-1-1 Kidamotomiya, Neyagawa-shi, Osaka 572-8570, Japan
yot-honma@exedy.com

² Protean Electric, 10B Coxbridge Business Park, Farnham GU10 5EH, UK

³ Professional University of Electric Mobility Systems, 1725-2, Hagyu, Iidemachi, Nishiokitama-Gun, Yamagata 999-0602, Japan

Abstract. This paper explores the effects of Direct Yaw Control (DYC) on driver's maneuverability feeling and vehicle dynamics. DYC is implemented in the experimental vehicle equipped with four-wheel independent controlled In-Wheel Motors (IWMs). The effects on vehicle dynamics are validated through open-loop testing. Subsequently, the closed-loop test is conducted to confirm the correlation between subjective evaluation and Vehicle dynamics data.

Keywords: In-wheel Motor · Torque Vectoring · Drivability · Comfortable · Independent Controlled

1 Introduction

The relationship between torque differentials characteristics on the left and right wheels by Direct Yaw Control (DYC) and vehicle dynamics has been well-established [1–5]. Less research has been conducted on the correlation between four-wheel independent yaw moment control and vehicle dynamic characteristics, as well as factors such as the maneuverability and the passenger lateral ride comfort. This paper presents an independent evaluation of a model based, yaw modifying, DYC system on an experimental vehicle with In-Wheel Motors (IWMs). The coordinate system is defined in Fig. 1.

2 Target Steering Response Using Torque Vectoring Control

2.1 Control Strategy

Torque vectoring systems have been included in production vehicles for more than 20 years. Originally this was achieved by electronic differential or brake control and is limited to relatively slow control algorithms which modify understeer/oversteer characteristics in near-limit situations. IWMs developments have enabled significantly higher

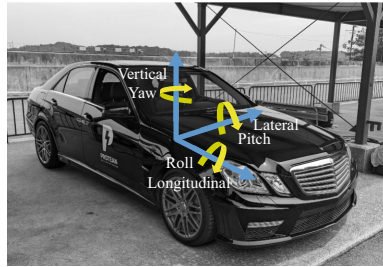


Fig. 1. Coordinate system.

bandwidth control algorithms which can subtly modify the yaw dynamics of the vehicle to change the feeling of ‘agility’ in sub-limit situations [6]. The experimental vehicle provided has a model based, agility modifying DYC control system called Torque Vectoring Control (TVC), enhancing the vehicle’s response to rapid steering inputs, known to influence driver ease of maneuver [7].

The control strategy developed is illustrated in Fig. 2. The development is carried out in three steps:

- 1) Identify the yaw transfer function of the vehicle from steering wheel to yaw angular velocity.
- 2) Identify the yaw transfer function for the vehicle from road wheel torque differential to yaw angular velocity.
- 3) Develop a control algorithm such that the overall transfer function from steering wheel angle (through traditional steering and through wheel torque differential) to yaw angular velocity matches some ideal characteristic.

The controller development is carried out in the frequency domain as this is a more natural environment for vehicle agility. Note that final tuning is carried out in the vehicle to ensure that non-linearities and model errors do not cause poor performance.

2.2 Experimental Vehicle

The experimental vehicle is equipped with the IWMs capable of independent control of all four wheels. It can switch between with and without TVC. In addition, the driving force distribution can be adjusted from FWD to RWD, continuously.

2.3 Steering Response Results

The results of the frequency response of lateral acceleration and yaw angular velocity to the sinusoidal steering inputs using the experimental vehicle are shown in Fig. 3. The frequency response of lateral acceleration and yaw angular velocity to the sinusoidal steering inputs clearly shows the improved steering response characteristics achieved by TVC. The implementation of TVC increased the gain of lateral acceleration and reduced the phase lag in yaw velocity. These observations indicate an overall improvement in the vehicle response to a rapid steering inputs.

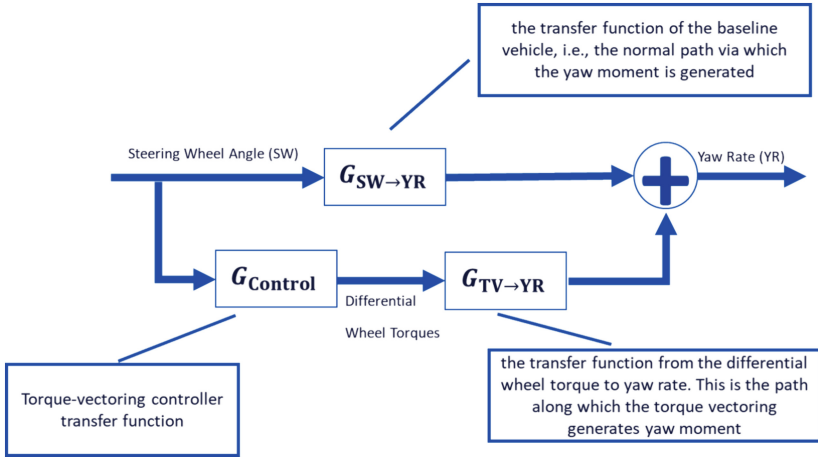


Fig. 2. A control block diagram of an experimental vehicle equipped with IWMs on all four wheels. The base vehicle is controlled to reduce the assumed yaw inertia. Note that the Yaw angular velocity has been represented to Yaw rate (YR) in this figure.

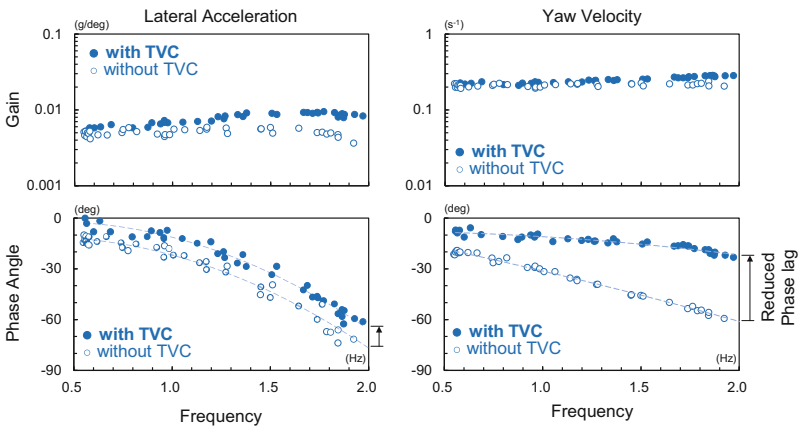


Fig. 3. Frequency Response Characteristics to Steering Inputs. Sinusoidal steering inputs at 40 kph constant speed, steering angle $\pm 30^\circ$ with moderate frequency incrementation ranging from 0.5 to 2.0 Hz.

3 Evaluation Methods

3.1 Open Loop Test

To clarify the effects of TVC under certain conditions, the angular velocities of the vehicle pitch, yaw and roll motion, and the lateral acceleration on the front and rear axles are measured when the driver input is an open loop step of approximately 30° at a car speed of 40 kph. These measurements are taken under conditions both with and without TVC activation. Furthermore, similar tests are executed with varying drive

configurations, specifically FWD and RWD, to elucidate the influence of distinct axes of TVC implementation on the dynamic behavior of the vehicle.

3.2 Closed Loop Test

To validate the effectiveness of TVC in steering response characteristics, a closed-loop test was conducted. Ten participants executed an emergency avoidance scenario shown in Fig. 4, wherein they travel at 35 kph and encounter an obstacle in their lane, and they move to the opposite lane and immediately return to their original lane to avoid oncoming vehicle with and without TVC. Subjective evaluations were conducted based on their individual experiences as both drivers and passengers. Participants were selected randomly, including both beginner and experienced drivers.

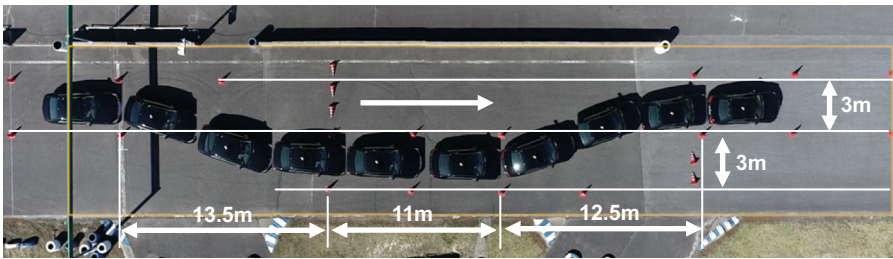


Fig. 4. The trajectory of the experimental vehicle executing the emergency avoidance scenario. The spacing between pylons is determined based on the vehicle's overall length and width, as well as the real world driving of a skilled driver.

4 Evaluation Results

4.1 Open Loop Test

Experimental results of a 30° step steering maneuver at 40 kph are shown in Fig. 5. Both the yaw angular velocity and lateral acceleration of the front and rear wheel axles exhibit quicker responses and increased peak values with TVC activation compared to when TVC is deactivated. The presence of TVC results in quicker responses and larger peak values in both yaw angular velocity and lateral acceleration on the front and rear axles compared to when TVC is deactivate.

Additionally, experiments are conducted with TVC activation in both FWD and RWD configurations. According to driver feedback, the sensation while driving differs between FWD and RWD configurations with TVC activation. In the case of FWD, subjective feelings of being pulled a front toward steered direction are noticed by driver. On the other hand, in the case of RWD, a feeling of being pushed a rear toward opposite direction of steering. The comparative results of FWD and RWD are shown in Fig. 6. However, the lateral acceleration data for both the front and rear axles do not exhibit significant differences as perceived by the drivers.

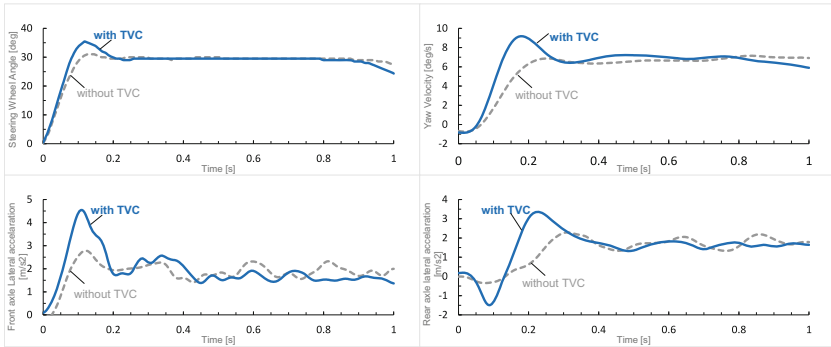


Fig. 5. Comparison results with and without TVC.

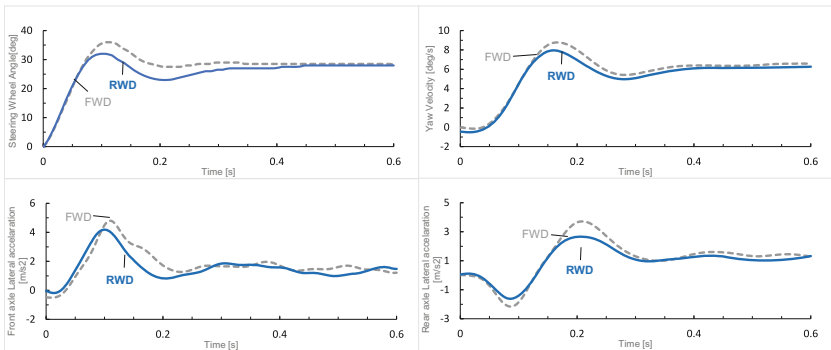


Fig. 6. Comparison between FWD and RWD configurations with TVC activation.

4.2 Closed Loop Test

The subjective evaluation results are presented in Fig. 7. All assessment criteria show the improvement with TVC. Particularly notable are the ease of avoidance perceived by drivers and the smoothness of lateral motion experienced by rear-seat passengers.

As representative data, Fig. 8 shows the measured data of steering angle and yaw angular velocity during the emergency avoidance scenario executed by driver G. TVC contributes to the reduction in time delay from driver input to vehicle response. Furthermore, it can be read from the Lissajous waveform that the hysteresis of the response has decreased. These indicate that the response has been improved.

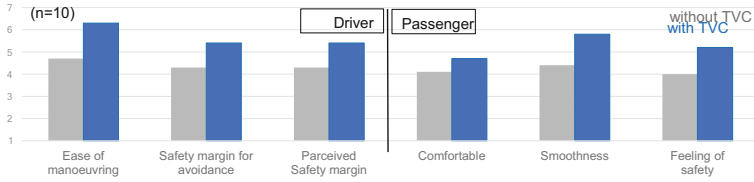


Fig. 7. Subjective Evaluation Results. Averaged subjective ratings of all participants on 7-point scale.

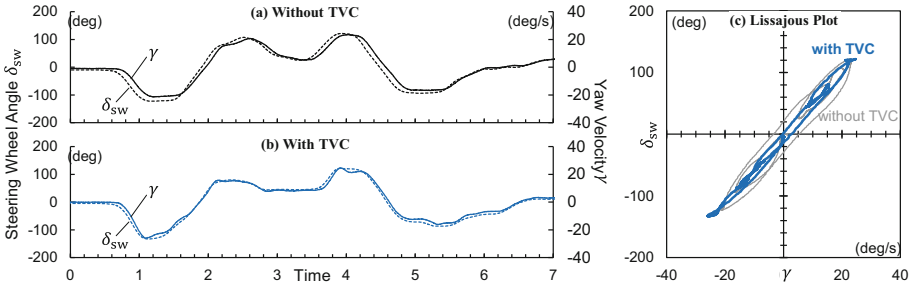


Fig. 8. Time-domain Waveform and Lissajous Waveform during Emergency Avoidance Scenario

5 Conclusion

Tests were conducted to validate the effectiveness of steering response enhancement using TVC with four-wheel independent controlled IWMs. The subjective evaluation results indicated the improvements in an ease of operation and in a perceived safety margin during emergency avoidance scenarios with the implementation of TVC. The improvement in subjective evaluation was proved by the physical data, indicating a reduction in phase lag and an increase in gain in vehicle yaw angular velocity and lateral acceleration with TVC under rapid steering inputs.

The vehicle dynamics under rapid steering input was improved by TVC with four-wheel independent controlled IWMs.

The subjective evaluation of maneuverability by drivers did not yield differences in data when altering the front-to-rear control distribution of TVC. These investigations will be the subject of further studies.

References

1. Shibahata, Y., Shimada, K., et al.: The improvement of vehicle maneuverability by direct yaw moment control. In: Proceedings of the AVEC92 (1992)
2. Shibahata, Y., Shimada, K., et al.: Improvement of vehicle maneuverability by direct yaw moment control. Veh. Syst. Dyn. **22**(5-6), 465-481 (1993)
3. Abe, M., Kano, Y., et al.: Improvement of vehicle handling safety with vehicle side-slip control by direct yaw moment. Veh. Syst. Dyn. **33**(sup1), 665-679 (1999)
4. Shibahata, Y., Abe, M., et al.: Improvement of limit performance of vehicle motion by Chassi Control. Veh. Syst. Dyn. (2000)

5. Shibahata, S., Shibahata, Y.: Principles and applications of DYC in transient state. J. JSAE (2022) (in Japanese)
6. Kostic Perovic, D.: Making the impossible, possible – Overcoming the design challenges of in wheel motors. World Electr. Veh. J. **5**(2), 514–519 (2012)
7. Sano, S., Furukawa, Y. et al.: Effects of vehicle response characteristics and driver's skill level on task performance and subjective rating. In: Proceedings of 8th International Technical Conference on Experimental Safety Vehicles, Wolfsburg (1980)

Open Access This chapter is licensed under the terms of the Creative Commons Attribution 4.0 International License (<http://creativecommons.org/licenses/by/4.0/>), which permits use, sharing, adaptation, distribution and reproduction in any medium or format, as long as you give appropriate credit to the original author(s) and the source, provide a link to the Creative Commons license and indicate if changes were made.

The images or other third party material in this chapter are included in the chapter's Creative Commons license, unless indicated otherwise in a credit line to the material. If material is not included in the chapter's Creative Commons license and your intended use is not permitted by statutory regulation or exceeds the permitted use, you will need to obtain permission directly from the copyright holder.





A Comprehensive Method for Computing Suspension Elasto-kinematics With Non-linear Compliance

Paolo Magri^(✉), Marco Gadola, Daniel Chindamo, Giulia Sandrini,
and Andrea Candela

Department of Mechanical and Industrial Engineering, University of Brescia, I-25123 Brescia,
Italy
p.magri003@unibs.it

Abstract. Since flexible bushings are used as the interface between the suspension arms and the chassis, the extra degrees of freedom make the design process a complex task. While the use of a multi-body model is common practice in the industry, a dedicated computational tool can be more practical and straightforward, especially when undertaking the design of a new suspension concept from the ground up. This paper presents a quasi-static method for calculating suspension compliance under the action of forces and moments, enabling real-time simulations. The algorithm proposed in this paper was devised with a threefold purpose: integrating elasto-kinematics into the kinematic design tool previously created by the authors, integrating real-time vehicle dynamics simulation, and overcoming the limitations of the traditional approach based on the superposition principle. Finally, a comparison of the proposed model with one based on the lookup-table and superposition principle is presented.

Keywords: Suspension · Kinematics · Elasto-kinematics · Bushing · Compliance · Simulation · Vehicle Dynamics

1 Introduction

Modern passenger cars require an intensive effort for the design of suspension elasto-kinematic properties because of their significant impact on ride, handling, stability, and steering feel. This importance is reflected in the vast engineering literature on the subject. The use of multi-body models, although the industry standard, is often considered demanding due to the high level of detail required. Additionally, a multi-body model is rarely suitable for real-time simulation. Instead, the development and application of relatively simple, dedicated design and simulation tools are often considered more practical, especially when designing a new suspension concept from the ground up. In fact, the proposed methodology is being implemented in the kinematics calculation tool developed by the authors [1]. This trend is evident in the related literature, where many publications describe self-developed, specific methodologies that vary in complexity

and computational approach. A multi-body model is commonly adopted for validation in these cases. Generally, however, most papers in the literature tend to neglect one or more factors of real-world design. In particular, they often overlook the non-linearity of bushings or linearize the suspension within a range of small displacements [2–4].

On the other hand, it is well known that correct modelling of elastokinematics, taking non-linearities into account, is crucial for several aspects: design [5], for handling [6] and also for ride & comfort [7]. The integration of models characterizing elastokinematics in vehicle dynamics simulations is a recurring topic, with the main challenge being the speed of computation [8].

With regard to real-time simulations, the current trend in the literature shows an approach based on modeling suspension compliance through artificial neural networks (ANN) [9]. In this way, it is also possible to consider dynamic effects as opposed to a quasi-static solver. However, a significant amount of data is needed to train the network, which can be particularly complicated or even impossible during the design phase. The purpose of this work is to provide a method for solving the suspension elastokinematic problem using a general procedure that enables the design of any layout under any combination of jounce and steering or load. Bushings can be described with real-world, non-linear stiffness curves for all six degrees of freedom. They can be located on either side of each suspension arm, i.e., on the chassis side and/or the wheel side. The axial flexibility of a track rod can also be represented by means of equivalent, non-linear bushings. The wheel bearing stiffness can be considered as well. Wheel movements, hence variations of vehicle dynamics-relevant parameters like camber, side view angle, toe, track, wheelbase, and vertical displacement, can be computed under any combination of road loads, also considering steering due to rack translation. Loads through suspension joints, components, and chassis pick-up points can also be computed.

In general, elastokinematics is implemented in vehicle dynamics simulations using look-up tables, often derived from experimental data obtained through K&C or SPMD, then applying the superposition principle [10]. This method is characterized by requiring negligible computational resources.

One of the aims of this work is to show how the superposition principle, which can work well in some cases, does not allow for a correct characterization of compliance when large lateral and longitudinal accelerations are involved, as mentioned in [10]. A comparison, through simulation, with a model based on look-up tables and the superposition principle is proposed to show how vehicle behavior can change in a test with large accelerations. The simulation is also carried out to demonstrate the possibility of using the method proposed in this work in real-time.

2 Methods

Two types of elements are considered in this model, Fig. 1 a). The first type of element is called “spring rod” and it is composed by a rod with a given axial stiffness complemented with a bushing at both ends. The second element is called “rigid element”: it is composed by a rigid body connected to any number of bushings.

The above elements can be attached to each other or to the chassis. By combining them it is possible to create any type of independent suspension. For example, in a

double wishbone both arms will consist of a rigid element connected to the chassis by two bushings and to the upright by one bushing. The upright will also be a rigid element with three bushings, two of them are connected to each wishbone and one to the steering tie rod; this one will instead be modelled using a spring rod element as in Fig. 1 b).

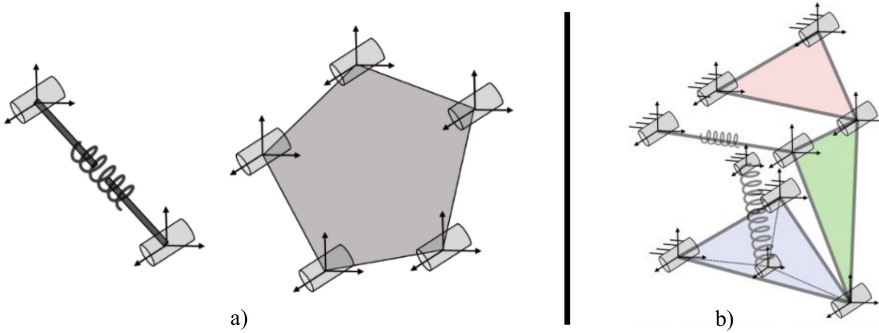


Fig. 1. a) General “spring rod” and “rigid element” of the suspension model. b) Example of a Double Wishbone suspension built using the general elements.

Each bushing is defined with its position, orientation, and the “Reaction Forces Vector” containing six functions that correspond to the three reaction forces and moments generated by the bushing as a function of the six deformations along or around its local reference system. A ball joint can be represented by means of a bushing with very high stiffness values. The suspension model is therefore composed of nonlinear equations representing the balance of forces and moments for each element as a function of bushing deformations. The number of degrees of freedom hence equations is a function of the type of elements used to compose the suspension: 6 degrees of freedom for each “rigid element” and 7 for each “spring rod”. The model, solved through the Newton-Raphson algorithm, enables the computation of the deformed configuration of the suspension as a function of forces and moments applied at any point on the wheel. It has been fully validated in [11] (currently under review).

A generic model of a double wishbone suspension was created as in Fig. 1 b), featuring nonlinear, force-displacement bushing characteristics defined with a fifth-degree polynomial to recreate their typically progressive, stiffening behavior.

The suspension model was implemented as a Matlab® function and transferred to Simulink®. This second function was then linked to Vi-CarRealTime®. A dynamic simulation has been carried out as a case study. The simulation is a corner-braking test where the vehicle starts from a speed of 108 km/h and enters in a cornering with a radius of 75 m. A virtual driver model controls the steering. After 2 s the driver brakes following a target deceleration of $10 \frac{m}{s^2}$.

The purpose is the comparison of the above model with a simpler one based on the superposition principle, where the effect of each force or moment on the suspension is considered as orthogonally decomposed. The suspension deflection is calculated as a simple summation of all effects of each external action.

A basic vehicle model was therefore used. Using the proposed algorithm, a series of 3-dimension look-up tables were generated in as a function of wheel travel, steer and external force, each describing the effect that each external force has on the suspension's 6 degrees of freedom.

The simulation has been carried out in the Vi-CarRealTime® environment with Simulink® co-simulation, with an integration step of 0.001 s. Only the compliance of the front axle was considered. To ensure that the simulation worked in real time, the algorithm calculating the elastokinematics has been compiled in C and has been run at 500 Hz, assigning the calculation of each wheel in parallel to one core of an Intel® Xeon Gold 6134 CPU.

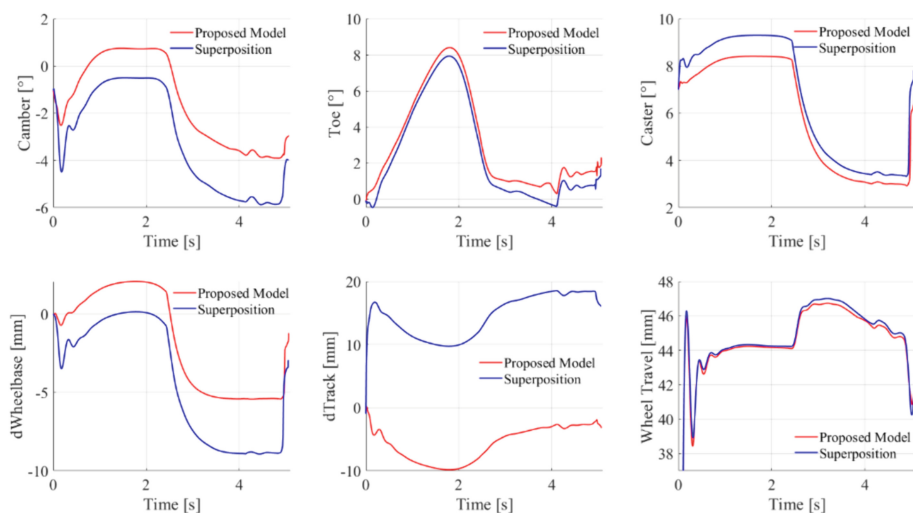


Fig. 2. Simulation results for left-hand wheel movements: camber, toe, caster, wheelbase variation and wheel travel. In red the comprehensive proposed model, in blue the model based on lookup-table and superposition.

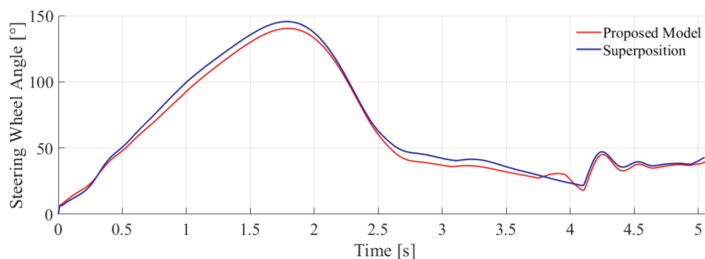


Fig. 3. Steering wheel angle over time in the simulation. In red the comprehensive proposed model, in blue the model based on lookup-table and superposition.

Figure 2 shows the simulation results for the movements of the left wheel (i.e. the most loaded as it is a right-hand bend): camber, toe, caster, wheelbase variation and wheel travel, comparing the two models.

Figure 3 represents the steering wheel angle over time. This is different between the two simulations as the test is in closed loop, i.e. virtual driver maintains an imposed trajectory and target deceleration.

3 Conclusion and Discussion

By using typical, strongly nonlinear force-displacement curves for the bushings, the difference between the two models becomes particularly apparent, as previously seen in Fig. 2, where large differences in track variation can be observed, even with opposite signs. The differences seen in camber, caster, and toe can significantly influence the handling and performance of the vehicle. This is also reflected in the varying values of steering angle, which alters the feedback for the driver. The difference in toe angle is opposite to the difference in steering angle, indicating a different contribution of elastokinematics in the two models.

Separating the effects of the various actions and combining them through the superposition principle does not lead to an accurate solution when large deformations occur, and large forces act on the wheel. In normal driving, the differences between the two models tend to be negligible. Even when examining the inner wheel during a turn, the differences are less significant.

For performance applications, the need arises for an appropriate solver to accurately calculate compliance effects, enabling an effective design and simulation process without limitations. Elasto-kinematic properties can be computed for any combination of wheel jounce and steering rack position, with the flexibility to change hardpoints or bushing stiffness curves at any time.

Unlike a multi-body model, the proposed model is a quasi-static solver that is well-suited for real-time applications, such as in a driving simulator. In this context, each solution of the problem is close to that of the previous instant, allowing the Newton-Raphson algorithm to converge in negligible time.

However, compared to a multi-body solver, dynamic features of rubber bushings, such as damping and hysteresis effects, are not accounted for. Another limitation of this model is the lack of an anti-roll bar model, which can transfer forces onto the suspension system and affect its elastokinematics.

In this work, the proposed model has been implemented in the simulation with its calculation frequency limited to 500 Hz, so that the vehicle model could operate at 1000 Hz, which is considered the minimum frequency for real-time. Lowering the update frequency of the elastokinematics does not significantly influence the vehicle model, as the dynamic effects of the suspension are not accounted for here. It is expected that with more powerful hardware, the suspension model frequency can also be increased to 1000 Hz.

In the author's opinion, an analytical approach suitable for both design and real-time operation is the best solution in the initial design phase of a vehicle with its suspension and steering systems. Additionally, with the proposed model, it is possible to calculate

the constraint reactions on each individual bushing, which is useful for FEM analyses, for example something that cannot be done with a model based on look-up tables or an artificial neural network.

References

1. Bonera, E., Gadola, M., Chindamo, D., Morbioli, S., Magri, P.: Integrated design tools for model-based development of innovative vehicle chassis and powertrain systems. In: *Lecture Notes in Mechanical Engineering*, pp. 118–128 (2020). https://doi.org/10.1007/978-3-030-31154-4_11/COVER
2. Burgess, M.J., Fleming, N.P., Wootton, M., Williams, S.J.: A tool for rapid vehicle suspension design. *SAE Technical Papers* (2004). <https://doi.org/10.4271/2004-01-3543>.
3. Kang, J.S., Yun, J.R., Lee, J.M., Tak, T.O.: Elastokinematic analysis and optimization of suspension compliance characteristics. *SAE Technical Papers* (1997). <https://doi.org/10.4271/970104>
4. Gerrard, M.B.: The equivalent elastic mechanism: A tool for the analysis and the design of compliant suspension linkages. *SAE Technical Papers* (2005). <https://doi.org/10.4271/2005-01-1719>
5. Yang, X.: Effects of bushings characteristics on suspension ball joint travels. *Veh. Syst. Dyn.* **49**(1–2), 181–197 (2011). <https://doi.org/10.1080/00423110903166300>
6. Morales, E.D.: Sensitivity study of front suspension parameters in elastokinematics and handling behavior of a vehicle. *SAE Technical Papers*, vol. Part F127082, no. October (2016). <https://doi.org/10.4271/2016-36-0182>
7. Knapczyk, J., Dzierzek, S.: Elastokinematic analysis of five-rod suspension with flexible joints, including effects of shock absorber. *Veh. Syst. Dyn.* **29**(sup1), 270–279 (1998). <https://doi.org/10.1080/00423119808969564>
8. Ammon, D., Gipser, M., Rauh, J., Wimmer, J.: High performance system dynamics simulation of the entire system tire-suspension-steering-vehicle. *Veh. Syst. Dyn.* **27**(5–6), 435–455 (1997). <https://doi.org/10.1080/00423119708969341>
9. Duan, Y., Zhang, Y., Wu, J., Lv, T.: A data-driven suspension kinematics and compliance model considering multi-axis coupling effects. *Proc. Inst. Mech. Eng., Part D: J. Autom. Eng.* (2023). <https://doi.org/10.1177/09544070231207160>
10. Park, J., Yi, J., Lee, D., Park, J., Yi, J., Lee, D.: Investigation into Suspension Dynamic Compliance Characteristics Using Direct Measurement and Simulation. *SAE Technical Papers* (2004). <https://doi.org/10.4271/2004-01-1065>
11. Magri, P., Gadola, M., Chindamo, D., Sandrini, G.: A comprehensive method for computing non-linear elastokinematic properties of passenger car suspension systems: double wishbone case study. *J. Comput. Nonlinear Dyn.* (2024)

Open Access This chapter is licensed under the terms of the Creative Commons Attribution 4.0 International License (<http://creativecommons.org/licenses/by/4.0/>), which permits use, sharing, adaptation, distribution and reproduction in any medium or format, as long as you give appropriate credit to the original author(s) and the source, provide a link to the Creative Commons license and indicate if changes were made.

The images or other third party material in this chapter are included in the chapter's Creative Commons license, unless indicated otherwise in a credit line to the material. If material is not included in the chapter's Creative Commons license and your intended use is not permitted by statutory regulation or exceeds the permitted use, you will need to obtain permission directly from the copyright holder.





A Novel Torque Vectoring Approach to Enhance Driving Experience

Marco Paparone¹(✉), Alessandro Pino¹, Filippo Giacomel², Giovanni Bussalai¹,
Andrea Macaluso¹, Antoine Lamps¹, and Basileios Mavroudakis¹

¹ Bugatti Rimac, 10431 Sveta Nedelja, Croatia

{marco.paparone, alessandro.pino, giovanni.bussalai,
andrea.macaluso, antoine.lamps, b.mavroudakis}@bugatti-rimac.com

² RSEngineering, 41053 Maranello, Italy

filippo.giacomel@rsengineering.com

Abstract. The current state of Direct Yaw Control literature has reached an advanced level, yielding compelling results in stabilizing vehicle behavior, and enhancing overall performance. However, conventional approaches exhibit limitations in addressing highly transient lateral dynamics, particularly during conditions of rapidly increasing vehicle sideslip angles, leading to poor controllability and reduced intuition for the driver. This paper introduces a novel extension to the established yaw rate tracking technique, integrating the trivial yaw rate feedback control with a less conventional model-based feedforward term, complemented by an innovative sideslip rate tracking loop. The primary objective of this term is to smoothen vehicle cornering response, effectively dampening oscillations in the vehicle's behavior without compromising time delays to driver inputs. The intended outcome is not only enhancing safety but also delivering a more intuitive and enjoyable driving experience. The effectiveness of the approach is demonstrated by the results obtained through detailed Driver-in-Motion (DiM) sessions.

Keywords: stability control · torque vectoring · sideslip rate control · driving feel

1 Introduction

In recent years, the research field of vehicle control algorithms has witnessed a significant surge in research endeavors, particularly directed towards enhancing handling, performance, and stability. Among the various performance-oriented algorithms, the Torque Vectoring (TV) stands out as the most widely adopted, whose concept is to impose a desired vehicle yaw rate (ω_z) or sideslip (β), derived from an ideal reference model, by generating an additional yaw moment (M_z) through proper control of actuators. A comprehensive coverage on the state-of-the-art feedback (FB) and feedforward (FF) algorithms is depicted in [1], therefore the authors will refrain from discussing further references at this stage. This paper proposes a novel approach to TV algorithms, building

upon the conventional yaw rate tracking method. The proposed method combines commonly used yaw rate feedback with a model-based feedforward control module and a novel damping term aimed at minimizing overshoots of vehicle sideslip rate ($\dot{\beta}$) (Fig. 1). A comparison between the passive vehicle and the controlled one through the proposed approach highlights how the latter results in a notably better damped and smooth vehicle response during transient cornering, with significantly reduced overshoot and oscillations in the closed loop tracking, without inducing any additional delay in the vehicle response. While discussing such topics, the focus is placed on how such novel algorithm is specifically designed for production road cars: emphasis is set on debugging efficiency and calibration simplicity, while ensuring high performance, which are crucial aspects for the cost-effective development of luxury hypercars.

2 Control Scheme

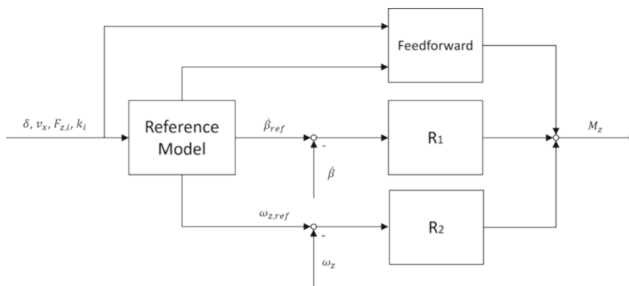


Fig. 1. Torque vectoring control scheme.

2.1 Reference Model

Aligned with the application efficiency, a simplified nonlinear bicycle model combined with a 4-parameter Pacejka tire formulation is selected to generate the reference vehicle response, guaranteeing both modeling precision and simplicity. The mathematical representation of this modeling approach can be described :

$$\dot{\omega}_z = \frac{1}{J_z} (F_{y,f} l_f \cos \delta - F_{y,r} l_r) \tag{1}$$

where J_z is the vehicle rotational inertia around its z-axis, $F_{y,i}$ the axles lateral force, δ the wheel steer angle, and l_i the distance between the axle and the center of gravity.

It is important to note that due to the presence of the lateral force, estimations of longitudinal speed (v_x), vertical load on the tires ($F_{z,i}$), and vehicle sideslip are essential. While the first two can be estimated with reasonable precision using standard algorithms, accurately estimating sideslip in all driving conditions remains a challenge.

To address this and enhance robustness while minimizing the calibration effort, the sideslip angle is computed by integrating the vehicle model using measurements of steering wheel angle and longitudinal speed. The dynamics are then evolved using Eq. 1 combined with the sideslip rate dynamics, derived by:

$$a_y = \frac{1}{M}(F_{y,f} \cos \delta + F_{y,r}) \quad (2)$$

$$\dot{\beta} = \frac{1}{v_x}(a_y - \omega_z v_x) \quad (3)$$

Here, a_y represents the lateral acceleration and M the total mass of the vehicle.

Since the model is based on a non-linear tire formulation, saturation limits are inherently considered, particularly with respect to the peak lateral force. Additionally, to capture the combined tire behavior, a scaling factor is applied to $F_{y,i}$ such that when high slip ratios k_i are experienced, the maximum lateral force is significantly reduced.

It is essential to emphasize that these equations describe the vehicle response to a given input steering wheel angle at a specific longitudinal speed. If the model is provided with ideal vehicle parameters, used as reference model calibration, it will yield an idealized transient behavior. Hence, for a specific set of calibration parameters, a unique model capable of producing a desired yaw rate and sideslip angle response can be defined, thus covering feedforward modeling and closed-loop reference definition.

At this stage, it is crucial to not introduce any control variables into the formulation, as this would alter the fundamental behavior, as the goal is to derive an ideal response that can then be delivered by the vehicle through torque vectoring. Control variables will be introduced in the next section for computing the feedforward action.

2.2 Feedforward Term

The feedforward action entails estimating the additional yaw torque needed to achieve the reference behavior in an open-loop manner, relying solely on knowledge of both the physical vehicle and the reference vehicle. The rationale behind this approach is to compare the yaw torque produced by the passive vehicle with the yaw torque that the target vehicle would generate under identical input conditions (such as steering wheel angle and longitudinal speed). The difference between these values indicates the adjustment that torque vectoring should apply to achieve the target response.

Enhancing Eq. 1 with the vehicle parameters and incorporating the torque vectoring contribution, the yaw moment generated by the real vehicle is described by equation:

$$\dot{\omega}_z = \frac{1}{J_z}(\hat{F}_{y,f} \hat{l}_f \cos \delta - \hat{F}_{y,r} \hat{l}_r + M_{z,FF}) \quad (4)$$

Alternatively, the ideal vehicle response can be calculated by exclusively evaluating Eq. 1 with the parameters of the target vehicle:

$$\dot{\omega}_z = \frac{1}{J_z} \left(\bar{F}_{y,f} \bar{l}_f \cos \delta - \bar{F}_{y,r} \bar{l}_r \right) \quad (5)$$

The required feedforward action can be computed by equating Eq. 7 and Eq. 8, as:

$$M_{z,FF} = \frac{\hat{J}_z}{J_z} \left(\bar{F}_{y,f} \bar{l}_f \cos \delta - \bar{F}_{y,r} \bar{l}_r \right) - \left(\hat{F}_{y,f} \hat{l}_f \cos \delta - \hat{F}_{y,r} \hat{l}_r \right) \quad (6)$$

Most of common state-of-the-art open-loop control methods are derived by mathematically inverting the vehicle model based on a single specific reference variable, such as yaw rate or sideslip angle. However, direct inversion is not always feasible due to the transfer function realization matter, typically requiring a simplified tire model. Instead, the proposed approach does not require model inversion and establishes a law that represents the response of the target vehicle whilst including multiple reference quantities, thus allowing for enhanced yet straightforward and intuitive reference calibration.

2.3 Feedback Term

The innovative approach proposed here incorporates a feedback tracking system for the sideslip rate in conjunction with the feedforward control. The primary advantage of this method lies in the introduction of a damping element within the loop. This ensures an improved driving experience for the driver by delivering a smoother transient response, significantly reducing instances of over- or undershooting of the sideslip angle, as well as avoiding snappy vehicle responses whilst offering an intuitive driving feeling.

For the sake of illustration, a proportional controller $R_1 = -|K_1|$ is used. Such a gain must be negative to ensure asymptotic stability, as it can be proven that the transfer function between the yaw torque M_z and sideslip rate $\dot{\beta}$ has a negative gain, thus:

$$M_z = -|K_1|(\dot{\beta}_{ref} - \dot{\beta}) \quad (7)$$

Equation 3 and Eq. 7 can be combined to derive a more explicit control law:

$$M_z = |K_1|(\omega_{z,ref} - \omega_z) - \frac{|K_1|}{v_x}(a_{y,ref} - a_y) \quad (8)$$

Equation 8 shows how the proposed control approach can be interpreted as a multivariable control system. The sideslip rate feedback inherently integrates a yaw rate tracking loop with a lateral acceleration feedback, whose gain dynamically varies with vehicle speed. However, this term has a negative gain opposing the yaw rate tracking action, therefore necessitating a tradeoff between yaw rate tracking and the damped transient responses.

It is crucial to underline that while tracking a reference yaw rate is pivotal for guaranteeing performance, driving feel and safety are equally important. The proposed approach

introduces an additional feedback loop that tracks the yaw rate with a positive feedback gain $R_2 = |K_2|$:

$$M_{z,FB} = (|K_1| + |K_2|)(\omega_{z,ref} - \omega_z) - \frac{|K_1|}{v_x}(a_{y,ref} - a_y) \quad (9)$$

This additional term serves two purposes: firstly, to introduce feedback robustness by coping with modeling uncertainties, delays, and noise in the plant, and secondly, as a means of calibration tradeoff. Indeed, by appropriately scheduling of the feedback controllers, more emphasis can be placed on yaw rate tracking during steady-state conditions, while ensuring a more damped response during highly dynamic maneuvers.

While the first term of Eq. 9 represents a conventional yaw rate tracking loop, it is the inclusion of this additional term that distinguishes this proposed approach as novel in the literature. For the sake of illustration, proportional feedback gains and the linear tire formulation are adopted here to derive the proof of asymptotic stability. However, through extension, it is possible to prove stability for a non-linear model and more elaborate control algorithms. By linearizing and combining Eqs. 1–3, an extended state-space system can be derived, whereby the steering effect is considered a disturbance:

$$\begin{bmatrix} \dot{\omega}_z \\ \dot{\beta} \end{bmatrix} = \begin{bmatrix} a_{11} & a_{12} \\ a_{21} & a_{22} \end{bmatrix} \begin{bmatrix} \omega_z \\ \beta \end{bmatrix} + \begin{bmatrix} b_1 \\ 0 \end{bmatrix} M_z \quad (10)$$

By deriving the sideslip dynamics with respect to time, the state-space system can be extended to include the sideslip rate as a state variable:

$$\begin{bmatrix} \dot{\omega}_z \\ \dot{\beta} \\ \ddot{\beta} \end{bmatrix} = \begin{bmatrix} a_{11} & a_{12} & 0 \\ a_{21} & a_{22} & 0 \\ a_{21}a_{11} & a_{21}a_{12} & a_{22} \end{bmatrix} \begin{bmatrix} \omega_z \\ \beta \\ \dot{\beta} \end{bmatrix} + \begin{bmatrix} b_1 \\ 0 \\ a_{21}b_1 \end{bmatrix} M_z \quad (11)$$

The stability condition for the state feedback gains can be derived using the Routh-Hurwitz criterion applied to the feedback matrix described by Eq. 12, obtained by substituting the control law $M_z = |K_2|(\omega_{z,ref} - \omega_z) - |K_1|(\dot{\beta}_{ref} - \dot{\beta})$ into Eq. 11.

$$A = \begin{bmatrix} a_{11} - |K_2|b_1 & a_{12} & |K_1|b_1 \\ a_{21} & a_{22} & 0 \\ a_{21}a_{11} - |K_2|a_{21}b_1 & a_{21}a_{12} & a_{22} + |K_1|a_{21}b_1 \end{bmatrix} \quad (12)$$

2.4 Tires Saturation

Although tires saturation has already been addressed in the feedforward modeling, the feedback term also influences the total yaw torque required. While it is relatively straightforward to develop a model-based saturation approach for the first component, deriving one solely for the feedback loop is not. In the interest of calibration efficiency and robustness, the total yaw torque is saturated with a calibratable function of tire slip ratios, steering wheel angle, and combined lateral acceleration vector.

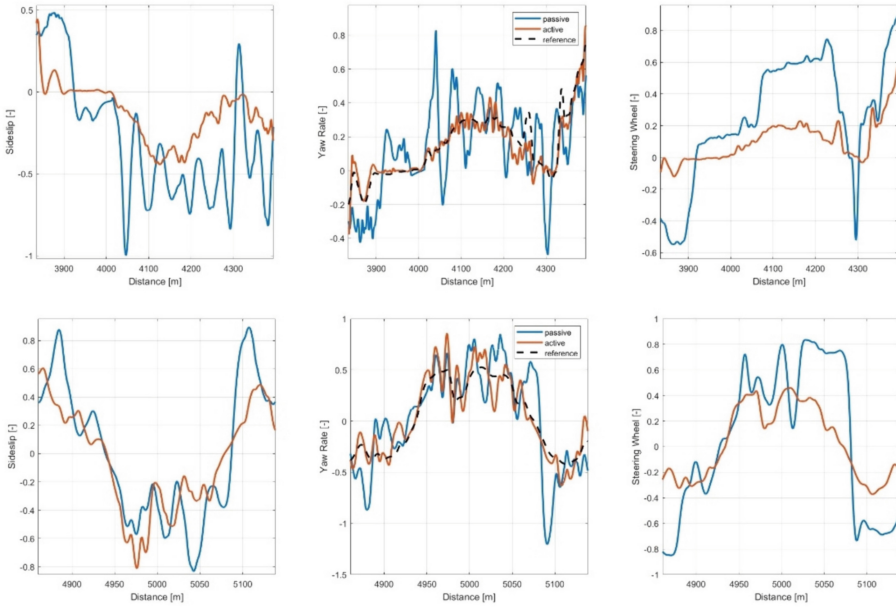


Fig. 2. NTC handling lap comparison, passive vs active; normalized states and control inputs.

3 Results and Conclusions

The proposed scheme has been very convincingly tested in numerous DiM and DiL-HiL sessions. Due to the limited space available, the results provided here will not focus on the comparison between the proposed and conventional approaches in terms of objective manoeuvres that can only offer a snapshot of the vehicle envelope. Likewise, elaborating on the brand's DNA and its reflection on objective metrics mapped against our experts' subjective attributes targets would not be feasible in this limited space. Instead the results presented (Fig. 2) focus on the benefits of the active vehicle on outright track performance, an attribute consciously balanced against intuitive dynamic responses, and benchmarked against the same vehicle optimally setup for track usage. Given the prerequisites of such a setup, it is evident that the benefits in dynamics and laptime ($-3.1s$) is the outcome of improved vehicle control and higher driver confidence.

The reference venue for the results presented is the Handling Track of the Nardo Technical Centre [2], a fast and highly technical track with a diverse combination of very high and low curvature corners as well as challenging elevation variance. The log extracts highlighting the delta in dynamics responses and driver effort through two particularly demanding track segments, whereby the dynamic composure achieved as well as the reference tracking ability of the proposed control scheme are evident.

References

1. Mazzilli, V., et al.: Integrated chassis control: classification, analysis and future trends. *Annu. Rev. Control.* **51**, 172–205 (2021)
2. <https://www.porscheengineering.com/nardo/en/services/theprovingground/testtracks/>

Open Access This chapter is licensed under the terms of the Creative Commons Attribution 4.0 International License (<http://creativecommons.org/licenses/by/4.0/>), which permits use, sharing, adaptation, distribution and reproduction in any medium or format, as long as you give appropriate credit to the original author(s) and the source, provide a link to the Creative Commons license and indicate if changes were made.

The images or other third party material in this chapter are included in the chapter's Creative Commons license, unless indicated otherwise in a credit line to the material. If material is not included in the chapter's Creative Commons license and your intended use is not permitted by statutory regulation or exceeds the permitted use, you will need to obtain permission directly from the copyright holder.





Iterative Learning Trajectory Tracking Control of an Autonomous Bicycle

Yixiao Wang^(✉), Fredrik Bruzelius, and Jonas Sjöberg

Department of Electrical Engineering and Department of Mechanical Engineering,
Chalmers University of Technology, Gothenburg, Sweden
{yixiaow,fredrik.bruzelius,jonas.sjoberg}@chalmers.se

Abstract. An autonomous bicycle has been developed for repeatable active safety tests of Advanced Driver Assistance Systems (ADAS). For effective interaction with other test objects, precise bicycle trajectory tracking control is essential. The repetitive nature of these tests suggest an Iterative Learning Control (ILC) approach.

In this paper, we present a design of an ILC controller tailored for the trajectory tracking problem of an autonomous bicycle. To illustrate the performance of the controller, simulations have been conducted.

Keywords: Motion control · Iterative learning control · Trajectory tracking

1 Introduction

Modern traffic safety is increasingly dependent on Advanced Driver Assistance Systems (ADAS). Test track testing is required to ensuring effectiveness and function of these systems. These tests are typically performed by replicating a real traffic scenario, and may include many actors. For scenarios including bicyclists, a bicycle robot is required that can be controlled according to the specific scenario be a specified trajectory. In response to the complexities of evaluating ADAS in cycling-related scenarios, we have developed a robotic bicycle equipped with self-balancing and path-tracking capabilities.

A common nature of ADAS test track test problem is repeatability. In practice, multiple test objects may be configured to repeat the same motion profile to simulate a traffic situation. However, lackness of prior knowledge about test uncertainties such as side wind, leaning pavement etc., might influence the robustness and precision of the test.

The problem formulation fits the framework of iterative learning control(ILC), where adaptive feed forward is learnt from previous test interactions. Iterative learning control have been proposed previously in the literature for vehicles. In Kapania and Gerdes, [3], controllers are proposed for race car driving, where the lateral control is improved over the laps. Both a PD and an LQ

Supported by VINNOVA, Swedish Innovation Agency.

© The Author(s) 2024

G. Mastinu et al. (Eds.): AVEC 2024, LNME, pp. 350–356, 2024.

https://doi.org/10.1007/978-3-031-70392-8_50

controller were proposed. With a similar concept but more innovation, [4] uses iterative learning scheme to realize an adaptive model predictive controller for a rover on Mars. The dynamical model of the system is improved after each iteration for better overall performance. Both of the papers reduce the lateral errors using ILC controllers.

ILC algorithms acquire information from the previous errors and utilize them to reduce the errors over iterations. For multiple-input multiple-output(MIMO) and nonlinear systems, more techniques need to be combined with ILC to guarantee convergence. The challenge comes from the coupled dynamics in different dimensions [5]. In this paper, to track the two-dimensional trajectory represented in Cartesian coordinates $(X(T), Y(T))$, we have decomposed the ILC trajectory tracking problem into a longitudinal and a lateral motion ILC tracking problems. This decomposition is based on several underlying assumptions related to lower level controllers and no tyre side-slip.

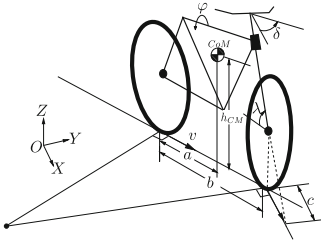


Fig. 1. Bike schematics

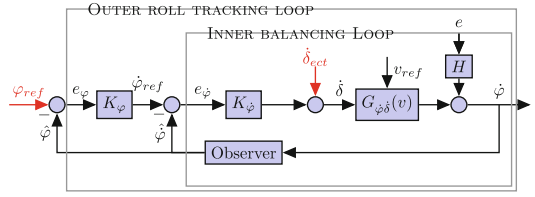


Fig. 2. Schematic Block of the roll tracking controller

2 Method

In this section, we first discuss the problem formulation and setup. Models will be given to describe the involved dynamics. Then the ILC framework will be introduced with the aim to reduce the tracking errors for each iteration. A theme across the approach taken is the separation in the dynamic states such that simpler control strategies can be applied. We start with the roll dynamics and its connection to the planar motion of the bicycle.

On the bicycle robot, tracking the planar position $(X(T), Y(T))$ can be achieved by lateral and longitudinal control using steering motor and drive motor respectively. The lateral control controls the steering angle δ and longitudinal control controls the rear wheel speed v .

The roll dynamics of the unstable bicycle $G_{\phi\delta}$ is given by (16) in [1]

$$\frac{d^2\varphi}{dt^2} = \frac{g}{h_{CM}}\varphi + \frac{av \sin \lambda}{bh_{CM}} \frac{d\delta}{dt} + \frac{(v^2 h_{CM} - acg) \sin \lambda}{bh_{CM}^2} \delta \quad (1)$$

where $g = 9.81 \text{ m/s}^2$ and other parameters are detailed in Fig. 1.

The unstable bicycle is balanced by a cascaded controller, as illustrated in Fig. 2. The inner balancing loop in Fig. 2 stabilizing the roll dynamics $G_{\varphi\delta}$ by controlling the steering angle rate $\dot{\delta}$. The outer loop is a roll angle tracking controller that tracks a roll angle reference φ_{ref} . There is a physical connection between the heading direction changes of the bicycle $\dot{\psi}$ and the leaning angle φ . Hence, the outer loop also influence the orientation of the bicycle. Under the assumption of fast closed loops in Fig. 2, we may neglect the dynamics from roll angle reference to heading. The model (1), can be used to obtain a function of a steering angle δ and a roll angle φ in steady state. Hence, the reference steering angle δ_{ref} can be translated into reference roll angle φ_{ref} and fed into the control loop (Fig. 4).

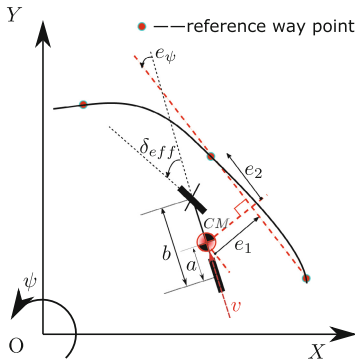


Fig. 3. Tracking error definitions

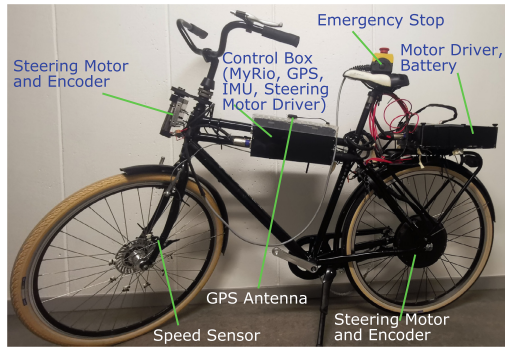


Fig. 4. The bicycle robot

The dynamics of position (X, Y) relates to the heading ψ and the steering angle δ :

$$\dot{X} = v \cos(\delta_{eff} + \psi) \qquad \dot{Y} = v \sin(\delta_{eff} + \psi) \qquad (2)$$

To evaluate the tracking performance, tracking errors can be computed in bicycle local coordinate, resulting in lateral and heading components (e_1 and e_ψ in Fig. 3):

$$\dot{e}_1 = v(\delta_{eff} + e_\psi) \qquad \dot{e}_\psi = \dot{\psi} - v\mathcal{K} \approx v\left(\frac{\delta_{eff}}{b} - \mathcal{K}\right) \qquad (3)$$

$$\frac{de_1}{dd_s} = (\delta_{eff} + e_\psi) \qquad \frac{de_\psi}{dd_s} \approx \left(\frac{\delta_{eff}}{b} - \mathcal{K}\right) \qquad (4)$$

In these formulations, $\delta_{eff} = \delta \sin(\lambda)$ represents the effective steering angle reference δ_{eff} computed by the lateral controller, and \mathcal{K} the path curvature. d_s is the travel distance, with $v = \dot{d}_s$ as its time derivative. A key insight derived from (4) is that, if the lateral controller only depends on position (X, Y) , or equivalently d_s , the lateral and heading errors e_1 and e_ψ are both time-independent. This is because δ_{eff} does not depend on time. This result is based on several

assumptions on the model (2): non-slip tyre ground contact and ideal control of steering angle δ . The slip-free assumption accords with the relatively slow speed (<4 m/s) and the ideal control of steering requires fast enough balancing and steering control loops, such that the transients can be neglected. We utilized a time-independent controller from [2] to reduce the lateral error, denoted as $K_{lat}(X, Y)$. Then the learned ILC feedforward signal $K_{\delta ILC}(T)$ can be re-indexed into $K_{\delta ILC}(d_s)$, independent of time T or speed v .

As another important factor, the longitudinal control relates to the test progress. The rear wheel speed v determines how fast the bicycle runs and the total duration of the iteration. Noticing path length to be roughly unaffected by the path deviation due to the lateral controller, we assume the speed v is independent on the lateral tracking errors e_1 and e_ψ . This assumption allows us to split the ILC trajectory tracking problem into a lateral ILC and a longitudinal ILC problem. Integrated into the motor microcontroller, a local speed PID controller tracks a given speed reference v_{ref} . By changing v_{ref} , ILC controller influences the progress indirectly. The propulsion motor dynamics can be modelled simply as resistor, inductor, voltage source and motor connected in series. The load of the motor in longitudinal dynamics can be modelled as a Mass-Damping system and a speed controller integrated in the motor driver tracks a reference speed v_{ref} . A longitudinal controller $K_v(X, Y, T) = v_0 + k_v e_2(T)$ tracks the progress with a constant gain k_v .

The ILC framework refines feedforward signals for steering angle δ and speed v over repetitions. As the lateral path is independent of speed variations, the lateral feedforward signals $K_{\delta ILC}(d_s)$ can also be indexed by the travel distance d_s , resulting in,

$$\delta_{ref}(X, Y) = K_{lat}(X, Y) + K_{\delta ILC}(d_s) \quad (5)$$

$$v_{ref}(X, Y, T) = K_v(X, Y, T) + K_{v ILC}(T) \quad (6)$$

where $K_{v ILC}(T)$ is the ILC feedforward for longitudinal speed v . δ_{ref} is converted into φ_{ref} and fed into the outer loop in Fig. 2 according to (1) in steady state.

The ILC controllers, $K_{\delta ILC}(d_s)$ and $K_{v ILC}(T)$ are chosen to be standard Proportional-Derivative controllers, as in e.g. [3]:

$$K_{v ILC}^+(T) = v_{ref}(T) - k_{vp}e_2(T) - k_{vd}(e_2(T) - e_2(T - 1)) \quad (7)$$

$$K_{\delta ILC}^+(d_s) = \delta_{ref}(d_s) - k_{\delta p}e_1(d_s) - k_{\delta d}(e_1(d_s) - e_1(d_s - \Delta d_s)) \quad (8)$$

$$d_s(T) = \int_0^T v dt \quad (9)$$

with the superscript $+$ denotes the variable in the new iteration. Δd_s is a constant longitudinal step to obtain equidistant samples. $k_{\star p}$ and $k_{\star d}$ denote the proportional and derivative gains in the dimension \star respectively. Zero-phase low-pass filters have been further added on $K_{v ILC}^+(T)$ and $K_{\delta ILC}^+(T)$ for robustness. See (16) in [3] for details (Fig. 5).

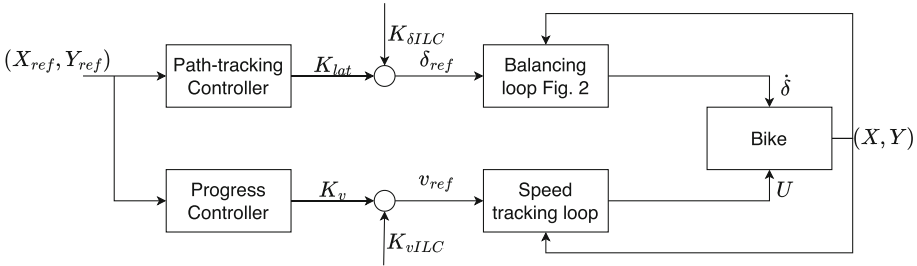


Fig. 5. Control structure of the overall system

3 Result

To assess the effectiveness of the ILC framework (5)(6), we conducted a simulation with the unstable linearized model of the bicycle in (1). A dynamical drive motor model is also used for longitudinal dynamics, together with the modeling of road inclinations and uneven road surfaces. Incorporating curves and straight lines, an infinite-shaped path with equidistant waypoints profile was selected for the simulation. The ILC speed controller is expected to dynamically adjust v_{ref} to counteract longitudinal speed v variations induced by steering actions δ . The results visualized in Fig. 6 show a progressive reduction in the root-mean-square(RMS) error across multiple iterations. Initial offsets in heading ψ and position (X, Y) have also been imposed to create initial transients. In 5 iterations, the RMS is reduced from 1.7 m to 0.6 m. The residual errors may be related to the coupling of longitudinal speed (acceleration) and steering with the lower level balancing loops (Fig. 2). They are neglected in our previous assumptions regarding ideal control in (3).

The absolute values of the lateral error e_1 and longitudinal error e_2 are further visualized in time domain, shown in Fig. 7. The errors during the beginning of each iteration (0–10 s) were similar, because of the overwhelming transients of the balancing and longitudinal speed control loops. While improvements can be seen after this start-up, where the maximum absolute errors are reduced from 1.49 m to 0.67 m and from 1.55 m to 0.73 m in e_1 and e_2 , respectively.

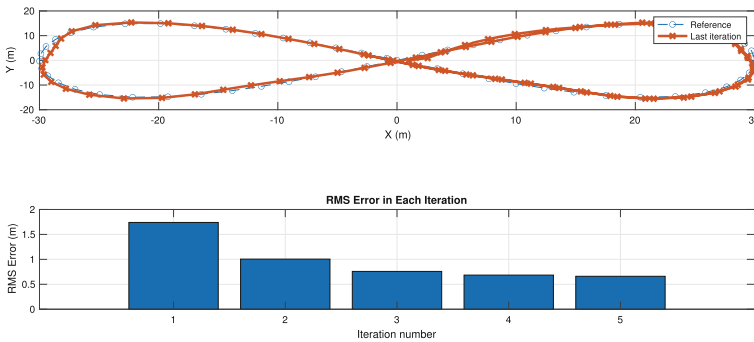


Fig. 6. Validation tests

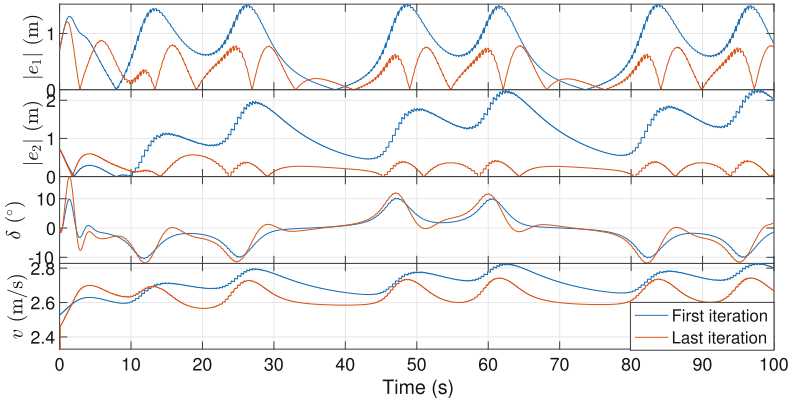


Fig. 7. $|e_1|$, $|e_2|$, δ and v in time domain.

4 Conclusions

This paper presents the design of a MIMO Iterative Learning Controller specifically tailored for the trajectory tracking of an autonomous bicycle. By assuming ideal control over steering and neglectable balancing transients, the task is effectively divided into longitudinal and lateral sub-problems. The lateral-longitudinal error separation is the crucial component in this approach. Simulation results demonstrate the effectiveness of this approach. Under the typical position dependent disturbances from slopes and resistances, the ILC controllers could reduce the errors over repeated test iterations.

However, the authors see more challenges in real application. Both the steering ILC controller $K_{\delta ILC}$ and the path-tracking controller [2] are based on linearization and may fail with large e_1 or e_ψ . Moreover, the real roll-longitudinal coupling may be more complicated than what we have modelled.

References

1. Astrom, K.J., Klein, R.E., Lennartsson, A.: Bicycle dynamics and control: adapted bicycles for education and research. *IEEE Control Syst. Mag.* **25**(4), 26–47 (2005)
2. Wen, G. Sjöberg, J.: Lateral control of a self-driving bike. In: *2022 IEEE International Conference on Vehicular Electronics and Safety (ICVES)*, pp. 1–6 (2022)
3. Kapania, N.R., Gerdes, J.C.: Path tracking of highly dynamic autonomous vehicle trajectories via iterative learning control. In: *2015 American Control Conference (ACC)*, pp. 2753–2758. IEEE, Conference Proceedings (2015)
4. Baldauf, N., Lubiniecki, T., Turnwald, A., Lakatos, K., Panagiotopoulos, N.: Learning-based motion control of a rover on unknown ground (2023)
5. Bristow, D., Tharayil, M., Alleyne, A.: A survey of iterative learning control. *IEEE Control Syst. Mag.* **26**(3), 96–114 (2006)

Open Access This chapter is licensed under the terms of the Creative Commons Attribution 4.0 International License (<http://creativecommons.org/licenses/by/4.0/>), which permits use, sharing, adaptation, distribution and reproduction in any medium or format, as long as you give appropriate credit to the original author(s) and the source, provide a link to the Creative Commons license and indicate if changes were made.

The images or other third party material in this chapter are included in the chapter's Creative Commons license, unless indicated otherwise in a credit line to the material. If material is not included in the chapter's Creative Commons license and your intended use is not permitted by statutory regulation or exceeds the permitted use, you will need to obtain permission directly from the copyright holder.





A General 3D Road Model for Motorcycle Racing

Thomas Fork^(✉) and Francesco Borrelli

University of California at Berkeley, Berkeley, CA 94708, USA
{fork, fborrelli}@berkeley.edu

Abstract. We present a novel control-oriented motorcycle model for nonplanar racetracks and use it for computing racing lines. The proposed model combines recent advances in nonplanar road models with the dynamics of motorcycles. Our approach considers the additional camber degree of freedom of the motorcycle body with a simplified model of the rider and front steering fork bodies. We demonstrate the effectiveness of our model by computing minimum-time racing trajectories on a nonplanar racetrack.

Keywords: Vehicle Dynamics · Motorcycles · Road Models

1 Introduction

Control-oriented vehicle models have seen widespread use for trajectory planning in consumer and motorsport applications. However, many such models have been limited to simple road geometry. This does not adequately capture vehicle behavior for safety-critical or high performance maneuvers and these limitations result from the lack of suitable road models [4].

Early literature [5] developed 3D road models for ribbon-shaped surfaces, which may curve and twist in 3D but are cross-sectionally linear. These works focused on four-wheeled vehicles, not motorcycles in part due to their more complicated dynamics and ability to camber. Later work [3] applied these road models to motorcycles. In [2] the authors developed a general 3D road model applied to cars. In this paper we extend our road model to motorcycles. We develop a procedure to extend [2] to vehicles which do not remain tangent to the road surface. We apply this to a particular motorcycle model which we use to compute racelines: periodic minimum-time trajectories around a 3D racetrack.

This paper is outlined as follows: In Sect. 2 we introduce a kinematic motorcycle model that allows for extension of our road model. We develop motorcycle dynamics and complete the motorcycle model in Sect. 3. We provide an example of the model's use for raceline optimization in Sect. 4.

Supported by Brembo Inspiration Lab.

© The Author(s) 2024

G. Mastinu et al. (Eds.): AVEC 2024, LNME, pp. 357–363, 2024.

https://doi.org/10.1007/978-3-031-70392-8_51

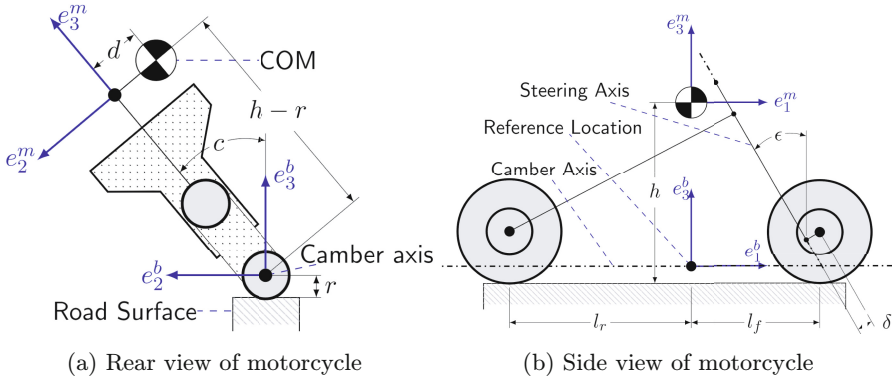


Fig. 1. Motorcycle geometry for nonplanar road model.

2 Road Model Extension for Motorcycles

Motorcycles are inherently multi-body systems comprised of wheels, front and rear suspension, rider, chassis, and more [7]. Control-oriented models invariably simplify some components to capture controllable behaviour while omitting finer details. We develop a motorcycle model kinematically similar to [3]. We neglect suspension motion and assume that there exists an axis fixed relative to the chassis of the motorcycle which remains a constant distance above the road: the “camber axis” shown Fig. 1a.

The camber axis will precisely link nonplanar road surface and motorcycle geometry. We use it to introduce a body reference frame along the camber axis and directly below the center of mass (COM), shown in Fig. 1b with the orthonormal basis $e_{1,2,3}^b$. Similarly, we introduce a motorcycle frame fixed to the motorcycle chassis at the height of the COM with basis $e_{1,2,3}^m$. We allow the COM itself to move laterally in the motorcycle frame due to rider motion as shown in Fig. 1a.

We follow the tire convention of [6] illustrated in Fig. 2. The tire camber angle c^t is the angle between the tire plane of symmetry and the body frame vertical e_3^b , and the steering angle γ^t is the angle between the e_1^b direction and the intersection of the tire plane of symmetry with the $e_1^b - e_2^b$ plane. These angles are dependent on camber angle c , rake angle ϵ , and the steering angle γ about the steering axis. We use superscripts f and r in place of t for quantities specific to the front and rear tire respectively.

We assume the rear tire is unsteered, as a result $\gamma^r = 0$ and $c^r = c$. For the front tire, we have [3]:

$$c^f = \sin^{-1}(\sin(c) \cos(\gamma) + \cos(c) \sin(\epsilon) \sin(\gamma)) \tag{1a}$$

$$\gamma^f = \tan^{-1} \left(\frac{\cos(\epsilon) \sin(\gamma)}{\cos(c) \cos(\gamma) - \sin(c) \sin(\epsilon) \sin(\gamma)} \right). \tag{1b}$$

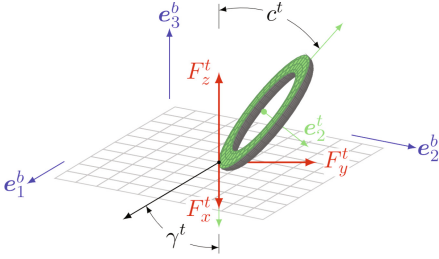


Fig. 2. Tire diagram, with the tire cross-sectioned through its plane of symmetry. Tire camber and steering angle c^t and γ^t are positive as shown, and differ from the steering angle of the motorcycle steering assembly and camber angle of the motorcycle body. Tire forces $F_{x,y,z}^t$ are discussed in Sect. 3.3.

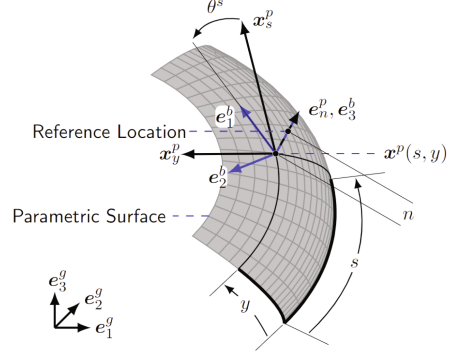


Fig. 3. Road surface model schematic. The surface is defined by $\mathbf{x}^p(s, y)$ and a vehicle reference location with the basis $\mathbf{e}_{1,2,3}^b$ is located at a fixed normal offset n from the surface.

We leverage the 3D road surface model proposed in [2]. With our road model, vehicle position is described by the surface parameterization $\mathbf{x}^p(s, y)$ and normal offset n . Orientation described by angle θ^s , and this is shown in Fig. 3. The main results are:

$$\begin{bmatrix} \dot{s} \\ \dot{y} \end{bmatrix} = (\mathbf{I} - n\mathbf{II})^{-1} \mathbf{J} \begin{bmatrix} v_1^b \\ v_2^b \end{bmatrix} \quad (2a)$$

$$\dot{\theta}^s = \omega_3^b + \frac{(\mathbf{x}_{ss}^p \times \mathbf{x}_s^p) \cdot \mathbf{e}_n^p}{\mathbf{x}_s^p \cdot \mathbf{x}_s^p} \dot{s} + \frac{(\mathbf{x}_{yy}^p \times \mathbf{x}_s^p) \cdot \mathbf{e}_n^p}{\mathbf{x}_s^p \cdot \mathbf{x}_s^p} \dot{y} \quad (2b)$$

$$\begin{bmatrix} -\omega_2^b \\ \omega_1^b \end{bmatrix} = \mathbf{J}^{-1} \mathbf{II} (\mathbf{I} - n\mathbf{II})^{-1} \mathbf{J} \begin{bmatrix} v_1^b \\ v_2^b \end{bmatrix} \quad (2c)$$

$$\begin{bmatrix} -\dot{\omega}_2^b \\ \dot{\omega}_1^b \end{bmatrix} \approx \mathbf{J}^{-1} \mathbf{II} (\mathbf{I} - n\mathbf{II})^{-1} \mathbf{J} \begin{bmatrix} \dot{v}_1^b \\ \dot{v}_2^b \end{bmatrix}. \quad (2d)$$

Here v_i^b and ω_i^b are the ISO body frame components of a vehicle's linear and angular velocity. \mathbf{I} and \mathbf{II} are the first and second fundamental forms of \mathbf{x}^p , with partial derivatives of \mathbf{x}^p denoted by subscripts. \mathbf{J} is the Jacobian between the body frame and x^p . Implicit in this road model is that the vehicle remains tangent to and in contact with the road, for instance that wheelie and stoppie behaviour of a motorcycle is prevented, and that the curvature of the surface is gradual relative to the length of the motorcycle. The former is considered explicitly later in this paper, while the latter is always subjective to the road and motorcycle considered.

For a motorcycle, we apply this to the body frame $\mathbf{e}_{1,2,3}^b$ of the motorcycle introduced in Fig. 1. However, additional variables c and d are necessary to describe its motion and behaviour, necessitating additional dynamic considerations compared to [2], which we introduce next.

3 Motorcycle Model

We derive our motorcycle model as follows:

1. Compute the momentum and time rate of change thereof of the system
2. Use 1) and Newtonian mechanics to obtain net force and moment
3. Equate 2) to the force and moment from tire forces, gravity, and drag

This process results in a differential algebraic equation of the form:

$$\dot{z} = f(z, u, a) \qquad 0 = g(z, u, a), \tag{3}$$

where g captures the force and moment equalities of step 3). u is a set of inputs while z and a are differential and algebraic states respectively. The components of z , a and u are:

$$z = \{s, y, \theta^s, v_1^b, v_2^b, \omega_3^b, c, \dot{c}, d, \dot{d}\} \tag{4a}$$

$$a = \{\dot{v}_1^b, \dot{v}_2^b, \dot{\omega}_3^b, \ddot{c}, F_z^f, F_z^r\} \tag{4b}$$

$$u = \{\gamma, \ddot{d}, F_x^f, F_x^r\}, \tag{4c}$$

where F_z^f and F_z^r are the front and rear tire normal forces and F_x^f and F_x^r are the longitudinal force of the same tires. Equation (2) provides \dot{s} , \dot{y} and $\dot{\theta}^s$ for \dot{z} . Other elements of \dot{z} are elements of z , u , or a .

3.1 Net Force from Mechanics

To obtain g we first determine the momentum and rate thereof of the motorcycle, beginning with the position of the COM relative to our reference location:

$$\mathbf{r}_{\text{com}} = \mathbf{e}_3^m(h - r) + \mathbf{e}_2^m d. \tag{5}$$

Basis vectors $\mathbf{e}_{1,2,3}^m$ are related to $\mathbf{e}_{1,2,3}^b$ via the camber angle c . Time derivatives of $\mathbf{e}_{1,2,3}^b$ follow from standard rotation theory and $\omega_{1,2,3}^b$. These expressions are omitted for brevity. As a result, the linear velocity of the center of mass is:

$$\mathbf{v}_{\text{com}} = \mathbf{v}^b + \frac{d}{dt} \mathbf{r}_{\text{com}} = \mathbf{v}^b + \dot{c} \partial_c \mathbf{r}_{\text{com}} + \dot{d} \partial_d \mathbf{r}_{\text{com}} + \sum_{k=1,2,3} \frac{d}{dt} (\mathbf{e}_k^b) \partial_{\mathbf{e}_k^b} \mathbf{r}_{\text{com}}, \tag{6}$$

where the \mathbf{r}_{com} derivative was expanded by using the chain rule.

The net force on the vehicle is then:

$$\mathbf{F} = \frac{d}{dt} \mathbf{p} = m \frac{d}{dt} \mathbf{v}_{\text{com}}. \tag{7}$$

Deriving $\frac{d}{dt} \mathbf{v}_{\text{com}}$ involves one more round of differentiation with additional derivatives of v_1^b , v_2^b , ω_3^b , \dot{c} , and \dot{d} in the chain rule. The result is a single expression with terms that include either \mathbf{e}_1^b , \mathbf{e}_2^b , or \mathbf{e}_3^b . Grouping all terms that include \mathbf{e}_k^b then provides the net force on the vehicle in direction \mathbf{e}_k^b .

3.2 Net Moment from Mechanics

For the angular momentum and net moment on the motorcycle we use a functionally identical approach with two main differences: First, we assume the moment of inertia matrix of the motorcycle and rider remains constant, i.e. rider displacement is small. Second, momentum is contributed by the spin of both the front and rear tires, approximated as:

$$\mathbf{l}^t = (\omega^t) I^t \mathbf{e}_2^m. \quad (8)$$

As in the previous section, deriving the net moment on the motorcycle involves derivatives and may be automated using symbolic algebra on a computer.

3.3 Force and Moment Laws

We complete our motorcycle model by considering several force models.

Gravitational forces on the motorcycle are fully determined by the orientation of the body frame, in turn determined by s, y, θ^s and found in [2].

Aerodynamic forces are often modeled with steady state equations based on vehicle speed, which are straightforward to consider.

We use the tire model proposed in [6, ch. 11]. Full equations and parameters of the tire model may be found in Equations (11.40) through (11.59) and Table 11.1 of [6]. Longitudinal and normal tire forces are treated as inputs, with lateral tire force a function of these inputs, camber angle, and slip angle of the tire, which follow from variables in $z, u,$ and $a,$ with slip angle defined in [6]. Importantly, the tire forces $F_{x,y,z}^t$ are relative to the road (Fig. 2) and must be transformed appropriately to the body frame, e.g. the normal force produces a moment about the center of mass when the motorcycle cambers.

In total, we can compute expressions for the net force and moment as a result of tires, aerodynamics, and gravity. We obtain g in (3) by equating these to the force and moment expressions that resulted from mechanics, which completes our vehicle model. Other sources of force and moment may be seamlessly considered by adding additional equations which model their effects.

4 Results

The core result of our work is the general road model applicable to motorcycles. To illustrate its use, we computed a raceline for a motorcycle on a racetrack. This is a well-studied problem [3] with the key difference being that our road model allows more general road surfaces to be considered. We set up the surface, motorcycle model, and raceline problem in CasADi [1], which was solved using IPOPT [8].

Racetrack and raceline are shown in Fig. 4. The 650 m long track includes many nonplanar features such as quarter-pipe turns, gullies, and undulating hills. Our method achieved a lap time of 31.1 s, with 33 s of compute time to converge to local optimality on an 11th Gen Intel® Core™ i7-11800H @2.3 GHz.

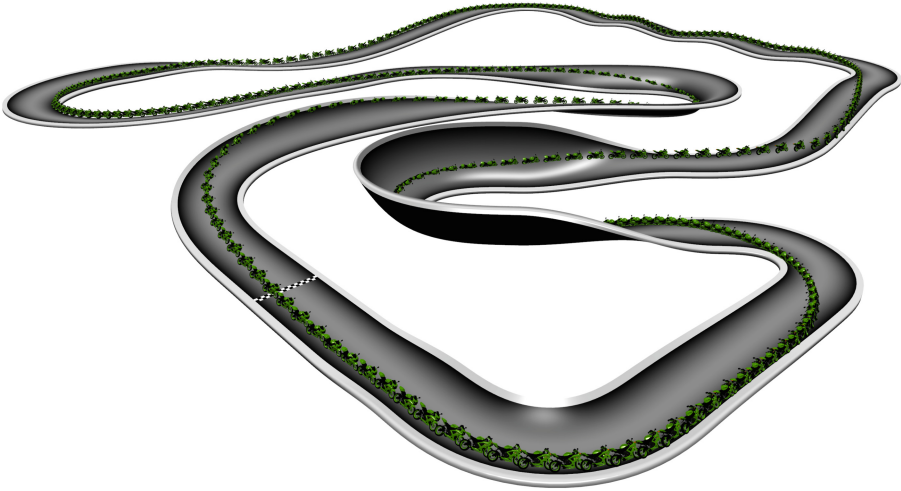


Fig. 4. Simulated nonplanar racetrack and motorcycle raceline. The graphical [motorcycle model](#) was made by Sketchfab user [nouter2077](#) and is [CC BY 4.0](#).

5 Conclusion

We extended the interpretation of a general nonplanar road model to apply it to the dynamics of motorcycles. In the process we added considerations for motorcycle camber and rider motion, and their impact on motorcycle dynamics. We discussed how the flexibility of the road model allows more general road geometry to be considered and used our model to generate time-optimal racelines on a complex nonplanar racetrack.

References

1. Andersson, J.A.E., Gillis, J., Horn, G., Rawlings, J.B., Diehl, M.: CasADi – a software framework for nonlinear optimization and optimal control. *Math. Program. Comput.* (2018)
2. Fork, T., Tseng, H.E., Borrelli, F.: Models for ground vehicle control on nonplanar surfaces. *Veh. Syst. Dyn.* **62**, 976–1000 (2023)
3. Leonelli, L., Limebeer, D.: Optimal control of a road racing motorcycle on a three-dimensional closed track. *Veh. Syst. Dyn.* **58**(8), 1285–1309 (2020)
4. Limebeer, D., Warren, E.: A review of road models for vehicular control. *Veh. Syst. Dyn.* **61**(6), 1449–1475 (2023)
5. Lot, R., Biral, F.: A curvilinear abscissa approach for the lap time optimization of racing vehicles. *IFAC Proc. Vol.* **47**(3), 7559–7565 (2014)
6. Pacejka, H.: *Tire and Vehicle Dynamics*, 3rd edn. Butterworth-Heinemann, Heine-
mann (2012)

7. Tanelli, M., Corno, M., Saveresi, S.: Motorcycle dynamics. In: *Modelling, Simulation and Control of Two-Wheeled Vehicles*, chap. 1, pp. 3–42. John Wiley & Sons (2014)
8. Wächter, A., Biegler, L.: On the implementation of an interior-point filter line-search algorithm for large-scale nonlinear programming. *Math. Program.* **106**, 25–57 (2006)

Open Access This chapter is licensed under the terms of the Creative Commons Attribution 4.0 International License (<http://creativecommons.org/licenses/by/4.0/>), which permits use, sharing, adaptation, distribution and reproduction in any medium or format, as long as you give appropriate credit to the original author(s) and the source, provide a link to the Creative Commons license and indicate if changes were made.

The images or other third party material in this chapter are included in the chapter's Creative Commons license, unless indicated otherwise in a credit line to the material. If material is not included in the chapter's Creative Commons license and your intended use is not permitted by statutory regulation or exceeds the permitted use, you will need to obtain permission directly from the copyright holder.





Energy-Efficient Straight-Line Driving Torque Vectoring for Electric Vehicles with Disconnect Clutches and Unequal Front/Rear Motors

Ivo Grđan, Branimir Škugor^(✉), and Joško Deur

Faculty of Mechanical Engineering and Naval Architecture, University of Zagreb, Zagreb, Croatia

branimir.skugor@fsb.hr

Abstract. This paper investigates potential of energy efficiency improvement for electric vehicle (EV) equipped with unequal front/rear-axle e-motors and disconnect clutches under straight-line driving conditions. First, a static optimization of front/rear torque distribution is performed for various driving cycles, which provides insights into energy efficiency gains and optimal powertrain operation including optimal torque switching curve for two- and four-wheel drive modes. Disconnect clutches enable inactive motors to be switched off when operating in the 2WD mode to avoid their drag losses. A dynamic programming (DP)-based optimization of torque vectoring control trajectories is carried out to find the globally optimal energy saving potential. For clutch durability reasons, the number of clutch state changes is minimized along with energy consumption. Finally, a rule-based (RB) control strategy is proposed and verified against the DP Pareto optimal frontier benchmark for different certification driving cycles.

Keywords: Electric Vehicles · Four-wheel Drive · Unequal Motors · Disconnect Clutches · Energy Efficiency · Torque Vectoring · Optimization · Control

1 Introduction

Electric vehicles (EV) can conveniently be realized in multiple e-motor configurations. These configurations are characterized by control redundancy that can be exploited to improve vehicle dynamics [1] and reduce energy consumption [1, 2]. For instance, the energy efficiency can be improved for straight-line driving by using two-wheel-drive (2WD) mode for low-torque demands, while switching to all-wheel drive (AWD) mode for mid-high torque demands [1]. Further energy efficiency gains can be achieved by avoiding the drag losses of inactive motors in the 2WD mode through disconnecting those motors via dog clutches [3].

EV torque vectoring literature is mostly focused on powertrains with no disconnect clutches and equal motors [4]. It is analytically proven in [5] that, under those conditions, the equal front/rear torque distribution is optimal in the AWD mode occurring above a vehicle velocity-dependent torque demand switching curve. When concerning the

use of disconnect clutches, the optimization problem becomes dynamic, and a global optimum can be found offline by using a dynamic programming algorithm [6, 7]. The DP benchmark can closely be approached by using rule-based (RB) control [6].

When concerning unequal front/rear motors, the optimal control problem becomes more complex, and it is solved in [8, 9] for the no-disconnect case. The main aim of this paper is to extend the numerical optimization and RB controller design studies from [6] to the disconnect case, in order to gain insights into optimal behavior and check the RB strategy applicability in this more general design task.

2 Model

The considered EV powertrain consists of two unequal pairs of e-motors (M/G_1 of 55 kW at front axle, and M/G_2 of 111 kW at rear axle), which are represented by the efficiency and maximum torque maps shown in Fig. 1b and c, and adopted from an extended-range EV from [12]. The motors are connected to wheels via single-speed transmissions and dog clutches (Fig. 1a).

The EV powertrain is represented by a backward-looking model [6, 11], which apart from the kinematic relations accounts for the tire and transmission losses. The front/rear torque distribution is defined by the torque distribution control input σ : $\tau_{w,f} = \sigma \tau_{w,t}$, $\tau_{w,r} = (1 - \sigma) \tau_{w,t}$, where $\tau_{w,t}$ is the total torque demand calculated from the vehicle longitudinal dynamics model fed by the velocity/acceleration profile defined by a simulated driving cycle. The only dynamics within the model relates to clutch state equation $\mathbf{c}(k + 1) = [0 \ 0 \ 0 \ 0] \cdot \mathbf{c}(k) + \mathbf{I} \cdot \mathbf{c}_R(k)$, where \mathbf{c} and \mathbf{c}_R are binary vectors of clutch state and clutch state reference, respectively, and k is the sampling step. The model includes \mathbf{c} - and \mathbf{c}_R -related e-drive transient losses corresponding to clutch connect synchronization and clutch-disconnect motor stopping process [6, 11]. The vehicle mass is increased compared to model in [6] to account for larger-size rear motors and provide wider-torque range utilization of motors for given, certification driving cycles.

3 Optimization and Control

The static optimization relies on a search over a grid of σ values, which is aimed at minimizing the battery power consumption. The results shown in Fig. 2a for the clutch disconnect case suggest that it is optimal to use the weaker, front motors ($\sigma = 1$; FWD) if the torque demand is lower than the torque switching curve (cyan; cf. EREV optimization results in [12]), which is close to the maximum torque curve for the FWD mode (red). Otherwise, all-wheel drive (AWD) is optimal, where σ mostly takes values in the range from 0.2 to 0.5, thus meaning that the torque is distributed towards stronger, rear motors. When not considering the disconnect clutches, the optimized σ -maps turn out to be very similar to those shown in Fig. 2a. These results contrast with those obtained for equal motors (M/G_1 all; [10]), where equal distribution ($\sigma = 0.5$) is optimal for AWD mode and the torque switching curves are distinctively different depending on whether the disconnect clutches are used or not. This is partly because the equal torque distribution is not feasible for high torque demands in the case of unequal motors (those larger than $4 \tau_{m,1,max} I_{t1}$, see Fig. 2a). For instance, the torque distribution ratio at the maximum wheel

torque demand is determined by $\sigma_{max} = 2\tau_{m,1,max}h_1/(2\tau_{m,1,max}h_1 + 2\tau_{m,2,max}h_2)$, which gives $\sigma_{max} = 0.2317$.

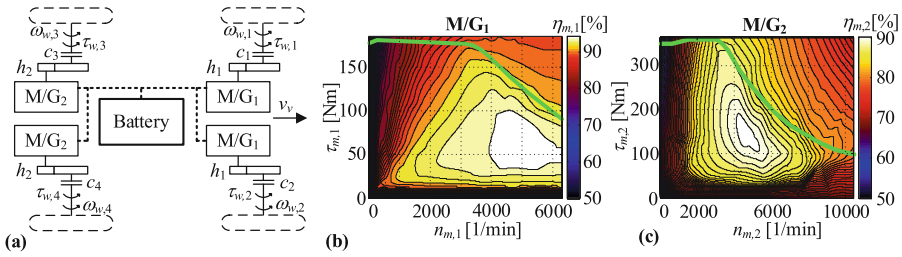


Fig. 1. Principal schematic of EV powertrain with unequal front/rear e-motors (a), given by efficiency maps and maximum torque curves (b, c).

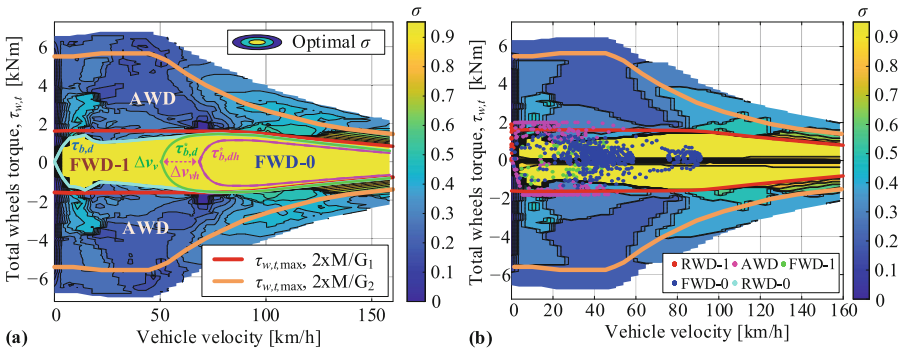


Fig. 2. Optimized torque distribution ratio map for clutch disconnect case (a) and DP optimization results corresponding to control setting denoted by orange-circle point in Fig. 4a.

Using the disconnect clutches introduces clutch state dynamics and related transient losses in the optimization problem. To establish a globally optimal benchmark for control strategy design and verification, offline optimizations of control trajectories $\sigma(k)$ and $\mathbf{c}_R(k)$ are performed by using the dynamic programming (DP) algorithm from [6, 10]. For the clutch durability and also drivability reasons, the energy consumption minimization cost function is extended with a term that penalizes the number of clutch state changes, with the corresponding weighting factor K_{sw} [10].

The RB control strategy, which is originally proposed for the powertrain with equal motors [6, 11], is somewhat adapted for the considered powertrain with unequal motors. It sets the AWD operating mode with the fixed $\sigma = 0.3$ (instead of $\sigma = 0.5$) for torque demands above the torque switching curve (cyan), while setting the FWD ($\sigma = 1$), otherwise (see Fig. 2a). The FWD mode is further divided into regions where the opposite-axle (rear) e-motors are connected (FWD-1) or disconnected (FWD-0), with the note that unlike in [6, 11] there are no separate switching curves for these two cases. This rule is motivated by DP optimization results shown in Fig. 2b, which indicate that the RWD clutches should remain connected in the FWD mode under low-velocity (urban-like)

condition, in order to reduce the clutch switching frequency including related transient losses. The FWD-1/FWD-0 boundary curve ($\tau_{b,d}^*$; green) has a two-parameter exponential form and it is supplemented with a hysteresis ($\tau_{b,dh}^*$; magenta) to suppress the number of clutch state changes [6, 11].

4 Results

Different control strategy variants are simulated over various certification driving cycles and compared based on the battery energy consumption (Table 1). The baseline strategy without clutch disconnect functionality, given in the first row of the table, simply iterates σ over the fine-resolution set $\{0, 0.01, \dots, 1\}$ at each simulation time step, to find the optimal value minimizing the energy consumption. Narrowing σ to only three discrete values $\{0, 0.35, 0.97\}$, selected on the basis of the static optimization results from Fig. 2a, leads to around only 1% higher energy consumption while simplifying the implementation. Adding clutch disconnect option within the static optimization in each simulation time step, and thus enabling FWD-0 and RWD-0 operating modes, improves the energy consumption up to 6% when compared to the baseline case (the third row of the table, cf. Similar results given in [10, 11] for the case of equal motors). The DP optimization accounting for transient losses further improves the results, with the percent margin shift of up to 2% for dynamic driving cycles (UDDS and US06), and negligibly (around 0.2%) for quasi-stationary cycles (HWFET and NEDC).

Table 1. Battery energy consumption [kWh] of control allocation and DP for various certification driving cycles.

METHOD	Disconnect	WLTP	UDDS	US06	HWFET	NEDC
Control allocation ($\sigma \in \{0, 0.01, \dots, 1\}$)	No	4.5189 (0%)	1.9941 (0%)	2.8620 (0%)	2.9525 (0%)	1.9178 (0%)
Control allocation ($\sigma \in \{0, 0.35, 0.97\}$)	No	4.5521 (+0.7%)	2.0089 (+1.2%)	2.8949 (+1.2%)	2.9703 (+0.6%)	1.9309 (+0.7%)
Control allocation ($\sigma \in \{0, 0.35, 1\}$)	Yes	4.3777 (−4.1%)	1.9904 (−2.6%)	2.7827 (−2.6%)	2.7827 (−5.9%)	1.8126 (−5.7%)
DP, $K_{sw} = 0$ ($\sigma \in \{0, 0.1, \dots, 1\}$)	Yes	4.3130 (−4.6%)	1.9064 (−4.4%)	2.7547 (−3.7%)	2.7713 (−6.1%)	1.8048 (−5.9%)

* $K_{sw} = 0$ relates to case of no clutch switching penalization within DP optimization.

Figure 3 shows the DP Pareto optimal frontiers (blue circles) obtained for $\sigma \in [0, 0.1, \dots, 1]$ and a wide range of K_{sw} values. The same figure shows the Pareto filtered frontiers corresponding to RB control strategies with and without hysteresis included (see [6, 11] for methodology details). The battery energy consumptions are expressed relative to the right-most minimum-energy Pareto frontier point ($K_{sw} = 0$). The number of clutch state changes can be reduced by up to 80% via increase of K_{sw} with a minor increase of energy consumption. Introduction of hysteresis brings consistent improvement of results,

which is most pronounced for the dynamic driving cycles (UDDS and US06; Fig. 3). The full-RB vs. DP relative energy consumption increase around the Pareto frontier knee point (i.e., in the region where the clutch switching frequency is well suppressed) is typically around 2%. This is somewhat inferior to the performance of the powertrain with equal motors, where the energy consumption increase margin is around 1% (see comparative results shown in Fig. 4). This implies that the expected benefit of predictive control would be higher for the case of unequal motors (see [6, 10, 11] for details of model predictive control approach and related results).

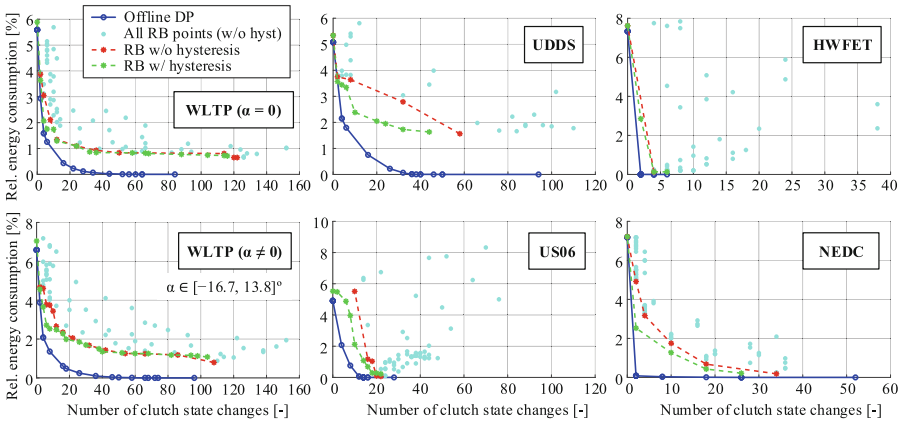


Fig. 3. Pareto optimal frontiers obtained by DP optimization, and RB control with and without hysteresis (a realistic non-zero road slope profile α is optionally appended to WLTP cycle).

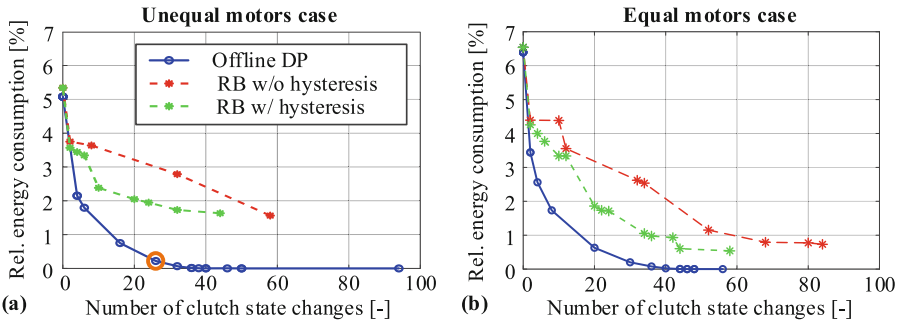


Fig. 4. DP and RB control Pareto optimal frontiers for powertrains with unequal (Fig. 3) and equal motors [11] (UDDS driving cycle).

5 Conclusion

An analysis of energy-efficient straight-line driving torque vectoring for electric vehicles equipped with unequal front/rear e-motors and disconnect clutches has been presented. The emphasis was on comparison of control strategy specifics and related performance with respect to the basic case of equal motors.

Control allocation optimization has revealed that there is an optimal velocity-dependent and clutch state-unaaffected torque switching curve, below which it is optimal to operate with front (weaker) motors only (front-wheel-drive, FWD), while all motors are activated, otherwise (all-wheel-drive, AWD). The optimal values of AWD front/rear torque distribution ratio lie in the range from 0.2 to 0.5 depending on the torque demand and velocity (unlike the value of 0.5, i.e. equal distribution, in the case of equal motors). It has been shown that the AWD torque distribution ratio can be fixed to a single value (0.35 for the particular vehicle) and still approach the optimal results (with the energy consumption increase margin of up to 1%). When enabling the clutch disconnect option, the energy consumption can be reduced by up to 6%, which is similar margin as in the case of equal motors.

Apart from the energy consumption criterion, the number of clutch state changes has also been considered for clutch durability reasons. Globally optimal and offline-obtained dynamic programming (DP) results have shown that the number of clutch state changes can be reduced by up to 80% with negligible influence on energy consumption. The previously proposed rule-based (RB) control strategy has been adjusted for the powertrain with unequal motors. The RB control performance approaches the DP benchmark energy consumption within the margin of 1% for a majority of considered driving cycles, while in the worst-case of UDDS cycle this margin increases to around 2%. Although small, these values are about doubled when compared with those observed for the powertrain with equal motors, which leaves a certain room for performance improvement through applying more sophisticated predictive control strategies.

References

1. Gruber, P., et al.: Energy efficient torque vectoring control. In: 13th AVEC, Munich (2016)
2. Koehler, S., et al.: Energy-efficiency optimization of torque vectoring control for battery electric vehicles. *IEEE ITSM* **9**(3), 59–74 (2017)
3. Yang, S., et al.: Disconnect actuator system (DAS) for AWD EV's driving system. SAE Technical Paper 2023-01-0451 (2023)
4. Sforza, A., et al.: A state-of-the-art review on torque distribution strategies aimed at enhancing energy efficiency for fully electric vehicles with independently actuated drivetrains. *Int. J. Mech. Control* **20**(2), 3–15 (2019)
5. Dizqah, A.M., et al.: A fast and parametric torque distribution strategy for four-wheel-drive energy-efficient electric vehicles. *IEEE Trans. Industr. Electron.* **63**(7), 4367–4376 (2016)
6. Deur, J., et al.: Energy-efficient straight-line driving torque vectoring for electric vehicles with multiple motors equipped with disconnect clutches. In: 18th SDEWES Conference, pp. 1–15, Sep (2023)
7. Xu, Y., et al.: Improved efficiency with adaptive front and rear axle independently driven powertrain and disconnect functionality. *Transp. Eng.* **13** (2023)
8. Lenzo, B., et al.: Torque distribution strategies for energy-efficient electric vehicles with multiple drivetrains. *J. Dyn. Syst. Meas. Control* **139**(12), 121004 (2017)
9. Dizqah, A.M., et al.: A non-convex control allocation strategy as energy-efficient torque distributors for on-road and off-road vehicles. *Control. Eng. Pract.* **95**, 104256 (2020)
10. Škugor, B., et al.: Optimization of straight-line driving torque vectoring for energy-efficient operation of electric vehicles with multiple motors and disconnect clutches. In review for a journal publication

11. Škugor, B., et al.: A parameter-optimized rule-based control strategy for front-rear torque vectoring in electric vehicles with multiple motors and disconnect clutches. In review for a journal publication
12. Deur, J., et al.: Modeling and low-level control of range extended electric vehicle dynamics. In: International Conference on Powertrain Modeling and Control (PMC 2012), Bradford, UK (2012)

Open Access This chapter is licensed under the terms of the Creative Commons Attribution 4.0 International License (<http://creativecommons.org/licenses/by/4.0/>), which permits use, sharing, adaptation, distribution and reproduction in any medium or format, as long as you give appropriate credit to the original author(s) and the source, provide a link to the Creative Commons license and indicate if changes were made.

The images or other third party material in this chapter are included in the chapter's Creative Commons license, unless indicated otherwise in a credit line to the material. If material is not included in the chapter's Creative Commons license and your intended use is not permitted by statutory regulation or exceeds the permitted use, you will need to obtain permission directly from the copyright holder.





Safety Filter for Lane-Keeping Control

Chenhuan Jiang¹, Hanyu Gan¹, Illés Vörös^{1,2(✉)}, Dénes Takács^{2,3},
and Gábor Orosz^{1,4}

¹ Department of Mechanical Engineering, University of Michigan,
Ann Arbor, MI 48109, USA

{chenhf,hanyugan,illesvoe,orosz}@umich.edu

² Department of Applied Mechanics, Budapest University of Technology
and Economics, Budapest 1111, Hungary

{illes.voros,takacs}@mm.bme.hu

³ HUN-REN-BME Dynamics of Machines Research Group,
Budapest University of Technology and Economics, Budapest 1111, Hungary

⁴ Department of Civil and Environmental Engineering, University of Michigan,
Ann Arbor, MI 48109, USA

Abstract. A safe lane-keeping controller is designed using a control barrier function (CBF) which ensures that if the vehicle starts between the lane boundaries then it does not leave the lane. The safety filter is applied on the top of a nominal path-following controller of the kinematic single-track model in order to modify the control input when the vehicle gets close to the boundary of the safe set in state space. Numerical simulations and phase portraits are used to demonstrate the performance of the proposed safety-critical controller.

Keywords: Automated vehicles · Control barrier function ·
Lane-keeping control · Safety critical control

1 Introduction

This paper presents the design of a safety-critical lane-keeping controller for passenger cars, which ensures that the vehicle is able to follow the lane center-line without leaving the lane boundaries. In order to stabilize the path following, a simple feedback controller can be set up that will aim to reduce the lateral position and yaw angle errors of the vehicle with respect to the lane center-line. However, to ensure that the path following can be achieved without the vehicle exiting the lane boundaries even in the presence of large initial deviations, the nominal controller has to be extended with some additional considerations.

In particular, we use a control barrier function (CBF) [1–4] to define a safety condition of the vehicle staying inside the lane boundaries. Based on this, a safe

C. Huang and H. Gan—The first two authors have the same contributions to this paper.

© The Author(s) 2024

G. Mastinu et al. (Eds.): AVEC 2024, LNME, pp. 371–377, 2024.

https://doi.org/10.1007/978-3-031-70392-8_53

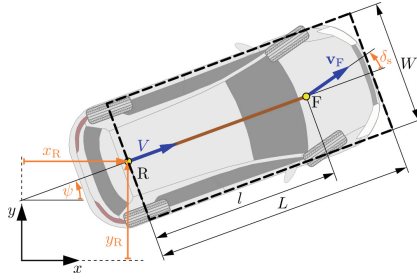


Fig. 1. Kinematic bicycle model with a bounding box excluding the rear overhang.

controller can be designed, which modifies the input of the nominal controller in a minimally-invasive fashion, in order to keep the system inside the safe set in state space, thereby ensuring safe lane-keeping of the vehicle.

The rest of the paper is organized as follows: in Sect. 2, the vehicle model and the nominal stabilizing controller are introduced. In Sect. 3, we present a brief overview of safe controller design using control barrier functions and define the safe set used for the lane-keeping problem. In Sect. 4, the resulting safe controller is analyzed using numerical simulations and phase portraits, highlighting the improvements over the case when only the nominal controller is used. Finally, Sect. 5 concludes the paper and gives an outlook for future research directions.

2 Vehicle Model and Nominal Controller

The kinematic bicycle model in Fig. 1 is applied in our analysis (see [5] for details), with the consideration of a straight-line reference path along the x -axis. The governing equations of the vehicle model are

$$\dot{x}_R = V \cos \psi, \quad \dot{y}_R = V \sin \psi, \quad \dot{\psi} = \frac{V}{l} \tan \delta_s, \tag{1}$$

where the state vector $x = [x_R \ y_R \ \psi]^T$ includes the coordinates of the rear axle center point x_R and y_R , and the yaw angle ψ . The vehicle speed V is considered to be constant and l denotes the wheelbase. We use $u = \tan \delta_s$ as the control input, where δ_s is the steering angle. This way the system can be written in the control affine form $\dot{x} = f(x) + g(x)u$.

We utilize a nominal steering controller of the form

$$u = k_d(x) = -P_y y_R - P_\psi \psi, \tag{2}$$

to stabilize the path-following, where P_y and P_ψ are the control gains. To ensure that the vehicle does not leave the lane boundaries, the vehicle model is extended with the bounding box of width W and length L shown in Fig. 1. For simplicity, the bounding box includes the wheelbase and the front overhang of the vehicle, while the rear overhang is neglected. In the next section, we extend the nominal controller to guarantee that if the bounding box starts inside the lane boundaries then it stays inside those boundaries.

3 Safety Filter with Control Barrier Function

In this sections we briefly review the theory behind control barrier functions (CBFs) and then apply it to the lane-keeping problem.

3.1 Control Barrier Function Background

Following [4], we define a safe set \mathcal{S} in the state space $\mathcal{X} = \mathbb{R}^2 \times (-\pi, \pi)$ and define a control barrier function $h : \mathcal{X} \rightarrow \mathbb{R}$ such that it is non-negative on \mathcal{S} :

$$\mathcal{S} = \{x \in \mathcal{X} : h(x) \geq 0\}, \quad (3)$$

while we require $h(x) = 0 \Rightarrow \nabla h(x) \neq 0$. Then it can be proven that \mathcal{S} is forward invariant (i.e., $\forall x(0) \in \mathcal{S} \Rightarrow x(t) \in \mathcal{S}, \forall t \geq 0$), if there exist a class- \mathcal{K} function $\alpha : \mathbb{R}_{\geq 0} \rightarrow \mathbb{R}_{\geq 0}$ such that

$$\sup_{u \in U} \underbrace{(\nabla h(x)f(x) + \nabla h(x)g(x)u)}_{\dot{h}(x,u)} \geq -\alpha(h(x)), \quad \forall x \in \mathcal{S}, \quad (4)$$

where U denotes the set of available control inputs. To find a controller that deviates from the nominal controller $k_d(x)$ as little as possible while still satisfying the safety condition (4), one may construct a quadratic program (QP):

$$k(x) = \underset{u \in U}{\operatorname{argmin}} \|u - k_d(x)\|^2, \quad \text{s.t.} \quad \dot{h}(x, u) \geq -\alpha(h(x)). \quad (5)$$

Considering a single unbounded input (as in (1) we have $u \in \mathbb{R} \Leftrightarrow \delta_s \in (-\frac{\pi}{2}, \frac{\pi}{2})$), one may obtain an analytical solution to the QP (5) as

$$k(x) = \begin{cases} \min\{k_d(x), k_s(x)\}, & \text{if } \nabla h(x)g(x) < 0, \\ k_d(x), & \text{if } \nabla h(x)g(x) = 0, \\ \max\{k_d(x), k_s(x)\}, & \text{if } \nabla h(x)g(x) > 0, \end{cases} \quad (6)$$

where

$$k_s(x) = -\frac{\nabla h(x)f(x) + \alpha(h(x))}{\nabla h(x)g(x)}. \quad (7)$$

This is often referred to as a safety filter.

3.2 Safe Boundary

In order to define the safe set for the lane-keeping scenario, we start by considering lateral position and yaw angle combinations for which the (bounding box of the) vehicle does not cross the lane boundaries. If we denote the half-width of the lane with y_{\max} and assume that the yaw angle does not exceed $\pm\frac{\pi}{2}$ (i.e., the vehicle is moving to the positive x direction), then the conditions for the front left and front right corners of the bounding box to stay inside the lane are

$$y_R + L \sin \psi \pm \frac{W}{2} \cos \psi \leq \pm y_{\max}, \quad (8)$$

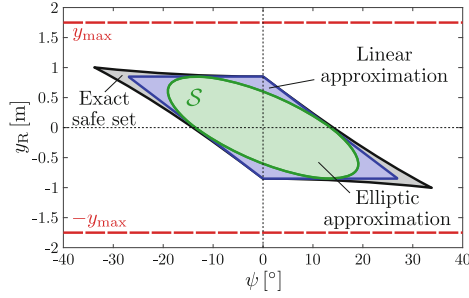


Fig. 2. Safe set in the plane of the yaw angle and lateral position.

where $+y_{\max}$ denotes the y coordinate of the left boundary of the lane, while $-y_{\max}$ corresponds to the right boundary of the lane. Similarly, the rear left and rear right corners of the bounding box stay inside the lane if

$$y_R \pm \frac{W}{2} \cos \psi \leq \pm y_{\max}. \tag{9}$$

We remark that for the kinematic bicycle model (1) without rear overhang, if the vehicle starts within the lane boundaries, then the condition (9) can only be violated after the condition (8) has already been violated. Nevertheless, (9) is still important to ensure that initially the vehicle is located between the lane boundaries. The contour lines corresponding to the four corners of the bounding box touching the lane boundaries are plotted in black in Fig. 2 and the safe set is the area encapsulated by these curves.

However, the non-smooth corners of the resulting safe set make it not suitable for direct safety filter design. In order to define a smooth CBF over the safe set, we first linearize the inequalities in (8) and (9) around $\psi = 0$. This way the safe set is approximated with a parallelogram in the phase plane, see the blue parallelogram in Fig. 2. Then we define the safe set to be used for the construction of the safety filter as the largest ellipse that can be inscribed in this parallelogram (shown in green in Fig. 2), resulting in a smooth inner approximation of the exact safe set.

It can be shown that the largest ellipse inscribed in a parallelogram touches the parallelogram at the midpoints of its edges. This ellipse can be written as

$$F(\psi, y_R) = a\psi^2 + b\psi y_R + cy_R^2 + d, \tag{10}$$

where the parameters a, b, c and d are

$$a = -\frac{(W - 2y_{\max})^2}{4}, \quad b = -\frac{(W - 2y_{\max})^2}{2L}, \tag{11}$$

$$c = -\frac{(W - 2y_{\max})^2}{2L^2}, \quad d = \frac{(W - 2y_{\max})^4}{16L^2}. \tag{12}$$

Based on this approximation, the safe set for the design of the safety filter is defined as

$$\mathcal{S} = \{y_R \in \mathbb{R}, \psi \in (-\pi, \pi) : F(\psi, y_R) > 0\}, \tag{13}$$

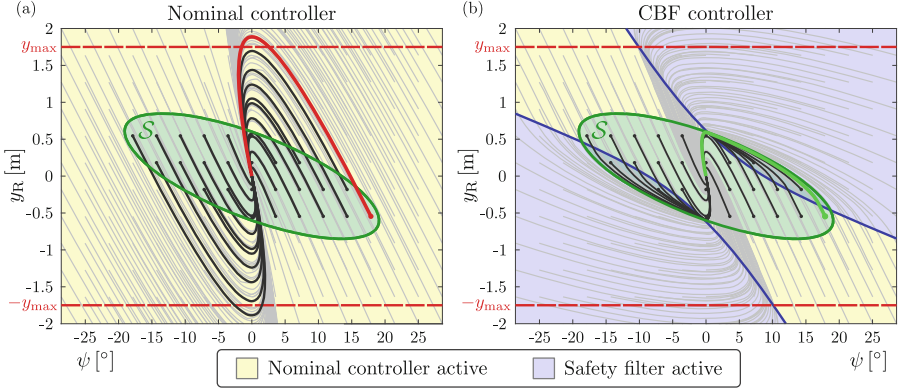


Fig. 3. Phase portraits of the controlled vehicle using (a) the nominal controller without the safety filter and (b) the safety-critical controller.

and the corresponding CBF is

$$h(x) = F(\psi, y_R). \quad (14)$$

Using $h(x)$ in (14) and the linear class- \mathcal{K} function $\alpha(r) = \gamma r$, the safety filter can be calculated according to (7).

4 Results and Discussion

Figure 3 shows multiple trajectories starting from different initial conditions in the (ψ, y_R) plane (without and with the safety filter), for parameter values $l = 2.7$ m, $L = 3.6$ m, $W = 1.8$ m, $y_{\max} = 1.75$ m and $V = 20$ m/s. The control parameters are $P_y = 0.0068$ m⁻¹, $P_\psi = 0.27$ and $\gamma = 5$. Red dashed lines show the lane boundaries, while the safe set \mathcal{S} is bounded by the green ellipse.

It can be seen in Fig. 3(b) that the controller with the safety filter is able to keep the vehicle within the safe set for all initial conditions that are already inside the safe set (see the trajectories in black). In addition, even for the trajectories starting outside of the safe set (colored in gray), the CBF controller greatly reduces the lateral displacement of the vehicle across the lane boundaries. The blue curves in Fig. 3(b) show the switching boundaries, where the controller switches over to the safety filter according to (6). It can be seen that using the selected control gains, the nominal controller in itself is able to keep a large part of the safe set forward invariant and the safety filter is only required near the boundaries of the safe set.

The benefits of the safety filter are further illustrated by the numerical simulations in Fig. 4(a) and (b) (the corresponding red and green trajectories are highlighted in Fig. 3), where the nominal controller in itself violates the safety constraint (panel (a)), while when the safety filter is applied in panel (b), the vehicle is able to return to the center without crossing the lane boundaries.

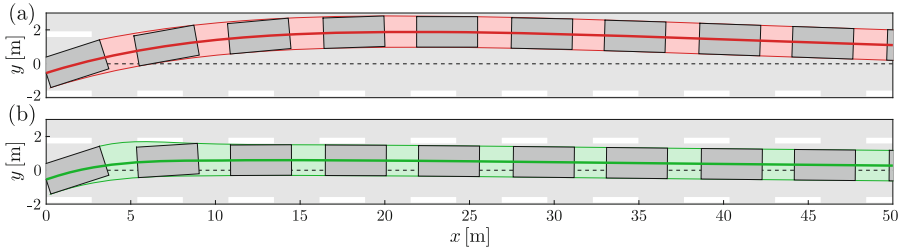


Fig. 4. Numerical simulations (a) without and (b) with the safety filter enabled.

5 Conclusion

A new approach to lane-keeping control by using a safety filter based on control barrier functions was presented to ensure that the vehicle does not cross the lane boundaries. A smooth and continuous CBF was derived using the kinematic bicycle model and the resulting controller was analyzed using numerical simulations and phase portraits. Phase portraits in the plane of the yaw angle and lateral displacement of the vehicle highlighted the improved dynamics of the controlled vehicle even for large initial conditions, thereby ensuring both stability and safety of lane-keeping.

Acknowledgments. The research reported in this paper was partly supported by the János Bolyai Research Scholarship of the Hungarian Academy of Sciences, the National Research, Development and Innovation Office under grant no. NKFI-146201 and 2020-1.2.4-TET-IPARI-2021-00012 and by the Rosztoczy Foundation.

References

1. Wieland, P., Allgöwer, F.: Constructive safety using control barrier functions. *IFAC Proc.* Vol. **40**(12), 462–467 (2007)
2. Ames, A.D., Xu, X., Grizzle, J.W., Tabuada, P.: Control barrier function based quadratic programs for safety critical systems. *IEEE Trans. Autom. Control* **62**(8), 3861–3876 (2017)
3. Ames, A.D., Coogan, S., Egerstedt, M., Notomista, G., Sreenath, K., Tabuada, P.: Control barrier function: theory and applications. In: *18th European Control Conference (ECC)*, pp. 3420–3431. IEEE (2019)
4. Molnár, T.G., Orosz, G., Ames, A.D.: On the safety of connected cruise control: analysis and synthesis with control barrier functions. In: *62th IEEE Conference on Decision and Control*, pp. 1106–1111 (2023)
5. Vörös, I., Orosz, G., Takács, D.: On the global dynamics of path-following control of automated passenger vehicles. *Nonlinear Dyn.* **111**(9), 8235–8252 (2023)

Open Access This chapter is licensed under the terms of the Creative Commons Attribution 4.0 International License (<http://creativecommons.org/licenses/by/4.0/>), which permits use, sharing, adaptation, distribution and reproduction in any medium or format, as long as you give appropriate credit to the original author(s) and the source, provide a link to the Creative Commons license and indicate if changes were made.

The images or other third party material in this chapter are included in the chapter's Creative Commons license, unless indicated otherwise in a credit line to the material. If material is not included in the chapter's Creative Commons license and your intended use is not permitted by statutory regulation or exceeds the permitted use, you will need to obtain permission directly from the copyright holder.





Neural Network Tire Force Modeling for Automated Drifting

Nicholas Drake Broadbent^(✉), Trey Weber, Daiki Mori,
and J. Christian Gerdes

Stanford University, Stanford, CA 94305, USA
{ndbroadb, tpweber, dmori, gerdes}@stanford.edu

Abstract. Automated drifting presents a challenge problem for vehicle control, requiring models and control algorithms that can precisely handle nonlinear, coupled tire forces at the friction limits. We present a neural network architecture for predicting front tire lateral force as a drop-in replacement for physics-based approaches. With a full-scale automated vehicle purpose-built for the drifting application, we deploy these models in a nonlinear model predictive controller tuned for tracking a reference drifting trajectory, for direct comparisons of model performance. The neural network tire model exhibits significantly improved path tracking performance over the brush tire model in cases where front-axle braking force is applied, suggesting the neural network’s ability to express previously unmodeled, latent dynamics in the drifting condition.

Keywords: Machine Learning · Tire Modeling · Autonomous Driving

1 Introduction

The maneuvering capability of a vehicle is fundamentally limited by the friction between the tires and the road. Vehicle operation at the friction limits may require large lateral and longitudinal tire slip, a regime that can be difficult to model accurately in the presence of parameter variation [1]. This is due in part to the many empirically defined characteristics of tire material composition (e.g. coefficient of friction between tire and road, cornering stiffness of the tire, thermal properties) and the geometry of tire and suspension subassemblies (e.g. camber, caster, and toe angles) that can significantly impact the overall vehicle dynamics [2]. The resulting force and moment computations of physics-based models are sensitive to the precise representation of these dynamic characteristics, particularly when operating in coupled slip regions at the limits of handling [1].

Recently, autonomous racing and drifting have emerged as challenge problems for demonstrating precise vehicle control at the friction limits. While interesting problems on their own, the insights gained from automated racing and drifting also lay the foundation for future automated systems that could improve safety. To succeed, controllers must reliably control tire forces in these nonlinear, coupled slip regions. Autonomous drifting, in particular, poses challenges as the tires are not only operating in these coupled slip regions but also heating and disintegrating over the course of the test [3].

Many examples in the literature have shown that an autonomous vehicle, with thoughtful modeling and control design, can drift. Velenis was one of the first to develop a controller for automated drifting, stabilizing the vehicle around an unstable cornering equilibrium with a large sideslip angle [4]. Subsequent control approaches by other authors have extended this result to path tracking and, with the use of front axle braking, simultaneous velocity control, demonstrated on full scale test vehicles [5]. The success of these approaches, applied to a variety of autonomous drifting problems, suggest that automated vehicles could harness these dynamics for greatly increased maneuverability.

Perhaps surprisingly, front axle braking while drifting poses an even more difficult modeling problem than the rear axle. Unlike the rear tires, the front tires are not always saturated and the tires are not coupled through a locked differential. Front suspension geometry while drifting with large steering angles further complicates modeling the coupled front tire forces. This is particularly true with dedicated drifting vehicles such as Takumi, our automated 2019 Toyota Supra built to Formula Drift specifications. Takumi features a custom front wheel alignment designed for high-performance drifting ($-7 \pm 0.3^\circ$ camber and $6 \pm 0.3^\circ$ caster at 0° steering angle). This setup creates effects in the coupled slip behavior that can be difficult to model, since the tire contact patch changes size and location based on steering angle.

Artificial intelligence offers a chance to address some of these challenges. Djeumou *et al.* developed front and rear tire force models for drifting using neural ordinary differential equations and neural-ExpTanh parameterization, ensuring physical accuracy by constraining predictions to a family of solutions and capturing higher-order effects from vehicle data. Compared to a nonlinear model predictive controller using the Fiala brush tire model, their models significantly improved tracking, smoothed control inputs, and sped up computation time in experiments [6]. Notably, their approach focused on steering and drive torque and did not include the front axle braking necessary for independent speed control. Given the particular challenges with modeling front axle tire force generation under braking, we propose a neural network for predicting front tire lateral force that makes no prior assumptions about the shape of the resulting tire curve (or constraining predictions accordingly), relying exclusively on capturing these dynamics with vehicle data. Comparing the performance to that of the Fiala brush model in an experimental setup similar to that of Djeumou *et al.*, the learning-based model achieved significantly better overall trajectory tracking performance with no increase in computational complexity. Deeper analysis of the results highlights the importance of training data coverage of the state space and potential opportunities for extending this approach to learn higher-order effects.

2 Experimental Setup

2.1 Neural Network Model Development

We structure the input layer of the neural network around the same terms that define lateral tire force generation within the Fiala brush model, as shown in

Fig. 1. We label vehicle states (yaw rate, velocity, and sideslip angle) and control inputs (steering angle and braking force) with raw measurements from the vehicle. The corresponding normal and lateral forces are labeled with estimates provided by an unknown input observer.

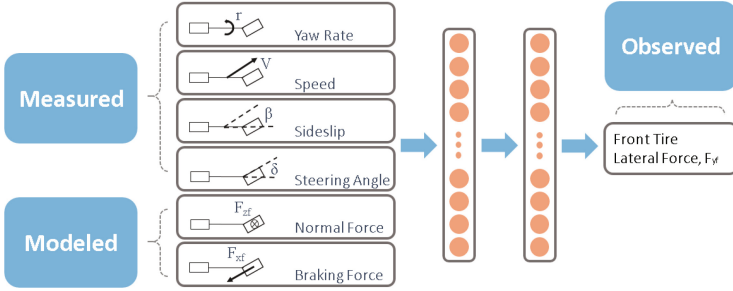


Fig. 1. Neural network architecture for predicting lateral tire force

The data used to train the neural network features a combination of automated and manual drifting, amounting to approximately 30 min recorded up to one month before these comparative experiments took place. One dataset, featuring automated drifting with instances of front axle braking collected the day before these experiments, is held out of the training data in order to iteratively tune the hyperparameters of the model including batch size, training epochs, activation function, and number of hidden elements. The resulting neural network consists of a three-layer feedforward architecture with 8 elements in the first hidden layer, 16 elements in the second hidden layer and tanh activation functions in both hidden layers. While quite small by neural network standards, this model size corresponds to a roughly 35 ms average solve time, approximately equivalent to that of the physics-based tire model used for comparisons. Therefore, a model of this size represents a drop-in replacement for a physical tire model. Training proceeds by cycling through mini-batches of 1000 samples over 1000 epochs, with loss optimization governed by the Adam optimizer and mean squared error loss function.

2.2 Trajectory Generation

The same tire force observer that generates front tire lateral force labels for the neural network training assists in fitting front and rear axle tire parameters. In addition to fully defining the Fiala brush model that served as the point of comparison for these experiments, these tire parameters and the resulting model are used in computing the offline reference trajectory, similar in approach to Weber [7]. This trajectory features a 15m radius circle path with a constant sideslip angle of -40° . By incorporating front axle braking, the target velocity decreases from the equilibrium value without the use of brakes (V_{sol}) with each

revolution of the map (lap 1: $V_{des} = V_{sol}$, lap 2: $V_{des} = 0.95 \cdot V_{sol}$, lap 3: $V_{des} = 0.875 \cdot V_{sol}$), allowing us to compare model performance in the condition of increasing front axle longitudinal force (lap 1: $F_{xf,ref} = 0$ N, lap 2: $F_{xf,ref} = 1000$ N, lap 3: $F_{xf,ref} = 2150$ N).

2.3 Control Architecture

Nonlinear Model Predictive Control (NMPC) can handle multi-input, multi-output systems with nonlinear dynamics and constraints on both states and inputs while predicting future system behavior. These properties are advantageous in trajectory tracking for automated drifting, as exhibited by both Goel and Weber [5, 7]. The implementation of NMPC for these experiments is very similar to that of the latter contribution, with a similar cost function (reformulated as a velocity tracking problem) and slightly different costs. The baseline physics-based MPC incorporates a Fiala brush front tire model. The neural network MPC (NNMPC) features an otherwise identical control framework with the same rear tire model and the learning-based front tire lateral force model as a drop-in replacement for the Fiala brush tire model.

3 Results and Discussion

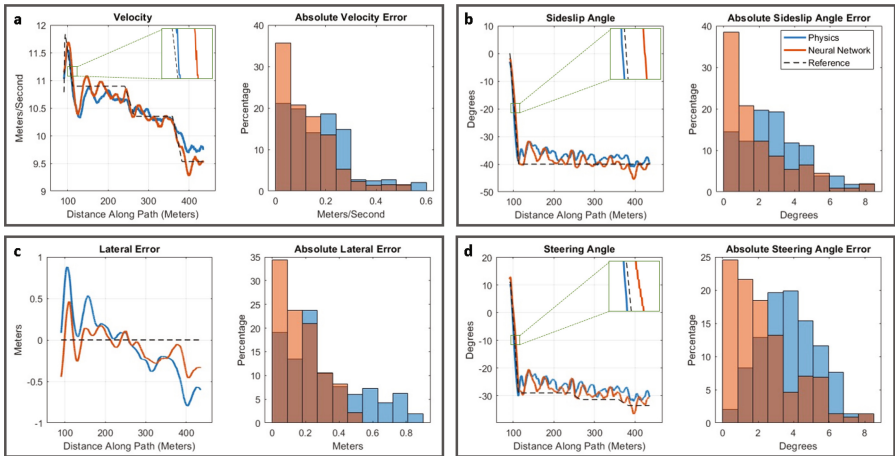


Fig. 2. Tire model comparison of tracking performance under braking

While both controllers slightly undershoot desired velocity after initiation, NNMPC is able to respond to the error more quickly and with less oscillation, as shown in Fig. 2a. This is consistent throughout the run, whereas the physics-based MPC tends to respond to changes in desired speed more slowly,

incurring a higher frequency of large absolute velocity errors in the process. This hesitation persists in sideslip angle tracking as well, where physics-based MPC shows some greater deviation from the desired -40° sideslip while negotiating control in the other states, as shown in Fig. 2b. Conversely, NNMPC is able to more quickly achieve and maintain the desired sideslip angle, leading to higher frequencies of small absolute sideslip angle errors in the process.

NNMPC's trend of high performance in the velocity states translates well to path tracking performance, where it exhibits a relatively low mean and max absolute lateral error, as shown in Fig. 2c. In contrast, the physics-based control appears to cause Takumi to slowly slide out from the desired path as the experiment progresses. This trend is consistent with the fact the tire temperature increases throughout the experiment and proportionally reduces friction, as shown by Kobayashi [3]. Conversely, the neural network-based model does not rely upon explicit tire parameterization for the front axle. The neural network may potentially be underfitting these temperature-dependent friction dynamics by generalizing to tire force generation characteristics that are indicative of a wide range of tire temperatures.

NNMPC's comparatively strong performance trends in both velocity and path state tracking appears to yield an overall reduced steering control effort required to maintain the drift equilibrium throughout the maneuver, as shown in Fig. 2d. However, if we decompose the stages of this experiment further into the drift initiation region ($s = 90.7:112.5$) and steady state equilibrium region ($s = 112.5:435.3$), we gain further insights into the advantages and disadvantages of each respective modeling approach-particularly when we focus into the initiation region dynamics, as shown in the insets of Fig. 2. For example, while it may appear that NNMPC is outperforming physics-based MPC in the initiation region, the mean absolute errors of velocity, sideslip angle, and steering angle are higher with NNMPC than with physics-based MPC-and the percent difference is significant (49%, 31%, and 26%, respectively). This is in stark contrast to the steady state equilibrium region of the experiment, where the mean absolute errors of velocity, sideslip angle, lateral error, and steering angle are lower with NNMPC than with physics-based MPC, where the percent difference is significant once again (41%, 46%, 55%, and 53%, respectively). One explanation for this behavior may be found in the way in which the neural network was trained. Of the approximately 30 min of data used to train the model, less than 5% can be prescribed to the drift initiation region. This imbalance in data representation can potentially lead to a bias toward solely capturing the dynamics of the steady state equilibrium region. Since the gradients calculated from the dominant region will have a greater influence on the network's parameter updates, this can cause the model to prioritize minimizing the loss in the steady state equilibrium region at the expense of capturing the dynamics of the drift initiation region, further exacerbating the imbalance represented in the data.

Another explanation for this behavior may be rooted in how the features and targets were labelled and synchronized. Latencies inherent in observers such as the one used to label tire force targets can cause a temporal misalignment

between the observed states and the actual system states—impairing the neural network’s ability to learn the correct temporal patterns and dynamics of the system. This may be particularly crucial in the drift initiation region, where the vehicle is highly dynamic, undergoing comparatively far greater velocity state derivatives (in yaw rate, velocity, and sideslip angle) than those indicative of the steady state equilibrium region.

4 Conclusion

This investigation presents a novel neural network architecture for predicting front tire lateral forces as a substitute for traditional physics-based models, with a specific focus on autonomous vehicle drifting maneuvers. Through comparative experimentation using a full-scale automated vehicle, we demonstrated that the neural network model significantly enhances path tracking performance, especially under conditions involving front-axle braking forces. The implications of this study are significant for the development of advanced control systems in autonomous vehicles, particularly those designed to operate in extreme conditions. As we continue to build trust and understanding in machine learning techniques, we may be able to achieve higher levels of precision and reliability in vehicle dynamics modeling, paving the way for safer and more efficient autonomous driving technologies.

This research may be extended in several ways to ultimately achieve similar closed-loop performance in trajectories of increasing complexity. Since observer latency and temporal misalignment of labeled data may have been an issue with this approach, we are currently investigating approaches with target labeling that rely solely upon vehicle-collected measurements to potentially eliminate this behavior. Additional performance enhancements can conceivably be obtained with the inclusion of additional relevant states as input to the neural network (e.g. tire temperature, in order to capture temperature-dependent dynamics) or simply expanding the complexity of the network itself as computational limitations allow.

References

1. Svendenius, J.: Tire Modeling and Friction Estimation. Lund University (2007)
2. Pacejka, H.B.: Tire and Vehicle Dynamics, 3rd edn. Butterworth-Heinemann, Heine-
mann (2012)
3. Kobayashi, T., Weber, T.P., Gerdes, J.C.: Trajectory planning using tire thermo-
dynamics for automated drifting. In: IEEE Intelligent Vehicles Symposium (2024)
4. Velenis, E., Katzourakis, D., Frazzoli, E., Tsiotras, P., Happee, R.: Steady-state
drifting stabilization of RWD vehicles. *Control Eng. Pract.* **19**, 1363–1376 (2011)
5. Goel, T.: In Complete Control; Simultaneous Path, Speed, and Sideslip angle Con-
trol of a Drifting Automobile. Stanford University, Stanford, CA (2022)
6. Djeumou, F., Goh, J., Topcu, U., Balachandran, A.: Autonomous drifting with 3
minutes of data via learned tire models. In: ICRA. IEEE, London (2023)
7. Weber, T.P., Gerdes, J.C.: Modeling and control for dynamic drifting trajectories.
IEEE Trans. Intell. Veh. (2023)

Open Access This chapter is licensed under the terms of the Creative Commons Attribution 4.0 International License (<http://creativecommons.org/licenses/by/4.0/>), which permits use, sharing, adaptation, distribution and reproduction in any medium or format, as long as you give appropriate credit to the original author(s) and the source, provide a link to the Creative Commons license and indicate if changes were made.

The images or other third party material in this chapter are included in the chapter's Creative Commons license, unless indicated otherwise in a credit line to the material. If material is not included in the chapter's Creative Commons license and your intended use is not permitted by statutory regulation or exceeds the permitted use, you will need to obtain permission directly from the copyright holder.





Basic Study on the Effect of Driver Condition on Steering Burden

Daigo Uchino¹(✉), Ri Kintou², Ikkei Kobayashi^{3,4}, Jumpei Kuroda^{3,4}, Kazuki Ogawa⁵, Keigo Ikeda⁶, Taro Kato⁷, Ayato Endo⁸, Hideaki Kato⁹, and Takayoshi Narita⁹

¹ Department of Mechanical Engineering, National Institute of Technology, Numazu College, Numazu, Japan

d.uchino@numazu-ct.ac.jp

² Course of Mechanical Engineering, Tokai University, Shibuya, Japan

³ Course of Science and Technology, Tokai University, Shibuya, Japan

⁴ Research Institute of Science and Technology, Tokai University, Shibuya, Japan

⁵ Department of Electronic Robotics, Aichi University of Technology, Gamagori, Japan

⁶ Department of Mechanical Engineering, Hokkaido University of Science, Sapporo, Japan

⁷ Department of Mechanical Engineering, Tokyo University of Technology, Hachioji, Japan

⁸ Department of Electrical Engineering, Fukuoka Institute of Technology, Fukuoka, Japan

⁹ Department of Mechanical System Engineering, Tokai University, Shibuya, Japan

Abstract. With the widespread use of steer-by-wire in automobiles, research is being conducted on high steering gear ratio systems that reduce the burden on the driver, which enables steering with high sensitivity. However, this decreases the resolution during steering and worsens operability, making steering operation more difficult. In addition, if the amount of steering operation and the magnitude of steering reaction torque are not appropriate for the driver, it may cause operation errors. In a highly sensitive steering system, a small change in steering reaction torque has a large potential to affect the driver. The driver's steering burden varies depending on conditions, so it is not always possible to reduce the steering burden. Therefore, we evaluated the driver's steering burden on different days and examined the effect of steering reaction force torque on the steering burden. The results confirmed that the deviation of the burden increases as the load increases.

Keywords: Steer-by-wire System · High Gear Steering Ratio · Steering Operation · Steering Burden · Surface Electromyogram · Steering Burden Evaluation

1 Introduction

Recent advances in automotive electronic control technology have led to the use of steer-by-wire systems in steering systems. Using a steer-by-wire system makes it possible to control the steering gear ratio [1]. Therefore, by setting the steering gear ratio to a high gear, it is possible to reduce the steering burden. However, the resolution of a steer-by-wire system with a high gear ratio is reduced, and there is concern that the system's

operability will deteriorate. Previously, it has been shown that if the torque is too heavy, it causes a physical burden, whereas if it is too light, it causes driving difficulties [2]. Therefore, there is also concern that inappropriate steering reaction torque may cause operating errors.

This research aims to construct a system to control steering reaction torque by evaluating parameters for each driver. However, the position of a human driving a car varies according to the physique of the upper limb in terms of joint angle, position, arm length, etc., and the moment generated at the shoulder joint differs from person to person. However, the position of a human driving a car varies according to the physique of the upper limb in terms of joint angle, position, arm length, etc., and the moment generated at the shoulder joint differs from person to person. This study proposes a load experiment in which drivers with different upper limb physiques can produce the same load at the shoulder joint. In this experiment, we confirmed that we have sufficiently replicated the burden of the steering operation.

With a high steering gear ratio, it is assumed that small driver inputs have a greater impact on the vehicle compared to a standard steering system. Therefore, the driver's condition is a concern regarding its effects on the vehicle. To address this, we will conduct load experiments to examine how the shoulder joint's burden varies daily.

2 Estimation of Steering Burden Using an Upper Limb Burden Model

2.1 Calculation of Shoulder Joint Moments Using the Upper Limb Burden Model

First, using Simscape, an analysis software by MathWorks, we created an upper limb burden model that reflects the driver's upper limb physique and replicates the steering operation (Fig. 1). Previous studies have demonstrated this model to replicate steering burden sufficiently [3, 4].

The x -axis is defined as the direction perpendicular to the vehicle's forward direction, the y -axis as the vehicle's forward direction, and the z -axis as the vehicle's vertical direction. The shoulder joint is denoted as the origin O, the elbow joint as Q, and the position where the steering wheel is grasped as P. A ball joint is used at the shoulder joint O and the gripping position P of the steering wheel, while a rotational joint is used at the elbow joint Q. The moments M_x , M_y , and M_z around the x , y , and z axes, respectively, at the shoulder joint O on the steering side, when the steering reaction force due to the steering torque applied to the steering wheel is applied at the gripping position P, with the weight of the lower arm and upper arm acting at the centers of mass R and S, respectively, were calculated using Eq. (1). The moments M_x , M_y , and M_z at the shoulder joint O, as shown in Fig. 1, are the moments occurring around the x , y , and z axes of the shoulder joint O in the upper limb load model. These represent the shoulder joint moments generated around the x -axis, y -axis, and z -axis, respectively.

$$M_x = y_P \cdot F_z + y_R \cdot m_1 g + y_S \cdot m_2 g \quad (1)$$

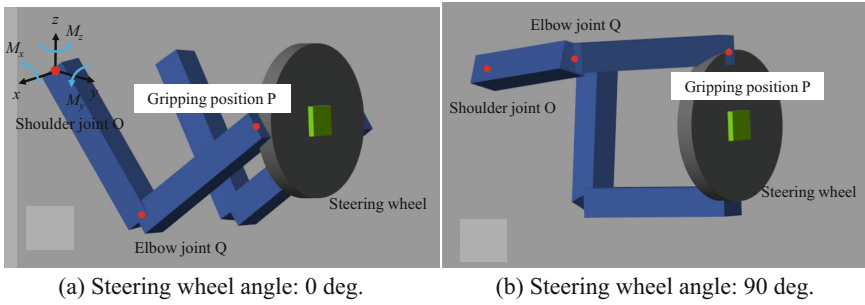


Fig. 1. A Simscape-created upper limb burden model.

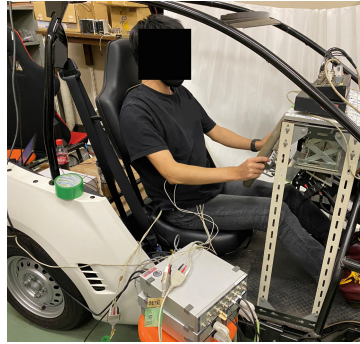


Fig. 2. Appearance of steering experiment in ultra-compact EV.

The parameters used in Eq. (1) is shown below. y_P : y -coordinate of the steering wheel grip position [m], y_U : y -coordinate of the upper arm's center of mass position [m], y_L : y -coordinate of the lower arm's center of mass position [m], F_z : z -axis component of the steering reaction force torque [N], m_1 : mass of the upper arm [kg], m_2 : mass of the lower arm [kg], g : gravitational acceleration [m/s^2],

2.2 Analysis Condition

In this study, the parameters of a 23-year-old male, as shown in Table 1, were utilized to reproduce the driving position of the experimental participant when riding in the ultra-compact EV (Fig. 2). The steering reaction torque was set to 0, 1.0, 2.0, 3.0, 4.0 [$N \cdot m$]. The steering operation is to turn the steering wheel from 0° to 90° in the left direction. The shoulder joint can evaluate the steering burden in the opposite side of the steering direction [5, 6]. Therefore, the maximum shoulder joint moment on the right side is calculated for each steering reaction torque. Figure 3 shows the shoulder joint moment M_x calculated at each steering reaction torque. The results show that shoulder joint moments occur in the range of 10 ~ 23 [$N \cdot m$].

Table 1. Parameter of a participant.

Length of upper arm [m]	Length of lower arm [m]	Weight of upper arm [kgf]	Weight of lower arm [kgf]
0.344	0.315	2.788	2.788

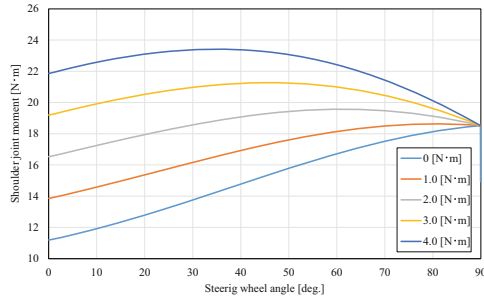
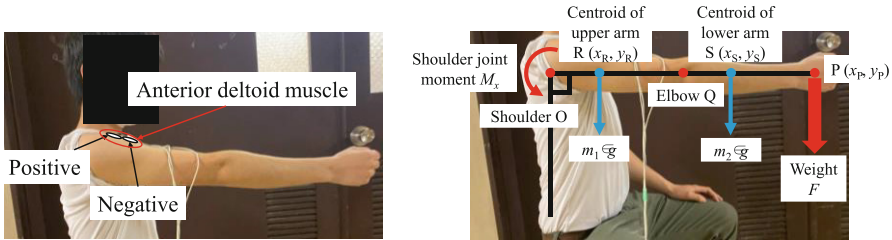


Fig. 3. The Result of the shoulder joint moment in steering operation.



(a) Position of electrodes and anterior deltoid muscle

(b) Appearance of load experiment

Fig. 4. The method of load experiment.

3 Variation in the Amount of Steering Burden Caused by the Driver’s Condition

3.1 Reproduction of Steering Burden by Load Experiment

The load experiment proposed in this paper can be applied mostly to the anterior deltoid muscle. In addition, the muscle activity of the anterior deltoid is known as a muscle that can be used to evaluate steering burden [5, 6]. Surface EMG measures muscle activity. The location of the electrodes for measuring the surface EMG of the anterior deltoid muscle is shown in Fig. 4 (a). The surface EMG was amplified using a Bio Amp ML132 (AD Instruments), passed through an A/D converter PowerLab ML825 2125 (AD Instruments), and recorded at a sampling frequency of 4 kHz. The original measured waveform was smoothed using the root mean square (RMS) every 0.1 s. A comparison of muscle activity between dynamic steering operations and load experiments was conducted as a

preliminary experiment. The results confirm that the burden is matched within 10% of the %MVC of the anterior deltoid muscle.

Table 2. Calculated weight from shoulder joint moment.

Shoulder joint moment [N · m] (Steering operation)	4.45	7.65	10.86	13.94	16.99	19.99	22.99
Weight [kgf] (Load experiment)	-1.02	-0.54	-0.06	0.42	0.90	1.38	1.86

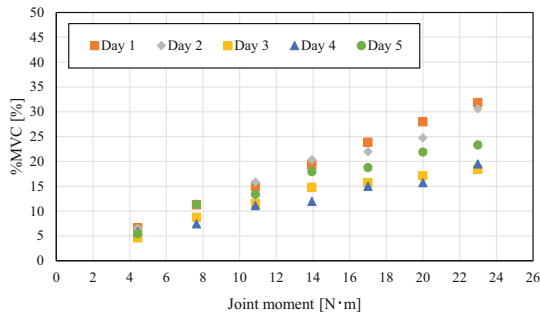


Fig. 5. .

The shoulder joint moment M_x calculated by the upper limb burden model during the steering operation is reproduced in the load experiment. Assuming a load experiment as shown in Fig. 4 (b), the weight is calculated such that the shoulder joint moment during steering can be calculated using Eq. (1). The calculated results are shown in Table 2. The range of shoulder joint moments was also set smaller than the range during steering operation. In addition, a negative weight is when the weight exceeds the arm's weight. Force is applied upward (opposite direction in Fig. 4 (b)).

A load experiment uses weights corresponding to the respective steering reaction torques. Teach the participant to hold the weights and measure the surface EMG potentials for 5 s. This will be done five times for each weight. This experiment was conducted for five consecutive days to evaluate the driver's daily burden. The surface EMG is evaluated using %MVC, expressed as a percentage of the MVC (Maximum Voluntary Contraction) at maximum effort.

3.2 Experiment Result and Consideration

The average daily %MVC measured for 5 s is shown in Fig. 5. As the shoulder joint moment increased, the load on the shoulder joint increased, resulting in a trend toward an increase in %MVC. When the shoulder joint moment was at its lowest, the difference was about 3% on different days. However, the greater the load on the shoulder joint, the greater the difference in %MVC. At 23 [N·m], the difference increased to over 10%. An

increase of 10% in load is equivalent to an increase from 14 [N·m] to 23 [N·m] on Day 1. This difference in shoulder joint moment is equivalent to the load difference when the steering reaction torque in Fig. 3 increases from 1.0 [N·m] to 4.0 [N·m]. Therefore, depending on the driver's condition, the burden due to the steering reaction torque may vary significantly.

4 Conclusion

If drivers are evaluated by their steering operation, the amount of steering burden cannot be normalized for each driver. Therefore, we proposed a load experiment that can normalize the steering burden for each driver. The load experiment subjected drivers to the same steering burden for five consecutive days, and the difference in load increased as the burden increased. A load experiment subjected the driver to the same steering burden for five consecutive days.

As a result, the difference in burden increased as the load increased. The load experiments also revealed that the steering reaction torque is felt very differently by drivers under different conditions. We also showed that the methods in this paper can be used to evaluate the effect of driver condition on the amount of burden.

However, this paper has not been able to address the causes of driver conditions. In the future, we are also going to evaluate the driver's fatigue level at the same time to examine what conditions affect the steering burden.

References

1. Wei, J., Shi, G., Lin, Y.: Design of new variable steering ratio for mechanical active steering system. In: Proceedings of 2013 IEEE International Conference on Vehicular Electronics and Safety (2013)
2. Hiraoka, T., Kumamoto, H.: Effect of steering reactive torque amplitude on state discrimination and driving behavior of Steer-By-Wire vehicle. *Trans. Hum. Interf. Soc.* **12**(2), 187–198 (2010)
3. Uchino, D., et al.: A basic study for active steering wheel system for steering burden evaluation by driving position focus on driver's arm size. *Vehicles* **5**(2), 846–858 (2023)
4. Uchino, D., et al.: Active steering wheel system for ultra-compact mobility vehicles: operability evaluation with steering burden in various drivers. *J. Robot. Mechatron.* **33**(5), 1169–1177 (2021)
5. Umemoto, T., Liu, X., Narita, T., Kato, H., Moriyama, H.: Steer-by-wire system for ultra-compact electric vehicle (fundamental consideration on the burden of the push side upper arm using EMG of anterior deltoid). *J. Japan Soc. Appl. Electromag. Mech.* **25**(2), 155–161 (2017)
6. Yoshida, T., Hase, K., Obinata, G., Hada, M.: Analysis of steering operation using a 3-dimensional musculo-skeletal model of the upper extremities and evaluation about the design parameters of steering wheel. *J. Soc. Biomech.* **34**(1), 41–52 (2010)

Open Access This chapter is licensed under the terms of the Creative Commons Attribution 4.0 International License (<http://creativecommons.org/licenses/by/4.0/>), which permits use, sharing, adaptation, distribution and reproduction in any medium or format, as long as you give appropriate credit to the original author(s) and the source, provide a link to the Creative Commons license and indicate if changes were made.

The images or other third party material in this chapter are included in the chapter's Creative Commons license, unless indicated otherwise in a credit line to the material. If material is not included in the chapter's Creative Commons license and your intended use is not permitted by statutory regulation or exceeds the permitted use, you will need to obtain permission directly from the copyright holder.





YOLOgraphy: Image Processing Based Vehicle Position Recognition

Ákos T. Köpeczi-Bócz^{1(✉)}, Tian Mi², Gábor Orosz^{2,3}, and Dénes Takács^{1,4}

¹ Department of Applied Mechanics, Budapest University of Technology and Economics, Budapest 1111, Hungary
{kopeczi,takacs}@mm.bme.hu

² Department of Mechanical Engineering, University of Michigan, Ann Arbor, MI 48109, USA
{tianm,orosz}@umich.edu

³ Department of Civil and Environmental Engineering, University of Michigan, Ann Arbor, MI 48109, USA

⁴ HUN-REN-BME Dynamics of Machines Research Group, Budapest University of Technology and Economics, Budapest 1111, Hungary

Abstract. A methodology is developed to extract vehicle kinematic information from roadside cameras at an intersection using deep learning. The ground truth data of top view bounding boxes are collected with the help of unmanned aerial vehicles (UAVs). These top view bounding boxes containing vehicle position, size, and orientation information, are converted to the roadside view bounding boxes using homography transformation. The ground truth data and the roadside view images are used to train a modified YOLOv5 neural network, and thus, to learn the homography transformation matrix. The output of the neural network is the vehicle kinematic information, and it can be visualized in both the top view and the roadside view. In our algorithm, the top view images are only used in training, and once the neural network is trained, only the roadside cameras are needed to extract the kinematic information.

Keywords: Image processing · Vehicle dynamics · Machine learning

1 Introduction

The detection of vehicles via real-time image processing is a crucial task not just for autonomous vehicles but also for intersection management systems. However, identifying bounding boxes and extracting vehicle kinematic data (like position, yaw angle, velocity and yaw rate) with satisfying accuracy are challenging problems. In [2], the problem is approached through object detection and post-processing with a trained network. The training data is collected through GPS and LIDAR sensors. As presented in [4], it is also possible to estimate the distance of an object based on the size of the bounding box. Instead of focusing

on object classification and tracking (position and speed), we introduce a novel methodology to extract vehicle kinematic data (position, velocity, orientation and yaw rate) with the help of a neural network trained on high-precision data.

In our experiments, the vehicle kinematic information is collected at an intersection of the Mcity Test Facility at the University of Michigan, Ann Arbor. A DJI Phantom 4 Pro drone is sent above the intersection, and a standing vehicle at the intersection equipped with a camera facing forward serves as the roadside camera. The movement of a truck at the intersection is captured by both the drone camera (top view) and the roadside camera (roadside view). The experimental setup is detailed in [3]. The ground truth data, i.e., the high-precision top view bounding boxes, are obtained by classic image processing algorithms of the drone view recordings, as shown in the top row of Fig. 1.

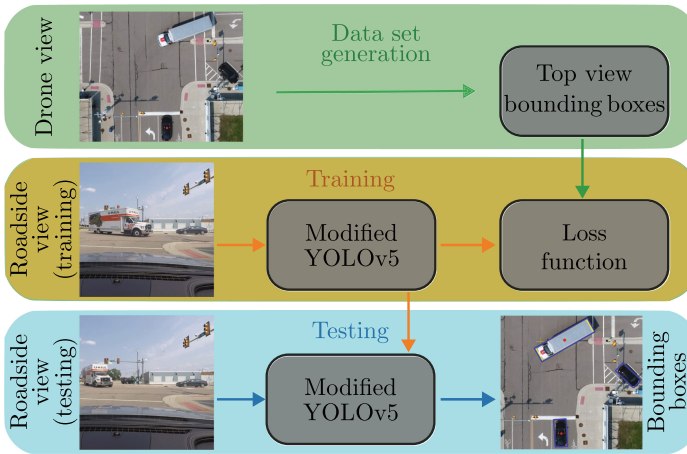


Fig. 1. Main steps of the kinematic data extraction method and the neural network training/testing.

2 Neural Network-Based Kinematic Data Extraction

The YOLOv5 [1] convolutional neural network serves as the basis of the proposed algorithm shown in Fig. 1. The structure of the original YOLOv5 network is modified to incorporate the discrepancy between the input (roadside view images) and the output (top view data), and the optimization method is modified to include kinematic information in the algorithm.

Originally, the YOLO network maps the bounding boxes onto the input image. Our goal, however, is not to obtain the bounding boxes on the roadside image but to reconstruct the top view bounding boxes of the vehicles. The top view perspective can be converted to the roadside view perspective with a homography transformation matrix, which can be obtained by selecting reference points from both perspectives. By decoupling the output space of the YOLOv5



Fig. 2. Sample output grid of the modified YOLOv5 network mapped on the (a) roadside and the (b) top view. The (a) roadside view is the input of the network.

from the input image and mapping the detection results on the top view, the network is trained to learn the homography transform connecting the top view images and roadside view images. We call this modified algorithm *YOLOgraphy*.

The original YOLOv5 output contains the center point, width, and height of the bounding boxes, while the orientation of the detected object is missing. To incorporate this, an additional parameter (representing the yaw angle) is added to the output of YOLOv5, and the loss function is extended with this parameter. Similar to the the original YOLOv5 algorithm, we detect the objects on three different grids (20×20 , 40×40 and 80×80). Depending on the size of the object, the network detects them on different grid layers, larger-sized objects on the coarser grids and smaller objects on the finer grids. A sample grid (6×6) is shown in Fig. 2. For each grid-cell we have the output

$$\mathbf{p} = [p_1 \ b_x \ b_y \ w_x \ w_y \ \varphi]^\top, \tag{1}$$

where $p_1 \in [0, 1]$ is the confidence of an object being present in the given grid-cell, b_x and b_y denote the bounding box center point positions within the cell relative to the top left corner of the grid-cell. For example, $b_x = b_y = 0.5$ represents the centerpoint, while $b_x = b_y = 1$ corresponds to the bottom right corner of the grid-cell. Outputs $w_x \geq 0$ and $w_y \geq 0$ are the width and height of the bounding box as the scaling factors of the anchor box, and $\varphi = \psi/2\pi \in [0, 1]$ is the newly introduced output, the normalized yaw angle of the bounding box (vehicle).

Originally, YOLOv5 used different anchor boxes. In many cases, it is optimal to have horizontal/vertical rectangles and a square as three anchor boxes, for example, vertical for a pedestrian, horizontal for a vehicle, and square for a cyclist in side view. In our solution, the introduction of the yaw angle makes such differentiation of the anchor boxes redundant, namely, horizontal and vertical rectangles can be transformed into each other by a 90-degree rotation. Hence, our algorithm is based on a single anchor box.

The loss function in the YOLOv5 training consists of three main parts: the classification loss (*cls_loss*), the objectness loss (*obj_loss*), and the bounding

box regression loss (*box_loss*). The classification loss corresponds to the classification of the detected objects and is excluded from the study at this stage, although it could be considered in the future. The objectness loss shows the confidence of an object being present in a grid cell and is kept as it is. Lastly, the bounding box regression is modified to include the yaw angle. Originally, the box loss was calculated based on the *Intersection over Union* (IoU) algorithm, which divided the area of the intersection of the predicted and ground truth bounding boxes with the area of the union of the two (IoU is 1 if they overlap perfectly). When the bounding boxes are not aligned horizontally/vertically due to their non-zero yaw angles, the calculation of the intersection of the boxes is a more complex geometric problem. Thus, it may be computationally more efficient to use a simple mean-squared-error-based loss for the regression instead of the IoU. We introduce the weighted sum of *position loss*, *size loss* and the *yaw loss* as

$$loss = obj_loss + \alpha \cdot pos_loss + \beta \cdot size_loss + \gamma \cdot yaw_loss, \quad (2)$$

where α , β and γ are tuneable dimensionless hyperparameters, and are chosen to be 5, 1 and 10, respectively. These hand-tuned parameters and the mean-squared-error-based loss function perform well for the current experiments (see Sect. 3), but may be learned and modified. These results provide a proof of concept that we will extend with additional measurements in the future.

Two recordings (with the corresponding datasets) are used to train the neural networks separately, as the roadside camera has slightly different perspectives in the two cases, yielding different homography transformation matrices. For each dataset, the frames are mixed randomly, with 75% for training, 15% for validation, and 10% for testing. The neck and heads of the upper layer YOLOv5 network are trained, while the main convolutional layers are frozen during the training. This way, the network does not need to learn what a vehicle looks like but only learns how to place it on the top view plane. Overall, the networks perform well even for the test and validation sets, which were not used during training. In Fig. 3, the output of one experiment is visualized both in the roadside view panel (a) and the top view panel (b). The yellow bounding boxes are the ground truth obtained from drone measurements, and the blue bounding boxes are the YOLOgraphy output. The trajectory of the center point of the bounding box is shown in panel (c). The blue curve (network prediction) and the yellow curve (ground truth) have good agreement, which validates our approach.

3 Data Analysis

We compare the results of the trained YOLOgraphy output with the drone measurements (ground truth). The positions of one experiment are shown in Fig. 4(a), where the blue dashed line is the YOLOgraphy output, and the orange solid line is the ground truth. The two curves overlap with minimal difference throughout the whole measurement. Note that the visualization includes all the training, validation, and test frames. The yaw angles are compared in Fig. 4(b). While the two curves have good agreement, the YOLOgraphy output looks more

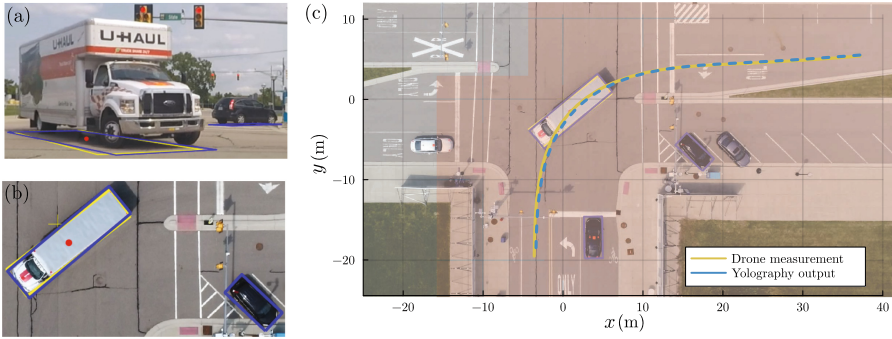


Fig. 3. YOLOgraphy output and its comparison with ground truth data: (a) roadside view, (b) top view, (c) trajectories.

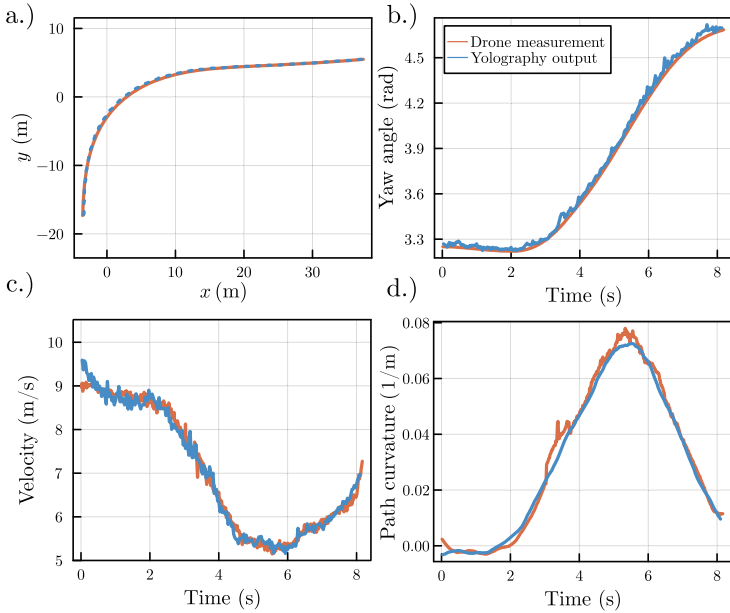


Fig. 4. Comparison of the drone measurements (ground truth) and the output of the trained Yolo network. (a) Trajectories, (b) yaw angles, (c) longitudinal velocities and (d) path curvatures for the rear axle center point (RAC).

noisy. This suggests that the YOLOgraphy struggles more with the prediction of the yaw angle, which is expected since it is a challenging task to predict the yaw angle based on the roadside view (cf. Fig. 2 and Fig. 3(a)).

In Fig. 4(c), the speed of the rear axle center (RAC) point is plotted, and since the RAC’s velocity aligns with the yaw angle, this is referred to as longitudinal velocity. Between 5 and 6 s, the velocity hits the minimum, which is at the apex

of the turning. The velocity of the drone measurement and the YOLOgraphy output show a good agreement. Since we calculate these values with the method of finite differences, it is expected to amplify the noise.

In Fig. 4(d), the curvature of the rear axle center (RAC) is shown. Assuming that the RAC's heading angle is close to the yaw angle, the curvature is calculated from the yaw angle as $\kappa = \frac{\Delta\psi}{\Delta s}$ where $\Delta\psi$ is the change in the yaw angle between two adjacent frames, and Δs is the distance between two positions. To smooth the data, a Savitzky-Golay filter is applied. The curvature from YOLOgraphy is (somewhat surprisingly) smoother compared to the drone measurement.

4 Conclusion and Discussion

This work provides a proof of concept of YOLOgraphy, based on a modified YOLOv5 neural network. The roadside view images are mapped to the top view, and the neural network essentially learns the transformation during training. After training, YOLOgraphy can take the images from a roadside camera as input and output the kinematic data of vehicles on the top view plane. The validation results demonstrate the feasibility of the proposed method.

As future work, we plan to extend the dataset by additional measurements using a fixed-location roadside cameras. With the roadside view angle being more steep, the robustness of the detection can be potentially increased. Generally, the higher the camera is positioned, the easier it is to detect the vehicle. We may face a potential challenge that a large vehicle close to the roadside camera may obstruct its view. To overcome this issue, we plan to include input images from multiple roadside cameras from different angles. We also plan to introduce kinematic vehicle models to filter the results and predict vehicle trajectories.

Acknowledgments. The research reported in this paper was supported by the János Bolyai Research Scholarship of the Hungarian Academy of Sciences, the National Research, Development and Innovation Office under grant no. NKFI-146201, and the University of Michigan's Center for Connected and Automated Transportation through the US DOT grant 69A3552348305. The project supported by the Doctoral Excellence Fellowship Programme (DCEP) is funded by the National Research Development and Innovation Fund of the Ministry of Culture and Innovation and the Budapest University of Technology and Economics, under a grant agreement with the National Research, Development and Innovation Office. The research is partly supported by the Foundation for Mechanical Engineering Education.

References

1. Jocher, G.: YOLOv5 repository. Software. <https://github.com/ultralytics/yolov5>
2. Fang, L., Malm, O., Wu, Y., Xiao, T., Zhao, M.: Using machine learning to estimate road-user kinematics from video data. Project report, Chalmers University of Technology (2024)
3. Mi, T., Takács, D., Liu, H., Orosz, G.: Capturing the true bounding boxes: vehicle kinematic data extraction using unmanned aerial vehicles. *J. Intell. Transport. Syst.* 1–13 (2024)

4. Xu, X., Chen, X., Wu, B., Wang, Z., Zhen, J.: Exploiting high-fidelity kinematic information from port surveillance videos via a YOLO-based framework. *Ocean Coastal Manag.* **222**, 106117 (2022)

Open Access This chapter is licensed under the terms of the Creative Commons Attribution 4.0 International License (<http://creativecommons.org/licenses/by/4.0/>), which permits use, sharing, adaptation, distribution and reproduction in any medium or format, as long as you give appropriate credit to the original author(s) and the source, provide a link to the Creative Commons license and indicate if changes were made.

The images or other third party material in this chapter are included in the chapter's Creative Commons license, unless indicated otherwise in a credit line to the material. If material is not included in the chapter's Creative Commons license and your intended use is not permitted by statutory regulation or exceeds the permitted use, you will need to obtain permission directly from the copyright holder.





Surrogate Modeling of Suspensions with High Stiffness Element for Real-Time Analysis Using Machine Learning

Tojuro Hiraga^(✉) and Taichi Shiiba

Department of Mechanical Engineering, Meiji University, 1-1-1 Higashi-Mita, Tama-Ku,
Kawasaki 214-8571, Japan

{ce232084, shiiba}@meiji.ac.jp

Abstract. The aim of this study is to generate a surrogate model of a suspension system with high stiffness elements for real-time analysis using machine learning. A Long Short-Term Memory networks was used as a machine learning method to generate surrogate models for three-degree-of-freedom quarter car model with a bush element. To evaluate the performance of the machine learning models, the simulation results and computation time were compared with the 3DOF model. As a result, it was confirmed that the response of the body acceleration was predicted with good accuracy by predicting the bush deformation and calculating the body acceleration based on the prediction results, instead of predicting the body acceleration directly. It was also confirmed that the machine learning model can accurately predict the body acceleration in less calculation time than the original model.

Keywords: Vehicle Dynamics · Suspension · Machine Learning · Surrogate Model · Long Short-Term Memory · Real-Time Calculation

1 Introduction

Rubber bushes in suspension systems are used to absorb vibrations from the road surface and improve the ride comfort of the vehicle. In addition, the deformation of rubber bushes changes the wheel alignment, which also affects the handling characteristics. Thus, it is important to consider the characteristics of rubber bushes in the analysis of a suspension system. Since rubber bushes have high stiffness, a numerical analysis of a suspension system which considers the effect of rubber bushes requires a small step size [1]. This increases the computational costs, making it difficult to apply the suspension model to real-time analysis such as driving simulators. Therefore, the aim of this study is to generate a surrogate model of a suspension system with high stiffness elements for real-time analysis using machine learning. The Long Short-Term Memory Network (LSTM) was used as the machine learning method because it is capable of long-term time series prediction [2]. The response and computational time of the LSTM suspension model were evaluated by comparison with those of the quarter car model with a bushing element.

© The Author(s) 2024

G. Mastinu et al. (Eds.): AVEC 2024, LNME, pp. 399–405, 2024.

https://doi.org/10.1007/978-3-031-70392-8_57

Table 1. Model Parameters

Parameters	Value
m_1	30 kg
m_2	300 kg
k_1	1.8e5 N/m
k_2	3.0e4 N/m
c_2	2.5e3 Ns/m
m_b	2.0 kg
k_b	2.0e6 N/m
c_b	1.0 e4 Ns/m

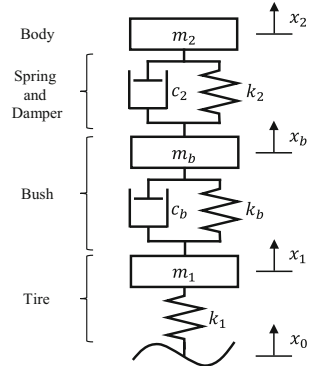


Fig. 1. 3 DOF quarter car model

2 Analysis Using Suspension Models with High Stiffness Elements

In this study, a three-degree-of-freedom quarter car model with a bush in the lower part of damper shown in Fig. 1 was created to evaluate the effect of the bush on ride comfort. The model parameters are shown in Table 1. The parameters were determined based on actual automobiles. Equations (1), (2) and (3) define the equations of motion for the quarter car model.

$$m_1 \ddot{x}_1 = k_b(x_b - x_1) + c_b(\dot{x}_b - \dot{x}_1) - k_1(x_1 - x_0) \tag{1}$$

$$m_b \ddot{x}_b = k_2(x_2 - x_b) + c_2(\dot{x}_2 - \dot{x}_b) - k_b(x_b - x_1) - c_b(\dot{x}_b - \dot{x}_1) \tag{2}$$

$$m_2 \ddot{x}_2 = -k_2(x_2 - x_b) - c_2(\dot{x}_2 - \dot{x}_b) \tag{3}$$

The quarter car model was subjected to the road surface displacement shown in Fig. 2a to examine the response of body acceleration when the stiffness values of the bush was changed. Figure 2b shows the body acceleration during the simulation, and Fig. 2c shows the deformation of the bush. It was confirmed that the peak value of the body acceleration increases as the bushing stiffness increases, while the deformation of the bush became smaller.

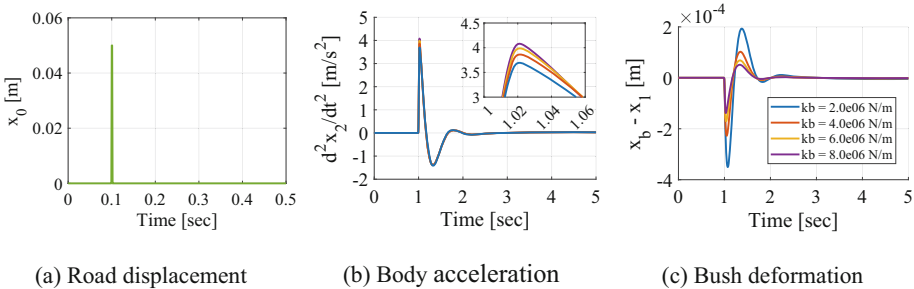


Fig. 2. Simulation results of the bump run using the 3DOF model

3 Procedure for Generating Surrogate Model

3.1 Construction of Surrogate Models

The objective of this study is to develop a surrogate model that can predict body acceleration, when the stiffness values of the bush was changed. A similar approach was taken in reference [3], but this study examined three different surrogate modeling methods as shown in Table 2. The machine learning model 1 predicts the body acceleration for the road surface inputs. On the other hand, the machine learning model 2 and model 3 predict the response of the bush for the displacement of the unsprung mass. The response of the body acceleration was calculated based on the machine learning prediction results and Eq. (3). Equation (2) that defines the equations of motion for the bush has a high natural frequency, which increases the calculation time of the system. Machine learning models 2 and 3 were examined to replace equations with a large computational load. The model 2 predicts the displacement and velocity of the bush, the model 3 predicts the bush deformation and bush deformation rate. The response of the body acceleration is influenced by various forces such as those from the spring, damper, and bush. The changes caused by the effect of the bush on body acceleration are small as shown in Fig. 2b, so it is difficult to predict the body acceleration directly with machine learning. It is expected to predict the changes in body acceleration caused by the bush with good accuracy by predicting bushing deformation and using the equations of motion to calculate body acceleration.

Table 2. Surrogate Model inputs and outputs

	Input	Output
ML 1	road surface displacement x_0	body acceleration \ddot{x}_2
ML 2	displacement of the unsprung mass x_1	displacement of the bush x_b velocity of the bush \dot{x}_b
ML 3	displacement of the unsprung mass x_1	bush deformation $x_b - x_1$ bush deformation rate $\dot{x}_b - \dot{x}_1$

3.2 Machine Learning Method

The long short-term memory network (LSTM) was used as the machine learning method, which can learn long time series data and ensure long-term dependability. Figure 3 shows the relationship between hyperparameter settings and performance in the machine learning model 3. The root mean squared error (RMSE) was used as the metric for prediction accuracy. Figure 3 shows that the machine learning model with a large number of units and layers makes more accurate predictions, but it also takes more computation time. The number of hidden layers was set to 2 and the number of units to 40 in each layer from the perspectives of the computation time and the accuracy. The other hyperparameters are shown in Table 3.

Table 3. Hyperparameters setting

Parameters	Value
<i>Number of Units</i>	40
<i>Number of Layers</i>	2
<i>Initial Learning Rate</i>	0.001
<i>Batch Size</i>	2 ⁵
<i>Sequence Length</i>	500
<i>Optimizer</i>	Adam
<i>State Activation Function</i>	tanh
<i>Gate Activation Function</i>	sigmoid

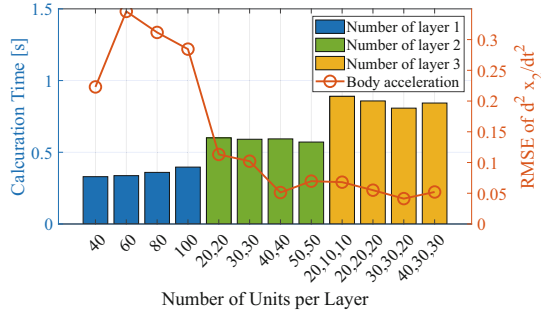
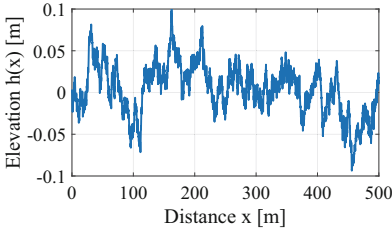


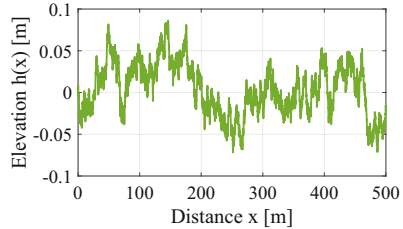
Fig. 3. Calculation time and RMSE with hyperparameters

3.3 Preparation of Road Surface Input Data

Two types of random road profiles were generated according to the ISO 8608 standard as shown in Fig. 4. Figure 4a shows the road surface for machine learning training, and Fig. 4b shows the road surface used to obtain predict data. Simulations were conducted on a quarter-car model, assuming a speed of 60 km/h on these road surfaces. The simulation results were used as training and predict data for machine learning.



(a) Road surface used for training data



(b) Road surface used for test data

Fig. 4. Road surface profile used for simulations

4 Surrogate Modeling and Accuracy Validation

Figure 5a shows the calculated body acceleration for machine learning models, and Fig. 5b shows its power spectral density (PSD). The hyperparameters of each machine learning model were set to the values shown in Table 3 to align the conditions. Figure 5b shows that the machine learning model 1 has a lower PSD than the quarter car model above 100 Hz, while the machine learning model 3 maintains good accuracy in predicting

body acceleration up to 200 Hz. Figure 6 shows the ratio of the maximum body acceleration predicted by each machine learning model to that of the quarter car model for different bushing parameters. It was confirmed that calculating body acceleration based on the model 3, which predicts bushing deformation, is more accurate than predicting vehicle body acceleration based on the model 1.

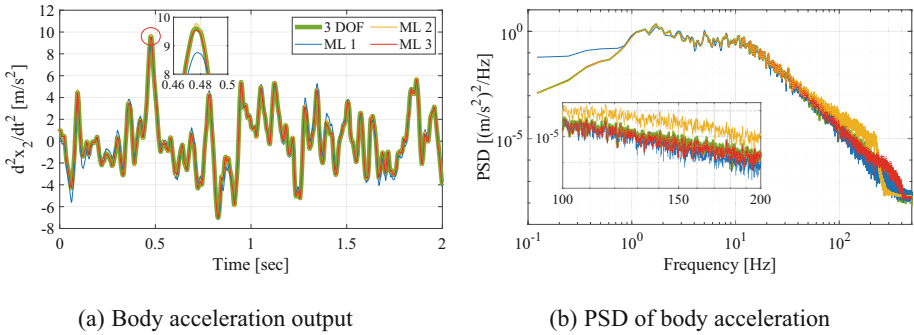


Fig. 5. Output data used for machine learning test data

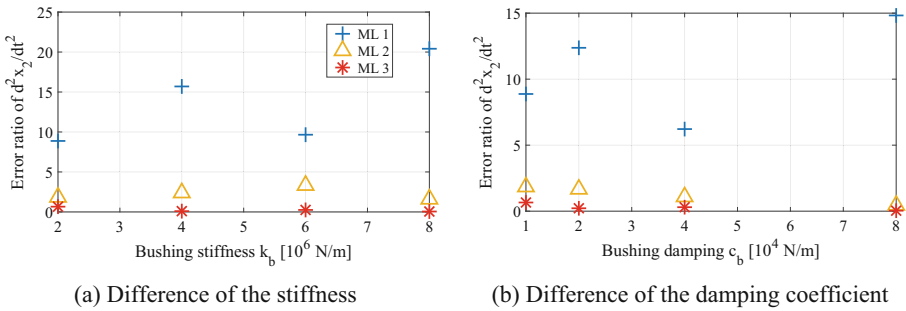


Fig. 6. Error ratio of the body acceleration for different bush parameter

In addition, the computational time for the quarter car model and machine learning model 3 were evaluated on the MATLAB environment on Windows 11. Both analyses were performed with the fixed-time step solver ode4 (Runge-Kutta). Figure 7 shows the RMSE calculated for each time step solution against the solution with a time step of $10e-8$ s. RMSE of the body acceleration increases with a large step time setting, and eventually the solution will diverge. If the stiffness of the bushing is constant at $k_b = 2.0e6$ N/m, the time step at which the solution diverges depends on the damping coefficient. On the other hand, the machine learning model was stable, meaning that the time step of this model can be adjusted according to the purpose. In this study, the machine learning model was set up with three different time steps of 0.1 ms, 1 ms, and 10 ms. Table 4 shows the computation time for a 5-s simulation for each model. These results show that even with large time steps, the predictions of the machine learning model were accurate and computationally fast. In particular, when the time step was

1 ms or 10 ms, the machine learning model was able to compute faster compared to the quarter-car model calculated at the maximum time step that can be analyzed with the settings in Table 1. Thus, for real-time analysis, the machine learning model with prediction accuracy has an advantage over quarter car model in terms of computational time.

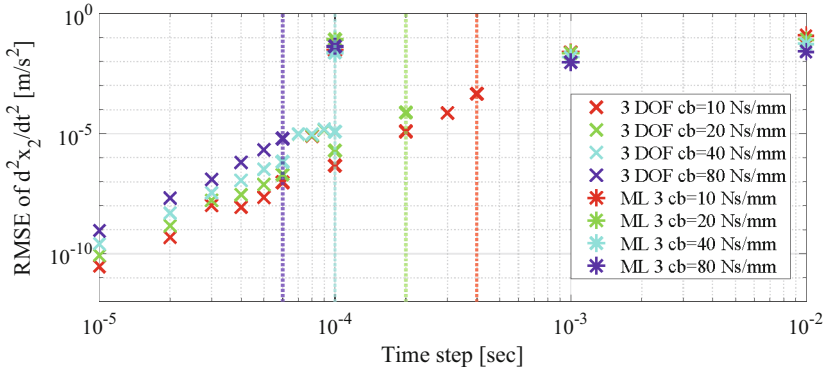


Fig. 7. RMSE of the body acceleration when the time step is changed

Table 4. Calculation time and accuracy for each model

	3 DOF model	LSTM model		
Step size (ms)	0.4	0.1	1	10
Calculation time (s)	1.44	3.51	0.59	0.04

5 Conclusion

In this study, the surrogate modeling methods of a suspension system with high stiffness elements using machine learning was investigated. It was confirmed that the response of the body acceleration changed depending on the stiffness and damping characteristics of the bush with a three-degree-of-freedom quarter car model with a bush element. Three surrogate modeling methods were examined to predict body acceleration. As a result, it was confirmed that the response of the body acceleration was predicted with good accuracy by predicting the bush deformation and calculating the body acceleration based on the prediction results, instead of predicting the body acceleration. It was also found that the machine learning model was stable and had an advantage over the quarter car model in terms of computation time.

References

- Kim, S.S., Jeong, W.H.: Real-time multibody vehicle model with bush compliance effect using quasi-static analysis for HILS. *Multibody Sys.Dyn.* **22**, 367–382 (2009)

2. Ono, T., Eto, R., Yamakawa, J.: Forecasting vehicle accelerations using LSTM. Mech. Eng. J. ID 21-00045 (2021)
3. Guarneri, P., Rocca, G., Gobbi, M.: A Neural-Network-Based Model for the Dynamic Simulation of the Tire/Suspension System While Traversing Road Irregularities. IEEE Trans. Neural Netw. **19**(9), 1549–1563 (2008)



Open Access This chapter is licensed under the terms of the Creative Commons Attribution 4.0 International License (<http://creativecommons.org/licenses/by/4.0/>), which permits use, sharing, adaptation, distribution and reproduction in any medium or format, as long as you give appropriate credit to the original author(s) and the source, provide a link to the Creative Commons license and indicate if changes were made.

The images or other third party material in this chapter are included in the chapter's Creative Commons license, unless indicated otherwise in a credit line to the material. If material is not included in the chapter's Creative Commons license and your intended use is not permitted by statutory regulation or exceeds the permitted use, you will need to obtain permission directly from the copyright holder.





Data-Driven Risk Assessment with Scenario Classification for Collision Avoidance in Left/Right Turn Across Path Conflicts

Wei Wang¹(✉) , Pongsathorn Raksincharoensak¹ , and Roman Henze²

¹ Department of Mechanical Systems Engineering, Tokyo University of Agriculture and Technology, Tokyo 184-8588, Japan

weiwang@go.tuat.ac.jp, pong@cc.tuat.ac.jp

² Technical University of Braunschweig, Braunschweig, Germany
r.henze@tu-braunschweig.de

Abstract. Traffic safety is one of the vital issues in developing autonomous and assisted driving systems. To achieve higher level of driving automation, it becomes necessary to have a reliable Risk Assessment (RA) method that not only responds to current traffic conditions but also anticipates future scenario propagation. Regardless of the driver intentions, traditional deterministic risk indicators like Time-To-Collision (TTC) have proven effective but fall short in addressing the inherent uncertainty in future propagation, especially under conflict scenarios influenced by interdependent decisions of traffic participants. Acceleration for Collision Avoidance (ACA) emerges as a flexible risk criterion adaptable to different collision-avoidance maneuvers. Focusing on the Left/Right Turn across path conflicts, this work aims to propose an innovative surrogate risk indicator for collision avoidance with the combination of ACA criteria and scenario classification using Hidden Markov Models (HMM). Based on a near-miss video database, we further train and evaluate the presented model, supplying interpretability and adaptability of risk assessment in complex conflict scenarios.

Keywords: Advanced driver assistance systems · Collision avoidance · Risk assessment · Surrogate safety indicator · Near-miss database · Hidden Markov Model

1 Research Background

In the development of future autonomous and advanced driver assistant systems (ADAS), a key technology is a reliable risk assessment method, which should not only react according to the current traffic states but also predict their future evolution to make appropriate actions.

The deterministic methods usually integrate the simple vehicle model like the constant yaw rate and acceleration (CYRA) with quantitative index like the Time-To-X metrics (such as the Time-To-Collision), Post-encroachment time,

and responsibility-sensitive safety (RSS). These common measures of the collision risk are proven to be effective in evaluating the severity of conflicts. However, the deterministic computation methods are inherently unable to reflect the uncertainty of future traffic evolution. To overcome this limitation, probabilistic inference methods such as Hidden Markov Model (HMM), Dynamic Bayesian Networks (DBN), Support Vector Machines (SVM), Recurrent Neural Network (RNN, include LSTM) are evaluated to be powerful in intention inference or direct trajectory prediction.

For the risk assessment problem in conflicts, the decision making of traffic participants are influenced by each other, resulting in different near-collision scenarios. Therefore, single deterministic matrix usually failed to reflect the actual severity. Recently, the concept of Acceleration for Collision Avoidance (ACA) appears as a more flexible risk criterion that can adaptive to various collision avoidance maneuvers. In this work, we focus on the Left/Right Turn Across Path (TAP) scenarios and combine the ACA criteria with the scenario classification based on HMM to propose a new surrogate indicator, which will be verified using a near-miss video database [1].

2 ACA Indicators in Left/Right Turn Across Path Conflicts

Figure 1 illustrates the potential ACA risk indicators in the Left/Right turn across path dilemma which can be divided into two scenarios. In scenario I, the ego vehicle passes the interaction before the turning vehicle entering the conflict area, following the driving intention of the ego vehicle driver. In scenario II, the ego vehicle lets the turning vehicle pass first and carried out a waiting maneuver, which would lead the vehicle to a complete stop or a relatively slow speed due to the driver braking maneuver. The calculation of proposed risk indicators based on the real-time measurements are expressed as follows, respectively.

$$R_1^{\text{TAP}} = ACA_{\text{pass}}^{\text{TAP}} \quad (1)$$

$$R_2^{\text{TAP}} = \begin{cases} ACA_{\text{yield}}^{\text{TAP}}, & \text{if: } \frac{(V_{e0} + G_{e0} \cdot \tau)}{ACA_{\text{yield}}^{\text{TAP}}} + \tau < t_{out} \\ ACA_{\text{stop}}^{\text{TAP}}, & \text{others} \end{cases} \quad (2)$$

with

$$\begin{cases} ACA_{\text{yield}}^{\text{TAP}} = \frac{G_{e0} \cdot \tau^2 - 2t_{out}(V_{e0} + G_{e0} \cdot \tau) + 2d_{ec}}{(t_{out} - \tau)^2} \\ ACA_{\text{stop}}^{\text{TAP}} = \frac{(V_{e0} + G_{e0} \cdot \tau)^2}{G_{e0} \cdot \tau^2 + 2V_{e0} \cdot \tau + 2(X_{e0} - d_{ec})} \\ ACA_{\text{pass}}^{\text{TAP}} = \frac{G_{e0} \cdot \tau^2 - 2t_{in}(V_{e0} + G_{e0} \cdot \tau) + 2(d_{ec} + L_e)}{(t_{in} - \tau)^2} \end{cases} \quad (3)$$

Where, the real-time measurements include the target vehicle speed V_{e0} , acceleration G_{e0} , displacement from vehicle front side to the cross-point d_{ec} , and the entry/leaving time of the opposite vehicle t_{in} and t_{out} calculated by the opposite vehicle speed. The target vehicle length is L_e and the human response delay is expressed by τ . Here we note that even though the two scenario can be clearly identified, e.g., for a sample case from the data-base, its hard to select the risk indicator according to the real-time interactive situation.

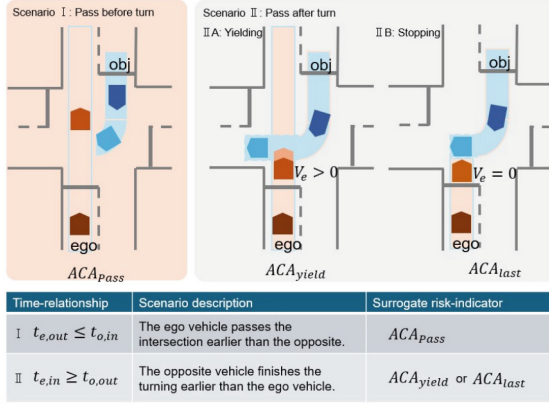


Fig. 1. Two collision avoidance scenarios and corresponding risk-indicator

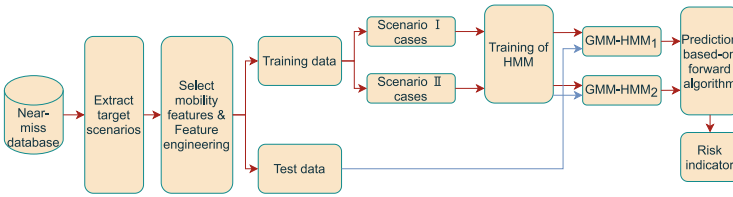


Fig. 2. Framework of the proposed risk assessment method

3 Stochastic Risk Indicator

In this work, we propose the conflict scenario prediction method based on HMM. The process of the presented method is illustrated in Fig. 2. For training the HMM models representing different conflict scenarios, the trails of mobility features (e.g., relative position, velocity) of vehicles in conflict situations are obtained. As the observation probabilistic model, Gaussian mixture model (GMM) is applied to characterize the continuous mobility features.

With trained HMM models for a given trail observation of the mobility features $O(t)$, we propose the stochastic risk indicator under Left/Right turn with conflicts, expressed as follows

$$\hat{R}^{TAP}(t) = \sum_{i=1,2} \omega_i \cdot R_i^{TAP} \tag{4}$$

where, the weighting factor $\sum \omega_i = 1, i = 1, 2$ indicates the predicted probability of scenario i , which can be calculated by the following logistic function

$$\omega_1 = \frac{1}{1 + e^{-(\log P(O(t)|\lambda_1) - \log P(O(t)|\lambda_2))}}, \omega_2 = 1 - \omega_1 \tag{5}$$

The probabilities $\log P(O(t)|\lambda_i)$ with regard to the observation $O(t)$ under different HMM models λ_i can be calculated by forward algorithm.

4 Scenario Prediction with GMM-HMM

Specifically, one particular HMM expressed by the parameter set λ_i is trained for each conflict scenario $i = 1, 2$. Each HMM model λ (index i is omitted) includes Q possible hidden states H , continuous output set V , state transmission probabilities $A = \{a_{q,p}\}$, observation GMM model Θ , and initial state probabilities π . The trail of each feature is represented by a column vector, expressed as

$$\mathbf{x}_n = [x_{n,1}, x_{n,2}, \dots, x_{n,T}]^T \tag{6}$$

where t is the time step index. For each scenario, all the mobility features from different conflict events are truncated to the same length T , and the set of all features can be expressed as the following data matrix, i.e.,

$$\mathbf{X} = [\mathbf{x}_1, \mathbf{x}_2, \dots, \mathbf{x}_N] \tag{7}$$

In this work, we apply the GMM to characterize the continuous mobility features, together with the training process of the HMM model. Every column in the data matrix represents the trail of every mobility features whose probability density can be fit by a super position of M Gaussian distribution, with the following expression

$$P(\mathbf{x}_n) = \sum_{m=1}^M \sum_{q=1}^Q \omega_{n,q,m} P(\mathbf{x}_n \mid \mathcal{N}(\mu_{n,q,m}, \sigma_{n,q,m})) \tag{8}$$

where $\omega_{n,q,m}$ means the weight when the type n feature probability is modeled by the m Gaussian component from the q hidden state, and $\mu_{n,q,m}, \sigma_{n,q,m}$ are the corresponding mean value and standard deviation of the Gaussian distribution component. Let $\Theta_n = \{\omega_{n,q,m}, \mu_{n,q,m}, \sigma_{n,q,m}\}$ express the GMM parameter set for the feature n , the observation model $\Theta = \{\Theta_1, \Theta_2, \dots, \Theta_N\}$ includes the parameter set for all N types of mobility features. For the HMM training, we use the maximum likelihood estimation (ME) algorithm to determine all the GMM parameters which most likely fit the data set \mathbf{x}_n , satisfying

$$\Theta_n = \arg \max_{\Theta_n} P(\mathbf{x}_n) = \arg \max_{\Theta_n} \prod_t^T P(\mathbf{x}_n(t)) \tag{9}$$

The training algorithm is started with an initial guess of Θ and then the probability of taking the value of $\mathbf{x}_n(t)$ by the Gaussian component of m from the hidden state q can be calculated as follows

$$\gamma_{n,q,m,t} = \frac{\omega_{n,q,m} \mathcal{N}(\mathbf{x}_n(t) \mid \mu_{n,q,m}, \sigma_{n,q,m})}{\sum_{j=1}^M \omega_{n,q,j} \mathcal{N}(\mathbf{x}_n(t) \mid \mu_{n,q,j}, \sigma_{n,q,j})} \cdot \gamma_t(q) \tag{10}$$

where, $\gamma_t(q) = P(Q_t = q \mid \mathbf{X}, \lambda)$. Then the corresponding updating rule for Θ_n can be obtained as

$$w_{n,q,m} = \frac{\sum_{t=1}^T \gamma_{n,q,m,t}}{\sum_{t=1}^T \gamma_t(q)} \tag{11}$$

$$\mu_{n,q,m} = \frac{\sum_{t=1}^T \gamma_{n,q,m,t} \mathbf{x}_n(t)}{\sum_{t=1}^T \gamma_{n,q,m,t}} \quad (12)$$

$$\Sigma_{n,q,m} = \frac{\sum_{t=1}^T \gamma_{n,q,m,t} (\mathbf{x}_n(t) - \mu_{n,q,m})^2}{\sum_{t=1}^T \gamma_{n,q,m,t}} \quad (13)$$

The complete algorithm is given as follows

Algorithm 1. GMMHMM Training Algorithm

- 1: Initialize model parameters: state transition probability matrix A , initial state distribution π , and the GMM parameters for each state
 - 2: **repeat**
 - 3: **E-step (Expectation Step):**
 - 4: Compute forward probabilities $\alpha_t(q)$ and backward probabilities $\beta_t(q)$
 - 5: Compute $\gamma_t(q)$
 - 6: Compute $\xi_t(q, p) = P(Q_t = q, Q_{t+1} = p \mid \mathbf{X}, \lambda)$
 - 7: Compute $\gamma_{n,q,m,t} = P(Q_t = q, M_t = m \mid \mathbf{X}, \lambda)$ using (10)
 - 8: **M-step (Maximization Step):**
 - 9: Update initial state probabilities $\pi_q = \gamma_1(q)$
 - 10: Update state transition probabilities $A_{qp} = \frac{\sum_{t=1}^{T-1} \xi_t(q, p)}{\sum_{t=1}^{T-1} \gamma_t(q)}$
 - 11: Update GMM parameters using (11)-(13)
 - 12: **until** convergence
-

5 Results and Analysis

A near-miss video database that focuses on collisions, near-misses, and normal driving data in real traffic has been developed in prior studies [1]. By using a drive-recorder installed on the front shield of vehicles, front-view video data, vehicle speed, accelerations, and GPS data were collected. The mobility features of the turning vehicle were obtained through image processing based on front-view videos. In the database we focus on the right turn across path conflicts and manually divide them into the two scenarios shown in Fig. 1. Then we trained the two GMM-HMM models respectively with the corresponding data trail of the mobility features. We first examine the accuracy of GMM-HMM models regarding the mobility feature predictions, as shown in Fig. 3. According to the prediction results, we notice that as general models of the two scenario classifications, the object vehicle's mobility features sometimes cannot be exactly predicted. However, the Ego vehicle's future behavior can be reasonably anticipated. In cases from scenario I, the Ego vehicle usually slows down to a low speed or stops and in scenario II cases, the global longitudinal/lateral speeds do not change much.

The scenario prediction results regarding the likelihoods of the 10 test cases are shown in Fig. 4. Treating the case no. 7 as a real-time scenario, the weight factor ω_i variation is also illustrated. The test cases no. 1-no. 5 are selected

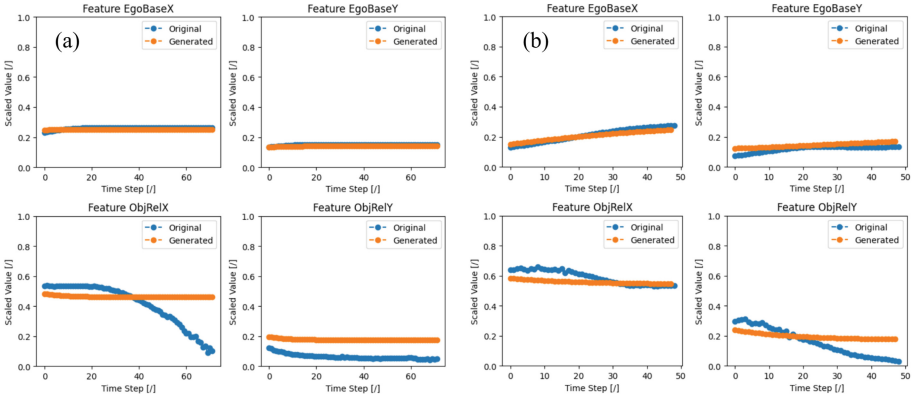


Fig. 3. Prediction results of Ego vehicle and Obj vehicle positions, (a) case from scenario I, (b) case from scenario II

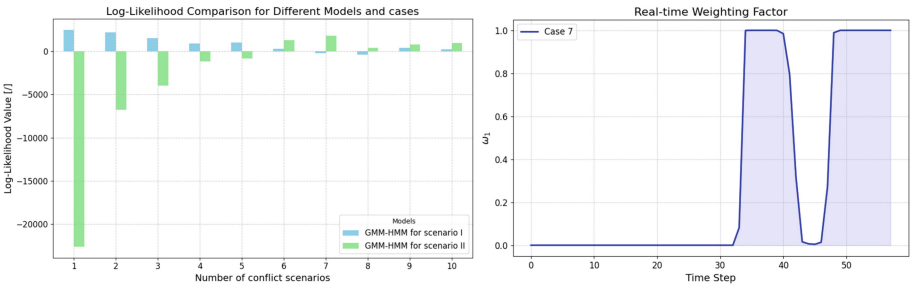


Fig. 4. Likelihood estimation of test cases, left: Comparison with different models, right: real-time estimation of a single case (observation within 0.5 s)

from the scenario I and others from scenario II. According to the calculation results, all the cases are correctly identified with the corresponding class. Some cases are with remarkable significance like case no. 1. We also note the real-time estimation sometimes leads to contrary prediction with real-time observations.

6 Conclusion

Focusing on the Left/Right Turn across path conflicts, this work proposed an innovative surrogate risk indicator including scenario classification using GMM-HMM models, which show good performances in scenario classifications.

References

1. Imaseki, T., et al.: Criticality metrics study for safety evaluation of merge driving scenarios, using near-miss video data. SAE Int. J. Transport. Saf. **12**(09-12-01-0002) (2023)

Open Access This chapter is licensed under the terms of the Creative Commons Attribution 4.0 International License (<http://creativecommons.org/licenses/by/4.0/>), which permits use, sharing, adaptation, distribution and reproduction in any medium or format, as long as you give appropriate credit to the original author(s) and the source, provide a link to the Creative Commons license and indicate if changes were made.

The images or other third party material in this chapter are included in the chapter's Creative Commons license, unless indicated otherwise in a credit line to the material. If material is not included in the chapter's Creative Commons license and your intended use is not permitted by statutory regulation or exceeds the permitted use, you will need to obtain permission directly from the copyright holder.





Design and Analysis of Traction Control Strategies for Icy Road Conditions

M. Mihalkov¹, C. Caponio¹, Z. Hankovszki², A. Sorniotti³, U. Montanaro¹,
and P. Gruber¹ (✉)

¹ Department of Mechanical Engineering Sciences, University of Surrey, Guildford, UK
p.gruber@surrey.ac.uk

² AVL List GmbH, 8020 Graz, Austria

³ Department of Mechanical and Aerospace Engineering, Politecnico di Torino, Torino, Italy

Abstract. Traction control (TC) plays a key role in improving vehicle safety, especially for driving scenarios involving extremely low levels of tyre-road friction. In this paper a novel deep reinforcement learning (DRL) based TC strategy is formulated and its performance is compared against a nonlinear model predictive control (NMPC) solution for a simulated straight-line acceleration manoeuvre on icy road conditions. The paper explores the design and assessment of the proposed controllers using a vehicle model experimentally validated on ice. The simulation results show that the DRL solution outperforms the NMPC strategy by reducing the wheel slip ratio peaks and oscillations at the start of an acceleration manoeuvre. Additionally, it converges more quickly to the reference slip and is more computationally efficient.

Keywords: Traction control · Vehicle dynamics · Artificial intelligence · Deep reinforcement learning · Model predictive control · Wheel slip · Electric vehicle

1 Introduction

Traction controllers (TCs) adjust the driver's traction torque request to limit wheel slip, and in doing so, maximise tyre force generation and maintain vehicle stability [1]. The functionality of TC is particularly beneficial for very low tyre-road friction coefficient conditions, like icy roads. In these conditions, relatively small torque requests can induce very fast wheel dynamics (beyond the driver's control), yielding significant wheel slips and potentially causing the vehicle to spin. Literature surveys on TC solutions, e.g., [2–4] show that most of the available TC strategies use model based and deterministic control approaches, such as Nonlinear Model Predictive Control (NMPC) based solutions [2]. In this work, a novel artificial intelligence based traction controller, using deep reinforcement learning (DRL), is designed and its effectiveness explored for low road-tyre friction conditions. The proposed DRL TC design uses feedforward neural networks (FFNNs). The choice of neural network (NN) architecture is based on the current vehicle dynamics control literature [5–7]. The analysis of different NN architectures such as recurrent neural networks (RNNs) for vehicle dynamics control is beyond the scope of this paper.

© The Author(s) 2024

G. Mastinu et al. (Eds.): AVEC 2024, LNME, pp. 413–419, 2024.

https://doi.org/10.1007/978-3-031-70392-8_59

To evaluate the DRL controller, its performance is compared against an NMPC strategy, serving as a benchmark state-of-the-art traction controller. The novelty points presented in this paper are: (i) the design of a DRL-based-TC trained on an experimentally validated vehicle model, and (ii) a simulation based analysis of the performance advantages of the DRL control strategy compared to a state-of-the-art NMPC TC.

The paper is organised as follows: Sect. 2 presents the case study electric vehicle (EV), vehicle model validation and the simulated control framework. Section 3 introduces the proposed TC strategies. Section 4 describes the simulation setup and the simulation results, which are quantitatively assessed. The conclusions and future developments are reported in Sect. 5.

2 Vehicle Validation and Traction Controller Framework

2.1 Case Study Vehicle and Validation

The EV case study considers a single motor, rear-wheel-drive vehicle available at the University of Surrey. Table 1 reports the main vehicle parameters. Straight-line acceleration tests were carried out with the vehicle driven on polished ice, see Fig. 1. The experimental results were used to validate the simulation model created in AVL VSM for the same acceleration manoeuvre, see Fig. 2. The tyres are simulated with the Pacejka Magic Formula (MF) 5.2. The electric motor dynamics are modelled with (i) a rate limiter of 226 %/s, and (ii) a communication time delay ($t_d = 82$ ms) between the torque request $T_{r_{exp}}$ and the feedback motor $T_{fb_{exp}}$ (see Fig. 2a). The longitudinal acceleration a_x of the vehicle was measured with an on-board accelerometer and the slip ratio was computed from the four wheel speed measurements.

2.2 Traction Controller Structure

The TC architecture is shown in Fig. 3. The driver presses the accelerator pedal, and the pedal's position (app) is fed into a drivability map to calculate a driver reference torque (T_{ref}). The TC block receives T_{ref} and the vehicle signals, and computes a torque correction T_{corr} that is subtracted from the driver torque request. The final torque request (T_{app}) is then applied to the vehicle. The controlled variable is the slip velocity $s_w = \omega_{wh}r - v_x$, where ω_{wh} is the angular speed of the driven wheels, r is the rolling radius of the tyre and v_x is the vehicle's longitudinal velocity. The practical slip ratio is defined as $\kappa = \frac{\omega_{wh}r - v_x}{v_x}$.

Table 1. Main vehicle parameters

Symbol	Description	Value
m	Vehicle mass	566 kg
a_F	Front semi-wheelbase	0.953 m
a_R	Rear semi-wheelbase	0.733 m
h_{CG}	Centre of gravity height	0.565 m
t_F	Front track width	1.094 m
t_R	Rear track width	1.08 m
r	Rear wheel rolling radius	0.279 m
J_{wh}	Rear wheel inertia	1.1 kgm ²
T_{max}	Peak motor torque	54 Nm
Gr	Gear ratio of the drivetrain	9.23:1
τ_m	Motor time constant	10 ms



Fig. 1. Case study EV tested on ice.

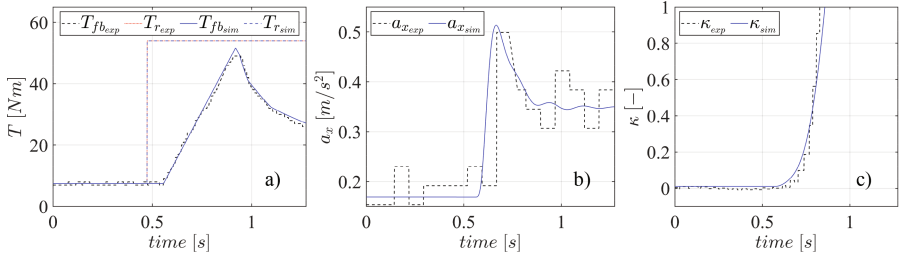


Fig. 2. Experimental (subscript *exp*) and simulated (subscript *sim*) straight-line acceleration manoeuvre. a) torque request (T_r) and feedback motor torque (T_{fb}); b) longitudinal acceleration, a_x ; c) practical slip ratio, κ .

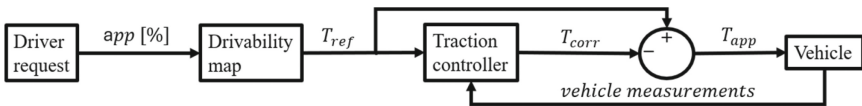


Fig. 3. Simplified schematic of the traction control architecture.

3 Control Strategies

3.1 NMPC Framework

The NMPC TC is a simplified version of the one presented in [1]. The internal model of the NMPC is based on the following four equations:

$$\frac{d}{dt}s_{w,L/R} = \left(-\frac{r^2}{J_{wh}} - \frac{1}{m_q} \right) D\mu_{L/R} \sin \left(C \arctan \left(\frac{Bs_{w,L/R}}{\omega_{wh,L/R}r} \right) \right) F_z + \frac{G_r T_{fb}}{2J_{wh}} r \quad (1)$$

$$\frac{d}{dt}\omega_{wh,L/R} = \frac{1}{J_{wh}} \left(\frac{G_r T_{fb}}{2} - D\mu_{L/R} \sin \left(C \arctan \left(\frac{Bs_{w,L/R}}{\omega_{wh,L/R}r} \right) \right) F_z r \right) \quad (2)$$

$$\frac{d}{dt}T_{fb} = \frac{T_{app} - T_{fb}}{\tau_m} \quad (3)$$

where the subscript “L/R” denotes the left or right wheel. m_q is the mass of the quarter car model, J_{wh} is the rear wheel inertia, B , C and D are the simplified MF parameters [8], G_r is the drivetrain gear ratio, μ is the friction coefficient and F_z is the vertical tyre load considered as constant in the formulation of the NMPC internal model, and τ_m is the motor time constant. The NMPC state vector is $x = [s_{wL}, \omega_{whL}, s_{wR}, \omega_{whR}, T_{fb}]$, where T_{fb} is the feedback motor torque. The control action is $u = T_{corr}$, whose maximum is equal to the torque requested by the driver. The stage cost is:

$$\min J = W_{\Delta s_w} \left(\Delta s_{w,L}^2(N) + \Delta s_{w,R}^2(N) \right) + \sum_{k=0}^{N-1} W_{\Delta s_w} \left(\Delta s_{w,L}^2(k) + \Delta s_{w,R}^2(k) \right) + W_u T_{corr}^2(k) \quad (4)$$

where the slip velocity error $\Delta s_{w,L/R} = s_{w,L/R} - \sigma_{x_{ref}} \omega_{wh,L/R}r$, with the theoretical slip reference $\sigma_{x_{ref}} = 5\%$. $W_{\Delta s_w}$ and W_u are weighting factors for slip tracking and control effort, respectively. Two versions of the same NMPC are proposed: the first one, denoted as “expert NMPC”, with $N = 50$ steps in the prediction horizon and sampling time of $T_s = 10$ ms, which is also used to guide the DRL TC training. The second one, denoted as “real-time NMPC”, is the real-time version with number of steps in the prediction horizon $N = 10$ and sampling time of $T_s = 10$ ms. To confirm the real-time capability of all proposed controllers, both NMPC configurations were run in real-time on a dSPACE MicroAutoBox II system (900 MHz, 16 Mb flash memory). The real-time NMPC has a peak turnaround time of 5.8 ms, guaranteeing real-time capability, while the “expert NMPC” had a peak turnaround time of 60.5 ms and 30 ms turnaround time subsequently, exceeding T_s .

3.2 Reinforcement Learning Framework

DRL controllers, known also as *agents*, decide *actions* (control input) based on observations (plant states) from the *environment*, which includes the nominal plant and relevant disturbances. The *policy* (control strategy) mapping observations to actions is learned through interactions with the environment by maximising a cumulative reward over multiple simulations, called *episodes*.

For the proposed DRL TC formulation, the control input (*action*) a is the torque correction, i.e., $a = [T_{corr}]$, while the observations vector is set as:

$$s = [a_x, T_{app}, \Delta s_{w,av}, \int \Delta s_{w,av}, app] \quad (5)$$

where $\Delta s_{w,av}$ is the average slip velocity error between left and right wheels. The reward function is:

$$R = -W_{\Delta s_{w,av}} |\Delta s_{w,av}| + W_{v_x} v_x - W_{IL} |T_{corr} - T_{corr,exp}|. \quad (6)$$

The first two rewards guide the agent to track the reference slip while keeping the vehicle accelerating. The third reward teaches the agent to follow the expert NMPC control action $T_{corr,exp}$. The third reward guides the agent to speed up the training process, while the first two rewards teach the agent to continue improving the TC performance. The weights for each term [$W_{\Delta s_{w,av}}$, W_{v_x} , W_{IL}] have been chosen to give the same priority to the first two rewards, while the third one has been tuned empirically. The DRL algorithm used is the state-of-the-art actor-critic DDPG algorithm [9]. This algorithm has the advantage of (i) handling complex plants with continuous control actions; (ii) improving performance, i.e., they are able to learn policies that achieve higher rewards on the same environment compared to value-based and policy-based algorithms; and (iii) providing a good trade-off between sample efficiency and computational expense [10]. The DDPG agent consists of 1 actor and 1 critic FFNNs. The actor network, i.e., the one computing the control action has two hidden layers with 40 neurons each and ReLU activation function after each layer, and one tanh output layer with one neuron, which is scaled by the peak rear motor torque. The critic network, i.e., which evaluates the actor's performance, has two hidden layers with 40 neurons each and a ReLU activation function in between for the state. The action path has two hidden layers, with 10 and 40 neurons respectively, and a ReLU activation function between them. The common path combines the two paths and applies a ReLU activation function before the single-neuron output.

4 Simulation Set up and Results

4.1 Test Scenario

The simulation analysis was carried out with the validated vehicle model presented in Sect. 2.1 using AVM VSM software. The DRL TC agent was trained for 1000 episodes and tested on a straight-line tip-in manoeuvre on a surface with a friction coefficient of $\mu_x = 0.085$. The manoeuvre consists of a step torque request T_{ref} with an initial value of 7.5 Nm and a final value of 54 Nm at a step time of 2.5 seconds.

4.2 Simulation Results

To evaluate the effectiveness of the DRL TC solution, the NMPC TC strategies presented in Sect. 3.1, i.e., the expert NMPC and the real-time NMPC, have been adopted as benchmark solutions. The sampling time of the DRL and NMPCs controllers is set

at $T_s = 10$ ms for a fair comparison. The reduction of sampling time implies a better tracking of the reference slip regardless of the selected control algorithm [11]. In addition, the controllers activate only when the slip is above of 5%. Figure 4 shows the simulation results for the tip-in manoeuvre with an initial velocity of 2.5 km/h. All control strategies manage to reduce the slip during the manoeuvre despite the presence of a pure time delay in the system. However, the DRL control solution outperforms the NMPC strategies in terms of residual steady-state error and converge time of the closed-loop slip response (see Fig. 4a). The inset in Fig. 4c shows that the DRL agent provides a quicker adjustment of the torque request compared to the NMPC controllers, resulting in a smaller overshoot in the slip response depicted in Fig. 4a. In addition, the smoother control action provided by the DRL also reduces the wear in the drivetrain components. In the interval between 1 and 2 seconds. The DRL agent starts to reduce the torque correction, leading to an increase in the final torque request. This allows the vehicle to reach higher accelerations compared to the NMPCs, up to 0.5 m/s² (see Fig. 4b).

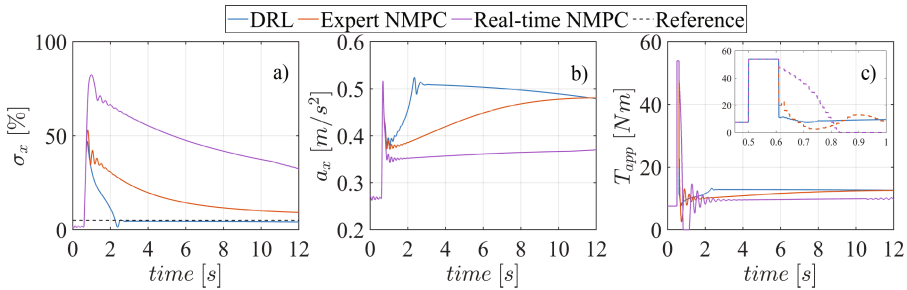


Fig. 4. Simulation results: a) Slip; b) longitudinal acceleration; c) final torque request with an inset in the interval [0.5, 1]s highlighting the intervention time and initial response of the TCs.

5 Conclusions

This paper proposes a novel DRL traction controller benchmarked against state-of-the-art NMPC controllers with two parametrisations: a real-time capable NMPC with a 10 step prediction horizon, and an expert NMPC with a 50 step prediction horizon. The expert NMPC provides better closed-loop tracking performance than the real-time capable NMPC, but is not real-time capable. The proposed DRL controller is trained for 1000 episodes using the control action of the expert NMPC as a term in the reward function allowing the agent to learn faster. The proposed DRL TC strategy can successfully reduce the peaks of the wheel slip and reduce the oscillations in the control action. In addition, the DRL agent reaches the reference slip faster while managing to maintain a higher longitudinal acceleration throughout the manoeuvre.

Future work will focus on extending the formulation of the DRL TC to different friction coefficients and more challenging manoeuvres to further improve closed-loop tracking performance. In addition, different NN structures will be explored and analysed.

Acknowledgements. The research leading to these results has been partially funded by the European Union’s Horizon Europe research and innovation programme under grant agreement No. 101096083 (EM-TECH). The views and opinions expressed are those of the author(s) only and do not necessarily reflect those of the European Union or CINEA – European Climate, Infrastructure and Environment Executive Agency. Neither the European Union nor the granting authority can be held responsible for them.

References

1. Scamacchio, A., et al.: Predictive anti-jerk and traction control for V2X connected electric vehicles with central motor and open differential. *IEEE Trans. Veh. Technol.* **6**, 7221–7239 (2023)
2. Ivanov, V., Savitski, D., Shyrokau, B.: A survey of traction control and anti-lock braking systems of full electric vehicles with individually-controlled electric motors. *IEEE Trans. Veh. Technol.* **9**, 3878–3896 (2015)
3. Fujimoto, H., Amada, J., Maeda, K.: Review of traction and braking control for electric vehicle. In: 2012 IEEE Vehicle Power and Propulsion Conference. pp. 1292–1299 (2012)
4. Kumar, A.: Review on traction control system. In: Garcia Márquez, F.P. (eds.) *International Conference on Intelligent Emerging Methods of Artificial Intelligence & Cloud Computing. Smart Innovation, Systems and Technologies*, vol 273. Springer, Cham (2022)
5. Wasala, A., Byrne, D., Miesbauer, P., O’Hanlon, J., Heraty, P., Barry, P.: Trajectory based lateral control: a reinforcement learning case study. *Eng. Appl. Artif. Intell.* **94**, 103799 (2020)
6. Wei, H., et al.: Deep reinforcement learning based direct torque control strategy for distributed drive electric vehicles considering active safety and energy saving performance. *Energy* **238**(Part B), 21725 (2022)
7. Mantripragada, V.K.T., Kumar, R.K.: Deep reinforcement learning-based antilock braking algorithm. *Veh. Syst. Dyn.* **61**(5), 1410–1431 (2022). <https://doi.org/10.1080/00423114.2022.2084119>
8. Pacejka, H.: *Tire and Vehicle Dynamics*. Butterworth, Oxford, U.K. (2012)
9. Lillicrap, T.P., et al.: Continuous Control with Deep Reinforcement Learning. *ArXiv:1509.02971 [Cs, Stat]*, September 9, 2015. <https://arxiv.org/abs/1509.02971>
10. Morales, M.: *Grokking Deep Reinforcement Learning*. Manning Publications (2020)
11. Tavernini, D., Metzler, M., Gruber, P., Sorniotti, A.: Explicit nonlinear model predictive control for electric vehicle traction control. *IEEE Trans. Control Syst. Technol.* **27**(4), 1438–1451 (2019)




Open Access This chapter is licensed under the terms of the Creative Commons Attribution 4.0 International License (<http://creativecommons.org/licenses/by/4.0/>), which permits use, sharing, adaptation, distribution and reproduction in any medium or format, as long as you give appropriate credit to the original author(s) and the source, provide a link to the Creative Commons license and indicate if changes were made.

The images or other third party material in this chapter are included in the chapter’s Creative Commons license, unless indicated otherwise in a credit line to the material. If material is not included in the chapter’s Creative Commons license and your intended use is not permitted by statutory regulation or exceeds the permitted use, you will need to obtain permission directly from the copyright holder.





Design and Verification of an Adaptive State-Tuned Power Management System for Series Hybrid Electric Tracked Vehicles

Dersu Çeliksöz¹ , İsmail Göçer² , and Kerim Arda Gülseren² 

¹ E-Mobility Design Solutions Unit, FNSS Savunma Sistemleri A.Ş. Ankara, Ankara, Turkey
dersu.celiksoz@fnss.com.tr

² Modelling and Simulation Unit, FNSS Savunma Sistemleri A.Ş. Ankara, Ankara, Turkey

Abstract. The accelerated shift towards electrification in the tracked vehicle industry, particularly concerning off-road and military vehicles, poses challenges due to their intensive power consumption and limited charging infrastructures. Addressing these challenges, this paper focuses on the development of an adaptive state-tuned power management system for a series hybrid electric tracked vehicle. The vehicle's architecture includes an electric traction unit and a hybrid powerpack. The core of this research involves designing a dynamic power allocation system that adjusts the power sharing between the battery and a generator set under varying operational conditions. Through a systematic approach, a power management algorithm featuring a hierarchical controller structure to manage the power flow is designed. Simulation tests, both Driver-in-the-Loop (DIL) and Model-in-the-Loop (MIL), were employed to verify the system's performance. Results indicate that the algorithm coordinates power distribution, ensuring optimal performance while adhering to the system's constraints and adapting to immediate power demands, demonstrating its potential for enhancing hybrid vehicle operations in demanding maneuvers.

Keywords: Series Hybrid Powertrain · Tracked Vehicle Electrification · Power Management · Power Following Control · Adaptive Control

1 Introduction

The industry trend toward off-road and military vehicle electrification offers benefits like performance and efficiency, but poses challenges, including higher power demands and limited charging access in off-road conditions. Hybridization, with its hybrid powerpack management, emerges as a key solution to these issues, with Sivakumar's research highlighting its benefits like improved fuel economy and quieter operation [1].

Several power management strategies for series hybrid tracked vehicles have been explored across various industries. Wang's research investigates the power allocation for a hybrid electric bulldozer, implementing a rule-based method with four key guidelines that relate to battery charge and the required power, subsequently demanding power from generator unit [2]. Furthermore, Shabbir has enhanced control strategies of thermostat

© The Author(s) 2024

G. Mastinu et al. (Eds.): AVEC 2024, LNME, pp. 420–426, 2024.

https://doi.org/10.1007/978-3-031-70392-8_60

and power following, aiming to reduce fuel usage by moderating the shifts between the rules [3]. Zhai has also contributed with a heuristic energy management system known as the Optimal Primary Source Strategy (OPSS), which is designed to improve fuel efficiency and battery management in series hybrid electric tracked vehicles [4]. Zhang has furthered the development of rule-based and optimization-based approaches by integrating intelligent control elements like fuzzy logic filters [5]. This integration aims to address the challenges of fuel consumption that arise from frequent variations in engine loads, the non-ideal operation of generator sets, and disturbances from hydraulic pump torque.

In addition to the researches on power management, environmental impact of military conditions on electric powertrains is also investigated from the existing literature. Studies show that for a military vehicle application both the high-power demands and the extreme temperatures that electric drive systems of military vehicles must endure, as highlighted in the report by Stott and colleagues from the US Army Engineer Research and Development Center (ERDC) [6], should be considered. Thus, priority is given to performance and adaptiveness of the power management algorithm in this work from military field.

In this paper, the focus is placed on an adaptive power management system specifically designed for a series hybrid electric tracked vehicle, incorporating the literature investigation combined with an emphasis on adaptiveness to operating conditions of powerpack components. Figure 1 presents main components of a series hybrid tracked vehicle. The architecture includes two principal units: the electric traction unit and hybrid powerpack. While the traction unit is combination of electric motors, gearboxes and brake systems, the powerpack consists of battery, generator set and power distribution unit that integrates the power generated from these sources. The objective of the power management system is to dynamically regulate power distribution between the battery and the generator set, considering system variables such as driver demands, and the battery's state of charge. The findings obtained are aimed to be tested on Kaplan Hybrid [7], which is a hybrid tracked vehicle developed by FNSS.

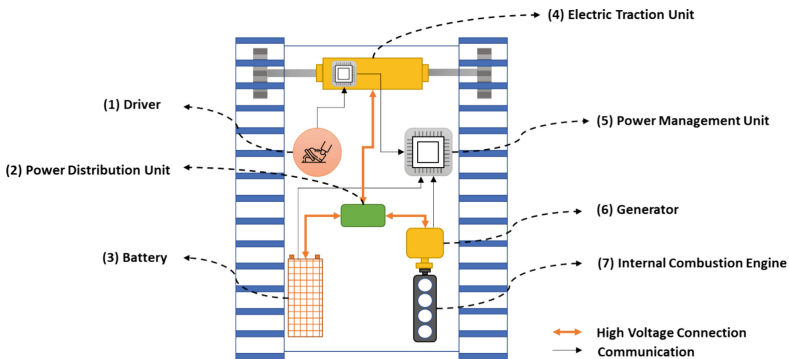


Fig. 1. Main Components of a Series Hybrid Tracked Vehicle

2 Power Management System (PMS) Development

The development of the PMS consists of several key stages: Modeling, Algorithm Design, and Verification.

2.1 Modeling the Hybrid Powerpack Plant

To test and evaluate PMS, a hybrid powerpack model with inputs including engine speed and generator torque requests, and actual outputs of these requests and the electric current at the powerpack's output bus is created.

The accelerator pedal position is first translated into a torque request for the traction unit by referencing the electric motor's full load curves at the given speed. This torque, when multiplied by traction motor speed and unit efficiency, produces the power demand, as illustrated in Eq. (1). P_D , App , $T_{M,max}$, ω_M and η_{Tr} represents driver power demand, accelerator pedal position, maximum motor torque, traction motor speed and traction unit efficiency respectively.

$$P_D = App T_{M,max}(\omega_M)\omega_M \eta_{Tr} \quad (1)$$

Next, the genset's power output is computed by multiplying the generator torque with engine speed which is controlled by output torque of the PI controller and informed by experiment-based lookup tables that factor in turbo lag and the engine's full load performance. Similar to the traction unit, the genset torque is limited by speed dependent full load curves. Computation is presented by Eq. (2) in which P_{GS} , $T_{G,req}$, $T_{G,max}$, ω_e and η_{GS} represents genset's power output, requested generator torque, maximum generator torque, engine speed and GenSet efficiency respectively.

$$P_{GS} = \min[T_{G,req}, T_{G,max}(\omega_e)]\omega_e \eta_{GS} \quad (2)$$

The genset's excess power over the driver's demand becomes the battery's power input illustrated by P_{BattIn} in Eq. (3) which may indicate discharge or charge. This power determines the battery's state of charge (SoC) through a simplified coulomb approach based on Movassagh's research [8]. Equation (4) shows the transient SoC calculation, including bus voltage (V_{Bus}), battery capacity (Q_{Batt}) in Ah, and time step (Δt).

$$P_{BattIn} = P_{GS} - P_D \quad (3)$$

$$SoC(t) = SoC(t - 1) + [P_{BattIn}(t)][V_{Bus}Q_{Batt}]^{-1} \Delta t \quad (4)$$

2.2 Algorithm Design of Power Management System

The developed power management algorithm combines a high-level controller for power allocation between the generator set (genset) and battery with a low-level controller that commands the genset to produce the required power. As outlined in Fig. 2, the power allocation algorithm employs an adaptive state-based power-following approach

to determine the share of power provided by the battery and genset, increasing the generator's contribution as demand rises or the state of charge (SoC) of the battery reduces to charge the battery up to a desired charge level. Based on actual state calculated using driver demand and battery SoC, PMS also decides whether requested traction power should be limited in order not to exceed the desired battery current limits at states 6 and 8. Meanwhile, the genset drive system controls the engine and generator through speed and torque commands respectively to fulfill the power generation demands.

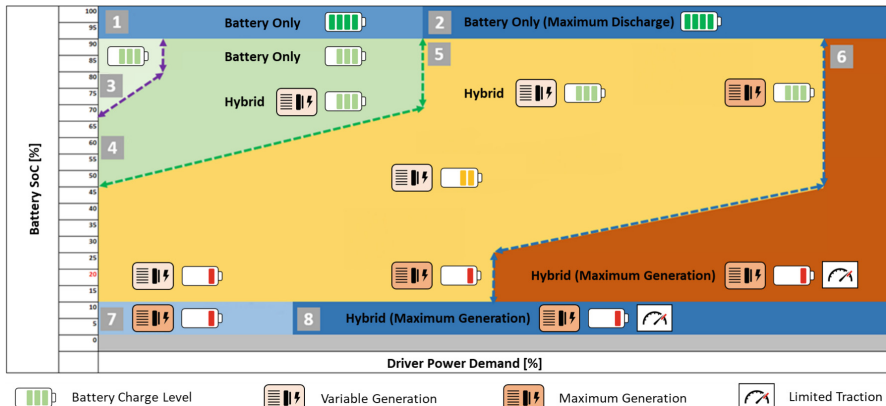


Fig. 2. Power Allocation Algorithm

This work's primary contribution lies in its adaptiveness to operating conditions of powerpack components, which is accomplished through dynamic normalization of boundary conditions. Initially, the instantaneous available hybrid power, sum of the maximum battery discharge and available genset power, is calculated based on operating factors such as auxiliary power, bus voltage, and the temperature of the battery cells as well as the engine coolant at that time step. Then, all power limits are normalized relative to the maximum hybrid power. As a result, the state boundaries change adaptively and they are illustrated in Fig. 2 in normalized format. In the final step, the driver's demand is also normalized, and the state is determined. This method allows vehicle to operate the generator at varying power levels, influenced by the operating conditions for same traction demand.

In addition to the state determination and transition algorithm, a power allocation function is designated and refined based on the vehicle concept. The powerpack is battery-driven in states 1 to 3, as depicted in Fig. 2, while state 4 ensures a smooth transition between states 3 and 5 through hysteresis by adhering to previous state rules. States 5 to 8 activate hybrid mode, with GenSet power outputs adjusted by a hybrid function, optimized via a real-time brute-force method and parameter adjustment during DIL simulations. For instance, when prioritizing silence, the function permits greater battery discharge in hybrid states 4 and 5. Conversely, if the vehicle's objective is high performance, PMS is operated at 5 and 6 states and battery's SoC is maintained at higher levels maximizing generator usage by fine-tuning the hybrid function accordingly. This hybrid function at state 5 operates similar to power following methods and is modeled as

a first-order polynomial in relation to the battery's state of charge. Its character is designated through the optimization of polynomial coefficients. Overall, PMS is designed to modulate the powerpack, promoting a higher discharge tendency at states with greater SoC and generator-driven charging tendency at states with lower SoC.

2.3 Simulations and Verifications

The power management system undergoes testing through Driver-in-the-Loop (DIL) and Model-in-the-Loop (MIL) methods. DIL testing utilizes a real-time driving simulator tailored for hybrid tracked vehicles, where the driver navigates the vehicle in a virtual environment transmitting the power demands to the ground through corresponding control blocks, powerpack blocks and the traction unit. The MIL approach, moreover, evaluates the system's performance with offline simulations, calibrating control parameters based on postprocessed results.

The battery power output distribution chart, observed during a model-in-the-loop (MIL) simulation, is presented in Fig. 3. In this simulation, the hybrid power allocation function has been optimized to ensure high performance while maintaining the battery's SoC at around 60%, charging below this level and discharging above it. Figure 3 also demonstrates that high SoC coupled with high power demand leads to maximum battery discharge, while lower SoC and power demand results in maximum battery charging, as expected in a vehicle with the main aim of performance. The hybrid function also ensures smooth transitions, effectively preventing undesired engine power fluctuations.

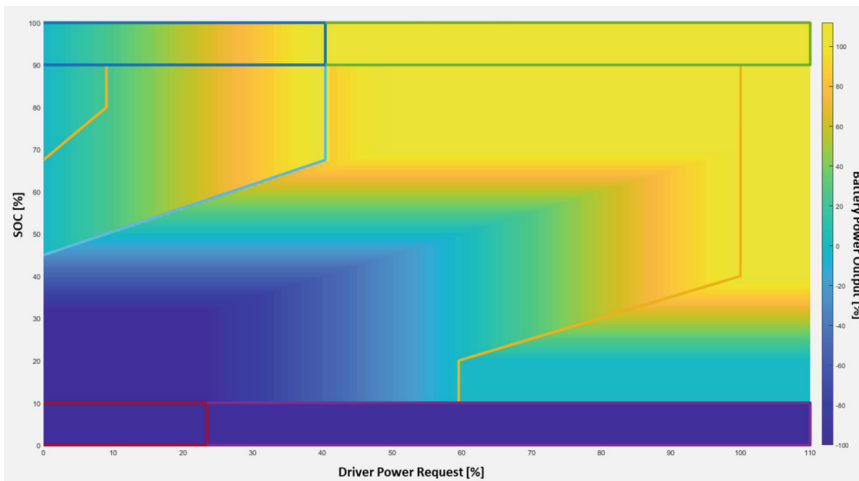


Fig. 3. Battery Power Output Distribution from MIL Simulation

Moreover, real-time driver-in-the-loop (DIL) simulations are conducted to evaluate the system under transient loading conditions, such as high-speed steering maneuvers, using the DIL simulator specifically developed for series-hybrid electric tracked vehicles. Real-time power requirements are monitored and recorded throughout the vehicle's

operation as illustrated in Fig. 4. Using the observations from these simulations, fine-tuning studies of power management system is supported.



Fig. 4. Steering Maneuver from DIL Simulation

3 Conclusion

An examination of the simulation outcomes shows that thanks to the algorithm's adaptive capacity, the power management system coordinates the power sources to dynamically meet demands without exceeding the battery's and generator set's limitations. Additionally, the genset fulfills the required power generation within acceptable delay thresholds. In summary, the abilities of the power management algorithm and developed MIL/DIL environments underscore their importance for the future of hybrid tracked vehicles.

References

1. Sivakumar, P., et al.: Configuration study of hybrid electric power pack for tracked combat vehicles. *Def. Sci. J.* **67**(4), 354–359 (2017)
2. Wang, H., et al.: Dynamic modeling and control strategy optimization for a hybrid electric tracked vehicle. *Mathematical Problems in Engineering* (2015)
3. Shabbir, W., Evangelou, S.A.: Threshold-changing control strategy for series hybrid electric vehicles. *Appl. Energy* **235**, 761–775 (2019)
4. Zhai, R.Q., et al.: A heuristic rule-based control strategy using for series hybrid tracked vehicles. *Journal of Physics: Conference Series* 1576 (2020)
5. Zhang, B., et al.: Adaptive smoothing power following control strategy based on an optimal efficiency map for a hybrid electric tracked vehicle. *Energies* **13**(8), 1893 (2020)
6. Stott, A.R., Callaghan, C.A., Punt, D.A., Elliott, T.J.: Cold Impacts on Vehicle Electrical Systems. The US Army Engineer Research and Development Center (ERDC) (2023)

7. FNSS Kaplan Hybrid web page: <https://www.fnss.com.tr/en/products/kaplan-hybrid>
8. Movassagh, K., Raihan, A., Balasingam, B., Pattipati, K.: A critical look at coulomb counting approach for state of charge estimation in batteries. *Energies* **14**(14), 4074 (2021)

Open Access This chapter is licensed under the terms of the Creative Commons Attribution 4.0 International License (<http://creativecommons.org/licenses/by/4.0/>), which permits use, sharing, adaptation, distribution and reproduction in any medium or format, as long as you give appropriate credit to the original author(s) and the source, provide a link to the Creative Commons license and indicate if changes were made.

The images or other third party material in this chapter are included in the chapter's Creative Commons license, unless indicated otherwise in a credit line to the material. If material is not included in the chapter's Creative Commons license and your intended use is not permitted by statutory regulation or exceeds the permitted use, you will need to obtain permission directly from the copyright holder.





A Study on the Control of Handling and Stability of a Four Wheel Independent Steering Electric Vehicle

Zhihao Wu, Ning Zhang^(✉), Pu Li, Zihong Li, and Jianrun Zhang

School of Mechanical Engineering, Southeast University, Nanjing 211189, People's Republic of China

nzhang_cn@seu.edu.cn

Abstract. The path-tracking control of electric vehicles with four wheel independent steering (FWIS) is crucial for enhancing vehicle stability. This paper aims to address the issue of multi-actuator redundancy by coordinating the control allocation of multiple actuators, thereby improving the handling stability and path tracking performance of FWIS vehicles. First, a model of FWIS electric vehicle is developed, taking into account both the nonlinear tyre and motor actuator characteristics. Subsequently, a path tracking model is established and a hierarchical control architecture is designed. The upper-level controller computes the generalized tracking force and the lower-level control force is distributed based on the principle of optimal tyre utilization rate. Finally, the simulation results demonstrate the effectiveness of the proposed control scheme in terms of tracking accuracy and handling and stability.

Keywords: Four Wheel Independent Steering · Electric Vehicle · Motor Characteristics · Handling and Stability · Path Tracking

1 Introduction

Vehicle electrification has not only provided a solution for reducing transportation emissions, but also new possibilities for enhancing the handling and stability performance. With advancements in electric motor technology and x-by-wire, the e-corner module, which consists of in-wheel motors, brake-by-wire, steer-by-wire, and active suspension, has been proposed as a next-generation modular platform for electric vehicles. Vehicles equipped with e-corner modules can realize FWIS and even special functions such as zero turn. Against the backdrop of a boom in skateboard platforms for EV designs, how to ensure stability at high speeds is a great challenge.

In recent decades, there has been a growing focus on the steering stability of FWIS systems. The intricate steering characteristics and over-actuated of these vehicles necessitate an effective control strategy to coordinate the actuators and ensure system stability, particularly at high speeds. In addition to traditional front wheel steering, various control strategies such as direct yaw moment control [2], torque vectoring control [3], active

rear wheel steering [4], and four wheel steering [5] have been proposed for FWIS and four wheel independent driving vehicles. However, these control strategy studies often overlook the influence of the actuators on control effectiveness. Consequently, ensuring stability in FWIS electric vehicles with e-corner modules at high speeds remains a challenging problem. Furthermore, most studies utilize linear tyre models and lack further analysis of tyre and motor characteristics [6].

The remainder of this paper is organized as follows. The vehicle path tracking model is established in Sect. 2. The modeling and design of the controllers have been fully studied in Sect. 3. Simulation and discussion are presented in Sect. 4 and the conclusion is drawn in Sect. 5.

2 Vehicle Path Tracking System Dynamics Modeling

The study focuses on a fully electric vehicle equipped with four drive motors and four steering motors. The objective is to effectively manage the torque and steering angle of each motor to coordinate the chassis control system and optimize tyre utilization. Figure 1 presents a top view of the vehicle, illustrating the yaw moment M_z and wheel forces F_x/F_y .

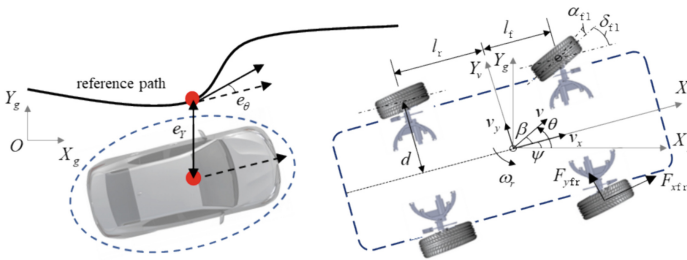


Fig. 1. Path tracking model and FWIS vehicle

2.1 FWIS Vehicle Dynamics Model

Referring to Fig. 1, the FWIS vehicle model is described as:

$$m(\dot{v}_x - v_y \dot{\psi}) = \sum_{i=1}^4 (F_{x,i} \cos \delta_i - F_{y,i} \sin \delta_i) - F_{res} \tag{1}$$

$$m(\dot{v}_y + \dot{v}_x \dot{\psi}) = \sum_{i=1}^4 (F_{x,i} \sin \delta_i + F_{y,i} \cos \delta_i) \tag{2}$$

$$I_z \ddot{\psi} = \sum_{i=1}^2 l_f (F_{x,i} \sin \delta_i + F_{y,i} \cos \delta_i) - \sum_{i=3}^4 l_r (F_{x,i} \sin \delta_i + F_{y,i} \cos \delta_i)$$

$$+ \sum_{i=1}^4 (-1)^i d (F_{x,i} \cos \delta_i - F_{y,i} \sin \delta_i) \quad (3)$$

where m is the total vehicle mass. v_x and v_y are the longitudinal and lateral speeds of the vehicle. ψ is the yaw angle. F_x and F_y are the longitudinal and lateral forces. $i = \text{fl}$ (front left), fr (front right), rl (rear left) and rr (rear right). δ is the wheel steering angle. F_{res} is the sum of aerodynamic resistance force and rolling resistance. I_z is the yaw moment of inertia. d is one-half of the tread width. The nonlinear tyre forces are described by means of the Pacejka Magic-Formula [1], where the independent variables are the tyre slip rate and tyre slip angle, as well as the dependent variables are the longitudinal and lateral tyre forces. The longitudinal wheel speed $v_{w,i}$ and tyre slip rate λ_i are defined as

$$v_{w,i} = (v_x \mp d\dot{\psi}) \cos \delta_i + (v_y + l_f \dot{\psi}) \sin \delta_i, i = 1, 2 \quad v_{w,i} = (v_x \mp d\dot{\psi}) \cos \delta_i + (v_y - l_r \dot{\psi}) \sin \delta_i, i = 3, 4 \quad (4)$$

$$\lambda_i = \frac{\omega_{w,i} r_w - v_{w,i}}{\omega_{w,i} r_w}, a > 0 \quad \lambda_i = \frac{\omega_{w,i} r_w - v_{w,i}}{v_{w,i}}, a < 0 \quad (5)$$

where $\omega_{w,i}$ and r_w are the rotational velocity and effective radius of the wheel. α_i is the tyre slip angle defined as:

$$\alpha_i = \arctan\left(\frac{v_y + l_f \dot{\psi}}{v_x \mp d\dot{\psi}}\right) - \delta_i, i = 1, 2 \quad \alpha_i = \arctan\left(\frac{v_y - l_r \dot{\psi}}{v_x \mp d\dot{\psi}}\right) - \delta_i, i = 3, 4 \quad (6)$$

In order to describe the tyre force characteristics under the combined conditions, the weight functions $G_{x\alpha}$ and $G_{y\lambda}$ are introduced. By multiplying the weight functions with Eq. (4), the tyre force output can be obtained. The vertical forces $F_{z,i}$ are dependent on steady-state component of the load transfer which is a function of longitudinal and lateral accelerations:

$$F_{z,i} = \frac{m}{2(l_f + l_r)} \left(l_f g - h_{cg} \dot{v}_x \mp \frac{l_f h_{cg} \dot{v}_y}{d} \right), i = 1, 2 \quad F_{z,i} = \frac{m}{2(l_f + l_r)} \left(l_r g + h_{cg} \dot{v}_x \mp \frac{l_r h_{cg} \dot{v}_y}{d} \right), i = 3, 4 \quad (7)$$

where h_{cg} is the height of the center of gravity. Wheels' dynamic equation as follows:

$$I_w \dot{\omega}_{w,i} = T_{w,i} - F_{x,i} r_w - F_{z,i} f r_w \quad (8)$$

where T_w is the drive motor output torque. f is the rolling resistance coefficient.

2.2 Motor Model

The drive system employs direct drive with electric motors. The primary function of the drive motor system is to deliver the specified torque to each wheel as dictated by the controller. The simplified ideal closed-loop dynamics of the motor can be described as follows:

$$T_w = \frac{1}{\tau_1 s^2 + \tau_2 s + 1} T_c \quad (9)$$

where τ_1 and τ_2 are close-loop response times and represent the control characteristic of the motor’s field-oriented controller. T_c is motor torque command.

To simplify the FWIS actuator, the dynamic equation of the steer-by-wire (SBW) system can be expressed as follows:

$$I_{eq}\ddot{\delta}_i + B_{eq}\dot{\delta}_i + T_e + T_f = i_g T_{m,i} \tag{10}$$

where equivalent moment of inertia of the SBW system $I_{eq} = I_w + i_g^2 I_m$. i_g is the steering gear ratio. I_w and I_m are the moments of inertia of the wheel and steering motor. Equivalent damping coefficient of SBW system $B_{eq} = B_w + i_g^2 B_m$. B_w and B_m are damping factors of wheel steering and steering motor. $T_{m,i}$ is the steering motor output torque. T_e and T_f are the internal friction torque of the SBW system and aligning torque.

2.3 Path Tracking Model

The path-following model is depicted in Fig. 1. A linear two-degree-of-freedom (2-DOF) vehicle dynamic model is employed to generate the desired yaw rate for maintaining vehicle stability. The state space equation can be given as follows:

$$\dot{X} = AX + BU \tag{11}$$

where $\dot{X} = [\beta \ \dot{\psi} \ \theta \ Y]^T$ is the state variable set. β is the vehicle body side-slip angle. θ is the heading angle. $U = \delta_f$ is the input variable.

$$A = \begin{bmatrix} \frac{-2C_f+2C_r}{mv_x} & \frac{-2C_{fl}-2C_{rl}}{mv_x^2} - 1 & 0 & 0 \\ \frac{-2C_{fl}-2C_{rl}}{mv_x} & \frac{-2C_{fl}^2+2C_{rl}^2}{mv_x^2} & 0 & 0 \\ \frac{-I_z}{mv_x} & \frac{-2C_{fl}I_z-2C_{rl}I_z}{mv_x^2} & 0 & 0 \\ v_x \cos \theta & 0 & v_x \cos \theta - v_x \beta \sin \theta & 0 \end{bmatrix}, B = \begin{bmatrix} \frac{2C_f}{mv_x} \\ \frac{2C_{fl}}{mv_x} \\ \frac{I_z}{mv_x} \\ 0 \end{bmatrix} \tag{12}$$

3 Multi-Controller Integrated Control Strategy

Figure 2 depicts the overall control scheme, including a path tracking controller and a hierarchical controller. It provides the ability to accurately assess the impact of coordinated control.

3.1 Model Predictive Control

The path tracking can be formulated for MPC by the following optimization problem. The cost function consists of two objectives penalizing the deviation from predefined idealized trajectory $X_{ref,i}$ for the system states X_i and control inputs U_i :

$$J = \min \left[\sum_{i=1}^{N_p} (X_i - X_{ref,i})^T Q (X_i - X_{ref,i}) + \sum_{j=0}^{N_c-1} U_j^T R U_j \right] \tag{13}$$

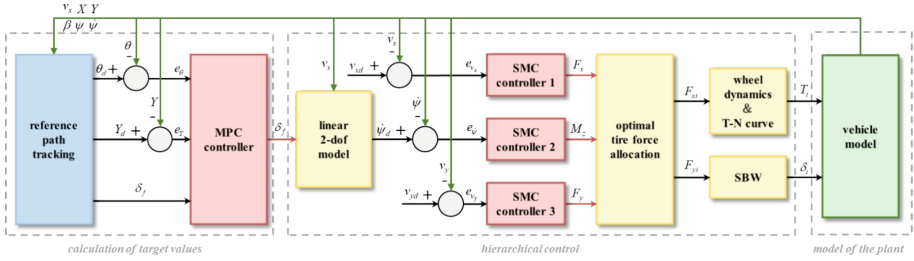


Fig. 2. Control system architecture.

where Q and R are the weight matrices of the states and control inputs. Subject to

$$X_i = f(X_i, U_i) \tag{14}$$

$$\delta_{\min} \leq \delta_i(k + j|k) \leq \delta_{\max}, j = 1, 2, \dots, N_c - 1 \tag{15}$$

3.2 Hierarchical Controller

The upper-level controller determines the desired forces and moment for tracking the desired path. The sliding mode control method is adopted to ensure the vehicle follows the reference states. The sliding surfaces are defined as follows.

$$S_1 = v_x - v_{xd}, S_2 = v_y - v_{yd}, S_3 = \psi - \psi_d, \tag{16}$$

To ensure that the errors between actual and desired values reach the sliding mode surface within a limited time and attenuate chattering, a combinatorial reaching law is applied in the controller:

$$\dot{S}_i = -\varepsilon_i \text{sat}(S_i) - k_i S_i \tag{17}$$

where ε_i and k_i are parameters of the controller. The required forces and moment are determined as follows:

$$F_{xd} = m[-\varepsilon_1 \text{sat}(S_1) - k_1 S_1 + a_x] \quad F_{yd} = m[-\varepsilon_2 \text{sat}(S_2) - k_2 S_2 + a_y] \tag{18}$$

$$M_{zd} = I_z[-\varepsilon_3 \text{sat}(S_3) - k_3 S_3 + \dot{\psi}] \tag{19}$$

The lower-level controller is used to realize better control performance through optimal tyre force allocation:

$$J = \min \sum_{i=1}^4 \frac{F_{x,i}^2 + F_{y,i}^2}{\mu^2 F_{z,i}^2} \tag{20}$$

where μ is the coefficient of road adhesion. The total F_x, F_y and M_z satisfy the equation and the linear constraints:

$$-0.9\mu F_{z,i} < F_{x,i}, F_{y,i} < 0.9\mu F_{z,i} - 0.9 \times \sqrt{2}\mu F_{z,i} < F_{x,i} \pm F_{y,i} < 0.9 \times \sqrt{2}\mu F_{z,i} \tag{21}$$

After the forces of each tyre are allocated, the motor model is used to transform the longitudinal force into drive or brake torque, and the lateral force into steering angle.

4 Simulation

In order to verify the effectiveness of the proposed integrated control strategy, the double line change (DLC) scenery is utilized to test the performance of the FWIS vehicle at different speeds.

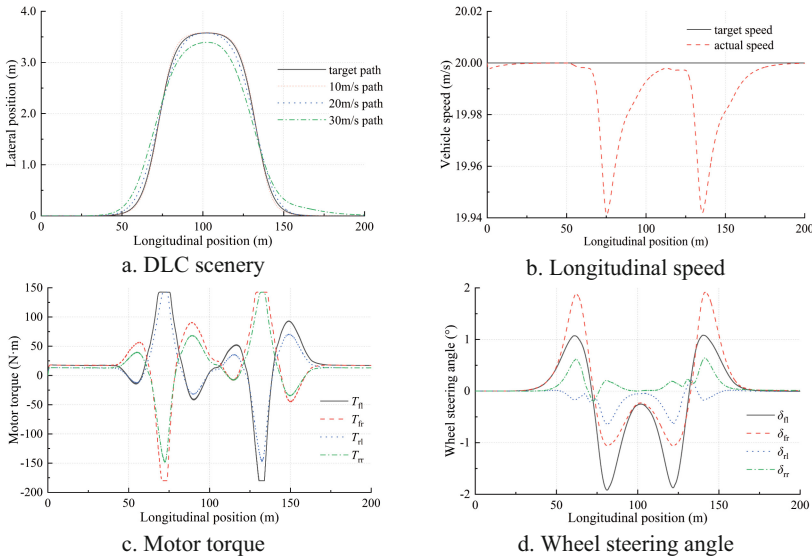


Fig. 3. Simulation result.

The simulation results are shown in Fig. 3a. Further analysis of the simulation results at 20 m/s speed is shown in Figs. 3b–d. The results show that the FWIS coordinated control maintains good speed and path tracking control accuracy from low to high speeds. Although there are some constraints and influences on the actuators, the independent wheels can still maintain coordinated torque and cornering control.

5 Conclusion

A FWIS electric vehicle path tracking system dynamics model considering nonlinear tyre and motor characteristics is proposed. In order to achieve coordinated stabilization of multiple actuators and the vehicle, a multi-controller integrated control strategy is proposed. The longitudinal and lateral forces are optimally distributed to the actuator layer of each wheel. Simulation results show that the method can achieve good path tracking performance at different driving speeds.

References

1. Pacejka, H.: *Tire and Vehicle Dynamics*, 3rd edn. Elsevier, Oxford (2012)
2. Peng, H., et al.: Path tracking and direct yaw moment coordinated control based on robust MPC with the finite time horizon for autonomous independent-drive vehicles. *IEEE Trans. Veh. Technol.* **69**(6), 6053–6066 (2020)
3. Vignati, M., et al.: A cooperative control strategy for yaw rate and sideslip angle control combining torque vectoring with rear wheel steering. *Vehicle Syst. Dyn.* **60**(5), 1668–1701 (2022)
4. Warth, G., et al.: Design of a central feedforward control of torque vectoring and rear-wheel steering to beneficially use tyre information. *Vehicle Syst. Dyn.* **58**(12), 1789–1822 (2020)
5. Liang, Y., et al.: Yaw rate tracking-based path-following control for four-wheel independent driving and four-wheel independent steering autonomous vehicles considering the coordination with dynamics stability. *Proc. Inst. Mech. Eng., Part D: J. Autom. Eng.* **235**(1), 260–272 (2021)
6. Liang, Y., et al.: Integrated lateral control for 4WID/4WIS vehicle in high-speed condition considering the magnitude of steering. *Vehicle Syst Dyn* **58**(11), 1711–1735 (2019)

Open Access This chapter is licensed under the terms of the Creative Commons Attribution 4.0 International License (<http://creativecommons.org/licenses/by/4.0/>), which permits use, sharing, adaptation, distribution and reproduction in any medium or format, as long as you give appropriate credit to the original author(s) and the source, provide a link to the Creative Commons license and indicate if changes were made.

The images or other third party material in this chapter are included in the chapter's Creative Commons license, unless indicated otherwise in a credit line to the material. If material is not included in the chapter's Creative Commons license and your intended use is not permitted by statutory regulation or exceeds the permitted use, you will need to obtain permission directly from the copyright holder.





Using a Smartwatch to Evaluate Subjective Ratings of Driving Functions

Panzer Anna^(✉), Lausch Hendryk, Iatropoulos Jannes, and Henze Roman

Institute of Automotive Engineering, Technische Universität Braunschweig,
Hans-Sommer-Straße 4, 38106 Braunschweig, Germany
a.panzer@tu-braunschweig.de

Abstract. Automating the driving task fundamentally changes the user's driving experience. The driving function now dictates the driving style, previously a product of individual decisions by the driver. Consequently, understanding what constitutes a comfortable driving style becomes essential for ensuring the optimal design of driving functions. This knowledge can be acquired through user studies. As self-reports are often distorted, physiological data can help provide a more objective insight into the emotions and feelings of the test subjects. Smartwatches serve as a convenient and uncomplicated measuring device in this context. The aim of this paper is to investigate whether the accuracy of a smartwatch is sufficient to infer user perceptions and subjective ratings. To achieve this, a subject study is conducted using a driving simulator.

Keywords: driver-vehicle systems · automated driving · advanced driver assistance systems · user study · driving simulator · driver state

1 Introduction

Human factors play an increasingly important role in the evolution of automobile development. The growing integration of vehicle automation, from assistance systems to autonomous driving, reshapes the traditional driver's role. Drivers are transitioning into more passive roles, resembling passengers, as vehicles assume greater control. Consequently, the conventional perception of the driving experience undergoes a major transformation [1].

To enhance the acceptance of novel driving functionalities, assessing the subjective driver experience is crucial. Recognizing that self-reports may be subject to distortion or inaccuracy, it is useful to employ objective measures based on physiological parameters. Some studies have previously identified correlations between (dis-)comfort or trust and physiological responses in automated driving functions. Common physiological measures for assessing the driver's mood and emotions are electroencephalography (EEG), electrocardiography (ECG), photoplethysmography (PPG), heart rate (HR), heart rate variability (HRV), electrodermal activity (EDA) and eye tracking [2].

Given the widespread popularity of smartwatches, they offer a convenient option for capturing physiological data in real-life scenarios. One notable advantage is the

ability to acquire data in a naturalistic setting. This paper explores the adequacy of smartwatch accuracy in monitoring the driver's state while experiencing an automated driving function.

2 Related Work

This paper focuses on the physiological parameters of electrodermal activity and photoplethysmography. EDA describes changes in the bioelectrical properties of the skin. The eccrine sweat glands in the skin are controlled by the sympathetic branch of the autonomic nervous system and respond to psychological stimuli. PPG sensors use an optical technique to detect changes in blood volume within the microvascular bed of tissue. Cardiovascular activity, specifically heart rate, can also be considered an arousal indicator. But unlike EDA, heart rate is regulated by both the sympathetic and parasympathetic nervous systems, making it less clear as an indicator of emotional arousal [2, 3].

Previous studies have examined the relationship between physiological data and subjective ratings. Dillen et al. [4] observed a correlation between self-reported comfort and skin conductance in their study. They demonstrated that the type of driving event and the interaction with other road users influence all physiological responses. They asserted that electrodermal activity could predict comfort and anxiety. In a study by Beggiato et al. [5], the correlation between self-reported discomfort and physiological parameters was investigated using a wearable device for measuring. Unlike other studies, no correlation was found between skin conductance level (SCL) and discomfort. However, HR was identified as a significant parameter. The study reported that HR consistently decreased during discomfort periods and returned to prior levels afterward. It was concluded that specific uncomfortable situations affect physiological parameters like HR, whereas situations with moderate to low reported discomfort did not show any changes.

This study employs the Empatica EmbracePlus, a medical wearable device designed to monitor and analyse a range of physiological parameters, including SCL and PPG. The application of the device has been demonstrated in other studies before. Menghini et al. [6] identified significant discrepancies in skin conductance measurements. Several participants exhibited flat and nonresponsive SC before the recording began. They suggested that the E4, a comparable model to the Empatica EmbracePlus, could be reliably used for measuring average HR in healthy adults. This implication also extends to HRV measures, but only under static and stationary conditions, indicating that the quality of the measurements is highly dependent on motion artefacts. This aligns with the findings of Milstein et al. [7].

The device was also used in studies relating to driver monitoring. Gruden et al. [8] utilised an Empatica E4 wristband and investigated the device's accuracy during manual driving. They identified substantial standard errors and elevated deviations in SCL and HRV measurements resulting from hand movements while steering. In a related study, Stephenson et al. [9] investigated the impact of unexpected events during autonomous driving. They found that elevated electrodermal activity persisted after such events, although they did not identify any statistically significant differences in heart rate.

3 Study Description

3.1 Participants

Before the study begins, participants are required to complete a preliminary questionnaire designed to provide a more detailed characterization of the test subject pool. There was a total of 10 participants recruited for this study (33% females) who were between 20 and 35 years old ($M = 28.6$, $SD = 3.2$). Six participants have a professional connection to automated driving. Most of the participants use a car at least three times a week or more.

3.2 Experiment Equipment

The driving simulation system used for the study was the Dynamic Vehicle Road Simulator from the Institute of Automotive Engineering, as shown in Fig. 1 (left). This setup features a modified Volkswagen Golf 7 vehicle, cut off behind the front seats. The cabin is mounted on a HEXaDRIVE motion platform from Simtec Systems GmbH (Braunschweig, Germany). Five 48-inch curved monitors provide a 180° visualisation of driving scenarios. The software utilised for the simulation is IPG CarMaker. The mockup is fully functional, including feedback from an electric power steering unit.

The Empatica EmbracePlus (Empatica Srl, Milan, Italy) smartwatch was selected for the study. This device is equipped with a ventral electrodermal activity sensor, which samples at 4 Hz, and a 4-channel multi-wavelength photoplethysmography sensor with a sampling frequency of 64 Hz. The internal Empatica software calculates the systolic peaks. The watch wristband was placed on the participants' non-dominant wrist and fastened as tightly as was comfortable for them. The wearable also collects acceleration data via a high-precision 3D microelectromechanical accelerometer, which monitors wrist movements. The sampling frequency of the accelerometer is 64 Hz.

3.3 Procedure

The entire procedure takes approximately one hour. The first step involves a detailed briefing of the test subjects, during which they are informed about the study's objective and instructed on how to use the driving simulator. Following this, a reference measurement for the physiological parameter is recorded. A familiarisation drive is conducted, lasting approximately ten minutes, to acclimate the test subjects to the driving simulator.

The actual test drive consists of four separate drives, each covering a 4-km route through an urban environment. These drives are conducted automatically. Each drive incorporates a potentially uncomfortable scenario: (1) a cyclist crosses the road from a parking space, (2) a vehicle pulls out of a parking spot, (3) a skateboarder crosses the road, and (4) a vehicle exits from a ramp. These events are strategically positioned at various points along the route to introduce an element of surprise. Participants are not informed about these specific situations during the initial briefing of the study.

In addition to measuring physiological data, we also assess the participants' subjective perceptions. We utilise an adapted questionnaire from Morra et al. [10] to identify their reactions to the test events. Therefore, we employ a five-point scale. Furthermore,



Fig. 1. Dynamic Vehicle Road Simulator (DVRS) of the Institute of Automotive Engineering (left) and scenario (1) with a crossing cyclist (right)

we assess the participants' subjective perceptions of comfort and safety for the overall drive using a five-point scale also.

4 Results

The results of the subjective ratings indicate that all participants perceived the four situations of the test drive as dangerous ($M = 4.44$, $SD = 0.71$) and surprising ($M = 4.27$, $SD = 0.65$). Conversely, the ride was generally perceived as comfortable and safe ($M = 4.55$, $SD = 0.49$).

Although the subjective ratings suggest a physiological reaction, the results indicate that there are problems in the correct measurement of the data from the Empatica EmbracePlus. Nine participants showed a flat and non-responsive SCL measurement. Only one participant showed reactions to the events, as shown in Fig. 2. However, the reactions were not significant either. In summary, the Empatica EmbracePlus was unable to provide reliable measurements. Given that the device has previously demonstrated that the quality of the data is highly sensitive to wrist movement, we also analysed the data from the accelerometer. As the entire drive was automatic, there was no movement at the wrist and it did not differ between scenarios.

A possible reason for the results could be that the participants had to adjust the wristband themselves, so it may not have been worn tightly enough. In some cases, the wearable was placed on dry skin. However, we also placed a few drops of warm water with the other participants and this did not make a significant difference to the results [11].

Furthermore, SCL measurements are typically obtained from the distal or intermediate phalanges of the ring and index fingers, which are areas with a greater density of active eccrine sweat glands [11]. The EmbracePlus, like many wearables, employs wrist sensors to measure skin conductance. Given that the wrist is less responsive to skin conductance, an underestimation of parameters could be anticipated [12].

The results for heart rate also present challenges. For the calculation, we utilized the internal Empatica software, which identifies the systolic peaks in the PPG signal. The number of peaks detected in a 10-s sliding window was multiplied by six to obtain the HR in beats per minute (BPM). We applied z-standardisation to the data to account

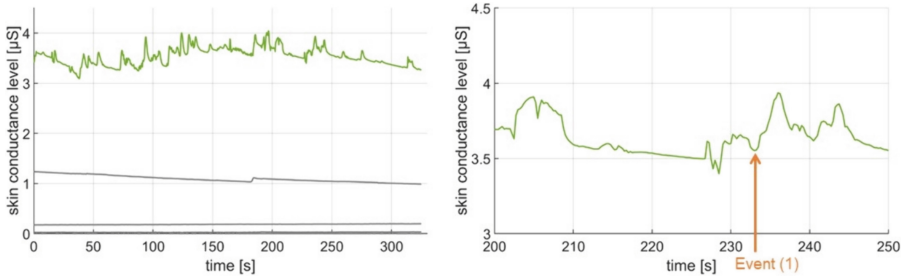


Fig. 2. Skin conductance level over all participants for scenario (1) (left) and the reaction to crossing cyclist from the only participant with a reaction (right)

for the individual variability of physiological responses. We examined two periods: 30 s before the stop and 30 s after the stop, as this was chosen in other research, as in [9]. The exemplary results are shown in Table 1.

Table 1. Results of the z-standardized HR before and after scenario (1) and (3)

Event	Before	After
scenario (1)	M = 0.15, SD = 1.77	M = 0.05, SD = 0.71
scenario (3)	M = 0.21, SD = 1.19	M = -0.07, SD = 0.43

It is not possible to detect a significant difference between the two periods. The HR over the entire trial is subject to considerable fluctuations. This is reflected in the high values for the standard deviation.

5 Conclusion

The results presented in this study investigate the physiological parameters measured by the Empatica EmbracePlus smartwatch. Despite the participants reporting that the situations during the study were perceived as dangerous, the SCL showed nearly no reaction. The same applies to HR, which demonstrated considerable variability. It is important to note that the sample size of 10 test subjects is relatively small, and that a larger pool of test subjects could provide a more reliable database. For future research, it would be beneficial to conduct a study utilising additional EDA and ECG sensors in order to rule out the possibility that the participants have no physiological reaction to the events.

References

1. Elbanhawi, M., Simic, M., Jazar, R.: In the passenger seat: investigating ride comfort measures in autonomous cars. *IEEE Intell. Transp. Syst. Mag.* 7(3), 4–17 (2015)

2. Möhring, W., Schlütz, D. (eds.): *Handbuch standardisierte Erhebungsverfahren in der Kommunikationswissenschaft*. Springer, Heidelberg (2013)
3. Allen, J.: Photoplethysmography and its application in clinical physiological measurement. *Physiol. Meas.* **28**(3), R1 (2007)
4. Dillen, N., et al.: Keep calm and ride along: Passenger comfort and anxiety as physiological responses to autonomous driving styles. In: *Proceedings of the 2020 CHI conference on human factors in computing systems*, pp. 1–13 (2020)
5. Beggiato, M., Hartwich, F., Krems, J.: Physiological correlates of discomfort in automated driving. *Transport. Res. F: Traffic Psychol. Behav.* **66**, 445–458 (2019)
6. Menghini, L., Gianfranchi, E., Cellini, N., Patron, E., Tagliabue, M., Sarlo, M.: Stressing the accuracy: Wrist-worn wearable sensor validation over different conditions. *Psychophysiology* **56**(11), e13441 (2019)
7. Milstein, N., Gordon, I.: Validating measures of electrodermal activity and heart rate variability derived from the empatica E4 utilized in research settings that involve interactive dyadic states. *Front. Behav. Neurosci.* **14**, 148 (2020)
8. Gruden, T., Stojmenova, K., Sodnik, J., Jakus, G.: Assessing drivers' physiological responses using consumer-grade devices. *Appl. Sci.* **9**(24), 5353 (2019)
9. Stephenson, A.C., et al.: Effects of an unexpected and expected event on older adults' autonomic arousal and eye fixations during autonomous driving. *Front. Psychol.* **11**, 571961 (2020)
10. Morra, L., Lamberti, F., Praticó, F.G., La Rosa, S., Montuschi, P.: Building trust in autonomous vehicles: Role of virtual reality driving simulators in HMI design. *IEEE Trans. Veh. Technol.* **68**(10), 9438–9450 (2019)
11. Boucsein, W., Fowles, D.C., Grimnes, S., Ben-Shakhar, G., Roth, W.T., et al.: Publication recommendations for electrodermal measurements. *Psychophysiology* **49**(8), 1017–1034 (2012)
12. van Dooren, M., Janssen, J.H.: Emotional sweating across the body: Comparing 16 different skin conductance measurement locations. *Physiol. Behav.* **106**(2), 298–304 (2012)



Open Access This chapter is licensed under the terms of the Creative Commons Attribution 4.0 International License (<http://creativecommons.org/licenses/by/4.0/>), which permits use, sharing, adaptation, distribution and reproduction in any medium or format, as long as you give appropriate credit to the original author(s) and the source, provide a link to the Creative Commons license and indicate if changes were made.

The images or other third party material in this chapter are included in the chapter's Creative Commons license, unless indicated otherwise in a credit line to the material. If material is not included in the chapter's Creative Commons license and your intended use is not permitted by statutory regulation or exceeds the permitted use, you will need to obtain permission directly from the copyright holder.





Speed Profile Generation for a Dual Motor Equipped Electrified Series Hybrid Tracked Vehicle Through Dynamic Programming Based Energy Optimization Procedure

Ismail Gocer¹  and S. Caglar Baslamisli² 

¹ Modeling and Simulation Engineer, FNSS Savunma Sistemleri A.S, Ankara, Turkey
ismail.gocer@fnss.com.tr

² Mechanical Engineering Department, Hacettepe University, Ankara, Turkey
scaglarb@hacettepe.edu.tr

Abstract. Electrification is a widely explored area in many fields and is becoming a widely researched topic in tracked vehicles. Achieving efficient operation for such vehicles is crucial similar to traditional vehicles. This paper introduces a speed profile generation procedure for a dual track – series hybrid tracked vehicle with an emphasis on fuel economy and trip time optimization. A Dynamic Programming method is proposed in spatial domain, considering the properties of predefined road geometries. The study includes examination of speed and torque estimation of the sprockets, particularly during steering maneuvers. Unlike wheeled vehicles, tracked vehicles have to overcome the turning resistance moment of skid steered tracks. Taking these dynamics into account, the study investigates efficient operation, presenting over a predefined road track including straight road, inclined road and curve sections, discussing the tradeoff between fuel economy and trip time optimality. As the result of problem solution, speed profiles are generated, and operation trends of the powertrain components are discussed.

Keywords: Dynamic Programing · Electrified Tracked Vehicles · Skid Steer · Time Optimality · Energy Optimality

1 Introduction

Energy efficient operation is the main driving force of improvement of hybrid electrified vehicles. This subject is mainly researched for straight road conditions, utilizing different type of control strategies e.g. rule based control, power following control, ECMS, etc. Dynamic Programming (DP) is generally used in these studies as benchmark of the optimal control. Most studies apply the rules of the DP in time domain, where speed profile is predefined. A good example for a dual track hybrid vehicle is given in [1], where energy management system is discussed for a tracked vehicle on straight road and includes also cornering sections in time domain. [2] discusses the improvement of fuel economy of a wheeled hybrid vehicle for an upcoming uphill and downhill

scenario. In [3] a speed profile generation study for a conventional truck is presented for upcoming inclined roads. This study is an example of the spatial domain DP problem applications. [4] provides a sample of spatial domain problem for a wheeled EV vehicle, covering energy efficiency of electrical motors and trip time minimization tradeoff, for a predefined track including curved road sections. Adaptive on-line optimization strategies are covered in literature, however scope of this paper limited with predefined road profile and off-line problem solution.

This study aims to provide optimized target speed profiles for a series hybrid – electrified tracked vehicle which provides efficient operation in terms of fuel economy & trip time. The DP approach is applied to solve the problem in spatial domain for predefined road geometries. Using the characteristics of created road profile sections, e.g. inclination, turning radius of the curves; required torque, speed and power demand of electrical motors are estimated. Trip time, fuel consumption and losses of other powertrain components are the key objectives used in DP to be minimized. The output of this problem is the optimized target speed profile. For a dual-motor, series hybrid tracked vehicle the traction is provided by only the electric motors. Supply of the electrical motors' power demand is shared between the generator and the battery with respect to applied control strategy. This relation is presented in Fig. 1. In the figure, two sided arrows show the possible bidirectional power flow.

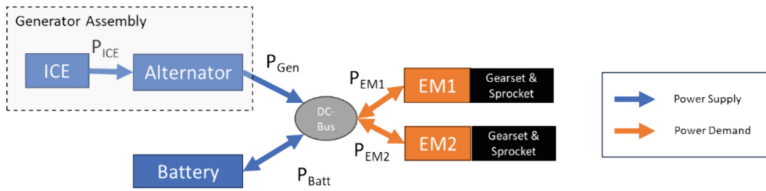


Fig. 1. Power flow diagram of the dual motor – series hybrid tracked vehicle

Unlike wheeled vehicles, braking of electrical motors does not occur only while slowing down; the inner track brakes during a steering maneuver to overcome the turning resistance moment of the skid steered tracks. In this scenario, outer tracks consume the supplied traction power, whereas inner track regenerates the kinetic energy during braking. In most generic form, required dynamic torque for electrical motors can be estimated as in Eq. (1) for a cornering maneuver [1]. In the equation, first square bracket section includes required torque due to steady state maneuver (Rolling resistance, resistance due to slope and turning resistance with respectively), whereas second square bracket section covers the inertial moments due to longitudinal and yaw motion with respectively. In the equation r_{spr} describes the sprocket radius, i_0 is cumulative gear ratio of the driveline, η is driveline efficiency, B is the tread of the vehicle and $\dot{\omega}_{EM_{o-i}}$ is the acceleration of outer and inner electrical motors with respectively.

$$\tau_{EM_{o-i}} = \left[(F_{Roll} + F_{Grad} \pm F_{Turn}) \frac{r_{spr}}{i_0 \eta} \right] + \left[\frac{m r_{spr}^2}{i_0^2 \eta} \frac{R}{(R \pm B/2)} \pm \frac{I_z r_{spr}^2}{i_0^2 \eta B (R \pm B/2)} \right] \dot{\omega}_{EM_{o-i}} \quad (1)$$

F_{Turn} parameter given in Eq. (1) occurs due to turning moment resistance of the tracks and it is expressed in Eq. (2). μ_t is effective turning resistance coefficient which

decreases with respect to increasing turning radius, as expressed in [5]. For the case of $R > B/2$ electrical motor velocities can be calculated as shown in Eq. (3) for outer and inner motors with respectively. V_c is the velocity of the centerline of the vehicle.

$$F_{Turn} = \frac{W \cdot \mu_t(R) \cdot L}{4 \cdot B} \quad (2)$$

$$\omega_{EM_{o-i}} = \left(V_c \cdot \left(1 \pm \frac{B/2}{R} \right) \right) \cdot \frac{i_0}{r_{spr}} \quad (3)$$

2 Formulation of the Dynamic Programming Problem

To reduce the burden of dimensionality problem of DP, it is assumed that vehicle perfectly follows perfectly the trajectory at each stage and lateral dynamics are only reflected in kinematic relations for the tracks in Eq. (3) and in Eq. (1) for calculating the electrical motor torques. Main dimensions of the DP problem are hence selected as 1) Distance, 2) Longitudinal velocity, 3) Longitudinal acceleration, 4) SoC of the battery and 5) Alternator torque. Velocity and SoC are the main states; longitudinal acceleration and alternator torque are considered as the inputs for the optimal control problem. Note that alternator in generator set is assumed operating in torque mode, altering the applied brake torque to provide required power output. Contrarily internal combustion engine operates in speed mode, maintaining its speed at rated speed. Therefore, control variable in the generator assembly is considered as only the alternator torque. At each stage of DP, longitudinal velocity and SoC at next stage is calculated with respect to corresponding inputs as shown in Eqs. (4) and (5). v_{k+1} is the calculated velocity at next stage using long. Acceleration input $a_{i,k}$ and $\Delta t_{j,k}$ which is the duration to complete constant road segment distance Δs . SoC_{k+1} is the calculated SoC at next stage using the battery current I_{Batt} and maximum charge capacity Q_{max} .

$$x_{1k+1} = v_{k+1} = v_{j,k} + a_{i,k} \cdot \Delta t_{j,k}, \text{ where } \Delta t_{j,k} = \frac{\Delta s}{v_{j,k}} \quad (4)$$

$$x_{2k+1} = SoC_{k+1} = SoC_k + I_{Batt} \cdot \frac{\Delta t_{j,k}}{Q_{max}} \quad (5)$$

In Eq. (5) battery current is calculated according to Eq. (6). V_{oc} is open circuit voltage and R_{Batt} is the internal resistance of the battery. Battery power depends on the power demand of electrical motors and power supply of the generator as defined in Eq. (7). If the generator power supply exceeds the electrical power demand of the motors, it charges the battery, otherwise they both supply the electrical motors. Also, battery is charged through recuperation during the braking of electrical motors.

$$I_{Batt \text{ chg-dischg}} = \frac{\mp V_{oc} \pm \sqrt{V_{oc}^2 \pm 4R_{Batt} \cdot P_{Batt}}}{2R_{Batt}} \quad (6)$$

$$P_{Batt} = -((P_{Elec-EM-o} + P_{Elec-EM-i}) - P_{Elec-Gen}) \quad (7)$$

The cost function of the DP problem, $g_k(u_k, x_k)$ consists of three main parts as shown in Eq. (8). Trip time cost and energy related cost have their own weighting parameters: w_T and w_E respectively. Energy cost include the fuel consumption, and power losses of the battery and the electrical motors. Constraints defined by restrictions of components and physical limits are penalized by the last term “ $L_{Constraints}$ ”. While solving the DP problem backwards from “ $N-1$ ”th stage back to 1st stage, minimum cost at each stage is stored in the so called “cost-to-go matrix” (Eq. (9)), and corresponding optimal control values ($u_k \rightarrow$ Long. Acceleration & Generator torque) are stored in other matrices. After these steps are completed, a forward calculation loop starts to obtain optimal velocity profile, and SoC calculations according to defined initial conditions. Constraints are applied in the problem according to inequalities (10), (11), (12), (13), (14) and (15):

$$g_k(u_k, x_k) = w_T \cdot \Delta t_{j,k} + w_E \cdot (Fc + P_{Losses}) \cdot \Delta t_{j,k} + L_{Constraints} \quad (8)$$

$$J_k(x_k) = \min_{u_k} (g_k(u_k, x_k) + J_{k+1}(f(u_k, x_k))) \quad (9)$$

$$\omega_{EMmin} \leq \omega_{EMo-i} \leq \omega_{EMmax} \quad (10)$$

$$\tau_{EMmin} \leq \tau_{EMo-i} \leq \tau_{EMmax} \quad (11)$$

$$|I_{Batt}| < I_{max} \quad (12)$$

$$a_{x-min} \leq a_x \leq a_{x-max} \quad (13)$$

$$v_x \leq v_{max-limit} \quad (14)$$

$$v_x \leq \sqrt{a_{y-max} \cdot R} \quad (15)$$

As the nature of DP, final stage has a separate solution step, where a special penalty for velocity and for battery SoC, as shown in Eq. (16), enforcing them to reach their final value at N^{th} stage to desired value Vel_{Fin} and SoC_{Fin} . Quadratic formation of these penalties is beneficial in problem solution of the DP method.

$$J_N(x_N) = g_N(x_N) + (Vel_N - Vel_{Fin})^2 \cdot 100 + (SoC_N - SoC_{Fin})^2 \cdot 10^6 \quad (16)$$

3 Results of Speed Profile Optimization

The DP problem is solved based on given road profile in Fig. 2. To present the concept in a clear way, length of the designed road is kept short. The profile consists of curvature sections as well as gradient sections including ascending and descending 10% slope. Maximum speed limit is shown in Fig. 2-b calculated and used as a constraint for DP, considering longitudinal and lateral acceleration limits. Solutions are obtained for three different weighting as shown in Fig. 3: Solution 1 reaches to higher speeds at road segments compared to others, whereas Solution 3 have overall better fuel economy as numeric results are listed in Table 1.

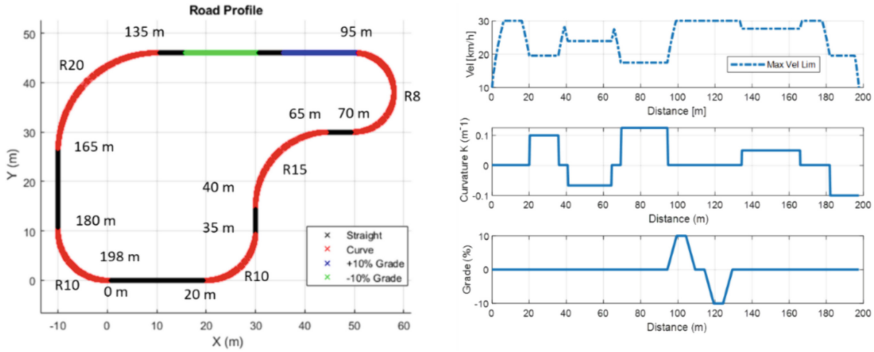


Fig. 2. a) Road Profile b) Velocity Limit & Road Data

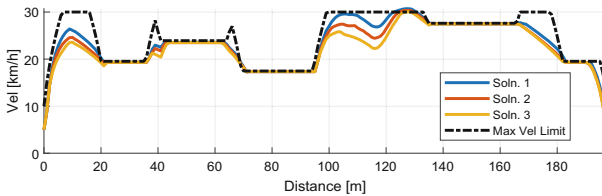


Fig. 3. Velocity profile results for 3 different Time – Fuel Cons. Tradeoff weightings

Table 1. Results for 3 different Time – Fuel Cons. Tradeoff weightings

Solution #	Duration (s)	Total Fuel Cons. (ml)	Final SoC
1	32.09	151.0	59.98
2	32.74	149.5	59.98
3	33.27	148.8	59.98

In Fig. 4 operation results for powertrain components are presented. Note that sign of the power values are with respect to the component perspective. For example, negative battery power means, power is distributed from the battery, whereas positive sign corresponds to power is absorbed: charging. According to results, alternator usage is more aggressive in Solution 1 which results with higher fuel consumption. At acceleration phases, alternator provides power supply, whereas, at near steady state velocity regions, flat road sections, alternator doesn't contribute. Battery is charged starting from about 70 m up to start of the +10% gradient uphill, then battery power is used at downhill and straight segments. It is also observed that the battery is slightly charged before R10 and R15 curve sections. At the end of 200 m road profile, SoC values and velocity get back to ~60% and ~5 km/h reaching to their initial values as enforced in DP problem.

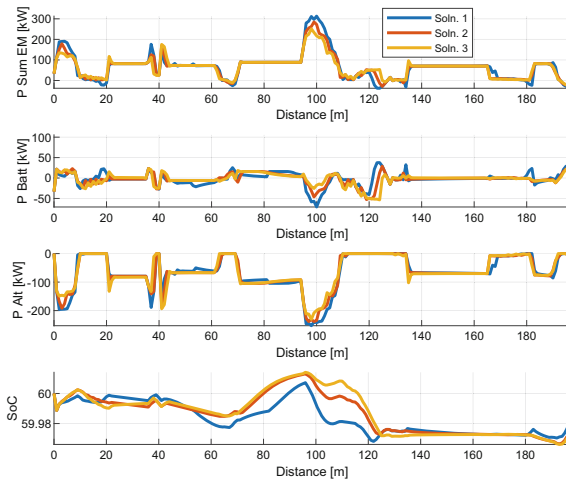


Fig. 4. Operation of the powertrain components

4 Conclusion

This study covers a 5D Dynamic Programming method for a Dual Motor – Series Hybrid Tracked vehicle. In the study, speed profile generation method is explained on a predefined road which cover curves, and inclination. According to results, tradeoff between fuel economy, and trip time can be presented operation of powertrain components are observed.

References

1. Zou, Y., Sun, F., Hu, X., Guzzella, L., Peng, H.: Combined optimal sizing and control for a hybrid tracked vehicle. *Energies* **5**(11), 4697–4710 (2012)
2. Kural, E., Guvenc, B.A.: Predictive-equivalent consumption minimization strategy for energy management of a parallel hybrid vehicle for optimal recuperation. *J. Polytech.* **18**(3), 113–124 (2015)
3. Hellström, E., Ivarsson, M., Åslund, J., Nielsen, L.: Look-ahead control for heavy trucks to minimize trip time and fuel consumption. *Control Eng. Pract.* **17**(2), 245–254 (2009)
4. Winter, C., de Castro, R.: Optimal Velocity Profile Generation for Semi-Autonomous Vehicles Deutsches Zentrum für Luft- und Raumfahrt (DLR), Oberpfaffenhofen
5. Ehlert, W., Hug, B., Schmid, I.C.: Field measurement and analytical models as a basis of test stand simulation of the turning resistance of tracked vehicles. *J. Terramechanics* **29**, 57–69 (1992)






Open Access This chapter is licensed under the terms of the Creative Commons Attribution 4.0 International License (<http://creativecommons.org/licenses/by/4.0/>), which permits use, sharing, adaptation, distribution and reproduction in any medium or format, as long as you give appropriate credit to the original author(s) and the source, provide a link to the Creative Commons license and indicate if changes were made.

The images or other third party material in this chapter are included in the chapter's Creative Commons license, unless indicated otherwise in a credit line to the material. If material is not included in the chapter's Creative Commons license and your intended use is not permitted by statutory regulation or exceeds the permitted use, you will need to obtain permission directly from the copyright holder.





Energy and Time Optimal Control of Autonomous Vehicles by Using Frenet Frame Modelling and over-Actuation

Wenliang Zhang¹ , Lars Drugge¹ , Mikael Nybacka¹ ,
Jenny Jerrelind^{1,2} , Derong Yang³, Rudolf Reiter⁴, Jonathan Frey⁴,
and Annika Stensson Trigell^{1,2} 

¹ Vehicle Dynamics, Department of Engineering Mechanics,
KTH Royal Institute of Technology, 10044 Stockholm, Sweden
wez@kth.se

² Centre for ECO2 Vehicle Design, KTH Royal Institute of Technology,
100 44 Stockholm, Sweden

³ Department of Vehicle Energy and Motion Control, Volvo Car Corporation,
405 31 Gothenburg, Sweden

⁴ Department of Microsystems Engineering, University of Freiburg,
79110 Freiburg im Breisgau, Baden-Württemberg, Germany

Abstract. Autonomous driving and electrification make over-actuation technologies more feasible and advantageous. Integrating autonomous driving with over-actuation allows for the effective use of their respective strengths, e.g., for studying energy and time optimal control. To model AVs, several vehicle coordinate systems have been used, e.g., Cartesian, Frenet and spatial coordinates. The present study aims to achieve energy and time optimal control of autonomous vehicles by using Frenet frame modelling and over-actuation. This study enhances the existing Frenet-based modeling by incorporating double-track dynamic vehicle models and torque vectoring. The problem is formulated in an optimal control framework, with carefully designed cost function terms and constraints. Two control strategies are examined, one for minimising travel time and the other for jointly optimising energy consumption and travel time. The results indicate that by considering both energy and time in the formulation, the energy consumption can be apparently reduced while the travel time is merely slightly increased.

Keywords: Energy efficient control · Time optimal control · Frenet frame · Over-actuation · Autonomous vehicle · Dynamic model · Torque vectoring · Vehicle dynamics

The authors gratefully acknowledge the financial support from the Swedish Electromobility Centre (SEC), the Swedish Energy Agency (Energimyndigheten), the Transport Research Environment with Novel Perspectives (TRENOP) and the Centre for ECO2 Vehicle Design at KTH Royal Institute of Technology, as well as the Karl Engver Foundation.

1 Introduction

Autonomous vehicles (AVs) have been advancing rapidly in recent years, primarily attributed to their potential in enhancing road safety and transport efficiency. In the meantime, vehicles are becoming increasingly electrified, making over-actuation technologies more feasible and advantageous.

There have been extensive studies exploring torque vectoring for enhancing vehicle safety, e.g., [1, 2], and energy efficiency, e.g., [3–5]. It is clear that combining autonomous driving with over-actuation technologies allows for the effective use of their respective strengths. For example, previous studies [6–8] have explored active camber, four-wheel steering and their integrations for improving the active safety of over-actuated AVs.

To model AVs, several vehicle coordinate systems have been used, including Cartesian, Frenet and spatial coordinates [9–12]. The spatial transformation allows for the natural consideration of obstacle constraints on the state vector [12], and the Frenet transformation facilitates a singularity-free formulation [13, 14]. Still, these transformations and formulations are either not implemented with dynamic vehicle models or not for over-actuated applications.

Based on the reviewed literature, the present study aims to achieve energy and time optimal control of autonomous vehicles by using Frenet frame modelling and over-actuation. This study enhances the existing Frenet-based modeling by incorporating double-track dynamic vehicle models and torque vectoring. This integration aims to leverage the advantages of both Frenet frame modelling and advanced models. Utilising this modelling method, this study focuses on optimising energy consumption and travel time simultaneously.

2 Vehicle Dynamics Modelling

By using the Frenet frame, the vehicle dynamics are modelled and presented in this section. The model includes a double-track dynamic vehicle model, road geometry, the Dugoff tyre model [15], load transfer as well as the possibility for controlling the individual wheel torques, i.e., torque vectoring. The vehicle motions in the longitudinal, lateral and yaw directions, the vehicle positions in the Frenet frame [13], as well as the wheel dynamics are described with the following equations:

$$m\dot{v}_x = mv_y\omega_z - (F_{yfl} + F_{yfr}) \sin \delta_f + (F_{xfl} + F_{xfr}) \cos \delta_f + F_{xrl} + F_{xrr} - C_d A_f \frac{D_a v_x^2}{2} \quad (1)$$

$$m\dot{v}_y = -mv_x\omega_z + (F_{yfl} + F_{yfr}) \cos \delta_f + F_{yrl} + F_{yrr} + (F_{xfl} + F_{xfr}) \sin \delta_f \quad (2)$$

$$I_z \dot{\omega}_z = l_f (F_{yfl} + F_{yfr}) \cos \delta_f - l_r (F_{yrl} + F_{yrr}) + \frac{B_f}{2} (F_{yfl} - F_{yfr}) \sin \delta_f + \frac{B_r}{2} (F_{xfr} - F_{xfl}) \cos \delta_f + \frac{B_r}{2} (F_{xrr} - F_{xrl}) + l_f (F_{xfl} + F_{xfr}) \sin \delta_f \quad (3)$$

$$\dot{\alpha} = \omega_z - \kappa_c(s) \frac{v_x \cos \alpha - v_y \sin \alpha}{1 - n\kappa_c(s)} \quad (4)$$

$$\dot{s} = \frac{v_x \cos \alpha - v_y \sin \alpha}{1 - n\kappa_c(s)} \quad (5)$$

$$\dot{n} = v_x \sin \alpha + v_y \cos \alpha \quad (6)$$

$$I_{wi}\dot{\omega}_i = T_i - r_e F_{xi}. \quad (7)$$

v_x and v_y are vehicle velocities at the centre of gravity (CoG), ω_z is the yaw rate, and ω_i is the angular velocity of the wheels. α denotes the yaw deviation with respect to the centreline of the road, and n and s are the lateral position deviation from the road centreline and the distance travelled along the road centreline, respectively. F_{xi} and F_{yi} are the longitudinal and lateral tyre forces, respectively. δ_f and T_i are the steering angles for the front wheels and the drive/braking torque on the wheel, respectively. m , I_z , I_{wi} , B_f , B_r , l_f , l_r , A_f , C_d , and r_e are the vehicle and tyre parameters, and D_a is the air density. Detailed explanations on these parameters, as well as tyre modelling, load transfer and torque vectoring can be found in [2].

The state-space form of the modelled vehicle dynamics is used in Sect. 3 and given as follows:

$$x_{k+1} = f(x_k, u_k). \quad (8)$$

3 Problem Formulation

Optimal control problems (OCPs) are used to formulate the energy and time optimal control of AVs. To achieve the objective of reducing energy consumption and optimising travel time, the cost function is carefully designed. Specifically, the power consumption of the wheels is minimised for energy efficiency. Moreover, the travel time is directly optimised in the cost function. Additionally, a term for actuator rate is included, to improve control efficiency and avoid actuator oscillations.

The OCPs are formulated based on the detailed vehicle dynamics as described in Sect. 2, with the capability of exploiting torque vectoring for energy and time optimal control. Moreover, various constraints are applied for considering factors such as road boundary, velocity, active safety and vehicle physical limits.

The OCP problem for jointly minimising energy consumption and travel time is given as follows:

$$\min_{x, u, \Delta u, s, T} Q_e \sum_{k=0}^{N_t-1} \sum_{i=0}^4 T_{k,i} \omega_{k,i} + \sum_{k=0}^{N_t-1} \|\Delta u_k\|_{R_{du}}^2 + \|s_k\|_{Q_s} + Q_T T \quad (9a)$$

$$\text{s. t. } x_{k+1} = f(x_k, u_k), \quad k \in \{0, 1, \dots, N_t - 1\} \quad (9b)$$

$$g(x_k, s_k) \leq 0 \quad (9c)$$

$$x_0 = \tilde{x}_0 \quad x_f = \tilde{x}_f \quad (9d)$$

$$u_{min} \leq u_{k,i} \leq u_{max} \quad (9e)$$

$$\Delta u_{min} \leq \Delta u_{k,i} \leq \Delta u_{max} \quad (9f)$$

where $\mathbf{x} = [x_1, \dots, x_{N_t}]$, $\mathbf{u} = [u_0, \dots, u_{N_t-1}]$, $\Delta\mathbf{u} = [\Delta u_0, \dots, \Delta u_{N_t-1}]$ and $\mathbf{s} = [s_0, \dots, s_{N_t-1}]$ are the sequences of states, control actions, variation of control actions, and slack vectors, respectively. T denotes the travel time to be optimised. x_0 and x_f are the initial and final states, respectively. Q_e , Q_T , R_{du} and Q_s are the weights on the energy consumption, travel time, control variation, slack vector, respectively.

Two sets of cost function terms are formulated to investigate two strategies: one focused on minimising travel time and the other aimed at simultaneously optimising energy consumption and travel time. For the second strategy, the cost function described in Eq. (9a) is employed. For the first strategy, the component related to energy usage is excluded from Eq. (9a). The results for both strategies are discussed in Sect. 4.

4 Results and Discussion

This section presents results for the two strategies examined: one for minimising travel time and the other for jointly optimising energy consumption and travel

Table 1. Comparison of energy usage and travel time with torque vectoring: Optimising travel time vs. Jointly optimising energy usage and travel time.

Strategy	Energy Usage (kWh)	Travel Time (s)
Time	0.5609	23.01
Energy + Time	0.5028	23.27
Energy + Time = 28	0.1060	27.91

^a “Energy + Time = 28” denotes the case where the travel time is limited to 28 s.

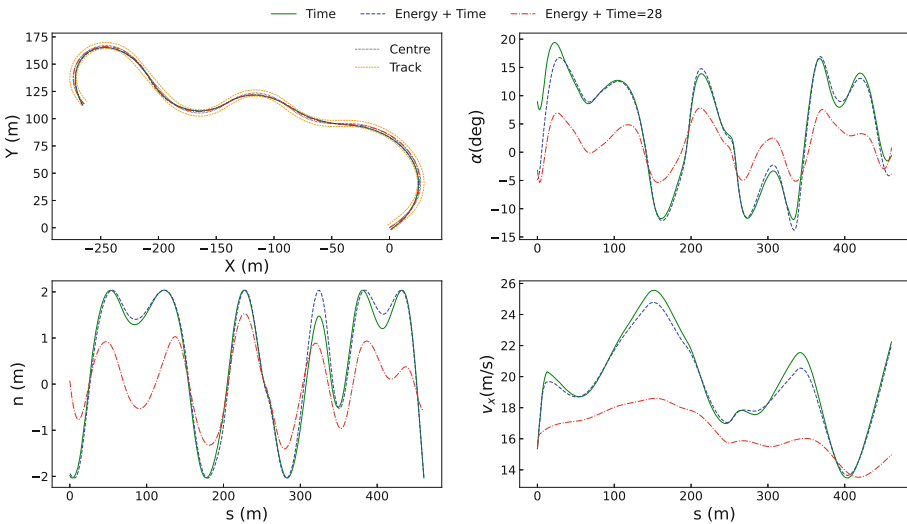


Fig. 1. Comparison of vehicle trajectories with torque vectoring: optimising travel time versus jointly optimising energy usage and travel time. “Centre” refers to the centerline of the road, and “Track” indicates the boundary of the road.

Table 2. Comparison of energy usage and travel time without torque vectoring.

Strategy	Energy Usage (kWh)	Travel Time (s)
Time	0.3916	23.93
Energy + Time	0.3542	24.09
Energy + Time = 28	0.1065	27.91

time. For the second strategy, two cases are analysed: one with free travel time and the other with a fixed travel time. In addition, these strategies are evaluated for the cases with and without torque vectoring. The evaluation is carried out based on a section of a handling test track. Implementation details regarding the strategies can be found in [2, 16, 17].

Table 1 presents a comparison of the results for purely optimising travel time versus jointly optimising both energy usage and travel time, utilising torque vectoring. As can be seen, by considering purely time in the formulation, the vehicle consumes 0.5609 kWh of energy and takes 23.01 s to complete the test. In contrast, by jointly considering energy usage and travel time in the formulation, it consumes 10.4% less energy but only travels 1.1% slower. Moreover, when the travel time is relaxed to 28 s, the energy consumption is significantly reduced.

Figure 1 shows the vehicle trajectories for the two investigated strategies while considering torque vectoring. Starting at the outer border of the track, the vehicle accelerates into the first corner with an initial velocity (v_x) around 15 m/s. To achieve minimum travel time, the vehicle consistently attempts to reach the maximum possible velocity, particularly during the first third and the final section of the track. Nevertheless, the vehicle at times decelerates to negotiate the cornering manoeuvres. When energy is considered in the problem formulation, the vehicle achieves lower peak velocities. Additionally, the vehicle aims to maintain a smoother trajectory to conserve energy, as evidenced by the larger lateral deviations around positions of 100 and 400 m in the strategy for optimising both energy and time. When the travel time is allowed to be larger, i.e., 28 s, the vehicle travels closer to the centreline of the track, as indicated by the smaller yaw and lateral deviations compared to the other two cases. However, the vehicle does not travel strictly along the centreline to maintain a smoother trajectory.

Table 2 presents the results for purely optimising travel time and jointly optimising energy usage and travel time without utilising torque vectoring. By comparing Table 2 with Table 1, it is evident that torque vectoring contributes to faster lap times at the expense of higher energy consumption. On the other hand, when completing the manoeuvre slower, i.e., 28 s, torque vectoring consumes a similar amount of energy. This is likely because the required energy to overcome the resistance forces is similar for both cases in such a low-dynamic manoeuvre.

5 Conclusions

This study investigated energy and time optimal control of autonomous vehicles using Frenet frame modelling and over-actuation. Enhancements have been made to the existing Frenet-based modelling, including the incorporation of a double-track dynamic vehicle model, an advanced tyre model and torque vectoring. The problem was formulated within an optimal control framework, featuring carefully designed cost function terms and constraints. Two control strategies were examined: one for minimising travel time and the other for jointly optimising energy consumption and travel time. The findings in the studied driving scenarios are summarised as follows. Firstly, considering both energy and time in the formulation can reduce energy consumption by 10.4% with only a slight increase in travel time. Secondly, maintaining a smoother trajectory contributes to energy conservation. Finally, torque vectoring results in faster lap times but at the cost of higher energy consumption. Additionally, torque vectoring consumes a similar amount of energy when traveling within the same time frame.

In the next step, the plan is to further study energy and time optimal control by exploring torque vectoring energy reduction and examining additional driving scenarios.

References

1. Zhai, L., Sun, T., Wang, J.: Electronic stability control based on motor driving and braking torque distribution for a four in-wheel motor drive electric vehicle. *IEEE Trans. Veh. Technol.* **65**(6), 4726–4739 (2016)
2. Zhang, W., Wang, Z., Drugge, L., Nybacka, M.: Evaluating model predictive path following and yaw stability controllers for over-actuated autonomous electric vehicles. *IEEE Trans. Veh. Technol.* **69**(11), 12807–12821 (2020)
3. Lenzo, B., et al.: Torque distribution strategies for energy-efficient electric vehicles with multiple drivetrains. *J. Dyn. Syst. Meas. Contr.* **139**(12), 121004 (2017)
4. Sun, P., Trigell, A.S., Drugge, L., Jerrelind, J.: Energy efficiency and stability of electric vehicles utilising direct yaw moment control. *Veh. Syst. Dyn.* **60**(3), 930–950 (2020)
5. Torinsson, J., Jonasson, M., Yang, D., Jacobson, B.: Energy reduction by power loss minimisation through wheel torque allocation in electric vehicles: a simulation-based approach. *Veh. Syst. Dyn.* **60**(5), 1488–1511 (2020)
6. Zhang, W., Drugge, L., Nybacka, M., Wang, Z.: Active camber for enhancing path following and yaw stability of over-actuated autonomous electric vehicles. *Veh. Syst. Dyn.* **59**, 1–22 (2020)
7. Zhang, W., Drugge, L., Nybacka, M., Jerrelind, J., Wang, Z.: Exploring four-wheel steering for trajectory tracking of autonomous vehicles in critical conditions. In: *IAVSD 2023* (2023)
8. Zhang, W., Drugge, L., Nybacka, M., Jerrelind, J.: Integrated control of motion actuators for enhancing path following and yaw stability of over-actuated autonomous vehicles. *Energies* **16**(12), 4776 (2023)
9. Falcone, P., Borrelli, F., Asgari, J., Tseng, H.E., Hrovat, D.: Predictive active steering control for autonomous vehicle systems. *IEEE Trans. Control Syst. Technol.* **15**(3), 566–580 (2007)

10. Werling, M., Ziegler, J., Kammel, S., Thrun, S.: Optimal trajectory generation for dynamic street scenarios in a frenet frame. In: 2010 IEEE International Conference on Robotics and Automation. IEEE (2010)
11. Verschueren, R., De Bruyne, S., Zanon, M., Frasch, J.V., Diehl, M.: Towards time-optimal race car driving using nonlinear mpc in real-time. In: 53rd IEEE Conference on Decision and Control. IEEE (2014)
12. Gao, Y., et al.: Spatial predictive control for agile semi-autonomous ground vehicles. In: AVEC 2012 (2012)
13. Kloeser, D., Schoels, T., Sartor, T., Zanelli, A., Prison, G., Diehl, M.: Nmpc for racing using a singularity-free path-parametric model with obstacle avoidance. IFAC-PapersOnLine **53**(2), 14324–14329 (2020)
14. Reiter, R., Nurkanović, A., Frey, J., Diehl, M.: Frenet-cartesian model representations for automotive obstacle avoidance within nonlinear mpc. Eur. J. Control **74**, 100847 (2023)
15. Dugoff, H., Fancher, P.S., Segel, L.: Tire performance characteristics affecting vehicle response to steering and braking control inputs. Technical Report. Contract CST-460, Washington, DC (1969)
16. Zhang, W., Drugge, L., Nybacka, M., Jerrelind, J., Wang, Z., Zhu, J.: Exploring model complexity for trajectory planning of autonomous vehicles in critical driving scenarios. In: Lecture Notes in Mechanical Engineering, pp. 1154–1165. Springer, Heidelberg (2022). https://doi.org/10.1007/978-3-031-07305-2_107
17. Zhang, W., Drugge, L., Nybacka, M., Jerrelind, J., Wang, Z., Zhu, J.: Exploring over-actuation and model complexity for trajectory planning of autonomous vehicles in critical manoeuvres. In: AVEC 2022 (2022)

Open Access This chapter is licensed under the terms of the Creative Commons Attribution 4.0 International License (<http://creativecommons.org/licenses/by/4.0/>), which permits use, sharing, adaptation, distribution and reproduction in any medium or format, as long as you give appropriate credit to the original author(s) and the source, provide a link to the Creative Commons license and indicate if changes were made.

The images or other third party material in this chapter are included in the chapter's Creative Commons license, unless indicated otherwise in a credit line to the material. If material is not included in the chapter's Creative Commons license and your intended use is not permitted by statutory regulation or exceeds the permitted use, you will need to obtain permission directly from the copyright holder.





Robust 3D On-Road Object Detection and Distance Estimation for Active Vehicle Control Systems Based on Monocular Camera Image Data

Xingguo Zhang^(✉), Daiki Ikami, and Pongsathorn Raksincharoensak

Tokyo University of Agriculture and Technology, Tokyo 184-8588, Japan
xgzhang@go.tuat.ac.jp

Abstract. 3D object detection from monocular camera videos constitutes a critical research domain. Achieving robust 3D object detection in databases lacking annotated information poses a highly challenging task. This paper proposes a simple yet effective transfer learning approach, integrating data alignment, 3D object detection, and dynamic result correction. Vanishing point detection is employed to infer camera angles in diverse scenes, and preprocessing of new data is conducted by considering the camera's pitch angle and vanishing point position. Subsequently, MonoDETR are applied for depth estimation and 3D object detection in monocular videos. Building upon the detection results, dynamic correction is achieved through inter-frame assistance, culminating in the final 3D object information. Validation on the TUAT Near-Miss Incident Database demonstrates the efficacy of the proposed approach. The results indicate a substantial reduction in the cost of annotating new domain data while simultaneously enhancing detection accuracy and robustness. Integration with onboard diagnostics (OBD) data allows the reconstruction of information about various traffic participants in hazardous scenarios, providing valuable insights for in-depth analysis of accident causes.

Keywords: Sensors and Actuators · Monocular Camera Videos · 3D Object Detection · Transfer Learning · Data Alignment · Dynamic Result Correction

1 Introduction

Autonomous driving systems rely on advanced perception, decision-making, and control technologies, utilizing various sensors such as cameras, and LiDAR to perceive the surrounding environment. While 3D object detection provides accurate descriptions of objects in the environment, achieving optimal results often requires the fusion of multiple sensors [1, 4]. However, due to the low cost of monocular cameras, they have become widely used at this stage. This study specifically focuses on the detection of 3-dimensional objects from videos captured by monocular cameras.

Current methods for monocular-based 3D object detection rely on depth inference from single images, demanding extensive depth annotation for model training [2]. Challenges arise from domain differences in training data, including variations in lighting,

camera parameters, and road topography. Overcoming these domain disparities is crucial for deploying models trained on existing domain knowledge directly to new domains without incurring additional costs. To address this issue, we propose a transfer learning solution incorporating data alignment, 3D object detection, and dynamic result correction. Validation on the Near-Miss Incident Database demonstrates enhanced detection accuracy and robustness while significantly reducing the cost of annotating new domain data. Integration with OBD data aids in reconstructing information about traffic participants in hazardous scenarios, facilitating a quantitative analysis of accident data.

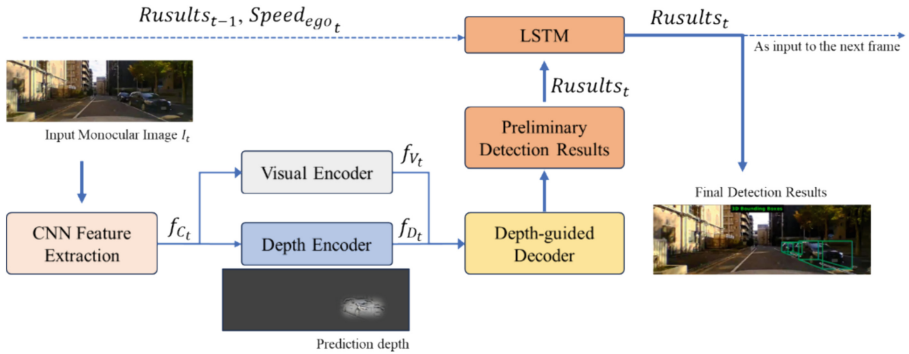


Fig. 1. Over pipeline of our proposed method.

2 Methodology

The pipeline of our proposed method is illustrated in Fig. 1. This approach achieves robust 3D object detection on new data lacking annotated information. Specifically, vanishing point detection infers camera angles, and preprocessing takes into account the camera's pitch angle and vanishing point position for new data. Subsequently, deep learning algorithms perform depth estimation and 3D object detection in monocular videos.

2.1 Image Detection Technologies for Relative Position Estimation

In the field of autonomous driving and safe driving, recognizing and understanding the environment and targets around the vehicle is a crucial issue. The environment includes vehicles, pedestrians, bicycles, road lines, and traffic signals. Especially, predicting information such as the speed and distance of target vehicles is expected to prevent car accidents. Currently, various technologies are used to detect this information, such as radar and ultrasonic sensors. However, these sensors are expensive and require complex installation, posing challenges for widespread adoption. Therefore, using onboard cameras, which allow for low-cost and easy installation, has been attracting attention recently.

2.2 2D and 3D Bounding Box Detection

When detecting targets such as vehicles from images, 2D Bounding Box detection technology is often considered first. While 2D Bounding Box detection is a mature technology that can achieve high-precision detection results in many fields, it only provides the upper-left and lower-right corner coordinates of the target in the image, making it difficult to understand detailed information such as the exact distance, rotation angle, and size of the target. Thus, 3D Bounding Box detection is introduced, which maps the exact position of the target in the world coordinate system based on rotation direction information and predicts how the target will move next.

2.3 Depth Encoder for 3D Bounding Box Prediction

3D object detection using monocular cameras has long been considered a challenging task. Most existing methods follow conventional 2D object detectors and predict 3D attributes based on features around the object's center. However, using only local features cannot understand the entire 3D spatial structure of the scene and ignores the depth relationships between objects in the image. We modified MonoDETR [3], a monocular image recognition framework using a depth-induced transformer, to perform 3D object detection from monocular images. MonoDETR adds a Depth Encoder to the conventional Visual Encoder to estimate depth information, achieving end-to-end 3D object detection from 2D images.

2.4 Transfer Learning to Reduce Manual 3D Labeling

In machine learning, preparing training data is essential. The algorithm uses this data to learn the parameters needed for prediction. Thus, the quality of training data is crucial for the algorithm to make accurate predictions. Annotating 3D Bounding Boxes is a challenging task that requires accurately capturing the three-dimensional shape of objects, which is much more difficult than 2D images.

Using public databases increases the diversity of datasets and improves the model's generalization performance. The KITTI dataset, widely used in the field of autonomous driving, includes tasks such as vehicle detection, 3D object detection, object tracking. KITTI, with high-quality manual annotations, serves as an ideal dataset for developing autonomous driving technologies. However, for the 3D Bounding Box detection task, differences in the cameras used, such as variations in pitch angle, focal length, and assumed height, can lead to suboptimal performance with the same model.

Our approach involves aligning the KITTI and TUAT near-miss databases based on their vanishing points. Specifically, we calculate the vanishing points for both databases, align Composition of the frames accordingly, and then crop and scale the TUAT near-miss database videos to closely match the frames of the KITTI database. Our experiments demonstrate that this preprocessing significantly enhances the accuracy of the predicted 3D bounding boxes and the precision of the target's pitch angle.

Subsequently, the 3D object detection model trained on the KITTI database is applied to the TUAT database. We input the images from the TUAT near-miss database into the model for object detection. During this process, the annotated bounding boxes from the

KITTI database are used to annotate the images in the TUAT near-miss database. This eliminates the need for manual creation of bounding boxes, thereby improving workflow efficiency.

2.5 Dynamic Correction of Target Trajectories by LSTM

The purpose of this study is to track the trajectories of road targets. However, fluctuations in the detection results over time can cause the targets to exhibit abnormal acceleration. This can negatively impact the decision-making behavior of autonomous vehicles. For example, consider a pedestrian walking normally, but due to fluctuations in the detection results, the predicted target appears to be accelerating across the road, forcing the autonomous vehicle to take emergency evasive actions. Therefore, it is crucial to address how to obtain reliable trajectories from image detection.

The simplest method is to filter out outliers, but in real-time processing tasks, simple filtering algorithms tend to maintain the status quo slowly and may miss genuine abrupt changes. To know the actual position and speed of the target vehicle, the ego vehicle's actual speed must be known. The TUAT near-miss database records the ego vehicle's speed information. In this study, we propose an algorithm for dynamically correcting tracking results. As shown in Fig. 1, by utilizing the previous moment's target detection results and the vehicle's speed, along with the current frame's detection results and current speed, we employ a Long Short-Term Memory (LSTM) network to construct a recurrent network that corrects the current results in real-time. This approach outputs the necessary corrections to the current detection results, improving detection accuracy and stabilizing the target trajectory over time.

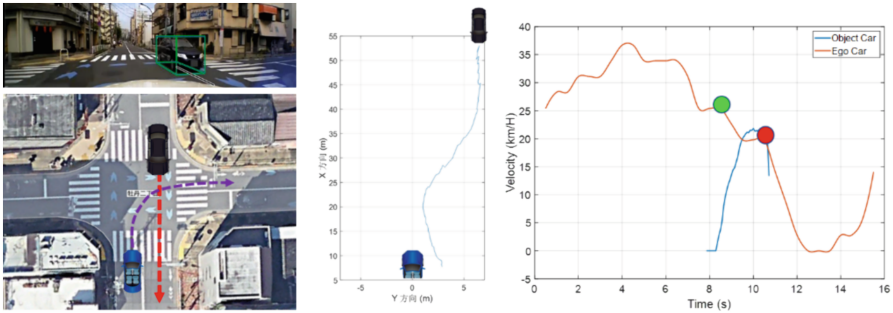


Fig. 2. Experiment results. (a) The 3D bounding box detection result and traffic scene restoration. (b) Relative distance from object car. (c) The velocity of ego car and object car.

3 Experimental Results

The 3D bounding box detection results on the TUAT database are illustrated in Fig. 2(a), showcasing not only the image category and 2D box coordinates but also the object's rotation angle, size, and distance from the camera. To assess the model's effectiveness

in estimating the relative motion states of vehicles within the TUAT Near-Miss Incident Database, we conduct both visual and quantitative tests. We use a specific example to elucidate the results. In a video depicting a right-turning vehicle at an intersection encountering a stationary black opposing vehicle that accelerates and enters the intersection, both vehicles engage emergency brakes. The trajectory of the detected relative position of the black vehicle is presented in Fig. 2(b), initiating at a distance of 54 m. As the video vehicle turns right, the X-direction relative distance decreases, and simultaneously, the Y-direction lateral distance also diminishes. Furthermore, the velocity changes of the estimated ego vehicle and the target vehicle are depicted in Fig. 2(c). The video vehicle decelerates in stages from the 6th second, while the target vehicle initiates acceleration from the 8th second. Both vehicles apply emergency brakes at the 10th second to avoid collision, validating the effectiveness of the proposed method in alignment with perceptual observations from video analysis.

4 Validation of Estimated Results

To quantitatively validate the estimated distances, we used Google Earth Pro to measure actual distances. By mapping the detected positions to the map and comparing them with the algorithm's estimated distances, we verified the accuracy of our method. For example, the Google Earth measurement showed a distance of 49.01 m, while our algorithm estimated 49.11 m, with an error of less than 0.1 m. Similar validation was performed for objects at closer distances, demonstrating the method's accuracy.

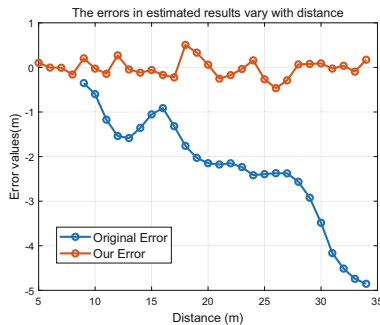


Fig. 3. The errors in estimated results varying with distance.

To further validate the effectiveness of the proposed method, we need to statistically verify the detection results across multiple vehicles. However, the TUAT database only contains the OBD data of the host vehicle and the video data from the onboard camera, lacking accurate positional information of surrounding vehicles in the road environment. How can we verify the accuracy of the predicted results? We target stationary vehicles in the road environment, using the predicted relative distance and the host vehicle's speed to estimate the speed of the road targets. By comparing the predicted results with a distance of zero, we can assess the validity of our method. Additionally, we examine the impact of errors based on the actual distance of the targets.

We selected 50 stationary vehicles distributed on both sides of the road. The experimental results are illustrated in the Fig. 3, showing the errors in estimated results varying with distance. The graph plots the error values (in meters) on the y-axis against the distance (in meters) on the x-axis. There are two sets of data presented: the “Original Error” (blue line with circular markers) and “Our Error” (orange line with circular markers).

From the graph, it is evident that the error values for the original method increase significantly as the distance increases, reaching up to approximately -5 m at 35 m distance. In contrast, the error values for our proposed method remain relatively stable around zero across all distances.

This comparison highlights the effectiveness of our method in maintaining low and consistent error values, demonstrating improved accuracy over the original method, especially as the distance increases. This stability is crucial for reliable target tracking in autonomous driving systems, ensuring more precise detection and reduced likelihood of erroneous behavior in decision-making processes.

5 Summary and Future Directions

This study introduces a refined transfer learning framework for robust 3D object detection in the Near-Miss Incident Database, which lacks annotated information. The proposed method effectively enhances detection accuracy and robustness while significantly reducing the cost of annotating new domain data. The integration with OBD data further facilitates the reconstruction of traffic participant information in hazardous scenarios, providing valuable insights for the development of Advanced Driver Assistance Systems (ADAS).

Future work will focus on extending the range of detectable objects and improving the accuracy of 3D detection and tracking algorithms. Enhancing the system’s performance under various environmental conditions such as nighttime and adverse weather will also be a priority. Additionally, further research will explore the integration of other sensor modalities to complement monocular camera data, aiming to achieve more comprehensive and reliable perception capabilities for autonomous vehicles.

References

1. Song, Z., et al.: Robustness-Aware 3D Object Detection in Autonomous Driving: A Review and Outlook. arXiv preprint [arXiv:2401.06542](https://arxiv.org/abs/2401.06542), 1–34 (2024)
2. Zhang, X., Xu, Q., Raksincharoensak, P.: Detection-Correction of Monocular 3D Bounding Box with LSTM Recurrent Networks. AVEC22, Tu1B-03, pp. 12–15 (2022)
3. Zhang, R., et al.: MonoDETR: Depth-guided transformer for monocular 3D object detection. In: Proceedings of the IEEE/CVF International Conference on Computer Vision (2023)
4. Yao, J., Ramalingam, S., Taguchi, Y., Miki, Y., Urtasun, R.: Estimating drivable collision-free space from monocular video. In: Proceedings of the 2015 IEEE Winter Conference on Applications of Computer Vision (WACV), pp. 420–427 (2015)

Open Access This chapter is licensed under the terms of the Creative Commons Attribution 4.0 International License (<http://creativecommons.org/licenses/by/4.0/>), which permits use, sharing, adaptation, distribution and reproduction in any medium or format, as long as you give appropriate credit to the original author(s) and the source, provide a link to the Creative Commons license and indicate if changes were made.

The images or other third party material in this chapter are included in the chapter's Creative Commons license, unless indicated otherwise in a credit line to the material. If material is not included in the chapter's Creative Commons license and your intended use is not permitted by statutory regulation or exceeds the permitted use, you will need to obtain permission directly from the copyright holder.





Occluded Area Detection Based on Sensor Fusion and Panoptic Segmentation

Hiroshi Yoshitake^{1(✉)}, Jinyu Gu¹, and Motoki Shino²

¹ The University of Tokyo, Kashiwa, Chiba 277-8563, Japan
hyoshitake@edu.k.u-tokyo.ac.jp

² Tokyo Institute of Technology, Ookayama, Tokyo 152-8550, Japan

Abstract. Detecting occluded areas in a driving environment is crucial to preventing traffic accidents against hidden road agents coming out from such occluded areas. Our previous work proposed a novel detection method that can offer geometric information of the detected areas by utilizing camera and LiDAR sensor fusion. However, it had difficulty identifying individual areas formed by different objects without information about distinct objects. Thus, the objective of this study was to improve our previous methodology, and panoptic segmentation, which can distinguish between individual objects and offer semantic class labels of the object, was adopted to overcome the limitation. Evaluation results revealed that our proposed methodology could achieve satisfactory results in occlusion area detection and superior accuracy in estimating hidden road agent types in the detected areas.

Keywords: occluded area detection · sensor fusion · panoptic segmentation

1 Introduction

Road safety is a pressing concern globally with the development of the automobile industry. According to traffic reports, traffic accidents could be briefly divided into two main categories: accidents involving visible road agents and accidents involving hidden road agents. Visible road agents refer to entities or objects on the road that are easily detectable and identifiable by drivers or sensors. On the other hand, hidden Road agents refer to entities or objects that cannot be directly detected by drivers or sensors by conventional means. Hidden road agents from occluded areas can pose significant threats to road safety as they are not readily visible to drivers. Therefore, detecting occluded areas is crucial. With successful detection, we can integrate the detection results into future Advanced Driver Assistance Systems (ADAS) to reduce the occurrence of collisions against hidden road agents.

Existing methods use external information, including information from other vehicles [1] and pedestrians [2], to detect the presence of hidden road agents within the occluded areas. These methods do not involve direct analysis of the surrounding environment to detect occluded areas that may contain hidden road

agents. On the contrary, we firmly believe that experienced drivers can perceive potential dangers by observing the surrounding environment. Thus, utilizing visual perception methods to detect occluded areas is essentially simulating human perception.

Several existing methods detect occluded areas based on visual perception methods [3–5]. Fukuda et al. [3] utilized a large dataset to train a predictor to estimate the occlusion area or recover the scene. Jeong et al. [4] utilize 2D LiDAR data from the bird’s eye view to estimate the occlusion areas in an occupancy grid map. Ding and Song [5] utilized the density of depth information derived from an RGB-D camera to estimate occlusion in human-related scenarios. However, these methods faced challenges in offering geometric information of the areas required for ADAS.

To overcome this limitation, we proposed a detection method utilizing sensor fusion of camera and LiDAR and a key point extractor identifying object boundaries forming the occlusion [6]. We succeeded in extracting key points, detecting occluded areas, and obtaining geometric information. However, identifying individual occluded areas was difficult because the key points were not classified into distinct objects. In other words, we can accurately detect individual areas if we can achieve information on individual objects.

As a method to achieve object information, we adopted panoptic segmentation [7]. This method can distinguish between individual objects and obtain class labels of each pixel simultaneously. Thus, we adopted this method and applied it to our previous method [6] to propose an improved detection method.

2 Methodology

Figure 1 shows the overview of the proposed methodology. This methodology consists of three main processes: 1. Data pre-processing, 2. Key point extraction, and 3. Occluded area reconstruction. The first and second processes were elaborated in our previous work [6]. Thus, this study focuses on the third process: Occluded area reconstruction.

The inputs to Process 3 are the key points, boundary points of occluded areas containing depth information, extracted in Process 2 and the image obtained by the RGB camera. Figure 2 shows a sample of extracted key points.

This process is designed to output individual occluded areas and estimated types of hidden road agents in the areas. The process consists of four steps. Firstly, panoptic segmentation is conducted to get segmented results of objects with class labels. Semantic edges of each object can be extracted from the segmented results. Secondly, the edge warping technique was adopted to obtain the depth edge of individual objects by integrating the semantic edges and the key points obtained in the previous process. Thirdly, Graham’s scan method was adopted to construct a convex hull of the depth edges of an individual object to reconstruct the occluded area. Lastly, a decision tree model was employed to estimate the types of potential road agents. Spatial information of occluded areas, such as depth, height, and width, and semantic information of occluded

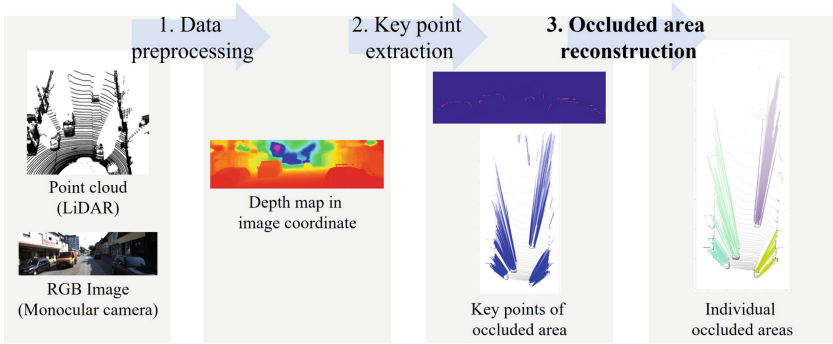


Fig. 1. Overview of the proposed methodology.



Fig. 2. Sample result of extracted key points of occluded areas. The top image is showing the original RGB image and the bottom image is showing the extracted key points of occluded areas made by the vehicles and building seen in the RGB image.

areas, the category label associated with the panoptic segmentation, were the input of the model.

3 Evaluation

3.1 Method

As the evaluation of the proposed methodology, the detection accuracy of occluded areas and the estimation accuracy of types of hidden road agents were evaluated. For the detection accuracy, the average Intersection of Union \overline{IoU} was adopted as the evaluation metric, which can be expressed as Eq. 1, where IoU_i denotes the IoU of area i and n denotes the number of areas. IoU between the detected results and manually labeled ground truth was evaluated for each area. For the estimation accuracy, Precision was adopted as the evaluation metric. As for the hidden road agent estimation, the model was trained with the ground truth dataset and tested with the same dataset.

$$\overline{IoU} = \frac{1}{n} \sum_i^n IoU_i \quad (1)$$

The method was evaluated for four different scenarios (S1–S4) included in the KITTI dataset [8]. Ground truth labels were annotated manually. Annotations of occluded areas were done by analyzing point cloud data, and annotations of types of hidden road agents were done by analyzing each area in RGB images.

3.2 Results

Table 1 shows the results of \overline{IoU} among different scenarios. The achieved results are acceptable, as the \overline{IoU} exceeded 0.5 in certain scenarios, indicating a satisfactory result. Figure 3 compares a sample scene’s detected areas and ground truths. From this result, it could be seen that our method was able to detect the same individual occluded areas as the ground truth. Although our method detected the same object, detected areas were larger than the ground truths, leading to a larger area of union, a smaller area of intersection, and a smaller IoU consequently.

Table 1. Evaluation results of \overline{IoU} .

Scene ID	\overline{IoU}
S1	0.62
S2	0.32
S3	0.28
S4	0.41

In terms of estimation of hidden road agent types, we achieved an accuracy of approximately 0.97. The high accuracy could be attributed to incorporating semantic information obtained in panoptic segmentation. We provided a higher-dimensional dataset by introducing semantic data alongside the original geometric information, enhancing linear separability.

4 Discussions

Although the evaluation metric was not high, the detection results of the proposed methodology were satisfactory and close to the ground truths, as shown in Fig. 3. This detection was possible because the key points of occluded areas were aligned with the object edges, thanks to the semantic edges obtained in the panoptic segmentation. Thus, it was confirmed that panoptic segmentation was effective in the occluded area reconstruction process.

However, at the same time, our method exhibited sub-optimal performance primarily due to the limitations of the panoptic segmentation. The segmentation

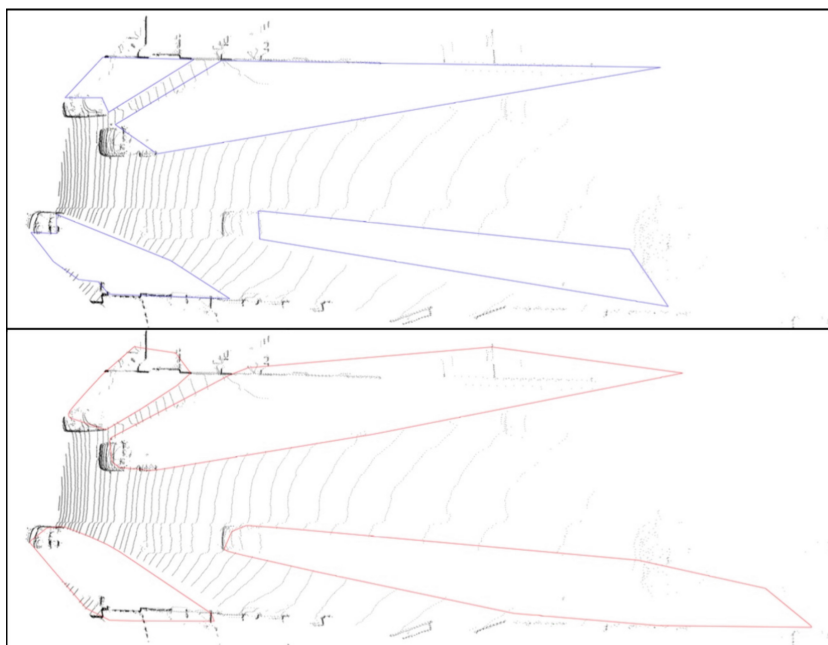


Fig. 3. Comparison of detected occluded areas and ground truths of the scene shown in Fig. 2. Red polygons are the detected occluded area and the blue polygons are the ground truths.

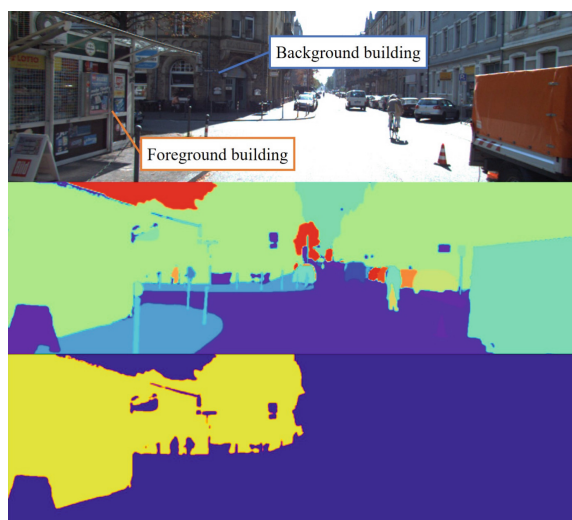


Fig. 4. Representative result of panoptic segmentation failing to distinguish foreground and background buildings as different objects. The top image is the original RGB image, the middle image is the panoptic segmentation result, and the bottom image is the segmentation result of the building on the left side.

struggled to distinguish background information. Figure 4 shows a sample of panoptic segmentation result, which failed to distinguish the foreground and background buildings on the left side. Since the foreground building was not segmented as a single object, the method failed to obtain the key points of the occluded area on the left side made by the foreground building. This type of failure was observed among vegetation such as trees. To overcome this issue, an update in the representation of segmentation is necessary to treat background objects as different objects.

5 Conclusions

This study proposed an occluded area detection method employing panoptic segmentation to improve our previous methodology, utilizing camera and LiDAR sensor fusion. The results showed that the proposed method could achieve satisfactory detection and superior accuracy in estimating hidden road agent types. From the results, it could be noted that our approach utilizing both geometric and semantic features obtained through sensor fusion and panoptic segmentation offered a more holistic perspective for detecting occluded areas. We plan to expand the size of the ground truth dataset to obtain more reliable evaluation results and analyze the strength of the proposed method in depth.

References

1. Zheng, X., et al.: Multivehicle multisensor occupancy grid maps (MVMS-OGM) for autonomous driving. *IEEE Internet Things J.* **9**(22), 22944–22957 (2022)
2. Hara, K., et al.: Predicting appearance of vehicles from blind spots based on pedestrian behaviors at crossroads. *IEEE Trans. Intell. Transp. Syst.* **23**(8), 11917–11929 (2021)
3. Fukuda, T., et al.: Blindspotnet: seeing where we cannot see. In: *Proceedings of European Conference on Computer Vision*, pp. 554–569 (2022)
4. Jeong, Y., et al.: Collision preventive velocity planning based on static environment representation for autonomous driving in occluded region. In: *Proceedings of 2020 IEEE Intelligent Vehicles Symposium*, pp. 425–430 (2020)
5. Ding, P., Song, Y.: Robust object tracking using color and depth images with a depth based occlusion handling and recovery. In: *Proceedings of 2015 12th International Conference on Fuzzy Systems and Knowledge Discovery*, pp. 930–935 (2015)
6. Gu, J., et al.: Occlusion detection method using key point extractor based on multiple sensor fusion. In: *Proceedings of 7th International Symposium on Future Active Safety Technology Toward Zero Traffic Accidents* (2023)
7. Kirillov, A., et al.: Panoptic segmentation. In: *Proceedings of 2019 IEEE/CVF Conference on Computer Vision and Pattern Recognition*, pp. 9404–9413 (2019)
8. Geiger, A., et al.: Vision meets robotics: the kitti dataset. *Int. J. Rob. Res.* **32**(11), 1231–1237 (2013)

Open Access This chapter is licensed under the terms of the Creative Commons Attribution 4.0 International License (<http://creativecommons.org/licenses/by/4.0/>), which permits use, sharing, adaptation, distribution and reproduction in any medium or format, as long as you give appropriate credit to the original author(s) and the source, provide a link to the Creative Commons license and indicate if changes were made.

The images or other third party material in this chapter are included in the chapter's Creative Commons license, unless indicated otherwise in a credit line to the material. If material is not included in the chapter's Creative Commons license and your intended use is not permitted by statutory regulation or exceeds the permitted use, you will need to obtain permission directly from the copyright holder.





Temporal and Frequency Analysis with Empirical Mode Decomposition for Vehicle Vibration Signals

Makoto Masuda^{1,2}(✉) and Taichi Shiiba²

¹ Two Wheeler and Powersports Business Unit, Bosch Corporation, Yokohama, Japan
Makoto.Masuda@jp.bosch.com

² Department of Mechanical Engineering, Meiji University, Kawasaki City, Japan

Abstract. This study presents the empirical mode decomposition method (EMD) for vehicle vibration and a correlation detection approach for input from road and vehicle body vibration using the Hilbert-Huang transform (HHT). Although the magnitude squared coherence is commonly used to examine the correlation of vehicle vibration with road input, it is not suitable for non-stationary vibration. On the other hand, the Hilbert-Huang transform (HHT) which consists of EMD and the Hilbert transform is proposed. This method is suitable for transient vibration analysis, while the drawbacks to intermittence signals are suggested. Vehicle vibration signals include intermittence signals in some cases. In this study, the masking EMD which adapts the mask signal to the amplitude of the target signal was applied to vehicle vibration to alleviate the drawbacks. By this method, the correlation analysis by HHT demonstrates higher temporal resolution compared to the continuous wavelet transform. Thus, it becomes possible to identify the components that caused vibrations at the moments when the passengers felt comfortable or uncomfortable, and to analyze the characteristics of the vibrations.

Keywords: Hilbert-Huang transform · Empirical Mode decomposition

1 Introduction

The testing of vehicle ride comfort still relies on subjective evaluations by test drivers. There are a lot of advantages to using the same method in vehicle tests as the general customers to evaluate cars. However, obtaining accurate physical information such as frequency and amplitude of vibration from subjective evaluation is usually challenging. The development of a quantitative analysis method for ride comfort vibration is not only useful for improving ride comfort but also development of new suspension components and their control logic. Although the magnitude squared coherence (the coherence) is commonly used to examine the correlation between the input from road surfaces and the output which is vehicle body vibration, the spectrum and phase obtained from the frequency analysis used in the method are averaged values within the window. That makes it difficult to capture the characteristics of transient vibrations. Moreover, the calculation of the coherence further deteriorates the temporal resolution by averaging

over a constant window for the spectrum and phase. On the other hand, the Hilbert-Huang transform (HHT) which is suitable for non-stationary vibration was proposed [1]. HHT consists of the empirical mode decomposition (EMD) and the Hilbert transform (HT), and the instantaneous amplitude and the instantaneous phase of the target signal are calculated by HT. In addition, the instantaneous frequency is obtained from the instantaneous phase. Since the signal that can be transformed by HT has to have only a single frequency component, the target signal is first decomposed into the intrinsic mode functions (IMFs) by EMD. EMD acts as a data-adaptive high-pass filter and has high temporal resolution. However, the drawback called mode mixing when EMD is applied to signals with intermittent signals is indicated by the author. In this study, we describe a method for mitigating the drawback when applying it to vehicle vibration and a correlation analysis with high temporal resolution using HHT.

2 Applying EMD to a Vehicle Vibration

2.1 Verification Method

The goal is to identify the characteristics of the instantaneous vibration when the vehicle behavior that the passengers perceive as comfortable or uncomfortable and to identify the components contributing to the vibration. For that goal, a road surface with a single convex input occurring on the ISO class D is used to conduct a full vehicle simulation using VI-CarRealTime. Figure 1a shows the road input and the simulation condition. The vertical displacement at the point of contacting the front tire and the road is shown in Fig. 1b. The vehicle parameters used in the simulation are the preset “Sedan car” model in VI-CarRealTime.

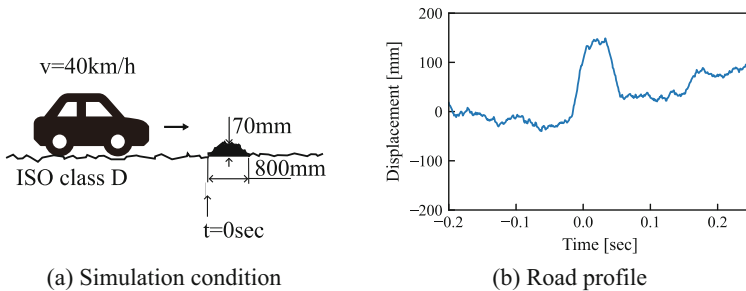


Fig. 1. Condition and road profile for simulation

2.2 Masking EMD

The procedure for processing EMD is first to take the difference between the average of the upper and lower envelope curves for the target signal. This process is repeated iteratively on the residual until achieving a threshold, at which point the residual is extracted as an IMF. Then, the difference between the extracted IMF and the target signal is taken, and the same process is repeated to sequentially decompose the signal

into IMF of progressively lower frequencies. On the other hand, EMD has been pointed out to have the problem of mode mixing where it decomposes signals with intermittent components into IMFs with non-monocomponents as mentioned earlier. As the vibration of a vehicle varies significantly depending on the driving location and conditions, the characteristics and frequency of inputs from the road are not constant. This becomes a challenge when EMD is applied to vehicle vibrations. In this study, the masking EMD [2] which is modified for intermittency signals is used to mitigate the drawback. The masking EMD adds a sinusoidal signal with single-frequency component across the entire range of the target signal as the masking signal. By executing EMD on the target signal, the components close to the frequency of the masking signal are extracted as an intrinsic mode along with the imposed signal. By removing the added masking signal from the intrinsic mode, the IMF of the target signal is obtained alone. According to the boundary map for masking EMD described by Fosso et al. [3], a smaller amplitude of a mask signal than the target signal is considered better. However, if the amplitude is too small compared to the target signal, the imposed signal may not work as a mask. Thus, we propose adapting the amplitude of the mask signal to an intermittency target signal using the sliding filter. This also acts to mitigate the drawback of EMD. Figure 2 shows an example of the target signal and a masking signal that adapts to the local amplitude of the target signal. In addition, by Fosso et al., the conditions of frequency between the mask signal and the two components that are to be extracted and separated are proposed with $f_1/f_m > 0.7$ and $f_2/f_m < 0.6$, where $f_1, f_2,$ and f_m represent the frequency of the signal to be extracted, the frequency of one to be separated and the masking frequency respectively. This study determines the masking frequencies are set to 1, 2, 4, 8, 16, 32, and 64 Hz by taking into account the logarithmic relationship of human sensory perception of vibration while meeting the aforementioned conditions. Figure 3a and Fig. 3b show the instantaneous frequency of IMFs obtained by HHT with the conventional EMD and with the masking EMD using the configuration mentioned above respectively. Instantaneous frequency from HHT is shown with lines in red. Furthermore, the background shows the scalogram using CWT for the same vibration data. The instantaneous frequency around 10 Hz in Fig. 3b which represents the maximum amplitude of the convex input is finely decomposed compared to Fig. 3a. In addition, the instantaneous frequency lines in Fig. 3b are less crossed compared to Fig. 3a, and the proposed method effectively decomposes the signal.

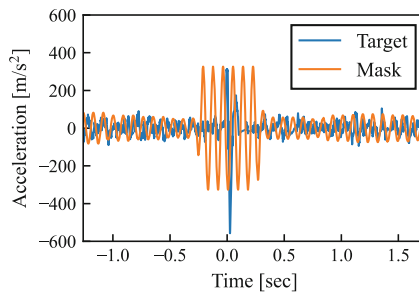


Fig. 2. An example of mask signal

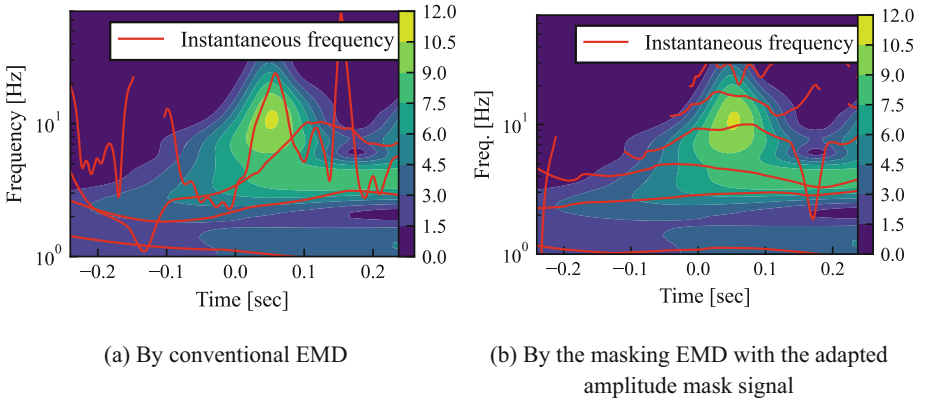


Fig. 3. Apply EMD to vehicle vibration

3 Correlation Analysis of Input and Output in Vehicle Vibration by HHT

The coherence is a common method for correlation analysis. It is calculated from the Fourier transform (FT), and the wavelet transform (WT) is represented by Eq. (1), where C_{xy} represents the cross spectrum of the input and the output signals, P_{xx} and P_{yy} represent the power spectrum of the input and output signal respectively, A_x and A_y represent spectra of input and output, θ_x and θ_y represents the phase of input and output, and the E represents an expected value.

$$coh^2 = \frac{|E(C_{xy})|^2}{E(P_{xx})E(P_{yy})} \quad (1)$$

$$= \frac{|E(A_x)|^2 |E(A_y)|^2}{E(P_{xx})E(P_{yy})} \cdot |E(e^{i(\theta_x - \theta_y)})|^2 \quad (2)$$

The first part of Eq. 2 is calculated based on the ratio of input and output amplitudes, while the second part is determined by the phase difference between the input and output. In the case of transient responses, although the amplitude ratio is not constant, the phase difference remains constant. Thus, the correlation analysis using HHT utilizes the second part of Eq. 2. Specifically, it is determined that input and output are correlated when the instantaneous frequency of input signals corresponds to the one of output for a certain duration. This method is possible because the instantaneous frequency can be obtained by HT, whereas the method with FT or WT deteriorates the accuracy of coherence. Figure 4a shows the correlation analysis of vertical acceleration on the front wheel and vertical acceleration of the center of gravity on the vehicle body obtained from the aforementioned simulation using HHT. The lines in orange represent the spots having the correlation of the input which is the acceleration of the wheel and output which is the acceleration of the vehicle body, and the coherence using CWT is shown in the background. The lines are within a region of high coherence using CWT in the time

axis direction, thereby correlation analysis using HHT exhibits high temporal resolution compared to coherence using CWT. Figure 4b illustrates the correlation analysis when the front bump rubber is replaced with the shorter one. It indicates that the correlation is detected at the moment when the bump rubber reaction force peaks around 30 - 40 Hz. Figure 4c illustrates the correlation when the greater damping force on the front damper is applied. It also indicates that the correlations affected by damping force around 10 - 20 Hz, 60 Hz are detected. Furthermore, features of Fig. 4b and Fig. 4c can be observed in Fig. 4a. This observation in Fig. 4a corresponds to the similarity of the bump rubber reaction force in Fig. 4a and Fig. 4b, and the similarity of the generated damping force in Fig. 4a and Fig. 4c. Consequently, HHT allows to find the characteristics of the vibration at the moment of forced vibration and the contribution of components. Figure 5 shows the characteristics of bump rubbers and dampers used in Fig. 4.

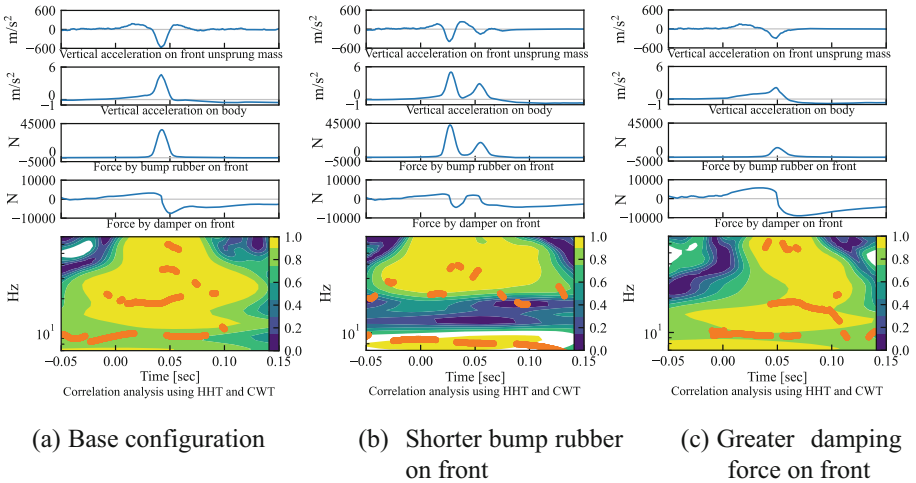


Fig. 4. Correlation analysis using HHT and CWT

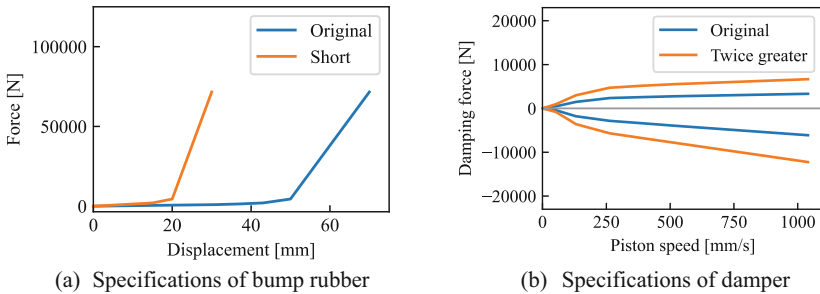


Fig. 5. Specifications of vehicle components used for the correlation analysis

4 Conclusion

This study presents the method for detecting the correlation between road inputs and vehicle behavior using HHT with the adaptive amplitude masking EMD. The adaptive amplitude masking EMD was demonstrated to alleviate mode mixing for intermittent road inputs and their corresponding vehicle vibrations. Furthermore, the correlation detection method using HHT has superior temporal resolution compared to the coherence with CWT, allowing for more localized correlation detection. This advantage enables the identification of components affecting vehicle vibration.

References

1. Huang, N.E., et al.: The empirical mode decomposition method and the Hilbert spectrum for non-stationary time series analysis. *Proc. Roy. Soc. London* **454A**, 903–995 (1998)
2. Deering, R., Kaiser, J.F.: The use of a masking signal to improve empirical mode decomposition. *IEEE International Conference on Acoustics, Speech, and Signal Processing*. vol. 4. pp. iv/485–iv/488 (2005)
3. Fosso, O.B., Molinas, M.: EMD mode mixing separation of signals with close spectral proximity in smart grids. In: 2018 IEEE PES Innovative Smart Grid Technologies Conference Europe (ISGT-Europe) (2018)

Open Access This chapter is licensed under the terms of the Creative Commons Attribution 4.0 International License (<http://creativecommons.org/licenses/by/4.0/>), which permits use, sharing, adaptation, distribution and reproduction in any medium or format, as long as you give appropriate credit to the original author(s) and the source, provide a link to the Creative Commons license and indicate if changes were made.

The images or other third party material in this chapter are included in the chapter's Creative Commons license, unless indicated otherwise in a credit line to the material. If material is not included in the chapter's Creative Commons license and your intended use is not permitted by statutory regulation or exceeds the permitted use, you will need to obtain permission directly from the copyright holder.





Dynamical Behaviours of the Nose Landing Gear with Freeplay and Stochastic Disturbance

Xiaolei Du¹ and Yong Xu²

¹ School of Mechanics, Civil Engineering and Architecture,
Northwestern Polytechnical University, Xi'an, China
duxiaolei970315@163.com

² School of Mathematics and Statistics, Northwestern Polytechnical University,
Xi'an, China
hsux3@nwpu.edu.cn

Abstract. Shimmy dynamics of a dual wheel nose landing gear system with torsional freeplay under stochastic lateral disturbances is studied. Dynamic characteristics of the deterministic case are numerically analyzed, especially the shimmy of the landing gear through bifurcation analysis. Meanwhile, the influences of the freeplay nonlinearity on shimmy behaviours are examined in detail. Impacts of stochastic lateral disturbances on the shimmy of the landing gear system are performed via time history and recurrence plots. Our results show that the interaction between the freeplay nonlinearity and the random load induces a significant reduction in the critical shimmy velocity, which has an adverse impact on the stability of the nose landing gear of an aircraft.

Keywords: Shimmy · Landing gear · Bifurcation analysis · Freeplay

1 Introduction

Landing gear shimmy is generally considered as an unexpected self-excited vibration of wheel and landing gear motion coupling with each degree of freedom. Many researches omitted the nonlinear effects caused by freeplay. The structural freeplay, like mechanical transmission clearance of the landing gear, also has a great impact on the wheel shimmy. In this work, the torsional freeplay caused by torque links is taken into account, and Gaussian white noise will be also considered to approximately describe the stochastic lateral excitation.

2 The Mathematical Model

The motion of each tire under the torsional and lateral bending effects of struts is based on [2]. A typical dual wheel NLG of a midsized passenger aircraft is

This work was partly supported by the NSF of China (Grant No. 12072264).

considered as sketched in Fig. 1. These two modes are coupled via the lateral deformation λ_L and λ_R of the left and right tyres. The torsional and lateral bending dynamics of the NLG can be described by Eq. (1a–b). The longitudinal mode is omitted here since it does not actively participate in the NLG dynamics [2]. The tire kinematic equation is obtained by the stretched string theory, which describes the wheel-ground interaction. The resultant lateral deformation can be expressed as an algebraic sum of the torsional and lateral bending modes where the natural frequencies of both modes are different. The motion of each tire under the torsional and lateral bending effects of struts is given by Eqs.(1a–b). Then the overall model of the dual wheel NLG system for torsional and lateral vibrational modes can be established as [2],

$$\dot{\lambda}_L + \frac{v}{\sigma} \lambda_L - v \sin(\theta) - l_g \dot{\delta} \cos(\delta) - (e_{\text{eff}} - h) \cos(\theta) \dot{\psi} \cos(\phi) - \frac{D}{2} \dot{\psi} \sin(\theta) \cos(\phi) = 0, \tag{1a}$$

$$\dot{\lambda}_R + \frac{v}{\sigma} \lambda_R - v \sin(\theta) - l_g \dot{\delta} \cos(\delta) - (e_{\text{eff}} - h) \cos(\theta) \dot{\psi} \cos(\phi) + \frac{D}{2} \dot{\psi} \sin(\theta) \cos(\phi) = 0, \tag{1b}$$

where D is the separation distance between the centres of two wheels, and each tyre has the moment of inertia I about the spinning axis.

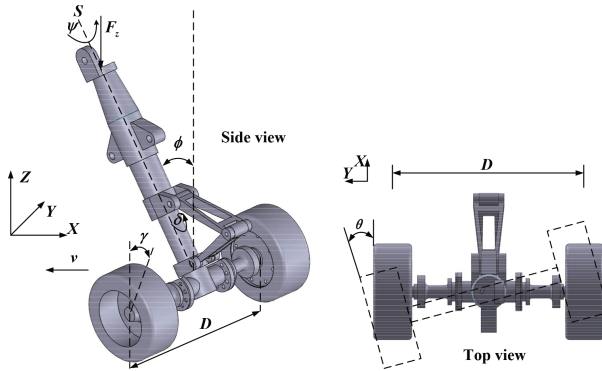


Fig. 1. Schematics of side and top views of the dual wheel NLG.

The torsional freeplay originating from the torque links of the NLG is studied here. The gap between the torque links will cause a reduction on the torsional stiffness that is expressed as [3]

$$M_{K_\psi} = \begin{cases} k_\psi (|\psi| - \theta_{FP}) \text{sgn}(\psi), & |\psi| > \theta_{FP}, \\ 0, & |\psi| \leq \theta_{FP}. \end{cases} \tag{2}$$

Specifically, a Gaussian white noise $\omega(t)$ is added to the lateral DOF as an additive noise excitation. The $\omega(t)$ satisfies the following property

$$E[\omega(t)] = 0, \quad E[\omega(t)\omega(t + \tau)] = \bar{N}\eta(\tau), \tag{3}$$

where $E[\cdot]$ means expectation, $\eta(\tau)$ is Dirac function, \bar{N} is the noise intensity.

3 Bifurcation Analysis

A bifurcation analysis is performed to explore the deterministic NLG system. The effects of the forward velocity and vertical loading force are to be analyzed regarded to the stability with freeplay.

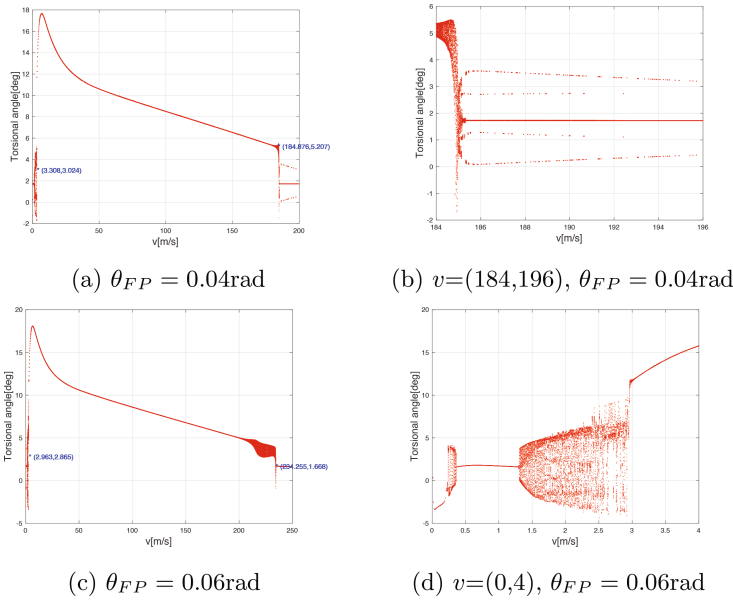


Fig. 2. The single parameter bifurcation with freeplay ($F_z = 500$ kN).

Figure 2 shows the bifurcation under high vertical load with the cases of freeplay (0.04/0.06 rad). Figure 2(a) indicates that the nonlinearity caused by freeplay still effects system at the high-speed stage. System does not return to the equilibrium after the second bifurcation, but oscillates in multiple periods as shown in Fig. 2(b). Increasing the freeplay will expand the shimmy area of the system. In addition, at the low speed stage, the freeplay will cause multi-period to single period and then to multi-period oscillation (Fig. 2(e)). System will oscillate in the negative axis in the torsional direction as shown in Figs. 2(a) and (d) and vibrate significantly in the lateral bending direction (Figs. 2(c) and

(f)). The bifurcation diagrams with freeplay shown in Fig. 2 display multi-period and quasi-period motions substansially extend the results of existing works. The freeplay may lead to chaos under specific conditions, and the impact of freeplay on the dynamics is more complex than discussed above.

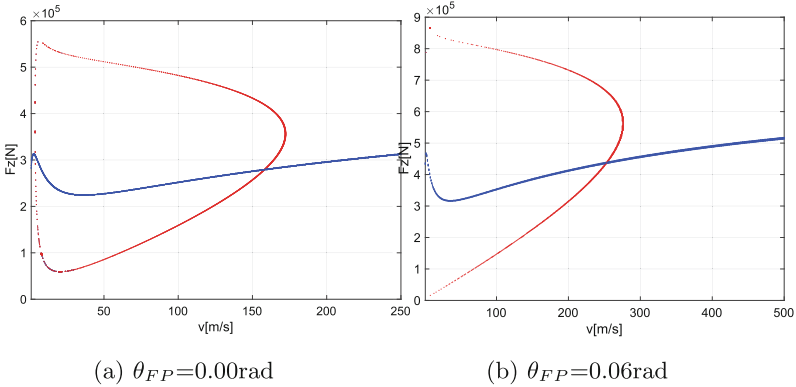


Fig. 3. The double parameter bifurcation (v - F_z plane).

As shown in Fig. 3, the double parameter bifurcation diagram of the v - F_z plane of the double wheel NLG system with and without considering the structural freeplay are obtained respectively. It can be seen from the Fig. 3(a) that system shimmies when forward velocity reaches 5.439 m/s. The intersection of the two areas is the area where system shimmies in both torsional and lateral bending directions. The result without freeplay shown in Fig. 3(a) completely corresponds to the one in [2]. From Fig. 3 (b), comparing with the case without freeplay, the critical speed of system shimmy is advanced from 5.439 m/s to about 1.028 m/s. The shimmy point in the torsional direction is extended from 175 m/s to about 270 m/s. The range of vertical load impact shimmy area is also expanded from 550 KN to 900 KN, which means that the existence of the freeplay makes the shimmy region in the torsional direction expand significantly. In the lateral bending direction, due to the coupling effect, the existence of freeplay will make the shimmy curve move up, indicating the vertical load required for system to lateral shimmy increases. In other words, the torsional freeplay inhibits the lateral shimmy to a certain extent.

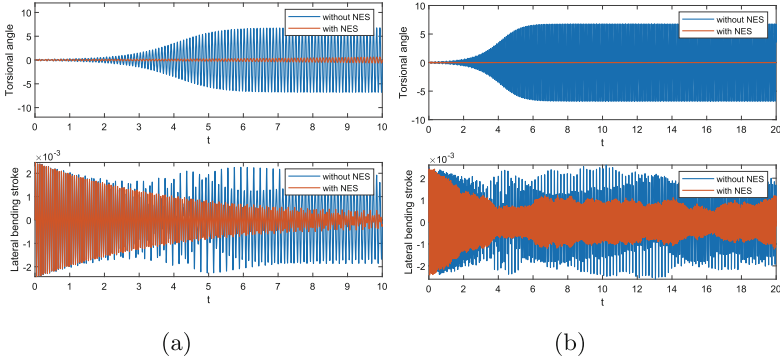


Fig. 4. The time histories with NES controller.

Figure 4 shows the time histories in the deterministic and stochastic cases respectively, the results indicate the shimmy can be well controlled by NES (Figs. 5 and 6).

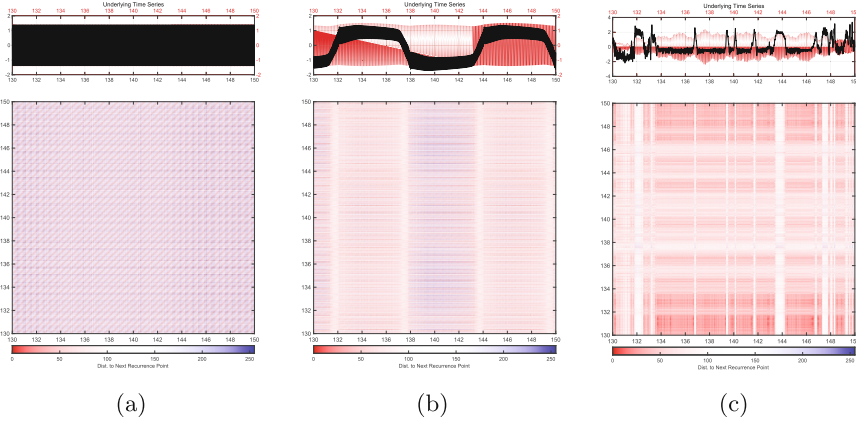


Fig. 5. The UCRP of the system with an embedding of $m = 3$, $\tau_1 = 10$ ($F_z = 500$ KN, $v = 0.25$ m/s). m is embedding dimension and τ_1 is delay time. The black line and red line on top of the UCRP represent the time history in the torsional direction and lateral bending direction respectively.

The unthreshold cross recurrence plot (UCRP) are obtained to compare the dynamics represented in torsional and lateral direction, showing the recursive structure characteristics from periodic to stochastic.

Moreover, the statistics on the cross correlation, recurrence rate and determinism are obtained. It can be seen that the system has strong cross-correlation, high recurrence rate and intensive determinism in the case without freeplay, and reduced after considering the freeplay and noise, indicating the coupling effect and periodicity in the torsion and lateral bending directions decreased.

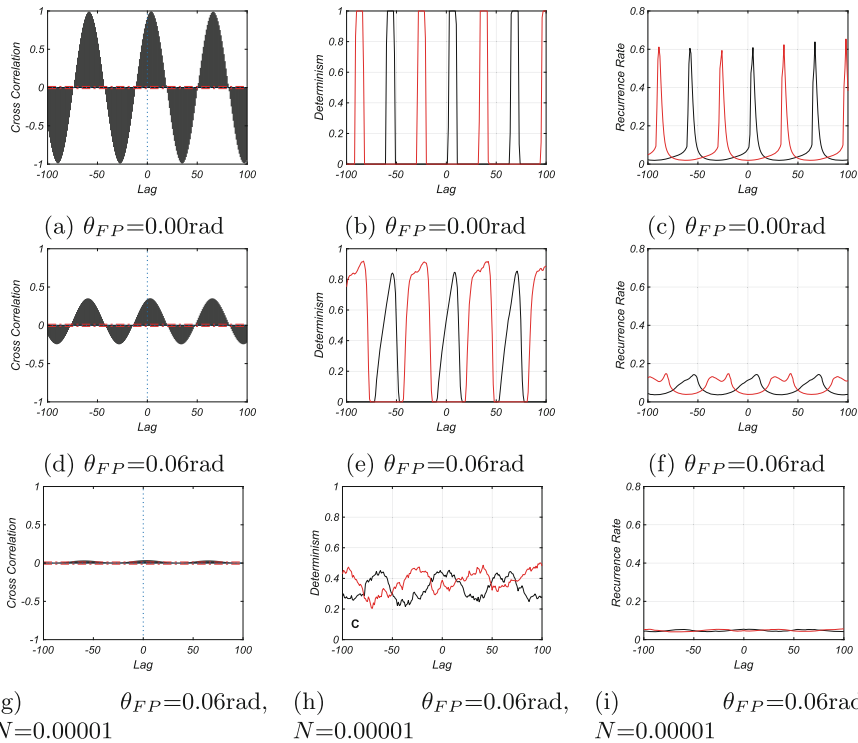


Fig. 6. The quantification analysis diagrams of UCRP for the torsional direction ($F_z = 500$ KN, $v = 0.25$ m/s). The black lines show positive relation, the red lines show negative relation. The dash-dotted line in (a), (d), (g) marks the 5% confidence interval. The lag domain is $[-100, 100]$.

4 Conclusion

Shimmy dynamics of a dual wheel NLG with torsional freeplay under stochastic lateral disturbances are investigated. We found that the torsional freeplay leads to an enlargement of the shimmy area and an enhancement of the shimmy characteristics compared to the case without freeplay. The stochastic lateral excitation enhances the lateral bending direction shimmy and brings out the random switching phenomenon of amplitude in the torsional mode of the system with torsional freeplay.

References

1. Du, X., Xu, Y., Liu, Q., et al.: Shimmy dynamics in a dual-wheel nose landing gear with freeplay under stochastic wind disturbances. *Nonlinear Dyn.* 1–23 (2024)
2. Thota, P., Krauskopf, B., Lowenberg, M.: Multi-parameter bifurcation study of shimmy oscillations in a dual-wheel aircraft nose landing gear. *Nonlinear Dyn.* **70**(2), 1675–1688 (2012)

3. Eret, P., Kennedy, J., Bennett, G.J.: Effect of noise reducing components on nose landing gear stability for a mid-size aircraft coupled with vortex shedding and freplay. *J. Sound Vib.* **354**, 91–103 (2015)

Open Access This chapter is licensed under the terms of the Creative Commons Attribution 4.0 International License (<http://creativecommons.org/licenses/by/4.0/>), which permits use, sharing, adaptation, distribution and reproduction in any medium or format, as long as you give appropriate credit to the original author(s) and the source, provide a link to the Creative Commons license and indicate if changes were made.

The images or other third party material in this chapter are included in the chapter's Creative Commons license, unless indicated otherwise in a credit line to the material. If material is not included in the chapter's Creative Commons license and your intended use is not permitted by statutory regulation or exceeds the permitted use, you will need to obtain permission directly from the copyright holder.





Tuning Time Delays to Improve the Performance of a Steering Controller

Jialin Li¹, Denes Takacs^{2,3}(✉), Jianwei Lu¹, Illes Voros², and Gabor Stepan²

¹ School of Automotive and Transportation Engineering,
Hefei University of Technology, Hefei, Anhui, China
janjananlin@163.com, jwlu75@163.com

² Faculty of Mechanical Engineering, Department of Applied Mechanics, Budapest
University of Technology and Economics, Budapest, Hungary

{takacs, illes.voros, stepan}@mm.bme.hu

³ HUN-REN-BME Dynamics of Machines Research Group, Budapest, Hungary

Abstract. Time delays and lags in control loops can cause instability and pose significant challenges to engineers. This study investigates a steering controller using the dynamic bicycle model, where the steering system dynamics are approximated by a steering lag. A higher-level controller calculates the desired steering angle based on the vehicle's lateral position and yaw angle by considering various time delays related to these states. Stability charts are plotted for delay combinations, and the most stable gain setups for the feedback controller are determined. The results indicate that an appropriate increase in one of the time delays expands the stable domain of control gains for the vehicle system, and it enhances the performance of the vehicle controller.

Keywords: time delay · steering control · stability analysis · feedback control

1 Introduction

In the past twenty years, autonomous vehicle (AV) research has seen incredible progress. One area that is crucial for making these vehicles safe and stable is active steering control [1–3]. Even though control systems have made essential progress, surprisingly little attention has been given to studying the effects of time delays within them, despite the fact that time delays persist as a critical issue.

Recent research often focuses on automated platforms with complex electric circuits and advanced actuators, which cause large time delays and lags in the control system. However, most of the studies on path-following controllers [4, 5] neglect the impact of the sensor and communication delays and steering dynamics, although these may lead to degraded system performance, such as steering oscillations and instability [6, 7]. One significant challenge for contemporary AV systems is signal congestion. These systems are increasingly complex and face difficulties in assimilating large volumes of data. Variations in sensor configurations and estimation methods at the upper controller levels result in differences

in feedback delays related to state variables [8]. Steering lag is another critical factor [9] representing the time it takes for the tire to rotate and the tire contact patch to develop the slip angle necessary for generating lateral tire force. This lag is influenced by hardware capabilities and the design of the lower level control system. Hence, ignoring these two factors can potentially cause unforeseen effects on system behavior.

Therefore, an in-depth investigation into the effects of time delays in upper-level controllers and steering lag in lower-level controllers is essential for developing robust and safe control systems for AV. In this study, the stability of a vehicle steering controller is analyzed considering time delays and steering lag. The stability domains of the control system and the most stable control gain setup can be determined under multiple time delay combinations. We can improve the performance of the control system via proper tuning of the delays.

2 Vehicle Dynamics and Control Design

The lateral dynamics of vehicles are commonly studied using the well-known bicycle model, which assumes a constant longitudinal speed V_x (see Fig. 1). This model is widely used due to its simplicity and effectiveness in capturing vehicle behavior.

In this case, the planar bicycle model for the vehicle is introduced in the form

$$m(\dot{V}_y + V_x\dot{\psi}) = F_{Fy} + F_{Ry}, \quad J_G\ddot{\psi} = aF_{Fy} - bF_{Ry}, \quad (1)$$

where V_y is the lateral speed, ψ is the yaw angle and δ is the steering angle. F_{Fy} and F_{Ry} are the lateral forces of the front and rear tires, respectively. The overall mass of the vehicle is m ; J_G is the mass moment of inertia of the vehicle. Parameters a and b refer to the distances of the front and rear axles to the center of gravity G, respectively.

In case of small tire deformations, the linearized brush tire model [10] provides:

$$F_{Fy} = -2C_F\alpha_F, \quad F_{Ry} = -2C_R\alpha_R, \quad (2)$$

where C_F and C_R are the so-called cornering stiffnesses of the front and rear tires, respectively. The tire slip angles are defined as follows:

$$\alpha_F = \arctan \frac{V_y + a\dot{\psi}}{V_x} - \delta, \quad \alpha_R = \arctan \frac{V_y - b\dot{\psi}}{V_x}. \quad (3)$$

3 Hierarchical Steering Control Strategy

In this study, we consider that the desired path of the vehicle is along the X -axis. Namely, the lateral error of the vehicle is the position Y_G of the vehicle's center of gravity, while the angular error is equal to the yaw angle ψ . To accomplish the vehicle path-following, a hierarchical steering control strategy is constructed.

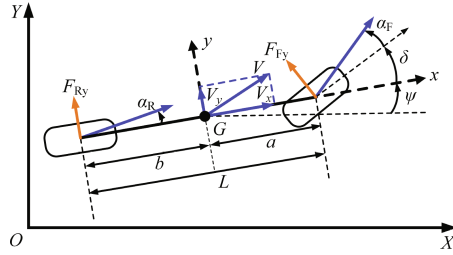


Fig. 1. Representation of planar bicycle model

The upper-layer control law for calculating the desired steering angle δ_d is designed to accommodate variations in feedback delays for lateral position and yaw angle. The control law is based on a linear state feedback:

$$\delta_d(t) = -P_y Y_G(t - \tau_y) - P_\psi \psi(t - \tau_\psi), \tag{4}$$

where P_y and P_ψ are the feedback control gains. The time delays corresponding to the different signals are τ_y and τ_ψ .

In order to achieve the desired steering angle in the lower-level controller, a simplified model of the steering system is used with the first-order differential equation

$$\tau_s \dot{\delta}(t) = \delta_d(t) - \delta(t), \tag{5}$$

where the steering lag τ_s describes the latency of the steering. This lag is set to $\tau_s=0.1$ s in the study [9]. $\delta(t)$ is the real steering angle of the front wheel, while $\delta_d(t)$ refers to the desired steering angle.

Table 1. Vehicle parameters.

Symbol (unit)	Description	Value
m (kg)	The total mass of the vehicle	1435
J_z (kg · m ²)	Yaw moment of inertia	2340
L (m)	Wheelbase	2.5
a, b (m)	The distance from G to front, rear axle	1.2, 1.3
C_F (N/rad)	Cornering stiffness of front wheel	$6 \cdot 10^4$
C_R (N/rad)	Cornering stiffness of rear wheel	$6 \cdot 10^4$
V_x (km/h)	Longitudinal velocity	60

4 Stability Analysis

By means of the D-separation and the semi-discretization methods (see [11]), stability charts are constructed in the plane (P_y, P_ψ) of the higher level control

gains while all the other parameters of the system are fixed as shown in Table 1. The control gain setup, for which the system has the most stable configuration (i.e., when the largest absolute value of the characteristic multipliers of the semi-discretized system is minimal), can also be determined. This setup varies as the parameters of the system are changed, like in case of the variation of the time delays.

The state vector \mathbf{x} of the vehicle system is defined as $\mathbf{x} = [Y_G \ \psi \ V_y \ \dot{\psi} \ \delta]^T$. From Eq.(1)-(5), the linear state space model can be obtained:

$$\dot{\mathbf{x}}(t) = \mathbf{A}\mathbf{x}(t) + \mathbf{B}u(t), \tag{6}$$

where $\mathbf{A} \in \mathbb{R}^{5 \times 5}$, $\mathbf{B} \in \mathbb{R}^{5 \times 1}$. They are listed as follows:

$$\mathbf{A} = \begin{bmatrix} 0 & 0 & 1 & 0 & 0 \\ 0 & 0 & 0 & 1 & 0 \\ 0 & \frac{2(C_F+C_R)}{m} & -\frac{2(C_F+C_R)}{mV_x} & -\frac{2(C_F a-C_R b)}{mV_x^2} & \frac{2C_F}{m} \\ 0 & \frac{2(C_F a-C_R b)}{J_z} & -\frac{2(C_F a-C_R b)}{J_z V_x} & -\frac{2(C_F a^2+C_R b^2)}{J_z V_x} & \frac{2C_F a}{J_z} \\ 0 & 0 & 0 & 0 & -\frac{1}{\tau_s} \end{bmatrix}, \quad \mathbf{B} = \begin{bmatrix} 0 \\ 0 \\ 0 \\ 0 \\ \frac{1}{\tau_s} \end{bmatrix}, \tag{7}$$

and the input u is the desired steering angle δ_d that is given by the proportional controller

$$u(t) = \mathbf{K}_y \mathbf{x}(t - \tau_y) + \mathbf{K}_\psi \mathbf{x}(t - \tau_\psi), \tag{8}$$

where the row vectors $\mathbf{K}_y = [-P_y \ 0 \ 0 \ 0 \ 0]$ and $\mathbf{K}_\psi = [0 \ -P_\psi \ 0 \ 0 \ 0]$.

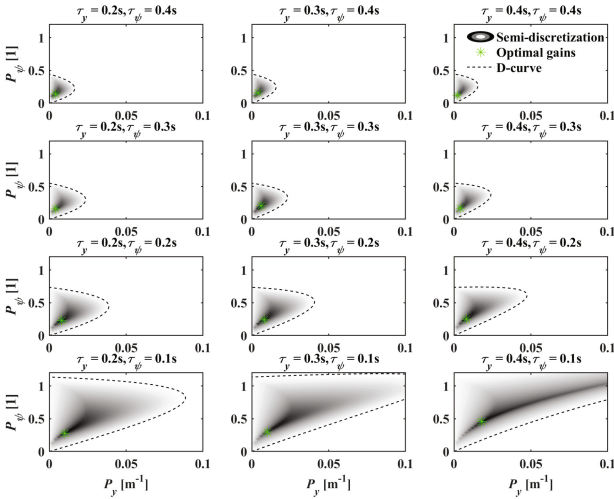


Fig. 2. Stability charts in the plane of control gains P_y and P_ψ for different combinations of time delays.

Figure 2 shows the stable regions for the control gains P_y and P_ψ in case of several varying feedback delay combinations. The black dashed line outlines

the stability domain, with darker gray shades indicating faster decaying signals, that is, indicating improved stability. The green star marks the optimal point for the fastest system decay, showing that maximum control gains do not yield the fastest decay. Increasing τ_ψ significantly reduces the stable region, while increasing τ_y primarily alters the shape of the stability domain. Some control gain combinations become stable as τ_y increases. In Fig. 3(a), the blue domain represents the fastest decay for the combination of the time delays where the modulus of the largest characteristic multiplier is the smallest (see the color-bar to the right of the stability chart). To verify the effectiveness of adjusting a specific time delay combination to enhance the system’s control performance, numerical simulations are conducted. The simulation duration is set to 10 s, and the initial values are $\mathbf{x}_0 = [3.5\ 0\ 0\ 0]^T$. Simulations are carried out for two combinations of time delays: A ($\tau_y = 0.2\text{ s}$; $\tau_\psi = 0.1\text{ s}$) and B ($\tau_y = 0.4\text{ s}$; $\tau_\psi = 0.1\text{ s}$). Figure 3(b) illustrates the simulation results for the lateral position of the system over time. Combination B exhibits a faster system response compared to Combination A, reaching a stable state earlier. Hence, adjusting a specific time delay combination for the system under the most stable (optimal) gain combinations can enhance the control performance.

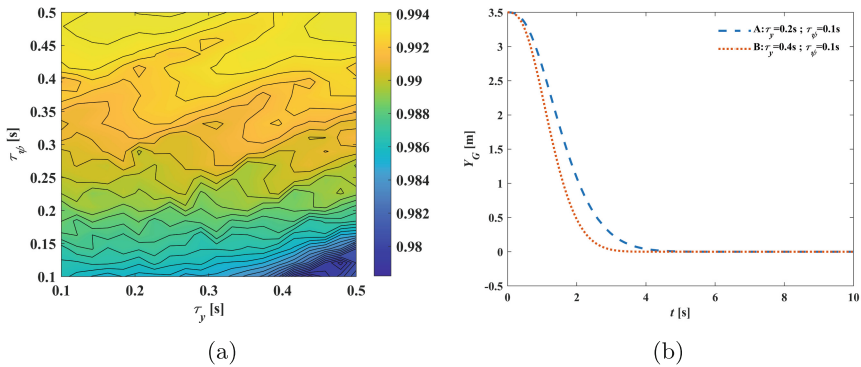


Fig. 3. The effect of different time delay combinations on the linear stability: (a) the value of the largest characteristic multiplier; (b) simulations for different time delay combinations.

5 Conclusion

In summary, the presented analysis identifies the control gain setup that yields the most robust parameter configurations against initial state perturbations by adjusting the time delays of the state signals processing. It is counter-intuitive that the optimal combinations of time delays are found with increasing one of the delays. These findings challenge the conventional wisdom that time delays tend to destabilize dynamical systems: certain scenarios may benefit from larger

time delays and these scenarios are also relevant in practical applications like the control of AV. Further investigation of complex hierarchical vehicle control systems with various delays is the task of future research.

Acknowledgements. The research reported in this paper was supported by the National Key Research and Development Program of the Ministry of Science and Technology of China under grant no. 2021YFE0116600, the Key Support Plan for Foreign Experts under grant no. zcgj2022017L, and the National Research, Development and Innovation Office of Hungary under grant no. 2020-1.2.4-TET-IPARI-2021-00012. D.T. was supported by the János Bolyai Research Scholarship of the Hungarian Academy of Sciences, J.L. was supported by the China Scholarship Council. I.V was supported by the Rosztoczy Foundation.

References

1. Eski, I., Temurlenk, A.: Design of neural network-based control systems for active steering system. *Nonlinear Dyn.* **73**, 1443–1454 (2013)
2. Kapania, N.R., Gerdes, J.C.: Design of a feedback-feedforward steering controller for accurate path tracking and stability at the limits of handling. *Nonlinear Dyn.* **53**(12), 1687–1704 (2015)
3. Fang, Z., Wang, J., Wang, Z., Chen, J., Yin, G., Zhang, H.: Human–machine shared control for path following considering driver fatigue characteristics. *Veh. Syst. Dyn.* (2024)
4. Guo, N., Zhang, X., Zou, Y., Lenzo, B., Zhang, T.: A computationally efficient path-following control strategy of autonomous electric vehicles with yaw motion stabilization. *IEEE Trans. Transport. Electrification.* **6**(2), 728–739 (2020)
5. Wang, W., Zhang, Y., Yang, C., Qie, T., Ma, M.: Adaptive model predictive control-based path following control for four-wheel independent drive automated vehicles. *IEEE Trans. Intell. Transp. Syst.* **23**(9), 14399–14412 (2021)
6. Chen, G., Zhao, X., Gao, Z., Hua, M.: Dynamic drifting control for general path tracking of autonomous vehicles. *IEEE Trans. Intell. Veh.* **8**(3), 2527–2537 (2023)
7. Botes, W., Botha, T.R., Els, P.S.: Real-time lateral stability and steering characteristic control using non-linear model predictive control. *Veh. Syst. Dyn.* **61**(4), 1063–1085 (2023)
8. Voros, I., Takacs, D.: Stability analysis of a hierarchical lane-keeping controller with feedback delay. *IFAC-PapersOnLine* **55**(36), 300–305 (2022)
9. Xu, S., Peng, H., Tang, Y.: Preview path tracking control with delay compensation for autonomous vehicles. *IEEE Trans. Intell. Transp. Syst.* **22**(5), 2979–2989 (2020)
10. Pacejka, H.: *Tire and Vehicle Dynamics*. Elsevier, Amsterdam (2005)
11. Insperger, T., Stepan, G.: *Semi-Discretization for Time-Delay Systems: Stability and Engineering Applications*. Springer, Heidelberg (2011). <https://doi.org/10.1007/978-1-4614-0335-7>

Open Access This chapter is licensed under the terms of the Creative Commons Attribution 4.0 International License (<http://creativecommons.org/licenses/by/4.0/>), which permits use, sharing, adaptation, distribution and reproduction in any medium or format, as long as you give appropriate credit to the original author(s) and the source, provide a link to the Creative Commons license and indicate if changes were made.

The images or other third party material in this chapter are included in the chapter's Creative Commons license, unless indicated otherwise in a credit line to the material. If material is not included in the chapter's Creative Commons license and your intended use is not permitted by statutory regulation or exceeds the permitted use, you will need to obtain permission directly from the copyright holder.





Vehicle Teleoperation: SRPT Approach Resilience to State Estimation Errors Through Simulation Insights

Jai Prakash^(✉), Michele Vignati, and Edoardo Sabbioni

Department of Mechanical Engineering, Politecnico di Milano, Milan, Italy
jai.prakash@polimi.it

Abstract. Vehicle teleoperation holds great promise but faces challenges in complex scenarios, limited awareness, and network delays, impacting human operators' cognitive workload. Our prior work introduced the Successive Reference Pose Tracking (SRPT) approach, transmitting poses instead of steering commands, potentially mitigating delays. Yet, SRPT's robustness in the face of state estimation inaccuracies and the necessary sensors remain unclear. In this study, we assess SRPT under various challenging environmental conditions and measurement errors using a Simulink-based 14-DOF vehicle model. Results show SRPT's consistent performance, using estimated states, in worst-case scenarios. Our minimalist sensor setup - IMU, wheel speed encoder, and steer encoder - underscores SRPT's resilience without relying on GPS, vital for urban environments. This paper highlights SRPT's robust teleoperation, setting the stage for future real-world vehicle tests prone to measurement errors.

Keywords: Vehicle teleoperation · Remote driving · Network delay · SRPT · NMPC · State estimation · Measurement noises · Simulink

1 Introduction

Vehicle teleoperation is the remote control of a vehicle, typically wirelessly. Automated vehicles (AVs) are promising for future mobility but face challenges in complex scenarios, limiting their effectiveness. Teleoperation can serve as a backup when AVs reach the limits of their Operational Design Domain (ODD) [1]. The goal of teleoperation is to offer a secure and effective method to overcome these limitations.

Key challenges in vehicle teleoperation include:

- ! **Human-machine interaction:** User experience with input modalities (e.g., touch, gesture, voice), feedback (e.g., haptic, visual, auditory), and cognitive load.
- ! **Network latency:** Variable delays degrade performance, especially in low-bandwidth or high-latency environments.

! Safety and reliability: Robust fault detection, recovery mechanisms, and handling communication failures or malfunctions (Fig. 1).

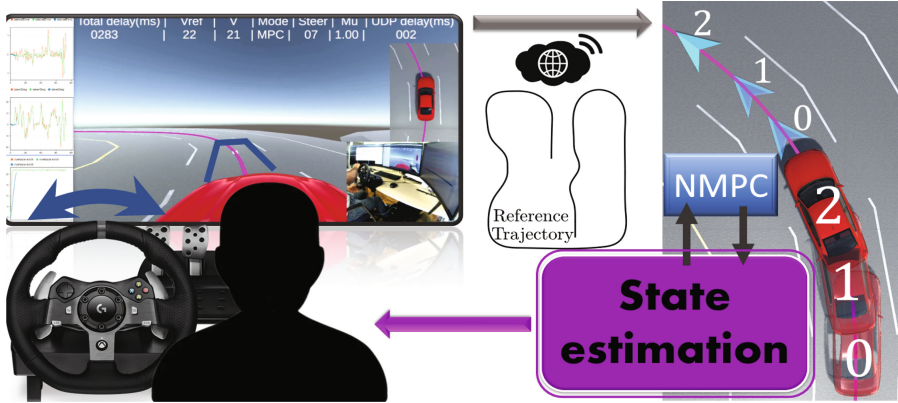


Fig. 1. Graphical depiction of the SRPT approach utilized for direct vehicle teleoperation. The remote vehicle is provided with successive reference poses as it progresses forward. The control-loop includes a state-estimation block.

Various teleoperation concepts [1], including direct control [2–4], shared control [5–7], and trajectory guidance [8, 9], face challenges such as latency and situational awareness. This paper focuses on mitigating the impact of network latency in vehicle teleoperation using the Successive Reference Pose Tracking (SRPT) approach, which falls under the direct control classification. SRPT transmits poses instead of steering commands. This method aims to improve safety and effectiveness by reducing human overcorrection and oscillations caused by delays.

1.1 Previous Work and Vehicle State Estimation

Our previous research introduced and assessed the SRPT approach [10–12]. Compared to predictive display-based teleoperation, SRPT, utilizing a Nonlinear Model Predictive Control (NMPC) block, demonstrated superior performance by dynamically adjusting vehicle speed and steer during rapid maneuvers and maintaining stability under variable network delays. The control-station generates closely spaced waypoints via joystick steering. Prior research works assumed perfect vehicle states; however, real-world scenarios necessitate evaluating SRPT’s robustness against state estimation inaccuracies.

State estimation is crucial for reliable teleoperation. Methods like the Extended Kalman Filter (EKF) and Unscented Kalman Filter (UKF) estimate vehicle states using inputs from IMUs and wheel encoders. Bersani et al. [13] employed a UKF with a kinematic model for pose and velocity estimation, while Doumiati et al. [14] used an EKF with a four-wheel model to estimate side-slip

angle and tire forces. Although high-accuracy methods using Lidar and GPS exist, they are costly. Our approach focuses on cost-effective, resilient solutions using only dead-reckoning sensors with EKF based state estimator to support SRPT.

1.2 Contribution of Paper

This paper assesses the performance of SRPT vehicle teleoperation under state estimation inaccuracies and challenging conditions. It highlights SRPT’s effectiveness using only dead-reckoning sensors, enhancing robustness without GPS dependency.

2 Method

The SRPT approach proposed in [11], requires vehicle states. Considering the single-track vehicle model, set of vehicle states are:

$$X = [\beta, \dot{\psi}, \psi, F_{y,F}, F_{y,R}, V_x, x, y, \delta]^T$$

The NMPC block optimizes for vehicle steer-speed commands, to keep the vehicle motion in sync with the received successive reference poses [11]. Figure 3 shows the incorporation of a state-estimator in the form of EKF. Its prediction model consists of the single-track version of the four-wheel vehicle model given in [14] and it is given by

$$\dot{X} = \begin{bmatrix} \frac{1}{mV_x} (F_{y,F} \cos \delta + F_{x,F} \sin \delta + F_{y,R}) - \frac{\beta \cdot a}{V_x} - \dot{\psi} \\ \frac{1}{I_z} [(F_{y,F} \cos \delta + F_{x,F} \sin \delta) l_F - F_{y,R} l_R] \\ \dot{\psi} \\ \frac{V_x}{\lambda} [C_{\sigma,F} \sigma_F - F_{y,F}] \\ \frac{V_x}{\lambda} [C_{\sigma,R} \sigma_R - F_{y,R}] \\ \dot{V}_x \\ V_x (\cos \psi - \sin \psi \tan \beta) \\ V_x (\sin \psi + \cos \psi \tan \beta) \\ \dot{\delta} \end{bmatrix}$$

$[\sigma_F, \sigma_R]$ are the tires slips given by

$$\begin{aligned} \sigma_F &\simeq \tan \delta - \beta - \dot{\psi} \frac{l_F}{V_x} \\ \sigma_R &\simeq -\beta + \dot{\psi} \frac{l_R}{V_x} \end{aligned}$$

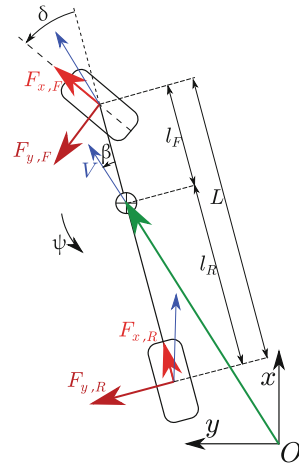


Fig. 2. Single-track vehicle model.

$[C_{\sigma,F}, C_{\sigma,R}]$ are the lumped cornering stiffness of front and rear axles respectively. $[m_f, m_R]$ are distribution of vehicle mass on front and rear axle based on $[l_F, l_R]$ respective distances of axles from CG (Fig. 2 and Table 1).

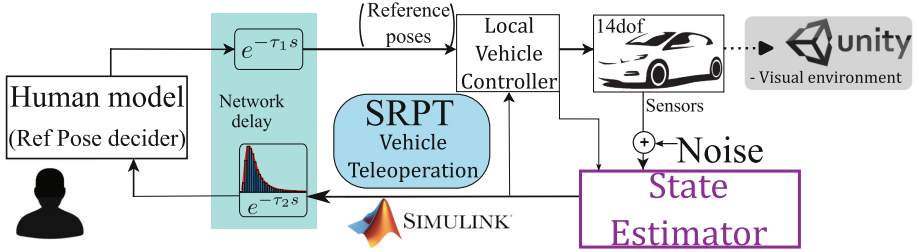


Fig. 3. Simplified block diagram of the simulation platforms set up on Simulink. Unity has no role in simulation, it is to display the manoeuvres while being performed.

Table 1. (Simulated) Vehicle parameters for the single-track model.

Parameter	Value
m	1680 kg
I_z	2600 kg s ²
$[m_F; m_R]$	[871.6; 809.4] kg
$[l_F; l_R]$	[1.3; 1.4] m
$[C_{\sigma,F}; C_{\sigma,R}]$	[1.057e+05; 1.050e+05] N
λ (Relaxation length)	0.3 m

2.1 Measurement Model

A dead-reckoning set of sensors, comprising a virtual IMU, a speed encoder and a steer encoder is considered. Hence the measurement vector and the measurement model are given by

$$Z = [a_{y,meas}, \dot{\psi}_{meas}, V_{x,meas}, \delta_{meas}]^T$$

$$h(X) = \left[\frac{1}{m} (F_{y,F} \cos \delta + F_{y,R}), \dot{\psi}, V_x, \delta \right]^T$$

3 Simulation Setup

A faster than real-time, vehicle teleoperation simulation test platform is developed using Simulink and Unity3D to emulate the network delayed vehicle teleoperation system, as shown in Fig. 3. In addition to environmental disturbances depicted in Fig. 4, measurement noises (Table 2) are also considered. These noise sources are grouped into following sets:

- i. Actual states, no EKF
- ii. Noise set 1 : EKF + Gaussian noises
- iii. Noise set 2 : EKF + Gaussian noises + gainV + biasδ + 3°tiltedImu
- iv. Noise set 3 : EKF + Gaussian noises + gainV + biasδ + 3°tiltedImu + C_{F,over} + C_{R,over}
- v. Noise set 4 : EKF + Gaussian noises + gainV + biasδ + 6°tiltedImu
- vi. Noise set 5 : EKF + Gaussian noises + gainV + biasδ + 6°tiltedImu + C_{F,over} + C_{R,over}

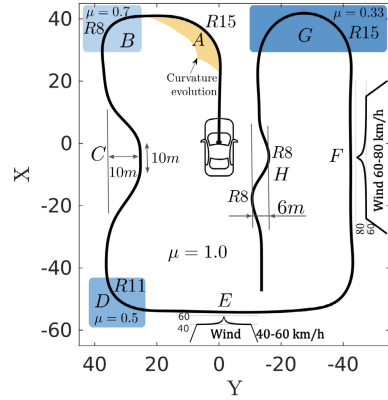


Fig. 4. The track.

Table 2. Sources of measurement noise

Noise sources	Description
Gaussian noise	AWGN; $R_k = diag([0.112^2, 0.005^2, 0.083^2, 0.003^2])$
gainV = 1.05	Inaccurate consideration of rolling radius.
biasδ = 0.5°	Constant bias in steer angle measurement.
3°tiltedImu	$a_{y,noisy} = a_y \cos(3^\circ) - 9.8 \sin(3^\circ)$; $\dot{\psi}_{noisy} = \dot{\psi} \cos(3^\circ)$
6°tiltedImu	$a_{y,noisy} = a_y \cos(6^\circ) - 9.8 \sin(6^\circ)$; $\dot{\psi}_{noisy} = \dot{\psi} \cos(6^\circ)$
C _{F,over} = 1.2C _F C _{R,over} = 1.2C _R	Overly estimated cornering stiffness.

Additionally, we include a teleoperation mode (under delays) with a look-ahead driver model, representing a typical human operator, steering the vehicle to align with the reference trajectory, serving as a baseline for comparing SRPT modes.

4 Results and Discussion

Simulations revealed significant oscillations with the look-ahead driver model during double lane change (C) and slalom (H) sections due to network delays. In contrast, the SRPT mode effectively eliminated these oscillations in all sections. The NMPC block considers steer-rate limitations and strategically decelerates the vehicle, allowing for more time to maneuver. Fig 5 compares cross-track errors across all modes. Key findings are:

- Obs I: Expectedly, Lookahead-Optimum consistently outperforms Lookahead-Suboptimum.
- Obs II: SRPT reduces error in high steer demand regions like C and H, countering instability in H better due to SRPT’s speed control.
- Obs III: SRPT performs better in regions with low adhesion (D), but shows a slight decrease in performance in regions with extremely low adhesion (G) due to significant changes in the system model. Nevertheless, this doesn’t significantly affect its overall performance.
- Obs IV: In windy conditions (E and F), SRPT maintains stability and outperforms Lookahead driver model in region F despite measurement noise.

SRPT vehicle teleoperation performs equal to or better than the lookahead driver mode in all regions.

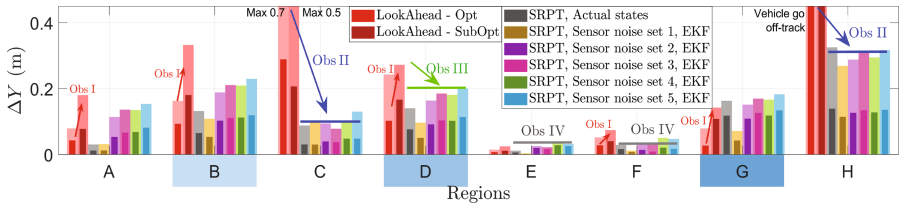


Fig. 5. Cross-track error for Lookahead and SRPT vehicle teleoperation modes at 22 km/h under network delays. SRPT maintains performance even with measurement noise.

4.1 How SRPT Is Unaffected from Diverging State Estimation?

Intrinsically, The SRPT approach relies on accurate vehicle pose estimation within a moving time window equal to the round-trip network delay (200–300 ms). Although global pose estimation may diverge over time, the proposed EKF provides accurate estimation within this small time window. This ensures SRPT’s robustness under varying network delays, demonstrating its resilience in adverse environmental conditions.

5 Conclusion

In our previous work, we introduced the SRPT approach for vehicle teleoperation, transmitting successive reference poses instead of steer commands. This study assessed SRPT's performance under state estimation errors using simulations and an EKF vehicle state estimation using dead-reckoning sensors. The remote vehicle was simulated with a 14-DOF vehicle model, and network delays were modeled with a FIFO nature GEV distribution, ranging from 200–300 ms. We simulated various adverse conditions, including challenging maneuvers, low-adhesion tracks, strong crosswinds, and significant measurement noise with dead-reckoning sensors.

Our findings show that SRPT outperforms the lookahead driver model under variable network delays during both normal and aggressive maneuvers. Especially during prompt maneuvers such as tight cornering, double lane changes, and slalom, SRPT mode exhibits significantly less cross-track error. This is desirable as these are common real-life maneuvers. SRPT achieves this by automatically moderating vehicle speed when needed. SRPT's resilience to network delay variability is promising for teleoperation systems, making them robust to measurement noise, network delays, and adverse conditions.

However, extreme network discontinuity can still strand the vehicle, and sensor failures require redundancy. Real-time computational resources are also necessary for optimizing the NMPC horizon. Notably, NMPC optimization performs within 5 ms on a standard office computer, which is sufficient given the 50 Hz optimization cycle frequency.

Future work will involve deploying SRPT on a real vehicle and control station, with operators generating reference poses using a steering joystick. Real-world experiments in urban scenarios, including online estimation of cornering stiffness and road adherence, will further enhance robustness.

References

1. Majstorovic, D., Hoffmann, S., Pfab, F., Schimpe, A., Wolf, M.-M., Diermeyer, F.: Survey on teleoperation concepts for automated vehicles (2022)
2. Mutzenich, C., Durant, S., Helman, S., Dalton, P.: Updating our understanding of situation awareness in relation to remote operators of autonomous vehicles. *Cogn. Res. Principles Implicat.* **6**, 1–17 (2021)
3. Hoffmann, S., Diermeyer, F.: Systems-theoretic safety assessment of teleoperated road vehicles. In: *Proceedings of the 7th International Conference on Vehicle Technology and Intelligent Transport Systems*, vol. 1: VEHITS, pp. 446–456, INSTICC, SciTePress (2021)
4. Prakash, J., Vignati, M., Vignarca, D., Sabbioni, E., Cheli, F.: Predictive display with perspective projection of surroundings in vehicle teleoperation to account time-delays. *IEEE Trans. Intell. Transport. Syst.* **24**(9), 9084–9097 (2023)
5. Saparia, S., Schimpe, A., Ferranti, L.: Active safety system for semi-autonomous teleoperated vehicles. In: *2021 IEEE Intelligent Vehicles Symposium Workshops (IV Workshops)*, pp. 141–147 (2021)

6. Qiao, B., Li, H., Wu, X.: Intelligent-assist algorithm for remote shared-control driving based on game theory. *J. Shanghai Jiaotong Univ. (Sci.)* **26**, 615–625 (2021)
7. Schitz, D., Graf, G., Rieth, D., Aschemann, H.: Model-predictive cruise control for direct teleoperated driving tasks. In: 2021 European Control Conference (ECC), pp. 1808–1813 (2021)
8. Hoffmann, S., Majstorović, D., Diermeyer, F.: Safe corridor: a trajectory-based safety concept for teleoperated road vehicles. In: 2022 International Conference on Connected Vehicle and Expo (ICCVE), pp. 1–6 (2022)
9. Schitz, D., Graf, G., Rieth, D., Aschemann, H.: Interactive corridor-based path planning for teleoperated driving. In: 2021 7th International Conference on Mechatronics and Robotics Engineering (ICMRE). IEEE (2021)
10. Prakash, J., Vignati, M., Sabbioni, E., Cheli, F.: Vehicle teleoperation: successive reference-pose tracking to improve path tracking and to reduce time-delay induced instability. In: 2022 IEEE Vehicle Power and Propulsion Conference (VPPC), pp. 1–8 (2022)
11. Prakash, J., Vignati, M., Sabbioni, E., Cheli, F.: Vehicle teleoperation: human in the loop performance comparison of smith predictor with novel successive reference-pose tracking approach. *Sensors* **22**(23), 9119 (2022)
12. Prakash, J., Vignati, M., Sabbioni, E.: Performance of successive reference pose tracking vs smith predictor approach for direct vehicle teleoperation under variable network delays. *IEEE Trans. Veh. Technol.* **73**(4), 4636–4645 (2024)
13. Bersani, M., et al.: An integrated algorithm for ego-vehicle and obstacles state estimation for autonomous driving. *Robot. Auton. Syst.* **139**, 103662 (2021)
14. Doumiati, M., Victorino, A.C., Charara, A., Lechner, D.: Onboard real-time estimation of vehicle lateral tire-road forces and sideslip angle. *IEEE/ASME Trans. Mechatron.* **16**(4), 601–614 (2011)

Open Access This chapter is licensed under the terms of the Creative Commons Attribution 4.0 International License (<http://creativecommons.org/licenses/by/4.0/>), which permits use, sharing, adaptation, distribution and reproduction in any medium or format, as long as you give appropriate credit to the original author(s) and the source, provide a link to the Creative Commons license and indicate if changes were made.

The images or other third party material in this chapter are included in the chapter's Creative Commons license, unless indicated otherwise in a credit line to the material. If material is not included in the chapter's Creative Commons license and your intended use is not permitted by statutory regulation or exceeds the permitted use, you will need to obtain permission directly from the copyright holder.





Advancing Autonomous Driving Safety Through LLM Enhanced Trajectory Prediction

Qian Cheng, Xinyu Jiao^(✉), Mengmeng Yang, Mingliang Yang, Kun Jiang^(✉),
and Diange Yang^(✉)

School of Vehicle and Mobility, Tsinghua University, Beijing, China
{jiaoxinyu, yangmm_qh, jiangkun}@tsinghua.edu.cn,
yml20@mails.tsinghua.edu.cn, ydg@mail.tsinghua.edu.cn

Abstract. In recent years, there has been remarkable progress in autonomous driving technology. To improve the safety of autonomous driving comprehensively, accurate predictions for all traffic agents are crucial. Typically, the graph neural network is widely employed for the trajectory prediction. To enhance the prediction accuracy rate, this paper utilizes a finetuned vision-to-language large model to extract driving intentions. With the well-designed prompt and the supervision of the specific dataset, the LLM (large language model) can analyze the current traffic condition and give the corresponding driving intention. This paper also combines the result of the LLM and the output of the traditional prediction model, and the future trajectory is modified with the driving intention, which can improve the final prediction accuracy. Finally, in the decision-making part, both the driving intention from the LLM and the trajectory from the traditional prediction model are considered in the boundary-based drivable area, and a safe planning path is then generated. According to the validation in the public motion forecasting dataset, this method has greatly improved the accuracy of the prediction and the safety of route planning.

Keywords: Autonomous driving · LLM · Trajectory prediction · Safety capability

1 Introduction

In order to ensure the safety of autonomous driving, predicting the future trajectory of traffic participants is essential. However, the trajectory prediction is a complex task due to the complicated traffic situation, especially during rush hours and interaction between different traffic participants [1]. In the traditional prediction model, the environmental information, such as the lane and other vehicles' positions is detected by the perception system and then input into a neural network. Current methods primarily utilize graph neural networks to extract key interaction information [2, 3]. Waymo's VectorNet model, for instance, encodes the environmental information as vectors and tensors, enhancing effectiveness and accuracy [4].

Recently, large language model (LLM) has been effectively applied in various fields. For trajectory prediction, LLMs' prior knowledge and understanding ability are used to

extract the scene information and interaction information. Based on this, model like Traj-LLM [5] and the transportation-context map [6] have enhanced the motion prediction performance. Unlike existing methods which enhance prediction performance by feeding enhanced scene information into prediction networks, this paper unitizes the high-level information generated by LLM for the adaptive modification of the output trajectory of the prediction network. Compared with the less interpretability of the network, our method can explicitly handle the output of the LLM and according to the modification result to improve the algorithm. In the meantime, we use a finetuned image-text large language model, trained on a specialized dataset, which can greatly enhance the understanding of the LLM for the specific traffic scene. The contributions of this paper are summarized as follows:

- 1) Innovatively utilizing a fine-tuned large language model to adaptively modify predicted trajectories with inferred driving intentions, enhancing prediction accuracy.
- 2) Considering both the driving intentions and predicted trajectories in the boundary-based drivable area model and allowing the safety margin to maximize the safety (Fig. 1).

2 Method

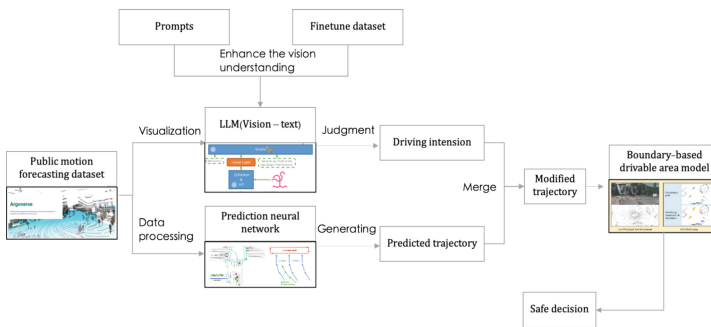


Fig. 1. The main process of this paper

Firstly, the dataset is processed and input into a prediction network to generate corresponding trajectory outputs. Simultaneously, the dataset is visualized in a specific form. Through the reasonable setting of prompts and supervised learning on a custom dataset, namely the finetuning process, the large language model's ability to recognize and understand the visualized dataset is significantly enhanced. The large language model then outputs assessments the driving intentions based on this recognition.

Secondly, the driving intention assessment is then utilized to modify the trajectory output by the prediction network, thereby improving prediction accuracy.

Finally, the modified trajectories are input into a boundary-based drivable area model, which comprehensively considers both driving intentions and predicted trajectories to achieve safe decision-making.

2.1 The Finetune of the LLM

Firstly, the public dataset needs to be visualized in a fixed form as a picture. The picture should contain all the related traffic elements, including the current position P_{cur} , the current velocity V_{cur} , the current yaw θ , and the trajectory of the past 2 s $\zeta_{2seconds}$, and the center line of the road M_{lane} . All the elements are described by specific geometric shapes.

$$\Theta_{per\ frame} = (X\{P_{cur}, V_{cur}, \theta, \zeta_{2seconds}\}, M_{lane}) \quad (1)$$

The setting of the prompt firstly should consider the explanation of the above traffic elements, and then describe the task for the driving intention judgement. The annotation of the custom is according to the ground truth of the dataset, and the label is stored in the corresponding JSON file.

According to the actual driving behavior, it can be divided into lateral intention and longitudinal intention. According to the amplitude, laterally it can be divided into left turn, left lane change, right turn, right lane change, going straight, U-turn, and longitudinally it can be divided into acceleration, deceleration, braking, and uniform speed.

2.2 Merge of the Driving Intention and the Predicted Trajectory

For the merge of the driving intention and the predicted trajectory, the prior information is the accuracy rate of the driving intention and the accuracy rate of the predicted trajectory, obtained by statistics on validation dataset. Also, in most cases, the vehicle follows the centerline of the road, which is regarded as an important reference.

And the final modified trajectory is related to the predicted trajectory $\zeta_{predicted}$, driving intention I , the accuracy rate of the LLM τ_{LLM} , the accuracy rate of the predicted trajectory τ_{NN} , and the neighbor centerline of the road M_{lane} , like in the Eq. (1) shows:

$$\zeta_{modified} = f(\zeta_{predicted}, I, \tau_{LLM}, \tau_{NN}, M_{lane}) \quad (2)$$

the detailed modification process is divided into three cases:

Case 1: When the driving intention is more consistent with the neighbor centerline of the road, the modified trajectory should follow the direction of the centerline.

Case 2: When the predicted trajectory is more consistent with the neighbor centerline of the road, the modified trajectory should follow the direction between the centerline and the predicted trajectory.

Case 3: When neither the driving intention and the predicted trajectory is not consistent with the neighbor centerline, the modified trajectory should follow the weighted average of the driving intention and the weight is related to the prior information. The Eq. (5) shows the modification process for the case 3.

$$\zeta_{modified,3} = \frac{\tau_{NN} * \zeta_{predicted} + \tau_{LLM} * I}{\tau_{LLM} + \tau_{NN}} \quad (3)$$

Case 4: When the driving intention is consistent with the predicted trajectory, the predicted trajectory will remain unchanged.

2.3 Decision-Making Based on Boundary-Based Drivable Area Model

Boundary-based drivable area model is an environmental model that considers the safety margin. With the modified trajectory, the future drivable area boundary will be drawn, and according to future boundaries, the safe decision-making can be generated.

The boundary of drivable area is shown in Fig. 2. The bounding boxes represents the perception result and the map limit represents the information of the HD map, after the pointing merging the final unified state-extended environment boundary is generated, and different color of the boundary represents the different attribute [7].

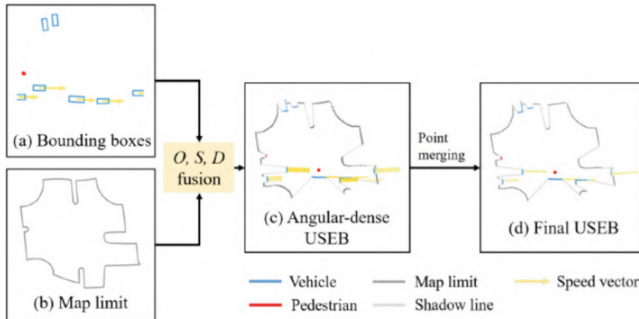


Fig. 2. The fusion process of the boundary-based drivable area model [7]

Combined with the driving intention and the modified predicted trajectory, it can ensure the safety of decision-making to the greatest extent.

3 Experiment

3.1 Finetune on the Vision-Text LLM

The public motion forecasting dataset Argoverse is utilized in this paper. And the LLM miniGPT4 is selected for the driving intention judgement.

Because the official finetune process only makes use of 3000 pictures for the whole scene, we utilize 500 frames in Argoverse with the annotation for the single scene. And the information of the hardware and the train parameter is in Table 1.

Table 1. Configuration of the finetune.

Environment	Value	Train parameter	
GPU	Nvidia L40*1	Batch size	2
GPU memory	48 GB	Epoch	20
Operating system	Ubuntu 18.04	Learning rate	3e-5
		Pretrained weight	13 B

3.2 Modification of the Predicted Trajectory

The typical prediction model Vectornet is selected as the baseline for the output of the trajectory and the network is trained for 25 epochs on the dataset Argoverse. And the typical modified trajectory is shown in the Fig. 3 below:

The red rectangle represents the target vehicle and the gray line represents the centerline of the road. The predicted trajectory by the Vectornet is in yellow, the modified trajectory is in green and the ground truth is in red. From the picture, it is demonstrated that the network predicts the wrong direction to straight, and with the modification of the driving intention, the green line is much close to the ground truth, which proves that the modification is effective.

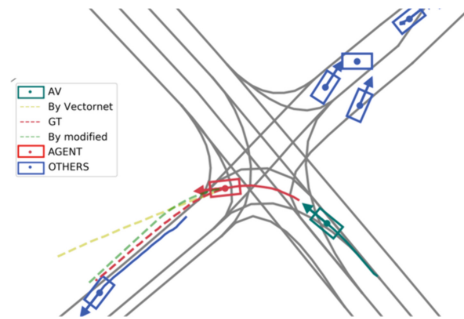


Fig. 3. The modified trajectory in the left-turn scenario

According to the modification method in Sect. 2.2, with the fusion of the driving intention of the LLM, the total prediction average distance error is greatly decreased by 31.9%, from 4.67 to 3.18.

3.3 Safe Decision-Making Based on Boundary-Based Drivable Area Model

The driving intention and the modified trajectory are considered in the boundary-based drivable area model, and the corresponding drivable space is generated. The planner for this part is the Werling planner based on the Frenet frame. The picture below shows the safety and the reliability of this method (Fig. 4):

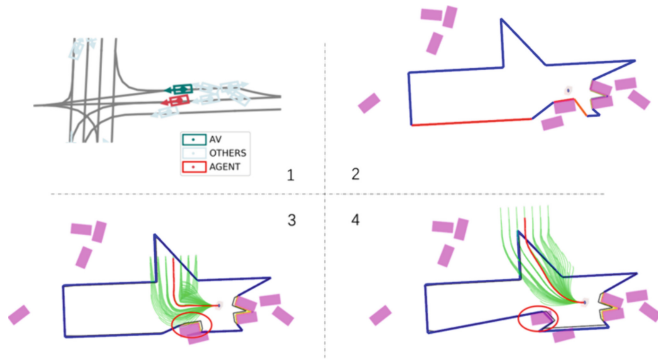


Fig. 4. The decision-making comparison between original prediction and modified prediction

Subpicture 1 represents the real scene of the dataset. The green car is the ego vehicle and chose to turn right in this scene, while the red car is the predicted vehicle and actually went straight. Subpicture 2 then shows the drivable space at the current moment. Subpicture 3 shows the drivable space at future moments and gives the planned trajectory of the ego vehicle going straight according to the prediction information of VectorNet. Subpicture 4 comprehensively considers the driving intention output by the LLM and the predicted trajectory to draw the drivable space and the planned trajectory of the ego vehicle at future moments, turning right.

In the subpicture 3, VectorNet model wrongly gives the prediction that the target vehicle (annotated with the red circle) will turn left, while subpicture 4 that comprehensively considers the LLM information to compensate the drivable boundary and reduces the drivable area. In terms of decision-making, the ego vehicle in subpicture 4 also avoids the target vehicle by an earlier right turn, thereby avoiding the safety risk of the ego vehicle crashing straight into the target vehicle which demonstrates that this method is safe and reliable.

4 Conclusion

This paper proposed a LLM enhanced trajectory prediction method. We finetune the large language model, so that the large language model has better prior knowledge of traffic scenes in general situations, and thus can give the driving intention of vehicles in the scene. At the same time, this paper designs an adaptive trajectory modification method, which utilizes the driving intention to modify the predicted trajectory, resulting in an improvement of the accuracy. Finally, combined with the boundary-based driving area model, this paper also adds the driving intention into the judgement of the drivable area, which generates a safer decision-making.

Acknowledgements. This work was supported in part by National Natural Science Foundation of China (U22A20104, 52102464), Beijing Natural Science Foundation (L231008), and Young Elite Scientist Sponsorship Program By BAST (BYESS2022153) and Shuimu Tsinghua Scholar Program.

References

1. Mozaffari, S., Al-Jarrah, O.Y., Dianati, M., Jennings, P., Mouzakitis, A.: Deep learning-based vehicle behaviour prediction for autonomous driving applications: a review. *IEEE Trans. Intell. Transport. Syst.* **23**(1), 33–47 (2020)
2. Brito, B., Agarwal, A., Alonso-Mora, J.: Learning Interaction-aware Guidance Policies for Motion Planning in Dense Traffic Scenarios. *arXiv* (2021)
3. Li, X., Ying, X., Chuah, M.C.: GRIP: graph-based interaction-aware trajectory prediction. In: 2019 IEEE Intelligent Transportation Systems Conference (ITSC), pp. 3960–3966. IEEE, Auckland, New Zealand (2019)
4. Gao, J., et al.: VectorNet: encoding HD maps and agent dynamics from vectorized representation. In: 2020 IEEE/CVF Conference on CVPR, pp. 11522–11530. IEEE (2020)
5. Lan, Z., et al.: Traj-LLM: A New Exploration for Empowering Trajectory Prediction with Pre-trained Large Language Models. *arXiv* (2024)
6. Zheng, X., et al.: Large language models powered context-aware motion prediction. *arXiv* (2024). Accessed: 29 May 2024
7. Jiao, X., et al.: Reliable autonomous driving environment model with unified state-extended boundary. *IEEE Trans. Intell. Transport. Syst.* **24**(1), 516–527 (2022)

Open Access This chapter is licensed under the terms of the Creative Commons Attribution 4.0 International License (<http://creativecommons.org/licenses/by/4.0/>), which permits use, sharing, adaptation, distribution and reproduction in any medium or format, as long as you give appropriate credit to the original author(s) and the source, provide a link to the Creative Commons license and indicate if changes were made.

The images or other third party material in this chapter are included in the chapter's Creative Commons license, unless indicated otherwise in a credit line to the material. If material is not included in the chapter's Creative Commons license and your intended use is not permitted by statutory regulation or exceeds the permitted use, you will need to obtain permission directly from the copyright holder.





Self-tuning of the Virtual-Bike Control for a Human-Powered Electric Bike with Series Architecture

Stefano Radrizzani^(✉), Giulio Panzani, and Sergio Matteo Savaresi

Dipartimento di Elettronica, Informazione e Bioingegneria, Politecnico di Milano,
Via G. Ponzio 34/5, 20133 Milan, Italy
`stefano.radrizzani@polimi.it`

Abstract. Motivated by environmental awareness, electric bikes (e-Bikes) diffusion as a means of transport has significantly increased in cities, thanks to their low emission and footprint. Among the different alternatives, series-parallel e-Bike architectures are interesting because they merge the advantages of the most common parallel bikes and the series ones, which can be exploited to improve the user experience. When an e-Bike is operating in series mode, a specific control action is needed to handle the absence of a mechanical transmission and so the chain-less nature of series or series-parallel e-Bikes. To this aim, the virtual-chain control law has been proposed and recently extended to a virtual-bike approach, respectively aiming at emulating the experience of the chain or an entire bike, whose parameters are user-chosen. In this work, a self-tuning strategy for the control parameters in the virtual-bike approach is formulated, making it independent of the specific bike and rider. Experimental results showed the advantages and limitations of the proposed solution.

1 Introduction

To reduce emissions and traffic in cities, electric bikes (e-Bikes) represent a suitable means of transport, whose diffusion significantly increased, see [1, 4] for a detailed review. Among the different alternatives, series-parallel e-Bike architectures, e.g., [8, 10], are interesting because they merge the advantages of parallel bikes, the most diffused on the market, and the series ones, which can increase the user experience when properly controlled to manage the absence of a mechanical chain. Indeed, an electrical transmission becomes, through the battery, the link between the in-wheel traction motor and the rider, whose power is converted into electrical by a generator directly mounted on the pedals. Therefore, when an e-bike can operate in series mode, a specific control law is necessary to deliver the human power to the wheel or to store it in the battery.

The current literature on series mode control is mainly focused on the control of the link between vehicle dynamics and human behavior. Indeed, it becomes a fundamental step before facing energy management, as in [3]. Particularly,

[2] explored the potential of a chain-less bike by virtually emulating a chain transmission, whose ratio can be freely designed by the rider. This approach is known as *virtual-chain*. Recently, [10] evolved this framework into a *virtual-bike*, in order to emulate not only the behavior of the chain but also the dynamics of a virtual bike, whose parameters are user-chosen.

In this work, we aim at improving the virtual-bike framework by proposing a self-tuning strategy, in order to adapt its control parameters, making them independent of a specific rider/bike pair. Specifically, vehicle/rider's parameters are identified in real-time while riding the bike: i.e., the bike coasting-down resistance and the total mass of the system, which are explicit parameters of the virtual-bike control law. Toward this aim, in this work, the virtual-bike control is integrated with a Recursive Least Squares (RLS) [7] approach in order to estimate the previously mentioned parameters. Indeed, RLS is an eligible solution for this application, where the identification problem is linear with respect to the parameters and the control law is an explicit function of the identified parameters.

The proposed approach has been experimentally tested to see the interaction of the control law and the adaptive strategy when the rider is on the bike. Experimental results show the general validity of the approach, but some limitations have been experienced. Indeed, the input applied to the system is not sufficiently exciting to correctly estimate the vehicle/rider's parameters. This happens with some combinations of the user-chosen design parameters of the virtual-bike.

The remainder of the paper briefly shows the vehicle modeling in Sect. 2, before introducing the adaptive virtual-bike control in Sect. 3. Then, the experimental results are shown in Sect. 4. Finally, the paper ends with some concluding remarks and future directions.

2 Vehicle Overview and Modeling

The considered vehicle is the one introduced in [10]. It is composed of a rear in-wheel electric motor, and a mid-drive generator, fed by a battery pack. Then, the key element is the free-wheel mechanism in the chain, which is responsible for the switch from a series to parallel architecture. Indeed, it can engage or disengage the chain, depending on the difference between the rotational speed on the wheel and pedal side [10]. Given that the vehicle is designed to engage the chain at low speed only, the parallel bike is just a transient architecture handled as in [9]. Hence, the vehicle control is for the series mode only, and so the model is presented for this scenario.

When an e-Bike works in series mode, the pedal and wheel side are mechanically decoupled. Therefore, the longitudinal dynamics can be effectively described by considering the longitudinal force balance below [2, 10]:

$$M \frac{dv}{dt} = \frac{T_m}{R_w} - F_{cd}(v), \quad (1)$$

where M is the total vehicle mass, composed of the bike M_b and the rider's one M_h . Then, v is the longitudinal speed, R_w is the wheel radius, and T_m is

the torque provided by the in-wheel electric motor. F_{cd} is the coasting-down force that is typically modeled through a second-order polynomial function of the speed:

$$F_{cd} = F_{cd}(v) = C + Bv + Av^2, \quad (2)$$

where A, B, C are model parameters. However, the longitudinal model in (1) can be simplified into a linearized one:

$$M \frac{dv}{dt} = \frac{T_m}{R_w} - \beta v, \quad (3)$$

where

$$\beta = \frac{dF_{cd}}{dv} = 2Av + B. \quad (4)$$

On the pedal side, due to the low inertia of the generator, the model is much simpler and the following torque balance holds:

$$T_h = -T_g \quad (5)$$

where T_h is the human torque applied by the rider and T_g the one applied by the generator.

3 Adaptive Virtual-Bike Control

The virtual-bike control law, introduced in [10] is the evolution of the virtual-chain control law from [2]. The virtual-chain is the solution of a bilateral control problem [11]: it returns a reference speed Ω_p for the generator on the pedals, as a function of the wheel speed Ω_w , and a reference torque T_m for the in-wheel traction motor, as a function of the cyclist's torque T_h . Then, if the reference pedal speed and motor torque share are designed to be respectively proportional to the wheel speed and rider's torque, the proportionality factor plays the role of a virtual chain ratio:

$$\Omega_p = \frac{\Omega_w}{\tau_v} \quad \text{and} \quad T_m = \frac{T_h}{\tau_v}. \quad (6)$$

It is worth mentioning that the virtual chain ratio is a user-chosen parameter, which can be freely designed, also as a function of the vehicle speed, according to the rider's preferences, even to keep a constant desired cadence.

This framework has been extended to the virtual-bike control by solving an impedance control problem [5] in the Laplace domain. In this way, the pedal speed and the reference torque become:

$$\Omega_p = \frac{\Omega_w}{\tau_v} \quad \text{and} \quad T_m = \frac{Ms + \beta}{M_v s + \beta_v} \frac{T_h}{\tau_v}, \quad (7)$$

where M_v and β_v represent the virtual mass and the virtual friction coefficient of the bike desired by the user. Considering that s is the Laplace operator, the

electric motor torque is now related to the rider's one through a transfer function and not by a static relationship as in the virtual-chain. The advantage of such an approach is the feeling experienced by the rider to be on a different bike, which can be freely designed. The main drawback of this control law is that the rider's mass and the bike coasting-down resistance are necessary to compute M and β .

Therefore, in this work, the main goal is the self-tuning of these parameters, in order to have a control law independent of their previous knowledge. To self-tune M and β , a recursive least-squares (RLS) problem has been formulated, exploiting that the vehicle dynamics in (3) can be re-written as:

$$a(t) = \frac{1}{M} (F_m(t) - Av^2(t) - Bv(t) - C), \quad (8)$$

where a is the vehicle acceleration and $F_m = T_m/R_w$. The RLS solution is computed by analytically [6] solving:

$$\theta^*(t) = \operatorname{argmin} \sum_k^t (a(k) - \phi^T(k)\theta)^2, \quad (9)$$

where θ is the vector of parameters and ϕ the vector of measurements sampled at time instant k :

$$\theta^T = \frac{1}{M} [1, -A, -B, -C,] \quad \text{and} \quad \phi^T(k) = [F_m(k), v^2(k), v(k), 1]. \quad (10)$$

Hence, the self-tuned virtual-bike control law becomes:

$$T_m(t) = \frac{M(\theta^*(t))s + \beta(\theta^*(t), v(t))}{M_v s + \beta_v} \frac{T_h}{\tau_v} = \frac{1}{\theta_1^*(t)} \frac{s - [2\theta_2^*(t)v(t) + \theta_3^*(t)]}{M_v s - \beta_v} \frac{T_h}{\tau_v}. \quad (11)$$

To conclude, the adaptive virtual-bike control law affects the link between the rider's torque and the motor one making it a transfer function with time-varying parameters. A graphical representation of the control scheme is given in Fig. 1.

4 Experimental Results

The effectiveness of the proposed methodology is experimentally tested on the same bike presented in [10] but with a different rider. Experimental tests showed the emulation capabilities of the self-tuning approach, despite a voluntary wrong parameter initialization $\theta^*(0)$. Moreover, different user-chosen parameters have been considered, ranging from a lighter to a heavier virtual tuning of the bike. Figure 2 shows the mismatch between the measured speed and the desired one, i.e., the speed computed imposing the chosen virtual-bike model, which is numerically quantified through the RMSE (Root Mean Square Error) comparing the adaptive approach and benchmark non-adaptive one developed in [10]. The adaptive solution was revealed to be superior except for one scenario. Indeed, when the virtual parameters represent a heavy bike, the cyclist rides at low speed; therefore, the RLS solution is not able to properly estimate the coasting-down force because of the lack of information. For such a reason, the emulation performance deteriorates. Opposite, in other cases, performance increases thanks to a better estimation of the coasting-down force.

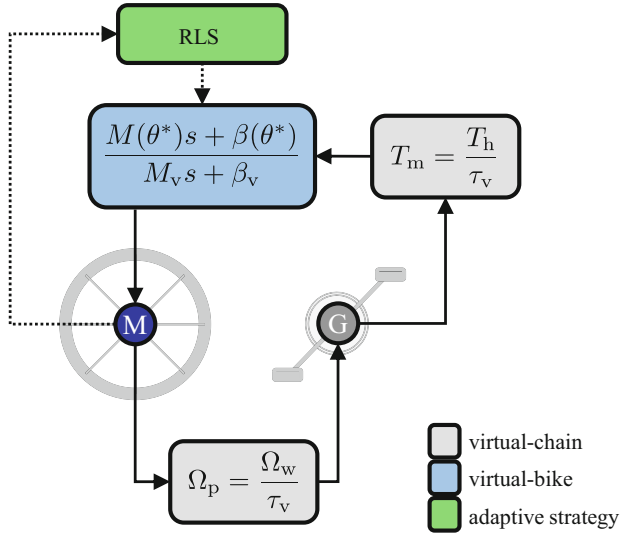


Fig. 1. Adaptive virtual-bike control scheme.

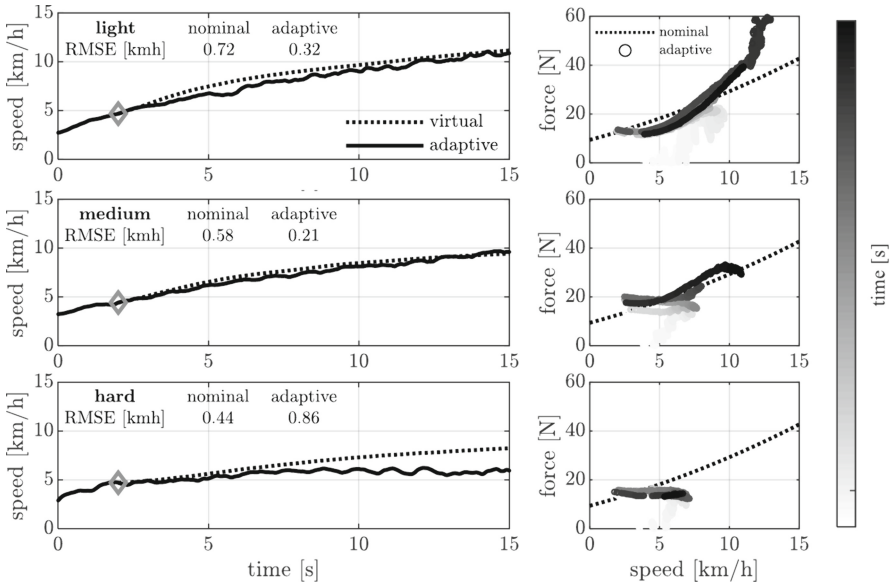


Fig. 2. Experimental results. (Left) Measured speed is compared, during an acceleration phase, with the reference when in series mode (after the diamond), and the error is compared with the nominal non-adaptive solution, in tables. (Right) Evolution of the adaptive estimation of the coasting-down force compared with the nominal non-adaptive model, during a longer test.

5 Conclusions

In this work, an RLS-based adaptive strategy for the virtual-bike control strategy in an e-Bike operating in series mode has been proposed. The effectiveness of the self-tuned solution has been experimentally evaluated and a general good behavior has been experienced. However, also some limitations have been noted with specific choices of the parameters, related to experience heavier virtual bikes. Therefore, further improvement or different approaches will be tested to increase the overall performance, also when emulating heavier bikes.

References

1. Contò, C., Bianchi, N.: E-bike motor drive: a review of configurations and capabilities. *Energies* **16**(1) (2023)
2. Corno, M., Roselli, F., Savaresi, S.M.: Bilateral control of SeNZA - a series hybrid electric bicycle. *IEEE Trans. Control Syst. Technol.* **25**(3), 864–874 (2017)
3. Guanetti, J., Formentin, S., Corno, M., Savaresi, S.M.: Optimal energy management in series hybrid electric bicycles. *Automatica* **81**, 96–106 (2017)
4. Harish Raaghav, S., Deepak, M., Swathika, O.V.G.: A Critical Review on the E-Bike and Its Evolution, chap. 34, pp. 123–147 (2024)
5. Hogan, N.: Impedance control: an approach to manipulation: part i-theory. *J. Dyn. Syst. Meas. Control* **107**(1), 1–7 (1985)
6. Ljung, L.: Recursive least-squares and accelerated convergence in stochastic approximation schemes. *Int. J. Adapt. Control Signal Process.* **15**(2), 169–178 (2001)
7. Lu, W.S., Meng, Q.H.: Impedance control with adaptation for robotic manipulations. *IEEE Trans. Robot. Autom.* **7**(3), 408–415 (1991)
8. Ongun, M.A., Kiran, U., Sakalli, A.: System design and simulation of a human electric hybrid vehicle in AVL cruise. In: 2020 IEEE International Symposium on Systems Engineering (ISSE), pp. 1–6 (2020)
9. Radrizzani, S., Panzani, G., Corno, M., Savaresi, S.M.: A concurrent controllers integration strategy to enhance the riding experience in bicycle driveline emulators. In: 2021 IEEE Conference on Control Technology and Applications (CCTA), pp. 1043–1048 (2021)
10. Radrizzani, S., Panzani, G., Savaresi, S.M.: Virtual-bike emulation in a series-parallel human-powered electric bike. *IFAC-PapersOnLine* **56**(2), 2558–2563 (2023). 22nd IFAC World Congress
11. Yokokohji, Y., Yoshikawa, T.: Bilateral control of master-slave manipulators for ideal kinesthetic coupling-formulation and experiment. *IEEE Trans. Robot. Autom.* **10**(5), 605–620 (1994)

Open Access This chapter is licensed under the terms of the Creative Commons Attribution 4.0 International License (<http://creativecommons.org/licenses/by/4.0/>), which permits use, sharing, adaptation, distribution and reproduction in any medium or format, as long as you give appropriate credit to the original author(s) and the source, provide a link to the Creative Commons license and indicate if changes were made.

The images or other third party material in this chapter are included in the chapter's Creative Commons license, unless indicated otherwise in a credit line to the material. If material is not included in the chapter's Creative Commons license and your intended use is not permitted by statutory regulation or exceeds the permitted use, you will need to obtain permission directly from the copyright holder.





Cooperative LiDAR-Aided Self-localization of CAVs in Real Urban Scenario

Akif Adas^(✉), Luca Barbieri, Pietro Morri, Simone Mentasti, Satyesh Awasthi,
Stefano Arrigoni, Edoardo Sabbioni, and Monica Nicoli

Politecnico di Milano, Milan, Italy
akif.adas@polimi.it

Abstract. In the rapidly advancing realm of Connected Autonomous Vehicles (CAVs), achieving reliable and precise positioning is of paramount importance. This paper presents a comprehensive approach integrating vehicular sensing, communication, and advanced filtering techniques to enhance vehicle positioning in urban areas. By leveraging LiDAR point clouds along with a light and accurate object detector, we create cohesive environmental sensing that improves situational awareness in autonomous systems. Central to our methodology is the integration of the Labeled Multi-Bernoulli Mixture (LMBM) filter, which offers a probabilistic framework for dynamic state estimation in environments characterized by high uncertainty and clutter. In turn, enhanced object locations are exploited as anchors for vehicular self-localization via an Extended Kalman filter (EKF). Our experimental results show that the proposed solution significantly enhances vehicular positioning accuracy.

Keywords: Cooperative sensing · Kalman filtering · Bernoulli tracking

1 Introduction

Global Navigation Satellite Systems (GNSSs) have widespread application in Connected Autonomous Vehicle (CAV) scenarios. However, conventional GNSS systems suffer from multipath propagation in urban environments, leading to high positioning errors [8] that can not be tolerated in safety-related vehicular services. A promising solution to overcome this problem is represented by collaborative sensing systems that leverage the presence of multiple actors in the same driving area to enhance positioning accuracy thanks to the coherent fusion of localization measurements acquired by nearby vehicles, as done in Implicit Cooperative Positioning (ICP) [2].

This work is financed by the European Union—NextGenerationEU project MOST (National Sustainable Mobility Center), grant # CN00000023, Italian Ministry of University and Research Decree n. 1033—17/06/2022, Spoke 9.

© The Author(s) 2024
G. Mastinu et al. (Eds.): AVEC 2024, LNME, pp. 510–516, 2024.
https://doi.org/10.1007/978-3-031-70392-8_73

This paper introduces a novel method for cooperative LiDAR-based vehicular self-positioning that leverages data sharing among vehicles to enhance localization accuracy. The innovative aspect of this method lies in its ability to address and mitigate key challenges such as false detections, object-measurement association, and measurement-measurement association which must be handled for real-world implementations. By integrating LiDAR data from various vehicles, the method ensures a more reliable and accurate vehicle positioning. Validation was conducted using a real-world dataset where multiple vehicles approached a zebra crossing on a two-way urban road featuring stationary road elements at the crossing. The results demonstrate the method’s effectiveness in improving positional accuracy and robustness in complex urban environments, underscoring its potential for practical applications in autonomous driving and advanced driver-assistance systems.

The rest of the paper is organized as follows. In Sect. 2, the cooperative sensing-based self-positioning solution is described. Section 3 presents the details of the experiment and provides a quantitative assessment, followed by concluding remarks in Sect. 4.

2 Cooperative Self-positioning

The proposed method fundamentals on implicit cooperative sensing and positioning. Vehicles equipped with LiDAR sensors generate point clouds. These point clouds encompass useful information for autonomous driving such as the location of road elements. In this end-to-end method, the object detector proposed in Sect. 2.1 clusters separable 3D points in the body reference system and identifies them as objects. Among these detected objects, there exist noise-derived detections. Besides, the other two onboard units are actively engaged, namely GNSS and Inertial Measurement Unit (IMU). Here, the GNSS positioning is enhanced with a Satellite-Based Augmentation System (SBAS), if available, which requires Line-Of-Sight (LOS) conditions with at least two geosatellites. Otherwise, Single-Point Positioning (SPP) is considered.

Additionally, vehicular heading is required for LiDAR-GNSS calibration. Some approaches used for the calculation of vehicular heading are visual odometry, dual-antenna GNSS localization, and fusion of GNSS and IMU [4]. Simply, we used single-antenna GNSS fixes to calculate vehicle heading and then calibrated the rotational component of LiDAR and GNSS reference frames.

While the proposed method can be implemented in a centralized or decentralized way, this paper focuses on centralized cooperation. In turn, the following data is exchanged with Road Side Unit (RSU) via Vehicle-to-Infrastructure (V2I) communications: detected object locations in the local framework and GNSS position fix. RSU synchronizes the aggregated data and projects objects onto the global reference system. At this step, a Multi-Target Tracking (MTT) filter tracks the static road elements in the presence of clutter. Here, vehicles are considered different sensors making observations in the same area and a special form of Labeled Multi-Bernoulli Mixture (LMBM), also known as multi-sensor

LMBM, is utilized. This operation returns object locations with lower uncertainty to be considered as anchors for the subsequent steps. It is worth noting that, the accuracy and precision of target locations in the global reference frame are tightly correlated to the number of vehicles as the higher the number of vehicles, the better the accuracy. These objects are back-propagated to each vehicle via V2I communications. Within this transmission, GNSS position fix, detected targets with clutters, and augmented object locations are available at each vehicle. Subsequently, vehicles individually employ a custom Extended Kalman Filter (EKF) given in Sect. 2.3 and leverage their global positioning.

2.1 Grid-Based Spatial Detector

The Grid-Based Spatial Detector (GSD) employed in this work is designed to isolate sets of points in the 3D space that objects have generated. The process is initiated by inserting a point cluster at a known position within the point cloud to mitigate segmentation noise. Subsequently, the point cloud is projected onto a 2D space and segmented to generate a density map. This density map is subsequently filtered to reduce noise-induced segments. At the core of this object detector is a density-based clustering method, namely density-based spatial clustering of application with noise (DBSCAN) [3] which is utilized to generate clusters in the density map. In turn, the inserted point cloud has been recognized among all detections and the segmentation bias has been eliminated by shifting clusters. Consequently, clusters with small dimensions are averaged and represented as single-point objects, ensuring accurate and reliable object detection.

2.2 Cooperative LMBM

MTT is a critical process performed in autonomous systems, for detecting and tracking multiple objects in a dynamic environment. An advanced MTT method is LMBM [5], efficiently handling measurement-target data association and clutter. This filter relies on a multi-Bernoulli birth model that initiates Bernoulli components at predefined locations.

The projection of detected objects on a global reference system depicts a multi-sensor configuration with independent imaging sensors. Likewise, the detected objects are independent. Therefore, Bernoulli components are independent and follow separate Bayesian recursions. A Bernoulli Random Finite Set (RFS) β is comprised of components at time t , $\text{RFS}_\beta \triangleq \{(T, L)_\beta, r_{e,t,\beta}, \mu_{t,\beta}, \Sigma_{t,\beta}\}$, where T_β is the birth time, L_β is a unique label assigned to Bernoulli β born at time t , and $\mu_{t,\beta}$ is the first central moment and $\Sigma_{t,\beta}$ is the covariance of Gaussian distribution. Bernoulli components follow a static motion model, namely $\mu_{t,\beta} = \mu_{t-1,\beta}$, as fixed targets in the driving scenario are considered.

For the propagation of existence probability, r_e , and marginal association probabilities over time, Gibbs's sampling [6] has been employed thanks to its capability to handle high dimensional problems. After conducting the gating,

pruning and capping steps, target states are obtained by processing the remaining Bernoulli components. These states contain the spatial attribute of objects in 2D, denoted by the object set $\mathcal{O} = \{\mathbf{x}_{o,t}\} : |\mathcal{O}| = N_o$, and their corresponding covariance to be used by the filter introduced in the following section.

2.3 Extended Kalman Filter-Based Refinement Stage

A set of vehicles $\mathcal{V} = \{1, \dots, N_V\}$ cruise in a 2D area. Each vehicle v , with $v \in \mathcal{V}$, is represented by its state $\mathbf{x}_{v,t} = [\mathbf{u}_{v,t}, \mathbf{v}_{v,t}]$ where $\mathbf{u}_{v,t}$ and $\mathbf{v}_{v,t}$ are the 2D position and 2D velocity, respectively. The vehicle's state changes over time according to a nearly constant velocity motion model [7], defined as

$$\mathbf{x}_{v,t|t-1} = \mathbf{F}\mathbf{x}_{v,t-1} + \mathbf{L}\mathbf{q}_{v,t-1}, \quad (1)$$

where $\mathbf{F} = [\mathbf{I}_2 T_s \mathbf{I}_2; \mathbf{0}_{2 \times 2} \mathbf{I}_2]$ and $\mathbf{L} = [0.5T_s^2 \mathbf{I}_2; T_s \mathbf{I}_2]$, T_s the sampling time, while $\mathbf{q}_{v,t-1} \sim \mathcal{N}(\mathbf{0}, \mathbf{I}_2 \sigma_{v,U}^2)$ is a zero-mean Gaussian random variable with standard deviation $\sigma_{v,U}$ modeling the acceleration uncertainty of the v -th vehicle.

EKF is employed for tracking as follows. States are predicted according to the motion model in (1) and are exchanged with RSU along with detected objects provided by GSD explained in Sect. 2.1. Subsequently, the LMBM filter (Sect. 2.2) is utilized. The leveraged object locations are then back-propagated to vehicles and object-object association between detected objects and leveraged targets is established according to the maximum likelihood criterion.

For the update step of the EKF, both GNSS and object-derived measurements are utilized to enhance vehicular positioning. The GNSS measurement of vehicle v is modelled as follows:

$$\rho_{g,t}^{(v)} = \mathbf{h}_g(\mathbf{x}_{v,t}) + \mathbf{n}_{v,t} = \mathbf{T}\mathbf{x}_{v,t} + \mathbf{n}_{v,t}, \quad (2)$$

where $\mathbf{T} = [\mathbf{I}_2, \mathbf{0}_{2 \times 2}]$, while $\mathbf{n}_{v,t} \sim \mathcal{N}(\mathbf{0}, \mathbf{I}_2 \sigma_v^2)$ is a zero-mean Gaussian random variable with standard deviation σ_v^2 characterizing the GNSS positioning accuracy of the v -th vehicle.

Any object $o \in \mathcal{O}$ with state $\mathbf{x}_{v,o,t} = [\mathbf{u}_{x,o,t}, \mathbf{u}_{y,o,t}]$ refined by the RSU is more accurate compared to the detection j , such that $\mathbf{x}_{v,j,t} = [\mathbf{u}_{x,j,t}, \mathbf{u}_{y,j,t}]$, generated by the same object on vehicle v . Leveraging this fact, so o and j , the measurement models $\rho_{r,t}^{(j,v)}$ and $\rho_{\alpha,t}^{(j,v)}$, define the distance and the clockwise angle from positive x-direction between object j and vehicle v , namely they are

$$\rho_{r,t}^{(j,v)} = \mathbf{h}_r(\mathbf{x}_{v,j,t}) + \mathbf{n}_{r,t}^{(j,v)} = \|\rho_{g,t}^{(v)} - \mathbf{x}_{v,j,t}\|^2 + \mathbf{n}_{r,t}^{(j,v)}, \quad (3)$$

$$\rho_{\alpha,t}^{(j,v)} = \mathbf{h}_\alpha(\mathbf{x}_{v,j,t}) + \mathbf{n}_{\alpha,t}^{(j,v)} = \angle(\rho_{g,t}^{(v)}, \mathbf{x}_{v,j,t}) + \mathbf{n}_{\alpha,t}^{(j,v)}, \quad (4)$$

where \angle is the angle while $\mathbf{n}_{r,t}^{(j,v)} \sim \mathcal{N}(\mathbf{0}, \mathbf{I}_2 \sigma_r^2)$ and $\mathbf{n}_{\alpha,t}^{(j,v)} \sim \mathcal{N}(\mathbf{0}, \mathbf{I}_2 \sigma_\alpha^2)$ are zero-mean Gaussian random variables with standard deviations σ_r and σ_α , respectively. EKF refinement exploits the measurements $\rho_{r,t}^{(j,v)}$ and $\rho_{\alpha,t}^{(j,v)}$ to improve the vehicle state. Accordingly, the state estimate of the vehicle is updated as

$$\mathbf{x}_{v,t} = \mathbf{x}_{v,t|t-1} + \mathbf{G}_t (\rho_{v,t} - \mathbf{h}(\mathbf{x}_{v,t|t-1}, \mathbf{x}_{v,1,t}, \dots, \mathbf{x}_{v,N_o,t})), \quad (5)$$

$$\mathbf{C}_t = \mathbf{C}_{t|t-1} - \mathbf{G}_t \mathbf{B} \mathbf{C}_{t|t-1}, \quad (6)$$

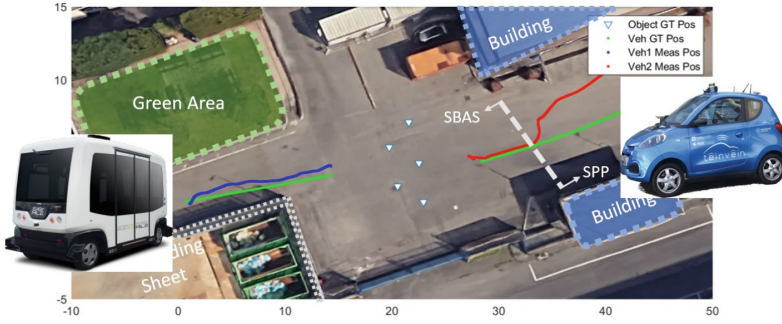


Fig. 1. Trajectories show GNSS measurements along with RTK-corrected ground truth (GT) positions, SBAS and SPP available regions along with prototypes

where $\mathbf{G}_t = \mathbf{C}_{t|t-1} \mathbf{B} (\mathbf{B} \mathbf{C}_{t|t-1} \mathbf{B}^T + \Sigma)^{-1}$ is the Kalman gain, $\mathbf{B} = [\mathbf{T}, \mathbf{J}_r, \mathbf{J}_\alpha]^T$ in which \mathbf{J}_r and \mathbf{J}_α are the Jacobian matrices extracted from (3) and (4), $\boldsymbol{\rho}_{v,t} \triangleq [\boldsymbol{\rho}_{g,t}^{(v)}, \boldsymbol{\rho}_{r,t}^{(1,v)}, \dots, \boldsymbol{\rho}_{r,t}^{(N_o,v)}, \boldsymbol{\rho}_{\alpha,t}^{(1,v)}, \dots, \boldsymbol{\rho}_{\alpha,t}^{(N_o,v)}]^T$, $\Sigma \triangleq \text{blkdiag}(\sigma_v^2 \mathbf{I}_2, \sigma_r^2 \mathbf{I}_{N_o}, \sigma_\alpha^2 \mathbf{I}_{N_o})$, $\mathbf{h} = [\mathbf{h}_g(\mathbf{x}_{v,t|t-1}), \bar{\mathbf{h}}_r^o, \bar{\mathbf{h}}_\alpha^o]^T$ with $\bar{\mathbf{h}}_\alpha^o = [\mathbf{h}_\alpha^o(\mathbf{x}_{v,1,t}), \dots, \mathbf{h}_\alpha^o(\mathbf{x}_{v,N_o,t})]^T$, and $\bar{\mathbf{h}}_r^o = [\mathbf{h}_r^o(\mathbf{x}_{v,1,t}), \dots, \mathbf{h}_r^o(\mathbf{x}_{v,N_o,t})]^T$ which are range and angle measurements calculated using augmented objects.

3 Experimentation and Results

To assess the performance of the proposed method, we collected real-world data through several experiments using two different instrumented prototype vehicles, an electric light quadricycle and a prototype bus as shown in Fig. 1, equipped with comprehensive sensor systems. Collected data includes RTK-corrected and uncorrected GNSS measurements as well as LiDAR point clouds. Five objects detectable by LiDAR were used to enhance positioning, aiming to evaluate localization improvement compared to ICP. The setup, shown in Fig. 1, featured both vehicles converging towards an area with the deployed objects. For further elaboration on the experimental campaign and dataset we refer to [1].

During the implementation of the proposed method, an assumption of lossless and zero-latency V2I communication has been made. Data collected by sensors were aggregated and processed at a central computational unit offline. As concerns the computational cost, the bottleneck is LMBM in which the number of measurement-target association hypotheses increases exorbitantly. While this problem can be overcome by investigating lighter MTT algorithms, we limited the number of hypotheses and Gibbs’s samples and initiated Bernoullis in the center of the surveillance area, so near to objects.

Figure 2 shows the Cumulative Density Function (CDF) of the vehicle positioning error considering ICP with [1] and without multipath compensation [2], raw GNSS ego vehicle position, proposed method, referred to as Cooperative Self-Positioning (CSP), along with Circular Error Probability with 95% confidence (CEP95). When CEP95 is concerned, CSP has a positioning improvement

of 68% and 66% compared to GNSS for veh1 and veh2 respectively. Besides, CSP has similar performance to the benchmark ICP which assumes perfect association among detected objects, making it unemployable in real applications.

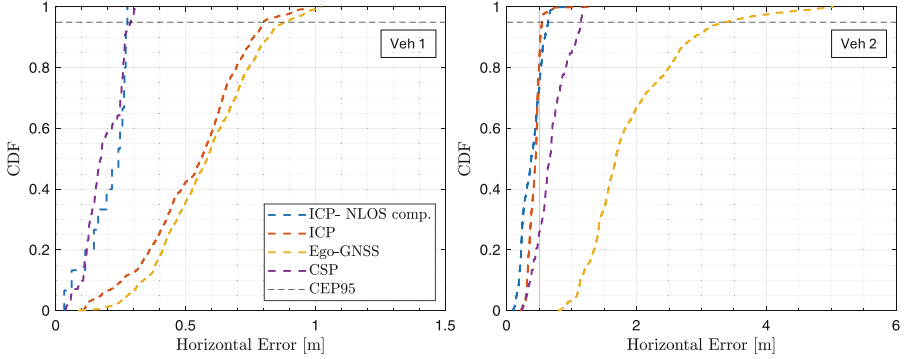


Fig. 2. Performance comparison of CSP against ICP with and without NLOS compensation and Ego-GNSS.

4 Conclusion

This paper proposed a cooperative sensing-aided positioning method relying on environmental perception with LiDAR sensors. This model-based algorithm handles the uncertainty of a dynamic environment by exploiting collaborative sensing and employing the LMBM filter. This method has been assessed in a real-world application and its effectiveness has been reported. The planned future work is to establish V2I communications and integrate RSU as both an observer and the central computational unit.

References

1. Adas, A., et al.: LiDAR-aided cooperative localization and environmental perception for CAVs. In: 2024 27th International Conference on Information Fusion (FUSION) (2024, to appear)
2. Barbieri, L., Tedeschi, B.C., Brambilla, M., Nicoli, M.: Deep learning-based cooperative lidar sensing for improved vehicle positioning. *IEEE Trans. Signal Process.* **72**, 1666–1682 (2024)
3. Hahsler, M., Piekenbrock, M., Doran, D.: dbscan: fast density-based clustering with R. *J. Stat. Softw.* **91**(1), 1–30 (2019)
4. Juang, J.C., Lin, C.F.: A sensor fusion scheme for the estimation of vehicular speed and heading angle. *IEEE Trans. Veh. Technol.* **64**(7), 2773–2782 (2015)
5. Reuter, S., Vo, B.T., Vo, B.N., Dietmayer, K.: The labeled multi-Bernoulli filter. *IEEE Trans. Signal Process.* **62**(12), 3246–3260 (2014)

6. Robert, C.P., Casella, G.: The two-stage Gibbs sampler. In: Robert, C.P., Casella, G. (eds.) *Monte Carlo Statistical Methods*, pp. 337–370. Springer, New York (2004). https://doi.org/10.1007/978-1-4757-4145-2_9
7. Thrun, S., Montemerlo, M.: The graph slam algorithm with applications to large-scale mapping of urban structures. *Int. J. Robot. Res.* **25**(5–6), 403–429 (2006)
8. Zhu, N., Marais, J., Bétaille, D., Berbineau, M.: GNSS position integrity in urban environments: a review of literature. *IEEE Trans. Intell. Transp. Syst.* **19**(9), 2762–2778 (2018)

Open Access This chapter is licensed under the terms of the Creative Commons Attribution 4.0 International License (<http://creativecommons.org/licenses/by/4.0/>), which permits use, sharing, adaptation, distribution and reproduction in any medium or format, as long as you give appropriate credit to the original author(s) and the source, provide a link to the Creative Commons license and indicate if changes were made.

The images or other third party material in this chapter are included in the chapter's Creative Commons license, unless indicated otherwise in a credit line to the material. If material is not included in the chapter's Creative Commons license and your intended use is not permitted by statutory regulation or exceeds the permitted use, you will need to obtain permission directly from the copyright holder.





Subjective-Objective Assessment of Different Torque Vectoring Control Strategies

Michele Asperti^(✉), Michele Vignati, and Edoardo Sabbioni

Department of Mechanical Engineering, Politecnico di Milano, Via La Masa N.1, 20156 Milan, Italy
michele.asperti@polimi.it

Abstract. With the increasing demand for enhanced vehicle performance and handling dynamics, torque vectoring has become a key technology in contemporary automotive engineering. Over the years, various control algorithms have been developed and their performance assessed using objective metrics that measure a vehicle's ability to follow a reference quantity for lateral dynamics. However, this evaluation approach is limited as it does not consider feedback from actual drivers. This paper addresses this critical gap by incorporating drivers' subjective evaluations through Driver-in-the-Loop simulations. The study conducts a comprehensive analysis of both objective metrics and subjective driver assessments, investigating the impact of different torque vectoring control strategies on vehicle dynamics. By correlating quantitative metrics with human perception, this integrated approach enhances the understanding of the effectiveness of torque vectoring control strategies and their real-world implications for driver satisfaction.

Keywords: Torque Vectoring · Vehicle Dynamics · Driver-in-the-Loop Simulation · Subjective Evaluation · Objective Assessment

1 Introduction

Electric vehicles are increasingly recognized as a viable alternative to traditional internal combustion engine vehicles due to their perceived sustainability [1]. The use of electric motors in these vehicles facilitates the implementation of multiple-motor powertrain layouts [2], enhancing vehicle dynamics through improved control capabilities. Notably, the adoption of In-Wheel Motors (IWMs) is widespread [3], as they allow independent control of driving torque at each wheel, enabling the implementation of Torque Vectoring Control (TVC). Indeed, Torque Vectoring (TV) controls vehicle lateral dynamics by generating a yaw moment through differential longitudinal forces on the wheels of the same axle.

Over the years, several TV controllers have been proposed [4, 5], with their performance typically evaluated using objective metrics that measure how closely they track reference quantities for lateral dynamics, such as yaw rate and sideslip angle. Recently, there has been a growing trend to incorporate driver preferences into TV control logics,

allowing the selection of driving modes [6, 7] to slightly modify the behavior of the controlled vehicle. This innovation tailors the vehicle response to driver desires, potentially increasing vehicle effectiveness and acceptability through appropriate feedback to the driver. Indeed, drivers' subjective evaluations of vehicle performance still are a fundamental process for car manufacturers [8]. However, there is a trend toward correlating subjective evaluations with objective indexes to reduce reliance on human testing in the future. For instance, ride comfort ratings are typically correlated with acceleration measurements at the seat level [9, 10]. On the other hand, vehicle handling ratings are typically correlated with system deadbands, delays, and gains in the vehicle's response to driver inputs [11–13].

This paper presents an in-depth analysis of the subjective and objective assessment of various torque vectoring control strategies through Driver-in-the-Loop simulations. The objective analysis provides a quantitative framework for evaluating the effectiveness of different torque vectoring control strategies. Conversely, the subjective assessments encompass factors such as perceived vehicle responsiveness, handling confidence, and overall driving satisfaction, offering crucial insights into user experience. Additionally, the study investigates the relationship between objective measurements and subjective evaluations, aiming to establish a correlation between quantitative metrics and human perception. This integrated approach enhances the understanding of torque vectoring control strategies' effectiveness and their real-world impact on driver satisfaction.

2 Torque Vectoring Controllers Design

Three alternative torque vectoring (TV) control strategies have been developed to enhance the cornering performance of the DinamiΣ PRC DP14 Formula SAE competition vehicle of Politecnico di Milano, shown in Fig. 1. These control strategies differ in their architectures, utilizing various combinations of feedforward and feedback yaw moment contributions. The objective of the feedback control action, regardless of its specific implementation, is to track the desired yaw rate response of the vehicle, which is defined as a function of vehicle speed and steering wheel angle input.



Fig. 1. DP14 Formula SAE vehicle of Politecnico di Milano.

Each TV controller features a unique formulation for defining the yaw moment applied to the vehicle, as detailed in the following:

- **PI Torque Vectoring Controller:** The PI torque vectoring controller consists in a pure feedback control aiming at tracking the desired yaw rate through the minimization of the yaw rate error ($\varepsilon_{\dot{\psi}}$)

$$M_{z,PI} = k_p(v_x) \cdot \varepsilon_{\dot{\psi}} + k_i(v_x) \cdot \int \varepsilon_{\dot{\psi}} dt \quad (1)$$

- **PI + DD Torque Vectoring Controller:** The PI + DD torque vectoring controller consists of the PI feedback control action described above with the addition of a DD feedforward control action function of the input steering wheel angle (δ) and steering wheel angle rate ($\dot{\delta}$) commanded by the driver

$$M_{z,PI+DD} = M_{z,PI} + M_{z,DD} = M_{z,PI} + k_{\delta}(v_x) \cdot \delta + c_{\delta}(v_x) \cdot \dot{\delta} \quad (2)$$

- **DD + ESC Torque Vectoring Controller:** The DD + ESC torque vectoring controller supplements the DD feedforward control action with an ESC-like discontinuous feedback contribution applying a discontinuous yaw moment contingent upon whether the absolute value of the yaw rate error falls below or exceeds a specified threshold ($\varepsilon_{\dot{\psi},TH}$).

$$M_{z,DD+ESC} = M_{z,DD} + M_{z,ESC} = M_{z,DD} + \begin{cases} 0 & IF \left| \varepsilon_{\dot{\psi}} \right| < \varepsilon_{\dot{\psi},TH} \\ k_p(v_x) \cdot \varepsilon_{\dot{\psi}} & IF \left| \varepsilon_{\dot{\psi}} \right| \geq \varepsilon_{\dot{\psi},TH} \end{cases} \quad (3)$$

For an effective and reliable performance of the proposed torque vectoring controllers, all their gains are scheduled as function of vehicle longitudinal speed (v_x).

3 Driver-in-the-Loop Simulator Testing Campaign

The effects of different TV control logics for a Formula SAE vehicle are assessed in this study through the adoption of Driver-In-the-Loop simulations at a static driving simulator. This allows testing in a safe environment while also ensuring a proper repeatability of the boundary conditions among the performed tests. Therefore, the resulting subjective evaluations from drivers can be considered as feedback about the torque vectoring control logic. Indeed, the 14 DOFs vehicle model implemented in VI-CarRealTime software has not been modified throughout the testing campaign.

The static driving simulator experimental campaign has been conducted by involving six drivers possessing significant familiarity with the FSAE competition vehicle both on track and in its development utilizing the same static driving simulator employed in this study. A tailored test track has been designed for the present study, where a double lane change maneuver is proposed. To ensure comprehensive evaluation, drivers were tasked with completing a minimum of 10 laps of the test track with each TV controller, rating vehicle response on a scale of 1 to 10, focusing on four key aspects being control, stability, easiness and repeatability.

4 Results

The performance of the proposed torque vectoring controllers is evaluated at first on a subjective basis through the ratings gathered from drivers. Then, an objective evaluation is performed to understand the effectiveness of each TV control logic in improving vehicle lateral dynamics. In the end, a correlation between subjective ratings and objective indexes is performed to understand which are the most important objective quantities that drive the human perception of vehicle lateral dynamics control.

4.1 Subjective Evaluation

The subjective evaluation of the proposed torque vectoring controllers relies on drivers' evaluations, which are reported in Fig. 2 for the double lane change maneuver. In there, the median rating is highlighted with a red bar, with the blue box that indicates the 25th and 75th percentiles of the ratings distribution. On average, the PI + DD TVC results the best control logic on a subjective basis for all the inspected rating categories, while the PI TVC results the control logic with the highest spread of ratings. This means that the addition of the feedforward component to the yaw moment generation is positively perceived by the driver. This could be due to a prompter vehicle response to the driver inputs, which also results in a more consistent rating in easiness and repeatability categories having a more direct vehicle behavior as function of the steering input. The DD + ESC TVC generally results the worst performing control logic, probably due to its discontinuous control action which is not positively perceived by humans.

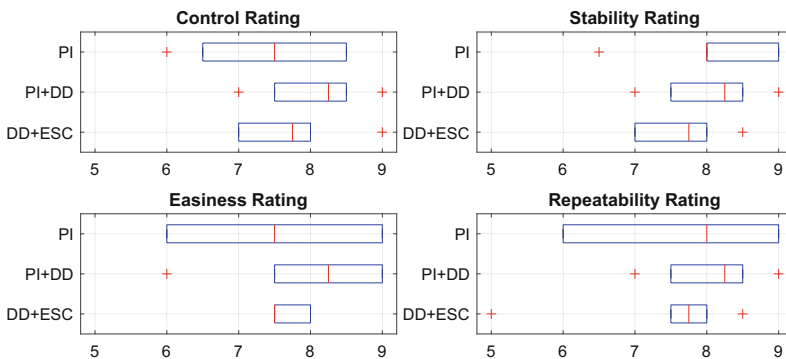


Fig. 2. Subjective evaluation of the proposed TV controllers about the vehicle cornering response during the double lane change maneuver.

4.2 Objective Evaluation

In this study, the objective analysis of vehicle handling performance is conducted using specifically defined Key Performance Indicators (KPIs) for transient maneuvers. To ensure consistency in the objective KPIs across different drivers, a normalization method

has been implemented to minimize the influence of driving style on the evaluation process. The normalization is expressed as follows.

$$KPI_{j,norm} = \frac{KPI_j - KPI_{PI}}{|KPI_{PI}|} \quad (4)$$

With this approach, the $KPI_{j,norm}$ values represent the relative variation of KPI_j obtained using the j^{th} TV control logic, compared to KPI_{PI} obtained with the PI TV control logic, which serves as the reference.

The evaluation of the relative objective performance of the proposed TV controllers during a double lane change maneuver is presented in Fig. 3. The results indicate that both the PI + DD and DD + ESC TVCs achieve lower section times compared to the PI TVC, with enhanced cornering performance attributed to an increased yaw rate gain in response to steering wheel angle inputs. Additionally, the PI + DD TVC demonstrates a significantly reduced hysteresis cycle area for the yaw rate response as a function of the steering wheel angle input, indicating improved repeatability of cornering response. However, this improvement is accompanied by several instances where the steering wheel torque opposes the steering wheel angle input, making vehicle control more challenging for the driver.

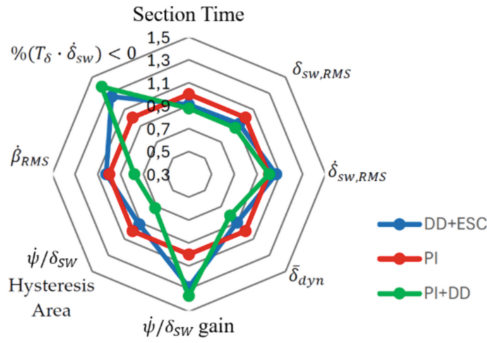


Fig. 3. Effects of the proposed TV controllers on the double lane change vehicle cornering response.

4.3 Subjective-Objective Evaluation Correlation

The objective evaluation of vehicle cornering performance is conducted in this study on a relative basis, using the PI TV control logic as a reference, thus also the subjective assessment is reverted to a relative basis for correlation purposes. This method eliminates driver bias in the evaluation of the TV control logics by considering only the variation in subjective evaluations ($Rating_i$) of the i^{th} driver relative to those obtained from the same driver using the reference TV control logic ($Rating_{PI}$).

$$Rating_{i,rel} = Rating_i - Rating_{PI} \quad (5)$$

The primary tool used for analyzing the level of correlation between subjective ratings and objective indexes is the Spearman rank correlation coefficient. This statistical measure evaluates the strength and direction of a monotonic relationship between two variables. The results regarding the correlation of subjective ratings with various objective KPIs is reported in Fig. 4 for the double lane change maneuver.

	Control	Stability	Easiness	Repeatability
DLC				
section time	0,03	0,78	0,36	0,18
RMS steering wheel angle	-0,50	0,37	-0,43	-0,44
RMS (steering - ideal steering)	-0,74	0,17	-0,21	-0,61
RMS steering wheel rate	-0,78	-0,17	-0,73	-0,67
MAX steering wheel angle rate	-0,71	0,07	-0,52	-0,60
CREST steering wheel angle rate	0,14	0,30	0,06	0,08
STD throttle	0,29	0,24	0,25	0,56
RMS sideslip angle	-0,71	-0,10	-0,54	-0,71
RMS sideslip angle rate	-0,78	-0,17	-0,62	-0,70
MAX sideslip angle rate	-0,71	-0,10	-0,54	-0,71
CREST sideslip angle rate	-0,15	0,00	-0,13	-0,19
RMS lateral acceleration	-0,29	-0,40	-0,59	-0,35
dynamic steering angle	0,53	-0,07	0,57	0,60
yaw rate gain	-0,05	-0,74	0,02	-0,19
hysteresis area	-0,81	-0,13	-0,79	-0,85
RMS (sidelip - ideal sideslip angle)	-0,60	-0,07	-0,51	-0,59
RMS (yaw rate - ideal yaw rate)	-0,60	-0,13	-0,57	-0,57
STD front tyre utilization factor	-0,32	0,13	-0,61	-0,43
STD rear tyre utilization factor	-0,43	-0,51	-0,69	-0,47
wheel-steer torque*wheel steer rate	-0,41	0,57	-0,39	-0,42

Fig. 4. Spearman correlation between subjective ratings and objective KPIs during double lane change maneuvers.

The analysis of control ratings reveals an inverse correlation with the steering wheel angle rate and sideslip angle rate KPIs. This is logical, as lower values for these rates likely correspond to fewer driver corrections needed to complete the maneuver. Additionally, control ratings are strongly correlated with changes in the yaw rate/steering hysteresis loop area. Stability ratings exhibit a strong correlation with section time and a strong inverse correlation with the yaw rate gain relative to steering input. This indicates that higher stability is perceived by the driver when the double lane change maneuver is completed at a lower average speed and the vehicle is slightly less responsive to steering input. Easiness ratings show a significant inverse relationship with the RMS value of the steering wheel angle rate and the standard deviation of the tires' utilization factor. This suggests that the vehicle is perceived as easier to drive when it requires fewer corrections. Repeatability ratings exhibit a very strong correlation with the hysteresis loop area of yaw rate relative to steering wheel angle input, indicating that drivers perceive

increased repeatability when the vehicle's yaw rate response is more predictable based on the steering wheel input.

5 Conclusions

The impact of three different torque vectoring control strategies on vehicle dynamics has been evaluated in this study. The standard approach, which relies on objective KPIs, has been enhanced by incorporating subjective evaluations from six drivers through a testing campaign on a static driving simulator. The subjective evaluations identify the PI + DD controller as the best perceived by humans. Additionally, the objective evaluation of torque vectoring controllers indicates that the PI + DD controller is the one most significantly enhancing vehicle cornering response, though it increases driver workload. The correlation between subjective and objective evaluations then is used to explain the reasons behind the improved or worsened ratings. Specifically, the PI + DD torque vectoring controller demonstrates the smallest hysteresis loop area between vehicle yaw rate response and steering wheel angle input, which correlates with higher ratings of controller capabilities. Additionally, the PI + DD controller also causes lower sideslip angle speeds, making the vehicle less challenging to drive and resulting in higher subjective ratings for vehicle easiness. This research not only contributes to optimizing torque vectoring control strategies but also provides a methodology for bridging the gap between objective performance metrics and subjective driver experience. These findings can guide the development of future torque vectoring systems, leading to vehicles that excel in objective performance measures while aligning with drivers' subjective preferences.

References

1. Requia, W.J., Mohamed, M., Higgins, C.D., et al.: How clean are electric vehicles? Evidence-based review of the effects of electric mobility on air pollutants, greenhouse gas emissions and human health. *Atmos. Environ.* **185**, 64–77 (2018)
2. Rinderknecht, S., Meier, T.: Electric power train configurations and their transmission systems. *SPEEDAM* **2010**, 1564–1568 (2010)
3. Murata, S.: Innovation by in-wheel-motor drive unit. *Veh. Syst. Dyn.* **50**, 807–830 (2012)
4. Mazzilli, V., De Pinto, S., Pascali, L., et al.: Integrated chassis control: Classification, analysis and future trends. *Annu. Rev. Control.* **51**, 172–205 (2021)
5. Katsuyama, E., Yamakado, M., Abe, M.: A state-of-the-art review: toward a novel vehicle dynamics control concept taking the driveline of electric vehicles into account as promising control actuators. *Veh. Syst. Dyn.* **59**, 976–1025 (2021)
6. De Novellis, L., Sornioti, A., Gruber, P.: Driving modes for designing the cornering response of fully electric vehicles with multiple motors. *Mech. Syst. Signal Process.* **64–65**, 1–15 (2015)
7. Mangia, A., Lenzo, B., Sabbioni, E.: An integrated torque-vectoring control framework for electric vehicles featuring multiple handling and energy-efficiency modes selectable by the driver. *Meccanica* **56**, 991–1010 (2021)
8. Badiru, I., Cwycyshyn, W.B., Badiru, I., Cwycyshyn, W.B.: Customer Focus in Ride Development. SAE International (2013)

9. Kim, M.S., Kim, K.W., Yoo, W.S.: Method to objectively evaluate subjective ratings of ride comfort. *Int. J. Automot. Technol.* **12**, 831–837 (2011)
10. Ghanwat, H., Gosavi, S., Sr., M chasker, et al.: Ride and comfort measurements - a challenge of subjective and objective correlation. *SAE Int. J. Adv. Current Prac. Mobi.* **4**, 828–835 (2021)
11. Crolla, D.A., Chen, D.C., Whitehead, J.P., et al.: Vehicle Handling Assessment Using a Combined Subjective-Objective Approach. SAE International (1998)
12. Gil Gómez, G.L., Nybacka, M., Bakker, E., Drugge, L.: Findings from subjective evaluations and driver ratings of vehicle dynamics: steering and handling. *Veh. Syst. Dyn.* **53**, 1416–1438 (2015)
13. Gil Gómez, G.L., Nybacka, M., Bakker, E., Drugge, L.: Objective metrics for vehicle handling and steering and their correlations with subjective assessments. *Int. J. Automot. Technol.* **17**, 777–794 (2016)

Open Access This chapter is licensed under the terms of the Creative Commons Attribution 4.0 International License (<http://creativecommons.org/licenses/by/4.0/>), which permits use, sharing, adaptation, distribution and reproduction in any medium or format, as long as you give appropriate credit to the original author(s) and the source, provide a link to the Creative Commons license and indicate if changes were made.

The images or other third party material in this chapter are included in the chapter's Creative Commons license, unless indicated otherwise in a credit line to the material. If material is not included in the chapter's Creative Commons license and your intended use is not permitted by statutory regulation or exceeds the permitted use, you will need to obtain permission directly from the copyright holder.





Retaining Cornering Performance and Reducing Energy Consumption with Torque Vectoring and Suspensions Tuning

Michele Asperti^(✉), Michele Vignati, and Edoardo Sabbioni

Department of Mechanical Engineering, Politecnico di Milano, Via La Masa N.1,
20156 Milan, Italy
michele.asperti@polimi.it

Abstract. With the automotive industry's shift towards sustainability and energy efficiency, optimizing vehicle handling dynamics has become secondary. Additionally, there is a growing trend towards comfort-oriented design over handling performance. However, advancements such as integrating multiple independently controlled electric motors enable torque vectoring, offering a promising solution for reconciling these conflicting objectives. This paper proposes a novel approach to jointly improve vehicle handling and energy efficiency. Advanced simulation techniques are used to explore various suspension configurations to balance cornering performance and energy consumption. A torque vectoring controller is then designed in combination with meticulously tuned suspensions. This innovative approach, which considers active control design alongside suspension setup, achieves superior performance. Desired vehicle cornering capabilities are attained while ensuring significant efficiency in straight-line driving, which constitutes most road driving.

Keywords: Torque Vectoring · Vehicle Dynamics · Suspensions Setup Tuning · Vehicle Handling · Energy Efficiency

1 Introduction

Road vehicle users continue to demand sporty and high-performance vehicles, despite the automotive industry's current focus on achieving sustainable and energy-efficient solutions [1]. Consequently, in the context of suspensions, the industry's attention has shifted away from enhancing vehicle handling performance [2, 3]. Instead, suspension design now prioritizes ride comfort, with numerous approaches aimed at optimizing suspensions to improve overall ride quality [4, 5]. While car setup optimization [6] remains a fundamental aspect, recent advancements enabling the use of multiple electric motors in a single vehicle [7] have facilitated more advanced improvements. The implementation of In-Wheel Motors (IWMs) [8] allows for the easy deployment of Torque Vectoring (TV) systems, which control lateral dynamics by applying a yaw moment. Over the years, numerous TV controllers have been proposed [9, 10] to enhance vehicle lateral dynamics by actively tracking a yaw rate and/or sideslip angle reference. Conversely,

some approaches utilize TV solely to improve overall vehicle efficiency [11]. A prevalent strategy lies between these two extremes, where TV controllers are designed to enhance lateral dynamics while allocating actuation torque to motors in a manner that minimizes power losses [12]. Additionally, TV controllers can adapt vehicle behavior to meet driver preferences by selecting a driving mode [13], allowing for on-demand modifications to the reference vehicle behavior, thus balancing vehicle handling and energy efficiency.

This paper investigates a novel approach to achieving optimal vehicle handling and high energy efficiency by jointly tuning vehicle suspensions and designing the torque vectoring control system. This integrated approach addresses the trade-off between vehicle cornering performance and energy efficiency by providing additional degrees of freedom. In particular, various configurations of combined suspension tuning and torque vectoring designs are evaluated in a simulation environment to assess their impact on cornering dynamics and energy efficiency.

2 Vehicle Model and Suspensions Tuning

The vehicle considered in this study belongs to the S-segment and is equipped with four independently controllable In-Wheel Motors (IWMs). The vehicle model for simulation purposes is developed using VI-CarRealTime software, incorporating five rigid bodies and 14 degrees of freedom. Specifically, the model used in this study is based on the validated SportCar model, originally representing an internal combustion engine vehicle, whose powertrain has been replaced with four In-Wheel Motors (IWMs).

Suspension angles, such as camber and toe, are typically set at neutral values in standard road cars to prevent excessive tire wear from scrubbing against the road. In contrast, these angles are often adjusted away from neutral in sports vehicles to enhance cornering response. Therefore, it is crucial to set these angles appropriately for the specific vehicle's purpose. In this study, two suspension setups are considered, as shown in Table 1. The baseline setup features suspension angles typical of road vehicles, ensuring proper drivability under all conditions. The sporty setup, instead, includes more aggressive suspension angles and a stiffened rear anti-roll bar to improve vehicle handling.

Table 1. Baseline and sporty vehicle suspensions setup details.

Parameter	Symbol	Baseline Setup	Sporty Setup
Front camber angle	γ_f	-0.5°	-4.5°
Front toe angle	τ_f	-0.05°	-0.15°
Rear camber angle	γ_r	-0.5°	-3.0°
Rear toe angle	τ_r	$+0.05^\circ$	$+0.15^\circ$
Front roll-bar stiffness	$k_{\theta,f}$	7040 Nm/rad	7040 Nm/rad
Rear roll-bar stiffness	$k_{\theta,r}$	21450 Nm/rad	42900 Nm/rad

3 Torque Vectoring Controller Design

The Torque Vectoring (TV) controller developed in this study is intended for implementation on a vehicle equipped with the baseline suspension setup, with the goal of replicating the cornering performance of the same vehicle when fitted with the sporty suspension setup. To achieve this goal, a reference generator for vehicle cornering has been designed. Specifically, the yaw rate has been chosen as the control variable, and the reference function incorporating exponential saturation, as outlined in [10], has been adopted in this study.

$$r_{ref} = \begin{cases} \frac{V}{l(1+K_{US}V^2)} \tau_{SW} \delta_{SW} = \alpha \delta_{SW} & \text{IF } \delta_{SW} \leq \delta_{SW}^* \\ r_{max} + (r^* - r_{max}) e^{\left(\frac{-\alpha(\delta_{SW} - \delta_{SW}^*)}{(r_{max} - r^*)}\right)} & \text{IF } \delta_{SW} > \delta_{SW}^* \end{cases} \quad (1)$$

In there, the maximum attainable yaw rate is the maximum achievable lateral acceleration normalized by the actual vehicle speed ($r_{max} = a_{y,max}/V$), r^* is the yaw rate value at which the transition between the linear and saturation regions occurs, $\delta_{SW}^* = r^*/\alpha$ is the steering wheel angle value at which this transition happens and τ_{SW} is the steering ratio between the steering wheel and the front wheels. Given the reference yaw rate function, its three main parameters (r_{max} , α , δ_{SW}^*) are obtained by fitting the reference to the yaw rate response of the sporty vehicle to steering pad constant speed maneuvers. These maneuvers have been performed at several different constant speeds by increasing the steering wheel angle at a rate of one degree per second until reaching the vehicle handling limits. The reference function characteristic coefficients are then regularized through a proper fitting over the achievable speed range for the vehicle for defining the yaw rate reference in each possible condition, with the results reported in Fig. 1.

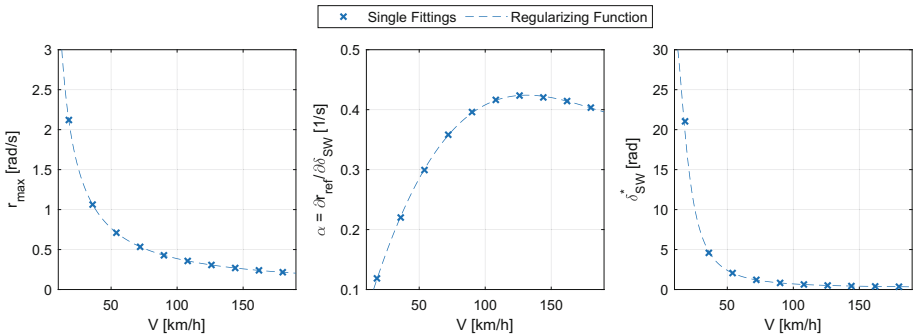


Fig. 1. Reference yaw rate function coefficients as function of vehicle speed.

The torque vectoring controller for tracking the desired yaw rate response defines the yaw moment to be deployed to the vehicle as the sum of a feedforward and a feedback contribution.

$$M_z = M_{z,FF} + M_{z,FB} = k_\delta \delta + k_P (r_{ref} - r) + k_I \int_0^t (r_{ref} - r) dt \quad (2)$$

The feedforward contribution is function of the wheel steering angle commanded by the driver, while the feedback contribution is the output of a PI controller aiming at minimizing the yaw rate deviation from its reference value. The feedforward gain (k_δ) is obtained by imposing that the static gain of the frequency response function relating the yaw rate response to the steering input is equivalent for the active and the sporty vehicle, resulting in the following

$$\mu_{\delta,ACTIVE} = \mu_{\delta,SPORTY} \rightarrow k_\delta = \frac{k_{y,f}k_{y,r}l}{k_{y,f}+k_{y,r}} \frac{\alpha_{SPORTY}-\alpha_{BASE}}{\alpha_{BASE}} \quad (3)$$

where $k_{y,f}$ and $k_{y,r}$ are the cornering stiffness of the front and rear axles respectively, l is the vehicle wheelbase and α_{BASE} and α_{SPORTY} are the slope of the linear yaw rate response region for the baseline and the sporty vehicles respectively. The feedback control gains (k_P, k_I) are instead tuned with a model-based approach with the objective of obtaining a robust and stable controlled system which performs as closely as possible to the sporty vehicle.

4 Results

The effectiveness of the proposed control strategy, implemented on a vehicle with the baseline suspension setup, in replicating the lateral dynamics performance of the vehicle with the sporty suspension setup, is evaluated through numerical simulations. The results encompass both transient and steady-state maneuvers, covering a range of scenarios from open-loop to closed-loop modalities, under high friction conditions ($\mu = 1.0$).

4.1 Straight Line Constant Speed Maneuver

A straight-line constant speed maneuver is simulated to evaluate the energy consumption effects of three different vehicle configurations. This maneuver was conducted at speeds ranging from 5 m/s to 50 m/s, in increments of 5 m/s. The simulation results are presented in Fig. 2 for the various running speeds. In there, the specific energy consumption (E_{sp}) increases more than linearly with vehicle speed due to aerodynamic resistance and

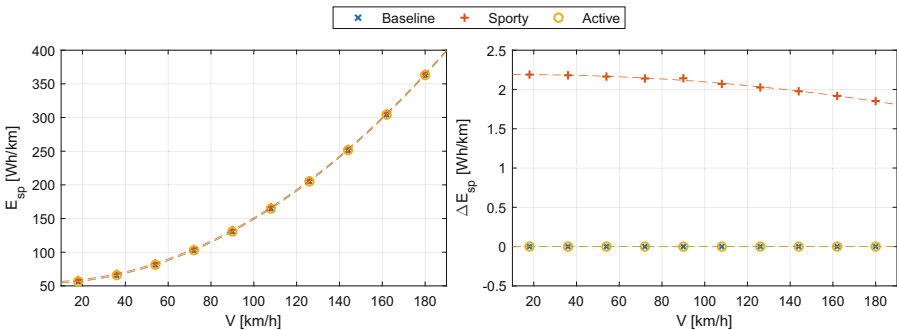


Fig. 2. Specific energy consumption and its variation with respect to the baseline vehicle for a straight-line constant speed maneuver across three vehicle configurations.

shows no significant differences among the three vehicle configurations. However, the variation in specific energy consumption (ΔE_{sp}) relative to the baseline vehicle indicates an increased energy demand for the sporty vehicle. This phenomenon may be attributed to the suspension angles, which causes tire scrubbing on the road, resulting in power losses due to lateral slip velocity at the tire-ground contact.

4.2 Constant Radius Cornering Maneuver

The steady-state handling performance of the proposed vehicle configurations under high friction conditions is evaluated using an ISO 4138 constant radius cornering maneuver. In this maneuver, the vehicle's speed is progressively increased at a constant rate, and the steering wheel angle is adjusted in close-loop to maintain a circular trajectory. The speed is increased from 10 km/h until the baseline vehicle achieves at least 99% of the maximum attainable lateral acceleration for the selected turn radius. The cornering results for a specific maneuver with a 100 m turn radius are presented in Fig. 3. Additionally, Fig. 4 summarizes the handling and energy consumption performance across all the inspected turn radii.

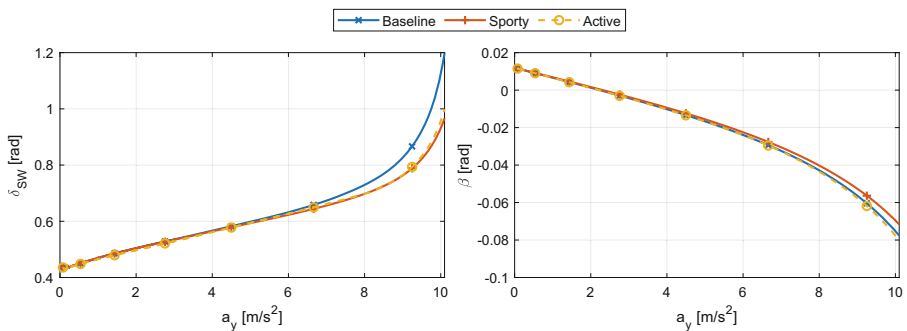


Fig. 3. Vehicle handling response during a constant radius cornering maneuver for a 100 m radius turn across three vehicle configurations.

The results in Fig. 3, illustrating the trend of the steering wheel angle as a function of vehicle lateral acceleration, indicate that the sporty and active vehicle configurations achieve almost equivalent cornering performance, both of which surpass that of the baseline configuration. Indeed, the baseline vehicle requires a greater steering wheel angle input to achieve the same turn radius. Additionally, both the baseline and active vehicle configurations exhibit similar sideslip angle responses, whereas the sporty vehicle is also capable of reducing the sideslip angle. The results in Fig. 4 indicate that the active vehicle configuration requires slightly more steering wheel angle input compared to the sporty configuration, while the baseline vehicle demands significantly more input than both. Furthermore, Fig. 4 demonstrates that both the sporty and active vehicle configurations consume less energy than the baseline configuration when executing a constant radius turn. Notably, the sporty vehicle achieves nearly five times the energy savings of the active vehicle. This significant reduction in energy consumption is primarily attributed to the lower longitudinal slip of the outer tires in the sporty vehicle, which

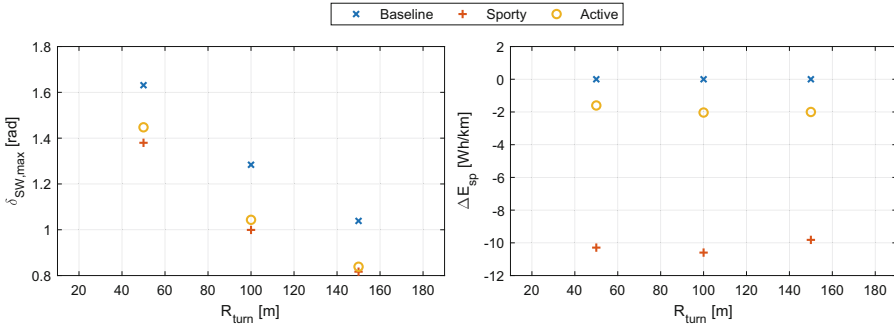


Fig. 4. Maximum steering wheel angle and specific energy consumption variation (ΔE_{sp}) with respect to the baseline vehicle during a constant radius cornering maneuver across three vehicle configurations.

is not employing increased longitudinal forces at outer wheels as the active vehicle is doing.

4.3 Double Lane Change Maneuver

The transient performance of the proposed vehicle configurations is evaluated using steering wheel closed-loop simulations based on an ISO 3888 double lane-change maneuver under high friction conditions. Figure 5 presents the results of this maneuver, comparing the performance of the three vehicle configurations.

An examination of the results in Fig. 5 reveals that the sporty and active vehicle configurations perform similarly under transient conditions, indicating an effective design and tuning of the torque vectoring controller. The trends observed in the steady-state tests are confirmed, showing that both the sporty and active vehicles generally enhance the cornering performance. Additionally, the active vehicle requires a slightly larger steering wheel angle input and exhibits a marginally higher sideslip angle compared to the sporty vehicle, which also confirms the steady-state results. In terms of power consumption, the baseline vehicle is the most demanding ($E_{sp,BASE} = 137.9$ Wh/km), followed by the active vehicle ($E_{sp,ACTIVE} = 132.4$ Wh/km), which consumes slightly more energy than the sporty vehicle ($E_{sp,SPORTY} = 130.8$ Wh/km).

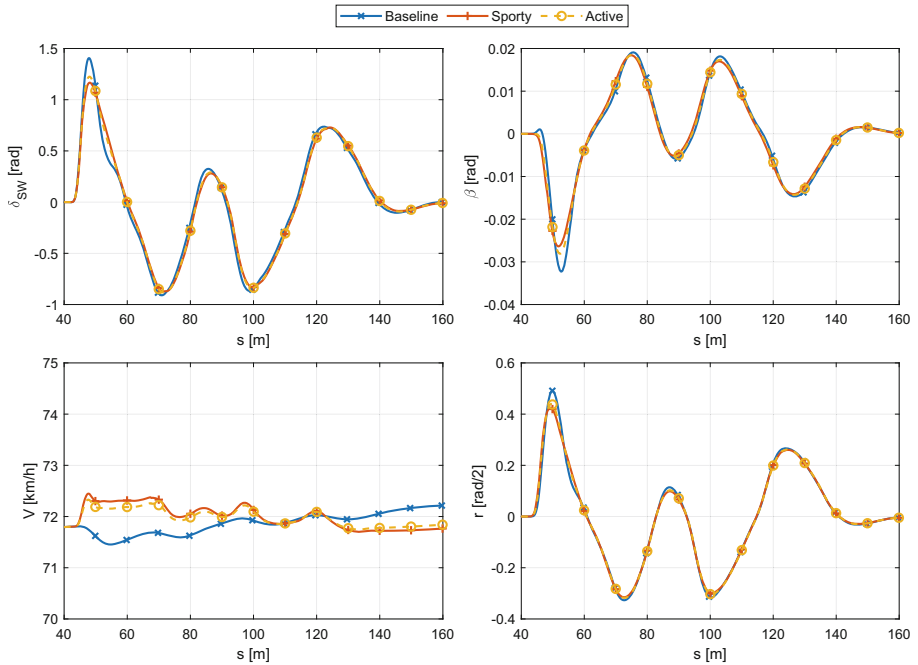


Fig. 5. Vehicle handling response during a double lane change maneuver in high friction conditions across three vehicle configurations.

5 Conclusions

The use of torque vectoring to enhance vehicle lateral dynamics has been extensively studied over the years. However, integrating a torque vectoring controller with suspension parameters tuning to improve cornering capabilities while ensuring good energy efficiency remains underexplored. In this study, baseline and sporty suspension setups have been defined and a torque vectoring controller designed for an active vehicle with the baseline suspension setup to emulate the handling characteristics of the sporty vehicle. Various steady-state and transient maneuvers have been simulated to demonstrate the method's effectiveness. Steady-state maneuver results confirm that the actively controlled vehicle can closely match the sporty vehicle performance by using torque vectoring to enhance the baseline vehicle handling. In terms of energy efficiency, the active vehicle outperforms the sporty vehicle in straight-line conditions but performs slightly worse in turns. Transient maneuver results corroborate the steady-state findings regarding handling, with the active vehicle's energy savings approaching those of the sporty vehicle.

References

1. Requia, W.J., Mohamed, M., Higgins, C.D., et al.: How clean are electric vehicles? evidence-based review of the effects of electric mobility on air pollutants, greenhouse gas emissions and human health. *Atmos. Environ.* **185**, 64–77 (2018)

2. Afkar, A., Mahmoodi-Kaleibar, M., Paykani, A.: Geometry optimization of double wish-bone suspension system via genetic algorithm for handling improvement. *Journal of Vibroengineering* **14**, 827–837 (2012)
3. Kwon, S.-J., Kim, T.-L., Kim, C.-J.: Optimal selection of suspension and tires for vehicles' cornering performance. *Machines* **10**, 1032 (2022)
4. Uys, P.E., Els, P.S., Thoresson, M.: Suspension settings for optimal ride comfort of off-road vehicles travelling on roads with different roughness and speeds. *J. Terramech.* **44**, 163–175 (2007)
5. Mitra, A.C., Soni, T., Kiranchand, G.R.: Optimization of automotive suspension system by design of experiments: a nonderivative method. *Adv. Acoust. Vibr.* **2016**, e3259026 (2016)
6. Wloch, K., Bentley, P.J.: Optimising the Performance of a Formula One Car Using a Genetic Algorithm. In: Yao, X., Burke, E.K., Lozano, J.A., et al. (eds.) *Parallel Problem Solving from Nature - PPSN VIII*, pp. 702–711. Springer, Berlin, Heidelberg (2004)
7. Rinderknecht, S., Meier, T.: Electric power train configurations and their transmission systems. *SPEEDAM* **2010**, 1564–1568 (2010)
8. Murata, S.: Innovation by in-wheel-motor drive unit. *Veh. Syst. Dyn.* **50**, 807–830 (2012)
9. Katsuyama, E., Yamakado, M., Abe, M.: A state-of-the-art review: toward a novel vehicle dynamics control concept taking the driveline of electric vehicles into account as promising control actuators. *Veh. Syst. Dyn.* **59**, 976–1025 (2021)
10. Asperti, M., Vignati, M., Sabbioni, E.: On torque vectoring control: review and comparison of state-of-the-art approaches. *Machines* **12**, 160 (2024)
11. De Filippis, G., Lenzo, B., Sorniotti, A., et al.: Energy-efficient torque-vectoring control of electric vehicles with multiple drivetrains. *IEEE Trans. Veh. Technol.* **67**, 4702–4715 (2018)
12. Pennycott, A., Novellis, L.D., Gruber, P., et al.: Enhancing the energy efficiency of fully electric vehicles via the minimization of motor power losses. In: 2013 IEEE International Conference on Systems, Man, and Cybernetics, pp. 4167–4172 (2013)
13. Mangia, A., Lenzo, B., Sabbioni, E.: An integrated torque-vectoring control framework for electric vehicles featuring multiple handling and energy-efficiency modes selectable by the driver. *Meccanica* **56**, 991–1010 (2021)

Open Access This chapter is licensed under the terms of the Creative Commons Attribution 4.0 International License (<http://creativecommons.org/licenses/by/4.0/>), which permits use, sharing, adaptation, distribution and reproduction in any medium or format, as long as you give appropriate credit to the original author(s) and the source, provide a link to the Creative Commons license and indicate if changes were made.

The images or other third party material in this chapter are included in the chapter's Creative Commons license, unless indicated otherwise in a credit line to the material. If material is not included in the chapter's Creative Commons license and your intended use is not permitted by statutory regulation or exceeds the permitted use, you will need to obtain permission directly from the copyright holder.





Enhancing Steer-by-Wire Systems with an Integrated E-Motor and MR-Brake Actuator – Feedback Control Strategy

Matthias Niegl¹(✉), Johannes Hendewerk¹, Matthias Becker², Stefan Battlogg³,
and Peter Pfeffer²

¹ MdynamiX AG, Heßstr. 89, 80797 Munich, Germany
matthias.niegl@mdynamix.de

² Munich University of Applied Sciences, Dachauerstraße 98b, 80335 Munich, Germany

³ INVENTUS Development GmbH, Montafonerstraße 68, 6771 St. Anton i.M, Austria

Abstract. This study introduces an innovative control strategy for a steer-by-wire (SbW) force feedback actuator, tailored for automotive use. The actuator integrates a direct drive electric motor and a magnetorheological brake (MR-brake) within a streamlined, compact design. This electric motor delivers torque essential for the desired steering feel and ensures swift responsiveness. Concurrently, the MR-brake, noted for its compactness and energy efficiency, contributes passive damping and robust end-stop torque capabilities. The synergistic use of these components allows for a smaller and more resource-efficient electric motor design. A critical aspect of this strategy is the implementation of a torque splitter, essential for replicating the steering feel associated with Electric Power Steering (EPS) systems. This splitter distributes the required feedback torque between MR-brake torque and e-motor torque, ensuring high fidelity and consistent stability across a range of vehicular dynamics and maneuvers. Notably, maintaining a subjectively satisfying steering feel under conditions where torque proportions vary between actuators presents a significant challenge. The proposed actuator design, with its focus on performance, safety, and reliability, is particularly well-suited for advanced SbW systems demanding high standards in these areas.

Keywords: Steer-by-Wire · Force Feedback Actuator · Magnetorheological

1 Differentiation to Current Force Feedback Actuator Designs

Current force feedback actuators which will be released in series production vehicles soon are using the same basic technology as column assisted electric steering systems. A small e-motor generates feedback torque with a worm gear towards the driver. A torque sensor is still required for a consistent steering feel to compensate friction tolerances from the manufacturing or wear [1]. A worm gear is a cost effective, simple and well-known component, the risk of a failing steer by wire system motivates the suppliers to use proven technology. Not all suppliers are focusing on this approach, e.g. Thyssenkrupp introduces a direct drive force feedback technology without a torque sensor [2]. Direct

drive e-motors promise a rigid steering feel with the possibility to generate frequencies up to 50 Hz. The drawback which prevents a more common use of direct drive e-motors is the requirement for the end stop torque which is typically higher than 20 Nm. The exact number is still to be discussed among the OEMs. This would result in heavy and large e-motors which are cost intensive and have major drawbacks in terms of packaging. Figure 1 shows close to series production SbW columns from Nexteer Automotive and Thyssenkrupp.

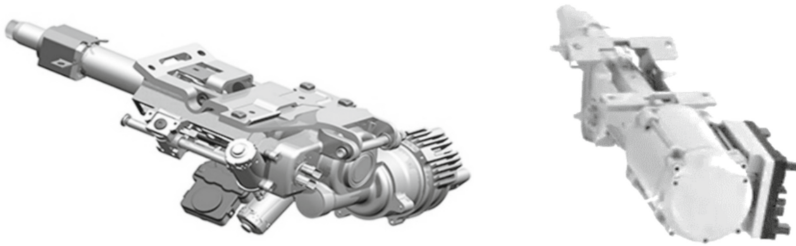


Fig. 1. SbW Force Feedback Actuators Nexteer Automotive [3] and Thyssenkrupp [2]

There are several possible solutions to using a small direct drive e-motor for functions related to steering feel but still providing high torque output:

- Use the maxed out peak torque of the e-motor
- Mechanical end stops in series to an e-motor
- Mechanical brake in series to an e-motor

The different approaches shows there is no simple solution for the direct drive force feedback actuator in existence. A combination of an e-motor with an MR-brake described in the following could solve the tradeoff between good steering feel and reduced costs or packaging.

2 Design and Theoretical Benefits of the Actuator Combination

A magnetorheological brake is a device that uses the properties of a special fluid or powder to control the braking force. An electric coil is attached to either the rotor or the stator, and can generate a magnetic field when a current is applied to it. The magnetic field closes from the rotor to the stator through the gap, and it causes the MRP particles to align and form magnetic bridges between the two surfaces. Figure 2 shows a simulation without and with a magnetic field.

The magnetorheological brake is a simple, reliable, and efficient way of braking. To reach a counter torque of 25 Nm the MR-brake prototype consumes 60 W electrical power at 12 V [5]. An electric motor wheelbase such the Simucube 2 Pro generates a maximum torque of 25 Nm at 450 Watts peak [6].

Figure 3 shows on the left side the INVENTUS SbW actuator concept dimensions are significantly smaller than a compared gaming wheelbase. This hybrid force feedback actuator includes a 5 Nm e-motor and a 25 Nm MR-brake.

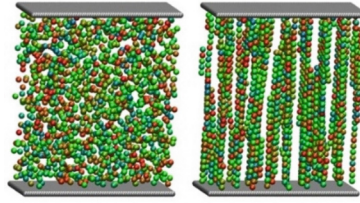


Fig. 2. Simulation of particle chains in an magnetic field [4] (© Fraunhofer IWM)

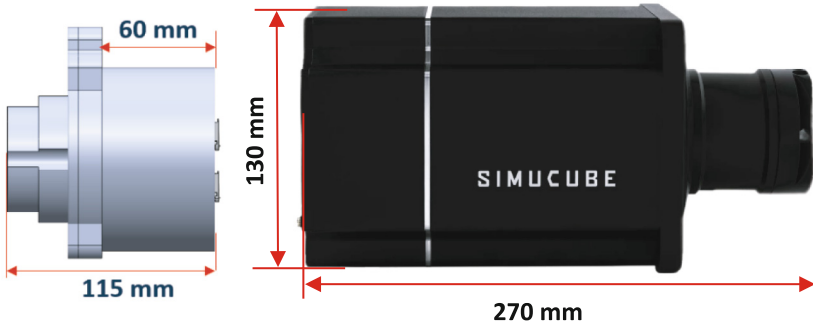


Fig. 3. INVENTUS SbW Force Feedback Actuator Concept Dimensions [5] vs. Simucube 2 Pro [6] (to scale)

The major question is whether a hybrid force feedback actuator can generate the same quality of steering feel as a pure e-motor. In order to answer that, the hybrid actuator designed for this study (Fig. 4) did not focus on size or packaging. The e-motor itself can generate up to 15.7 Nm of continuous torque and 30.0 Nm of peak torque. This enables a direct comparison on one system between the hybrid design and the pure e-motor with a disabled MR-brake. If both actuators are enabled, the e-motor torque can be limited to any low peak torque from a close to series production concept.

The actuator further has a MR-brake designed by INVENTUS Development GmbH with a peak torque of 8 Nm. Figure 4 shows the hybrid actuator cross-section and the real actuator including a high precision angle sensor.

3 Controller and Torque Splitter

An MR-brake can only be controlled semi-actively and can therefore only take over two of four quadrants in the steering wheel torque- steering wheel angle velocity diagram during steering. An electric motor is required for e.g. active return. To design a control system for distributing the torque with good steering feel, the control must be advanced. This includes blending of actuator torques in the steering off-center and more e-motor proportion in the on-center region, thereby moving away from the ideal areas. Sudden changes in e.g. SWV may lead to unwanted behaviors due to settling time and minor differences in actual torque. To realize blending, factors between 0 and 1 were introduced

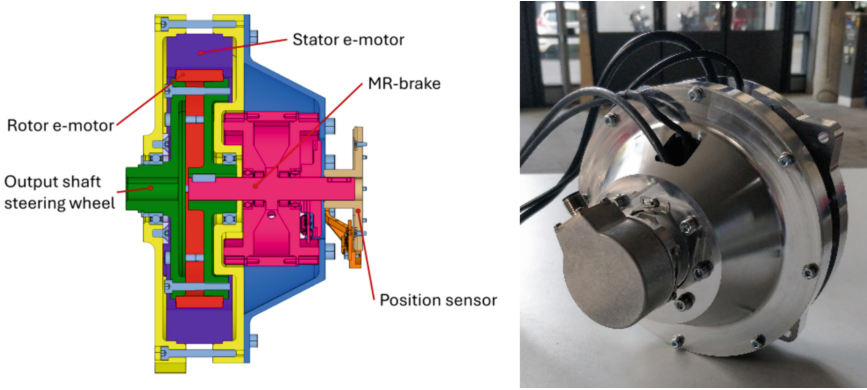


Fig. 4. SbW Force Feedback Actuator with Direct Drive E-Motor and MR-Brake

and multiplied with the respectable torque command value of MR-brake and e-motor. The factors are realized via a characteristic field as shown in Fig. 5. At lower SWVs, the MR-brake factor is 0 and reaches a factor of 1 at a given SWV, called transition speed. A full takeover of torque from the brake only happens in areas where the MR-brake factor is 1 (resulting in an e-motor factor of 0). In areas where the MR-brake is active, but the factor is smaller than 1, the e-motor is partially taking over the torque in low SWV section, achieving torque blending of each actuator torques.

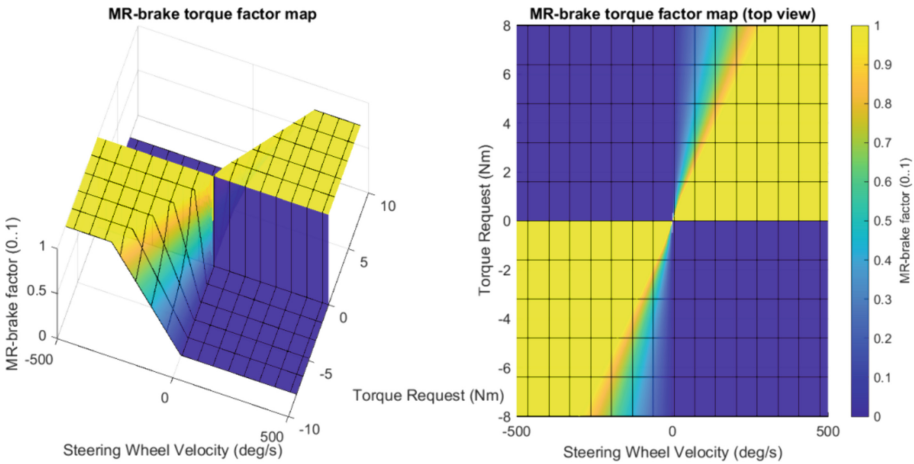


Fig. 5. Torque factor map of MR-brake for torque splitter

For end stop behavior, a similar logic is used with two main differences. Firstly, since the achieved SWVs are low compared to driving even when pushing over the end stop torque limits, the transition speeds of the characteristic field are kept low, resembling more the ideal torque splitter. Secondly, the e-motor is not disabled in areas where the MR-brake is active to avoid fast on and off switching of e-motor torque due to the steeper

map. Steering into the end stops results in an added torque of e-motor and MR-brake, steering away from the end stops is only controlled by the e-motor.

4 Simulation and Driver in the Loop Results

For the execution of Driver-in-the-Loop (DiL) tests, the hybrid actuator was implemented within a static driving simulator stationed in the laboratory of the Munich University of Applied Sciences. The control unit for the MR-brake and the inverter for the e-motor are connected to an embedded computer. This embedded computer handles the torque splitter and simulates a Pfeffer steering model [8].

To evaluate the functionality of the torque splitter, a Weave Test, 100 km/h, 30 °, 0.2 Hz, 4 m/s² and End Stop Tests are performed. For both scenarios the actual torque values were computed utilizing the currents and their respective torque constants. It's important to note that the setup did not incorporate a torque sensor. The graph in Fig. 6 shows the torques against the SWA for the Weave Test. The MR-brake becomes active during turning the steering wheel into the sine wave according to the torque-velocity diagram. Arriving at the peak of SWA sine wave, the MR-brake torque ramps down due to decreasing SWV. The e-motor takes over completely to generate the counter torque and a smooth transition can be seen. By superimposing the torques of each actuator, a well-defined hysteresis can be generated.

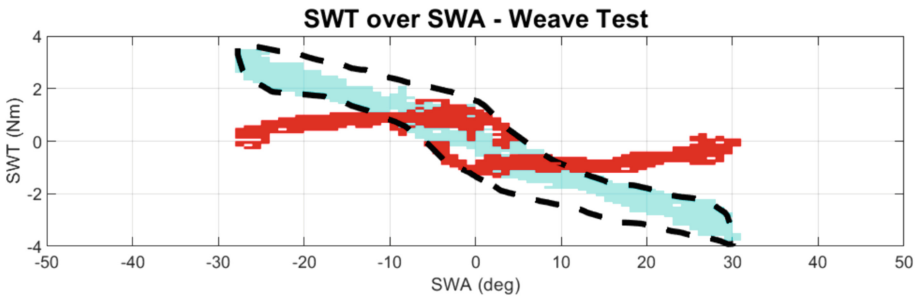


Fig. 6. E-motor and MR-brake torque splitting for Weave Test

The graph in Fig. 7 shows the torques of the actuators over the measurement time, for the End Stop Test. The MR-brake becomes already active during slowly turning the steering wheel towards the end stop and the e-motor is inactive. At 4.5 s, when the end stop limit is reached the MR-brake and the e-motor torques are rising to the parametrized maximum. At 11 s during steering back to the center the e-motor torque is reduced slowly as well. The end stop transitions can be generated as a sum of the actuators or independently as shown in the measurement.

An expert evaluation of both scenarios in a DiL environment shows good subjective results, the transitions between the actuators were hardly noticeable, only the end stops were described as “little sticky”. The MR-brake is not released early enough, because the driver’s intention is sensed after oversteering the MR-brake torque.

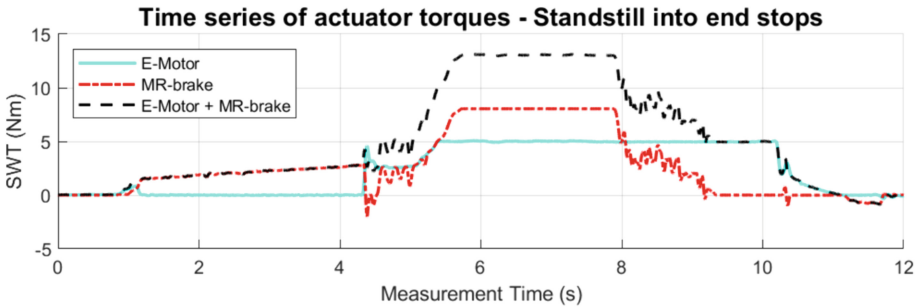


Fig. 7. E-motor and MR-brake torque splitting for End Stop Test

5 Summary and Outlook

In this study the potential advantages for a force feedback actuator with direct drive e-motor and MR-brake are presented. The design is cost effective, delivers a high maximum torque at low energy consumption and ensures flexible end stops. The steering feel of the design was analyzed objectively and evaluated subjectively by experts. The results show that the developed torque splitter feels smooth in the transitions, but the MR-brake tends to stick in the end stops. The reason for the behavior was identified in the angle sensor position at the end of the actuators. The sensor type will be changed towards a hollow shaft type and positioned between the steering wheel and the e-motor to improve the sticky feel. The torque input from the driver is measured early to release the MR-brake instead of first oversteer it. A second demonstrator with a series production EPS-motor including an updated MR-brake is currently being built up to further investigate the potential of the presented force feedback actuator with direct drive e-motor and MR-brake.

Acknowledgement. This study was supported by the European Union “Interreg Bayern-Österreich”.

References

1. Wilhelm, F., Tamura, T., Fuchs, R., Müllhaupt, P.: Friction compensation control for power steering. *IEEE Trans. Control Syst. Technol.* **24**(4), 1354–1367 (2016)
2. <https://www.thyssenkrupp.com/en/stories/automotive-and-new-mobility/steer-by-wire-thyssenkrupp-schlaegt-innovativen-weg-in-der-entwicklung-ein>
3. <https://www.nexteer.com/columns-intermediate-shafts/stowable-steering-column/>
4. <https://www.iwm.fraunhofer.de/en/services/manufacturing-processes/powder-technology-particle-simulation/magnetorheological-fluids.html>
5. https://www.inventus.at/de_de/rotary-haptic-solutions/steer-by-wire/
6. <https://simucube.com/simucube-2-pro/?v=3a52f3c22ed6>
7. Strecker, Z., Roupec, J., Mazurek, I., Machacek, O., Kubik, M., Klapka, M.: Design of magnetorheological damper with short time response. *J. Intell. Mater. Syst. Struct.* **26**(14), 1951–1958 (2015)
8. Pfeffer, P.E., Harrer, M., Johnston, D.N.: Interaction of vehicle and steering system regarding on-centre handling. *Veh. Syst. Dyn.* **46**(5), 413–428 (2008)

Open Access This chapter is licensed under the terms of the Creative Commons Attribution 4.0 International License (<http://creativecommons.org/licenses/by/4.0/>), which permits use, sharing, adaptation, distribution and reproduction in any medium or format, as long as you give appropriate credit to the original author(s) and the source, provide a link to the Creative Commons license and indicate if changes were made.

The images or other third party material in this chapter are included in the chapter's Creative Commons license, unless indicated otherwise in a credit line to the material. If material is not included in the chapter's Creative Commons license and your intended use is not permitted by statutory regulation or exceeds the permitted use, you will need to obtain permission directly from the copyright holder.





A Rule-Defined Adaptive MPC Based Motion Planner for Autonomous Driving Applications

Mohammed Irshadh Ismaaeel Sathyamangalam Imran^(✉),
Satyesh Shanker Awasthi, Michael Khayyat, Stefano Arrigoni,
and Francesco Braghin

Department of Mechanical Engineering, Politecnico di Milano, Via Giuseppe La
Masa, 1, 20156 Milan, Italy

mohammedirshadh.sathyamangalam@polimi.it

Abstract. In autonomous driving systems, motion planning to reach a given destination while avoiding obstacles becomes a task entirely managed by the on-board unit. In this work, we present a rule-defined motion planning algorithm for autonomous driving applications based on an adaptive Model Predictive Controller (MPC) framework. The motion planning task is first formulated as an Optimal Control Problem (OCP) subject to time-varying Control Barrier Function (CBF) constraints. It is then integrated within an MPC framework with adaptive weights settings, enabling the algorithm to dynamically adjust the MPC weights according to the rule-defined driving scenarios. The developed motion planner generates optimized trajectories for a high-fidelity Autonomous Vehicle (AV) model within IPG CarMaker software. Simulations performed showed that the developed motion planner adeptly facilitates successful overtaking, following, and stopping of the AV behind the Obstacle Vehicle (OV) based on rule-defined scenarios perceived by the AV.

Keywords: Autonomous Vehicle · Model Predictive Control · Optimal Control Problem · Obstacle Avoidance · Control Barrier Functions · High Fidelity Simulation Environment

1 Introduction

Motion planning algorithms ensure the safety of Autonomous Vehicles (AVs) in the presence of Obstacle Vehicles (OVs) and also ensure that AVs reach their target destinations. Obstacle avoidance is an important aspect of motion planning. One of the earliest implementation was based on Artificial Potential Fields (APF), where repulsive forces are used to avoid obstacles [1]. However, a limitation of APF-based algorithms is their poor performance in the presence of highly nonlinear systems and the oscillations that occur when operating at low frequencies. To overcome this issue, a model-dependent Control Barrier Function

(CBF) [2] was used to handle obstacles in more complex non-linear optimization algorithms.

To fulfill the second fundamental goal of a motion planning algorithm, which is goal reaching, approaches based on way-point tracking or Control Lyapunov Functions (CLFs) [3] have been widely adopted in literature. Research work has shown that it is possible to combine CBFs and CLFs and other essential constraints through a Quadratic Programming (QP) to form an OCP [4]. The OCP can then be propagated along a predefined receding time horizon resulting in an MPC framework and is one of the current state-of-the-art techniques [5,6] for AV motion planning in addition to data-driven techniques. Data-driven approaches are becoming increasingly popular due to their ability to efficiently optimize in diverse environments [7]. However, these approaches have the disadvantage of not providing security guarantees defined through a mathematical formulation of constraints. For this reason, in safety-critical tasks and when proper modeling of the physical problem is available, model-based approaches are still a viable solution for motion planning. This is confirmed by the extensive literature available on automated control of vehicles, such as in [8–10] where MPC is used for obstacle avoidance control, automatic highway overtaking and urban low speed autonomous driving respectively.

The most common solution to handle multiple driving scenarios in a model-based motion planner is a hierarchical approach. Each scenario is characterized by a specific problem formulation, and a high-level algorithm identifies the situation and selects the appropriate algorithm. To develop a single algorithm capable of handling multiple scenarios, this paper proposes a rule-based motion planner for an AV using a waypoint-assisted MPC formulation subjected to time-varying CBF constraints. The formulated motion planner can overtake, follow, and fully stop behind OV depending on the autonomous driving scenario sensed by the AV. This adaptability eliminates the need for transition planners for each scenario, making the algorithm versatile. This is achieved by making the MPC adapt the weights based on predefined driving rules corresponding to the sensed scenario. The first section of the paper focuses on the mathematical modeling of the vehicle and the formulation of the motion planner. The second section deals with simulation methodology while the third section presents the simulation results.

2 Mathematical Modelling

2.1 Vehicle Model

The AV to be controlled has been mathematically approximated by using a Single Track Model (STM) [11] and the kinematic expressions that describe the motion of STM along the constrained XY space are expressed in (1)

$$\begin{cases} \dot{x} = v \sin(\theta + \beta) \\ \dot{y} = v \cos(\theta + \beta) \\ \dot{\theta} = \frac{v \sin(\beta)}{L_r} \end{cases} \quad (1)$$

where

$$\beta = \text{atan} \left(\frac{L_r \tan(\delta)}{L} \right)$$

The parameters L and L_r denote the total length of the vehicle and length of the vehicle from rear axle to the vehicle’s Center of Gravity (CoG) point respectively. The variables v , δ and θ represent velocity of the vehicle, steering angle imposed at front wheel and orientation of the vehicle with respect to the global XY plane respectively. Integrating (1) yields x , y and θ where the quantities x and y denote the position of the vehicle along global XY frame.

The variables v and δ are the control variables to vehicle. To have a smoother control, the control actions are placed on acceleration u_{acc} and steering rate ψ and are defined in (2).

$$\begin{cases} \dot{v} = u_{acc} \\ \dot{\delta} = \psi \end{cases} \tag{2}$$

The expressions (1) and (2) are collectively taken as \underline{X} and \underline{U} respectively and are combined to define the total non-linear dynamic Eq. (3) of STM and is fed as a dynamic equality constraint to the optimization algorithm.

$$\dot{\underline{X}} = f(\underline{X}, \underline{U}) \tag{3}$$

2.2 Development of the Motion Planning Algorithm

The specific problem formulation developed is analyzed as follows. In particular, the CBF formulation is described in detail and then the overall problem formulation is reported.

2.2.1 CBF Constraint Formulation The OV in this work is formulated as a circular entity centered at its CoG point and this circular entity is described mathematically in (4)

$$B(\underline{X}_{AV}, \underline{X}_{OV}) = (\underline{X}_{AV} - \underline{X}_{OV})^\top (\underline{X}_{AV} - \underline{X}_{OV}) - D_{OV}^2 \tag{4}$$

where \underline{X}_{AV} is a vector containing position states of the AV (x and y), while \underline{X}_{OV} corresponds to the OV’s positional state vector (x_{OV} and y_{OV}) and finally, D_{OV} defines the region of influence around the OV. The first-order time derivative of (4) is taken and is described in (5)

$$\dot{B}(\underline{X}_{AV}, \underline{X}_{OV}, \dot{\underline{X}}_{AV}, \dot{\underline{X}}_{OV}) = 2(\underline{X}_{AV} - \underline{X}_{OV})^\top (\dot{\underline{X}}_{AV} - \dot{\underline{X}}_{OV}) \tag{5}$$

where $\dot{\underline{X}}_{AV}$ points to the AV’s velocity vector (\dot{x} and \dot{y}), while $\dot{\underline{X}}_{OV}$ corresponds to the OV’s velocity vector (\dot{x}_{OV} and \dot{y}_{OV}) with $\dot{x}_{OV} = 0$. The generalized expression for CBF constraint in continuous form [12] after substituting the B and its derivative \dot{B} is defined in (6)

$$\dot{B}(\underline{X}_{AV}, \underline{X}_{OV}, \dot{\underline{X}}_{AV}, \dot{\underline{X}}_{OV}) + \gamma B(\underline{X}_{AV}, \underline{X}_{OV}) \geq 0 \tag{6}$$

where γ defines the rate at which the AV is guided away from the region confined to the OV. A high value of gamma makes the AV overtake OV closer to it, while a small value makes the AV overtake OV by going very wide of it. The setting of the parameters D_{OV} and γ values are done by the rules defined in the motion planner and are optimally tuned for each specific driving scenario. Under the OV overtaking rule, D_{OV} and γ are set at 2.5 m and 100 to allow the AV to overtake the OV within the available lane width. In the scenario of OV vehicle following, D_{OV} is extended to 15 m while γ is reduced to 1 to ensure the AV maintains a safe following distance. Lastly, for the fully stopping rule, D_{OV} is further increased to 20 m while γ is brought to around 0.35 to prevent the AV from overtaking the OV. The constraint Eq. (6) when satisfied creates a forward invariant safe set \mathcal{S} that assists the AV to keep it away from the space confined to that of the OV.

2.2.2 Definition of Way-Points Assisted MPC Based OCP From the fundamentals of optimal control theory, a problem formulation based on a quadratic cost function can be defined. This cost function is then subjected to the constraints arising from the vehicle dynamics (3), OV induced CBFs (6) and from vehicle state and control limits. This OCP is then propagated in time along a predefined receding time horizon T leading to a MPC based formulation as defined in (7).

$$\left\{ \begin{array}{l} \min_{\underline{U}} \quad J(\underline{X}, \underline{U}) = \frac{1}{2} \sum_{k=0}^{N-1} \left[\|\underline{X}_k - \underline{X}_{ref,k}\|_{\mathbf{Q}}^2 + \|\underline{U}_k - \underline{U}_{ref,k}\|_{\mathbf{R}}^2 \right] + \frac{1}{2} \|\underline{X}_N - \underline{X}_{ref,N}\|_{\mathbf{P}}^2 \\ \text{s.t.} \quad \left\{ \begin{array}{ll} \dot{\underline{X}}_k - f(\underline{X}_k, \underline{U}_k) = 0 & \text{Dynamic Constraints} \\ \dot{B}(\underline{X}_{AV}, \underline{X}_{OV}, \dot{\underline{X}}_{AV}, \dot{\underline{X}}_{OV}) + \gamma B(\underline{X}_{AV}, \underline{X}_{OV}) \geq 0 & \text{CBF Constraint} \\ \underline{U}_{min} \leq \underline{U} \leq \underline{U}_{max} & \text{Control Constraints} \\ \underline{X}_{min} \leq \underline{X} \leq \underline{X}_{max} & \text{State Constraints} \end{array} \right. \end{array} \right. \quad (7)$$

where N indicates the number of discretization time steps distributed along the MPC time horizon and is fixed as 50 steps while T is set at 2.5 s leading to a ΔT of 0.05 s for the MPC.

\underline{X}_N stands for terminal states of AV, while \mathbf{P} , \mathbf{Q} and \mathbf{R} correspond to the weights for the MPC. The way-points that define the path along which AV needs to travel have been set in $\underline{X}_{ref,k}$ in the problem definition (7). In this paper, the MPC is optimized based on the hypothesis that the distance between AV and OV is known and AV knows whether it is travelling on a road consisting of a single lane or a double lane. The MPC is numerically solved thanks to an open source `acados` solver based on `sqp-rti` [13]. The formulation is developed to properly handle 3 common driving scenarios: overtaking, following and full stopping by defining them as rules set by weights to the MPC. In particular, the default driving rule is OV overtake, but if the speed of OV relative to AV is greater than a threshold defined in this paper, vehicle following rule is applied.

In situations when AV is travelling along a single lane road and there is an OV stopped along that lane vehicle stopping rule is applied to the MPC. The mathematical relationship between OV velocities for different AV velocities that causes change of rule between OV overtaking and vehicle following scenario is shown in Fig. 1a.

The MPC is able to automatically toggle between these 3 rules depending upon the information about OV velocity, AV velocity and lane width datum by changing the weight matrices \mathbf{P} , \mathbf{Q} and \mathbf{R} and parameters γ and D_{OV} that are defined and set for each rule. For the overtaking maneuver, less emphasis is placed on the weights associated with lateral and longitudinal position tracking error (δx and δy) compared to the weights assigned to velocity tracking error (δv). This approach allows the CBF constraint to push the AV away from region occupied by OV while trying to maintaining the reference velocity $v_{ref,AV}$. Regarding the vehicle following and fully stopping maneuvers, the weights for both scenarios focus primarily on δx , with near-zero weights on δy and δv . This configuration ensures that the AV strictly adheres to the reference lane with minimal lateral movement and aligns its driving behavior based on the parameters D_{OV} and γ . In the vehicle following scenario, as discussed in Sect. 2.2.1, D_{OV} is set to 15 m and γ is reduced to 1. This enables the AV to decelerate and match the velocity of the preceding OV while maintaining a safe following distance. For the fully stopping scenario, as outlined in Sect. 2.2.1, the parameter D_{OV} is increased to 20 m, while γ is adjusted to 0.35. This ensures that the AV comes to a complete stop behind the stationary OV while maintaining a safe stopping distance with minimal lateral movement.

3 Methodology

Extensive virtual simulations were conducted to test the adaptiveness of the MPC-based motion planner and an integrated scenario comprising of an ego vehicle and four OVs is reported in this work. The ego vehicle encounters the four OVs one after the another and performs different manoeuvres based on the velocity of the obstacle vehicle which defines the rule set for the MPC weight adaptation. The algorithm is expected to seamlessly transition between the overtaking, following or safety-critical fully stopping manoeuvres. Further details are included in Sect. 4. The simulations were performed using Simulink platform of MATLAB environment in combination with high-fidelity simulation environment of IPG CarMaker. At each time-step, the environment and the multi-body vehicle model of the simulator take as input the control outputs from the motion-planner. The details of the information exchanged between the Simulink and IPG CarMaker is schematically represented in Fig. 1b. Since ego-localization and obstacle tracking is out of scope of this research, the initial states of the AV and the OV are provided to the motion planning algorithm which in real life would be given by localization and perception modules.

The control algorithm outputs the optimized acceleration (u_{acc}) and steering rate (ψ) of the AV, latter of which is integrated to obtain the steering angle (δ)

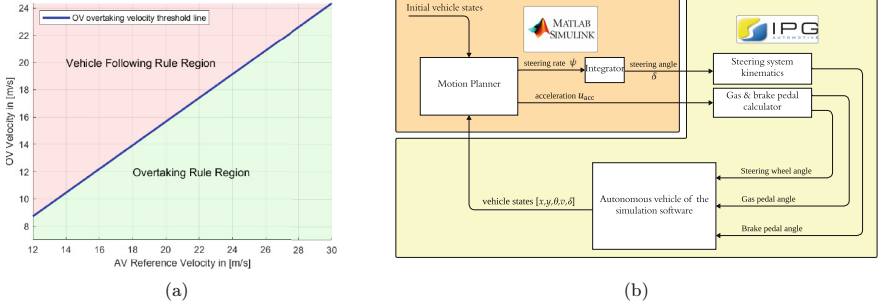


Fig. 1. (a) Plot between the AV reference velocity and the OV velocity that defines the threshold velocity limit that separates vehicle following maneuver from the overtaking maneuver by the AV. (b) Layout of feedback loop established between the developed motion planner and the high-fidelity simulation software.

at the front wheels from the given initial steering angle. u_{acc} is used to derive brake pedal angle and gas pedal angle of IPG CarMaker vehicle by utilizing the in-built PID control block of IPG CarMaker. δ is used to obtain steering angle of the steering wheel of IPG CarMaker vehicle using the steering system kinematics. The obtained states of the simulator model are fed to the algorithm, which acts as a feedback to the optimizer.

4 Simulation Results

The simulated scenario could be divided into four functional sub-scenarios occurring sequentially as follows:

- The AV, driving at a reference cruise velocity overtakes a stationary OV.
- The AV, driving at a reference cruise velocity overtakes a slow-moving OV.
- The AV, driving at a reference cruise velocity decelerates and follows an OV moving at a considerably high velocity which then takes a right turn at the road junction allowing the AV to accelerate back to its reference speed.
- The AV accelerates back to its stated reference velocity and then stops while detecting a stationary OV when overtaking option is not possible because of a divider in between the 2 lanes.

Table 1. Obstacle Vehicle characteristics for Integrated Simulation

OV Number	OV type	v_{OV}	$y_{0,OV}$	MPC Rule
OV ₁	Stationary	[0 m/s]	100 m	Overtake
OV ₂	Moving	[6 m/s]	170 m	Overtake
OV ₃	Moving	[13.6 m/s]	200 m	Follow
OV ₄	Stationary	[0 m/s]	1300 m	Stop

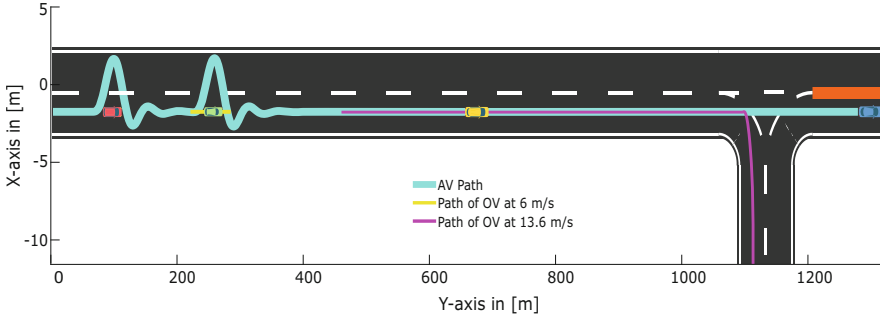


Fig. 2. The path and positions of the AV and the OVs in the integrated scenario simulation. The red car indicates the stationary OV_1 , while green and yellow cars represent OV_2 and OV_3 respectively. The dark orange line denotes the barrier that divides the two lanes. Finally the blue car denotes OV_4 .

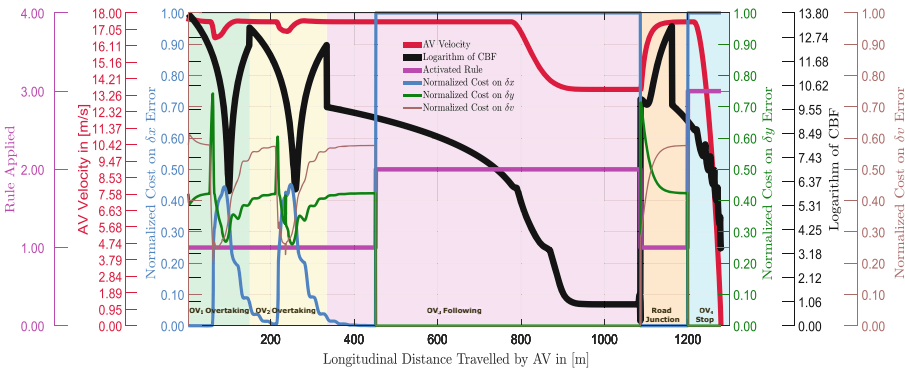


Fig. 3. Results from the integrated scenario simulation

The scenario consists of 4 OVs along the path of the AV as seen in Fig. 2. The OV characteristics are stated in Table 1.

All the sub-scenarios proceed continuously on a two-lane straight road, with each lane having a width of 3.5 m. Before the junction, the lanes are separated by lane markings, and after the junction, they are separated by a barricade. The initial and the reference velocity for the AV are set to 17.5 m/s and the simulation results are shown in Fig. 3. The OV_1 gets overtaken by the AV since it is stationary (shown in green region of Fig. 3). The AV then overtakes OV_2 as it is travelling within the vehicle following threshold limit of 13.5 m/s (shown in yellow region of Fig. 3). The AV then approaches OV_3 and decelerates to follow the OV since OV_3 is travelling above the set threshold limit. The AV keeps following OV_3 (shown in pink region of Fig. 3) till a junction located at about 1100 m from the starting position of the AV (shown in Fig. 3), where OV_3 shifts to another path different from that of the AV. The AV now is free to accelerate to its stated reference velocity $v_{ref,AV}$ of 17.5 m/s and this could be inferred from

orange region of Fig. 3. Once the AV crosses the junction and approaches OV_4 , the presence of barricades between the lanes prevents the AV from performing any further overtaking maneuver. Since there is no adjacent lane for AV now to overtake OV_4 , even though OV_4 is stationary AV decelerates and stops behind OV_4 (shown in indigo region of Fig. 3).

The logarithm of the CBF value during the simulation run over time is plotted in Fig. 3 as the black line and it could be inferred that constraint values are always greater than zero with a minimum value of 0.22 confirming that the constraints are always satisfied. As previously mentioned, the weights assigned to the MPC cost function are instantaneously adjusted according to the OV handling rules. This adjustment can be observed from the magenta line in Fig. 3, which defines the rule activated based on the scenario observed by the AV. A value of 1 indicates that the vehicle overtaking rule is followed, while values of 2 and 3 indicate that vehicle following and vehicle stoppage rules are followed by the MPC. Notwithstanding the fact that the MPC weights are shifted instantaneously, the AV does not exhibit any significant transient behaviours which could be observed from AV path in Fig. 2, which in-turn signifies that sudden change of the weights does not lead to instability of the AV. This behaviour was possible by setting the weights to control inputs on the ψ relatively higher compared to all other weights for all the scenarios in addition to the rule specific weight setting on tracking errors discussed earlier. A twofold advantage of such setting is that AV does not show high fluctuation in acceleration and steering rate values thereby resulting in smoother velocity profile which can be observed from the velocity plot in Fig. 3 (red line).

The normalized δx error cost is shown in Fig. 3 as the blue line. It can be inferred that this cost increases when the AV steers away from its reference line to perform an overtaking maneuver around the OV. The motion planner then works to bring the AV back to the reference line while satisfying the CBF constraints to reduce this cost. A similar pattern is observed for the δy error cost, also normalized and depicted as the dark green line in Fig. 3, during the overtaking maneuver. During the vehicle following and fully stopping scenarios, it could be inferred that the δx error cost is almost equal to 1 with near-zero cost values for δy and δv (also normalized and shown as brown line) error. This occurs because the AV tries to follow the OV_3 while maintaining a safe following distance with minimal lateral deviation from the reference line, achieved by heavily penalizing the δx error for the vehicle following maneuver. Similar behavior is observed in the vehicle stopping scenario where the AV decelerates from its stated reference velocity $v_{ref,AV}$ and completely stops behind OV_4 with minimum lateral deviation from its reference by sacrificing the cost on δy and δv errors. Additionally, when OV_3 steers right from the junction, the δy error cost is initially higher and gradually declines. This is because the AV is now free to track the way-points set for $v_{ref,AV}$, which was not possible earlier due to the vehicle-following rule enforced because of OV_3 . The AV reaches these way-points by accelerating through the road junction. The δv error cost is higher during the overtaking maneuvers around OVs because a reduction in the AV velocity is

necessary to safely overtake the OVs as observed in the red line. The normalized δv error cost is also higher when the AV accelerates along the road junction to reach $v_{\text{ref,AV}}$ as OV_3 moves right at the junction.

The maximum solving time for the combined setup (Simulink + IPG CarMaker) during the entire simulation time range is found to be 4.2 milliseconds which is less than ΔT of 0.05 s (20 Hz) required by MPC thereby demonstrating the real-time integration capability of the developed motion planner. This 20 Hz control frequency ensures the system can dynamically react to unexpected situations within a suitable reaction time, as highlighted in the research work of [10].

5 Conclusion

In this paper, a rule-based adaptive motion planner for an AV capable of autonomously overtaking, following, and stopping behind an OV is developed using an adaptive MPC framework. Based on the lane width available and relative speed between the AV and the OV, rules are defined that enables the motion planner to consider the proper driving scenario. The simulation results for these rule-defined scenarios are presented which confirms that the motion planner is able successfully adapt to different driving scenarios without colliding with any of the OV by seamlessly transitioning between weights assigned for different driving conditions.

Acknowledgement. The authors would like to acknowledge IPG Automotive for providing the CarMaker software, which was crucial for the simulations and analysis in this research.

References

1. Vadakkepat, P., Tan, K.C., Ming-Liang, W.: Evolutionary artificial potential fields and their application in real time robot path planning, vol. 1, pp. 256–263 (2000)
2. Choi, J.J., Lee, D., Sreenath, K., Tomlin, C.J., Herbert, S.L.: Robust control barrier–value functions for safety-critical control. IEEE Press (2021)
3. Artstein, Z.: Stabilization with relaxed controls. *Nonlinear Anal. Theory Methods Appl.* **7**(11), 1163–1173 (1983)
4. Desai, M., Ghaffari, A.: CLF-CBF based quadratic programs for safe motion control of nonholonomic mobile robots in presence of moving obstacles. In: 2022 IEEE/ASME International Conference on Advanced Intelligent Mechatronics (AIM), pp. 16–21 (2022)
5. Zeng, J., Zhang, B., Sreenath, K.: Safety-critical model predictive control with discrete-time control barrier function. In: 2021 American Control Conference (ACC), pp. 3882–3889 (2021)
6. Buyval, A., Gabdullin, A., Sozykin, K., Klimchik, A.: Model predictive path integral control for car driving with autogenerated cost map based on prior map and camera image, pp. 2109–2114 (2019)
7. Schperberg, A., Tsuei, S., Soatto, S., Hong, D.: Saber: data-driven motion planner for autonomously navigating heterogeneous robots. *IEEE Robot. Autom. Lett.* **6**(4), 8086–8093 (2021)

8. Shibata, K., Shibata, N., Nonaka, K., Sekiguchi, K.: Model predictive obstacle avoidance control for vehicles with automatic velocity suppression using artificial potential field. *IFAC-PapersOnLine* **51**, 313–318 (2018). 6th IFAC Conference on Nonlinear Model Predictive Control NMPC 2018
9. Arrigoni, S., et al.: Autonomous vehicle controlled by safety path planner with collision risk estimation coupled with a non-linear MPC, pp. 199–208 (2016)
10. Arrigoni, S., Braghin, F., Cheli, F.: MPC trajectory planner for autonomous driving solved by genetic algorithm technique. *Veh. Syst. Dyn.* **60**(12), 4118–4143 (2022)
11. Althoff, M., Koschi, M., Manzingler, S.: Commonroad: composable benchmarks for motion planning on roads, pp. 719–726 (2017)
12. Ames, A.D., Coogan, S., Egerstedt, M., Notomista, G., Sreenath, K., Tabuada, P.: Control barrier functions: theory and applications, pp. 3420–3431 (2019)
13. Verschueren, R., et al.: acados - a modular open-source framework for fast embedded optimal control. *Math. Program. Comput.* **14**(1), 147–183 (2021)

Open Access This chapter is licensed under the terms of the Creative Commons Attribution 4.0 International License (<http://creativecommons.org/licenses/by/4.0/>), which permits use, sharing, adaptation, distribution and reproduction in any medium or format, as long as you give appropriate credit to the original author(s) and the source, provide a link to the Creative Commons license and indicate if changes were made.

The images or other third party material in this chapter are included in the chapter's Creative Commons license, unless indicated otherwise in a credit line to the material. If material is not included in the chapter's Creative Commons license and your intended use is not permitted by statutory regulation or exceeds the permitted use, you will need to obtain permission directly from the copyright holder.





Towards Friction Potential Estimation for Motorcycles

Florian Klinger^(✉), Christoph Ott, Agnes Poks, Johannes Edelmann,
and Manfred Plöchl

Institute of Mechanics and Mechatronics, TU Wien, Austria
florian.klinger@tuwien.ac.at

Abstract. Estimation of the actual friction potential from measured vehicle states has been extensively explored for passenger cars, but lacks attention for motorcycles. Several aspects towards friction potential estimation for motorcycles are discussed in this study: (i) analysis of the characteristics of motorcycle tyres on different surfaces and conditions by using an instrumented motorcycle, (ii) analysis of the theoretical performance of an EKF-based friction potential estimation approach by means of simulation studies, and (iii) analysis of the feasibility of using a wetness sensor on the motorcycle to gain information on actual road conditions.

Keywords: Friction Potential Estimation · Extended Kalman Filter · EKF · Motorcycle · Tyre Characteristics · Road Conditions · Wetness Sensor

1 Introduction

The forces transmitted in the contact area of the tyres with the road are decisive for the handling dynamics and safety properties of road vehicles. Demanded forces that exceed the limits of friction may lead to a loss of stability, with potentially dangerous consequences, especially for motorcycle riders. Knowledge of the actual friction potential, however, may improve the performance of safety systems such as Anti-Lock Braking System (ABS), Traction Control System (TCS), and Stability Control System, and may also be helpful for the development of further Advanced Driver Assistance Systems (ADAS).

Methods for online estimation of the actual tyre–road friction potential can be basically classified into *cause-based* and *effect-based* [1]. The former methods are based on the detection of environmental (temperature, rain, etc.) or road surface conditions (water, ice, etc.). This can be done predictively within certain limits, but usually allows just for a classification of the actual friction potential. The latter methods rely on measurable effects of the current tyre–road contact conditions on the dynamic behaviour of vehicle and tyres. This allows for an estimation of the friction potential, but valid and yet sufficiently simple models of vehicle and tyres are required to adequately represent their behaviour at different friction conditions.

Various approaches for friction potential estimation are presented in vehicle dynamics literature, but refer almost exclusively to two-track vehicles, see e.g. [2–4]; an exception thereof is [5], wherein nonlinear regression methods are applied to estimate the friction potential during braking manoeuvres for a motorcycle. In this proceedings, selected aspects of an ongoing study towards friction potential estimation for motorcycles based on the magic formula (MF) tyre model and an extended Kalman Filter (EKF) approach are discussed, along with the first results from an analysis using a wetness sensor on a motorcycle.

2 Tyre Characteristics at Different Road Conditions

In a first step, the longitudinal characteristics of the front and rear tyres of an actual motorcycle have been analysed in order to identify applicable effects with regard to friction potential estimation. Starting from an available MF tyre parametrisation (from measurements on a flat track test rig), the scaling factors of the MF tyre model were adjusted to adapt the tyre characteristics to different surfaces and conditions found at the braking platform of the ZalaZONE proving ground in Hungary. Respective measurement data was collected by means of an instrumented motorcycle, and a procedure similar to [6] was employed to derive tyre forces and slip values at the front and rear tyres from coast down, constant speed, and acceleration and braking manoeuvres.

Figure 1 shows the resulting tyre characteristics of the front and rear tyres with the traction coefficient $\mu = F_x/F_z$ and the corresponding longitudinal slip κ . Comparing the orange and blue lines reveals a remarkable drop of the friction potential from dry asphalt to wet polished concrete, while the slope at small values of longitudinal slip κ remains unchanged. Note, that for the rear tyre, the friction potential is fully exploited

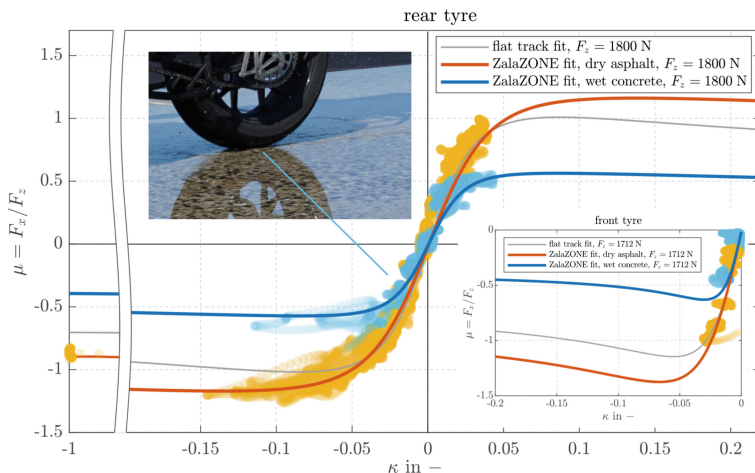


Fig. 1. Comparison of the longitudinal characteristics of the motorcycle tyres derived from measurements on a flat track test rig (grey) as well as from road tests with an instrumented motorcycle on dry asphalt (orange) and wet polished concrete (blue).

in wet conditions, while maximum tyre forces at higher positive slip values cannot be reached in dry conditions since a lift-off of the front tyre would occur (wheelie).

The same limitation applies to the front tyre under braking (stoppie). Besides, and due to the lack of driving forces, only negative slip values are used for the characterisation of the front tyre from on-road measurements. Yet, one may conclude that an effect-based friction potential estimation approach based on pure longitudinal excitation due to acceleration and braking, and relying on the diverging characteristics of the tyres in the (beginning of the) non-linear region seems promising.

3 Performance of EKF Based Friction Potential Estimation

It seems reasonable to investigate the performance of effect-based friction potential estimation approaches in idealised simulation studies first, before real-world measurements are taken into account. The former is addressed in this section, aiming to gain experience w.r.t. required excitation intensities for reliable estimation results, as well as related adaption time delays.

A discrete-time extended Kalman-Filter (EKF) according to [7] is implemented in Matlab. The selected structure of the algorithm is based on the planar three-dof motorcycle model depicted in the top left part of Fig. 2. In case of acceleration, the drive torque T_2 is the input to the estimator; longitudinal velocity \hat{v}_x , angular velocity $\hat{\omega}_2$ and friction potential $\hat{\mu}_{\max,2}$ comprise the estimated states of the EKF, which are updated at each time step by taking the chosen measurements in form of the longitudinal acceleration a_x and the angular velocity ω_2 of the rear wheel into account. Within the EKF, a simplified MF with $F_{x2} = F_{x2}(F_{z2}, \kappa_2, \mu_{\max,2})$ is applied. The vertical tyre forces F_{z1} and F_{z2} required within the EKF are related via the c.g. coordinates a , b , and h to the longitudinal acceleration a_x from the previous time step. In the case of braking at the front wheel only, a corresponding approach is realised.

The model of Fig. 2 is used as simulation model with the full MF tyre model in longitudinal direction, and with overlaid white noise. For simplicity, the front and rear tyre characteristics are presumed to be equal, such that only one friction potential $\hat{\mu}_{\max}$ is estimated for both tyres by the EKF. Variations of the tyre-road friction potential are realised by altering the scaling factor $\lambda_{\mu x}$ of the MF tyre model. A synthetic, sawtooth-like torque profile was selected, with alternating drive and braking inputs $T_2 > 0$ and $T_1 < 0$ at the rear and front wheel, respectively, resulting in acceleration and braking sections for a duration of two seconds each. Several instantaneous changes of $\lambda_{\mu x}$ and thus μ_{\max} are included in the manoeuvre. The linear increase of torque during a sawtooth provokes increasing wheel slips, and the peaks of the torques were selected that the traction coefficients μ_1 and μ_2 reach a certain fraction of the friction potential μ_{\max} during each segment, which will be referred to as “excitation intensity” in the following. In the bottom plot in Fig. 2, the dashed lines show the traction coefficients μ_1 and μ_2 for the front and rear tyre, respectively, and the dash-dotted line indicates the excitation intensity, which is set here to approx. 80% of μ_{\max} . In this form, the manoeuvre provides ideal conditions for testing the EKF by comprising persistent and high excitations while remaining within the wheelie and stoppie limitations.

The estimated friction potential $\hat{\mu}_{\max}$ converges in steps to the predefined μ_{\max} as can be observed by the blue line in the bottom plot of Fig. 2. It was found that the

traction coefficients need to exceed an excitation intensity of 0.6 for the algorithm to reliably converge. In Fig. 2, the related adaption time delays of the EKF are summarized as bar chart. The adaptation time delay is the time from the instantaneous change of $\lambda_{\mu x}$ until $\hat{\mu}_{\max}$ converges to a $\pm 10\%$ error range of μ_{\max} . Adaptation time delays of few seconds can be observed, and tend to increase with increasing downward-steps of the friction potential: for the steps towards $\lambda_{\mu x} = 0.4$, more than one sawtooth-excitation are required for the algorithm to converge. Adaptation time delays w.r.t. the upward steps appear to be close to each other. This effect can be explained in the present case by the fact that the traction coefficients μ_1 and μ_2 quickly exceed the former μ_{\max} after an upward-step, which gives a clear sign to the EKF that μ_{\max} must have raised as well.

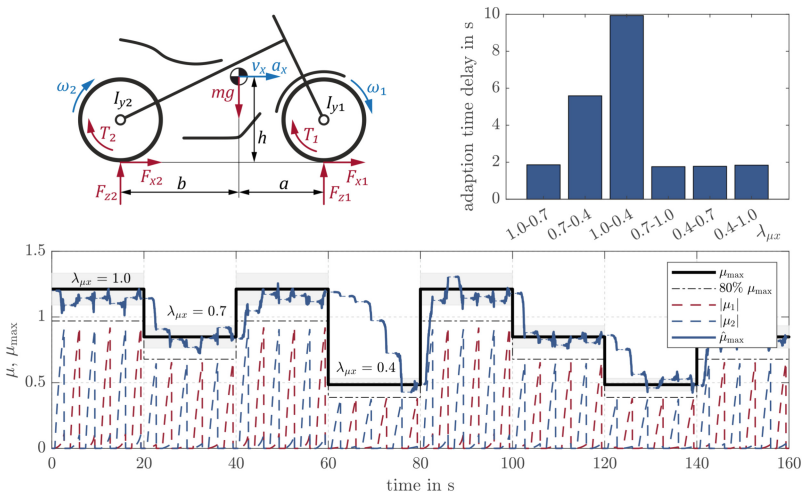


Fig. 2. Top left: three-dof motorcycle model for EKF and simulation. Bottom: simulated acceleration and braking manoeuvres with changing and estimated friction potential. Top right: adaption time required by the EKF to detect changes of the friction potential.

4 Analysis of Sensor-Based Detection of Wet Road Surfaces

To overcome limitations of the effect-based estimation method w.r.t. required excitation intensity and adaption time delays, the potential of a cause-based method to gain information on the actual road conditions is analysed in this section.

Multiple sensor principles for the purpose of detecting and quantifying road wetness are discussed in literature, see e.g. [8, 9], and recommendations for the positioning of such sensors at passenger cars are given based on different mechanisms of water spray ejection of rotating tyres.

In order to analyse the potential at motorcycles, two identical piezo-electric wetness sensors were applied to the instrumented motorcycle. First, a decision had to be made about the position of the sensors. Having in mind that the front tyre experiences changes in road conditions first, and already displaces some water from the road such that the

rear wheel experiences less road wetness when following the front wheel in the same track, it seems reasonable to place both sensors in the area of the front wheel. Two distinct positions have been selected, and are illustrated as orange rectangles in the top left sketch in Fig. 3: the first one is attached to the guard plate below the engine, such that the sensor is most directly hit by the water picked up by the tread of the front tyre; the second one is placed beneath the front fender, such that the sensor gets in contact with the spray circumferential to the front tyre. Impinging water droplets excite vibrations of the membrane of each sensor, resulting in oscillating analogous voltage output signals, which were recorded with a sampling rate of 50 kHz at the instrumented motorcycle.

Multiple measurements with different water heights on different surfaces have been conducted, with different velocities and different engine speeds. The recorded sensor signals were then analysed in both time and frequency domains, and from a comparison between the different mounting positions, the one beneath the front fender was found to be favourable. This may be due to the reasons described in [8, 9] that there is not enough water picked up by the front tyre to impinge on the first sensor at lower water heights, or the sensor position was too high above the road; another dominant reason is attributed to the engine noise, which is more dominant in the signal of the sensor at the engine plate than beneath the front fender.

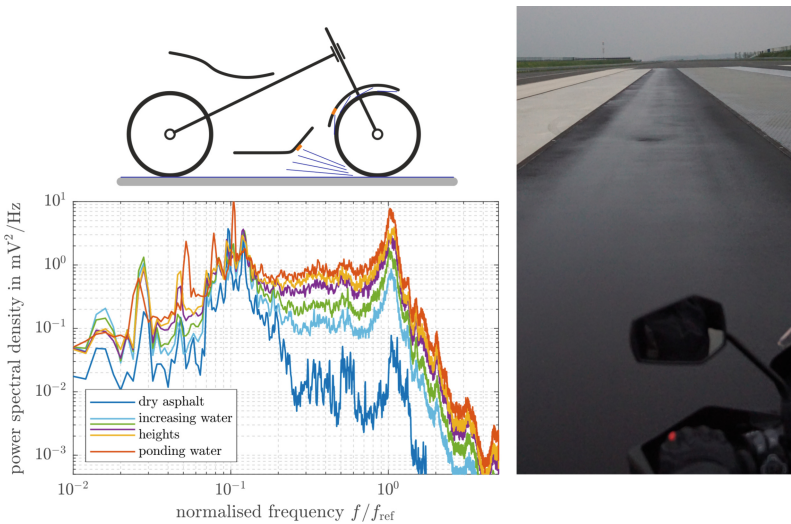


Fig. 3. Top left: selected positions of the wetness sensors at the motorcycle. Bottom left: power spectra for different water heights at an asphalt road resulting from the sensor mounted beneath the front fender. Right: asphalt road with different water heights at different tracks.

Power spectra of the signal of the sensor beneath the front fender are shown in the bottom left diagram in Fig. 3, resulting from different water heights on an asphalt road, which was traversed with a constant speed of 80 km/h in 4th gear. At lower frequencies, the sensor signal is influenced by engine noise, which possibly masks effects from impinging water. At higher frequencies above the sensor resonance frequency f_{ref} , the

spectra quickly decay with increasing frequency. The frequency range in between, however, allows for a clear distinction between dry asphalt (dark blue) and full wet asphalt with ponding water (dark orange), as well as between intermediate water heights at different tracks as depicted in the right picture in Fig. 3.

5 Summary

Analyses of the tyre characteristics of an actual motorcycle on different road surfaces and conditions reveal the possibility of effect-based friction estimation based on an extended Kalman Filter, relying on pure longitudinal driving and braking inputs. A performance analysis in a simulation environment confirms the feasibility in principle, but also shows that rather high excitation intensities and respective high longitudinal slip of the tyres are required, and that an estimation time of at least 2 s has to be accepted. As a possible solution, wetness sensors were investigated on the motorcycle. Encouraging results towards a quicker detection of wet road surfaces were found with a sensor positioned beneath the front fender of the motorcycle.

Acknowledgements. The measurement was carried out for R&D purposes at the ZalaZONE Automotive Proving Ground within the framework of scientific cooperation.

References

1. Müller, S., Uchanski, M., Hedrick, K.: Estimation of the maximum tire-road friction coefficient. *J. Dyn. Syst. Meas. Contr.* **125**(4), 607–617 (2004)
2. Gustafsson, F.: Slip-based tire-road friction estimation. *Automatica* **33**(6), 1087–1099 (1997)
3. Tanelli, M., Piroddi, L., Savaresi, S.M.: Real-time identification of tire-road friction conditions. *IET Control Theory Appl.* **3**(7), 891–906 (2009)
4. Fichtinger, A., Edelmann, J., Plöchl, M., Höll, M.: Aquaplaning detection using effect-based methods. *IEEE Veh. Technol. Mag.* **16**(3), 20–28 (2021)
5. Savino, G., Baldanzini, N., Pierini, M.: Real-time estimation of road–tyre adherence for motorcycles. *Veh. Syst. Dyn.* **51**(12), 1839–1852 (2013)
6. Bartolozzi, M., Savino, G., Pierini, M.: Novel high-fidelity tyre model for motorcycles to be characterised by quasi-static manoeuvres. *Veh. Sys. Dyn.* **60**(12), 4290–4316 (2022)
7. Simon, D.: *Optimal State Estimation*. John Wiley & Sons, New Jersey (2006)
8. Schmiedel, B., Gauterin, F., Unrau, H.-J.: Study of system layouts for road wetness quantification via tire spray. *Autom. Engine Technol.* **4**(1), 63–73 (2019)
9. Döring, J., Beering, A., Scholtyssek, J., Krieger, K.L.: Road surface wetness quantification using a capacitive sensor system. *IEEE Access* **9**, 145498–145512 (2021)

Open Access This chapter is licensed under the terms of the Creative Commons Attribution 4.0 International License (<http://creativecommons.org/licenses/by/4.0/>), which permits use, sharing, adaptation, distribution and reproduction in any medium or format, as long as you give appropriate credit to the original author(s) and the source, provide a link to the Creative Commons license and indicate if changes were made.

The images or other third party material in this chapter are included in the chapter's Creative Commons license, unless indicated otherwise in a credit line to the material. If material is not included in the chapter's Creative Commons license and your intended use is not permitted by statutory regulation or exceeds the permitted use, you will need to obtain permission directly from the copyright holder.





On the Stability of the Closed-Loop Teleoperated Vehicle and Teledriver System

Ypti Hossain¹, Mathias Metzler²(✉), Johannes Edelmann¹,
and Manfred Plöchl¹

¹ Institute of Mechanics and Mechatronics, TU Wien, Vienna, Austria

² Vay Technology GmbH, Mariendorfer Damm 1, Berlin, Germany
mathias.metzler@vay.io

Abstract. Teleoperated vehicles are gaining importance during the transition to fully automated vehicles since at the current state of development automated vehicles are not capable of operating in all conditions and environments. Despite the high potential of the concept of teleoperated vehicles, there are still challenges to be dealt with. As the teledriver is physically not present in the vehicle during teleoperation, the communication between the teledriver and the vehicle takes place via internet. That could lead to a delayed transmission of the telemetry and visual signals. Additionally, the teledriver's perception of the vehicle motion is reduced. This study demonstrates the differences between teledriving and normal driving from a theoretical perspective and how the stability of the vehicle-teledriver system is affected by the communication delay and the reduced perception of the vehicle motion. To increase the driver's perception and the ease of control of the teleoperated vehicle, a simple structured and tunable steering wheel torque emulation concept is introduced.

Keywords: Teledriver model · torque emulation · teleoperated vehicle · stability · time delay · perception · steering feel

1 Introduction

In recent years, autonomous driving has become a focal point of research and development. As a matter of fact, there is currently no automated vehicle that is capable of operating in all conditions and environments, as defined in SAE level 5 [6]. Automated vehicles still require human intervention in unknown driving environments or the event of hardware or software failure. As a transition to fully automated vehicles, teledriving also known as remote operation of vehicles over the internet plays an important role. Teleoperated vehicles can be employed in various practical scenarios, including taxi services, delivery services [2] and shared mobility platforms such as from Vay Technology GmbH [8]. In [7], the

structure of a teleoperated vehicle system is described. During vehicle teleoperation, the control signals of the teledriver such as steering input, throttle and brake pedal positions are transmitted to the vehicle control unit (VCU) over the internet and thus the signal transmission is delayed. To provide the teledriver with appropriate visual and acoustic feedback, the teleoperated vehicle has to be equipped with cameras and speakers. Likewise, there is a time delay to reach the telestation. In Fig. 1, the schematic structure of the telestation and the teleoperated vehicle is illustrated.

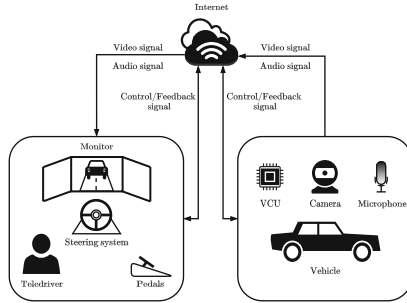


Fig. 1. Teleoperated vehicle system based on [7]

Despite the high potential of the concept of teleoperated vehicles, an investigation into the dynamics and the stability of the vehicle-teledriver system remains absent in the current literature to the best of the author’s knowledge. This paper studies the influence of the communication time delay and the reduced perception of the teledriver on the vehicle-teledriver system. Furthermore, a torque emulation concept is introduced that considers the telestation signals and the vehicle states to improve the teledriver’s haptic perception and the ease of control of the teleoperated vehicle [3].

2 Vehicle-Teledriver System

In this section, the vehicle-teledriver system is derived from the conventional vehicle-driver system. As described in [5], the vehicle-driver system consists of the vehicle model $G_{Veh}(s) = \frac{y_{CG}(s)}{\delta_{sw}(s)}$, the driver model $Dr(s) = \frac{\delta_{sw}(s)}{\Delta y(s)}$ and a prediction transfer function $Pr(s) = \frac{y(s)}{y_{CG}(s)}$. The steering wheel angle is δ_{sw} , y_{CG} is the current lateral position of the vehicle, y is the predicted lateral position and Δy is the deviation between the predicted position and the lateral position reference in the local road frame. Firstly, the parameter set of the driver model $Dr(s)$ is derived for conventional driving based on [5] and [3].

When the driver is physically not present in the vehicle, the communication between the driver and the vehicle takes place via the internet. The teledriver

inputs are transmitted to the vehicle with a communication delay. The vehicle’s output and the visual information are transmitted to the driver with a communication delay as well. Therefore, the delay transfer function $G_{Com}(s) = e^{-T_C s}$ is added. The resulting closed-loop vehicle-teledriver system is shown in Fig. 2. For the purposes of this investigation, the communication time delay is assumed to be constant $T_C = 0.04$ s. The stability of the closed-loop system is evaluated based on the Nyquist stability criterion. The open-loop transfer function is

$$G_{o,TS}(s) = Dr(s) G_{Com}(s) G_{Veh}(s) G_{Com}(s) Pr(s). \tag{1}$$

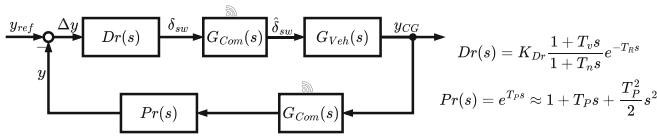


Fig. 2. Block diagram of the vehicle-teledriver system

As shown in Table 1, the phase margin φ_R decreases with increasing time delay until it reaches a negative value. That demonstrates that the closed-loop motion can leave the stable regime due to communication delay. The crossover frequency $\omega_c = 0.285$ Hz does not change with varying communication delay.

Table 1. Influence of the time delay on the system stability

T_C	0 s	0.04 s	0.08 s	0.12 s	0.16 s
φ_R	30.00°	21.80°	13.59°	5.39°	-2.82°

Now, it is assumed that the human operator is able to adapt to the situation of driving a vehicle remotely, based on experience. Therefore, it is further assumed that the teledriver is trained to operate the vehicle at a certain speed, e.g. $v_x = 30$ km/h, and with a communication delay $T_C = 0.04$ s. The parameters of the teledriver model are derived accordingly for this speed. In Table 2, the crossover frequency and phase margin of the closed-loop system are given. As the vehicle velocity is changing, but the teledriver does not adapt due to the reduced perception of speed, it can be seen that the crossover frequency shifts to higher values and the phase margin decreases with increasing velocity, until the phase margin is negative. This results from the non-minimum phase behaviour which becomes more dominant at higher frequencies. The closed-loop motion with the teledriver leaves the stable regime at 45 km/h due to the reduced perception. This phenomenon can also be observed with teledrivers in real application.

Table 2. Influence of the reduced perception on the system stability

v_x	30 km/h	35 km/h	40 km/h	45 km/h
φ_R	30.00°	21.14°	10.60°	-0.62°
ω_c	0.285 Hz	0.355 Hz	0.424 Hz	0.490 Hz

In conclusion, a teledriver can steer the vehicle in a stable fashion despite the time delay. However, if the teledriver's perception of the changing speed is reduced, the vehicle motion can become unstable. There might be teledrivers who are able to adapt themselves to different speeds, but the motion could still become unstable due to the communication time delay. To increase the stability of the teleoperated vehicle-teledriver system, a phase-boosting element, such as lead-steering as proposed in [4], could be introduced, which is however beyond the scope of this paper. Alternatively, a steering wheel torque emulation could also be helpful for the driver to better adapt to changing speed.

3 Torque Emulation

In literature, there are many concepts to emulate the feedback torque at the steering wheel. However, most of them require a profound knowledge of the steering system parameters. In the scope of this study, a tunable torque emulation concept is introduced and implemented in a teledriving simulator and a real telestation. Since there are no physical links between the telestation steering system and the vehicle steering system, the feedback torque can be generated freely. The torque emulation concept has a modular structure that can be tuned as described in [3]. The emulated torque considers the telestation steering wheel angle $\delta_{sw,TS}$, telestation steering wheel rate $\dot{\delta}_{sw,TS}$, lateral acceleration a_y and the yaw rate r of the vehicle. A spring torque is calculated based on the steering wheel angle and a damping torque based on the steering wheel rate. The lateral acceleration and the yaw rate based torques are used to provide the teledriver with information of the vehicle motion. Each torque component T_i is evaluated with a two-dimensional characteristic curve that considers the longitudinal velocity v_x and the corresponding signal. The characteristic curves are generated with the hyperbolic tangent function as described in [1]. The maximum value and the slope around the origin are varied with the parameters $A_i(v_x)$ and $\xi_i(v_x)$. The variable χ and the index i describe the individual signal to generate the torque component ($\chi = i = \delta_{sw,TS}, \dot{\delta}_{sw,TS}, a_y, r$)

$$T_i = A_i(v_x) \tanh(\xi_i(v_x) \cdot \chi). \quad (2)$$

For test purposes, a slalom is build up in a teledriving simulator. In Fig. 3, the view of a telestation is shown. The tests at the real telestation can be found in [3].



Fig. 3. Telestation with operator in real environment [8]

The reaction of a teledriver with little teledriving experience is tested with different torque contributions. For this study, the results with no torque emulation (mode 0) are compared with two different torque emulation modes. The investigated torque emulation mode 5 only includes the spring and damping torque. Whereas mode 9 considers all four torque components. In the left graph of Fig. 4, the trajectories with the different torque emulation modes at $v_x = 30$ km/h are illustrated. In comparison to mode 0, where no feedback torque is applied, the driver successfully navigates through the slalom with the assistance of the feedback torque. Moreover, the amplitudes are reduced with a feedback torque at the steering wheel. However, in mode 5 the driver leaves the track after passing the exit gate of the slalom. In contrast, in mode 9 the driver finishes the slalom without touching any cones and not coming off the track. Additionally, the driver manages to steer the vehicle with a slightly smaller amplitude than in mode 5. The steering inputs of the driver and the corresponding vehicle states with different torque emulation modes are compared in the right graph of Fig. 4. With the feedback torque at the steering wheel, the driver steers less than without a feedback torque. Furthermore, in mode 9 the driver reacts earlier passing the cones than in mode 5 or mode 0. Additionally, the

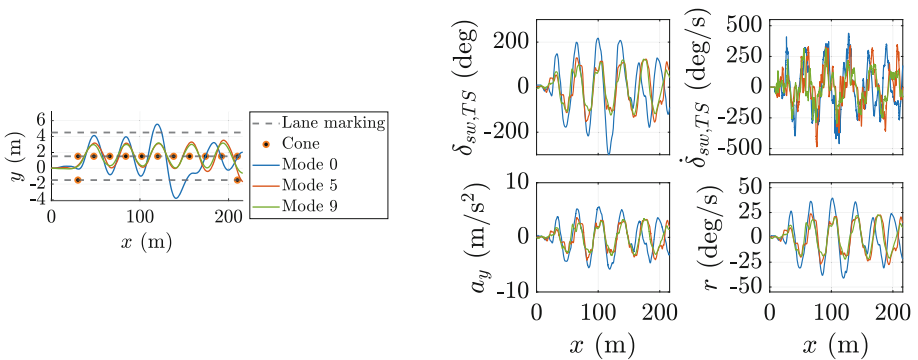


Fig. 4. Trajectory with different torque emulation modes at $v_x = 30$ km/h (left); Steering inputs and vehicle states with different torque emulation modes (right)

steering wheel angle rate is lower in torque emulation mode 5 and 9 than with mode 0. Due to the lower steering wheel angle input in modes 5 and 9, the lateral acceleration and the yaw rate are also lower. The tuning parameters of mode 5 are chosen such that the spring torque has the greatest contribution. This steering wheel angle based torque may give the driver the feeling of having an immediate response, but the information of the vehicle's response is not provided. In mode 9 the contribution of the spring torque is smaller, but there are additional torque components such as the lateral acceleration and the yaw rate based torque. The torque emulation component was also introduced to a real telestation. The tests in the real system show that torque emulation assists the steering of a teleoperated vehicle and improves the teledriver's perception of speed and the road, which is helpful when performing the slalom manoeuvre from simulation in a real environment [3].

4 Conclusion

This study shows from a theoretical perspective how the teleoperation of a vehicle differs from driving a normal vehicle. In general, the teledriver has to cope with the influences of the varying time delay and the reduced perception. The combination of these two impacts makes the teleoperation of a vehicle more challenging than conventional driving. To increase the driver's perception and the ease of control of a vehicle, a basic and tunable torque emulation concept is introduced, that considers the steering wheel angle, steering wheel rate, lateral acceleration and the yaw rate. Due to the simple structure, it is possible to run the torque emulation component in real-time on a simulator and the real telestation.

A teledriving simulator for testing the driving behaviour in a safe environment is used. The tests at the teledriving simulator demonstrate that a non trained teledriver may have difficulties driving without any torque feedback. Generally, the absence of feedback torque gives drivers an unusual light feeling. That leads to heavy steering due to the reduced perception. It could be demonstrated that the motion gets unstable whenever big steering wheel angle inputs are applied in combination with a high steering wheel angle rate. In this case, the driver tries to steer more due to the delayed reaction of the vehicle. Furthermore, it became clear that it is beneficiary to have a component in the teleoperated vehicle-teledriver system that boosts the phase of the open-loop system and therefore ensures the stability of the closed-loop system. For further investigations the torque emulation component could be integrated into the system model to investigate its influence on stability.

References

1. Fankem, S., Müller, S.: A new model to compute the desired steering torque for steer-by-wire vehicles and driving simulators. *Veh. Syst. Dyn.* **52**, 251–271 (2014). <https://doi.org/10.1080/00423114.2014.896469>

2. Goodall, N.: Non-technological challenges for the remote operation of automated vehicles. *Transp. Res. Part A Policy Pract.* **142**, 14–26 (2020). <https://doi.org/10.1016/j.tra.2020.09.024>
3. Hossain, Y.: Torque emulation for teleoperated vehicles. Diploma thesis, Technische Universität Wien (2023). <https://doi.org/10.34726/hss.2023.110790>
4. Limpibuntern, T., Fujioka, T.: Bilateral driver model for steer-by-wire controller design. *Veh. Syst. Dyn.* **41**, 381–390 (2003)
5. Mitschke, M., Wallentowitz, H.: *Dynamik der Kraftfahrzeuge*. Springer Fachmedien, Wiesbaden (2014). <https://doi.org/10.1007/978-3-658-05068-9>
6. On-Road Automated Driving (ORAD) Committee: *Taxonomy and Definitions for Terms Related to Driving Automation Systems for On-Road Motor Vehicles* (2021). https://www.sae.org/standards/content/j3016_202104
7. Su, C., Li, H., Wu, X.: Artificial steering feel for teleoperated road vehicle with disturbance observer. In: *2021 5th CAA International Conference on Vehicular Control and Intelligence (CVCI)*, Tianjin, pp. 1–6 (2021). <https://doi.org/10.1109/CVCI54083.2021.9661125>
8. Vay Technology: *Our teledriving-first approach* (2024). <https://vay.io/our-teledriving-first-approach-how-we-build-teledrive-technology-around-safety-and-the-human-driver/>

Open Access This chapter is licensed under the terms of the Creative Commons Attribution 4.0 International License (<http://creativecommons.org/licenses/by/4.0/>), which permits use, sharing, adaptation, distribution and reproduction in any medium or format, as long as you give appropriate credit to the original author(s) and the source, provide a link to the Creative Commons license and indicate if changes were made.

The images or other third party material in this chapter are included in the chapter's Creative Commons license, unless indicated otherwise in a credit line to the material. If material is not included in the chapter's Creative Commons license and your intended use is not permitted by statutory regulation or exceeds the permitted use, you will need to obtain permission directly from the copyright holder.





Increasing Performance of Differential Braking as Steering Backup Using Combined Slip Effects

Leon Salzwedel¹(✉), Christian Frohn¹, Cedric Heise¹, Jannes Iatropoulos²,
and Roman Henze²

¹ Volkswagen AG, Berliner Ring 2, 38436 Wolfsburg, Germany
leon.salzwedel@volkswagen.de

² Institute of Automotive Engineering, Technische Universität Braunschweig,
Hans-Sommer-Straße 4, 38106 Braunschweig, Germany

Abstract. Redundancies provide essential fail-operationality and are commonly utilized in design of Steer-by-Wire systems. Operationality of steering rack actuators can therefore be increased using differential braking as additional redundancy level. Research in this field has shown boundaries for lateral control to be mitigated compared to conventional steering systems. This paper focuses on performance increases by drive-line torque and stability control, both yielding effects of combined longitudinal and lateral tire slip during cornering.

Coping with the tradeoff between under- and oversteer whilst increasing performance was the major aim during controller design. For vehicle prototype testing a model following control scheme for differential braking was derived and implemented. Measurements on a low friction proving ground in suitable driving maneuvers were carried out subsequently. The results show new boundaries of vehicle dynamics and address variations of steering kinematics parameters as well as driveline configurations. Investigated interactions of longitudinal and lateral tire slip in the field of differential braking brings up promising potential to increase cornering ability in the fallback level for steering rack actuators.

Keywords: Steer-by-Wire · Differential Braking · Vehicle Dynamics

1 Introduction

Recent legislation has released further development of Steer-by-Wire systems [7]. Published standards describe supplementary redundancies in steering systems with limited performance [2] as optional design method. Implementation of differential braking has therefore been topic of several research in the past. Jonasson [6], Gauger [3], Sharma [10] and our recent work investigated limits regarding driving dynamics in steady-state conditions [9]. Maximum curvature depends on maximum feasible brake forces due to road wheel friction.

The constraint of differential braking in terms of Steer-by-Wire can be equivalent to understeer since desired yaw rate would not be achieved. We are demonstrating theoretically and practically how understeer can be reduced. Therefore

overlying drive torque and increased longitudinal slip was used to change the vehicle’s driving behavior.

A stability controller within a model following control scheme was implemented. As a result we were able to show the impact of longitudinal slip and drive torque on the vehicle’s driving behavior in practical application. To achieve greater magnitudes of yaw rate, increasing side slip was necessary. This can theoretically be considered as oversteer, but might be compensated due to vehicle free steer behavior and active countermeasures.

The results show increases in potential for lateral control using effects of combined slip. Variations in driveline configurations and steering kinematics give an outlook towards further vehicle applications. These findings extend previous research.

2 Vehicle Dynamics

Differential braking differs from conventional front axle steering regarding control input and front wheel steering system behavior. Literature [4,6,9] has described single track models where the front wheel steering angle is treated as an additional degree of freedom. Figure 1 shows the model considered within this paper. (a) is an extended single track model with differential brake forces [6]. (b) shows the steering model to describe mechanics of the vehicle’s free steer behavior. The model was parametrized by test bench measurements with the test vehicles steering system. Phenomena of combined tire slip are modeled through a coupled brush tire model according to Pacejka [8] by Eq. (1). Its output vector \mathbf{F} effectively describes the resulting forces F_x and F_y depending on the combination of theoretical slip quantities σ_x and σ_y .

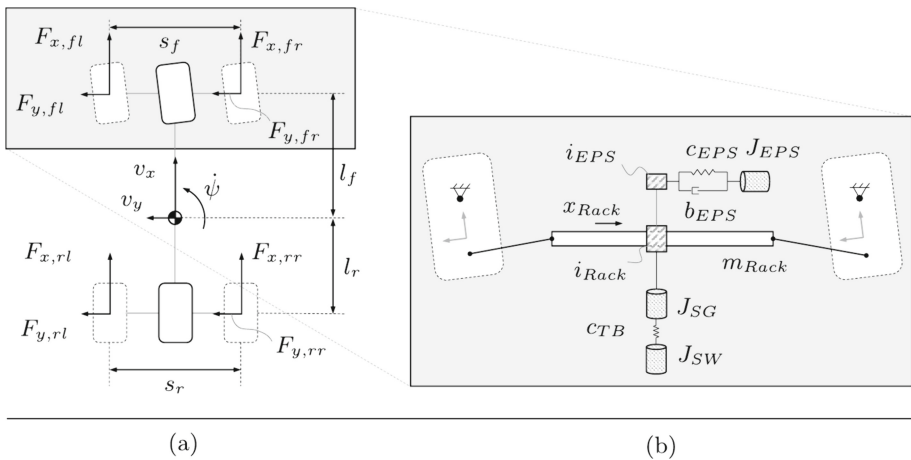


Fig. 1. (a) Vehicle Model [6] (b) Steering Model

$$\mathbf{F} = \sigma \frac{F}{\sigma} \tag{1}$$

Yielded vehicle model behavior is nonlinear due to steering system friction and tire behavior. Therefore the phase plane method can describe system dynamics as practiced by Bobier-Tiu [1] to describe differential braking control. Figure 2 shows side slip and yaw rate ($\beta - \dot{\psi}$) phase portraits with free steering as a result of approximate differential brake forces $F_{b,fl/rl}$ on front and rear axle.

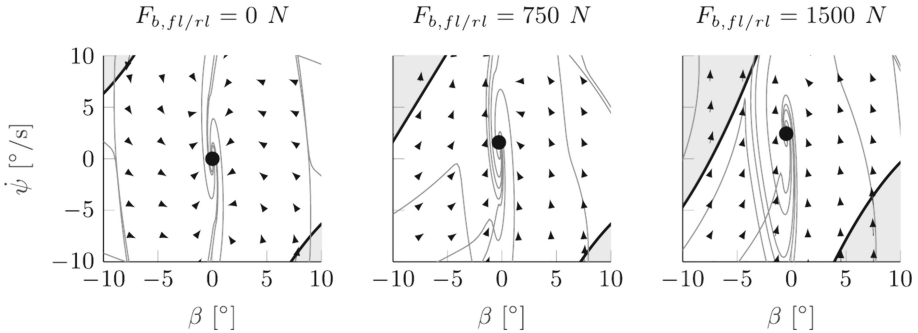


Fig. 2. Nonlinear behavior represented by phase portraits for differential brake forces at $v_0 = 20$ m/s and $\mu = 0.3$

The system reaches a steady state for all three variants. It has fewer yaw rate but is more stable at higher velocities than the same system would with steering angle fixed to zero. Greater dynamics can be achieved using two different methods. On the one hand, differential brake forces $F_{b,fl/rl}$ can be increased by overlaying drive torque. Rear axle understeer interventions can be utilized to increase yaw rate on the other hand. They cause the vehicle to turn into the corner by transiently increasing side slip angles on front and rear axle. Both options yield potential oversteer and the necessity of equivalent countermeasures.

3 Controller Design

We implemented a model following controller in a vehicle with rapid prototyping platform to investigate performance improvement. Figure 3 shows the scheme. It comprises a reference model, feedforward block, a slip controller and stability controller as well. The stability controller in this scheme can bypass the slip controller with an additional brake input disregarding the separate anti-lock functionality of the slip controller. The controller prevents under- and oversteer depending on the driving state.

The feedforward block computes necessary brake inputs by the reference model's desired yaw rate $\dot{\psi}$ and takes into account vehicle longitudinal speed

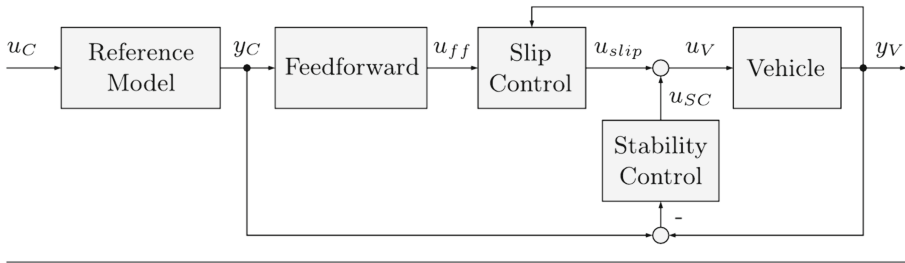


Fig. 3. Control concept for differential braking as steering backup with stability control. Inputs u_C : Driver steering wheel angle δ_{SW} , longitudinal velocity v_x , yaw rate ψ . Outputs u_V : Brake pressures $p_{b1\dots4}$

v_x and steering wheel angle δ_{SW} . The steering angle resulting from the rack position x_{Rack} is not considered as an input in the control algorithm. Sensor data for the rack position might not be available in the considered use case of differential braking.

The control scheme is used to determine the possible performance increase by understeer interventions yielding greater magnitudes of tire slip. Triggering drive torque overlay is not shown.

4 Vehicle Testing and Performance Evaluation

Differential braking's limit is primarily understeer, therefore the main goal was to determine the performance increase with understeer countermeasures on the rear axle. Since it is also able to impact stability and maximum yaw moment, a variant with drive torque overlay was tested as well. The maneuver "slowly increasing steering-wheel angle" from straight line driving according to ISO 4138 [5] was chosen for performance evaluation regarding circular driving behavior. To determine the effectiveness of understeer countermeasures, the tests were carried out in a modified prototype vehicle on a snow-covered driving dynamics surface with low friction. Vehicle behavior for conventional steering was measured as a reference and compared to the results of differential braking with positive scrub radius in three variants. The results with feedforward differential braking were compared to adding the stability controller and drive torque. To eliminate the impact of the positive scrub radius, the test sequence was repeated only applying brake and drive forces on the rear axle to analyze an equivalent vehicle with negative scrub radius. Initial vehicle speed was 20 m/s.

Figure 4 shows the results. Thereby steering-wheel and side slip angle are shared over lateral acceleration for both sequences and corresponding measurements. For each case, three measurement series have been examined to ensure statistical validity. Steering by feedforward differential braking shows to lead to expected understeer behavior for the front and rear axle braking as well as rear axle only. For both test sequences, understeer interventions through the stability controller and drive torque overlay increased feasible lateral acceleration

compromising slip angle β . Shown driving behavior can further be adjusted by controller design.

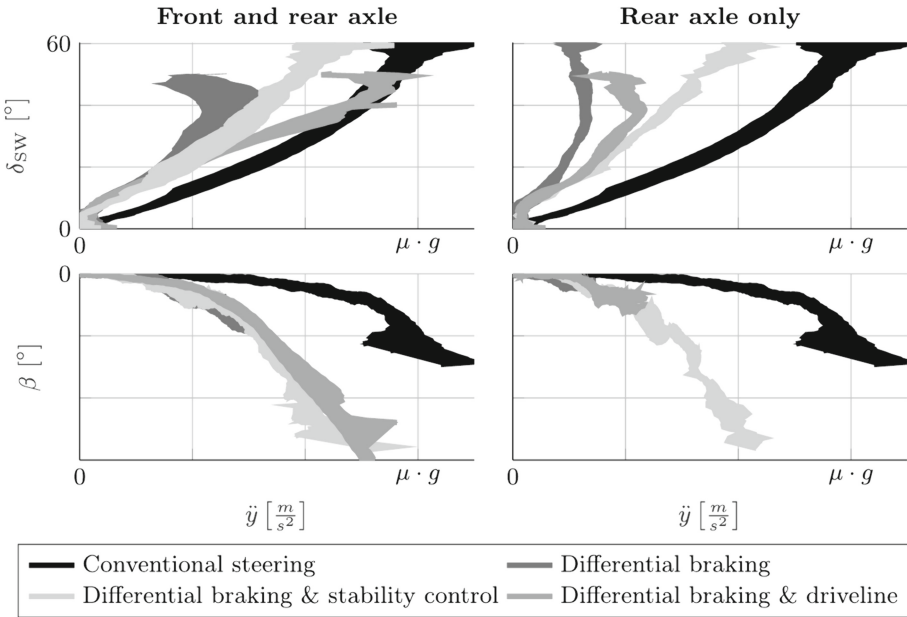


Fig. 4. Slowly increasing steering-wheel angle according to [5] at $v_0 = 20$ m/s

Results again show strong dependency of differential braking on road wheel friction and scrub radius. Analyzing effects of combined slip indicates novel improvements towards feasible lateral acceleration during low friction tests. Drive torque overlay has also shown promising results towards feasible vehicle dynamics. The downside of drive torque overlay was the negative effect on driving stability and that vehicle speed was reduced less to decrease accident severities regarding the steering failure. Another challenge is the impact of the front axle’s free steering behavior.

5 Outlook and Summary

This paper shows earlier derived limits of lateral control for differential braking to be extendable by effects of combined slip. We focussed on maximum lateral vehicle dynamics regarding circular driving behavior. Measurements for two vehicle variants have shown expectable different results in the linear region. Achieved vehicle reactions using greater magnitudes of longitudinal slip were comparable for both setups.

Feasible yaw moment was increased overlaying drive torque at both axles and analyzed in the same driving maneuver. The result in real vehicle tests

was a performance increase as well as a tendency to oversteer, which yields the necessity for a stability controller as well.

Considering potential increase in vehicle dynamics as a chance and the risk of oversteer as a fact of differential braking, a stability controller seems essential for full use of differential braking's capabilities as backup steering. Further testing has to be carried out in real world and virtual development for implementation.

References

1. Bobier-Tiu, C.G., Beal, C.E., Kegelman, J.C., Hindiyeh, R.Y., Gerdes, J.C.: Vehicle control synthesis using phase portraits of planar dynamics. *Veh. Syst. Dyn.* **57**(9), 1318–1337 (2018). <https://doi.org/10.1080/00423114.2018.1502456>
2. DIN-Normenausschuss Automobiltechnik: DIN 70065: Kraftfahrzeuge - Anforderungen an ein Steer-by-Wire-System (2023)
3. Gauger, A.: HIGHLY AUTOMATED DRIVING – potential of wheel-individual brake interventions as a backup for steering system failures during automated driving. In: Pfeffer, P. (ed.) 7th International Munich Chassis Symposium 2016. P, pp. 485–503. Springer, Wiesbaden (2017). https://doi.org/10.1007/978-3-658-14219-3_33
4. Iatropoulos, J., Ahrenhold, T., Henze, R.: Lateral control of automated vehicles with braking interventions as a fallback level for failures in the steering system. In: 7th International Symposium on Future Active Safety Technology Toward Zero Traffic Accidents (2023)
5. International Organization for Standardization: Passenger cars - Steady-state circular driving behaviour - Open-loop test methods (2021)
6. Jonasson, M., Thor, M.: Steering redundancy for self-driving vehicles using differential braking. *Veh. Syst. Dyn.* **56**(5), 791–809 (2018). <https://doi.org/10.1080/00423114.2017.1356929>
7. Official Journal of the European Union: Regulation No 79 of the Economic Commission for Europe of the United Nations (UN/ECE) — Uniform provisions concerning the approval of vehicles with regard to steering equipment [2018/1947] (2018)
8. Pacejka, H.B.: *Tire and Vehicle Dynamics*, 3rd edn. SAE International, Elsevier, Amsterdam (2012)
9. Salzwedel, L., Iatropoulos, J., Henze, R.: Potential of differential braking as backup system for steering actuators. In: 32nd Aachen Colloquium Sustainable Mobility 2023 (2023)
10. Sharma, A.: Steering by braking individual wheels. Master thesis, Eindhoven University of Technology, Eindhoven (2018). <https://research.tue.nl/en/studentTheses/steering-by-braking-individual-wheels>

Open Access This chapter is licensed under the terms of the Creative Commons Attribution 4.0 International License (<http://creativecommons.org/licenses/by/4.0/>), which permits use, sharing, adaptation, distribution and reproduction in any medium or format, as long as you give appropriate credit to the original author(s) and the source, provide a link to the Creative Commons license and indicate if changes were made.

The images or other third party material in this chapter are included in the chapter's Creative Commons license, unless indicated otherwise in a credit line to the material. If material is not included in the chapter's Creative Commons license and your intended use is not permitted by statutory regulation or exceeds the permitted use, you will need to obtain permission directly from the copyright holder.





Laboratory Abrasion Tester to Estimate Tyre Grip and Cornering Stiffness

Francesco Colombo¹, Samuel Sonnino¹, Federico Mantovani², Andrea Ronchi², Luca Michielan², Michele Vignati¹, and Edoardo Sabbioni¹(✉)

¹ Politecnico di Milano, 20133 Milan, Italy
{francesco.colombo, edoardo.sabbioni}@polimi.it
² Pirelli Tyre S.p.A., 20126 Milan, Italy

Abstract. Identification of tyre grip is crucial for ensuring safety and performance. To develop new tyres matching the requirements for grip, extensive testing is required both indoor and outdoor, which is time-consuming and costly. Therefore, the possibility to assess their performance in laboratory before manufacturing a full tyre appears very attractive. On this purpose, the present paper compares the peak of the friction coefficient, evaluated using a Laboratory Abrasion Tester (LAT100) on two compounds and the grip assessed through MTS Flat-Trac machine tests on two full tyres having the same structure and made of the compounds tested on the LAT100. An ad hoc procedure for driving the test on the LAT100 and make them comparable with the full-tyre data was developed. A good correlation was found for the dependency of the friction coefficient on temperature and load, highlighting the possibility of using LAT100 tests to gain information about tyre performance, before the manufacturing of the full tyre.

Keywords: Grip · Cornering Stiffness · VMI LAT100 · MTS Flat-Trac

1 Introduction

Tyre grip is crucial for evaluating vehicle handling performance and design effective vehicle dynamics controllers, such as ABS and ESP. Assessing tyre grip in the early stage of its design is therefore of utter importance in the tyre development. Under this point of view, the possibility to assess tyre performance using laboratory tests on compound samples before manufacturing a full tyre appears very attractive. The present paper considers tests carried out on a Laboratory Abrasion Tester (LAT100) on two compound samples (referred as “*CompoundA*” and “*CompoundB*”) and Lateral Steady State test performed on MTS Flat-Trac. The *CompoundB* is a more performing compound than the *CompoundA* and so it experiences higher value of grip and cornering stiffness.

The LAT100 machine consists of a spinning disc on which a solid rubber test wheel (Grosch wheel) is pressed under a normal load F_z at a slip angle. The tangential velocity of the sample wheel is induced by the disc angular velocity.

The traveling speed, slip angle, and load can be varied over a wide range. The average slip velocity in the contact area is created by combining the angular velocity and slip angle [1]. Although the machine was originally designed to assess the abrasion loss of the test wheel according with different experimental test conditions, the objective of this study is to verify if it can also be used to assess its grip by performing tests similar to ones carried out on the MTS Flat-Trac machine on a full tyre.

2 Methodology

As mentioned earlier, the present research investigates the possibility of using the LAT100 machine to measure friction coefficient as a function of load and temperature and assess possible correlations between these measurements and their counterparts on full tyre grip measured on MTS Flat-Trac. On this purpose, an ad hoc procedure was developed for testing compound samples, in the form of a solid wheel, in steady-state cornering conditions. The idea is to replicate on the LAT100 machine tests similar to the ones performed on the MTS Flat-Trac machine on a full tyre, so to compare the outputs. Specifically, two compounds were tested in the LAT100 machine. Tests on the MTS Flat-Trac machine were carried out with two full tyres, having an identical structure, but with the tread made of the two compounds tested on the LAT100.

2.1 MTS Flat-Trac Tests

Only steady-state cornering tests are considered in this work since these conditions are replicable on the LAT100. These tests are performed applying a triangular wave slip angle input at constant vertical load. The test is then repeated by varying the vertical load. Figure 1 shows on the left the cornering (or lateral) force (F_y) vs. the slip angle (α) curve obtained during tests carried considering three different vertical loads: the blue curve refers to the nominal load, the red curve to the 65% of the nominal load and the yellow curve to the 125% of the nominal load. Data are reported in a non-dimensional form for industrial privacy reasons: the cornering force is made non-dimensional by the vertical load applied during the test, while the slip angle is made non-dimensional by maximum slip angle imposed during the test. From these tests, the following information can easily be obtained:

- tyre grip: the peak cornering force divided by the vertical load imposed during the test;
- cornering stiffness: the slope of the lateral force curve near the origin ($\alpha = \pm 0.5$ deg);
- the nonlinear dependency of the tyre grip on the vertical load.

2.2 LAT100 Tests

Similarly to the MTS Flat-Trac tests, the procedure involves the application of a triangular repeated slip angle time history profile to the test wheel. In particular, LAT100 tests are performed by placing the test wheel on the actuator (right side) and then repeated with the specimen flipped, i.e. by rotating the specimen 180° with respect to its vertical axis (left side). In fact, since the testing surface is a rotating disc, the velocity profile is not uniform in the contact patch, thus by repeating the test on both sides, the non-uniform speeds distribution, and the consequent conicity effects on the specimen, should be compensated [2]. An example of the results obtained on the LAT100 machine are shown on the right of Fig. 1, which reports the cornering force vs. the slip angle for three different vertical loads: the nominal load (blue), the 75% of the nominal vertical load (red) and the 125% of the nominal load. The same non-dimensional form used for the MTS Flat-Trac data (left of Fig. 1) is used. The influence of the disc speed, the maximum slip angle, the slip angle rate, the powder sprayed on the contact patch and test duration was investigated during the research. Parameters were tuned in order to improve the matching with the MTS Flat-trac data. Results are shown in the next section in terms of grip and cornering stiffness and their dependence on vertical load and test temperature.

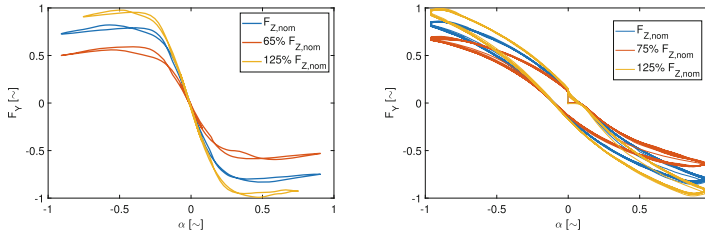


Fig. 1. Lateral force vs SSA on MTS Flat-Trac (left) and LAT100 (right)

3 Results

In this section, the comparison between LAT100 and MTS Flat-Trac data is reported. From Fig. 2 and 3 is possible to appreciate the similarities and the differences between the grip (Ed. Note: for simplicity of comparison, we will use the not entirely appropriate term “grip” for the LAT100 wheel as well, aware that the more suitable term would be “coefficient of friction”) and the cornering stiffness as a function of the vertical load evaluated on MTS Flat-Trac and LAT100. Data are reported in a normalized form for industrial privacy reasons, in particular the vertical load is normalized on the nominal one and the temperature range on the central value of the test (same for MTS Flat-Trac and LAT100 data). Consequentially, each key performance indicator (KPI) is normalized on

the corresponding “nominal value”. LAT100 data were compared with MTS Flat-Trac data to assess the correlation in terms of grip (maximum of the normalized lateral force with respect to the side slip angle) and cornering stiffness (slope of the lateral force trend for null side slip angle). Each graph shows the same scales between MTS Flat-Trac and LAT100 data for grip and temperature representation but different ones for what concern cornering stiffness and loads, since the two machines work at very different loads.

As expected considering the characteristics of the two compounds, grip and cornering stiffness of *CompoundB* are larger than the ones of *CompoundA* at each tested vertical load. This ranking is confirmed both by MTS Flat-Trac and LAT100 data. As it can be seen the trend of the grip with the vertical load is well correlated in MTS Flat-Trac and LAT100 tests. Indeed, tyre grip is mainly influenced by tread compound characteristics. Viceversa, the trend of the cornering stiffness on the vertical load differs between MTS Flat-Trac and LAT100 data. For what concerns the cornering stiffness, in fact, the tyre structure (not present in the Grosch Wheel) plays a crucial role. The tyre cornering stiffness is actually given by two contributions: tread and belt/sidewall stiffness. Obviously, the Grosch Wheel’s cornering stiffness is instead determined only by the tread contribution. The influence of temperature was also investigated.

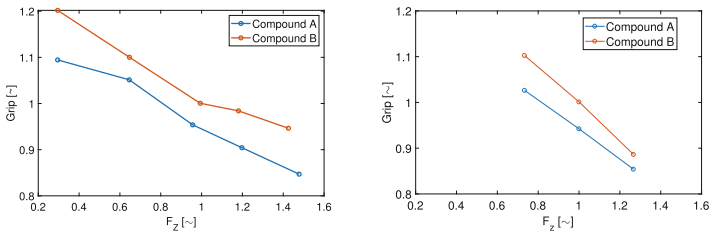


Fig. 2. Grip vs load on MTS Flat-Trac (left) and LAT100 (right)

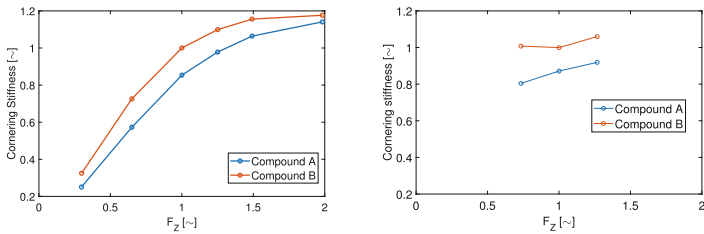


Fig. 3. Cornering Stiffness vs load on MTS Flat-Trac (left) and LAT100 (right)

Figures 4 and 5 respectively show the trend of the grip and the cornering stiffness vs. the tread temperature during the tests carried out on the MTS Flat-Trac and the LAT100 for the *CompoundB*.

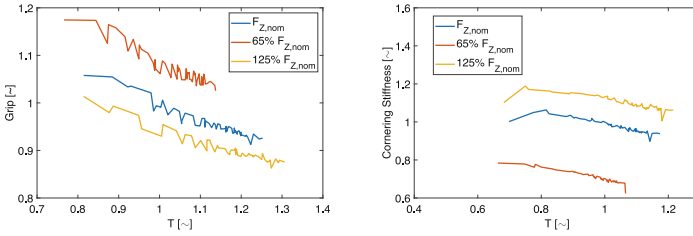


Fig. 4. Grip and Cornering Stiffness vs temperature for the *CompoundB* on MTS Flat-Trac

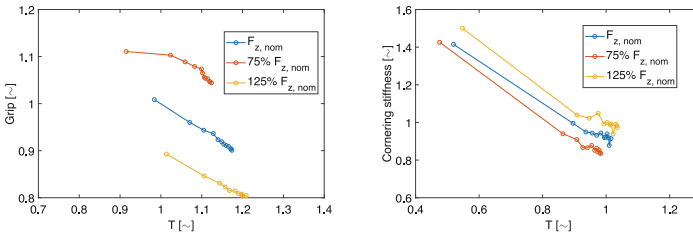


Fig. 5. Grip and Cornering Stiffness vs temperature for the *CompoundB* on LAT100

A good correlation between MTS Flat-Trac and LAT100 data can be seen for the dependency of the grip on the temperature for all the tested loads. For what concerns the cornering stiffness, unless the trend with temperature and load is captured, more remarkable differences can be noticed: the effect of the load is more evident on the MTS Flat-Trac, while the effect of temperature is higher on the LAT100, where it is possible to observe that the temperature range is bigger than the MTS Flat-Trac one, since the first acquisition is at a lower temperature with respect to the MTS Flat-Trac tests: a more severe “Run-In” has to be implemented in order to obtain a preconditioning similar to MTS Flat-Trac tests, matching the entire temperature range.

Figure 6 compares the trend of grip vs. the tread temperature for *CompoundA* and *CompoundB* during the tests carried out on the MTS Flat-Trac and the LAT100 at the nominal load. As already noticed, the trend for *CompoundB* both for grip and cornering stiffness is in good agreement between MTS Flat-Trac and LAT100 data, instead the *CompoundA* shows a less temperature dependent behavior on LAT100 than on MTS Flat-Trac.

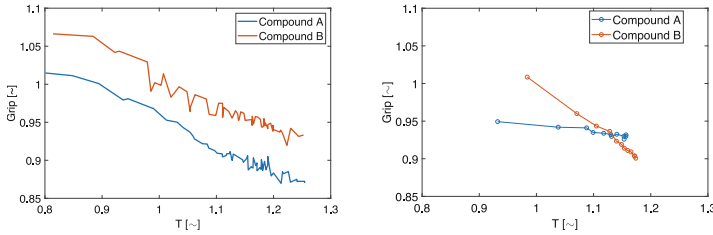


Fig. 6. Grip vs temperature comparison for MTS Flat-Trac (left) and LAT100 (right)

4 Conclusions

The objective of this work was to evaluate the effect of different compounds on tyre grip and cornering stiffness through indoor tests at the LAT100 and correlate obtained results with full tyre data collected on a Flat Track machine. The developed procedure offered the opportunity to assess the behavior of two test wheels made of different compounds (*CompoundA* and *CompoundB*) as function of the normal load and temperature, performing tests similar to the ones carried out on the real tyre on the MTS Flat-Trac. The results of the LAT100 tests align qualitatively with those obtained from the MTS Flat-Trac tests. While the overall trends of the key performance indicators (KPIs) remain consistent, there is a scaling effect due to the substantial difference between the experimental subjects (Grosch wheel and pneumatic tyre) and the two machines.

In particular, a qualitative correlation between LAT100 and MTS Flat-Trac exists for the grip against the load for both the *CompoundA* and *CompoundB*. On the other hand, the trends of the grip against the temperature only finds a correlation for the *CompoundB*. The behavior of the *CompoundA* in fact tends to remain almost constant over all the temperature range.

Regarding the cornering stiffness, instead, a qualitative correlation against load and temperature holds for both the compounds.

Although the complexity of the mechanics involved precludes an immediate quantitative correlation, a finite element simulation approach generally allows for the incorporation of structural and geometrical differences between the Grosch wheel and the tyre during validation. This enables the prediction of the tyre grip using the coefficient of friction measured in the laboratory.

References

1. Salehi, M., Noordermeer, J.W.M., Reuvekamp, L.A.E.M., Dierkes, W.K., Blum, A.: A new horizon for evaluating tire grip within a laboratory environment. *Tribol. Lett.* **68**, 1–18 (2020)
2. Salehi, M., Noordermeer, J.W.M., Reuvekamp, L.A.E.M., Dierkes, W.K., Blum, A.: Measuring rubber friction using a laboratory abrasion tester (LAT100) to predict car tire dry abs braking. *Tribol. Int.* **131**, 191–199 (2019)

Open Access This chapter is licensed under the terms of the Creative Commons Attribution 4.0 International License (<http://creativecommons.org/licenses/by/4.0/>), which permits use, sharing, adaptation, distribution and reproduction in any medium or format, as long as you give appropriate credit to the original author(s) and the source, provide a link to the Creative Commons license and indicate if changes were made.

The images or other third party material in this chapter are included in the chapter's Creative Commons license, unless indicated otherwise in a credit line to the material. If material is not included in the chapter's Creative Commons license and your intended use is not permitted by statutory regulation or exceeds the permitted use, you will need to obtain permission directly from the copyright holder.





Indoor Tyre Tread Wear Testing Driven by Outdoor Data Clustering

Lorenzo Maglia¹, Davide Fantin², Stefano Pontoglio², Matteo Stella²,
and Edoardo Sabbioni¹(✉)

¹ Politecnico di Milano, 20133 Milan, Italy
{lorenzo.maglia,edoardo.sabbioni}@polimi.it
² Pirelli Tyre S.p.A, 20126 Milan, Italy

Abstract. Wear is becoming a topic of major attention for tyres, affecting also other performances. Therefore, its estimation is of utter importance under several points of view, such as predictive maintenance and vehicle dynamics controllers. Indoor testing is emerging as an alternative way for predicting wear compared to on-road outdoor tests, which nowadays represent the standard methodology. Indoor tests, in fact, are performed in a more controllable environment, reducing testing time and costs. However, several challenges must be faced to reproduce indoor the same wear rate/shape obtained in real on-road working conditions. The present paper focuses one of the critical aspects for indoor testing: the definition of the load cycle to be applied to a tyre, i.e. the time history of forces, slip and angles to be provided as an input to the wear machine. Specifically, a clustering approach able to extract from outdoor data a limited set of manoeuvres representative of a given outdoor wear track is proposed.

Keywords: Tyre Wear · Indoor Testing · Clustering · Vehicle Dynamics

1 Introduction

Nowadays, the standard process to assess the wear performance of a tyre involves outdoor tests, during which a convoy of vehicles travels along predefined road courses. Although well consolidated, this testing methodology has several limitations: long duration, high costs and subjected to uncontrollable variables such road conditions, weather and traffic; nonetheless, it is responsible for environmental pollution. Indoor wear testing is emerging as a viable alternative to road testing, with the advantage of being performed in an environment where boundary conditions are controlled and with the possibility of rigorous monitoring of key performance indicators. In addition to that, the development of an indoor methodology can enhance the understanding of the underlying mechanisms to wear phenomena; similarly, smart systems for monitoring tyre conditions could undoubtedly benefit from data of indoor testing process. Nevertheless, to drive

indoor tests that are representative of on-road conditions, several issues must be addressed: a) definition of the machine-input time histories of forces, slip ratio, inclination angle and speed able to reproduce the wear induced by a given track and vehicle combination; b) identification of indoor testing conditions such as abrasiveness of sandpaper.

This paper focuses on the first aspect, aiming to identify the manoeuvres to be performed on the indoor testing machine in order to replicate the wear rate/shape achieved outdoor. Telemetry data acquired on outdoor sessions are processed and clustered in terms of accelerations and speed, with the aim of extrapolating from the whole time history a reduced number of significant conditions, which can be representative of the full outdoor wear session.

2 Objective and Methodology

The indoor wear machine considered for this study is a new facility by ZF (Fig. 1), composed of two testing stations and a 3m diameter drum with a width of 600 mm, actuated by an AC electric motor. The tyres, mounted on the rim, are fixed to a load carriage that features four degrees of freedom: the three rotations, and the axial translation with respect to the drum. The machine is able to provide radial and lateral forces, driving and braking torque and camber angle to the wheel. Each testing station has a powder feeding system to prevent gumming of the drum surface, typically covered in abrasive sandpaper; in addition, a laser monitors the tread wear evolution during the test.



Fig. 1. ZF indoor wear tester

The wear machine input file required to run a wear test is typically derived from telemetry data acquired during outdoor testing campaigns. The main steps in the generation of the input file to the wear machine (Drive-File), which include the time history of forces, speed, angles and slips to apply to the tyre, are:

1. **Processing of acquired outdoor data:** the data coming from outdoor sessions are processed through a properly designed routine, with the aim of removing outliers and filter unwanted disturbances.
2. **Clustering:** accelerations and speed time histories are clustered in order to extrapolate from the whole dataset a reduced number of significant manoeuvres, able to describe the chosen outdoor wear course. This is a key step when building the indoor wear machine input since it allows to rationalize and simplify a complex time history in a reduced set of manoeuvres with increased control and insight capability; same procedure could be applied for virtual track replicas via FEA simulations as well. The description of the procedure followed in this work will be addressed later on.
3. **manoeuvres simulation and Drive-File composition:** the representative manoeuvres obtained by means of clustering contain only kinematics information about the global motion of the vehicle, i.e. speed and accelerations in the CoG. These data must be simulated by means of an inverse dynamics model, in order to obtain forces, torques and inclination angles acting on each car corner. During typical outdoor wear courses, the vehicle experiences soft handling manoeuvres with accelerations up to 0.5 g, in which the behaviour of the car can be assumed as linear; this enables a validated dynamics model that accounts for some simplification to be chosen. This vehicle dynamics model has been validated by comparing its output to those obtained either via VI-Grade CarRealTime or directly to outdoor data. After the vehicle dynamics simulation phase, the significant manoeuvres are re-arranged to build a suitable Drive-File for the indoor test.

The present paper focuses on the clustering process, which is crucial in the Drive-File definition.

Indeed, the proposed procedure (Fig. 2) is not the only one when dealing with indoor tyre testing. A similar approach was described in [1], but with no specific mention to clustering. Another viable procedure consists of defining a set of standardised manoeuvres by default. These do not represent any real course, but are able to summarise the typical working conditions of a tyre. Alternatively, the indoor load history can be derived from direct measurements on the car wheels [2].



Fig. 2. Drive-File generation workflow

3 Clustering

Clustering is a crucial step in the generation of the input file for the indoor wear machine. This procedure allows to reduce the number of conditions to be replicated from the thousands of samples acquired outdoor to few significant manoeuvres, able to fully reproduce a complete wear course.

The extrapolation of such manoeuvres has to combine two different principles. In fact, the number of conditions to be replicated indoor must be sufficient to avoid the loss of significant information from the original acquisition. At the same time, it has to include the fewest manoeuvres possible, in order to keep the test simple and not over-complicated. In this work, a statistical clustering procedure has been adopted. The *k - medoids* data mining algorithm is used to achieve a reduction in the number of conditions from the thousands of samples acquired outdoor to few hundreds of manoeuvres, based on vehicle longitudinal and lateral acceleration (a_x , a_y), speed (v) and travelled distance. The resulting set of conditions can be effectively visualised in Fig. 3. It is a bubble plot in which each point represents a cluster center defined by longitudinal and lateral accelerations and speed. The size of the bubbles identifies the time spent in each condition. A cluster identified by a larger dot is highly representative of the outdoor acquisition, therefore a longer time must be spent in such manoeuvre.

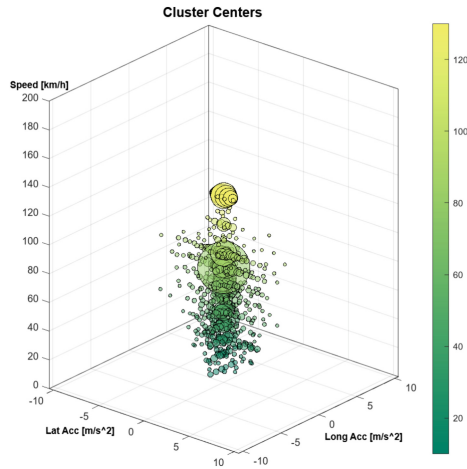


Fig. 3. Bubble plot of clustered manoeuvres. The size of each point refers to the time spent in a certain condition, i.e. the frequency of occurrence of such manoeuvre. The colors refer to the speed level.

As said, the choice of the number of cluster (i.e. manoeuvres) is not trivial. In this work, a sensitivity analysis to clusters number has been performed through FEA with a model defined on a chosen tyre specification and on a selected wear route. The aim was to find the minimum manoeuvres number providing a sufficient fidelity level to the original course. To do that, the energy dissipated on

each tyre groove in the contact patch was computed after the clustering procedure. Then, that values compared to those obtained with the full outdoor acquisition. The acceptance threshold was set to $\pm 5\%$ of relative percentage error. Figure 4 shows the trend of such error on dissipated energy for each tyre groove. As can be evinced, about 150 clusters are sufficient to achieve an error within the imposed threshold. Increasing the manoeuvres number even more, such discrepancy tends to zero, while in case of decreasing them an accuracy reduction can be assessed anyhow. Nevertheless, choosing larger sets of conditions (for instance 600) would not be beneficial since leading to over complicated indoor tests. Same considerations would apply if same approach were used for virtual track replica by means of FE analyses.

This sensitivity analysis, here only briefly reported, showed that this clustering approach is able to fulfil the previously mentioned requirements: adequate similarity to the unclustered time history of speed and accelerations by using a small number of extrapolated conditions. Extensions to multiple cases confirmed the considerations hereby reported.

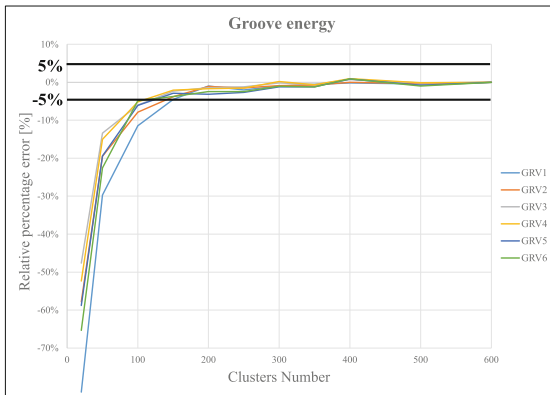


Fig. 4. Relative percentage error on dissipated energy computed with respect to the full outdoor acquisition, as function of increasing clusters number. Each line refers to a single tyre groove (GRV).

4 Results and Conclusions

In this section, results of indoor and outdoor tests are compared. The indoor test was driven by an input file obtained using the proposed clustering approach. The correlation between outdoor and indoor tests was assessed comparing the weight loss rate [mg/km], the abrasion rate [mm/1000 km] and wear shape.

Figure 5 shows the wear profile evolution (tread height vs. tread width) over travelled distance both for indoor and outdoor test (data are presented in a non-dimensional way for industrial privacy reasons). As it can be seen, the indoor tests result to be an accelerated version of the outdoor ones: a comparable wear

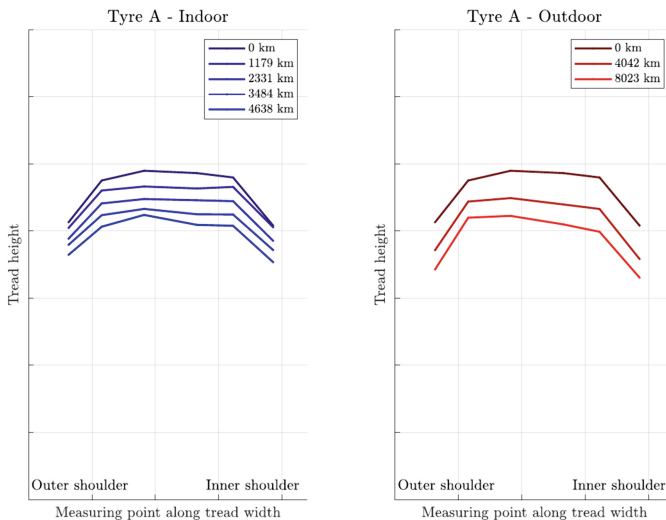


Fig. 5. Wear profile indoor vs outdoor

amount can be reached in around half travelled distance. This aspect is primarily related to the higher abrasiveness of the sandpaper used for indoor testing. Compared to road asphalt, it exhibits higher levels of micro-roughness and lower of macro-roughness. This can be considered as beneficial, since indoor tests take shorter time than outdoor ones. Coming to the wear profiles, a good agreement between indoor and outdoor can be appreciated. Main differences are concerned with a higher material loss on the inner shoulder, which is likely to be induced by the different tyre footprint on a curved surface compared to a flat road and the difference between the kinematics of vehicle suspension and the wear machine load carriage.

Concluding, the main results obtained in this work are related to the implementation of a validated clustering procedure. This is able to extract from large dataset only few significant manoeuvres, helping in saving time and resources both in FEA and experimental tests. Then, concerning the latter, the indoor procedure exhibited a larger wear rate compared to the outdoor one. As said, this was expected and can be attributed to the different abrasiveness of the two contact surfaces. Also the wear shape obtained indoor showed good similarities to that outdoor.

References

1. Knuth, E.F., Stalnaker, D.O., Turner, J.L.: Advances in indoor tire tread wear simulation. *SAE Trans.* **115**, 1390–1410 (2006). <http://www.jstor.org/stable/44667842>
2. Stalnaker, D., Turner, J., Parekh, D., Whittle, B., Norton, R.: Indoor simulation of tire wear: some case studies. *Tire Sci. Technol. TSTCA* **24**(2), 94–118 (1996). <https://doi.org/10.2346/1.2137517>

Open Access This chapter is licensed under the terms of the Creative Commons Attribution 4.0 International License (<http://creativecommons.org/licenses/by/4.0/>), which permits use, sharing, adaptation, distribution and reproduction in any medium or format, as long as you give appropriate credit to the original author(s) and the source, provide a link to the Creative Commons license and indicate if changes were made.

The images or other third party material in this chapter are included in the chapter's Creative Commons license, unless indicated otherwise in a credit line to the material. If material is not included in the chapter's Creative Commons license and your intended use is not permitted by statutory regulation or exceeds the permitted use, you will need to obtain permission directly from the copyright holder.





Trailer Reversing Supported by Steer-by-Wire

Chang Liu^{1,2}, Jakob Roempke^{1,2}, Matthijs Klomp^{2,3}, and Lars Drugge¹

¹ Royal Institute of Technology, Stockholm, Sweden

² Volvo Cars, Gothenburg, Sweden

matthijs.klomp@volvocars.com

³ Chalmers University of Technology, Gothenburg, Sweden

Abstract. Backing up a trailer can be a daunting task, even for experienced drivers. The main challenge being the unstable property of car-trailer kinematics when reversing. With steer-by-wire systems, the mechanical connection between the steering wheel and the road wheels is replaced by an electrical connection. This means that road wheels no longer have to be directly connected to the steering wheel input. The aim of this paper is to help the driver to steer the trailer directly by stabilising the car-trailer kinematics during reversal. This is achieved by developing a steer-by-wire system coupled with a closed-loop trailer reversal control using the necessary feedback. How to obtain this feedback is further investigated in this paper as well as how to use the steering wheel input and torque feedback to interact with the backup assist function. The developed control and user interaction is subjectively and objectively evaluated using computer simulation and a physical prototype of a vehicle equipped with steer-by-wire.

The results from the simulation experiments demonstrate that drivers with and without experience of driving a trailer can do the wanted manoeuvres with higher accuracy as well as within a short time span with the controller that is developed in this work. The results from the real life experiments also appears to indicate that the system can remove stress from the driver and move the trailer in an accurate way during a parking manoeuvre.

Keywords: Steer-by-Wire · Trailer · Backup Assist

1 Introduction

There are many benefits with the introduction of steer-by-wire into vehicles. There are both economic and functional reasons for this introduction, examples of economic reasons can be, fewer modifications for left- or right-hand driven vehicles, simpler axle geometry as seen in Fig. 1, and weight/space reduction. The main functional reason for steer-by-wire is the possibility of having a steering ratio that changes with speed, surface, etc. [1].

Reversing with a trailer is known to be a difficult manoeuvre and a lot of experience is needed for being able to do it in a good and accurate way. The main challenge lies in that the system is unstable during reversal. If you drive the car-trailer system in a straight line, sooner or later the trailer angle will diverge unless stabilised by the driver. It is also challenging from the drivers perspective since the trailer will initially move in the opposite direction of the drivers steering input due to offset between tow hitch and the rear axle of the vehicle [2].

The system developed in this project will be different to a traditional “non-steer-by-wire” car since it takes the input from the driver of what the desired car-trailer angle should be instead of what the wheel angle should be. While this manoeuvre could also be achieved in a traditional car without steer-by-wire, there are drawbacks, as noted in [3]. The primary challenge lies in the difficulty for the driver to translate their desired trailer movements through the steering wheel, which is mechanically linked to the wheels. Consequently, the steering wheel must constantly mirror the wheel angles, necessitating the use of alternative mechanisms, such as a knob, for the driver to specify the desired car-trailer angle i.e. the ϕ angle. This setup results in the steering wheel rotating during manoeuvres, sometimes at high speeds, causing discomfort for the driver and potentially posing safety risks.

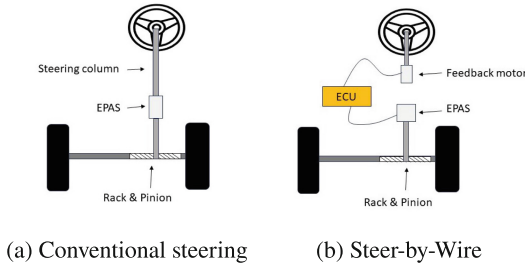


Fig. 1. The difference between conventional steering and Steer-by-Wire.

2 Car-Trailer Motion and Controller Design

2.1 Bicycle Model for the Car Based on Geometry

The way that the kinematic model of the car-trailer system will be derived for this thesis will be based on the method that is used in [4] and [6]. This model, which is based on a bicycle model of a car-trailer system, is going to be implemented in a car-trailer system so that the angle between the car and the trailer (i.e. hitch angle) can be controlled.

There are both fixed variables such as the wheelbase, length from the tow hook to the rear axle of the car as well as the length from tow hook to the axle on the trailer, and also values that will change with time such as, actual and

demanded car-trailer angle ϕ , the actual and demanded angular rate $\dot{\phi}$ as well as the speed of the car.

The angle and the angular rate of the hitch angle ϕ is defined in this thesis as seen in Eq. 1 where θ_1 and θ_2 is the car and trailer global angle respectively. This can be seen in Fig. 2:

$$\phi = \theta_2 - \theta_1, \quad \dot{\phi} = \dot{\theta}_2 - \dot{\theta}_1 \quad (1)$$

The points IC_T and IC_V are the trailer and car rotational centres, respectively. These are defined as the points around which the bodies rotate.

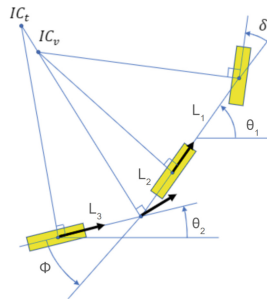


Fig. 2. An overview of the kinematic model.

Based on the bicycle model in Fig. 2 equations can be derived on how the angular rate of the hitch angle ($\dot{\phi}$) depends on the hitch angle (ϕ) and the steering angle (δ) [4], which can be seen in Eq. 2.

$$\dot{\phi} = -\frac{v}{L_3} \cdot \sin(\phi) - \frac{v}{L_1} \cdot \left(1 + \frac{L_2}{L_3} \cdot \cos(\phi)\right) \cdot \tan(\delta) \quad (2)$$

2.2 Stability Analysis of the Open-Loop System

To analyse the stability of the open-loop system Eq. 2 an eigenvalue analysis is performed.

In order to do so, a first-order Taylor expansion of Eq. 2 is made such that:

$$\dot{\phi} = -\frac{v}{L_3} \cdot \phi - \frac{v}{L_1} \cdot \left(1 + \frac{L_2}{L_3}\right) \cdot \delta \quad (3)$$

From Eq. 3 it can be seen that the car-trailer system without any backup assist, the eigenvalue of the linearised system is $-\frac{v}{L_3}$, which lies in the left-hand side of the complex plane if and only if v takes on a positive value, indicating forward driving. Conversely, we can confirm what we know from experience, namely that the system is unstable when reversing. The instability of reversing raises the need for an assist system to ensure that the eigenvalue is in the left-hand side of the complex plane.

2.3 Controller Design

In this paper, the controller by solving for the steering angle, δ , from Eq. 3 such that:

$$\delta_{target} = -\frac{L_1}{v} \cdot \frac{L_3 \cdot \dot{\phi}_{target} + v \cdot \phi}{L_2 + L_3} \tag{4}$$

with $\dot{\phi}_{target}$ being the control value.

The control value is based on the difference between the real-time ϕ and the target ϕ as a P-controller:

$$\dot{\phi}_{target} = k \cdot (\phi_{target} - \phi) \tag{5}$$

The value is fed to a P controller with the output as the $\dot{\phi}$ input to the steering angle, that is the target front wheels angle of the car. The value of ϕ is also given as an output from the system, which can be used as feedback to the driver in a way that the “zero-torque” position of the steering wheel always corresponds to the angle of ϕ . A block diagram of the controller is shown in Fig. 3.

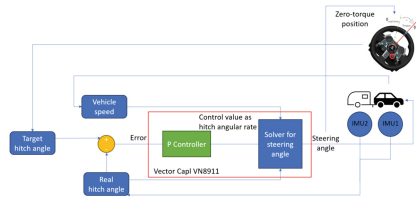


Fig. 3. The flow chart for controlling ϕ .

2.4 Stability Analysis of the Closed-Loop System

By combining Eq. 4, Eq. 5 and Eq. 3, the eigenvalue of the system is changed to $-k$. This means that, all that is required to ensure the stability of reversing is that k needs to be larger than zero so that the eigenvalue lies in the left-hand side of the complex plane.

3 Length Estimation of Trailer

For the model that is developed in this project to work, there is a need to know the length of the trailer to its wheel axle. The length of the trailer is not always known and it can also be difficult to accurately measure the length. This could be a cumbersome process if it must be done by the driver. Therefore it would be beneficial if the trailer length could be determined automatically. This could be done using an error prediction method, using a parameter value that minimises

the quadratic sum of the prediction errors [3]. However, to make the system compact and more efficient, another simple yet effective way of determining the length of the trailer is created and utilised. This is by using Eq. 2 to derive the length of the trailer L_3 . The equation for L_3 can be seen in Eq. 6.

$$L_3 = -\frac{v \cdot (\sin(\phi) \cdot L_1 + L_2 \cdot \cos(\phi) \cdot \tan(\delta))}{\dot{\phi} \cdot L_1 + v \cdot \tan(\delta)} \quad (6)$$

This equation will give the length of the trailer whenever all of the variables in the equation are steady-state. The car-hitch angle as well as its angular rate, steering angle, and car speed will be recorded during a short period when reaching steady-state and the distance between the trailer axle and the tow hook can be calculated using Eq. 6. The easiest way to get stable inputs is to start the length estimation while going forward in a turn with a fixed steering angle. This means that $\dot{\phi}$ will move towards zero and the speed and ϕ will move towards steady values respectively. This will make the equation easier to solve as well as make the result more stable. If the trailer gets replaced by a different one, the system will work again to estimate the new geometry. In theory, the estimation also works during reversing if the trailer back-up assist system is not active. After the automatic length estimation, the result will be sent to the controller as input of trailer length. The driver can also choose to manually input the length.

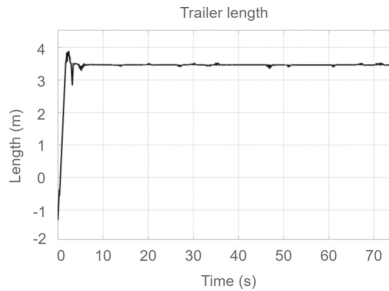


Fig. 4. Simulation results of the length estimation of a 3.5 m long trailer.

As can be seen from Fig. 4, the trailer length estimation gives reasonable values after about 5 s. This delay is due to the road being straight in the beginning and leads to that there is no steering angle to start with.

4 Determining the Car-Trailer Angle

In the trailer backup assist system, estimating the hitch angle is a key for controlling the required steering during trailer reversing. This angle can be determined direct measurement or by using yaw-rate sensors, as was done in this project. This works by having one yaw-rate sensor on the car and the other on the trailer.

The hitch angle is then determined by integrating the difference between the car and trailer yaw angular rate ($\dot{\theta}_1$ and $\dot{\theta}_2$) over time.

One challenge with this way of determining the trailer-car angle is that there is no way for the car and trailer to know their global angle relationship at the start of integration, therefore a calibration of what is zero degree of the hitch angle must be done. This is done by resetting the integration to zero when the yaw rate of both car and trailer has been close to zero for some time during forward driving.

Another challenge with this setup is that it is very common to have integration drift due to sensor bias. There are several more or less complicated ways to reduce the influence of the IMU drift. In this paper sensor bias is observed over time and when the car is stand still, the observed bias is removed from the yaw rate and thereby reduce the influence of the integration drift.

5 How to Avoid Jack-Knifing

Jack-knifing is when the car-trailer angle can no longer be reduced but increases until there is contact between the car and trailer. This so-called critical angle is reached the moment the car and the trailer share the same yaw rate and the front wheels are steered to its maximum value [3] [5]. To find the critical hitch angle, calculations can be done to find when the car and trailer share the same instant centre of rotation when the maximum geometrical angle on the front wheels is reached.

An estimate of the critical angle $\dot{\phi}_{crit}$ can be found from Eq. 3 when $\dot{\phi} = 0$ and $\delta = \delta_{max}$ such that

$$\dot{\phi}_{crit} = -\frac{L_3}{L_1} \cdot \left(1 + \frac{L_2}{L_3}\right) \cdot \tan(\delta_{max}); \quad (7)$$

This means that to prevent jack-knifing from occurring, ϕ should not be allowed to pass the critical angle. The width of the car and trailer is not considered in this calculation which might lead to that the critical angle might not be reached before the car and trailer hit each other if the car or the trailer is very wide.

6 Experiments

6.1 Experimental Setup

For the driving simulator studies conducted in this research, IPG CarMaker was used. Two experiments were conducted to discover if the trailer back-up assist is improving the drivers' performance to reverse with a trailer. For the straight reverse experiment, the trace of the car was recorded and compared with a reference lane that it should follow. Mean squared errors of the comparison were computed to determine the accuracy of the car-trailer system motion with or without the back-up system. Time for movement was also recorded for each of

them. For the parking experiment, similarly, a reference lane was given for the driver to follow, with and without the back-up assist system. In this case the time it took to complete the manoeuvre is shown for comparisons and not mean squared errors since was found to be difficult to compare the actual trace with the reference in a good way.

For the real-world tests using a test vehicle with a trailer, steering wheel data were recorded and are plotted to show the difference between manual and assisted manoeuvres.

6.2 Experiment Results Driving Simulator

The first experiment was conducting using a Volvo XC90 demo model with user-defined steering system based on steer-by-wire with the trailer back-up assist. The experiment was made up by two parts: the straight-line reverse test and the parking into a designated parking lot on the simulated parking space test. For the straight-line reverse, the test drivers drove the trailer-car system to reverse for 80 m on a straight road, with and without the assist system. Driving traces of the car, for three test drivers, are shown in Fig. 5 to make comparisons between driving with and without the assist system.

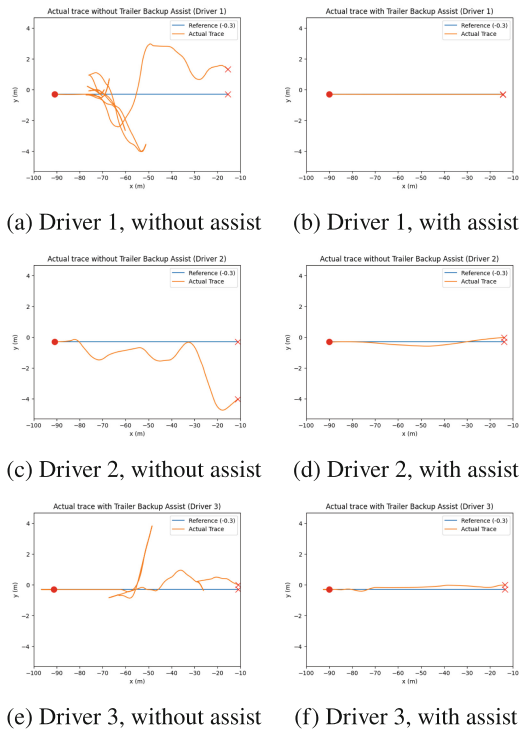


Fig. 5. Results from the straight line experiment.

In Fig. 5, the blue line is the reference straight line to follow for the test driver, which starts from the left side of a figure. The red lines are the traces of the cars driven by test drivers, with a sampling rate of 2 Hz. It is clear that the drivers can follow the reference lane more accurately with the help of the assist system. Without the assist system, some drivers have to undergo several trials and errors to correct the direction of the trailer. To quantitatively show the differences of lane-following accuracy, a mean squared error based on the deviation between the trace and the reference lane is defined and computed. Results are shown in Table 1.

Table 1. Mean squared errors (MSE) of three test drivers

	Non-assisted	Assisted
Driver 1	3.005 m ²	0.0 m ²
Driver 2	3.149 m ²	0.042 m ²
Driver 3	1.308 m ²	0.037 m ²

A smaller MSE value stands for a higher accuracy in following the reference lane. Without the back-up assist system, none of the drivers can easily control the car-trailer system even though driver 2 is experienced in reversing a trailer in the real world. Comparatively, with the assist system, all the drivers can follow the reference lane effortlessly.

In Table 2, time-to-reach for each driver has been recorded as well and the difference in time between being assisted and not is not as large as the difference in MSE.

Table 2. Time for passing the distance of three test drivers

	Non-assisted	Assisted
Driver 1	187 s	31 s
Driver 2	62 s	71 s
Driver 3	169 s	109 s

In the second experiment, the reference lane is no longer a straight road, but a path to park the trailer into a parking lot. Here, time-to-reach is the main output for evaluation shown in Table 3 and the three test drivers are put into a parking scenario. Their driving traces with and without the assist are recorded and shown in Fig. 6.

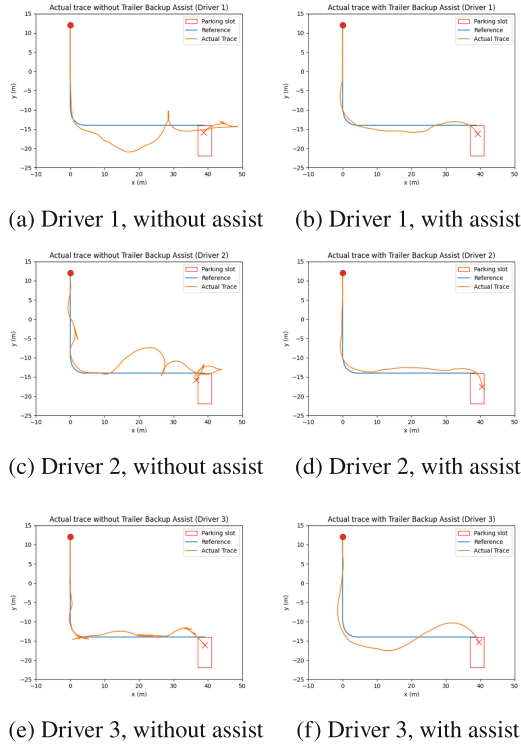


Fig. 6. Results from the parking experiment.

Table 3. Time for parking the trailer in the parking slot of 3 test drivers.

	Non-assisted	Assisted
Driver 1	192 s	43 s
Driver 2	131 s	41 s
Driver 3	170 s	46 s

It can be seen in Fig. 6 that driving without the assist normally requires more correction movement and less possibility in keeping to the reference lane due to greater challenge in hitch angle control compared with having the assist. With these disadvantages, time-to-reach shows a great difference between assisted and non-assisted driving. For driver 1 and 3 who do not have much trailer parking experience, time-to-reach has been significantly reduced by 4 to 5 times. For driver 2 who is experienced, it has also been reduced by 3 times.

6.3 Experiment Results Real World

Due to lack of time the system that is implemented into a Volvo V60 was not tested by any test persons other than the developers of the system. The main experiment that was conducted in the car is to study the steering wheel angle, ϕ and the velocity of the car through a parking manoeuvre. The data can be seen in Fig. 7.

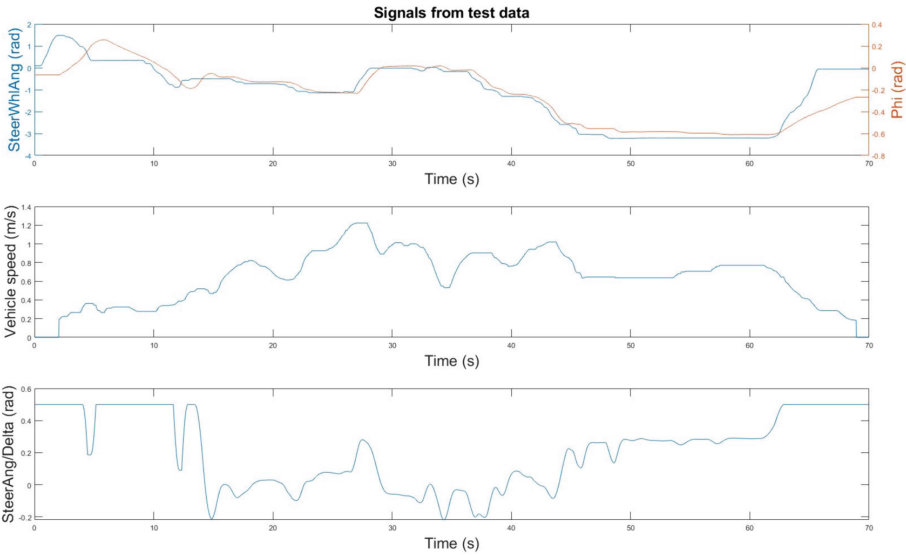


Fig. 7. Data gathered from the car in the experiment. The first graph show steering wheel angle in blue and ϕ in orange. The second graph shows how the speed is changing under time and the last graph show how δ changes with time.

As shown in Fig. 7, the steering wheel angle input by the driver, the hitch angle ϕ , the steering angle δ , as well as vehicle speed from a 70-second trailer parking manoeuvre with regard to time were all recorded. The manoeuvre starts from stand-still and ends when the trailer reaches the target spot. To analyse the delay between the driver input and the hitch angle ϕ , the steering wheel angle and the hitch angle ϕ are overlaid.

The system is speed-sensitive since the steering angle δ was frozen below speeds of 0.1 m/s to reduce the stress on the steering rack at standstill. Also an amplitude limiter 0.5rad for the steering angle δ was implemented. When the vehicle starts from stand-still, the steering angle δ was kept at 0 until the speed of the system reaches the safety limit. During this process, delay was accumulated since the system does not output required steering angle. After several seconds, the controller finishes compensating for the error and the delay is controlled under one second during the parking process. The delay also occurs

during braking. Vehicle speed v controlled by the driver does not influence the delay unless it is smaller than the safety limit of 0.1 m/s. The last graph in Fig. 7 shows how the steering angle δ is changing to fulfil the driver's request. A large difference can be seen between the steering wheel input in the first graph and the actual steering angle in the last graph. The steering wheel angle is changing slowly and predictable while the steering angle is more erratic. This difference is showing how much strain that has been taken off from the driver during a parking manoeuvre.

7 Discussion and Conclusion

The overall stability of the trailer back-up assist that is developed in this thesis can be considered as stable and does not seem to be restricted due to the linearisation of the equations used in the controller.

The main issue with reversing and controlling the motion of the trailer without the trailer back-up assist system that was noticed in the simulation experiments is that the driver must control the car direction in order to adjust the trailer direction in a nonlinear fashion. When the car-trailer system is moving, it is hard to predict how the trailer will react to the steering wheel input, and corrections must be made constantly. The delay in the change of trailer direction is also large. That explains for the large curves and less accuracy in the traces of the simulator experiments without the assist. When the driver becomes anxious due to lack of control over the trailer direction, the driver tends to overreact and give large inputs on the steering wheel, leading to more errors.

However, with the trailer back-up assist, the intensity of the above issues were reduced. The hitch angle follows the steering wheel input directly and ease the burden from drivers so that they had enough time to avoid obstacles and move the trailer in a stable manner. Also, since the car could react to very small changes of the angle in the car-trailer system, the driver could react before any large deviations occur in the wanted car-trailer angle and hence the stability of the system was vastly increased compared to the non-assisted system.

It can be seen from the experiments in the driving simulator that both the time to finish the manoeuvres as well as the accuracy of the manoeuvres was greatly improved using the system that is developed in this work, both for experienced and non-experienced trailer drivers. The real life experiments shows that there was a large difference between the requested car-trailer angle (i.e. steering wheel angle) and the actual steering angle. This difference shows how much strain that was taken from the driver since the driver could focus on the path of the trailer instead of focusing on controlling the steering angle on the car and through that the path of the trailer. Hence, the experiments show that the trailer back-up assist can be a great help to drivers with different levels of driving skills.

One thing that is not considered in this work is the motion of the vehicle and therefore the risk of hitting obstacles with the vehicle. This means that since that the driver is mostly checking the motion of the trailer it might be so that the driver forgets to check the motion of the car and may drive into an obstacle

with the car. However, this is something that can easily be avoided by using the proximity/camera sensors that are available on the car to alert the driver if the car get close to any obstacle. Another way to tackle this issue is by switching between the trailer backup assist mode and a normal driving mode.

References

1. Mortazavizadeh, S.A., Ghaderi, A., Ebrahimi, M., Hajian, M.: Recent developments in the vehicle steer-by-wire system. *IEEE Trans. Transp. Electrification*. **6**(3), 1226–1235 (2020)
2. Belco Trailers. How to reverse a trailer (2022). <https://belcocustomtrailers.com.au/trailer-tips/how-to-reverse-a-trailer/>. Accessed Mar 2024
3. Enqvist, O.: AFS-assisted trailer reversing. Master thesis, Linköping universitet (2006)
4. Abraham, S., Nilsson, J.: Trailer parking assist (TPA). Master thesis, Chalmers University of Technology (2013)
5. Zhao, J.: A review of wearable IMU (inertial-measurement-unit)-based pose estimation and drift reduction technologies. *J. Phys. Conf. Ser.* **1087**(4), 042003 (2018)
6. Elhassan, A.: Autonomous driving system for reversing an articulated vehicle. Master thesis, KTH (2015)

Open Access This chapter is licensed under the terms of the Creative Commons Attribution 4.0 International License (<http://creativecommons.org/licenses/by/4.0/>), which permits use, sharing, adaptation, distribution and reproduction in any medium or format, as long as you give appropriate credit to the original author(s) and the source, provide a link to the Creative Commons license and indicate if changes were made.

The images or other third party material in this chapter are included in the chapter's Creative Commons license, unless indicated otherwise in a credit line to the material. If material is not included in the chapter's Creative Commons license and your intended use is not permitted by statutory regulation or exceeds the permitted use, you will need to obtain permission directly from the copyright holder.





A Yaw Rate Based Stability Control Tuning via Virtual Methods

Luca D'Avico¹(✉), Fabio Carbone¹, Lucas Baudry¹, Fabrizio Forni¹,
Pietro Caresia¹, and Gerardo Amato²

¹ Brembo N.V., Via Stezzano, 87, 24126 Stezzano, BG, Italy
{luca.davico, fabio.carbone, lucas.baudry, fabrizio.forni,
pietro.caresia}@brembo.com

² Teoresi S.p.A., Via Perugia, 24, 10152 Torino, TO, Italy
gerardo.amato@teoresigroup.com

Abstract. Electronic Stability Control (ESC) allows to prevent safety-critical scenarios and vehicle sideslip angle estimation plays a crucial role in such applications. Time to market and safety concerns in the development and validation of such algorithms are leading the automotive industry towards virtual methods. The recent introduction of driving simulator technologies on vehicle development process allows to develop calibrate and test in advance virtual prototypes of full vehicle and its controls obtaining objective and subjective evaluation during the early stage of the vehicle development. This paper presents the methodology and results related to the development and calibration of a yaw rate based stability control grounded on a mixed-kinematic sideslip estimator. This work has been carried out leveraging tools provided by simulation platforms, scalable configurations of driving simulators and results from road tests.

Keywords: Stability Control · Sideslip Angle · Virtual Methods · Simulation Platforms · Vehicle Control · Vehicle State Observer

1 Introduction

Electronic Stability Control (ESC) has been introduced to prevent cars from losing driveability [1–4] and vehicle (or body) sideslip angle is of paramount importance in such algorithm [5–7]. In this paper the estimation performances of sideslip estimators are outlined at first [8–10]. A yaw rate based stability control is then presented and the results outlined. Virtual methods provide powerful tools to speed up the development process following the V-model approach [11, 12]; in this work such methodology has been applied for the evaluation of both estimation and control achievements. This paper outlines at first an overview of the system, development environments and use cases considered

for this activity. Then the adopted estimation, control strategies and dedicated KPIs are introduced for evaluation of the performances. A comparison between results on different development environments is illustrated. Finally, the conclusions portrays the main outcomes and summary of the achieved results.

2 System Overview, Virtual Environments and Use Cases

This work has been accomplished following the V-model approach by leveraging the information from several development environments with decreasing virtualization levels (Fig. 1). Simulation activities have been performed in a completely virtual Model-In-the-Loop (MIL) environment while Driver-Hardware-In-the-Loop (DHIL) tests on a COMPACT Simulator by VI-grade [13]. The virtual environment development results of this activity have been achieved based on a vehicle model provided by VI-grade CarRealTime software [14]. Vehicle activities have been carried out on a AWD fully electric vehicle equipped with Brembo braking system [15–17] portrayed in Fig. 1. The designated use case for this activity is the Lane Change maneuver following test protocol as in ISO 3888-1 [18].

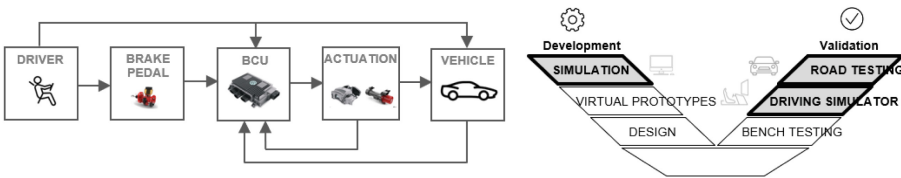


Fig. 1. (Left) Brembo braking system. (Right) V-model diagram.

3 Vehicle (or Body) Sideslip Angle Estimation

Vehicle (or body) sideslip angle is of great importance in the development of stability control algorithms. In this work, the following body sideslip angle (β) estimators have been adopted and compared: BSAE presented in [8, 9] and BSAA outlined in [10] and results are illustrated in Fig. 2. Main idea is to confront such methods in order to assess the best appropriate solution for the control purposes and to determine whether consistent results can be achieved in environments with different level of virtualization. To evaluate the estimation performances, the EAM (Error At Maximum) indicator delineated in (1) has been adopted: it focuses on the relative error between the estimated sideslip angle at the time instant \bar{t} when the ground-truth (GT) signal is at its maximum value; ground-truth signal is provided by VI-grade CarRealTime software on MIL and DHIL environments, Kistler Correvit S-Motion optical sensor on vehicle. Although this is not a complete evaluation of the estimation behaviour and features of the algorithms, it provides a concise assessment of the estimation outcomes during

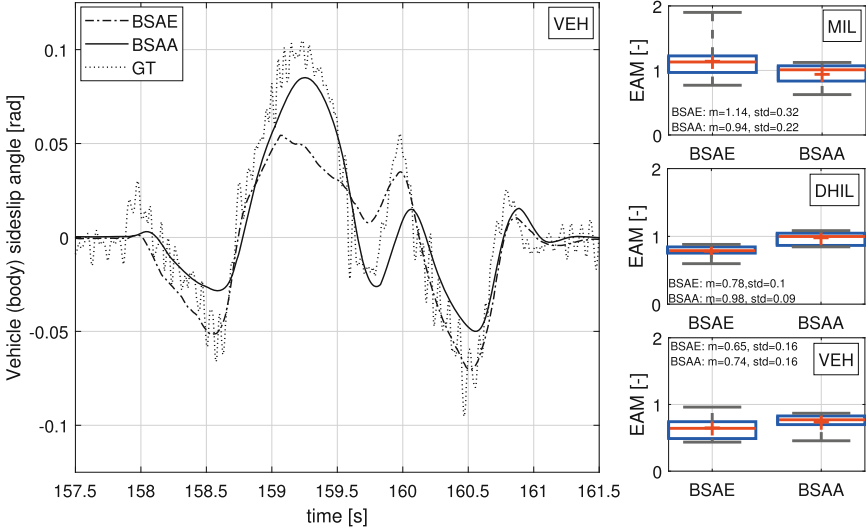


Fig. 2. (Left) Example of a vehicle test during a Lane Change maneuver (ISO 3888-1). (Right) KPI to assess body slip angle estimation performances (VEH = vehicle, GT = Ground-Truth, m = mean, std = standard deviation).

several repetitions of lane-change maneuvers where the maximum sideslip angle (β) is a major concern. The closer the EAM is to the unit value 1, the better the estimation performances. Based on this criteria, BSAA outperforms BSAE in terms of both mean value and standard deviation in all environments; thus, it is the most suitable solution for the purposes of stability control. Furthermore, this analysis shows coherent results among different development environments demonstrating the effectiveness of using a virtualization approach to anticipate road testing activities.

$$EAM[-] = \frac{BSAx(\bar{t})}{GT(\bar{t})}, x = \{E, A\} \quad (1)$$

4 Yaw Rate Based Stability Control

The stability control adopted for this activity is portrayed in Fig. 3 where both the wheel slip controller and the yaw rate controller are based on a PID algorithm enhanced with additional non linear contributions. The methodologies behind these logics are similar to the ones described in [19,20] and [21,22] respectively. The reference generator is developed starting from the definition of maximum admissible yaw rate as in [23]. The vehicle state observer (VSO) provides the information required by the stability control but not included among the available measurements; the estimators of the sideslip angle (β) presented in the previous section are included in this block. The stability control exploits the

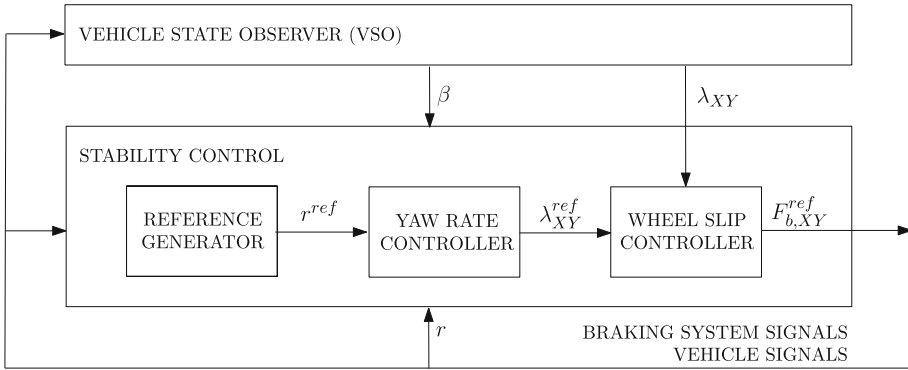


Fig. 3. Yaw rate based stability control scheme where β = body sideslip angle, ref = reference, r = yawrate, λ = wheel slip, F_b = brake force, $X = \{\text{Front,Rear}\}$, $Y = \{\text{Left,Right}\}$

benefits of the independent wheels braking system generating a reference brake force for each corner ($F_{b,XY}^{ref}$) in order to enhance performance and safety.

The tuning of the yaw rate controller is the main goal of this work. For this purpose, four different set of parameters have been defined based on an increasing degree of control intervention: standard control intervention (SD), less invasive control intervention (LC), more invasive control intervention (MC) and stability control deactivated (OFF). In order to take into account environments with the variability of the driver’s inputs only, driving simulator (DHIL) environment and vehicle testing have been considered. To carry out this analysis, the following objective criteria have been applied: (1) vehicle (body) sideslip angle peak defined as the maximum absolute value of the measured angle during the maneuver; this criteria focuses on the vehicle lateral stability; (2) yaw rate peak defined as the maximum absolute value of the yaw rate during the maneuver; this criteria highlights the vehicle steerability; (3) speed loss ratio defined as the ratio between the minimum speed within the maneuver and the speed at the beginning of maneuver, this criteria aims to measure the level of the brake intervention. Since vehicle activities have been carried out on a mixed dry and wet/dry condition, DHIL maneuvers have been performed using 2 grip levels (1, 0.8) to take into account the tire-road grip (μ) variability during road testing. As outlined in Fig. 4, results follow the expected behaviour: increasing the degree of control leads to decrease both body sideslip angle and yaw rate peaks, while speed loss ratio tends to increase. In terms of comparison between development environments, the results show a consistent trend between driving simulator (DHIL) and the vehicle.

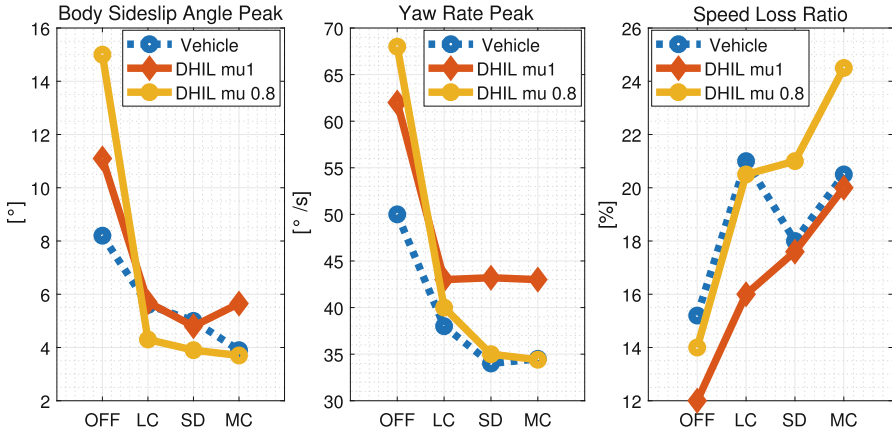


Fig. 4. Stability control results: comparison between vehicle data and DHIL tests (μ refers to the tire-road grip) during Lane Change maneuvers (ISO 3888-1).

5 Conclusions

In this work the tuning and validation of a yaw rate based stability control has been described. The strategy have been carried out based on virtual methods following the V-model approach which has been used to assess the most suitable estimation algorithm and parameter sets to be tested on vehicle. Despite a significant effort is required to implement realistic virtual environments and define representative KPIs to evaluate the outcomes, the results have shown that virtual methods provide useful information in order to support and speed up the development of vehicle estimation and control strategies prior to any vehicle activity leading to significant time and cost reduction.

Acknowledgements. We would like to thank Matteo Corno, Alberto Dubbini and Stefano Carnier from Dipartimento di Elettronica e Informazione, Politecnico di Milano, Piazza L.da Vinci, 32, 20133 Milano, Italy that have provided the sideslip angle estimation algorithms adopted in this work.

References

1. Rajamani, R.: Vehicle Dynamics and Control (2006)
2. Liebemann, E., Meder, K., Schuh, J., Nenninger, G.: Safety and performance enhancement: the Bosch electronic stability control (ESP) (2004)
3. Gimondi, A., Corno, M., Savaresi, S.: A yaw rate based stability control for under-actuated vehicles, pp. 1–6 (2020)
4. Mazzilli, V., et al.: Integrated chassis control: classification, analysis and future trends. *Annu. Rev. Control.* **51**, 172–205 (2021)
5. Erke, A.: Effects of electronic stability control (ESC) on accidents: a review of empirical evidence. *Accid. Anal. Prev.* **40**, 167–73 (2008)

6. Dang, J.: Statistical Analysis of the Effectiveness of Electronic Stability Control (ESC) Systems - Final Report. OT HS 810 794 July 2007 NHTSA Technical Report DC: US Department of Transportation (2007)
7. Piyabongkarn, N., Rajamani, R., Grogg, J., Lew, J.: Development and experimental evaluation of a slip angle estimator for vehicle stability control. *IEEE Trans. Control Syst. Technol.* **17**, 78–88 (2009)
8. Selmanaj, D., Corno, M., Panzani, G., Savaresi, S.: Vehicle sideslip estimation: a kinematic based approach. *Control Eng. Pract.* **67**, 1–12 (2017)
9. Galluppi, O., Corno, M., Savaresi, S.M.: Mixed-kinematic body sideslip angle estimator for high performance cars. In: 2018 European Control Conference (ECC), pp. 941–946 (2018)
10. Carnier, S., Corno, M., Savaresi, S.M.: Hybrid kinematic-dynamic sideslip and friction estimation. *J. Dyn. Syst. Meas. Control* **145**(5), 051004 (2023)
11. Forsberg, K., Mooz, H.: The relationship of system engineering to the project cycle. *Eng. Manag. J.* **4**, 36–43 (2015)
12. ASPICE guide. <https://knuevenermackert.com/wp-content/uploads/2021/03/ASPICE-Guide-KM2021-01.pdf>. Accessed 08 May 2024
13. VI-grade. Compact simulator. <https://www.vi-grade.com/en/products>
14. VI-grade. Carrealtime. <https://www.vi-grade.com/en/products/vi-carrealtime/>
15. Forni, F.: Method for controlling a braking system of a vehicle and system thereof (2022). US Patent, 20220017049
16. Forni, F.: Method for controlling the wheel slip in a braking system with b-b-w technology of a vehicle and system thereof (2023). US Patent, 20230303043
17. Galizzi, V.: A method for controlling the deceleration of a vehicle and a braking system (2024). US Patent, 20240042978
18. ISO 3888-1:2018 Standard. Passenger Cars-Test Track for a Severe Lane-Change Manoeuvre-Part 1: Double Lane-Change. <https://www.iso.org/standard/67973.html>. Accessed 08 May 2024
19. Johansen, T.A., Petersen, I., Kalkkuhl, J., Ludemann, J.: Gain-scheduled wheel slip control in automotive brake systems. *IEEE Trans. Control Syst. Technol.* **11**(6), 799–811 (2003)
20. Pretagostini, F., Ferranti, L., Berardo, G., Ivanov, V., Shyrokau, B.: Survey on wheel slip control design strategies, evaluation and application to antilock braking systems. *IEEE Access* **8**, 10951–10970 (2020)
21. Amato, G., Marino, R.: Adaptive slip vectoring for speed and yaw-rate control in electric vehicles with four in-wheel motors. *Control. Eng. Pract.* **135**, 105511 (2023)
22. Canale, M., Fagiano, L.: Stability control of 4WS vehicles using robust IMC techniques. *Veh. Syst. Dyn.* **46**, 1011–991 (2008)
23. Kiencke, U., Nielsen, L.: Automotive control systems: for engine, driveline, and vehicle. *Meas. Sci. Technol.* **11**, 1828 (2000)

Open Access This chapter is licensed under the terms of the Creative Commons Attribution 4.0 International License (<http://creativecommons.org/licenses/by/4.0/>), which permits use, sharing, adaptation, distribution and reproduction in any medium or format, as long as you give appropriate credit to the original author(s) and the source, provide a link to the Creative Commons license and indicate if changes were made.

The images or other third party material in this chapter are included in the chapter's Creative Commons license, unless indicated otherwise in a credit line to the material. If material is not included in the chapter's Creative Commons license and your intended use is not permitted by statutory regulation or exceeds the permitted use, you will need to obtain permission directly from the copyright holder.





Optimal Braking and Steering Control Under Split Friction on Curved Roads

Ektor Karyotakis^{1,2}(✉) , Derong Yang¹, Mats Jonasson³ ,
and Jonas Sjöberg² 

¹ Vehicle Energy and Motion Control, Volvo Car Corporation,
405 31 Gothenburg, Sweden

ektor.karyotakis@volvocars.com

² Department of Electrical Engineering, Chalmers University of Technology,
412 96 Gothenburg, Sweden

³ Department of Maritime and Mechanical Engineering,
Chalmers University of Technology, 412 96 Gothenburg, Sweden

Abstract. This paper aims to maximize deceleration on split friction roads by combining steering and individual wheel braking. For this, a previously tested optimization problem is adapted to curved roads. The optimal brake force and steering allocation is investigated as a function of the split friction asymmetry. Results show that low friction is more detrimental to maximum braking on the inner side of the curve due to load transfer. Finally, the paper showcases a control strategy for braking on split friction, which enhances safety and manoeuvrability in critical split friction scenarios.

Keywords: split · friction · optimization · cornering · curve · braking

1 Introduction

Split friction is an edge case of a slippery road where one side of the vehicle is on the regular road surface while the other is on a low-friction surface, like snow or fallen leaves. The road condition asymmetry creates an asymmetry in the brake forces, which in turn creates a yaw moment disturbance. The disturbance must be countered, typically by the driver, but can be abrupt and surprise the driver [8]. Making it autonomous would be beneficial to reduce accidents.

Contributions in literature have primarily focused on designing a controller for steering, assuming the ABS handles the brake control, as in [2, 10]. However, our research shows that using ABS on all wheels can be dangerous when there is a significant friction difference between the two vehicle sides. More advanced control solutions focus on designing the steering compensation and the brake control together [5, 9]. However, none of these have investigated the effects of friction on vehicle dynamics and maximum braking.

When braking under split friction, the maximum deceleration potential without deviating from the lane depends on the friction asymmetry [3]. In [7], the authors investigate the maximum deceleration potential on curved roads for

several steering/braking configurations and varying road friction coefficients. They showed a significant maximum deceleration potential reduction when the brake forces are constrained not to produce any yaw moment. Balancing the yaw moment on split friction braking is critical, but restricting the brakes implies longer stopping distances.

This paper analyses the maximum deceleration potential under split friction as a function of lateral acceleration and friction asymmetry. The resulting allocation of brake forces and steering can be used to design control algorithms better suited to varying friction. Inspired by this analysis, a control implementation is tested in simulation to show the potential.

2 Maximum Static Deceleration on Curved Roads

With the focus on maximising braking in a curve, an optimization problem (OP) is built upon a double-track vehicle model with combined slip and longitudinal and lateral load transfer; for details, see [1,3]. The focus of the OP on a high level is illustrated in Fig. 1.

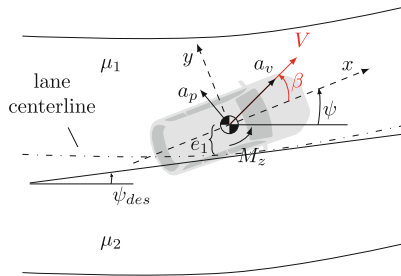


Fig. 1. Vehicle trajectory and orientation

The velocity vector is denoted with V , and its orientation, the side slip angle, with β . The vehicle's orientation is defined by the yaw angle ψ . In the static case of no dynamics, the acceleration along V , a_v , should be minimized. In contrast, the acceleration perpendicular to V , a_p , keeps the vehicle in the curve to a desired lateral acceleration $a_{p,des}$. Further, for a constant radius, yaw acceleration $\ddot{\psi}$ is unwanted; thus, the yaw torque $M_z = I_{zz}\ddot{\psi}$ should be zero. At the same time, the yaw rate $\dot{\psi}$ is chosen as a desired one.

For the desired lateral acceleration and yaw rate, the circular motion ones can be used, defined as

$$a_{p,des} = \frac{v_x^2}{R} \quad (1)$$

$$\dot{\psi}_{des} = \frac{v_x}{R} \quad (2)$$

where R is the road radius, and v_x the longitudinal speed. More advanced definitions can be obtained from [6].

The maximum static deceleration optimization problem is expressed as

$$\begin{aligned}
 \min_q \quad & a_v(q) \\
 \text{s.t.} \quad & a_p(q) = a_{p,des} \\
 & M_z(q) = 0 \\
 & \dot{\psi} = \dot{\psi}_{des} \\
 & F_{xi} = \frac{\sigma_{xi}(q)}{\sigma_i(q)} F_i(q) \\
 & F_{yi} = \frac{\sigma_{yi}(q)}{\sigma_i(q)} F_i(q) \\
 & \sqrt{F_{xi}^2 + F_{yi}^2} \leq k_F F_{\max,i}
 \end{aligned} \tag{3}$$

with $q = [\kappa_i, \delta, \beta]^\top$ the optimization variables, κ_i the longitudinal slip ratio, δ the steering angle. The control inputs are $u = [\kappa_i, \delta]^\top$, while $[\beta, \psi]$ are states. Equality constraints are needed for the forces $[F_{xi}, F_{yi}]$ to include the load transfer. Further, an inequality constraint is added for the friction circle, multiplied by a factor $0.95 < k_F < 1$ to avoid numerical instabilities at the friction peak and excessive slips.

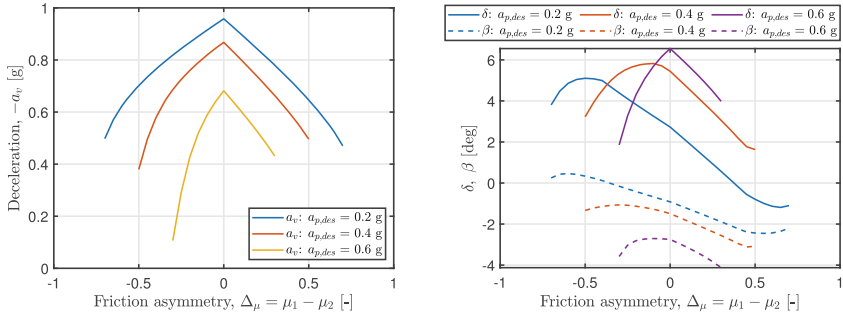
The solution to the OP (3) is static, without dynamics. In reality, as speed reduces, $a_{p,des}$ also reduces, and the vehicle brakes harder, giving a larger magnitude of a_v every instant. Instead, the solution can be seen as an upper limit to what deceleration can be achieved with the current speed and radius. For a straight road, the solution converges to a steady state instead as R becomes large and $1/R \rightarrow 0$ in (2). Next, the analysis of the OP is presented as a function of the friction difference between the vehicle sides.

3 Split Friction Effects

The *friction asymmetry* between the left (inner side for a left turn) μ_1 and right (outer) μ_2 vehicle side is defined as

$$\Delta_\mu = \mu_1 - \mu_2 \tag{4}$$

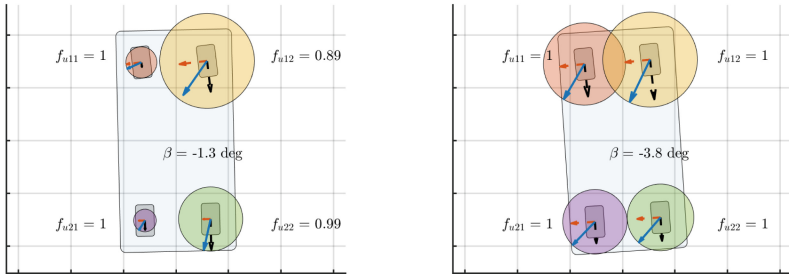
Several outputs from the OP (3) are depicted in Fig. 2 for several Δ_μ values. For positive Δ_μ , the outer curve side μ_2 varies, while the inner $\mu_1 = 1$, and vice versa for negative Δ_μ . The maximum deceleration potential is depicted in Fig. 2a. The curves are asymmetric. Less deceleration can be achieved when the inner side has lower friction ($\Delta_\mu < 0$) than when the outer side is on low friction ($\Delta_\mu > 0$). The main mechanism behind this is the lateral load transfer. The more lateral acceleration, the more pronounced the asymmetry becomes. The steering input and side slip angle are depicted in Fig. 2b. Some counter-steering is observed at large Δ_μ for the blue curve at low lateral acceleration. As lateral acceleration increases, the magnitude of steering inputs and side slip angles increase.



(a) Vehicle deceleration vs friction asymmetry (b) Vehicle steering and side slip angles vs friction asymmetry

Fig. 2. Vehicle deceleration, steering angle and side slip angle for several lateral acceleration values as a function of friction asymmetry

The optimal brake force and seeing allocations are depicted in Fig. 3 for two cases when the friction is low on the inner or outer curve side, respectively. The effect of load transfer is more important when the inner side has low friction, as the inner side friction circles are smaller, see Fig. 3a. Due to this mechanism, the side slip angle is also smaller, and the outer front circle moves away from the friction circle.



(a) Vehicle sketch for $\mu_1 = 0.6, \mu_2 = 1$ (b) Vehicle sketch for $\mu_1 = 1, \mu_2 = 0.6$

Fig. 3. Brake force/steering allocation for $a_{p,des} = 0.4$ g; The friction circles are scaled with the load; f_{ui} denotes how much of the friction circle is utilized

4 Vehicle Closed-Loop Simulations

Figure 4 shows the control logic. The human driver is replaced by a path-following *PD* steering controller using look-ahead measurements y from a vision system and is complemented by a feedforward steering angle based on friction. The brake controller controls the high-friction brakes to reduce excessive yaw torque using yaw rate $\dot{\psi}$ and the look-ahead measurement y as feedback. The low-friction side is controlled by the ABS. The details of the control logic are given in [4].

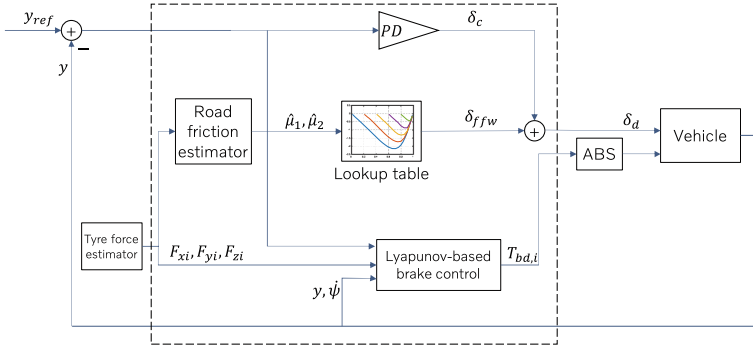
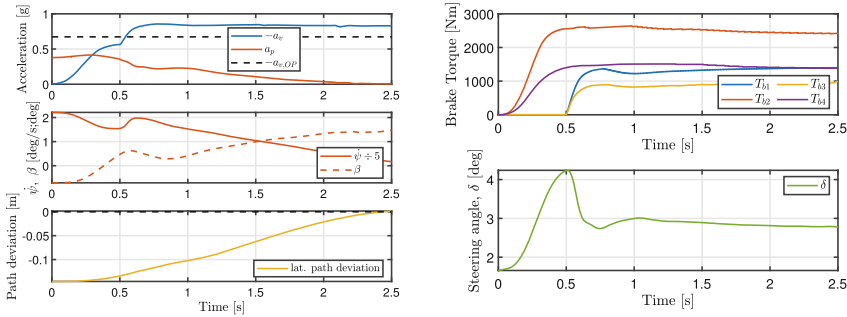


Fig. 4. Block diagram of control logic

Vehicle simulations are conducted in IPG CarMakerTM to validate the optimization, presented in Fig. 5. The simulation is performed for an initial speed of $V_0 = 70$ km/h and radius $R = 100$ m, corresponding to a lateral limit of $a_{p,des} \approx 0.4$ g. In Fig. 5a, the vehicle trajectory and motion states are depicted, while the states' targets are depicted with black dashed lines. The deceleration a_v surpasses the limit set by the OP $a_{v,OP}$ after a transient phase of about 0.7 s. The lateral acceleration a_p gradually decreases as a_v increases and velocity drops. At the same time, the yaw rate decreases linearly, as the side slip angle is almost constant, fluctuating around 1° . Also, the steering controller keeps path deviations small. The small side slip angle and path deviation at high deceleration show the vehicle's good manoeuvrability. In Fig. 5b, the control inputs are depicted. Interestingly, the ABS turns off the inner side brake torques up to 0.5 s due to excessive slip. It is also when the steering angle is at its peak.



(a) Vehicle states: accelerations, yaw rate & side slip angle, and path deviation (b) Control inputs: brake torques and steering wheel angle

Fig. 5. Closed loop simulation of a vehicle braking in a curve of $R = 100$ m on split friction with $\mu = [0.6 \ 1]$ and initial speed $V_0 = 70$ km/h

5 Conclusion

This paper presented a way to find the maximum braking during cornering on split friction roads. The maximum braking and the active front steering/differential brake torque allocations were investigated as a function of the friction difference between the vehicle's sides and the lateral acceleration. The analysis revealed that low friction on a curve's inner side is more dangerous than on the outer side due to the lateral load transfer. Further, a control logic was showcased that achieves good path-following and keeps the vehicle side slip small while achieving optimal deceleration. Future work includes using prior friction knowledge to predict optimal speed in a curve for varying friction road conditions.

References

1. Fors, V., Nielsen, L., Olofsson, B.: Models for Optimization of Vehicle Maneuvers. Vehicular Systems, ISY, Linköping University (2023)
2. Hebden, R.G., Edwards, C., Spurgeon, S.K.: Automotive steering control in a split- μ manoeuvre using an observer-based sliding mode controller. *Veh. Syst. Dyn.* **41**, 181–202 (2004). <https://doi.org/10.1076/vesd.41.3.181.26511>
3. Karyotakis, E., Jonasson, M., Yang, D., Sjöberg, J.: Minimizing stopping distance on split friction via steering and individual wheel braking optimization. In: The 28th IAVSD Symposium on Dynamics of Vehicles on Roads and Tracks (2023)
4. Karyotakis, E., Jonasson, M., Yang, D., Sjöberg, J.: Minimum stopping distance on split friction roads via joint control of steering and individual wheel braking. *Veh. Syst. Dyn.* (2024, to be submitted)
5. Mirzaeinejad, H., Mirzaei, M., Kazemi, R.: Enhancement of vehicle braking performance on split- μ roads using optimal integrated control of steering and braking systems. *Proc. Inst. Mech. Eng. Part K J. Multi-body Dyn.* **230**, 401–415 (2016)
6. d'Andrea Novel, B., Ellouze, M.: Tracking with stability for a vehicle braking in a corner. In: Proceedings of the 40th IEEE Conference on Decision and Control (Cat. No. 01CH37228), vol. 5, pp. 4427–4432. IEEE (2001)
7. Peng, H., Hu, J.S.: Traction/braking force distribution for optimal longitudinal motion during curve following. *Veh. Syst. Dyn.* **26**, 301–320 (1996). <https://doi.org/10.1080/00423119608969313>
8. Tagesson, K., Jacobson, B., Laine, L.: Driver response to automatic braking under split friction conditions. In: Proceedings of the 12th International Symposium on Advanced Vehicle Control (AVEC), pp. 666–671 (2014)
9. Xue, Z., Li, C., Wang, X., Li, L., Zhong, Z.: Coordinated control of steer-by-wire and brake-by-wire for autonomous emergency braking on split- μ roads. *IET Intell. Transp. Syst.* **14**, 2122–2132 (2020)
10. Yu, L., Zheng, S., Dai, Y., Abi, L., Liu, X., Cheng, S.: A feedback-feedforward steering controller designed for vehicle lane keeping in hard-braking manoeuvres on split- μ roads. *Veh. Syst. Dyn.* **60**, 1763–1787 (2022)

Open Access This chapter is licensed under the terms of the Creative Commons Attribution 4.0 International License (<http://creativecommons.org/licenses/by/4.0/>), which permits use, sharing, adaptation, distribution and reproduction in any medium or format, as long as you give appropriate credit to the original author(s) and the source, provide a link to the Creative Commons license and indicate if changes were made.

The images or other third party material in this chapter are included in the chapter's Creative Commons license, unless indicated otherwise in a credit line to the material. If material is not included in the chapter's Creative Commons license and your intended use is not permitted by statutory regulation or exceeds the permitted use, you will need to obtain permission directly from the copyright holder.





A Fallback Approach for In-Lane Stop on Curved Roads Using Differential Braking

Jihoon Sung¹(✉), Seungwon Choi¹, and Kunsoo Huh²

¹ Department of Automotive Engineering (Automotive-Computer Convergence), Hanyang University, Seoul 04763, Republic of Korea
{wlgns8900, seung5049}@hanyang.ac.kr

² Department of Automotive Engineering, Hanyang University, Seoul 04763, Republic of Korea
khuh2@hanyang.ac.kr

Abstract. Due to the importance of safety in the development of Automated Driving Systems (ADS), research is ongoing on fallback functions for ADS. Scenarios involving steering actuator failures during curved road driving are particularly dangerous, with limited available fallback options. This paper proposes a method for achieving a safer in-lane stop using differential braking when steering actuator failure occurs. Lateral motion is induced by the difference in longitudinal forces between the left and right sides, facilitating an in-lane stop maneuver. The vehicle's lateral behavior under differential braking and changes in front-wheel steering angle are modeled. A model-based estimator using a Kalman filter estimates the vehicle's state and steering angle. Based on these estimations and lane information, a controller employing a linear quadratic regulator (LQR) is developed. The effectiveness of the differential braking in-lane stop system is validated through simulation.

Keywords: Differential braking · Minimal risk maneuver · In-lane stop

1 Introduction

Automated Driving Systems (ADS) are being developed for a variety of applications, aiming to enhance driving safety, efficiency, and convenience. However, it is crucial to prepare for scenarios where ADS may not function normally due to various reasons, such as sensor failures, actuator failures, software glitches, or unforeseen road conditions. To address such situations, fallback functions are being researched extensively. One notable fallback function is the Minimal Risk Maneuver (MRM) [3], which is designed to bring the vehicle to a safe, stable stop when the ADS encounters a failure.

Typically, the primary consideration during an MRM is a straight stop. This maneuver is performed when only longitudinal deceleration control is possible,

and lateral control is compromised due to lane detection failures or steering actuator malfunctions. As a result, straight stops can lead to collisions with roadside structures or others in certain situations. Conversely, an in-lane stop allows for lateral control, enabling the vehicle to halt within its lane, even on curved roads.

Previous research has explored various methods to achieve safe stopping maneuvers under ADS failures. However, many of these methods focus on straight stops or rely on fully functional steering systems [1,5]. There remains a significant gap in addressing the safe stopping of vehicles on curved roads when the steering system fails.

In this paper, a differential braking in-lane stop system is proposed to execute the in-lane stop maneuver on curved roads, specifically addressing scenarios involving steering system failures. The proposed method employs differential braking to generate the necessary lateral motion, thus enabling safer in-lane stops compared to straight stops. The proposed approach is distinctive in that it does not rely on the steering system, making it particularly useful in scenarios where steering control is lost. Simulation results demonstrate that the proposed approach effectively performs in-lane stops, enhancing safety during ADS failures.

2 Vehicle Model

The behavior of the vehicle and changes in the front wheel steering angle occur directly due to the differential longitudinal force [4].

The extended two-track model [2,4] is used to consider the differential longitudinal force in the commonly used bicycle model. At the same time, the simplified steering model is utilized.

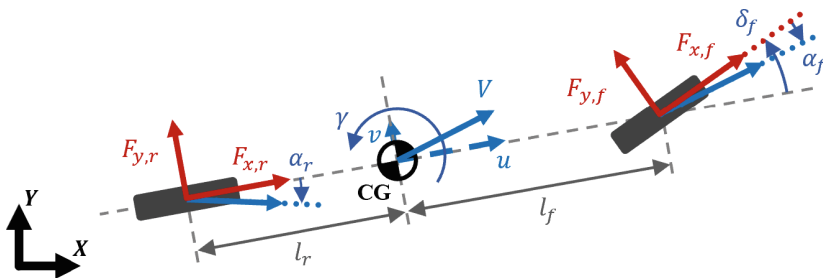


Fig. 1. Single-track model with vehicle geometric parameters, applied forces and motion characteristics.

The geometric parameters of the vehicle and the forces generated at each wheel are illustrated in Fig. 1. $F_{x,i}$ and $F_{y,i}$ represent the longitudinal and lateral tire forces with $i = \{f, r\}$ denoting the front and rear tires. u and v are the

longitudinal and lateral velocity, γ is the yaw rate, δ_f is the front wheel steering angle and α_i are the tire slip angles. l_f and l_r are the distance of the front and rear axles from the vehicle's center of gravity (CG).

The combined state space equation for the lateral dynamics motion model and the steering system model can be expressed as follows:

$$\dot{x} = Ax + Bu \tag{1}$$

$$x = [v \ \gamma \ \delta_f \ \dot{\delta}_f]^T, \quad u = \begin{bmatrix} \Delta F_{x,f} \\ \Delta F_{x,r} \end{bmatrix} \tag{2}$$

$$A = \begin{bmatrix} -\frac{C_f+C_r}{mu} & -\frac{l_f C_f - l_r C_r}{mu} & -u \frac{C_f}{m} & 0 \\ -\frac{l_f C_f - l_r C_r}{J_z u} & -\frac{l_f^2 C_f + l_r^2 C_r}{J_z u} & \frac{l_f C_f}{J_z} & 0 \\ 0 & 0 & 0 & 1 \\ 0 & 0 & -\frac{k_\delta}{J_\delta} & -\frac{b_\delta}{J_\delta} \end{bmatrix}, \quad B = \begin{bmatrix} 0 & 0 \\ \frac{w}{2J_z} & \frac{w}{2J_z} \\ 0 & 0 \\ \frac{s_{eff}}{J_\delta} & 0 \end{bmatrix} \tag{3}$$

$\Delta F_{x,i}$ are the differential longitudinal forces, m is the vehicle mass, J_z is the moment of inertia about its z-axis and w is the track width of the vehicle. The coefficients of the tires slip, C_i , are the cornering stiffness. In addition, J_δ , b_δ , and k_δ are the effective moments of inertia, effective damping, and effective stiffness of the steering system, respectively. s_{eff} is the effective scrub radius, which is defined as the distance between the point of application of resultant longitudinal force and the steering axis at ground level.

3 Differential Braking In-Lane Stop System

The differential braking in-lane stop system consists of four modules: reference generator, state estimator, controller, and brake pressure distributor.

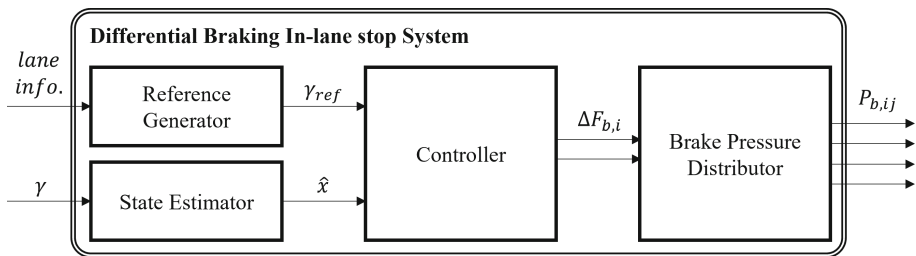


Fig. 2. Block diagram of the differential braking in-lane stop system.

The system architecture is shown in Fig. 2. γ_{ref} is the reference yaw rate and \hat{x} is the estimated states. In addition, $\Delta F_{b,i}$ are the differential braking forces and $P_{b,ij}$ are the braking pressures with $j = \{L, R\}$ denoting the left and right tires.

The reference generator module determines a reference state based on lane detection. It calculates the reference yaw rate to reach the look-ahead point, which is determined based on the vehicle’s speed. Simultaneously, the state estimator module obtains the estimated states using a model-based state observer with a Kalman filter. Based on both the reference state and the estimated vehicle state, the controller then calculates the necessary differential braking amounts for the front and rear wheels. A Linear Quadratic Regulator (LQR) algorithm is utilized in the controller. The brake pressure distributor module calculates the appropriate signal for braking pressure.

4 Simulation Result

The proposed system is verified through a joint simulation using CarSim and MATLAB/Simulink. The simulation cycle is set to 1 ms, while the controller’s output cycle is set to 20 ms. The scenario assumes a steering system failure and includes an in-lane stop maneuver on curved roads. Despite the lack of torque input to the steering wheel due to the steering system failure, a front wheel steering angle can be generated by the differential braking.

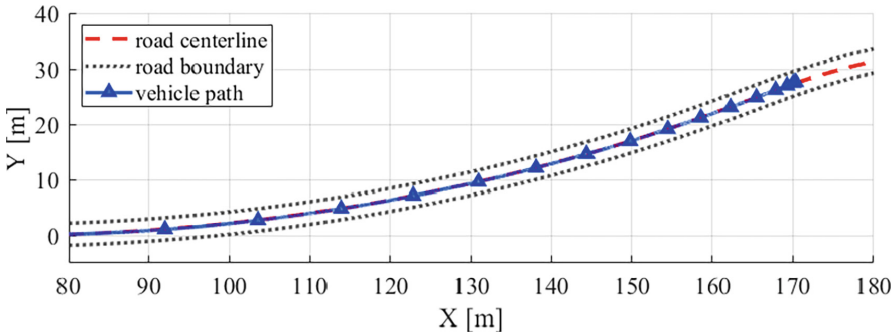


Fig. 3. Vehicle Path for the in-lane stop maneuver on a curved road.

Figure 3 shows the path of the vehicle as it comes to a stop on a curved road with the differential braking in-lane stop system active. The distance to the road center line after stopping is 0.047 m, successfully performing the in-lane stop maneuver without crossing the lane.

Figure 4 presents the speed, distance to the center line, yaw rate, front wheel steering angle and brake pressure inputs over time. After approximately 13s, the vehicle speed is sufficiently reduced. At this point, differential braking is ceased, with brake pressure applied to all wheels to achieve a complete stop. The simulation results demonstrate that the in-lane stop maneuver is successfully performed without deviating from the road.

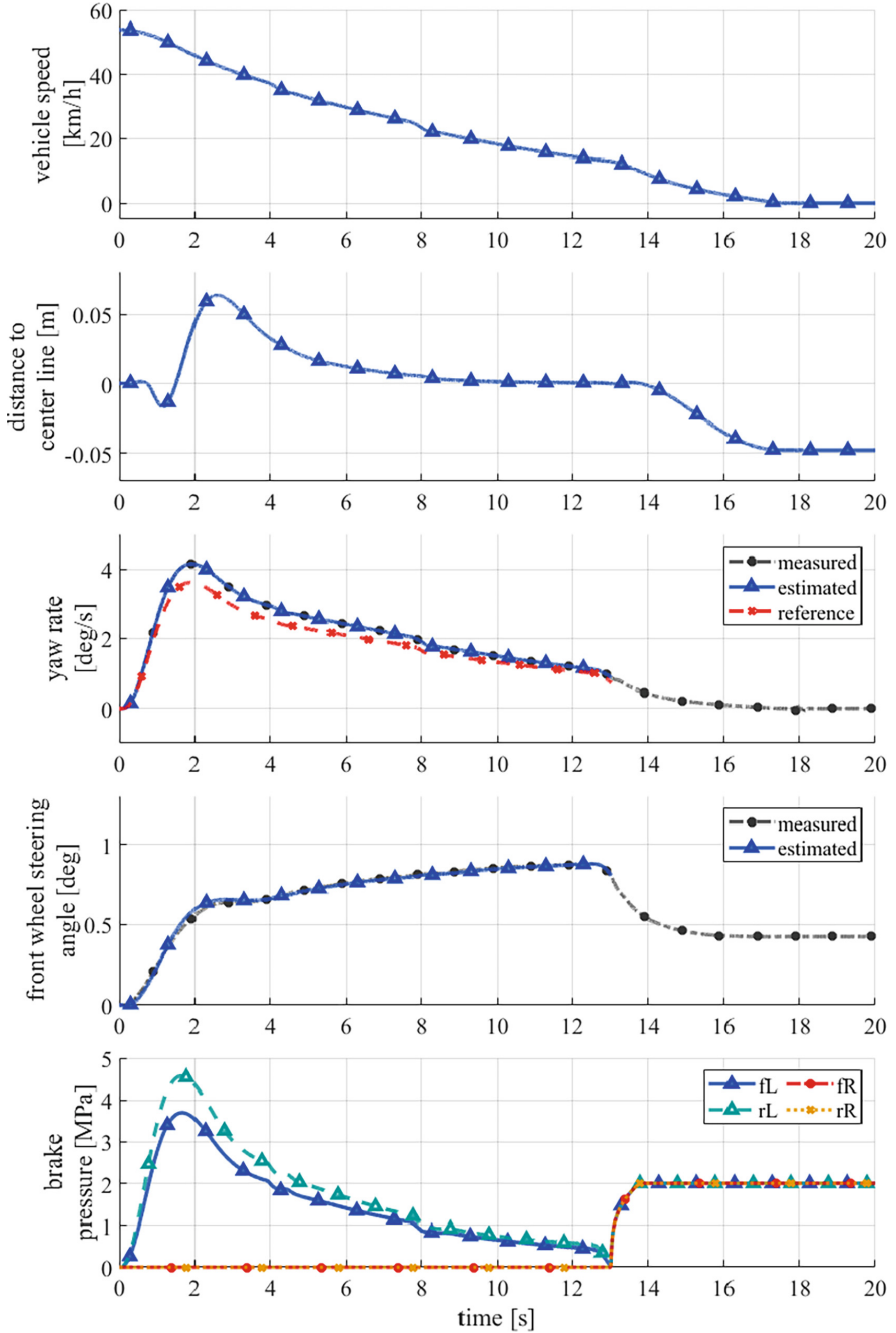


Fig. 4. Simulation results for the in-lane stop maneuver on a curved road.

5 Conclusion

In this paper, we proposed a reliable system that utilizes differential braking to perform in-lane stop maneuvers in the event of a steering system failure. The reference state was calculated using road information to ensure the vehicle remains within the lane. To account for the steering angle generated by differential braking, the steering system model was integrated with the vehicle lateral motion model. An estimator and controller were designed using the integrated model.

Simulations confirmed that the proposed differential braking in-lane stop system can decelerate and stop the vehicle within the lane on curved roads without deviating. Our results demonstrate that differential braking is an effective method for maintaining vehicle control and safety when a steering system failure occurs. The integration of the steering system model with the vehicle lateral motion model allows for precise control of the vehicle's trajectory, even on curved roads.

Future research is expected to extend this work to more complex road environments and different maneuvers, such as road shoulder stops. Additionally, experiments with actual vehicles will be conducted to validate the system's performance in real-world conditions.

Acknowledgment. This work was supported by the Ministry of Trade, Industry, and Energy (MOTIE), South Korea, through the Technology Innovation Program (Development on Automated Driving with Perceptual Prediction Based on T-Car/Vehicle Parts to Intelligent Control/System Integration for Assessment) under Grant 20018101.

References

1. Coll-Perales, B., et al.: Prototyping and evaluation of infrastructure-assisted transition of control for cooperative automated vehicles. *IEEE Trans. Intell. Transp. Syst.* **23**(7), 6720–6736 (2021)
2. Dominguez-Garcia, A.D., Kassakian, J.G., Schindall, J.E.: A backup system for automotive steer-by-wire, actuated by selective braking. In: 2004 IEEE 35th annual power electronics specialists conference, vol. 1, pp. 383–388. IEEE, Germany (2004)
3. ISO/DIS 23793-1, Intelligent transport systems - Minimal Risk Maneuver (MRM) for automated driving - Part 1: Framework, straight-stop and in-lane stop, ISO, under development
4. Sung, J., Choi, S., Huh, K.: A differential brake-actuated steering system for redundancy of steer-by-wire. *IEEE Trans. Intell. Veh.* **9**(1), 993–1004 (2023)
5. Xue, W., Yang, B., Kaizuka, T., Nakano, K.: A fallback approach for an automated vehicle encountering sensor failure in monitoring environment. In: 2018 IEEE Intelligent Vehicles Symposium (IV), pp. 1807–1812. IEEE, China (2018)

Open Access This chapter is licensed under the terms of the Creative Commons Attribution 4.0 International License (<http://creativecommons.org/licenses/by/4.0/>), which permits use, sharing, adaptation, distribution and reproduction in any medium or format, as long as you give appropriate credit to the original author(s) and the source, provide a link to the Creative Commons license and indicate if changes were made.

The images or other third party material in this chapter are included in the chapter's Creative Commons license, unless indicated otherwise in a credit line to the material. If material is not included in the chapter's Creative Commons license and your intended use is not permitted by statutory regulation or exceeds the permitted use, you will need to obtain permission directly from the copyright holder.





Steering Noise Cancelling for Drift Assist Control

Yiwen Sun¹(✉), Efstathios Velenis¹, and Ajinkya Krishnakumar²

¹ Cranfield University, Cranfield MK43 0AL, UK
{Yiwen.Sun, e.velenis}@cranfield.ac.uk

² Rimac Technology, Ljubljanska 7, 10431 Sveta Nedelja, Croatia

Abstract. In this paper we consider a driver assist system concept for the stabilization of the vehicle during high sideslip angle cornering (drifting). Unregulated steering inputs (steering noise) from inexperienced drivers, can disturb the drift equilibria and oppose to the controller’s stabilization task. Therefore, this paper presents a drift assist control concept to cancel the steering effects from the driver by torque vectoring. In detail, first by equilibria analysis for four-wheel drive vehicle, the steering effects on drift equilibria are analyzed, which indicates a contradiction between stabilizing the yaw rate and the sideslip angle. Then, by nonlinear programming, it is proven that the path angle rate together with the speed which determine the trajectory, could be stabilized with torque vectoring against the steering noise. Finally, a steering noise cancelling and trajectory tracking controller structure is designed and further evaluated with CarMaker.

Keywords: Drift Assist Control · Torque Vectoring · Trajectory Tracking · Vehicle Dynamics

1 Introduction

Vehicle control systems that enable cornering at high sideslip angle (drifting) have recently been the focus of significant research effort. These approaches have been developed mainly in the context of Autonomous Vehicles (AVs) to demonstrate that the AV controllers are able to operate in regimes that are challenging and non-intuitive for average human drivers [1–5].

Drift-assist control, where the driver still maintains authority over the control of the vehicle in the context of Advanced Driver Assist Systems (ADAS), has been introduced by several high-performance vehicle manufacturers (“Variable Drift Control” of McLaren [6], “Drift Mode” of BMW [7]). These systems allow the vehicle to operate outside the envelope of stability control systems, or even provoke instability to achieve high sideslip angle [8, 9]. However, maintaining a drift condition, even with drift-assist control, currently still requires driving skills beyond average and understanding of the non-intuitive vehicle behavior in such operating regimes. One of the reasons is the steering input provided by the driver can prevent the control system from achieving its task, if it is not properly coordinated with the wheel torque control of the drift assist system [10].

In this paper, we introduce a concept of drift-assist system to stabilize the vehicle in high sideslip cornering using torque vectoring interventions against uncoordinated steering inputs (steering noise) by the driver. In particular, we calculate drifting equilibria for vehicles equipped with four-wheel torque vectoring capability, and explore the effects of steering angle in the required wheel-slip for four wheels to achieve the same equilibrium states. This study reveals a conflict in maintaining the same yaw rate and vehicle sideslip angle when the steering angle changes. Therefore, we formulate a trajectory tracking task where the vehicle speed and path angle rate (instead of both yaw rate and sideslip angle) are sought to be stabilized by means of torque vectoring when the steering angle is being disturbed. The control task is formulated as a nonlinear programming problem to demonstrate the feasibility of the concept, and a control structure is designed and further validated in CarMaker.

2 Drift Equilibria for Four-Wheel Drive Vehicle

Based on typical parameters of a high-performance vehicle, a four-wheel drive vehicle model (Fig. 1) is considered for longitudinal/lateral dynamics (speed v , yaw rate r and sideslip angle β), with steering δ and four-wheel slip ratio s_{ri} ($i = fl, fr, rl, rr$) as inputs. The model considers nonlinear tire characteristics and load transfer effects.

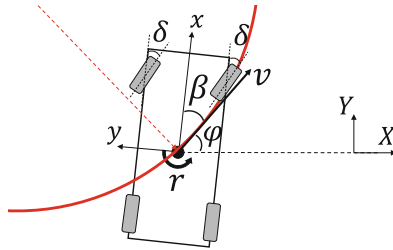


Fig. 1. The four-wheel drive vehicle model for drift equilibrium analysis.

Unlike rear-wheel drive drift analysis where there are only two controlled variables (steering and throttle), now with four-wheel drive that allows different slip ratio for each wheel, there are more unknown variables involved. But with three equilibrium equations ($\dot{v}, \dot{r}, \dot{\beta} = 0$) we can only solve for three variables. Therefore, we set the steering δ and the slip ratio s_{ri} as known before solving the equilibria [11]. With equal slip ratio for wheels of the same axle ($s_{fl,fr} = s_{rf}$, $s_{rl,rr} = s_{rr}$), the solved equilibria at different δ are shown in Fig. 2 (counterclockwise drifting with counter steering) as surfaces marked in different color. One of the most important findings of this steady-state analysis is the steering effects on the drift equilibria: i.e., when the counter steering increases from -10° to -20° (green surface to orange surface in Fig. 2), to maintain the previous r_{eq} , the rear wheel slip ratio s_{rr} has to increase and s_{rf} to decrease, however for keeping the sideslip β_{eq} , the trend is opposite that s_{rr} has to decrease and s_{rf} to increase. This leads to a preliminary conclusion that r_{eq} , β_{eq} are unlikely to be both stabilized when the steering has changed (the effects of different slip ratio for wheels on the same axle will be discussed in detail in our future work).

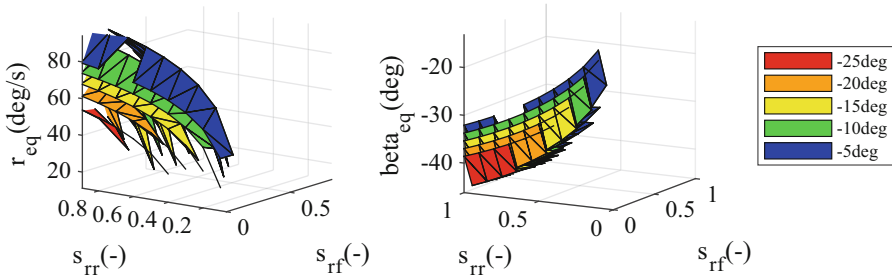


Fig. 2. The four-wheel drive drift equilibria at different steering angle δ .

3 Nonlinear Programming Based Steering Noise Cancelling

As discussed in previous section, when the drift equilibrium is disturbed by additional steering inputs, r_{eq}, β_{eq} are not likely to be stabilized separately. Therefore, we discuss the steering noise cancelling problem in the aspect of path angle rate $\dot{\varphi}$, which is the sum of yaw rate r and sideslip rate β (Fig. 1), and directly decides the trajectory. To explore whether stabilizing $\dot{\varphi}$ is possible, nonlinear programming method [12] is applied to the previous four-wheel vehicle dynamics model in a counterclockwise drift, and the cost function J is written as:

$$J = \varepsilon_1(\dot{\varphi} - \dot{\varphi}_{eq})^2 + \varepsilon_2(v - v_{eq})^2 \tag{1}$$

where φ_{eq}, v_{eq} are the equilibria path angle rate and speed, $\varepsilon_1, \varepsilon_2$ are the weighting coefficients. The result is shown in Fig. 3, a sinusoidal noise (180°) is added to the equilibrium steering wheel angle (-380°). With torque vectoring that independently controls the slip ratio for each wheel, the desired speed, path angle rate and the trajectory could be kept against the steering noise from unskilled driver.

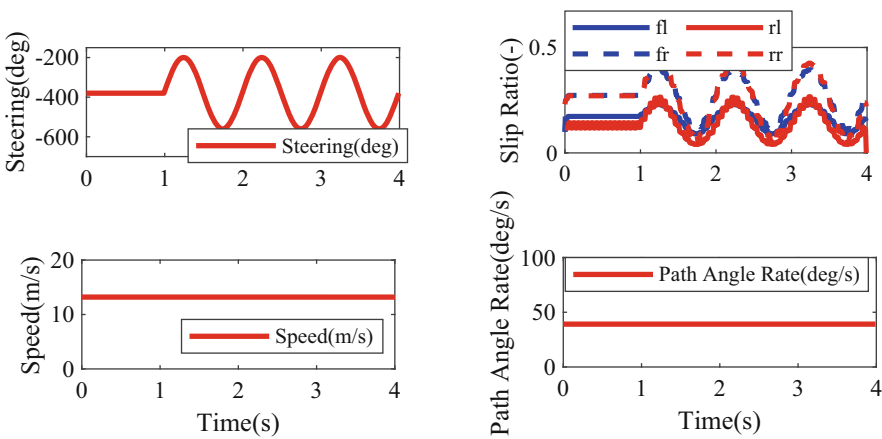


Fig. 3. The steering noise cancelling results of nonlinear programming.

4 Steering Noise Cancelling Controller and Simulation Results

In the preceding section, we discussed the possibility to cancel the steering effects of an inexperienced driver and maintain the desired trajectory for drifting with torque vectoring. In this section, we design a steering noise cancelling controller and evaluate it in CarMaker. As shown in Fig. 4, the proposed structure could be divided into three parts, which will be discussed respectively.

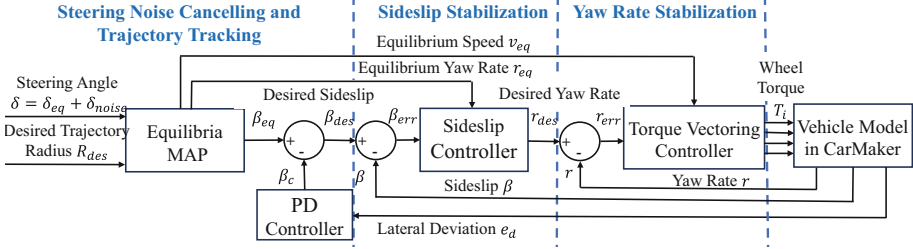


Fig. 4. The structure of the steering noise cancelling and trajectory tracking controller.

4.1 Steering Noise Cancelling and Trajectory Tracking

Known the desired trajectory radius R_{des} and the disturbed steering angle δ (which deviates from the equilibrium δ_{eq} with a noise of δ_{noise}), we firstly calculate a new equilibrium sideslip angle β_{eq} as feedforward based on the previous equilibrium map (Fig. 2). Next, to account for the lateral deviation e_d from the desired trajectory, a feedback sideslip angle β_c based on a Proportional-Derivative (PD) controller is adopted. Then, the desired sideslip angle β_{des} could be written as Eq. (2), in which k_{pd} , k_{dd} are coefficients. The desired trajectory could be tracked as higher sideslip generates more centripetal force which drives the vehicle drift deeper into the corner thus reduce the trajectory radius, and vice versa.

$$\beta_{des} = \beta_{eq} + \beta_c = \beta_{eq} - k_{pd}e_d - k_{dd}de_d/dt \quad (2)$$

4.2 Sideslip Stabilization

To stabilize the sideslip angle at the desired β_{des} , the equilibrium yaw rate r_{eq} is considered together with the sideslip error β_{err} ($\beta_{err} = \beta_{des} - \beta$). And the desired yaw rate r_{des} could be written as Eq. (3), in which τ is a time constant.

$$r_{des} = r_{eq} - \dot{\beta}_{err} = r_{eq} - \beta_{err}/\tau \quad (3)$$

4.3 Yaw Rate Stabilization and Torque Vectoring

With the desired yaw rate r_{des} and the yaw rate error $r_{err} = r_{des} - r$, a Proportional-Integral (PI) controller is implemented to calculate the desired yaw moment ΔM_z for torque vectoring, as shown in Eq. (4), in which k_{pr} , k_{ir} are constant coefficients. Then, together with the total drive force F_{xdes} in order to maintain the equilibrium speed v_{eq} , also assuming all wheel torque is delivered as drive force [13], the drive torque for each wheel $T_{fl,fr,rl,rr}$ could be written as Eq. (5). Here w is the wheel track width, r_w is the wheel rolling radius, and c_{tf} is a coefficient to decide the torque allocation between front and rear wheels.

$$\Delta M_z = k_{pr}r_{err} + k_{ir} \int r_{err}dt \tag{4}$$

$$\begin{aligned} T_{fl,fr} &= c_{tf}(1/2F_{xdes} \mp \Delta M_z/w)r_w \\ T_{rl,rr} &= (1 - c_{tf})(1/2F_{xdes} \mp \Delta M_z/w)r_w \end{aligned} \tag{5}$$

4.4 Simulation Results

To evaluate the above steering noise cancelling controller, a circular track with 20 m radius is built in CarMaker. The vehicle is drifting in counterclockwise direction until 2 s a steering noise with increasing frequency and amplitude is added to imitate the steering behavior of an inexperienced human driver. As shown in Fig. 5, the steering effects are effectively reduced by varying the sideslip angle and yaw rate, that the lateral deviation is lower than 1 m and the desired trajectory is basically maintained as shown in Fig. 6.

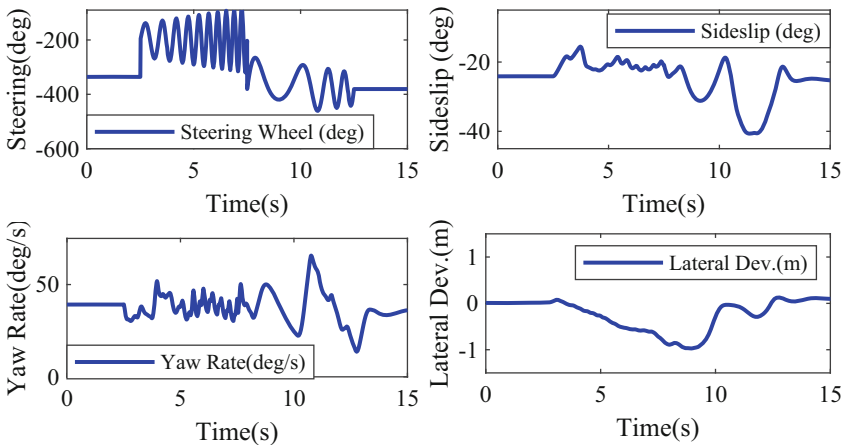


Fig. 5. Vehicle motion with steering noise cancelling controller.

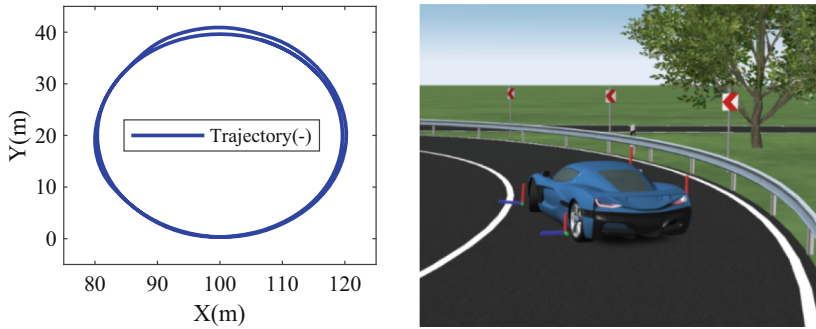


Fig. 6. Trajectory with steering noise cancelling controller.

5 Conclusion

In this paper we propose a driver assist system concept for the stabilization of the vehicle during drifting, as undesired steering inputs (steering noise) from inexperienced drivers can disturb the drift equilibria and deviate the vehicle from the desired track. Therefore, this paper presents a steering noise cancelling and trajectory tracking concept to cancel the steering effects from the driver by torque vectoring. In detail, first by equilibrium analysis specifically for four-wheel drive vehicle, the steering effects on drift equilibria are analyzed, which indicates a contradiction between stabilizing yaw rate and sideslip angle. Then, by nonlinear programming, it is proven that the path angle rate together with the speed which determines the trajectory could be regulated with torque vectoring against the steering noise, by independently controlling the slip ratio for all four wheels. Finally, a control structure is proposed and further evaluated in CarMaker, where the vehicle successfully maintains drifting on the desired circular track under a sinusoidal steering disturbance.

References

1. Velenis, E., et al.: Steady-state drifting stabilization of RWD vehicles. *Control. Eng. Pract.* **19**(11), 1363–1376 (2011)
2. Goh, J.Y., et al.: Toward automated vehicle control beyond the stability limits: drifting along a general path. *J. Dyn. Syst. Meas. Control* **142**(2) (2019)
3. Acosta Reche, M., et al.: A hybrid hierarchical rally driver model for autonomous vehicle agile maneuvering on loose surfaces. In: *International Conference on Informatics in Control, Automation and Robotics* (2017)
4. Joa, E., et al.: A new control approach for automated drifting in consideration of the driving characteristics of an expert human driver. *Control. Eng. Pract.* **96**, 104293 (2020)
5. Baars, M., et al.: Control of a scaled vehicle in and beyond stable limit handling. *IEEE Trans. Veh. Technol.* **70**(7), 6427–6437 (2021)
6. Jalopnik. Here's What The McLaren 720S' Drift Mode Really Does (2017). <https://www.youtube.com/watch?v=oEa5R1dM5rM>
7. BMW M. How To Adjust the DSC and Drift in an Electric BMW M Model (2023). <https://www.youtube.com/watch?v=yJZFpF8FCLc>

8. Werling, M., et al.: Robust power-slide control for a production vehicle. *Int. J. Veh. Auton. Syst.* **13**, 27 (2015)
9. Park, M., Kang, Y.: Experimental verification of a drift controller for autonomous vehicle tracking: a circular trajectory using LQR method. *Int. J. Control. Autom. Syst.* **19**(1), 404–416 (2021)
10. Voser, C., et al.: Analysis and control of high sideslip manoeuvres. *Veh. Syst. Dyn.* **48**(sup1), 317–336 (2010)
11. Milani, S., et al.: Vehicle drifting dynamics: discovery of new equilibria. *Veh. Syst. Dyn.* **60**(6), 1933–1958 (2022)
12. Andersson, J.A.E., et al.: CasADi: a software framework for nonlinear optimization and optimal control. *Math. Program. Comput.* **11**(1), 1–3 (2019)
13. Nakano, H., et al.: Trajectory tracking control of a vehicle with a large sideslip angle. In: 2015 IEEE International Conference on Advanced Intelligent Mechatronics (AIM) (2015)

Open Access This chapter is licensed under the terms of the Creative Commons Attribution 4.0 International License (<http://creativecommons.org/licenses/by/4.0/>), which permits use, sharing, adaptation, distribution and reproduction in any medium or format, as long as you give appropriate credit to the original author(s) and the source, provide a link to the Creative Commons license and indicate if changes were made.

The images or other third party material in this chapter are included in the chapter's Creative Commons license, unless indicated otherwise in a credit line to the material. If material is not included in the chapter's Creative Commons license and your intended use is not permitted by statutory regulation or exceeds the permitted use, you will need to obtain permission directly from the copyright holder.





A Decoupling Control Scheme for Path Tracking with Model Predictive Path Integral and Output Regulator

Hang Wan, Hui Liu, Shida Nie^(✉), and Lijin Han

Beijing Institute of Technology, Beijing 100081, China
nieshida@bit.edu.cn

Abstract. The coupling and nonlinearity of vehicle dynamics present considerable challenges to path tracking of autonomous vehicles. In this paper, a necessary condition is derived to decouple the translational motion from yawing motion based on the time-scale separation. Consequently, the translational motion is regulated over an extended control horizon to generate a human-like tracking trajectory. The yawing motion is regulated based on a high-fidelity control model. In addition, model predictive path integral (MPPI) is developed to mitigate the computational burden of nonlinear motion planning through sampling-based optimization. A predictive output regulator is developed to solve the underactuated problem in the 2-DOF lateral dynamics with only 1-DOF of control input. Simulation results show that the proposed method enhances computing efficiency and reduces the lateral jerk by an average of 50% with only one set of parameters.

Keywords: Autonomous vehicle · Decouple · MPPI · Underactuated control

1 Introduction

While a short-term step can improve tracking accuracy and stability of motion control system, a long-term prediction/control horizon is necessary to make a reasonable future guess and make impacts on the translational motion and speed profile of vehicles [4]. However, the limited computing power causes a dilemma between them. Besides, the coupling control of states envolving over different time scales leads to difficult controllers tuning in different driving conditions.

This paper derives the necessity for path tracking problem. As a result, the translational motion can be decoupled from the rotational. And states envolving over different time scales can be regulated with different control loops. Thus, the computational load can be reduced and the control horizon can be extended without sacrificing tracking accuracy. To further mitigate the computational

Supported by National Natural Science Foundation of China (Grant No. 52394262).

© The Author(s) 2024

G. Mastinu et al. (Eds.): AVEC 2024, LNME, pp. 625–631, 2024.

https://doi.org/10.1007/978-3-031-70392-8_88

burden, The path integral control framework is incorporated into the model predictive control, where the control sequence is constantly optimized via parallel sampling [6]. Moreover, a predictive output regulator is proposed to solve the underactuated problem in lateral tracking. Simulation results show that the proposed method reduces the computational complexity of nonlinear optimization effectively and improves the steering smoothness without sacrificing tracking accuracy.

2 Formulation of Path Tracking Problem

We consider the path tracking problem as the Point to Points problem (P2Ps). The original P2Ps solve the path tracking problem in a single loop, which leads to difficult bandwidth allocating and controllers tuning. In this paper, the coupling P2Ps is decoupled as the simplified P2Ps problem through deriving a necessity as shown in Fig. 1.

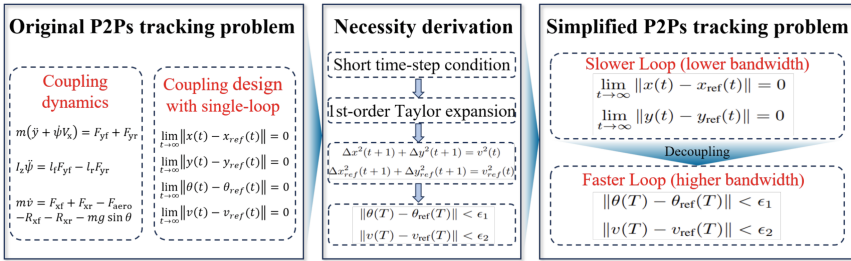


Fig. 1. Formulation of the P2Ps tracking problem.

In the coupling design with single-loop, path convergency needs the following equations hold.

$$\lim_{t \rightarrow \infty} \|x(t) - x_{ref}(t)\| \rightarrow 0, \tag{1a}$$

$$\lim_{t \rightarrow \infty} \|y(t) - y_{ref}(t)\| \rightarrow 0, \tag{1b}$$

$$\lim_{t \rightarrow \infty} \|\theta(t) - \theta_{ref}(t)\| \rightarrow 0, \tag{1c}$$

$$\lim_{t \rightarrow \infty} \|v(t) - v_{ref}(t)\| \rightarrow 0. \tag{1d}$$

In the necessity derivation, we prove that the last two equations, i.e., Eq. 1c and 1d, are the necessary condition of the first two equations. Then the single loop control scheme can be transformed into cascade control scheme.

3 Decoupling Control Scheme

In this section, we propose a decoupling control scheme with the translational regulator and the attitude regulator as shown in Fig. 2. Because any rotation maneuver required to point the heading in the right direction or desired yaw rate for translational control can be achieved quickly, the control authority of the attitude regulator has a higher bandwidth than the translation regulator.

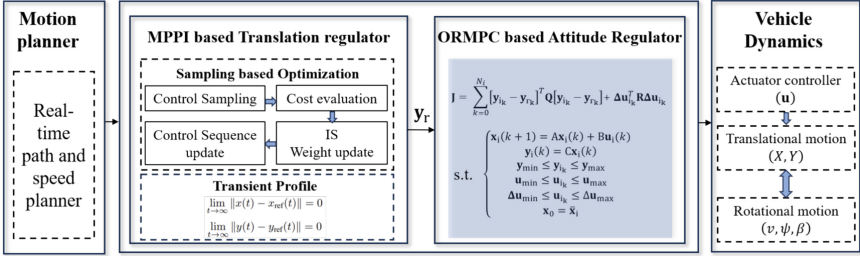


Fig. 2. Decoupling control scheme.

3.1 Translation Regulator

For a mobile vehicle with nonholonomic constraints, where the control actions may affect not only the immediate result but also the next situation and, through that, all subsequent results, which we called the delayed effect of the actions. With a guidance law generating the transient profile, dynamics controller can output more reasonable manipulation signal and provide smoother steering.

Control systems with long-term control horizon and short sampling step bear significant computational burden. Due to decoupling design, cascade control scheme enable different sampling steps and control horizons between slow translational regulator and attitude regulator. Although linear tracking law in translational regulator reduces the computational burden [1], it needs explicit method to handle the large deviation from reference path [5]. We propose to formulate a nonlinear programming (NLP) for translational regulator as follows,

$$\text{minimize } \phi(\mathbf{x}_T) + \int_t^T (q(\mathbf{x}_t) + \frac{1}{2} \mathbf{u}_t^T \mathbf{R} \mathbf{u}_t) dt. \quad (2a)$$

$$\text{subject to } \dot{\mathbf{x}} = \mathbf{f}(\mathbf{x}_t, \mathbf{u}_t, t), \quad (2b)$$

Assume the dynamics equation given in Eq. (2) can be transformed into system which is affine in control input. Define the value function of system states,

$$V(\mathbf{x}_t) = \min_{\mathbf{u}} \mathbb{E}_{\mathcal{Q}} [\phi(\mathbf{x}_T) + \int_t^T (q(\mathbf{x}_t) + \frac{1}{2} \mathbf{u}(\mathbf{x}_t)^T \mathbf{R} \mathbf{u}(\mathbf{x}_t)) dt]. \quad (3)$$

The expectation of the second-order Taylor expansion of $V(\mathbf{x}_t)$ with respect to the state variable is as following,

$$\mathbb{E}_{\mathbb{Q}}[V(\mathbf{x}_k + \delta)] = V(\mathbf{x}_k) + \Delta(\mathbf{f}^T + \mathbf{u}^T \mathbf{G}^T)V_x(\mathbf{x}_k). \tag{4}$$

Under the small enough sampling step Δ , the Bellman principle can be used to approximate the value equation as a recursive equation,

$$V(\mathbf{x}_k, k) = \min_{\mathbf{u}} \{ \Delta(q(\mathbf{x}_k) + \frac{1}{2} \mathbf{u}^T \mathbf{R} \mathbf{u}) + \mathbb{E}_{\mathbb{Q}}[V(\mathbf{x}_k + \Delta \mathbf{f} + \Delta \mathbf{G} \mathbf{u}, k + 1)] \}. \tag{5}$$

Substituting the Eq. (4) into Eq. (5), the optimal control input can be derived under unconstrained conditions. Then, calculating the limits respect to time, we can derive the Hamilton-Jocabi-Bellman (HJB) equation as following,

$$V_t(\mathbf{x}_t, t) = q(\mathbf{x}_t, t) + \mathbf{f}(\mathbf{x}_t, t)^T V_x - \frac{1}{2} V_x^T \mathbf{G} \mathbf{R}^{-1} \mathbf{G}^T V_x. \tag{6}$$

Normally, it is difficult to solve this backward PDE due to the curse of dimensionality. The path integral control scheme provides an elegant method to derive the optimal control distribution based on Feynman Kac lemma [3]. It allows to represent the solution of the PDE as an exception of a stochastic function,

$$V(\mathbf{x}_t, t) = -\lambda \log(\mathbb{E}_{\mathbb{P}}[\exp(-\frac{1}{\lambda} S(\tau))]), \tag{7}$$

where $S(\tau)$ is the state-dependent cost function. Supposing that we have known the probability density function $q^*(\mathbf{u}|U, \sigma)$ of the optimal control distribution \mathbb{Q}^* , the optimal control inputs at each sampling step t can be generated through sampling from \mathbb{Q}^* .

$$\mathbf{u}_t^* = \mathbb{E}_{\mathbb{Q}^*}[\hat{\mathbf{u}}_t] \quad \forall t \in 0, 1, \dots, T - 1. \tag{8}$$

However, it's inaccessible to explicitly provide the optimal control distribution because the precise environment models cannot be established for autonomous vehicles. So we cannot directly sample from the optimal control distribution. Importance sampling (IS) can be utilized to sample from another known distribution $\mathbb{Q}_{\hat{U}, \sigma}$ and monte carlo (MC) method can be utilized to provide the unbiased estimation of the optimal control sequence.

$$\begin{aligned} \mathbb{E}_{\mathbb{Q}^*}[\hat{\mathbf{u}}_t] &= \int q^*(\mathbf{u}|U, \sigma) \hat{\mathbf{u}}_t d\hat{\mathbf{u}} \\ &= \int w(\mathbf{u}) q(\mathbf{u}|\hat{U}, \sigma) \hat{\mathbf{u}}_t d\hat{\mathbf{u}} \\ &= \mathbb{E}_{\mathbb{Q}_{\hat{U}, \sigma}}[w(\mathbf{u}) \hat{\mathbf{u}}_t], \end{aligned} \tag{9}$$

where $w(\mathbf{u}) = \frac{q^*(\mathbf{u}|U, \sigma)}{q(\mathbf{u}|\hat{U}, \sigma)}$ is the IS weight.

Providing the optimal control distribution as follows [6],

$$q^*(\mathbf{u}) = \frac{1}{\eta} \exp(-\frac{1}{\lambda} S(\mathbf{u})) p(\mathbf{u}), \quad \eta = \int \exp(-\frac{1}{\lambda} S(\mathbf{u})) p(\mathbf{u}) d\mathbf{u}, \tag{10}$$

where $p(\mathbf{u}) = q(\mathbf{u}|\hat{U}, \sigma)$ is the base distribution. Substituting Eq. (10) into IS weight and abandoning the non-optimization elements, we can estimate the IM weight as following,

$$\begin{aligned}
 w(\mathbf{u}) &= \frac{\exp(-\frac{1}{\lambda}S(\mathbf{u}) - \sum_{t=0}^{T-1}(\hat{\mathbf{u}}_t - \tilde{\mathbf{u}}_t)^T \sigma^{-1} \mathbf{v}_t)}{\int \exp(\sum_{t=0}^{T-1}((\hat{\mathbf{u}}_t - \tilde{\mathbf{u}}_t)^T \sigma^{-1} \mathbf{v}_t))q(\mathbf{u}|\hat{U}, \sigma) \exp(-\frac{1}{\lambda}S(\mathbf{u}))} \\
 &= \frac{\exp(-\frac{1}{\lambda}S(\mathbf{u}) - \sum_{t=0}^{T-1}(\hat{\mathbf{u}}_t - \tilde{\mathbf{u}}_t)^T \sigma^{-1} \mathbf{v}_t)}{\int q(\mathbf{u}|\hat{U}, \sigma) \exp(-\frac{1}{\lambda}S(\mathbf{u}) - \sum_{t=0}^{T-1}(\hat{\mathbf{u}}_t - \tilde{\mathbf{u}}_t)^T \sigma^{-1} \mathbf{v}_t)}
 \end{aligned} \tag{11}$$

The computational cost evaluations of MPPI with NLP and single loop linear MPC are provided in Table 1.

Table 1. Computational Cost Evaluation

Method	Number of nonzeros in Lagrangian Hessian	Execution time (s)
Decoupling (MPPI)	41	0.01+0.001
Decoupling (NLP)	439	0.0209 + 0.001
L-MPC (Single loop)	610	0.032

3.2 Attitude Regulator

In the decoupled cascade control scheme, the master controller, i.e., translational regulator, provides the set point for the slave controller (attitude regulator). Then the attitude regulator manipulates the steering mechanism to guide the vehicle to achieve desired yaw rate and sideslip angle. Methods that do not consider the side-slip angle probably lead to non-zero steady-state yawing error and poor performance when driving in the tight radii curves [2]. The tangent direction of the reference path is commonly chosen as the desired heading angle of the attitude controller in these methods. We take the side-slip angle into consideration through designing a MPC based output regulator and generate the transient profile for output regulator to improve the transient response and the driving comfort. The finite-time optimal control problem is transformed into a standard quadratic program (QP).

4 Result

J-shape path consisting of a straight line with a length of 70 m and an arc with a radius of 47.8 m is fed as the reference path. The vehicle is controlled at a speed of 36 km/h. Figure 3 shows the simulation results of proposed decoupling ORMPC (D-ORMPC), compared with Error-based MPC (E-MPC) and its variants (PMPC) with a preview item of path curvatures.

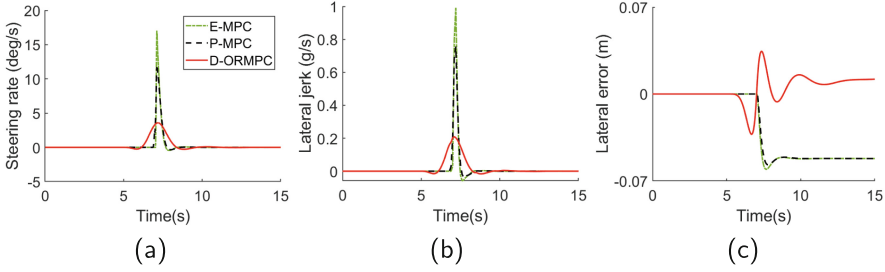


Fig. 3. Simulation results in J-shape path. (a) Steering rate. (b) Lateral jerk. (c) Lateral tracking error. Simulation results of steering rate and lateral jerk show that our method achieves more elegant steering without sacrificing tracking accuracy.

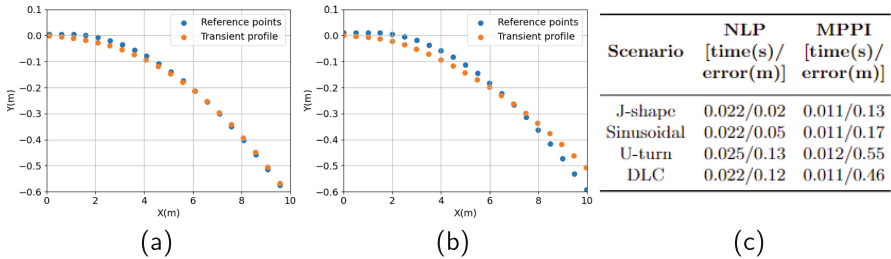


Fig. 4. (a) Transient profile generated by NLP in Sinusoidal path at one sampling interval. (b) Transient profile generated by MPPI. (c) Solving time and tracking error comparisons in different driving scenario.

More comparisons about MPPI with NLP are presented in Fig. 4. In all four driving scenarios, two controllers share the same control parameters, which prove the proposed scheme achieves good parameters adaptability. The results show that the tracking performance of MPPI deteriorates in tight radii curves, which is mainly because it does not sample sufficiently in action space and there is a bias in the estimation of state value.

References

- Borrelli, F., Falcone, P., Keviczky, T., Asgari, J., Hrovat, D.: MPC-based approach to active steering for autonomous vehicle systems. *Int. J. Veh. Auton. Syst.* **3**(2–4), 265–291 (2005). <https://doi.org/10.1504/IJVAS.2005.008237>
- Hu, C., Wang, R., Yan, F., Chen, N.: Should the desired heading in path following of autonomous vehicles be the tangent direction of the desired path? *IEEE Trans. Intell. Trans. Syst.* **16**(6), 3084–3094 (2015)
- Karatzas, I., Shreve, S.E.: *Stochastic Integration*, pp. 128–238. Springer, New York (1998). <https://doi.org/10.1007/978-1-4612-0949-2>
- Laurense, V.A., Gerdes, J.C.: Long-horizon vehicle motion planning and control through serially cascaded model complexity. *IEEE Trans. Control Syst. Technol.* **30**(1), 166–179 (2022). <https://doi.org/10.1109/TCST.2021.3056315>

5. Raffo, G.V., Gomes, G.K., Normey-Rico, J.E., Kelber, C.R., Becker, L.B.: A predictive controller for autonomous vehicle path tracking. *IEEE Trans. Intell. Trans. Syst.* **10**(1), 92–102 (2009). <https://doi.org/10.1109/TITS.2008.2011697>
6. Williams, G., Drews, P., Goldfain, B., Rehg, J.M., Theodorou, E.A.: *Information theoretic model predictive control: theory and applications to autonomous driving* (2017)

Open Access This chapter is licensed under the terms of the Creative Commons Attribution 4.0 International License (<http://creativecommons.org/licenses/by/4.0/>), which permits use, sharing, adaptation, distribution and reproduction in any medium or format, as long as you give appropriate credit to the original author(s) and the source, provide a link to the Creative Commons license and indicate if changes were made.

The images or other third party material in this chapter are included in the chapter's Creative Commons license, unless indicated otherwise in a credit line to the material. If material is not included in the chapter's Creative Commons license and your intended use is not permitted by statutory regulation or exceeds the permitted use, you will need to obtain permission directly from the copyright holder.





A Learning-Based Model Predictive Contouring Control for Vehicle Evasive Manoeuvres

Alberto Bertipaglia¹ (✉) , Mohsen Alirezaei² , Riender Happee¹,
and Barys Shyrokau¹ 

¹ Delft University of Technology, 2628 CD Delft, The Netherlands
{A.Bertipaglia,R.Happee,B.Shyrokau}@tudelft.nl

² Siemens PLM Software, 5708 JZ Helmond, The Netherlands
mohsen.alirezaei@siemens.com

Abstract. This paper presents a novel Learning-based Model Predictive Contouring Control (L-MPCC) algorithm for evasive manoeuvres at the limit of handling. The algorithm uses the Student-t Process (STP) to minimise model mismatches and uncertainties online. The proposed STP captures the mismatches between the prediction model and the measured lateral tyre forces and yaw rate. The mismatches correspond to the posterior means provided to the prediction model to improve its accuracy. Simultaneously, the posterior covariances are propagated to the vehicle lateral velocity and yaw rate along the prediction horizon. The STP posterior covariance directly depends on the variance of observed data, so its variance is more significant when the online measurements differ from the recorded ones in the training set and smaller in the opposite case. Thus, these covariances can be utilised in the L-MPCC's cost function to minimise the vehicle state uncertainties. In a high-fidelity simulation environment, we demonstrate that the proposed L-MPCC can successfully avoid obstacles, keeping the vehicle stable while driving a double lane change manoeuvre at a higher velocity than an MPCC without STP. Furthermore, the proposed controller yields a significantly lower peak sideslip angle, improving the vehicle's manoeuvrability compared to an L-MPCC with a Gaussian Process.

Keywords: Learning-based model predictive control · Student-t process · Evasive manoeuvre · Obstacle avoidance · Limit of handling

1 Introduction

A crucial safety element of automated driving is to prove the capacity to avoid obstacles at the limit of handling. A common solution is based on Nonlinear

The Dutch Science Foundation NWO-TTW supports the research within the EVOLVE project (nr. 18484). European Union's Horizon 2020 research and innovation programme under the Marie Skłodowska-Curie actions, under grant agreement (nr. 872907).

Model Predictive Control (NMPC), which optimises the steering angle and the longitudinal force of a vehicle. However, in such scenarios, where longitudinal and lateral dynamics are coupled, the uncertainties and inaccuracies due to the tyre's non-linear behaviour pose a particularly challenging problem [1, 2]. Therefore, we focus on developing a Student-t Process (STP) combined with a Model Predictive Contouring Control (MPCC), which improves the prediction model, reducing the tyre model mismatches and minimising the vehicle lateral state uncertainties. An L-MPCC based on a sparse Gaussian Process (GP) has recently been proposed for lap-time optimisation [4]. It leverages the capacity of the GP to predict the mismatches between the prediction model and the measured vehicle states: longitudinal and lateral velocity and yaw rate. Furthermore, the vehicle is constrained inside the track, tightening the track boundaries with the vehicle position uncertainty. The latter is first computed as the GP's posterior covariance, then open-loop propagated along the prediction horizon using successive linearisation similar to an Extended Kalman Filter (EKF) [4]. However, the propagated position uncertainty can increase exponentially over the prediction horizon, strongly limiting or eliminating the allowable driving area. This results in a very conservative controller. A possible alternative is to consider the uncertainty in the vehicle velocity states rather than in the vehicle position [3]. For instance, the NMPC cost function can be extended by the vehicle lateral velocity and yaw rate variance. Thus, the latter can be minimised to reduce the operating time in the unstable region of the vehicle. However, these variances are computed and propagated by linearising the prediction model with a constant tyre model uncertainty optimised offline. This simplification does not consider the remarkably different accuracy of the tyre model in different operating regions, and therefore, it does not reduce the prediction model mismatches in all regions.

We propose an L-MPCC based on an STP, which predicts the mismatches between the prediction model and the vehicle yaw rate and the lateral tyre forces measured by intelligent (force sensing) bearings [5]. The proposed controller minimises the vehicle's operating time at unstable working points, thanks to the STP posterior covariance of the tyre forces. The latter ones are used to compute and propagate the vehicle lateral state uncertainties along the prediction horizon.

The contributions of this paper are threefold. The first is the development of the L-MPCC based on an STP, which directly reduces the prediction model mismatches in the tyre model rather than in the vehicle velocity states typically used [4]. This results in successfully performing evasive manoeuvres at 8.5% higher velocity than the current state-of-the-art MPCC [1]. The second contribution is related to the STP, which improves the outlier resistance of the state-of-the-art GP. Furthermore, the STP posterior covariance depends on the observed measurements, providing a higher variance than a GP for operating points different than in the training set and a lower one in the opposite situation [8]. The third contribution is improving the vehicle stability by reducing the sideslip angle peak of a 76% during an evasive manoeuvre, thanks to the reduction of the model mismatches and the minimisation of the vehicle lateral

state uncertainties. Thus, the controller decreases the time the vehicle spends in operating points close to the vehicle’s handling limits.

2 Learning-Based Model Predictive Contouring Control

The proposed L-MPCC controller is based on an MPCC for obstacle avoidance at the limit of handling [1]. The prediction model is a nonlinear single-track vehicle model. The Cartesian reference system describes the vehicle kinematics, as the contouring formulation requires. The vehicle dynamics, the longitudinal (v_x) and lateral (v_y) velocity, and the vehicle yaw rate (r) are described as follows:

$$\begin{cases} \dot{v}_x = \frac{(F_{x,F} \cos(\delta) - (F_{y,F} + \Delta F_{y,F}) \sin(\delta) + F_{x,R} - F_{drag})}{m} + (r + \Delta r) v_y \\ \dot{v}_y = \frac{(F_{x,F} \sin(\delta) + (F_{y,F} + \Delta F_{y,F}) \cos(\delta) + F_{y,R} + \Delta F_{y,R})}{m} - (r + \Delta r) v_x \\ \dot{r} = \frac{((F_{y,F} + \Delta F_{y,F}) \cos(\delta) l_f - (F_{y,R} + \Delta F_{y,R}) l_r + F_{x,F} \sin(\delta) l_f)}{I_{zz}} \end{cases} \quad (1)$$

where the road-wheel angle (δ) and the longitudinal force at the front ($F_{x,F}$) and rear axle ($F_{x,R}$). The lateral front and rear tyre forces, respectively $F_{y,F}$ and $F_{y,R}$, are computed using validated Fiala tyre model [2]. However, during an evasive manoeuvre, the prediction model inaccuracies can increase significantly, so the model mismatches of the front ($\Delta F_{y,F}$) and rear ($\Delta F_{y,R}$) lateral tyre forces and the yaw rate (Δr) are computed by an STP.

The proposed L-MPCC cost function is responsible for ensuring path tracking, maintaining the physical feasibility of the control inputs, prioritising obstacle avoidance in case of collision risk, and minimising the uncertainties of the prediction model, thus limiting the operating time in nonlinear regions. The cost function (J) is defined as follows:

$$\begin{aligned} J = & \sum_{i=1}^N \left(\sum_{j=1}^{N_{Obs}} (q_{e_{Obs,j,i}} e_{Obs,j,i}^2) + \sum_{k=1}^{N_{Edg}} (q_{e_{Edg,ki}} e_{Edg,ki}^2) + q_{\delta} \delta_i^2 + q_{\dot{F}_x} \dot{F}_{x,i}^2 \right. \\ & \left. + q_{e_{Con}} e_{Con,i}^2 + q_{e_{Lag}} e_{Lag,i}^2 + q_{e_{Vel}} e_{Vel}^2 \right) + \sum_{j=1}^{N_{Prob}} \left(q_{\sigma_r} \sigma_{r,j}^2 + q_{\sigma_{v_y}} \sigma_{v_y,j}^2 \right) \end{aligned} \quad (2)$$

where N is the length of the prediction horizon, N_{Obs} and N_{Edg} are respectively the number of obstacles and road edges, and $q_{e_{Obs}}$, e_{Obs} , $q_{e_{Edg}}$ and e_{Edg} are used to prioritise obstacle avoidance and keeping the vehicle away from the road edges in case of emergency [1]. The tracking performance is ensured by the minimisation of the contouring (e_{Con}), lag (e_{Lag}) and velocity e_{Vel} errors with their respective cost terms, i.e. $q_{e_{Con}}$, e_{Lag} , $q_{e_{Vel}}$. The lateral velocity and yaw rate uncertainties are minimised through the σ_{v_y} and σ_r parameters of the cost function. The σ_{v_y} and σ_r are propagated open-loop, so they can increase rapidly, potentially overpowering the other elements of the cost function. To avoid the problem, they are propagated not over the entire prediction horizon, $N = 30$, but only for the reduced horizon $N_{Prob} = 20$ [4]. Furthermore, the cost parameters,

$q_{\sigma_{v_y}}$ and q_{σ_r} , are tuned not to exceed the cost related to obstacle avoidance prioritisation. Therefore, the proposed controller pushes the vehicle to work at operating points close to normal driving. However, it allows the vehicle to drive at operating points close to the handling limits if it helps avoid a collision.

3 Student-T Process and Uncertainty Propagation

This study uses an STP as a stochastic process with a Laplace inference to estimate model mismatches and uncertainties for two reasons. First, the Student-t distribution allows the algorithm to define the level of Kurtosis, reducing the influence of the outliers and improving the accuracy of the predictions [7,9]. The robustness to outliers is an essential property for L-MPCC, which relies on online measurements with sensor noise. For instance, a single outlier can highly influence the GP prediction; pushing the posterior means far away from the level of the other observations, which is not the case in an STP [9]. The second reason is that the STP posterior covariance directly depends on the observed measurements and not only on the location of the observed measurements. This implies that the covariance increases when the measurements vary more than expected, i.e., a higher difference between training and test sets, and vice-versa decreases when the difference is lower [7,8]. Once again, this is an essential property for an L-MPCC, which can work in conditions with a high discrepancy from the training scenario. Regarding the kernel selection, this work opts for the automatic relevance determination Matérn 5/2 function due to its generalisation capabilities and interpretability properties. The STP is implemented using the GPML Matlab Code version 4.2 [6].

We predict the $\Delta F_{y,F}$, $\Delta F_{y,R}$ and Δr model mismatches, rather than the errors in v_x and v_y as usually done in literature [4] because it allows the reduction of the mismatches in a proactive way. It also directly targets the source of the errors, i.e., the tyre forces, and not the states that depend on them. This is possible thanks to the availability of tyre lateral forces at the front and rear axle, measured by the intelligent bearings [5], the vehicle yaw rate and the control inputs F_x and δ . Thus, we assume that the discrepancies are independent of the vehicle position [4] and that the velocity states, not measurable through the standard sensor setup for passenger vehicles, are entirely dependent on the tyre forces. The training data is derived from the algebraic difference between the measurements and the nominal model predictions. The training set is composed of 2 double lane changes at respectively 55 km/h and 80 km/h, and a double lane change with collision avoidance prioritisation at 55 km/h. The manoeuvres are selected to identify the mismatches in the linear and nonlinear regions of the vehicle. The test set comprises a double lane change at 60 km/h and the same manoeuvre with collision prioritisation. Despite the high prediction model accuracy and the reduction of the model mismatches, some unmodeled effects can still influence the prediction model. These are captured by the STP posterior covariance for the front and rear lateral tyre force, respectively $\sigma_{F_{y,F}}$ and $\sigma_{F_{y,R}}$. Thus, the tyre forces are not only evaluated as a single point but also as a

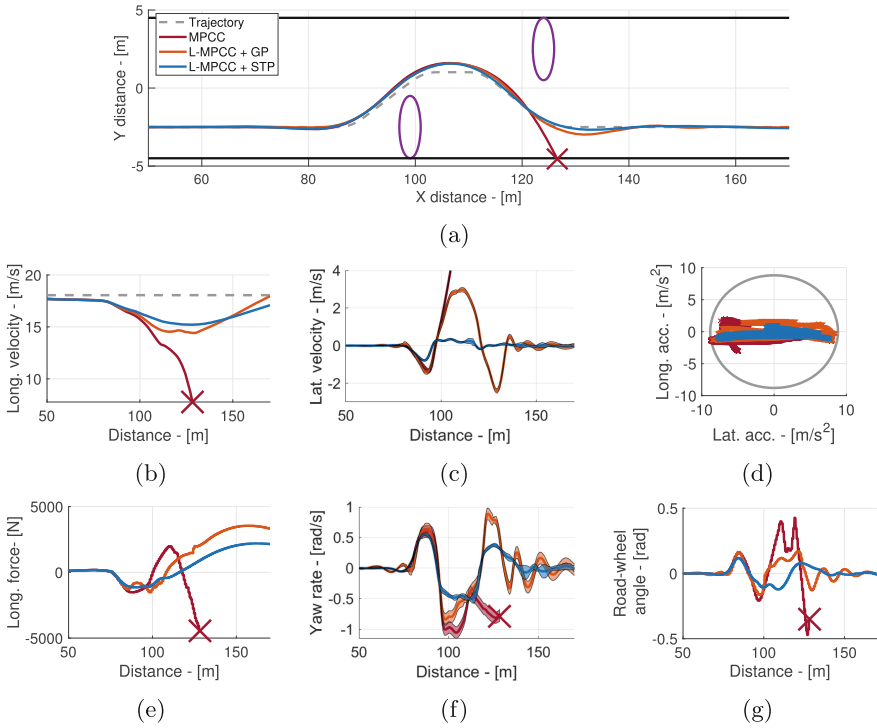


Fig. 1. States and control inputs in a double lane change.

distribution [3]. The STP variance and degrees of freedom are transformed and simplified into a Gaussian variance to be able to propagate it through the prediction horizon and relate them to the lateral states related to vehicle stability, i.e. v_y and r , using a procedure similar to an EKF [3,4].

4 Results

Figure 1 shows the performance of the evaluated controllers in a double lane change with collision avoidance prioritisation at 65 km/h. Figure 1a shows that only the learning-based controllers can successfully avoid the two obstacles and stay inside the road track. Vice versa, the MPCC baseline [1] leaves the track on the right side at 130 m. The improvement is due to reduced model mismatches in the L-MPCC. For instance, the proposed L-MPCC+STP reduces the root mean square of the $F_{y,F}$, $F_{y,R}$ and r mismatches by respectively 33.14%, 24.85% and 60.61% compared to the MPCC and further 20.14%, 11.85% and 61.33% with respect to the L-MPCC+GP. This proves the importance of implementing an STP rather than a GP to predict the model mismatches. The enhanced performance of the proposed controller is also visible from the reduction of the vehicle lateral velocity peak; see Fig. 1c. Furthermore, the L-MPCC+STP can reduce the

lateral velocity and, consequently, the sideslip angle peak by 76%, maintaining an overall higher velocity during the manoeuvre than the L-MPCC+GP. Figures 1c and 1f show that the vehicle sideslip angle reduction and the increased operating time in the stable vehicle behaviour are not only due to the lower model mismatches but also to the reduced uncertainties for the vehicle lateral states. However, it has a lower vehicle longitudinal acceleration when the obstacle avoidance manoeuvre is over to achieve the desired velocity, Fig. 1e.

5 Conclusions

This paper presented a novel Learning-based Model Predictive Contouring Control based on a Student-t Process for evasive manoeuvres with an online minimisation of model mismatches and uncertainties. In a high-fidelity simulation environment, we demonstrate that our proposed controller successfully avoids obstacles, keeping the vehicle stable while driving a double-lane change manoeuvre at a higher velocity compared to a non-learning-based baseline. Furthermore, the proposed controller reduces the peak of vehicle sideslip angle by 76%. The performance enhancement is due to the properties of the Student-t Process, which can further reduce the prediction model mismatches and better capture the vehicle state uncertainties. Future work involves the proposed controller implementation on rapid prototyping hardware to prove its real-time capability.

References

1. Bertipaglia, A., Alirezai, M., Happee, R., Shyrokau, B.: Model predictive contouring control for vehicle obstacle avoidance at the limit of handling. arXiv preprint [arXiv:2308.06742](https://arxiv.org/abs/2308.06742) (2023)
2. Bertipaglia, A., et al.: Model predictive contouring control for vehicle obstacle avoidance at the limit of handling using torque vectoring. arXiv preprint [arXiv:2405.10847](https://arxiv.org/abs/2405.10847) (2024)
3. Brown, M., Gerdes, J.C.: Robust stabilization and collision avoidance through minimizing open-loop velocity uncertainty. In: IEEE Intelligent Vehicles Symposium, pp. 259–264 (2020)
4. Kabzan, J., Hewing, L., Liniger, A., Zeilinger, M.N.: Learning-based model predictive control for autonomous racing. *IEEE Robot. Autom. Lett.* **4**(4), 3363–3370 (2019)
5. Kerst, S., Shyrokau, B., Holweg, E.: A model-based approach for the estimation of bearing forces and moments using outer ring deformation. *IEEE Trans. Industr. Electron.* **67**(1), 461–470 (2020)
6. Rasmussen, C.E., Nickisch, H.: Gaussian processes for machine learning toolbox. *J. Mach. Learn. Res.* **11**, 3011–3015 (2010)
7. Shah, A., Wilson, A., Ghahramani, Z.: Student-t processes as alternatives to gaussian processes. In: Artificial Intelligence and Statistics, pp. 877–885 (2014)
8. Tracey, B.D., Wolpert, D.: Upgrading from gaussian processes to student-T processes. In: AIAA Non-Deterministic Approaches Conference, p. 1659 (2018)
9. Vanhatalo, J., Jylänki, P., Vehtari, A.: Gaussian process regression with student-T likelihood. In: Advances in Neural Information Processing Systems, vol. 22 (2009)

Open Access This chapter is licensed under the terms of the Creative Commons Attribution 4.0 International License (<http://creativecommons.org/licenses/by/4.0/>), which permits use, sharing, adaptation, distribution and reproduction in any medium or format, as long as you give appropriate credit to the original author(s) and the source, provide a link to the Creative Commons license and indicate if changes were made.

The images or other third party material in this chapter are included in the chapter's Creative Commons license, unless indicated otherwise in a credit line to the material. If material is not included in the chapter's Creative Commons license and your intended use is not permitted by statutory regulation or exceeds the permitted use, you will need to obtain permission directly from the copyright holder.





Predictive Braking on a Nonplanar Road

Thomas Fork¹(✉), Francesco Camozzi², Xiao-Yu Fu², and Francesco Borrelli¹

¹ University of California at Berkeley, Berkeley, CA 94708, USA
{fork, fborrelli}@berkeley.edu

² Brembo Inspiration Lab, Sunnyvale, CA 94089, USA
{FCamozzi, XFu}@us.brembo.com

Abstract. We present an approach for predictive braking of a four-wheeled vehicle on a nonplanar road. Our main contribution is a methodology to consider friction and road contact safety on general smooth road geometry. We use this to develop an active safety system to preemptively reduce vehicle speed for upcoming road geometry, such as off-camber turns. Our system may be used for human-driven or autonomous vehicles and we demonstrate it with a simulated ADAS scenario. We show that loss of control due to driver error on nonplanar roads can be mitigated by our approach.

Keywords: Active Safety Systems · Predictive Control · Road Models

1 Introduction

Nonplanar road geometry plays a major role in the behaviour and safety of ground vehicles that operate in such environments. Operating limits due to road adherence change while new effects appear, such as losing contact when cresting a hill. This paper develops an approach to consider these effects generally on a smooth nonplanar road surface. We develop a novel predictive safety system algorithm for safe vehicle operation on nonplanar road geometry. We show that our safety system maintains safe vehicle speed on a simulated off-camber turn.

This manuscript addresses gaps in current ADAS systems in the treatment of road geometry. Namely, most solutions are designed for flat roads [6, 8]. Approaches that consider more complicated geometry limit their considerations to road curvature, slope, and bank [1, 7]. These variables are not sufficient to describe roads with curved cross-section and subsequent analysis of vehicle safety is simplified in existing literature. The work in [1] ignores changes in vehicle orientation due to road slope and bank when assessing rollover and friction limits. Furthermore, centripetal effects, such as a vehicle driving over a crest or off-camber turn, are absent. The authors of [7] consider changes in the components of gravity on a vehicle due to slope but not bank angle, and weight distribution of the vehicle is not considered for rollover prevention.

Supported by Brembo Inspiration Lab.

© The Author(s) 2024

G. Mastinu et al. (Eds.): AVEC 2024, LNME, pp. 639–645, 2024.

https://doi.org/10.1007/978-3-031-70392-8_90

This paper presents a new active safety system for predictive braking on nonplanar roads which addresses these shortcomings in a systematic and general manner applicable to general, smooth nonplanar road surfaces.

2 Vehicle Operating Limits

We consider three operating limits for a single-body vehicle on a smooth road surface: Tire friction, road contact, and velocity continuity. The last refers to the inability instantly change vehicle speed, and is necessary to anticipate vehicle behaviour on variable road geometry. To consider road geometry in a general sense we use the road model developed in [2], which we introduce and use next (Fig. 1).

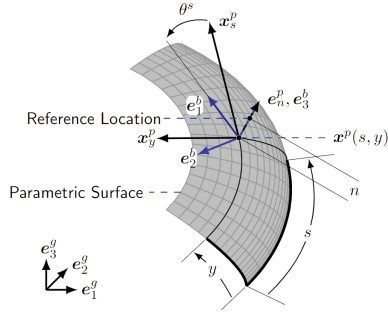


Fig. 1. Parametric road surface \mathbf{x}^p . Coordinates s , y , and θ^s describe vehicle pose relative to the surface.

2.1 Nonplanar Road Model

The paper [2] extends the approach of modeling a car as a body tangent to and in contact with a surface to a general parametric surface. The road surface \mathbf{x}^p is parameterized by coordinates s and y , which then describe a vehicle positioned at normal offset n from the road. Vehicle orientation is described by the angle θ^s between the longitudinal vehicle axis \mathbf{e}_1^b and the s tangent vector of the surface: \mathbf{x}_s^p . Surface coordinates may be chosen flexibly, such as to follow the center of a lane. The main results hold for any surface parameterization and are:

$$\begin{bmatrix} \dot{s} \\ \dot{y} \end{bmatrix} = (\mathbf{I} - n\mathbf{II})^{-1} \mathbf{J} \begin{bmatrix} v_1^b \\ v_2^b \end{bmatrix} \quad \begin{bmatrix} -\omega_2^b \\ \omega_1^b \end{bmatrix} = \mathbf{J}^{-1} \mathbf{II} (\mathbf{I} - n\mathbf{II})^{-1} \mathbf{J} \begin{bmatrix} v_1^b \\ v_2^b \end{bmatrix}. \quad (1a)$$

$$\dot{\theta}^s = \omega_3^b + \frac{(\mathbf{x}_{ss}^p \times \mathbf{x}_s^p) \cdot \mathbf{e}_n^p}{\mathbf{x}_s^p \cdot \mathbf{x}_s^p} \dot{s} + \frac{(\mathbf{x}_{yy}^p \times \mathbf{x}_s^p) \cdot \mathbf{e}_n^p}{\mathbf{x}_s^p \cdot \mathbf{x}_s^p} \dot{y} \quad (1b)$$

Here v_i^b and ω_i^b are the ISO body frame components of a vehicle’s linear and angular velocity. \mathbf{I} and \mathbf{II} are the first and second fundamental forms of \mathbf{x}^p , with partial derivatives of \mathbf{x}^p denoted by subscripts. \mathbf{J} is the Jacobian between the body frame and \mathbf{x}^p , used here in the form of a Q-R decomposition:

$$\theta^p = -\sin^{-1} \left(\frac{\mathbf{x}_s^p \cdot \mathbf{x}_y^p}{\|\mathbf{x}_s^p\| \|\mathbf{x}_y^p\|} \right) \quad \mathbf{Q} = \begin{bmatrix} \|\mathbf{x}_s^p\| & 0 \\ -\sin(\theta^p) \|\mathbf{x}_y^p\| & \cos(\theta^p) \|\mathbf{x}_y^p\| \end{bmatrix} \quad (2a)$$

$$\mathbf{J} = \begin{bmatrix} \mathbf{x}_s^p \cdot \mathbf{e}_1^b & \mathbf{x}_s^p \cdot \mathbf{e}_2^b \\ \mathbf{x}_y^p \cdot \mathbf{e}_1^b & \mathbf{x}_y^p \cdot \mathbf{e}_2^b \end{bmatrix} = \mathbf{Q} \begin{bmatrix} \cos \theta^s & -\sin \theta^s \\ \sin \theta^s & \cos \theta^s \end{bmatrix}. \quad (2b)$$

The Q-R form for \mathbf{J} simplifies expressions in this manuscript, while Eq. (1) captures nonplanar behaviour. Coriolis forces and moments on the vehicle will follow from part of the Newton Euler equations:

$$F_1^b = m(\dot{v}_1^b - \omega_3^b v_2^b) \quad F_2^b = m(\dot{v}_2^b + \omega_3^b v_1^b) \quad F_3^b = m(\omega_1^b v_2^b - \omega_2^b v_1^b) \quad (3)$$

$$K_1^b = I_1^b \dot{\omega}_1^b + (I_3^b - I_2^b) \omega_2^b \omega_3^b \quad K_2^b = I_2^b \dot{\omega}_2^b + (I_1^b - I_3^b) \omega_3^b \omega_1^b \quad (4)$$

$v_3^b = 0$ per the road model [2] and thus is not present. For motion planning purposes, we will describe vehicle velocity using signed speed v , sideslip angle β , and rates of change of θ^s and β proportional to v as follows:

$$v_1^b = v \cos(\beta) \quad v_2^b = v \sin \beta \quad \dot{\theta}^s = \kappa^s v \quad \dot{\beta} = \kappa^\beta v \quad (5)$$

Expressions for \dot{v}_1^b and \dot{v}_2^b follow via standard calculus. v^2 and \dot{v} will be decision variables in our safety system, with s , y , θ^s , β , κ^s , and κ^β treated as parameters. These choices will allow our safety system to be implemented as a convex optimization problem. Another result is an expression for ω_3^b from $\dot{\theta}^s$ using (1):

$$\omega_3^b = \kappa^s v - \frac{(\mathbf{x}_{ss}^p \times \mathbf{x}_s^p) \cdot \mathbf{e}_n^p}{\mathbf{x}_s^p \cdot \mathbf{x}_s^p} \dot{s} - \frac{(\mathbf{x}_{yy}^p \times \mathbf{x}_s^p) \cdot \mathbf{e}_n^p}{\mathbf{x}_s^p \cdot \mathbf{x}_s^p} \dot{y} \quad (6)$$

2.2 Friction Cone Constraint

Using (3), constraint (1a), and (5), the net vehicle normal force is:

$$F_3^b = mv^2 [\cos(\beta + \theta^s) \sin(\beta + \theta^s)] \mathbf{Q}^{-1} \mathbf{\Pi} (\mathbf{I} - n\mathbf{\Pi})^{-1} \mathbf{Q} \begin{bmatrix} \cos(\beta + \theta^s) \\ \sin(\beta + \theta^s) \end{bmatrix} \quad (7)$$

F_3^b is linear in v^2 , meaning the net normal tire force (F_3^t) is affine in v^2 for a given s , y , and θ^s as gravity forces are constant (found in [2]) and aerodynamic forces are often approximated as linear in v^2 .

Linear expressions for F_1^b and F_2^b follow from the same equation blocks used to derive (7) and are not expanded here. As a result, net longitudinal and lateral tire forces F_1^t and F_2^t are affine in \dot{v} and v^2 by the same assumptions. The complete friction cone constraint is then:

$$\|F_1^t \ F_2^t\|_2 \leq \mu F_3^t \quad (8)$$

where μ is a road adherence parameter. This constraint is a convex second order cone constraint as the tire forces are affine functions of \dot{v} and v^2 .

2.3 Road Contact Constraint

Enforcing road contact requires modeling weight distribution, which requires modeling the roll and pitch moment on the vehicle. These follow from (4), where the $\omega_{1,2,3}^b$ coefficients are linear in v due to (1a) and (6). For $\dot{\omega}_{1,2}^b$ we use the approximation from [2] that

$$\begin{bmatrix} -\dot{\omega}_2^b \\ \dot{\omega}_1^b \end{bmatrix} \approx \mathbf{J}^{-1} \mathbf{II} (\mathbf{I} - n\mathbf{II})^{-1} \mathbf{J} \begin{bmatrix} \dot{v}_1^b \\ \dot{v}_2^b \end{bmatrix}. \tag{9}$$

Expansion of (4) using (1), (5), (6), and (9) provides expressions for roll and pitch moments K_1^b and K_2^b . These are linear in v^2 and \dot{v} and omitted for brevity. For weight distribution we consider moments from tire normal forces. The dominant source of other moments are longitudinal and lateral tire forces, which produce moments about the height of the center of mass h . Moments due to tire normal forces K_1^N and K_2^N are then:

$$K_1^N = K_1^b - F_2^t h \qquad K_2^N = K_2^b + F_1^t h \tag{10}$$

These are affine in v^2 and \dot{v} , and may be extended to include v^2 terms for aerodynamic moments. To model the forces on individual tires, we use the load-transfer model of [4] with wheelbase dimensions in Fig. 2:

$$N_f = \frac{F_3^t l_r - K_2^N}{l_r + l_f} \qquad N_r = \frac{F_3^t l_f + K_2^N}{l_r + l_f} \qquad \delta = \frac{K_1^N}{2(t_f^2 + t_r^2)} \tag{11a}$$

$$N_{fr} = N_f - \delta t_f \quad N_{fl} = N_f + \delta t_f \quad N_{rr} = N_r - \delta t_r \quad N_{rl} = N_r + \delta t_r \tag{11b}$$

The four tire normal forces N_{fr} (front right) through N_{rl} (rear left) are affine in v^2 and \dot{v} , meaning that constraining them to be positive to avoid loss of road contact is a convex constraint:

$$N_{fr} \geq 0 \qquad N_{fl} \geq 0 \qquad N_{rr} \geq 0 \qquad N_{rl} \geq 0 \tag{12}$$

2.4 Velocity Continuity Constraints

To develop our safety system, friction cone and road contact constraints are introduced at fixed points in space in a multistage control problem presented next. These stages must be connected together with velocity constraints relating v^2 and \dot{v} at adjacent stages to capture vehicle speed changing over time. We use a midpoint integration scheme similar to [5]:

$$(v^2)^{k+1} = (v^2)^k + \frac{1}{2} (\dot{v}^k + \dot{v}^{k+1}) (l^{k+1} - l^k) \tag{13}$$

Here superscript k denotes the stage of the control problem, and l^k is the arc length traveled by a vehicle to reach stage k .

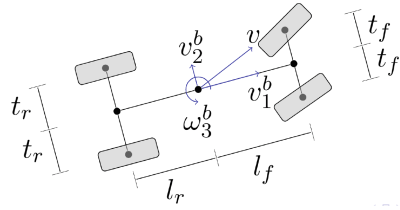


Fig. 2. Wheelbase dimensions used for weight distribution.

3 Active Safety System

We develop an active safety system with safety limits encoded by constraints (8), (12), and (13). These constraints are convex in v^2 and \dot{v} for fixed $s, y, \theta^s, \beta, \kappa^s$, and κ^β , which we respectively make decision variables and parameters for optimization problem (14). We introduce stages 0 through $N - 1$

$$\min_{(v^2)^k, \dot{v}^k} \sum_{k=0}^{N-1} \left| (F_1^t)^k - B \right| \tag{14a}$$

subject to Eq. (8) $\forall k$ (14b)

Eq. (12) $\forall k$ (14c)

Eq. (13) $\forall k$ (14d)

$$(v^2)^0 = (v_0)^2 \tag{14e}$$

with decision variables and parameters present at each stage. (13) constrains the speed between adjacent stages, while (8) and (12) constrain individual stages. We introduce parameter v_0 for initial speed of the vehicle, and B for a nominal brake force input. We use the objective function (14a) which is the total absolute difference between B and the longitudinal tire force at each stage.

The main output of this optimization problem is $F_1^t - B$ at each stage, which informs how much tire forces must change relative to B for continued safe vehicle operation. As an example application, B could be a pedal request from a driver and $F_1^t - B$ being nonzero indicates active safety measures must be taken, such as an automated brake procedure. Minimizing $F_1^t - B$ corresponds to intervening only when necessary, such as if a driver fails to slow down for an off-camber turn.

We note that the core novelty of this safety system is the nonplanar road safety constraints. These are not limited to speed-limiting applications, and may be used for active steering, suspension, and powertrain systems as well.

4 Simulation Environment

We tested our active safety system using a simulated lane-keeping scenario on a nonplanar road surface. We used a nonplanar two-track vehicle model with suspension motion based on [2] with a combined-slip Pacejka tire model [3]. Driver behaviour was simulated with a PI steering controller. Brake actuators and slip control were simulated with a proprietary Brembo model. We implemented our safety system (14) with parameters for each stage corresponding to following the center of a lane, with brake force targets handled by a nonplanar electronic brakeforce distribution (EBD) algorithm described here:

The core component of EBD is distributing a target brake force and moment over the four wheels of a car. This is fundamentally limited by the road adherence of each tire and any limits of the brake actuators. We consider weight distribution effects in a general manner by careful use of accelerometer data. The raw output of any accelerometer is proper acceleration, which is related to coordinate acceleration in an inertial frame via gravitational acceleration \mathbf{g} .

$$\mathbf{a}_{\text{proper}} = \mathbf{a}_{\text{coordinate}} - \mathbf{g} = \frac{1}{m} \mathbf{F}^b - \mathbf{g} \tag{15}$$

The far-right expression follows from Newtonian mechanics, telling us the accelerometer measures every force but gravity. We use this to estimate tire force components directly, which are used to compute the net normal force and moments in (11). The four normal forces then inform our EBD algorithm, which distributes target net brake force and moment over the four wheels.

Two test cases were considered: First, impulsive brake application after an initial delay, modeling a delayed driver. Second, driver brake application was removed and the test repeated with the active safety system present. All simulations used the same steering control, brake control, vehicle simulator, and road surface: a u-turn with a 30% off-camber bank.

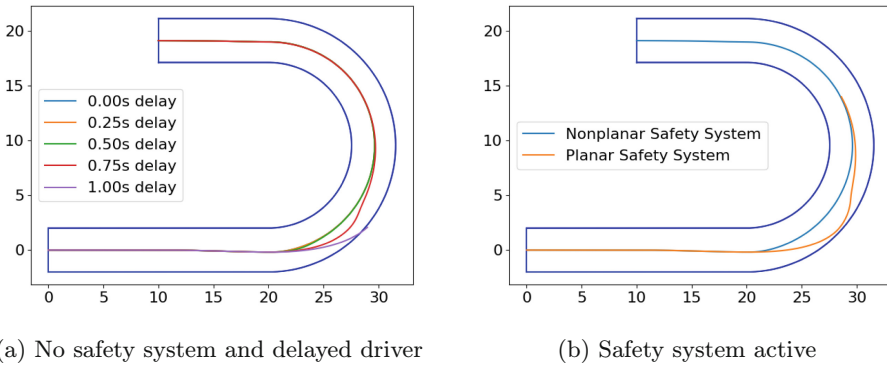


Fig. 3. Vehicle trajectories on nonplanar u-turn, starting from bottom left

5 Results and Conclusion

Closed loop vehicle trajectories with and without safety system are shown in Fig. 3. As evidenced in Fig. 3a, a proactive driver can maintain control of the vehicle, but must brake almost immediately to follow the lane. With the nonplanar safety system (Fig. 3b) no longitudinal driver intervention is necessary. However, implementation of the same system with a planar road model results in loss of control. Our safety system mitigates loss of control of a vehicle using knowledge of the road surface and intended vehicle motion.

References

1. Barreno, F., Santos, M., Romana, M.G.: A novel adaptive vehicle speed recommender fuzzy system for autonomous vehicles on conventional two-lane roads. *Expert Syst.* e13046 (2022)
2. Fork, T., Tseng, H.E., Borrelli, F.: Models for ground vehicle control on nonplanar surfaces. *Veh. Syst. Dyn.* 1–25 (2023)
3. Pacejka, H.: *Tire and Vehicle Dynamics*, 3rd edn. Butterworth-Heinemann (2012)

4. Rucco, A., Notarstefano, G., Hauser, J.: Development and numerical validation of a reduced-order two-track car model. *Eur. J. Control.* **20**(4), 163–171 (2014)
5. Verschuer, D., Demeulenaere, B., Swevers, J., De Schutter, J., Diehl, M.: Time-optimal path tracking for robots: a convex optimization approach. *IEEE Trans. Autom. Control* **54**(10), 2318–2327 (2009)
6. Weigel, H., Cramer, H., Wanielik, G., Polychronopoulos, A., Saroldi, A.: Accurate road geometry estimation for a safe speed application. In: 2006 IEEE Intelligent Vehicles Symposium, pp. 516–521. IEEE (2006)
7. Yan, X., Zhang, R., Ma, J., Ma, Y., et al.: Considering variable road geometry in adaptive vehicle speed control. *Math. Probl. Eng.* **2013** (2013)
8. Zhang, Y., et al.: Toward a more complete, flexible, and safer speed planning for autonomous driving via convex optimization. *Sensors* **18**(7), 2185 (2018)

Open Access This chapter is licensed under the terms of the Creative Commons Attribution 4.0 International License (<http://creativecommons.org/licenses/by/4.0/>), which permits use, sharing, adaptation, distribution and reproduction in any medium or format, as long as you give appropriate credit to the original author(s) and the source, provide a link to the Creative Commons license and indicate if changes were made.

The images or other third party material in this chapter are included in the chapter's Creative Commons license, unless indicated otherwise in a credit line to the material. If material is not included in the chapter's Creative Commons license and your intended use is not permitted by statutory regulation or exceeds the permitted use, you will need to obtain permission directly from the copyright holder.





Variable-Step-Length Hybrid A* Based on Dichotomy Optimization for Path Planning of Autonomous Mining Trucks*

Yichen Zhang, Yafei Wang^(✉), Mingyu Wu, and Ruoyao Li

School of Mechanical Engineering, Shanghai Jiao Tong University, Shanghai, China
{ethanzhang, wyfjlu}@sjtu.edu.cn

Abstract. Global path planning for autonomous mining trucks in shovel-loading areas requires path optimality and high computational efficiency. However, generating qualified paths for the loading process is more difficult for conventional methods under accurate final pose constraints. Furthermore, due to large-scale maps with variable obstacle distribution, considerable computation time needs to be allocated for path planning when using conventional methods. To address this problem, a novel Variable-Step-Length Hybrid A* based on Dichotomy Optimization (DO-VSLHA*) algorithm is proposed to generate obstacle-free paths considering mountain morphology and vehicle constraints while reducing computation time. To avoid U-shape obstacles and unnecessary node search, the clustering method is applied to the grid map to generate convex polygon obstacles. Subsequently, with joint sampling of step length and steering angle, we put forward dichotomy optimization based on the cost function in order to generate near-optimal nodes in each loop of the node expansion process, thus reducing the overall computing time of path planning. Field experiments are carried out on autonomous mining trucks at an open-pit mine, validating the improvement in effectiveness and computational efficiency of our method compared to conventional methods.

Keywords: mining truck · path planning · Hybrid A star

1 Introduction

The emergence of autonomous mining trucks (AMTs) shows great promise in addressing safety hazards and the aging workforce [1]. However, the deployment of AMTs in typical mining operations is still challenging [2]. Shovel-loading operation is one of the most complex scenarios in open-pit mines, which significantly influences the ore production efficiency [3]. To ensure the safety and efficiency of the loading process, the loading position and orientation of AMTs are strictly

Supported by the National Natural Science Foundation of China under Grant No. 52372417 and Grant 52072243.

© The Author(s) 2024
G. Mastinu et al. (Eds.): AVEC 2024, LNME, pp. 646–652, 2024.
https://doi.org/10.1007/978-3-031-70392-8_91

constrained [4]. Under this restriction, the global path planning of AMTs is crucial to generate an obstacle-free reference path with accurate final orientation for subsequent motion control [5].

The global path planning of AMTs in the shovel-loading area encounters two primary challenges. Firstly, the global reference path must satisfy non-holonomic constraints of AMTs and final pose constraints to ensure the safety of the loading process. Thus, some conventional methods are not suitable for AMTs due to their neglect of final orientation and vehicle kinematics, such as A* [6] and Rapidly-exploring Random Tree [7]. In addition, the irregular massif and scattered rocks form various obstacle distributions in large-scale shovel-loading areas. Under this circumstance, conventional methods that adopt a fixed step exhibit a dramatic decrease in search efficiency and path quality.

At present, global path planning for autonomous mining trucks mainly adopts Hybrid A* [8] and its variants, which utilize motion primitives and Reeds-Shepp curve to satisfy non-holonomic and final pose constraints respectively. In [9], Hybrid A* considering tire cost is designed based on a high-precision digital map for global path planning of AMTs. In [10], the dichotomy process is introduced to Hybrid A* to determine a near-optimal steering angle in the node expansion stage, thus improving the smoothness of the global reference path. In [11], a modified Hybrid A* using different curvature in forward and backward motion primitives is proposed to generate a global feasible path for subsequent trajectory optimization. However, the state space of Hybrid A* increases significantly when encountered with large-scale areas, leading to unacceptable computation time. To tackle this problem, prior research has proposed the concept of variable step length. In [12], a variable-step-length A* based on an improved cost function is proposed to reduce the overall computation time. In [13], a step selection strategy based on dangerous area construction is proposed for sparse A*. Nevertheless, these approaches determine step length from discrete value sets based on simple rules, thus lacking the adaptability required for the intricate environment in shovel-loading scenarios.

In summary, the strict restrictions on the final pose and complex environment result in performance degradation of conventional methods. To deal with these challenges, this paper focuses on improving computational efficiency and path quality of global path planning. The contribution of the paper lies in proposing a novel joint dichotomy optimization method to determine near-optimal step length and steering angle in the node expansion stage of Hybrid A*. The generated near-optimal nodes typically have lower costs, contributing to the improvement of computation time and path quality of global path planning.

2 Methodology

Our proposed method contains the map pre-processing stage and the path planning stage. The overall framework of the proposed DO-VSLHA* is shown in Fig. 1.

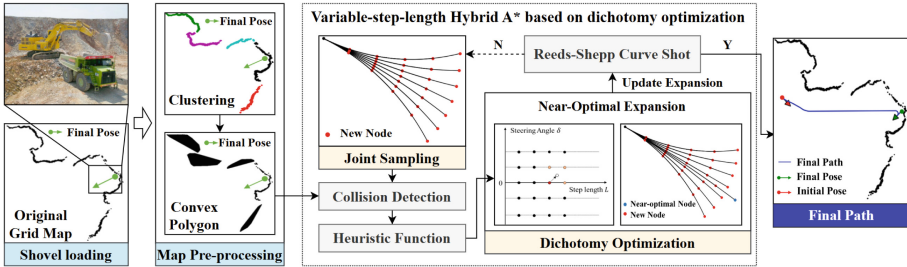


Fig. 1. The overall framework of the proposed DO-VSLHA*. The original grid map is pre-processed to eliminate U-shape obstacles which typically lead to unnecessary node exploration. The obstacle grids are clustered into groups and transformed into convex polygons, forming a new map for collision detection in the path planning stage. In each node expansion iteration of the path planning stage, joint sampling on step length and steering angle is applied to generate the initial successor nodes. Subsequently, the cost of each initial node is updated based on collision detection and heuristic function. Then, a dichotomy optimization is proposed to determine near-optimal step length and steering angle based on dichotomy optimization. The near-optimal nodes are subsequently generated and added to the open set of Hybrid A*.

In map pre-processing, DBSCAN [14] is applied to cluster obstacle grids into different groups. The eps-neighbourhood $N_\epsilon(\cdot)$ and core object in DBSCAN is defined as follows:

$$N_\epsilon(p) = \{q \in \mathcal{G} | dist(p, q) < \epsilon\} \tag{1}$$

$$p \text{ is } \begin{cases} \text{core object} & \text{if } \|N_\epsilon\| \geq Minpts \\ \text{others} & \text{if } \|N_\epsilon\| < Minpts \end{cases} \tag{2}$$

where p and q represent the obstacle grid. $dist(\cdot)$ represents the distance function and adopts Euclidean distance in our case. $Minpts$ and ϵ represent the number threshold of obstacle grids and distance threshold respectively. In our case, we let

$$\begin{cases} \epsilon = w + 2d \\ Minpts = 2 \end{cases} \tag{3}$$

where w represents the width of ATMs and d represents the safety margin on each side. After clustering, the convex hull algorithm is applied to every cluster to generate a convex polygon. Ray-casting method is utilized to filter invalid convex polygons when the loading point and starting point are located inside them. With map pre-processing, U-shape obstacles are eliminated, thus avoiding unnecessary node searches.

In the path planning stage, the node expansion of Hybrid A* is described as follows

$$\begin{bmatrix} x_s \\ y_s \\ \theta_s \end{bmatrix} = \begin{bmatrix} x_c \\ y_c \\ \theta_c \end{bmatrix} + d \cdot L \begin{bmatrix} \cos \theta_c \\ \sin \theta_c \\ \frac{\tan \delta}{l_w} \end{bmatrix} \tag{4}$$

where $N_c(x_c, y_c, \theta_c, d_c)$ and $N_s(x_s, y_s, \theta_s, d_s)$ represent the state of the current node and the successor node respectively. $d \in \{-1, 1\}$ denotes the forward or backward motion and l_w denotes the wheelbase of AMTs. L and δ denote the step length and steering angle. By determining near-optimal L and δ , successor nodes with less cost are generated to accelerate the overall node expansion process.

A joint optimization of step length and steering angle based on dichotomy is proposed to generate near-optimal nodes. The pseudo-code of the dichotomy optimization is shown in Algorithm 1. A joint sampling on step length and steering with a given discrete interval is performed to generate an initial successor set. Then, we generate near-optimal nodes with a given number of iterations. In each iteration, the node with the least cost and its corresponding step length s_m and steering angle δ_m are selected. Then, the adjacent value of step length and steering angle can be found, denoted as $s_l, s_r, \delta_l, \delta_r$. Subsequently, we generate four new nodes based on the mean value of these parameters, as shown in line 11 and 12 in Algorithm 1. The node with the least cost among the generated nodes is chosen to generate a new node with n_m . By repeating the dichotomy process, the step length and angle will converge to a near-optimal value, and these near-optimal nodes will be added to the initial node set.

Algorithm 1. Dichotomy(*Nodes*)

Input: Node list *Nodes* $\leftarrow \emptyset$

Output: Node list *Nodes*

```

for  $i \leftarrow 1$  to MaxAngle do
  for  $j \leftarrow 1$  to MaxStep do
     $n \leftarrow \text{CreateNode}(i \times \text{AngleSize}, j \times \text{StepSize}); \text{Nodes.add}(n)$ 
  end for
end for
for  $i \leftarrow 1$  to Num do
   $n_m \leftarrow \text{MinCostNode}(\text{Nodes}); s_m \leftarrow \text{Step}(n_m); \delta_m \leftarrow \text{Angle}(n_m)$ 
   $s_l, s_r \leftarrow \text{NeighbourStep}(s_m); \delta_l, \delta_r \leftarrow \text{NeighbourAngle}(\delta_r)$ 
   $n_{ll} \leftarrow \text{CreateNode}(\frac{\delta_l + \delta_m}{2}, \frac{s_l + s_m}{2}); n_{lr} \leftarrow \text{CreateNode}(\frac{\delta_l + \delta_m}{2}, \frac{s_m + s_r}{2})$ 
   $n_{rl} \leftarrow \text{CreateNode}(\frac{\delta_m + \delta_r}{2}, \frac{s_l + s_m}{2}); n_{rr} \leftarrow \text{CreateNode}(\frac{\delta_m + \delta_r}{2}, \frac{s_m + s_r}{2})$ 
   $n_t \leftarrow \text{MinCostNode}(\text{set}(n_{ll}, n_{lr}, n_{rl}, n_{rr})); s_t \leftarrow \text{Step}(n_t); \delta_t \leftarrow \text{Angle}(n_t)$ 
   $n_{new} \leftarrow \text{CreateNode}(\frac{\delta_m + \delta_t}{2}, \frac{s_m + s_t}{2})$ 
   $\text{Nodes.add}(n_{new});$ 
end for
return Nodes

```

3 Experiments

To validate our proposed method, we conduct field tests on an AMT at an open-pit mine, as shown in Fig. 2a. The original grid map is generated according to a 913m \times 1037m shovel loading platform with the resolution of 1m for path

planning, as shown in Fig. 2b. We compared our method with Hybrid A* and D-HA* [10]. Path length L , smoothness Φ and computation time T are calculated to verify the effectiveness of path planning methods. Smoothness Φ is calculated with $\Phi = \sum_{i=1}^N |\phi_i - \phi_{i-1}|$, where N represents the number of path points and ϕ represents yaw angle of each path point.

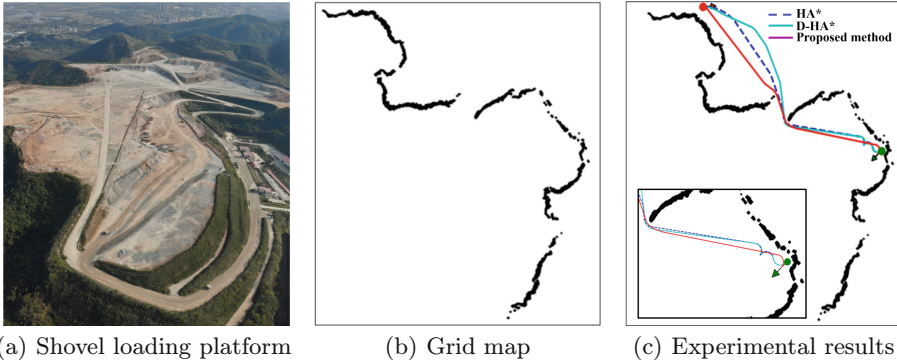


Fig. 2. The shovel-loading scenario, grid map, and experimental results of field tests.

Results are shown in Fig. 2c and Table 1. Our method outperforms conventional methods in path length, smoothness, and computation time. Unlike Hybrid A* using fixed parameters in node expansion, the proposed dichotomy optimization generates near-optimal nodes with optimized exploration parameters, thus reducing the number of iterations and the overall computation time. In addition, compared to D-HA* which only optimizes steering angle by dichotomy process and faces more computation burden, our method jointly optimizes step length and steering angle, thus improving the path quality and overall computational efficiency.

Table 1. The comparison results between our proposed method and others.

Method	L (m)	ϕ (rad)	T (s)
Hybrid A*	610.89	22.08	50
D-HA*	625.58	24.22	105
DO-VSLHA*	591.43	5.01	24.60

4 Conclusion

This paper presents a novel variable-step-length Hybrid A* based on dichotomy optimization which jointly optimizes step length and steering angle and generates near-optimal nodes in the node expansion stage. The experiment demonstrates that our proposed method outperforms other conventional methods in

computation time and path quality, indicating better adaptability in complex environments at open-pit mines.

References

1. Ge, S., et al.: Making standards for smart mining operations: Intelligent vehicles for autonomous mining transportation. *IEEE Trans. Intell. Veh.* **7**(3), 413–416 (2022)
2. Li, Y.M., Xu, G.Y., Li, H., Zhou, B., Chen, P., Yu, G.Z.: Optimization-based trajectory planning for autonomous driving at mining area with irregular boundary. In: *Proceedings of the 2023 International Conference on Frontiers of Artificial Intelligence and Machine Learning*, pp. 199–204 (2023)
3. Zhang, X., Guo, A., Ai, Y., Tian, B., Chen, L.: Real-time scheduling of autonomous mining trucks via flow allocation-accelerated tabu search. *IEEE Trans. Intell. Veh.* **7**(3), 466–479 (2022)
4. Lei, Y., Wang, Y., Wu, S., Gu, X., Qin, X.: A fuzzy logic-based adaptive dynamic window approach for path planning of automated driving mining truck. In: *2021 IEEE International Conference on Mechatronics (ICM)*, pp. 1–6. IEEE (2021)
5. Li, H., Chen, P., Yu, G., Zhou, B., Han, Z., Liao, Y.: Collaborative trajectory planning for autonomous mining trucks: a grouping and prioritized optimization based approach. *IEEE Trans. Veh. Technol.* **73**(5), 6283–6300 (2024)
6. Hart, P.E., Nilsson, N.J., Raphael, B.: A formal basis for the heuristic determination of minimum cost paths. *IEEE trans. Syst. Sci. Cybern.* **4**(2), 100–107 (1968)
7. LaValle, S.: Rapidly-exploring random trees: a new tool for path planning. *Research Report 9811* (1998)
8. Dolgov, D., Thrun, S., Montemerlo, M., Diebel, J.: Path planning for autonomous vehicles in unknown semi-structured environments. *Int. J. Robot. Res.* **29**(5), 485–501 (2010)
9. Zhao, Z., Bi, L.: A new challenge: path planning for autonomous truck of open-pit mines in the last transport section. *Appl. Sci.* **10**(18), 6622 (2020)
10. Hu, M.J., Yang, Z., et al.: A hybrid A* path planning method based on DBSCAN and dichotomy. *Autom. Eng.* **45**(3), 341–349 (2023)
11. Li, B., Ouyang, Y., Li, X., Cao, D., Zhang, T., Wang, Y.: Mixed-integer and conditional trajectory planning for an autonomous mining truck in loading/dumping scenarios: a global optimization approach. *IEEE Trans. Intell. Veh.* **8**(2), 1512–1522 (2022)
12. Da, K., Xiaoyu, L., Bi, Z.: Variable-step-length A* algorithm for path planning of mobile robot. In: *2017 29th Chinese Control And Decision Conference (CCDC)*, pp. 7129–7133. IEEE (2017)
13. Yi-Han, W., Wen-Jun, Z., Tian-Xin, Z.: Path planning of surface unmanned craft based on variable step-length sparse a-star algorithm. In: *2021 33rd Chinese Control and Decision Conference (CCDC)*, pp. 1917–1920. IEEE (2021)
14. Ester, M., Kriegel, H.-P., Sander, J., Xu, X., et al.: A density-based algorithm for discovering clusters in large spatial databases with noise. In: *KDD*, vol. 96, no. 34, pp. 226–231 (1996)

Open Access This chapter is licensed under the terms of the Creative Commons Attribution 4.0 International License (<http://creativecommons.org/licenses/by/4.0/>), which permits use, sharing, adaptation, distribution and reproduction in any medium or format, as long as you give appropriate credit to the original author(s) and the source, provide a link to the Creative Commons license and indicate if changes were made.

The images or other third party material in this chapter are included in the chapter's Creative Commons license, unless indicated otherwise in a credit line to the material. If material is not included in the chapter's Creative Commons license and your intended use is not permitted by statutory regulation or exceeds the permitted use, you will need to obtain permission directly from the copyright holder.





Study on Continuous Road Friction Measurement Under Various Environmental Conditions

Ichiro Kageyama^{1,2}(✉), Atsushi Watanabe², Yukiyo Kuriyagawa²,
Tetsunori Haraguchi^{1,2}, Tetsuya Kaneko³, and Minoru Nishio⁴

¹ Consortium on Advanced Road-Friction Database, Sakura, Japan
kageyama.ichiro@nihon-u.ac.jp

² Nihon University, Chiyoda City, Japan

³ Osaka Sangyo University, Daito, Japan

⁴ Absolute Co., Ltd., Isehara, Japan

Abstract. This paper deals with a study to construct a road friction characteristic database as the first step in building a system to estimate road friction characteristics ahead, which is one of the major issues in traffic safety. To achieve this goal, we proposed a new method that can continuously measure the peak μ in the μ -s characteristic and showed the measurement results on different road surfaces. Based on these results, in this paper we measure the friction characteristics of snow and ice surfaces at a well-maintained test site and present the continuous μ -s characteristics on the surfaces and the peak μ regions on each surface. Furthermore, measurements are also performed on ordinary roads under snowy conditions, and a comparison with the results from the proving ground, it is shown that we need to examine the dynamics of the μ -s characteristics.

Keywords: Road friction · Breaking force · Measurement · Tire characteristics

1 Introduction

In recent years, various ADAS have been developed to ensure road traffic safety, and to further promote these effects, the effect of autonomous driving is expected in the next stage. Currently, various sensing systems and algorithms for safety management have been improved one after another from the viewpoint of reducing accidents, reducing the burden on drivers, and improving reliability, compared to when ADAS was first introduced, and it is believed that the effectiveness of safety support has been greatly improved. For these various safety systems to function effectively, it is important to fully understand the friction characteristics of the road surface, which is a prerequisite for the control systems to function effectively. Road surface friction characteristics generally vary greatly depending on road conditions, weather, temperature, region, etc., and the friction coefficient of road surfaces that ordinary vehicles face varies greatly from approximately 0.15 to approximately 1.2. On roads with large differences in the friction coefficients, emergency braking distances can vary by several times or even ten

times more depending on changing road conditions, which poses a major problem from the perspective of safety management. When driving on snowy or icy roads in snowy or mountainous regions in winter, building a road friction estimation system is one of the extremely important research subjects from the perspective of safety management. However, to build such a system, it is important to construct a database related to road friction, but such a system has not yet been constructed. Given this situation, our research purposes are to establish a method for continuous measurement of road surface friction, to construct a broad database of road surface friction, and to construct an environmental database that is highly correlated with the friction characteristics. This paper presents the results of continuous measurement results of the road friction coefficient for various paved road surfaces that have been developed through past activities, as well as the results of continuous measurements of road friction on snowy and icy roads.

2 Measurement Device on Road Friction

Road friction measuring devices have been developed for various purposes and are now widely used for various purposes. Roughly speaking, these can be divided into two types: one is a system for evaluating the road surface itself, and the other is a system for measuring the characteristics of tires to understand the vehicle behaviors. The required friction characteristics need to be considered separately for the longitudinal and lateral directions, but since the characteristics of normal tires can be roughly considered in terms of a friction circle, we will focus on the braking characteristics especially for μ -s characteristics, which are important from the perspective of safety. Figure 1 shows various road friction measurement systems.

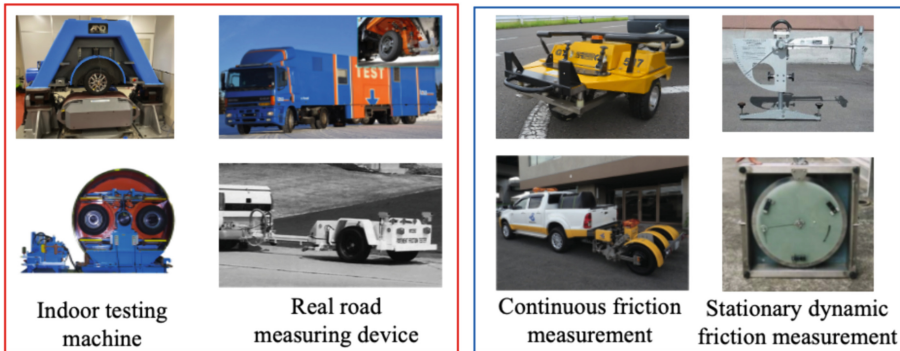


Fig. 1. Differences in road friction measurement equipment

These two groups of road friction characteristic measuring devices have different characteristics due to their different purposes. Road surface evaluation instruments are designed to measure road surface friction at measurement points on the road surface, because the relationship between the measurement position and the road surface characteristics is important. Currently, instruments used on highways and airport runways

can measure the surface friction continuously. These devices are used for continuous measurements to grasp changes over time and identify areas of damage, but they cannot measure the detailed lateral force characteristics and/or braking /driving characteristics required for vehicle dynamics analysis. On the other hand, dynamic vehicle tire characteristic measuring devices are designed to measure tire characteristics under various road surface conditions, and measure tire characteristics by continuously changing brake torque and/or sideslip angle under the assumption that the friction coefficient in the measurement section is constant. Therefore, although it is suitable for measurements on maintained road conditions such as proving grounds, it is not suitable for measurements on road surfaces such as ordinary roads where friction characteristics change. To build a road friction database, it is important to measure both characteristics, especially the ability to continuously measure road friction characteristics as well as the ability to measure μ - s characteristics at each point. To simultaneously satisfy both requirements, we developed a new road friction measurement system. The basic idea behind the construction of this system is to measure a finite set of μ and s , and use these results to estimate μ - s characteristics. An important element in the construction of this system is the introduction of a function that represents the μ - s characteristics well. The magic formula proposed by Pacejka describes very well the characteristics of the tire, including not only lateral force characteristics but also braking force and torque characteristics¹⁾. A simplified description of this formula can be written as in Eq. 1.

$$\mu = a \sin \left\{ b \tan^{-1} (c \cdot s) \right\} \quad (1)$$

The three constants a , b , and c in the formula are used to identify the μ - s characteristic from as few experimental results as possible. Figure 2 shows the estimated peak μ and locked μ when three sets of μ and s are measured, using the data on the μ - s characteristics measured so far and the characteristics of snow-and-ice roads extracted from literature. In this identification, the friction coefficients of slip ratios of 2%, 12%, and 22% are assumed to be known. These results show that sufficient braking characteristics can be obtained by using this method.

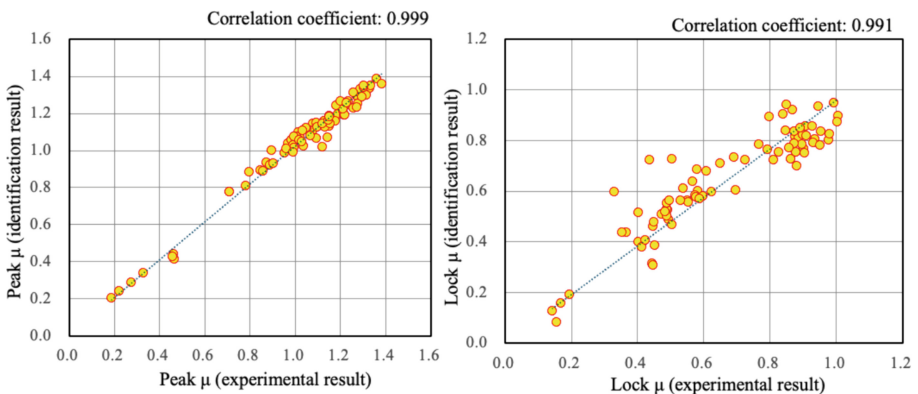


Fig. 2. Peak μ and lock μ on μ - s characteristic estimated from three sets of μ and s ($s = 2\%$, 12% , 22%).

3 Constructed Measurement Device

A road friction characteristic measuring device with the above-mentioned structure was constructed. Figure 3 shows a trailer-type measuring device having three measuring tires, which are driven by chains from the trailer tires using different teeth of sprocket.

The basic idea behind the construction of this system is to measure a finite set of μ and s , and use these results to estimate μ - s characteristics. An important element in the construction of this system is the introduction of a function that represents the μ - s characteristics well.

For this reason, various control methods have been adopted to improve safety and comfort, and their effectiveness has been demonstrated. Road friction characteristics are extremely important for the various systems for these safety measures, and ensuring these friction characteristics is a prerequisite for the control.

The coefficient of road friction on an actual road surface varies greatly depending on the road surface material, road surface condition, tire structure, and other factors. Furthermore, the reduction of the coefficient of friction on snowy and icy roads in wintertime in snowy regions poses a significant threat to road traffic safety. In the past, road surface friction measurements have used sliding friction such as BPN, or truck/bus/trailer type road surface friction measurement systems to measure μ - s characteristics by gradually applying braking. In particular, the measurement of peak μ at each location on the road is important for estimating road friction characteristics since the widespread use of ABS in recent years has enabled braking near peak μ and automatic braking system is based on such control. However, the road friction measurement systems required the assumption that the friction characteristics of the measured section are constant. However, it can be inferred that the friction characteristics may always change between a road surface where frequent braking is applied just before an intersection and a section where most vehicles pass at a constant speed, and that the friction characteristics always change on partially frozen or partially snow-covered road surfaces. In such measurements related to road surface friction, it is important to understand the continuous change in peak μ , but until now, there has been no system capable of continuously measuring this characteristic. In recent years, the authors have proposed a new road friction measurement system to overcome this problem and have shown its measurement results.

In this paper, we present an overview of the system we have constructed and the measurement results, followed by the results of continuous measurement of peak μ under various conditions, including snow and ice on actual roads. Furthermore, we summarize the identification of these measurement problems and future issues.

This document is a guide for MS Word users. If you are reading the PDF version of this document, please download:

<https://www.springer.com/it/authors-editors/book-authors-editors/resources-guidelines/rights-permissions-licensing/manuscript-preparation/5636>.

This template fits both for the Extended Summary and the Full paper

The Extended Summary for AVEC'24 is 3 pages

Please restrict your document to 6 pages for the Full paper of AVEC'24.

Page Size, Margins and Font

The page size is standard A4, with the margins listed in Table below. The text area is

12.3 × 19.1 cm. The document is based on the font Times New Roman. The standard font size is 10pt. The paper title is 14pt bold faced. Section titles are 12pt bold faced; subsection titles are 10pt italics. Figure and table captions are 9pt.

Page	Top	Bottom	Left	Right
First	5.0	5.6	4.7	4.6
Rest	5.0	5.6	4.7	4.6

4 First Section

4.1 A Subsection Sample

Please note that the first paragraph of a section or subsection is not indented. The first paragraphs that follows a table, figure, equation etc. does not have an indent, either.

Subsequent paragraphs, however, are indented.

Figures/Tables should be centred within the page width and numbered sequentially. Figures/Tables should be numbered separately. Multiple figures should be referred using letters (e.g. Figure 1a or 1b).

In the text a figure/table is referred as “Fig. 1a shows the drag coefficient...” or “the slope of the lift coefficient switches from negative to positive at the critical Re (Fig. 1b)”.

Sample Heading (Third Level). Only two levels of headings should be numbered. Lower level headings remain unnumbered; they are formatted as run-in headings.

Sample Heading (Fourth Level). The contribution should contain no more than four levels of headings. The following Table 1 gives a summary of all heading levels.

Table 1. .

Heading level	Example	Font size and style
Title (centered)	Lecture Notes	14 point, bold
1 st -level heading	1 Introduction	12 point, bold
2 nd -level heading	2.1 Printing Area	10 point, bold
3 rd -level heading	Run-in Heading in Bold. Text follows	10 point, bold
4 th -level heading	<i>Lowest Level Heading.</i> Text follows	10 point, italic

Displayed equations are centered and set on a separate line, and numbered sequentially. Equations must be referred in the text as “Eq. (1) defines strain sensitivity”. Equations must be referred in the text as “Eq. (1)” for one equation or “Eqs. (1), (2) and (3)” for multiple equations.

$$x + y = z \quad (2)$$

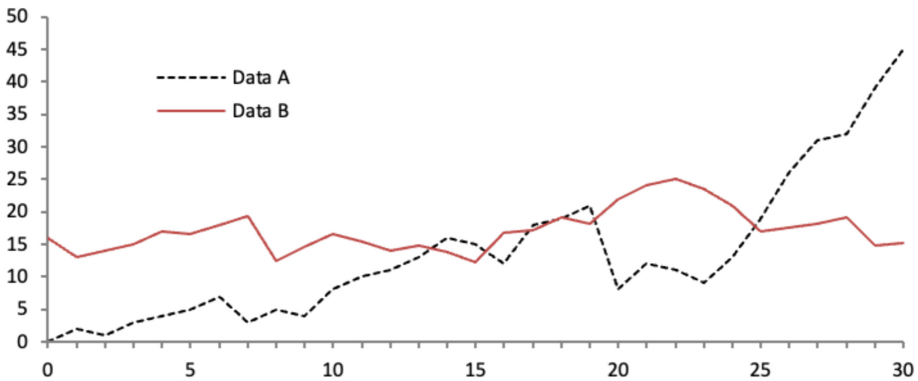


Fig. 3. A figure caption is always placed below the illustration. Short captions are centered, while long ones are justified. The macro button chooses the correct format automatically.

Please try to avoid rasterized images for line-art diagrams and schemas. Whenever possible, use vector graphics instead (see Fig. 3).

For citations of references, we prefer the use of square brackets and consecutive numbers. Citations using labels or the author/year convention are also acceptable. The following bibliography provides a sample reference list with entries for journal articles [1], an LNCS chapter [2], a book [3], proceedings without editors [4], as well as a URL [5].

References

1. Author, F.: Article title. *Journal* 2(5):99–110 (2016)
2. Author, F., Author S.: Title of a proceedings paper. In: Editor F, Editor S (eds.) *Proceedings Title*, pp. 1–13. Springer, Heidelberg (2017)
3. Author, F., Author, S., Author, T.: *Book title*, 2nd edn. Publisher, Location (1999)
4. Author, F.: Contribution title. In: *9th International Proceedings on Proceedings*, pp. 1–2. Publisher, Location (2010)
5. LNCS Homepage. <http://www.springer.com/lncs>. Accessed 21 Nov 2016

Open Access This chapter is licensed under the terms of the Creative Commons Attribution 4.0 International License (<http://creativecommons.org/licenses/by/4.0/>), which permits use, sharing, adaptation, distribution and reproduction in any medium or format, as long as you give appropriate credit to the original author(s) and the source, provide a link to the Creative Commons license and indicate if changes were made.

The images or other third party material in this chapter are included in the chapter's Creative Commons license, unless indicated otherwise in a credit line to the material. If material is not included in the chapter's Creative Commons license and your intended use is not permitted by statutory regulation or exceeds the permitted use, you will need to obtain permission directly from the copyright holder.





Observer Design for Estimating Road Elevations at All Tire Contact Patches Using Only an Inertial Sensor

Hosik Choi^(✉)  and Juhui Gim 

Changwon National University, Changwon 51140, Korea
hosikchoi1998@gmail.com, juhuigim@changwon.ac.kr

Abstract. This paper designs an observer for estimating road elevations at all tire contact patches using only an inertial sensor with high accuracy, comparable to that of laser scanning. The observer is constructed within the framework of the unknown input Kalman filter to estimate road elevations, which act as disturbances to vehicle dynamics. The model for the observer is based on vertical-pitch-roll dynamics, encompassing road elevations at all tire contact patches. The introduction of virtual measurements for all tires ensures the observability of the model in the inertial sensor-based observer without requiring both additional sensors and model simplification. Additionally, a bias model is added to compensate for sensor installation errors for practical realization. Experimental validation demonstrates that the proposed observer can estimate road elevation with high accuracy, regardless of vehicle speed and dynamics, even when utilizing only an inertial sensor, making it suitable for rapid and robust road maintenance.

Keywords: Road elevation estimation · Inertial sensor signals · Virtual measurement · Observable model design · Unknown Input Kalman Filter

1 Introduction

Road maintenance is of paramount importance for ensuring ride comfort, stable vehicle control, and even safety against road cracks or potholes [1, 2]. A critical initial step in road maintenance is the measurement of road bumpiness [3, 4]. Accurate measurement of the road profile typically employs direct-contact devices called profilometers, albeit at a significant cost in terms of both time and money.

Inertial sensors offer a more affordable alternative because road elevation variations affect inertial sensor signals. However, a challenge arises as road elevation changes are not directly observable using only inertial sensor signals. This limitation stems from the fact that the inertial sensor is attached to the sprung mass, with the excitation caused by road elevation changes being filtered by the unsprung masses. To address this, previous methods have either incorporated additional sensors at an increased cost [5] or utilized a vehicle model without unsprung masses, compromising accuracy [6].

Previous work by J. Gim et al. showcased the potential for road elevation estimation using only inertial sensor signals by introducing virtual measurement and synthesizing the Unknown input Kalman filter [7]. However, this research primarily focused on

estimating longitudinal road elevations for vehicle localization, emphasizing consistency and repeatability, without extending its applicability to road maintenance, which requires high precision.

This paper proposes an observer design for the accurate estimation of road elevations at all tire contact patches, with a specific emphasis on its applicability to road maintenance. The vehicle model in the observer is extended to an eight-degree-of-freedom (8-DOF) model to encompass road elevation changes at all four tire contact patches. To ensure observability, virtual measurement is also extended for all tires, and a bias model is introduced to compensate for sensor installation errors. The effectiveness of the designed observer is validated by comparing it with directly measured road elevations using profilometers, establishing its potential utility in practical road maintenance applications.

2 Observer Design

Figure 1 shows the scheme of the proposed road elevation observer.

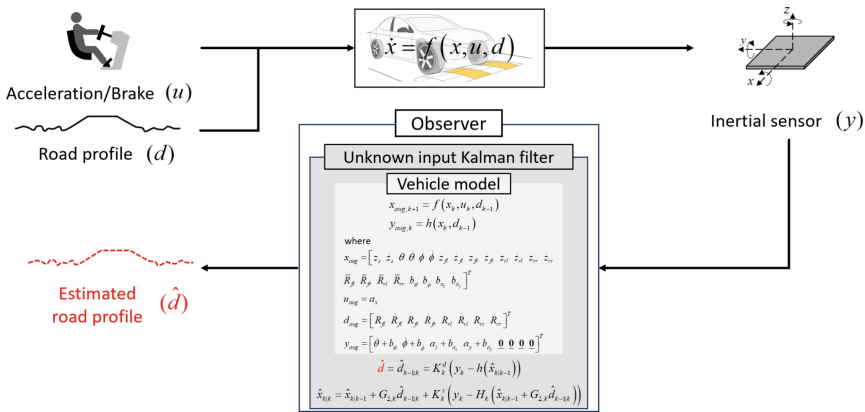


Fig. 1. Scheme of the proposed observer for estimating road elevation changes using only inertial sensor signals.

Vehicle dynamics is excited by alterations in road elevation and the driver’s acceleration or brake input, and the inertial sensor mounted on the vehicle measures this vehicle dynamics in terms of accelerations and angular velocities. The discretized model for both vehicle dynamics and the inertial sensor are derived as:

$$\begin{aligned}
 x_{k+1} &= f(x_k, u_k, d_{k-1}), \\
 y_k &= h(x_k, d_{k-1}),
 \end{aligned}
 \tag{1}$$

where vehicle state $x \in \mathbb{R}^n$ encompasses the vertical displacements of sprung and unsprung masses and their rates, as well as the pitch and roll angles of the sprung mass and their rates. The known input $u \in \mathbb{R}^1$ represents the longitudinal acceleration.

The disturbance $d \in \mathbb{R}^q$ signifies the road elevations at all tire contact patches and their rates, which are the parameters to be estimated. The measurement $y \in \mathbb{R}^p$ consists of only the inertial sensor signals.

The designed observer employs an 8-DOF vehicle model, incorporating vertical, pitch, and roll dynamics representing the responses excited by road elevation changes at all tire contact patches, as illustrated in Fig. 2 [8]. The measurement model y includes four inertial sensor signals—vertical acceleration, lateral acceleration, pitch rate, and roll rate signals—to design a road profile observer based only on inertial sensors.

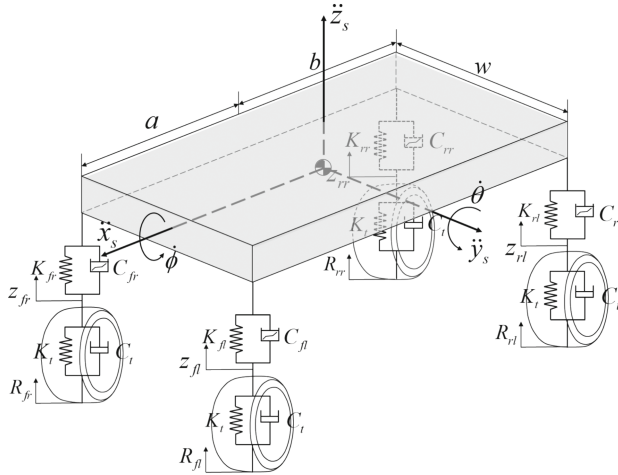


Fig. 2. 8-DOF vehicle model.

A observer framework is based on the unknown input Kalman filter, which estimate disturbances with rapid responses, provided the system satisfies the following two conditions [9]:

$$\text{rank} \left(\begin{bmatrix} H_k \\ H_k F_k \\ \vdots \\ H_k F_k^{n-1} \end{bmatrix} \right) = n \text{ and } \text{rank}(H_k G_k) = \text{rank}(G_k) = q, \quad (2)$$

where $F_k = \frac{\partial}{\partial x_k} f(x_k, u_k, d_k)$, $G_k = \frac{\partial}{\partial d_k} f(x_k, u_k, d_k)$, $H_k = \frac{\partial}{\partial x_k} h(x_k)$.

However, the employed 8-DOF vehicle model does not satisfy the observability conditions, meaning that the road profile cannot be estimated using only inertial sensor signals. This is because the inertial sensors are not responsive to changes in the road profile that are longer than the wheelbase, such as hills. The concept of virtual measurement involves continuously monitoring low-pass-filtered road profiles as zero, under the assumption that road profiles longer than wheelbase should be flat. Therefore, four virtual measurements, corresponding to each tire contact patch, are augmented into the measurement model involving the only inertial sensor signals:

$$y_{aug,k} = [y_k \ \bar{R}_{fl,k} \ \bar{R}_{fr,k} \ \bar{R}_{rl,k} \ \bar{R}_{rr,k}]^T = [y_k \ 0 \ 0 \ 0 \ 0]^T, \tag{3}$$

where $\bar{R}_{ij,k} = \alpha R_{ij,k-1} + (1 - \alpha)\bar{R}_{ij,k-1}$,

\bar{R}_{ij} and R_{ij} are the virtual measurements and the vertical road heights at all tire contact patches, where i denotes the front or rear tires, and j are left or right side. α determines how much the estimated road height influences the virtual measurement. Consequently, the model guarantees observability by augmenting the original states with four virtual measurements for each tire contact patch.

Finally, a bias model is incorporated to compensate inertial sensor installation errors. Inertial sensor signals involve the sensor biases with constant or slowly changing dynamics. The final model for a road profile observer is designed with:

$$\begin{aligned} x_{final,k} &= [z_{s,k} \ \dot{z}_{s,k} \ \theta_k \ \dot{\theta}_k \ \phi_k \ \dot{\phi}_k \ z_{fl,k} \ \dot{z}_{fl,k} \ z_{fr,k} \ \dot{z}_{fr,k} \ z_{rl,k} \ \dot{z}_{rl,k} \ z_{rr,k} \ \dot{z}_{rr,k} \\ &\ R_{fl,k} \ R_{fr,k} \ R_{rl,k} \ R_{rr,k} \ \bar{R}_{fl,k} \ \bar{R}_{fr,k} \ \bar{R}_{rl,k} \ \bar{R}_{rr,k} \ b_{z_s,k} \ b_{\theta,k} \ b_{\phi,k} \ b_{\dot{y}_s,k}]^T, \\ u_{final,k} &= \ddot{x}_{s,k}, \\ d_{final,k} &= [\dot{R}_{fl,k} \ \dot{R}_{fr,k} \ \dot{R}_{rl,k} \ \dot{R}_{rr,k}], \\ y_{final,k} &= [\dot{z}_{s,k} \ \dot{\theta}_k \ \dot{\phi}_k \ \ddot{y}_{s,k} \ \bar{R}_{fl,k} \ \bar{R}_{fr,k} \ \bar{R}_{rl,k} \ \bar{R}_{rr,k}]. \end{aligned} \tag{4}$$

The proposed observer synthesizing the designed observable model into the unknown input Kalman filter estimates the vehicle states and the one-time-step delayed road profiles at all tire contact patches.

3 Validation

Figure 3 shows the validation results through comparative analysis of road elevations measured by laser sensors on profilometers for four distinct cases. The estimated results demonstrate that the designed observer can accurately estimate road elevations for all tire contact patches using only inertial sensor signals, with high accuracy similar to that achieved by laser scanning. This accuracy remains consistent across different vehicle types, vehicle speeds, and driver’s acceleration intentions.

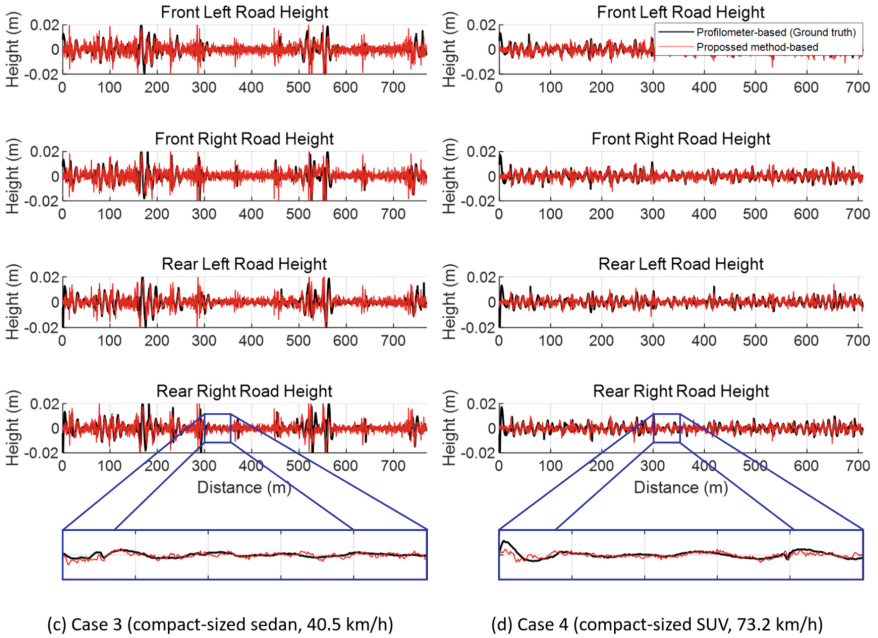
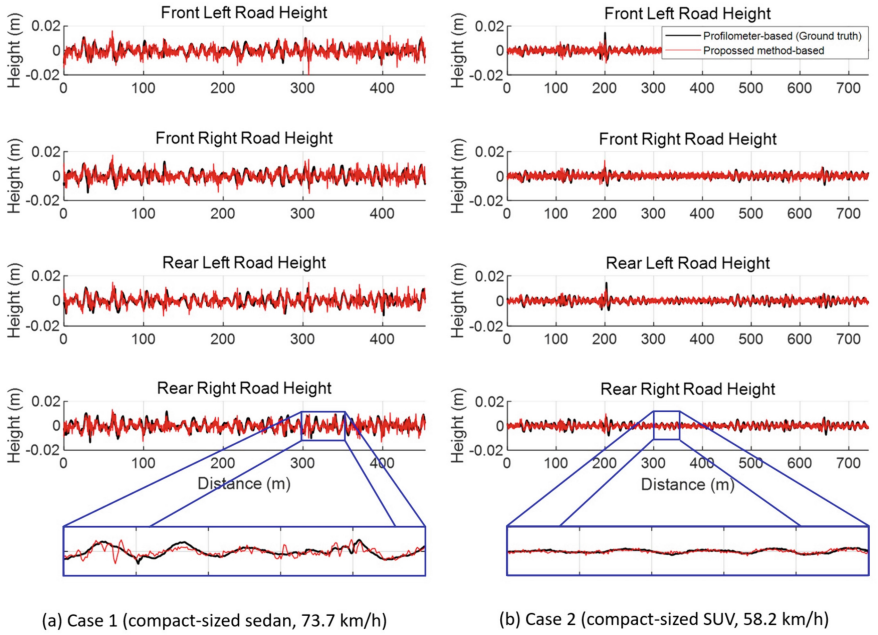


Fig. 3. Estimated results of the designed observer for four cases.

4 Conclusion

This paper proposes an observer for estimating road elevation changes at all tire contact patches using only inertial sensors, achieving accuracy comparable to that obtained with laser sensors. Therefore, the designed observer can be an alternative to direct contact measurement approaches requiring special devices with a short time horizon.

Acknowledgement. This work was supported by the Advanced Materials and Components Laboratory Project for Defense Industry, Under grant no. DCL2020L, funded by Korea Research Institute for Defense Technology Planning and Advancement (KRIT).

References

1. Norrman, J., Eriksson, M., Lindqvist, S.: Relationships between road slipperiness, traffic accident risk and winter road maintenance activity. *Climate Res.* **15**(3), 185–193 (2000)
2. Kat, C.J., et al.: Vibration-induced discomfort in vehicles: a comparative evaluation approach for enhancing comfort and ride quality. *SAE Int. J. Veh. Dyn. Stabil. NVH* **8**(2) (2024)
3. Ruochen, W., et al.: Switching control of semi-active suspension based on road profile estimation. *Veh. Syst. Dyn.* **60**(6), 1972–1992 (2022)
4. Ni, T., Li, W., Zhao, D., Kong, Z.: Road profile estimation using a 3D sensor and intelligent vehicle. *Sensors* **20**(13), 3676 (2020)
5. Jeongyun, L., Kukjin, Y.: Temporally consistent road surface profile estimation using stereo vision. *IEEE Trans. Intell. Transp. Syst.* **19**(5), 1618–1628 (2018)
6. Göhrle, C., Schindler, A., Wagner, A., Sawodny, O.: Road profile estimation and preview control for low-bandwidth active suspension systems. *IEEE/ASME Trans. Mechatron.* **20**(5), 2299–2310 (2015)
7. Juhui, G., Changsun, A.: IMU-based virtual road profile sensor for vehicle localization. *Sensors* **18**(10), 3344 (2018)
8. Setiawan, J.D., Safarudin, M., Singh, A.: Modeling, simulation and validation of 14 DOF full vehicle model. In: *International Conference on Instrumentation, Communication, Information Technology, and Biomedical Engineering*, pp. 1–6. IEEE, Bandung (2009)
9. Darouach, M., Zasadzinski, M., Onana, A.B., Nowakowski, S.: Kalman filtering with unknown inputs via optimal state estimation of singular systems. *Int. J. Syst. Sci.* **26**(10), 2015–2028 (1995)

Open Access This chapter is licensed under the terms of the Creative Commons Attribution 4.0 International License (<http://creativecommons.org/licenses/by/4.0/>), which permits use, sharing, adaptation, distribution and reproduction in any medium or format, as long as you give appropriate credit to the original author(s) and the source, provide a link to the Creative Commons license and indicate if changes were made.

The images or other third party material in this chapter are included in the chapter's Creative Commons license, unless indicated otherwise in a credit line to the material. If material is not included in the chapter's Creative Commons license and your intended use is not permitted by statutory regulation or exceeds the permitted use, you will need to obtain permission directly from the copyright holder.





Physics-Informed Neural Network for Mining Truck Suspension Parameters Identification

Mingyu Wu , Yafei Wang  , Yichen Zhang, and Zexing Li

School of Mechanical Engineering, Shanghai Jiao Tong University, Shanghai, China
wmy_marvin@sjtu.edu.cn

Abstract. Mining truck suspensions are prone to performance degradation under complex external excitation of the mining area, leading to high safety risks and maintenance costs. However, the lack of unsprung kinematic information and harsh operating environments lead to inadequate accuracy of current physical models. On the other hand, data-driven methods partially address the issue of incomplete information, but suffer from the absence of interpretability and generalization. To address these challenges, this paper introduces a Physics-Informed Neural Network (PINN) for precise suspension characteristic identification of mining trucks. Specifically, the physical model of the longitudinal-vertical dynamics of the mining truck is established. Then, based on the model, baseline values of suspension parameters are regressed through the instrumental variable method. Therefore, the hybrid modeling architecture is established to precisely identify suspension parameters by utilizing a recurrent neural network. Under this architecture, the states of the mining truck can be effectively updated. Real truck experiments demonstrate the proposed hybrid model outperforms traditional physical and data-driven models in estimating suspension nonlinear parameters and truck dynamic characteristics under typical longitudinal motions.

Keywords: Mining Truck · Hybrid Model · Neural Network · Parameter Identification

1 Introduction

Accurate suspension parameter identification of mining trucks is essential to its dynamic modeling and subsequent control strategy [1]. Existing models can be roughly divided into physics and data-driven models for the vertical dynamic modeling of vehicles and their coupling effects.

Existing models can be roughly divided into physics and data-driven models for the vertical dynamic modeling of vehicles and their coupling effects. Physical models are typically expressed using Newton's law or Lagrange equations to describe the vehicle's dynamic characteristics [2]. Dynamics modeling and parameter identification are then

Supported by the National Natural Science Foundation of China under Grant No. 52372417 and Grant 52072243, and the Postdoctoral Fellowship Program of CPSF under Grant Number GZC20231585.

conducted using filtering methods or their combination [3]. Although the physical model has significant advantages in generalization, it is necessary to clarify all parameters and may fall short in transient conditions and extreme scenarios [4]. Data-driven models are superior to physical models in many fields and have a more comprehensive range of applications, but they still cannot escape the shortcomings of poor generalization and interpretability [5].

In recent years, physics-informed neural network has received widespread attention. Data-driven models can effectively compensate for parts that are challenging or impossible to model with physical models. Physical models can extend the applicability range of data-driven models, effectively expanding the applicable state space concerning vehicle dynamics [6]. In [7], a simplified vehicle model was integrated with a recurrent neural network to estimate the vehicle's lateral motion behavior, and results demonstrated that the hybrid architecture achieved excellent estimation quality while demonstrating generalization across various tires, surfaces, and driving scenarios. A novel car-following control model combining machine learning and kinematics models for automated vehicles was established in [8], the real vehicle trajectory data sets demonstrated better performance for controlling the longitudinal movements under a hybrid approach.

Considering the aforementioned limitations and challenges, this paper primarily focuses on establishing a longitudinal-vertical dynamic model for mining trucks during transportation. A hybrid-driven framework that combines data-driven and physical models to identify the suspension parameters of mining trucks is employed. At first, the nonlinear mapping relationship of the inertial measurement unit to the measured point is proposed for determining the vertical motion. Secondly, the mining truck longitudinal-vertical dynamics model is established considering the differences in parameters between the front and rear suspensions. Subsequently, the instrumental variable method derives baseline values for suspension parameter identification. The hybrid modeling architecture combining physics and learning methods is given for precise identification and prediction of the mining truck's suspension parameters and dynamic characteristics.

2 PINN Architecture

The proposed method integrates a deep learning network into a physics model of the mining truck to establish an accurate mining truck longitudinal-vertical dynamic model and identify precise suspension parameters. Figure 1 shows the schematic diagram of the proposed algorithm. Firstly, the sequence states of the mining truck maneuver are collected by monitor sensors. The critical suspension parameters (such as stiffness and damping coefficients) are roughly determined by a linear dynamic model considering the longitudinal-vertical coupling effect. Meanwhile, the sequence states are the input of the deep learning network, which can calculate the parameter correlation factors. The modified parameters are fed into the mining truck dynamic model to estimate the state of the next time step. The state loss L_p between predicted and target states can be used as the loss error term of the neural network and update the neural network weights.

The overall hybrid modeling architecture is shown in Fig. 2. According to the state of two consecutive moments as the input of the network and the physical model, the correction coefficients of the suspension parameters are calculated through the network

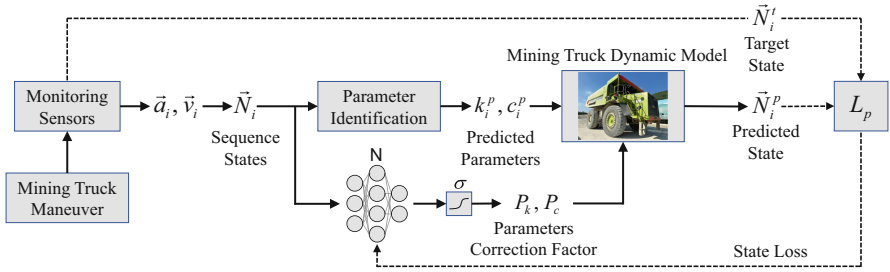


Fig. 1. Schematic diagram of the proposed PINN algorithm.

and then input into the physical model to estimate the state of the next moment. The selected loss function is utilized to calculate the MSE after dimensional unification and perform backpropagation and weight training on the network. Since the parameters input to the network model in this article are time series signals, a recurrent neural network (RNN) is considered. The Long Short-Term Memory (LSTM) network is selected as the RNN network, with 3 layers and a hidden size of 128. The suspension correction parameters are calculated through a fully connected layer during output. In the network model, in order to avoid problems such as gradient disappearance or gradient explosion during the neural network training process, the Xavier initialization method is used to initialize the RNN network. The normal distribution initialization method is employed for the linear output layer to enhance the training stability and accelerate the convergence speed of the network.

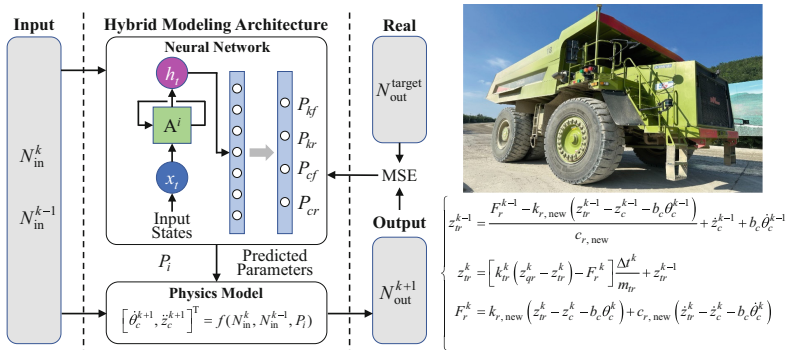


Fig. 2. Hybrid modeling architecture and experimental platform TR100A mining truck.

The mining truck longitudinal-vertical dynamic modeling and suspension parameter identification have been proposed by combining physics and deep learning methods. In order to verify the validity and accuracy of the proposed theory, the real test of the mining truck is carried out below.

3 Experiments and Results

In order to verify the accuracy and effectiveness of the proposed method, we conducted experiments on a real mining truck. The TR100A mining truck made by TEREX was selected as the experimental platform (Fig. 2). The experiments were conducted on a flat paved road, and the mining truck was in the unloaded state. For simplification, the ground’s excitation is neglected compared to the tire dimension during transportation. The experiments include longitudinal acceleration and deceleration tests, and specific tests are shown in Table 1.

Table 1. Mining Truck Experiment Conditions

Part number	Status	Conditions
1	Acceleration	0–20 km/h
2		20–30 km/h
3	Deceleration	10–0 km/h
4		20–0 km/h
5		30–0 km/h

The hybrid model proposed in this article can give the suspension parameters of the mining truck, which is crucial to the structural design and performance prediction of the mining truck. Figure 3 and Fig. 4 show the change regulations of identified front and rear suspension stiffness, respectively.

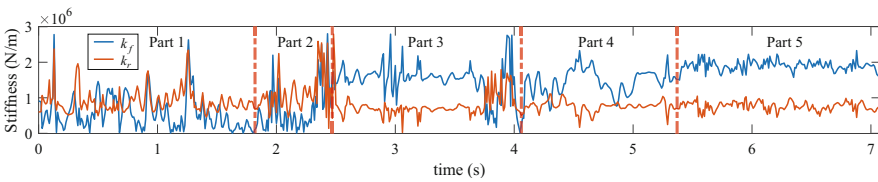


Fig. 3. Change regulations of front and rear suspension stiffness.

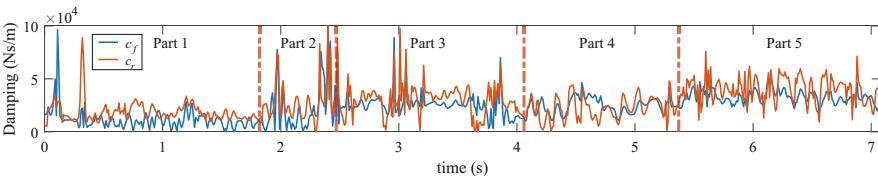


Fig. 4. Change regulations of front and rear suspension damping.

Working conditions Part 1 and Part 5 are selected for display to verify the model effect during acceleration and deceleration. Figure 5 show the comparison results of the vertical

acceleration of the center of gravity in the testing set of the two working conditions. It can be seen that the hybrid model proposed in this article has more robust applicability and accuracy than the physical model and data-driven model. In the physical model, the calculation of the unsprung position requires solving differential equations during the calculation process. This process will introduce errors and oscillations, leading to violent oscillations in the final state calculation at the next moment. The accuracy of the data-driven model is higher than that of the pure physical model, but it is affected by limited samples and a more significant number of iterations (about 10–15 epochs, depending on the size of samples), which limits its generalization ability. The model-based hybrid-driven model proposed in this article can effectively reflect the real motion state and converge within a limited number of iterations (about 2–3 epochs). It can also be seen from the comparison results that under some severe working conditions and sharp points, the hybrid model still has strong robustness.

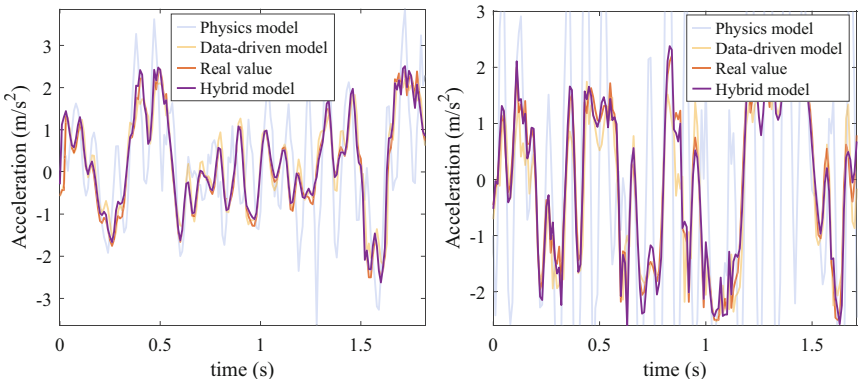


Fig. 5. Comparison of the vertical acceleration at CoG (Part 1, 5).

In order to give qualitative comparison results of the three models, this article uses the MSE of all testing sets as the measurement index. The smaller the value, the higher the accuracy of the model. The MSE comparison results for the vertical acceleration of the center of gravity a_c , the sprung velocity of the front suspension v_f and the sprung velocity of the rear suspension v_r are shown in Table 2.

Table 2. The comparison of MSE in the experiment

MSE value	Physics model	Data-driven model	Hybrid model
$a_c \text{ (m/s}^2\text{)}^2$	13.69	0.18	0.13
$v_f \text{ (}\times 10^{-2}\text{m/s)}^2$	2.36	0.76	0.32
$v_r \text{ (}\times 10^{-2}\text{m/s)}^2$	2.23	0.78	0.31

It can be seen that the hybrid model method proposed in this article has good performance in predicting different motion parameters. It is worth mentioning that the hybrid

model method in this paper only relies on the sensor signals of the vehicle body and does not require unsprung information. This advantage makes it possible to directly predict the dynamic characteristics of the mining truck without building a complex mining truck sensor measurement system.

4 Conclusion

For precise prediction of mining truck vertical dynamic characteristics and accurate identification of the suspension parameters during the transportation process, a hybrid modeling architecture is proposed by combining physics and learning methods. Experimental results from real mining truck tests demonstrate enhanced accuracy and efficiency of the proposed hybrid model compared to traditional physical and data-driven models in estimating suspension nonlinear parameters and predicting the mining truck vertical dynamic characteristics under various working conditions.

References

1. Zhou, Z., Wang, Y., Zhou, G., Nam, K., Ji, Z., Yin, C.: A twisted gaussian risk model considering target vehicle longitudinal-lateral motion states for host vehicle trajectory planning. *IEEE Trans. Intell. Transp. Syst.* **24**(12), 13685–13697 (2023)
2. Cao, D., et al.: Future directions of intelligent vehicles: potentials, possibilities, and perspectives. *IEEE Trans. Intell. Veh.* **7**(1), 7–10 (2022)
3. Xue, Z., Cheng, S., Li, L., Zhong, Z., Mu, H.: A robust unscented m-estimation-based filter for vehicle state estimation with unknown input. *IEEE Trans. Veh. Technol.* **71**(6), 6119–6130 (2022)
4. Li, Z., Chen, H., Liu, H., Wang, P., Gong, X.: Integrated longitudinal and lateral vehicle stability control for extreme conditions with safety dynamic requirements analysis. *IEEE Trans. Intell. Transp. Syst.* **23**(10), 19285–19298 (2022)
5. Yue, B., Che, W.: Data-driven dynamic event-triggered fault-tolerant platooning control. *IEEE Trans. Industr. Inf.* **19**(7), 8418–8426 (2023)
6. Yao, H., Li, X., Yang, X.: Physics-aware learning-based vehicle trajectory prediction of congested traffic in a connected vehicle environment. *IEEE Trans. Veh. Technol.* **72**(1), 102–112 (2023)
7. Gräber, T., Lupberger, S., Unterreiner, M., Schramm, D.: A hybrid approach to side-slip angle estimation with recurrent neural networks and kinematic vehicle models. *IEEE Trans. Intell. Veh.* **4**(1), 39–47 (2019)
8. Yang, D., Zhu, L., Liu, Y., Wu, D., Ran, B.: A novel car-following control model combining machine learning and kinematics models for automated vehicles. *IEEE Trans. Intell. Transp. Syst.* **20**(6), 1991–2000 (2019)

Open Access This chapter is licensed under the terms of the Creative Commons Attribution 4.0 International License (<http://creativecommons.org/licenses/by/4.0/>), which permits use, sharing, adaptation, distribution and reproduction in any medium or format, as long as you give appropriate credit to the original author(s) and the source, provide a link to the Creative Commons license and indicate if changes were made.

The images or other third party material in this chapter are included in the chapter's Creative Commons license, unless indicated otherwise in a credit line to the material. If material is not included in the chapter's Creative Commons license and your intended use is not permitted by statutory regulation or exceeds the permitted use, you will need to obtain permission directly from the copyright holder.





Point Cloud Interpolation by RGB Image to Estimate Road Surface Profile for Preview Suspension Control

Masato Inoue¹(✉), Yosuke Kawasaki¹, Takuma Suzuki², Yuta Washimi²,
Tutomu Tanimoto², and Masaki Takahashi³

¹ Graduate School of Keio University, Hiyoshi 3-14-1, Yokohama, Japan
{masato_7121, kawasaki.yosuke}@keio.jp

² Research Division, EV System Laboratory, Nissan Motor Co., Ltd., Yokohama, Japan
{takuma_s, y-washimi, tanimoto-t}@mail.nissan.co.jp

³ Keio University, Hiyoshi 3-14-1, Yokohama, Japan
takahashi@sd.keio.ac.jp

Abstract. The growing prevalence of autonomous driving is expected to shift passengers' attention from driving, increasing the demand for enhanced ride comfort. Studies addressing ride comfort have prominently explored active suspension control with recent research on preview suspension control using on-board sensors. The proposed systems often include LiDAR deployment at the front for high-precision road surface profiles. However, these systems often involve costly sensors such as LiDAR, making it impractical for on-board installation. Nonetheless, in recent autonomous vehicles, LiDAR tend to be mounted on the roof. It would be beneficial to leverage this LiDAR for preview control, the point cloud obtained from the roof has insufficient density to accurately perceive the unevenness on the road surface. To overcome the low-density issue in point cloud data obtained from less channels LiDAR, this study applies a supervised machine learning model, developed for autonomous driving, to estimate road surface profiles and enhance the precision of these estimations.

Keywords: Depth completion · Autonomous car · LiDAR · Neural Network · Point cloud densification · Preview control

1 Introduction

In the last few years, extensive research and development have been conducted towards the widespread adoption of autonomous vehicles. With the anticipated proliferation of autonomous driving, there is an expectation that occupants, including drivers, will engage in activities other than driving, further increasing the demand for enhanced ride comfort. In these considerations, studies focused on improving ride comfort of autonomous vehicles have prominently explored active suspension control. Recently, attention has shifted towards preview control using on-board sensors that have evolved in conjunction with autonomous driving technologies.

© The Author(s) 2024

G. Mastinu et al. (Eds.): AVEC 2024, LNME, pp. 672–678, 2024.

https://doi.org/10.1007/978-3-031-70392-8_95

For preview suspension control, various systems have been proposed to estimate road surface profiles. These include a system achieving high-precision road surface profile acquisition by mounting LiDAR at the front of the vehicle [1], and a system using optical sensors mounted on the roof of the vehicle to obtain road surface profiles [2]. While these preview sensing systems can independently detect the undulations of the road surface with high precision, their implementation often involves expensive sensors for preview control. Particularly, LiDAR stands out as one of the most costly sensors among those integrated into autonomous vehicles, and its use should be limited to the minimum necessary quantity and specific mounting positions for ensuring safe autonomous driving. For example, as point cloud dataset [3] shown in Fig. 1, frequently LiDAR installed for acquiring information about the surroundings of autonomous vehicles is a roof-mounted 32 channels. LiDAR used for environmental perception is often positioned on a high elevation such as on the roof, and the point cloud density is relatively low for use in preview control. Therefore, this study clarifies the differences in road surface profile estimation from the data obtained from roof-mounted LiDAR, as typically proposed for autonomous vehicles, contrasted with front-mounted, as suggested in conventional preview control studies. Moreover, to obtain a sufficient road surface profile for preview control from the sparse point cloud from LiDAR installed on autonomous vehicles, proposes that utilizes RGB image information obtained from onboard cameras.

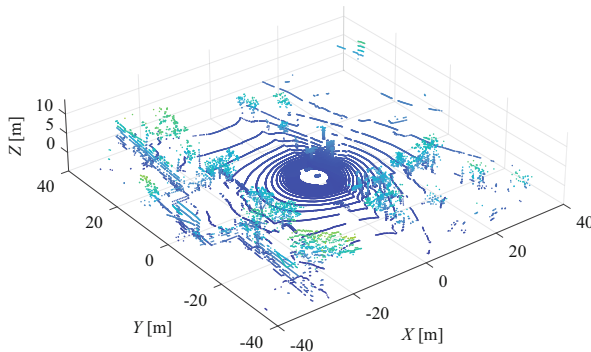


Fig. 1. An example of point cloud data from roof [3]

2 Experiments of Measuring Speed Bump

In this paper, to investigate the differences on road surface measurement by the mounting position and the number of channels of LiDAR, experiments were conducted using a system shown in Fig. 2a to measure speed bumps. Both roof-mounted and front-mounted 128 channels LiDARs (Ouster) were utilized, with an RGB camera installed near the LiDAR mounted on the roof. By using the system, a bump that has a cross-section shape as shown in Fig. 2b placed on a flat road surface was measured. In addition to the obtained 128 channels raw point cloud data, the point clouds were downsampled to 32 and 64 channels to create comparative data. For example, the point cloud data obtained from

the front-mounted 128 channels LiDAR, which is suitable for preview control when both LiDARs capture the bump simultaneously, were compared with the point cloud data obtained from the roof-mounted LiDAR assumed to have 32 channels for use in autonomous vehicles, as shown in Fig. 3. Note that both plots have the distance from the front wheels as the X-axis. As shown in Fig. 3, there is a significant difference in point cloud density due to the different mounting positions and the number of channels. Additionally, it is considered highly disadvantageous from the perspective of capturing road surface shapes if the density decreases to the level shown in Fig. 3b, even when using LiDAR.

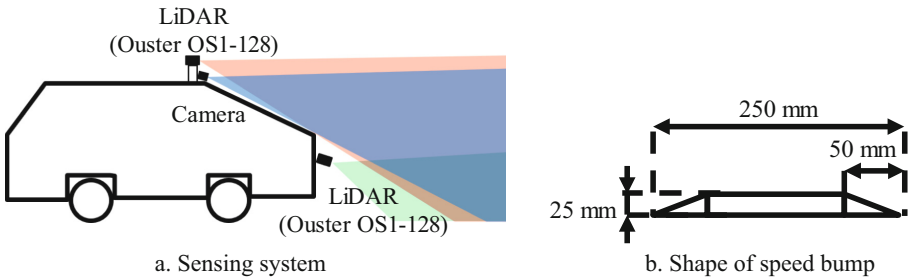


Fig. 2. Experimental Setups

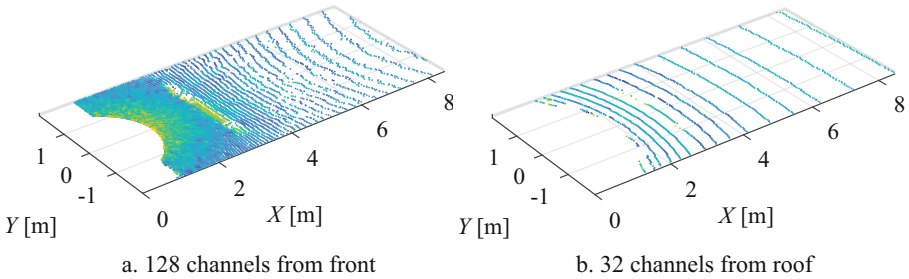


Fig. 3. Examples of Point Cloud from the System

To conduct a specific comparison, data with the width of 1 m capturing the bump from the obtained point clouds were extracted, and 2D road surface profiles with the origin at beneath the front wheels were presented for each condition in Fig. 4. The red dashed lines in the figure represent the moving average of the raw point clouds, simplified estimating the road surface shape. It can be confirmed from Fig. 4 that front-mounted LiDARs capture the undulating shape better than roof-mounted ones, and larger number of channels LiDARs captures more detailed undulations. However, in the case of roof-mounted installation, except for 128 channels, the obtained point clouds are insufficient for capturing the undulating shape adequately, making it difficult to estimate the road surface profile. Besides, the Root Mean Square Error (RMSE) of the bump shape estimated by moving average compared to the true value and the ascending order based on the RMSE including the results for 64 channels are shown in Table 1. This

study aims to enable the estimation of 2D road surface profiles with the same degree of precision as those obtained from high-density point clouds by front-mounted LiDAR, as typically handled in conventional studies on preview control, even from such sparse point clouds.

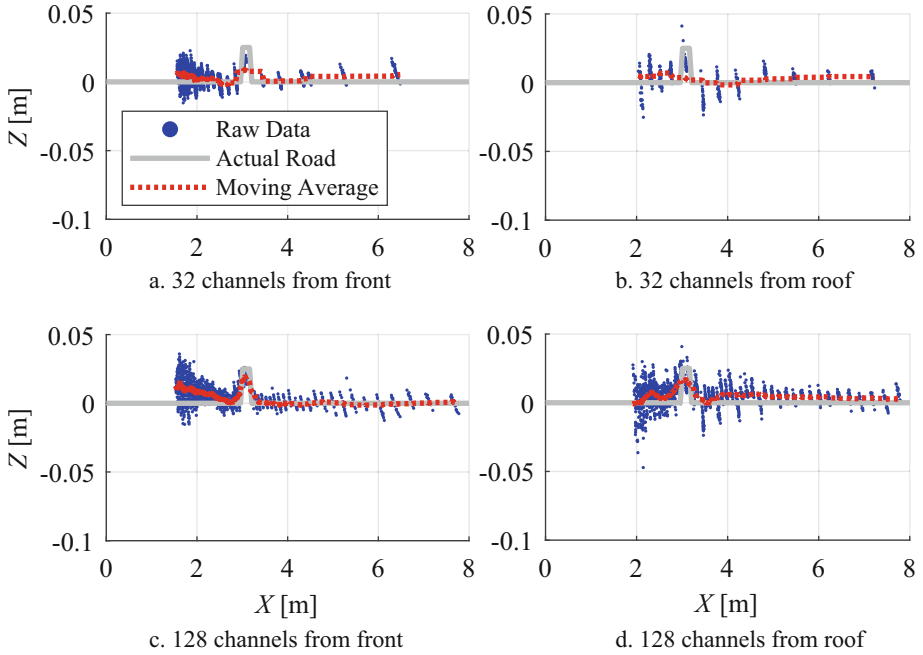


Fig. 4. Road Surface Profile from Raw LiDAR Point Cloud of Each Condition

Table 1. RMSE of Bump Shape Estimation

Front/Roof - Number of channels	F-128	F-64	F-32	R-128	R-64	R-32
RMSE [m]	0.0067	0.0095	0.0146	0.0098	0.0147	0.0208
Ascending order of RMSE value	1	2	4	3	5	6

3 Interpolation Method by RGB Using FusionNet

In this study, to densify point clouds for road surface profile estimation, FusionNet that is a supervised machine learning framework proposed by Gansbeke *et al.* [4] is employed to perform depth completion from sparse depth images generated from low-density point clouds and their corresponding RGB images. This framework has an architecture as shown in Fig. 5. By combining part of the dataset used for training the original model

with the data obtained from the current experiments, a new training dataset is created. This aims to construct a model more focused on depth of road surface than the original one.

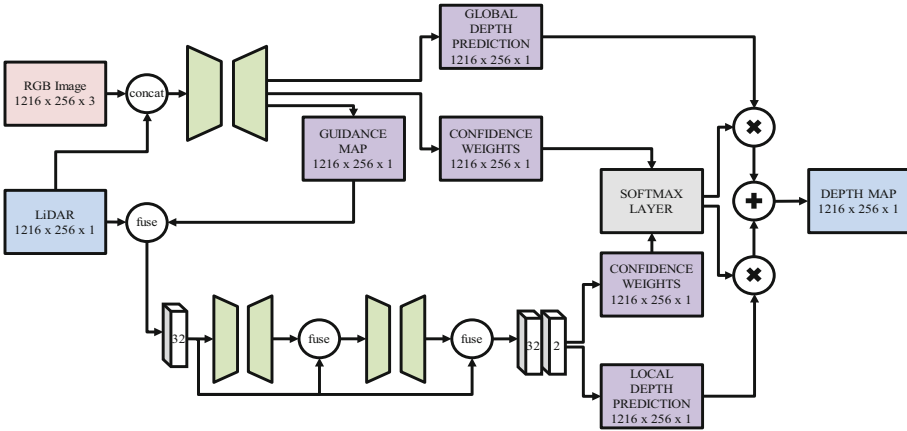


Fig. 5. Architecture of FusionNet [4]

4 Training and Results

In this training, depth map scaled to 15-m range from 32 and 64 channels front-mounted LiDAR, along with their corresponding RGB images, were provided as input data, with the ground truth data based on the 128 channels data as supervision. An example frame used in the training data is shown in Fig. 6. Our dataset provides 6650 frames for training, 2490 frames for evaluation, and 1091 frames for testing. In this paper we tried to achieve densification from 32 channels front-mounted LiDAR data. However, directly using the raw 128 channels data as the ground truth can make it challenging to estimate planes accurately due to noise. Therefore, denoising was performed as shown in Fig. 7. This involved segmenting the planes from the point clouds, removing the points recognized as planes, and inserting grids based on plane equations to denoise the data.

The results of point cloud densification by using our trained model at the same location as in Fig. 4 are shown in Fig. 8. The best RMSE between the dense depth map as an output and the ground truth was 0.023 m. Additionally, the RMSE of the undulating shape in estimated road surface profile from predicted dense depth map by the same method as those in Fig. 4 was 0.0118 m.

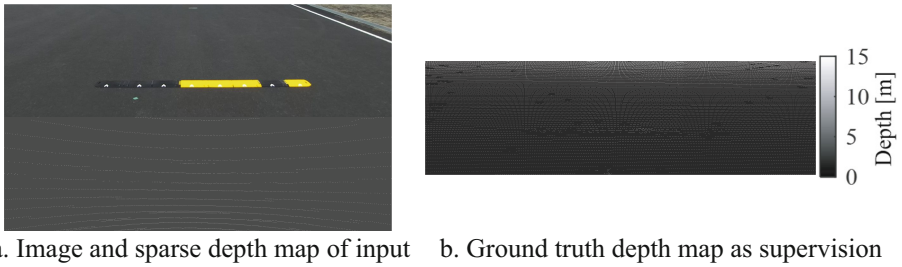


Fig. 6. One Frame of our Dataset

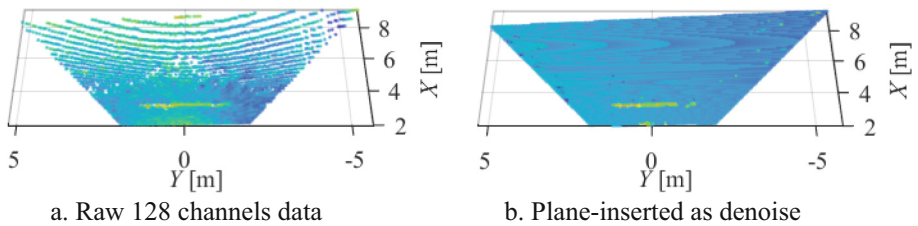


Fig. 7. Ground Truth

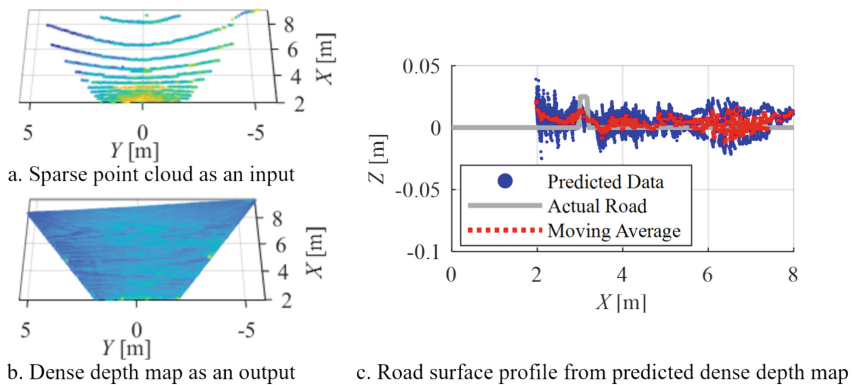


Fig. 8. Prediction Results with Trained Model

5 Conclusion

In this paper, we compared measurement accuracy differences due to LiDAR installation position and the number of channels. The results indicate significant challenges in estimating undulating shapes with LiDAR mounted on autonomous vehicles. To address this, we trained a model to densify low-density road point clouds. Future work will focus on enhancing accuracy by applying object detection techniques.

References

1. Wu, J., Zhou, H., Liu, Z., Gu, M.: Ride comfort optimization via speed planning and preview semi-active suspension control for autonomous vehicles on uneven roads. *IEEE Trans. Veh. Technol.* **69**(8), 8343–8355 (2020)
2. Papadimitrakis, M., Alexandridis, A.: Active vehicle suspension control using road preview model predictive control and radial basis function networks. *Appl Soft Compute* **120**, 108646 (2022)
3. Udacity Self-Driving Car Data Subset. <https://github.com/mathworks/udacity-self-driving-data-subset/tree/master>. Accessed 6 Jan 2024
4. Van Gansbeke, W., Neven, D., De Brabandere, B., Van Gool, L.: Sparse and noisy LiDAR completion with RGB guidance and uncertainty. In: 16th International Conference on Machine Vision Applications, Tokyo, Japan (2019)

Open Access This chapter is licensed under the terms of the Creative Commons Attribution 4.0 International License (<http://creativecommons.org/licenses/by/4.0/>), which permits use, sharing, adaptation, distribution and reproduction in any medium or format, as long as you give appropriate credit to the original author(s) and the source, provide a link to the Creative Commons license and indicate if changes were made.

The images or other third party material in this chapter are included in the chapter's Creative Commons license, unless indicated otherwise in a credit line to the material. If material is not included in the chapter's Creative Commons license and your intended use is not permitted by statutory regulation or exceeds the permitted use, you will need to obtain permission directly from the copyright holder.





Gain-Scheduled Bicycle Balance Controller Based on System Identification

Yixiao Wang^(✉), Fredrik Bruzelius, and Jonas Sjöberg

Department of Electrical Engineering and Department of Mechanical Engineering,
Chalmers University of Technology, Gothenburg, Sweden
{yixiaow, fredrik.bruzelius, jonas.sjoberg}@chalmers.se

Abstract. Balancing a bicycle through steering is similar to balancing an inverted pendulum, with a travel-speed-dependent pivot point. This paper derives a speed-dependent balancing controller for a self-balancing bicycle. This controller is based on an identified gray box model. The identification procedure is formulated as a weighted least squares problem with the time-varying parameter of the model. Identification data was generated on a controlled bicycle robot. Excitation experiments were designed to account for the unstable nature of the problem. Based on this identified model, a gain-scheduled controller is derived for a speed-independent closed-loop performance for a speed range. The controller is further implemented on the bicycle and tested for a set of speeds. Tests performed on the bicycle illustrate the gain-scheduled controller's performance gain.

Keywords: Bicycle dynamics · Gray-box identification · Gain-scheduled controller

1 Introduction

Modern traffic safety relies heavily on Advanced Driver Assistance Systems (ADAS). Testing these systems often requires specific scenarios that include a cyclist target to ensure safety and repeatability. To address the challenges of testing ADAS in cyclist scenarios, a bicycle robot with self-balancing and path-tracking capabilities has been developed. Compared to existing solutions with a stable moving robot platform [1], this bicycle robot is inherently unstable and hence will exhibit more natural leaning behavior.

Obtaining a reliable model usually requires measuring and computing physical parameters. However, such methods require additional tools and time to dismantle the bicycle and measure its individual parts. In contrast, this paper adopts an alternative approach: using system identification techniques to estimate these model parameters from experimental data.

Gray-box identification offers an advantage in this context. It employs a model structure informed by physical principles, which can enhance robustness

Supported by VINNOVA, Swedish Innovation Agency.

© The Author(s) 2024

G. Mastinu et al. (Eds.): AVEC 2024, LNME, pp. 679–685, 2024.

https://doi.org/10.1007/978-3-031-70392-8_96

against varying operational conditions. Given its benefits, we apply a gray-box identification method, to compute a bicycle model parameterized by longitudinal speeds. This strategy combines the merits of a physically-informed model with system identification, enabling the identified model to extrapolate dynamics across multiple speeds.

In this paper, we introduce a gray-box identification method to obtain a semi-linear bicycle model. Tests are done in a closed loop and a model with an explicit speed dependency is obtained. The speed-dependent model is then used to derive a controller that achieves a speed independent closed loop using gain scheduling (Fig. 2).

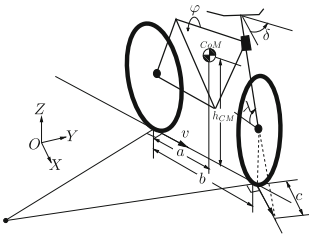


Fig. 1. Bike schematics

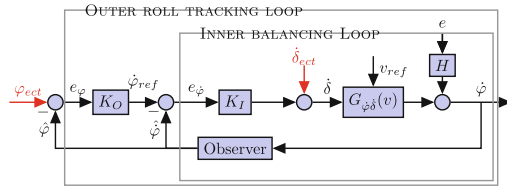


Fig. 2. Schematic Block of the Control loops

2 Method

The steering angle of the bicycle is assumed to be controlled perfectly. Hence, we do not need to consider models that include the interaction between the leaning angle and the steering torque. Instead we adopted a point-mass model from [2] for its simplicity and relevance to our actuator settings, as shown in Fig. 1. The bicycle’s roll dynamics from steering angle δ to roll φ are given by, assuming small caster,

$$J_{xx} \frac{d^2\varphi}{dt^2} - mgh_{CM}\varphi = \frac{J_{xz}v \sin(\lambda)}{b} \frac{d\delta}{dt} + \frac{mv^2 h_{CM} \sin(\lambda)}{b} \delta, \tag{1}$$

where J_{xx}, J_{xz} are the inertia with respect to the xz -axes and x -axes. Other parameters are depicted in Fig. 1. The equation above can be recast to a LTI transfer function for a constant speed with the structure,

$$G_{\varphi\delta}(s, v) = \frac{A_0vs + A_1v^2}{s^2 + B_0} \tag{2}$$

where s is the Laplace operator and A_i, B_i are constant coefficients. This equation describes the roll dynamics, i.e., $G_{\varphi\delta}(v)$ in Fig. 1.

To identify the parameters of the roll dynamics in (2), identification experiments were conducted in closed loop. To mitigate biases induced by closed loop,

periodic excitation signals were used and frequency responses are collected [3]. This was done by applying these periodic signals to the reference φ_{ect} and noise to $\hat{\delta}_{ect}$. Further, to use the frequency response for our unstable system $G_{\hat{\varphi}\hat{\delta}}$, the definition of transfer functions are also extended to include the imaginary axis, since the imaginary axis is not in its region of convergence.

A next step in the identification process was to form empirical transfer function estimate (ETF) $\hat{F}(j\omega, v_i)$ based on the measured tests,

$$\hat{F}(j\omega, v_i) = \frac{1}{P_i} \sum_{l=1}^{l=P_i} \frac{\mathcal{F}\{\hat{\varphi}_{[l]}(j\omega, v_i)\}}{\mathcal{F}\{\hat{\delta}_{[l]}(j\omega, v_i)\}} = R(j\omega, v_i) + jI(j\omega, v_i) \tag{3}$$

where subscript l denotes the l th response out of P_i periodic responses conducted at speed v_i . $\mathcal{F}\{x\}$ denotes the Fourier transform of time series data x , and R and I denote the coefficients of real and imaginary components, respectively. Such an averaged ETFE is asymptotically unbiased if the noise e is Gaussian [3].

A final step in the identification process was to use the obtained ETFE in (3) to fit the model (2).

To minimize the difference between the identified model $G_{\hat{\varphi}\hat{\delta}}(j\omega, v)$ and the empirical transfer function $\hat{F}(j\omega, v_i)$, a cost function of frequency responses $\varepsilon(j\omega, v)$ can be defined

$$\varepsilon(j\omega, v) = \hat{F}(j\omega, v) - G_{\hat{\varphi}\hat{\delta}}(j\omega, v) = \hat{F}(j\omega, v) - \frac{N(j\omega, v)}{D(j\omega, v)} \tag{4}$$

$$D\varepsilon = D\hat{F} - N = a(j\omega, v) + jb(j\omega, v) \tag{5}$$

where N and D are numerator and denominator of the transfer function in (2).

With a total of n experiments at speeds $v_i, i \in \mathcal{Z}^+$ and each containing $m+1$ frequency points in frequency responses, we may sum the cost function $\varepsilon(j\omega, v)$ over all the experiments

$$E = \sum_{i=1}^n \sum_{k=0}^m [a^2(j\omega_k, v_i) + b^2(j\omega_k, v_i)]. \tag{6}$$

Here k denotes the index of the frequency points in Fourier Transformation of the experiment data and i denotes the index of speeds. For simplicity in notation, variables to the functions $(j\omega_k, v_i)$ will be omitted henceforth. We notice that, (6) is a weighted cost function of the difference between the identified model $G_{\hat{\varphi}\hat{\delta}}$ and the empirical transfer function \hat{F} . Therefore, we can minimize (6) with respect to all unknown coefficients - A_i 's and B_i 's in the transfer function

$$\frac{\partial E}{\partial A_i} = 0, \quad \frac{\partial E}{\partial B_i} = 0. \tag{7}$$

To minimize the differences (6) over all the experiments spanned in a speed range $\{v_1, \dots, v_n\}$, we construct the equations into a linear regression form. Define

intermediate variables λ_h, S_h, T_h and U_h

$$\lambda_h = \sum_{k=0}^m W_k \omega_k^h, S_h = \sum_{k=0}^m W_k \omega_k^h \hat{R}_k, T_h = \sum_{k=0}^m W_k \omega_k^h \hat{I}_k, U_h = \sum_{k=0}^m W_k \omega_k^h (\hat{R}_k^2 + \hat{I}_k^2)$$

where m denotes the number of frequency points in a frequency response. W_k , which provides design freedom compared to the weight D from problem construction in (5), is a user-defined weight for individual frequency points.

Substitute these variables and rewrite (7) in matrix form

$$\begin{aligned} \sum_{i=1}^n \begin{bmatrix} 2\lambda_0 v_i^4 & 0 & -2S_0 v_i^2 \\ 0 & 2\lambda_2 v_i^2 & -2T_1 v_i \\ -2S_0 v_i^2 & -2T_1 v_i & 2U_0 \end{bmatrix} \begin{bmatrix} A_0 \\ A_1 \\ B_0 \end{bmatrix} &= \sum_{i=1}^n M(v_i)N \\ &= \sum_{i=1}^n \begin{bmatrix} -2S_2 v_i^2 \\ -2T_3 v_i \\ 2U_2 \end{bmatrix} = \sum_{i=1}^n C(v_i). \end{aligned} \tag{8}$$

Further, experiments can also be weighted individually

$$\sum_{i=1}^n W_i M(v_i)N = \sum_{i=1}^n W_i C(v_i) \tag{9}$$

where W_i is the user-defined weight for individual speeds $i \in \{1, \dots, n\}$. This complex linear curve fitting problem is thus solvable in a weighted least square formulation. The weights for individual experiments and frequency points, i.e. W_i and W_k , may be used as a tuning parameter, depending on the number of periods in each experiment and frequency range of confidence.

Based on the derived parameter dependent LTI model of the roll dynamics, a gain-scheduled PD controller was designed. The design criteria was a speed independent closed loop performance for a range of speeds. Specifically, $K_I(v)$ and $K_O(v)$ are computed, such that inner balancing and outer roll tracking loop in Fig. 1 have speed-independent bandwidths.

3 Result

On the bicycle presented in Fig. 3, identification experiments have been conducted, at speeds of 2.2, 2.4, 2.6, 2.8 m/s. Although these experiments were conducted without a human dummy, our algorithm is prepared for scenarios involving a dummy, which can be modeled as a mass rigidly attached to the saddle. Periodic multisine signals up to 25 Hz are chosen for φ_{ect} and δ_{ect} to control the excitation frequency range. After the decay of initial transients, the periodic responses are processed following (3). Table 1 summarizes the number of identification periods and Fig. 3 visualizes the averaged frequency responses at each speed. It is noteworthy that, in lower frequency range, a clear dependency can be seen between the magnitudes of frequency responses and the speeds. At

higher frequencies, this dependency dies out and it might be attributed to other system dynamics in the control loop, e.g. sensors.

Substituting the computed averaged empirical transfer functions $\hat{F}(j\omega, v_i) = \tilde{G}_i(j\omega)$ and letting the weights W_k, W_i be identity for simplicity, a model is identified:

$$\hat{G}_{\phi\delta}(s, v) = \frac{0.8285vs + 1.9699v^2}{s^2 - 20.2663} \tag{10}$$

To evaluate this model and with a rough approximation of $D = -J_{xz} \approx -mah_{CM}$ and $J \approx mh_{CM}^2$, a comparison between the identified parameters of the roll dynamics and direct measurements of center of gravity is given in Table 2. It can be observed that the differences are small in magnitude.

Based on the identified model, we compute $K_I(v)$ and $K_O(v)$ to limit the closed-loop bandwidth of the inner balancing loop to be 1.5 Hz and the outer roll-tracking loop 0.15 Hz respectively.

Against a same step references of $\pm 3^\circ$, this gain-scheduled PD controller was tested on the bicycle robot. For comparison, a speed-independent P-D controller is tested as well, referred to as conventional P-D controller. Figure 3 illustrates the roll-tracking performance. While both the gain-scheduled (Blue) and conventional P-D controllers (Red) performed similarly at the higher speed, the gain-scheduled controller has better performance at the lower speed. This highlights the limitations of conventional controllers and confirm the practical need of our gain-scheduled approach. With the same roll reference, the gain-scheduled controller is further tested at an even lower speed of 1.7 m/s, visualized in Fig. 6. Despite of constraints in the steering motor and IMU signal-to-noise ratio, the gain-scheduled controller stabilized the bicycle, showing the potential of speed extrapolation (Figs. 5 and 4).

Table 1. The experiment profile

Speed (m/s)	total number of Periods
2.2	11
2.4	19
2.6	12
2.8	7

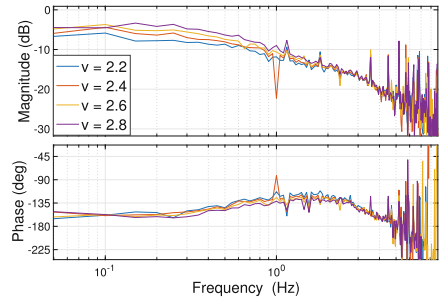


Fig. 3. Figure to the right: the averaged empirical transfer function (3)

Table 2. The calculated physical parameters illustrated in Fig. 1

	calculated (m)	measured (m)
a	0.4206	0.6687
b	0.9580	1.1549
h_{CM}	0.4841	0.534

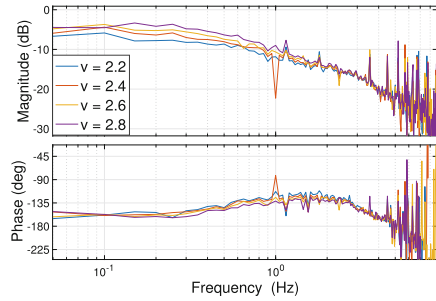


Fig. 4. Bike modules overview

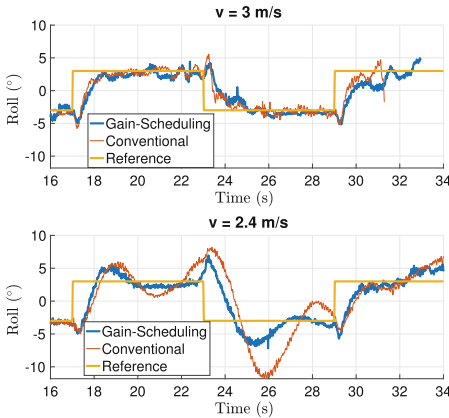


Fig. 5. Figure to the right: Tests of the Gain-scheduled controller (Blue) and conventional P-D controller (Red) at 2.4 and 3.0 m/s with $\varphi_{ref} = \pm 3^\circ$

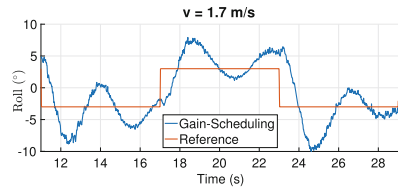


Fig. 6. Experiment with the extrapolated Gain-scheduling controller at lower speeds

4 Conclusions

An approach to obtain a gain scheduled controller for a balancing bicycle robot using grey box identification is presented. The performance of the controller is illustrated on a prototype bicycle robot. The gray box identification employs periodic excitation signal to asymptotically remove the bias and the excitation frequency ranges are tailored with multisine excitation signals.

Future work will focus on enhancing controller robustness and adapting the model for changing conditions, e.g., loading different human dummies. Besides, adaptive control and online identification based on dual-Youla method may be explored as it fits our purpose well [5].

References

1. 4 Active Systems. 4activemc (EuroNCAP) - 4ActiveSystems - Solutions for ADAS and Autonomous Driving (2022). <https://www.4activesystems.at/4activemc-gmt>. Accessed 20th May 2024
2. Astrom, K.J., Klein, R.E., Lennartsson, A.: Bicycle dynamics and control: adapted bicycles for education and research. *IEEE Control Syst. Mag.* **25**(4), 26–47 (2005)
3. World Health: Bias of indirect non-parametric transfer function estimates for plants in closed loop. *Automatica* **37**(10), 1529–1540 (2001). <https://www.sciencedirect.com/science/article/pii/S0005109801001054>
4. Levy, E.C.: Complex-curve fitting. *IRE Trans. Autom. Control* **AC-4**(1), 37–43 (1959). <https://doi.org/10.1109/tac.1959.6429401>
5. Mahtout, I., Navas, F., Milanes, V., Nashashibi, F.: Advances in Youla-Kucera parametrization: a review. *Annu. Rev. Control* **49**, 81–94 (2020). <https://www.sciencedirect.com/science/article/pii/S1367578820300249>

Open Access This chapter is licensed under the terms of the Creative Commons Attribution 4.0 International License (<http://creativecommons.org/licenses/by/4.0/>), which permits use, sharing, adaptation, distribution and reproduction in any medium or format, as long as you give appropriate credit to the original author(s) and the source, provide a link to the Creative Commons license and indicate if changes were made.

The images or other third party material in this chapter are included in the chapter's Creative Commons license, unless indicated otherwise in a credit line to the material. If material is not included in the chapter's Creative Commons license and your intended use is not permitted by statutory regulation or exceeds the permitted use, you will need to obtain permission directly from the copyright holder.





Investigating Reversing Motion of Truck-Semitrailer Along Clothoid Curve

Levente Mihályi¹(✉) and Dénes Takács^{1,2}

¹ Department of Applied Mechanics, Faculty of Mechanical Engineering,
Budapest University of Technology and Economics, Műegyetem rkp. 3.,
Budapest 1111, Hungary

{mihalyi,takacs}@mm.bme.hu

² HUN-REN-BME Dynamics of Machines Research Group, Műegyetem rkp. 3.,
Budapest 1111, Hungary

Abstract. The focus of the research is on the most common transport vehicle, the truck-semitrailer combination. A single-track kinematic model is used, supplemented by the dynamics of the steering system, to design a linear state feedback controller for the low-speed path-following problem in reverse. Despite the significant time delay considered in our study, the linear stability of the system is ensured, even for complicated maneuvers. The advantages of the adaptive gain tuning method are presented based on simulations of the commonly used 90-degree alley dock.

Keywords: truck-semitrailer · reverse maneuvering · time delay · path-following

1 Introduction

Autonomous vehicles imply a fundamental change in modern engineering. Optimizing safety, speed, and operating costs is the task and responsibility of engineers. Beyond safety, the competition among automotive designers now focuses on reducing travel time and costs, even more so, in the case of commercial trucks. Key tasks on highways involve operating long convoys with only one human driver in the front, i.e., platooning. Vehicle-to-vehicle communication decreases fuel consumption through real-time traffic data.

Maneuvering articulated vehicles, especially in reverse motion, demands special attention due to potential accidents like the Jackknifing phenomenon [1, 2]. Driver Assistance Systems (DAS) are available, but these features only assist human drivers, not replace them in complicated situations. Auto-parking systems at docking stations address the dwelling time problem of transport companies [3]. The implementation of automated maneuvers cannot be realized without developing path-following controls in reverse motion [4]. Installing fully automated parking systems into loading bays allows drivers to spend more time on the road.

Our research focuses on the most common freight transport vehicle, the truck-semitrailer combination. Due to the dwelling time problem, we are interested in realizing complicated maneuvers in reverse motion. The single-track kinematic model is applied with the assumption of rigid wheels. The paper presents and analyzes a control scheme for solving the path-following problem in low-speed reverse motion. Neglecting the time delay of localization and control-related computations on stability may be irresponsible; thus, the stability of reversing along curves with constant curvatures is investigated in the presence of significant time delay. Based on stability charts - produced by the semi-discretization method, see [5] - related to reversing along circular arcs (constant curvature), three different gain tuning strategies for varying curvature are selected, and their performances are compared via simulations.

2 Model Setup

The vehicle combination is modeled with the single-track kinematic model, see Fig. 1. The wheels at points F, R and T are assumed rigid. The constant longitudinal speed of the rear axle of the towing truck is V . The geometry is described by the wheelbase l of the towing vehicle, the distance a between the kingpin (K) and the rear axle (R), and the length L of the trailer's axle measured from the kingpin. During the path-following problem, the prescribed point of the vehicle combination is the center point T of the trailer's axle. Table 1 contains the numerical values of the parameters.

The vector of the state variables is $\mathbf{q} = [e \ \Theta \ \varphi \ \delta \ \omega]$, where e is the lateral deviation between the prescribed point of the vehicle combination (T) and the closest point on the desired path (C); Θ denotes the yaw angle error; and φ is the relative yaw angle between the two vehicle parts. The dynamics of the steering system are considered using the steering angle δ of the front wheel (which is related to the only actuation) and steering rate ω . The control gains p and d of the steering servo control are listed in Table 1.

The equations of motion are derived from the kinematic constraints of the vehicle. On the one hand, the velocity vectors of points F, R and T are parallel to the related wheel planes, described by the unit vectors \mathbf{e}_F , \mathbf{e}_R and \mathbf{e}_T in Fig. 1. On the other hand, the longitudinal speed of the truck's rear axle (point R) is constant (V). Finally, the equations of motion are formulated in

$$\dot{e} = V \left(\sin(\theta - \varphi) - \frac{a}{l} \tan \delta \cos(\theta - \varphi) + \cos \theta \left(\sin \varphi + \frac{a}{l} \cos \varphi \tan \delta \right) \right), \quad (1)$$

$$\dot{\theta} = \frac{V}{l} \tan \delta + \dot{\varphi} - \kappa \dot{s}, \quad (2)$$

$$\dot{\varphi} = -\frac{V}{lL} (l \sin \varphi + (L + a \cos \varphi) \tan \delta), \quad (3)$$

$$\dot{\delta} = \omega, \quad (4)$$

$$\dot{\omega} = -p\delta - d\omega + p\delta_{\text{des}}, \quad (5)$$

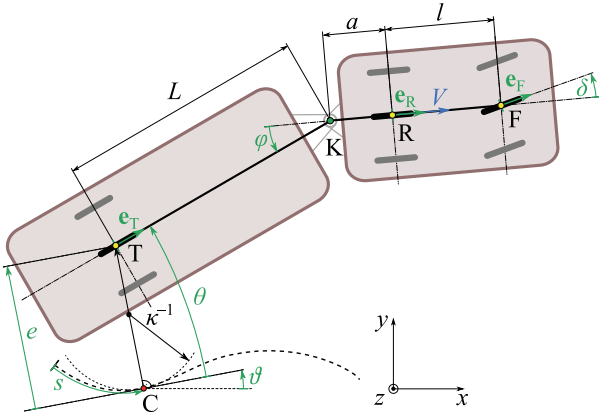


Table 1. Numerical values of the parameters.

Parameter	Value
V	-1.5 m/s
a	-0.8 m
l	3.5 m
L	10 m
p	300 1/s^2
d	34.6 1/s

Fig. 1. Single-track kinematic model of the truck-semitrailer.

The reverse path-following motion is achieved by a linear feedback controller:

$$\delta_{\text{des}}(t) = \delta_{\text{ff}}(\kappa) - P_e e(t - \tau) - P_\theta \theta(t - \tau) - P_\varphi (\varphi(t - \tau) - \varphi^*), \quad (6)$$

where τ is the feedback delay; P_e , P_θ and P_φ are the control gains (representing the feedback term) related to the lateral deviation, the angle error and the relative yaw angle between the truck and the trailer, respectively. The feedforward term $\delta_{\text{ff}}(\kappa)$ and the reference value $\varphi^*(\kappa)$ of the relative yaw angle are the steady-state solutions of (1)–(5), which depend on the curvature κ , of course. Note that the steady-state solution could be generated from geometric considerations as well.

3 Stability and Optimization

Figure 2(a) shows the linear stability chart of the path-following motion when the time delay is $\tau = 0.5 \text{ s}$. Colored areas represent the stable gain configurations; white crosses denote the most stable gain setup (in the sense of the smallest real part of the rightmost eigenvalues) for each curvature value. As can be seen, the most stable gain setup for one specific case may be located outside of the stable domain for a different curvature value. However, reversing along a path with varying curvature may still be possible if control gains are selected from the intersection of stable domains (assuming that the rate of change is relatively small).

The main contribution of this study is the comparison of control gain tuning methods. One of the most common maneuvers in loading bays is the so-called 90-degree alley dock in reverse. This maneuver can be realized along a path consisting of three clothoid arcs (i.e., the curvature κ changes linearly, see [6]), and a straight-line run-out at the end. The desired position and orientation of

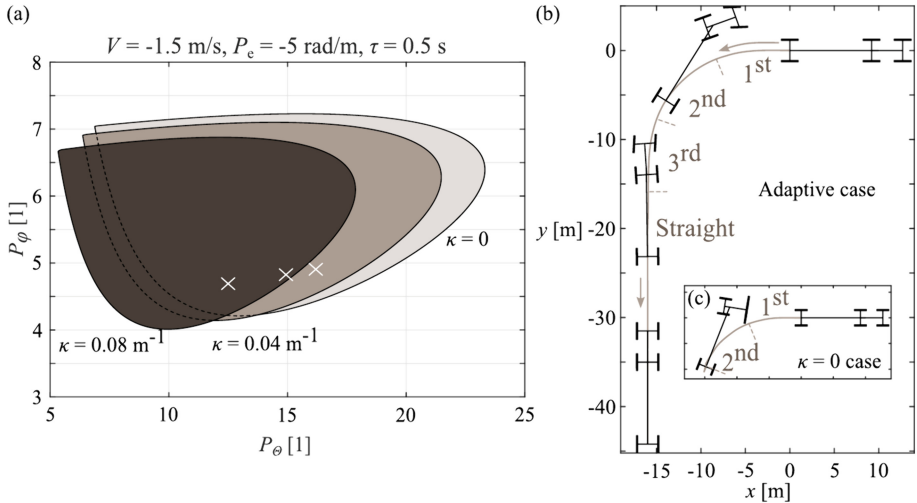


Fig. 2. (a) Stability chart in the plane of control gains. Shaded areas denote the stable domains for different curvature values. White crosses represent the most stable gain setups within each stable region. (b)–(c) Trajectories of the trailer's axle (prescribed point) during the investigated 90-degree alley dock with the skeleton model of the vehicle combination at some specific time steps. The clothoid segments and the straight run-out are labeled along the trajectories.

the trailer, and the curvature of the path can be adjusted at the start and end points of the maneuver. The trajectory with the explanation of the segments is plotted in Fig. 2(b).

The differences in the performance between three different gain tuning methods are shown in Fig. 3. The comparison is based on simulation results by solving the nonlinear equations of motion (1)–(5) using the *Matlab* built-in solver *dde23* with adaptive time stepping. The steady-state solution related to zero curvature (i.e., the starting of the maneuver) is set as the initial condition. Panels (a)–(e) represent the time series of the state variables, while (f) shows the change of curvature in time along the entire path. The path segments are separated by brown dashed lines in each panel. Real vehicles have a physical limit to the steering angle. Let this limit be $\delta_{\max} = 40^\circ = 0.7$ rad, as also marked with gray dashed line in panel (d). Three distinct methods for tuning the control gains are presented: the green thick line represents the case when the gains are adaptively tuned to the most stable setup according to the instantaneous curvature; the blue thin line is the most stable for the largest occurring curvature value; while the orange dashed line is the most stable for the zero curvature, i.e. assuming straight-line motion.

Figure 2(b) also helps visualize the motion in the case of adaptive gain tuning that provides a smooth and precise parking maneuver. In panel (c), the motion is illustrated when the gains of the controller are tuned for $\kappa = 0$. The

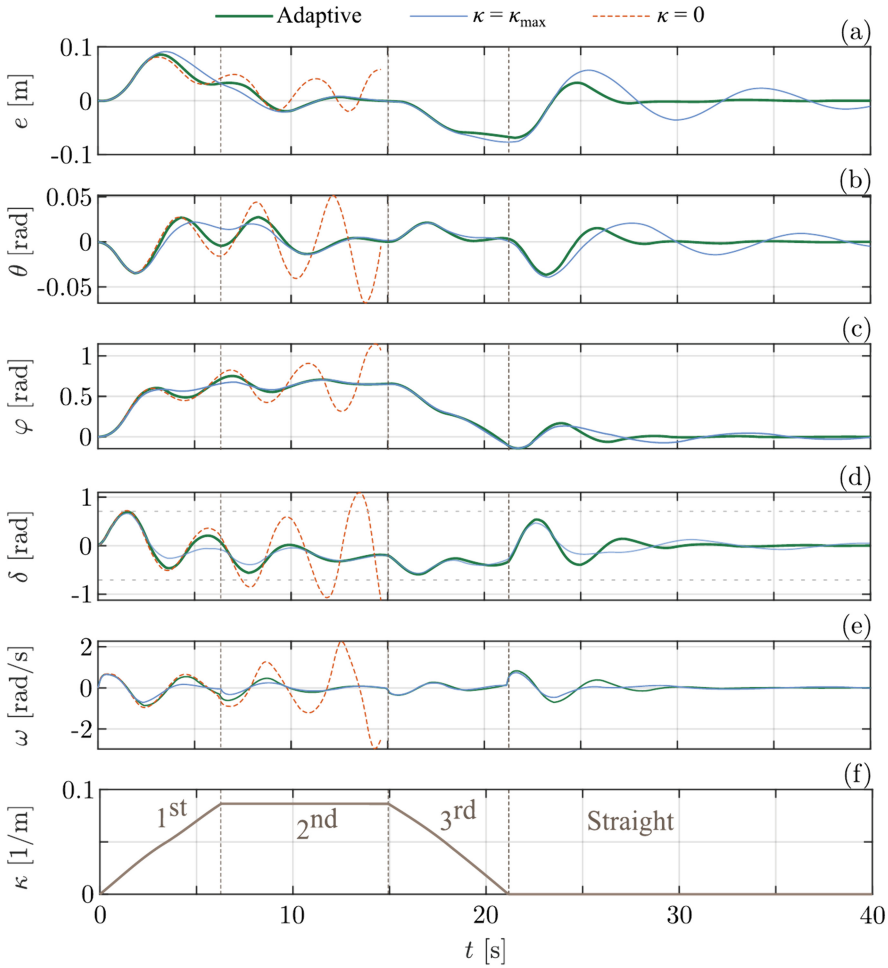


Fig. 3. Simulated time series of the state variables during the 90-degree alley dock (i.e., reversing along a path with varying curvature) with time delay $\tau = 0.5$ s in order to demonstrate the differences between the three distinct gain tuning methods. The control gain related to the lateral deviation is $P_e = -5$ rad/m. Vertical dashed lines separate the segments of the path. Horizontal dashed lines in (d) mark the physical limit of the steering angle.

motion becomes unstable as the steering angle exceeds its limitation and the truck overturns in this latter case.

As a main contribution, using adaptive control gain tuning is recommended to solve the reversing problem along the path of varying curvature. However, considering the largest occurring curvature in the gain tuning method can also lead to an acceptable solution, although precise positioning may not be achievable at the straight-line segment (when $\kappa = 0$). Finally, neglecting the path curvature in the 90-degree alley dock maneuver in reverse can easily lead to unstable motion.

4 Conclusion

A possible control algorithm for reversing a truck-semitrailer combination along a path was constructed using the single-track kinematic model. The time delay in the control loop and the dynamics of the steering mechanism were also included in the model. An adaptive control gain tuning method was established besides two other strategies by which reversing may be stabilized even in case of a large time delay. These methods were implemented via a typical parking maneuver involving varying path curvature. In order to achieve the best performance in solving the path-following problem, the adaptive control scheme is recommended based on the presented comparison.

Acknowledgement. The research reported in this paper was partly supported by the János Bolyai Research Scholarship of the Hungarian Academy of Sciences and by the National Research, Development and Innovation Office under grant no. NKFI-146201; and by 2020-1.2.4-TET-IPARI-2021-00012, and by the Foundation for Mechanical Engineering Education.

References

1. Roh, J., Chung, W.: Reversing control of a car with a trailer using the driver assistance system. *Int. J. Adv. Robot. Syst.* **8**(2) (2011). <https://doi.org/10.5772/10578>
2. Chiu, J., Ambarish, G.: The critical hitch angle for jackknife avoidance during slow backing up of vehicle-trailer systems. *Veh. Syst. Dyn.* **52**(7), 992–1015 (2014). <https://doi.org/10.1080/00423114.2014.909944>
3. Shin, H., Kim, M.J., Baek, S., et al.: Perpendicular parking path generation and optimal path tracking algorithm for auto-parking of trailers. *Int. J. Control Autom. Syst.* **20**, 3006–3018 (2022). <https://doi.org/10.1007/s12555-021-0268-9>
4. Hamaguchi, Y., Raksincharoensak, P.: Study on path planning and tracking algorithm for autonomous parking system of semi-trailers. *Mech. Eng. J.* **10**(3) (2023). <https://doi.org/10.1299/mej.22-00361>
5. Insperger, T., Stepan, G.: *Semi-Discretization for Time-Delay Systems – Stability and Engineering Applications*. Springer, New York (2011). <https://doi.org/10.1007/978-1-4614-0335-7>
6. Bertolazzi, E., Frego, M.: On the G2 Hermite interpolation problem with clothoids. *J. Comput. Appl. Math.* **341**, 99–116 (2018). <https://doi.org/10.1016/j.cam.2018.03.029>

Open Access This chapter is licensed under the terms of the Creative Commons Attribution 4.0 International License (<http://creativecommons.org/licenses/by/4.0/>), which permits use, sharing, adaptation, distribution and reproduction in any medium or format, as long as you give appropriate credit to the original author(s) and the source, provide a link to the Creative Commons license and indicate if changes were made.

The images or other third party material in this chapter are included in the chapter's Creative Commons license, unless indicated otherwise in a credit line to the material. If material is not included in the chapter's Creative Commons license and your intended use is not permitted by statutory regulation or exceeds the permitted use, you will need to obtain permission directly from the copyright holder.





A Way Beyond Drifting: Cornering at the Unexploited Region of Dynamics

Hangyu Lu^{1,2(✉)}, Xiaodong Wu¹, and Liang Yan¹

¹ Institute of Intelligent Vehicles, Shanghai Jiao Tong University, Shanghai, China
{hangyulu95,xiaodongwu}@sjtu.edu.cn

² Budapest University of Technology and Economics, Budapest, Hungary

Abstract. Linear range considerations in the tire-road contact restrict the potential of dynamic control designs of passenger vehicles, while strong nonlinear dynamics such as drifting are intrinsically dangerous. In this paper, based on the chassis with independent wheel drive/brake torque control, we propose a model-based strategy to exploit the potentials of all four tires in combined slips to elevate the cornering performance in critical maneuvers. The model-inversed results indicate that the maximal achievable steady-state (SS) yawing is larger than the widely-used boundary for control system design. Nonlinear dynamics around the created stable motions are further analyzed by plotting phase planes. With feedback control incorporated, the proposed strategy is verified in simulations for both local and global dynamics. The method also shows a distinctive availability of tuning different vehicles into desired driving characteristics and elevating their performance levels through independent powertrains.

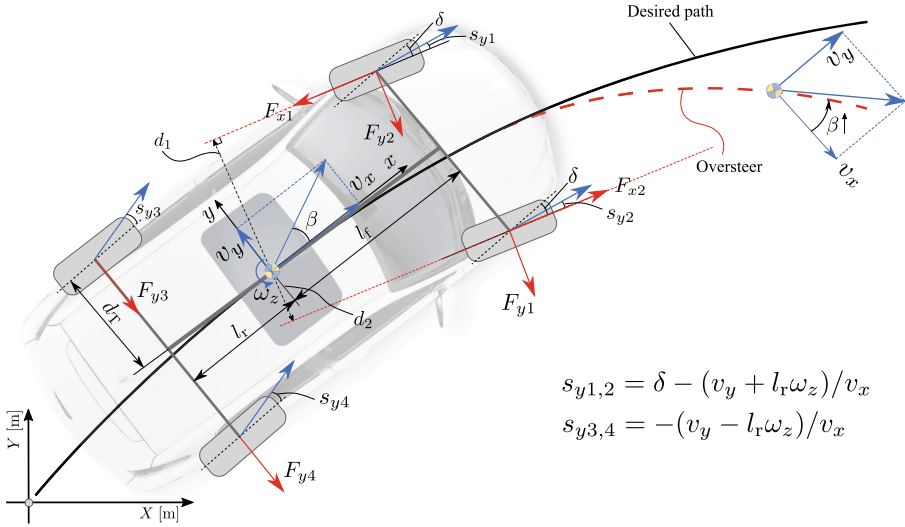
Keywords: Vehicle dynamics · Steering characteristics · Combined slip · Cornering performance · Vehicle stability control

1 Introduction and Motivation

The development of vehicular technology has led to a surge of innovations in chassis control. Still, such advancement is restricted by the very basic mechanics mechanism of the tire-ground contacts. To maintain steerability for drivers, classical active systems (e.g., ESC) commonly keep the vehicle within the linear SS boundaries that in return, give up the potential in the nonlinear regions [1, 2]. In advanced chassis with independent torque control, more possibilities are shown with the utilization of large combined slips, such as drifting control in [3] and obstacle avoidance in [4]. Indeed, such large-side slip motion is stabilizable while not elevated since the maximal yawing is yet within the SS boundary in [1, 5].

1.1 Problem Formulation

The motivation of the paper comes from the demand to stabilize the oversteer vehicle after global instability is induced by Saddle-Node bifurcation [1]. Instead



$$s_{y1,2} = \delta - (v_y + l_r \omega_z) / v_x$$

$$s_{y3,4} = -(v_y - l_r \omega_z) / v_x$$

Fig. 1. (a) Modification of SS steering chara (-OL: open-loop; -C: with proposed control; US: understeer; OS: oversteer; NS: neutral); (b) Visualised control intervention.

of moving towards drifting where a large body side-slip is required, we aim to achieve high cornering speed while retaining a small body side-slip. The key finding traces that the maximal achievable yaw rate $\omega_{z,max,c}$ in SS is extended than the well-known open-loop one $\omega_{z,max,ol}$:

$$\omega_{z,max,c} \left(\approx \frac{\mu_f + \mu_r}{2} \frac{1}{v_x g} \right) > \omega_{z,max,ol} \left(= \frac{\min\{\mu_f, \mu_r\}}{v_x g} \right), \tag{1}$$

where μ is the contact coefficients and g is the gravitational constant (see [5] for detailed parameter definitions).

1.2 Key Contributions

- I) we propose a new mechanics-based approach to manipulate the vehicle dynamics in critical maneuvers, while maintaining predictable body motions in either yaw or lateral side-slip.
- II) a desired SS equilibrium can be created even for oversteered vehicles in globally unstable domains, where an elevated performance of SS cornering can be achieved;
- III) methodology for the control systems development based on the proposed strategy is demonstrated, and the simulated results verify its feasibility and functionality.

2 Methodology

The proposed method is applied to a 3-DOF (degree of freedom) planar vehicle model where control system development is also introduced.

2.1 Vehicle and Tire Model in Combined Slips

A planar 3-DOF vehicle model assumes the form [1] (check [6] for parameters):

$$\begin{aligned}
 m(\dot{v}_x - v_y\omega_z) &= (F_{x1} + F_{x2}) \sin \delta + (F_{y1} + F_{y2}) \cos \delta + (F_{x3} + F_{x4}), \\
 m(\dot{v}_y + v_x\omega_z) &= (F_{y1} + F_{y2}) \cos \delta + (F_{y3} + F_{y4}) + (F_{x1} + F_{x2}) \sin \delta, \\
 I_z\dot{\omega}_z &= (F_{y1} + F_{y2}) l_f \cos \delta - (F_{y3} + F_{y4}) l_r + F_{x2}d_2 - F_{x1}d_1,
 \end{aligned} \tag{2}$$

where $F_{..}$ are the tire forces (1,2,3,4 refer to four wheels, see Fig.1) and v_x, v_y, ω_z are the motion states. The tire force at the combined slip is described by adopting the combination of the steady-state Magic formula and non-steady-state TMeasy model, which finally gives the force calculation in the form of

$$F_i = \mu_i F_{zi} \sin(C(Bs_i - EBs_i + E \arctan Bs_i)), i \in [1, 2, 3, 4]. \tag{3}$$

The longitudinal and lateral forces are derived based on (3), respectively:

$$F_{xi} = \frac{s_{xi}}{s_i} F_i, F_{yi} = \frac{s_{yi}}{s_i} F_i. \tag{4}$$

where s_{xi}, s_{yi} are the slip ratios defined in two dimensions [5] and $s_i = \sqrt{s_{xi}^2 + s_{yi}^2}$.

2.2 Preliminaries of Extending Steady-State Cornering

Using OS vehicles as a demonstration, the contact force in front wheels cannot be fully used due to the imbalance of yawing moment $\sum M_z \neq 0$, thus, we apply certain opposite longitudinal forces in the side wheels to create extra yaw torque $M_{z,x} = F_{x2}d_2 - F_{x1}d_1$ in (2) while generating no sum in longitudinal acceleration $\sum F_x = 0$. This $M_{z,x}$ contributes in a similar way to ESC, but not for stabilization, to directly modify the combined tire characteristics in the axle which consequently, leads to the enlarged lateral force generation ΔF_y and additional yaw moment $M_{z,y}$. To reach SS motions, balances in three planar dimensions $\mathbf{x} = [v_x, v_y, \omega_z]^T$ in (2) have to be satisfied:

$$\sum F_{x,...}(\bar{\mathbf{x}}; \mathbf{u}) = -\bar{v}_y \bar{\omega}_{z,ss}, \sum F_{y,...}(\bar{\mathbf{x}}; \mathbf{u}) = \bar{v}_x \bar{\omega}_{z,ss}, \sum M_{z,...}(\bar{\mathbf{x}}; \mathbf{u}) = 0, \tag{5}$$

where $\bar{\mathbf{x}}$ denote the equilibrium of state variables and \mathbf{u} is the controllable inputs that are the longitudinal slip ratios $[s_{x1}, s_{x2}]^T$.

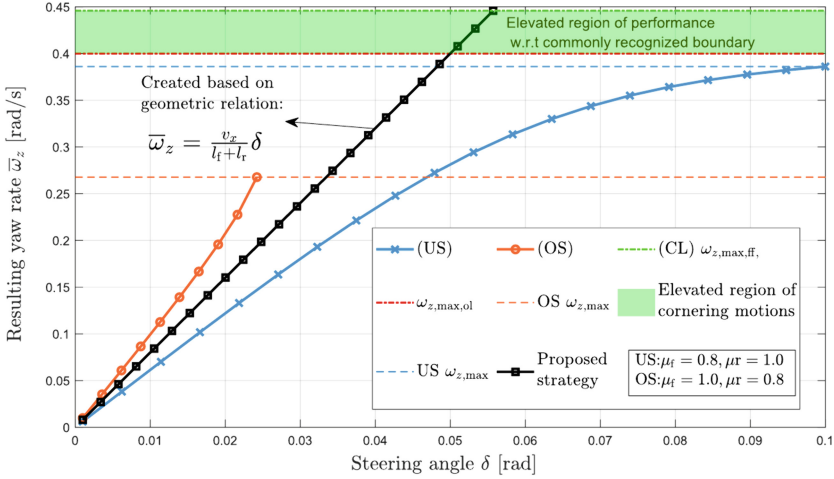


Fig. 2. Extension and modification of SS steering chara (-OL: open-loop; -CL: with proposed control; US: understeer; OS: oversteer), where the red dot-dash line refers to the OL boundary in (1).

Analytically, in maximal conditions, full contact forces both in the front and rear axle are generated and balanced assuming an SS condition:

$$\sum_{i=1}^4 F_{y,i} + \Delta F_y = \bar{v}_x \bar{\omega}_{z,ss}, \sum M_{z,\dots} = \Delta F_y l_f - (F_{x1} d_1 - F_{x2} d_2) = 0, \quad (6)$$

where in the case of the open-loop system, $\sum_{i=1}^4 F_{y,i} = v_x \omega_{z,max,ol}$. Thus, the increment of the SS yaw rate can be derived $\Delta \omega_{z,max} = \Delta F_y / v_x$, and the unbalanced moment is compensated through longitudinal tire forces.

The solution of Eq. (5) satisfying (6) can be numerically found by inverting the nonlinear systems as shown in Fig. 2, where the external input parameters are $[\omega_{z,des}, v_{x,des}, \delta]$, and the solution set is $[\bar{v}_y, \bar{s}_{x1}, \bar{s}_{x2}]$. The black line refers to the SS cornering achieved by the proposed methodology, where the green region indicates the absolute elevated performance w.r.t classical boundary (check (1)).

Stability around the new elevated equilibrium \bar{x} in Fig. 1 is checked through phase planes in Fig. 3. In this maneuver, driver is not able of stabilizing the motions (left of Fig. 3), and even the drifting would be restricted in the OL boundaries (red dotted line). While in the right-side panel, one can achieve an out-of-limit yawing speed in a more stable and simple manner. The quick demonstration in Figs. 2 and 3 points out the capability of the proposed methodology in critical conditions.

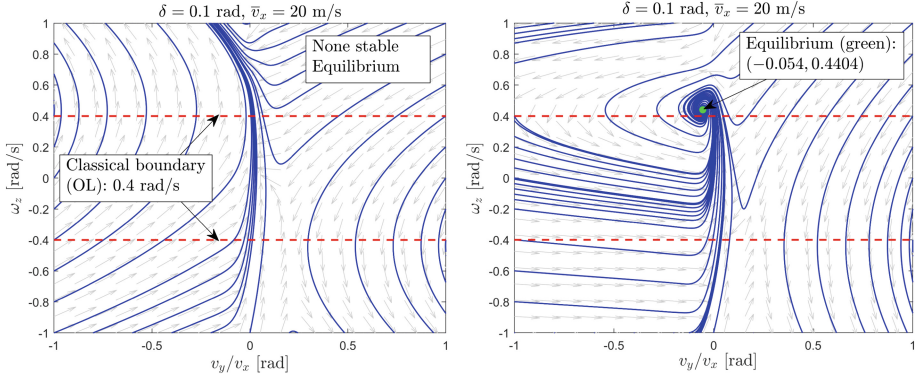


Fig. 3. Phase planes of (a) an uncontrolled open-loop OS vehicle system and of (b) a same OS vehicle but with feedforward control torque.

2.3 Control System Development

Based on the created equilibrium $\bar{\mathbf{x}}$ and the calculated longitudinally controlled slips $\bar{s}_{x1}, \bar{s}_{x2}$, the control law \mathbf{T}_c in the side wheels is structured as

$$\mathbf{T}_c = \mathbf{T}_{c,ff}(\bar{s}_{x1}, \bar{s}_{x2}) + \mathbf{T}_{c,fb}(\mathbf{x}, \bar{\mathbf{x}}), \quad (7)$$

where the feedforward term $\mathbf{T}_{c,ff}$ calculated from (6) is applied for creating the SS equilibrium and the feedback term $\mathbf{T}_{c,fb}$ is to accomplish better local stability against deviations. By substituting $\bar{s}_{x1}, \bar{s}_{x2}$ into the tire formula (3, 4), one can derive that

$$\mathbf{T}_{c,ff} = [F_{x1}(\bar{s}_{x1})R_w, F_{x2}(\bar{s}_{x2})R_w]^T. \quad (8)$$

Consequently, the feedback controller can be assumed in an elegant way that

$$\mathbf{T}_{c,fb} = \left[\frac{d_2}{d_1 + d_2} M_{pd}, \frac{d_1}{d_1 + d_2} M_{pd} \right]^T, M_{pd} = \mathbf{K}(\mathbf{x}(t) - \bar{\mathbf{x}}), \quad (9)$$

where \mathbf{K} is the coefficient matrix for control gains of motion states. This torque \mathbf{T}_c is further applied to the rotational dynamic model of wheels, which for simplicity here, is not listed. The matrix of control gains is

$$\mathbf{K} = \frac{1}{I_z} [0 \ P_y \ P_\omega] \quad (10)$$

where $P_y = -0.0772 \text{ N}^2 \text{ ms}^3$ and $P_\omega = 1.2375 \text{ N}^2 \text{ m}^2 \text{ s}^3$ are the optimal gains derived at the new equilibrium (check [6] for methods).

3 Simulated Result and Discussion

Simulations are carried out in Matlab/Simulink with the Vehicle Dynamics Toolbox, and a path with a radius of 48 m is designed to test the cornering capability.

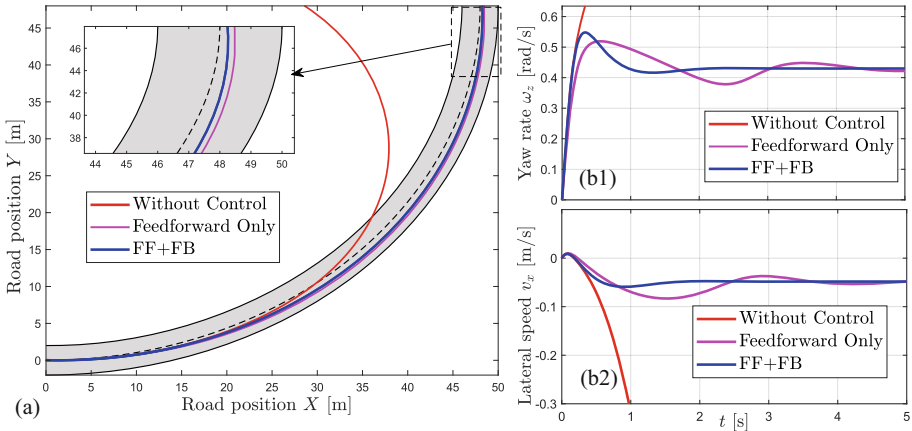


Fig. 4. Three types of external control intervention are compared: without control, with only feedforward torque $\mathbf{T}_{c,ff}$, with both \mathbf{T}_c , where the (a) road map, (b1-b2) motion state variables are checked, respectively.

The longitudinal speed is set at 20 m/s, which means that to stably exit the corner, the minimum yaw rate is $20/48 = 0.417$ rad/s larger than the $\omega_{z,max,ol} = 0.4$ rad/s of the oversteered vehicle in Fig. 2. Thus, without control, theoretically the corner cannot be passed at this speed.

Figure 4 presents the kinematics and dynamics data in passing the corner. Compared to the case without control, the proposed controller helps the vehicle to get through the corner successfully, and in road maps, little difference can be spotted. While in the dynamic responses, further incorporation of feedback portion improve the settling processes by faster decaying, which finally gets the vehicle stabilized at $\bar{\omega}_z = 0.43$ rad/s exceeding the road requirement.

4 Conclusion

In sum, the proposed method demonstrates the effectiveness and advantages of motion stabilization and performance elevation for OS vehicles compared to naturally unstable drifting. A more promising application is for vehicles at different steering characteristics, where on the basis of advanced chassis, one can create desired motions way beyond the classical handling boundary.

References

1. Rossa, F.D., Mastinu, G., Piccardi, C.: Bifurcation analysis of an automobile model negotiating a curve. *Veh. Syst. Dyn.* **50**(10) (2012)
2. Lugner, P.: *Vehicle Dynamics of Modern Passenger Cars*. Springer, Cham (2019)
3. Goh, J.Y., Goel, T., Christian Gerdes, J.: Toward automated vehicle control beyond the stability limits: drifting along a general path. *J. Dyn. Syst. Measur. Control* **142**(2) (2020)

4. Edelmann, J., Plöchl, M.: Handling characteristics and stability of the steady-state powerslide motion of an automobile. *Regular Chaotic Dyn.* **14** (2009)
5. Bobier-Tiu, C.G., Beal, C.E., Kegelman, J.C., Hindiye, R.Y., Gerdes, J.C.: Vehicle control synthesis using phase portraits of planar dynamics. *Veh. Syst. Dyn.* **57**(9) (2018)
6. Lu, H., Stepan, G., Lu, J., Takacs, D.: Dynamics of vehicle stability control subjected to feedback delay. *Eur. J. Mech.-A/Solids* **96**, 104678 (2022)

Open Access This chapter is licensed under the terms of the Creative Commons Attribution 4.0 International License (<http://creativecommons.org/licenses/by/4.0/>), which permits use, sharing, adaptation, distribution and reproduction in any medium or format, as long as you give appropriate credit to the original author(s) and the source, provide a link to the Creative Commons license and indicate if changes were made.

The images or other third party material in this chapter are included in the chapter's Creative Commons license, unless indicated otherwise in a credit line to the material. If material is not included in the chapter's Creative Commons license and your intended use is not permitted by statutory regulation or exceeds the permitted use, you will need to obtain permission directly from the copyright holder.





Design and Implementation of a Slip Control for Electric Formula Student Vehicle Using Sliding Mode Control

Ádám Alföldi^(✉), Dániel Fényes, and Péter Gáspár

HUN-REN Institute for Computer Science and Control,
Kende utca 13-17, Budapest 1111, Hungary
{adam.alfoldi,daniel.fenyas,peter.gaspar}@sztaki.hu

Abstract. This paper presents a slip control design method for a four wheel driven electric race car with low hardware requirements. In addition, to achieve robustness against the changing frictional conditions, a discrete-time Luenberger tractive force observer is designed. The tuning is carried out using the high-precision vehicle dynamics simulation software CarMaker. The performance of the controller is demonstrated in real-world tests. An extensive comparison is given to show the advantage of the proposed method over a previously designed PID controller.

Keywords: Sliding mode control · Wheelslip control · Electric race car

1 Introduction

In the past decades, the development of wheelslip control solutions has been a challenging task both for passenger and race vehicles. When dealing with the former one, the main goal is to maintain stability of the vehicle. Racing cars on the other hand have more requirements, such as to achieve the best possible lap time. To accomplish this, it is necessary to maximize the accelerations of the vehicle. In order to achieve this in the longitudinal direction, it is vital to extract the maximum tractive and braking forces from the tires (Fig. 1).

When examining the longitudinal tire characteristics, it is evident that the tractive force is significantly impacted by the longitudinal slip. Therefore, it is crucial to maintain optimal wheelslip during braking and acceleration. The longitudinal wheelslip - in case of acceleration - can be calculated using the following formula:

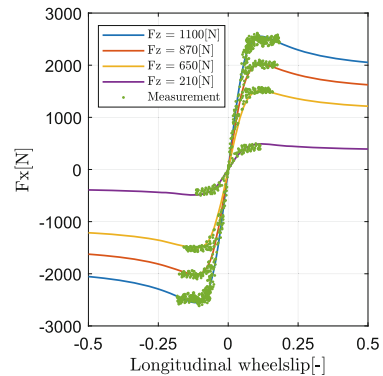


Fig. 1. Longitudinal characteristics of the Hoosier R20 tire

$$\kappa = \frac{r\omega - v_x}{r\omega} \quad (1)$$

where κ is the slip, r is the dynamic wheel radius, ω is the rotational velocity of the given tire and v_x is the longitudinal velocity.

Designing a controller capable of maintaining optimum wheel slip is still a challenging task today due to the highly nonlinear behaviour of the tire/road interface. Several solutions can be found in the literature: the most recent ones include model predictive control (MPC) [1] or application of neural network [2]. MPC has the advantage of being able to handle constraints, but it requires significant computational capacity. A Formula Student car have limited capacity due to financial causes and weight limitations. The use of a neural network requires a substantial amount of reliable data for training. Conducting sufficient testing within the available time is not feasible. Therefore, it is advisable to consider classical control solutions that do not require significant computing capacity. In this paper a design of SMC for controlling slip is proposed.

2 Design of the Sliding Mode Controller

2.1 Longitudinal Model

To achieve optimal longitudinal wheelslip using sliding mode control, a longitudinal model must be established. It contains the longitudinal forces acting on the vehicle, as well as the forces and moments acting on a specific wheel. These forces and moments can be expressed as:

$$m\dot{v}_x = F_{x_{FL}} + F_{x_{FR}} + F_{x_{RL}} + F_{x_{RR}} - F_{aero} - F_r \quad (2)$$

where m is the mass of the car, F_{x_i} are the tractive forces on the four wheels, F_{aero} is the aerodynamic drag, F_r is the tire resistance.

$$\theta\dot{\omega} = M_{wheel} - F_x r + F_r r \quad (3)$$

where θ is the wheel inertia, $\dot{\omega}$ is the angular acceleration of the wheel, M_{wheel} is the torque applied to the wheel, r is the wheel radius.

2.2 Idea Behind Sliding Mode Control

Sliding mode control is a nonlinear control technique that aims to achieve the optimal trajectory/reference even in the presence of significant uncertainties. The controller is a variable structure controller containing a discontinuous switching function. Its design ensures that the system always approaches and remains at the switching point of the function. This state is the sliding surface, defined by $S(x) = 0$. The function $S(x)$ is typically a linear combination of the state variables x , which equals to 0 if and only if the desired control objective is met. The controller design consists of creating the sliding surface, defining the switching function to ensure that the system always moves towards the sliding

surface and finally deriving the equivalent function make sure that the system slides along this surface. In the case of wheelslip control the configuration space can be

$$S(\kappa, \omega) = (\kappa - \kappa_{opt})\omega \tag{4}$$

where κ is the longitudinal wheelslip, κ_{opt} is the optimal slip, ω is the angular velocity of the given tire. This is a common solution that can be found in the literature [3].

2.3 Equivalent Control

The goal of the equivalent control is to keep the system in the sliding mode defined in Sect. 2.2. It is obtained by satisfying the equation

$$\dot{S}(v, \omega) = 0 \tag{5}$$

The derivative of the longitudinal velocity from Eq. 2 after coupling tractive forces losses into one term each yields:

$$\dot{v}_x = \frac{F_{x_{sum}} - F_{loss}}{m} \tag{6}$$

The derivative of the angular velocity of the wheel can be expressed from 3:

$$\dot{\omega}_i = \frac{M_{wheel_i} - F_{x_i}r + T_{r_i}}{\theta} \tag{7}$$

The configuration space 4 can be rewritten using 1:

$$S(v, \omega) = \frac{r\omega_i - v}{r\omega_i}\omega_i - \kappa_{opt}\omega_i, \rightarrow S(v, \omega) = (1 - \kappa_{opt})\omega_i - \frac{v}{r} \tag{8}$$

Taking the derivative of this, and by substituting the terms from 6 and 7, we can get:

$$\dot{S}(v, \omega) = (1 - \kappa_{opt})\dot{\omega}_i - \frac{\dot{v}}{r}, \quad \dot{S}(v, \omega)_i = \frac{1 - \kappa_{opt}}{\theta} (M_{wheel_i} - F_{x_i}r + F_{r_i}r) \tag{9}$$

The control input is the torque applied to the wheel. The equivalent part can be expressed using 5 and 9:

$$u_{i(eq)} = \frac{(1 - \kappa_{opt})(r(F_{x_i} - F_{r_i}))}{\theta} + \frac{\theta}{1 - \kappa_{opt}} \cdot \frac{F_{x_{sum}} - F_{loss}}{rm} \tag{10}$$

2.4 Switching Function

The idea behind the switching function is to drive the system from its initial state towards the sliding surface. Once it has reached sliding mode, it is also necessary to reject noise and uncertainties that the equivalent control could not handle. In order to move towards the desired sliding mode, the expression $S\dot{S} = -\eta|S|$

must be satisfied, where η is a positive constant. This means that the sign of $S(x)$ is always opposite to the sign of its derivative, which drives S to 0. To achieve this, the required input signal is

$$u_{sw} = -\eta \operatorname{sgn}(S) \quad (11)$$

In theory, the switching function should be a discontinuous signum function. Due to the highly oscillatory nature of this input signal, it is replaced by a sigmoid function to avoid unnecessary wear on the mechanical components:

$$u_{sw} = -\eta \frac{s}{|s| + \delta} \quad (12)$$

where δ is a parameter that “softens” the chatter. Given the characteristics of the tire, the main objective is to ensure that the slip remain in the optimal region, rather than tracking a specific reference value.

3 State Estimation

3.1 Tractive Force Observer

The input signal is the sum of the switching and the equivalent functions. Accurate estimation of tractive forces is crucial as it significantly influences the latter. Tire-road friction can vary in a wide range due to various factors such as surface, temperature, etc. Therefore, it is necessary to implement a force observer. The estimated states at time step $k+1$ of the discretized Luenberger observer are written as $\hat{x}(k+1) = A_d \hat{x}(k) + B_d u(k) + L_d (y(k) - \hat{y}(k))$, where $\hat{x}(k)$ are the estimated states, $u(k)$ are the inputs, $y(k)$ are the measured states, $\hat{y}(k)$ are the estimated outputs at time k . A_d is the state matrix, B_d is the input matrix, L_d is the observer gain matrix [4].

The aim is to estimate the tractive forces using the introduced Luenberger observer. By writing Eqs. 2 and 3 into state-space form, the estimator can be designed. The states are $x^T = [v_x \ \omega_{FL} \ \omega_{FR} \ \omega_{RL} \ \omega_{RR} \ F_{FL} \ F_{FR} \ F_{RL} \ F_{RR}]$ and the inputs are: $u^T = [T_{FL} \ T_{FR} \ T_{RL} \ T_{RR} \ F_{loss}]$, where $[FL, FR, RL, RR]$ marks the front left, front right, rear left and rear right wheels.

The system is then discretized using Tustin transform. The observer gain is calculated via pole allocation and simulation results. The final poles in continuous time are $p = [-1 - 2 \dots -9] \cdot 50$. The formula $p_{disc} = e^{pT_s}$ is used to obtain the discrete poles, where T_s is the sampling time, which is 0.005 s. To demonstrate the performance of the observer, I made test runs in Carmaker with different friction coefficients. The results can be seen in Fig. 2.

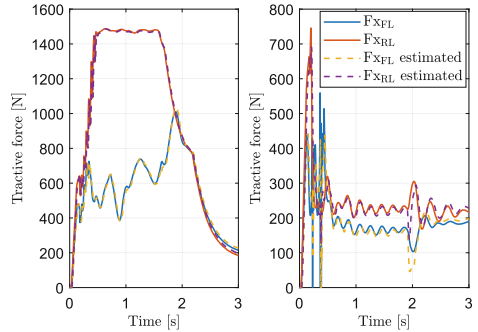


Fig. 2. Actual and estimated tractive forces

3.2 Velocity Estimation

In reality, the longitudinal velocity cannot be measured with low-cost sensors, so its estimation is crucial to the successful implementation of the controller. The idea is to use Kalman filter in order to take advantage of the accuracy of the GPS and the quickness of the inertial sensors. This method is introduced in [5] and the realization for this particular race car can be found in [6].

4 Results, Comparison with PID

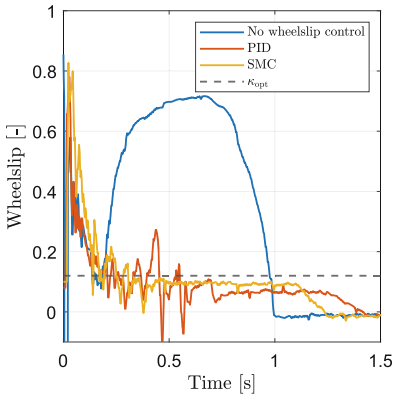


Fig. 3. Front left wheelslip

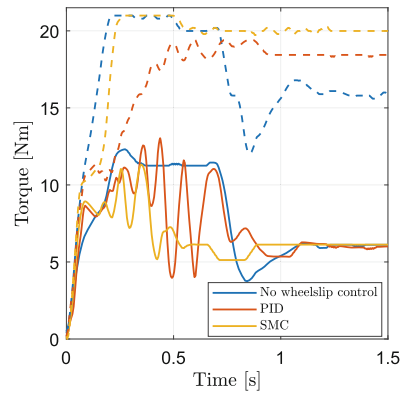


Fig. 4. Torques (front and rear left)

The controller has been designed using Matlab/Simulink. C code is generated from the model, which runs on a Texas Instruments TMS570LS1227 microcontroller. The SMC is compared to a run with a previously designed PID controller and to a run without wheelslip control.

Figure 3 shows that the wheelslip oscillates less with SMC than with PID. This also means that the torques oscillate more with PID (Fig. 4), which can cause the premature failure of certain drive train elements. In terms of performance, the SMC has a slightly higher overshoot, but is also faster. Its settling time is around 0.4 s, while the PID only settles after 0.75 s, also with a larger settling error. During the test, the car completed the 70 m straight in under 3.56 s without controller, 3.52 s with PID and under 3.4 s with SMC. The latter is an improvement of 4.495%. Looking at Fig. 5, we can see that the maximum acceleration was around $11.75 \frac{m}{s^2}$ without control, $12.25 \frac{m}{s^2}$ with PID and $12.5 \frac{m}{s^2}$ with SMC. It can be seen that the SMC performs better especially in the 0.3–0.75 s time interval, which is consistent with the fact that it settles faster (Fig. 6).

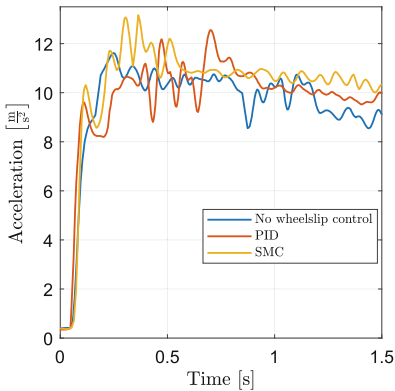


Fig. 5. Longitudinal acceleration

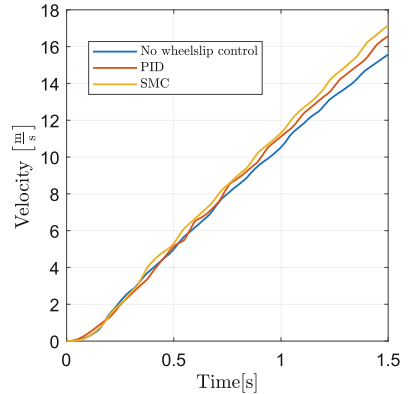


Fig. 6. Longitudinal velocity

5 Conclusion, Further Recommendations

This paper demonstrated that the proposed SMC is more advantageous than the previously designed PID wheelslip controller. The current design is only suitable for operation in straight-line acceleration scenarios. It would be advantageous to incorporate lateral dynamics in the future. This implies that the combined slip must be considered in lieu of the pure longitudinal, and that the force observer must also consider losses resulting from turning. Furthermore, with a slightly faster microcontroller it would be worth considering a simple MPC, as its attributes are highly suitable for this particular problem.

Acknowledgment. The paper was funded by the National Research, Development and Innovation Office under OTKA Grant Agreement No. K 143599. The research was also supported by the National Research, Development and Innovation Office through the project “Cooperative emergency trajectory design for connected autonomous vehicles” (NKFIH: 2019-2.1.12-TÉT VN). The work of Daniel Fényes was supported by the János Bolyai Research Scholarship of the Hungarian Academy of Sciences.

References

1. Luping, G., et al.: MPC-based slip control system for in-wheel-motor drive EV. In: 5th IFAC Conference on Engine and Powertrain Control, Simulation and Modeling E-COSM, pp. 578–582 (2018). <https://doi.org/10.1016/j.ifacol.2018.10.140>
2. Velimir, C., Dragan, A., Dusan, S.: Longitudinal wheel slip control using dynamic neural networks. *Mechatronics* **23**(1), 135–146 (2013). <https://doi.org/10.1016/j.mechatronics.2012.11.007>
3. Suwat, K.: Traction control of electric vehicles using sliding-mode controller with tractive force observer. *Int. J. Veh. Technol.* (2014). <https://doi.org/10.1155/2014/829097>

4. Matlab Luenberger Observer. <https://www.mathworks.com/help/sps/ref/luenbergerobserver.html>. Accessed 4 Apr 2024
5. Ryu, J., Gerdes, J.C.: Integrating inertial sensors with global positioning system (GPS) for vehicle dynamics control. *ASME J. Dyn. Syst. Meas. Control* **126**(2), 243–254 (2004). <https://doi.org/10.1115/1.1766026>
6. Facskó, V.: Estimation of vehicle states with on-board sensors (2023)

Open Access This chapter is licensed under the terms of the Creative Commons Attribution 4.0 International License (<http://creativecommons.org/licenses/by/4.0/>), which permits use, sharing, adaptation, distribution and reproduction in any medium or format, as long as you give appropriate credit to the original author(s) and the source, provide a link to the Creative Commons license and indicate if changes were made.

The images or other third party material in this chapter are included in the chapter's Creative Commons license, unless indicated otherwise in a credit line to the material. If material is not included in the chapter's Creative Commons license and your intended use is not permitted by statutory regulation or exceeds the permitted use, you will need to obtain permission directly from the copyright holder.





Long Combination Vehicles Reverse Strategies Based on Articulation Angle Gradient

Zhaohui Ge^(✉), Fredrik Bruzelius, and Bengt Jacobson

Chalmers University of Technology, 41296 Gothenburg, Sweden
zhaohui.ge@chalmers.se

Abstract. To guide the development of driver assistant systems and fully automated solutions for reversing long combination vehicles (LCVs), the principles for reversing LCVs are investigated using the articulation angle gradient. The widely used *Steady-state Circling Limitation* (SSCL) in reversing LCVs has two main drawbacks: it restricts vehicles from operating with large articulation angles crucial for tight spaces and lacks a well-defined feasible range. Two new reverse principles are introduced that can provide better insight. The first principle extends SSCL to include more extreme articulation angles for single-articulated vehicles. It also addresses the necessity of considering articulation gradients when developing the continuous reverse limitation for multi-articulated vehicles. The second principle introduces limited distance reversing for vehicles that no longer meet the first principle's requirements, providing additional vehicle ending poses useful for tasks like loading and coupling.

Keywords: Combination Vehicle · Kinematic Model · Reverse · Articulation Angle Gradient

1 Introduction

High-capacity transport using multi-articulated LCVs increases efficiency and reduces the emission of the transportation [1]. Reversing those vehicles is a difficult and time-consuming task for drivers [2]. A potential solution to this challenge is developing driver assistant systems or fully automated solutions for reverse tasks.

Matsushita et al. controlled reversing a double-trailer vehicle with a velocity and a trajectory controller [3]. Morales et al. presented a reverse control algorithm that transformed a virtual steering angle at the last trailer into the tractor steering angle and pointed out that their algorithm is feasible only under the condition that none of the articulation angles within the vehicle exceed the corresponding magnitude reached during the vehicle's minimal radius steady-state circling state [4, 5]. That limitation is referred to as the SSCL. Within the SSCL, articulation vehicles are claimed to be able to reverse continuously without any inter-unit clashes. Some research on control algorithms for reversing combination vehicles [6–8] are using paths that follow SSCL for validations. Therefore, SSCL is considered as the basic reverse limitation for LCVs.

The drawbacks of the existing research are that they lack boundaries for their feasible region or that the feasible region is defined incompletely.

2 Kinematic Model

A kinematic vehicle model shown in Fig. 1 is used in this study.

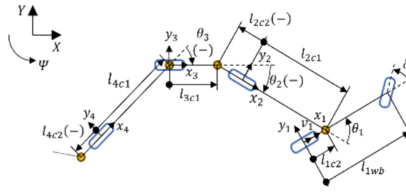


Fig. 1. Vehicle Model

The yaw gradient with respect to the 1st unit’s rear axle travel distance is:

$$\frac{\partial \Psi_i}{\partial s_1} = \begin{cases} f_{\frac{\partial \Psi_i}{\partial s_1}}(\delta, \mathbf{l}_i), & i = 1 \\ f_{\frac{\partial \Psi_i}{\partial s_1}}(\delta, \mathbf{l}_i, \boldsymbol{\theta}_{i-1}), & i = 2, 3, 4, \dots \end{cases} \quad (1)$$

where Ψ_i is the heading in the global coordinate system, s_1 is the travel distance at the 1st unit’s rear axle, δ is the steering angle at the 1st unit’s front axle, \mathbf{l}_i is the dimensions, as stated in Fig. 1, from the 1st to the i^{th} unit, and $\boldsymbol{\theta}_{i-1}$ is the articulation angle vector of the 1st to the i^{th} articulation angle.

Using Eq. (1), the articulation angle gradient with respect to s_1 is given as:

$$\frac{\partial \theta_i}{\partial s_1} = \frac{\partial \Psi_i}{\partial s_1} - \frac{\partial \Psi_{i+1}}{\partial s_1} = f_{\frac{\partial \theta_i}{\partial s_1}}(\delta, \mathbf{l}_i, \boldsymbol{\theta}_i), \quad i = 1, 2, 3, \dots \quad (2)$$

3 Articulation Angle-Based Reverse Principles Analysis

This section introduces two principles that can be used to develop future reverse strategies. They are established from the articulation angle gradient in Eq. (2) with parameters from several combination vehicles.

As shown in Table 1, the dimensions of nine vehicle combinations [9] are used in the following discussions. Cfg. 1 is a regular tractor and semi-trailer combination. Cfg. 2 to 5 are double-articulated vehicles within 25.25 m limitation. Cfg. 6 to 9 are double- or triple-articulated vehicles within 34.5 m limitation.

All the combinations follow two mechanical constraints. The steering angle δ is limited within $[-45^\circ, 45^\circ]$ [6] and the articulation angles are limited to $[-90^\circ, 90^\circ]$ to avoid inter-unit clashes within the combination.

3.1 Controllable Articulation Angle-Oriented Reverse Principle (CAARP)

For a reversing combination vehicle, it is vital to be able to change the evolution of the articulation angle to avoid inter-unit clashes, which the articulation angles should

Table 1. Vehicle combinations selected for following discussions.

Cfg. No.	1	2	3	4	5	6	7	8	9
Combination in the report [9]	402	602	604	606	705	11	13	1	9

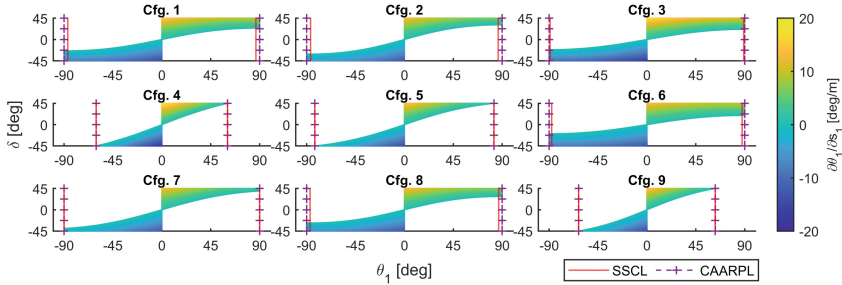


Fig. 2. Comparison between SSCL and CAARPL for single-articulated combinations vehicles.

be able to be controlled to avoid their mechanical limitations. They are called *Controllable Articulation Angles*, a concept introduced in this research. For a single-articulated vehicle, they can be described as:

$$\forall |\theta_1| < \theta_{1,CAARP}, \exists \delta \in [-45^\circ, 45^\circ], \frac{\partial \theta_1}{\partial s_1} \cdot \text{sgn}(s_1) \cdot \theta_1 \leq 0 \tag{3}$$

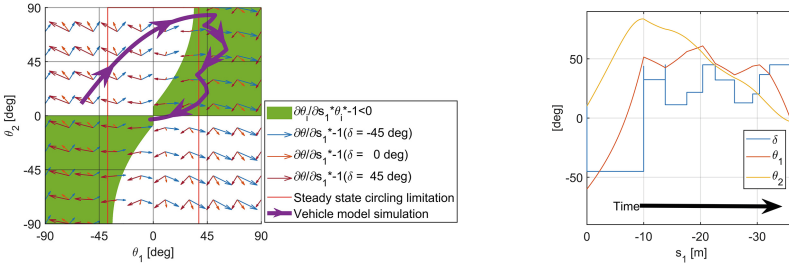
where $\theta_{1,CAARP}$ is the first articulation angle limitation for controllable articulation angle, $\text{sgn}(s_1)$ indicates the travel direction of unit 1.

All the following discussion is based on reversing, which means $\text{sgn}(s_1) = -1$. As shown in Fig. 2, colored zones show the articulation angle gradient that satisfies $\frac{\partial \theta_1}{\partial s_1} \cdot \text{sgn}(s_1) \cdot \theta_1 \leq 0$; θ_1 between two red lines are within SSCL; and θ_1 between two purple marked dash lines are feasible for CAARP. The CAARP feasible range is defined as an interval on the one-dimensional articulation angle space.

Equation (3) is satisfied outside the domain described by the SSCL in Cfg. 1, 2, 3, 6 and 8, which indicates CAARP allows for higher articulation angle limitations. This is because these configurations have their rear coupling points on unit 1 in front of their rear axles, and SSCL lacks steady states where the instantaneous rotation center is on different sides of unit 1 and unit 2. For the remaining vehicles, SSCL and CAARP have the same limitation. However, when θ_1 is close to the CAARP limitation, as limited by $\left| \frac{\partial \theta_1}{\partial s_1} \right|$, there will be only limited possibility of reducing the articulation angle. Therefore, one needs to have a margin to this border.

The next step is to extend CAARP to multi-articulated vehicles. To find out how to define the feasible range of CAARP for multi-articulated vehicles, the later part of the statement in Eq. (3) is extended to all articulation angles, and the new statement is given in Eq. (4).

$$\exists \delta \in [-45^\circ, 45^\circ], \frac{\partial \theta_i}{\partial s_1} \cdot \text{sgn}(s_1) \cdot \theta_i \leq 0 (i = 2, 3, \dots) \tag{4}$$



a) Articulation angle trajectory b) Steering and articulation angles with respect to the travel distance of Unit 1

Fig. 3. Simulation of reverse Cfg. 2 from $\theta_1 = -60^\circ$, $\theta_2 = 10^\circ$ towards a straight pose.

The green areas in Fig. 3a show that the articulation angles satisfy Eq. (4) of a double-articulated vehicle formed with units 1 to 3 of Cfg. 2. Double-articulated combinations formed with the first three units of Cfg. 3 to 9 show similar behaviors. If the same ideal from SSCL is applied, the first part of Eq. (3) should be extended to $\forall|\theta_i| < \theta_{i,lim}$. This should create a rectangular area in Fig. 3a and fully covered by green areas. It is impossible to define such a rectangular in Fig. 3a. This indicates that the CAARP feasible range for multi-articulated vehicles cannot be defined by independently limiting each articulation angle.

Equation (4) is insufficient in defining the feasible range for CAARP of multi-articulated vehicles. Therefore, the articulation angle gradients are considered to further study the feasible range of CAARP. As shown in Fig. 3a, the articulation angle gradient range for a specific pose is expressed by a set of arrows: $\left(-\frac{\partial\theta_1}{\partial s_1}, -\frac{\partial\theta_2}{\partial s_1}\right)_{\delta=-45^\circ, 0^\circ, 45^\circ}$. For any steering angle within the steering limitation, the articulation angle gradient vector will be within the sector between the arrows for $\delta = -45^\circ$ and $\delta = 45^\circ$ via $\delta = 0^\circ$. This can be proved by the continuity of $\frac{\partial^2\theta_i}{\partial s_1\partial\delta}$.

As shown in Fig. 3a, the feasible articulation gradient vector plots on the articulation angle plane can offer subjective guidance on whether a vehicle pose is within the CAARP feasible range. For a vehicle pose which is close to the corners of SSCL in the second quadrant, it is impossible to continuously reverse due to all articulation angle vectors in surrounding areas increasing $|\theta_2|$ towards its mechanical limitations. Hence, forward driving is the only possibility before applying CAARP to a vehicle from that pose. We classified long combination vehicles in similar states as NO-NO states, an abbreviation for “if NO forward driving, then NO continuous reversing”.

A simulator based on Sect. 2 is built to test the controllability of vehicles’ poses outside SSCL. Figure 3 shows one of the simulation results from it. This simulation shows that a pose outside SSCL may still have controllable articulation angles, and articulation angle gradient vectors can guide steering control.

The dimension of the articulation angle space will increase with the number of articulation joints. To describe the articulation gradients of a triple-articulated vehicle, one additional dimension will be added for θ_3 , which will turn the 2-D plane in Fig. 3a into a 3-D articulation angle cube. The internal high dimension planning problem, and space constraints are expected to bring additional challenges.

3.2 Locked Articulation Angle-Oriented Reverse Principle (LAARP)

LAARP means the combination vehicle aims for *NO-NO* states, poses outside the CAARP limitation. The *Locked Articulation Angle* appears when at least one articulation angle within a combination vehicle reaches its mechanical limitation, and forward driving is required to avoid clashes. The idea behind LAARP is that the vehicle does not need to reverse further after it arrives at its desired position.

This study shows primary results that show the potential of LAARP. This is done by simulating the combination vehicles with the model from Sect. 2. The vehicle in the simulation will start to reverse with a specific pose, and the steering angle is kept fixed during the reverse. The resolution is 1° for initial articulation angles and 0.1° for the steering angle. The simulation step is given as $\Delta s_1 = 0.1$ m. The simulation ends when the vehicle reaches a locked pose. For a rough estimation, the longer the vehicle can reverse, the greater the potential to manoeuvring the last unit.

Figure 4 shows the maximum reverse distance with fixed steering angles of Cfg. 9, where the position on the articulation angle plane shows the initial pose. Figure 4a and b show the result of a single-articulated vehicle formed by the first two and three units of Cfg.9, respectively. Figure 4c and d show the results of the triple-articulated Cfg.9 that sliced at two different θ_3 .

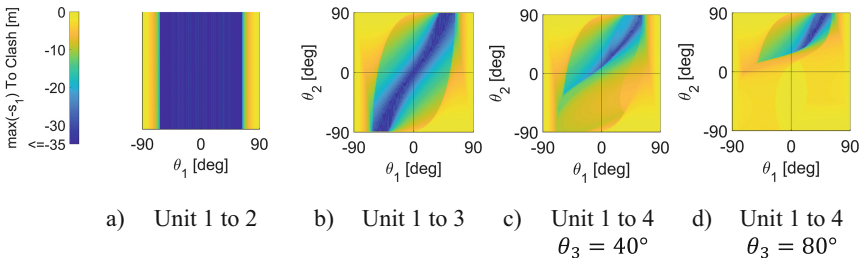


Fig. 4. Maximum reverse distances with fixed steering angles of Cfg. 9.

Recall from Fig. 2, the single-articulated vehicle based on Cfg. 9 will no longer satisfy the requirement for CAARP at large articulation angle magnitudes. According to Fig. 4a, the vehicle may still reverse for meters outside CAARP limitations. Figure 4c to d also show non-zero reverse distances appearing in many initial poses of the multi-articulated vehicles, showing the potential outside CAARP feasible range in reverse.

4 Conclusion

This paper investigates principles that can guide the development of reverse strategies for long combination vehicles from the view of kinematical model-based articulation angle gradients. Two principles are established in this paper.

Controllable Articulated Angle-oriented Reverse Principle aims to maintain the vehicles' ability to avoid inter-unit clashes. The feasible range of CAARP can be easily

defined by articulation angle limitations for single-articulated vehicles. A more complex limit on each articulation angle dependent on the other articulation angles is necessary for multi-articulated vehicles, which must consider the articulation angle gradients. Analysing the instantaneous kinematics of multi-articulated vehicles of a specific initial pose is insufficient to identify whether the pose is within the feasible range of CAARP. A planning algorithm for vehicle pose change in the articulation angle space is required to define the feasible range for multi-articulated vehicles based on the CAARP.

Locked Articulation Angle-oriented Reverse Principle uses vehicle poses outside the feasible range of CAARP. The preliminary study confirmed the feasibility of LAARP by observing the non-zero reverse distance of the first unit between the nonlocked to locked articulation angle pose.

Compared with the SSCL, the two new reverse principles show possibilities of expanding the feasible vehicle pose ranges for reverse path planning, including additional intermediate poses from CAARP and final poses from LAARP. CAARP excludes certain poses from SSCL intermediate poses for reverse.

References

1. Lindqvist, D., Salman, M., Bergqvist, R.: A cost benefit model for high capacity transport in a comprehensive line-haul network. *Eur. Transp. Res. Rev.* **12** (2020)
2. Vesmes, A.: Drivers' needs while reversing with a high capacity transport combination. Master's thesis 2023, Chalmers University of Technology (2023)
3. Matsushita, K., Murakami, T.: Backward motion control for articulated vehicles with double trailers considering driver's input. In: *IECON Proceedings (Industrial Electronics Conference)*, pp. 3052–3057 (2006)
4. Morales, J., Martínez, J.L., Mandow, A., Garcia-Cerezo, A.J.: Steering the last trailer as a virtual tractor for reversing vehicles with passive on-and off-axle hitches. *IEEE Trans. Ind. Electron.* **60**, 5729–5736 (2013)
5. Morales, J., Martínez, J.L., Mandow, A., Medina, I.J.: Virtual steering limitations for reversing an articulated vehicle with off-axle passive trailers. In: *IECON Proceedings (Industrial Electronics Conference)*, pp. 2385–2390 (2009)
6. Rimmer, A.J., Cebon, D.: Planning collision-free trajectories for reversing multiply-articulated vehicles. *IEEE Trans. Intell. Transp. Syst.* **17**, 1998–2007 (2016)
7. Beghini, M., Lanari, L., Oriolo, G.: Anti-jackknifing control of tractor-trailer vehicles via intrinsically stable MPC. In: *Proceedings of the IEEE International Conference on Robot Automation*, pp. 8806–8812 (2020)
8. Kusumakar, R.: *Autonomous Parking for Articulated Vehicles*. HAN University of Applied Sciences (2017)
9. Fröjd, N., Emil, P., Larsson, L.: Svenska HCT Typfordonskombinationer utvärderade mot år 2020 gällande regelverk för BK4 (Swedish HCT Typical Vehicle Combinations Evaluation Based Regulations of Year 2020 for BK4) (2021). https://nvfnorden.org/wp-content/uploads/2021/04/2021-04-15_Svenska_HCT_Typfordon.pdf

Open Access This chapter is licensed under the terms of the Creative Commons Attribution 4.0 International License (<http://creativecommons.org/licenses/by/4.0/>), which permits use, sharing, adaptation, distribution and reproduction in any medium or format, as long as you give appropriate credit to the original author(s) and the source, provide a link to the Creative Commons license and indicate if changes were made.

The images or other third party material in this chapter are included in the chapter's Creative Commons license, unless indicated otherwise in a credit line to the material. If material is not included in the chapter's Creative Commons license and your intended use is not permitted by statutory regulation or exceeds the permitted use, you will need to obtain permission directly from the copyright holder.





A Comparative Study of Discomfort Using Electrical and Friction Braking at Low Speed Driving

Samira Deylaghian^(✉), Mats Jonasson, and Petri T. Piiroinen

Chalmers University of Technology, Gothenburg, Sweden
{samira.deylaghian,mats.jonasson,petri.piiroinen}@chalmers.se

Abstract. In this study, we conduct an analysis of the longitudinal dynamics of a vehicle model in an incline, with a specific focus on its behavior, at low speeds, when starting and stopping. The model is minimal, yet an effective representation of a vehicle that includes the effects of springs and dampers as well as friction and electric braking models, which allows for easy analysis into their interplay at low speed. One important feature that this early study shows is how the acceleration and jerk is affected by static and dynamic friction coefficients in different driving situations. Our study further demonstrates the interplay between the electric and friction braking systems and the differences in oscillatory motion they generate. Such insights are vital if we want to improve vehicle control at low speeds and suggest ways to reduce problems like excessive acceleration and jerk. Additionally, our findings could also provide valuable insights when developing active friction braking systems.

Keywords: Longitudinal dynamic · Standstill · Braking system

1 Introduction

1.1 Background and Literature Review

Most everyday driving involves non-extreme maneuvers, nevertheless, ride comfort is often compromised by frequent starts and stops. Ride discomfort is caused by acceleration and jerk (the rate of change in acceleration). As the vehicle accelerates, passengers experience inertia forces, leading to discomfort when these forces are large or change rapidly. Additionally, both uphill and downhill driving affect comfort by shifting weight distribution between the two axles, which in turn influences the potential for regenerative braking power. Specifically, in downhill driving, Chen *et al.* [1] investigate a regenerative braking strategy for electric vehicles on varied slopes. They analyzed the effect of the slope on braking, and introduced an online co-estimation of road slope and vehicle mass using neural networks and a least-squares algorithm.

Supported by Chalmers University of Technology.

© The Author(s) 2024

G. Mastinu et al. (Eds.): AVEC 2024, LNME, pp. 714–720, 2024.

https://doi.org/10.1007/978-3-031-70392-8_101

Many studies have been done on longitudinal ride comfort. Hou *et al.* [2] present a novel control strategy using residual reinforcement learning to enhance vehicle ride comfort during the post-braking phase in urban environments. Experimental tests on a skateboard chassis confirm its effectiveness in improving comfort across different braking scenarios. The relationship between acceleration, jerk, and passenger discomfort was examined in [3], using a driving simulator with 23 participants. That test showed that discomfort increases with acceleration amplitude, and that the strength of this effect depends on the direction of motion. Lee and Choi [4] focused on enhancing ride comfort in low-risk braking situations. Their research was conducted on Electro-Mechanical-Brake (EMB) and Brake-by-Wire (BBW) systems, which allow for more precise control of braking actuators. A control algorithm was developed that significantly improved ride comfort by generating an acceleration trajectory designed to minimize discomfort caused by sudden changes in acceleration and jerk. A key aspect of this improvement is the reduction of jerk, ensuring smoother transitions and a more comfortable driving experience. In order to control and minimize jerk, Singh *et al.* [5] introduced an autonomous emergency braking system. The system's stopping distance was analytically calculated, and a simple controller tracked the desired velocity profile. In [6], a novel braking method using an integrated electro-hydraulic brake system was proposed to improve ride comfort. The proposed method comprises target acceleration generation, revision of target acceleration, and acceleration tracking control. The tracking control included both feedforward and feedback control, which were used to precisely track the target acceleration.

1.2 Motivation

In this study, we investigate and analyze the behavior of vehicle motion at low-speeds using a minimal vehicle model that captures the main longitudinal dynamics phenomena. Our research specifically focuses on scenarios of starting and stopping in an uphill, where both propulsion and friction braking torques are engaged. We do this by testing how the relation between static and dynamic friction coefficients affect the dynamics. We then study acceleration and jerk under different conditions to understand the conceptual comfort difference between using a shaft torque, generated from for example an electrical motor, and a friction brake force. By gaining a deeper understanding of vehicle dynamics in this particular scenario, we seek to pave the way for further understanding of how to reduce excessive jerk when starting and stopping, and thus provide solutions for better ride comfort in everyday driving conditions.

2 Modelling

2.1 Model Description

For the current study, we have developed a minimal vehicle model to capture a few aspects of longitudinal comfort at low speed, which is shown in Fig. 1(b). The

model includes a vehicle body, a wheel hub and wheel. The body is supported by a spring-mass suspension system that is attached to a wheel hub.

The vehicle body has a sprung mass m_b , the wheel hub has mass m_a and the wheel has mass m_w , radius r , and moment of inertia J . Further, the suspension system comprises a spring and damper, with parameters k and d , respectively, which allow the wheel to have a translational motion in relation to the vehicle body. We let x_1 and x_2 , respectively, be the vehicle's body and wheel displacement relative to the surface, \dot{x}_1 and \dot{x}_2 their respective velocities, and \ddot{x}_1 and \ddot{x}_2 their accelerations. The angular velocity of the wheel is ω , the propulsion torque acting on the wheel is T_p , and the clamp force of the brake is F_c . We finally assume that here is no slip between the tyre and ground, and thus $\dot{x}_2 - r\omega = 0$.

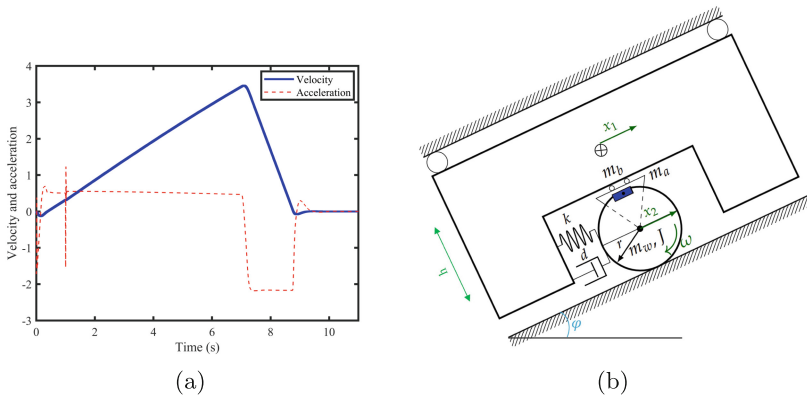


Fig. 1. (a) Vehicle velocity and acceleration from Carmaker, (b) The minimal vehicle model.

We note that the model simplifies a vehicle's complexity by lumping all wheels into a single representative wheel. Here we considered wheel as a solid model and the stiffness and damping characteristics from the tires and suspension are consolidated into a spring and damper setup. The model has two degrees of freedom, which are the movement of the sprung mass and the wheel. The effects of motion resistance such as air drag, rolling, etc. are omitted.

Taking all this into consideration, the equations of motion for the system on a road with an inclination angle φ are given by

$$m_b \ddot{x}_1 - k(x_2 - x_1) - d(\dot{x}_2 - \dot{x}_1) = m_b g \sin(\varphi), \tag{1}$$

$$\frac{J + r^2 m_s}{r} \ddot{x}_2 + rk(x_2 - x_1) + rd(\dot{x}_2 - \dot{x}_1) = T_p(t) - rF_b(\dot{x}_2) + r m_s g \sin(\varphi), \tag{2}$$

where $m_s = m_a + m_w$ and the friction force F_b is given by

$$F_b(\dot{x}_2) = \begin{cases} [-\mu_s F_c, \mu_s F_c], & \dot{x}_2 = 0, \\ -\left(\mu_d + (\mu_s - \mu_d) \cdot \exp\left(-\left(\frac{\dot{x}_2}{v_s}\right)^\alpha\right)\right) \text{sign}(\dot{x}_2/r) \cdot F_c, & \dot{x}_2 \neq 0. \end{cases} \quad (3)$$

and includes the Stribeck effect (with Stribeck velocity v_s), and static and dynamic friction coefficients μ_s and μ_d , respectively.

2.2 Parameter Selection

The lumped parameters of the model were selected through a comparative analysis between our proposed model and a standard model provided by the simulation tool Carmaker. This comparison was conducted to ensure that both models exhibited similar natural frequencies. Results from Carmaker (for an example see Fig. 1(a)) were used to adjust the parameters until the frequency response of the minimal model matched that of the Carmaker model. This process helped in ensuring that the simplified model well represents the dynamics of a Carmaker vehicle model.

3 Simulation

3.1 Driving Scenario

Simulations and solving the equations of motion were done using MATLAB & Simulink. The two scenarios we analysed were starting and stopping in a hill. During all simulations the propulsion torque $T_p(t)$ varies, while the clamp force F_c remains constant, ensuring that there is always a sufficient friction braking torque to bring the model to a complete stop.

3.2 Results

By analyzing the jerk of the main body, some levels of rapid changes are observed when the wheel starts moving and when it comes to a complete stop. To analyze role the friction in the brake has in these scenarios, the body acceleration and jerk were calculated for different static and dynamic friction coefficients, as shown in Fig. 2. In order to minimize noise when calculating signal derivatives, such as jerk, and to ensure accurate analysis and detection, we employ a 6 Hz low-pass filter [7]. This significantly reduced noise and minimized fluctuations in the derivatives, which enhanced the clarity and reliability of the results for analysis.

As can be seen in Fig. 2(a) and 2(b), jerk and acceleration of the body increases significantly with higher static friction coefficients μ_s and lower dynamic friction coefficients μ_d , when the vehicle starts moving. Here the friction brake must transition from a static to a dynamic state, which means that when the static friction coefficient is big, the maximum static friction force will be greater and requires more force to overcome in order to initiate motion. A

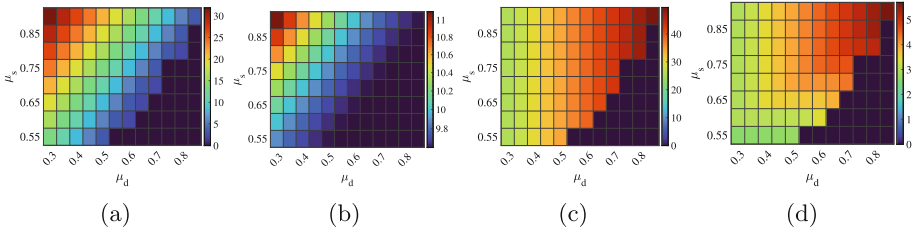


Fig. 2. The maximum body (a) jerk and (b) acceleration during start, an maximum (c) jerk and (d) acceleration during stop are shown for μ_s and μ_d .

consequence is that this results in greater jerk. Conversely, a small μ_s and a large μ_d lead to smoother transitions and reduced jerk. This indicates that very high μ_s and very low μ_d gives discomfort in start scenarios on uphill. Instead, when stopping, Fig. 2(c) and (d) show the jerk and body acceleration after the wheel has stopped rotating. As seen in the figures, μ_s seems to have a small effect when stopping while μ_d plays an important roll. An increase in μ_d increase both jerk and acceleration, but they are both almost constant for a given μ_d and varying μ_s . To observe the effects the difference $\Delta\mu = \mu_s - \mu_d$ between the two coefficients have, we chose three different cases to analyze. The body acceleration and jerk for these cases are shown in Fig. 3.

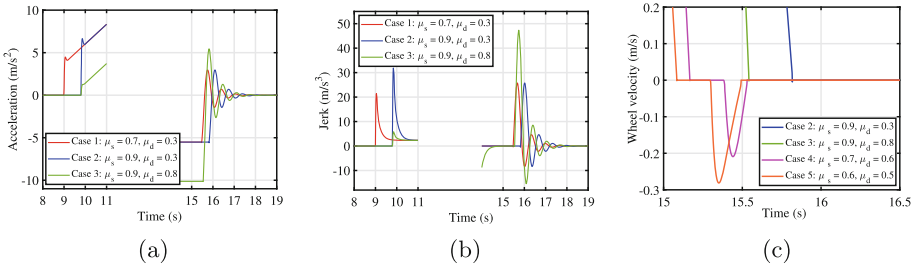


Fig. 3. Time histories for (a) body acceleration, (b) body jerk and (c) wheel speed.

As can be seen in Fig. 3(a), when the model starts moving, we see for all three cases that there is a jump in acceleration, resulting in a large jerk (see corresponding plot in Fig. 3(b)). In particular, jerk is largest for Case 2, with the largest $\Delta\mu$, and the smallest for Case 3, with the smallest $\Delta\mu$. However, when stopping, Case 3 has the largest jerk. It can also be seen that the three cases have similar oscillations when stopping, and for Cases 1 and 2 the maximum jerk and acceleration is the same since they have the same μ_d . From Fig. 2 we know that a change in μ_s only has a small effect on the jerk, when stopping. In general, μ_s has no effect when stopping, but when μ_s is small and close to μ_d , the wheel may start rotating again, thereby affecting and reducing acceleration. Cases 4 and 5 in Fig. 3(c) demonstrate this behavior.

4 Conclusion

In the present study, we introduce a minimal longitudinal model that incorporates the effects of springs and dampers as well as friction and electric braking. We examined the behavior of the vehicle at low speeds when starting and stopping in an uphill when varying the friction coefficients of the friction break. The results indicate that μ_d and μ_s have different impact depending on the scenario. The combination of a small value for μ_d and a large value for μ_s increases discomfort when starting. Conversely, a large μ_d , independent of μ_s , when stopping also increases discomfort. Additionally, as the difference $\Delta\mu$ between the friction coefficients decreases, increased oscillations are experienced when stopping. This study can be used to enhance the understanding of the interplay between friction and electric brake close to zero speed, and thus help us improve comfort by reducing jerk. In future research, we can utilize this model to develop a controller for managing jerk more effectively as well as including a more realistic tire model and enhance the current friction model, and thereby improving both performance and validity in special scenarios.

References

1. Chen, Z., Xiong, R., Cai, X., Wang, Z., Yang, R.: Regenerative braking control strategy for distributed drive electric vehicles based on slope and mass co-estimation. *IEEE Trans. Intell. Transp. Syst.* (2023)
2. Hou, X., Gan, M., Zhang, J., Zhao, S., Ji, Y.: Vehicle ride comfort optimization in the post-braking phase using residual reinforcement learning. *Adv. Eng. Inform.* **58**, 102198 (2023)
3. de Winkel, K.N., Irmak, T., Happee, R., Shyrokau, B.: Standards for passenger comfort in automated vehicles: acceleration and jerk. *Appl. Ergon.* **106**, 103881 (2023)
4. Lee, J., Choi, S.: Braking control for improving ride comfort. In: *MATEC Web of Conferences*, vol. 166, p. 02002 (2018)
5. Singh, A.S.P., Nishihara, O.: Modeling of autonomous emergency braking system with minimum jerk. In: *2022 22nd International Conference on Control, Automation and Systems (ICCAS)*, pp. 40–44. *IEEE* (2022)
6. Shi, B., Xiong, L., Yu, Z.: A control method for improving ride comfort in braking. In: *2021 5th CAA International Conference on Vehicular Control and Intelligence (CVCI)*, pp. 1–6. *IEEE* (2021)
7. Bagdadi, O., Várhelyi, A.: Development of a method for detecting jerks in safety critical events. *Accid. Anal. Prev.* **50**, 83–91 (2013)




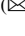

Open Access This chapter is licensed under the terms of the Creative Commons Attribution 4.0 International License (<http://creativecommons.org/licenses/by/4.0/>), which permits use, sharing, adaptation, distribution and reproduction in any medium or format, as long as you give appropriate credit to the original author(s) and the source, provide a link to the Creative Commons license and indicate if changes were made.

The images or other third party material in this chapter are included in the chapter's Creative Commons license, unless indicated otherwise in a credit line to the material. If material is not included in the chapter's Creative Commons license and your intended use is not permitted by statutory regulation or exceeds the permitted use, you will need to obtain permission directly from the copyright holder.





Deriving Models from Field Test Data to Forecast Brake System Limits in Fuel Cell Heavy-Duty Trucks

Seongjae Mun¹ , Jinhui Park² , Hongwoo Lee² , and Changsun Ahn¹  

¹ Pusan National University, Pusan 46241, South Korea
sunahn@pusan.ac.kr

² Hyundai Motor Company, Hwaseong 18280, South Korea

Abstract. Evaluating braking system limits is crucial in designing heavy-duty trucks, often requiring extensive time and resources through field and dynamometer testing. To reduce these demands, modeling approaches have been widely adopted. However, it faces challenges in complex configurations like fuel cell trucks due to interactions between brake and energy systems, particularly regenerative braking, a feature absent in conventional heavy-duty trucks. This paper presents a model that simplifies the representation of these systems in fuel cell trucks, using data-driven models based on field tests. It details constructing and validating a comprehensive brake system model specifically for downhill scenarios in fuel cell trucks, achieving around 99% accuracy in predicting brake limits.

Keywords: fuel cell heavy-duty truck · braking system modeling · simulation · braking limit point · retarder oil temperature

1 Introduction

As the transition from fossil fuels to hydrogen gains momentum for carbon neutrality [1], the development of eco-friendly fuel cell heavy-duty trucks has become a focal point [2–4]. Predicting the braking performance of these trucks is a critical design challenge, usually assessed through costly and time-consuming field and dynamometer tests. A need exists for a method to forecast braking performance beforehand amid changing design specifications. Accessing vehicle data such as states of the powertrain, braking, and control systems is crucial for accurate performance prediction [5]. However, obtaining comprehensive data, especially for new vehicle development, is often challenging. This requires a modeling technique that can forecast braking performance using field test data. This paper proposes a modeling approach using experimental data to forecast braking system limits in fuel cell heavy-duty trucks. The method enables deriving algorithms for complex components and diverse systems, even with minimal knowledge of the underlying mechanism and control algorithms.

Table 1. Details of field test driving scenarios

Scenario	Total driving duration	Total distance covered	Remarks
#1	1727 s	29.47 km	–
#2	1162 s	12.85 km	driving at low speeds
⋮	⋮	⋮	⋮
#14	2372 s	37.17 km	exclusive use of regenerative braking, no retarder
#15	578 s	10.79 km	–

2 Braking System of Fuel Cell Heavy-Duty Trucks

The braking system of a fuel cell heavy-duty truck can be classified into two main components: the primary brake and two auxiliary brakes. The primary brake utilizes air disc brakes with the operational limit dependent on the temperature of the disc. The two auxiliary brakes, namely the regenerative brake and retarder, operate through distinct mechanisms. The regenerative brake converts kinetic energy into electrical energy using a generator during deceleration, and its operational limit is influenced by the battery's state of charge (SOC) [6]. Fuel cell and cooling fan operations play crucial roles in SOC changes during deceleration, and the control algorithms for fuel cell operation and the cooling fan significantly impact both SOC and the operational limit of regenerative braking. On the other hand, the retarder generates braking force by slowing down the output shaft of the transmission, with the braking torque produced by fluid friction [7]. The operational limit of the retarder is determined by the retarder oil temperature.

3 Brake System Modeling

To construct a brake system model, diverse vehicle states during braking were obtained through a series of field tests. The tests were conducted on long downhill descents, with the truck endeavoring to maintain a consistent speed range as much as possible. The dataset includes 52 signals. The dataset was collected from 15 distinct driving scenarios (see Table 1). These scenarios were executed by a 6x4 tractor, specifically a fuel cell heavy-duty truck.

The model structure for the fuel cell heavy-duty truck is shown in Fig. 1. Model of each component is described below.

The vehicle is modeled as a simple lumped mass model as follows:

$$m_{eq}\dot{v}_x = \tau_{traction}/R_{wheel} - F_{brake} - m_{eq}g \sin \theta - k_{rr}m_{eq}g \cos \theta - 0.5C_dA_f\rho v_x^2. \quad (1)$$

The structure of the retarder oil temperature model is illustrated in Fig. 2a, and the temperature dynamics are defined as follows:

$$m_{rd}c_{p,rd} \frac{dT_{rd}}{dt} = P_{rd} - \dot{m}_{clnt}c_{p,clnt}(T_{rd} - T_{clnt,rd_in}) - h_{rd}A_{rd}(T_{rd} - T_{air}), \quad (2)$$

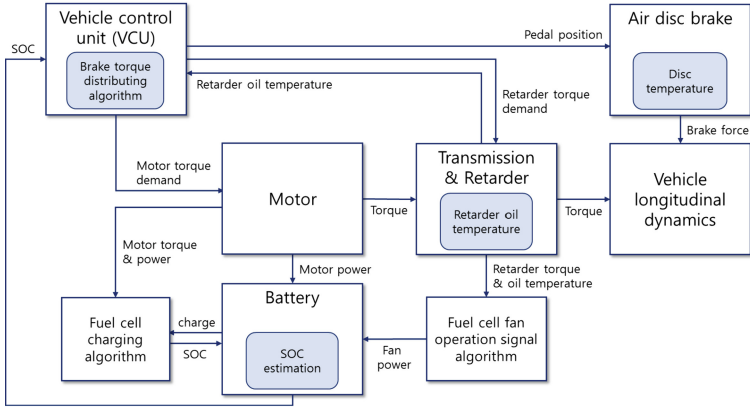


Fig. 1. Model structure for brake system modeling of a fuel cell heavy-duty truck

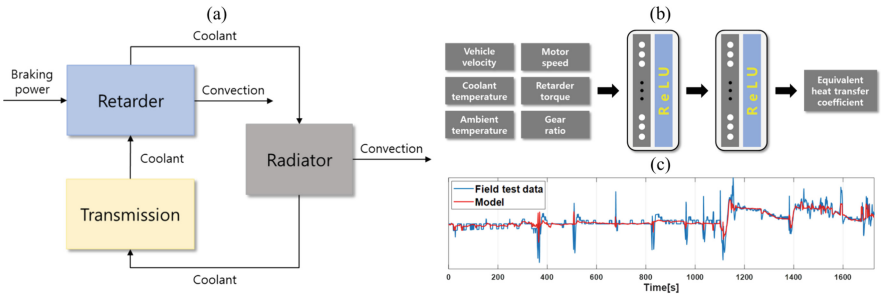


Fig. 2. (a) Structure of retarder oil temperature model, (b) Structure of neural network (NN) for equivalent heat transfer coefficient, (c) Validation of the parameter modeled by NN

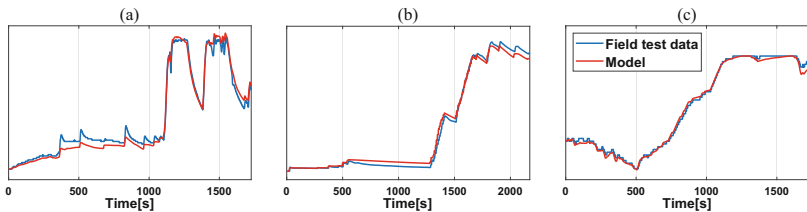


Fig. 3. Validation of models for (a) retarder oil temperature, (b) disc temperature and (c) SOC

where m_{rd} , $c_{p,rd}$, T_{rd} , P_{rd} , h_{rd} and A_{rd} are mass, specific heat, temperature, power, convective heat transfer coefficient and convection area of retarder, \dot{m}_{clnt} and $c_{p,clnt}$ are

mass flow rate and specific heat of coolant, T_{clnt,rd_in} is coolant temperature at retarder inlet and T_{air} is ambient temperature.

The equation for the temperature difference through the radiator is

$$\dot{m}_{clnt}c_{p,clnt}(T_{clnt,rad_in} - T_{clnt,rad_out}) = h_{rad}A_{rad}((T_{clnt,rad_in} + T_{clnt,rad_out})/2 - T_{air}), \quad (3)$$

where T_{clnt,rad_in} and T_{clnt,rad_out} are coolant temperature at radiator inlet and outlet, h_{rad} and A_{rad} are convective heat transfer coefficient and convection area of radiator. Assuming that the amount of heat generated by the transmission is the same as the energy change in the coolant, the following equation is derived:

$$\dot{m}_{clnt}c_{p,clnt}(T_{clnt,TM_out} - T_{clnt,TM_in}) = \dot{Q}_{TM}, \quad (4)$$

where T_{clnt,TM_out} is coolant temperature at transmission outlet, \dot{Q}_{TM} is heat generated by the transmission. Combining Eqs. (2), (3) and (4), the following temperature equation can be derived:

$$m_{rd}c_{p,rd} \frac{dT_{rd}}{dt} \approx P_{rd} - K_{eq}(T_{rd} - T_{air}), \quad (5)$$

where K_{eq} is equivalent heat transfer coefficient of retarder.

The temperature model for the retarder oil is intricately linked to the transmission, both of which are cooled by the same coolant. Accounting for this, modeling the transmission temperature becomes imperative, necessitating the inclusion of several other unknown variables. Additionally, the mass flow rate of the coolant is influenced by an internal algorithm whose specifics are unknown. To address this challenge, this paper introduces the utilization of a neural network to model the equivalent heat transfer coefficient described in Eq. (5). Inputs (vehicle speed, motor speed, retarder torque, coolant and ambient temperatures, gear ratio) obtained from the model feed into the neural network shown in Fig. 2b. This model, operating as a two-hidden-layer feedforward neural network with 64 nodes in each layer and utilizing the Rectified Linear Unit (ReLU) activation function, outputs the equivalent heat transfer coefficient. Figure 2c shows the validation results of the equivalent heat transfer coefficient model.

$$K_{eq} = f_{NN}(x), \quad x = [v_{vehicle}, \omega_{motor}, \tau_{rd}, T_{coolant}, T_{ambient}, R_{gear}]. \quad (6)$$

Figure 3a shows the validation results of the retarder oil temperature model.

The differential equation for the disc temperature is designed as follows:

$$m_{brk}c_{p,brk} \frac{dT_{brk}}{dt} = P_{brk} - \dot{Q}_{conv} = P_{brk} - h_{brk}A_{brk}(T_{brk} - T_{air}), \quad (7)$$

where P_{brk} is the power generated by the air disc brake, m_{brk} , $c_{p,brk}$, h_{brk} , and A_{brk} are the mass, specific heat, convective heat transfer coefficient, and convection area of the air disc brake, respectively. The experimental formula for the convective heat transfer coefficient of a disc brake in turbulent flow [8] is given by

$$h_{brk} = 0.04(k/D)Re^{0.8} = \left(0.04k\rho^{0.8}L^{0.8}/D\mu^{0.8}\right)v^{0.8}. \quad (8)$$

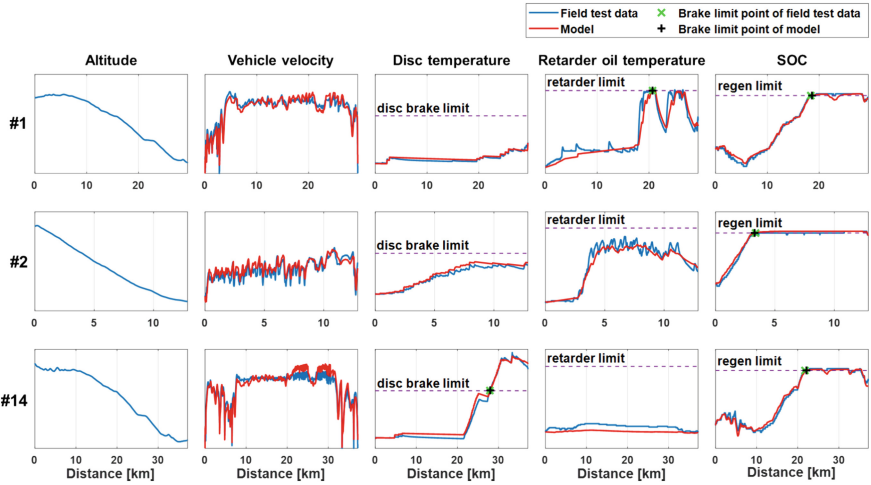


Fig. 4. Comparison of results between simulation and field test data in 3 scenarios

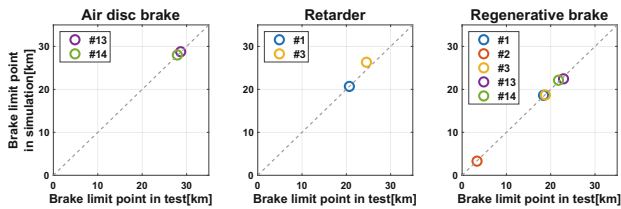


Fig. 5. Comparison of brake point operational limit points caused by temperature or SOC constraints in simulations and field tests

Figure 3b shows the validation results of the disc temperature model.

The battery model is designed based on the equivalent circuit model [9] by open circuit voltage, internal resistance, battery capacity, and battery charge/discharge power as follows:

$$\dot{SOC} = \left(V_{oc} - \sqrt{V_{oc}^2 - 4P_{bat}R_i} \right) / 2Q_{bat}R_i. \tag{9}$$

Figure 3c shows the performance validation results of the battery model.

4 Model Validation

To validate the braking system model, we systematically compare field test data and simulation results for Scenarios #1, #2, and #14, as illustrated in Fig. 4. Directly comparing field test data with simulation is challenging due to variations in drivers; the truck was operated by a human driver in the field test, while a driver model controlled the truck in the simulation. However, our primary focus is on ensuring the consistency of the braking limit point during downhill driving under the same gradient road conditions.

In both the field tests and simulation, the order of brake demand distribution was regenerative brake first, followed by the retarder, and then the disc brake. If a brake in priority reaches its torque limit, the next one is engaged. In Scenarios #1 and #2, all three brake systems were activated, whereas in Scenario #14, the retarder was intentionally deactivated to simulate a retarder failure case. Consequently, Scenario #14 underscores the predominant engagement of the primary braking system, surpassing the braking limit point.

Figure 5 demonstrates the consistency of the proposed model in terms of the distance to the brake operational limit caused by temperature or SOC constraints. Across several scenarios, the model's distance to the brake limit exhibits a very high correlation. These robust findings affirm the effectiveness of the proposed modeling approach.

5 Conclusion

This paper presents an approach utilizing field test data to model the braking system of fuel cell heavy-duty trucks when internal details are unavailable. It models the primary braking system (air disc brake) and auxiliary systems (regenerative braking and retarder). Specific models for disc temperature, SOC, and retarder oil temperature, representing braking limit points, are developed. Validation against field test data confirms the simulation model's accuracy in forecasting braking limit points to be over 99%. The proposed method allows for advanced forecasting of braking performance in fuel cell heavy-duty trucks based on design specification changes, optimizing vehicle stability and efficiency through simulation.

References

1. Chen, L., et al.: Strategies to achieve a carbon neutral society: a review. *Environ. Chem. Lett.* **20**(4), 2277–2310 (2022)
2. de las Nieves Camacho, M., Jurburg, D., Tanco, M.: Hydrogen fuel cell heavy-duty trucks: Review of main research topics. *Int. J. Hydrogen Energy* **47**(68), 29505–29525 (2022)
3. Muthukumar, M., et al.: The development of fuel cell electric vehicles—a review. *Mater. Today: Proc.* **45**, 1181–1187 (2021)
4. Pramuanjaroenkij, A., Kakaç, S.: The fuel cell electric vehicles: the highlight review. *Int. J. Hydrogen Energy* **48**(25), 9401–9425 (2023)
5. Alpaslan, E., et al.: A review on fuel cell electric vehicle powertrain modeling and simulation. *Energy Sources Part A: Recov. Utilization Environ. Effects* 1–37 (2021)
6. Bravo, R.R.S., De Negri, V.J., Oliveira, A.A.M.: Design and analysis of a parallel hydraulic–pneumatic regenerative braking system for heavy-duty hybrid vehicles. *Appl. Energy* **225**, 60–77 (2018)
7. Ganesh Prasad, M.V.: Engine retarders. In: Lakshminarayanan, P., Agarwal, A. (eds.) *Design and Development of Heavy Duty Diesel Engines*, pp. 637–678. Springer, Singapore (2020). https://doi.org/10.1007/978-981-15-0970-4_18
8. Limpert, R.: *Brake Design and Safety*. SAE International, Warrendale (2011). <https://doi.org/10.4271/R-398>
9. He, H., Xiong, R., Fan, J.: Evaluation of lithium-ion battery equivalent circuit models for state of charge estimation by an experimental approach. *Energies* **4**(4), 582–598 (2011). <https://doi.org/10.3390/en4040582>

Open Access This chapter is licensed under the terms of the Creative Commons Attribution 4.0 International License (<http://creativecommons.org/licenses/by/4.0/>), which permits use, sharing, adaptation, distribution and reproduction in any medium or format, as long as you give appropriate credit to the original author(s) and the source, provide a link to the Creative Commons license and indicate if changes were made.

The images or other third party material in this chapter are included in the chapter's Creative Commons license, unless indicated otherwise in a credit line to the material. If material is not included in the chapter's Creative Commons license and your intended use is not permitted by statutory regulation or exceeds the permitted use, you will need to obtain permission directly from the copyright holder.





Numerical Study on Vibration Characteristics of Non-pneumatic Tire Coupled with Quarter-Car Model

Yuta Washimi^(✉), Takuma Suzuki, Toshihiko Okano, and Kensuke Sasaki

Nissan Motor Co., Ltd., 1-1 Morinosatoayama, Atsugi 243-0123, Japan
y-washimi@mail.nissan.co.jp

Abstract. Non-Pneumatic Tires are primarily recognized for their puncture-free attributes, particularly suitable for specialized vehicles. However, not only the advantages, but also vehicle characteristics such as noise, vibration, and harshness need to be considered in case of application to standard passenger cars. To address this, estimating the vibration characteristics of NPT, considering the nonlinear behavior of the tire and its interaction with other car components, is important for vehicle development and chassis control. In this study, tire finite element analysis combined with the multibody simulation of a quarter-car model is employed. The vibration characteristics of a passenger car equipped with NPT are investigated on a specific tire construction and a car model in comparison to a pneumatic tire. It was found that the NPT exhibits high-frequency characteristic vibrations, although the overall trend is qualitatively similar to that of the pneumatic tire when the vertical stiffness and the contact properties are set to be close to those of the pneumatic tire.

Keywords: Non-pneumatic tire · Cleat Impact · Vibration · Ride Comfort

1 Introduction

A non-Pneumatic tire (NPT, airless tire) has been used in specialized applications such as all-terrain vehicles. The previous study mentioned that the application of the NPT to standard passenger needs consideration of potential performances such as noise, vibration, harshness and rolling resistance [1]. In the previous research [2], an NPT structure with a circular deformable shear beam which has an advantage in reducing energy loss during impacting a cleat is proposed. The vibration analysis induced by discrete spokes was reported in the study [3]. However, estimating the vehicle vibration characteristics of NPT involving the nonlinear behavior of the tire and its interaction with other chassis components is not conducted very well, although it is crucial for vehicle development and chassis control. The main goals of the present work are to investigate and improve the vibration characteristics of a passenger car equipped with NPT. In the present study, tire finite element (FE) analysis combined with a multibody quarter-car model is performed. The vibration characteristics is investigated on a specific NPT construction in comparison to a pneumatic tire by using the method.

2 The Detail of NPT Structure

Figure 1 shows the specific structure of the NPT, based on the concept proposed in the previous work [4]. The spoke is made of elastomer with relatively low-hysteresis-loss properties compared to the rubber used for conventional pneumatic tire to mitigate the rolling resistance. The spoke geometry has an advantage of transferring stress concentration in tire bottom region to entire region by connecting angled spokes. The geometry helps reduce strain energy which is proportional to square of stress when linear elastic material property is assumed. The tread ring is composed of tread rubber, steel belts, and elastomer layer. The elastomer layer enables shear deformation of the tread ring, allowing the NPT to have a contact length comparable to that of a pneumatic tire. The steel belts are designed to transfer stress in the circumferential direction and positioned outside the elastomer layer to accommodate deformation of the spokes, which have relatively low-hysteresis-loss to reduce the rolling resistance.

The geometry is configured to provide comparable vertical static stiffness and footprint length with the tolerance of 10% to those of a similar size pneumatic tire as shown in Fig. 2, specifically 165/70R14.

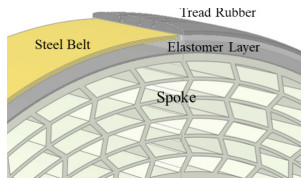


Fig. 1. Structure of NPT in this study

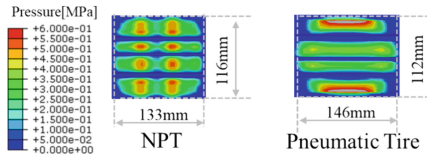


Fig. 2. Contact properties of NPT in comparison to pneumatic tire

3 Modeling Description and Computational Process

3.1 Computational Process

In this study, a methodological approach based on finite element structural analysis is employed. Linear frequency-domain finite element analysis involving rolling effect is widely used to simulate rolling tire. However, as the tread ring of the NPT undergoes large deformations during rolling over a cleat, it is crucial to consider geometric nonlinearity of the structure. Additionally, the vibration caused by rotating discrete spokes contacting road surface also needs to be considered. For these reasons, nonlinear (rolling) tire simulation is employed in this study.

3.2 Modeling Description

The schematic diagram of the model is described in Fig. 3. In this study, a combination of a FE tire model and a multibody quarter-car model is employed. This approach is suitable when the input forces between the left and right wheels are in-phase, such as in case of a cleat impact, to directly capture the tire-suspension interaction and the nonlinear behavior of the NPT while mitigating computational cost.

The quarter-car model consists of tire and suspension link FE models, rigid car body, joints, and bushings. The physical properties of the model are determined based on a specific front suspension of a B-segment car. The material properties used in the tire FE model such as elasticity and viscoelasticity are determined based on the laboratory material tests.

As shown in Fig. 3, the calculation assumes the condition to roll over a 10 mm high step-shaped cleat. In this study, the spindle forces under speed of 10 km/h, 40 km/h and 60 km/h are calculated and compared between the NPT and the pneumatic tire. Once the spindle forces are calculated, they can be utilized as input information for vibration predictions analysis of the entire vehicle system.

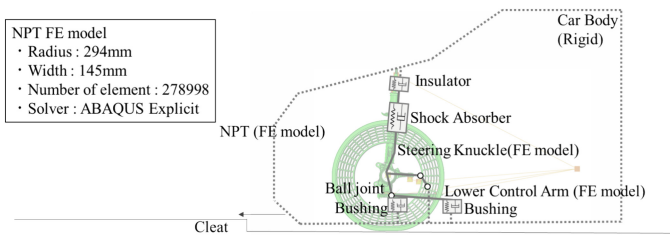


Fig. 3. Schematic diagram of simulation model

4 Results and Discussions

4.1 Vibration Characteristics of NPT

Time and frequency domain response of the spindle force in vertical direction is described in Fig. 4 and 5, respectively. At 10 km/h condition, the time domain spindle force of the NPT shows a similar tendency compared to that of the pneumatic tire and has a dip after the initial impact of the cleat. The dip can be explained by the bending deformation of the tread ring during rolling over the cleat, which is commonly referred to the envelope property. As the spindle force during cleat crossing at lower speed is influenced by enveloping and footprint length properties [5], the NPT is considered to have the envelope property similar to that of the pneumatic tire. The major difference at 57 Hz can be attributed to the vibration generated while the individual spoke hits the road surface. The vibration around 190 Hz is a result of the characteristic vibration caused by the mass and stiffness of the spokes themselves, as shown in Fig. 6. This type of vibration can be referred to spring surge in general.

At 40 km/h condition, the time-domain spindle force exhibits the unsprung mass vibration around 10–20 Hz and the first-order vertical vibration mode around 90 Hz as shown in Fig. 6. The NPT shows the major difference in the vibration amplitude around 90 Hz compared to the pneumatic tire while the amplitudes of lower frequency are at the same level. Since the NPT has the envelope property similar to that of the pneumatic tire, the frequency characteristics of the input force generated when rolling over the cleat can be assumed to be qualitatively equivalent, and the difference in the spindle force can be attributed to the difference in the vibration characteristics of the tire structure. One possible factor is that the spokes of the NPT are composed of low-hysteresis-loss materials, which may explain the higher gain in this frequency range.

At 60 km/h condition, vibration amplitude of NPT is comparable to that of the pneumatic tire. It is well-known that tire vertical force resulting from cleat impact depends on the speed, as the frequency characteristics of the input force vary with the speed during cleat crossing.

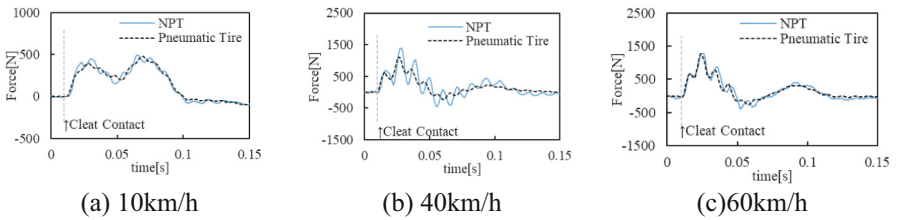


Fig. 4. Time domain spindle force

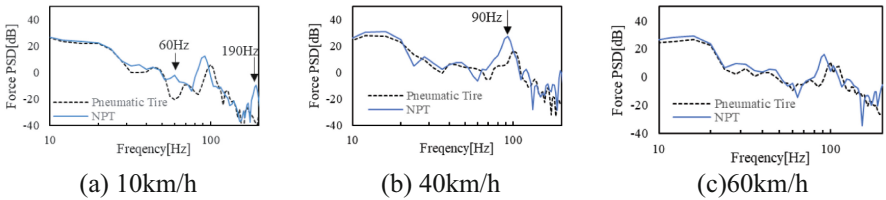


Fig. 5. Frequency domain spindle force

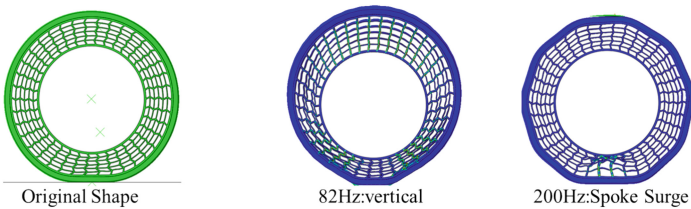


Fig. 6. Mode shapes affecting spindle force

In summary, significant differences were observed in the high frequency range such as the vibration caused by the rotating discrete spokes, the spoke surge, and the tire

characteristic vibration at certain vehicle speed while the overall trends are similar. While these trends can potentially change through innovative designs of the spoke shape, the fundamental tendencies are estimated to remain the same. Addressing these differences would require improvements in both vehicle and tire construction.

4.2 Vibration Characteristics Between Different Structure

The results introduced in the previous section show the vibration characteristics of the NPT. However, these results are based on the examination of a specific structure. In particular, the NPT has an opportunity to change the vibration characteristic around 90 Hz by adjusting the enveloping property to change the frequency characteristics of input force during rolling over the cleat, leveraging its design flexibility. To verify this, a study was conducted by individually adjusting the elastic modulus of the spokes and elastomer layer to maintain the constant vertical stiffness while changing the envelope property.

In this study, two NPT models with almost identical vertical stiffness were examined, with different design properties as shown in Table 1. Spec A has the same specification as discussed in the previous section while the tread groove is omitted for simplicity. Figure 7 illustrates the contact properties of tires. Spec B, the construction with a tread ring of higher rigidity exhibits the shorter contact length, indicating the lower envelope property.

Table 1. Elastic modulus and vertical stiffness of NPTs for parametric study

NPT Spec	Elastic modulus [MPa]		Tire Vertical stiffness[N/mm]
	Elastomer Layer	Spokes	
A(BASE)	6	45	186 N/mm
B	200	40	187 N/mm

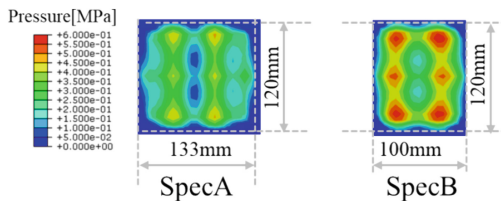


Fig. 7. Contact properties of NPT

Figures 8 and 9 compare the time and frequency domain spindle force in vertical direction, respectively. For the NPT with the higher rigidity of the tread ring (Spec B), the characteristic vibration around 90 Hz at 40 km/h is reduced compared to Spec A. This result suggested that the frequency characteristics of the input force during rolling over the cleat has a peak close to the eigen frequency of the first-order vertical vibration

mode of Spec A, which is qualitatively similar behavior to pneumatic tires [6], while it is separated for Spec C. However, the vibration around this frequency range is larger at 60 km/h. This can be explained by the speed dependency of the frequency characteristics of input force generated during cleat crossing.

As mentioned above, the trend of the NPT in this study, which exhibits a larger amplitude of high-frequency vibration, remains consistent across different structures. However, it can be described that the NPT has design flexibility to change the vibration characteristics at a specific speed by adjusting the envelope property.

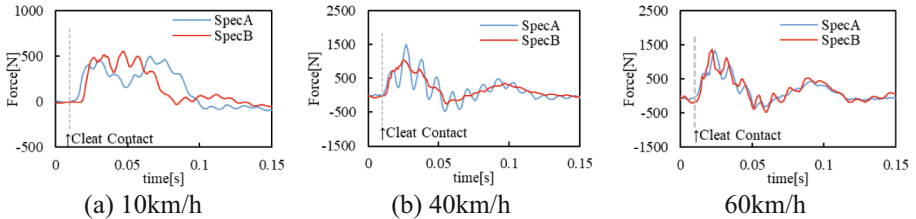


Fig. 8. Time domain spindle force between different construction

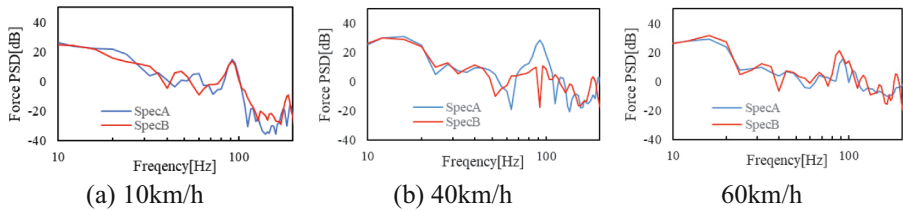


Fig. 9. Frequency domain spindle force between different construction

5 Conclusion

In the present study, the vibration characteristics of a specific NPT construction was evaluated within a comprehensive vehicle simulation, considering the nonlinear behavior of the tire. The spindle force was investigated in comparison to the pneumatic tire and found that the NPT has high-frequency characteristic vibrations, although overall trends are similar. However, it was also described that the NPT possesses the design flexibility to change the frequency characteristics at a specific speed by adjusting the envelope property. Future efforts will focus on exploring performance improvements including the tire and the vehicle design properties.

References

1. Nakajima, Y.: [The Picture of Future Tire] Taiya no shorai zou. J. Soc. Rubber Sci. Technol. Jpn. **93**(9), 305–311 (2020). (in Japanese)

2. Rhyne, T.B., Cron, S.M.: Development of a non-pneumatic wheel. *Tire Sci. Technol.* **34**(3), 150–169 (2006)
3. Narasimhan, A., Ziegert, J., Thompson, L.: Effects of material properties on static load-deflection and vibration of a non-pneumatic tire during high-speed rolling. *SAE Int. J. Passeng. Cars – Mech. Syst.* **4**(1), 59–72 (2011)
4. Suzuki, T., et al.: Rolling resistance evaluation of non-pneumatic tire with linked zig-zag structure using scale model. In: *The 13th TSME International Conference on Mechanical Engineering* (2023)
5. Clark, S.K.: *Mechanics of Pneumatic Tires*. U.S. Department of Transportation, National Highway Traffic Safety Administration (1981)
6. Ketzmerick, E., Angrick, C., Heimann, P., Kubenz, J., et al.: A Dynamic Tire Concept Model for Early Phases of Ride Comfort, Development. SAE Technical Paper 2023-01-5002 (2023)

Open Access This chapter is licensed under the terms of the Creative Commons Attribution 4.0 International License (<http://creativecommons.org/licenses/by/4.0/>), which permits use, sharing, adaptation, distribution and reproduction in any medium or format, as long as you give appropriate credit to the original author(s) and the source, provide a link to the Creative Commons license and indicate if changes were made.

The images or other third party material in this chapter are included in the chapter's Creative Commons license, unless indicated otherwise in a credit line to the material. If material is not included in the chapter's Creative Commons license and your intended use is not permitted by statutory regulation or exceeds the permitted use, you will need to obtain permission directly from the copyright holder.





Study on the Effects of Long-Term Vibration and Visual Tasks on Visual Acuity in the Car

Masateru Amano^(✉), Aya Kubota, Hiroyuki Yamaguchi, Yuji Muragishi,
and Yoshikazu Hattori

Toyota Central R & D Laboratory, 41-1, Yokomichi, Nagakute, Aichi 480-1192, Japan
m-amano@mosk.tytlabs.co.jp

Abstract. In this research, to maintain a passenger's good visual acuity during long riding, we investigated the effects of long-term vibration and visual task on the visual acuity. The results showed that after performing the prolonged visual tasks in the vibration-exposed state, the visual acuity in the stationary state remained unchanged, but the visual acuity in the vibration-exposed state decreased. From these results, it is assumed that among the functions of the eye, the function of stabilizing the eye against vibrations is most likely to deteriorate due to fatigue caused by visual loads. Consequently, to maintain visibility in the car during long car trips, it is important to suppress head movement. This helps prevent fatigue in the eye stabilization function.

Keywords: Human engineering · Visual acuity · Whole-body vibration

1 Introduction

Recently, there has been an increasing demand for performing visual tasks such as computer work and video viewing in the car. In future vehicle development, it is important for passengers to have good visibility of objects even while exposed to car vibrations. It is known that visual acuity, which indicates the ease of seeing objects, decreases due to whole-body vibration [1].

Motivated by this background, to clarify the factors behind the decline in visual acuity, we investigated the relationship between visual acuity and eye movements during vibration. As the result, we showed that the visual acuity during vibration is anticipated by a percentage of visual target's projection outside fovea centralis [2]. This implies that eye motor control to project a visual target on fovea centralis stably is important for the good visual acuity under whole body vibration such as car riding.

On the other hand, our previous study was on visual acuity during a relatively short period of vibration. Other research showed that long-term exposure to vibration gradually reduces vision acuity [3]. In this research, to evaluate the effects of long-term vibration and visual tasks on the visual acuity, we measured changes in visual acuity before and after playing a video game for long time in the condition of exposure to whole body vibration.

2 Visual Acuity During a Short Period of Vibration

In our previous study [2], we investigated the impact of whole-body vibration on visual acuity using a shaker shown in Fig. 1a. Our findings revealed that the experimental collaborator, who initially had a visual acuity of -1.0 LogMAR (equivalent to 6/4.8 vision), exhibited a visual acuity of 0.0 LogMAR (equivalent to 6/6 vision) under vibrations mimicking car movement with a peak amplitude of 0.05G. Furthermore, the collaborator’s visual acuity was measured at 0.1 LogMAR (equivalent to 6/7.5 vision) under vibrations with a maximum amplitude of 0.1G. We confirmed that the passenger’s visual acuity decreases even under car vibration, consistent with previous research.

To elucidate the mechanism of poor visual acuity under vibration mimicking car movement, we measured the movements of eye, head and visual target under vibration and showed the following relationships between these values and the visual acuity:

- (1) The reduction in visual acuity due to vibration exposure can be anticipated by a nonlinear function of a retinal slip ratio (Fig. 1b). The retinal slip ratio is defined as a percentage of visual target’s projection outside fovea centralis shown in Fig. 1c.
- (2) The reduction in visual acuity is independent on the visual acuity in a stationary state.

It can be interpreted that the passenger is no longer able to project the visual target stably on fovea centralis stably under vibration, and the visual target becomes blurred and difficult to see. The eye motor control under vibration is important for good visual acuity in car riding.

On the other hand, our previous study evaluated the visual acuity over a short duration. To make it easier for passengers to see objects during long rides, it is necessary to investigate how long-term vibration and visual tasks affect visual acuity.

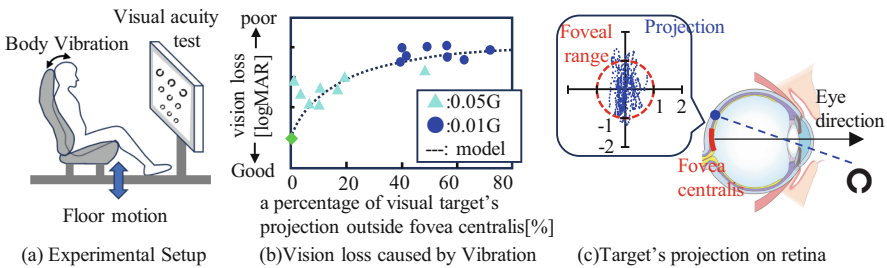


Fig. 1. Visual acuity during a short period of vibration mimicking car movement

3 Experimental Setup for Effects of Long-Term Vibration and Visual Tasks on the Visual Acuity

In this section, we show a new experimental method to investigate how long-term vibration and visual tasks affect visual acuity. Figure 2a shows the new experimental setup in this research. We installed the visual acuity test chart 0.75m and a display for visual

task 0.6 m ahead from the experimental collaborator's eye position. The experimental collaborator, which sits a passenger car seat installed on the floor of shaker having 6 degrees of freedom, can take a vision test before and after performing the visual task.

To investigate the effects of long-term vibration and visual task, the requirement for visual task is that experimental collaborator can focus on performing the task for a long time feeling tired. For this reason, we use a video game "TETORIS" [4] as a visual task.

We use the Early Treatment of Diabetic Retinopathy Study (ETDRS) chart with the Landolt rings arranged in an inverted triangle shown in Fig. 2a as visual acuity test chart. The unit of visual acuity of ETDRS chart is Logarithm of the Minimum Angle of Resolution (logMAR), defined as the common logarithm of viewing angle of the slit of the Landolt ring. An advantage of using LogMAR is that it can be mathematically calculated including addition, average and so on, because the LogMAR is recognized as interval scale [5].

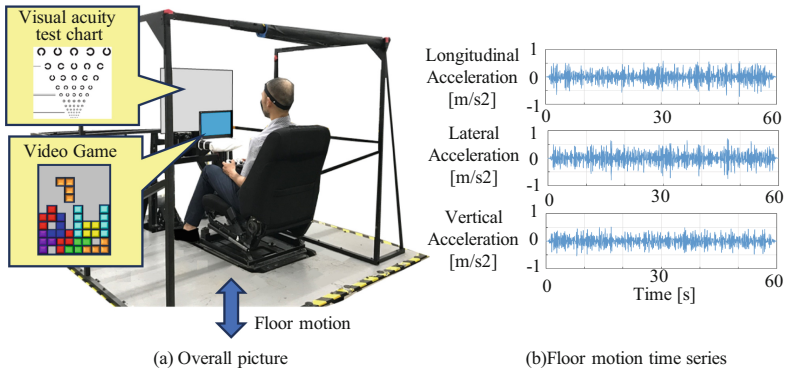


Fig. 2. New Experimental setup

Using the experimental setup, we investigated the effect of long-term vibration and visual task on visual acuity in following three steps.

Step 1. Measurement of visual acuity before visual task

The experimental collaborator sits the passenger car seat installed on the shaker, laying their hands on the knee and their head off the headrest with their eyes close. When the collaborator hears a start signal from the experimenter, the collaborator opens their eyes and answer the directions of the slits of the Landolt rings by voice. The possible answers are only 4 choices such as 'Upper', 'Down', 'left' and 'right'. We ask them for answering one direction of one Landolt ring in about 1 s even if they are not confident in the answer.

They start to answer the directions of the slits of the Landolt rings corresponding to 0.6 LogMAR from left to right and continue to answer the directions of the lower Landolt rings in the same way when all directions of upper Landolt rings are answered correctly.

When the collaborator answers the wrong direction, we finish 1 trial of the visual acuity test after their answering all remaining slits of Landolt rings on the same line.

Using a correct answer rate for the Landolt ring with incorrect answers, we calculate the collaborator's visual acuity. For example, in the case of the correct answer rate 60% (3 out of 5 rings are correct) for the Landolt ring with 0.3 LogMAR, the collaborator's visual acuity is considered 0.34 LogMAR.

As with our previous research [1], we measure the visual acuity before visual task in a stationary state as well as in a vibration-exposed state. Figure 2b shows the translational accelerations in each direction of the floor of the shaker used as vibration input. The translational accelerations are the random noise signals superimposed on sin wave signals at a frequency of 1, 1.1, and 1.4 Hz, filtered through a band pass filter at a frequency of 0 to 5 Hz and have a maximum amplitude of 0.05G. Before the visual task, the visual acuity measurements are taken four times, twice in the stationary state and twice in the vibration-exposed state.

Step 2. Performing the visual task (playing the video game "TETORIS" for a total of 1 h)

After the measurement of visual acuity before visual task of Step 1, to apply loads of the prolonged visual task to the experimental collaborator, we ask them to play the video game "TETORIS" for a total of 1 h.

The collaborator plays "TETORIS" using the display 0.6m ahead from their eye position and the game controller at hand as shown in Fig. 2a. The duration of each playing "TETORIS" is 15 min. The collaborator performs this 4 times, getting out of the shaker and taking a about one-minute break between each playing.

To evaluate the loads of vibration, we use two vibration conditions during playing "TETORIS": stationary and vibration-exposed. The same data used in Step 1 is utilized for vibration input. The experimental with and without vibration is conducted on different days to avoid interaction between the two.

Step 3. Measurement of visual acuity after visual task

After performing the visual task, we measure the visual acuity in same way of Step 1 and complete this experiment.

The requirement for the experimental collaborator is that the collaborator's visual acuity is 0.6 LogMAR (equal to 6/24 normal vision) or higher with the naked eye or soft contacts. In this study, four male collaborators (mean age: 36 years) in their 30s to 40s participated. We performed above Step 1, 2, 3 on each collaborator and got A total of 64 samples (2 cases of visual acuity before and after the task, 2 cases of presence or absence of vibration during visual acuity measurement, 2 cases of presence or absence of vibration during visual task, 2 repetitions, 4 collaborators, multiplication number) of visual acuity data. This study was approved by the Ethics Review Committee of Toyota central R & D Laboratory (No.21B-11).

4 Results and Discussions

Figure 3 shows averages and standard deviations of visual acuity measured under various conditions. Clearly, the followings are shown:

- (1) There are no significant changes in visual acuity before and after playing the game in the stationary state,

- (2) After performing the prolonged visual tasks in the vibration-exposed state, the visual acuity in the stationary state remained unchanged, but the visual acuity in the vibration-exposed state decreased.

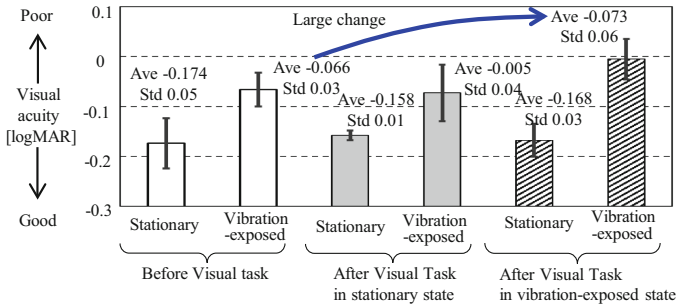


Fig. 3. Visual acuity under various condition

Table 1 shows the results of a three-way ANOVA for differences in the visual task, presence or absence of vibration during visual acuity measurement, and between-subject differences. We consider only an interaction between the differences in the visual task and the presence or absence of vibration because the interaction between the differences among experimental collaborators and other factors is less effective. As is clear from Table 1, the visual acuity changes can be expressed by incorporating the differences in the visual task and the presence or absence of vibration.

Table 1. Three-way ANOVA results

		P values
Main factor	Differences in the visual task:3 levels (Before task, after task in stationary, after task in vibration)	ns
	Presence or absence of vibration during visual acuity measurement: 2 levels (stationary, vibration)	***
	Experimental collaborator: 4 levels (4 person)	***
Interaction	Differences in the visual task and presence or absence of vibration during visual acuity measurement	**

The above results show that the only effect of prolonged visual tasks under vibration is a decrease in visual acuity under vibration. It is thought that the blurring of the projected image on the fovea caused by whole-body vibration results in reduced visual acuity. Therefore it is assumed that among the functions of the eye, the function of stabilizing the eye against vibrations is most likely to deteriorate due to fatigue caused by visual loads. To maintain visibility in the car during long car trips, it is important to suppress head movement. This helps prevent fatigue in the eye stabilization function. The vibration

characteristics of the seated head are characterized by high sensitivity to longitudinal and pitch motion. It is increasingly important to design and control vehicles based on these specific human vibration characteristics.

5 Conclusion

In this research, to investigate how long-term vibration and visual tasks affect visual acuity, we studied the changes in visual acuity before and after playing a video game as a visual task under prolonged vibration. The following results were shown:

- (1) There are no significant changes in visual acuity before and after playing the game in the stationary state,
- (2) After performing the prolonged visual tasks in the vibrating state, the visual acuity in the stationary state remained unchanged, but the visual acuity in the vibrating state decreased.

From these results, it is assumed that among the functions of the eye, the function of stabilizing the eye against vibrations is most likely to deteriorate due to fatigue caused by visual loads. To maintain visibility in the car during long car trips, it is important to suppress head movement. This helps prevent fatigue in the eye stabilization function.

Acknowledgement. The authors are grateful to TOYOTA MOTOR CORPORATION, DENSO CORPORATION, AISIN CORPORATION, JTEKT Corporation, TOYOTA BOSHOKU CORPORATION, TOYOTA AUTO BODY CO., LTD., TOYOTA MOTOR EAST JAPAN, INC. DAIHATSU MOTOR CO., LTD., ADVICS Co., Ltd., and Toyota Technical Development Corporation for supporting and useful discussions. We also thank Toshiyuki Taguchi for leading this research for so long time.

References

1. Ishitake, T., et al.: Changes of visual performance induced by exposure to whole-body vibration. *Kurume Med. J.* **45**, 59–62 (1998)
2. Taguchi, T., et al.: Study of the dynamic visual acuity under whole-body vibration (first report) - evaluation of visual acuity based on head motion and ocular movement measurements. In: JSAE Annual Congress (Autumn) Proceedings 20236190. The Society of Automotive Engineers of Japan, Inc., Yokohama, Japan (2010). (in Japanese)
3. Harazin, B.: Study of effects of whole-body vibration on visual acuity. *Vibr. Active Control* **18**(1), 13–19 (1999)
4. Tetris. <https://en.wikipedia.org/wiki/Tetris>. Accessed 10 Dec 2023
5. CooperVision (in Japanese). <https://coopervision.jp/sites/coopervision.jp/files/drsalmonnews201204.pdf>. Accessed 10 Dec 2023

Open Access This chapter is licensed under the terms of the Creative Commons Attribution 4.0 International License (<http://creativecommons.org/licenses/by/4.0/>), which permits use, sharing, adaptation, distribution and reproduction in any medium or format, as long as you give appropriate credit to the original author(s) and the source, provide a link to the Creative Commons license and indicate if changes were made.

The images or other third party material in this chapter are included in the chapter's Creative Commons license, unless indicated otherwise in a credit line to the material. If material is not included in the chapter's Creative Commons license and your intended use is not permitted by statutory regulation or exceeds the permitted use, you will need to obtain permission directly from the copyright holder.





Human-Centered Collaborative Decision-Making and Steering Control with Reinforcement Learning

Liang Yan¹(✉), Xiaodong Wu², and Hangyu Lu^{2,3}

¹ School of Mechanical Engineering, Shanghai Jiao Tong University, Shanghai, China
y1950726@sjtu.edu.cn

² Institute of Intelligent Vehicle, Shanghai Jiao Tong University, Shanghai, China
xiaodongwu@sjtu.edu.cn

³ Department of Applied Mechanics, Budapest University of Technology and Economics, Budapest, Hungary

Abstract. This paper presents a novel human-centered collaborative driving scheme using model-free reinforcement learning (RL) approach. The human-machine cooperation is achieved in both decision-making and steering control levels to improve driving safety while leaving space for human freedom as much as possible. A Markov decision process is firstly derived from the collaborative driving problem, then a RL agent is developed and trained to cooperatively control the vehicle steering under the guidance of a heuristic reward function. Twin delayed deep deterministic policy gradient (TD3) is conducted to attain the optimal control policy. In addition, two extended algorithms with distinct agent action definitions and training patterns are also devised. The effectiveness of the RL-based copilot system is finally validated in an obstacle avoidance scenario by simulation experiments. Driving performance and training efficiency of different RL agents are measured and compared to demonstrate the superiority of the proposed method.

Keywords: Human-machine coordination · Steering control · Reinforcement learning · Driver intention

1 Introduction

Subject to the inadequacies of fully autonomous driving technology, it is still the mainstream practice to retain human drivers in the vehicle control loop [1]. Nowadays a new technical architecture called human-machine collaborative driving has emerged as the times require. Through close collaboration in vehicle motion planning and control, the integrated system can easily benefit from the hybrid intelligence of the human and the machine [2].

Supported by the National Natural Science Foundation of China under Grant 51775331.

© The Author(s) 2024

G. Mastinu et al. (Eds.): AVEC 2024, LNME, pp. 742–748, 2024.

https://doi.org/10.1007/978-3-031-70392-8_105

In order to achieve the coordination, traditional methods for driving authority allocation usually include constructed functions, model predictive control, fuzzy system and game theory [3]. Recently, with the development of machine learning and neural networks, several researchers have attempted to use such techniques to settle the co-driving problem. For example, [4] proposed a shared steering control framework based on miscellaneous RL methods to achieve a flexible and efficient path-following maneuver. In [5], a lane change decision-making strategy was developed with deep Q-learning, in which the driving risk was evaluated by probabilistic models beforehand. Nevertheless, few of the existing works pay attention to the control freedom or the realization of individual preference of the driver, thus is detrimental to volume up the superiority of human intelligent in the hybrid system.

A human-centered collaborative driving paradigm adheres to the minimal intervention principle [6], which means the machine partner only intervenes as necessary. Otherwise, the human entities are allowed to do whatever they want, such as choosing the desired path and speed, under the premise of safety. Therefore, it improves the driving flexibility in face of some ambiguous environments, and also facilitates the user acceptance of the assistance system. Several human-centered shared control schemes have been elaborated in the robotics domain, like [7] and [8], but that relevant to the ground vehicle is rare. To this end, the main contributions of this paper are concluded as:

- A novel human-centered collaborative driving scheme is proposed, which is the first effort to achieve human-machine coordination in the integrated decision-making and control links with reinforcement learning (RL).
- Two extended RL agents adapted for the collaborative driving task are devised and validated in a challenging obstacle avoidance scenario, which provides directions for structural optimization and training acceleration.

2 Driver-Vehicle System Modeling

Vehicle Modeling. The lateral dynamic characteristics of a vehicle can be represented by a 2-DOF bicycle model:

$$\dot{\beta} = \frac{2}{Mu} \left[C_f \delta - (C_f + C_r) \beta + \frac{-aC_f + bC_r}{u} r \right] - r \quad (1a)$$

$$\dot{r} = \frac{2}{I_z} \left[aC_f \delta - (aC_f - bC_r) \beta - \frac{a^2 C_f + b^2 C_r}{u} r \right] \quad (1b)$$

where M is the vehicle mass; I_z is the yaw inertia; a and b are the distances of the front and rear axles from the center of gravity; C_f and C_r are the cornering stiffnesses of the front and rear tires; β is the sideslip angle; r is the yaw rate. The longitudinal speed is u and the system incentive is the front steering angle δ . Note that the vehicle model is only used for environmental simulation during training and validation since the RL-based method is a model-free approach. Therefore, the model uncertainty will not downgrade the performance of the controller.

Driver Modeling. The optimal preview model is utilized to describe the driver steering control behavior during the path-following process. At an instant t_0 , the optimal steering angle can be obtained by:

$$\delta_d^* = \frac{2(a+b)}{d^2} \left[f\left(t_0 + \frac{d}{u}\right) - y(t_0) - \frac{\dot{y}(t_0)d}{u} \right] \quad (2)$$

where d is the preview distance; f is the reference path; y, \dot{y} is the lateral displacement and velocity respectively. Likewise, the driver model is not necessary a priori knowledge for the controller design, but plays a role in the interaction with the RL agent.

3 Reinforcement Learning Approach

The collaborative driving control can be considered as a Markov decision process (MDP), which is denoted by a tuple $(\mathcal{S}, \mathcal{A}, P, R, \gamma)$ composed of states \mathcal{S} , actions \mathcal{A} , transitions P , rewards R and discount factor $\gamma \in [0, 1]$. An optimal policy π^* that maximizes the expected discounted return in the future can be found through a training process with interaction of the external environment. The policy is usually represented by a parametric neural network.

Observation. The agent observation in this paper consists of the driver action $a_H = [\delta_d, \dot{\delta}_d]$ and the environment states o_E . The environment states contain positions and status of both ego vehicle and surroundings, including information of lanes, road boundaries and obstacles.

Action. The action space is discussed as two situations here. Considering the end-to-end capability of neural networks, the agent output can be defined as either the steering angular velocity or the target lateral displacement of the ego vehicle. For the latter, a low-level Stanley controller [9] is employed to figure out the executable front-wheel steering angle.

Reward. The step reward is comprised of human reward r_H and environmental reward r_E , which is given by:

$$r_H = k_1 e^{-\sigma_1(\delta - \delta_d)^2} \quad (3a)$$

$$r_E = k_2 e^{-\sigma_2 d_c^2} - k_3 e^{-\sigma_3 d_o^2} \quad (3b)$$

where d_c is the offset of the ego vehicle to the lane centerline; d_o is the distance to the nearest obstacle; k_1, k_2, k_3 are weighting coefficients; $\sigma_1, \sigma_2, \sigma_3$ are adjustable softmax coefficients.

Policy Gradient. To obtain the optimal policy, twin delayed deep deterministic policy gradient (TD3) is adopted in this paper. TD3 establishes two Q-function networks Q_{θ_1} , Q_{θ_2} as the critic and a deterministic policy network π_θ as the actor, which is updated by the policy gradient:

$$\nabla_\theta J(\pi) = \frac{1}{N} \sum \nabla_a Q_{\theta_1}(s, a) |_{a=\pi_\theta(s)} \nabla_\theta \pi_\theta(s) \tag{4}$$

where J is the return function and N is the number of transitions in a mini-batch. Figure 1 shows the overall framework of the proposed collaborative driving scheme.

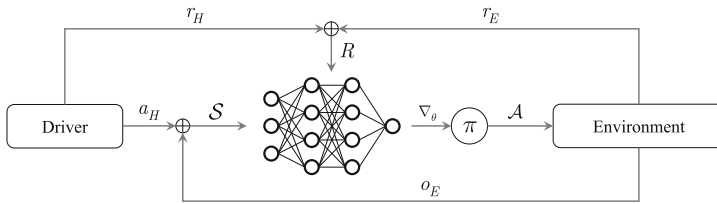


Fig. 1. An overview of the collaborative driving control loop using RL.

Besides vanilla TD3 (where the agent output is the direct steering action), two extended versions are also developed and investigated in this paper: TD3-SC and TD3-SF. Both of them has target lateral displacement as their action space with a subsequent Stanley tracker. The difference is that TD3-SC agent is trained under changeable episode steps, which means an episode ends as collision occurs, while TD3-SF agent is trained under fixed episode steps (collision does not abort the episode). Performance of the three agents will be compared and discussed in the next section.

4 Validation

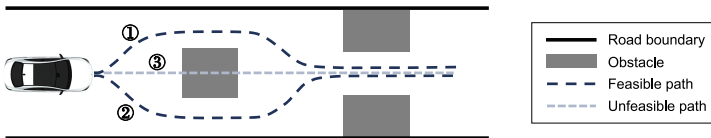


Fig. 2. The testing environment of the collaborative driving scheme.

The collaborative driving agents are trained and validated in the scenario shown in Fig. 2. As illustrate by the diagram, there exist two feasible paths for the

Table 1. Comparison of the training time for the three agents.

Agent	TD3	TD3-SC	TD3-SF
Training time [h]	3.63	1.81	0.97

vehicle to bypass the obstacles. These paths serve as the reference trajectories for human drivers. In addition, one straight-line path representing the driver takes no action in face of the oncoming obstacle is also involved. Basically, the driver randomly choose one of the three reference paths for each episode. It is expected that with the assistance of the collaborative control, the vehicle can travel along the desired path consistent with driver’s intention when there is no risk of collision, or actively steer to avoid the obstacle in case of danger (Fig. 4).

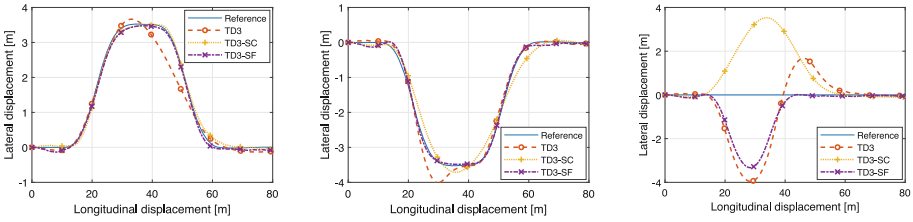


Fig. 3. Trajectory plots for various driver’s reference choices.

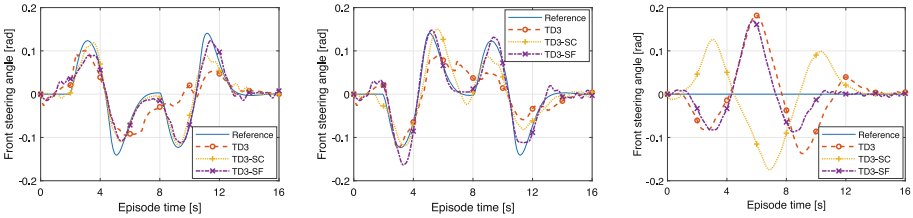


Fig. 4. Action plots for various driver’s reference choices.

As depicted in Fig. 3, for path ① and ②, all three agents can follow the reference and make the correct steering decisions that align with the driver’s intention. However, the trajectories of vanilla TD3 have more deviations than the others, owing to the arbitrary variations and jitters in the steering angle output, which is also plotted in Fig. 3 accordingly. For path ③, it can be seen that all agents successfully bypass the obstacle, but some of them choose to turn left while others choose to turn right. This is also interpretable that the agents stochastically make their own strategies due to the symmetrical nature

of the field. Besides, Table 1 lists the total training time for the three agents to convergence. Obviously, TD3-SF has the highest training efficiency as well as the best path-following accuracy among the three agents.

5 Conclusion

In this paper, a novel human-centered collaborative steering strategy based on RL is proposed and validated in an obstacle avoidance driving scenario. The result shows that the RL-based controller can effectively decode driver's intention from the steering behavior and correct the risky action to enhance the driving safety. In the comparison of three different agents, the adjustment of agent output to target displacement helps to improve the stability of steering control, while the fixed-step discipline can greatly increase the convergence speed. Future work may include to explore more advanced RL algorithms like soft actor-critic (SAC), and to conduct additional driver-in-the-loop experiments where real-world human drivers are engaged.

References

1. Guo, W., et al.: Toward consumer acceptance of cooperative driving systems: a human-centered shared steering control approach within a hierarchical framework. *IEEE Trans. Consum. Electron.* **70**(1), 635–645 (2024)
2. Ning, H., Yin, R., Ullah, A., Shi, F.: A survey on hybrid human-artificial intelligence for autonomous driving. *IEEE Trans. Intell. Transp. Syst.* **23**(7), 6011–6026 (2022)
3. Ansari, S., Naghdy, F., Du, H.: Human-machine shared driving: challenges and future directions. *IEEE Trans. Intell. Veh.* **7**(3), 499–519 (2022)
4. Xie, J., Xu, X., Wang, F., Liu, Z., Chen, L.: Coordination control strategy for human-machine cooperative steering of intelligent vehicles: a reinforcement learning approach. *IEEE Trans. Intell. Transp. Syst.* **23**(11), 21163–21177 (2022)
5. Li, G., Yang, Y., Li, S., Qu, X., Lyu, N., Li, S.E.: Decision making of autonomous vehicles in lane change scenarios: deep reinforcement learning approaches with risk awareness. *Transp. Res. Part C: Emerg. Technol.* **134**, 103452 (2022)
6. Anderson, S.J., Karumanchi, S.B., Iagnemma, K.: Constraint-based planning and control for safe, semi-autonomous operation of vehicles. In: 2012 IEEE Intelligent Vehicles Symposium, pp. 383–388 (2012)
7. Carlson, T., Demiris, Y.: Collaborative control for a robotic wheelchair: Evaluation of performance, attention, and workload. *IEEE Trans. Syst. Man Cybern. Part B (Cybern.)* **42**(3), 876–888 (2012)
8. Javdani, S., Admoni, H., Pellegrinelli, S., Srinivasa, S.S., Bagnell, J.A.: Shared autonomy via hindsight optimization for teleoperation and teaming. *Int. J. Robot. Res.* **37**(7), 717–742 (2018)
9. Hoffmann, G.M., Tomlin, C.J., Montemerlo, M., Thrun, S.: Autonomous automobile trajectory tracking for off-road driving: controller design, experimental validation and racing. In: 2007 American Control Conference, pp. 2296–2301 (2007)

Open Access This chapter is licensed under the terms of the Creative Commons Attribution 4.0 International License (<http://creativecommons.org/licenses/by/4.0/>), which permits use, sharing, adaptation, distribution and reproduction in any medium or format, as long as you give appropriate credit to the original author(s) and the source, provide a link to the Creative Commons license and indicate if changes were made.

The images or other third party material in this chapter are included in the chapter's Creative Commons license, unless indicated otherwise in a credit line to the material. If material is not included in the chapter's Creative Commons license and your intended use is not permitted by statutory regulation or exceeds the permitted use, you will need to obtain permission directly from the copyright holder.





A Study on Giant Magnetostrictive Actuator Used in Active Noise Control System for Ultra-compact Electric Vehicles (Analytical Consideration on Output Performance of the Actuator)

Taro Kato¹ (✉), Ryusei Naganuma¹, Koki Bando¹, Ikkei Kobayashi², Jumpei Kuroda³,
Daigo Uchino³, Kazuki Ogawa⁴, Keigo Ikeda⁵, Ayato Endo⁶, Xiaojun Liu⁷,
Hideaki Kato⁸, Takayoshi Narita⁸, and Mitsuaki Furui¹

¹ Department of Mechanical Engineering, Tokyo University of Technology, Hachioji, Japan
katohtr@stf.teu.ac.jp

² Course of Mechanical Engineering, Tokai University, Hiratsuka City, Japan

³ Course of Science and Technology, Tokai University, Hiratsuka City, Japan

⁴ Department of Electronic Robotics, Aichi University of Technology, Gamagori, Japan

⁵ Department of Mechanical Engineering, Hokkaido University of Science, Sapporo, Japan

⁶ Department of Electrical Engineering, Fukuoka Institute of Technology, Fukuoka, Japan

⁷ OMRON Corporation, Kyoto, Japan

⁸ Department of Mechanical System Engineering, Tokai University, Hiratsuka City, Japan

Abstract. The interiors of ultra-compact electric vehicles (EVs) can be uncomfortable owing to the noise caused by the road and wind. To address this issue, we propose an active noise control (ANC) system that uses a giant magnetostrictive actuator. The proposed system allows estimating ride comfort by analyzing the biological information of passengers and controlling the interior acoustic environment. The proposed ANC system employs wall-surface vibrations generated by a giant magnetostrictive actuator. We analytically investigated the thrust characteristics of giant magnetostrictive materials deformed by a magnetic field through electromagnetic field analysis. The results showed that the effect of thrust on frequency changes depends on the characteristics of the giant magnetostrictive material.

Keywords: Ultra-compact Electric Vehicle · Interior Sound Control · Giant Magnetostrictive Actuator · Ride Comfort · Electromagnetic Field Analysis

1 Introduction

As ultra-compact electric vehicles (EVs) employ electric motors as their power source, the noise within the vehicle primarily comprises road and wind noise [1]. This is because the bodies of ultra-compact EVs are compact and lightweight owing to the rigidity of their lower outer plates. Generally, hard felt and urethane are employed on the interior

walls and roofs of vehicles to minimize external noise. However, the installation of these passive noise control materials in an ultra-compact EV is difficult owing to interior-space limitations. Additionally, the demand for ultra-compact EVs is expected to increase in the future. However, the research and development of noise control systems for ultra-compact EVs have been insufficient. To address this issue, we investigated an active noise control (ANC) system for ultra-compact EVs using a giant magnetostrictive actuator (GMA) [2–4]. Giant magnetostrictive materials (GMMs) feature an elastic displacement exceeding 1000 ppm, high-speed response, and high durability [5]. Therefore, a GMA can output low to high frequencies.

In this study, we determined the output characteristics of GMAs using the finite element method to develop two GMA models for ultra-compact EVs. Their output performance was evaluated through electromagnetic field analysis based on the differences in the material properties of the proposed GMAs.

2 Giant Magnetostrictive Material

Terfenol-D, exhibits the largest room-temperature magnetostriction. Terfenol-D is an alloy composed of terbium, dysprosium, and iron. GMMs are functional materials that can transform energy into other forms and generate 100 times more magnetostriction than conventional magnetic materials. Furthermore, their magnetostriction force and Curie temperature can be changed by altering their metal structure [6, 7]. Most GMMs developed thus far feature a metal composition of $Tb_{0.3}Dy_{0.7}Fe_{1.9-2.0}$. The selected Tb/Dy ratio minimizes their anisotropy energy at room temperature owing to the competition of the TbFe-DyFe pseudo-dielement system. The characteristics of GMMs can be altered by altering their manufacturing method and the compounding ratio of the metal powder. Table 1 lists the physical properties of Terfenol-D [8].

3 GMA Structure and Flux Density Generated by GMM

3.1 GMA Structure

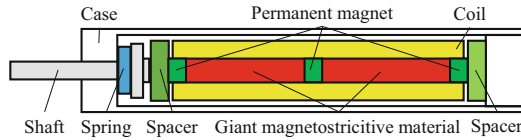
Figure 1 shows the structure of a GMA comprising a columnar GMM, permanent magnet (that applies a bias magnetic field), solenoid coil, and spacer. The coil is connected to an alternating current (AC) source and a magnetic field is generated as the current flows through the coil. The magnetic field stretches the GMM, and the control sound is output by the wall surface, generating vibrations via the shaft and spring. Table 2 lists the fundamental components and materials of the GMA.

3.2 Magnetostriction Force Generated by AC Flowing Through the Coil

Figure 2 shows a model of the GMA along the longitudinal cross-section. The *N* pole of the permanent magnet around the GMM is on the shaft side and the *S* pole is on the opposite side. In this scenario, the magnetostrictive force generated on the surface in contact with the shaft has a positive value. This is because, as shown in Fig. 2, the *x*-axis originates from the shaft side, and the left direction is positive. Therefore, the

Table 1. Nominal physical properties of Terfenol-D.

Physical properties	Values
Density [ρ]	9.3×10^3 [kgf/m ³]
Elastic modulus [Y^H]	$2.5\text{--}3.5 \times 10^{10}$ [N/m ²]
Elastic modulus [Y^B]	$5.0\text{--}7.0 \times 10^{10}$ [N/m ²]
Speed of sound [c^H]	1.72×10^3 [m/s]
Speed of sound [c^B]	2.45×10^3 [m/s]
Magnetic permeability [μ^T]	$9.2 \times 4\pi \times 10^{-7}$ [Tm/A]
Magnetic permeability [μ^S]	$4.5 \times 4\pi \times 10^{-7}$ [Tm/A]
Coupling coefficient [k]	0.7–0.75 [-]
Resistivity [ρ_e]	60×10^{-8} [$\Omega\cdot\text{m}$]
Impedance [ρc^H]	1.57×10^7 [Rayls]
Impedance [ρc^B]	2.27×10^7 [Rayls]
Frequency [$f^H l$]	0.845×10^3 [Hzm]
Frequency [$f^B l$]	1.255×10^3 [Hzm]

**Fig. 1.** GMA structure.**Table 2.** Nominal physical properties of the GMM.

Components	Material	Electrical resistivity
Permanent magnet	Neodymium sintered	–
Shaft/ Spring /Spacer	SUS303	0.7×10^{-6}
Coil	Cu	1.7×10^{-8}
GMM	Terfenol-D	6.0×10^{-7}

direction in which the stretched GMM is pushed out of the shaft is positive. This GMA employs permanent magnets as the bias magnets. Therefore, it can generate a constant magnetostrictive force under the effect of the magnetic field applied by the permanent magnet, even though no AC flows through the coil. Subsequently, when an AC flows through the coil, the magnetostriction force generated by the operating GMM increases or decreases. This magnetostrictive force causes the shaft to transmit vibrations to the wall surface, resulting in the generation of sound waves.

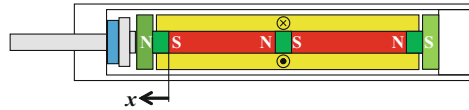


Fig. 2. Model of the GMA along the longitudinal cross-section.

3.3 Analysis Model and Material Characteristics of the GMM

In this study, we considered the magnetic flux density for the output band of road noise using finite element models of the GMA through an electromagnetic field analysis using JMAG Designer Version 16.0 (JSOL Corporation). A permanent magnet was magnetized along the axial direction of the GMM. The coil conductor featured a diameter of 0.5, 1000 turns, and an inductance of 3.5 μH .

In this analysis, the characteristics of the GMM were used as the values for the magnetic field and flux density, based on the research conducted by Sugawara [9]. The size change under the effect of an external magnetic field applied to the GMM was determined according to the method proposed by Mori [10]. The Young's modulus of the GMM was set to 26.5 GPa and its Poisson's ratio was 0.3. Based on these, a 3D analysis was conducted. The number of divided elements and nodes was 29653 and 5570, respectively. The electromagnetic field analysis considered the eddy currents in the shaft and GMM.

4 GMA Structures and Magnetic Flux Density Generated by the GMM

Figure 3 shows the finite element models of the two GMAs employed in this study. Figure 4a shows a GMA in which two Terfenol-D components with lengths and diameters of 20 and 4 mm, respectively, are arranged in series. By contrast, the GMM shown in Fig. 4b has a length of 43 mm and comprises two permanent magnets. As GMAs output the displacement owing to the axial strain of the material, we analytically examined the magnetic flux density characteristics of the two GMMs by changing the AC voltage and varying the frequency applied to the coil from 100–500 Hz based on the road-noise frequency band. In this analysis, a sampling frequency of 20 kHz and voltage amplitude of 1–5 V were employed.

Figure 4 shows the vector plots of the magnetic flux densities for each model under an applied voltage of 3 V. Model A exhibits a large magnetic flux density at the interface between the GMM and permanent magnet, whereas Model B exhibits a large magnetic flux density at the center of the GMM. Figure 5 shows sample vector plots for the amplitude of the magnetic flux density of each model when the AC voltage was changed from 1–5 V. In both figures, the vertical and horizontal axes represent the magnetic flux density and AC frequency, respectively. The magnetic flux density is the value at the surface center on the shaft side. These were higher for Model A than for Model B at 100 and 300 Hz. Based on these results, we determined that the magnetic flux density changes depending on the GMM shape and the arrangement of the permanent magnets. However, a detailed study of the correlation between the magnetic flux density and the magnetostriction force is required.

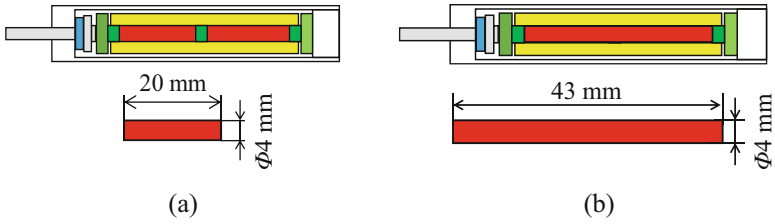


Fig. 3. Finite element models of the two GMAs: Models (a) A and (b) B

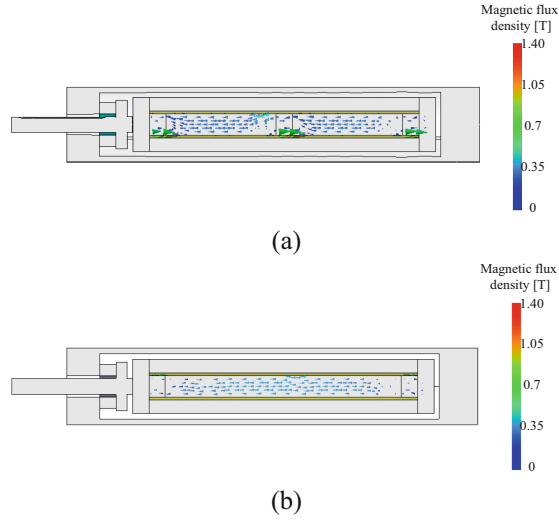


Fig. 4. Vector plot samples of the magnetic flux density for each model at the maximum voltage: Models (a) A and (b) B.

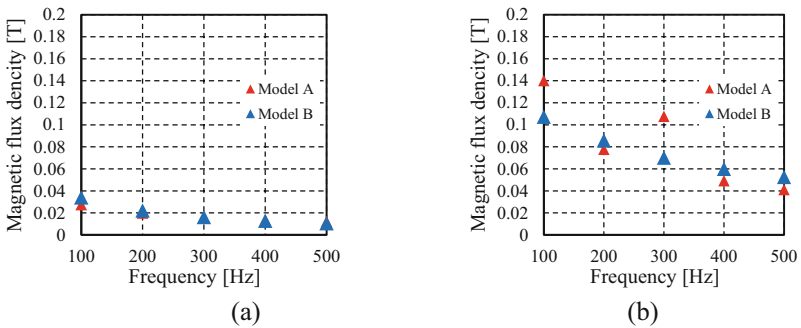


Fig. 5. Sample vector plots of the magnetic flux density for each model at the maximum voltage: Models (a) A and (b) B.

5 Conclusion

This study analyzed the output performances of two GMAs with different material properties to develop an acoustic device for an ANC system for ultra-compact EVs. We determined the low-frequency output control sound via electromagnetic field analyses of finite element models of the GMA. The analysis results indicated that the magnetic flux density changes depending on the shape of the GMM and the arrangement of the permanent magnets. However, a more detailed study on the correlation between the magnetic flux density and the magnetostriction force is required. Therefore, in future studies, we plan to vary the size, weight, shape, and components of the actuator, and employ a material with a higher magnetic permeability.

References

1. The ministry of Land, Infrastructure Transport, and Tourism. Profits on ultra-compact mobility lead to investigation utilizing experiments (2011). (in Japanese)
2. Kato, T., et al.: Design of giant magnetostrictive actuator for ultra-compact EV: fundamental consideration on frequency characteristics of magnetostriction force. *J. Magn. Soc. Jpn.* **46**(3), 70–75 (2022)
3. Kato, T., Suzuki, R., Miyao, R., Kato, H., Narita, T.: A fundamental consideration of active noise control by small actuator for ultra-compact EV. *Actuators* **7**(3) (2016)
4. Kato, T., et al.: Development of noise control system for ultra-compact mobility by plate vibration (Fundamental consideration on performance of giant magnetostrictive actuator). *Trans. Magn. Soc. Jpn. Spec. Issues* **5**(1), 44–49 (2021). (in Japanese)
5. Matsui, Y.: Giant Magnetostrictive actuator. *Trans. Jpn. Soc. Mech. Eng.* **111**(1072), 188–189 (2008). (in Japanese)
6. Mori, T.: Investigation of power metallurgical RFe₂ compound and their applications. *J. Jpn. Soc. Precis. Eng.* **60**(12), 1691–1694 (1994). (in Japanese)
7. Kobayashi, T., Sakai, I.: Giant magnetostrictive material and actuator application. *J. Jpn. Soc. Precis. Eng.* **60**(12), 1695–1698 (1994). (in Japanese)
8. Clark, A.E., Eda, H.: Giant magnetostrictive material. *The Nikkan Kogyo Shimibun* (1995). (in Japanese)
9. Sugasawa, M., Arai, M.: Evaluation of eddy current characteristics for applied high frequency voltage to the giant magnetostrictive material. *Trans. Jpn. Soc. Comput. Method Eng.* **7**(2), 235–238 (2008). (in Japanese)
10. Mori, T.: Giant magnetostrictive actuator. *J. Robot. Soc. Jpn.* **15**(3), 334–337 (1997). (in Japanese)

Open Access This chapter is licensed under the terms of the Creative Commons Attribution 4.0 International License (<http://creativecommons.org/licenses/by/4.0/>), which permits use, sharing, adaptation, distribution and reproduction in any medium or format, as long as you give appropriate credit to the original author(s) and the source, provide a link to the Creative Commons license and indicate if changes were made.

The images or other third party material in this chapter are included in the chapter's Creative Commons license, unless indicated otherwise in a credit line to the material. If material is not included in the chapter's Creative Commons license and your intended use is not permitted by statutory regulation or exceeds the permitted use, you will need to obtain permission directly from the copyright holder.





Collision Prediction for a Mining Collision Avoidance System

J. C. van Aswegen, H. A. Hamersma^(✉) , and P. S. Els 

Department of Mechanical and Aeronautical Engineering, University of Pretoria, Pretoria,
South Africa
hermanh@up.ac.za

Abstract. Accidents caused by wheeled mining machines contribute to approximately 30% of injuries and fatalities in the global mining industry. Wheeled mining machines have limited driver assist features when compared to the passenger vehicle market and are typically limited to collision avoidance by braking. These products are often subject to false positive interventions leading to production losses, increased wear, and resistance to adopt the technology by end users. This study proposes a sampling-based method to expand the collision avoidance by braking approach to include steering. The sampling method is based on the vehicle's kinematics and the application of a Gaussian distribution to the steering rate to determine the probability of a collision occurring. Initial results indicate that the inclusion of steering rate on the collision prediction model may increase the operator's situational awareness, leading to fewer false positives.

Keywords: Automatic emergency braking · mining safety · collision avoidance system · situational awareness · heavy vehicle dynamics

1 Introduction and Background

New technologies are transforming the mining industry, making it cleaner and safer. One of the focus areas is the safe operation of mine transport and mobile equipment. The International Council on Mining and Metals (ICMM) reports that approximately a third of all fatalities at their member company operations are due to transport and mobile equipment accidents [1].

Mining machine Collision Avoidance Systems (CAS) are under the spotlight in South Africa, where the use of Collision Prevention Systems (CPS) is regulated [2]. Where a significant risk of injury exists due to collisions between mining machines and pedestrians (for underground mines) and between mining machines (for surface mines), mines are required to implement CPS. The regulation stipulates three distinct stages of the interaction and the subsequent response by the CPS: 1) The remote object is detected, 2) the operator(s) and pedestrian(s) (if applicable) are given an effective warning and (3) the machine is slowed and stopped [2]. Within the South African context, mobile machines include any self-propelled machine used for the purpose of mining, transport, or associated operations. Effectively, this means that all wheeled vehicles,

such as light vehicles, forklifts, load-haul-dumpers (LHDs) and haul trucks are subject to these regulations. At the time of writing, South Africa is the only region in the world that regulates the use of collision avoidance technology [3].

Mining collision avoidance products currently available on the market are almost exclusively retrofits that are installed on existing mining machines. Collision avoidance is provided by interfacing with the machine's SAE J1939 CAN-bus through a standardized interface [4]. The standardized interface only makes provision for the application of the machine's braking system. This limits the collision avoidance system to a single degree of freedom (effectively only half a degree of freedom since the throttle cannot be applied). Any action other than slowing and stopping the machine is left up to the operator. Existing systems typically do not instruct the operator to change direction; rather, they rely on instructions such as 'warning' or 'caution' before automatically applying the brakes [3].

The result of limiting the automatic intervention to braking, and only warning the operator, is that mining collision avoidance systems tend to be very conservative, erring on the side of caution. The result is that numerous false positives are reported, resulting in increased wear and tear, production losses and resistance to adoption from the end users [5]. It is hypothesized that improved situational awareness of the operator through increasing the design envelope of the collision avoidance system, may result in fewer false positive detections, resulting in improved performance and wider adoption.

2 Approach

Collision prediction is a vital part of CAS. Without an accurate collision prediction model that can provide a computationally inexpensive solution, a collision can be falsely predicted or neglected. Both situations are dangerous and could lead to a collision, an injury or/and a reduction in the productivity of the mining operations. The proposed method will be explained with a passing scenario. This is a scenario that frequently occurs on mining sites and is included in the User Requirements for CPS developed by the Minerals Council South Africa [6]. Figure 1 shows the passing interaction scenario, with the ego and actor vehicles indicated.

2.1 Trajectory Prediction

Collision prediction works on the principle that the future states of one vehicle are compared to the future states of another vehicle. If the predictions simultaneously occupy the same location, it is assumed that the machines will collide [7]. For this reason, a trajectory must be predicted for all relevant vehicles.

The proposed approach uses linear kinematic equations (see Eq. (1) to (7)) to predict the vehicles' future states. By applying different steering rates to a geometric Ackermann steer single-track model in conjunction with kinematic equations for yaw and the predicted x and y Cartesian coordinates, the future states of a vehicle are predicted. This provides a range of predicted vehicle states at the center of gravity of the vehicle within the kinematic constraints and steering rate limits of the vehicle. Figure 1 shows the result of the sampling-based prediction method.

Equations (1), (2), (3), (5), (6) and (7) represent the kinematic equations that calculate the predicted x and y Cartesian coordinates. Equation (4) computes steering angles by integrating different steering rates over a small time increment Δt . Equations (8), (9) and (10) represent the equations for the geometric Ackermann single-track model, which is used to constrain the maximum steering angle based on the maximum allowable lateral acceleration a_y , chosen to be 0.3 g.

$$x = x_0 + V_x \Delta t \quad (1)$$

$$y = y_0 + V_y \Delta t \quad (2)$$

$$\psi = \psi_0 + \dot{\psi} \Delta t \quad (3)$$

$$\delta = \delta_0 + \dot{\delta} \Delta t \quad (4)$$

$$V_x = V \cos(\psi) \quad (5)$$

$$V_y = V \sin(\psi) \quad (6)$$

$$V = \dot{\psi} R \quad (7)$$

$$\delta = \frac{L}{R} \quad (8)$$

$$a_{y_{\max}} = \frac{V^2}{R} \quad (9)$$

$$\delta = \frac{a_{y_{\max}} L}{V^2} \quad (10)$$

2.2 Trajectory Uncertainty

Trajectory prediction also includes the modelling of the uncertainty of the predicted states. Common methods include applying a Gaussian distribution to the predicted x and y Cartesian coordinates [8].

This study applies a Gaussian distribution to the steering rate of the vehicle. Figure 1 shows the trajectory prediction model for the head-on passing scenario with blue areas indicating lower probabilities. By integrating the Gaussian distribution, the probability for each steering rate is computed and applied to each predicted future vehicle state accordingly. To ensure that the predicted states of the vehicle fully represent the spatial domain, samples are added based on the width, length and heading angle of the vehicle.

The next step is a detailed analysis of the trajectory probabilities. The Euclidian distance between the predicted states of different vehicles at a certain predicted time increment is used to construct a uniform grid of collision probabilities. Using the Euclidean

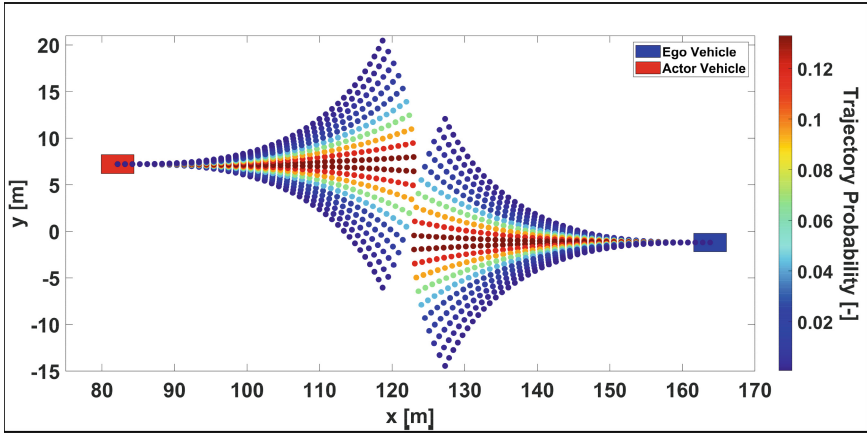


Fig. 1. Trajectory prediction for the ego and actor vehicles for a passing scenario.

distance between the predicted future states, a uniform probability grid is populated with the probabilities of each trajectory. The maximum probabilities in relevant regions of the grid are kept with a convolutional moving maximum method [9], ensuring a conservative uncertainty model. The probabilities must be normalized for all the vehicle grids to ensure consistency. Figure 2 shows the probability grids for the ego and actor vehicles, where the blue areas indicate the lowest trajectory probabilities.

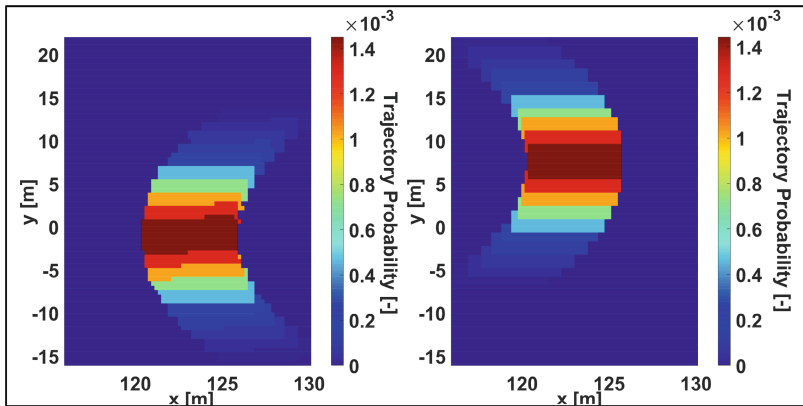


Fig. 2. Ego (left) and actor (right) vehicle trajectory probability for passing scenario.

Considering the uncertainty of the trajectory based on the steering rate of the vehicle, the safest steering direction can be determined, based on the collision prediction metric. From this information an effective warning can be supplied to the driver. This may improve the situational awareness of the operator.

2.3 Collision Metric

Common collision prediction metrics integrate probability distributions over a region to determine the probability of a collision based on the joint probability distribution of multiple vehicles [8]. The proposed model introduces a novel collision metric based on the highest trajectory probability of the different vehicles. Since it is impossible to convert the probability distributions based on the steering rate to a grid of probabilities without influencing the probability distribution, the following method is proposed: multiplying the probability grids based on the trajectory of different vehicles, a new probability grid is created. This is referred to as the collision probability grid. Since this produces very small numbers due to the multiplication of probabilities, a method is developed to provide a collision metric between 0 and 100, based on the probability of the steering rate, which can be converted to a percentage (Eq. (11)). P(ego) and P(actor) are all the probabilities across each uniform probability grid for the ego and actor vehicles.

$$\text{Max Collision \%} = \max\left(\frac{P(\text{ego})P(\text{actor})}{\max(P(\text{ego})P(\text{actor}))} \times 100\right) \tag{11}$$

This collision metric provides a percentage value which can be seen in Fig. 3. By applying a threshold to the proposed collision prediction metric, a collision can be predicted.

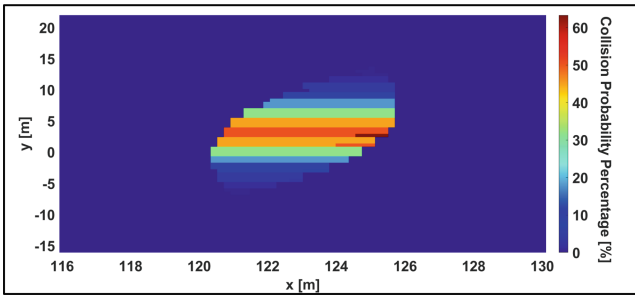


Fig. 3. Collision prediction metric for passing scenario.

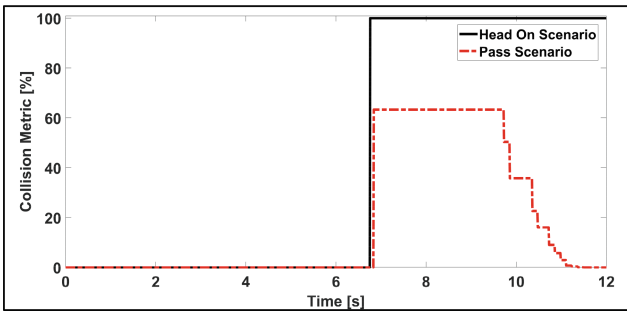


Fig. 4. Collision metric vs simulation time for different scenarios.

3 Initial Results

A passing and head-on scenario, based on [6], are modelled and simulated in RoadRunner [10]. These scenarios are used to do initial tests of the model, specifically to investigate the use of a collision prediction metric threshold to predict a collision. Figure 4 shows the collision metric of the two scenarios. The results indicate that the maximum collision metric is notably different for the two scenarios. This indicates that, for these two scenarios, it is possible to apply a threshold to the collision prediction metric, such that the head-on scenario and passing scenario will not both state that a collision will occur. The threshold can be tuned based on the maximum allowable separation distance between the different vehicles.

4 Discussion

This paper introduced a physics constrained, sampling-based collision prediction method for mining CAS. The collision prediction model used a maximum possible percentage collision probability method to determine whether a collision will occur, while the trajectory uncertainty is modelled using the steering rate. Initial results indicate that the collision prediction model has potential in terms of predicting collisions, but further investigation is needed to apply a reasonable threshold to the collision metric and test the robustness of the model. Since the probability is applied to the steering rate of the vehicle, this approach has the potential to increase the situational awareness of the operator.

It is important to note that the Gaussian distribution applied to the steering rate has a significant influence on the collision prediction metric and must be carefully chosen. The grid size, predicted steering rate samples and predicted time increment, all significantly influence the performance and computational efficiency of the proposed method and needs to be investigated in more detail.

References

1. International Council on Mining and Metals. Cleaner and Safer Vehicles (2024). <https://www.icmm.com/en-gb/our-work/cleaner-safer-vehicles>. Accessed 27 May 2024
2. South Africa. Mine Health and Safety Act 29 of 1996 and Regulations (1996)
3. Hamersma, H.A., Els, P.S., Doran, C.E. (eds.): Evaluation of trackless mobile machine collision management systems. In: 39th International Symposium 'Application of Computers and Operations Research in the Mineral Industry' (APCOM 2019), Wroclaw, Poland, 4–6 June 2019 (2019)
4. International Organisation of Standardisation. ISO/TS 21815-2 Earth-moving machinery - Collision warning and avoidance - Part 2: On-board J1939 communication interface. Geneva, Switzerland (2021)
5. Jacobs, J., Hamersma, H.A., Preis, E., Els, S.: Glencore Waterval East - Pedestrian Vehicle Detection System (PVDS) Technology Capability Assessment. Earth Moving Equipment Safety Round Table (EMESRT) (2018). <https://emesrt.org/stream/technology/digital-ops/technology-capability-assessment-of-the-glencore-waterval-pedestrian-vehicle-detection-system-pvds/>. Accessed 28 May 2024

6. Minerals Council South Africa. Test Specification for Collision Prevention Systems (2022). <https://www.mosh.co.za/transport-and-machinery/documents>. Accessed 28 May 2024
7. Huang, Y., Du, J., Yang, Z., Zhou, Z., Zhang, L., Chen, H.: A survey on trajectory-prediction methods for autonomous driving. *IEEE Trans. Intell. Veh.* 7(3), 652–674 (2022)
8. Jansson, J.: Collision Avoidance Theory: With application to automotive collision mitigation (Doctoral dissertation, Linköping University Electronic Press) (2005)
9. MathWorks. Help Center – movmax Moving maximum (2024). <https://www.mathworks.com/help/matlab/ref/movmax.html>. Accessed 30 May 2024
10. MathWorks. RoadRunner (2024). <https://www.mathworks.com/products/roadrunner.html>. Accessed 28 May 2024

Open Access This chapter is licensed under the terms of the Creative Commons Attribution 4.0 International License (<http://creativecommons.org/licenses/by/4.0/>), which permits use, sharing, adaptation, distribution and reproduction in any medium or format, as long as you give appropriate credit to the original author(s) and the source, provide a link to the Creative Commons license and indicate if changes were made.

The images or other third party material in this chapter are included in the chapter's Creative Commons license, unless indicated otherwise in a credit line to the material. If material is not included in the chapter's Creative Commons license and your intended use is not permitted by statutory regulation or exceeds the permitted use, you will need to obtain permission directly from the copyright holder.





Interactive and Robust Prevention of Lane Departure

Syouma Edamoto^(✉), Shuuji Kimura, Tsutomu Tamura, Richard Gao,
and Robert Fuchs

Systems Innovation R&D Department, JTEKT Corporation, Kashihara 634-8555, Japan
syouma_edamoto@jtekt.co.jp

Abstract. Lane Keeping Assistance (LKA) is one of the most common Advanced Driver Assistance System (ADAS) functions on the market, yet it is still not well accepted by drivers. Although LKA can reduce the occurrence of traffic accidents by correcting the vehicle heading in the event of an unintentional lane departure, poor usability often results in manual deactivation of the function. We provide considerations on how to specify LKA functions in general and propose admittance control as a solution to improve the state-of-the-art from the widely used concept of torque overlay, which is limited by a trade-off between automated and manual driving modes. Using the proposed LKA function, unintentional lane departure is prevented while maintaining comfortable reaction torque which allows the driver to easily steer the vehicle.

Keywords: Advanced driver assistance system · Shared control · Lane keeping assistance · Human machine interaction · Haptic feedback

1 Introduction

Unintentional lane departure due to driver inattention or fatigue can cause tragic accidents. According to NHTSA data, 42% of traffic fatalities are caused by lane departure [1]. The Lane Keeping Assistance (LKA) function is now a common feature in new vehicles to help avoid fatal accidents. The European Union has even made LKA mandatory for M1 and N1 vehicles [2].

The Handbook of Driver Assistance Systems published by Springer describes the requirements of LKA to help prevent unintentional vehicle lane departure [3].

1. Inform the driver of imminent lane departure in a timely manner.
2. Steer the departing vehicle back into the lane if possible.

However, unnecessary warning or intervention from the LKA system should be avoided. In addition, intervention should be avoided for intentional lane changes e.g. during overtaking or if the driver intentionally “cuts corners”. LKA intervention on unintentional lane departures should be clearly perceptible without hindering the driver.

The torque overlay method, in which the LKA torque is added on the existing assist torque for manual driving, has often been used as a steering based LKA mechanism. Torque overlay can exist in both open-loop and closed-loop format. The open-loop format adds the LKA torque for an arbitrary period of time when the system detects an imminent lane departure. The amount of torque applied to the steering wheel is small and can be easily overcome so that the driver keeps control of the vehicle. However, the LKA performance is expectedly low because the open-loop system does not consider feedback of the vehicle position and heading with respect to the lane marking. Furthermore, the haptic warning disappears even if the risky situation exists. To resolve this problem, closed-loop torque overlay, also known as blended control, is now widely implemented [4]. Blended control improves the LKA performance by incorporating steering angle feedback and provides continuous risk communication to the driver. However, the overlaid torque is modulated to ensure that the driver does not require excessive steering torque leading to a trade-off between manual and automated driving modes. Hence, a method for switching the control authority between driver and automation is required based on estimating driver intention [3].

We propose an LKA system based on admittance-type haptic shared control [5] which removes the need for complex authority switching controllers. The experiment results, which were performed on a real vehicle, show improved acceptance of intentional lane crossing and LKA performance when the driver is hands-off. Additionally, the risk of lane departure is continuously communicated to the driver via the steering wheel.

2 Requirements Specification of LKA

The main requirements for LKA are haptic risk communication and safe vehicle motion. However, the driver’s steering feel should not be impaired by the LKA function. Additionally, the LKA function must cope with a wide range of operating situations across driver intentions, vehicle states, traffic environments and so on. The LKA specification can be summarized by the flowchart in Fig. 1.

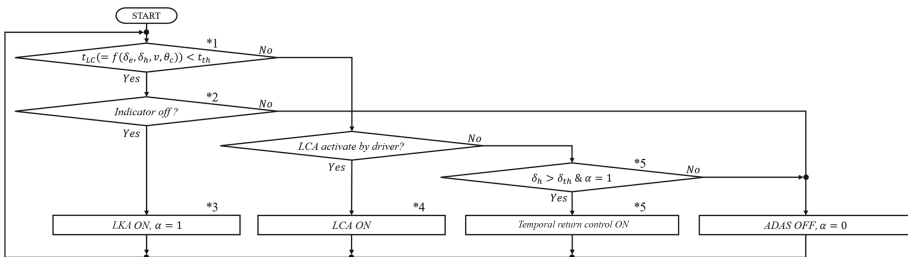


Fig. 1. LKA specification flowchart.

1. The estimated time until lane crossing t_{LC} is calculated by the distance between the vehicle and lane marking δ_e , heading angle δ_h , vehicle speed v and steering column angle θ_c as $t_{LC} = f(\delta_e, \delta_h, v, \theta_c)$. The threshold time t_{th} determines when the LKA

function is activated. A small t_{th} reduces the impact of the LKA function on manual driving while a large t_{th} allows more comfortable vehicle motion when the function is activated.

2. Intentional lane crossing by drivers must be accepted by the LKA function which, until now, has required complex driver intention estimation methods. The proposed LKA control scheme shall eliminate this requirement. Therefore, it is sufficient for the controller to observe the indicator as the driver intention.
3. When the driver is hands-on, continuous haptic warning is necessary while high-risk conditions persist. When the driver is hands-off or “out-of-the-loop”, safety features must prevent lane departure ideally in all situations. The maximum lateral acceleration and jerk which may be induced by the LKA function has been specified in ISO 11270 and UN ECE-R79 [6, 7] as 3 m/s^2 and 5 m/s^3 respectively. However, this may be insufficient in certain situations. For example, a vehicle travelling at 50 km/h on a road with the minimum curvature of 80 m [8] experiences a lateral acceleration of 2.41 m/s^2 which is already approaching the limit. The lateral acceleration which would be induced by the LKA function would be even greater as the vehicle must follow a smaller radius of curvature. Therefore, strict LKA in all situations would merit a revision of the current regulations.
4. When Lane Centering Assist (LCA) is available, the LKA function should quickly transition to LCA in order to prevent jerky motion as illustrated by Fig. 2. As LCA is merely a convenience feature, the centering torque is much smaller than the LKA torque which is a safety feature.

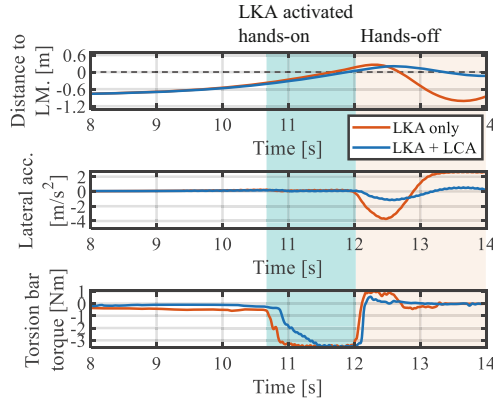


Fig.2. Example of jerky motion due to lack of LCA.

5. Even when LCA is not active, some centering functionality must be present to prevent the vehicle from “bouncing” between lane markings due to the LKA heading correction. A temporary return control is therefore required to obtain smooth vehicle motion once the LKA heading correction is completed.

The proposed LKA based on admittance control will primarily focus on improving point 2 and 3. It is shown to provide high lane keeping performance and continuous haptic warning while being receptive of driver intentional lane crossing.

3 Admittance Control Based LKA

Figure 3a shows the block diagram of LKA based on admittance control. Closed-loop torque overlay based LKA is also shown as a benchmark in Fig. 3b; note the presence of a gain k_t which modulates the torque command generated by the angle controller. θ_{LKA} is the angle command to prevent lane departure and is generally calculated by $\theta_{LKA} = f(\delta_e, \delta_h, v)$. T_{tb} is the torsion bar torque of the Electric Power Steering (EPS) which is used to measure the driver torque T_d . Upon activation of the LKA function, θ_c tracks θ_{cmd} using the angle controller which is implemented by PD control.

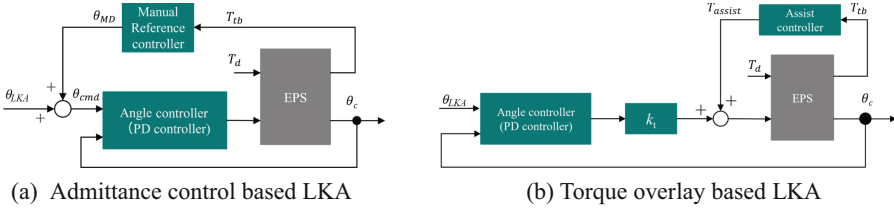


Fig. 3. Block diagrams of LKA control schemes.

In Fig. 3a, the Manual Reference Controller (MRC) is used to estimate the manual deviation angle θ_{MD} created by the driver input. θ_{MD} is then superposed with θ_{LKA} to create the command angle θ_{cmd} for the angle controller, thereby incorporating the driver intention directly into the angle control. The dynamics of the steering column during hands-off situations is given by Eq. 1 and the reaction torque felt by the driver during hands-on situations is given by Eq. 2:

$$J_c \ddot{\theta}_c = k_p(\theta_{LKA} - \theta_c) + k_d(\dot{\theta}_{LKA} - \dot{\theta}_c) + J_c \ddot{\theta}_{LKA} \quad (1)$$

$$T_{tb} = k_{MD}(\theta_{LKA} - \theta_c) + c_{MD}(\dot{\theta}_{LKA} - \dot{\theta}_c) + J_{MD}(\ddot{\theta}_{LKA} - \ddot{\theta}_c) \quad (2)$$

where J_c is the moment of inertia of the steering column, k_p and k_d are the PD controller gains. J_{MD} , c_{MD} and k_{MD} are the MRC parameters.

From Eqs. 1 and 2, it can be seen that the LKA performance in hands-off situations and the driver torque required to intentionally change lanes have been decoupled.

The PD controller gains k_p and k_d can be tuned to improve the angle tracking performance independent of the reaction torque. The MRC parameters k_{md} and c_{md} allow flexible adjustment of reaction torque with respect to distance to the lane marking, as $\theta_{LKA} = f(\delta_e, \delta_h, v)$. Crucially, θ_c can perfectly track θ_{cmd} where $\theta_{cmd} = \theta_{LKA} + \theta_{MD}$ and $\theta_{MD} = 0$ during hands-off situations. Deactivation of the LKA function is unnecessary for intentional lane crossing which means that the system can continuously provide haptic information while high-risk conditions persist.

4 Performance of LKA

In this section, the admittance control based LKA is evaluated on a real vehicle using the closed loop torque overlay as a benchmark. The experiment procedure is shown in Fig. 4. First the driver intentionally steers the vehicle across the lane marking (Fig. 4a). Next, the

vehicle approaches the lane marking without driver input and risking unintentional lane crossing (Fig. 4b). Ideally, intentional lane crossing can be achieved without excessive driver torque and unintentional lane crossing is prevented by the LKA function.

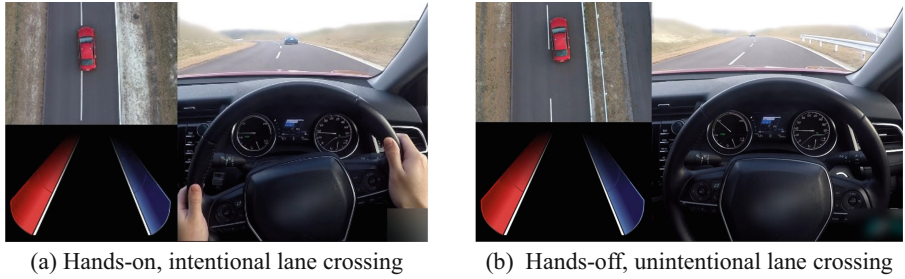


Fig. 4. Experimental procedure.

The torque overlay experiment results are shown in Fig. 5. The blue highlighted area corresponds to the intentional lane crossing scenario and the beige highlighted area corresponds to the unintentional lane crossing scenario. In Fig. 5a, a high value of the gain k_t is used to prioritize the angle tracking performance and unintentional lane departure is prevented. However, the reaction torque during intentional lane crossing is high at around 6 Nm. In Fig. 5b, a low value of k_t is used and the reaction torque during intentional lane crossing has been reduced to around 2 Nm. However, angle tracking performance is reduced, and unintentional lane departure is observed.

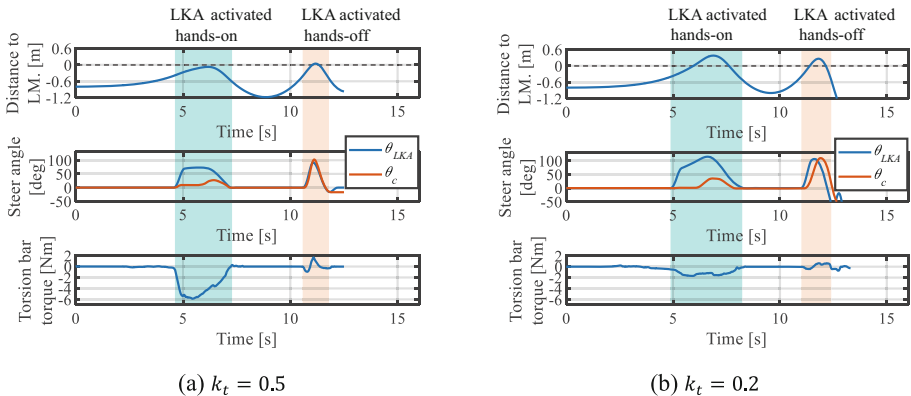


Fig. 5. Performance of torque overlay based LKA.

Figure 6a shows the experiment results using the proposed admittance control based LKA. The high angle tracking performance derived from the admittance control structure prevents unintentional lane departure. In addition, the reaction torque observed during intentional lane crossing is comparable to that from Fig. 6b at around 2 Nm. Thus, the requirements of LKA outlined in Sect. 2 have been achieved without the need for complex

authority switching mechanisms which rely on estimation of driver intention. Figure 6b demonstrates how the reaction torque may be easily tuned using the MRC parameter k_{MD} . The reaction torque grows linearly until the vehicle has crossed the lane marking at which point it plateaus. The LKA function is never turned off and continuous risk information is communicated to the driver even when driving along the lane marking. Exploring the optimal MRC parameters is an important step in combining appropriate haptic risk communication and driver acceptance.

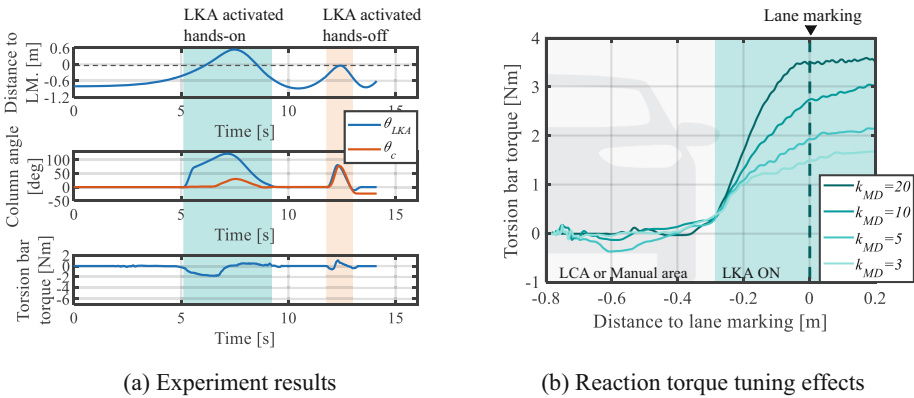


Fig. 6. Performance of admittance control based LKA.

5 Conclusion

This paper has proposed an LKA system based on admittance-type haptic shared control. The admittance control scheme has been shown to allow high lane keeping performance when the driver is hands-off while being receptive of driver intentional lane crossing. Figures 5 and 6 demonstrate how the trade-off required of conventional torque overlay LKA has been resolved using the proposed admittance control based LKA.

Maintaining a comfortable steering feel and smooth vehicle motion when the LKA function is activated are the primary challenge to driver acceptance of the function in the future. The requirements of LKA outlined in Sect. 2 aim to improve driver acceptance rates by addressing both of these issues.

References

1. Run-Off-Road Crashes: An On-Scene Perspective. NHTSA, July 2011
2. REGULATION (EU) 2019/2144. Official Journal of the European Union (2019)
3. Bartels, A., Rohlf, M., Hamel, S., Saust, F., Klauske, L.K.: Lateral guidance assistance. In: Winner, H., Hakuli, S., Lotz, F., Singer, C. (eds.) Handbook of Driver Assistance Systems, pp. 1207–1233. Springer, Cham (2016). https://doi.org/10.1007/978-3-319-12352-3_49

4. Kim, W., Son, Y.S., Chung, C.C.: Torque-overlay-based robust steering wheel angle control of electrical power steering for a lane-keeping system of automated vehicles. *IEEE Trans. Veh. Technol.* **65**(6), 4379–4392 (2016)
5. Nakade, T., Fuchs, R., Bleuler, H., Schiffmann, J.: Haptics based multi-level collaborative steering control for automated driving. *Commun. Eng.* **2**, 2 (2023)
6. ISO DIS standard 11270. Intelligent transport systems – lane keeping assistance systems (LKAS) – performance requirements and test procedures (2013)
7. ECE-R 79. Uniform provisions concerning the approval of vehicles with regard to steering equipment (2005)
8. MLIT - Ministry of Land, Infrastructure Transport and Tourism, Article 15

Open Access This chapter is licensed under the terms of the Creative Commons Attribution 4.0 International License (<http://creativecommons.org/licenses/by/4.0/>), which permits use, sharing, adaptation, distribution and reproduction in any medium or format, as long as you give appropriate credit to the original author(s) and the source, provide a link to the Creative Commons license and indicate if changes were made.

The images or other third party material in this chapter are included in the chapter's Creative Commons license, unless indicated otherwise in a credit line to the material. If material is not included in the chapter's Creative Commons license and your intended use is not permitted by statutory regulation or exceeds the permitted use, you will need to obtain permission directly from the copyright holder.





Effect of Control Laws for Torque-Vectoring Systems on Steady-State Cornering in Race Cars

Ikkei Kobayashi^{1,2}, Fumiya Yoshida³, Liting Fu³, Yusuke Ebashi³, Hayato Yamada³,
Jumpei Kuroda^{1,2}, Daigo Uchino⁴, Kazuki Ogawa⁵, Keigo Ikeda⁶, Taro Kato⁷,
Ayato Endo⁸, Mohamad Heerwan Bin Peeie⁹, Hideaki Kato¹⁰,
and Takayoshi Narita¹⁰(✉)

¹ Course of Science and Technology, Tokai University, Hiratsuka City, Japan

² Research Institute of Science and Technology, Tokai University, Hiratsuka City, Japan

³ Course of Mechanical Engineering, Tokai University, Hiratsuka City, Japan

⁴ Department of Mechanical Engineering, National Institute of Technology,
Numazu College, Numazu, Japan

⁵ Department of Electronic Robotics, Aichi University of Technology, Gamagori, Japan

⁶ Department of Mechanical Engineering, Hokkaido University of Science, Sapporo, Japan

⁷ Department of Mechanical Engineering, Tokyo University of Technology, Hachioji, Japan

⁸ Department of Electrical Engineering, Fukuoka Institute of Technology, Fukuoka, Japan

⁹ Faculty of Mechanical and Automotive Engineering, University Malaysia Pahang,
Pekan, Malaysia

¹⁰ Department of Mechanical System Engineering, Tokai University, Hiratsuka City, Japan
tnarita@tokai.ac.jp

Abstract. This paper presents an analysis of the control law for a torque-vectoring system that actively distributes left and right drive torques to maximize the steady-state cornering performance of a rear-wheel drive race car. The control law allocates torque to the left and right vertical load distribution. Steady-state analysis results show that the maximum lateral acceleration could be improved by 7.8% by decreasing the maximum slip ratio and altering the point at which the yaw moment is trimmed compared to the existing passive system. Furthermore, the stability of the system is reduced, and measures to ensure stability are presented.

Keywords: Torque-Vectoring · Steady-State Cornering · Performance Optimization · Moment Method · Simulation

1 Introduction

In race cars, operating at the limit of tire performance, enhancing cornering performance is crucial to minimize lap times. The most important of these is the steady-state performance at the corner apex, which determines the minimum speed during the cornering process, and requires maximizing the grip of the four tires and balancing the yaw moment. Typical measures for improving cornering performance include various

approaches aimed at uniformly improving overall performance. These may include initiatives such as mass reduction, tire performance improvement, and increased down-force. In scenarios where cornering performance potential is constrained by regulations, the steady-state cornering capability of a rear-wheel-drive vehicle primarily hinges on achieving equilibrium between lateral forces acting on all four tires and longitudinal forces exerted on the left and right rear tires. Ensuring that the lateral forces on all four tires reach their limits is crucial. The key lies in the distribution of torque applied to the left and right rear tires, known as torque-vectoring (TV). While TV is typically induced by a passive differential mechanism, achieving precise control for each vehicle in motion presents challenges. Active yaw moment control systems have been extensively researched to improve vehicle maneuverability and stability in recent years. Among these, active TV systems, including those investigated by our research group [1] have garnered significant attention. Different TV control laws that change the dynamic characteristics have been studied so far. Among them, a torque distribution strategy proportional to the vertical load was devised to suppress stability changes associated with load transfer during acceleration and deceleration [2].

This study presents an analytical investigation of the contribution of a TV control law proportional to the vertical load to maximizing the steady-state lateral acceleration of a rear-wheel-drive race car. Although this control law has been recognized and much investigated for some time, the purpose of this paper is to emphasize its importance compared to conventional passive systems for maximizing the steady-state lateral acceleration of race cars. The analysis method used is the moment method [3, 4], which can comprehensively analyze the behavior changes caused by nonlinear tire characteristics. This analysis method has the advantage of being able to quantify stability indices for whether or not a turn can be maintained. The analysis results were then compared with those obtained with conventional passive systems.

2 Vehicle Dynamics Model

2.1 Equations of Motion with 7 Degrees of Freedom

As shown in Fig. 1(a), the vehicle is constrained on a two-dimensional plane, exhibiting 7 degrees of freedom, which encompass the rotational motion of each wheel. To accurately the model's behavior, roll/pitch load transfers were calculated based on the height of the center of gravity and the tire positions under static equilibrium conditions. In addition, anti-roll stiffness distribution was considered for rolling effects.

The equations of translational motion for two degrees of freedom in the longitudinal and lateral directions at the vehicle's center of gravity are shown in Eqs. (1) and (2). Equation (3) shows the equation of rotational motion in the yaw direction.

$$m(\dot{V}_x - rV_y) = -(F_{yFL} + F_{yFR}) \sin \delta + F_{xRL} + F_{xRR} - F_d, \quad (1)$$

$$m(\dot{V}_y + rV_x) = (F_{yFL} + F_{yFR}) \cos \delta + F_{yRL} + F_{yRR}, \quad (2)$$

$$I_{zz}\dot{r} = l_f(F_{yFL} + F_{yFR})\cos\delta - l_r(F_{yRL} + F_{yRR}) + t_f/2(-F_{yFL} + F_{yFR})\sin\delta + t_r/2(F_{xRL} - F_{xRR}), \quad (3)$$

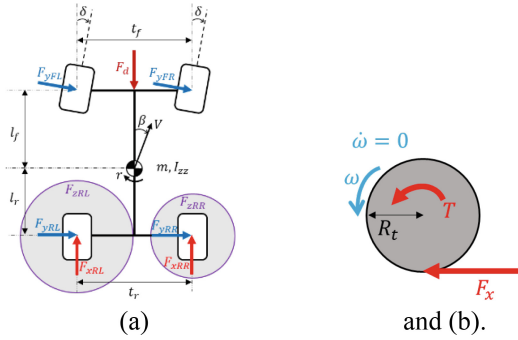


Fig. 1. (a) Free body diagram showing all external forces applied to a vehicle body. (b) Free body diagram showing all external forces on the tire and wheel assembly.

2.2 Application to Moment Method

The moment method is a quasi-static analysis method that uses a combination of the steering wheel angle δ_{sw} and the sideslip angle β at a given longitudinal velocity V_x as inputs. Developed in the 1990s, primarily as an analytical tool for race cars, this method offers a significant advantage in that it can comprehensively represent the relationship between the vehicle’s lateral acceleration a_y and yaw moment N for each input condition. In this study, as shown in Eq. (4), the time derivatives of the longitudinal velocity V_x and lateral velocity V_y were constrained to zero in the moment method calculation.

$$[a_y, N] = f(\delta_{sw}, \beta, V_x) \text{ with } \dot{V}_x = \dot{V}_y = 0, \tag{4}$$

Specifically, a moment diagram was created as shown in Fig. 2. The horizontal axis represents the lateral acceleration, indicating the cornering performance, whereas the vertical axis represents the yaw moment. The inputs are represented by two lines: the red line represents the constant steering angle, and the black dashed line represents the constant sideslip angle. The endpoint of the constant steering angle line represents the limit of the front tire, whereas the endpoint of the constant sideslip angle line signifies the limit of the rear tire.

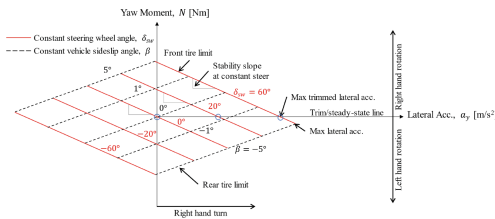


Fig. 2. Schematic diagram describing the moment method.

The trim line, where the yaw moment was balanced, and the trimmed maximum lateral acceleration were used as indices of cornering performance. In addition, as a

stable system must maintain turning for a steady-state, we focused on the stability index. The slope of the constant steering angle in the Fig. 2 indicates stability; specifically, the stability index SI shown in Eq. (5) was used.

$$SI = \partial N / \partial \{a_y m(l_f + l_r)\}, \quad (5)$$

3 Study of Control Law for Active TV Systems

In this study, our focus lies in examining whether the yaw moment, resulting from the disparity in longitudinal forces, can alter the trimming point of the cornering performance depicted in Fig. 2, consequently improving overall cornering performance. Another important consideration is the interdependence between the lateral and longitudinal forces generated by the tires. Figure 3 shows the lateral force values against the slip ratio along the line of constant slip angle, as determined using the tire model. The convex shape of the graph, with its apex at zero slip ratio, indicates the undesirability of employing extremely high slip ratios when aiming to maximize lateral force on the tire for enhanced lateral acceleration. This issue remains unresolved with existing passive differentials. In passive systems, TV is governed by the grip state of the left and right tires, affected by factors such as the frictional torque of the clutch or the yaw angular velocity. Consequently, one wheel may experience strain, resulting in a high slip ratio and a loss of the lateral force necessary for improving cornering performance.

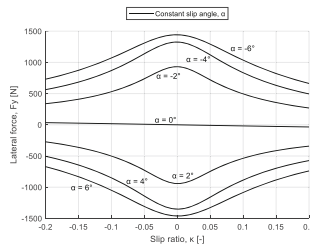


Fig. 3. Lateral force against slip ratio calculated from tire model.

The control law of the torque vectoring system proportional to the vertical load in this study based on the relationship between slip ratio and lateral force for improving the problem and cornering performance of the passive system is shown in Eq. (6).

$$T_{RL,RR} = T_{in} [p \{ |F_{zRL,RR} / F_{zRL} + F_{zRR}| - 0.5 \} + 0.5], \quad (6)$$

Here, T_{in} represents the input torque. This control law allocates torque to the rear wheels according to the vertical load distribution on the left and right sides. The parameter p is set, where $p = 1$ signifies distribution in accordance with the vertical load distribution on the left and right sides. For $p = 0$, TV was performed, equivalent to an open differential.

4 Analysis to Validate the Proposed Control Law

The proposed active TV control law was compared to the existing open differential, limited-slip differential (LSD), and locked differential during steady-state turning to determine its effects on lateral acceleration and stability. The analysis was conducted on a vehicle used in Formula SAE events [5], where competition vehicles were built by students from universities worldwide. Test data specific to FSAE vehicles were used for tires [6] and differentials. Table 1 lists the fundamental vehicle parameters. Figure 4 shows the moment diagram of each system. The longitudinal velocity was 15 m/s, and the steering wheel angle was calculated for combinations in the range of 0° – 100° , with the sideslip angle ranging from -5° – 5° .

Table 1. FSAE vehicle parameters

Parameters	Value
Total mass	268 kg
CoG height	275 mm
Front axle to CoG distance	832.4 mm
Rear axle to CoG distance	697.6 mm
Front/Rear track width	1200 mm
Anti-roll stiffness distribution	60%Fr

The lateral acceleration of the proposed system improved by approximately 7.8% compared to the maximum value of the passive system. Among the passive systems, the locked differential system exhibits the lowest lateral acceleration.

Figure 5 shows the stability index at the trim line for each system. The larger the stability index in the negative direction, the higher the stability; if the value is in the positive direction, the vehicle cannot continue turning. In the passive system, the directly connected locked differential exhibited the highest stability, up to approximately 10 m/s^2 of lateral acceleration. In the region where the lateral acceleration exceeded 10 m/s^2 , the other systems were more stable, and the situation was reversed. The proposed control law for TV was found to be unstable, indicating a trade-off between stability and steady-state cornering performance. If stability becomes an issue at speeds higher than those used in this study, the TV ratio in Eq. (6) should be adjusted closer to zero. Two factors contributed to the increase in the lateral acceleration of the proposed system. First, the increase in the slip ratio of the inner rear wheel was suppressed to increase the lateral force, as the control law intended. In fact, the slip ratio was reduced by approximately 66% compared to the direct-coupling case. The second factor is thought to be that the addition of yaw moment increased the grip in the negative yaw moment region of the moment diagram to zero.

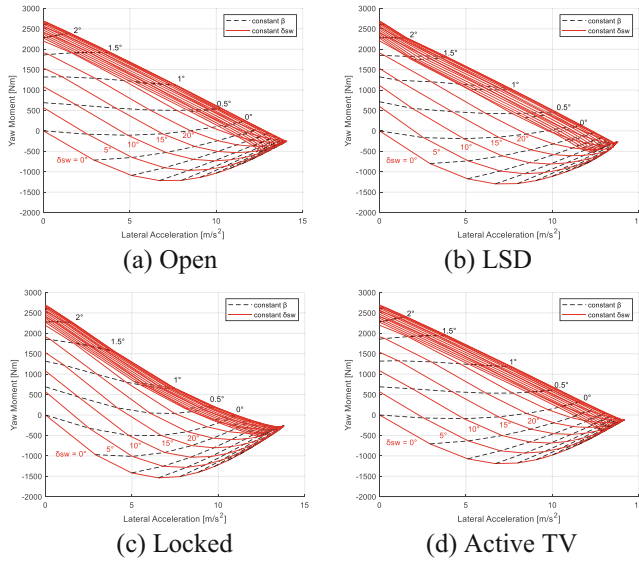


Fig. 4. Moment diagram for each system.

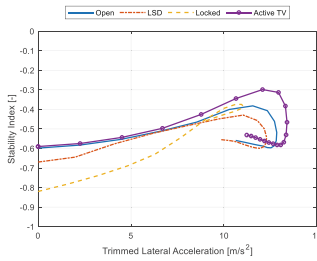


Fig. 5. Trimmed lateral acceleration relative to the stability index.

5 Conclusion

Moment method analysis compares the proposed torque vectoring control law with the passive system and shows that significant performance improvement can be expected without weight reduction or additional downforce. However, since the reduction in stability, which is considered to be a trade-off with lateral acceleration, could be a serious problem, the same analysis will be performed at higher vehicle speeds where the yaw damping is reduced. In addition, since the estimation of vertical loads is necessary to fully apply the control law to reality, the estimation and calculation of load changes due to load transfers and aerodynamics will also be investigated.

References

- Ikkei, K., et al.: Research on yaw moment control system for race cars using drive and brake torques. *Vehicles* **5**(2), 515–534 (2023)

2. Yasuji, S., et al.: Improvement of vehicle maneuverability by direct yaw moment control. *Veh. Syst. Dyn.* **22**(5–6), 465–481 (1993)
3. William, M., Douglas, M.: Race car vehicle dynamics. In: SAE International, Warrendale USA (1995)
4. William, M., Wright, P., et al.: Moment Method - A Comprehensive Tool for Race Car Development, SAE Technical Paper 942538 (1994)
5. Formula SAE Rules. <https://www.fsaonline.com/>. Accessed 01 June 2024
6. Formula SAE Tire Test Consortium, Round 9 test data. <https://www.fsaettc.org/>. Accessed 01 June 2024

Open Access This chapter is licensed under the terms of the Creative Commons Attribution 4.0 International License (<http://creativecommons.org/licenses/by/4.0/>), which permits use, sharing, adaptation, distribution and reproduction in any medium or format, as long as you give appropriate credit to the original author(s) and the source, provide a link to the Creative Commons license and indicate if changes were made.

The images or other third party material in this chapter are included in the chapter's Creative Commons license, unless indicated otherwise in a credit line to the material. If material is not included in the chapter's Creative Commons license and your intended use is not permitted by statutory regulation or exceeds the permitted use, you will need to obtain permission directly from the copyright holder.





Mapping and Localization Method for Autonomous Vehicles on Roads Using Environmental Magnetic Field

Kyoya Ishii¹(✉), Keisuke Shimono², Yoshihiro Suda², Takayuki Ando³,
Hirotaka Mukumoto³, and Kazuo Urakawa³

¹ Graduate School of Engineering, The University of Tokyo, 4-6-1 Komaba,
Meguro-ku, Tokyo 1538505, Japan
kyoyai@iis.u-tokyo.ac.jp

² Institute of Industrial Science, The University of Tokyo, 4-6-1 Komaba, Meguro-ku,
Tokyo 153-8505, Japan

³ Aichi Steel Corporation, 1 Wanowari Arao-machi, Tokai, Aichi 476-8666, Japan

Abstract. Vehicle localization is one of the key technical factors for autonomous vehicles. It requires high accuracy, precision, and robustness towards various road conditions. Popular localization methods include global navigation satellite system (GNSS) and visual methods, but their accuracy can degrade in some conditions. This work proposes to use the environmental magnetic field (EMF) for localization to complement the shortcomings of existing methods. EMF is a combination of the Earth's geomagnetic field and magnetic field induced by man-made objects. It has local fluctuations that can be paired with coordinate positions and is time-invariant within a practical timescale. Past works considering the localization of road vehicles had few problems when applying them to the localization of autonomous vehicles. This work overcomes the problems in the existing method by creating a two-dimensional magnetic field map using Gaussian Process regression, using magnetic markers to enhance EMF fluctuations, and utilizing the Monte Carlo localization algorithm. The proposed method was validated through actual vehicle tests, and its robustness towards other vehicles was examined.

Keywords: Autonomous Vehicle · Localization · Environmental Magnetic Field

1 Introduction

Autonomous vehicles (AVs) can not only free people from driving but are also expected to solve various social problems. One key technical factor for autonomous vehicles on the road is vehicle localization. It is important because the autonomous system will maneuver the vehicle based on this understanding.

Supported by JST SPRING, Grant Number JPMJSP2108.

© The Author(s) 2024

G. Mastinu et al. (Eds.): AVEC 2024, LNME, pp. 777–783, 2024.

https://doi.org/10.1007/978-3-031-70392-8_110

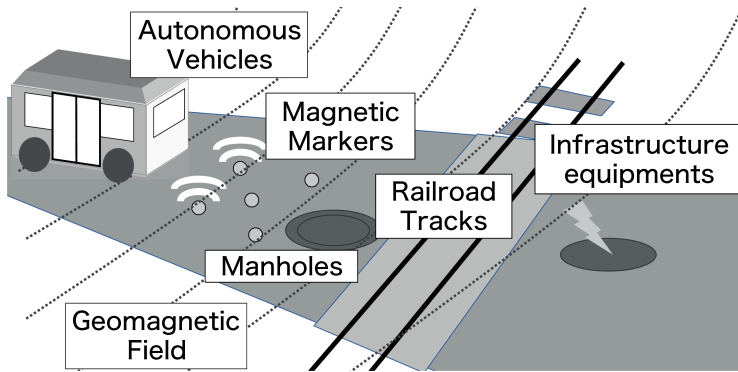


Fig. 1. Image of vehicle localization by EMF. The geomagnetic field is altered by artificial objects such as manholes and other ferromagnetic objects.

It requires high accuracy, precision (the modest error accepted for a typical 2 m wide vehicle running in a 3 m wide lane is 50 cm), and robustness towards various road conditions. Conventional localization methods use GNSS (global navigation satellite system) or visual sensors such as cameras and LiDARs (light detection and ranging) [3]. However, these methods have conditions where their localization accuracy can degrade. Therefore, in practice, multiple methods complement each other to increase robustness.

This work proposes to use the environmental magnetic field (EMF) for AV localization to complement the conventional methods. Here, EMF refers to the combination of the Earth's geomagnetic field and magnetic field induced by man-made objects. EMF has two features that are useful for localization: it has local fluctuations that can be paired with coordinate positions and is time-invariant within a practical time scale [9]. Figure 1 shows the concept image of the proposed AV localization method using EMF. Various ferromagnetic objects can be found in road environments, such as manholes, railroad tracks, and underground structures. Fluctuations of the magnetic field caused by these objects are used for localization.

EMF localization has recently been studied for relatively small indoor mobile robots such as in [1, 5, 7]. However, there are a few examples of EMF localization for road vehicles and problems when applying the works for AV localization. One of them is that their localization accuracy is unacceptable, possibly because there are less useful magnetic field features in outdoor environments. [6] proposed a method using only the magnetometer data, but the localization accuracy was poor, with several hundred meters of error in worst cases. Another problem is that previous works have only made a topological map of the measured magnetic field along the vehicle trajectory. However, this is insufficient for AV localization since the vehicle needs information about the position along the path and within the road or lane width.

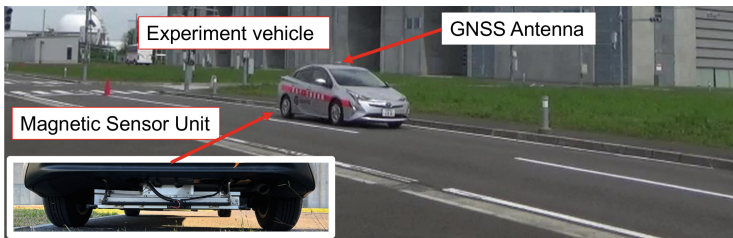


Fig. 2. Image of experimental vehicle running on the experimental field. Magnetic markers are embedded in the lane where the experiment vehicle is running.

2 Proposed Localization Method

This work proposes to overcome the problems of the current EMF localization for road vehicles by the following methods: First, a two-dimensional magnetic field map is created using Gaussian process (GP) regression. Second, magnetic markers can be embedded on roads in places with few magnetic features to enhance such features. Finally, the Monte Carlo method is utilized for the localization algorithm.

GP regression is a non-parametric and Bayesian approach to regression that can model non-linear function relations [4]. Therefore, it is suitable for modeling EMF with limited observation points, and previous works aimed at an indoor environment produced a 2D EMF map from limited observations [1, 7].

In areas where EMF fluctuations are expected to be scarce, magnetic markers are added to enhance the fluctuations of EMF. Unlike the conventional methods such as the magnetic positioning system [2], where the markers' coordinate information is measured and stored in a database for localization, the proposed method does not require such coordinate information. This is because the fluctuations of EMF caused by magnetic markers are modeled into the EMF map with other EMF fluctuations caused by various other reasons.

The Monte Carlo localization (MCL) algorithm utilizes the particle filter algorithm, expressing the vehicle states, such as its coordinate position and heading, as multiple “particles.” Unlike other localization methods, such as Kalman filtering, MCL can approximate any distribution without an explicit landmark [8].

3 Experimental Condition

The proposed method was validated through data obtained from the experiment vehicle. Figure 2 shows the overview of the experimental setup. Data collection was conducted at the ITS R&R experimental field at the University of Tokyo. The experimental field has an actual scale model of a road environment. Some sections have magnetic markers embedded at the center of the lane at 2 m intervals, which can be used to generate the EMF fluctuations needed for the pro-

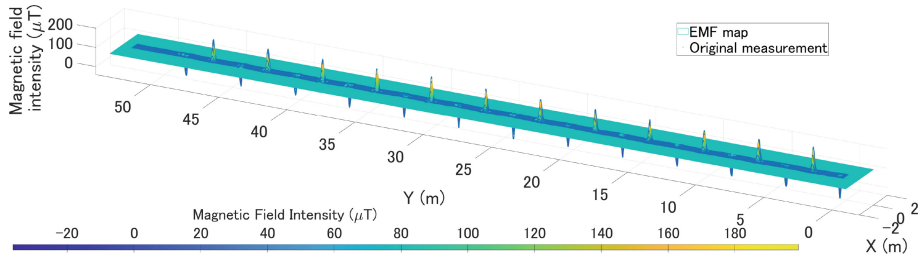


Fig. 3. The generated Z-axis EMF map.

posed method. EMF measurement was conducted at a 50 m straight section with magnetic markers embedded in the road.

Measurements were done by a sensor unit attached to an experiment vehicle provided by Aichi Steel Corporation. The sensor unit is attached to the vehicle's rear, as shown in Fig. 2. The sensor unit comprises 16 3-axis magnetometers installed in a straight line 50 mm apart. The vehicle also has a velocity sensor, inertial measurement unit (IMU), and GNSS antenna.

Conditions with and without other vehicles were conducted to assess the proposed method's robustness towards other road members. An electric vehicle (Mitsubishi iMiev) was used for the other nearby vehicle, with 4 different situations considered: the vehicle being parked with its power off, the vehicle parked with power on, the vehicle running next to the experiment vehicle, and the vehicle running towards the vehicle in the adjacent lane.

4 EMF Map Generation and Discussion

Figure 3 shows the EMF map generated by the proposed method. It was generated within $X = -2\text{ m}$ to $+2\text{ m}$ and $Y = -1\text{ m}$ to $+53\text{ m}$ at the resolution of 1 cm. The figure is plotted with the original measurement data plotted in blue points. The X and Y axes show the coordinate positions, and the Z-axis with the color bar shows the magnetic field intensity in μT .

As seen in Fig. 3, the proposed method generated the EMF map that retained the magnetic field fluctuations of the original measurements. A distinctive spike shape can be seen around the locations of magnetic markers.

5 Localization Results and Discussion

The proposed localization method was applied to measurement data obtained from the experiment vehicle to validate the proposed method. Figure 4 shows the localization result of the condition without any other vehicles nearby. The X and Y axis show the coordinates, and the vehicle ran in the upward direction of the figure. The blue dots show the reference GNSS positions, the red line shows the estimated path of the proposed localization algorithm, and the yellow dots

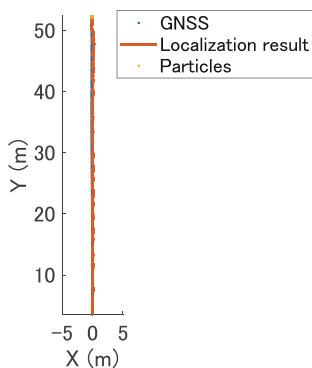


Fig. 4. The localization result of the condition without any other vehicles.

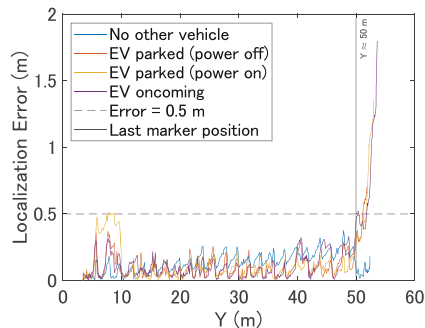


Fig. 5. The localization error of different conditions.

show the final state of the particles. It can be seen that the localization result follows the reference GNSS positions.

Figure 5 shows the localization error from the reference GNSS position of various conditions. The horizontal axis shows the GNSS position in the direction of the Y axis, and the vertical axis shows the localization error at each Y coordinate. The blue line shows the error of the condition with no other vehicle, as we saw in Fig. 4, the red line shows the error of the condition with an EV parked with its power off, the yellow line shows the error of the condition with an EV parked with its power on, and the purple line shows the error of the condition with an EV coming towards the experiment vehicle in the adjacent lane. The horizontal dashed line shows the 0.5 m error border, and the vertical line shows the Y coordinate position of the last marker observed within the experiment condition.

As seen in Fig. 5, the proposed method was able to localize the vehicle for most of the length of the experiment in the conditions listed in the legend. In the condition with an EV parked and oncoming, the vehicles passed by at around $Y = 25$ m, but very little effect on localization is seen. A relatively large localization error is seen for EV parked and EV oncoming conditions after the vehicle passes the last marker. This was mainly caused by a large measurement error by IMU when the vehicle stopped at the end of the measurement.

However, the localization of the condition with an EV running in parallel with the experimental vehicle was not successful, and it is not plotted in the figure. The localization failure may be due to the continuous offset from the original EMF in the measurement caused by the presence of a nearby vehicle. Our preliminary analysis in a simulated environment had a similar outcome when the measured EMF had some offset error from the original EMF.

6 Conclusion

This paper proposes a new vehicle localization method for AVs. The method uses EMF, which is a combined magnetic field of the Earth's geomagnetic field and magnetic field induced by manmade objects. The proposed method generates a 2-D EMF map using GP regression, utilizes magnetic markers where EMF fluctuation is less present, and uses the MCL method to localize the vehicle using the generated EMF reference map.

The proposed method was validated by data obtained from an actual vehicle. It successfully localized the vehicle with high accuracy. The method also showed some robustness towards the existence of other vehicles, but it failed to localize in a condition where an EV was running parallel to the experiment vehicle. We will continue to refine the method to localize the vehicle even in the constant existence of a surrounding vehicle.

References

1. Akai, N., Ozaki, K.: Gaussian processes for magnetic map-based localization in large-scale indoor environments. In: 2015 IEEE/RSJ International Conference on Intelligent Robots and Systems (IROS), pp. 4459–4464 (2015). <https://doi.org/10.1109/IROS.2015.7354010>
2. Ando, T., et al.: Localization using global magnetic positioning system for automated driving bus and intervals for magnetic markers. *IEEE Trans. Intell. Veh.* **8**(1), 878–887 (2023). <https://doi.org/10.1109/TIV.2022.3155324>
3. Kuutti, S., Fallah, S., Katsaros, K., Dianati, M., Mccullough, F., Mouzakitis, A.: A survey of the state-of-the-art localization techniques and their potentials for autonomous vehicle applications. *IEEE Internet Things J.* **5**, 829–846 (2018). <https://doi.org/10.1109/JIOT.2018.2812300>
4. Mochihashi, D., Oba, S.: *Gaussian Process and Machine Learning*. Kodansha LTD. (2019). (in Japanese)
5. Rahok, S.A., Koichi, O.: Odometry correction with localization based on landmarkless magnetic map for navigation system of indoor mobile robot. In: 2009 4th International Conference on Autonomous Robots and Agents, pp. 572–577 (2009). <https://doi.org/10.1109/ICARA.2000.4803938>
6. Shockley, J.A.: Ground vehicle navigation using magnetic field variation. Ph.D. thesis, Graduate School of Engineering and Management Air Force Institute of Technology (2012)
7. Solin, A., Kok, M., Wahlstrom, N., Schon, T.B., Sarkka, S.: Modeling and interpolation of the ambient magnetic field by gaussian processes. *IEEE Trans. Robot.* **34**, 1112–1127 (2018). <https://doi.org/10.1109/TRO.2018.2830326>
8. Thrun, S., Burgard, W., Fox, D.: *Probabilistic Robotics*. Mynavi Publishing Corporation (2007). (in Japanese)
9. Wei, D., Ji, X., Li, W., Yuan, H., Xu, Y.: Vehicle localization based on odometry assisted magnetic matching. In: 2017 International Conference on Indoor Positioning and Indoor Navigation, IPIN 2017, pp. 1–6. Institute of Electrical and Electronics Engineers Inc. (2017). <https://doi.org/10.1109/IPIN.2017.8115941>

Open Access This chapter is licensed under the terms of the Creative Commons Attribution 4.0 International License (<http://creativecommons.org/licenses/by/4.0/>), which permits use, sharing, adaptation, distribution and reproduction in any medium or format, as long as you give appropriate credit to the original author(s) and the source, provide a link to the Creative Commons license and indicate if changes were made.

The images or other third party material in this chapter are included in the chapter's Creative Commons license, unless indicated otherwise in a credit line to the material. If material is not included in the chapter's Creative Commons license and your intended use is not permitted by statutory regulation or exceeds the permitted use, you will need to obtain permission directly from the copyright holder.





Consideration of Restoration in Yaw Resonance

Hideki Sakai^(✉)

Kindai University, Higashihiroshima 739-2116, Japan
sakai@hiro.kindai.ac.jp

Abstract. Yaw resonances cause the rear-end of the vehicle to swing, which is related to the feeling of handling. As a basis for improving this motion, this paper considers the restoration of yaw resonance. The equilibrium position of the yaw resonance is the extension of the velocity vector at the “heading point,” where the vehicle median line is perpendicular to the turning radius in a steady state turn. Toward this position, the center of percussion at the rear-end of the vehicle travels. This travel is the restoration of yaw. Observing the vehicle behavior from the earth-fixed coordinate system at the moment when the heading point changes direction of travel, the heading point and the center of percussion travel in their respective directions. Each motion continues for a distance from the rear wheel to the heading point to reach the equilibrium position. This continues time equals “yaw lead time constant.” Therefore, when the yaw lead time constant is small, the vehicle is restored in a short time.

Keywords: Yaw natural frequency · Yaw restoration · Yaw lead time constant

1 Introduction

The swinging motion of the rear-end of the vehicle, as in the hand gesture that begins at the 223-second point in a video [1], interferes with the pleasantness of the handling. This paper proves that this swing is the yaw resonance, discusses its mechanism, and proposes a method to improve it.

2 Vehicle Model and Its Yaw Resonance

The vehicle planar motion, represented by the yaw velocity “ r ” and the sideslip angle at C.G. “ β ,” are represented by a linear model shown in Fig. 1. Its vehicle mass m is represented by portion masses divided into front and rear masses [2],

$$m_f = \frac{l_r}{l}m, \quad m_r = \frac{l_f}{l}m \quad (\text{kg}) \quad (1)$$

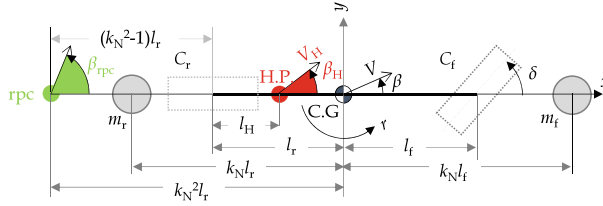


Fig. 1. A planar 2-DOF model for center of gravity

according to the vertical loads. The yaw moment of inertia I_z is expressed as

$$I_z = m_f(k_N l_f)^2 + m_r(k_N l_r)^2 = k_N^2 m l_f l_r \quad (\text{kgm}^2) \tag{2}$$

where k_N^2 is a coefficient called *dynamic index* [3].

Newton’s second law equations of the model are described by

$$k_N^2 m l_f l_r \dot{r} = 2F_f l_f - 2F_r l_r \quad (\text{Nm}) \tag{3}$$

$$mV(r + \dot{\beta}) = 2F_f + 2F_r \quad (\text{N}). \tag{4}$$

The front and rear cornering forces $2F_f$ and $2F_r$ are respectively

$$2F_f = -C_f m_f \alpha_f, \quad 2F_r = -C_r m_r \alpha_r \quad (\text{N}) \tag{5}$$

where C_f and C_r are the cornering coefficients in the acceleration dimension, respectively. Their typical values are $C_f = 100$ and $C_r = 200$ [(m/s²)/rad], respectively. The front slip angle α_f and the rear slip angle α_r are written as

$$\alpha_f = \beta_f - \delta, \quad \alpha_r = \beta_r \tag{6}$$

$$\beta_f = \beta + \frac{l_f}{V} r \quad \beta_r = \beta - \frac{l_r}{V} r \quad (\text{rad}). \tag{7}$$

Algebraic manipulation of the above equations yields

$$\dot{r} = -\frac{C_f l_f + C_r l_r}{k_N^2 l V} r - \frac{C_f - C_r}{k_N^2 l} \beta + \frac{C_f}{k_N^2 l} \delta \quad (\text{rad/s}^2) \tag{8}$$

$$\dot{\beta} = -\left[1 + \frac{(C_f - C_r) l_f l_r}{l V^2}\right] r - \frac{C_f l_r + C_r l_f}{l V} \beta + \frac{C_f l_r}{l V} \delta \quad (\text{m/s}^2). \tag{9}$$

The yaw natural frequency “ ω_n ” of the model is described by

$$\omega_n = \sqrt{\frac{C_r + \left(\frac{C_r l}{V^2} - 1\right) C_f}{k_N^2 l}} \quad (\text{rad/s}). \tag{10}$$

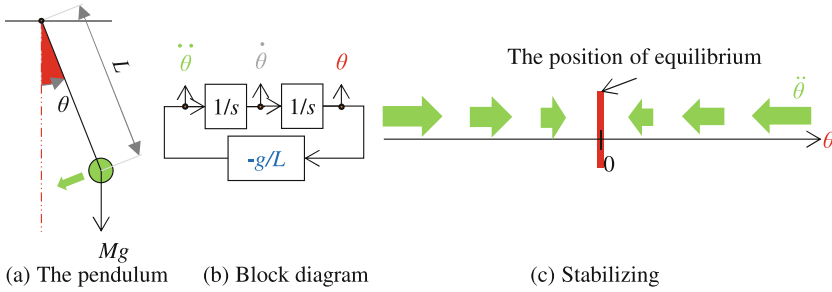


Fig. 2. The pendulum

3 Motion Equations Representing the Resonance Explicitly

To understand resonances, that of a single pendulum is suitable. Its Newton’s second law shown in Fig. 2a is represented in Fig. 2b. This figure expresses the phenomenon that $\ddot{\theta}$ occurs in the opposite direction of θ as shown in Fig. 2c. Therefore, the equilibrium position is at $\theta = 0$. Thus transforming the equations of motion of the vehicle into a form similar to that in Fig. 2b can reveal its equilibrium position and the variable that accelerates toward it.

The final term of Eq. (8) is eliminated by replacing β with β_{rpc} shown in Fig. 1. Subtracting $k_N^2 l_r / V$ times Eq. (8) from Eq. (9) yields

$$\frac{d}{dt} \left(\beta - \frac{k_N^2 l_r}{V} r \right) = - \left(1 - \frac{C_r l_r}{V^2} \right) r - \frac{C_r}{V} \beta. \tag{11}$$

The term in round brackets on the left-hand side means the sideslip angle “ β_{rpc} ” at rpc behind $k_N^2 l_r$ from the center of gravity. Hence

$$\beta_{\text{rpc}} = \beta - \frac{k_N^2 l_r}{V} r. \tag{12}$$

Position rpc is the center of percussion where no acceleration occurs when a percussion force is applied to the front wheel position in the lateral direction of the vehicle [3]. By using Eq. (12), eliminating β from Eqs. (8) and (9) obtains

$$\dot{r} = - \left[1 + \frac{(k_N^2 - 1) l_r}{l} \frac{C_f - C_r}{C_f} \right] \frac{C_f}{k_N^2 V} r - \frac{C_r - C_f}{k_N^2 l} \beta_{\text{rpc}} + \frac{C_f}{k_N^2 l} \delta \tag{13}$$

$$\dot{\beta}_{\text{rpc}} = - \left[1 + \frac{C_r (k_N^2 - 1) l_r}{V^2} \right] r - \frac{1}{T_r} \beta_{\text{rpc}} \tag{14}$$

where T_r is yaw lead time constant [4] expressed as

$$T_r = \frac{V}{C_r} \quad (\text{s}). \tag{15}$$

The time constant is the coefficient of Laplace variable s in the numerator of the transfer function relating the steer angle to the yaw rate.

The first term on the right-hand side of Eq. (14) is eliminated by replacing r with sideslip angle “ β_H ” at *Heading Point* “H.P.” where the radius is perpendicular to the vehicle median line in a steady state turn. H.P. is located near the rear wheels at very low speeds and moves forward with increasing vehicle speed. As typical examples, H.P. is at the midpoint of the wheelbase at 60 (km/h) and on the front axle at 80 (km/h). H.P. is represented as l_H ahead of the rear wheels, as shown in Fig. 1. The length l_H is expressed as

$$l_H = \frac{V^2}{C_r} = T_r V \quad (\text{m}). \quad (16)$$

Using β_H and β_{rpc} , yaw velocity is written as

$$r = \frac{\beta_H - \beta_{\text{rpc}}}{l_H + (k_N^2 - 1)l_r} V \quad (\text{rad/s}). \quad (17)$$

Substituting this expression into the expressions (8) and (9) and performing the algebraic operations yields

$$\dot{\beta}_H = -2\zeta\omega_n\beta_H + \omega_n^2 T_r \beta_{\text{rpc}} + \left[1 + \frac{(k_N^2 - 1)l_r}{l} \cdot \frac{C_r l}{V^2} \right] \frac{C_f}{k_N^2 l} T_r \delta \quad (18)$$

$$\dot{\beta}_{\text{rpc}} = -\frac{1}{T_r} \beta_H \quad (19)$$

where ζ is *yaw damping ratio*.

The first and last terms on the right-hand side of Eq. (18) are eliminated by assuming a steering where they cancel each other out. That is

$$\delta = \frac{2\zeta\omega_n}{\left[1 + (k_N^2 - 1)\beta_H \frac{l_r}{l} \cdot \frac{C_r l}{V^2} \right] \frac{C_f}{k_N^2 l} T_r} \beta_H \quad (20)$$

Numerical simulation results are omitted, but under non-zero initial conditions, the steering proportional to β_H causes the yaw resonance to continue. Under this steering, Eq. (19) is reduced as

$$\dot{\beta}_H = \omega_n^2 T_r \beta_{\text{rpc}}. \quad (21)$$

Comparing Eqs. (19) and (21) with Fig. 2b with attention to the negative sign, we obtain Fig. 3a.

4 Yaw Resonance and Its Restoration

Figure 3a means that the yaw resonance equilibrium position is at $\beta_H = 0$ and $\dot{\beta}_{\text{rpc}}$ is restored toward this position, as shown in Fig. 3b.

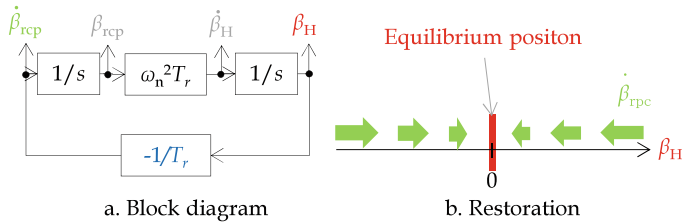


Fig. 3. Resonance and Restoration of Yaw: ω_n and T_r denote the yaw natural frequency and yaw lead time constant, respectively.

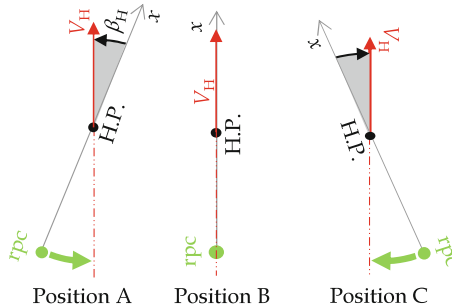


Fig. 4. Yaw resonance mode

Yaw resonance is a phenomenon in which the rear wheels accelerates toward the extension of H.P.'s vehicle speed vector. The meaning of Fig. 3 is represented by the behavior of the vehicle in Fig. 4. The equilibrium state of the yaw resonance is position B, where $\beta_H = 0$ as in steady-state turning. At this time, the rear wheels position r is on the extension of H.P.'s vehicle speed vector \vec{V}_H . Hence, \vec{V}_H is located at position r in the extension of \vec{V}_H is a balanced state. Therefore, yaw resonance is a phenomenon in which rpc accelerates toward the extension of \vec{V}_H like positions A and C.

This motion rotates the vehicle around H.P. It is shown in the H.P. path, which is closer to a straight line than the front or rear wheel paths in Fig. 5, which shows a restoring behavior after an unbalanced condition are given. For concise analysis, rpc is assumed to be on the rear wheel.

Intuitively, the restoration is the behavior in which rpc maintains its former motion to the vicinity of the ground position where H.P. was at the moment of imbalance, and then follows the trajectory of H.P. This phenomenon is seen in Fig. 5, where rpc moves almost straight ahead to the vicinity of the initial H.P. ground position, and then follows the trajectory of H.P.

The restoration mechanism is represented in schematic Fig. 6. The schematic shows the result of H.P. and rpc continuing to travel $l_H(m)$ in each direction at the moment of disproportionation. The vehicle median line is on the vehicle speed vector at H.P., thus $\beta_H = 0$, which means the equilibrium position, as shown at position B in Fig. 4.

The time required for the vehicle to travel l_H (m) is T_r (s). T_r is located in the block $-1/T_r$ that represents the strength of restoration in Fig. 3a. This block corresponds to the $-g/L$ block, which represents the restoration of the pendulum, shown in Fig. 2b. Thus, a small T_r or l_H immediately restore the vehicle.

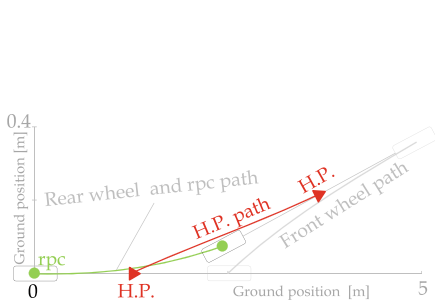


Fig. 5. Vehicle trajectories (initial conditions: $\beta_H \neq 0$, $\beta_{rpc} = 0$ and $\delta = 0$)

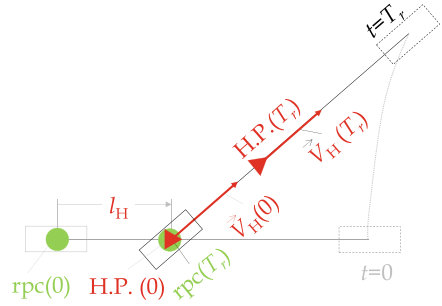


Fig. 6. Schematic of the restoration in yaw resonance implied in Fig. 5

5 Handling Improvement

To emphasize the restoration, yaw lead time constant and the length can be shortened by increasing the rear cornering coefficient from Eq. (16).

To suppress the manifestation of yaw resonance pointed out in the movie [1], it is necessary to increase the yaw damping ratio, which can be achieved by increasing the front cornering coefficient [5].

6 Conclusion

This research has revealed that the swaying phenomenon at the rear-end of the vehicle is a manifestation of yaw resonance. Restoration of the yaw resonance is the running of the rpc to the H.P. position at the moment of imbalance. This suggests that the vehicle planar motion can be improved by controls that focus on the heading point and rpc.

References

1. Tsuchiya, K., Hattori, N.: Mazda AZ-1 appeared!!!. Best MOTORing (1992). <https://youtu.be/1jUbZy2qbZA>. (in Japanese)
2. Gillespie, T.: Fundamentals of Vehicle Dynamics. SAE (1992)
3. Milliken, W., Milliken, D.: Chassis Design. SAE (2002)
4. Sakai, H.: Automobile Vehicle Dynamics. Morikita Publishing (2015). (in Japanese)
5. Dixon, J.C.: Tires, Suspension and Handling, 2nd edn. SAE (1996)

Open Access This chapter is licensed under the terms of the Creative Commons Attribution 4.0 International License (<http://creativecommons.org/licenses/by/4.0/>), which permits use, sharing, adaptation, distribution and reproduction in any medium or format, as long as you give appropriate credit to the original author(s) and the source, provide a link to the Creative Commons license and indicate if changes were made.

The images or other third party material in this chapter are included in the chapter's Creative Commons license, unless indicated otherwise in a credit line to the material. If material is not included in the chapter's Creative Commons license and your intended use is not permitted by statutory regulation or exceeds the permitted use, you will need to obtain permission directly from the copyright holder.





Testing Urban Interaction Scenarios Between Automated Vehicles and Vulnerable Road Users Using a Vehicle-in-The-Loop Test Bench and a Motion Laboratory

Michael Kaiser¹ (✉), Lisa Marie Otto¹, Steffen Müller¹, André Hartwecker², and Christian Schyr²

¹ Chair of Automotive Engineering, Technische Universität Berlin, Berlin, Germany
michael.georg.kaiser@tu-berlin.de

² AVL Deutschland GmbH, Wiesbaden, Germany

Abstract. For testing and analyzing urban vehicle-pedestrian or vehicle-bicyclist interactions as realistically and safely as possible, new types of test environments are required. This paper presents and analyzes a test environment in which a Vehicle-in-the-Loop test bench is combined with a motion laboratory. In this test setup, a real automated vehicle can interact with a human pedestrian or cyclist in a virtual test field in the same way as in real road traffic. Employing a walking platform ensures that the pedestrian's range of movement is not restricted during the test. This test environment is used to stimulate vehicle perception with a pedestrian avatar animated by a test subject. The test results are compared with measurements taken with a human pedestrian in reality, and strengths and weaknesses of the approach are discussed.

Keywords: Advanced Driver Assistance Systems · Automated Driving Systems · Testing and Validation · Motion Capture · Vehicle-in-the-Loop · Mixed Reality

1 Introduction

Due to safety concerns, testing and analyzing safety-critical urban interaction scenarios involving vehicles, pedestrians, and bicycles on real roads or proving grounds is challenging. On the one hand, current approaches, which utilize moving dummy pedestrian or bicycle targets on proving grounds or avatars in numerical simulations represent human interaction behavior only to a very limited extend. On the other hand, analyses in motion laboratories, an approach which has been increasingly used in recent years for evaluating pedestrian and bicycle behavior in traffic in a safe test environment, consider the automated vehicle only in simulation. With both approaches, the behavior of the interaction partner is always only realistically depicted to a limited extend; real behavior is only approximately or not at all possible.

In this paper, we introduce a new cyber-physical test environment for a realistic and safe analysis of the interaction of advanced driver assistance systems or automated driving systems with vulnerable road users (VRUs) and we analyze the strengths and weaknesses of such an approach. Such an approach has been theoretically proposed in [1], but, to the best knowledge of the authors, no realization of their idea or experimental results have been shown so far.

2 Method

For safe and realistic studies of Vehicle-VRU interaction scenarios, we combine a Vehicle-in-the-Loop test bench (ViL) with a Pedestrian-in-the-Loop test bench (PiL) and a Cyclist-in-the-Loop (CiL) test bench via a virtual test field as shown in Fig. 1.

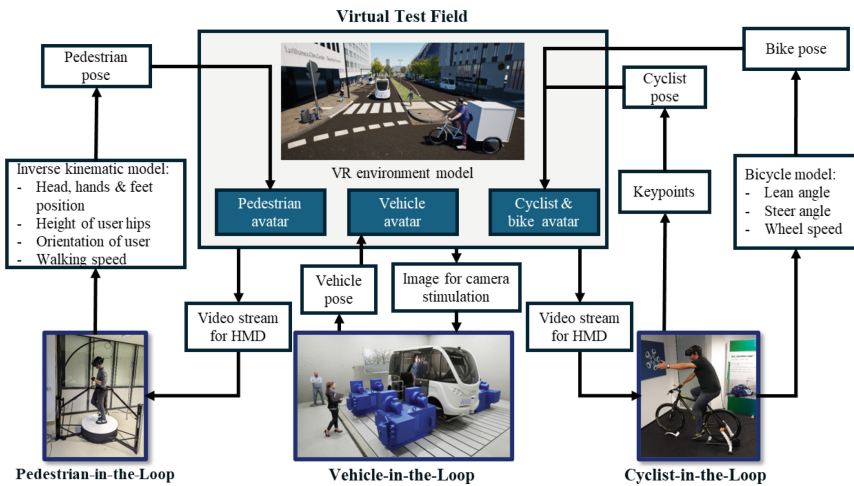


Fig. 1. MotionLab - Connected test benches for human-machine interaction of automated vehicles with VRUs

The real automated vehicle on the ViL test bench perceives information about other traffic participants from the virtual test field via its camera filming a projected image from a virtual reality (VR) environment model. It can respond by steering, accelerating, or braking against electrical motors that provide realistic force and torque feedback and update the pose of a vehicle avatar in the same VR environment model. More detailed information about the ViL test bench is available in our previous works [2–4].

On the PiL test bench, a real human test subject wears a head mounted display (HMD) and perceives information from the VR environment model. The subject moves on a low- μ walking platform with adaptive incline and is fixated at the hips for this purpose. The position and orientation of the subject’s head (from the HMD), hands, and feet (from trackers), together with the position and orientation of the test subject’s hips, as well as walking speed and direction (from the walking platform) are provided to an Unreal Engine 5 implementation. There, this tracking information is used to calculate

the local pose of a human skeleton model [5]. Excessive degrees of freedom of this model are derived using inverse kinematics (e.g., the positions of elbows and knees). Using the walking speed and direction, the pedestrian avatar changes its global position in the environment and is animated accordingly.

On the CiL test bench, a real human test subject wears an HMD and perceives information from the VR environment model while riding a bike on a bicycle trainer. A camera-based 3D human pose estimation (HPE) system is used to determine the precise position of the human rider relative to the bike as an additional signal into a multi-body system (MBS) model of the bicycle with rider. The camera-based 3D HPE has been integrated as an efficient and flexible alternative to the previous purely laboratory-based motion capture using marker-based systems as part of a collaboration with Subsequent GmbH (<https://www.subsequent.ai>). The AI method used enables the use of simple video data, such as from smartphones or vehicle cameras, to evaluate the detailed 3D movement data of the human skeleton in real time. The solution has so far been used in professional and elite sports, neurological rehabilitation, home fitness, and security [6]. Additionally, the measured steering angle and wheel speed are used as inputs. The MBS model controls the resistance torque on the eddy-current dynamometer on the bike's rear axle. The pose of the bike and the rider is sent from the MBS model in real time to an Unreal Engine 5 implementation and animates a cyclist and bike avatar in the virtual test field in the same way as on the PiL test bench.

Information from the virtual test field then again feeds into the vehicle's sensor input, allowing it to react to the VRUs' actions without endangering the subjects in any way.

3 Experimental Validation

For the analysis of the strengths and weaknesses of the proposed method, we conduct tests both in real-world conditions and in our test environment. The general functionalities of the ViL test bench, such as the integration of the real vehicle and the transfer of the real vehicle's motion to the motion of the vehicle in the virtual environment, have been previously demonstrated by us [2, 4]. Therefore, our tests focus on the integration of the PiL test bench and its influence on the vehicle's perception. If the perception works similarly, we expect only minor differences in all subsequent vehicle functions.

For our tests, we use a real automated shuttle bus that employs a monocular camera (1280 × 960 px, 20 fps) and feeds the images to an instance of the 3D HPE algorithm, which we also use in the CiL test bench, to estimate a skeleton representation of the pedestrians pose. We treat the anchor point of the skeleton as position of the pedestrian.

For different pedestrian poses, the skeleton estimation accurately represents the position of various limbs (see Fig. 2, left and middle). As expected, the estimation is accurate for visible limbs but shows higher deviation for covered limbs. However, the skeleton estimation may not always represent the pose of the human test subject correctly if untracked joints are highly bent. In such cases, there is a deviation between the test subject's pose and the avatar's pose (see Fig. 2, middle and right; note the deviation in the position of the left and right elbows) and the HPE algorithm is fed a divergent visual representation of the test subject. This issue mainly concerns elbow positions and, to a lesser extent, knee positions.

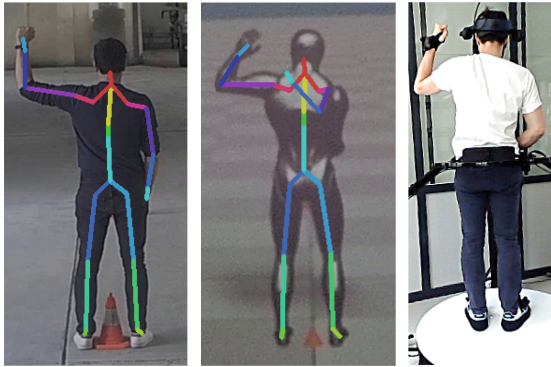


Fig. 2. Skeleton estimation in reality (left), skeleton estimation on test bench (middle), and respective pose of the test subject (right)

To compare the performance for static objects, we position test subjects of small (166 cm), medium (178 cm), and large (189 cm) heights, or similarly sized human avatars, in defined positions and compare the output of the HPE algorithm. The pedestrians are detected in similar positions (see Fig. 3). For test subjects placed closer to the vehicle ($x < 12$ m) the position's standard deviations fall within the interval between 0.7 cm and 7.9 cm; for test subjects further away, they fall within the interval between 4.2 cm and 53.7 cm. The measurements for both real-world conditions and the test bench setup are similar for mean value and standard deviation, especially for smaller distances to the vehicle. We are also able to reproduce the systematic measurement error for different test subject heights.

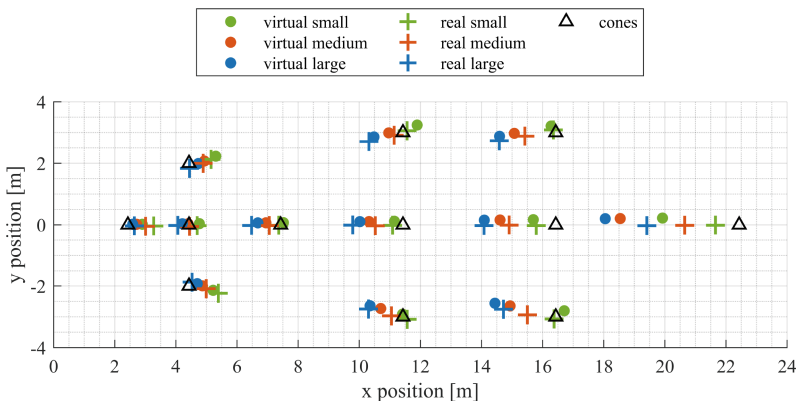


Fig. 3. Static pedestrian position estimations

To compare the performance for dynamic objects, the test subject had the task of walking past the vehicle at predefined distances (laterally back and forth both closer and further away). In the real-world scenario, these distances were marked with cones; for the test bench setup, ground truth data of the test subject's position is available from

the VR environment model. In the results (see Fig. 4), we can see that the pedestrian is detected with a similar deviation from the real path in both environments. However, we note higher uncertainty in the position estimation for higher distances in the test bench scenario. We assume, this is due to the unrealistic reflective surface of the pedestrian avatar (see Fig. 2, middle).

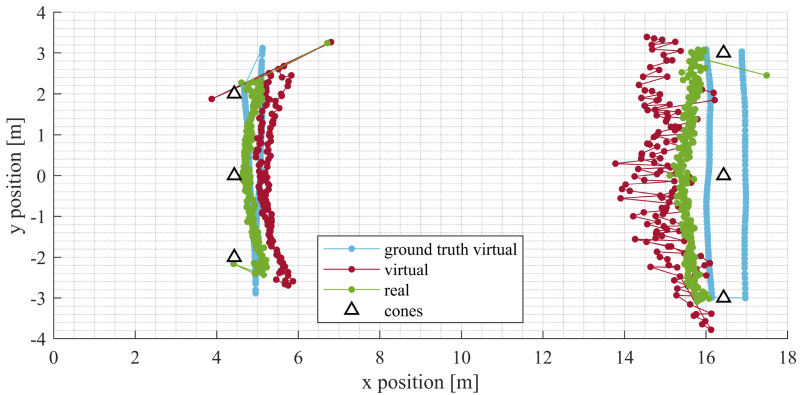


Fig. 4. Dynamic pedestrian position estimations with ground truth

To estimate the latency of our test bench, we recorded both the test subject in the motion laboratory and the image projected for camera stimulation of the vehicle using a camera (see Fig. 5), which can record at 240 frames per second - this corresponds to a temporal resolution of approximately 4.2 ms. A test subject raises or lowers their arm in a semi-circular motion, which in turn animates the pedestrian avatar accordingly. We counted the number of camera frames between when the test subject's arm is at a 90° angle to the torso and when the avatar's arm reaches the same position. Considering the recording frequency, we observed an average latency of 134 ms with a standard deviation of 15 ms across ten individual measurements. All measured latencies fall within the interval between 104 ms and 154 ms.



Fig. 5. Setup for latency measurement

4 Summary and Outlook

This paper presents a test environment in which a Vehicle-in-the-Loop test bench is combined with a motion laboratory to include a human pedestrian and a human cyclist. We demonstrate that vehicle perception can be stimulated in the test environment in a manner comparable to real-world conditions. Our approach surpasses traditional test benches and motion laboratory concepts while maintaining the safety of laboratory environments, unlike proving ground tests.

In the future, we plan to add tests for vehicle-cyclist interaction scenarios. To improve pedestrian depiction in the test bench, we want to use more realistic pedestrian avatars. Additionally, we aim to integrate the human pose estimation algorithm within the Pedestrian-in-the-Loop test bench to increase the accuracy of the pedestrian avatar's animation, particularly for otherwise untracked limbs.

Acknowledgement. This work was partly funded by the German Federal Ministry for Economic Affairs and Climate Action (BMWK) and partly financed by the European Union in the frame of NextGenerationEU within the project "Solutions and Technologies for Automated Driving in Town" [7] (grant FKZ 19A22006P).

References

1. Hartmann, M., Viehweger, M., Desmet, W., Stolz, M., Watzenig, D.: Pedestrian in the loop: an approach using virtual reality. In: 2017 XXVI International Conference on Information, Communication and Automation Technologies (ICAT), pp. 1–8. IEEE (2017)
2. Schyr, C., Brissard, A.: DrivingCube - a novel concept for validation of powertrain and steering systems with automated driving. In: AVEC 2016, Munich (2016)
3. Schyr, C., Inoue, H., Nakaoka, Y.: Vehicle-in-the-loop testing - a comparative study for efficient validation of ADAS/AD functions. In: 2022 International Conference on Connected Vehicle and Expo on Proceedings, ICCVE, Lakeland, FL, USA, pp. 1–8 (2022)
4. Hartwecker, A., Müller, S., Schyr, C.: Safety of use analysis for autonomous driving functions under laboratory conditions. In: Orlova, A., Cole, D. (eds.) IAVSD 2021. LNME, pp. 1183–1192. Springer, Cham (2022). https://doi.org/10.1007/978-3-031-07305-2_110
5. Unreal Engine - Mannequins Pack. <https://www.unrealengine.com/marketplace/en-US/product/mannequins-asset-pack>. Accessed 31 May 2024
6. Schyr, C., Hartwecker, A., Zimmermann, P., Seebacher, D.: Absicherung der kamerabasierten Bewegungs- und Gestenerkennung von vulnerablen Verkehrsteilnehmern in hochautomatisierten Fahrzeugen. 17. Tagung Diagnose in mechatronischen Fahrzeugsystemen, Dresden (2024)
7. STADT:up – Solutions and Technologies for Automated Driving in Town: an urban mobility project. <https://www.stadtup-online.de>. Accessed 31 May 2024

Open Access This chapter is licensed under the terms of the Creative Commons Attribution 4.0 International License (<http://creativecommons.org/licenses/by/4.0/>), which permits use, sharing, adaptation, distribution and reproduction in any medium or format, as long as you give appropriate credit to the original author(s) and the source, provide a link to the Creative Commons license and indicate if changes were made.

The images or other third party material in this chapter are included in the chapter's Creative Commons license, unless indicated otherwise in a credit line to the material. If material is not included in the chapter's Creative Commons license and your intended use is not permitted by statutory regulation or exceeds the permitted use, you will need to obtain permission directly from the copyright holder.





Robust Inverse Vehicle Map Regression Based on Laplace Distribution

Maxime Penet^(✉) and Gaetan Le Gall

Valeo Mobility Tech Center, 6 rue Daniel Costantini, 94000 Créteil, France
{maxime.penet,gaetan.le-gall}@valeo.com
<https://www.valeo.com/en/comfort-driving-assistance-systems/>

Abstract. This paper deals with the identification of the relationship between vehicle acceleration and driver available actuators. The vehicle is modeled based on how a driving task is performed. The model is constructed using neural networks whose weights are identified using data collected through non tailored driving sessions. To take into account disturbances, the model follows a Laplace distribution. This leads to a more robust estimate of the vehicle knowledge and the confidence we have in it. The approach is illustrated on a prototype vehicle equipped with a petrol engine, plus a device to actuate the pedals.

Keywords: Neural network · Laplace distribution · Pedal control

1 Introduction

The development of autonomous driving features considerably boomed over the past years, leading to their deployment in commercially available vehicle. Yet, many challenges sustain which rely on innovative solutions to be solved (see [1]). When dealing with such complex problems, it is advantageous to work with an agile mindset as frequent testing to rapidly apprehend the current level of performance is considered a smart strategy.

This drives the need to design prototype vehicles to validate solutions in real driving situations. As many vehicle software are developed by non-car manufacturers, it is a common approach to use commercially available vehicles that are then upgraded as needed. These users usually assume that a car can be controlled at high level such as via the acceleration (see e.g. [2]). Since this is not a standard interface, low level controllers have to be designed. This paper focuses on the longitudinal dynamic and considers the problem of tracking an acceleration using throttle and brake pedals.

A proficient control strategy consists in using an inverse model obtained from a mechanical description of the vehicle (see e.g. [5]). If this has proven to work well (see e.g. [3] or [4]), it however requires too deep vehicle knowledge and too many measurements in order to be efficiently deployed on a large scale. A generic solution thus needs to consider a black box approach to the nature of the vehicle, from an end user perspective.

In this paper, we consider a data driven inverse model design taking a driver viewpoint. Data from non-tailored driving sessions are used. To compensate for the expected uncertainties and significant noise levels, the model output is selected as a Laplace distribution. This brings robustness in the estimation process, quite similarly as when a least absolute deviation criteria is used to fit a model. Vehicle types variability is handled by using neural networks because they offer strong descriptive power.

The paper is organized as follows. In Sect. 2, we describe how to model the vehicle behavior taking a driver perspective. In Sect. 3, we present the chosen model structure. In Sect. 4 we provide some pointers to solve the challenges related to the specifics of our data collection process. In Sect. 5, results using real vehicle data are presented. Finally, the paper is concluded in Sect. 6.

2 A Driver Perspective on the Longitudinal Dynamic

Our objective is to model an inverse map, from vehicle acceleration to actuators, to design a low level controller used to track a desired acceleration. It is known that using mechanical descriptions to model the dynamics of a vehicle (see e.g. [5]) is costly. For instance, the innumerable parameters can only be obtained through complex experiments, or the acquisition of data is hardly accessible or data inaccurate. This is in contrast to the relative ease with which people can drive. Consequently, we focus on a driver's point of view.

There is a vast literature dealing with driver modeling (see e.g. [6]). They describe how drivers adjust acceleration to cruise or to follow a leading vehicle, and how brake and throttle pedals positions are modified accordingly to vehicle gear or speed. This means that the inverse vehicle model is a mapping from vehicle speed, engaged gear and target acceleration to brake and throttle pedals positions. The advantage of this driver oriented approach is that only a few signals are needed, namely vehicle odometry (e.g. acceleration and speed coming from an IMU) and some CAN information (gear number and pedals positions).

3 Model Selection

As most drivers consider the vehicle as an unknown system which reacts to some inputs, we consider a black box model. Instead of relying on tailored experiments, we simply include any driving sessions data as long as they cover the expected operating domain. We can thus rely on easy access to a significant amount of data. The inconvenience though is that we shall also expect significant noise levels. By interpreting external factors as having stochastic effects, the output is chosen to be a probability distribution. This approach only works well if external factors have a non deterministic effect during the data collection phase.

We assume that this distribution is both monomodal and symmetrical. Indeed, disturbances can reasonably be approximated by such distributions (e.g. average road is flat and whenever going uphill we can go downhill as well). To reduce numerical complexity, it is worth working with distributions represented

by a small numbers of parameters like the Gaussian distribution. However, in our case, the latter is not fit for purpose as the external factors can induce significant noise which could bias our variance estimate. We thus need a heavier tail distribution, which can be obtained through a Laplace distribution. The inverse map hence generates the probability p

$$p(U|X, Y, \theta) = \frac{1}{2b(X, Y, \theta)} e^{-\frac{|U - \mu(X, Y, \theta)|}{b(X, Y, \theta)}} \quad (1)$$

where θ are parameters to be defined, X is the input vector (speed and gear), Y is the target acceleration and U is a signal which can be mapped unambiguously to a brake and throttle position. The Laplace distribution is fully described by μ and b . Basically, μ embeds the vehicle dynamic that is reflected through data while b monitors how much it can be trusted. They can take various shapes depending on the actual vehicle and data set. This is why a generic function structure is needed. We thus select neural networks.

Assuming that the actuator response time is fast and/or the requests are varying slowly, actuators internal dynamic can be neglected. This means that an internal memory is not required. We select a direct feedforward architecture (see e.g. [7]). As its numerical evaluation is simple, it has the additional benefits of enabling real time operation on a wide range of ECU. To determine a pedal position, we build the probability density function (1). We then use it to select an appropriate value according to a meaningful criteria such as the mode, or any other criteria including risk management (see e.g. [8]).

4 Estimating the Distribution Parameter

Firstly, we need to consider the data causality issue. Indeed, when estimating network weights, we need to apprehend the relationship between pedal displacement and the corresponding observed acceleration. This is challenging as actuators can exhibit very dissimilar responses. Therefore, we model lag basically through constant delays. Signal distortion is taken into account through a DDTW algorithm (see e.g. [9]). The median index mapping variation is used as an estimate of our delays. The delay estimation strategy is based on the fact that the mapping from pedal to acceleration should define a monotone operator, i.e. if we push harder on a pedal we shall see more effect on the acceleration. Delay variations are assumed to be small and are included as the source of additional noises. The variations around the value of the delay are monitored to ensure that our assumption is viable.

Once delays are estimated, we can synchronize speed, gear and acceleration with pedal positions. To find the set of parameters which best explains the observed data, we use a log likelihood criteria. To ensure well-posedness of the problem, a Lasso regularization is chosen. Since pedal positions are assumed to follow a Laplace distribution (1), θ is given as the solution of the following minimization problem

$$\theta = \operatorname{argmin}_w \sum_i \left(\log(2b(X_i, Y_i, w)) + \frac{|U_i - \mu(X_i, Y_i, w)|}{b(X_i, Y_i, w)} \right) + \lambda|w|. \quad (2)$$

where λ is a regularization parameter which is selected to achieve the best compromise between model smoothness and data explanation. Using a Laplace distribution means that the model is trained via a (modified) least absolute deviation problem. This implies a reduced sensitivity to disturbances and external factors.

To solve (2) we use an ADAM solver (see e.g. [10]) which is based on stochastic gradients (see e.g. [11]). It estimates true gradient using a subset of randomly drawn samples. It is commonly assumed that all samples are equally important using uniform sampling. In our case, this is an issue as data are collected in inverse proportion to their safety relevance. Indeed, we are more likely to collect a soft braking than a heavy braking data point. There is thus a risk that those safety cases will not be properly captured, implying that the model will be biased. To circumvent this issue, we propose to use stratified sampling (see [12]). Since we consider a low dimensional input vector, we suggest to stratify through a full gridding of the input space. We also use a drop out strategy (see [13]) to avoid learning specifics related to external disturbances.

5 Results

The approach is illustrated on data collected from a petrol engine vehicle. First, we estimated the delays to correct the causality issue. Its distribution over the record as well as the synchronized normalized signals are depicted in Fig. 1.

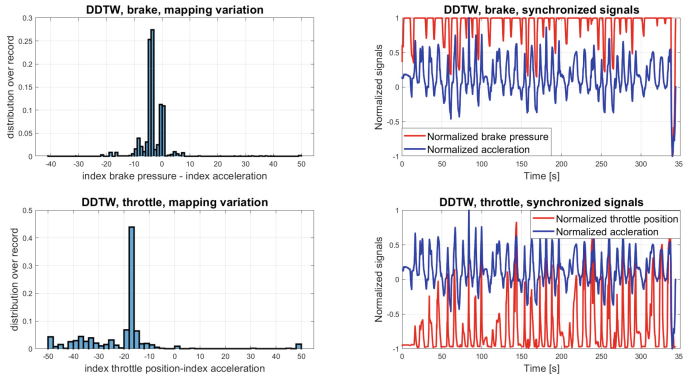


Fig. 1. Instantaneous delay estimation using DDTW

Then, by using (2), we estimated the networks weights. The mode results (i.e. μ in (1)) can be seen in Fig. 2. The brake and throttle positions are coded with negative and positive percentage values respectively.

The mapping has been used in a low level controller, which includes a feedback, to control the vehicle on a rural road, see Fig. 3. The tracking accuracy is satisfying with the inverse model (feedforward) being the main contributor. The feedback is mainly active to compensate for external factors such as pitch.

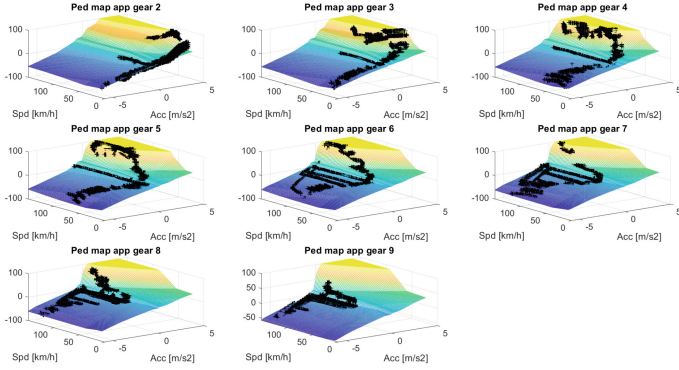


Fig. 2. Mode petrol engine, black cross: synchronized data set.

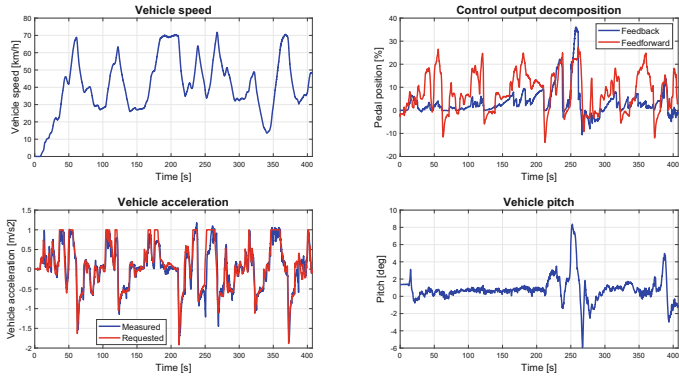


Fig. 3. Inverse map validation, vehicle control on a rural road.

6 Conclusions

This paper tackles the problem of building and deploying an inverse vehicle model from acceleration to actuator by non expert through a driver oriented approach. The vehicle is described by a black box model based on a small set of easily available signals. Data are collected in a non-tailored way, which implies cheap access to a significant amount of data. To compensate for expected significant noise level, the model output is probabilistic. The density function was selected as a Laplace distribution as it leads to more robust estimates. Assuming that users cannot provide *a priori* knowledge, model structure was chosen to be a neural network. It provides a huge descriptive power, though at the cost of challenges when estimating its weights where algorithms are usually based on uniform sampling of data. To remove potential bias related to the density of corner cases, we suggest to use a stratified sampling. This model was estimated from a petrol engine vehicle, showing its ease of deployment and its performances. Future works will consist in introducing a reinforcement learning framework in order to keep improving this map online. The probabilistic map being handy as it provides a natural way to explore alternatives.

References

1. Contreras-Castillo, J., Zeadally, S., Guerrero-Ibáñez, S.: Autonomous cars: challenges and opportunities. *IT Prof.* **21**(6), 6–13 (2019)
2. Li, L., Li, J., Zhang, S.: Review article: state of the art trajectory tracking for autonomous vehicles. *Mech. Sci.* **12**, 419–432 (2021)
3. Kebbati, Y., Ait-Oufroukh, N., Vigneron, V., Ichalal, D., Gruyer, D.: Optimized self-adaptive PID speed control for autonomous vehicles. In: 26th Proceedings International Conference on Automation and Computing (2021)
4. Naranjo, J.E., Alonso, F.J., Zato, J.G.: Low level control layer definition for autonomous vehicles based on fuzzy logic. *Intell. Autom. Soft Comput.* **18**, 333–348 (2012)
5. Guiggiani, M.: *The Science of Vehicle Dynamics*, 2nd edn. Springer, Dordrecht (2016)
6. Negash, N.M., Yang, J.: Driver behavior modeling toward autonomous vehicles: comprehensive review. *IEEE Access* **11**, 22788–22821 (2023)
7. Aggarwal, C.C.: *Neural Networks and Deep Learning: A Textbook*. Springer, Cham (2018)
8. Emmer, S., Kratz, M., Tasche, D.: What is the best risk measure in practice? A comparison of standard measures. *J. Risk* **18**, 31–60 (2015)
9. Keogh, E.J., Pazzani, M.J.: *Derivative Dynamic Time Warping*. SDM (2001)
10. Kingma, D.P., Ba, J.L.: Adam: a method for stochastic optimization. In: *ICLR* (2015)
11. Wojtowytsch, S.: Stochastic gradient descent with noise of machine learning type. Part 1: discrete time analysis. *J. Nonlinear Sci.* **33**, 45 (2023)
12. Sadaiyandi, J., Arumugam, P., Sangaiah, A.K., Zhang, C.: Stratified sampling-based deep learning approach to increase prediction accuracy of unbalanced dataset. *Electronics* **12**(21), 4423 (2023)
13. Srivastava, S., Hinton, G., Krizhevsky, A., Sutskever, I., Salakhutdinov, R.: Dropout: a simple way to prevent neural networks from overfitting. *J. Mach. Learn. Res.* **15**(1), 1929–1958 (2014)




Open Access This chapter is licensed under the terms of the Creative Commons Attribution 4.0 International License (<http://creativecommons.org/licenses/by/4.0/>), which permits use, sharing, adaptation, distribution and reproduction in any medium or format, as long as you give appropriate credit to the original author(s) and the source, provide a link to the Creative Commons license and indicate if changes were made.

The images or other third party material in this chapter are included in the chapter's Creative Commons license, unless indicated otherwise in a credit line to the material. If material is not included in the chapter's Creative Commons license and your intended use is not permitted by statutory regulation or exceeds the permitted use, you will need to obtain permission directly from the copyright holder.





Energy-Efficient Optimal Torque Vectoring for a Four-Motor High-Performance Electric Vehicle

Mattéo Prost¹ , Ivan Cvok¹ , and Efstathios Velenis² 

¹ Rimac Technology, Ljubljanska 7, 10431 Sveta Nedelja, Croatia
matteo.prost@rimac-technology.com

² Cranfield University, Cranfield MK43 0AL, UK

Abstract. The paper presents and compares an optimal control allocation (CA) and model predictive control (MPC)-based torque vectoring (TV) for improved energy efficiency of electric vehicle with four independent electric motors. Offline and online (instantaneous) optimisation-based CA are designed for front-rear torque distribution. For overall wheel torque allocation, a production-ready MPC-based TV is extended with energy consumption minimisation terms. CA and MPC rely on power loss curves of differently sized front and rear powertrains that are fitted with polynomial regression models. Performance of both strategies is evaluated in high-fidelity nonlinear simulation environment in terms of energy efficiency improvement on standard driving cycles and impact on the vehicle dynamics in lateral manoeuvres. Results demonstrate consistent reduction of the energy consumption and preservation of the vehicle handling behaviour.

Keywords: Energy Efficiency · Control Allocation · Torque Vectoring · Vehicle Dynamics · Model Predictive Control

1 Introduction

Battery electric vehicles with four independent motors offer improved vehicle dynamics performance and energy efficiency due to their all-wheel drive and torque vectoring capabilities, achieved through independent wheel torque control. In the literature, different approaches have been applied to solve this efficient torque allocation problem, typically with the assumption of equal powertrains. These approaches range from rule-based/analytical solutions [1], offline and online instantaneous optimisation [2, 3], and various model predictive control concepts for powertrains with [4] and without disconnect clutch actuation [5, 6]. For equal motor assumption, it is demonstrated in [7] that optimal longitudinal bias is either single axle for low torque demand or 50:50 for high torque demand. Similar conclusions have been drawn for lateral motion, where outer-track motors are first considered. In this paper, a 4MEV with differently sized front and rear powertrains is considered, and the optimal control allocation (CA)

and model predictive control (MPC) based torque vectoring (TV) are designed with an emphasis on improving the overall vehicle energy efficiency and driving range, while accounting for induced effect on vehicle dynamics [8].

2 Energy-Efficient Torque Vectoring Design

2.1 Power Losses Modeling

The powertrain power losses models are developed based on experimental data obtained from bench tests of inverters, surface-mounted permanent-magnet electric motors, and gearboxes originating from an electric hypercar. The power loss maps are a function of respective torque, speed, and battery voltage. They are fitted with polynomial regression models for use in the online optimisation problems to capture the complex and nonlinear relationships between the variables.

Figure 1 shows the power loss characteristics of the front and rear powertrains as a function of the electric motor torque request for multiple motor speed operating points and constant battery voltage (normalized axes). Each rear axle powertrain can be used in a free-rolling configuration with inverter switches opened, i.e. in open circuit with mechanical losses predominant (represented by * in Fig. 1b).

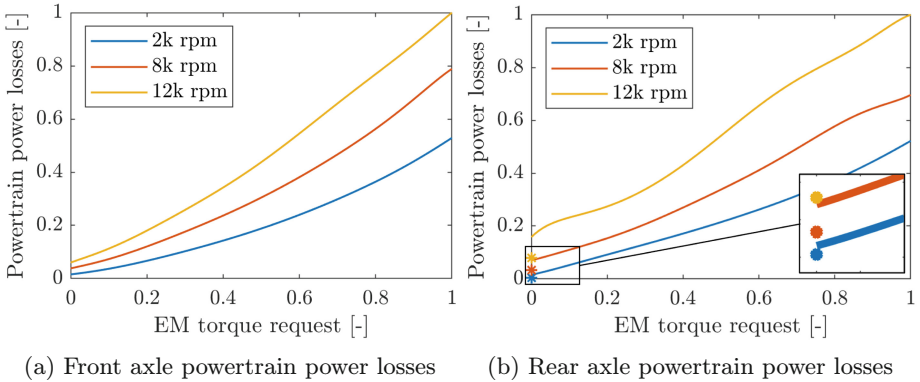


Fig. 1. Individual power losses characteristics for specific EMs angular velocities

Tyres introduce controllable energy dissipation attributable to longitudinal slip, which is a function of wheel torque. Herein, the tyre losses are excluded from offline optimisation to reduce computational complexity. We observed in simulation that tyre power losses never exceed 10% of a Front-Wheel Drive (FWD) vehicle's global power losses on a demanding driving cycle (EPA-US06).

2.2 Optimal Torque Control Allocation Problem

The CA strategy determines the longitudinal torque split between front and rear axles. The nonlinear multi-parametric optimisation problem, given by Eq. 1, minimises the overall powertrain power losses subject to driver-demanded force request and velocity-dependent actuator torque constraints. The optimisation yields a front-to-total bias for the overall range of achievable inputs.

$$J = \min_{\mathbf{T}} \sum_{i=1}^2 P_i(T_i, V_{bat}, \omega_i) \tag{1}$$

where $i = [Front, Rear]$, T_i is the vector of front and rear motor torques [Nm], V_{bat} is the battery voltage [V] and Ω_i is the front and rear motor speed [rad/s].

The objective function value of optimal solution is compared to the one of a FWD strategy with rear powertrains disabled, i.e., free rolling (cf. Fig. 1b), and more efficient torque allocation is selected. Such switching between strategies can yield excessive bias transitions and, thus, instantaneous torque steps on both axles which compromise drivability. A rate limit is therefore applied to the bias after the optimisation to avoid selection of possible local minima as illustrated in Fig. 2 where points *A*, *B*, *C*, and *D* correspond respectively to previous sample time ($t - 1$) solution, locally optimal solution with the rate constraint (red line) included in the optimisation, selected suboptimal solution, and globally optimal solution without rate constraints included in the optimisation. Rate limit can be scheduled with yaw rate to avoid unsafe behaviour and/or driver demand to protect drivetrain components from torque steps, while maximum value should be set for acceptable drivability (low jerk).

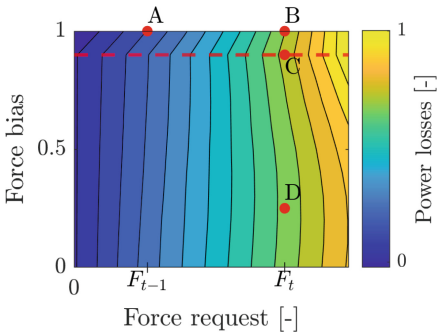


Fig. 2. Vehicle trajectories (Power losses against force bias and force request at constant v_x and V_{bat})

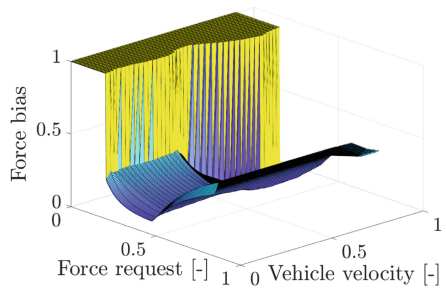


Fig. 3. Optimal front-to-total force bias for constant V_{bat} , positive F_{req} and low tyre slip

In the offline case using a fixed lateral distribution of 50:50, the results are stored in 3D map as shown in Fig. 3 to facilitate vehicle implementation and

reduce computational effort. The optimisation tool is implemented in Matlab and uses the `fmincon` SQP solver.

The same optimisation problem is solved online using the `fmincon` SQP solver and implemented in real-time on a production ECU. The benefit of this approach is the adaptation to varying motor torque limits that can be changed by the driver (directly or through driving modes) or inverter due to, e.g., temperature derating. The offline optimisation in that case requires pre-computed maps.

2.3 Model Predictive Control Torque Vectoring Architecture

For the overall torque distribution control, a production-ready Linear Time-Varying (LTV) MPC TV [9] is expanded with energy efficiency terms. It is based on a 7-degree-of-freedom handling model as seen in Fig. 4, extended with energy loss state fed by the aforementioned, polynomial regression power loss functions for each powertrain where tyre slip losses can be considered independently. The cost function S that includes driver demand tracking terms (yaw rate and force request) and control input penalization terms is extended with energy state minimisation term to account for energy efficiency as shown in Eq. 2.

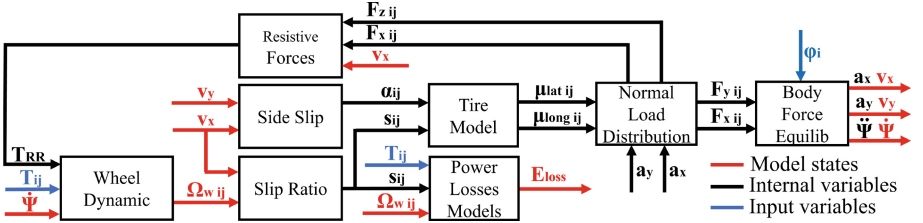


Fig. 4. Simplified 7deg of freedom vehicle handling model including power losses calculation where $i = Front, Rear$ and $j = Left, Right$

A high cost set on yaw rate tracking $W_{\dot{\psi}}$ gives authority to the safety/performance character of the problem over the efficiency cost. The efficiency term weight W_E is scheduled based on yaw rate and surface adhesion to maintain safety during high slip or high lateral dynamic manoeuvres.

$$\begin{aligned}
 S(X(k), T_{ij}(k), X_{dev}(k)) = & W_{\dot{\psi}} \cdot (\dot{\psi}_{ref}(k) - \dot{\psi}(k))^2 \\
 & + W_{F_x} \cdot (F_{x,ref} - (\sum_{ij} T_{ij}(k) \cdot \frac{1}{R_{w,ij}}))^2 \\
 & + W_E \cdot (E_{loss}(k))^2 \\
 & + W_{U_{rate}} \cdot (T_{ij}(k-1) - T_{ij}(k))^2
 \end{aligned} \quad (2)$$

where X is the state vector, X_{dev} is a vector of controller inputs, $\dot{\psi}$ is the yaw rate [rad/s], $F_{x,ref}$ is the longitudinal force request [N], $R_{w,ij}$ are the wheel radii [m], E_{loss} is the energy losses estimation [J], k is the current discretization step, and W are the weights applied to each cost term of the objective function.

The MPC TV problem is solved using a quadratic problem solver with linear constraints and runs on a production ECU at a sampling rate of 10 ms.

3 Longitudinal Motion Simulations

A longitudinal vehicle model consisting of a closed-loop driver model, longitudinal vehicle dynamics with suspension effects included, powertrain model with compliance and inertia effects, and Pacejka tyre model is used to assess the vehicle efficiency on standard driving cycles. Table 1 compares the results of the different torque allocation strategies relative to a fixed 50:50 All-Wheel Drive (AWD) strategy in terms of energy losses ΔE_{loss} and total energy consumed ΔE_{cons} . Results from online CA and energy efficient MPC TV are equal.

Table 1. Efficiency variation compared to fixed AWD for different drive cycles

	WLTP (class 3)	EPA US06	UC LA92
Fixed FWD (100:0)	$\Delta E_{loss} = -31.45\%$ $\Delta E_{cons} = -13.05\%$	$\Delta E_{loss} = -16.95\%$ $\Delta E_{cons} = -4.85\%$	$\Delta E_{loss} = -21.69\%$ $\Delta E_{cons} = -10.01\%$
Fixed RWD (0:100)	$\Delta E_{loss} = +8.10\%$ $\Delta E_{cons} = +3.60\%$	$\Delta E_{loss} = +6.06\%$ $\Delta E_{cons} = +2.36\%$	$\Delta E_{loss} = +7.42\%$ $\Delta E_{cons} = +4.34\%$
Offline CA	$\Delta E_{loss} = -31.46\%$ $\Delta E_{cons} = -13.14\%$	$\Delta E_{loss} = -22.40\%$ $\Delta E_{cons} = -7.39\%$	$\Delta E_{loss} = -23.40\%$ $\Delta E_{cons} = -11.34\%$
Online CA	$\Delta E_{loss} = -32.05\%$ $\Delta E_{cons} = -13.40\%$	$\Delta E_{loss} = -22.63\%$ $\Delta E_{cons} = -7.49\%$	$\Delta E_{loss} = -23.61\%$ $\Delta E_{cons} = -11.42\%$

It is evident that the FWD configuration presents efficiency results close to those of the offline and online CA and MPC efficient TV due to the unusually high capacity of the front powertrain for the low force demand of most driving cycles. The online CA exhibits minor improvement compared to the offline CA as it circumvents the inaccuracy of fixed step breakpoints in the offline map.

4 Lateral Motion Simulations

The weights associated to the cost function of the MPC TV are tuned to conserve the safety, performance and driving characteristic of the baseline MPC TV while improving efficiency. Steady-state skidpad tests in Fig. 5 demonstrate that both efficient CA and TV provide efficiency improvement at low values of lateral acceleration, with the efficient TV surpassing the CA for $a_y \in [2.5 : 5.5]$ m/s² due to a yaw moment request allowing for a favorable left-right torque distribution.

ISO Ramp steer test presented in Fig. 7 showcase the weight associated to energy efficiency at low values of lateral acceleration a_y and the convergence of the energy efficient TV yielded torque commands towards the baseline TV ones.

While the energy efficient MPC TV reduces the vehicle responsiveness (understeer gradient increased by approx. 9%), the maximum value of lateral acceleration is preserved. Note that the efficient TV torque allocation corresponds to the successive enabling of the outside and inside rear wheels as shown in Fig. 6.

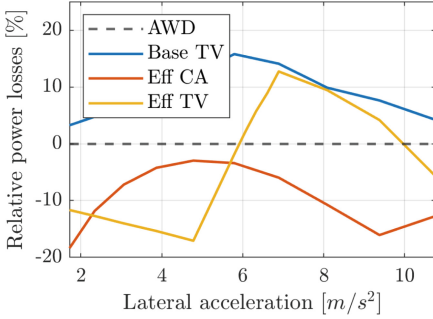


Fig. 5. Vehicle trajectories (PSteady-state skidpad test ($R = 42 \text{ m}/\mu = 1$)) AWD relative power losses

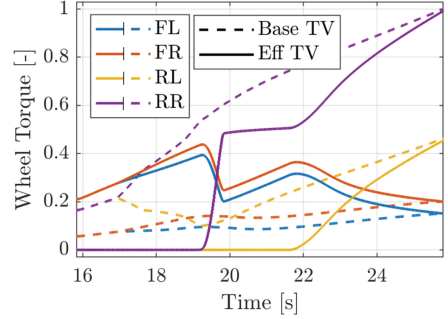
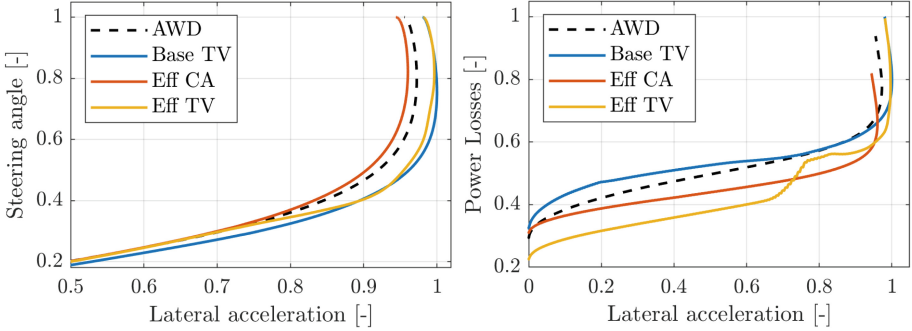


Fig. 6. Wheel torque during steady-state ($v_x = 100 \text{ km/h}$) ramp steer manoeuvre



(a) Focus max a_y of different architectures (b) Power losses of different architectures

Fig. 7. Steady-state ($v_x = 100 \text{ km/h}$) ramp steer with tyre slip induced $F_{x_{req}}$ increase

The control allocation strategies are implemented on a production specification vehicle equipped with 4 electric powertrains, i.e. one for each wheel, to validate integration and real-conditions behaviour during dynamic manoeuvres.

Conclusion

This paper presents strategies to enhance vehicle efficiency and dynamic performance, including an optimal offline torque allocation strategy, an online torque allocation strategy, and a model predictive control-based energy-efficient torque vectoring system. Through simulation testing on an EV, these solutions proved effective for vehicles with multiple electric motors of varying sizes. The control allocation strategy efficiently distributes force requests between front and rear axles, enhancing overall vehicle efficiency by up to 32.05% compared to a baseline 50:50 AWD architecture and up to 5.68% compared to a fixed FWD architecture on typical driving cycles. However, the performance gains were tempered by the unusually high capacity of the demonstrator vehicle powertrains. Furthermore, the strategy preserved the dynamic behaviour of the baseline vehicle, ensuring stability, maneuverability, and safety across various driving conditions, including cornering manoeuvres at the handling limit. Vehicles equipped with efficient torque vectoring maintained lateral performance and improved overall efficiency by up to 17% compared to fixed lateral distribution configurations at specific vehicle operating points.

References

1. Filippis, D., et al.: Torque distribution strategies for energy-efficient electric vehicles with multiple drivetrains. *J. Dyn. Syst. Meas. Control* **139**(12), 121004 (2017)
2. Torinsson, J., et al.: Energy reduction by power loss minimisation through wheel torque allocation in electric vehicles: a simulation-based approach. *Veh. Syst. Dyn.* **60**(5), 1488–1511 (2022)
3. Chatzikomis, C., et al.: An energy-efficient torque-vectoring algorithm for electric vehicles with multiple motors. *Mech. Syst. Sig. Process.* **128**(1), 655–673 (2019)
4. Deur, J., et al.: Energy-efficient straight-line driving torque vectoring for electric vehicles with multiple motors equipped with disconnect clutches. In: 18th Conference on Sustainable Development of Energy, Water, and Environment Systems (SDEWES), pp. 1–15 (2023)
5. Parra, A., et al.: On nonlinear model predictive control for energy-efficient torque-vectoring. *IEEE Trans. Veh. Technol.* **70**(1), 173–188 (2021)
6. Hongqian, W., et al.: Optimal energy allocation strategy for electric vehicles based on the real-time model predictive control technology. *Sustain. Energy Technol. Assess.* **50**(2), 101797 (2022)
7. Dizqah, A., et al.: A fast and parametric torque distribution strategy for four-wheel-drive energy-efficient electric vehicles. *IEEE Trans. Ind. Electron.* **67**(7), 4367–4376 (2016)
8. Diez, D., et al.: Front/rear axle torque vectoring control for electric vehicles. *J. Dyn. Syst. Meas. Control* **141**(6), 061002 (2019)
9. Hrvatinic, K., et al.: Controlling motion of a vehicle. United States Patent (2023)

Open Access This chapter is licensed under the terms of the Creative Commons Attribution 4.0 International License (<http://creativecommons.org/licenses/by/4.0/>), which permits use, sharing, adaptation, distribution and reproduction in any medium or format, as long as you give appropriate credit to the original author(s) and the source, provide a link to the Creative Commons license and indicate if changes were made.

The images or other third party material in this chapter are included in the chapter's Creative Commons license, unless indicated otherwise in a credit line to the material. If material is not included in the chapter's Creative Commons license and your intended use is not permitted by statutory regulation or exceeds the permitted use, you will need to obtain permission directly from the copyright holder.





A Lateral Control Based on Physics Informed Neural Networks for Autonomous Vehicles

Tamás Hegedűs¹(✉) , Dániel Fényes¹, Balázs Németh¹, Vu Van Tan²,
and Péter Gáspár¹

¹ HUN-REN Institute for Computer Science and Control (SZTAKI), Kende u. 13-17,
Budapest 1111, Hungary

{[tamas.hegedus](mailto:tamas.hegedus@sztaki.hun-ren.hu),[daniel.fenyas](mailto:daniel.fenyas@sztaki.hun-ren.hu),[balazs.nemeth](mailto:balazs.nemeth@sztaki.hun-ren.hu),
[peter.gaspar](mailto:peter.gaspar@sztaki.hun-ren.hu)}@sztaki.hun-ren.hu

² Department of Automotive Mechanical Engineering, Faculty of Mechanical
Engineering, University of Transport and Communications, Cau Giay Street, Hanoi
100000, Vietnam
vvtan@utc.edu.vn

Abstract. In the paper, a lateral control strategy is presented using Physics-Informed Neural Network (PINN) for automated vehicles. The main idea is that the physics information is incorporated into the training process, which leads to an improvement in the performance level of the control algorithm. Moreover, in the highly nonlinear range of the lateral dynamics, which is not properly covered by the training dataset, the stability of the vehicle is guaranteed. The results are compared to a conventional neural network trained to control the vehicle.

Keywords: Automated vehicles · Neural networks · Lateral control

1 Introduction

In general, the modeling process of an arbitrarily chosen system often relies on large datasets, which must cover the whole operational range of the system. This can be a challenging task, and the presence of nonlinearities and uncertainties makes it even harder. However, the modeling phase is essential since the reachable performance level highly depends on the accuracy of the model in several applications such as control and observer design.

In the field of control design, the applied methods can be sorted into two main groups, based on how the collected dataset is utilized. The first group contains the classical methods, in which the dataset is used for constructing a nominal mathematical model. Whilst the second group consists of methods, which directly use the data points during the control design [1]. In practice, the machine learning-based solutions cannot be used for control purposes in safety-critical systems. However, combined control structures give an option for the control-oriented use of machine learning-based methods [5].

Although the combined solutions can guarantee the robustness of the control loop, the neural network-based layer must have a high accuracy, which can be achieved using non-conventional training methods such as Physics-Informed Neural Network (PINN). The main idea behind this approach is to consider the physical information of the system during the training process [2, 7]. The goal of the paper is to present a high-performance level neural network for combined control structures. In the paper, a comparison study can be found between the conventional and the modified training process of the network. The whole method is validated through an automated vehicles-motivated problem: trajectory tracking.

The paper is structured as: In Sect. 2 the data generation process, and the nonlinear system are presented. In Sect. 3 the physics-informed neural network is detailed in terms of control purposes. The results of the simulations can be found in Sect. 4. Finally, the paper is summarized in Sect. 5.

2 System Description and Data Generation

In this section, the mathematical formulation of the vehicle dynamics and the data acquisition of the training process is presented. The main equations of the vehicle dynamics rely on the lateral forces, which can be computed from the slip angles (α_i), where $i = \{f, r\}$, f denotes the front, while r is the rear axis [8]. The axle positions measured from the center of gravity are denoted by l_i . Using these values and the tire characteristics (Magic formula), the lateral forces of both the front and the rear tires can be computed using [6]:

$$F_{y,i} = mgl_{f,r}L^{-1}\mu_i\sin(c \cdot \tan^{-1}(b \cdot \alpha_i)). \quad (1)$$

The shape of the nonlinear tire characteristics is determined by the parameter c, b . The distance between the rear and front axis is: $L = l_f + l_r$. The vehicle mass is m , while the gravitational acceleration is g . Based on the tire characteristics and the slip angles, the lateral forces can be computed for the axles. The vehicle motion is described by two main equations:

$$\frac{d^2\psi}{dt^2} = \frac{1}{I_z}(l_f F_{y,f} - l_r F_{y,r}), \quad \frac{dv_y}{dt} = \frac{1}{m}(F_{y,f} + F_{y,r}), \quad (2)$$

where $\dot{\psi}$ is the angular velocity (yaw-rate), and the lateral velocity is given by v_y . The goal is to calculate the derivatives during the training process of these signals, which can be done using the continuous dynamical equations: $\dot{x} = \mathcal{F}(x_0, u, p_i)$, where \mathcal{F} is the dynamical system, x_0 gives the initial conditions, u is the control input and the varying parameters are given by p_i . In practice, the continuous systems are discretized to fulfill the requirements of the implementation [3], for the time-varying system: $x(k+1) = A(k)x(k) + B(k)u(k)$, $y(k) = C^T(k)x(k)$. Using the discrete state space model of the system, the output can be predicted based on the input signals sequence ($\mathcal{U} = [u(1), u(2) \dots u(N_p)]$). The tracking error can be computed from the predicted output and the reference value ($y_{ref} \in \mathbb{R}^{n \times N_p}$) as $\epsilon(k) = y_{ref}(k) - y(k)$. Then, using the predicted error signal, the following quadratic optimization can be formed [3]:

$$\min_{\mathcal{U}} \sum_{i=1}^{N_p} (\gamma(y_{ref}(i) - y(i))^2 + \lambda u^2(i)), \text{ s.t. } \phi \mathcal{U} < b \text{ and } l_b \leq u \leq l_u, \quad (3)$$

where $\gamma \in \mathbb{R}$ and $\lambda \in \mathbb{R}$ are weights, which make the balance between the tracking accuracy and the energy used for the control purposes. The upper and lower bounds for the control input signal are denoted by l_b, l_u . Moreover, a bound is defined for the chosen, predicted states of the system (b), and ϕ can be constructed from the system matrices.

In the next step, the data generation process is presented. Considering that the tire characteristics significantly depend on the operational point of the vehicle, the nonlinear system is linearized at each operational point. Furthermore, it is assumed, that the reference longitudinal velocity is known over the prediction horizon. The data generation process is carried out by driving the vehicle along the reference trajectory, which is defined as:

$$y_{ref}(t) = \beta(p_1x(t)^3 + p_2x(t)^2 + p_3x(t) + p_0)\sin(\omega t), \quad (4)$$

where t provides the simulation time. The parameters of the reference lateral position are varied randomly to generate trajectories with different radius. The parameters of the reference positions are selected to: $p_1 \in [-1, 1], p_2 \in [-2, 2], p_3 \in [-0.5, 0.5], \omega \in [0, 0.5], \beta = 0.1$. The sampling time is set to $T_s = 0.02$ s, and the longitudinal velocity is set between 10 and 20 m/s.

Firstly, the initial states and the parameters of the reference trajectory are randomized. Secondly, the vehicle is driven along the route solving the optimization problem (3), which calculates the control input signal sequence, and several signals are saved during the simulation. The measured states of the vehicle are: $x = [y_0, v_y, \dot{\psi}, \psi,]^T$, and the control input is the steering angle (δ). Moreover, the output of the system is the lateral position. During the data generation the weights are set to $\gamma = 1, \lambda = 5$ to ensure smooth trajectory tracking. Moreover, the yaw-rate ($\dot{\psi}$) is limited to $0.7 \text{ rad/s} \geq |\dot{\psi}|$ and the limits for the control input is set to $0.2 \text{ rad} \geq |u| \forall u \in \mathcal{U}$ to ensure stable motion requirements. Finally, the prediction horizon is selected to $N_p = 45$.

3 Physics Informed Neural Network in Control Structure

In Fig. 1, the whole training structure is presented of the neural network. The input vector consists of the initial states of the vehicle (x_0). Since the neural network is implemented for trajectory tracking, the input vector is augmented with a sequence of the reference signal ($y_{ref,1} \dots y_{ref,k}$), where k denotes the length of the reference signal. Moreover, taking into account

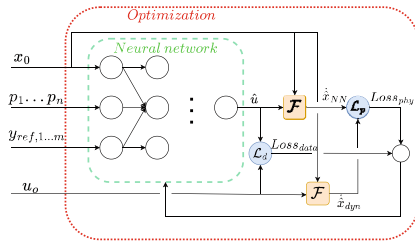


Fig. 1. Structure of the training process

the varying parameters of the system ($p_1 \dots p_n$), these values are also incorporated into the input vector. In practice, the horizon length for the reference signal and for the changing parameters should be chosen to the same. Finally, the u_{MPC} gives the reference control signal value, which is computed from (3). In Figure \mathcal{L} gives the computation method of the loss function within one iteration step.

3.1 Computation of the Loss Function

The loss function, which is the base of the optimization process, is built up from two main parts: the data-based part and the physics-based part. Firstly, the data-based loss function is detailed. In every iteration step, the predicted output signal of the neural network is denoted as \hat{u} and computed as:

$$\hat{u} = \hat{F}(x_0, p_{1,2\dots n}, y_{ref,1}, y_{ref,2}, y_{ref,m}), \quad (5)$$

where \hat{F} is the approximated function of the system. Using the predicted value of the network, for the given set of training datasets the error between the target and the predicted data can be computed as $\epsilon_{data} = \hat{u} - u_{MPC}$. Secondly, the physics-based loss function is calculated. The derivative(s) of the specific states can be computed using the nonlinear function of the system (2). Using the initial states, the varying parameters, and the predicted neural network output: $\dot{\hat{x}} = \mathcal{F}(x_0, \hat{u}, p_i)$. Since the real output of the neural network is known (u_{MPC}), the real derivatives can be also computed by the nonlinear description of the systems. The calculated error between the derivatives is crucial during the training process. This part of the algorithm takes into account the nonlinear effects of the dynamics for the error between the real and the results of the neural network. This makes the estimation more accurate within the ranges, where a small deviation between the real and the estimated value results in a significant error in the changes of the system states. This effect is observable, especially within the ranges influenced by highly nonlinear effects. This makes the performance level of the neural network higher within these ranges, which makes the neural network more reliable. Both the data-based loss function ($Loss_{data}$), and the physics-based part ($Loss_{phy}$) is computed using L_2 loss:

$$\mathcal{L}_{NN} = Q_1 \frac{1}{N} \sum_i^N \|\epsilon_{data,i}\|^2 + \frac{1}{M} \sum_j^M Q_j \frac{1}{N} \sum_i^N \|\dot{\hat{x}}_{i,j} - \dot{x}_{i,j}\|^2, \quad (6)$$

where M gives the number of the computed derivatives and Q_1, Q_i aims to scale the loss values to each other. These values are computed for each mini-batch of the neural network and also computed for every epoch. The training process of the neural network can be made using an optimizer such as the ADAM optimization algorithm [4]. In the following, the effectiveness of the proposed training process is demonstrated through a lateral trajectory tracking problem of automated vehicles.

3.2 Training Dataset and the Neural Network

The whole training dataset consists of 60000 data points, which are saved during the 4000 randomly generated test scenarios. The output of the neural network is computed through the input vector (5). In the vehicle-oriented implementation, the input vector is $T = [v_y, \psi, \dot{\psi}, v_{1,p}, \epsilon_{1\dots n}]$. ϵ_i gives the predicted error between the current lateral position and the reference trajectory. However, for training purposes, not the whole reference trajectory is used, but it is sampled along the prediction horizon as $i = \{1, 12, 23, 34, 45\}$. Moreover, the first and the predicted last longitudinal velocity is used. Since the goal is the trajectory tracking, the output of the network is the steering angle. During the training process, based on the nonlinear differential equations, the predicted derivatives of the lateral displacement and the yaw-rate are considered (see: (2)) in the data-based part of the loss function. Moreover, the weights in the loss function are $Q_{data} = 10, Q_{\dot{\psi}} = 5, Q_{\dot{v}_y} = 1$.

The size of the input vector of the neural network is 10, while the output is 1. The network has 3 hidden layers and the number of neurons is 25, 40, 20. Moreover, the activation functions are Hyperbolic tangent, ReLU, and Hyperbolic tangent. The training process of the network is carried out using the Adaptive Moment Estimation (ADAM) algorithm [4]. During the optimization the Learning rate is selected to 0.01, the size of the mini batch is 256, while the maximum epoch number is 200.

4 Simulation Results

In this section, the conventionally trained and the PINN are compared to each other in terms of tracking performance. The test scenarios are implemented in CarMaker vehicle dynamics simulation software, in which a Tesla Model S vehicle is used. For training purposes, a small amount of data is used to highlight the advantage of the incorporation of physical information. Moreover, dynamical ranges are eliminated from the training dataset in terms of yaw-rate: $(0.35 \leq |\dot{\psi}| \leq 0.45) \vee (0.55 \leq |\dot{\psi}| \leq 0.65)$. The results are summarized in Table 1.

Table 1. Test results using different neural networks

Size of data	$n = 2000$	$n = 4000$	$n = 8000$	$n = 12000$	$n = 16000$
PINN	✗	✓	✓	✓	✓
Conv. NN	✗	✗	✗	✓	✓

The test is said to be successful if the vehicle fulfills the stable motion requirements during the scenario. In Table 1, successful tests are marked with a checkmark (✓), while unsuccessful tests are marked with a crossmark (✗). Considering the results shown in the table, it can be observed, that the PINN-based solution was successful in reference trajectory tracking with the use of 4000 data points,

whereas the conventionally trained network required at least 12000 data points. Furthermore, the lateral positions are depicted in Fig. 2a, for three cases: PINN, with 4000 and 8000 training data points, and the conventionally trained with 12000 points. Although the conventional trained model used more data points, the physics-based extension in the loss function increased tracking accuracy as shown in Fig. 2a. In Fig. 2b the yaw-rates during the trajectory tracking can be examined. The regions, which are not covered by the training dataset, are highlighted in red.

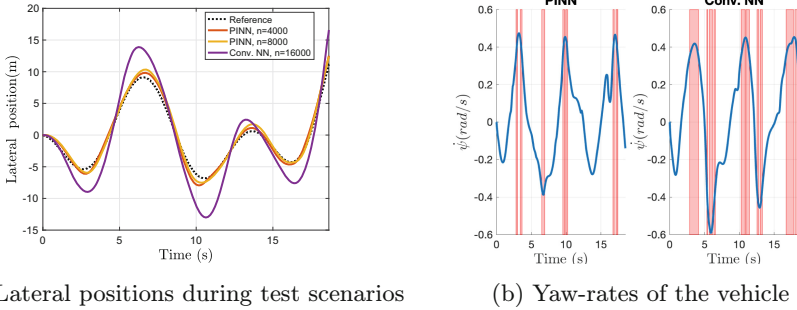


Fig. 2. The velocity and the trajectory of the vehicle

5 Conclusion

The paper presented a novel PINN-based lateral control strategy for autonomous vehicles. The physics-based information of the vehicle has been utilized during the training process of the vehicle. As the simulation examples have shown the this information can significantly improve the performance level of the controller and guarantee the stable motion even under extreme circumstances.

Acknowledgement. The research was supported by the National Research, Development and Innovation Office through the project “Cooperative emergency trajectory design for connected autonomous vehicles” (NKFIH: 2019-2.1.12-TÉT-VN). The paper was partially funded by the National Research, Development and Innovation Office under OTKA Grant Agreement No. K135512. The work of Daniel Fenyés was supported by the Janos Bolyai Research Scholarship of the Hungarian Academy of Sciences.

References

1. Aradi, S.: Survey of deep reinforcement learning for motion planning of autonomous vehicles. *IEEE Trans. Intell. Transp. Syst.* **23**(2), 740–759 (2020)
2. Arnold, F., King, R.: State-space modeling for control based on physics-informed neural networks. *Eng. Appl. Artif. Intell.* **101**, 104195 (2021)

3. Grune, L., Pannek, J.: *Nonlinear Model Predictive Control*. Springer, London (2011)
4. Kingma, D.P., Ba, J.: Adam: a method for stochastic optimization (2017)
5. Nemeth, B., Hegedus, T., Gaspar, P.: Performance guarantees on machine-learning-based overtaking strategies for autonomous vehicles. In: 2020 European Control Conference (ECC), pp. 136–141 (2020)
6. Pacejka, H.: *Tire and Vehicle Dynamics*. Elsevier Science (2005)
7. Raissi, M., Perdikaris, P., Karniadakis, G.: Physics-informed neural networks: a deep learning framework for solving forward and inverse problems involving nonlinear partial differential equations. *J. Comput. Phys.* **378**, 686–707 (2019)
8. Rajamani, R.: *Vehicle Dynamics and Control*. Springer, New York (2005)

Open Access This chapter is licensed under the terms of the Creative Commons Attribution 4.0 International License (<http://creativecommons.org/licenses/by/4.0/>), which permits use, sharing, adaptation, distribution and reproduction in any medium or format, as long as you give appropriate credit to the original author(s) and the source, provide a link to the Creative Commons license and indicate if changes were made.

The images or other third party material in this chapter are included in the chapter's Creative Commons license, unless indicated otherwise in a credit line to the material. If material is not included in the chapter's Creative Commons license and your intended use is not permitted by statutory regulation or exceeds the permitted use, you will need to obtain permission directly from the copyright holder.





Enhancing Electric Vehicle Remaining Range Prediction Through Machine Learning

Byunggun Kim^(✉) and Haeyoun Kim

Control Solution Center, Hyundai Kefico, 102 Gosan-ro, Gunpo, Gyeonggi-do,
Republic of Korea

ByungGun.Kim@hyundai-kefico.com

Abstract. Many automakers are announcing electric vehicle (EV) models in response to environmental regulations. However, charging times still exceed those of traditional internal combustion engine vehicles. Moreover, the supply of electric vehicle charging stations has not kept pace with the rapid expansion of electric vehicle adoption. This incongruity raises ongoing concerns for drivers regarding Distance To Empty (DTE) or remaining range. However, accurate DTE prediction faces challenges due to various factors. Therefore, predicting effective remaining range is attracting researchers' attention. However, most algorithms are based on long-term historical driving data, which presents limitations in a shared vehicle scenario with frequently changing drivers. To address these challenges, this paper introduces a novel algorithm employing machine learning to classify driving styles and predict remaining range. This approach can integrate expected future road information and current driving conditions, offering a solution to the uncertainties associated with traditional methods.

Keywords: Electric Vehicles (EVs) · Machine Learning · Drive Style · Remaining Range Prediction · Distance To Empty (DTE)

1 Introduction

1.1 Background

The importance of sustainable energy solutions in the automotive industry has led global automakers to promote electric vehicles (EVs) to meet environmental regulations. Despite technological advancements, challenges persist, hindering a smooth transition to EVs. While fast charging is available, EV charging times still exceed those of conventional internal combustion engine vehicles. Additionally, the growth of EV charging infrastructure has not kept pace with EV adoption, leaving drivers uncertain about charging availability when needed. Moreover, drivers experience ongoing fatigue from monitoring the Distance To Empty

Supported by Hyundai Motor Group.

© The Author(s) 2024

G. Mastinu et al. (Eds.): AVEC 2024, LNME, pp. 819–825, 2024.

https://doi.org/10.1007/978-3-031-70392-8_116

(DTE) and the distance to charging stations or destinations. DTE is determined by multiplying the vehicle's total energy by its power efficiency, which decreases as the vehicle's battery charge level (State of Charge (SoC)) nears 0%. Consequently, drivers may experience heightened anxiety once the SoC drops below a certain threshold. Accurately predicting DTE is thus a critical challenge for EVs. However, designing precise DTE prediction logic is challenging due to its complexity, influenced by factors such as driving style, external conditions, air conditioning usage, battery health, and driving mode. Furthermore, predicting remaining range becomes even more challenging due to unknown future driving conditions. (see Fig. 1).

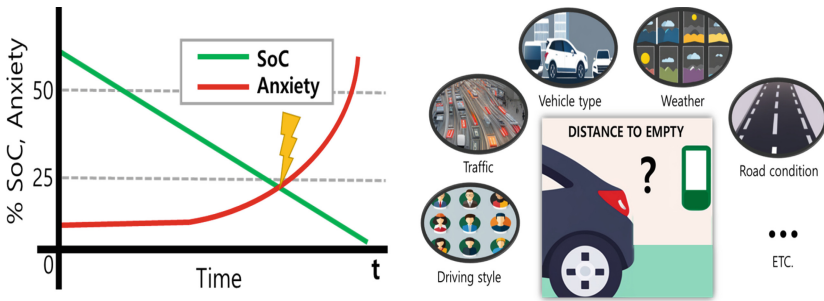


Fig. 1. Sharp rise in anxiety once the SoC has crossed a certain point and Various factors affecting Distance To Empty (DTE).

In addition, current remaining range prediction methods use calibration values because it is difficult to define the effects of various factors in a fixed formula. To determine energy efficiency for future routes, official efficiency values for each road type are calibrated and used as constants. Similarly, driving mode weights are fixed through calibration. Setting these values requires extensive data collection to match actual vehicle specs and standard values for general drivers, a process that demands significant resources from automakers. However, these calibration values are averages and do not account for individual driving styles or conditions, limiting the accuracy of the actual Distance to Empty (DTE).

Recent advances in artificial intelligence are impacting the automotive industry, with significant research being conducted using machine learning [2]. Remaining range prediction in electric vehicles is a critical task, and various methods have been proposed. Some studies estimate energy consumption based on past driving records [1, 6], which is accurate for familiar routes but less so for new ones. Modeling approaches also predict energy consumption using vehicle dynamics equations [3]. Recently, machine learning methods have emerged [4, 5], though they heavily depend on data.

This paper introduces an improved DTE algorithm that works with minimal data, leveraging past, present, and future vehicle data and machine learning. The algorithm can classify the driver's style from past data and predicts DTE using future driving environment information, like road gradient, and the current

vehicle state. This approach addresses the uncertainties of existing DTE methods by learning and adapting to the current driver’s style in real-time, enhancing DTE accuracy with less data.

2 Proposed Algorithm

2.1 Proposed Algorithm Structure

The integrated algorithm consists of a driving style assessment network and a remaining range prediction network (see Fig. 2).

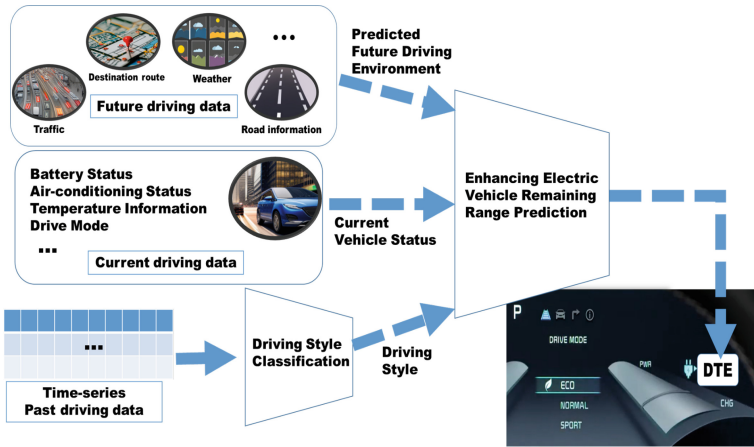


Fig. 2. Schematic diagram of the proposed algorithm.

The driving style assessment network leverages machine learning techniques to analyze driving data and determine driving styles. Simultaneously, the remaining range prediction network considers various factors and incorporates the assessed driving style to enhance prediction accuracy. In practical driving scenarios, diverse drivers operate vehicles in various situations, making it challenging to determine specific driving styles. This study aims to assess driving style based solely on data obtainable through the vehicle’s Controller Area Network (CAN) communication.

From this, we propose a remaining range prediction algorithm that incorporates the evaluated driving style. The integration of these networks aims to provide a comprehensive solution for predicting remaining range by considering both driving style and relevant factors in real-time EV driving scenarios.

2.2 Data Acquisition

The creation of a high-quality dataset is crucial for enhancing machine learning performance. In this study, real-world driving data from a HYUNDAI electric

vehicle was collected to build the dataset. Twelve factors were obtained through CAN (Controller Area Network) communication, including vehicle speed, road gradient, accelerator position sensor (APS), brake position sensor (BPS), steering wheel angle, steering wheel angular velocity, outside temperature, odometer, total power consumption, air conditioning power consumption, and Distance to Empty (DTE) value. Diverse scales among selected factors can adversely affect the learning process. To mitigate this, normalization was applied, ensuring that data characteristics of each factor were represented on a similar scale. Additionally, synchronization for the timestamp was performed. The processed datasets were then divided into a randomly selected test set and a training set for network training and performance evaluation. The test set-to-training set ratio was set at 0.1:0.9 for this study. The total driving data acquired amounted to approximately 5,000 s and 40 km, comprising short driving sessions from different days using the company’s test car. During testing, half of the driving sessions were conducted under normal conditions, while the remaining sessions involved diverse driving behaviors, including rapid acceleration/deceleration maneuvers and adjustments to the air conditioner. From the collected data, five features were utilized to assess driver behavior, including APS, BPS, steering wheel manipulation, and longitudinal vehicle velocity. These feature data were segmented into 500-s intervals and categorized into three label classes (Bad, Normal, Good) to classify driver styles (see Fig. 3).

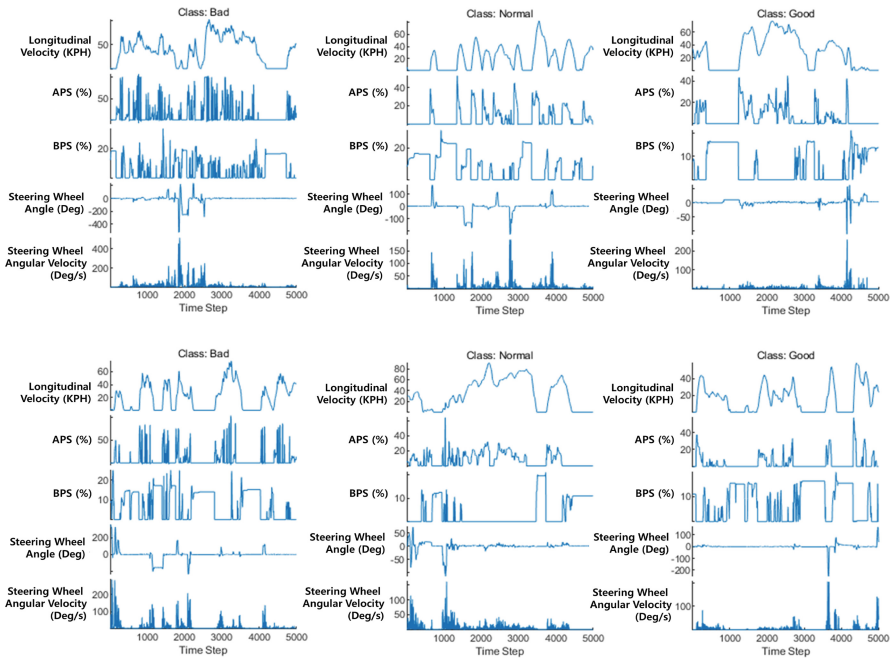


Fig. 3. Labeled collection data.

The remaining features were input into the second network to predict the vehicle’s power efficiency, considering the current vehicle conditions. These feature data were divided into 100-s intervals, and clustering was employed to determine the class label based on the actual travel distance divided by the total energy consumption of the corresponding driving data.

2.3 Network Layer

The order and outline of the layers used to optimize the performance of the proposed algorithm are as follows. (see Table 1).

Table 1. Layer Descriptions

Order	Layer	Description
1	Sequence Input Layer	Entry point for sequence data, accommodating specified input dimensionality
2	Layer Normalization Layer	Stabilizes learning by normalizing inputs across features, improving training efficiency
3	Bidirectional LSTM Layer	Processes sequences bidirectionally to capture comprehensive dependencies and contextual info
4	Dropout Layer	Applies 50% dropout rate to prevent overfitting and enhance generalization
5	Fully Connected Layer	Contains 50 neurons to learn complex patterns from sequence data
6	ReLU Activation Layer	Introduces non-linearity with ReLU activation for learning complex data relationships
7	Fully Connected Layer	Maps learnt features to output classes for final classification, with neurons matching output classes
8	Softmax Layer	Converts outputs to probability distributions for multi-class classification tasks

3 Conclusion

The power efficiency classification results of the network are depicted in Fig. 4.

The distance calculated by multiplying the network’s final output, the predicted power efficiency, by the vehicle’s total energy, proved to be more effective in determining the practical remaining range value compared to the existing method. This success can be attributed to the algorithm’s effective handling of shorter distances, unlike existing Distance To Empty (DTE) logic, which relies on power efficiency calculated from previous driving data. This paper presents a practical approach to predict the remaining range, alleviating anxiety for EV drivers. The proposed method demonstrates effectiveness even with limited data

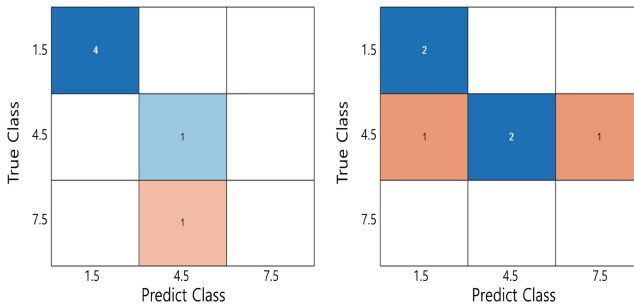


Fig. 4. Results of the test data set.

and holds promise for real-world electric vehicles with further development. Moreover, it is expected to be particularly effective in scenarios where drivers change frequently, such as shared vehicles or corporate fleets. Future studies will consider additional factors and the impact of regenerative braking on electric vehicles.

Acknowledgment. This work was supported by the Hyundai Motor Group.

References

1. Fukushima, A., Yano, T., Imahara, S., Aisu, H., Shimokawa, Y., Shibata, Y.: Prediction of energy consumption for new electric vehicle models by machine learning. *IET Intell. Transp. Syst.* **12**(9), 1174–1180 (2018)
2. Kim, B., et al.: Vehicle speed optimization based on predicted traction torque using machine learning. *Trans. Korean Soc. Autom. Eng.* **30**(6), 511–518 (2022)
3. Miri, I., Fotouhi, A., Ewin, N.: Electric vehicle energy consumption modelling and estimation—a case study. *Int. J. Energy Res.* **45**(1), 501–520 (2021)
4. Shen, H., et al.: Electric vehicle velocity and energy consumption predictions using transformer and Markov-chain Monte Carlo. *IEEE Trans. Transp. Electrification* **8**(3), 3836–3847 (2022)
5. Ullah, I., Liu, K., Yamamoto, T., Al Mamlook, R.E., Jamal, A.: A comparative performance of machine learning algorithm to predict electric vehicles energy consumption: a path towards sustainability. *Energy Environ.* **33**(8), 1583–1612 (2022)
6. Yavasoglu, H., Tetik, Y., Gokce, K.: Implementation of machine learning based real time range estimation method without destination knowledge for BEVs. *Energy* **172**, 1179–1186 (2019)

Open Access This chapter is licensed under the terms of the Creative Commons Attribution 4.0 International License (<http://creativecommons.org/licenses/by/4.0/>), which permits use, sharing, adaptation, distribution and reproduction in any medium or format, as long as you give appropriate credit to the original author(s) and the source, provide a link to the Creative Commons license and indicate if changes were made.

The images or other third party material in this chapter are included in the chapter's Creative Commons license, unless indicated otherwise in a credit line to the material. If material is not included in the chapter's Creative Commons license and your intended use is not permitted by statutory regulation or exceeds the permitted use, you will need to obtain permission directly from the copyright holder.





Fuel Economy Assessment of MPC-ACC on Powertrain Testbed

Stefano Favelli^{1,3}(✉), Luis M. Castellanos Molina^{1,3}, Alessandro Mancarella^{2,3},
Omar Mareello^{2,3}, Eugenio Tramacere^{1,3}, Raffaele Manca^{1,3}, Mario Silvagni^{1,3},
Andrea Tonoli^{1,3}, and Nicola Amati^{1,3}

¹ Department of Mechanical and Aerospace Engineering, Politecnico di Torino,
Turin, Italy

stefano.favelli@polito.it

² Department of Energy “Galileo Ferraris”, Politecnico di Torino, Turin, Italy

³ Center for Automotive Research and Sustainable Mobility, Politecnico di Torino,
Turin, Italy

<https://www.cars.polito.it/>

Abstract. The development and testing of Advanced Driver Assistance Systems (ADAS) is one of the most active fields in the automotive industry towards Automated Driving (AD). This work presents the deployment and testing of an Adaptive Cruise Control (ACC) based on Model Predictive Control (MPC). The goal is to design and validate through the experimental campaign a computationally efficient longitudinal dynamics controller and assess its fuel economy potential. The development of the control structure as well as the definition of the testing method for energy efficiency assessment are central aspects of this work. The performance of the approach is tested on a light-duty commercial vehicle on a state-of-the-art 4-axis powertrain testbed. The findings demonstrate that the speed profile can be optimized to achieve a fuel reduction of up to 13% while maintaining mission timing and comfort.

Keywords: Advanced Driver Assistance Systems · Adaptive Cruise Control · Model Predictive Control · 4-axis powertrain testbed

1 Introduction to ADAS for Fuel Economy

In the past decades, vehicles have been increasingly equipped with connectivity and automation technologies with the introduction of communication infrastructures and onboard sensors [1]. Compared to manual driving, vehicles equipped with Advanced Driver Assistance Systems (ADAS) can be controlled more precisely, improving road safety and traffic flow stability [2]. In recent years, there has been a marked interest in using ADAS beyond safety and comfort to also address vehicle efficiency improvement [3].

Supported by [CARS](#) - Center for Automotive Research and Sustainable Mobility.

© The Author(s) 2024

G. Mastinu et al. (Eds.): AVEC 2024, LNME, pp. 826–832, 2024.

https://doi.org/10.1007/978-3-031-70392-8_117

Adaptive cruise control (ACC) is one of the most popular ADAS available on a wide variety of mass-production vehicles. ACC has proven to be well-suited to enhance fuel economy because of the possibilities opened by prescribing a target lead vehicle speed [4]. A wide variety of strategies have been proposed to minimize fuel consumption, especially when the following policy is solved under a predictive control framework [5–7]. Recent literature on the topic only partially focuses on systematic assessment of energy savings from ADAS with experimental testing [8], while great attention is paid to the impact of low-level control policies on stability [9].

This work presents a novel experimental framework to assess fuel economy improvement introduced by a predictive controller deployed in real-time and tested in a powertrain testbed. The proposed ACC sets the optimal target acceleration to guarantee passenger comfort and reduce fuel consumption. Special attention is paid to a low-level controller to guarantee a good enough tracking of the desired acceleration. Experimental results demonstrate fuel consumption reduction up to 13% especially when relaxed headway time values are set.

The work is organized as follows. Section 2 presents the proposed ACC controller, the MPC problem formulation, and the inner feedforward-feedback acceleration tracking controller. Section 3 concludes with the ACC real implementation on powertrain testbed.

2 Adaptive Cruise Control on Powertrain Testbed

The proposed ACC is implemented on a vehicle installed in a powertrain testbed (hereinafter called host vehicle) as depicted in Fig. 1.

The lead vehicle speed profile is emulated together with the host vehicle radar to properly generate the relative distance and relative speed profiles. The high-level predictive controller uses kinematic vehicle constraints to determine the optimal target acceleration for the host vehicle. Then, a low-level controller with combined feedback and feedforward action properly tracks the given reference. The powertrain testbed automation system made it possible to conduct a systematic assessment of vehicle performance.

In the following, the two proposed control layers are briefly described.

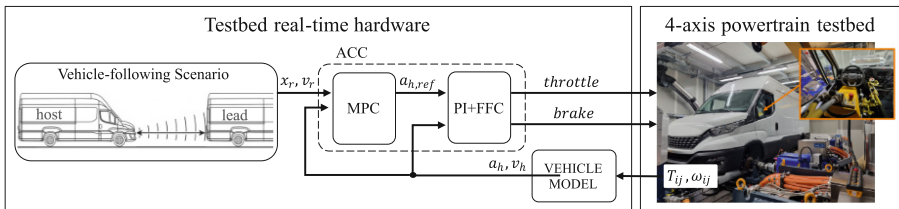


Fig. 1. Scheme of the experimental framework on the 4-axis powertrain testbed in which the MPC-ACC has been tested.

2.1 MPC Controller Design

Assuming that the low-level control action ensures perfect tracking of the desired acceleration $a_{h,ref}(t)$, it can be modeled together with the internal vehicle dynamics as a single integrator. In this way, the host vehicle speed $v_h(t)$ is related to the desired acceleration $a_{h,ref}(t)$ with the following set of equations [10]:

$$\begin{cases} x_r(t) = x_r(0) + \int_{t_0}^t v_r(t) dt \\ v_r(t) = v_r(0) + \int_{t_0}^t a_r(t) dt \\ v_h(t) = v_h(0) + \int_{t_0}^t a_h(t) dt \end{cases} \quad (1)$$

where $x_r(t)$ is the relative position between the lead and the host vehicle, $v_r(t) = v_l(t) - v_h(t)$ the relative velocity, $a_r(t) = a_l(t) - a_h(t)$ the relative acceleration, $v_h(t)$ the host vehicle velocity, and $a_h(t)$ the host vehicle acceleration at time t . The values of $x_r(t)$ and $v_r(t)$ are given by the radar, and the host vehicle speed $v_h(t)$ is assumed available in vehicle control unit. The relative acceleration becomes $a_r(t) \equiv -a_h(t)$, as the acceleration of the lead vehicle $a_l(t)$ is unknown, and assumed to be zero for the prediction model. The host vehicle acceleration $a_h(t)$ is used as a control decision variable, and $a_l(t)$ acts as a disturbance on the system.

In ACC, an important performance parameter is the desired headway time ($t_{hw,d}$) i.e., a way for the driver to communicate how closely the vehicle should follow the preceding one. The desired headway time is used to define a reference distance

$$x_{r,d}(k) = x_{r,0} + \bar{v}_h(k)t_{hw,d} \quad (2)$$

that depends on a constant $x_{r,0}$, representing the minimum distance, and the host vehicle's speed v_h . The latter is saturated as:

$$\bar{v}_h(k) = \begin{cases} v_h(k) & \text{if } v_h(k) < V_{\max} \\ V_{\max} & \text{if } v_h(k) \geq V_{\max} \end{cases}$$

where V_{\max} is the road limit speed.

Correspondingly, the tracking error at time step k is defined as $e(k) = x_{r,d}(k) - x_r(k)$. Hence, a primary control objective is minimizing the absolute tracking error $e(k)$.

Constraints related to safety and comfort are detailed in the following:

- **Safety:** the inter-vehicle distance should always be greater than a minimum safe distance, i.e. $x_r > x_{r,\min}$, thus avoiding collisions. Furthermore, the relative velocity between the vehicles should be minimized, $|v_r(k)|$.
- **Comfort:** the peak values of the host vehicle acceleration $|a_h(k)|$ and jerk $|j_h(k)|$ should be kept small to guarantee the comfort of driving action. To accommodate the jerk constraints into the MPC problem, the host acceleration is written as a state, and its variation

$$\frac{da_h}{dt} \equiv j_h(t) \equiv u(t)$$

is treated as an input u , which written in discrete-time domain becomes

$$a_h(k) = a_h(k-1) + T_s u(k) \quad (3)$$

The proposed MPC-ACC needs a dynamic model to predict the evolution of the vehicle and its surroundings. To do that, the equations in (1) are firstly written in discrete-time domain with sample time T_s and then combined with (3) to obtain a discrete-time state space model:

$$\xi(k+1) = A\xi(k) + Bu(k) \quad (4)$$

with states $\xi = [x_r(k), v_r(k), v_h(k), a_h(k-1)]^\top$, and matrices

$$A = \begin{pmatrix} 1 & T_s & 0 & -\frac{1}{2}T_s^2 \\ 0 & 1 & 0 & -T_s \\ 0 & 0 & 1 & T_s \\ 0 & 0 & 0 & 1 \end{pmatrix}, \quad B = \begin{pmatrix} 0 \\ 0 \\ 0 \\ T_s \end{pmatrix}. \quad (5)$$

The following MPC problem is proposed for the ACC:

$$\min_{\xi, u} \sum_{k=1}^N \|\xi_k - \xi_k^{ref}\|_Q^2 + \|u_k\|_R^2 \quad (6a)$$

subj. to

$$\xi_{k+1} = A\xi_k + B\delta u_k \quad k = 0, \dots, N-1 \quad (6b)$$

$$x_{r,\min} < x_r(k) \quad (6c)$$

$$a_{h,\min} \leq a_h(k) \leq a_{h,\max}(v_h(k)), k \in N \quad (6d)$$

$$|u(k)| \leq j_{h,\max}. \quad (6e)$$

Weight matrix $Q \succeq 0$ is properly set to track the relative distance with the minimum effort in terms of acceleration, while $R \succ 0$ is tuned to normalize the variations of the acceleration with the state deviations. Constraints on relative distance, acceleration, and jerk are set to guarantee comfort. Hence, the controller tries to properly follow the lead vehicle with minimum effort in terms of acceleration command. This approach produces a smoother speed profile, which indirectly reduces fuel consumption and improves comfort.

The resulting control problem (6) is cast into a quadratic programming (QP) problem once and offline. At each time step, the problem is updated with the current state and then solved to obtain the optimal acceleration deviation $u^*(t)$. Finally, the target acceleration is updated using Eq. (3) and set as the new reference for the inner acceleration control layer, as explained in Subsect. 2.2. The proposed method allows real-time implementation on the testbed's hardware. It is worth mentioning that, to avoid infeasibility issues, a slack variable is added to the acceleration state constraints. During the implementation, its activation has been noticed only in critical conditions, like panic braking of the lead vehicle or when running on aggressive driving cycles.

2.2 Low-Level Acceleration Tracking Control

The low-level controller generates accelerator and brake pedal signals to accurately track the target acceleration $a_{h,ref}$. It combines a feedforward (FFC) and a feedback (FBC) controller. The FFC generates throttle and braking commands by inverting the vehicle model. The FBC, which uses a PI (Proportional-Integral controller), compensates for plant-model mismatches by tracking the speed reference $v_{h,ref}$ generated from the integration of $a_{h,ref}$. For the sake of brevity, this work excludes all calibration details and instead presents a simplified control scheme, as depicted in Fig. 2. Note that the information about the actual gear and road grade (RG) profile is used by the feedforward to guarantee a better plant model inversion and hence improve the open-loop tracking of the desired vehicle acceleration.

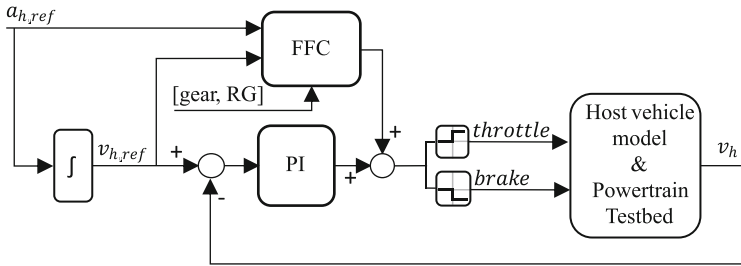


Fig. 2. Simplified low-level controller scheme.

3 Experimental Results and Conclusions

The proposed MPC-ACC is evaluated at a vehicle level in the powertrain testbed. This setup enables a systematic assessment of the fuel consumption in repeatable conditions over different driving cycles by directly measuring the fuel rate of the internal combustion engine. Experimental results obtained on a 2.5-ton light-duty commercial vehicle are reported in Table 1.

Table 1. Fuel Consumption (FC) reduction achieved by the MPC-ACC with 3s headway time. The results are mean values of FC with dispersion, obtained by giving the host and lead speed profiles references 3 times to the same driver model, thus allowing the assessment of different vehicle responses to the same speed profiles.

Scenario	Lead FC [L]	Host FC [L]	FC Reduction [%]
Urban	1.30 ± 0.01	1.14 ± 0.01	13.5 ± 0.1
Extra-urban	3.82 ± 0.02	3.32 ± 0.01	13.0 ± 0.3
Highway	5.54 ± 0.02	5.40 ± 0.01	2.6 ± 0.2

The difference in fuel consumption is evaluated by giving the lead and the host speed profiles to the same vehicle under test. The speed profiles and fuel consumption in both cases are reported in Fig. 3. The results show that by adopting a headway time of 3 seconds, the proposed MPC-ACC can improve fuel consumption by up to 13% in urban and mixed extra-urban driving scenarios while respecting mission timing. Minor effects on fuel economy have been highlighted in highway scenarios, where well-known state-of-the-art techniques remain more suitable.

The results have demonstrated the promising application of Vehicle-in-the-Loop (ViL) testing on a 4-axis powertrain testbed. Future works will use cutting-edge hardware stimulators to replace emulated radar and camera with real data from the vehicle's onboard sensors.

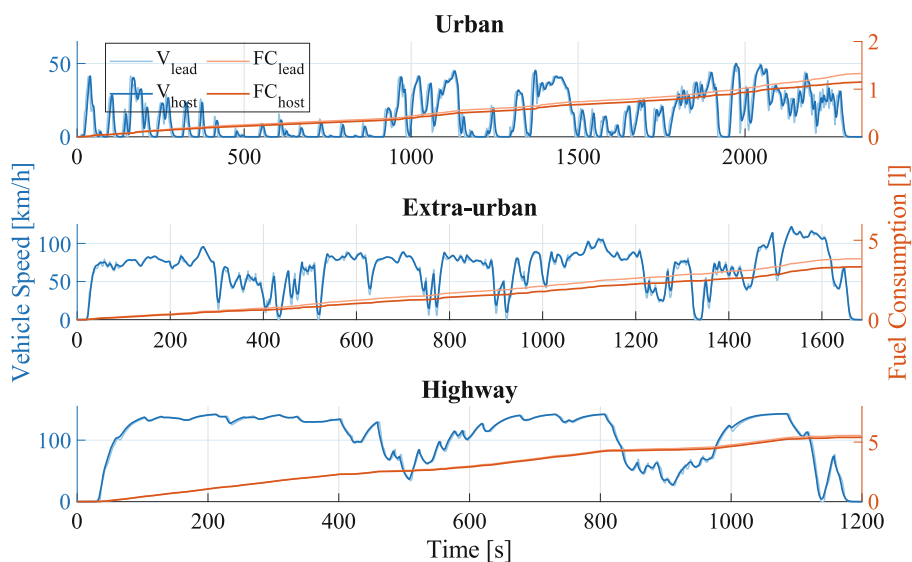


Fig. 3. Fuel consumption results of the MPC-ACC on Real-Driving Emissions (RDE) profiles, i.e. RDE Urban (top), RDE Rural (center), and RDE Motorway (bottom). The host and lead speed profiles are performed by the same vehicle, namely the light-duty commercial vehicle, to highlight the potential fuel consumption reduction.

References

1. Schrotten, et al.: Research for TRAN Committee - The impact of emerging technologies on the transport system. European Parliament Policy Department for Structural and Cohesion Policies (2020)
2. Hagl, M., Kouabenan, D.R.: Safe on the road - does advanced driver-assistance systems use affect road risk perception? *Transp. Res. F: Traffic Psychol. Behav.* **73**, 488–498 (2020). <https://doi.org/10.1016/j.trf.2020.07.011>

3. Vahidi, A., Sciarretta, A.: Energy saving potentials of connected and automated vehicles. *Transp. Res. Part C: Emerg. Technol.* **95**, 822–843 (2018). <https://doi.org/10.1016/j.trc.2018.09.001>
4. Schmied, R., et al.: Extension and experimental validation of fuel efficient predictive adaptive cruise control. In: 2015 American Control Conference (ACC) (2015). <https://doi.org/10.1109/ACC.2015.7172078>
5. Asadi, B., Vahidi, A.: Predictive cruise control: utilizing upcoming traffic signal information for improving fuel economy and reducing trip time. *IEEE Trans. Control Syst. Technol.* **19**(3), 707–714 (2011). <https://doi.org/10.1109/TCST.2010.2047860>
6. Li, S., et al.: Model predictive multi-objective vehicular adaptive cruise control. *IEEE Trans. Control Syst. Technol.* **19**(3), 556–566 (2011). <https://doi.org/10.1109/TCST.2010.2049203>
7. Li, S.E., et al.: Fast online computation of a model predictive controller and its application to fuel economy-oriented adaptive cruise control. *IEEE Trans. Intell. Transp. Syst.* **16**(3), 1199–1209 (2015). <https://doi.org/10.1109/TITS.2014.2354052>
8. He, Y., et al.: Adaptive cruise control strategies implemented on experimental vehicles: a review. *IFAC-PapersOnLine* **52**(5), 21–27 (2019). <https://doi.org/10.1016/j.ifacol.2019.09.004>
9. Zhou, H., et al.: Significance of low-level control to string stability under adaptive cruise control: algorithms, theory and experiments. *Transp. Res. Part C: Emerg. Technol.* **140**, 103697 (2022). <https://doi.org/10.1016/j.trc.2022.103697>
10. Naus, G.J.L., et al.: Design and implementation of parameterized adaptive cruise control: an explicit model predictive control approach. *Control. Eng. Pract.* **18**(8), 882–892 (2010). <https://doi.org/10.1016/j.conengprac.2010.03.012>

Open Access This chapter is licensed under the terms of the Creative Commons Attribution 4.0 International License (<http://creativecommons.org/licenses/by/4.0/>), which permits use, sharing, adaptation, distribution and reproduction in any medium or format, as long as you give appropriate credit to the original author(s) and the source, provide a link to the Creative Commons license and indicate if changes were made.

The images or other third party material in this chapter are included in the chapter's Creative Commons license, unless indicated otherwise in a credit line to the material. If material is not included in the chapter's Creative Commons license and your intended use is not permitted by statutory regulation or exceeds the permitted use, you will need to obtain permission directly from the copyright holder.





MLIO: Multiple LiDARs and Inertial Odometry

Pragyan Dahal¹(✉), Stefano Arrigoni¹, Mario Bijelic², and Francesco Braghin¹

¹ Politecnico di Milano, 20156 Milan, Italy

{pragyan.dahal, stefano.arrigoni, francesco.braghin}@polimi.it

² Princeton University, Princeton, NJ 08544, USA

mario.bijelic@princeton.edu

Abstract. With the decreasing cost of LiDAR sensors, sensor setups with multiple LiDARs are becoming available. In such advanced setups with multiple LiDARs the sensor temporal asynchronicity and spatial miscalibration are critical factors for vehicle localization increasing measurement uncertainty. Hence, simple merging of synchronized point clouds as done in some literature can lead to sub-optimal results. To tackle this problem we propose MLIO, a factor graph-based odometry computation algorithm that fuses multiple LiDARs with an inertial measurement unit (IMU) and provides an accurate solution mitigating the effect of temporal asynchronicity and spatial miscalibration.

The proposed algorithm is validated using a custom dataset. We compare the proposed algorithm with the state-of-the-art LiDAR-only odometry algorithms, such as KISS-ICP, and LiDAR-IMU fusion LIO-SAM and demonstrate its superiority. We were able to achieve up to 40% and 16% increment in positional and orientation accuracy compared to KISS-ICP and 25% increment in positional accuracy compared to LIO-SAM.

Keywords: LiDAR Odometry · multi-LiDAR Odometry · Factor Graph

1 Introduction

The localization of autonomous machines in a reference coordinate frame is a fundamental task and prerequisite for downstream applications reasoning about objects and tasks within this world frame. Dependent tasks are for example perception, planning, control, and many more [1]. Accurate localization can be achieved either through state estimation or simultaneous localization and mapping (SLAM). Usually, a Global Navigation Satellite System (GNSS) along with other sensors like an Inertial Measurement Unit (IMU) and In-Vehicle sensors (steering and velocity encoders) are employed for state estimation [2] while LiDARs and Cameras are primary sensors for SLAM [3]. Vehicle motion estimation through LiDAR odometry, even though can be prone to drift if not corrected with loop closures [6], provides a robust solution. LiDAR odometry and

mapping for the sensor setups with the single LiDAR are studied extensively in [4–6]. Lately, decreasing LiDAR cost, caused the emergence of multi-sensor setups and works with multiple LiDARS are becoming available [8, 11]. Authors in [8] extend the LOAM [7] algorithm to accommodate multiple LiDARS, however, it is designed to work with LiDARS with common Field of View (FoV) for online calibration and sensors with higher resolution with feature-rich point cloud. Similarly, in [11], a multi-LiDAR localization and mapping pipeline is proposed based on KISS-ICP algorithm. The authors apply a separate scan registration for each LiDAR point cloud and create an offline map which is later used for online localization.

Departing from multiple sensors from the same type to setups with multiple LiDARs from various manufacturers or different tasks as short range and long range sensing, increases the difficulty to perform precise localization. Further, the LiDARs can be asynchronous with different update rates and hence pose a significant challenge to perform odometry estimation. In particular in cases where the sensor setup do not have overlapping FoV as in our experimental vehicle, EasyMile [10], calibrating them to a common reference frame can be challenging due to missing jointly available information.

In this work, we propose a factor graph-based LiDAR odometry algorithm for an asynchronous multi-LiDAR setup. We employ an IMU as a base sensor to build the factor graph similar to our previous work [2] and architecture proposed in [3]. Kiss-ICP [6] is used to compute the odometry for each LiDAR using the locally constructed LiDAR map. Instead of trying to synchronize the LiDAR point-cloud or fusing them neglecting the time asynchronicity, we treat each LiDAR separately and estimate the odometry for each IMU update. We can turn the odometry estimation framework into state estimation by integrating the GNSS measurements into the factor graph. The major contribution of the proposed framework is threefold:

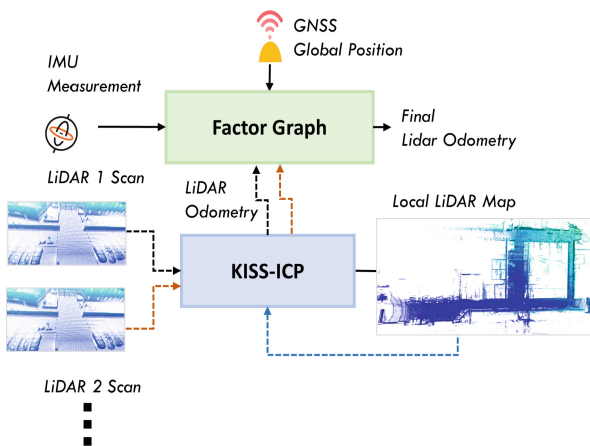


Fig. 1. Tightly coupled multi-LiDAR odometry for the odometry computation from two different LiDARs in the EasyMile setup

- We propose a novel and modular LiDAR Odometry prediction framework for multiple asynchronous LiDARs with a non-aligning FoV.
- The architecture is devised so that GNSS sensor can be added to perform state estimation.
- We validate the proposed algorithm using a custom dataset collected using the EasyMile vehicle with 4 LiDARs, a GNSS Sensor, and an IMU.

2 Problem Formulation

Given the use of multiple sensors with diverse sets of information, we not only estimate the vehicle position and orientation but also its velocity and IMU’s bias. Assuming that X_t^G represents the state for the factor graph,

$$X_t^G = [{}_I P^G, {}_I R^G, {}_I V^G, B^I]_t \quad (1)$$

where, ${}_I P^G$, ${}_I R^G$, and ${}_I V^G$ are the IMU’s position, orientation, and velocity in the Global Reference Frame (\mathbf{G}). B^I consists of the estimated accelerometer and gyroscope biases. The subindex t is used to represent the time instance.

We differentiate two case with GNSS measurements and without. In the first case we apply the algorithms as odometry computer and as in the latter case as state estimator. The major focus of the manuscript is dedicated to the odometry computer component and we will additionally demonstrate the state estimation capability.

3 Factor Graph Construction

The IMU sensor is used as the base sensor to develop the factor graph, and multiple LiDAR odometry factors are added online as they become available. The overall architecture of the proposed algorithm is illustrated by Fig. 1. The modular nature of the algorithm enables the addition and removal of sensors based on their availability. Since this study focuses on the LiDAR odometry component only, we will focus on how multiple LiDARs can be easily integrated into the framework using Robot Operating System (ROS). The architecture is based on the IMU timestamps, hence requiring to have IMU in the sensor setup, besides that, any other sensor providing relative odometry or absolute positions can also be added. The EasyMile sensor setup consists of the following sensor installation:

- GNSS Sensor, located at the top of the vehicle
- two 16 Plane Velodyne Lidars with 180^0 FoV facing front and back of the EasyMile vehicle, providing PointCloud at 10 Hz
- two 4 Plane Sick long range Lidars with 180^0 FoV facing front and back of the EasyMile vehicle, providing PointCloud at 10 Hz
- XSens IMU sensor providing acceleration and angular velocity measurements at 100 Hz

3.1 Graph Initialization

Initially, when the vehicle is stationary, IMU measurements are stored in a buffer for a predefined time window. The measurements are then analyzed to compute the orientation of the IMU in the local frame, except the yaw angle, which is initialized to zero. The IMU provides the acceleration and angular velocity measurements along the IMU reference frame. Using the gravity component measurement of the acceleration, the initial orientation of the IMU is computed using the following equations:

$$\begin{aligned}
 a_X &= -g \sin(\theta) \\
 a_Y &= g \sin(\psi) \cos(\theta) \\
 a_Z &= g \cos(\psi) \cos(\theta)
 \end{aligned}
 \tag{2}$$

where, a_X , a_Y , and a_Z are the mean values of the buffered accelerometer measurements while the vehicle is stationary. θ and ψ are the IMU roll and pitch angle in the Local Reference Frame \mathbf{L} . g is the acceleration due to gravity. We neglect the bias and noise contribution in the IMU measurements in this initialization phase. The initial roll and pitch angle are calculated using Eq. 2.

Position and velocity values are initialized to zero. The roll and pitch angles are initialized using the step discussed above while the yaw angle is initialized to zero. For bias values of the accelerometer, user input or prior knowledge is utilized while the gyroscope bias is initialized as the mean value of the angular velocities when the vehicle is stationary. Once the initial state is defined, the factor graph is constructed by adding values at the IMU timestamps and factors connecting the corresponding sensor timestamps.

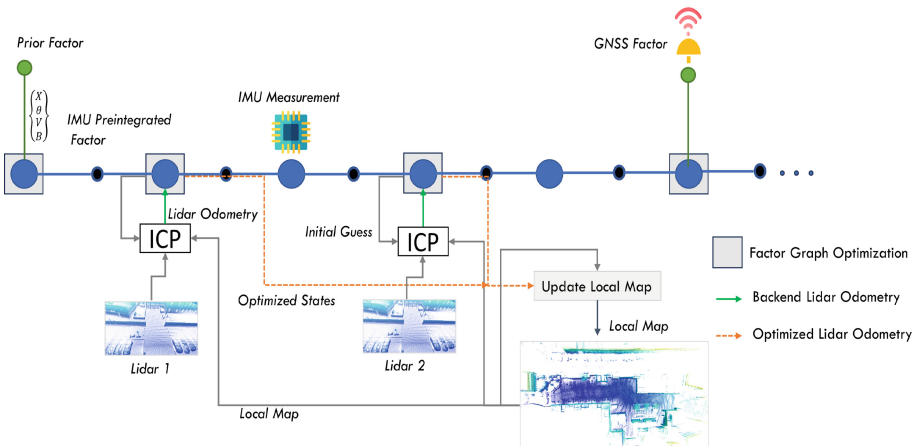


Fig. 2. Tightly coupled multi-LiDAR odometry for the odometry computation from two different LiDARs in the EasyMile setup

3.2 IMU Factor

First for each received IMU measurement, a value is added to the factor graph, in a similar approach to [3]. We apply the widely used pre-integrated factor proposed by [9]. Adding a value to the graph with each measurement is suitable for the IMUs with the lower frequency ranges, till 100 Hz, while for the IMUs with the higher frequency, some IMU measurements are stored in a buffer and values are added as per the user-defined, but lower frequency. The raw IMU measurements at time instance t consists of linear acceleration ${}^I\hat{a}_t$ and the angular velocities ${}^I\hat{\omega}_t$. The accelerometer and gyroscope models are then defined as:

$$\begin{aligned} {}^I\hat{\omega}_t &= {}^I\omega_t + {}^Ib_{\omega_t} + {}^I\eta_t \\ {}^I\hat{a}_t &= {}^I R_t({}^W a_t - {}^W g) + {}^Ib_{a_t} + {}^I\nu_t \end{aligned} \quad (3)$$

where, ${}^I\omega_t$ and Ia_t are the true angular velocities and linear accelerations of the IMU. ${}^Ib_{\omega_t}$ and ${}^Ib_{a_t}$ are the angular velocity biases and linear acceleration biases. They are modeled as a random walk. The noise terms, ${}^I\eta_t$ and ${}^I\nu_t$, follow Gaussian distributions. ${}^I R_t$ is the rotation matrix from the \mathbf{L} frame to IMU reference frame. Readers are referred to [9] for further reading on the development of this factor.

3.3 Lidar Odometry and Odometry Factors

We study two approaches to creating a LiDAR odometry factor for the factor graph. The first approach is a lightly coupled odometry computer based on the work of [6]. In this approach, the odometry computer directly subscribes to the point cloud topics obtained from the LiDAR sensors, and the computed odometry is used as a binary factor connecting two values in the factor graph corresponding to the point cloud timestamps. The relative transformation between the two locations of the two consecutive point clouds in the local map is used as the factor between the values in the graph closest to these timestamps. A lightly coupled and completely separate mapping approach for sensor setup with multiple LiDARs can create unnecessary overhead to the algorithm if we create multiple LiDAR maps. In case of employing the ICP [6] approach for multiple LiDARs, different local maps need to be constructed, stored, and maintained for each LiDAR separately. Our previous work in [2] employed this technique to compute LiDAR odometry for two Velodyne LiDARs of the EasyMile sensor setup. In this work, the loosely coupled approach creates a single LiDAR map and localizes the newly obtained point cloud in the cumulative local map created using the point cloud of all the LiDARs instead of a single LiDAR. The local map is updated using the downsampled point cloud from each LiDAR following techniques employed in [6].

The second approach is a tightly coupled LiDAR odometry with the possibility to integrate multiple LiDARs into a single local map and use the optimized factor graph state to update the local map. The complete architecture of the multi-LiDAR odometry applied in this work is illustrated in Fig. 2. Note, that

the LiDAR point cloud from different LiDARs is received asynchronously by the ROS network. Contrary to the common practices of fusing the point cloud from different LiDARs into one single point cloud and performing the odometry computation, our approach deals with the LiDAR point cloud separately. The addition of values to the factor graph with high-frequency IMU measurement allows to fuse asynchronous LiDARs odometry with IMU. As soon as the factor graph is initialized, the mapping module receives the point cloud from each LiDAR and adds the downsampled point cloud to the local map. The local map is stored in the IMU frame as the origin, hence the static transformation from IMU sensor to each LiDAR is used to add the LiDAR point cloud to the map. When the point cloud from each LiDAR is received at least once, the ICP algorithm based on KISS-ICP proposed on [6] is run to compute the odometry of the LiDAR in the \mathbf{L} frame. Contrary to the [6], where a constant velocity model is used to predict the initial guess of the ICP algorithm, we use the predicted state from the IMU pre-integration model closest to the point cloud timestamp. This is illustrated in the Fig. 2.

Once the Lidar is localized in the \mathbf{L} frame, the computed transformation is added as a unary factor connecting the corresponding IMU value. Fixed lag factor graph optimization is done to compute the estimated state at the LiDAR timestamp. This estimated transformation is used to update the local map instead of the ICP computed transformation as done in [6]. This is repeated for the asynchronous point clouds arriving from different LiDARs and is enabled easily by the design choice of using the IMU timestamps to create values in the factor graph.

3.4 GNSS Unary Factor

GNSS sensor provides the location of the vehicle in the \mathbf{G} frame. They are transformed to the IMU reference point in the vehicle to be added to the factor graph as the unary factor using the known static transformation between the GNSS and the IMU.

$${}^I\hat{p}^G = \hat{p}_t^G + {}_{GN}R^I {}_{GN}p^I \quad (4)$$

where, ${}^I\hat{p}^G$ is the GNSS measurement transformed to the IMU location in the vehicle expressed in the \mathbf{G} frame. ${}_{GN}R^I$ and ${}_{GN}p^I$ represent the rotation and translation component of the static transformation between IMU and the GNSS sensor.

4 Results and Comparison

To validate the proposed algorithm, we use the EasyMile vehicle and its sensor setup. We validate the algorithm against the LiDAR only odometry computation algorithm KISS-ICP [6] and LiDAR IMU fusion SLAM algorithm LIO-SAM [4]. The test is performed with the data collected around the Department of Mechanical Engineering, Politecnico Di Milano Bovisa Campus. We collect three

distinct scenes to demonstrate the suitability of the proposed algorithm for the multi-lidar sensor setup.

Figures 3a, 3b and 4a show the qualitative results of the trajectory of the vehicle computed using the baseline algorithms and the proposed MLIO algorithm. For the baselines, the point cloud received from the different LiDARs are synchronized and then merged to provide a 360 FoV around the vehicle. The points in the vehicle trajectory are first aligned with the GNSS measurements temporally to find the correspondence and then Umeyama alignment algorithm [12] is used to perform the alignment. Qualitative observation of these trajectories obtained from the proposed and baseline algorithms shows that the proposed MLIO algorithm can provide the most consistent and accurate LiDAR odometry estimate at high frequency. In Fig. 4b, we also demonstrate the state estimation capability of the algorithm, which also takes as input the GNSS unary factor.

This observation is further buttressed by the results shown in Table 1. The results obtained in this table are for the input point cloud from the two Velodyne LiDARs only. The point clouds are first temporally synchronized using ROS message filters, merged and then fed to the baselines for LiDAR odometry estimation. However, for MLIO, such temporal synchronization is not necessary. In this table, we have listed results for two different variants of MLIO algorithm, *MLIO-0* for the loosely coupled variant and *MLIO-1* for the tightly coupled one. We can see that both the *MLIO* algorithms provide similar level of accuracy in average. In average, they provide approximately 25% increase in positional estimation accuracy while maintaining similar level of accuracy in terms of yaw angle estimation compared to LIO-SAM. They outperform KISS-ICP significantly by improving positional accuracy by 40% and yaw angle estimation by 16%.

We also conduct some ablation studies about the LiDAR choice and the possibility of choosing LiDARs with different parameters and from different manufac-

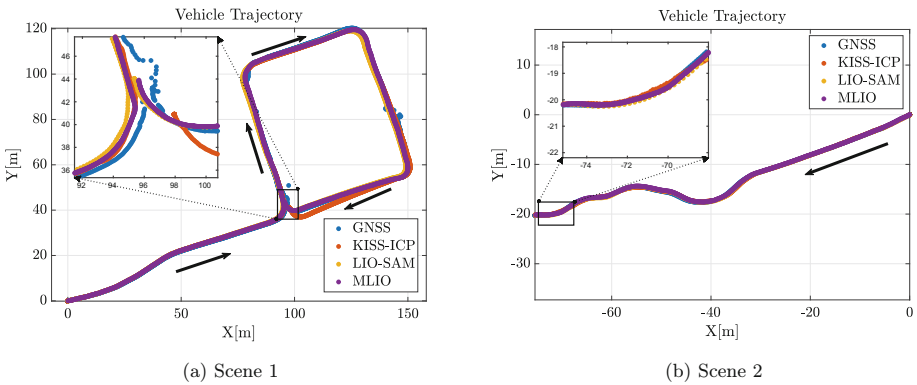


Fig. 3. Ground truth and estimated vehicle trajectories. The red and green circles indicate the start point and GNSS failure point while the arrow shows the vehicle motion direction. Bottom Figure: Ground truth and estimated side slip angle

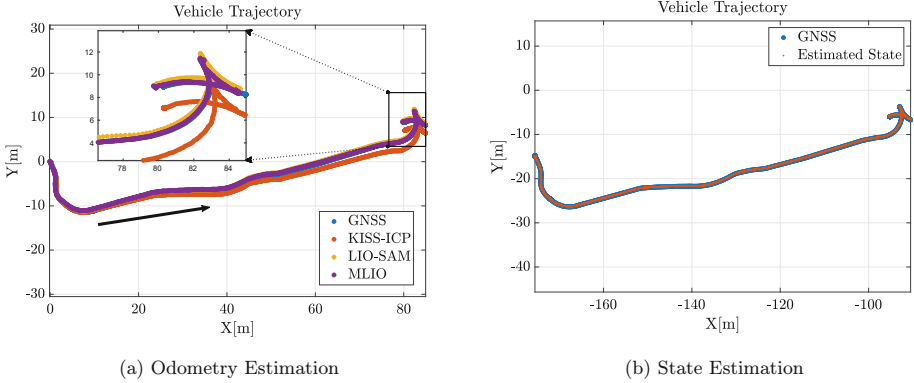


Fig. 4. Odometry and State estimation results from the proposed and the baseline algorithms

tracers into a single framework. In Table 2, the results of this study are illustrated. The *KISS – S* and *MLIO – S* refer to the framework only taking input from the SICK front and rear LiDARs, while *KISS – SV* and *MLIO – SV* take input from the front SICK and rear Velodyne LiDARs. We can observe that MLIO outperforms KISS-ICP for both frameworks in all the scenes. Furthermore, we can observe an interesting result, the performance of both the KISS-ICP and MLIO degrade when using the point clouds from the LiDARs from the different manufacturers. This degradation is more pronounced for the KISS-ICP algorithm. This could be because the LiDARS are calibrated approximately in the spatial frame due to their lack of common FoV. The temporal and spatial miscalibrations easily introduce noises into the local map and the point cloud fed to the algorithm. This effect is minimized in the MLIO algorithm due to the use of the factor graph to optimize the poses, hence the performance is not degraded to the same degree of KISS-ICP. This also demonstrates the capability of the algorithm to integrate multiple LiDARs from different manufacturers.

Table 1. Positional Root Mean Square Error (RMSE), Absolute Positional Error (APE) at the trajectory end and Yaw RMSE for predicted odometry computed using the baselines KISS-ICP [6], LIO-SAM [4] and the proposed Multiple LiDAR and Inertial Odometry (MLIO)

Algorithm	Scene 1	Scene 2	Scene 3
KISS-ICP [6]	0.92, 2.75,0.06	0.26,0.1,0.07	1.12,2.76,0.047
LIO-SAM [4]	1.17,1.41,0.025	0.32,0.21,0.07	0.29,0.67,0.043
MLIO-0	0.90,1.5,0.049	0.24,0.14,0.06	0.29,0.41,0.041
MLIO-1	0.78,1.15,0.049	0.26,0.19,0.06	0.31,0.79,0.038

Table 2. Positional RMSE, APE and Yaw RMSE values for predicted odometry computed using the baselines KISS-ICP [6] and the proposed Multiple LiDAR and Inertial Odometry (MLIO)

Algorithm	Scene 1	Scene 2	Scene 3
KISS-S	0.68,0.34,0.06	0.17,0.06,0.06	0.21,0.53,0.037
KISS-SV	2.75,3.27,0.075	0.29,0.57,0.067	1.18,2.95,0.046
MLIO-S	0.45,0.43,0.054	0.15,0.048,0.06	0.15,0.16,0.036
MLIO-SV	1.09,2.06,0.05	0.35,0.54,0.068	0.30,0.76,0.038

5 Conclusions

In this work, we propose MLIO, a framework to estimate the LiDAR odometry using the input from multiple asynchronous LiDARs and an IMU sensor. The backend odometry for each LiDAR is computed using KISS-ICP while the factor graph using IMU pre-integration factors is used to compute optimized LiDAR odometry. We validate the algorithm on the dataset collected using EasyMile vehicle with the installation of the required sensor. We can demonstrate that the proposed MLIO algorithm is able to outperform the considered baselines, the LiDAR-only KISS-ICP and LiDAR and IMU based LIO-SAM in this custom dataset.

The proposed algorithm could be extended to include online calibration of the LiDARS which could significantly improve the overall odometry estimation result.

References

1. Jo, K., Kim, J., Kim, D., Jang, C., Sunwoo, M.: Development of autonomous car-part i: distributed system architecture and development process. *IEEE Trans. Ind. Electron.* **61**, 7131–7140 (2014)
2. Dahal, P., Prakash, J., Arrigoni, S., Braghin, F.: Vehicle state estimation through modular factor graph-based fusion of multiple sensors, 2023
3. Nubert, J., Khattak, S., Hutter, M.: Graph-based multi-sensor fusion for consistent localization of autonomous construction robots. In: 2022 IEEE International Conference on Robotics and Automation (ICRA). IEEE (2022)
4. Shan, T., Englot, B., Meyers, D., Wang, W., Ratti, C., Rus, D.: LIO-SAM: tightly-coupled lidar inertial odometry via smoothing and mapping. In: IEEE/RSJ International Conference on Intelligent Robots and Systems (IROS) 2020, pp. 5135–5142 (2020)
5. Frosi, M., Matteucci, M.: ART-SLAM: accurate real-time 6dof lidar slam, 2021
6. Vizzo, I., Guadagnino, T., Mersch, B., Wiesmann, L., Behley, J., Stachniss, C.: KISS-ICP: in defense of point-to-point ICP - simple, accurate, and robust registration if done the right way. In: *IEEE Robotics and Automation Letters (RA-L)*, vol. 8, no. 2, pp. 1029–1036 (2023)
7. Zhang, J., Singh, S.: LOAM: lidar odometry and mapping in real-time. In: *Robotics: Science and Systems Conference (RSS)*, pp. 109–111, January 2014

8. Jiao, J., Ye, H., Zhu, Y., Liu, M.: Robust odometry and mapping for multi-lidar systems with online extrinsic calibration. *IEEE Trans. Robot.* **PP**, 1–10 (2021)
9. Forster, C., Carlone, L., Dellaert, F., Scaramuzza, D.: IMU preintegration on manifold for efficient visual-inertial maximum-a-posteriori estimation, July 2015
10. Awasthi, S.S., Arrigoni, S., Awasthi, P., Braghin, F.: An interactive human-machine control interface for an autonomous shuttle. In: 2021 AEIT International Conference on Electrical and Electronic Technologies for Automotive (AEIT AUTOMOTIVE), Torino, Italy (2021)
11. Sauerbeck, F., Kulmer, D., Pielmeier, M., Leitenstern, M., Weiß, C., Betz, J.: Multi-LiDAR Localization and Mapping Pipeline for Urban Autonomous Driving (2023)
12. Umeyama, S.: Least-squares estimation of transformation parameters between two point patterns. *IEEE Trans. Pattern Anal. Mach. Intell.* (TPAMI) **13**(4), 376–380 (1991)

Open Access This chapter is licensed under the terms of the Creative Commons Attribution 4.0 International License (<http://creativecommons.org/licenses/by/4.0/>), which permits use, sharing, adaptation, distribution and reproduction in any medium or format, as long as you give appropriate credit to the original author(s) and the source, provide a link to the Creative Commons license and indicate if changes were made.

The images or other third party material in this chapter are included in the chapter's Creative Commons license, unless indicated otherwise in a credit line to the material. If material is not included in the chapter's Creative Commons license and your intended use is not permitted by statutory regulation or exceeds the permitted use, you will need to obtain permission directly from the copyright holder.





Vehicle State Estimation Through Dynamics Modeled Factor Graph

Pragyan Dahal¹(✉), Stefano Arrigoni¹, Mario Bijelic², and Francesco Braghin¹

¹ Politecnico Di Milano, 20156 Milan, Italy

{pragyan.dahal, stefano.arrigoni, francesco.braghin}@polimi.it

² Princeton University, Princeton, NJ 08544, USA

mario.bijelic@princeton.edu

Abstract. Ego Vehicle state estimation is integral to every autonomous driving software stack. Thereby, the estimation of the state and its components as for example the side slip angle, is a crucial component to track the vehicle maneuvers. In the absence of a direct sensor measuring side slip angle, most of the existing literature either use observers like Kalman Filters or non-modular factor graphs by modeling lateral dynamics. However, the modularity of such graphs, to integrate multiple asynchronous sensors that provide disentangled measurements, like LiDAR, GNSS, and IMU is still overlooked in the literature. In this work, we propose a novel factor graph-based architecture that builds upon the vehicle dynamics at its core to enable the fusion of multiple sensors asynchronously and enables to perform robust and accurate state estimation.

We validate the proposed algorithm against two baselines, a model-based Extended Kalman Filter and a factor graph-based state estimator that uses the IMU pre-integration factor as a reference factor. The algorithms are validated in a custom dataset collected using an in-house vehicle.

Keywords: State Estimation · Robustness · Sensor Fusion · Factor Graph · EKF

1 Introduction

Any robotic application like Autonomous Driving requires knowledge of its location, i.e. position, orientation, velocity, etc. to provide autonomous functionality. The measurements obtained from different sensors cannot be directly interpreted as the vehicle state due to various challenges including, noisy measurements, asynchronous sensor readings, discrepancies in the sensor measurement format compared to state representation, etc. Hence, the state is estimated using the measurements obtained from different sensors. In literature, these state estimation algorithms can be broadly categorized into filtering-based built upon the Kalman Filter and its different variants: Extended Kalman Filter (EKF) [2, 8], Unscented Kalman Filter [1, 8], and Graph-based methods either using a pose

graph [12] or a factor graph [4, 5]. While Filtering-based approaches are primarily employed for state estimation, graph-based approaches are the primary choice for Simultaneous Localization and Mapping (SLAM). With the advancement of learning-based algorithms, some works in literature use deep learning techniques to perform state estimation. [9–11, 14]. Even though deep learning-based algorithms provide reliable solutions, they are often constrained to the systems they are trained for due to measurable domain gaps and require the ground truth data to optimize the algorithm.

The representation of the Vehicle state varies across different works, with each adopting distinct formats and modeling approaches for their components. Among these components, side slip angle estimation proves to be one of the most challenging, particularly within the context of modeling vehicle lateral dynamics. The absence of a dedicated sensor for direct side slip angle measurement has prompted the exploration of various techniques in the literature, often involving GNSS and optical sensors. However, the reliability of GNSS sensors in urban canyons and the cost associated with optical sensors present significant challenges. The UKF filtering approach in [1] models the vehicle motion using the single-track vehicle kinematic model and doesn't explicitly compute the side slip angle. [2] address this by including vehicle side slip angle in state representation and modeling vehicle motion with a single-track version of the four-wheel vehicle model, however, the filtering-based approach is not modular and hence not designed to include additional sensors into the framework. The authors in [3] propose a state estimator based on a factor graph. This estimator models the vehicle's lateral dynamics using a single-track vehicle dynamics model. Nevertheless, it is noteworthy that this research is confined to representing only the vehicle's lateral dynamics. Unfortunately, this limitation restricts the incorporation of additional sensors such as the Inertial Measurement Unit (IMU), GNSS, LiDAR, Cameras, and others into the broader state estimation framework. Our earlier work, [4] is similar to the proposed architecture, but only tests the inclusion of the vehicle kinematic factor into the factor graph without explicitly modeling vehicle lateral dynamics.

In this work, we propose a factor graph-based state estimation architecture that takes the single-track vehicle dynamics model as the reference factor and integrates GNSS measurements and LiDAR odometry for vehicle state estimation. We demonstrate the superiority of the proposed algorithm in terms of modeling vehicle lateral dynamics compared to the baselines and its modularity in integrating multiple asynchronous external sensors enabling robust state estimation in GNSS outage scenarios. The major contribution of the proposed framework is threefold:

- We propose a novel and modular factor graph-based state estimation framework that can utilize measurements from IMU, LiDAR, GNSS, and In-Vehicle sensors (i.e. velocity and steering encoders) to provide consistent and reliable state estimation.
- Filter-like implementation of the architecture enables real-time state estimation at high frequency. The frequency can be regulated to meet user's need.

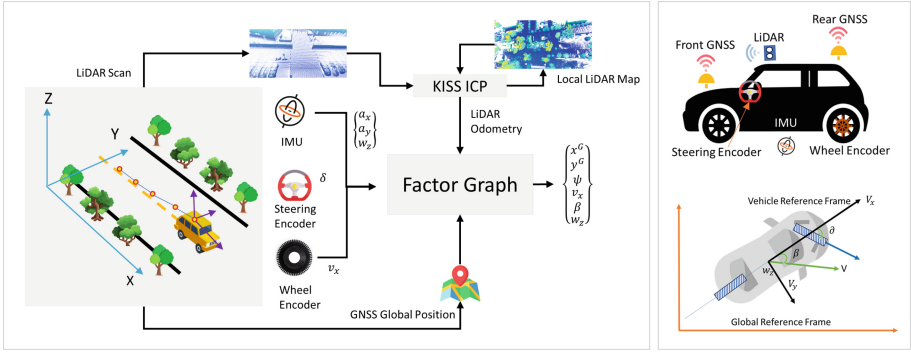


Fig. 1. Left: Overall Architecture of the proposed factor graph based state estimator illustrating inputs from multiple sensors, Right: Vehicle Sensor setup and Reference frames definition for problem formulation

- We demonstrate that the proposed algorithm can provide robust and accurate lateral dynamics state estimate when compared to the IMU preintegration based factor graph [4] and baseline EKF [2].

2 Problem Formulation

For state representation, we take the position of the IMU as the reference point and assign it as the origin of the Vehicle Reference Frame (\mathbf{V}). \mathbf{X}_t represents the state or values for the factor graph,

$$\mathbf{X}_t = [{}_I x^G, {}_I y^G, {}_I \psi^G, V_x^I, \beta^I, \omega^I]_t \quad (1)$$

where, $[{}_I x^G, {}_I y^G]$ and ${}_I \psi^G$ are the IMU's position and orientation in the Global Reference Frame (\mathbf{G}). V_x^I, β^I , and ω^I are longitudinal velocity, side slip angle and yaw rate in IMU frame. The subindex t corresponds to the time instance.

If we represent \mathbf{X}_t^G as a set of the factor graph state till time instance t , the algorithm needs to estimate the posterior distribution $p(\mathbf{X}_t^G | \mathbf{Z}_t)$. Where \mathbf{Z}_t represents all the measurements from sensors till time instance t . Estimation can be performed using the Maximum A Posteriori (MAP) inference, for \mathbf{X}_t^G , which is represented as:

$$\mathbf{X}_t^G = \underset{\mathbf{X}_t^G}{\operatorname{argmax}}(p(\mathbf{X}_t^G | \mathbf{Z}_t)) \quad (2)$$

while we can approximate the posterior $p(\mathbf{X}_t^G | \mathbf{Z}_t)$ using the Baye's law as,

$$p(\mathbf{X}_t^G | \mathbf{Z}_t) \propto p(\mathbf{Z}_t | \mathbf{X}_t^G) p(\mathbf{X}_0) \quad (3)$$

where, $p(\mathbf{Z}_t | \mathbf{X}_t^G)$ is the measurement likelihood density and $p(\mathbf{X}_0)$ is the prior of the states. Given the measurements obtained from the LiDAR in the point cloud

format, linear acceleration, and angular velocities measurements from IMU, global position measurements in the latitude, longitude, and altitude format from the GNSS sensor, steering angle measurement from the steering encoder and longitudinal velocity measurement from the velocity encoder, the algorithm provides the estimates of \mathbf{X}_t^G at time instance t by solving Eq. (3) for the respective states.

The overall architecture of the algorithm is illustrated in Fig. 1 and detailed representation is provided in Fig. 2. The factor graph is designed to accommodate the vehicle dynamics factor as a base factor and add additional sensor measurements as per their availability.

2.1 Factor Graph

A factor graph is constructed by taking the synchronized In-Vehicle sensor's measurements as the reference points in a temporal sense. These sensors have the highest frequency in most sensor setups and hence can provide connection points to other sensors with a high degree of flexibility. Using the Robot Operating System (ROS) framework, the factor graph is constructed by taking their timestamps as the reference points, and new values are added to the graph concurrently. The modular nature of the graph enables the addition and removal of sensors based on their availability. The sensor setup consists of 2 GNSS Sensors, located at the front and the rear of the vehicle operating at 10 Hz, one Hesai 32 plane LiDAR operating at 20 Hz, one Bosch 5-axis IMU, and In-Vehicle sensors, all operating at 100 Hz.

Filter Like Architecture. The posterior distribution in Eq. 3 is proportional to the product of a prior distribution $p(\mathbf{X}_0)$ and the measurement likelihood $p(\mathbf{Z}_t|\mathbf{X}_t^G)$. This allows for an iterative solution to the MAP problem by moving the optimization horizon into a computationally tractable threshold [5]. The MAP inference referred to by Eq. 2 is solved by using factor graph [13] in this work. A factor graph is a bipartite graph, $\mathcal{G} = (\mathcal{V}, \mathcal{F})$ with \mathcal{V} being the set of values, \mathcal{F} being the set of factors. For a given factor graph, MAP inference in Eq. 2 can be rewritten as a product of multiple factors:

$$\mathbf{X} = \underset{\mathbf{X}}{\operatorname{argmax}} \prod_i \psi_i(X^i) \quad (4)$$

where the subscript i refers to the factor number. Each factor can be a result of measurement or constraint received from different sensors. Assuming that each factor is of a type,

$$\psi_i(X^i) \propto \exp\left\{-\frac{1}{2}\|h^i(X^i) - z^i\|_{\Sigma_i}^2\right\} \quad (5)$$

measurements from different sensors can be easily integrated into the factor graph if the measurement model given by $h^i(X^i)$ can be defined. The MAP inference problem can be modeled as a least square optimization problem with

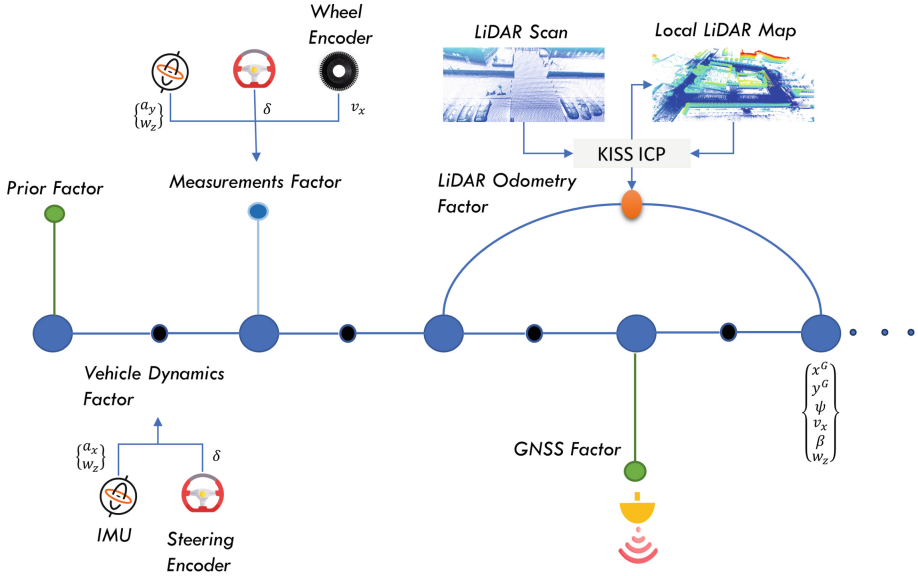


Fig. 2. Factor Graph construction displaying all the factors

the residual error given by $e^i = h^i(X^i) - z^i$. z^i is a measurement received from a sensor. The measurements are assumed to be normally distributed with zero mean and Σ_i covariance. This factorized implementation facilitates the modular architecture of the factor graph-based algorithm and hence enables sensor fusion for measurements coming from different sensors with different modalities.

In this work, we implement a filter-like factor graph-based state estimator taking inspiration from the work in [5]. Given that In-Vehicle sensors are the sensor with the highest frequency in most vehicles, its timestamp is used to add values to the factor graph. Having established a factor graph with reference values at high frequency, a variety of sensors can be easily integrated. Most control algorithms require the state to be estimated at a high frequency for smooth operation, however, LiDAR odometry and GNSS measurements are usually available at a lower frequency of (10–20) Hz. This filter-like implementation is designed using predict-optimize iterations to provide state estimates at In-Vehicle sensors' frequency. With each In-Vehicle sensor measurement, the state is predicted to the next time instance using single-track vehicle dynamics model, and once a LiDAR or GNSS factor is added to the graph, it is optimized to obtain an updated or optimized state.

2.2 Vehicle Dynamics Factor

To construct the factor graph within the framework, the vehicle dynamics are incorporated into residual error functions aimed at minimizing through factor graph optimization. Equation 6 represents the residual errors pertaining to

vehicle dynamics and connects two states or values, denoted as X^k and X^{k-1} within the graph. Here, v_y , v_x , and ω_z are the lateral, longitudinal, and angular velocities of the vehicle, respectively. Additionally, C_f and C_r denote the cornering stiffness of the front and rear tires, while l_f and l_r represent the distances from the vehicle’s center of gravity to the front and rear axles, respectively. The steering angle δ and longitudinal acceleration a_x are measured from the steering encoder and IMU. A single dynamic factor is established by linearizing Eq. 6. In the factor graph, values are added at the frequency of the In-Vehicle sensors, and two consecutive values are linked by factors, as depicted in Eq. 6.

$$\begin{aligned}
 e_x^{k-1} &= x^k - x^{k-1} - \Delta t(v_x^{k-1}(\cos(\psi^{k-1}) - \sin(\psi^{k-1})\beta^{k-1})) \\
 e_y^{k-1} &= y^k - y^{k-1} - \Delta t(v_x^{k-1}(\sin(\psi^{k-1}) + \cos(\psi^{k-1})\beta^{k-1})) \\
 e_\psi^{k-1} &= \psi^k - \psi^{k-1} - \Delta t\omega_z^{k-1} \\
 e_{v_x}^{k-1} &= v_x^k - v_x^{k-1} - \Delta ta_x^{k-1} \\
 e_\beta^{k-1} &= \beta^k - \beta^{k-1} + \Delta t \left(-\frac{C_f + C_r}{mv_x^{k-1}}\beta^{k-1} - \left(\frac{C_f l_f - C_r l_r}{m(v_x^{k-1})^2} + 1 \right) \omega^{k-1} + \frac{C_f \delta^{k-1}}{mv_x^{k-1}} \right) \\
 e_{\omega_z}^{k-1} &= \omega_z^k - \omega_z^{k-1} - \Delta t \left(-\frac{C_f l_f - C_r l_r}{J_z}\beta^{k-1} - \frac{C_f l_f^2 + C_r l_r^2}{J_z v_x^{k-1}} + \frac{C_f l_f \delta^{k-1}}{J_z} \right)
 \end{aligned} \tag{6}$$

2.3 Measurements Factor

The measurement factor incorporates lateral acceleration \hat{a}_y^k and yaw rate $\hat{\omega}_z$ measurements from IMU. It also includes longitudinal velocity measurement, \hat{v}_x from the velocity encoder. This integration is expressed through the residual of these measurements connected with the value at time instance k , denoted as X^k , as illustrated in Eq. 7. Additionally, the steering angle at time instance k , δ^k is also considered in the formulation.

$$\begin{aligned}
 e_{\hat{v}_x}^k &= \hat{v}_x - v_x^k \\
 e_{\hat{\omega}_z}^k &= \hat{\omega}_z - \omega_z^k \\
 e_{\hat{a}_y}^k &= \hat{a}_y^k + \frac{C_f + C_r}{m}\beta^k + \frac{C_f l_f - C_r l_r}{mv_x^k}\omega_z^k - \frac{C_f \delta^k}{m}
 \end{aligned} \tag{7}$$

2.4 GNSS and LiDAR Factors

GNSS sensor provides the location of the vehicle in the frame \mathbf{G} . The sensor setup has two RTK-corrected GNSS sensors located at the front and rear of the vehicle and hence can also provide information on the vehicle’s global yaw and pitch angle. The GNSS measurements are transformed into the IMU reference point of the vehicle and are subsequently added to the factor graph as a Unary factor using the known static transformation between the GNSS sensor and the IMU sensor.

$${}^I \hat{p}_t^G = \hat{p}_t^G + {}_{GN} R^I {}_{GN} p^I \tag{8}$$

where ${}^I\hat{p}^G$ is the GNSS measurement transformed to the IMU location in the vehicle expressed in the \mathbf{G} frame. ${}_{GN}R^I$ and ${}_{GN}P^I$ represent the rotation and translation component of the static transformation between IMU and the GNSS sensor.

To compute LiDAR Odometry we employ a lightly coupled odometry computer based on the work of [6]. In this approach, the odometry computer directly subscribes to the point cloud topics obtained from the LiDAR sensor and is used as a binary factor between two values corresponding to the timestamps of the consecutive LiDAR scan. The relative transformation between the two consecutive point clouds is used as the factor between the values in the graph closest to these timestamps.

3 Implementation

We design the factor graph and perform state estimation using the Fixed Lag Smoother in the GTSAM [7] framework. We use the ROS framework to establish callbacks to acquire sensor measurements and test real-time applicability. The proposed algorithm is validated against two model-based state estimators: an EKF [2] and an IMU preintegration-based factor graph [4]. We acquire test data with difficult maneuvers to demonstrate the algorithm’s ability to model vehicle lateral dynamics and its modularity to integrate arbitrary other sensors in the state estimation framework. We use a Datron optical sensor to measure the vehicle’s longitudinal and lateral velocities and validate the estimated state against it in complex maneuvers.

4 Results

A series of slalom maneuvers is performed to create the first scene. The trajectory of the vehicle’s motion along with the states estimated by the proposed algorithm and the baselines are illustrated by Fig. 3. Position estimation from the proposed algorithm and the baselines are very similar as they both use the RTK-corrected GNSS sensors, however, a significant improvement can be seen in the estimation of the side slip angle. We can observe that the side slip angle estimation from the proposed factor graph that utilizes a vehicle dynamics model for motion prediction matches closely to the estimation from the EKF and the Datron side slip computation, while estimation from the IMU factor graph is significantly worse in maneuver end situations.

In the second scenario, we use two scenes as shown in Fig. 4, to validate the algorithm, where we investigate a GNSS failure case. We eliminate the availability of both GNSS measurements to the algorithm after a certain time instance from the algorithm’s initiation and analyze its performance in terms of state estimation. This same procedure is applied to the baseline algorithms. Note, for the baseline EKF, the IMU and In-Vehicle sensors’ measurements are made consistently available and update respective states even in the absence of GNSS measurements in the failure scenario. Ground truth for position and yaw angle

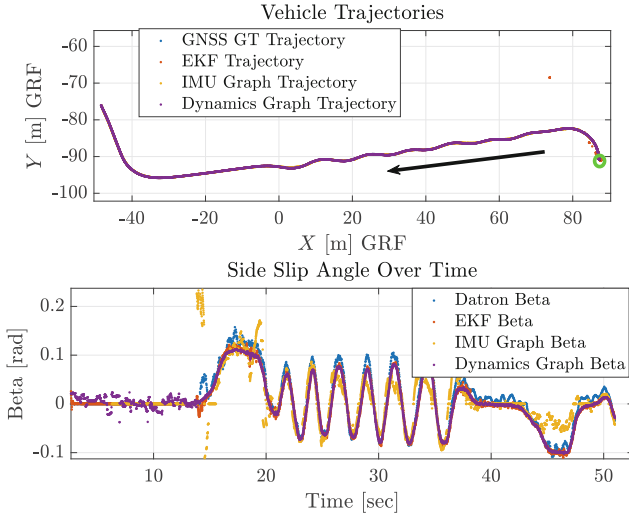


Fig. 3. Top Figure: Ground truth and estimated vehicle trajectories using the proposed and the baselines algorithms. The green circle indicates the start point while the arrow shows the vehicle motion direction. Bottom Figure: Ground truth and estimated side slip angles using the proposed and baseline algorithms

Table 1. Root Mean Square Error (RMSE) values for estimated states (Position, Yaw angle values) computed using the baselines EKF [2], IMU Graph [4] and the proposed algorithm

Algorithm	Scene 1	Scene 2
EKF [2]	3.0692, 0.1387	11.6245, 0.1520
IMU Graph [4]	1.1523, 0.0587	6.1375, 0.0827
Dynamics Graph	0.6005 , 0.0597	2.2953 , 0.0491

is computed using two RTK-corrected GNSS positions. Notably, since GNSS positions are unavailable from 5s onward for Scene 1 and 50s onward for Scene 2 into the algorithm run, the unused GNSS measurement serves as a reliable ground truth reference. This further emphasizes the robust performance of the proposed dynamics graph under GNSS failure conditions. The qualitative analysis presented in Fig. 4a reveals that the proposed algorithm consistently outperforms both the EKF [2] and the IMU factor graph [4] in terms of vehicle position estimation. Moreover, the estimation of the side slip angle from the proposed graph appears to be more accurate compared to the IMU graph and EKF. A similar level of performance is observed in the GNSS failure scenario in Scene 2, illustrated by Fig. 4b. The quantitative results are depicted in Table 1, supporting the findings and show that the proposed dynamics graph consistently outperforms both baseline algorithms in positional and yaw angle estimation. In

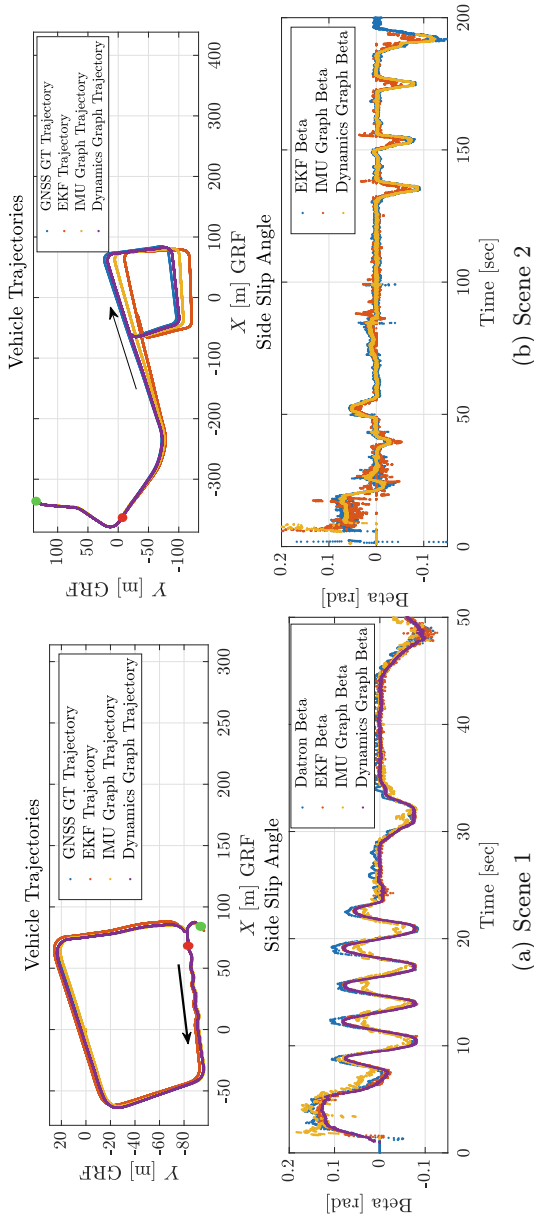


Fig. 4. Top Figure: Ground truth and estimated vehicle trajectories expressed in GRF. The green and red circles indicate the start point and GNSS failure point while the arrow shows the vehicle motion direction. Bottom Figure: Ground truth and estimated side slip angle in radians

total, we can observe up to 60% and 23% performance improvement on average, in terms of positional and yaw angle estimation respectively compared to the IMU graph.

5 Conclusion

We present a novel factor graph-based state estimation algorithm. The algorithm uses a vehicle dynamic factors to establish a base factor graph and integrates multiple asynchronous sensors like LiDAR, GNSS, etc. to provide consistent and accurate state estimation at high frequency. We validate the algorithm using data collected by an in-house vehicle with the defined sensor setup and multiple scenarios, where we simulate the GNSS sensor failure to check the reliability of the algorithm in urban settings. We were able to demonstrate that the proposed algorithm is highly modular and can seamlessly integrate multiple asynchronous sensors while providing reliable and robust state estimates compared to the baselines.

References

1. Bersani, M., et al.: An integrated algorithm for ego-vehicle and obstacles state estimation for autonomous driving. *Robot. Auton. Syst.* **139**, 103662 (2021)
2. Prakash, J., Vignati, M., Sabbioni, E.: Vehicle teleoperation: performance assessment of SRPT approach under state estimation errors, 2023
3. Leanza, A., Reina, G., Blanco-Claraco, J.-L.: A factor- graph-based approach to vehicle sideslip angle estimation. *Sensors* **21**(16) (2021). <https://www.mdpi.com/1424-8220/21/16/54093>
4. Dahal, P., Prakash, J., Arrigoni, S., Braghini, F.: Vehicle state estimation through modular factor graph-based fusion of multiple sensors. In: *IEEE Vehicle Power and Propulsion Conference (VPPC)*. Milan, Italy 2023, pp. 1–6 (2023). <https://doi.org/10.1109/VPPC60535.2023.10403196>
5. Nubert, J., Khattak, S., Hutter, M.: Graph-based multi-sensor fusion for consistent localization of autonomous construction robots. In: *2022 IEEE International Conference on Robotics and Automation (ICRA)*. IEEE (2022)
6. Vizzo, I., Guadagnino, T., Mersch, B., Wiesmann, L., Behley, J., Stachniss, C.: KISS-ICP: in defense of point-to-point ICP - simple, accurate, and robust registration if done the right way. In: *IEEE Robotics and Automation Letters (RA-L)*, vol. 8, no. 2, pp. 1029–1036 (2023)
7. Dellaert, F., Contributors, G.: “Borglab/ch1gtsam,” May 2022. <https://github.com/borglab/gtsam>
8. Bersani, M., Vignati, M., Mentasti, S., Arrigoni, S., Cheli, F.: Vehicle state estimation based on Kalman filters. In: *2019 AEIT International Conference of Electrical and Electronic Technologies for Automotive (2019)*
9. Kong, D., et al.: Vehicle lateral velocity estimation based on long short-term memory network. *World Electr. Veh. J.* **13**(1) (2021)
10. Revach, G., Shlezinger, N., Ni, X., Escoriza, A.L., van Sloun, R.J.G., Eldar, Y.C.: KalmanNet: neural network aided Kalman filtering for partially known dynamics. *IEEE Trans. Signal Process.* **70**, 1532–1547 (2022)

11. Dahal, P., Mentasti, S., Paparusso, L., Arrigoni, S., Braghin, F.: Robust-statenet: robust ego vehicle state estimation for autonomous driving. *Robot. Auton. Syst.* 104585 (2023). <https://www.sciencedirect.com/science/article/pii/S0921889023002245>
12. Frosi, M., Matteucci, M.: ART-SLAM: accurate real-time 6dof lidar slam, 2021
13. Dellaert, F., Kaess, M.: Factor graphs for robot perception. *Found. Trends Robot.* **6** (2017). <http://www.cs.cmu.edu/kaess/pub/Dellaert17fnt.pdf>
14. Chindamo, D., Gadola, M.: Estimation of vehicle side-slip angle using an artificial neural network. In: *MATEC Web of Conferences*, vol. 166, p. 02001, January 2018

Open Access This chapter is licensed under the terms of the Creative Commons Attribution 4.0 International License (<http://creativecommons.org/licenses/by/4.0/>), which permits use, sharing, adaptation, distribution and reproduction in any medium or format, as long as you give appropriate credit to the original author(s) and the source, provide a link to the Creative Commons license and indicate if changes were made.

The images or other third party material in this chapter are included in the chapter's Creative Commons license, unless indicated otherwise in a credit line to the material. If material is not included in the chapter's Creative Commons license and your intended use is not permitted by statutory regulation or exceeds the permitted use, you will need to obtain permission directly from the copyright holder.





Nonlinear Model Predictive Control for Enhanced Path Tracking and Autonomous Drifting Through Direct Yaw Moment Control and Rear-Wheel-Steering

Gaetano Tavolo¹(✉), Pietro Stano¹, Davide Tavernini¹, Umberto Montanaro¹,
Manuela Tufo^{2,3}, Giovanni Fiengo^{2,3}, Pietro Perlo⁴, and Aldo Sorniotti⁵

¹ University of Surrey, Guildford GU2 7XH, UK
g.tavolo@surrey.ac.uk

² University of Sannio, 82100 Benevento, Italy

³ Kineton R&D, 80146 Naples, Italy

⁴ Interactive Fully Electrical VehicleS (IFEVS), 10040 Turin, Italy

⁵ Politecnico di Torino, 10129 Turin, Italy

Abstract. Path tracking (PT) controllers capable of replicating race driving techniques, such as drifting beyond the limits of handling, have the potential of enhancing active safety in critical conditions. This paper presents a nonlinear model predictive control (NMPC) approach that integrates multiple actuation methods, namely four-wheel-steering, longitudinal tyre force distribution, and direct yaw moment control, to execute drifting when this is beneficial for PT in emergency scenarios. Simulation results of challenging manoeuvres, based on an experimentally validated vehicle model, highlight the substantial PT performance improvements brought by: i) vehicle operation outside the envelope enforced by the current generation of stability controllers; and ii) the integrated control of multiple actuators.

Keywords: active safety systems · electrified vehicles · modelling · testing and validation · autonomous drifting · nonlinear model predictive control

1 Introduction

Since 2014, the EU has mandated vehicle stability controllers (VSCs), enhancing active safety during emergency manoeuvres, through the limitation of the yaw rate error, sideslip angle, and longitudinal tyre slip [1, 2]. While these systems are effective in supporting the average human driver, they may be overly conservative for highly automated vehicles (AVs) [3]. In parallel, powertrain electrification and active chassis control systems offer new AV control opportunities [4]. A current trend in AV research involves

This work was supported by the Horizon 2020 Programme of the European Commission under Grant 101006953 (Multi-Moby project).

© The Author(s) 2024

G. Mastinu et al. (Eds.): AVEC 2024, LNME, pp. 854–861, 2024.

https://doi.org/10.1007/978-3-031-70392-8_120

emulating expert driving techniques, such as drifting, by using path tracking (PT) controllers that push the vehicle beyond the conventional VSC-related stability constraints, potentially improving road safety [5]. Several PT algorithms from the literature, e.g., [6, 7], achieve controlled drifting by tracking dedicated sideslip angle and yaw rate profiles, in addition to the reference trajectory. However, such controllers are not designed to induce drifting only when necessary to track a challenging trajectory, and are often demonstrated in scenarios with negligible vehicle speed variations or increasing speed, along circular paths or during drift parking, typically with rear-wheel-drive AVs [8, 9]. On the contrary, typical real-world emergency manoeuvres involve significant speed reductions through braking, imposed either by the human/automated driver and/or the VSC. Although the recent studies in [5] and [10] demonstrate the safety benefits of autonomous drifting in realistic scenarios, the literature lacks a performance assessment of different chassis actuation suites, and especially rear-wheel-steering (RWS), in terms of accident avoidance through AV control beyond the VSC-related boundaries. This paper targets the gap by proposing an NMPC algorithm that integrates four-wheel-steering, longitudinal tyre force distribution, and direct yaw moment (DYM) actuation. Simulation results with a high-fidelity model along two challenging manoeuvres show the controller's capability to perform drifting, and the benefit of rear steering actuation for achieving tighter cornering.

2 Control Architecture

Three alternative NMPC PT formulations are considered: i) $NMPC_{M_z, \delta_r}$, which is the novelty of the study, and controls (independently from each other) the time derivatives of the front and rear steering angles, $\dot{\delta}_f$ and $\dot{\delta}_r$; the time derivative of the longitudinal tyre force on the front axle, $\dot{F}_{x,f}$; the front-to-total force distribution factor in braking, p_b ; and the time derivative of the DYM, \dot{M}_z ; ; ii) $NMPC_{M_z}$, which, compared to $NMPC_{M_z, \delta_r}$, excludes $\dot{\delta}_r$ control; iii) $NMPC_{bas}$, which, compared to $NMPC_{M_z}$, excludes \dot{M}_z and p_b control. The control allocation (CA) algorithm is detailed in [5], and is integrated with a rule-based VSC, including a PID anti-lock braking system (ABS). In the $NMPC_{M_z, \delta_r}$ and $NMPC_{M_z}$ simulations, the VSC intervention thresholds are relaxed, to allow operation beyond the limits of handling.

2.1 Prediction Model Formulations

The prediction models are based on the single-track formulation in [5]. For brevity, only the updated longitudinal and lateral force balance and yaw moment balance equations for the $NMPC_{M_z, \delta_r}$ case are reported:

$$\begin{aligned} \dot{v}_x &= \frac{1}{m} [F_{x,f} \cos(\delta_f) - F_{y,f} \sin(\delta_f) + F_{x,r} \cos(\delta_r) \\ &\quad - F_{y,r} \sin(\delta_r) - F_{x,M_z} - F_{drag} - F_{roll} + mv_x \dot{\psi}] \\ \dot{v}_y &= \frac{1}{m} [F_{x,f} \sin(\delta_f) + F_{y,f} \cos(\delta_f) \\ &\quad + F_{x,r} \sin(\delta_r) + F_{y,r} \cos(\delta_r) - mv_x \dot{\psi}] \end{aligned}$$

$$\ddot{\psi} = \frac{1}{I_z} [F_{x,f} \sin(\delta_f) l_f + F_{y,f} \cos(\delta_f) l_f - F_{y,r} \cos(\delta_r) l_r - F_{x,r} \sin(\delta_r) l_r + M_z] \tag{1}$$

where m is the vehicle mass; I_z is the yaw mass moment of inertia; l_f and l_r are the front and rear semi-wheelbases; F_{drag} and F_{roll} are the aerodynamic drag and rolling resistance force; $F_{x,i}$ and $F_{y,i}$ are the longitudinal and lateral tyre forces of the axle i , where the subscript $i = f, r$ refers to the front or rear axles; and M_z is the direct yaw moment generated through the actuation of the friction brakes, while F_{x,M_z} is the corresponding longitudinal tyre force contribution. The lateral axle forces, $F_{y,i}$, are calculated through a simplified version of the Pacejka magic formula, whose vertical tyre force inputs account for both the static contribution and the longitudinal load transfer, based on the measured longitudinal acceleration, $a_{x,meas}$.

2.2 Optimal Control Problem

At each time step, the NMPC algorithm computes an optimal control sequence that minimizes a cost function, see its discrete form in [5], based on the outputs from the prediction models, which are expressed through the following continuous time formulation:

$$\dot{x}(t) = f(x(t), u(t), w(t)) \tag{2}$$

where x is the state vector, and u is the control input vector, which, for the three considered controller configurations, are expressed as:

$$\begin{aligned} x_{M_z, \delta_r} &= [v_x, v_y, \dot{\psi}, s, e_y, e_\psi, \delta_f, F_{x,f}, M_z, \delta_r] & u_{M_z, \delta_r} &= [\delta_f, \dot{F}_{x,f}, p_b, \dot{M}_z, \varepsilon_{M_z}, \delta_r] \\ x_{M_z} &= [v_x, v_y, \dot{\psi}, s, e_y, e_\psi, \delta_f, F_{x,f}, M_z] & u_{M_z} &= [\delta_f, \dot{F}_{x,f}, p_b, \dot{M}_z, \varepsilon_{M_z}] \\ x_{bas} &= [v_x, v_y, \dot{\psi}, s, e_y, e_\psi, \delta_f, F_{x,f}] & u_{bas} &= [\delta_f, \dot{F}_{x,f}] \end{aligned} \tag{3}$$

where s is the distance along the path; e_y is the lateral position error; e_ψ is the heading angle error; and ε_{M_z} is the slack variable associated with a soft constraint on the DYM. The online data vector, w , is the same for $NMPC_{M_z, \delta_r}$ and $NMPC_{M_z}$, i.e., $w_{M_z, \delta_r} =$

$w_{M_z} = [a_{x,meas}, \mu, \rho_{ref}, M_{z,min}, M_{z,max}]$, where μ is the tyre-road friction factor, which is assumed constant along the prediction horizon (H_p), while the reference road curvature (ρ_{ref}) and the maximum and minimum DYM values ($M_{z,max}$ and $M_{z,min}$) vary according to [5]. In $NMPC_{bas}$, w excludes $M_{z,min}$ and $M_{z,max}$. The output vectors and their reference values include the PT error variables and the states associated with the control inputs:

$$\begin{aligned} z_{M_z, \delta_r} &= [v_x, e_y, e_\psi, \delta_f, \delta_r, F_{x,f}, M_z] & z_{M_z, \delta_r, ref} &= [v_{x,ref}, 0, 0, 0, 0, 0, 0] \\ z_{M_z} &= [v_x, e_y, e_\psi, \delta_f, F_{x,f}, M_z] & z_{M_z, ref} &= [v_{x,ref}, 0, 0, 0, 0, 0] \\ z_{bas} &= [v_x, e_y, e_\psi, \delta_f, F_{x,f}] & z_{bas, ref} &= [v_{x,ref}, 0, 0, 0, 0] \end{aligned} \tag{4}$$

where the reference longitudinal speed, $v_{x,ref}$, is assumed to be known and variable along H_p . For all controllers, hard constraints are set on the steering angles, the front longitudinal tyre force, and their variation rates, as well as on the rear longitudinal tyre force:

$$\begin{aligned}
-\delta_{i,max} &\leq \delta_i \leq \delta_{i,max} \\
-\mu_{id} F_{z,f} &\leq F_{x,f} - F_{x,M_z} \frac{F_{z,f}}{\bar{F}_{z,f} + \bar{F}_{z,r}} \leq \mu_{id} F_{z,f} \\
-\hat{\delta}_{i,max} &\leq \hat{\delta}_i \leq \hat{\delta}_{i,max} \\
\hat{F}_{x,f,min} &\leq \hat{F}_{x,f} \leq \hat{F}_{x,f,max} \\
-\mu_{id} F_{z,r} &\leq F_{x,r} - F_{x,M_z} \frac{F_{z,r}}{\bar{F}_{z,f} + \bar{F}_{z,r}} \leq \mu_{id} F_{z,r}
\end{aligned} \tag{5}$$

where μ_{id} is an ideal friction factor, which marginally overestimates the real one used in the high-fidelity vehicle model to avoid underbraking, while the slip ratios are limited by the ABS, with relaxed intervention thresholds in case of $NMPC_{M_z, \delta_r}$ and $NMPC_{M_z}$; and the term F_{x, M_z} is present only in $NMPC_{M_z, \delta_r}$ and $NMPC_{M_z}$. $NMPC_{M_z}$ and $NMPC_{M_z, \delta_r}$ also include a hard constraint on p_b , a soft constraint on M_z , and a hard constraint on \dot{M}_z :

$$\begin{aligned}
p_{b,min} &\leq p_b \leq p_{b,max} \\
-\varepsilon_{M_z} + M_{z,min} &\leq M_z \leq M_{z,max} + \varepsilon_{M_z}, \text{ with } \varepsilon_{M_z} \geq 0 \\
\dot{M}_{z,min} &\leq \dot{M}_z \leq \dot{M}_{z,max}
\end{aligned} \tag{6}$$

where $M_{z,min}$ and $M_{z,max}$ are computed by the CA algorithm, based on the prediction of the control inputs at the previous time step.

3 Model Validation and Simulation Results

3.1 Case Study Vehicle

A four-wheel-drive electric vehicle (EV) prototype by IFEVS, with a centralized on-board electric machine per axle, is used as case study, see Fig. 1a. The EV is equipped with: i) a set of vehicle dynamics sensors, e.g., to measure the individual wheel speeds and the longitudinal and lateral velocity components; ii) an integrated GPS device with inertial measurement unit; iii) a modified commercial VSC unit to independently control the friction brake torque of each corner; and iv) a dSPACE MicroAutoBox III system for rapid control prototyping. The vehicle simulation model was implemented in the IPG CarMaker environment, and was experimentally validated along a handbrake manoeuvre, see Fig. 1b. The very good match between the experiments and the high-fidelity and prediction model results confirms: i) the reliability of the CarMaker model as a control system assessment tool; and ii) the ability of the proposed prediction models to accurately capture the system dynamics at the limit of handling.

3.2 Simulation Results

The NMPC implementations were evaluated along two manoeuvres, i.e., a 135-deg turn and a U-turn with braking from an initial speed of 45 km/h. For $NMPC_{M_z, \delta_r}$, different RWS angle limits, equal to 5, 10, and 15 deg, were set. Although higher than those for typical RWS systems, these values were selected to assess the potential advantages of

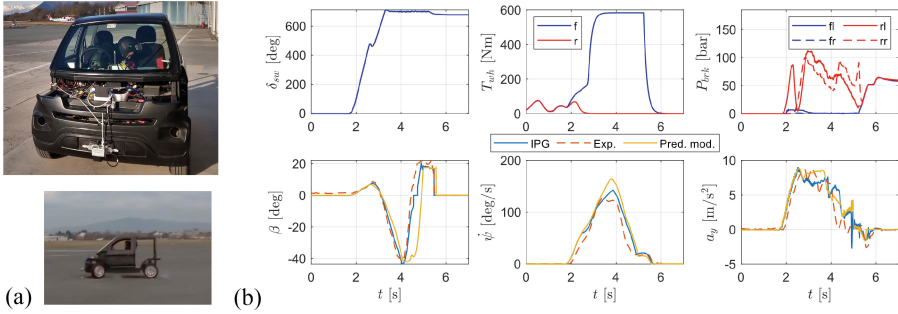


Fig. 1. (a) Case study EV prototype. (b) Time profiles of the hand-brake manoeuvre inputs, i.e., steering wheel angle δ_{sw} , wheel torque T_{wh} , and braking pressures P_{brk} , along with the associated sideslip angle β , yaw rate $\dot{\psi}$, and lateral acceleration a_y . IPG: CarMaker simulation model results; Exp.: experimental results; Pred. Mod.: prediction model results. The notations ‘fl’, ‘fr’, ‘rl’ and ‘rr’ refer to the front left, front right, rear left, and rear right corners.

enhanced rear steering capabilities. The 135-deg turn results are reported in Fig. 2a. The vehicle with $NMPC_{bas}$ significantly deviates from the reference trajectory, and exits the turn with unsafe lateral and orientation errors. On the contrary, the drifting behaviour induced by $NMPC_{M_z}$ and $NMPC_{M_z, \delta_r}$ enables the EV to effectively complete the manoeuvre. The DYM interventions create an asymmetric braking force distribution between the EV sides, resulting in increased yaw rate and rear slip angle magnitudes, which enhance manoeuvring agility. However, the M_z profile requested by the PT controller is very different from the one generated by the vehicle through the CA algorithm, see the mismatch between the ‘NMPC’ and ‘Plant’ curves in the M_z plot. This is caused by the absence of the lateral load transfer in the prediction model, and the purposely relaxed constraints on the longitudinal force and DYM, to fully utilise the tyre-road friction capability. While the δ_r actuation does not improve performance in the 135-deg turn, the counterphase actuation of δ_f and δ_r can facilitate vehicle oversteer [11], with potential benefits during more aggressive manoeuvres, such as the U-turn in Fig. 2b, for which a higher initial destabilizing effect is desirable. Since the inner wheel tends to be saturated during high lateral acceleration manoeuvring, the DYM intervention struggles generating the destabilizing effect required to induce controlled drifting, which, instead, can be more effectively induced with the RWS intervention. As a result, $NMPC_{M_z, \delta_r}$ generates higher yaw rates, reducing the DYM intervention as well as the lateral and speed tracking errors. For $NMPC_{M_z}$ and $NMPC_{M_z, \delta_r}$, Table 1 includes a set of PT key performance indicators (KPIs), including the maximum and root mean square (RMS) errors of the lateral position and speed, along with the maximum sideslip angle magnitude, indicating the extent of the controlled drifting behaviour. The RWS actuation of $NMPC_{M_z, \delta_r}$ reduces the lateral error by ~ 1.8 m during the U-turn test, compared to DYM intervention alone of $NMPC_{M_z}$. The best trade-off between the lateral and speed tracking errors is achieved with a maximum rear steering angle magnitude of 10 deg. A further increase to 15 deg results in higher $|\beta|_{max}$ (up to 44 deg), lower $RMS_{e_{v_x}}$, and increased $|e_y|_{max}$ (by 0.17 m).

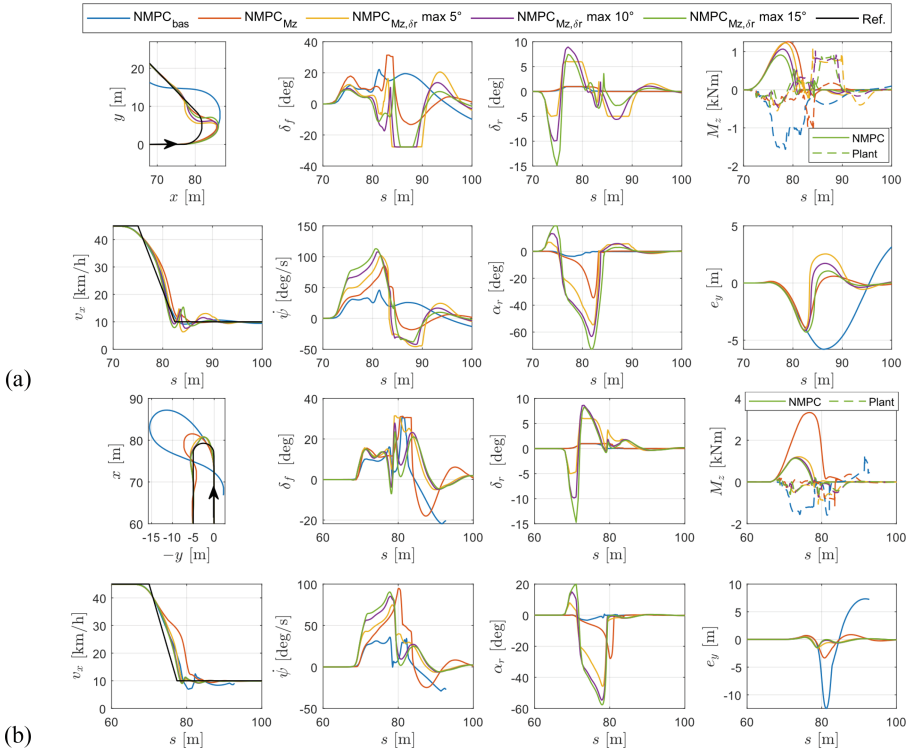


Fig. 2. Simulation results for (a) the 135-deg turn and (b) the U-turn, for $NMPC_{bas}$, $NMPC_{M_z}$, and $NMPC_{M_z, \delta_r}$ with maximum RWS angle constraints equal to 5, 10, and 15 deg.

Table 1. KPIs along the 135 deg-turn and U-turn (the best values are highlighted in bold).

Case	Configuration	$ e_y _{max}$	RMS_{e_y}	$RMS_{e_{v_x}}$	$ \beta _{max}$
		[m]	[m]	[km/h]	[deg]
135-deg turn	$NMPC_{M_z}$	3.88	0.988	1.574	17.3
	$NMPC_{M_z, \delta_r}, \delta_{r,max} = 5 \text{ deg}$	4.09	1.227	1.553	38.6
	$NMPC_{M_z, \delta_r}, \delta_{r,max} = 10 \text{ deg}$	4.16	1.131	1.176	53.1
	$NMPC_{M_z, \delta_r}, \delta_{r,max} = 15 \text{ deg}$	4.30	1.139	1.211	63.0
U-turn	$NMPC_{M_z}$	3.347	0.945	3.265	16.9
	$NMPC_{M_z, \delta_r}, \delta_{r,max} = 5 \text{ deg}$	1.572	0.397	1.618	27.8
	$NMPC_{M_z, \delta_r}, \delta_{r,max} = 10 \text{ deg}$	1.476	0.337	1.223	39.6
	$NMPC_{M_z, \delta_r}, \delta_{r,max} = 15 \text{ deg}$	1.493	0.329	1.110	44.2

4 Conclusion

The study introduced a nonlinear model predictive controller ($NMPC_{M_z, \delta_r}$) for the concurrent actuation of the front and rear steering angles, the total longitudinal tyre force and its distribution between the axles, as well as the direct yaw moment, to execute drifting manoeuvres when beneficial to the path tracking (PT) performance in emergency conditions. The simulation results, based on an experimentally validated vehicle model, highlight that: i) drifting is very effective in dealing with challenging trajectories that PT controllers coupled with conventional vehicle stability controllers cannot achieve (see the $NMPC_{bas}$ results), thereby enhancing the collision avoidance capability; and ii) in the more demanding scenario, i.e., the U-turn test, the rear steering actuation of $NMPC_{M_z, \delta_r}$ significantly enhances the tracking performance, by reducing the maximum lateral error by ~ 1.8 m compared to $NMPC_{M_z}$.

References

1. Tavolo, G., et al.: On antilock braking systems with road preview through nonlinear model predictive control. *IEEE Trans. Ind. Electron.* **71**(8), 9436–9448 (2024)
2. Chen, Y., et al.: Path tracking and handling stability control strategy with collision avoidance for the autonomous vehicle under extreme conditions. *IEEE Trans. Veh. Technol.* **69**(12), 14602–14617 (2020)
3. Stano, P., et al.: Model predictive path tracking control for automated road vehicles: a review. *Annu. Rev. Control.* **55**, 194–236 (2022)
4. Skrickij, V., et al.: Review of integrated chassis control techniques for automated ground vehicles. *Sensors* **2024**(24), 600 (2024)
5. Stano, P., et al.: Enhanced active safety through integrated autonomous drifting and direct yaw moment control via nonlinear model predictive control. *IEEE Trans. Intell. Veh.* **9**(2), 4172–4190 (2024)
6. Goh, J., et al.: Nonlinear Model Predictive Control for Highly Transient Autonomous Drifting. *AVEC'22* (2022)
7. Weber, T.P., Gerdes, J.C.: Modeling and control for dynamic drifting trajectories. *IEEE Trans. Intell. Veh.* **9**(2), 3731–3741 (2024)
8. Chen, G., et al.: Dynamic drifting control for general path tracking of autonomous vehicles. *IEEE Trans. Intell. Veh.* **8**(3), 2527–2537 (2023)
9. Bellegarda, G., Nguyen, Q.: Dynamic vehicle drifting with nonlinear MPC and a fused kinematic-dynamic bicycle model. *IEEE Control Syst. Lett.* **6**, 1958–1963 (2022)
10. Li, D., Zhang, J., Lin, S.: Planning and control of drifting-based collision avoidance strategy under emergency driving conditions. *Control. Eng. Pract.* **139**, 105625 (2023)
11. Shimada, K., Shibahata, Y.: Comparison of three active chassis control methods for stabilizing yaw moments. *SAE Trans.* **103**, 1178–1187 (1994)

Open Access This chapter is licensed under the terms of the Creative Commons Attribution 4.0 International License (<http://creativecommons.org/licenses/by/4.0/>), which permits use, sharing, adaptation, distribution and reproduction in any medium or format, as long as you give appropriate credit to the original author(s) and the source, provide a link to the Creative Commons license and indicate if changes were made.

The images or other third party material in this chapter are included in the chapter's Creative Commons license, unless indicated otherwise in a credit line to the material. If material is not included in the chapter's Creative Commons license and your intended use is not permitted by statutory regulation or exceeds the permitted use, you will need to obtain permission directly from the copyright holder.





Powerslide Control with Deep Reinforcement Learning

Florian Jaumann^{1,2}(✉), Tobias Schuster¹, Michael Unterreiner²,
Torben Gräber², Johannes Edelmann¹, and Manfred Plöchl¹

¹ TU Wien, Institute of Mechanics and Mechatronics, Vienna, Austria
tobias.schuster@tuwien.ac.at

² CARIAD SE, Vehicle Motion & Energy, Wolfsburg, Germany
florian.jaumann@cariad.technology

<https://www.mec.tuwien.ac.at/vsd>, <https://cariad.technology>

Abstract. Controlling a vehicle's powerslide motion in the presence of a human driver is a challenging control task, but one that may have a significant impact on vehicle safety, for example, during rapid evasive manoeuvres. Reinforcement Learning, a data-driven optimal control strategy, has gained increasing attention in recent years, demonstrating its effectiveness in successfully controlling various nonlinear systems. In this work, a novel powerslide controller is designed for an all-wheel drive battery electric vehicle with individually driven front and rear axles and a human driver in closed-loop using Reinforcement Learning. The performance of the proposed controller is analysed, and its robustness to steering disturbances and changes in road friction is demonstrated.

Keywords: Powerslide · Reinforcement Learning · Driver Assistance System · Powerslide Control · Drift Assistance · Optimal Control

1 Introduction and Related Work

The ability to control a vehicle in extreme driving conditions, such as the powerslide, where large vehicle sideslip angles, large traction forces and large negative steering angles occur, is of great interest to the automotive industry. Since the powerslide is an unstable motion, [4] addresses the observability and controllability characteristics for both rear-wheel drive (RWD) and all-wheel drive (AWD) vehicles. Depending on the drive concept, the powerslide can be stabilised in different ways. In recent years, Reinforcement Learning (RL), a data-driven control approach, has become increasingly popular and has been considered to stabilise the powerslide in this work. In [1] and [9], RL is used to control the steering wheel angle and the drive train in simulation, while in [2], RL-based controllers are successfully tested on radio-controlled (RC) model cars in real world. The development of battery electric vehicles (BEVs) and the possibility of using individual electric motors on each axle opens up new control strategies. While previous works considered the autonomous drift controlling both the vehicle's

drive train and the steering system, [3] proposes a linear controller that controls front and rear axle torques in the presence of a human driver. This controller shows great performance in simulation; however, when tested in the real world, it requires application effort to handle specific road conditions. In this work, a novel RL-based controller is proposed for an AWD BEV to control the individually driven front and rear axles with a human driver in the loop. Moreover, the robustness of the proposed controller in terms of steering disturbances from the driver and sudden road friction changes is analysed. Further, the controller is integrated into a test vehicle and the control performance is proven in a real-world test case. The remainder of this paper is structured as follows. In Sect. 2, the general problem setup, the vehicle model and the RL problem are introduced, while in Sect. 3, the test configuration and the results in simulation and in real world are presented. Section 4 gives a brief summary and an outlook.

2 Problem Formulation

This section introduces the vehicle and driver model used in the simulation environment, and the general methodology of RL.

Vehicle and Driver Model. The nonlinear two-wheel vehicle model in Fig. 1 at time step $t \in \mathbb{N}_0$

$$\mathbf{x}_{t+1} = \mathbf{f}_{\text{car}}(\mathbf{x}_t, \mathbf{u}_t), \tag{1}$$

is considered, with vehicle state $\mathbf{x} \in \mathcal{X}$ and input $\mathbf{u} = [\delta, T_{\text{front}}, T_{\text{rear}}]^T \in \mathcal{U}$, where T_{front} and T_{rear} denote the front and rear axle torques, respectively. In the presence of a human driver, the steering angle δ is defined by the nonlinear driver model [6]

$$\delta = \mathbf{f}_{\text{driver}}(\beta, v, e, \Delta\psi) \tag{2}$$

based on vehicle sideslip angle β , velocity v , lateral deviation e and orientation $\Delta\psi$ relative to the desired path.

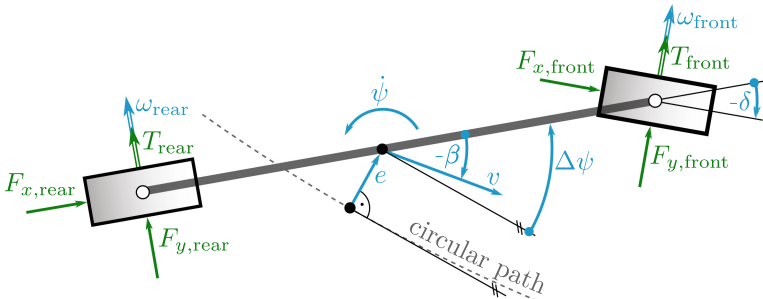


Fig. 1. Two-wheel vehicle model with independently driven front and rear axles.

Control Goal. While the driver (model) in (2) focuses only on path-tracking by applying δ , the RL-based controller’s task is to initiate and stabilise the powerslide by applying T_{front} and T_{rear} . Although the control tasks are separated, they are expected to interfere with each other.

Reinforcement Learning. In RL, an agent learns a policy based on the interaction with its environment. The agent acts on the environment using control $\mathbf{u}_t \in \hat{\mathcal{U}} = \mathcal{U} \setminus \{\delta\}$ sampled from policy $\pi_\theta(\mathbf{u}|\mathbf{x})$ with policy parameters θ based on the current environment state \mathbf{x}_t . The agent observes the next environment state \mathbf{x}_{t+1} and receives a reward r_{t+1} defined by the reward function R associated with the tuple $[\mathbf{x}_t, \mathbf{u}_t, \mathbf{x}_{t+1}]$. A Markov Decision Process (MDP) described by $\langle \mathcal{X}, \hat{\mathcal{U}}, R, \mathbf{f}_{\text{car}}, \mathcal{X}_0 \rangle$ is assumed, where $\mathcal{X}_0 \subseteq \mathcal{X}$ denotes the initial state distribution. Starting from an initial state $\mathbf{x}_0 \in \mathcal{X}_0$, the MDP forms a trajectory τ of states, actions and rewards. The central objective is to find an optimal control policy π^* that maximises the expected sum of discounted rewards

$$\pi^* = \arg \max_{\pi_\theta} \mathbb{E}_{\tau \sim \pi} \left[\sum_{t=0}^{\infty} \gamma^t r_t \right] \tag{3}$$

with discount factor $\gamma \in [0, 1]$ balancing the present impact of future rewards. To find policy parameters θ , optimisation problem (3) can be solved using policy gradient methods, e.g. Proximal Policy Optimization (PPO) [7,8].

Observation Space and Action Space. At each time step, only a subset of the entire environment state is visible to the agent. The observation space $\mathbf{o} = [\beta \ \dot{\psi} \ v \ \omega_{\text{front}} \ \omega_{\text{rear}} \ \delta \ \beta_{\text{target}} \ \beta_{\text{ref}}]^T$ comprises vehicle sideslip angle β , yaw rate $\dot{\psi}$, velocity v , angular speed of front axle ω_{front} and rear axle ω_{rear} , respectively, and the steering angle δ . Moreover, the agent receives information about the target steady-state vehicle sideslip angle β_{target} and the predefined vehicle sideslip angle reference trajectory β_{ref} on how to reach β_{target} . The vehicle sideslip angle reference is a ramp function with a slope of $-9^\circ/\text{s}$, derived from expert knowledge, converging to β_{target} . While the first six entries in \mathbf{o} reflect sensor information available in the car, the last two entries are required to fulfil the control task. To stabilise the powerslide, the agent can individually control both the front axle torque T_{front} and the rear axle torque T_{rear} , however only positive torque values are feasible, which excludes the possibility of braking.

Reward Function. During training, the agent tries to learn a policy that maximises the reward function. To simultaneously encourage the agent to stabilise the powerslide and to stay on the circular path,

$$R(\beta, e) = \sum_{i=1}^2 w_i R_i = w_{\text{slip}} R_{\text{slip}}(\beta) + w_{\text{path}} R_{\text{path}}(e), w_i \in [0, 1] \tag{4}$$

is chosen as a weighted sum of the reference vehicle sideslip angle tracking and the trajectory following reward R_{slip} and R_{path} , respectively. The reward terms $R_i = \exp(-c_i \Delta_i^2)$ with the deviation of the control target Δ_i and shaping parameter c_i ensure a positive learning signal.

3 Experiments

The agent is trained in simulation and evaluated in simulation and in real world.

Training and Network Architecture. Throughout the training, two multi-layer perceptron (MLP) networks are trained, one for the policy and one for the value function. Both networks share the same architecture, namely three hidden layers and use Exponential Linear Unit (ELU) activation functions. Before the observations are passed into the policy network, they are normalised to the range $[-1,1]$. The output of the policy network is clipped to the range $[-1,1]$ and scaled to the admissible torques. To improve exploration during the training, generalised state-dependent exploration (gSDE) is used. The learning rate is set to $2e-4$ and the discount factor to 0.9999 . ADAM is used to optimise the networks [5]. To accelerate the training, 40 environments are run in parallel. A training episode is terminated when it exceeds 40 seconds. However, it is prematurely terminated when the vehicle leaves the track or when the difference between the current vehicle sideslip angle and the reference exceeds a certain threshold. A rollout buffer size of 409600 and a batch size of 5120 are used.

3.1 Testing

The trained controller is tested in both simulation and real world.

Simulation. The controller is trained on different configurations of the environment, where each configuration is randomly initialised. In the first example, the controller is exemplarily evaluated with a target vehicle sideslip angle of -30 deg on a circular path with radius $R = 60$ m and friction coefficient $\mu = 0.21$, see Fig. 2. The vehicle starts with an initial velocity of 20 km/h and transitions into a stable powerslide motion following the vehicle sideslip angle reference β_{ref} . Figure 2 shows that the controller successfully learnt to transition the vehicle from regular steady-state cornering into powerslide and to stabilise the powerslide motion. To initiate the powerslide and to increase the vehicle sideslip angle, a high rear axle torque compared to the front axle torque is applied. Once the target vehicle sideslip angle is reached, front and rear torque converge to a fixed drive torque distribution of $\gamma = T_{rear}/(T_{rear} + T_{front}) = 0.84$.

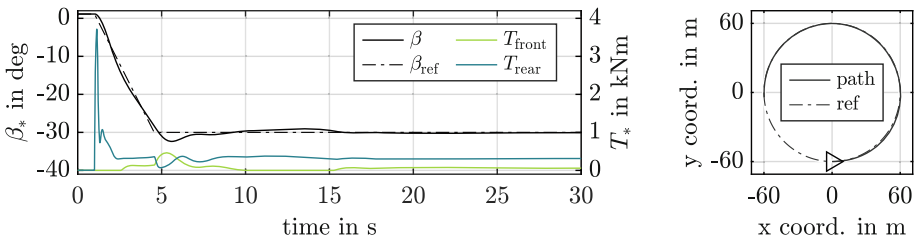


Fig. 2. Simulation of the powerslide with a target vehicle sideslip angle of -30° on a circular path with radius $R = 60$ m and friction coefficient $\mu = 0.21$.

In the second example, the controller’s robustness to steering and road friction disturbances is focussed. In the first scenario, a disturbance of the steering angle δ is considered, while in the second scenario, the road friction μ is instantaneously increased (μ_{\uparrow}) and decreased (μ_{\downarrow}). The steering angle disturbance is represented by a shifted cosine function over a single period of 0.5 s with an amplitude of 1.5° towards the inside (δ_{\uparrow}) and the outside (δ_{\downarrow}) of the turn. For these evaluations, the environment configuration is adapted to radius $R = 18.5$ m and friction coefficient $\mu = 0.35$, corresponding to the real-world setting. Figure 3 shows the vehicle sideslip angle trajectories resulting from the steering wheel angle disturbance and the change of the friction value. In both scenarios, the vehicle motion is successfully stabilised by the controller.

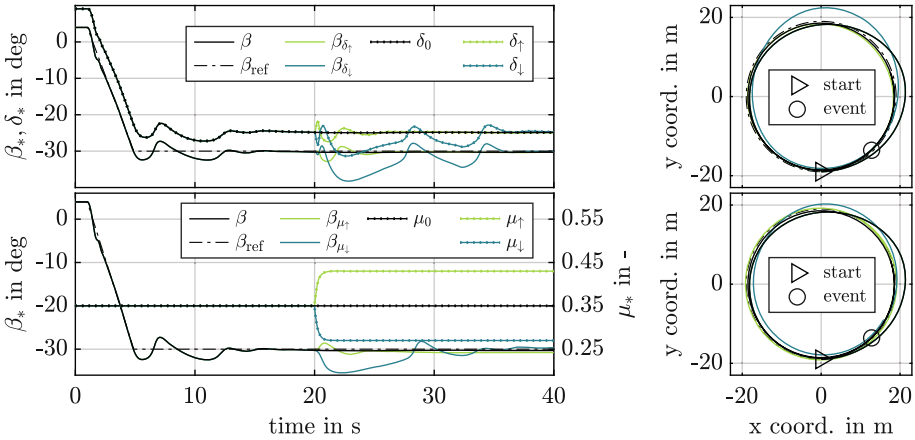


Fig. 3. Simulation of the powerslide with a target vehicle sideslip angle of -30° on a circular path with radius $R = 18.5$ m and friction coefficient $\mu = 0.35$. Robustness is analysed by applying a disturbance to the steering angle (upper plots) and a change of the road friction (lower plots) at time $t = 20$ s.

Real World. The controller is deployed on a conventional, consumer-grade computer, which is connected to the vehicle’s embedded hardware. The test vehicle is a series production electric sports car. Vehicle sensor data and computed controls are exchanged between the computer and the vehicle via the XCP-protocol using prototype hardware. The controller runs cyclically with a sampling frequency of 100 Hz. For the control task, only built-in sensor signals of the vehicle are used, except for the vehicle sideslip angle, which is provided by an additional inertial measurement unit (IMU) mounted in the car. The measurements are collected on a watered circuit with 18.5 m radius and an estimated friction coefficient of 0.35. In the experiment, the vehicle starts in regular steady-state cornering with an initial speed of 20 km/h and after time step $t = 5$ s, it transitions to the powerslide with a target vehicle sideslip angle of -30° , see Fig. 4. The controller stabilises the powerslide motion, however, oscillations of the vehicle side slip

angle are present. This could be due to the driver influence, latencies or sensor noise in the control loop.

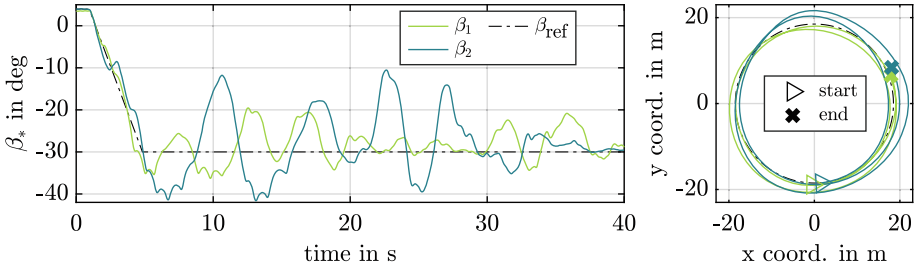


Fig. 4. Measurements of the powerslide with a target vehicle sideslip angle of -30° on a circular path with 18.5 m radius and an estimated friction coefficient of 0.35. Vehicle sideslip angles β_1 and β_2 were recorded with different drivers.

4 Summary and Outlook

In this paper, an RL-based controller is developed to stabilise the powerslide of a vehicle with a human driver in charge of steering only. This is achieved by controlling the front and rear axle torques of an AWD BEV. The control performance of the powerslide controller on a circular path both in simulation and in the real world is demonstrated. For the latter case, the controller is tested in a series production electric sports car. The experiments clearly show that the proposed controller reacts appropriately to steering disturbances and instantaneous changes in the friction coefficient, revealing the robustness of the controller. Moreover, the tests prove that the controller, which was exclusively trained in simulation is also capable of stabilising the powerslide motion in real-world application. This indicates the capability of RL controllers to bridge the simulation to reality gap, since it has to deal with unmodelled real-world phenomena.

Future work should investigate the performance of RL-based controllers across a broader range of drivers, friction coefficients, and vehicle platforms.

Acknowledgements. We thank the ÖAMTC Fahrtechnikzentrum Wachau for providing the test track, Dr. Ing. h.c. F. Porsche AG for their support, and the Vienna Scientific Cluster for computational resources.

References

1. Cai, P., Mei, X., Tai, L., Sun, Y., Liu, M.: High-speed autonomous drifting with deep reinforcement learning. *IEEE Robot. Autom. Lett.* **5**(2), 1247–1254 (2020)
2. Domberg, F., Wemmers, C.C., Patel, H., Schildbach, G.: Deep drifting: autonomous drifting of arbitrary trajectories using deep reinforcement learning. In: *International Conference on Robotics and Automation (ICRA)*, pp. 7753–7759 (2022)

3. Eberhart, M., Plöchl, M., Unterreiner, M., Edelmann, J.: Insights into the stability and control of the powerslide for variable drive torque distribution applied to a driver assistance system. (submitted)
4. Edelmann, J., Plöchl, M.: Controllability of the powerslide motion of vehicles with different drive concepts. *Procedia Eng.* **199**, 3266–3271 (2017). x Int. Conf. on Structural Dynamics, EUROLYN
5. Kingma, D., Ba, J.: Adam: a method for stochastic optimization. In: International Conference on Learning Representations (ICLR). San Diego, CA, USA (2015)
6. McRuer, D., Graham, D., Krendel, E., Reisener, W.: Human-pilot dynamics in compensatory systems: an abstract of U.S. government report AFFDL-TR-65-15. *IEEE Trans. Hum. Factors Electron.* **HFE-6**(1), 84–84 (1965)
7. Raffin, A., Hill, A., Gleave, A., Kanervisto, A., Ernestus, M., Dormann, N.: Stable-baselines3: reliable reinforcement learning implementations. *J. Mach. Learn. Res.* **22**(268), 1–8 (2021)
8. Schulman, J., Wolski, F., Dhariwal, P., Radford, A., Klimov, O.: Proximal policy optimization algorithms. arXiv preprint [arXiv:1707.06347](https://arxiv.org/abs/1707.06347) (2017)
9. Tóth, S.H., Ádám Bárdos, Viharos, Z.J.: Tabular q-learning based reinforcement learning agent for autonomous vehicle drift initiation and stabilization. *IFAC-PapersOnLine* **56**(2), 4896–4903 (2023). 22nd IFAC World Congress

Open Access This chapter is licensed under the terms of the Creative Commons Attribution 4.0 International License (<http://creativecommons.org/licenses/by/4.0/>), which permits use, sharing, adaptation, distribution and reproduction in any medium or format, as long as you give appropriate credit to the original author(s) and the source, provide a link to the Creative Commons license and indicate if changes were made.

The images or other third party material in this chapter are included in the chapter's Creative Commons license, unless indicated otherwise in a credit line to the material. If material is not included in the chapter's Creative Commons license and your intended use is not permitted by statutory regulation or exceeds the permitted use, you will need to obtain permission directly from the copyright holder.





Simulating Effects of Suspension Damper Degradation on Common Sensor Signals for Diagnosis Models in the Context of Condition-Based Maintenance

Lorenz Ott^{1,2}(✉), Torben Gräber¹, Michael Unterreiner¹, Johannes Edelmann²,
and Manfred Plöchl²

¹ TU Wien, Institute of Mechanics and Mechatronics, Vienna, Austria
lorenz.ott@cariad.technology

² CARIAD SE, Vehicle Motion & Energy, Wolfsburg, Germany

Abstract. Degraded suspension dampers strongly influence vehicle safety and ride comfort, but often occur after several years of operation. Related workshop checks are usually not degradation-adaptive, so they can be significantly delayed to the need for maintenance. To make the maintenance adaptive to degradations, onboard diagnosis methods can be used, which rely on the degradation status extracted from sensor signals. To support the development of sensitive yet robust diagnosis models, a model that can simulate and explain the effects of damper degradation in common sensor signals is proposed. This paper focuses on low-frequency effects in signals of the wheel speed sensors, which are ultra low cost and always available in modern vehicles. As a result, the model shows a good qualitative match to real-world test drives, specifically in the frequency domain. Therefore, various real-world measurements were conducted, in particular, test bench measurements of degraded dampers and vehicle on-road tests.

Keywords: condition-based maintenance · damper degradation · diagnosis models

1 Introduction

New trends in automotive mobility, such as shared vehicles and highly automated driving, require advanced methods to self-responsibly diagnose maintenance needs. In contrast to regular, pre-scheduled, or reactive maintenance, advanced maintenance strategies have a decisive advantage: the maintenance activity can be adapted to the actual degradation state. These maintenance strategies include so-called condition-based maintenance, based on diagnostic models that continuously monitor the degradation status of one or more components. The paper focuses on the suspension damper, which often degrades over time; according to a report, more than every hundredth vehicle fails a regular

check after seven years due to faults related to suspension springs and dampers, [1]. Wheel speed sensors are ultra low cost, available in every modern vehicle and are close to suspension dampers, which makes them attractive as limited sensor set. The analysis of wheel speed signals in the presence of degraded dampers shows that effects from degradation occur in the frequency domain, see Fig. 1.

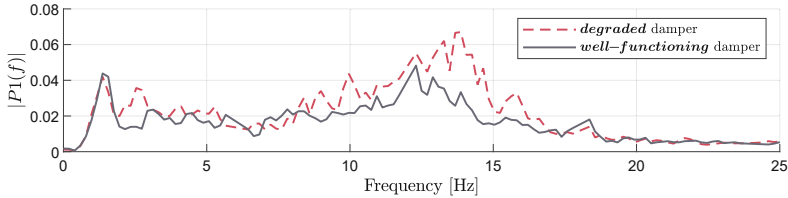


Fig. 1. Measured effects of damper degradation on wheel speed signals

Therefore, the focus of this paper is to explain, how these effects are transmitted from the damper to the signals and how they depend on chassis parameters and environmental conditions. Existing studies focus directly on the development of diagnosis models, e.g., [2–4], rather than on explanations of these effects. Building up a deeper understanding of these effects could potentially help to develop sensitive yet robust diagnosis models. In contrast, approaching the diagnosis model development purely data-driven demands excessive data collection due to the high variance of chassis parameters, including different suspension damper and spring variants and different tyres, in different vehicle models.

2 System Model

Dynamics simulation that can handle degradation effects and parameter variations can help to better understand these effects. To select a suitable model, an approximately constant vehicle speed is assumed, thus pitch and roll motions are neglected. Consequently, a quarter-car model with single-point excitation serves as a base model for this study, see, e.g., [5]. The frequency range of interest is limited to the vertical natural frequency of the un-sprung mass m_2 , typically between 12–15 Hz [6]. To simulate the wheel speed signals, the quarter-car model is extended by a rotational degree of freedom of the wheel. The angular velocity of the wheel is denoted ω . Consequently, we add to the equations of motion of the quarter-car model, Euler’s law for the wheel, equation (2), where I_2 denotes the wheel polar moment of inertia, r_l is the loaded radius and F_x the longitudinal tyre force. In addition, a moment M_y is introduced, which represents rolling resistance effects and the influence of tyre eccentricity. Typically, the natural frequency related to the un-sprung mass in the longitudinal direction lies in the frequency range of interest. Thus, the model is further extended by the equation of motion (1) in the longitudinal direction, with longitudinal suspension stiffness c_{S_x} and damping coefficient k_{S_x} . For all model-based analyses, the model is parametrised with values from [7]. A schema of the model is depicted in Fig. 2.

The road is modeled as stochastic excitation, [5], whereby the waviness is kept constant with a value of 2, and the degree of unevenness is varied in typical values. A single-contact-point transient tyre model, [7], is applied; decoupling of belt and rim mass is not considered since the frequency range of interest is well below the in-plane first natural frequency. Due to the assumed constant vehicle speed v_1 , the slip states are small, and tyre forces are assumed to be linear with respect to the transient longitudinal slip κ' in (3), where $C_{F\kappa}$ denotes the longitudinal slip stiffness, κ' the longitudinal transient slip, u the longitudinal tyre deflection in the contact patch and σ_κ , the relaxation length. The first-order differential Eq. (4) is employed, where the input is the longitudinal slip velocity $V_{sx} = V_2 - r_{\text{eff}} \cdot \Omega$. For the simulation of the effects of the degradation of the suspension damper, the damping coefficient k_{Sz} is reduced by 30%.

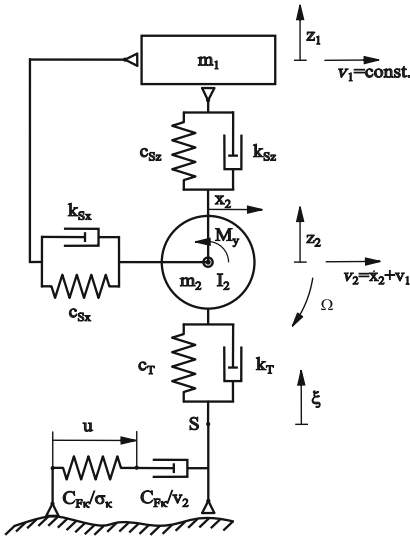


Fig. 2. Schema of the system model

$$m_2 \ddot{x}_2 + c_{Sx} x_2 + k_{Sx} \dot{x}_2 - F_x = 0 \quad (1)$$

$$I_2 \dot{\omega} + r_L F_x + M_y = 0 \quad (2)$$

$$F_x = C_{F\kappa} \cdot \kappa', \quad \kappa' = u / \sigma_\kappa \quad (3)$$

$$\dot{u} + v_2 u / \sigma_\kappa = -v_2 + r_{\text{eff}} \cdot \Omega \quad (4)$$

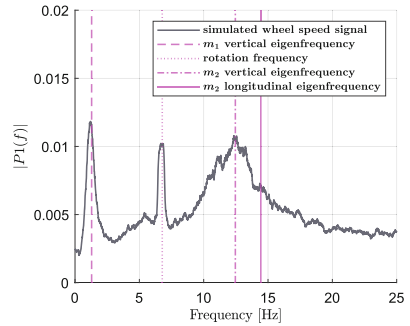


Fig. 3. FFT of simulated wheel speed signal

For a more detailed analysis and later comparison of simulation and measurement results, measurements with an Audi A6 are performed. The relevant model parameters are measured on a Kinematic and Compliance Test Rig. Further measurements include measuring the suspension spring and the damper in new condition and with 50% oil loss, and the suspension stiffness in the longitudinal direction.

3 Results

The simulation results are analysed in the frequency domain. Figure 3 shows the relevant characteristic frequencies. These frequencies include the natural frequencies related to the sprung mass, to the un-sprung mass in vertical and longitudinal directions, and to the rotation frequency of the wheel. In the following, the influence of M_y is neglected in the simulation results and related effects in the measurement signals are filtered out.

From (2), it is evident that the wheel speed ω is influenced by the term $r_L F_x$, which depends on the parameters r_{eff} , σ_κ , $C_{F\kappa}$, all functions of wheel load F_z , [7]. Variations of σ_κ and $C_{F\kappa}$ with F_z do not exhibit significant effects on the simulated wheel speed. Therefore, the subsequent analysis focuses on the parameters r_L and r_{eff} . For both, a linear dependency on F_z is assumed based on values from [7]. If dependencies are set to zero, degradation effects cannot be observed. It becomes clear that r_{eff} and r_L couple the vertical motion and effects of a degraded damper (influencing the wheel load) with the rotational wheel motion and wheel speed ω .

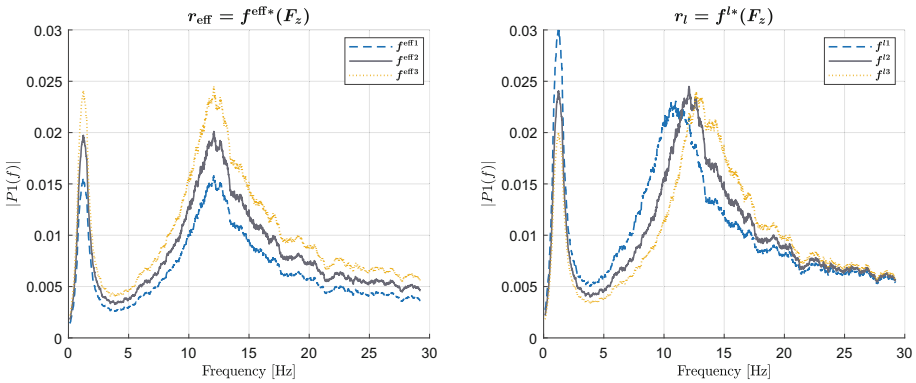


Fig. 4. Sensitivity analysis of wheel speed signals to tyre parameter variations

Figure 4 illustrates that a variation of the loaded radius with wheel load, $f^{\text{eff}*}(F_z)$, affects the simulated wheel speed across the investigated frequency range; an increasing slope in the linear relationship amplifies the vibrations. The dependency of the effective rolling radius on the wheel load, $f^{l*}(F_z)$, affects the simulated wheel speed vibrations below 20 Hz. In addition to changes in magnitude, also the vertical natural frequency of m_2 is shifted. An increasing slope shifts the natural frequency towards greater values.

Besides the tyre parameters, road roughness and vehicle speed show considerable effects on the wheel speed in simulation, which are not addressed here in more detail.

Figure 5 depicts the simulated wheel speeds for a well-functioning and a degraded suspension damper. In comparison to Fig. 1, it is remarkable, that degradation-induced effects within the frequency range related to the natural

frequency of the sprung mass, at approximately 1.4 Hz, are observable in the simulated signals but remain absent in the measurements. Furthermore, the measurements reveal effects spanning the frequency spectrum from 3 to 11 Hz, which are not evidently mapped by the simulation results. The measurements show an influence concentrated around the vertical natural frequency of the un-sprung mass, approximately within the range of 11 to 16 Hz. This phenomenon is captured by the simulation. Beyond 16 Hz, both the simulated and measured signals show negligible effects.

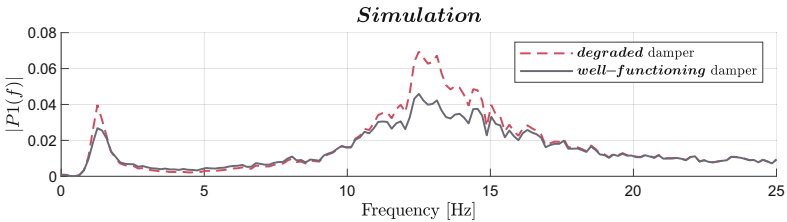


Fig. 5. Spectra of simulated wheel speeds for a well-functioning and a degraded suspension damper

The influence of road roughness can be observed in other measurements, which is mapped well by the simulation. However, the simulation results show a strong dependency on vehicle speed, which cannot be confirmed by the measurements. If the vertical tyre stiffness c_T and the effective rolling radius r_{eff} become functions of vehicle velocity and inflation pressure, as addressed in [8], the simulation to reality gap is decreased.

4 Discussion and Conclusion

The above findings outline the potential of physics-based models to simulate the effect of suspension damper degradation on wheel speed signals. The model can be parameterised with few parameters, and it can be used to explain measured degradation effects and further to systematically develop a diagnosis model for condition-based maintenance. A respective physics-informed machine learning diagnosis will be published in a further research paper soon, which uses physics-based knowledge derived from the system model above.

First, the simulation of degradation effects can be used to engineer features with a high degradation-information to noise ratio. The simulation results indicate that frequency-based features in the range of 12 to 15 Hz are particularly suitable.

Second, the sensitivity analysis reveals that the model parameters influencing wheel speed signals, aside from damper degradation, can be confined to a limited set. This knowledge is significant as it gives an argued indication of critical parameter combinations for the development and testing of a diagnosis

model, where the challenge is to remain robust against varying vehicle and environmental parameters while also being efficient, e.g., collecting no data of not influencing parameters.

The results demonstrate that vehicle speed, road roughness and the influence of tyre radii depending on wheel load should be considered for a diagnosis model. The sensitivity analysis shows, that these parameters influence the wheel speed signals within the frequency range associated with a damper degradation effect, which indicates that diagnosis purely based on wheel speed signals is difficult.

Future research may focus on methods that can fuse information from estimated environment and vehicle parameters and features that include information about the degradation state, enhancing both diagnostic sensitivity and robustness in real-world scenarios. Moreover, discrepancies between simulated and measured signals revealed areas for further refinement.

References

1. TÜV Süd. Die häufigsten Mängel, 2024. <https://www.tuvsud.com/de-de/publikationen/tuev-report/die-haeufigsten-maengel>. Accessed 16 Jan 2024
2. Jautze, M.: Ein Signalmodellbasiertes Verfahren zum Erkennen von Dämpferschäden bei Kraftfahrzeugen: Zugl. Erlangen-Nürnberg, Univ., PhD-Thesis (2002)
3. Zehelein, T., Merk, A., Lienkamp, M.: Damper diagnosis by artificial intelligence. In: 9th International Munich Chassis Symposium 2018: Chassis. Tech Plus, pp. 461–482. Springer, Wiesbaden (2019). https://doi.org/10.1007/978-3-658-22050-1_31
4. Zehelein, T., Hemmert-Pottmann, T., Lienkamp, M.: Diagnosing automotive damper defects using convolutional neural networks and electronic stability control sensor signals. *J. Sens. Actuator Netw.* **9**(8) (2020)
5. Mitschke, M., Wallentowitz, H.: Dynamik der Kraftfahrzeuge. Springer Fachmedien Wiesbaden, Wiesbaden (2014). <https://doi.org/10.1007/978-3-658-05068-9>
6. Klinger, F.: Kombinierte Betrachtung passiver und (semi-)aktiver Radaufhängungen mittels äquivalenter Fahrwerksparameter. TU Wien, PhD-Thesis (2018)
7. Pacejka, H.B.: Tyre and Vehicle Dynamics, 2nd edn. Butterworth-Heinemann, Oxford (2006)
8. Besselink, I.J.M., Schmeitz, A.J.C., Pacejka, H.B.: An improved Magic Formula/Swift tyre model that can handle inflation pressure changes. *Veh. Syst. Dyn.* **48**(S1) (2010)

Open Access This chapter is licensed under the terms of the Creative Commons Attribution 4.0 International License (<http://creativecommons.org/licenses/by/4.0/>), which permits use, sharing, adaptation, distribution and reproduction in any medium or format, as long as you give appropriate credit to the original author(s) and the source, provide a link to the Creative Commons license and indicate if changes were made.

The images or other third party material in this chapter are included in the chapter's Creative Commons license, unless indicated otherwise in a credit line to the material. If material is not included in the chapter's Creative Commons license and your intended use is not permitted by statutory regulation or exceeds the permitted use, you will need to obtain permission directly from the copyright holder.





Controllability of Steer-by-Wire Steering Angle Faults at the Limits of Driving Dynamics

Janick Birkemeyer¹ (✉), Lukas Borkowski¹, Ingo Wülfing², and Steffen Müller²

¹ Volkswagen AG, Berliner Ring 2, 38436 Wolfsburg, Germany
janick.birkemeyer@volkswagen.de

² Chair of Automotive Engineering, Technische Universität Berlin, Gustav-Meyer-Allee 25,
13355 Berlin, Germany

Abstract. To ensure functional safety of vehicle dynamics controllers, monitoring functions are used to limit the effectiveness of lateral dynamic inputs to a safe, controllable level. For this purpose, driving situation dependent limits for maximum permissible lateral dynamic inputs are determined with the help of subject studies. To exploratively investigate limits of a steer-by-wire superposition function in a nonlinear driving situation, a subject study (N = 52) was conducted in a semi-dynamic driving simulator. This paper presents the study design and discusses the results obtained. A 4 × 4 within subject design including an additional baseline condition was used to investigate the independent variables steering angle fault and side slip angle. First, significant effects on the maximum lateral deviation and the integral of the side slip angle are demonstrated with a two-way ANOVA, thus proving the methodical approach. Second, limits for permissible additional steering input of a steer-by-wire system in an oversteering driving situation are determined from the obtained data.

Keywords: Steer-by-Wire · Functional Safety · Controllability

1 Introduction

Controllability in vehicle dynamics is generally considered as the driver's ability to follow a desired course by having a direct feedthrough of control inputs via the steering wheel [1]. It is the task of functional safety to ensure this controllability even in the event of failures by limiting their effectiveness [2]. For this purpose, driving situation dependent limits for maximum permissible dynamic inputs are determined with the help of subject studies where system faults are systematically injected [3]. With the use of new actuators such as steer-by-wire systems, which offer additional degrees of freedom for lateral control, the limits of driving dynamics are of increasing interest for such controllability studies. Thus, this paper presents the design and the results of a subject study investigating the effects of faults of a steer-by-wire superposition function.

Previously published studies have largely defined the driving situation by variations of vehicle speed and lateral acceleration and are therefore based on common standards [4]. Neukum et al. [5] have previously investigated superposition steering system faults,

but restricted their analysis to a maximum steering fault of 3° at tire level and only considered straight-ahead driving. Schneider [6] also examines higher yaw moment disturbances, triggered by faults in the ESC actuators, but also refers to straight-ahead driving. In both cases, the authors argue that straight-ahead driving represents a worst-case scenario when assessing lateral dynamic malfunctions [7]. However, it remains open to what extent the limits shift during transient maneuvers. To investigate the impact of steering torque recommendation, Mehrjerdian et al. [8] investigated the driver's reaction in an oversteer situation, reproducing side slip angles of approx. 3° using a kickplate.

In contrast to the research mentioned above, the study presented in this paper is intended to take the increased potentials of steer-by-wire based superposition systems into account by assessing larger fault amplitudes in more critical driving situations characterized by higher side slip angles. It focusses on faults which decrease the yaw reaction since this is the effective operating area of superposition steering systems in oversteering driving situations. The following research questions are mainly addressed: (1) Do steering faults of a superposition steer-by-wire system which decrease the yaw reaction lead to a reduction in controllability at the limits of driving dynamics? (2) How do the effects of such steering angle faults differ depending on the criticality of the initial driving situation?

To answer the research questions a subject study on a semi-dynamic driving simulator was conducted. The study design uses a new methodical approach to conduct subject tests at the limits of driving dynamics in a reproducible manner. Thus, the evaluation of the applied methods and evaluation criteria is also part of this paper's contribution. Methods and design of the subject study are explained in more detail hereinafter.

2 Study Design

In total, 52 (age range = 20–65 years) participants took part in the study. The participants had a valid driving license for an average of 18 years and reported a yearly driving amount from 5.000 to more than 50.000 km. Two thirds of the participants reported having prior experience in simulated driving environments. 33% of the participants attended safe-driving trainings.

2.1 Driving Maneuver and Fault Injection

To investigate the research questions described above, the participants experienced the following driving situation: Driving on a rural road with a reference trajectory defined by a pylon lane and a center line. The road consisted of 32 consecutive curves with a length of 240 m and a radius of 75 m. To simplify the driving task and to standardize the driving situation, a constant speed of 86 km/h was set using cruise control. This speed results in stationary circular driving close to the maximum adhesion utilization of the tires.

The cornering was divided into three phases (Fig. 1b). In phase I, the vehicle was set to a defined side slip angle β_0 by a controlled traction stimulus at the rear axle in order to create a reproducible unstable driving situation. A reversible, initially yaw-decreasing steering angle fault δ_F was then injected near the curve apex over a period of 1 s. It is

known from literature that compensatory actions of a driver generally start 250 ms after fault injection and are completed after 1.5 s [5]. Thus, the chosen fault duration is within the most critical time frame. Figure 1a shows an example of stimulus \bar{M} relative to the maximum drive torque and steering fault δ_F .

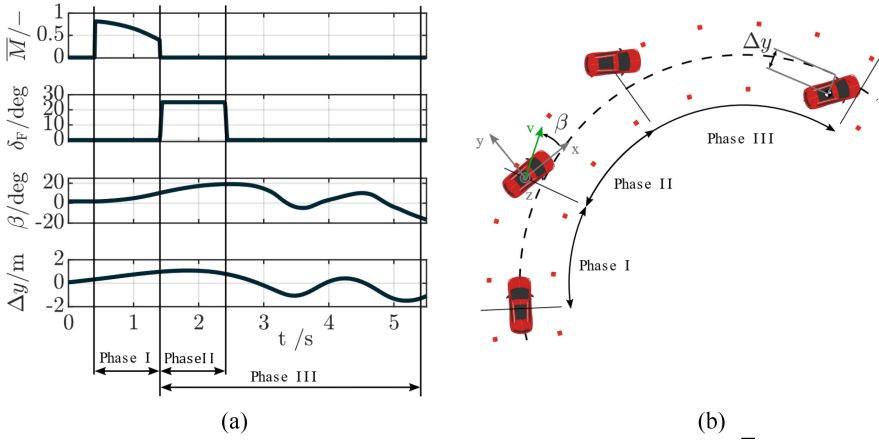


Fig. 1. Side slip angle β and lateral deviation Δy based on the lateral stimuli \bar{M} and δ_F (a) during an example cornering with separated phases for destabilization (Phase I), fault injection (Phase II) and evaluation (Phase III) (b).

2.2 Study Design and Procedure

A 4×4 within-subject design including additional baseline conditions was used to examine the independent variables initial side slip angle $\beta_{0,m}$ at the end of phase I and amplitude of steering angle fault $\hat{\delta}_{F,n}$. Each combination of $\beta_{0,m}$ and $\hat{\delta}_{F,n}$ defines a specific test condition (TC_{mn}). During baseline conditions (BL_{m0}), the participants experienced solely an unstable driving situation without any steering angle fault. The baseline conditions serve as controllability references of the nonlinear driving situation to objectively evaluate the criticality of injected steering angle faults. Each participant experiences conditions shown in Table 1 two times, once for left and once for right hand curves.

Two dependent variables were chosen to evaluate the criticality of the test conditions defined above. First, the integral of the absolute side slip angle $|\beta|$ during phase III generally indicates the instability of the driving situation [9]. Second, the maximum lateral deviation $|\Delta y|_{\max}$ from the reference line is used to evaluate the ability to follow the track. In the following, both values are used as indicators for the criticality of a steering angle fault. In contrast to former controllability studies, no absolute criterion was used to assess pass or fail of a test condition. Instead, we use baseline-related values for the dependent variables:

$$\overline{f|\beta|}_{TC_{mn}} = \frac{\int |\beta|_{TC_{mn}}}{\max(\int |\beta|_{BL_{m,R}}; \int |\beta|_{BL_{m,L}})} \quad (1)$$

Table 1. Test conditions of the 4×4 within-subject design including baseline conditions ($\hat{\delta}_{F,0} = 0^\circ$)

		Amplitude of steering angle fault $\hat{\delta}_{F,n}$ (deg)			
		0	25	50	75
Initial side slip angle $\beta_{0,m}$ (deg)	0	BL ₁₀	TC ₁₁	TC ₁₂	TC ₁₃
	5	BL ₂₀	TC ₂₁	TC ₂₂	TC ₂₃
	10	BL ₃₀	TC ₃₁	TC ₃₂	TC ₃₃
	15	BL ₄₀	TC ₄₁	TC ₄₂	TC ₄₃

$$\overline{|\Delta y|_{\max \text{TCmn}}} = \frac{\Delta |y|_{\max, \text{TCmn}}}{\max(\Delta |y|_{\max, \text{BLm,R}}; \Delta |y|_{\max, \text{BLm,L}})} \quad (2)$$

For each $\beta_{0,m}$ there is a baseline value for a left-hand (L) and a right-hand (R) curve. In Eqs. (1) and (2), the maximum of these two values is used to consider the most critical cornering without steering angle fault. According to these definitions, a baseline-related value greater than 1 corresponds to increased criticality as a consequence of a steering angle fault.

3 Results

For the analysis a data set of 48 valid test runs was used. A significance level of $\alpha = 0.05$ was defined for all inferential statistical tests. The curve direction had no significant effect on the dependent variables ($p_{f\beta} = 0.26$, $p_{\Delta y} = 0.21$). Therefore, the measurements for left and right curves were combined into a repeated measures model in the following analyses. The Mauchly test revealed that the requirement for sphericity of the measurement data is not fulfilled. The differences in variance are plausible due to the changed criticality of the driving situations caused by the independent variables. However, in the following evaluation Huynh-Feldt (HF) corrected p-values are used to compensate the violation of sphericity.

3.1 General Inferential Statistics

The results of a two-way ANOVA carried out for the repeated measures model are listed in Table 2. The results of the significance test (p_{HF}) reveal significant effects of β_0 and δ_F on both dependent variables ($p_{HF} < .001$). Based on the explained variation ($\eta^2 p$), the effect size f can be determined according to Cohen [10]. Following Cohen's classification of the effect size f , the measurement data shows an almost entirely strong effect ($f > 0.4$) of the within-subject factors on $\overline{f|\beta|}$ and $\overline{\Delta |y|_{\max}}$. A medium effect can be observed for the interaction $\delta_F : \beta_0$ on the dependent variable $\overline{f|\beta|}$ ($f > 0.25$). These results show that the study design effectively captures the relationship between independent and dependent variables in a nonlinear driving situation.

Table 2. Metrics for the assessment of the chosen study design

		Dependent variables	
		$\overline{f \beta }_{TCmn}$	$\overline{\Delta y _{max}}_{TCmn}$
Within-subject factor	δ_F	$p_{HF} < .001; \eta^2 p = 0.47; f = 0.94$	$p_{HF} < .001; \eta^2 p = 0.53; f = 1.06$
	β_0	$p_{HF} < .001; \eta^2 p = 0.32; f = 0.68$	$p_{HF} < .001; \eta^2 p = 0.23; f = 0.54$
	$\delta_F : \beta_0$	$p_{HF} < .001; \eta^2 p = 0.08; f = 0.29$	$p_{HF} < .001; \eta^2 p = 0.19; f = 0.48$

3.2 Descriptive Analysis

To determine maximum permissible yaw-decreasing faults, the medians of the baseline-related maximum lateral deviation $\overline{\Delta|y|_{max}}$ and integral of side slip angle $\overline{f|\beta|}$ are examined. Figure 2 summarizes the results for all test conditions. Values greater than 1 correspond to an increase in the lateral deviation or integral of side slip angle compared to the baseline condition and thus indicate reduced controllability resp. Increased instability of the driving situation. The comparison shows that the impact of the steering angle fault δ_F on both dependent variables tend to diminish as the initial side slip angle β_0 increases. For lower initial side slip angles ($\beta_0 = \{0^\circ, 5^\circ\}$) the median values of both dependent variables increase with increasing steering fault. Whereas for $\beta_0 = \{10^\circ, 15^\circ\}$ even improvements in stability and controllability are observable.

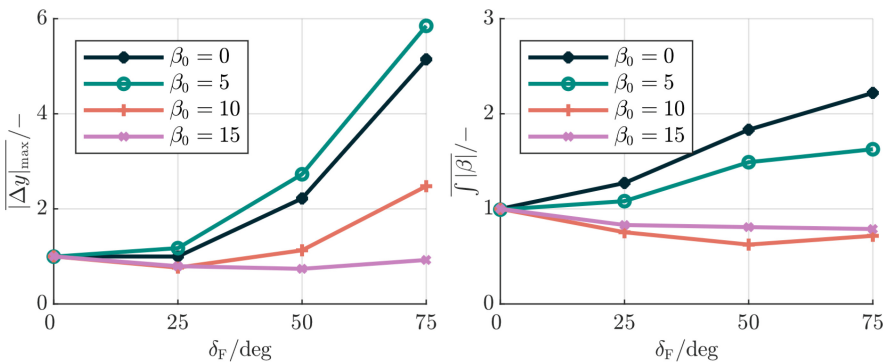


Fig. 2. Median values for baseline-related values of the maximum lateral deviation and the integral of side slip angle

This descriptive observation is supported by one-tailed t-tests. The results show a significant increase in the mean values of $\overline{f|\beta|}$ for all test conditions compared to the baseline conditions ($p < .01$) at lower initial side slip angles ($\beta_0 = \{0^\circ, 5^\circ\}$). For higher

initial side slip angles $\beta_0 = \{10^\circ, 15^\circ\}$, no significant difference in mean values could be detected ($p > .99$).

No significant differences between mean values of baseline and test conditions were also found for $\overline{\Delta|y|_{max}}$ at $\beta_0 = 15^\circ$ ($p = .28$). For $\beta_0 = 10^\circ$, there is a significant increase for test conditions with $\delta_F = \{50^\circ, 75^\circ\}$ ($p < .01$). For a steering angle fault of 25° , there is no significant difference in the means ($p = .78$).

4 Discussion

The subject study identified significant effects caused by steering angle faults which decrease the yaw reaction in the nonlinear region of driving dynamics. Due to the high effect sizes, the proposed study design is suitable for investigating controllability in oversteering driving situations. Based on the descriptive analysis, the initially formulated research questions can be answered as follows: Yaw decreasing steering angle faults can reduce controllability at the limits of driving dynamics. The impact depends on the amplitude of the steering angle fault and the criticality of the initial situation. The steering angle faults investigated in this study were even found to improve controllability as the initial side slip angle increased. In summary, only the test conditions TC₃₁, TC₄₁, TC₄₂ and TC₄₃ (see Table 1) show an improvement in stability and controllability according to the analysis in Sect. 3.2 and can therefore be assessed as permissible. In further investigations, additional grid points of the independent variables, especially at smaller side slip angles, should be examined to enable correlation analysis.

References

1. Hoffman, R.C., Stein, J.L., Louca, L.S., Huh, K.: Using the Milliken moment method and dynamic simulation to evaluate vehicle stability and controllability. In: ASME International Mechanical Engineering Congress and Exposition, Dynamic Systems and Control, Parts A and B (2004)
2. RESPONSE-Consortium: Code of practice for the design and evaluation of ADAS (2009)
3. ISO 26262-10: Road vehicles - Functional safety – Part 10: Guidelines on ISO26262 (2011)
4. VDA: Situationskatalog E-Parameter nach ISO 26262-3:2018 (2023)
5. Neukum, A., Ufer, E., Paulig, J., Krueger, H.P.: Controllability of superposition steering system failures. In: Steering Tech 2008 (2008)
6. Schneider, N., Schmitz, M., Ahrens, L., Löffler, C., Neukum, A.: Der Toleranzansatz als Methodik zur Bewertung der Kontrollierbarkeit höherer Eingriffsstärken bei Falschauslösung eines systeminitiierten Ausweichmanövers mit ESP-Aktorik. In: Workshop Fahrerassistenzsysteme und automatisiertes Fahren (2018)
7. Neukum, A., Ufer, E., Schwab, M.: Kontrollierbarkeit potenzieller Fehleingriffe des elektronischen Stabilitätsprogramms (ESP). In: Ika, vol. 7 (2010)
8. Mehrjerdian, E., Gaedke, A., Greul, R., Bertram, T.: Efficiency of steering torque recommendation in limits of driving dynamics: an empirical study. In: 6th IFAC Symposium Advances in Automotive Control (2010)
9. Wey, T., Weimann, U., Esser, F.: Methoden und Kriterien zur objektiven Beurteilung der Sicherheit von Fahrstabilitätssystemen. In: 1. Tagung Aktive Sicherheit durch Fahrerassistenzsysteme (2004)

10. Cohen, J.: Statistical Power Analysis for the Behavioral Sciences, 2nd edn. Erlbaum, Mahwah (1988)

Open Access This chapter is licensed under the terms of the Creative Commons Attribution 4.0 International License (<http://creativecommons.org/licenses/by/4.0/>), which permits use, sharing, adaptation, distribution and reproduction in any medium or format, as long as you give appropriate credit to the original author(s) and the source, provide a link to the Creative Commons license and indicate if changes were made.

The images or other third party material in this chapter are included in the chapter's Creative Commons license, unless indicated otherwise in a credit line to the material. If material is not included in the chapter's Creative Commons license and your intended use is not permitted by statutory regulation or exceeds the permitted use, you will need to obtain permission directly from the copyright holder.





An Automated Lane-Change System Based on Probabilistic Trajectory Prediction Network

Yoonyong Ahn¹(✉), Sangwon Han¹, Jihoon Sung¹, Jaeho Choi¹,
and Kunsoo Huh²

¹ Department of Automotive Engineering (Automotive-Computer Convergence),
Hanyang University, Seoul 04763, Republic of Korea

yahoo0515@hanyang.ac.kr

² Department of Automotive Engineering, Hanyang University,
Seoul 04763, Republic of Korea

Khuh2@hanyang.ac.kr

Abstract. In highway driving, understanding the intentions of surrounding vehicles is a crucial prerequisite to ensure collision-free lane changes. In this study, an automated lane change system framework is proposed for highway driving. A Long Short-Term Memory (LSTM)-based network is utilized to predict the paths of surrounding vehicles as probability distributions. When initiating a lane change, multiple candidate paths are generated, and the collision probability is then calculated by considering the generated paths of the host vehicle and the predicted paths of surrounding vehicles. Using the vehicle as a reference, the collision risk area is defined first related to the lane change. Secondly, the probability of the predicted distribution of the surrounding vehicles existing within this area is integrated to derive the collision probability. Subsequently, the collision-free optimal path is adopted, and Model Predictive Control (MPC) is employed for path tracking. The proposed framework was validated on a highway-like proving ground.

Keywords: trajectory prediction · risk assessment

1 Introduction

The safety and importance of lane changes on highways are critical in autonomous driving. Ensuring these maneuvers are safe is essential for efficient navigation and obstacle avoidance. Recent advancements have emphasized the need for reliable automated lane-change systems, drawing significant attention from researchers and industry professionals [8].

Trajectory prediction of surrounding vehicles is essential for safe lane changes. Despite progress in predicting vehicle trajectory using various learning-based models, real-world application remains limited [4]. Few studies have implemented these systems in actual vehicles, highlighting a gap between theory and practice.

© The Author(s) 2024

G. Mastinu et al. (Eds.): AVEC 2024, LNME, pp. 883–889, 2024.

https://doi.org/10.1007/978-3-031-70392-8_124

Although various studies have been conducted on risk assessment, it is common to predict the trajectories of surrounding vehicles using simple models such as constant velocity and acceleration models [5].

Therefore, this paper aims to bridge these gaps by presenting an automated lane-change system using a probabilistic trajectory prediction network. Through risk assessment between the predicted trajectory and the generated lane change candidates, the optimal lane change trajectory is generated. The real-time effectiveness of the proposed framework is validated through real vehicle experiments.

2 Probabilistic Trajectory Prediction Network

In this study, an efficient LSTM encoder-decoder network structure [3], ensuring real-time performance, is employed to predict the trajectories of surrounding vehicles in the form of a probability distribution.

2.1 Input and Output Representation

The input of the network at timestep $t = T$ is the past trajectory of the target vehicle, X_{hist} , in the following form.

$$X_{hist}(T) = [(x^{T-T_h}, y^{T-T_h}), \dots, (x^{T-1}, y^{T-1}), (x^T, y^T)] \quad (1)$$

where x , y indicate the position of the target vehicle and T_h is the length of the history. The output of the network is a bivariate normal distribution of the future trajectory, represented by mean and variance.

$$Y_{pred}(T) = [f_{xy}^{T+1}, \dots, f_{xy}^{T+T_f-1}, f_{xy}^{T+T_f}] \quad (2)$$

where T_f is the length of the predicted future trajectory and

$$f_{xy} = [(\mu_x, \mu_y, \sigma_x, \sigma_y, \rho)] \quad (3)$$

is the parameters of the bivariate normal distribution. The interaction between the ego and target vehicle is considered by extracting the spatial vehicle interaction feature using convolutional social pooling [1].

2.2 Input Data Preprocessing

Since surrounding vehicles are detected through perception sensors, the initially obtained position of the target vehicle are based on the local coordinate of the ego vehicle. To enable the network to effectively learn the dynamic characteristics of the target vehicle and its relationship with the lane, the trajectory of the target vehicle are transformed into lane coordinate-based position.

Therefore, a two-step coordinate transformation is applied. First, the position of the target measured in the local coordinate system $(x, y)_{lo}$ is transformed

into the position in the global coordinate system $(x, y)_g$ using the vehicle's localization data:

$$(x, y)_g = T_1((x, y)_{lo}; (X, Y, \theta)_{ego}) \quad (4)$$

where T_1 is the rigid transformation matrix and $(X, Y, \theta)_{ego}$ represents the global position and heading angle of the ego vehicle. Next, with the stacked trajectory history in the global coordinate $X_{hist,g}$, using the map data of the current driving lane, the lane heading is calculated and the global position is transformed into the lane coordinate system:

$$X_{hist,la} = T_2(X_{hist,g}; \theta_{la}) \quad (5)$$

where T_2 is the rigid transformation matrix and θ_{la} is the lane heading angle in the global coordinate. Note that $X_{hist,la}$ is transformed so that the current position $X_{hist,la}(T_h + 1) = (0, 0)$. Once the prediction is performed, the output (lane coordinate) is transformed back to the local coordinate.

2.3 Dataset and Training

The proposed method is trained using a dataset that combines the HighD dataset with data acquired from real-world vehicle experiments. Since the network's output follows a normal distribution, we employ the negative log-likelihood as the training loss.

3 Collision Risk Assessment

3.1 Lane Changing Trajectory Candidate Generation

Using the lane information, lane change (LC) trajectories are generated in the Frenet frame [2], allowing for easy and intuitive application of planning. Polynomial trajectories are generated based on conditions such as initial position, final position, and acceleration constraints. This process results in several candidate trajectories $X_{plan}^{(n)}$, where $1 \leq n \leq N$ and N is the number of the candidates.

3.2 Risk Probability Calculation

When approximating the shapes of the ego vehicle and target vehicle as rectangles, the trace of the center point of the target vehicle in situations where the two rectangles overlap can be defined as the collision area S_{col} . The bivariate normal distribution predicted for the center point of the target vehicle is integrated within this area to calculate the collision probability. Since the probability of collision can be considered as the maximum collision probability during the prediction horizon, the collision probability between the candidate n and the predicted trajectory of the target vehicle during the prediction horizon can be defined as follows.

$$P_{col}^{(n)}(T) = \max_{T \leq t \leq T+T_f} p^{(n)}(t) \quad (6)$$

where

$$p^{(n)}(t) = \int_{(x,y) \in S_{col}^{(n)}(t)} g(x, y; t) dx dy \tag{7}$$

and $g(x, y)$ is the probability density function of the bivariate normal distribution which is formed by the network output f_{xy} .

Meanwhile, if the ego vehicle is steering to change lanes, the shape of S_{col} becomes an octagon, making integration difficult. Since the shape is still convex, it can be replaced with a rectangular shape S'_{col} satisfying $S_{col} < S'_{col}$, where the area is approximately similar [6]. This does not underestimate the collision probability since $P_{col} < P'_{col}$ is always satisfied because $g(x, y) > 0$. Assuming the size of the ego and target vehicle is similar, S'_{col} can be defined as:

$$S'_{col}(t) = \{(x, y) | x_{min} \leq x \leq x_{max}, y_{min} \leq y \leq y_{max}\} \tag{8}$$

where

$$\begin{aligned} x_{min} &= x_{plan}^{(n)}(t) - \frac{\sqrt{w^2 + l^2}}{2} \cos(\tan^{-1}(\frac{w}{l} - \Theta)) - l \\ x_{max} &= x_{min} + 2l + l \cos \Theta + w \sin \Theta \\ y_{min} &= y_{plan}^{(n)}(t) - \frac{\sqrt{w^2 + l^2}}{2} \sin(\tan^{-1}(\frac{w}{l} + \Theta)) - w \\ y_{max} &= y_{min} + 2w + w \cos \Theta + l \sin \Theta \end{aligned} \tag{9}$$

Here, w and l are the width and length of the vehicle, and Θ is the heading angle difference between the vehicles. $x_{plan}^{(n)}(t)$ and $y_{plan}^{(n)}(t)$ indicate the planned position of candidate n at time t .

The bivariate normal distribution does not have an explicit integration form (i.e., cumulative distribution). Therefore, the risk probability P_{col} is calculated using the numerical method known as the Darboux integral. To avoid underestimating the probability due to errors caused by the method, the upper Darboux sum is considered. Defining finite sequences with equal intervals $x_{min} = x_0 < x_1 < \dots < x_m = x_{max}$ and $y_{min} = y_0 < y_1 < \dots < y_k = y_{max}$, Eq. (7) can be approximated as follows:

$$p = \sum_{i=0}^{m-1} \sum_{j=0}^{k-1} \sup_{\substack{x \in [x_i, x_{i+1}] \\ y \in [y_j, y_{j+1}]}} g(x, y) \Delta x \Delta y \tag{10}$$

where Δx and Δy are intervals along the local coordinate.

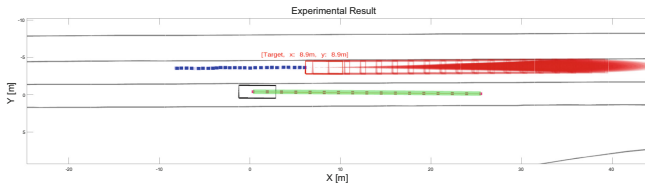
If there exists a lane change candidate within the collision probability threshold, and among them, candidate n^* with the smallest lateral acceleration is selected as the final reference $X_{ref} = X_{plan}(n^*)$.

4 Lane Change Controller

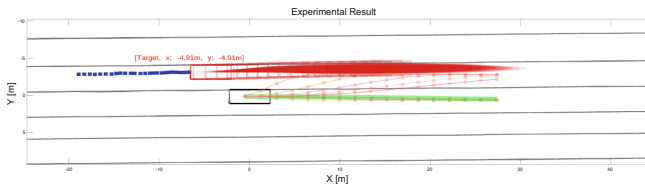
Given the reference lane change trajectory X_{ref} , a linear MPC is constructed based on the lateral bicycle model of the vehicle [7]. The optimal steering angle is achieved by minimizing the cost function of the MPC, which mainly consists of lateral error and steering angle rate.

5 Experimental Results

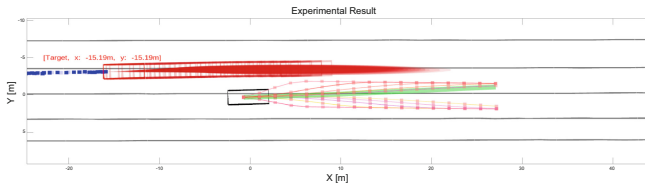
To validate the proposed framework, actual experiments were conducted. The experiments took place at a proving ground, designed in the form of a highway. The prediction network was implemented on a mid-performance laptop in a Robot Operating System environment, while the controller was developed in the MATLAB/Simulink environment. Real-time control was executed through the MicroAutobox II. The sampling time for the prediction network and risk assessment is 70 ms and 50 ms for the controller.



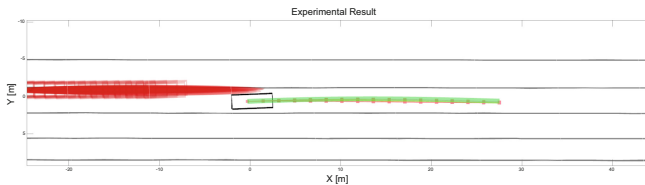
(a) The target vehicle (red) traveling in the left adjacent lane at a speed similar to that of the ego vehicle (black)



(b) Despite the LC intention, a collision is anticipated in the generated LC trajectory candidate (pink). As a result, the optimal trajectory is determined to be the lane keeping trajectory (green).



(c) As the target vehicle decelerates, a collision-free trajectory is generated (green)



(d) After the lane change, lane keeping is initiated again

Fig. 1. Experimental result

Figure 1 shows the result when the ego vehicle attempts a lane change to the left while there is a vehicle traveling at a similar speed in the left lane. The results show that the proposed framework has been validated to ensure a collision-free and safe lane change in real-time scenarios.

6 Conclusion

In this paper, a novel framework for automated lane change system is proposed. The framework is consist of trajectory prediction network, collision risk assessment module, and the controller. The proposed framework was validated in a highway-like proving ground. Applications of more complicated scenarios is planned for future work.

Acknowledgments. This work was supported by the Technology Innovation Program (Industrial Strategic Technology Development Program, Development of Test Procedure Standards for Vehicle-to-Infrastructure (V2I) Connected Automated Driving Systems) funded by the Ministry of Trade, Industry and Energy (MOTIE), South Korea, under Grant 20014460.

References

1. Deo, N., Trivedi, M.M.: Convolutional social pooling for vehicle trajectory prediction. In: Proceedings of the IEEE Conference on Computer Vision and Pattern Recognition Workshops, pp. 1468–1476 (2018)
2. Huang, Z., Liu, H., Wu, J., Lv, C.: Differentiable integrated motion prediction and planning with learnable cost function for autonomous driving. *IEEE Trans. Neural Netw. Learn. Syst.* (2023)
3. Hui, F., Wei, C., ShangGuan, W., Ando, R., Fang, S.: Deep encoder–decoder-NN: a deep learning-based autonomous vehicle trajectory prediction and correction model. *Phys. A: Stat. Mech. Appl.* **593**, 126,869 (2022)
4. Jeong, Y., Yi, K.: Bidirectional long shot-term memory-based interactive motion prediction of cut-in vehicles in urban environments. *IEEE Access* **8**, 106,183–106,197 (2020)
5. Meng, D., Xiao, W., Zhang, L., Zhang, Z., Liu, Z.: Vehicle trajectory prediction based predictive collision risk assessment for autonomous driving in highway scenarios. arXiv preprint [arXiv:2304.05610](https://arxiv.org/abs/2304.05610) (2023)
6. Song, Y., Huh, K.: Driving and steering collision avoidance system of autonomous vehicle with model predictive control based on non-convex optimization. *Adv. Mech. Eng.* **13**(6), 16878140211027,669 (2021)
7. Wang, H., Liu, B., Ping, X., An, Q.: Path tracking control for autonomous vehicles based on an improved MPC. *IEEE Access* **7**, 161,064–161,073 (2019)
8. Ye, F., Cheng, X., Wang, P., Chan, C.Y., Zhang, J.: Automated lane change strategy using proximal policy optimization-based deep reinforcement learning. In: 2020 IEEE Intelligent Vehicles Symposium (IV), pp. 1746–1752. IEEE (2020)

Open Access This chapter is licensed under the terms of the Creative Commons Attribution 4.0 International License (<http://creativecommons.org/licenses/by/4.0/>), which permits use, sharing, adaptation, distribution and reproduction in any medium or format, as long as you give appropriate credit to the original author(s) and the source, provide a link to the Creative Commons license and indicate if changes were made.

The images or other third party material in this chapter are included in the chapter's Creative Commons license, unless indicated otherwise in a credit line to the material. If material is not included in the chapter's Creative Commons license and your intended use is not permitted by statutory regulation or exceeds the permitted use, you will need to obtain permission directly from the copyright holder.





Development of Vehicle State Estimation Method for Dedicated Sensor-Less Semi-active Suspension Using AI Technology

Yoshifumi Kawasaki¹(✉), Akai Akihito², and Ryusuke Hirao¹

¹ Hitachi Astemo, Ltd., Atsugi, Japan
yoshifumi.kawasaki.bf@hitachiastemo.com

² Hitachi, Ltd., Chiyoda, Japan

Abstract. This paper presents a sensor-less vehicle state estimation method using a neural network for semi-active suspensions. This method surpasses conventional mathematical models in performance and reduces calibration effort. The developed system, logic, and learning method are designed to address AI-specific challenges such as increased processing load and learning techniques, and their performance is validated through simulations and real-world tests. The results show that this system performs on par with those using dedicated sensors.

Keywords: Chassis Control · Semi-active Suspension · Neural Network · Damping Force Control

1 Introduction

Recently, various sensor configurations for semi-active suspension systems have been mass-produced. Among these, sensor-less systems, which use wheel speed data instead of dedicated sensors to reduce costs, remain relatively rare [1–4]. This study applies neural networks (NN) to a sensor-less system that omits conventional dedicated sensors, proposing a solution that combines high performance with low cost [5, 6].

2 Sensor-Less AI Semi-active Suspension System

2.1 Overview of Sensor-Less AI Semi-active Suspension

Figure 1 illustrates the sensor-less AI semi-active suspension logic configuration. The system estimates vehicle states using wheel speeds without sensors like G-sensors. Recurrent neural networks (RNN) replace formula-based logic, using CAN signals such as wheel speeds that vary with road surface inputs. The system outputs the vehicle body's vertical speed and the suspension's stroke speed, eliminating the need for dedicated sensors and enabling a cost-effective semi-active suspension system that enhances ride comfort.

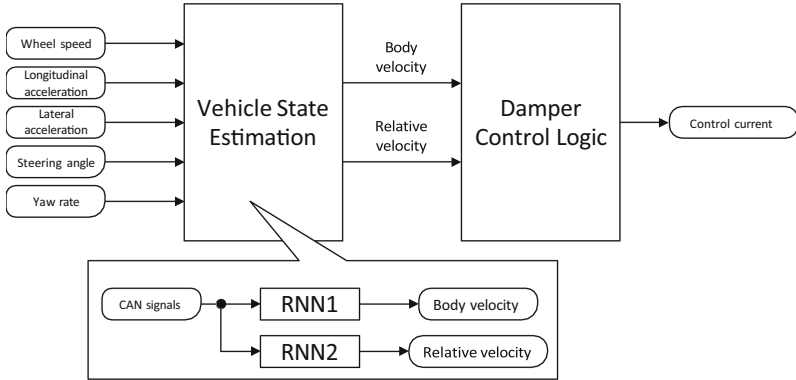


Fig. 1. AI semi-active suspension logic configuration

2.2 Learning Data

This system is designed to control frequencies related to primary and secondary rides. Consequently, the learning data focuses on vehicle vibrations within the 0.8 to 5 Hz range. Figure 2 illustrates the frequency distribution of the training data.

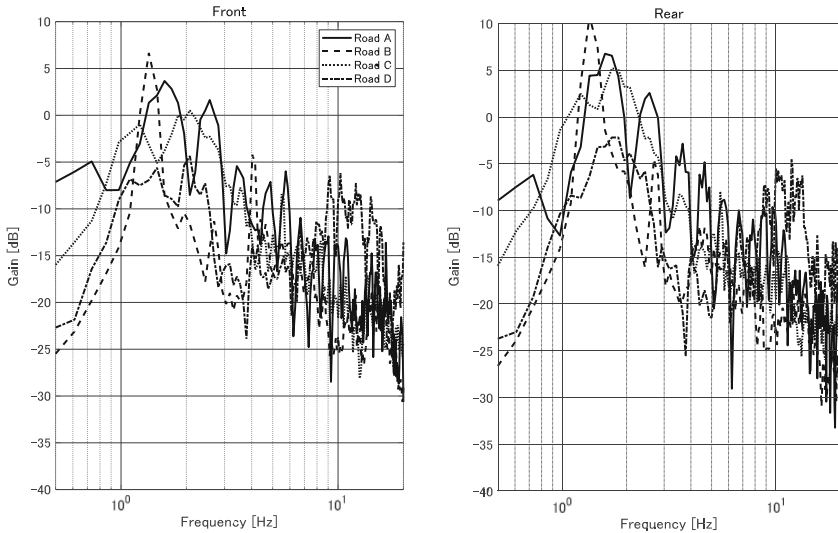


Fig. 2. An example of the frequency distribution of the training data

3 Features of AI Semi-active Suspension

3.1 Using Synthetic Data to Enhance Ride Comfort

A notable advantage of AI is the ability to use synthetic data for learning. Synthetic data is artificially generated rather than naturally occurring. Figure 3 depicts the NN learning flow.

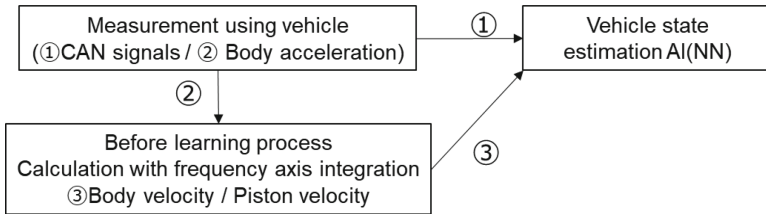


Fig. 3. NN learning flow with synthetic data

Using a test vehicle, we measure CAN data such as wheel speed and the corresponding vehicle behavior. The measured vehicle behavior undergoes frequency axis integration, allowing the calculation of body speed and piston speed with optimal frequency characteristics for artificial control. Training the NN with this CAN data and the artificially generated vehicle behavior results in an NN with characteristics that are difficult to achieve with traditional formulas. The integral characteristic is shown in Figure 4.

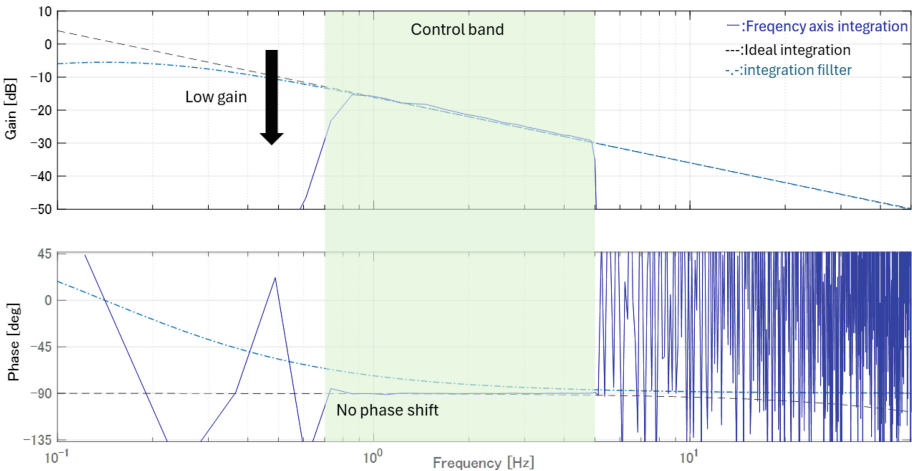


Fig. 4. Integral characteristics

The integral filter characteristic used in formulas reduces low-frequency gain to minimize the impact of gradients and sensor tilt. However, this causes the control band's

phase to shift from the ideal characteristics. In contrast, the frequency axis integral characteristic prevents phase shift in the control band while reducing low-frequency gain. This improvement reduces the impact of gradients and enhances ride comfort near the sprung resonance frequency.

3.2 Enhanced Robustness with Relative Wheel Speed

AI robustness is a significant challenge, requiring accurate state estimation even under unlearned conditions. By setting the input signal's wheel speed as a relative value to other wheels rather than an absolute value, it becomes easier to detect wheel speed variations caused by road surface inputs. This approach improves robustness across various unlearned road surfaces and vehicle speeds.

4 Result

4.1 NN Estimation Results

Figure 5 displays the measured and estimated vertical body velocity. The NN provides high estimation accuracy over a wide range by learning the suspension's characteristics.

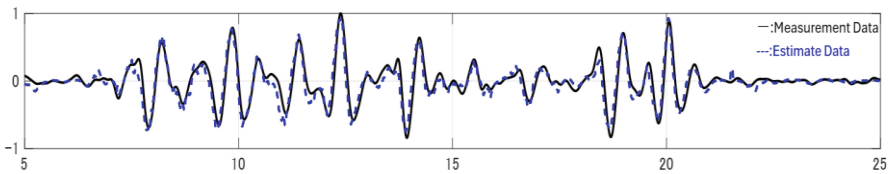


Fig. 5. Measured and estimated vertical body velocity of uneven road

Figure 6 shows the transfer function of the learning data and the NN output. Due to the small amplitude of the NN output, a gain error occurs in the control band. However, the phase at the sprung resonance frequency matches the learning data, exhibiting the intended phase characteristics.

5 Ride Comfort Evaluation Results

Figure 7 shows the floor displacement, pitch angle, and sprung acceleration PSD when driving on a swell road with the AI system without sensors and a non-AI system with sensors. The AI system's displacement and sprung acceleration PSD match those of the sensor-equipped system, but the pitch angle is smaller, enhancing ride comfort.

Figure 8 illustrates the floor displacement, pitch angle, roll angle, and sprung acceleration PSD when driving on an uneven road with the AI system without sensors and a non-AI system with sensors. The AI system's displacement, roll angle, and sprung acceleration PSD are similar to those of the sensor-equipped system, but the pitch angle is smaller, enhancing ride comfort.

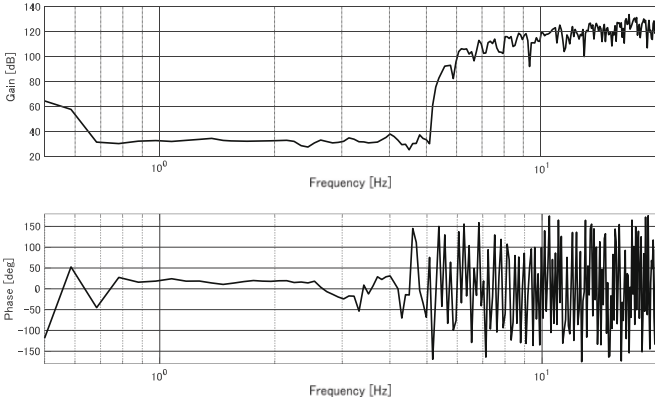


Fig. 6. Transfer function of the learning data and the NN output

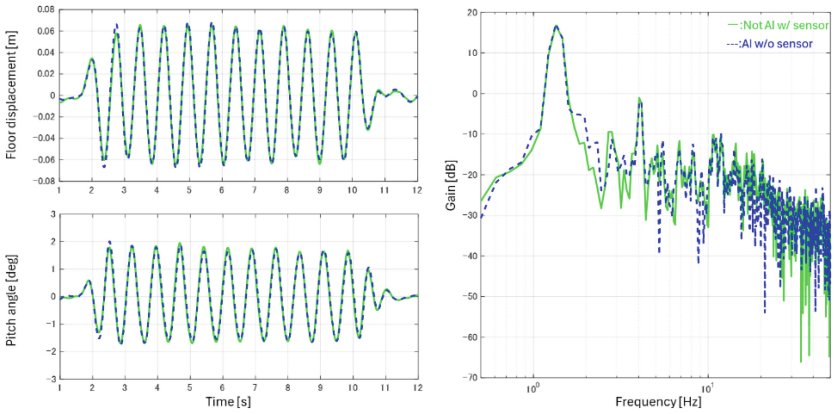


Fig. 7. Floor displacement, pitch angle and floor acceleration PSD when driving a swell road with AI system without sensor and non-AI system with sensor

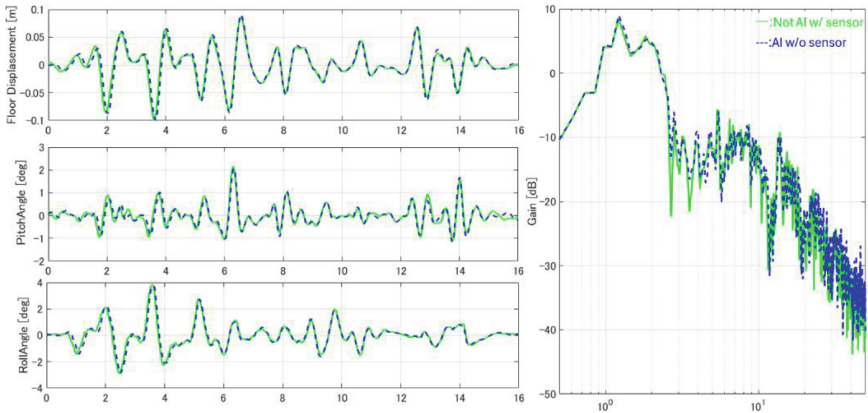


Fig. 8. Floor displacement, pitch angle and floor acceleration PSD when driving a uneven road with AI system without sensor and non-AI system with sensor

6 Conclusion

We have developed a dedicated sensor-less semi-active suspension system using AI and confirmed its performance surpasses that of sensor-equipped systems.

References

1. Hirao, R., et al.: Development of vehicle state estimation method considering driver input and suspension geometry non-linearity for dedicated sensor-less semi-active suspension. In: Proceedings of AVEC'22 No.Th1D-01, pp. 1–6
2. Liu, Y., et al.: Body attitude state estimation using wheel rolling speed variations. *Int. J. Autom. Eng.* **6-4**, 135–142 (2015)
3. Izawa, M., et al.: A skyhook control using estimated vehicle state by wheel speed sensors. In: Proceedings of Society of Automotive Engineers of Japan (JSAE) Annual Congress (Spring), No. 35–14, pp. 1–4 (2014)
4. Kikuchi, H., et al.: Ride performance on wheel rotation speed driven controlled damper system. *Int. J. Automot. Technol.* **23**(5), 1451–1470 (2022). <https://doi.org/10.1007/s12239-022-0127-6>
5. Akai, A., et al.: Research on AI semi-active suspension without dedicated sensors. *Trans. Soc. Automot. Eng. Japan* **54**(3), 492–497 (2023)
6. Yamamoto, A., et al.: Study of state estimation using LSTM for semi-active suspension. *Trans. Soc. Automot. Eng. Japan* **54**(5), 1038–1043 (2023)

Open Access This chapter is licensed under the terms of the Creative Commons Attribution 4.0 International License (<http://creativecommons.org/licenses/by/4.0/>), which permits use, sharing, adaptation, distribution and reproduction in any medium or format, as long as you give appropriate credit to the original author(s) and the source, provide a link to the Creative Commons license and indicate if changes were made.

The images or other third party material in this chapter are included in the chapter's Creative Commons license, unless indicated otherwise in a credit line to the material. If material is not included in the chapter's Creative Commons license and your intended use is not permitted by statutory regulation or exceeds the permitted use, you will need to obtain permission directly from the copyright holder.





Validation of Control Method to Improve Posture Stability of Narrow Tilting Vehicles Using Real-Vehicle Dynamic Tests

Keizo Araki^(✉), Jongseong Gwak, and Yoshihiro Suda

The Institute of Industrial Science, The University of Tokyo, Tokyo, Japan
k-araki@iis.u-tokyo.ac.jp

Abstract. Narrow Tilting Vehicles (NTVs) have been proposed as a solution to traffic problems such as congestion and limited parking spaces. However, their small footprint can lead to a reduction in postural stability. To address this issue, NTVs have been designed to reduce the lateral acceleration experienced by occupants by tilting the vehicle body inwards during turns, depending on the driving situation. Three types of tilt control methods have been proposed for NTVs: direct tilt control (DTC), steering tilt control (STC), and combined steering and direct tilt control (SDTC). In this study, we proposed a simplified method to control SDTC using a single roll directional motion equation, focusing on the yaw angular acceleration and roll inertia of the vehicle body. The proposed method was found to result in a 84% reduction in the lateral acceleration experienced by occupants during turning maneuvers in the evaluation of real-vehicle dynamic tests.

Keywords: Narrow tilting vehicles · Tilt control · Posture stability · Lateral acceleration

1 Introduction

As the demand for personal mobility increases in urban areas, traffic problems such as congestion, fuel consumption, air pollution, and limited parking space are expected to worsen. To address these issues, one- and two-seater personal mobility vehicles, known as Narrow Tilting Vehicles (NTVs), have been developed. NTVs are expected to help alleviate traffic congestion during commuting hours. However, compared to conventional vehicles, NTVs are prone to impairing postural stability, making it essential to address this issue. As a solution, NTVs equipped with lean actuators that can control the vehicle's posture in the roll direction have been proposed [1–3].

In NTVs with lean actuators, the method of directly controlling the roll angle via the lean actuator is referred to as Direct Tilt Control (DTC), while the method of tilting the vehicle body via centrifugal force generated by counter-steering, as seen in motor-bikes and bicycles, is known as Steering Tilt Control (STC). DTC is superior in roll angle stability at low speeds, but requires a large roll torque to change the roll angle and generates large lateral acceleration to the occupants along with the roll angular acceleration [4–8]. In contrast, STC does not require a lean actuator because to tilt the vehicle

body by counter-steering, and the lateral acceleration to the occupant is relatively small. However, the roll angle becomes unstable at low speeds and the roll angle cannot be controlled when the vehicle is stationary [9, 10].

Based on the aforementioned considerations, two primary control challenges for NTVs are identified: (i) reducing the lateral acceleration experienced by occupants, thereby enhancing postural stability, and (ii) maintaining stable roll angle control across all vehicle speeds. To address these challenges, a control strategy has been proposed that either switches between DTC and STC based on vehicle speed, or employs a combined control approach integrating both DTC and STC, referred to as SDTC [11, 12]. One of the factors complicating the control of NTVs is the necessity for counter-steering in steering control. Front-wheel steering NTVs require counter-steering similar to that used in motorcycles and bicycles to reduce lateral acceleration caused by roll angle acceleration, thereby complicating steering angle control during turns. For example, a counter-steering control method utilizing a transfer function with unstable zeros has been proposed [13].

The authors proposed a method to control leaning and steering based on a single roll direction equation of motion, focuses on the yaw angular acceleration and roll inertia of the vehicle body. This approach aimed to avoid the complex combination control of STC and DTC in front-wheel steering vehicles while ensuring that occupants do not experience significant lateral acceleration. The effectiveness of this method was verified through driving simulations using a multi-degree-of-freedom dynamic model [14].

In this study, we conducted real vehicle evaluations using the proposed method and confirmed its effectiveness. Figure 1 and Table 1 show the appearance and main specifications of an NTV used in this research.



Fig. 1. A view of narrow tilting vehicle

Table 1. Specifications of Narrow Tilting Vehicle.

Length	2.1 [m]
Height	1.55 [m]
Tread	0.55 [m]
Wheel base	1.575 [m]
Tire size	130/60R13
Minimum turning radius	3.0 [m]
Occupancy	1
Powertrain	2 electric motors
Maximum speed	50 [km/h]
Battery type	Lithium-ion

2 Vehicle and Control Specification

2.1 Vehicle Specification

Figure 2 shows the vehicle configuration of the NTV used in this study. This vehicle is a four-wheeled model with two front wheels and two rear wheels. It is equipped with lean actuators on both the front and rear wheels, which determine the target roll angle based on the driver's steering input. The lean actuators rotate the parallel links to raise and lower the left and right wheels, thereby tilting the vehicle body. Additionally, the front wheels are fitted with a steering actuator that controls the steering torque according to the proposed control method. Each rear wheel is equipped with an in-wheel motor that drives the wheels based on the driver's throttle input. Furthermore, the vehicle has a very narrow tread width of 550 mm, aiming to achieve stable driving with a width comparable to that of a motorcycle.

2.2 Control Specification

Figure 3 shows a block diagram of the proposed control system. The "in-wheel motor" is the in-wheel motor for the left and right rear wheels, "Steer act." is the steering actuator, "Lean act." is the lean actuator, and "Controller" is a control system that adds a steering torque based on roll speed to the control method proposed in a previous paper [14]. The term τ_{wh} denotes the torque command to the in-wheel motor, determined by the driver's accelerator opening, V is the translational speed, and θ , $\dot{\psi}$, and $\ddot{\psi}$ denote the roll angle, yaw rate, and yaw angle acceleration of the vehicle's upper body, estimated by the inertial sensor, respectively. The term θ_d denotes the roll command angle, derived from the steering wheel angle and vehicle speed, $LeanTrq$ and $SteerTrq$ are the torque command derived from θ_d to the lean actuator and to the steering actuator.

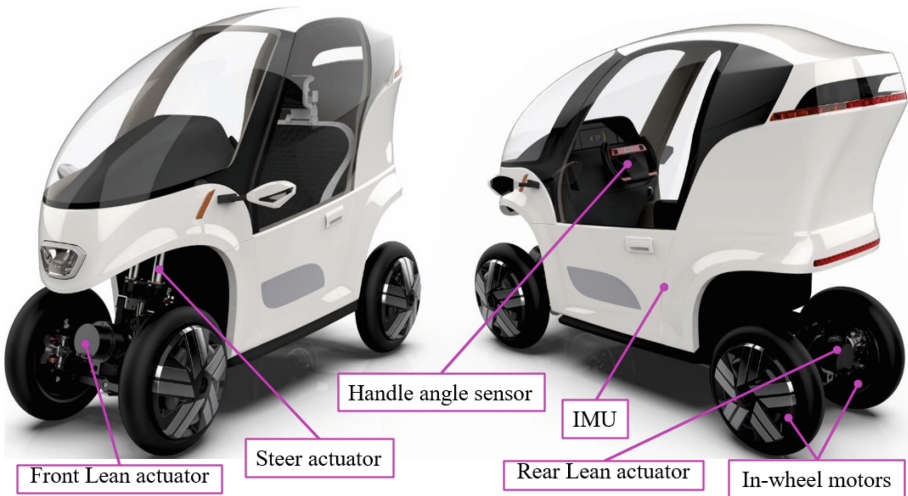


Fig. 2. Mechanical structure.

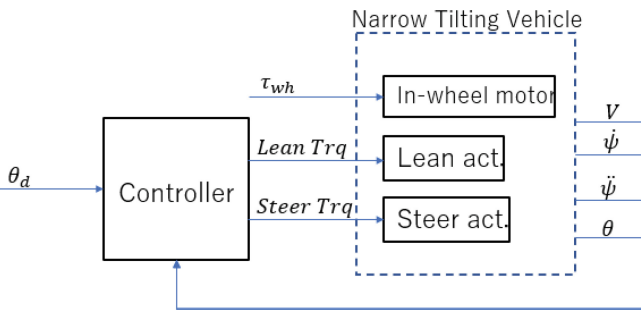


Fig. 3. Control block diagram of Narrow Tilting Vehicle.

3 Validation

To verify the effectiveness of the proposed method, a 180° turning maneuver was conducted using the experimental vehicle. Figure 4 shows the results for DTC, while Fig. 5 shows the results for the proposed method. The lean angle was varied from 0° to 18° and back to 0°, and the vehicle speed was maintained at 20 km/h. Graph [a] represents the roll angle, graph [b] represents the yaw rate, and graph [c] represents the lateral acceleration near the sprung mass center of gravity. In the DTC, significant lateral acceleration occurred during transitions from straight to turning and from turning to straight, with a maximum value of 0.19G, causing uncomfortable G-force variations for the occupants. In contrast, the maximum lateral acceleration with the proposed method was 0.03G, and the occupants barely felt any G-force variations. This indicates that the proposed method can reduce the lateral acceleration experienced by occupants during turning maneuvers by 84%, thereby enhancing passenger comfort. Additionally, concerns about degraded line tracing due to counter-steering were largely unfounded.

In the future, we will verify the effectiveness of the proposed method during 180° turning maneuvers at different speeds and during slalom maneuvers, ensuring that significant reductions in lateral acceleration are achieved, consistent with the simulation results.

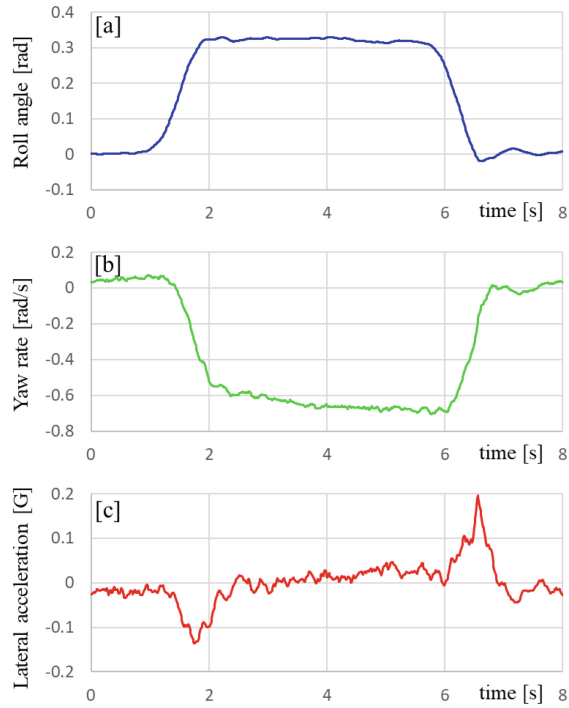


Fig. 4. Results of the DTC.

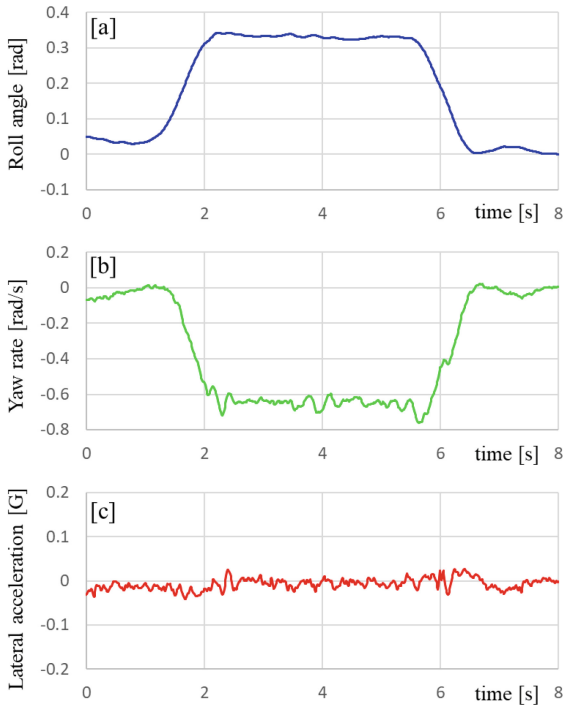


Fig. 5. Results of the Proposal.

4 Conclusion

The following conclusions can be drawn from this study:

- (1) Using the method proposed in our previous paper, which focuses on the yaw angular acceleration and roll inertia of the vehicle body to determine the torque distribution between the lean actuator and the steering actuator, we conducted an evaluation with a developed experimental vehicle. This evaluation confirmed that the lateral acceleration experienced by occupants can be reduced by 84%.
- (2) By employing the proposed method, the maximum lateral acceleration during turning maneuvers was reduced to 0.03G, ensuring that occupants barely perceive any variations in lateral acceleration.
- (3) The deterioration in line tracing performance due to counter-steering, which was a concern with the proposed method, was barely perceptible.

In the future, we will verify the effectiveness of the proposed method during 180° turning maneuvers at different speeds and during slalom maneuvers, ensuring that significant reductions in lateral acceleration are achieved, consistent with the simulation results.

References

1. Maakaroun, S., Khalil, W., Gautier, M., Chevrel, P.: Modeling and simulating a narrow tilting car using robotics formalism. *IEEE Trans. Intell. Transp. Syst.* **15**(3), 1026–1038 (2014)
2. Hibbard, R., Karnopp, D.: Twenty first century transportation system solutions—A new type of small, relatively tall and narrow active tilting commuter vehicle. *Veh. Syst. Dyn.* **25**(5), 321–347 (1996)
3. Rajamani, R., Gohl, J., Alexander, L., Starr, P.: Dynamics of narrow tilting vehicles. *Math. Comput. Model. Dyn. Syst.* **9**(2), 209–231 (2003)
4. Piyabongkarn, D., Keviczky, T., Rajamant, R.: Active direct tilt control for stability enhancement of a narrow commuter vehicle. *Int. J. Automot. Technol.* **5**(2), 77–88 (2004)
5. Mourad, L., Claveau, F., Chevrel, P.: Design of a two DOF gain scheduled frequency shaped LQ controller for narrow tilting vehicles. In: 2012 American control conference (ACC), pp. 6739–6744. IEEE (2012)
6. Haraguchi, T., Kageyama, I., Kaneko, T.: Inner wheel lifting characteristics of tilting type personal mobility vehicle by sudden steering input. *Trans. Soc. Automot. Eng. Japan, Inc.*, **50**(1), 96–101 (2019)
7. Karamuk, M., Alankus, O.B.: Development and experimental implementation of active tilt control system using a servo motor actuator for narrow tilting electric vehicle. *Energies* **15**(6), 1996 (2022)
8. Karamuk, M., Alankus, O.B.: Direct tilt controller design with disturbance compensation and implementation for a narrow tilting electric vehicle. *Energies* **16**(15), 5724 (2023)
9. Gohl, J., Rajamani, R., Starr, P., Alexander, L.: Development of a novel tilt-controlled narrow commuter vehicle (2006)
10. Van Poelgeest, A., Edge, K.A., Darling, J.: Development of a steer tilt controller for a three wheeled tilting vehicle. In: ASME International Mechanical Engineering Congress and Exposition, vol. 43106, pp. 149–156 (2007)
11. Kidane, S., Alexander, L., Rajamani, R., Starr, P., Donath, M.: A fundamental investigation of tilt control systems for narrow commuter vehicles. *Veh. Syst. Dyn.* **46**(4), 295–322 (2008)
12. Mourad, L., Claveau, F., Chevrel, P.: Direct and steering tilt robust control of narrow vehicles. *IEEE Trans. Intell. Transp. Syst.* **15**(3), 1206–1215 (2014)
13. Kaneko, T., Haraguchi, T., Kageyama, I.: A study on characteristics of the vehicle response by abrupt operation and an improvement method for personal mobility vehicle with leaning mechanism. *Trans. Soc. Automot. Eng. Japan* **50**(3), 796–801 (2019)
14. Araki, K., Gwak, J., Sugimachi, T., Kubo, N., Suda, Y.: Control method to improve posture stability of narrow tilting vehicles. *Int. J. Intell. Transp. Syst. Res.* **20**, 1–8 (2022). <https://doi.org/10.1007/s13177-021-00282-1>







Open Access This chapter is licensed under the terms of the Creative Commons Attribution 4.0 International License (<http://creativecommons.org/licenses/by/4.0/>), which permits use, sharing, adaptation, distribution and reproduction in any medium or format, as long as you give appropriate credit to the original author(s) and the source, provide a link to the Creative Commons license and indicate if changes were made.

The images or other third party material in this chapter are included in the chapter's Creative Commons license, unless indicated otherwise in a credit line to the material. If material is not included in the chapter's Creative Commons license and your intended use is not permitted by statutory regulation or exceeds the permitted use, you will need to obtain permission directly from the copyright holder.





Gradient Correction for Asynchronous Stochastic Gradient Descent in Reinforcement Learning

Jiaxin Gao¹(✉) , Yao Lyu¹ , Wenxuan Wang¹ , Yuming Yin² , Fei Ma³ ,
and Shengbo Eben Li¹ 

¹ Tsinghua University, Beijing 100084, China
gaojiaxin2017@163.com, {y-lv19,wang-wx18}@mails.tsinghua.edu.cn,
lishbo@tsinghua.edu.cn

² Zhejiang University of Technology, Hangzhou 310014, China
yinyuming@zjut.edu.cn

³ University of Science and Technology Beijing, Beijing 100083, China
yeke@ustb.edu.cn

Abstract. Distributed stochastic gradient descent techniques have gained significant attention in recent years as a prevalent approach for reinforcement learning. Current distributed learning predominantly employs synchronous or asynchronous training strategies. While the asynchronous scheme avoids idle computing resources present in synchronous methods, it grapples with the stale gradient issue. This paper introduces a novel gradient correction algorithm aimed at alleviating the stale gradient problem. By leveraging second-order information within the worker node and incorporating current parameters from both the worker and server nodes, the gradient correction algorithm yields a refined gradient closer to the desired value. Initially, we outline the challenges associated with asynchronous update schemes and derive a gradient correction algorithm employing local second-order approximations. Subsequently, we propose an asynchronous training scheme incorporating gradient correction within the generalized policy iteration framework. Lastly, in the context of trajectory tracking tasks, we compare the impact of employing gradient correction versus its absence in an asynchronous update scheme. Simulation results underscore the superiority of our proposed training scheme, demonstrating notably faster convergence and higher policy performance compared to the existing asynchronous update methods.

Keywords: Asynchronous training · Autonomous driving · Reinforcement learning · Second-order approximation · Stochastic gradient descent

S. E. Li—This work is supported by NSF China with 52072213 and U20A20334. It is also partially supported by Tsinghua-Toyota Joint Research Institute Inter-disciplinary Program.

© The Author(s) 2024
G. Mastinu et al. (Eds.): AVEC 2024, LNME, pp. 904–910, 2024.
https://doi.org/10.1007/978-3-031-70392-8_127

1 Introduction

Reinforcement learning (RL) embodies a learning paradigm inspired by biological systems and demonstrates significant potential in various domains such as computer games [1, 2], robotics [3, 4], and autonomous driving [5–7]. However, RL often requires extensive data gathering, making distributed training techniques like synchronous and asynchronous stochastic gradient descent (SGD) essential.

Synchronous SGD, as used in OpenAI’s advantageous synchronous advantage actor-critic (A2C), requires servers to wait for gradient updates from all workers before updating models. While enabling linear scaling, this approach suffers from delays caused by slower workers that can undermine intended acceleration [8]. Asynchronous SGD methods like DeepMind’s asynchronous advantage actor-critic (A3C) mitigate this issue by allowing more frequent model updates without synchronization [9, 10]. However, asynchronous training faces the challenge of potentially using outdated model gradients, which can disrupt training stability [11]. Mitigating gradient staleness is thus a critical challenge. Dutta et al. [12] proposed an adaptive algorithm to balance straggling and staleness by regulating synchronous workers. Chen et al. [11] suggested using backup workers to handle stragglers and prevent staleness. However, these methods merely aim to strike a delicate balance between the challenges of gradient straggling and gradient staleness, without effectively addressing the underlying systemic issues that lead to these problems in distributed training.

To tackle this issue, this paper proposes a gradient correction algorithm designed specifically for asynchronous SGD in RL, with a primary focus on addressing the stale gradient issue in asynchronous parallelism. Our primary contributions can be summarized as follows:

1. We propose a gradient correction algorithm that leverages second-order information within the worker process and incorporates current parameters from both worker and server processes. This approach yields an improved gradient closer to the target value, effectively harnessing parallel resources while ensuring model convergence and stability.
2. We present an asynchronous training scheme incorporating gradient correction within the generalized policy iteration framework. The simulation results on an autonomous vehicle demonstrate that this innovative approach exhibits significantly improved convergence speed and policy performance compared to the current asynchronous update scheme.

2 Preliminaries

Reinforcement Learning. RL involves an agent interacting with the environment to learn behaviors that maximize the objective. Given state $x_t \in \mathcal{X}$ at time t , the agent takes action $u_t \in \mathcal{U}$ based on its policy $\pi_\theta : \mathcal{X} \rightarrow \mathcal{U}$ parameterized by θ . It then receives utility l_t and transitions to the next state x_{t+1} . The primary goal of RL is to find the optimal policy π_θ^* that minimizes expected

accumulated utilities, i.e., $\min J(\theta) = \mathbb{E} \sum_{t=0}^T l(x_t, \pi_\theta(x_t))$. The generalized policy iteration (GPI) framework is commonly employed to iteratively solve RL problems. Specifically, the policy evaluation step utilizes the current policy to forecast accumulated future utilities, while the policy improvement step updates the policy parameters θ in order to minimize the objective J [7].

Stochastic Gradient Descent Optimization. RL commonly employs stochastic gradient descent (SGD) optimization. At iteration k , given the stochastic gradient $\nabla_\theta J(\theta^k)$ obtained by utilizing a batch of randomly sampled data, the parameter updating rule is as follows:

$$\theta^{k+1} = \theta^k - \alpha \nabla_\theta J(\theta^k), \quad (1)$$

where α is the learning rate that determines the extent of parameter adjustments.

Synchronous Training. In synchronous training, a parameter server aggregates gradients from all worker nodes. Upon accumulating gradients from all workers, the parameter server updates the policy parameters and communicates the updated parameters back to the workers, ensuring all workers maintain consistent and up-to-date parameters. However, this synchronization can introduce delays from waiting for all workers to synchronize, potentially leading to the slow straggler issue where updates only occur after the slowest worker completes the batch assembly and gradient computation.

Asynchronous Training. In the asynchronous approach, workers independently update shared policy parameters without waiting for synchronization, enabling immediate parameter updates once each worker finishes gradient computation. However, this naive asynchronous approach is vulnerable to the stale gradient issue, where workers compute gradients based on outdated networks. For instance, while one worker is still processing data, other workers may have already updated the network multiple times due to variations in their computing intervals.

3 Asynchronous Training with Gradient Correction

In this section, we propose a gradient correction algorithm to mitigate the stale gradient issue that arises from the lack of synchronization during the asynchronous training process. For simplicity, we consider a scenario where only two workers (A and B) are involved in the asynchronous training process. However, it is worth noting that our analysis also applies to more general cases.

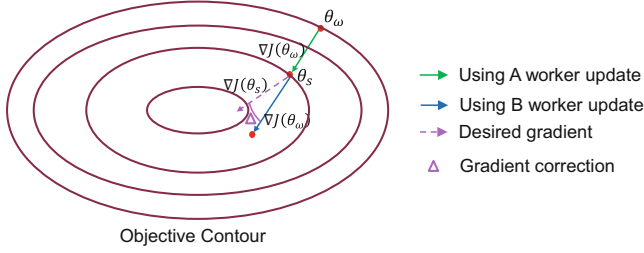


Fig. 1. Gradient correct process.

The gradient correction process is shown in Fig. 1, where purple ellipses outline the objective contours. We assume that both workers A and B have identical policy parameters θ_w , and worker A completes the gradient calculation first. However, when the server uses worker A’s gradient to update parameters to θ_s , worker B’s gradient becomes stale as it lags behind the policy parameters on the server. Specifically, at point θ_s , the desired gradient $\nabla J(\theta_s)$ should resemble the dotted purple line, deviating from the stale gradient $\nabla J(\theta_w)$ represented by the solid blue line.

To correct the stale gradient by aligning it with the desired gradient, we first employ Taylor expansion on the objective, yielding:

$$J(\theta_s) = J(\theta_w) + \nabla J(\theta_w)^\top (\theta_s - \theta_w) + \frac{1}{2} (\theta_s - \theta_w)^\top H(\theta_s) (\theta_s - \theta_w). \quad (2)$$

By deriving both sides and treating higher-order terms as infinitesimal, we further derive:

$$\nabla J(\theta_s) = \nabla J(\theta_w) + H(\theta_w) (\theta_s - \theta_w), \quad (3)$$

where H is the Hessian matrix, and the gradient correction can be defined as

$$\Delta = H(\theta_w) (\theta_s - \theta_w). \quad (4)$$

Hence, the utilization of second-order information enables the correction of stale gradients caused by parameter discrepancies between the worker and server. Moreover, we seamlessly integrate this gradient correction mechanism into asynchronous training, where workers are required to transmit gradient, Hessian matrix, and local parameters to the server for computing the corrected gradient:

$$G_c = G_i + H_i(\theta_i) (\theta^k - \theta_i), \quad (5)$$

where G_i, H_i, θ_i denote the gradient, Hessian matrix, and policy parameters from worker i respectively, θ^k are the current parameters on the server, and G_c represents the corrected gradient. Figure 2 illustrates the proposed asynchronous training scheme with gradient correction within the GPI framework.

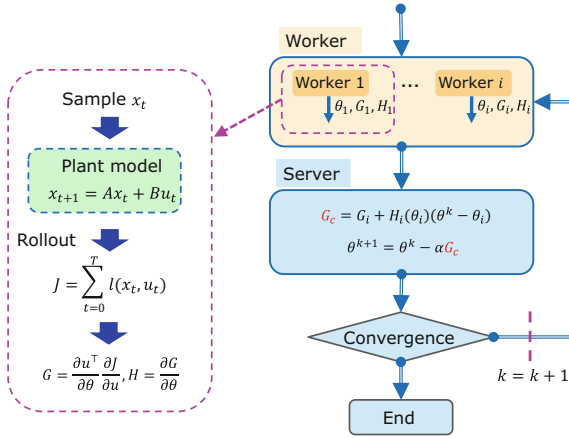


Fig. 2. Asynchronous training with gradient correction.

4 Simulation

In this section, the efficacy of our proposed asynchronous training scheme with gradient correction is evaluated in sinusoidal trajectory tracking tasks for an autonomous vehicle. The learning curves are depicted in Fig. 3, where the naive asynchronous scheme is labeled as “Async”, and our proposed approach is denoted as “Modify”.

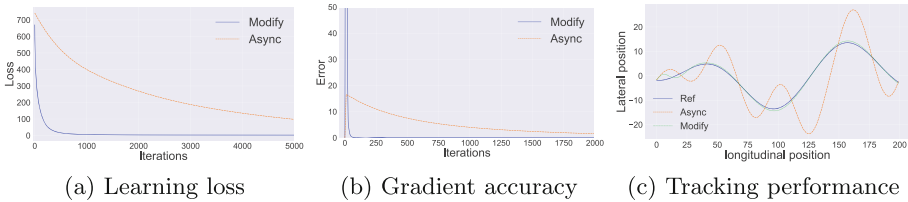


Fig. 3. Learning curves.

Figure 3a illustrates loss curves plotted against training iterations. For a fair comparison, we employ identical random seeds and hyperparameters for two training schemes. It is evident that both loss curves initially decrease from the same level. However, our scheme exhibits a more rapid decline and achieves convergence in approximately only 1,000 iterations. Conversely, the naive scheme displays a slower reduction in loss and fails to converge within the specified maximum iterations set for the experiment. These findings indicate that our scheme demonstrates superior effectiveness in algorithm convergence without being affected by stale gradients.

Figure 3b demonstrates the comparison of gradient accuracy between the two distinct training schemes during the training process. In both schemes, the server consistently retains and updates the latest policy parameters, which are considered as ground truth for computing desired gradients. On the other hand, the stale gradient is derived from gradients returned by workers. Therefore, we quantify gradient accuracy through error analysis between these two gradients. As shown in Fig. 3b, our proposed scheme initially exhibits higher gradient errors but rapidly reduces this error to ultimately converge to zero. In contrast, the naive scheme demonstrates a relatively slow decline in gradient error over iterations. These results highlight the effectiveness of our proposed training scheme in mitigating stale gradient issues by incorporating second-order information, further supporting experimental observations depicted in Fig. 3a.

Figure 3c presents the tracking performance on the sinusoidal curve. By utilizing the policy parameters saved at the maximal iteration and starting from the same initialization, our proposed training scheme successfully achieves precise trajectory tracking, closely following the reference trajectory. Conversely, employing the naive training scheme results in a policy that merely learns a rudimentary feedback control, demonstrating poor tracking capabilities.

5 Conclusion

This paper presents a gradient correction algorithm aimed at tackling the stale gradient issue in asynchronous RL training. By leveraging second-order information from the worker and considering the current parameters from both the worker and server, this algorithm refines the stale gradient to closely align with the desired one. Moreover, we incorporate this gradient correction mechanism into an asynchronous training scheme, offering a novel approach. Validation through sinusoidal trajectory tracking tasks of an autonomous vehicle demonstrates its accelerated convergence speed and effective resolution of gradient staleness. An avenue for future exploration involves addressing the challenge of generalizing neural network approximate functions while utilizing second-order information. Additionally, our method holds promise for comprehensive investigation into its application in enhancing training speed and driving policy performance in autonomous vehicles.

References

1. Mnih, V., Kavukcuoglu, K., Silver, D., et al.: Human-level control through deep reinforcement learning. *Nature* **518**, 529–533 (2015)
2. Vinyals, O., Babuschkin, I., Czarnecki, W.M., et al.: Grandmaster level in StarCraft II using multi-agent reinforcement learning. *Nature* **575**, 350–354 (2019)
3. Levine, S., Pastor, P., Krizhevsky, A., Quillen, D.: Learning hand-eye coordination for robotic grasping with deep learning and large-scale data collection. In: 2016 International Symposium on Experimental Robotics (2016)
4. Andrychowicz, O.M., Baker, B., Chociej, M., et al.: Learning dexterous in-hand manipulation. *Int. J. Robot. Res.* **39**(1), 3–20 (2020)

5. Duan, J., Ren, Y., Zhang, F., et al.: Encoding distributional soft actor-critic for autonomous driving in multi-lane scenarios. *IEEE Comput. Intell. Mag.* (2023)
6. Duan, J., Guan, Y., Li, S.E., et al.: Distributional soft actor-critic: off-policy reinforcement learning for addressing value estimation errors. *IEEE Trans. Neural Netw. Learn. Syst.* **33**(11), 6584–6598 (2022)
7. Li, S.: Eben. Springer Verlag, Singapore, Reinforcement Learning for Sequential Decision and Optimal Control (2023)
8. Dean, J., Barroso, L.A.: The tail at scale. *Commun. ACM* **56**, 74–80 (2013)
9. Mnih, V., Badia, A., Mirza, M., et al.: Asynchronous methods for deep reinforcement learning. In: *ICML'16: Proceedings of the 33rd International Conference on International Conference on Machine Learning*, pp. 1928–1937 (2016)
10. Dalton, S., Frosio, I.: Accelerating reinforcement learning through GPU Atari emulation. In: *34th Conference on Neural Information Processing Systems, NeurIPS 2020* (2020)
11. Chen, J., Pan, X., Monga, R., et al.: Revisiting Distributed Synchronous SGD (2017). [arXiv:1604.00981](https://arxiv.org/abs/1604.00981)
12. Dutta, S., Wang, J., Joshi, G.: Slow and stale gradients can win the race. *IEEE J. Sel. Areas Inf. Theory* **2**(3), 1012–1024 (2021)

Open Access This chapter is licensed under the terms of the Creative Commons Attribution 4.0 International License (<http://creativecommons.org/licenses/by/4.0/>), which permits use, sharing, adaptation, distribution and reproduction in any medium or format, as long as you give appropriate credit to the original author(s) and the source, provide a link to the Creative Commons license and indicate if changes were made.

The images or other third party material in this chapter are included in the chapter's Creative Commons license, unless indicated otherwise in a credit line to the material. If material is not included in the chapter's Creative Commons license and your intended use is not permitted by statutory regulation or exceeds the permitted use, you will need to obtain permission directly from the copyright holder.





Indoor Test-Rig to Measure the Lateral Characteristics of Bicycle Tyres

Gabriele Dell'Orto^{1,2}  and Giampiero Mastinu¹ 

¹ Department of Mechanical Engineering, Politecnico di Milano, Via La Masa 1, 20156 Milano, Italy

gabriele.dellorto@polimi.it

² Faculty of Mechanical Engineering ME, Delft University of Technology, Mekelweg 2, 2628 CD Delft, The Netherlands

Abstract. Tyre characteristics can strongly affect bicycle dynamics, therefore the overall bicycle performances. However, it may be hard to measure lateral characteristics with low uncertainty. Proper test-rigs are needed to obtain reliable tyre parameters, to be used then for modelling. The paper presents VeTyT, acronym of “Velo Tyre Testing”, a new test-rig specifically developed for bicycle tyres at the Department of Mechanical Engineering of Politecnico di Milano. It is the first test-rig for bicycle tyres in compliance with the standard ISO 9001-2015. We also present the results of an experimental campaign conducted on a road racing bicycle tyre. In particular, the impact of rim stiffness is relevant to tyre characteristics, leading to a 13% increase in cornering stiffness under the same test conditions.

Keywords: Tyre · test-rig · modeling · lateral characteristics · bicycle

1 Introduction

The use of bicycles as a cheap and healthy way to travel the “last mile” is widely spreading in cities. This new way of dealing with short trips in the city, labeled “micro-mobility”, is even fostered by the new awareness on the global impact of ICE vehicles as well as the fluctuations of fuel prices.

As the popularity of two-wheeled vehicles grows, concerns about road safety are growing as well. Injuries related to bicycle and moped falls have increased in recent years, enlightening the need to prevent them with proper strategies. With the aim of improving the self-stability and deepening the knowledge on bicycle dynamics, advanced numerical models are required [1, 2]. Furthermore, existing mechanical models of bicycles mostly ignore tyre dynamics and need to be complemented with realistic tyre models [3]. Therefore it is necessary to characterize bicycle tyres to proper understand the bicycle dynamics. At the Department of Mechanical Engineering of Politecnico di Milano, a new test bench has been designed specifically for the characterization of bicycle tyres [4–6]. It is possible to measure the lateral force and the self-aligning torque at varying slip and camber angle, vertical load and inflation pressure.

The aim of this study is present a new test-rig able to ensure accurate measurements on bicycle tyres lateral characteristics, varying working parameters such as vertical load and inflation pressure. This may be really useful to assess tyres, and set the proper strategy for improving both performances and bicycle stability. A number of previous works on test-rigs for bicycle tyre testing have been investigated in the last decades [5]. The still existing gaps are as follows. First, the values of uncertainty are generally not declared. Second, there is the request of both accuracy and data production efficiency. Reliable tyre data have to be exploited both by tyre and bicycle manufacturers. VeTyT tries to bridge the gap between accuracy and efficiency.

We also present the verification procedure of the test-rig, necessary to fulfill the requirements for ISO 9001 (Sect. 3). In Sect. 4, we show the results of an experimental campaign conducted on a 26 mm wide road racing bicycle tyre. In particular, we focus on the impact of inflation pressure and rim stiffness to the cornering stiffness (Sect. 4).

2 Test-Rig

VeTyT (short of “Velo Tyre Testing”) is a testing machine specifically designed for bicycle tyres (Fig. 1). It can measure lateral forces and self-aligning moment of bicycle tyre, varying many parameters, including slip angle α , camber (or lean) angle, and vertical load. It consists of a welded Aluminum 6060 T6 square-section bars, reinforced with plates and steel rods to ensure lightness and sufficient stiffness. It is connected to the ground by means of Watt’s linkage (Fig. 2(a)) and universal joint. The kinematics of Watt’s linkage allows for a sufficient vertical displacement while it constrains the lateral motion of the structure. The lateral force F_y can be derived by mounting two load cells in between rods.

VeTyT has been conceived so that the longitudinal axis passes from the universal joint, the contact point tyre/surface and the center of the Watt’s linkage (Fig. 2(b)). In this way, by rotating a shaft rigidly connected to the universal joint, the camber angle can be set. Furthermore, this solution allows compensating vertical vibrations of the wheel due to unevenness on the rolling surface. The tyre/road contact point can be displayed only in vertical direction, resulting in zero longitudinal speed [1].

The test-rig can be placed both on a drum or on a flat track (Fig. 1). The drum has an outer diameter of 2.6 m, and it can reach a peripheral speed of 122 m/s. The flat track consists of a poly-V belt moved by a 5 kW three-phase asynchronous electric motor. A maximum speed of 21 m/s can be achieved. An aluminum plate supports the flat track belt in the contact region. Pressured air mixed with silicone oil is blown between the plate and the flat track belt to reduce the friction. As the shape of a bicycle tyre contact patch is similar to an ellipse [7], i.e. narrow and elongated, the flat track results the best tool to appreciate the forces exchanged along the entire contact area.

In addition to standard commercial rims, the apparatus has been designed to accommodate special high-stiffness laboratory rim (the one mounted on in Fig. 2). In this way, the compliance of the rim does not affect the experimental measurements.

A vertical shaft used to hold the wheel represents the vertical axis of VeTyT. It crosses the longitudinal axis in the contact point tyre/surface (Fig. 2). The slip angle α can be adjusted by rotating the steering shaft. Once the desired slip angle is set, the position can

be fixed, and the test can start. An axial load cell used to fix the set slip angle measures the reaction force generated by the steered tyre. The self-aligning moment can be derived being the distance between the steering shaft axis and the load cell longitudinal axis known. The vertical load acting on the wheel can be varied by adding masses on the frame. Its magnitude F_z is recorded by a load cell positioned at the top of the steering shaft.

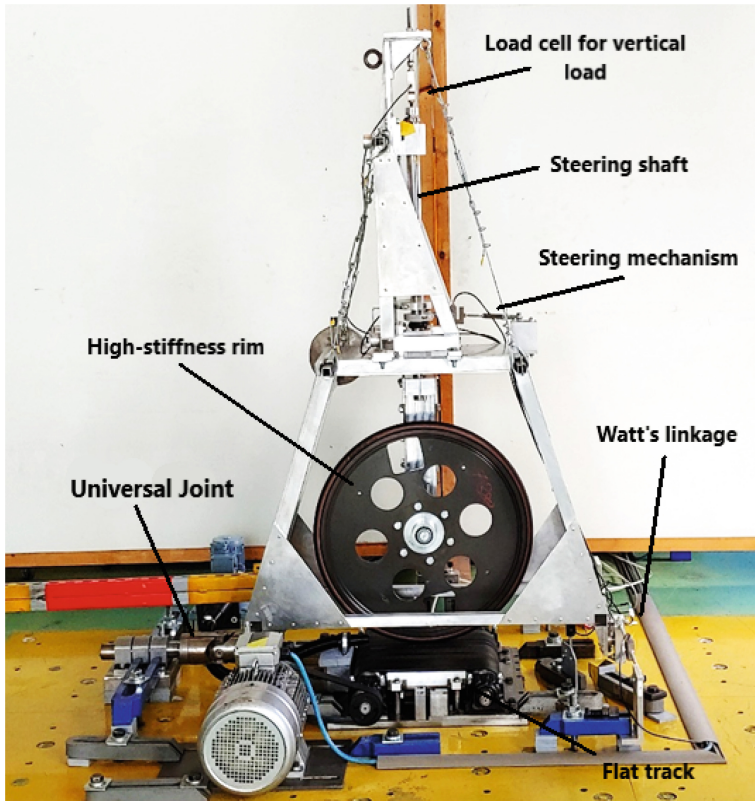


Fig. 1. VeTyT test-rig. The frame carries the bicycle tyre running on flat track. In this picture, tyre is mounted on high-stiffness laboratory rim [7].

3 Static Verification

VeTyT has been statically verified, to ensure the effectiveness of the measurements. In this way, we can compensate for any possible systematic error. The procedure has been conducted both for lateral force and self-aligning torque by using special set-up (Fig. 3).

Regarding the lateral force, the fork for commercial rim was mounted on the steering shaft. It was loaded with a treaded bar in series with a load cell, proper placed to ensure

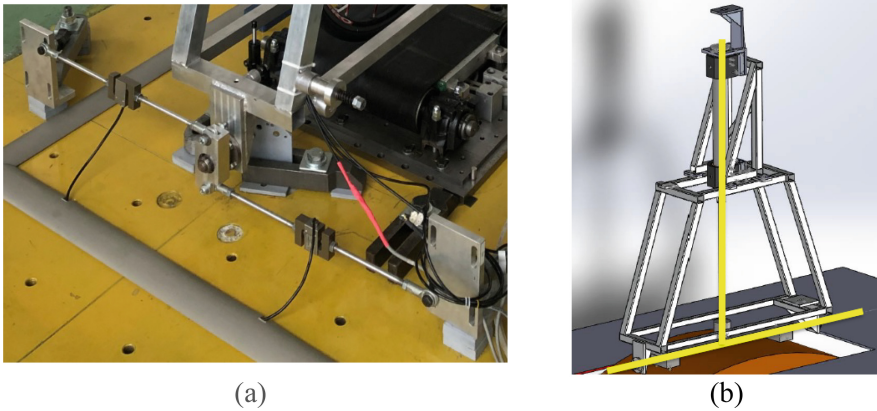


Fig. 2. (a) Watt's linkage on VeTyT. The central part is connected to VeTyT, the rods with load cells are fixed to the ground [4]. (b) VeTyT main axes are enlightened in yellow. The vertical axis defined by the steering shaft crosses the longitudinal axis in the center of tyre contact patch [4].

the perpendicularity with respect to the longitudinal axis of VeTyT. Assuming the self-aligning torque equal to zero by hypothesis, the applied force was compared to the actual value of lateral force given by the test-rig [4]. The measured force was found to be slightly higher than the applied one, for a systematic error of about 4.5 N. Referring to accuracy, the lateral force read by VeTyT corresponds to the actual applied force with a mean error less than 0.3%. Referring to precision, the standard deviation is less than 2% with respect to the mean value.

As for the self-aligning torque, we used the high-stiffness rim and an instrumented threaded bar fixed at a given distance from the hub. The torque can be generated by applying a force to the bar. Then, we measure the output given by the test-rig VeTyT [4]. The measured self-aligning torque was underestimated with respect to the actual torque applied. The deformation of chassis during the tests may slightly misalign the bearings, thus increasing the declared friction. During experimental tests, the maximum difference between measured and applied torque was equal to 0.55 Nm.

In this case, referring to accuracy self-aligning torque measured by VeTyT corresponded to the actual applied torque with a mean error lower than 1%. The standard deviation was found to be less than 2.5% with respect to the mean value.

4 Tests and Results

Several tests can be conducted with VeTyT. The static tests involve tyre not rolling on the contact surface, e.g. tyre deflection and contact patch measurements varying inflation pressure and vertical load. The dynamic tests are performed with tyre rolling on the contact surface to measure the lateral force and the self-aligning torque [8]. In this paper, we focus on dynamic tests, in particular on the role of rim stiffness and inflation pressure on the cornering stiffness C_{F_y} .

We conducted the test on a 26 mm wide road racing bicycle tyre, under different vertical loads, inflation pressure and mounted on a commercial aluminum rim and the

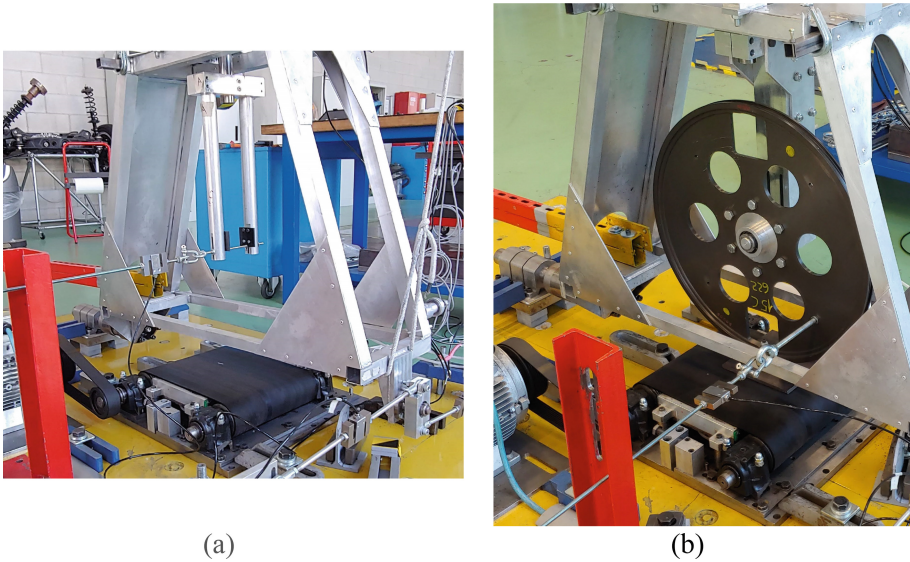


Fig. 3. (a) Watt's linkage on VeTyT. The central part is connected to VeTyT, the rods with load cells are fixed to the ground. (Adapted from [4]) (b) Set-up used to verify the measurement of self-aligning torque. We used the high-stiffness rim with a threaded bar fixed to the rim at a known distance from the hub. (Adapted from [4]).

laboratory high-stiffness rim. The latter is approximately five times stiffer in lateral direction than a standard aluminum rim [8]. Flat track surface was covered by sand of controlled granulometry (1.2 mm).

The value of C_{F_y} largely changes with inflation pressure. As depicted in Fig. 4, the values at inflation pressure of 7.5 bar are higher than those at inflation pressure of 3.5 bar. The peak of cornering stiffness for inflation pressure 7.5 bar corresponds to the maximum tested vertical load of 490 N. As for lower inflation pressures, the peak of cornering stiffness can be found for lower vertical loads. Mounting the same tyre on high-stiffness rim (also named “Rigid rim”), we obtain larger values of cornering stiffness under the same test conditions (inflation pressure and vertical load, Fig. 5). Independently on the inflation pressure or on the vertical load, the value of C_{F_y} is on average 13% higher for the high-stiffness rim. The values of cornering stiffness C_{F_y} were then interpolated with high-order polynomial, to show the trend of cornering stiffness over the applied vertical load.

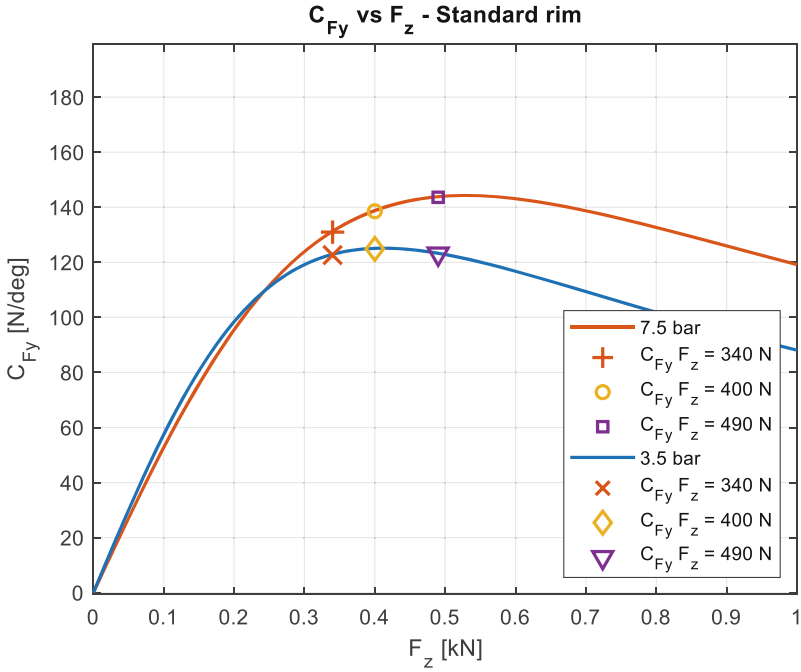


Fig. 4. Cornering stiffness C_{F_y} as function of the vertical load F_z [kN]. The red curve is for inflation pressure of 7.5 bar, the blue one is for 3.5 bar. Tyre was tested on flat track, mounted on aluminum commercial rim [8].

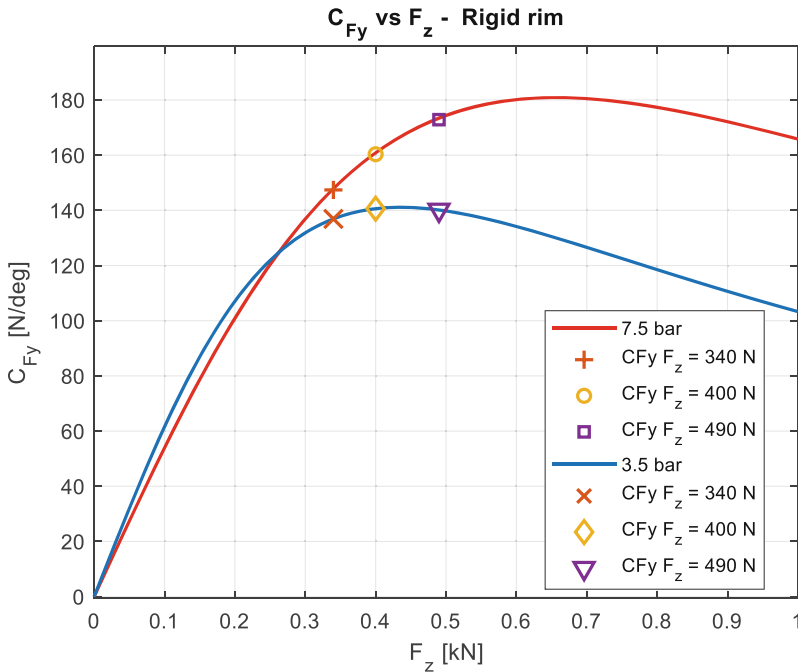


Fig. 5. Cornering stiffness C_{F_y} as function of the vertical load F_z [kN]. The red curve is for inflation pressure of 7.5 bar, the blue one is for 3.5 bar. Tyre was tested on flat track, mounted on high-stiffness rim [8].

5 Conclusion

This paper presents VeTyT, a test-rig specifically designed for bicycle tyres. An experimental verification of the results was carried out. Given known loads, measurements were performed through VeTyT. We found a systematic error of about 4.5 N for the lateral force, which can be easily compensated in post-processing. As for the self-aligning torque, we found a mean error for the measured torque lower than 1%. The standard deviation was found to be less than 2.5% with respect to the mean value.

The results of an experimental campaign were then presented. A 26 mm wide road racing bicycle tyre mounted on aluminum commercial rim and on high-stiffness rim was tested to derive the cornering stiffness by varying some working parameters (inflation pressure and vertical load). The stiffness of the rim largely affects the lateral characteristics of the tyre. It was found that the use of high-stiffness rim can ensure up to 13% higher cornering stiffness for tyres tested under the same working conditions.

The upgrades made to VeTyT allowed it to fulfill the requirements of standard ISO 9001-15. To our knowledge, VeTyT is first test-rig to measure the lateral characteristics of bicycle tyres in compliance with ISO standards.

References

1. Previati, G., Magnani, G., Mastinu, G.: Analysis of bicycle shimmy and relevant bicycle compliances. In: Proceedings, Bicycle and Motorcycle Dynamics 2019 Symposium on the Dynamics and Control of Single Track Vehicles (2019). https://bmd2019.figshare.com/articles/conference_contribution/Analysis_of_Bicycle_Shimmy_and_Relevant_Bicycle_Compliances/12363707. Accessed 05 Jan 2023
2. Tomiati, N., Colombo, A., Magnani, G.: A nonlinear model of bicycle shimmy. *Veh. Syst. Dyn.* **57**(3), 315–335 (2019). <https://doi.org/10.1080/00423114.2018.1465574>
3. Bultink, V.E., Doria, A., Van De Belt, D., Koopman, B.: The effect of tyre and rider properties on the stability of a bicycle. *Adv. Mech. Eng.* **7**(12) (2015). <https://doi.org/10.1177/1687814015622596>
4. Dell'Orto, G., Ballo, F.M., Mastinu, G., Gobbi, M.: Bicycle tyres – development of a new test-rig to measure mechanical characteristics. *Measurement* **202**, 111813 (2022). <https://doi.org/10.1016/j.measurement.2022.111813>
5. Dell'Orto, G., Ballo, F.M., Mastinu, G.: Experimental methods to measure the lateral characteristics of bicycle tyres – a review. *Veh. Syst. Dyn.* **61**, 2738–2760 (2022). <https://doi.org/10.1080/00423114.2022.214488>
6. Dell'Orto, G., Mastinu, G., Happee, R., Moore, J.K.: Measurement of the lateral characteristics and identification of city and cargo bicycle tyres. *Veh. Syst. Dyn.* 1–26 (2024). <https://doi.org/10.1080/00423114.2024.2338143>
7. Dell'Orto, G., Ballo, F.M., Mastinu, G., Gobbi, M., Magnani, G.: Racing bicycle tyres – experimental indoor evaluation of relaxation length. *Meccanica* **58**, 1523–1537 (2023). <https://doi.org/10.1007/s11012-023-01684-z>
8. Dell'Orto, G., Ballo, F.M., Mastinu, G., Gobbi, M., Magnani, G.: Racing bicycle tyres – Influence on mechanical characteristics of internal pressure, vertical force, speed and temperature. *Eur. J. Mech. A/Solids*, **100** (2023). <https://doi.org/10.1016/j.euromechsol.2023.105010>

Open Access This chapter is licensed under the terms of the Creative Commons Attribution 4.0 International License (<http://creativecommons.org/licenses/by/4.0/>), which permits use, sharing, adaptation, distribution and reproduction in any medium or format, as long as you give appropriate credit to the original author(s) and the source, provide a link to the Creative Commons license and indicate if changes were made.

The images or other third party material in this chapter are included in the chapter's Creative Commons license, unless indicated otherwise in a credit line to the material. If material is not included in the chapter's Creative Commons license and your intended use is not permitted by statutory regulation or exceeds the permitted use, you will need to obtain permission directly from the copyright holder.





Driver Behaviour Characterization Using an Instrumented Steering Wheel Conscious/Unconscious Muscle Activation

Xabier Carrera Akutain¹, Francesco Comolli², Massimiliano Gobbi²(✉), Giampiero Mastinu², and Giovanni Radaelli¹

¹ Toyota Motor Europe, Zaventem, Belgium

² Politecnico di Milano, Milan, Italy

massimiliano.gobbi@polimi.it

Abstract. The paper presents an Instrumented Steering Wheel (ISW) that measures the forces and moments that the driver applies at each hand. The ISW is equipped with two six-axis load cells and has the same inertia of a reference steering wheel fitted on normal production cars. The ISW is used to assess the conscious or unconscious application of forces at the steering wheel during a set of manoeuvres. The conscious steering actions refer both to sinusoidal steering input and handling circuit driving. A statistical analysis is performed to characterize the conscious driver behaviour. Referring to unconscious activation of muscles, a kick-plate pass-by manoeuvre is studied. Several drivers are employed for such tests. Typical behavioural patterns are found, describing how drivers apply forces and moments in conscious steering actions. The unconscious moment applied during a kick-plate manoeuvre may be even 20% of the maximum torque applied during counter-steering. The results can be used to develop new driver models, additionally, the ISW is proposed as a tool for properly defining the ADAS intervention logic to reduce the intrusiveness feeling felt by the driver and increase safety in case of unconscious steering actions.

Keywords: Driver-Vehicle Systems · ADAS · Sensors and Actuators

1 Introduction

The knowledge of the forces applied by the driver to the steering wheel is of great utility for assessing the driver-vehicle interaction, either for normal or emergency driving manoeuvres. Such a knowledge is crucial for developing new driver models based on Neuro-Muscular System (NMS) activation [1]. NMS can be activated consciously or unconsciously, if a kick or a shock is applied to the vehicle. Improving ADAS requires the knowledge of forces applied by the hands at the steering wheel [2]. During normal driving, the driver controls the steering wheel by applying forces and moments in all the directions and not only tangentially, the investigation of such a fact has been attempted in the literature. Simple torque sensors have been successfully employed for a long time for measuring the torque applied to the steering wheel and developing the control logic

of Electric Power Steering (EPS) systems. In [3], an ISW able to measure the three forces and moments was presented. Such a device was made from a normal steering wheel divided into three sectors. The ISW was tested on a driving simulator. In this paper, an innovative ISW has been used to measure the forces and the moments applied by the driver during steering manoeuvres. The steering wheel has been designed for the application on real vehicles. The mass, the stiffness, the eigenfrequencies, the power system have been defined for the use on a passenger vehicle. In Sect. 2, the ISW is shown and a brief description of its components is provided, in particular the six axis load cells and the grip force detection system. In Sect. 3, the forces and moments applied by each hand on the ISW have been considered to analyse the behaviour of different drivers in certain driving scenarios. The common attitudes and behaviours of the drivers have been highlighted and analysed. Two cases have been considered, namely conscious and unconscious steering actions.

2 Experimental Setup

2.1 Instrumented Steering Wheel

An ISW which measures the six forces and six moments applied by the driver is presented [2]. The ISW, shown in Fig. 1, has a carbon fiber composite body, two six-axis load cells to measure forces and moments, two handles that the driver must grasp and an electronic-box for signal conditioning. Furthermore, by six mono-axial load cells positioned in the handles, it is possible to measure the grip forces at each hand.

The force and moment signals are sent to an on-board vehicle acquisition system which stores the data, together with the vehicle dynamics data published on the CAN network. Due to the fast transient manoeuvres in which the steering wheel has been used, the compensation of the static weight and of the inertial contribution due to the vehicle dynamics [2] and to the steering rotation is necessary.

2.2 Test Setup

The kinematics of the vehicle were acquired with an OxTS inertial measurement unit, capable of measuring vehicle accelerations in three directions, together with roll, pitch, yaw angles and their derivatives. A GPS antenna was used to track the path of the vehicle. Speed and steering angle data were obtained from the vehicle's CAN network.

Conscious Steering Action: Sine Test. In the sine test the task of the driver is to steer the vehicle at a fixed frequency and fixed amplitude of steering wheel angle oscillation. This sine input is chosen as a high-consistency method, due to its “open-loop” characteristic.

Conscious Steering Action: Handling Circuit Test. The drivers are asked to follow a reference trajectory as close as possible, while driving at high speed. The reference trajectory is a white solid line at the inner edge of the racetrack's width, and it does not correspond to a racing line.



Fig. 1. Instrumented Steering Wheel

Unconscious Steering Action. The vehicle is driven in a kick-plate test, where a moving platform introduces a lateral sliding to the rear axle of the vehicle when it passes over it. In this way, an emergency situation is simulated in which the driver suffers an unexpected lateral disturbance and must keep the vehicle in trajectory by acting on the steering.

3 Data Analysis

3.1 Conscious Steering Action

Sine Test Results. When asked to perform the sine test manoeuvre, different drivers show different approaches when comparing tangential forces applied on the steering wheel. Considering that tangential forces are the main contributors to the steering action, Fig. 2 shows that the more experienced driver (in green) uses a balanced approach, with the two hands mostly cooperating during the steering action. The other two drivers show a “4th quadrant” behaviour, which means that the tangential forces do not cooperate but rather fight each other.

In other words, less experienced drivers prefer to pull downwards with the inner hand rather than pushing upwards with the outer hand and as a result, the force applied by the inner hand has a higher absolute value for them with respect to the professional driver.

Handling Circuit Test Results. In this test the same pattern of dominance of the inner hand is seen once again, as shown in Fig. 3. In this example, as drivers turn the steering wheel clockwise, the tangential force exerted by the inner hand (right one) increases significantly, while the left hand exerts a smaller force in the opposite direction (i.e. without cooperation). In this test all drivers showed a similar behaviour, regardless of skill level.

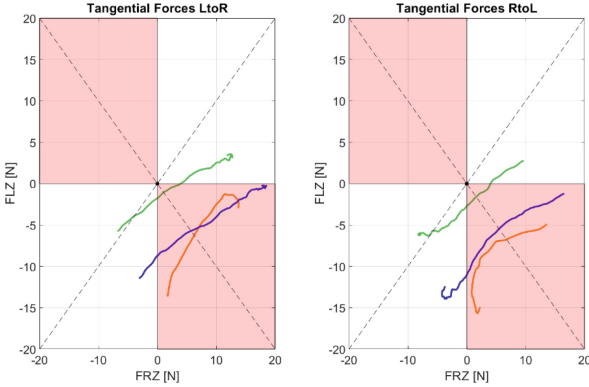


Fig. 2. Tangential Forces in sine test, comparison of 3 different drivers

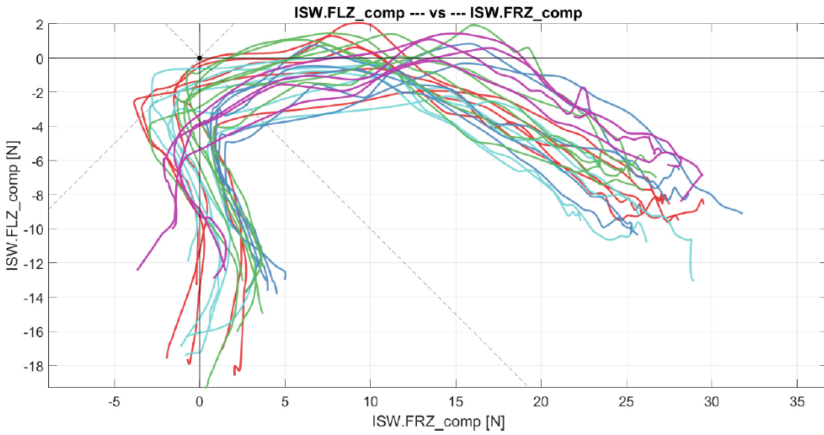


Fig. 3. Tangential forces during a left-to-right chicane, dominant inner hand of different drivers

Steering Quality Index. The classification of the drivers' behaviour is based on heuristic algorithms [4, 5]. For each driving scenario, various analyses have been completed and, when possible, some Key Performance Indicators (KPI) have been calculated to reflect the driving perception. A KPI for the correlation between objective performance of the vehicle and subjective evaluation of the drivers has been defined as follows [4]: *The steering quality index is the standard deviation of the intersection points between the sum of the resultant forces for both hands and a plane perpendicular to the average sum of resultant forces, set at a fixed distance of 0.5 [m].* This index has been measured during the end of the *steer-in* phase, where the steering wheel torque |SWT| has a local minimum. The idea behind this objective indicator is that a subjectively bad *steer-in* manoeuvre is characterized by a high jerkiness of forces at the end of this phase. This jerkiness is reflected both by a change in direction of the forces and by a change in amplitude, the former being the main contributor.

In Table 1, the steering quality index has been computed for 5 vehicle setups used by the professional driver. Vehicle 2 has been used as a benchmark for its well-known good steering characteristics. The steering quality index correctly ranks the benchmark vehicle as the better one.

Table 1. Steering quality index

Steering quality index	Ranking	Vehicle + tyre
0.0113	3	V1_T1
0.0120	4	V1_T2
0.0139	5	V1_T3
0.0100	2	V1_T4
0.0070	1	V2_T5

3.2 Unconscious Steering Action

The ISW is used to assess the unconscious application of forces and moments at the steering wheel during a kick-plate pass-by manoeuvre. The vehicle passes over a plate that is kicked sideways to cause a spin. A prompt counter-steering action is requested to the driver. Due to the side kick, an unconscious steering action is generated, due to the activation of the Neuro-Muscular System.

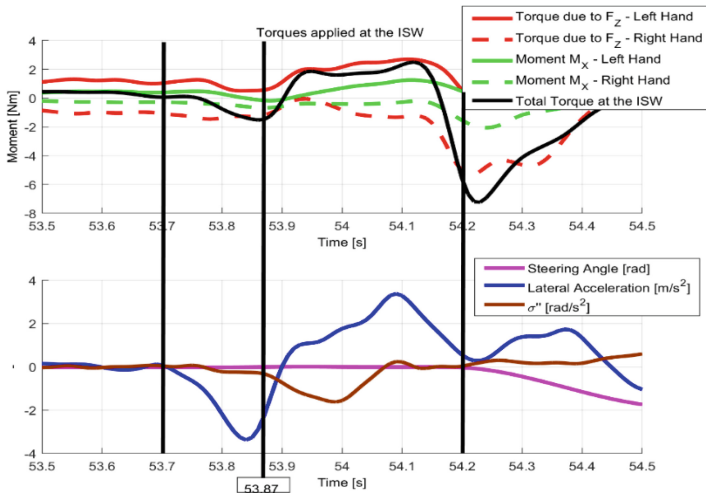


Fig. 4. Unconscious activation of NMS and steering action due to side kick applied.

In Fig. 4, the unconscious activation of the NMS is shown. Actually, at $t = 53.7$ s the vehicle is kicked, as is possible to note from the lateral acceleration graph. Then, at

$t = 53.87$ s the unconscious reflex action reaches its maximum to counter the undesired vehicle motion. At $t = 54.2$ s the conscious steering action is initiated. The unconscious torque is 20% of the absolute value of the maximum torque during the recovering manoeuvre. Analysing a panel of nine different drivers, the maximum of the reflex torque occurs at 0.13 ± 0.03 s after the vehicle disturbance and at 0.28 ± 0.11 s before of the actual steering. Moreover, the unconscious moment applied by the driver influences the vehicle dynamics, e.g. the yaw acceleration. Such an effect highlights the need of a proper modelling of the unconscious driver action, because of its influence on the vehicle dynamics.

4 Conclusion

The presented ISW appears to be the most accurate device for detecting forces and moments applied to the steering wheel by each hand of the driver. The ISW has been used to characterize driving patterns of both professional and regular drivers. Relevant differences exist between forces and moments applied by regular and professional drivers during the sine wave test or the handling circuit test: the professional driver is more efficient in using tangential forces to perform the steering action. The steady state turning analysis has also been considered for analyzing the distribution of tangential forces that is different at the two arms. These forces distribution looks quite consistent between different drivers. A steering quality index has been computed to correlate the measurements of the ISW with the subjective evaluation of the professional driver. Further validation of the index could focus on more repeatable manoeuvres such as U-turns, lane changes and 90° corners as well as on a robust detection of the steer-in phase. Referring to unconscious manoeuvres, occurring when a kick or shock is applied to the vehicle, the forces and moments due to the muscular unconscious activation are considerable, up to 20% of the maximum ones. The muscular activation occurs tenths of second before of the actual steering of the steering wheel, influencing the vehicle dynamics and highlighting the need to model the unconscious reflex muscular activation in the NMS driver models. Such an information could be helpful in designing innovative ADAS (Advanced Driver Assistance Systems) that can intervene in much less time that the actual control systems, increasing the road safety.

References

1. Pick, A.J., Cole, D.J.: A mathematical model of driver steering control including neuromuscular dynamics. *J. Dyn. Syst. Measur. Control* **130**(3) (2008)
2. Gobbi, M., Comolli, F., Hada, M., Mastinu, G.: An instrumented steering wheel for driver model development. *Mechatronics* **64**, 102285 (2019)
3. Gabrielli, F., Pudlo, P., Djemai, M.: Instrumented steering wheel for biomechanical measurements. *Mechatronics* **22**(5), 639–650 (2012)
4. Akutain, X.C., Ono, K., Comolli, F., Gobbi, M., Mastinu, G.: Further understanding of steering feedback and driver behavior through the application of an instrumented steering wheel. In: Pfeffer, P. (ed.) 10th International Munich Chassis Symposium 2019, pp. 481–502. Springer, Heidelberg (2020). https://doi.org/10.1007/978-3-658-26435-2_33

5. AVL-DRIVE The objective assessment of vehicle attributes. www.avl.com/-/avl-drive-4. Accessed 08 Feb 2020

Open Access This chapter is licensed under the terms of the Creative Commons Attribution 4.0 International License (<http://creativecommons.org/licenses/by/4.0/>), which permits use, sharing, adaptation, distribution and reproduction in any medium or format, as long as you give appropriate credit to the original author(s) and the source, provide a link to the Creative Commons license and indicate if changes were made.

The images or other third party material in this chapter are included in the chapter's Creative Commons license, unless indicated otherwise in a credit line to the material. If material is not included in the chapter's Creative Commons license and your intended use is not permitted by statutory regulation or exceeds the permitted use, you will need to obtain permission directly from the copyright holder.





Interaction Between L4 AVs and Human Drivers in Italian Take-over Scenarios

Linda Boscaro², Veronica De Guglielmo¹, Andrea Fossati², Andrea Galbiati²,
Massimiliano Gobbi¹✉, Gianpiero Mastinu¹, Giorgio Previati¹,
Edoardo Sabbioni¹, Maria Gabriella Signorini¹, Antonella Somma²,
Luca Subitoni¹, and Lorenzo Uccello¹

¹ Politecnico di Milano, Milan, Italy
massimiliano.gobbi@polimi.it

² Università Vita-Salute San Raffaele, Milan, Italy
fossati.andrea@hsr.it

Abstract. Automated Driving (AD) technologies are rapidly transforming road transportation, emphasizing the critical role of Human-Machine Interaction (HMI). In this regard, the paper examines the interaction between Level 4 Autonomous Vehicles (L4 AVs) and human drivers in take-over scenarios within Italian traffic environments. Employing the Dynamic Driving Simulator at Politecnico di Milano, the study presents two simulation environments: an urban roundabout and a Ligurian highway. The research aims to measure the driver response during take-over requests. Questionnaires are used to psychologically analyse the participants. Physiological signals, including ECG, EEG, and EDA, are acquired throughout the entire simulation.

Keywords: Automated driving · L4 AVs · Dynamic Driving Simulator

1 Introduction

The rapid advancement of Automated Driving (AD) technologies and their connection to Intelligent Transportation Systems (ITS) is revolutionizing road transport, promising safer roads, reduced pollution, and human-centred solutions [1, 2]. In this regard, Human-machine interaction in Autonomous Vehicles (AVs), particularly during take-over scenarios, emerges as a pivotal research domain. Many are the factors to be carefully studied. The Take-Over Time (TOT) [3] and its relation to the driver state and performance. The Operational Design Domains (ODDs), its correct definition and extension, considering geographical, technological and design limitations [4]. Furthermore, bidirectional human-machine interaction should drive all the technologies related to advanced Automated Vehicles. Specifically, the current trust paradigm, in which the human evaluates the vehicle's ability to drive in a given condition, should be assessed, investigating whether an AV should let the driver regain control [5]. This research aims to study L4 AVs, employing the state-of-the-art Dynamic Driving Simulator at DriSMi Laboratory of Politecnico di Milano [6, 7]. Specifically, the paper

analyzes the take-over manoeuvre, during which the driver is asked to regain control of the vehicle. The study is part of “Interaction of Humans with Level 4 AVs in an Italian Environment - HL4IT” project, stemmed from the necessity to test the admittance of Level 4 AVs in a unique scenario, such as the Italian one. The project, therefore, aims to deploy automated mobility in Italy, pursuing the subsequent objectives:

- the psychophysiological characterization of the driver, interacting with an automated vehicle Level 4 in the Italian environment;
- the definition of an Operational Design Domain adequately representing 80% of the Italian road network and traffic conditions.

Hence three scenarios, representative of the majority of Italian traffic networks, were selected to assess the humans’ capability of regaining control after a TOR respectively in an urban, suburban and highway environment:

1. A urban four-leg roundabout replicated from a real one in Milan.
2. The industrial area of a town located in Friuli-Venezia Giulia, near Udine.
3. An highway scenario, modelled on Ligurian motorways.

The paper is organized as follows. Firstly, it presents a brief literature review to frame the topic covered. Secondly, the two currently developed simulation scenarios are described, focusing on the factor causing ODD exit. The last chapter collects the sensors employed to measure the driver’s response and interaction with the vehicle and the surrounding road elements.

2 Literature Review

L4 AVs, as defined by the Society of Automotive Engineers (SAE), can perform all driving tasks within specific Operational Design Domains (ODDs) [8]. ODDs can be contained by different limitations, such as geographical or technological, making it highly mutable [4]. If an event causes the exit from the ODD, they must give back the control to the human driver or achieve a minimal risk condition. During these events, a Take-Over-Request (TOR) is issued, prompting the driver to take over [9]. The critical period between the TOR and the driver regaining control is known as the Take-Over Time (TOT). Many factors influence the extent of TOT, such as handheld device usage, non-visual tasks, auditory or vibrotactile TORs, and anticipatory cues [3]. Furthermore, studies suggest that a time budget of 10 s is generally adequate for a safe take-over.

Monitoring driver states during this process is complex, possibly involving bio-telemetry systems, such as Electrocardiography (ECG), Electroencephalography (EEG) and Electrodermal Activity (EDA) [10]. Effective warning methods, including auditory, visual, and haptic stimuli, are essential to improve driver response and reduce TOT [11].

2.1 Roundabout Scenario

To test the interaction between humans and AVs Level 4 in an urban context, a network constituted by an orbital and intercity roads and a mini-roundabout has been developed, as shown in Fig. 1. Specifically, a four-leg, single-lane mini-roundabout, located in Milan, was selected as one of the most representative scenarios of the Italian urban environment. The following roundabouts' characteristics justified the choice:

- The presence of a crosswalk at each leg, positioned directly before the entrance to the roundabout.
- The high volume of traffic at two of the legs of the roundabout.
- The standard roundabout's configuration, widely spread in Italy.

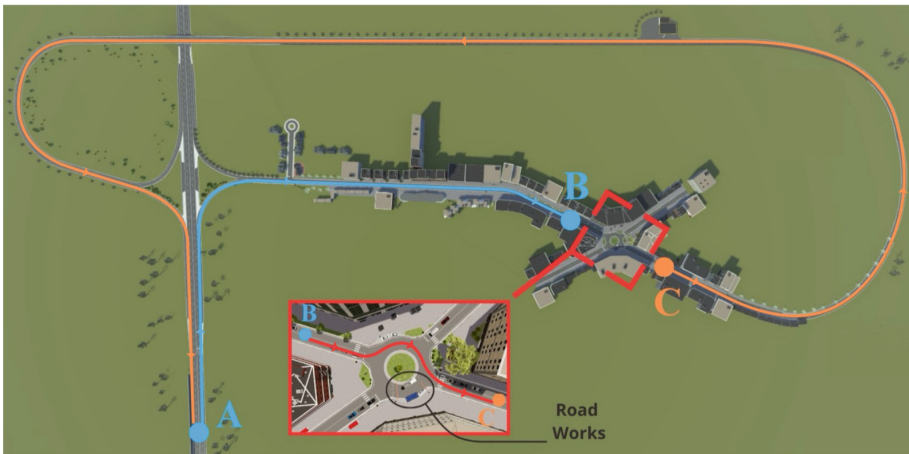


Fig. 1. Simulation environment created using VI-WorldSim.

The simulation environment created was divided into three zones:

1. *Zone 1 (blue section in Fig. 1)*: in the initial part of the route, going from point A to point B and corresponding to an orbital road, the DDT is entirely performed by the ADS. Hence the human being is not driving and is, instead, asked to watch a video on a hand-held device.
2. *Zone 2 (red section in Fig. 1)*: the central part of the route, going from point B to point C, corresponds to the roundabout, where the presence of roadworks caused an alteration of the traffic flow. Specifically, the direction of traffic flow became clockwise, causing the exit from the ODD. Hence the driver is asked to regain control of the vehicle, within the time budget, and to proceed along the route, following the instructions provided on the dashboard. If the driver could not take control of the vehicle, they were asked to remain inside the cockpit, while the Automated Driving System (ADS) achieved the minimal risk condition.

3. *Zone 3 (orange section in Fig. 1)*: the last part of the route, going from point C to point A and corresponding to an orbital road, is travelled solely in the case the driver regained control of the vehicle. While driving in this zone, the driver had to comply with ordinary road rules. An auditory signal warns the driver of exceeding the speed limit, simulating warnings usually installed on the most recent vehicles.

2.2 Highway Scenario

To further investigate the interaction between humans and AVs Level 4, a simulation environment representing a Ligurian motorway has been developed, as shown in Fig. 2. Specifically, a three-lane highway has been selected, including the emergency lane. The subsequent motorway's characteristics justified the choice:

- The presence of tunnels and bridges;
- The risk of wind gusts;
- The standard highway configuration, widely spread in the Italian coastline.

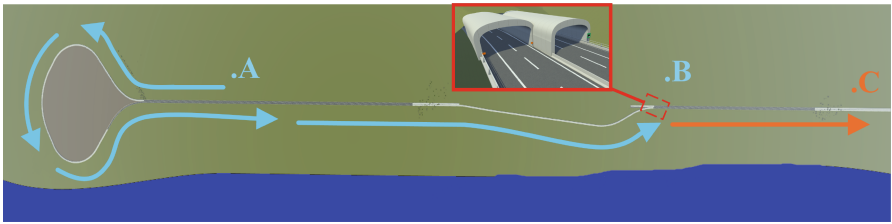


Fig. 2. Simulation environment created using VI-WorldSim.

During the simulation, three driving phases are considered:

1. *Phase 1 (blue section in Fig. 2)*: in the first part of the manoeuvre, going from point A to point B and corresponding primarily to a tunnel, the DDT is entirely performed by the ADS. Hence the human being is not driving and they are asked to watch a video on a hand-held device.
2. *Phase 2*: At the exit of the tunnel, corresponding to point B, a wind gust caused the exit from the ODD. Hence the ADS prompted a TOR to the driver, who was asked to regain control of the vehicle within the TOT, proceeding along the route. If the driver could not perform the DDT, they were asked to remain inside the cockpit, while the ADS achieved the minimal risk condition.
3. *Phase 3: (orange section in Fig. 1)*: the last part of the route, starting from point C, was travelled solely in the event the driver regained control of the vehicle.

3 Overview of the Collected Physiological and Psychological Measures from Drivers

Drivers’ physiological signals are continuously monitored throughout the driving simulation. Figure 3 illustrates the recorded set of data, which includes ECG [12,13], EEG, and EDA [15] signals, as well as eye-tracking data and the forces applied to the steering wheel [14,16]. Additionally, questionnaires are used to describe the drivers’ psychological status. Before the driving session, participants completed several psychological measures. Specifically, the Technological Optimism Scale (TOS), assesses views on technology, the Perception of Driving an Automated Vehicles Scale (PDAV) gauges disposition towards automated vehicles, and the Differential Emotions Scale (DES) rates emotional states, based on a 5-point and a 7-point Likert’s scale, respectively. Furthermore, the Manchester Driver Behaviour Questionnaire (DBQ) measures self-reported driving behaviours and the Big Five Inventory (BFI) evaluates personality traits are also considered. After the driving session, additional measures, such as the Simulator Sickness Questionnaire (SSQ), the Presence Questionnaire (PQ), measuring the sense of presence in the virtual scenario, and the PDAV and the DES, were administered.

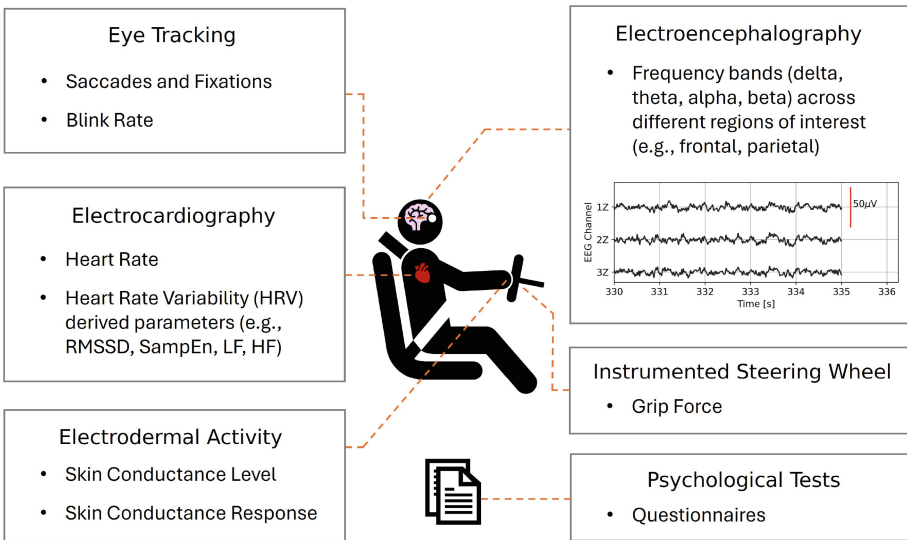


Fig. 3. Outline of the physiological and psychological data collected from each subject, along with relevant parameters. The EEG signals shown in the figure illustrate actual pre-processed data from three exemplary midline electrodes, acquired during a driving simulation session.

The project has been funded by NextGenerationEU, M4C2 I1.1, Progetto PRIN 2022 “HL4IT”, Prot. 2022L3M25K - CUP D53D23003750006.

References

1. Campi, E., et al.: Roundabouts: traffic simulations of connected and automated vehicles—a state of the art. *IEEE Trans. Intell. Transp. Syst.* **25**(5), 3305–3325 (2024). <https://doi.org/10.1109/TITS.2023.3325000>
2. Ferrarotti, L., et al.: Autonomous and human-driven vehicles interacting in a roundabout: a quantitative and qualitative evaluation. *IEEE Access* **12**, 32693–32705 (2024). <https://doi.org/10.1109/ACCESS.2024.3370469>
3. Zhang, B., et al.: Determinants of takeover time from automated driving: a meta-analysis of 129 studies. *Transp. Res. Part F Traffic Psychol. Behav.* **64**, 285–307 (2019). <https://doi.org/10.1016/j.trf.2019.04.020>
4. Committee, On-Road Automated Driving (ORAD). Taxonomy and Definitions for Terms Related to Driving Automation Systems for On-Road Motor Vehicles (2021). <https://doi.org/10.4271/J3016.202104>
5. Wang, C., et al.: Traffic safety improvement through evaluation of driver behavior - an initial step towards vehicle assessment of human operators. SAE Technical Paper (2023). <https://doi.org/10.4271/2023-01-0569>
6. DriSMi - Driving Simulator Politecnico di Milano. Accessed 1 Mar 2024
7. Previati, G., et al.: Influence of the inertia parameters on a dynamic driving simulator performances. In: 81st Annual Conference on Savannah, 2022. Society of Allied Weight Engineers. 3775. <https://www.sawe.org/papers/3775/buy>
8. SAE Levels of Driving Automation™ Refined for Clarity and International Audience. <https://www.sae.org/blog/sae-j3016-update>. Accessed 4 Mar 2024
9. Bahram, M., Aeberhard, M., Wollherr, D.: Please take over! An analysis and strategy for a driver take over request during autonomous driving. In: 2015 IEEE Intelligent Vehicles Symposium (IV), pp. 913–919 (2015). <https://doi.org/10.1109/IVS.2015.7225801>
10. Minea, M., et al.: Advanced e-call support based on non-intrusive driver condition monitoring for connected and autonomous vehicles. *Sensors* **21**(24) (2021). <https://doi.org/10.3390/s21248272>
11. Yun, H., Yang, J.: Multimodal warning design for take-over request in conditionally automated driving. *Eur. Transp. Res. Rev.* **12**(1), 34 (2020). <https://doi.org/10.1186/s12544-020-00427-5>
12. Signorini, M.G., et al.: Monitoring fetal heart rate during pregnancy: contributions from advanced signal processing and wearable technology. *Comput. Math. Methods Med.* **2014** (2014). <https://doi.org/10.1155/2014/707581>
13. Task Force European Society of Cardiology. “Heart rate variability: standards of measurement, physiological interpretation, and clinical use.” *Circulation*, vol. 93, no. 5, pp. 1043–1065 (1996). <https://doi.org/10.1161/01.CIR.93.5.1043>
14. Reali, P., et al.: Integrated data analysis for the quantification of emotional responses during video observation. In: 2017 IEEE 3rd International Forum on Research and Technologies for Society and Industry (RTSI) (2017). <https://doi.org/10.1109/RTSI.2017.8065945>
15. Reali, P., et al.: Towards the development of physiological models for emotions evaluation. In: 2018 40th Annual International Conference of the IEEE Engineering in Medicine and Biology Society (EMBC) (2018). <https://doi.org/10.1109/embc.2018.8512236>
16. Healey, J.A., Picard, R.W.: Detecting stress during real-world driving tasks using physiological sensors. *IEEE Trans. Intell. Transp. Syst.* **6**(2), 156–166 (2005). <https://doi.org/10.1109/TITS.2005.848368>

Open Access This chapter is licensed under the terms of the Creative Commons Attribution 4.0 International License (<http://creativecommons.org/licenses/by/4.0/>), which permits use, sharing, adaptation, distribution and reproduction in any medium or format, as long as you give appropriate credit to the original author(s) and the source, provide a link to the Creative Commons license and indicate if changes were made.

The images or other third party material in this chapter are included in the chapter's Creative Commons license, unless indicated otherwise in a credit line to the material. If material is not included in the chapter's Creative Commons license and your intended use is not permitted by statutory regulation or exceeds the permitted use, you will need to obtain permission directly from the copyright holder.





A Moving Laboratory for Automotive Components Safety Testing (MoLAS)

A. Biffi, F. Ballo, M. Gobbi^(✉), and G. Mastinu

Politecnico di Milano, Milan, Italy
massimiliano.gobbi@polimi.it

Abstract. The MoLAS is a moving laboratory able to fully characterize the tire behavior in the real working environment. The basic structure of the moving laboratory is represented by a semi-trailer. A rotating frame that supports the measuring system is used to set the camber level by using an electric actuator. An electric steering actuation system guarantees high output torque and high output power. A pneumatic actuator is used to apply the vertical load, allowing to generate a large range of vertical force up to SUVs values. A complex driveline including an internal combustion engine (ICE) coupled with the gearbox and an electromagnetic (EM) retarder is used to apply both driving and braking torques. This aspect constitutes a new feature of the system.

Keywords: tire testing · outdoor · driving/braking torque

1 Introduction

With the aim of designing and developing safe and efficient vehicles, tire characterization covers a crucial role. Multi-body models employed for vehicle handling simulations require detailed descriptions of forces and moments exchanged at the tire-terrain contact area [10]. *Pacejka's Magic Formula* (MF) is the most employed tire model for simulating vehicle handling in different conditions, offering a good compromise among accuracy, reliability and computational effort. However, MF model requires the identification of a set of coefficients, which has to be done by means of a curve fitting procedure over a large number of physical tests. For this reason, proper testing facilities are mandatory to accurately measure tire forces and tire slip in well defined loading conditions [12]. Concerning with tire testing facilities, both indoor and outdoor test rigs can be found [10, 12]. Indoor-type testing facilities allow to replicate tire working conditions within a controlled laboratory environment. On the other hand, outdoor test rigs allow for tire testing under more realistic operative conditions, i.e. on real road surfaces like asphalt or tarmac. Such kind of machines are generally mounted on moving trailers that can be driven on public roads like the Simcenter Tire (formerly TNO/TASS Delft Tyre) semi-trailer [11] and the skid trailers by Dufournier Industries [4]. The Simcenter Tire semi-trailer, developed by the

TU-Delft university, features a structure able to accommodate up to two wheels (one per side), one side has car tire measurement setup, while the other allows to apply camber angles up to 70° for motorcycle tire measurement. The Dufournier skid-trailer test rig is composed by a dual-axle lightweight trailer and it is able to characterize C1 and C2 car tires. The wheel is mounted on an actuated tower, while 6 axes hub sensor is located on the spindle and allows to measure tire contact forces and moments. In the mentioned outdoor test rigs, dedicated actuators are able to control vertical load, camber angle, steering angle and braking force. However, the main limitation of these laboratories lies in the fact that longitudinal forces can be applied only by braking, meaning that only longitudinal positive slip conditions can be actually investigated. In this paper, an innovative Moving Laboratory for Automotive components Safety (MoLAS) assessment is presented. MoLAS is a moving laboratory for tire testing and its aim is that of providing a comprehensive suite of testing conditions within a single unit. Its main innovation with respect to current state of the art test rigs relies in the possibility of testing tires both in traction and braking slip condition, allowing for a complete characterization of the tire. This is obtained thanks to the introduction of an internal combustion engine (ICE) in the drive line, enabling testing the tire also in traction slip conditions. The MoLAS is able to characterize tire sizes ranging from 16 to 24 in., with a width up to 345 mm. Tire forces are measured by means of a 6-axis measuring wheel mounted on the spindle.

2 MoLAS Equipment

The basic structure of the moving laboratory is represented by a semi-trailer frame, characterized by three different containers: the electric generator and warehouse container, the measuring unit and the control room. The total length of the semi-trailer is approximately 11 m, with a total mass of 17000 kg (Fig. 1, left).



Fig. 1. MoLAS test system (left), MoLAS measuring unit structure (right).

The core structure of the measuring unit (Fig. 1, right), is represented by a double-framed solution

- a fixed frame (orange in Fig. 1, right) linked to the semi-trailer chassis, providing stiffness and supporting all the suspended parts;
- a rotating frame (gray in Fig. 1, right), pinned to the fixed frame and able to rotate to apply the desired camber angle.

A double stage suspension system, designed to filter out vertical disturbances coming from road irregularity, holds the wheel. The vertical load (up to $20kN$) is imposed by means of a pneumatic spring placed on top of the wheel supporting structure (see the red arrow in Fig. 1, right).

The camber angle is provided by an electro-mechanical linear actuator mounted on top of the structure (see the green arrow in Fig. 1, right). The linear actuator is moved by a three-phase 230 V electric motor coupled with a linear ball screw drive, reaching a maximum force of 13 kN and a camber angle in the range $\pm 5^\circ$. The steering angle, varying between $\pm 20^\circ$, is controlled by means of a second electric motor mounted on the steering axis. The electric motor features an output power of 3 kW and is coupled with a planetary gear reduction, the maximum deliverable output torque is around 1250 Nm. Thanks to this arrangement, the steering axis falls exactly in the middle plane of the wheel, removing any tire scrub effect during the steering maneuver. Moreover, being the steering system mounted on the moving frame, this condition holds also for any value of imposed camber angle.

The main innovation introduced by the MoLAS system is the possibility of testing tires both in braking and traction slip conditions, thanks to its complex driveline, which is composed by a V6 2.9 liters ICE coupled with a 8-speed automatic transmission, providing the driving torque; an electromagnetic retarder, applying and controlling the braking torque; an electro-magnetic clutch able to decouple the wheel from the transmission; two angular drives, transferring the rotating motion between perpendicular axes; three torsional joints, connecting the shafts.

2.1 Forces and Moments Acquisition

Contact forces and moments acting at the wheel center are measured by means of the six-axis dynamometric wheel sensor shown in Fig. 2, right.

The sensor is constituted by a three-spoked structure connected to an outer ring by means of specifically designed laminae. The proposed structure realizes a “quasi”-statically determined structure, which allows to obtain the highest measuring accuracy [2, 7, 9]. A set of strain gauges is able to compute the three forces and three moments acting at the hub by measuring the bending strain on the three spokes. The proposed structure has been successfully employed for the realization of six-axis load cells [2, 3, 7, 9] and smart wheels for road vehicles [6] and motorcycles [5]. A wireless communication system has been specifically set up to transmit the signals related to the six-forces/moments and to the wheel rotation angle to the telemetry system located on board of MoLAS. The computed signals are sent to an on-board receiver via Bluetooth connection; the receiver is connected to a Controlled Area Network (CAN) and transmits the

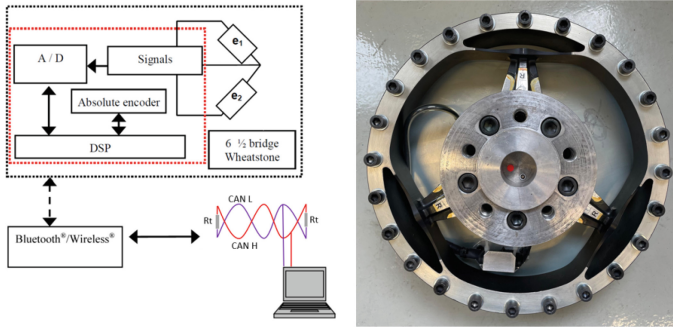


Fig. 2. Six-axis force sensor telemetry system (left), six-axis hub sensor for tire forces and moments measurement (right).

signals to the MoLAS datalogger. The scheme of the wheel telemetry system is depicted in Fig. 2, left.

3 Indoor Tire Characterization

A complete characterization of a 245/45 R18 100 Y radial tire was performed on the MoLAS test bench. The characterization was done by placing the MoLAS semi-trailer over the RuotaVia drum at the Laboratory for the Safety of Transportation (LaST) of Politecnico di Milano as shown in Fig. 3.



Fig. 3. MoLAS semi-trailer on the RuotaVia drum.

The tire was inflated at 210 kPa, the drum tangential speed was set to 22.2 m/s and a series of tests in pure lateral, pure longitudinal and combined lateral-longitudinal conditions have been conducted. The drum surface was covered with a specific sandpaper tape (see Fig. 3) to replicate high-grip dry asphalt conditions. Three different vertical loads were set for the tests, namely 2900 N, 4000 N and 5200 N. The lateral force was applied by imposing a steering motion law in the range $\pm 10^\circ$ following a triangular waveform. The longitudinal force was applied by setting different levels of the retarder brake intensity.

Signals related to the tire forces, actuators position and angular speeds were synchronously sampled at a frequency of 500 Hz and filtered down to 25 Hz in post-processing stage. Experimental data were used for characterizing the tire behavior under pure cornering, pure longitudinal and combined slip conditions. A curve fitting procedure was implemented to identify the MF parameters. Post-processed experimental data, coming from the tests, were collected in different TYDEX files [13] which were used as input for the Adams tire data fitting toolkit (TDFT) [1]. The PAC 2002 MF tire model [1, 10] was selected for interpolating the experimental data. The selected model was proven to be applicable for tires with camber angles not exceeding 15° , travelling on smooth roads up to frequencies of 12 Hz [8]. The Adams TDFT outputs the coefficients of the MF in a *tire property file* (*.tir), containing all the information regarding the tire behavior under the possible operative conditions. In Fig. 4, the experimental data (circles) and the MF model (solid lines) are reported. On the left, the identified curves of the lateral force F_y for pure cornering slip condition under three different vertical loads and zero camber angle. On the right side, the longitudinal force F_x as function of the longitudinal slip is shown for pure braking conditions. The comparison shows that the identified model is well fitting the experimental data for the three considered vertical loads, showing a good agreement both in the linear and saturation regions.

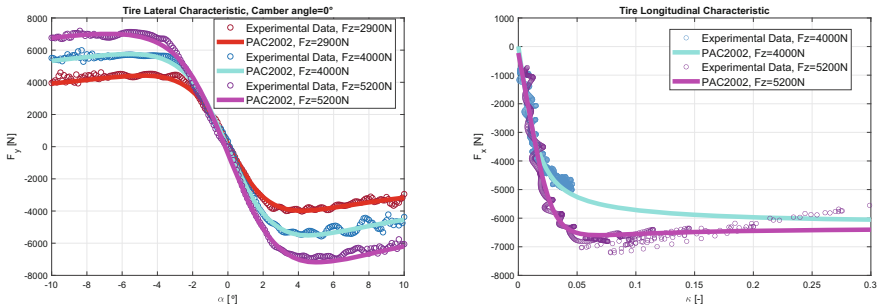


Fig. 4. Characteristic curves of 245/45 R18 tire. Circles represent experimental data, solid lines represent PAC2002 fitted curve.

4 Conclusions

The MoLAS is a cutting edge testing laboratory, as it allows to obtain a complete characterization of road vehicles tires under a large variety of working conditions in a single unit. The main innovation introduced by this test rig relies in the ability to test the tire under both braking and traction slip conditions, thanks to the combined action of a controlled electromagnetic brake retarder and an ICE installed on the driveline. Tire-terrain contact forces and moments are measured

by means of a specifically designed 6-axes force sensor mounted on the rotating hub. In this paper, the MoLAS trailer was placed on on the RuotaVia drum of the LaST laboratory of Politecnico di Milano for a complete indoor characterization of a 245/45 R18 100 Y radial tire. A PAC 2002 MF tire model was selected to characterize the tire behaviour under lateral, longitudinal and combined steady-state conditions. Experimental data were employed to identify the required set of coefficients of the MF model, by means of the TDFT implemented in Adams. Results confirmed the ability of the MoLAS to provide reliable experimental data to be used for tire characterization and modelling, which are essential for accurately create vehicle dynamics simulations.

References

1. Adams: Adams 2020 adams tire user's guide (2020). <http://msc-documentation.questionpro.com>
2. Ballo, F., Gobbi, M., Mastinu, G., Previati, G.: Advances in force and moments measurements by an innovative six-axis load cell. *Exp. Mech.* **54**(4), 571–592 (2014)
3. Ballo, F., Gobbi, M., Mastinu, G., Previati, G.: A six axis load cell for the analysis of the dynamic impact response of a hybrid III dummy. *Measurement* **90**, 309–317 (2016). <https://doi.org/10.1016/J.MEASUREMENT.2016.04.047>
4. Doufornier-Industries: Skid Trailer (2024). <https://www.dufournier.com/testing-equipment/skid-trailer>
5. Gobbi, M., Mastinu, G., Ballo, F., Previati, G.: Race motorcycle smart wheel. *SAE Int. J. Passenger Cars Mech. Syst.* **8**(1), 119–127 (2015). <https://doi.org/10.4271/2015-01-1520>
6. Gobbi, M., Mastinu, G., Previati, G., Pennati, M.: 6-axis measuring wheels for trucks or heavy vehicles. *SAE Int. J. Commer. Veh.* **7**(1), 141–149 (2014). <https://doi.org/10.4271/2014-01-0816>
7. Gobbi, M., Previati, G., Guarnieri, P., Mastinu, G.: A new six-axis load cell. part ii: error analysis, construction and experimental assessment of performances. *Exp. Mech.* **51**(3), 389–399 (2011)
8. Kuiper, E., Van Oosten, J.J.: The PAC2002 advanced handling tire model. *Veh. Syst. Dyn.* **45**(SUPPL. 1), 153–167 (2007). <https://doi.org/10.1080/00423110701773893>
9. Mastinu, G., Gobbi, M., Previati, G.: A new six-axis load cell. Part I: Des. *Exp. Mech.* **51**(3), 373–388 (2011)
10. Pacejka, H.: *Tyre and Vehicle Dynamics*, 3rd edn. Butterworth-Heinemann, Oxford (2012)
11. Simcenter-Tire: Tire modeling made easy with off-the shelf parameter sets (2020). <https://blogs.sw.siemens.com/simcenter/off-the-shelf-parameter-sets-for-tire-modelling/>
12. Smith, G.: The development of an efficient tyre testing procedure to gather data for the parameterisation of Magic Formula 6.1 tyre models. Ph.D. thesis, Coventry University (2018)
13. Unrau, H.J., Zamow, J.: Tydex-format, description and reference manual. release 1.3 (1997). <https://doi.org/10.5445/IR/1000158921>

Open Access This chapter is licensed under the terms of the Creative Commons Attribution 4.0 International License (<http://creativecommons.org/licenses/by/4.0/>), which permits use, sharing, adaptation, distribution and reproduction in any medium or format, as long as you give appropriate credit to the original author(s) and the source, provide a link to the Creative Commons license and indicate if changes were made.

The images or other third party material in this chapter are included in the chapter's Creative Commons license, unless indicated otherwise in a credit line to the material. If material is not included in the chapter's Creative Commons license and your intended use is not permitted by statutory regulation or exceeds the permitted use, you will need to obtain permission directly from the copyright holder.





Force Sensors for the Active Safety of Road Vehicles

M. Milivinti, M. Amadini, F. Ballo, M. Gobbi^(✉), and G. Mastinu

Politecnico Di Milano, Milan, Italy
massimiliano.gobbi@polimi.it

Abstract. Force and moment measurement within road vehicles plays a break-through role in automotive engineering. Both wheel force transducers and instrumented hub carriers are considered in the paper. Both technologies have advantages and disadvantages. Active safety systems (ABS, ESP, up to full automated driving) are expected to be impacted by the measurement of forces and moments at the wheels. Friction potential evaluation and driver model development and monitoring are major field of research. Force and moment measurement technology may also be exploited for lightweight construction purposes. Promising technologies are the ones that don't need RF data transfer, providing low latency for data transfer and are resiliency against cyber-attacks.

Keywords: Force and moment sensor · active safety · stability enhancement systems · structural safety · cooperative connected and automated

1 Introduction

Most of the algorithms used in Vehicle Dynamics Control are based on on-line measurements of the state of the vehicle. Some measurements are directly taken, such as wheels angular velocities [21]. The measure of the force can be provided by components that measure the forces exchanged at the tyres. A state-of-the-art review on the topic is provided in [12]. In [3,6,8,9], the development of an instrumented wheel to measure the forces acting at the wheel hub is presented. The measure is obtained through a patented six-axis load cell [11]. The same technology can be adapted and used by resorting to an instrumented hub carrier [13,20]. Differently to the RF data transfer implemented on the wheel, the hub carrier permits to use a wired measurement system that leads to a lower latency. The component includes a three-spokes structure. The spokes connect the hub case to the external case. To make the structure statically determined, the spokes have an additional degree of freedom along their own axis. On the spokes surface a system of strain gauges detect the deformation of the material that is converted into force measurement. The moment around the wheel axis cannot be detected since it is the degree of freedom of the wheel respect to the suspension. An instrumented brake caliper can be fitted in order to measure the brake torque.

Active safety systems (ABS, ESP, up to full automated driving) are impacted by the measurement of forces and moments at the wheels [1, 8, 12, 13, 21]. New strategies for the control of road vehicles dynamics based on the measurements of the forces acting on the tyres can be implemented

2 Method

Several control algorithm can be applied to ABS system and the main ones are analyzed in [14]. Rule-based ABS are robust to disturbances coming from changes in the road friction coefficient. This is due to the fact that these systems work with the level of acceleration and deceleration of the wheel. As these levels depend only on the difference between the brake and road torque, and not their actual magnitudes, road friction coefficient has little influence on the performance of the system [21]. On the other hand, if the ABS control algorithm is supposed to work based on tyre force measurements (as in this case), the algorithm must be robust enough to guarantee an equivalent performance in the presence of disturbances, model inaccuracies and so on. Under these assumptions, Sliding Mode Control (SMC) seems to meet all the requirements for this particular application. Force based Anti-Lock Braking Systems (ABS) can be developed by using Sliding Mode Control. In literature it is possible to see many example of its application [1, 2, 4, 7, 15–18]. A complex four-wheels multibody model (14 degrees of freedom) has been used to simulate the force based implementation of the ABS logic in comparison with the standard one. The model represents an high-performance sportscar for motorsport applications. Each wheel has an independent ABS control respect to the other wheels. The control computes the optimal brake torque that is applied to the wheel. To the brake torque is applied a filter that modifies the signal with a time delay, a first order delay, a 100 Hz signal resampling and a random noise addition. Two straight braking events have been selected to compare the two ABSs. The first is a 100 km/h braking with high friction coefficient ($\mu = 1.12$) to simulate a dry road. The second is a mixed surface (high $\mu = 1.4$ and low $\mu = 0.7$) μ -split road. Every 4 m, the high μ and low μ sections are inverted giving to the road the shape of a chessboard. The initial speed for this maneuver is 90 km/h.

2.1 Rule-Based ABS Control Logic

Rule-based ABS control logic is based on thresholds on the wheel rotational speed and wheel slip. The check on the variables is done sequentially: firstly the brake torque is adjusted to maintain the wheel acceleration inside the predefined thresholds. If the acceleration is acceptable, the brake torque is adjusted to maintain the wheel slip inside the predefined thresholds.

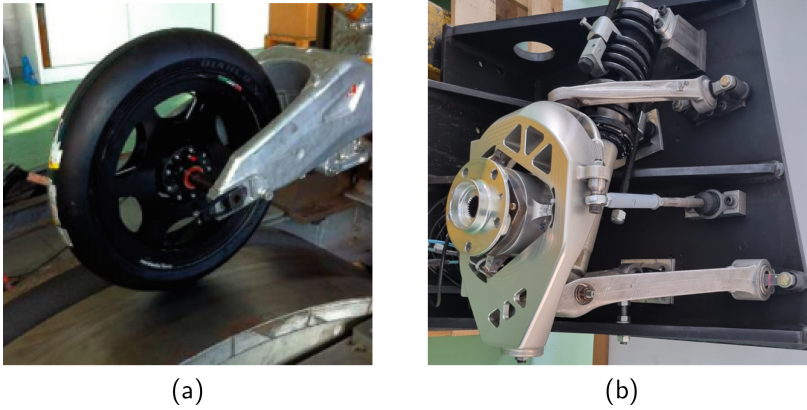


Fig. 1. Race motorcycle smart wheel (a). Instrumented wheel carrier featuring a six-axis load cell (b).

2.2 Sliding Mode Control ABS

The SMC is based on the sliding surface defined as:

$$s = \kappa - \kappa_{des} + K_i \int (\kappa - \kappa_{des}) dt \quad (1)$$

where κ is the slip defined as $\kappa = \frac{V - \Omega R}{V}$, κ_{des} is the desired slip target, K_i is the coefficient of the integral term. The sliding surface was chosen based on the work conducted in [1, 2, 4, 10, 15, 18, 19].

From the sliding surface it is possible to obtain the value of braking torque to be applied to the wheel. The SMC calculates the optimal braking torque to keep the wheel from locking and to maintain the slip close to the desired slip target. The braking torque T_b is defined as:

$$T_b = \hat{T}_b - K sat\left(\frac{s}{\phi}\right) \quad (2)$$

To have a complete mathematical derivation of Eq. 2, please refer to [1, 2, 4, 7, 10, 15, 18]. The presented work to exploit the capabilities of the SMC, it integrates an online tyre-road friction coefficient estimation. Based on the work conducted in [3, 20], the measured forces are used to estimate the friction coefficient. The information is then used to calculate the optimal slip target in order to maximize the braking force [5, 21].

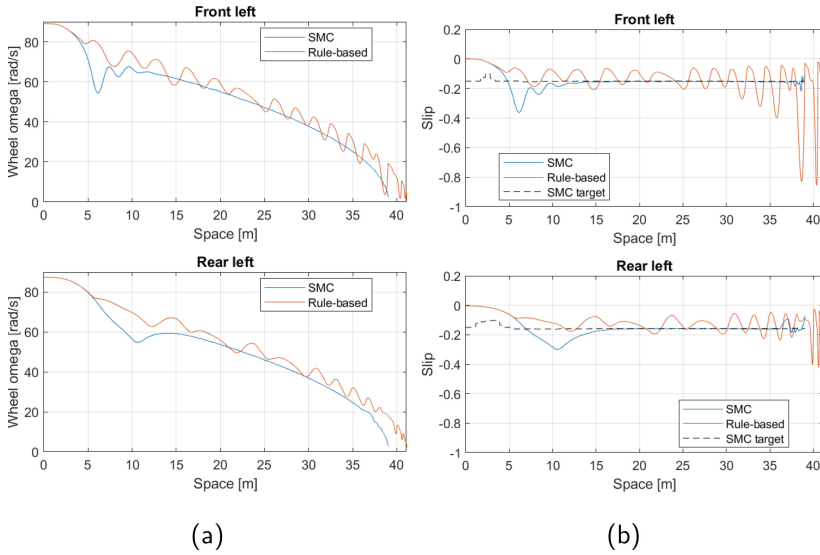


Fig. 2. Wheels angular speed(a) and wheel slips (b). Emergency braking maneuver on high- μ road ($\mu = 1.12$).

3 Results

The results confirm the relevant improvement by using the direct measurement of the wheel forces respect to the actual ABS technology. The simulations have been performed on an emergency brake test in different scenario conditions. The dry braking scenario is representative of conditions where ABS should not be stressed heavily in maintaining the optimal braking force. Results are shown only for the left wheels of the vehicle for symmetry in the results. In both Fig. 2a and Fig. 2b it is possible to see how the rule-based ABS is prone to oscillation. Instead, it is possible to appreciate how the SMC ABS is more precise and less affected by them. figure 2b shows with the black dotted line, the online estimation of the optimal slip target. Once identified the optimal slip target, the SMC ABS is able to almost overlap the real slip to the target one. This lead to the force based ABS to stop the car in 38.9m respect to the 41.2m required by the rule-based ABS. While considering a mixed surface, the benefit is particularly relevant. The force based ABS formulation allows to stop the car in 36.7m, while the rule-based requires 40.8m. In Fig. 2b it is possible to see even better how the optimal slip target changes whenever the wheel passes from one type of asphalt to the other. On the other hand, the rule-based ABS struggle to keep the wheel from locking when the wheel runs on the low adherence block.

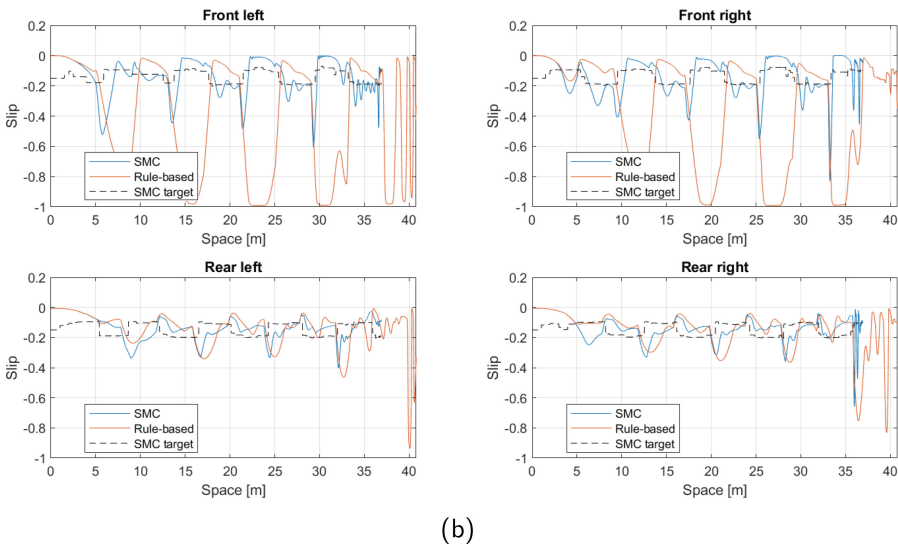
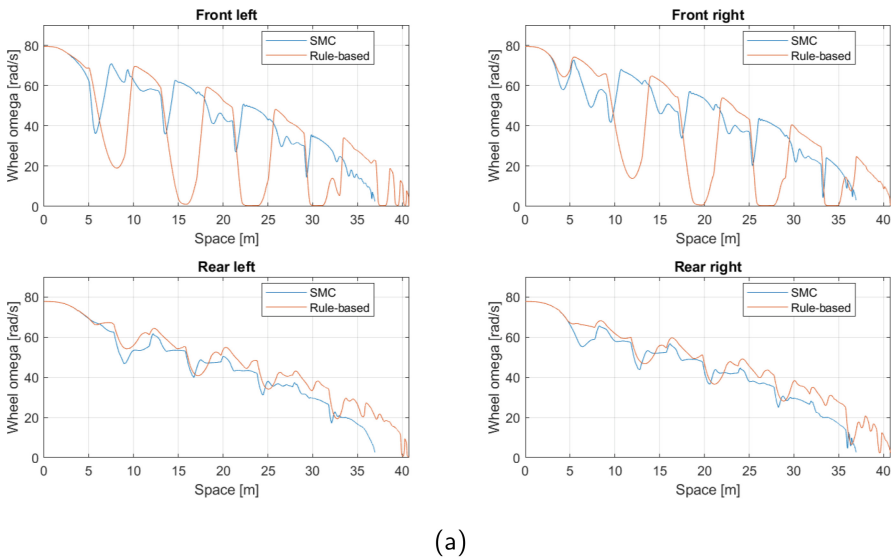


Fig. 3. Wheels angular speed (a) and wheel slip (b). Emergency braking maneuver on a mixed surface road.

References

1. Botero, J.C., Gobbi, M., Mastinu, G., Piazza, N.D., Martorana, R.: On the reformulation of the abs logic by sensing forces and moments at the wheels, pp. 265–272. IFAC Secretariat (2007). <https://doi.org/10.3182/20070820-3-us-2918.00037>

2. Decarlo, R., Zak, S.: A quick introduction to sliding mode control and its applications (2008). Lecture note, Università degli studi di Cagliari
3. Edelmann, J., Gobbi, M., Mastinu, G., Ploechl, M., Previati, G.: Friction estimation at tire-ground contact (2020). <https://doi.org/10.4271/2015-01-1594>
4. Edwards, C., Spurgeon, S.: Sliding Mode Control. CRC Press, Boca Raton (1998). <https://doi.org/10.1201/9781498701822>
5. Gobbi, M.: A $k, k-\epsilon$ optimality selection based multi objective genetic algorithm with applications to vehicle engineering. *Optim. Eng.* **14**, 345–360 (2013). <https://doi.org/10.1007/s11081-011-9185-8>
6. Gobbi, M., et al.: Measurement of the forces and moments acting on farm tractor pneumatic tyres. *Veh. Syst. Dyn.* **43**, 412–433 (2005). <https://doi.org/10.1080/00423110500140963>
7. Gobbi, M., Botero, G., Mastinu, G.: Global chassis control by sensing forces/moments at the wheels. *International J. Veh. Auton. Syst.* **7** (2009). <https://doi.org/10.1504/IJVAS.2009.033262>
8. Gobbi, M., Mastinu, G., Ballo, F., Previati, G.: Race motorcycle smart wheel. *SAE Int. J. Pass. Cars - Mech. Syst.* **8**, 2015–01–1520 (2015). <https://doi.org/10.4271/2015-01-1520>
9. Gobbi, M., Mastinu, G., Comolli, F., Ballo, F., Previati, G.: Motorcycle smart wheels for monitoring purposes (2019). <https://doi.org/10.3390/vehicles2040037>
10. Gusikhin, O., Madani, K., Zaytoon, J. (eds.): Informatics in Control, Automation and Robotics, vol. 793. Springer, Cham (2022). <https://doi.org/10.1007/978-3-030-92442-3>
11. Mastinu, G., Gobbi, M.: Dispositivo e metodo per la misura di forze e momenti (2003). <https://hdl.handle.net/11311/262882>
12. Mastinu, G., Gobbi, M.: Force sensors for active safety, stability enhancement and lightweight construction of road vehicles. *Veh. Syst. Dyn.* **61**, 2165–2233 (2023). <https://doi.org/10.1080/00423114.2023.2240447>
13. Mastinu, G., Gobbi, M., Ballo, F.: Hub carrier comprising force and/or moment sensors (2021). WO2021160629
14. Pretagostini, F., Ferranti, L., Berardo, G., Ivanov, V., Shyrokau, B.: Survey on wheel slip control design strategies, evaluation and application to antilock braking systems. *IEEE Access* **8** (2020). <https://doi.org/10.1109/ACCESS.2020.2965644>
15. Rajendran, S., Spurgeon, S., Tsampardoukas, G., Hampson, R.: Time-varying sliding mode control for abs control of an electric car. *Sci. Direct* (2017). <https://doi.org/10.1016/j.ifacol.2017.08.823>
16. Rajendran, S., Spurgeon, S.K., Tsampardoukas, G., Hampson, R.: Estimation of road frictional force and wheel slip for effective antilock braking system (abs) control. *Int. J. Robust Nonlinear Control* **29**, 736–765 (2019). <https://doi.org/10.1002/rnc.4366>
17. Savaresi, S.M., Tanelli, M., Cantoni, C., Charalambakis, D., Previdi, F., Bittanti, S.: Slip-deceleration control in anti-lock braking systems. *IFAC Proc. Vol.* **38**, 103–108 (2005). <https://doi.org/10.3182/20050703-6-CZ-1902.01905>
18. Slotine, J.J., Li, W.: Applied non linear control. Prentice Hall, Hoboken (1991). <https://doi.org/10.1007/978-1-84628-615-5>
19. Tanelli, M., Piroddi, L., Piuri, M., Savaresi, M.: Real-time identification of tire-road friction conditions. *IEEE* (2008)
20. Viani, G., Chiodarelli, F.: Tyre force and moment measurement using an instrumented upright (2022)
21. Zanten, A.V.: Control of horizontal vehicle motion, pp. 1093–1177 (2006). <https://doi.org/10.1201/b15560>

Open Access This chapter is licensed under the terms of the Creative Commons Attribution 4.0 International License (<http://creativecommons.org/licenses/by/4.0/>), which permits use, sharing, adaptation, distribution and reproduction in any medium or format, as long as you give appropriate credit to the original author(s) and the source, provide a link to the Creative Commons license and indicate if changes were made.

The images or other third party material in this chapter are included in the chapter's Creative Commons license, unless indicated otherwise in a credit line to the material. If material is not included in the chapter's Creative Commons license and your intended use is not permitted by statutory regulation or exceeds the permitted use, you will need to obtain permission directly from the copyright holder.





Design of Explicit and Lateral-Longitudinal Integrated Motion Controller with Safety Guarantee for Autonomous Vehicles

Haoyu Gao¹(✉) , Chang Liu², Yingxi Piao¹ , Sen Yang¹ , Beiyang Jiang³ ,
and Shengbo Eben Li¹ 

¹ Tsinghua University, Beijing 100084, China
ghy22@mails.tsinghua.edu.cn, lishbo@tsinghua.edu.cn

² Peking University, Beijing 100871, China
changliucoe@pku.edu.cn

³ Beijing Union University, Beijing 100101, China
jqrbeiyang@buu.edu.cn

Abstract. Model predictive control (MPC) is an effective method in lateral-longitudinal integrated control with safety guarantee for autonomous vehicles. But its computational burden is significant, making it challenging to meet real-time requirements. The contribution of this paper is to propose an explicitly solvable autonomous vehicle motion controller with lateral-longitudinal integrated characteristics and safety guarantee, achieved by integrating input-output controllers from exponential control Lyapunov function (ECLF) and exponential control barrier function (ECBF). We performed simulations using a high-fidelity dynamics model in CarSim for simple urban traffic scenarios. The simulation results demonstrate that our designed controller has good trajectory tracking performance, safety guarantee, low computational burden and a certain level of robustness.

Keywords: autonomous vehicles motion control · lateral-longitudinal integration · safety guarantee · explicit · nonlinear system · high-order

1 Introduction

Lateral-longitudinal integrated control is an important research direction in autonomous vehicle motion control [1, 8]. Integrated control can more fully consider the coupling characteristics between the longitudinal and lateral dynamics of the vehicle, thereby having a higher performance potential [6]. However, due to the increase in the number of system states and the nonlinearity of the system, the design of control law becomes more challenging, and the computational load during usage is also increased.

Supported by NSF China with 52072213 and U20A20334. It is also partially supported by Tsinghua-Toyota Joint Research Institute Inter-disciplinary Program.

© The Author(s) 2024

G. Mastinu et al. (Eds.): AVEC 2024, LNME, pp. 947–953, 2024.

https://doi.org/10.1007/978-3-031-70392-8_133

Another important research direction is to design motion controllers with safety guarantee. Due to the tracking error and lag, collisions may still occur even if path planning includes safety constraints. While MPC does offer safety guarantee, it comes with a significant computational burden [4, 5]. Therefore, designing a vehicle lateral-longitudinal integrated controller that ensures safety and has a low computational burden is of significant importance.

Control Lyapunov function (CLF) given by Artstein in [3] is an essential tool for the stable control design of affine nonlinear system. Later, based on the idea of CLF and the foundation of barrier certificates theory [9], Wieland introduced the control barrier function (CBF) in [10], a widely favored approach for designing safety control laws among scholars. However, the aforementioned works can only address problems with relative degree 1. Exponential stabilizing control Lyapunov function (ES-CLF) were introduced in [2] to achieve stability of zero dynamics, and later evolved into exponential control Lyapunov function (ECLF) which was commonly used in the stability design of higher-order systems. Inspired by ECLF, exponential control barrier functions (ECBF) were first introduced in [7] as a way to easily enforce high relative-degree safety constraints.

The contribution of this paper is to propose an explicitly solvable autonomous vehicle motion controller with lateral-longitudinal integrated characteristic and safety guarantee, achieved by using exponential control Lyapunov function to address high-order tracking problem and using exponential control barrier function to address high-order constraint problem. We performed simulations using a high-fidelity dynamics model in CarSim for simple urban traffic scenarios. The simulation results demonstrate that our designed controller has good trajectory tracking performance, safety guarantee, low computational burden and a certain level of robustness.

2 Contribution

2.1 Autonomous Vehicles Trajectory Tracker Using Exponential Control Lyapunov Function

The vehicle dynamics model used in the controller design is a six-state system with relative degree 2, given by the following equation:

$$\begin{bmatrix} \dot{X} \\ \dot{Y} \\ \dot{\varphi} \\ \dot{U} \\ \dot{V} \\ \dot{\omega} \end{bmatrix} = \begin{bmatrix} U \cos \varphi - V \sin \varphi \\ U \sin \varphi + V \cos \varphi \\ \omega \\ V\omega \\ -U\omega + \frac{k_f}{m} \left(\frac{V+l_f\omega}{U} \right) + \frac{k_r}{m} \left(\frac{V-l_r\omega}{U} \right) \\ \frac{l_f k_f}{I_z} \left(\frac{V+l_f\omega}{U} \right) - \frac{l_r k_r}{I_z} \left(\frac{V-l_r\omega}{U} \right) \end{bmatrix} + \begin{bmatrix} 0 & 0 \\ 0 & 0 \\ 0 & 0 \\ 1 & -\frac{k_f}{m} \left(\frac{V+l_f\omega}{U} \right) \\ 0 & -\frac{k_f}{m} \\ 0 & -\frac{l_f k_f}{I_z} \end{bmatrix} \begin{bmatrix} a \\ \delta \end{bmatrix} \quad (1)$$

All the variables are illustrated in Fig. 1. To facilitate future use, define $x = [x_1 \ x_2]^T$, $x_1 = [X \ Y \ \varphi]^T$ and $x_2 = [U \ V \ \omega]^T$. The reference trajectory is a time dependent sequence of reference state $x_1^{\text{ref}}(t) = [X^{\text{ref}}(t) \ Y^{\text{ref}}(t) \ \varphi^{\text{ref}}(t)]^T$ which

is located at a distance L from the perpendicular foot of mass center along the reference path, it is also illustrated in Fig. 1. L is proportionally related to the reference speed, and the scale factor is set to 0.5.

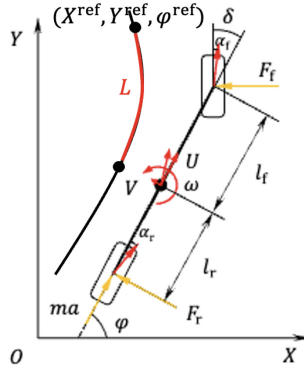


Fig. 1. Vehicle dynamics model and design of reference trajectory

For tracking problem with time-varying reference state $x^{\text{ref}}(t)$, to use ECLF for tracker design, we can treating time-varying reference states as time-varying equilibria. The neglect of the derivatives of reference states may result in some loss of tracking performance, but the impact is minimal, especially when the derivatives is not significant. The original exponential control Lyapunov function for autonomous vehicles trajectory tracker is designed as follows

$$V(x) = (x_1 - x_1^{\text{ref}})^T \begin{bmatrix} 0.3 & 0 & 0 \\ 0 & 0.3 & 0 \\ 0 & 0 & 500 \end{bmatrix} (x_1 - x_1^{\text{ref}}) \tag{2}$$

It can be determined that the relative degree of V is 2 under the system (1). According to the theory of ECLF, we can establish a linear system as follows

$$\dot{\eta}_v(x) = F\eta_v(x) + G\mu, \tag{3a}$$

$$V(x) = C\eta_v(x) \tag{3b}$$

where $\eta_v(x) = \begin{bmatrix} V(x) \\ \dot{V}(x) \end{bmatrix} = \begin{bmatrix} V(x) \\ L_f V(x) \end{bmatrix}$, $F = \begin{bmatrix} 0 & 1 \\ 0 & 0 \end{bmatrix}$, $G = \begin{bmatrix} 0 \\ 1 \end{bmatrix}$, $C = [1 \ 0]$ and $\mu = L_f^2 V(x) + L_g L_f V(x)u$. Using linear control design techniques, we can choose $\mu = -K_v \eta_v(x)$, with K_v ensuring that $A_v = F - GK_v$ has eigenvalues with negative real parts. Furthermore, we can obtain the following control law

$$u^{\text{track}} = (L_g L_f V(x))^+ (-K_v \eta_v(x) - L_f^2 V(x)) \tag{4}$$

Under the assumption that ego vehicle and the obstacle are treated as point masses, the constraint $h(x)$ can be formulated as follows

$$h(x) = (X - X_{\text{obs}})^2 + (Y - Y_{\text{obs}})^2 - d_{\text{safe}}^2 < 0 \tag{5}$$

where X_{obs} and Y_{obs} are the coordinates of the obstacle, and d_{safe} is the minimum safe distance that must be maintained between the vehicle and any obstacles. We construct the following ECBF by $h(x)$

$$B(x) = k^b h(x) = k^b [d_{\text{safe}}^2 - (X - X_{\text{obs}})^2 - (Y - Y_{\text{obs}})^2] \tag{6}$$

where $k^b \in \mathbb{R}_+$. Likewise, the relative degree of B under the system (1) is also 2. According to the theory of ECBF, we can establish a linear system as follows

$$\dot{\eta}_b(x) = F\eta_b(x) + G\mu, \tag{7a}$$

$$B(x) = C\eta_b(x) \tag{7b}$$

where $\eta_b(x) = \begin{bmatrix} B(x) \\ \dot{B}(x) \end{bmatrix} = \begin{bmatrix} B(x) \\ L_f B(x) \end{bmatrix}$, $F = \begin{bmatrix} 0 & 1 \\ 0 & 0 \end{bmatrix}$, $G = \begin{bmatrix} 0 \\ 1 \end{bmatrix}$, $C = [1 \ 0]$ and $\mu = L_f^2 B(x) + L_g L_f B(x)u$. Likewise, we can choose $\mu \geq -K_b \eta_b(x)$, with K_b ensuring that $A_b = F - GK_b$ has eigenvalues with negative real parts. Furthermore, we can obtain the following control law

$$u^{\text{safe}} = (L_g L_f B(x))^+ (-K_b \eta_b(x) + \tau - L_f^2 B(x)) \tag{8}$$

where $\tau \in \mathbb{R}_+$. The final step is to fuse u^{track} and u^{safe} , resulting in a controller that achieves both tracking performance and safety. We adopt the method proposed by Wieland in [10], replacing CBF with ECBF. The method is as follows

$$u = \begin{cases} u^{\text{track}} & \text{if } B(x) \leq -\epsilon, \\ \sigma u^{\text{track}} + (1 - \sigma)u^{\text{safe}} & \text{if } B(x) \in (-\epsilon, 0), \\ u^{\text{safe}} & \text{if } B(x) \geq 0, \end{cases} \tag{9}$$

where $\sigma = -2 \left(\frac{B(x)}{\epsilon}\right)^3 - 3 \left(\frac{B(x)}{\epsilon}\right)^2 + 1$, $\epsilon \in \mathbb{R}_+$.

3 Simulation

The controller parameters are selected as follows: $K_v = [2 \ 3]$, $K_b = [2 \ 3]$, $k_b = 0.2$, $\tau = 1$ and $\epsilon = 0.25$. The control object in the simulation is the CarSim high-fidelity vehicle dynamics model.

3.1 Pure Trajectory Tracking

Pure trajectory tracking simulation including straight through intersection and right turn through intersection. In the multi-lane setup, the reference driving speed is established at 10 m/s. However, this speed is adjusted to 8 m/s at intersections, and further reduced to 5 m/s when executing turns at intersections. The simulation results are shown in Fig. 2 and Fig. 3.

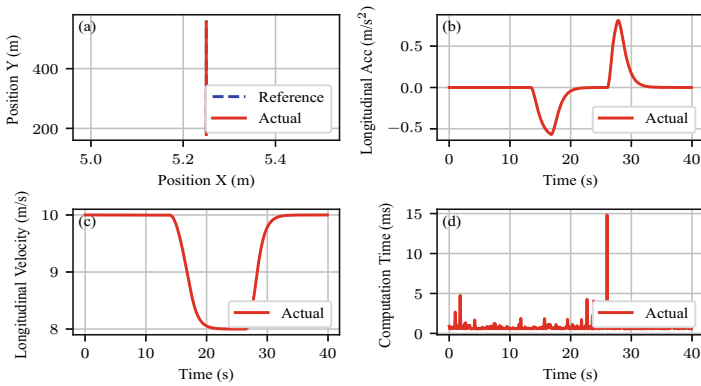


Fig. 2. Parameters in Variable-Speed Straight-Line Scenario

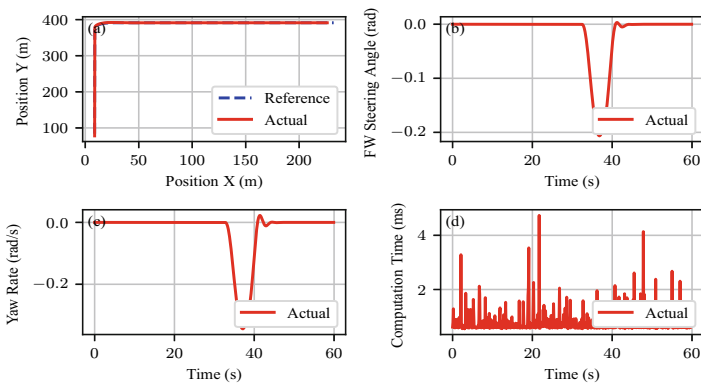


Fig. 3. Parameters in Variable-Speed Right-Turn Scenario

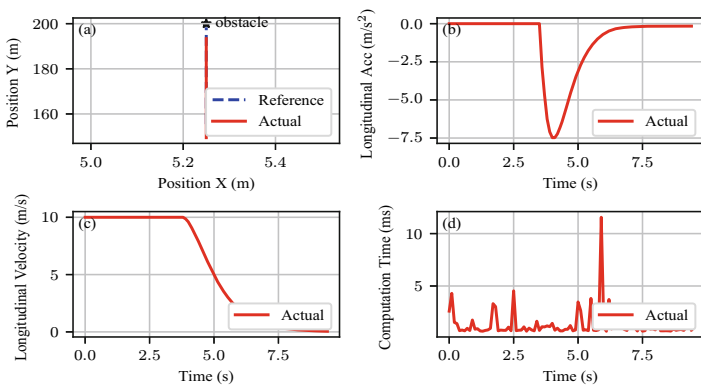


Fig. 4. Parameters in Straight-Line Collision Avoidance Scenario

3.2 Trajectory Tracking with Collision Avoidance

The vehicle is traveling in a straight line when a stationary obstacle suddenly appears ahead. d_{safe} is set to 6 m. It was observed that the vehicle executed a reasonable braking maneuver, ultimately coming to a stop at a distance of 6.24 m from the obstacle. The simulation results are shown in Fig. 4.

4 Conclusion

The simulation results demonstrate that our designed controller has good trajectory tracking performance, safety guarantee, low computational burden and a certain level of robustness. As a next step, we aim to propose an integrated optimization method for the tunable parameters in the controller to enhance its optimality.

References

1. Amer, N.H., Zamzuri, H., Hudha, K., Kadir, Z.A.: Modelling and control strategies in path tracking control for autonomous ground vehicles: a review of state of the art and challenges. *J. Intell. Robot. Syst.* **86**, 225–254 (2017)
2. Ames, A.D., Galloway, K., Sreenath, K., Grizzle, J.W.: Rapidly exponentially stabilizing control lyapunov functions and hybrid zero dynamics. *IEEE Trans. Autom. Control* **59**(4), 876–891 (2014). <https://doi.org/10.1109/TAC.2014.2299335>
3. Artstein, Z.: Stabilization with relaxed controls. *Nonlinear Anal. Theor. Methods Appl.* **7**(11), 1163–1173 (1983). [https://doi.org/10.1016/0362-546X\(83\)90049-4](https://doi.org/10.1016/0362-546X(83)90049-4), <https://www.sciencedirect.com/science/article/pii/0362546X83900494>
4. Gao, Y.: Model Predictive Control for Autonomous and Semiautonomous Vehicles. University of California, Berkeley (2014)
5. Gao, Y., Lin, T., Borrelli, F., Tseng, E., Hrovat, D.: Predictive control of autonomous ground vehicles with obstacle avoidance on slippery roads. In: *Dynamic Systems and Control Conference*, vol. 44175, pp. 265–272 (2010)
6. Lim, E.H., Hedrick, J.K.: Lateral and longitudinal vehicle control coupling for automated vehicle operation. In: *Proceedings of the 1999 American Control Conference* (Cat. No. 99CH36251), vol. 5, pp. 3676–3680. IEEE (1999)
7. Nguyen, Q., Sreenath, K.: Exponential control barrier functions for enforcing high relative-degree safety-critical constraints. In: *2016 American Control Conference (ACC)*, pp. 322–32 (2016). <https://doi.org/10.1109/ACC.2016.7524935>
8. Paden, B., Čáp, M., Yong, S.Z., Yershov, D., Frazzoli, E.: A survey of motion planning and control techniques for self-driving urban vehicles. *IEEE Trans. Intell. Veh.* **1**(1), 33–55 (2016). <https://doi.org/10.1109/TIV.2016.2578706>
9. Prajna, S., Jadbabaie, A.: Safety verification of hybrid systems using barrier certificates. In: Alur, R., Pappas, G.J. (eds.) *HSCC 2004*. LNCS, vol. 2993, pp. 477–492. Springer, Heidelberg (2004). https://doi.org/10.1007/978-3-540-24743-2_32
10. Wieland, P., Allgöwer, F.: Constructive safety using control barrier functions. *IFAC Proc.* **40**(12), 462–467 (2007). <https://doi.org/10.3182/20070822-3-ZA-2920.00076>, <https://www.sciencedirect.com/science/article/pii/S1474667016355690>

Open Access This chapter is licensed under the terms of the Creative Commons Attribution 4.0 International License (<http://creativecommons.org/licenses/by/4.0/>), which permits use, sharing, adaptation, distribution and reproduction in any medium or format, as long as you give appropriate credit to the original author(s) and the source, provide a link to the Creative Commons license and indicate if changes were made.

The images or other third party material in this chapter are included in the chapter's Creative Commons license, unless indicated otherwise in a credit line to the material. If material is not included in the chapter's Creative Commons license and your intended use is not permitted by statutory regulation or exceeds the permitted use, you will need to obtain permission directly from the copyright holder.





Towards Automated Driving: Findings and Comparison with ADAS

Riccardo Donà¹✉, Konstantinos Mattas¹, Giovanni Albano²,
Sandor Váss¹, and Biagio Ciuffo¹

¹ Joint Research Centre for the European Commission, 21027 Ispra, VA, Italy
{riccardo.dona,konstantinos.mattas,sandor.vass,
biagio.ciuffo}@ec.europa.eu
² Píksel Italia, Milan, Italy
giovanni.albano@ext.ec.europa.eu

Abstract. The present contribution provides preliminary empirical findings concerning the first-in-literature independent experimental characterization of a commercially viable automated driving system in Europe. In particular, the paper reports on the testing campaign involving a type-approved Automated Lane Keeping System (ALKS) equipped vehicle and its comparison with the comparable driving assistance feature technology from the same vehicle: the Adaptive Cruise Control (ACC) system. The results suggest that the ALKS shows substantially enhanced performances with respect to ACC. In particular, both the string stability metrics and the reaction time show remarkable improvements. Additionally, the increased stability is not obtained via resorting to a significantly higher time gap which further motivates that string stable car-following is indeed feasible.

Keywords: Adaptive Cruise Control · Automated Lane Keeping System · Driving Automation

1 Introduction

The Automated Lane Keeping System (ALKS) was the first Automated Driving System (ADS) application to have been regulated by the United Nations Economic Commission for Europe (UNECE) via Regulation 157 (UN-R157). ALKS is a system enabling automated driving on motorways with physical separation among opposite driving lanes at a cruising speed of up to 60 km/h. The latest amendment increased the operational speed up to 130 km/h and introduced automatic lane change [5]. A stand-out feature of any ADS feature with respect to Advanced Driver Assistance Systems (ADAS) is that the driver is no longer responsible for the driving task when the system is engaged. Thus, an ADS achieves automation Level 3 or 4 according to SAE J3016 [4]. At the time of

The work was supported by the Joint Research Centre for the European Commission.

© The Author(s) 2024

G. Mastinu et al. (Eds.): AVEC 2024, LNME, pp. 954–960, 2024.

https://doi.org/10.1007/978-3-031-70392-8_134

writing, only two vehicles exist in Europe that were type-approved according to the ALKS provisions: the Mercedes S-Class and Mercedes EQS.

In terms of user-perceived functionality and target operational domain, the ALKS L3 *automation* is in direct competition with the Adaptive Cruise Control (ACC) L2 *assistance*. In contrast to ALKS, ACCs are envisioned as SAE J3016 Level 1/2 systems meaning that the driver shall always be ready to take back control and the same will remain legally liable. ACCs have reached nowadays a substantial market penetration which eases carrying out testing to understand real-world behavior. Despite the undoubted comfort benefit that ACC can deliver, several concerns have been raised in the literature about the traffic implications [1]. For instance, the empirical evidence suggests that ACCs exhibit poor string stability performances and slow reaction times thus contradicting many fundamental hypotheses which advocated for the introduction of such systems.

To the end of providing an empirically-informed study that could give practitioners more realistic assumptions and monitor the implementation of the legal provisions, the authors have organized a testing campaign in Germany involving one of those ALKS-featured vehicles. The objective was to provide a quantitative assessment of the system's capabilities with respect to the competing ACC. Due to the limited Operational Design Domain (ODD) of the ALKS feature (the manufacturer according to UN-R 157 is free to select the ODD), the authors could only test the system in a selection of German motorways where the following conditions applied simultaneously: no roadworks, no tunnel, good weather, good visibility, and traffic speed up to 60 km/h due to congestion.

This paper provides the preliminary findings of a testing campaign aimed at assessing the real impact of driving automation on public roads. The first results suggest that ALKS show remarkably better string stability performance when traveling under comparable headway in relation to the traditional Adaptive Cruise Control (ACC) system.

2 Methodology

2.1 Testing Campaign

The experimental campaign took place in November 2023, about 3000 km were driven in Germany using 2 vehicles equipped with state-of-the-art ADAS and a vehicle equipped with ALKS from different OEMs while trying to maximize the use of the driving assistance/automation features. The vehicles were instrumented with external GNSS antennas to record the positions and velocities to enable the later post-processing vehicle-independent analysis.

2.2 String Stability

String stability refers to the capability of a platoon to absorb a traffic perturbation. Conversely, a string stable platoon will dampen disturbances whereas

a string unstable platoon will magnify the same leading to potentially unsafe driving scenarios. String stability, w_{SS} , is given by

$$w_{SS} = \frac{v_{FF,leader} - \min(v_{follow})}{v_{FF,leader} - \min(v_{leader})}, \quad (1)$$

where $v_{FF,leader}$ is the free-flow velocity of the leader before the perturbation occurs, $\min(v_{follow})$ is the minimum velocity recorded for the follower, and $\min(v_{leader})$ is the minimum velocity recorded for the leader. $w_{SS} \leq 1$ indicates a string stable platoon.

2.3 Headway Policy

The headway refers to the spacing policy adopted by a follower vehicle when cruising at equilibrium in car-following mode. The headway policy and string stability have been demonstrated to exist in a trade-off interconnection. On one side, a low spacing policy enables high theoretical flow. However, the poor string stability associated with such reduced distances will in practice deteriorate the flow as soon as a perturbation occurs or due to the intrinsic instability of the system. On the other hand, increasing the headway will make the platoon more robust against traffic perturbations but at the expense of reduced theoretical maximum flow. As such, the quantification of the string stability cannot be decoupled from the corresponding headway characterization.

In our testing campaign, we included in the dataset long portions of constant speed driving segments to estimate at the post-processing phase the corresponding headway settings. From the collected evidence the time-gap t_g , which together with the length of the vehicle originates the headway, can be estimated as

$$t_g = \frac{dist_{long}}{v_{follow}}, \quad (2)$$

where $dist_{long}$ is the bumper-to-bumper longitudinal distance at equilibrium.

2.4 Reaction Time

The reaction time is a relevant metrics for the safety assessment of a driving automation technology. In the following, the definition suggested in [3] is adopted where the reaction time t_r is the time offset that maximizes the Pearson correlation $r(\cdot)$ between the speed difference of two adjacent traffic participants (Δv) and the follower's produced acceleration (a_{follow}) in response to a perturbation as of

$$t_r = \arg \max(r_{\Delta v, a_{follow}}(\Delta v(t), a_{follow}(t + t_r))). \quad (3)$$

3 Results

3.1 String Stability

Figure 1 depicts, on the left, the string unstable behavior denoted for the ACC system whereas, on the right, the completely different behavior reported when

the same vehicle traveled in ALKS mode is shown. The behavior illustrated for one specific scenario in Fig. 1 has been consistent throughout the several perturbations recorded in the testing campaign.

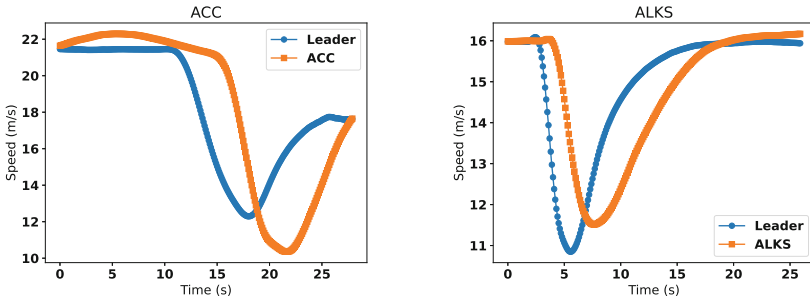


Fig. 1. ACC (left) string unstable behavior vs. ALKS (right) string stable behavior.

By aggregating the string stability metrics computed per each disturbance scenario reported, Fig. 2 can be obtained which shows the median values and the corresponding Q1/Q3 quartiles. Overall, significantly better performances can be denoted for the ALKS since the entire distribution is contained in the region $w_{SS} < 1$ suggesting that the system has always been string stable in the dataset collected. The same considerations do not apply to the ACC where the distribution is always above the string stability threshold. Concerning the numerical assessment, the median w_{SS} for the ALKS is 0.83 with an Inter Quartile Range (IQR) of 0.14. Conversely, the ACC displays a median w_{SS} of 1.31 and an IQR of 0.20.

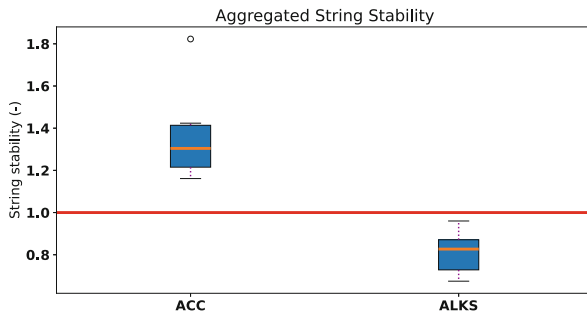


Fig. 2. ACC vs. ALKS aggregated string stability margins.

3.2 Headway Policy

Figure 3 depicts the aggregated data concerning the time-gap t_g for the ACC and ALKS. The numerical assessment returns a median t_g for the ALKS equal to 1.60 s with an IQR of 0.07 s. Conversely, the ACC displays a median t_g of 1.50 s and an IQR deviation of 0.41 s.

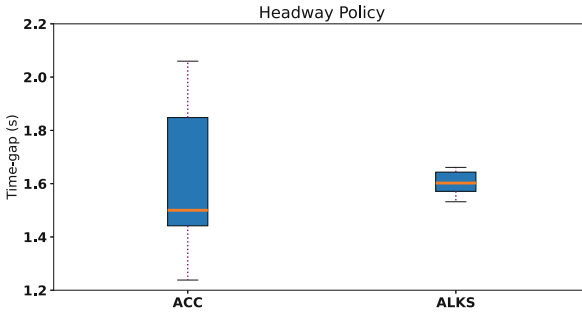


Fig. 3. ACC vs. ALKS aggregated headway policies.

The ACC has a slightly lower median headway ($\approx 6\%$) than the ALKS which would imply a theoretically higher maximum flow. However, the poor string stability performance as of Fig. 2 while operating such a short time-gap will most likely annihilate any potential theoretical advantage in traffic flow in a real-world scenario. Additionally, the ALKS has a minimum time-gap of 1.60 s when traveling at 60km/h as mandated by UN-R157, a provision which is proven to be fulfilled. Eventually, the ACC also exhibits a substantially larger dispersion that can be ascribed to the mentioned poorer stability performance and generally less precise tracking of the leader’s speed.

3.3 Reaction Time

Figure 4 depicts the aggregated data concerning the reaction time for the ACC and ALKS estimated using (3). The same perturbations used to identify the string stability margin were adopted to compute the aggregate reaction time. The median reaction time for the ALKS has been identified as 0.80 s with an IQR of 0.20 s. The ACC is significantly slower with a median r_t of 2.60 s and IQR of 0.90 s.

The results show the clearly different nature of ALKS vs ACC. The automation system is tuned to be more reactive to traffic disturbance since it is not only designed for comfort applications, in contrast to its driving assistance counterpart, but for tackling safety-critical scenarios as it bears the driving responsibility.

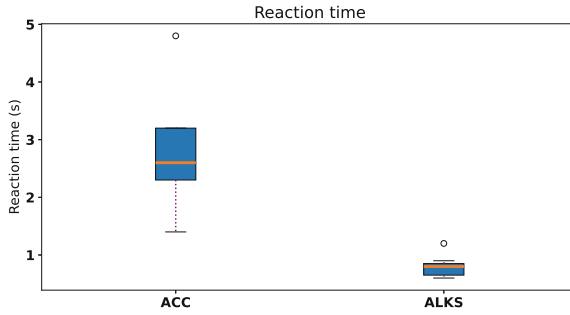


Fig. 4. ACC vs. ALKS aggregated reaction time.

4 Conclusion

The study summarized the results of the first commercially available ALKS system in Europe. To the best of the authors' knowledge, this scientific effort is the first independently assessed documented evidence regarding commercial automation solutions moving beyond SAE J3016 Level 2.

The preliminary outcomes look encouraging. The ALKS managed to substantially improve the string stability metrics with negligible impact on the headway policy thus contributing to increased real-world flow and potentially better fuel consumption. Additionally, the legal provisions mandating a minimum level of safety culminate in a safety less prone to delayed reaction.

Still, the very limited ODD remains the main challenge OEMs will have to face in order for the benefits to become tangible to the wider transportation network. Further work will be devoted to extending the performance comparison to embrace also previously tested ACC systems in the past [2] and to release publicly the data to the wider practitioners' community.

References

1. Ciuffo, B., et al.: Requiem on the positive effects of commercial adaptive cruise control on motorway traffic and recommendations for future automated driving systems. *Transp. Res. Part C: Emerg. Technol.* **130**, 103305 (2021)
2. Makridis, M., Mattas, K., Anesiadou, A., Ciuffo, B.: Openacc. an open database of car-following experiments to study the properties of commercial ACC systems. *Transp. Res. Part C: Emerg. Technol.* **125**, 103047 (2021)
3. Makridis, M., Mattas, K., Borio, D., Giuliani, R., Ciuffo, B.: Estimating reaction time in adaptive cruise control system. In: 2018 IEEE Intelligent Vehicles Symposium (IV), pp. 1312–1317. IEEE (2018)

4. SAE On-Road Automated Vehicle Standards Committee: Taxonomy and Definitions for Terms Related to Driving Automation Systems for On-Road Motor Vehicles. Technical Report, SAE (2021). https://www.sae.org/standards/content/j3016_202104/
5. United Nations Economic Commission for Europe: UN Regulation No. 157. Technical Report, UNECE, May 2022. <https://unece.org/sites/default/files/2022-05/ECE-TRANS-WP.29-2022-59r1e.pdf>






Open Access This chapter is licensed under the terms of the Creative Commons Attribution 4.0 International License (<http://creativecommons.org/licenses/by/4.0/>), which permits use, sharing, adaptation, distribution and reproduction in any medium or format, as long as you give appropriate credit to the original author(s) and the source, provide a link to the Creative Commons license and indicate if changes were made.

The images or other third party material in this chapter are included in the chapter's Creative Commons license, unless indicated otherwise in a credit line to the material. If material is not included in the chapter's Creative Commons license and your intended use is not permitted by statutory regulation or exceeds the permitted use, you will need to obtain permission directly from the copyright holder.





Stability Issues in Adaptive Cruise Control Systems and Traffic Implication

Riccardo Donà¹ , Konstantinos Mattas¹ , Giovanni Albano² ,
Sandor Váss¹ , and Biagio Ciuffo¹ 

¹ Joint Research Centre for the European Commission, 21027, Ispra, VA, Italy

{riccardo.dona,konstantinos.mattas,sandor.vass,
biagio.ciuffo}@ec.europa.eu

² Pikel Italia, Milan, Italy

giovanni.albano@ext.ec.europa.eu

Abstract. Adaptive Cruise Control (ACC) systems under short headway configurations have been found to have a potentially detrimental impact on the transport network due to the string instability effect. Such phenomenon results in traffic perturbations amplification downstream causing increasing fuel consumption and posing safety threats. However, recent findings summarized in this paper show how even the simpler platoon stability might not be attained with current ACC-equipped vehicles raising additional concerns regarding their unregulated operation. In fact, as part of a recent campaign involving state-of-the-art assisted vehicles, an ACC displayed a low-frequency oscillatory behavior around the equilibrium speed. This work, by leveraging a mixed simulation/empirical approach, uncovers the harmful influences of such behavior. Ultimately, we found that despite the poor stability phenomenon might not be impactful for one vehicle, the overall repercussions on the transportation network can be dramatically detrimental raising the need for a regulatory framework for lower-level automation.

Keywords: Adaptive Cruise Control · Asymptotic/String Stability

1 Introduction

Adaptive Cruise Control (ACC) is a driving assistance feature that provides the driver with additional comfort when traveling on highways by adjusting the speed while following a leader vehicle. ACC is commonly classified as an SAE J3016 Level 1 system (or Level 2 when coupled with lane-centering assistance) meaning that the driver will always have to be ready to take control at any time and the same will remain legally liable. ACCs have been investigated for a long time both via theoretical simulation studies [7] and, more recently, via real-world experiments [1, 5]. Frequently, the two types of assessment have led to contrasting outcomes: on one side theoretical studies have envisaged a beneficial

The work was supported by the Joint Research Centre for the European Commission.

© The Author(s) 2024

G. Mastinu et al. (Eds.): AVEC 2024, LNME, pp. 961–967, 2024.

https://doi.org/10.1007/978-3-031-70392-8_135

effect of ACC introduction based on the adopted assumptions, on the other side, the actual mass-market ACCs did not prove to deliver increased stability performance with respect to human driving [1].

Albeit higher-level automation systems, *i.e.*, systems where the feature provides proper driving automation thus transferring the legal liability to the manufacturer in contrast to driving assistance, are gradually approaching the market [2], driving assistance still has the largest market penetration share.

To the end of monitoring the evolution of driving assistance technologies, the authors have organized a testing campaign in Germany involving three vehicles featuring advanced Level 2 systems. During the testing, it became apparent to the driver sitting in one specific vehicle that the same was never able to achieve a constant speed while following a leader. The present contribution characterizes the specific instability phenomenon. The paper reports on the effect and the potential implications of a similar ACC design on the transportation network if left uncorrected by the car manufacturer. The effort leverages a mixture of experimental characterization together with a simulation-based approach to enlarge the scope.

2 Methodology

2.1 Perturbation Identification

The experimental campaign took place in November 2023, about 3000 km were driven in Germany using 3 vehicles equipped with state-of-the-art SAE J3016 Level 2 systems while trying to maximize the use of the driving assistance features. The vehicles were instrumented with external GNSS antennas to record the positions and velocities. To isolate the oscillation effect, the testers drove for long sections of the motorway while the leader kept a constant speed with no disturbance upfront. By repeating the procedure multiple times, 40 intervals were identified covering a range of different target speeds. The oscillations were analyzed by removing the mean component of the speed and fitting a sine wave to the residual speed profile. The sine functions calibration procedure returned the wave's frequency, amplitude, and phase. The latter signal was disregarded as it did not provide useful information. On the contrary, two distributions could be obtained for the oscillation frequency and amplitude, respectively, by repeating the sine function fitting procedure to all the 40 intervals produced.

Additionally, the extra fuel consumption associated with the oscillation behavior was characterized using the CO₂MPAS software tool (<https://code.europa.eu/jrc-ldv/co2mpas>) developed by the Joint Research Centre for European Commission to establish the fuel/energy consumption of passenger cars and light duty vehicles. The CO₂MPAS microsimulation tool has been executed on the trajectory exhibiting the oscillation and on the same trajectory subject to a non-causal low-pass filter removing the oscillatory component while maintaining the same average speed to match the distance traveled. The procedure was repeated for the whole set of identified perturbations to identify the average additional energy expenditure.

2.2 Traffic Flow Implications

Following the characterization of the oscillation abnormality, a stochastic simulation study was put in place to assess the foreseen implications on longer and heterogeneous platoons which were not possible to accomplish during the public road testing. A thorough validation effort for the simple simulation model to match the behavior of the vehicle under test goes beyond the article’s aim. Instead, the simulation uses a stochastic approach to enlarge the scope to embrace vehicles with different controllers’ tuning but similar undamped follow behavior.

The simulation setup was derived from earlier authors’ work [3,4] and leveraged a simple car-following model where the well-known linear controller model gives the car-following control law [6]:

$$u_{\text{ACC}}(t) = k_d(v_L(t - T) - v(t)) + k_p(s(t - T) - t_g v(t) - \eta). \quad (1)$$

In Eq. (1), $s(\cdot)$ represents the ego-leader distance, $v_L(\cdot)$ the leader’s speed, $v(\cdot)$ the ego’s speed and $u(\cdot)$ the control action. k_d and k_p are the controller’s gains, t_g the desired time-gap, T is the estimation delay, and η is the standstill spacing. The target acceleration u_{ACC} is saturated in the interval $[-5.0, 2.0]$ m/s². Each virtual vehicle is calibrated by randomly sampling its parameters from the intervals reported Table 1 assuming uniform distribution assumptions. The intervals are derived from real-world characterizations of ACC behavior as of [5].

Table 1. Vehicle platoon simulation parameters.

k_p (s ²)	k_d (s)	t_g (s)	τ_a (s)	T (s)	η (m)
[0.03, 0.10]	[0.25, 0.70]	[1.20, 2.50]	[0.20, 0.50]	[0.75, 1.50]	[2.00, 3.00]

The simulation setup is such that a platoon of ACC-equipped vehicles, starting from a steady-state condition, is subject to a perturbation induced by the leader vehicle. In particular, a set of 15 mild perturbations derived from the “highD” dataset [8] were adopted for the purpose. To replicate the effect of the leader vehicle experiencing the oscillatory behavior observed during the testing campaign, which is not present in the highD dataset, a sinusoidal wave speed profile has been superimposed on top of the original leader’s trajectory. Each simulation is repeated 20 times by randomizing over the vehicle parameters in Table 1 and over the calibrated oscillation parameters frequency and amplitude as described in Sect. 2.1. The analysis was repeated twice for two platoon reference lengths: 5 vehicles and 20 vehicles (including the leader). Thus, the impact of the oscillation propagation can be better grasped. The assessment is carried out via computing the average root mean square (RMS) platoon longitudinal acceleration $a_{x,\text{RMS}}$ and the number of rear-end collisions as a proxy for comfort and safety degradation metrics.

3 Results

3.1 Oscillations Characterization

Figure 1 shows a recorded oscillation (blue dots) together with the calibrated sine wave (red line) and leader’s speed (black dots). Albeit the leader is traveling at constant velocity the follower is exhibiting a clearly undamped oscillation which can be effectively fitted with a sine function.

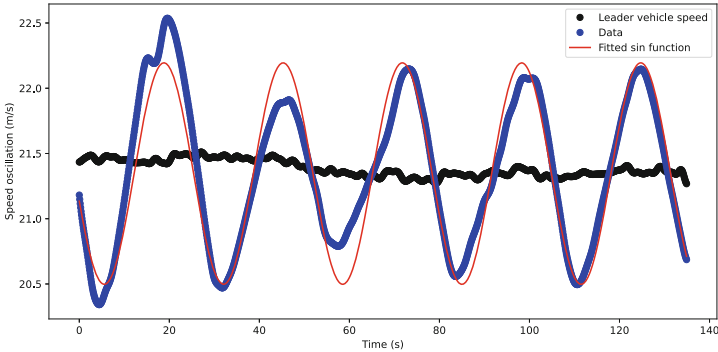


Fig. 1. Example of recorded oscillation and fitted sine wave.

The computation of the Pearson correlation between the amplitude of the oscillatory component and the mean speed component returns a negative statistic (-0.0108) and a p -value equal to 0.947 suggesting that the quantities are uncorrelated.

The median oscillation corresponds to a low-frequency 0.225 rad/s ($T = 27.3$ s) wave having a mean 0.873 m/s amplitude as shown in Fig. 2. The standard deviations are 0.00248 (rad/s) and 0.0955 (m/s) respectively. The statistical test assessing the normality of the distributions returns a value higher than 0.05 , suggesting that the null hypothesis of the distributions being normal cannot be rejected.

Concerning the fuel consumption analysis, for the particular vehicle model considered, an average reduction of 3.30% could be accomplished by filtering the oscillatory component of speed while maintaining the same traveled distance. Overall, the oscillation only contributes to a marginal increase in fuel consumption that would be barely noticeable in a real-world scenario considering an individual vehicle only.

3.2 Traffic Simulation Results

The simulation assessment of longer platoons provides insightful findings.

Figure 3 displays the 5-vehicles long platoon aggregated results in terms of $a_{x,RMS}$ and virtual crashes. Similarly, Fig. 4 shows the outcome associated with the longer 20 vehicles platoon.

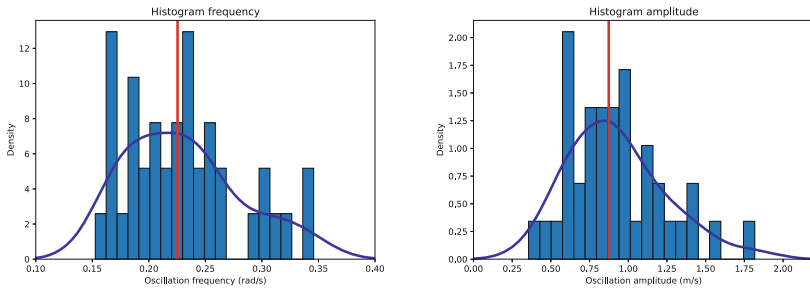


Fig. 2. Histogram of oscillation frequencies (left) and amplitude (right).

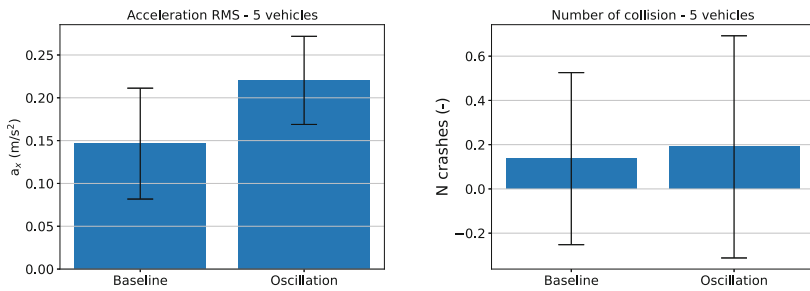


Fig. 3. Bar charts: acceleration RMS (left) and collision (right). 5 vehicles platoon.

The introduction of the oscillatory components marks a clear surge in the acceleration RMS value which is increased by approximately 50% in the 5 vehicles long platoon suggesting that comfort and energy consumption are sensibly affected. On the contrary, safety is marginally reduced. The situation gets substantially worse when the longer platoon is considered. In this case, the RMS acceleration more than doubles and the platoon is hardly capable of maintaining a stable car-follow with a substantial increase in rear-end collisions.

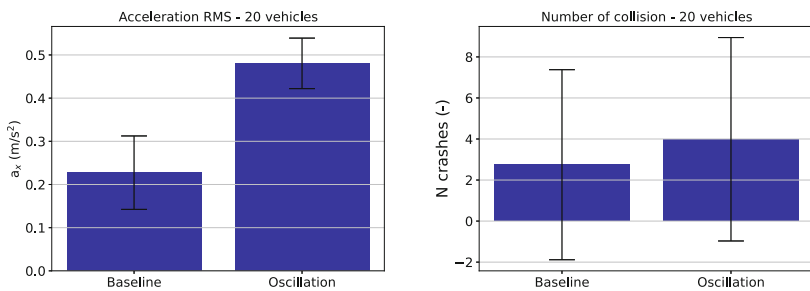


Fig. 4. Bar charts: acceleration RMS (left) and collision flow (right). 20 vehicles platoon.

4 Conclusion

The study summarized the testing results of SAE J3016 Level 2 assisted driving vehicles, highlighting concerns about poor stability in one vehicle's ACC mode. Firstly, the phenomenon has been characterized in terms of its frequency and amplitude showing that the oscillation has a relatively slow period of $T \approx 27$ s and a mean amplitude slightly inferior to 1 m/s. The energy consumption analysis demonstrated how, for one vehicle only, the phenomenon yields only a slight increase in fuel consumption which could be hardly measurable. However, once the phenomenon is enlarged via simulation to multiple vehicles exhibiting a string unstable behavior significant safety and comfort/energy worsening effects were reported, in particular in longer platoons. The results support the need for a regulation framework for lower automation systems to prevent potentially harmful impacts on traffic networks.

References

1. Ciuffo, B., Mattas, K., Makridis, M., Albano, G., Anesiadou, A., He, Y., Josvai, S., Komnos, D., Pataki, M., Vass, S., et al.: Requiem on the positive effects of commercial adaptive cruise control on motorway traffic and recommendations for future automated driving systems. *Transp. Res. Part C: Emerg. Technol.* **130**, 103305 (2021)
2. Donà, R., et al.: Recent advancements in automated vehicle certification: How the experience from the nuclear sector contributed to making them a reality. *Energies* **15**(20), 7704 (2022)
3. Donà, R., Mattas, K., Albano, G., Ciuffo, B.: Multianticipative adaptive cruise control compared with connectivity-enhanced solutions: simulation-based investigation in mixed traffic platoons. *Transp. Res. Record* **2677**, 573–587 (2023)
4. Donà, R., Mattas, K., He, Y., Albano, G., Ciuffo, B.: Multianticipation for string stable adaptive cruise control and increased motorway capacity without vehicle-to-vehicle communication. *Transp. Res. Part C: Emerg. Technol.* **140**, 103687 (2022). <https://doi.org/10.1016/j.trc.2022.103687>
5. Gunter, G., et al.: Are commercially implemented adaptive cruise control systems string stable? *IEEE Trans. Intell. Transp. Syst.* **22**(11), 6992–7003 (2020)
6. He, Y., et al.: Adaptive cruise control strategies implemented on experimental vehicles: a review. *IFAC-PapersOnLine* **52**(5), 21–27 (2019)
7. Ioannou, P.A., Chien, C.C.: Autonomous intelligent cruise control. *IEEE Trans. Veh. Technol.* **42**(4), 657–672 (1993)
8. Krajewski, R., Bock, J., Kloeker, L., Eckstein, L.: The highd dataset: a drone dataset of naturalistic vehicle trajectories on German highways for validation of highly automated driving systems. In: 2018 21st International Conference on Intelligent Transportation Systems (ITSC), pp. 2118–2125. IEEE (2018)

Open Access This chapter is licensed under the terms of the Creative Commons Attribution 4.0 International License (<http://creativecommons.org/licenses/by/4.0/>), which permits use, sharing, adaptation, distribution and reproduction in any medium or format, as long as you give appropriate credit to the original author(s) and the source, provide a link to the Creative Commons license and indicate if changes were made.

The images or other third party material in this chapter are included in the chapter's Creative Commons license, unless indicated otherwise in a credit line to the material. If material is not included in the chapter's Creative Commons license and your intended use is not permitted by statutory regulation or exceeds the permitted use, you will need to obtain permission directly from the copyright holder.





The Influence of Transient Tire Force Transmission on Sideslip Angle Estimation

Dženana Puščul^(✉) , Martin Schabauer , and Cornelia Lex 

Institute of Automotive Engineering, Graz University of Technology,
Inffeldgasse 11/2, 8010 Graz, Austria
dzenana.puscul@tugraz.at

Abstract. Knowledge of the sideslip angle is significant in development, testing and validation of advanced driver assistance systems and vehicle control systems, to enhance vehicle performance and stability. This article investigates the influence of having additional information about transient tire behavior during estimation of the sideslip angle. Since transient behavior depends on the dynamic excitation, the effect during different driving maneuvers (excitations) such as steady-state cornering, slalom and general handling as well as on different road surfaces is investigated. The results show that considering transient force transmission even by a pragmatic approach leads to a significant improvement.

Keywords: Sideslip angle · State estimation · Transient tire behavior · Tire force dynamics · Tire relaxation · Vehicle handling dynamics

1 Introduction

The sideslip angle β , as a main indicator of dynamic stability, describes the orientation of the horizontal velocity in the center of gravity (COG) of a vehicle and is given as a function of longitudinal v_x and lateral velocity v_y by $\beta = \arctan(v_y/v_x)$. Estimating β has garnered significant attention from researchers over the past few decades and observer-based methods such as KALMAN filters (KF) or sliding-mode observers (SMO) are often used. Within such observers, different types of uncertainties in the lateral tire forces are typically modeled without distinction. These uncertainties include deviations from the real cornering stiffness, deviations from the real vertical force, transient tire behavior, effects based on nonlinear tire behavior, e.g. assuming linear force transmission, as well as imperfect or missing knowledge of the maximum coefficient of tire-road friction. Being able to distinguish these effects will enable improved modeling of the uncertainties in the observers, especially of effects such as transient tire forces and vertical load, that can be linked to a certain dynamic excitation.

2 Transient Tire Force Transmission

The theory of steady-state (static) tire force transmission $F_{x,y}^S$ is based on the fundamental assumption that when the sliding condition in the contact patch

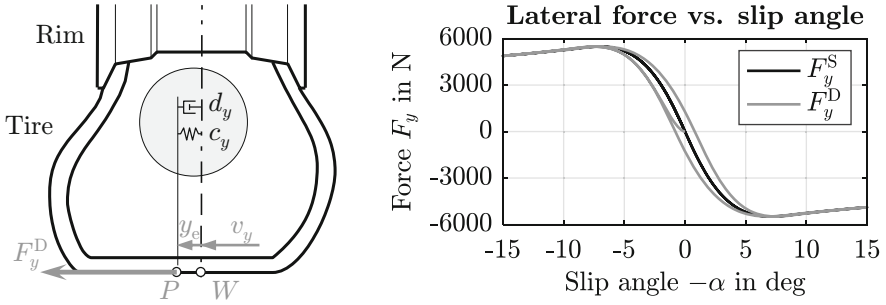


Fig. 1. Principles of modeling visco-elastic tire compliance y_e by a KELVIN-VOIGT element (left), based on [6], and resulting transient tire force transmission F_y^D (right)

changes, a certain steady-state force value is reached immediately. In general, a certain time delay between a change of the sliding velocity and the build up of a steady-state tire force value occurs. Consequently, transient effects and a hysteresis behavior of horizontal force characteristics $F_{x,y}^D$ occur, see Fig. 1 (right). A simple and widely used approach in vehicle handling dynamics analyses is to approximate the dynamic behavior of tire forces by first-order systems

$$\tau_{x,y} \dot{F}_{x,y}^D + F_{x,y}^D = F_{x,y}^S \quad \text{with} \quad \tau_{x,y} = \frac{r_{x,y}}{v_t}. \quad (1)$$

The key parameter in such approaches is the relaxation time $\tau_{x,y}$, which is linked to the relaxation length $r_{x,y}$ and the transport velocity of the tire tread elements through the contact patch v_t . Relaxation time and length are only constant in a specific operating point. Several literature sources deal with a detailed modeling of these two parameters and their dependencies on e.g. slip $s_{x,y}$, vertical load F_z and visco-elastic effects d_y and c_y of tire compliance y_e , see Fig. 1 (left) and e.g. [5, 6]. The determination of relaxation lengths based on experimental investigations with a certain accuracy is still a cumbersome and challenging task as well as a research topic, see e.g. [2].

Based on the enhanced first-order tire force dynamics of the semi-physical TMeasy 5 handling tire model, [6], relaxation time and length for pure lateral slip are given by

$$\tau_y = \frac{v_t d_y + f_y}{v_t c_y} = \frac{d_y}{c_y} + \frac{f_y}{v_t c_y} \quad \text{and} \quad r_y = v_t \tau_y, \quad (2)$$

where nonlinear steady-state tire force characteristics $F_y^S = F_y^S(s_y, F_z)$ are described by the global derivative $f_y = F_y^S/s_y$ with respect to the lateral slip $s_y = -v_y/v_t = \tan \alpha$ or slip angle α . For pure lateral slip, $v_t = |v_x|$ holds. Based on the considerations in Eqs. (1)–(2), the transient behavior of the lateral tire force transmission F_y^D is fully determined by nonlinear steady-state contact force characteristics f_y as well as visco-elastic stiffness c_y and damping properties d_y of the tire structure. Thus, tire force dynamics are approximated in an effective and efficient semi-physical manner by a KELVIN-VOIGT element.

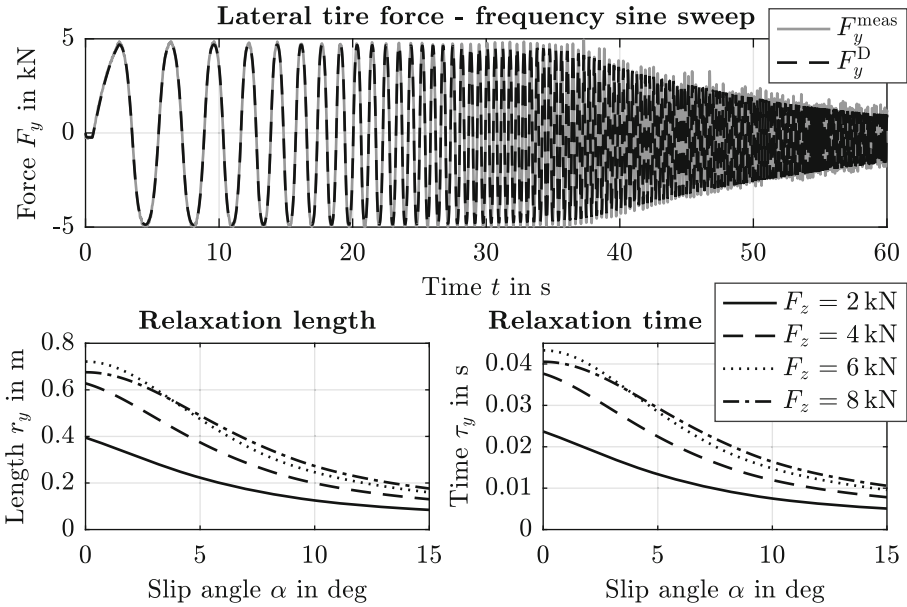


Fig. 2. Identified relaxation length $r_y = r_y(\alpha, F_z)$ and time $\tau_y = \tau_y(\alpha, F_z)$ (bottom left and right) of a tire of size 245/40 R 2099 W based on measured lateral tire force responses F_y^{meas} (top) at different vertical loads $F_z = \text{const.}$ and $v_t = |v_x| = 60 \text{ km/h}$

An extensive tire testing series with five different tires was conducted on an industrial flat track tire test rig, as presented in [4] for two tires. An example of measured dynamic responses of the lateral tire force F_y^{meas} of a tire of size of 245/40 R 2099 W due to a frequency based sine sweep maneuver of the slip angle α from $0 \rightarrow 5 \text{ Hz}$ at constant tire load F_z and velocity v_t is presented in Fig. 2 (top). Based on such measurements, the KELVIN-VOIGT parameters, lateral tire stiffness c_y and damping d_y , can be identified by optimization of the computed transient lateral tire force F_y^{D} , see also [4]. Consequently, a reasonable prediction of the behavior of relaxation length $r_y = r_y(\alpha, F_z)$ and time $\tau_y = \tau_y(\alpha, F_z)$ according to Eq. (2) is possible, see Fig. 2 (bottom left and right).

3 Sideslip Angle Estimation

The cascaded observer structure from [1] was implemented. First, a discrete-time extended KALMAN filter (EKF) is used to estimate front longitudinal F_{x1} , front and rear lateral tire forces F_{yi} . System and measurement models for the force observer are given by Eqs. (1)–(10) in [1]. Subsequently, these estimates are treated as inputs to the sideslip angle observer.

The sideslip angle observer is based on a combination of a single track vehicle model and a linear adaptive tire force model, where the cornering stiffness $C_{\alpha i}$ is corrected by $\Delta C_{\alpha i}(t)$. The lateral tire force is $F_{yi}(t) = (C_{\alpha i} + \Delta C_{\alpha i}(t)) \alpha_i(t)$

Table 1. System model for both sideslip angle observers (first set) and measurement models for observer O_1 (second set) and O_2 (third set)

$\dot{\beta} = \frac{1}{mv} [F_{x1} \sin(\delta - \beta) + (C_{\alpha 1} + \Delta C_{\alpha 1}) \left(\delta - \beta - \frac{l_1 \dot{\psi}}{v} \right) \cos(\delta - \beta) + (C_{\alpha 2} + \Delta C_{\alpha 2}) \left(-\beta + \frac{l_2 \dot{\psi}}{v} \right) \cos \beta] - \dot{\psi}, \quad \Delta \dot{C}_{\alpha 1} = 0 \quad \text{and} \quad \Delta \dot{C}_{\alpha 2} = 0$	
$y_1 = (C_{\alpha 1} + \Delta C_{\alpha 1}) \left(-\beta + \delta - \frac{l_1 \dot{\psi}}{v} \right)$	$\text{and} \quad y_2 = (C_{\alpha 2} + \Delta C_{\alpha 2}) \left(-\beta + \frac{l_2 \dot{\psi}}{v} \right),$
$y_3 = \frac{1}{m} \left[(C_{\alpha 1} + \Delta C_{\alpha 1}) \left(\delta - \beta - \frac{l_1 \dot{\psi}}{v} \right) \cos \delta + (C_{\alpha 2} + \Delta C_{\alpha 2}) \left(-\beta + \frac{l_2 \dot{\psi}}{v} \right) + F_{x1} \sin \delta \right]$	
$y_1 = (C_{\alpha 1} + \Delta C_{\alpha 1}) \left(-\beta + \delta - \frac{l_1 \dot{\psi}}{v} \right)$	$\text{and} \quad y_2 = (C_{\alpha 2} + \Delta C_{\alpha 2}) \left(-\beta + \frac{l_2 \dot{\psi}}{v} \right),$
$y_3 = \frac{1}{m} \left[(C_{\alpha 1} + \Delta C_{\alpha 1}) \left(\delta - \beta - \frac{l_1 \dot{\psi}}{v} \right) \cos \delta + (C_{\alpha 2} + \Delta C_{\alpha 2}) \left(-\beta + \frac{l_2 \dot{\psi}}{v} \right) + F_{x1} \sin \delta \right],$	
$y_4 = \delta - \beta - \frac{l_1 \dot{\psi}}{v}$	$\text{and} \quad y_5 = -\beta + \frac{l_2 \dot{\psi}}{v}$

with $i = 1, 2$ distinguishing between front and rear axle, respectively. By adjusting the cornering stiffness, $\Delta C_{\alpha i}(t)$ accounts for nonlinear effects as well as different uncertainties that can arise. This adjustment is included as a state variable and modeled as the random walk. The system model is given in Table 1 (first set) with the state $\mathbf{x} = [\beta \Delta C_{\alpha 1} \Delta C_{\alpha 2}]^T$ and input vector $\mathbf{u} = [\delta \dot{\psi} v F_{x1}]^T$, where δ is the steering angle, $\dot{\psi}$ the yaw rate, and v the vehicle velocity in the COG. The measurement model is given in Table 1 (second set) with measurement vector $\mathbf{y} = [F_{y1} F_{y2} a_y]^T$, where a_y is the lateral acceleration. Together with the EKF, this forms the basis of the first observer named O_1 . The model covariance matrix is set to $\mathbf{Q} = \text{diag}(10^{-12}, 10^9, 10^9)$, whereas measurement covariance matrix is set to $\mathbf{R} = \text{diag}(10^3, 10^3, 10^{-5})$.

The present work investigates the impact of additional information regarding transient tire forces, represented by τ_{yi} , on the sideslip angle estimation. The estimated lateral force F_{yi} is the dynamic force in Eq. (1), i.e. $F_{yi} = F_{yi}^D$. With this information and the knowledge of τ_{yi} , the static force F_{yi}^S can be obtained using the discrete version of Eq. (1). The static force in the linear region can be described by a linear model, $F_{yi,k}^S = C_{\alpha i} \alpha_{i,k}$, where k represents the current time step. Consequently, $\alpha_{i,k} = \alpha_{i,k}^{\text{meas}}$ can be calculated in every time step by

$$F_{yi,k}^S = \tau_{yi} \frac{F_{yi,k}^D - F_{yi,k-1}^D}{\Delta t} + F_{yi,k}^D \quad \text{and} \quad \alpha_{i,k}^{\text{meas}} = \frac{F_{yi,k}^S}{C_{\alpha i}}, \quad i = 1, 2. \quad (3)$$

Therefore, if the observer is operating within the linear region of tire force characteristics, sufficiently accurate values of the slip angle $\alpha_{i,k}$ are obtained. Hence, the measurement vector can be augmented by incorporating this values, for both front and rear, $\mathbf{y} = [F_{y1} F_{y2} a_y \alpha_1 \alpha_2]^T$. The index k is omitted but implied. Relationships between the slip angles α_i and the sideslip angle β read $\alpha_1 = \delta - \beta - l_1 \dot{\psi}/v$ and $\alpha_2 = -\beta + l_2 \dot{\psi}/v$. These equations are combined with the measurement model from O_1 to form the novel measurement model of the second observer named O_2 , see Table 1 (third set). The system model is the same

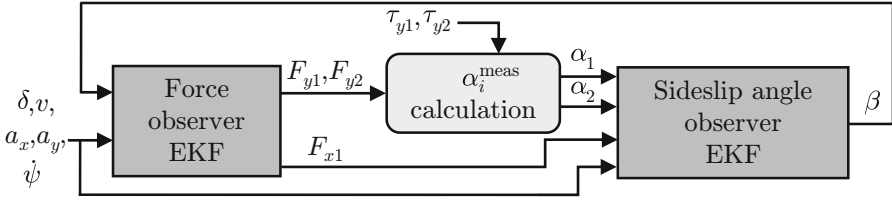


Fig. 3. Algorithm structure with the proposed adapted sideslip angle observer O_2

for both observers. Discrete-time EKF is employed and the algorithm structure with O_2 is shown in Fig. 3. Using the POPOV-BELEVITCH-HAUTUS (PBH) criterion, [3], it is proven that the system is locally observable. However, only in the linear region, sufficiently accurate slip angle values are obtained. Consequently, the values of R corresponding to slip angles are changed depending on the region. In the linear region, the corresponding value is set to 10^{-7} rad^2 , while in the nonlinear region, it is $5 \cdot 10^{-1} \text{ rad}^2$. This is done for both the front and rear separately. To decide whether the observer is in the linear or nonlinear region, pragmatic threshold values of $F_{yi} = \{5, 3.5\} \text{ kN}$ are implemented.

4 Results and Discussion

Observers O_1 and O_2 were tested based on vehicle dynamics measurements obtained with a front wheel driven standard VW Golf 7 GTI TCR with tires of size 235/35 R 1991 Y. The total vehicle mass is $m = 1574 \text{ kg}$, the distances between the COG and the front and rear axle are $l_i = \{0.992, 1.634\} \text{ m}$. The cornering stiffnesses of the front and rear axle are $C_{\alpha i} = \{150, 142.4\} \text{ kN/rad}$.

Different driving maneuvers with a mean vehicle speed of $v \approx 60 \text{ km/h}$ for a wide range of sideslip angle values were performed on road surfaces with different maximum tire-road friction. Although the tires of the test vehicle were not part of the tire testing series, similar tire properties were assumed. Based on the measured vertical tire load F_{zi} and slip angle α_i variations during different sinusoidal steering maneuvers, overall mean values of the relaxation times were determined with $\tau_{yi} = \{38, 31\} \text{ ms}$ by Eq. (2), cf. Figure 2 (bottom right), and were assumed constant for all maneuvers.

The results show that the proposed adapted observer O_2 can improve the estimate of β , see Fig. 4. Significant improvement can be seen in steady-state cornering (top right), where the result of O_1 drifts from the real value. Due to the steady-state inputs, the errors accumulate over time. However, O_2 is able to correct this error and track the true value of β . Additionally, the performance of O_2 is quite robust against uncertainties of τ_{yi} . This is supported by tests on different road surfaces. Figure 4 (bottom) shows that both O_1 and O_2 perform well on the ice-like surface around $t = 20 \text{ s}$, although no information on the surface is available to the observers. In both observers, the change in tire-road friction is compensated in the estimates of $\Delta C_{\alpha i}(t)$. However, during the low excitation on wet asphalt, O_1 again drifts and is not able to converge again until around $t \approx 115 \text{ s}$. In contrast, O_2 is again able to correct the error.

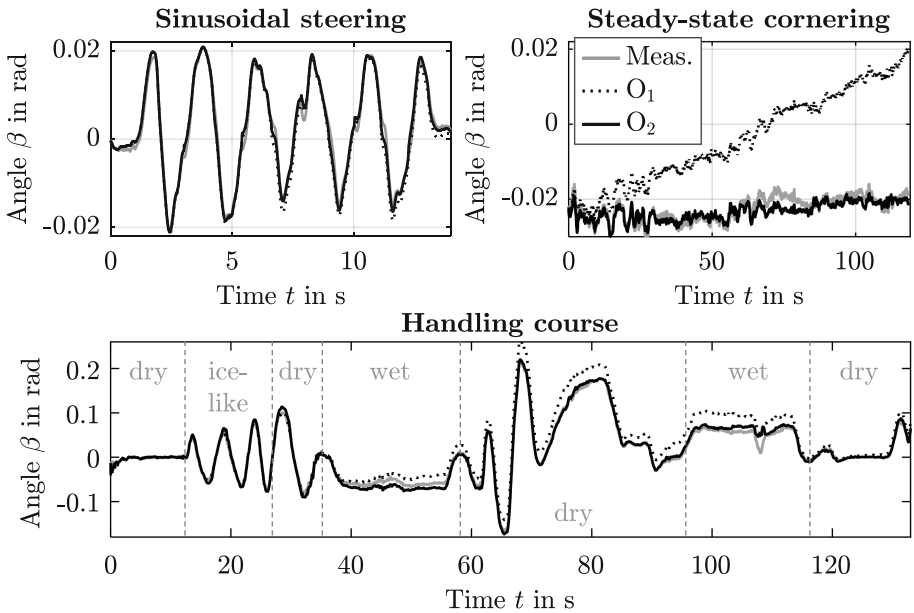


Fig. 4. Comparison of measurement and estimation results of observers O_1 and O_2 for different maneuvers (excitation) and on different road surfaces (tire-road friction)

To summarize, the overall results show that including even simplified and pragmatic assumptions on the transient tire force transmission can significantly improve the estimation of the sideslip angle.

References

1. Baffet, G., Charara, A., Lechner, D., Thomas, D.: Experimental evaluation of observers for tire-road forces, sideslip angle and wheel cornering stiffness. *Veh. Syst. Dyn.* **46**(6), 501–520 (2008). <https://doi.org/10.1080/00423110701493963>
2. Besselink, I.J.M., Aertssen, A.J., Thakkar, D., Lugaro, C.: Measurement of tire vertical damping, carcass deflection and longitudinal relaxation length. In: 28th Symposium of the International Association of Vehicle System Dynamics, IAVSD 2023, Ottawa, Canada (2023)
3. Ghosh, B., Rosenthal, J.: A generalized Popov-Belevitch-Hautus test of observability. *IEEE Trans. Autom. Control* **40**(1), 176–180 (1995). <https://doi.org/10.1109/9.362874>
4. Hackl, A.: Enhanced Tyre Modelling for Vehicle Dynamics Control Systems. PhD thesis. Graz University of Technology, Graz, Austria (2019). ISBN 978-3-85125-7281
5. Pacejka, H.B.: *Tire and Vehicle Dynamics*, 3rd edn. Elsevier Ltd., Oxford, United Kingdom, Butterworth-Heinemann (2012). 978-0-08-097016-5
6. Rill, G., Castro, A.A.: *Road Vehicle Dynamics, Fundamentals and Modeling with MATLAB*, 2nd edn. CRC Press/Taylor & Francis Group, Boca Raton, United States (2020). 978-0-367-19973-9

Open Access This chapter is licensed under the terms of the Creative Commons Attribution 4.0 International License (<http://creativecommons.org/licenses/by/4.0/>), which permits use, sharing, adaptation, distribution and reproduction in any medium or format, as long as you give appropriate credit to the original author(s) and the source, provide a link to the Creative Commons license and indicate if changes were made.

The images or other third party material in this chapter are included in the chapter's Creative Commons license, unless indicated otherwise in a credit line to the material. If material is not included in the chapter's Creative Commons license and your intended use is not permitted by statutory regulation or exceeds the permitted use, you will need to obtain permission directly from the copyright holder.





AI-Based Power Split Strategy for Hybrid Commercial Vehicle Applications

Pratheesh Sivaraman Nair^(✉), Tomislav Bukic, Dominik Burnner,
Georgios Koutroulis, and Milan Zivadinovic

AVL List GmbH, Graz, Austria
pratheesh@gmx.at, tom@ac8.ai,
{Dominik.Brunner, Georgios.Koutroulis, Milan.Zivadinovic}@avl.com

Abstract. In the rapidly evolving landscape of hybrid commercial vehicle technology, integrating artificial intelligence (AI) with fuel cell applications offers a promising frontier for efficient, sustainable and eco-friendly road freight system. There has been many different approaches on optimization of power split between the electric motor and the fuel cell system (FCS). Conventional approaches use quadratic optimization to determine the optimal power from the electric motor at each discrete grid point along the route, with initial and final battery state of charge (SoC) as constraints. This paper proposes a deep reinforcement learning-based approach to optimize the power split between the electric motor and the FCS in a hybrid vehicle at every time point during the vehicle's trip. The agent demonstrated the ability to autonomously learn and improve power split decisions, resulting in enhanced fuel efficiency.

Keywords: hybrid commercial vehicles · power split strategy · artificial intelligence · machine learning · deep reinforcement learning

1 Introduction

1.1 Hybrid Commercial Vehicles

Hybrid commercial vehicles with hydrogen Fuel Cell System (FCS) are powered by a combination of fuel cell system and an electric propulsion system. We are considering hybrid vehicles in which both the power sources can drive the vehicle independently and simultaneously and the battery of the electric motor is charged from recuperation. Most of the power requirement is met by the FCS. This type of hybrid systems are called series-parallel hybrid system. Along with the FCS, electric motor and battery pack, this type of vehicle contains a power split device which manages the distribution of power between the FCS and the electric motor. The power split device runs on certain logic to split the total required power at a particular instance between the FCS and the electric motor. It also charges the battery from recuperation when the total required energy goes negative. We use deep reinforcement learning for deriving the logic to split the required power between the above power sources.

1.2 Reinforcement Learning

Reinforcement Learning (RL) is a machine learning technique where an agent learns to make decisions in an environment to maximize returns based on specific objectives. The environment is a bounded system that changes its state in response to the agent's actions. An agent, an external entity, observes the system's state and influences it to achieve and maintain a favorable state. Therefore, the agent's objective is to learn the action-state dynamics and control the system with actions that result in the desired system state.

Rewards are defined to meet the system's output objectives and are calculated based on the observed state of the system. During the learning phase, the agent observes the system's state, performs actions to change it, and evaluates the new state by calculating the return. The return consists of the immediate reward and the discounted future reward at the new state. Over time, the agent adjusts its actions based on the returns to transition from the current state to a favorable state.

Artificial neural networks, which can learn complex non-linear relationships between variables, are used to represent the agent in deep reinforcement learning. These networks serve as universal function approximators, enabling the agent to learn and adapt effectively. The objective of the agent is to learn a policy $\pi(\mathcal{D}|\sim, \theta)$, which is a mapping from state s to a probability distribution over action a , parameterized by a neural network θ , that maximizes the expected return $\mathbf{J}_\theta = \mathbb{E}_\pi[\mathbb{G}_t]$. The return $\mathbb{G}_t = \sum_{k=0}^{\infty} \gamma^k \mathbb{R}_{t+k+1}$ where γ is the discounting factor for future rewards and \mathbb{R}_{t+k+1} is the reward at time step $t+k+1$. The policy is improved over iterations by updating θ from the gradient of the return $\nabla_{\theta} \mathbb{J}_\theta = \mathbb{E}_\pi[\nabla_{\theta} \log \pi(a|s, \theta) \mathcal{Q}^\pi(s, a)]$.

2 Related Work

Ferrara et al. [2] used quadratic optimization for optimal power split in hybrid commercial vehicles. Liessner et al. [6] addressed the power split problem using RL with Deep Deterministic Policy Gradient (DDPG) [7] algorithm. DDPG is a breakthrough in off-policy continuous action space RL applications, but is sensitive to hyper parameters [3]. Manio et al. [8] used Q-learning to address the problem with explicit inclusion of SoC conservation in the reward function. Hu et al. [4] uses deep Q-learning with reward function discretized on the value of SoC. Q-learning suffers from over estimation bias. We use Soft Actor Critic (SAC) [3] algorithm for learning the optimal power split. SAC is robust to hyper parameters and converges fast in high dimensional control problems. SAC avoids hyper parameter sensitivity by incorporating policy entropy term in policy update, thereby encouraging exploration.

3 Training Architecture

The objective of this exercise is to develop a model that optimally splits the total required power between the electric motor and the FCS. Optimal power

split involves minimizing hydrogen fuel consumption, preventing battery drain, and battery charging when the wheels do not require power (e.g. during downhill travel). The model considers look ahead information on the next downhill travel and the total battery charge during the next downhill travel. The architecture consists of two main components: the vehicle model and the reinforcement learning (RL) module. The RL module receives observations from the vehicle model at each time instance and outputs the power split ratio between the FCS and electric motor. Based on this ratio, the vehicle model calculates the power from the FCS and the electric motor at every time point of the trip (Fig. 1).



Fig. 1. Training architecture. The agent forms a deep reinforcement learning algorithm, which takes observations from the vehicle model as inputs and outputs the action. The environment sends a step/reset command along with the action to the vehicle model. The vehicle model integrates the next step's power requirement and the current power split observations based on the action and sends it back to the environment. The environment checks for termination/truncation of the episode based on the observations from the vehicle model. The environment then calculates the reward, which is used to update the agent's network. Additionally, the environment normalizes the observations and feeds them back into the network.

3.1 Vehicle

The vehicle model consist of two sub modules- vehicle configuration and road data. Vehicle configuration consist of vehicle mass, FCS configuration, battery configuration, auxiliary power and vehicle dynamics including acceleration, deceleration, velocity, traction power and driving resistance. Road data consist of road slope, curvature, speed limits etc. which are captured using sensors on vehicle while driving along 8 different routes in Austria. Driving mode is a variable in the range (0,1) representing economy to aggressive driving. From the road data, vehicle dynamics and the driving mode, the required power for the vehicle at each instant of time is calculated. When the RL module sends the power split ratio as an action through the environment module, the vehicle model calculates the power from FCS as (total power * power split ratio) and power from electric motor as (total power * (1-power split ratio)). The SoC expenditure from the battery for the power from electric motor is calculated according to the battery configuration and dynamics. Subsequently, the remaining SoC is calculated as

the difference between the current SoC and the SoC expenditure for the power. The FCS fuel consumption and efficiency are then determined from the FCS model. When the total power goes negative, the battery is charged and FCS power is kept at zero.

3.2 Deep RL Module

This is an episodic task involving finding the optimal power split at any given time point of truck’s trip.

Observation Space: The observations space consist of the total required power at the wheels at the moment in time, the battery SoC at the moment, altitude and curvature of the road, desired velocity, time steps to episode end, time steps till next downhill descent and total SoC charge in the next descent. The total required power is a continuous value in kW and is derived from the vehicle and route data. The battery SoC is also a continuous value ranging from 0 to 1.

Action Space: The action space is the power split ratio between FCS and electric motor which is a continuous value in the range [0,1].

Algorithm: With the episodic task setting with continuous action space, Soft Actor Critic (SAC) [3] algorithm best suits the problem. SAC is an off-policy actor critic deep reinforcement algorithm suited for continuous action space. Off-policy algorithms are sample efficient algorithms which uses past experience gathered in a replay buffer for learning. This suits our scenario where the route and vehicle dynamics are constants and environment exploration is bounded.

Reward: Table 1 shows the observations used for reward calculation. A reward of 100 is given when the agent navigates successfully to the end of the episode without SoC drain. A small reward is given for every step towards the episode end which promotes saving SoC since the episode gets terminated when the SoC goes to 0. A negative reward is given for cumulative H2 consumption during the travel with the objective of reducing H2 consumption. A penalty is given when the SoC goes below 10%.

Table 1. Reward components, positive/negative (+/-) contribution and their weights.

Component	+/-	Weight
Truncated (episode end)	+	100
Non terminated	+	0.1
Cumulative H2 consumption	-	10
SoC below 10%	-	100

4 Experiment

4.1 Setup

Building on the methodology and tool chain by Bukic et al. [1] created around Ray [5], an open-source distributed computing framework, we trained the network with 16 CPUs and 1 GPU. A vehicle model with 40 ton weight, initial battery SoC of 0.5 and driving style of 0.5 were used for training. The driving style effect the acceleration, deceleration and velocity calculation and subsequently the required power at the wheels. Total of 8 routes were used for training. Policy and Q value network used 256,256 fully connected network with a learning rate of 0.003 for both the networks. A prioritized replay buffer with a capacity of 10,00,000 was used and a train batch size of 512 was used. Training was done for 50,000 iterations.

4.2 Results

Figure 2 shows the power split between FCS and electric motor using SAC method on the Brenner route. The approach splits the total power almost equally. The battery charges when the total power goes negative. The Brenner route is a high uphill/downhill route.

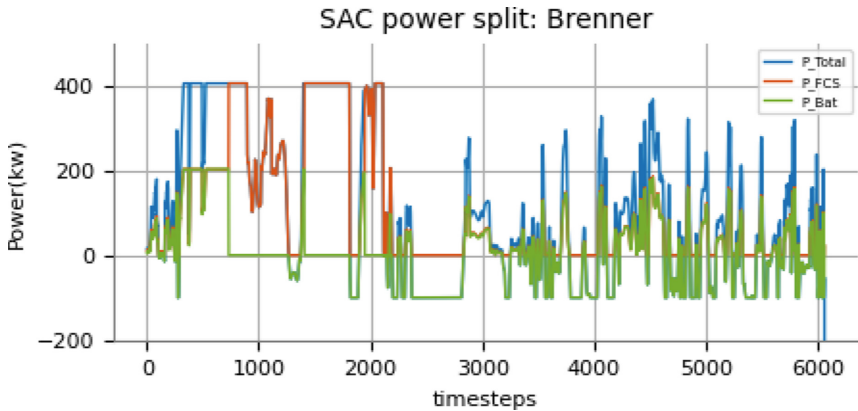


Fig. 2. Power split by Soft Actor Critic(SAC) method on the Brenner route. P.total is the total required power, P_FCS is the power from FCS and P_Bat is the power from battery(electric motor)

Figure 3 shows the battery SoC comparison between SAC and QO approaches on Brenner route. The red line shows the altitude of the route. Table 2 shows the comparison of H2 consumption with SAC power split method and Quadratic

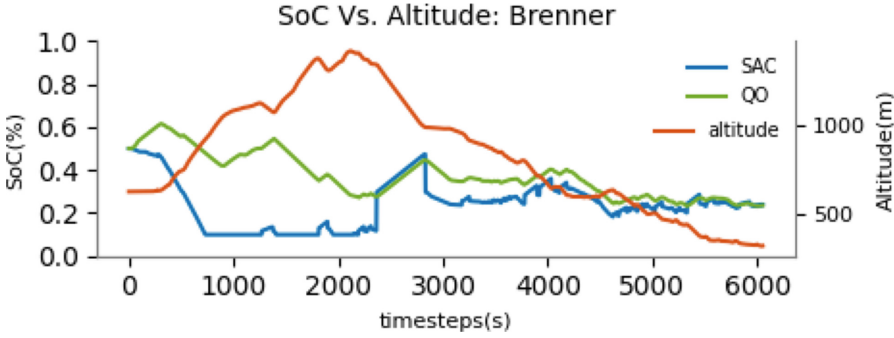


Fig. 3. Battery SoC with Soft Actor Critic(SAC) method and Quadratic Optimization(QO) method on the Brenner route against the altitude of the road.

Optimization method on the 8 routes. On all routes, SAC approach has shown less H2 consumption with an highest improvement of 6% and the lowest improvement of 1.4 % compared to quadratic optimization approach.

Table 2. Drive cycles, distance covered and H2 consumption with SAC power split approach and quadratic optimization(QO) approach from Ferrara et al. [2]

Drive Cycle	Distance(km)	H2 Consumption(kg)		Improvement(%)
		SAC	QO	
Steyr ⇒ Linz	43	2.39	2.81	1.4
Graz ⇔ Wiener Neustadt	358	31.49	32.71	3.7
Graz ⇒ Wiener Neustadt	181	14.64	15.09	2.9
Goettingen ⇒ Ulm	428	42.56	44.52	4.4
Ulm ⇒ Trient	383	33.16	35.30	6.0
Innsbruck ⇒ Bozen (Brenner)	120	8.70	9.82	11
Steyr ⇒ Graz	200	16.90	17.37	2.7
Graz ⇒ Wiener Neustadt	187	16.22	17.10	5.1

4.3 Conclusion

RL based power split strategy has demonstrated its effectiveness in reducing fuel consumption in hybrid vehicles. The above approach relies on offline pre-determined route information and ideal velocity profile to calculate the power requirement. However, enhancing this strategy by predicting real-time power requirements using sensor data from the moving vehicle will improve its applicability and accuracy in real-world scenarios. Additionally, incorporating battery health parameters into the model will yield more sustainable battery performance. The current experiment is limited to vehicles of a specific weight.

Acknowledgement. This work is funded by the European Union under Grant Agreement No. 101138110. Views and opinions expressed are however those of the author(s) only and do not necessarily reflect those of the European Union or CINEA. Neither the European Union nor the granting authority can be held responsible for them.

References

1. Bukic, T., et al.: Advanced reinforcement learning-based thermal management strategy for battery electric vehicles. In: *Fisita World Congress (2023)*
2. Ferrara, A., et al.: Optimal calibration of an adaptive and predictive energy management strategy for fuel cell electric trucks. *Energies* **15**(7), 2394 (2022)
3. Haarnoja, T., Zhou, A., Abbeel, P., Levine, S.: Soft actor-critic: off-policy maximum entropy deep reinforcement learning with a stochastic actor. In: *International Conference on Machine Learning*, pp. 1861–1870. PMLR (2018)
4. Yue, H., Li, W., Kun, X., Zahid, T., Qin, F., Li, C.: Energy management strategy for a hybrid electric vehicle based on deep reinforcement learning. *Appl. Sci.* **8**(2), 187 (2018)
5. Johri, S., Goyal, M., Jain, S., Baranwal, M., Kumar, V., Upadhyay, R.: A novel machine learning-based analytical framework for automatic detection of covid-19 using chest x-ray images. *Int. J. Imaging Syst. Technol.* **31**(3), 1105–1119 (2021)
6. Liessner, R., Schroer, C., Dietermann, A.M., Bäker, B.: Deep reinforcement learning for advanced energy management of hybrid electric vehicles. In: *ICAART (2)*, pp. 61–72 (2018)
7. Lillicrap, T.P., et al.: Continuous control with deep reinforcement learning. *arXiv preprint arXiv:1509.02971* (2015)
8. Maino, C., Mastropietro, A., Sorrentino, L., Busto, E., Misul, D., Spessa, E.: Project and development of a reinforcement learning based control algorithm for hybrid electric vehicles. *Appl. Sci.* **12**(2), 812 (2022)



Open Access This chapter is licensed under the terms of the Creative Commons Attribution 4.0 International License (<http://creativecommons.org/licenses/by/4.0/>), which permits use, sharing, adaptation, distribution and reproduction in any medium or format, as long as you give appropriate credit to the original author(s) and the source, provide a link to the Creative Commons license and indicate if changes were made.

The images or other third party material in this chapter are included in the chapter's Creative Commons license, unless indicated otherwise in a credit line to the material. If material is not included in the chapter's Creative Commons license and your intended use is not permitted by statutory regulation or exceeds the permitted use, you will need to obtain permission directly from the copyright holder.





Risk-Predictive Path Planning in Urban Autonomous Driving: A Geometric Approach to VRU Crossing

Yohei Fujinami^(✉)  and Pongsathorn Raksincharoensak 

Tokyo University of Agriculture and Technology, Koganei, Tokyo 184-8858, Japan
y-fujinami@go.tuat.ac.jp

Abstract. This research introduces a method for autonomous driving systems to safely overtake bicycles in urban environments. It identifies the risk of sudden crossing when overtaking a bicycle and proposes a solution to minimize this risk. The method classifies the situation into three conditions related to the drivable space of the road and speed of the bicycle, and it determines the target speed and positions. The proposed algorithm uses onboard sensor information and assumptions of the bicycle's virtual sudden-crossing motion, enabling real-time calculations in a practical environment. Simulations demonstrate the method's effectiveness, showing it can generate a natural overtaking speed and lateral gap based on road width and bicycle speed. The proposed method is compatible with waypoint-based path generation methods we have proposed in previous research, making it a promising solution for future autonomous driving systems. Future research will discuss the method's implementation in automated vehicles, contributing to safer and more efficient autonomous driving systems.

Keywords: Autonomous Driving System · Risk Prediction · Crossing Bicycle · Overtake · Urban Area

1 Introduction

Autonomous driving systems or advanced driver assistance systems in urban environment presents a significant challenge, particularly when navigating narrow roads shared with other traffic participants, including vulnerable road users (VRUs). Human drivers, when navigating these scenarios, maintain a safe longitudinal and lateral distance from objects to prepare for unexpected crossing. At the same time, drivers select an appropriate speed for overtaking objects. In particular, we focused on the scenario when a bicycle suddenly drifts out or crosses the ego vehicle's driving lane while the ego vehicle is overtaking. According to a near-miss incident database HHDB, the near-miss incidents involving overtaking bicycles have reached 624 cases out of 3005 of entire bicycles' near-miss incidents that are recorded in the database [1].

As legislative measures for overtaking bicycle, the Japanese Cabinet decided to impose on car drivers a duty to make an effort to overtake the bicycles at a safe speed

when the lateral gap is insufficient [2]. In the United States, 3-foot passing laws were widely employed across states [3]. However, neither the safe speed nor the sufficient lateral gap has been quantitatively defined by the Japanese Cabinet. Also, the research investigated the effect of 3-foot law suggested that the effect to the driver behavior by the law was limited [4]. In addition, much research has been conducted on autonomous driving for overtaking bicycles [5, 6]. This research required huge amounts of driving data of the real drivers. Moreover, motion prediction and path planning with MPC requires more computational resources. Furthermore, the stochastic method seems to reasonably defines the motion of the object, however, we must note that most high-risk scenarios occur due to behaviors that happen in low probabilities. Therefore, it may be difficult to avoid the collision like the case that unusually happens with the stochastic method.

Therefore, this research aims to define, both theoretically and geometrically, the risk of sudden crossing in risk predictive scenario especially when overtaking bicycle in the same driving lane. Also, it proposes a method to minimize this risk to avoid collisions within the context of Autonomous Driving Systems and Advanced Driver Assistance Systems in urban driving. Previous research conducted by our team has revealed the safe speed and safe lateral gap to manage potential risks from blind object, such as blind intersections and parked vehicles [7]. Building on this research, this paper aims to geometrically determine and calculate the safe speed and lateral overtaking distance to safely overtake the ongoing bicycles, with a rationally lower computational cost.

2 Definitions of Safe Lateral Gap and Safe Speed

2.1 Conditions for Overtaking Bicycle

In this study, a following collision avoidance scenario by an autonomous vehicle was considered. A bicycle is driving straight on the same lane of the autonomous vehicle and the vehicle is catching up to the bicycle. When an onboard sensor on the autonomous vehicle detects a target bicycle, the system assumes that the object virtually moves into the driving trajectory. In generating the trajectory and speed profiles, the system considers three conditions to handle the scenario, as shown in Fig. 1. To prevent collisions, the system is designed to ensure side-face collision avoidance by maintaining sufficient lateral time gap, as in condition (a), or to decelerate to a safe speed to ensure frontal collision avoidance, as in condition (b). As another option, when the lateral gap is not enough to ensure both frontal and side-face collision, the system needs to judge to follow the object as condition (c).

As previously explained, we considered three conditions related to the width of the lateral drivable space. The virtual target object is presumed to start crossing at a certain time while maintaining the speed v_{obj} . The timing t_1 is derived from the geometrical relationships as depicted in the figures. Subsequently, the virtual target object sways out at an angle ψ_{vir} . The crossing angle is determined from the statistical measurements in a previous study [8]. The following subsections introduces the definitions of safe speed and safe lateral gap for each condition.

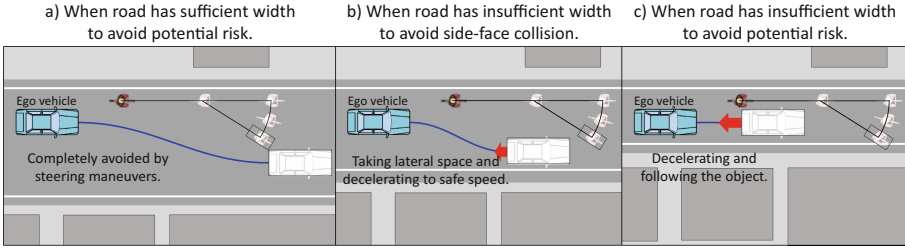


Fig. 1. Three conditions to handle the preceding slower bicycle.

2.2 Condition (a): Avoiding Through Steering Maneuvers

When the road has enough width, the system aims to avoid the virtual crossing object by providing a safe-sufficient time-to-conflict of the virtual object t_{vir} . We have defined the lateral gap distance when the ego vehicle can completely avoid the collision as the safe lateral gap D_{safe} (see Fig. 2). When the vehicle can maneuver to keep the safe lateral gap, it avoids entering the virtual crossing area and traverses the area at the current speed or higher as in condition (a). The safe lateral gap D_{safe} is calculated using the following equation:

$$D_{safe}(t) = v_{obj}(t)t_{vir} \sin(\psi_{vir}) + C \tag{1}$$

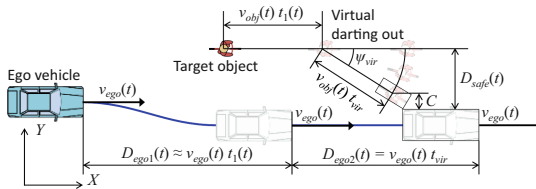


Fig. 2. Schematic definitions of safe speed, lateral gap, and parameters at condition (a).

Under condition (a), the vehicle needs to complete the overtaking, therefore, the collision avoidance is guaranteed only when the vehicle is driving faster than the current velocity v_{ego} . In this scenario, the target speed v_{tar} and target position (X_{tar}, Y_{tar}) for the vehicle control are as:

$$\begin{cases} v_{tar}(t) = v_{ego}(t) \\ X_{tar}(t) = X_{ego}(t) + D_{ego1}(t) \\ Y_{tar}(t) = Y_{obj}(t) - D_{safe}(t) - W_{ego}/2 \end{cases} \tag{2}$$

2.3 Condition (b): Avoiding Through Deceleration and Steering Maneuvers

Conversely, as in the scenario (b), when the situation presents insufficient drivable space, the system maintains the maximum possible lateral gap D_{max} without deviating from

the road boundary. Then the vehicle decelerates to the safe speed v_{safe} that can avoid the collision with the virtual crossing object by performing emergency braking (see Fig. 3). The formula for calculating the safe speed v_{safe} is as follows:

$$v_{safe}(t) = -a_{EB}(t_2(t) - \tau_{EB}) + v_{obj}(t) \cos \psi_{vir} \quad (3)$$

where a_{EB} is the estimated acceleration of emergency braking and τ_{EB} is the latency before emergency braking activation. The time t_2 can be calculated using the following equation:

$$t_2(t) = (D_{max}(t) - C) / (v_{obj}(t) \sin \psi_{vir}) \quad (4)$$

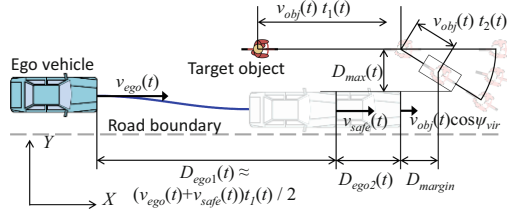


Fig. 3. Schematic definitions of safe speed, lateral gap, and parameters at condition (b).

By decelerating the vehicle speed to the safe speed v_{safe} and taking the safe lateral gap $D_{safe} = D_{max}$ at the collision estimated point, the system can guarantee the frontal collision avoidance by performing emergency braking. In this scenario, the target speed v_{tar} and target position (X_{tar}, Y_{tar}) are as:

$$\begin{cases} v_{tar}(t) = v_{safe}(t) \\ X_{tar}(t) = X_{ego}(t) + D_{ego1}(t) \\ Y_{tar}(t) = Y_{obj}(t) - D_{safe}(t) - W_{ego} / 2 \end{cases} \quad (5)$$

2.4 Condition (c): Following Object

When the time t_2 is shorter than the latency τ_{EB} , the emergency braking may not be able to stop the vehicle if the ongoing object starts crossing in front of the vehicle. In this scenario, regarding $t_2 = \tau_{EB}$, the target speed v_{tar} and target position (X_{tar}, Y_{tar}) are as:

$$\begin{cases} v_{tar}(t) = v_{obj}(t) \\ X_{tar}(t) = X_{ego}(t) + D_{ego1}(t) \\ Y_{tar}(t) = Y_{ego}(t) \end{cases} \quad (6)$$

2.5 Summary

The proposed algorithm can determine the target speed, positions, and longitudinal acceleration simply from the onboard sensor information and several assumptions of the virtual motion of the bicycle. This simple calculation method enables real-time calculations in practical environment. Therefore, the target speed and positions will be iteratively updated until the loss of detection of the target object.

The target points can be used as control waypoints, and the path generation methods that follow the waypoint enable automated driving [7]. Moreover, the proposed algorithm allows easy combination with other waypoint generation methods and can extend the scenario to more complex and practical scenes [7].

3 Simulations and Results

From the definitions of safe speed and lateral gap, and considering the environmental factors, the safe speed and lateral gap are determined from the road width and speed of the ongoing target object. Simulations were conducted to demonstrate the calculation of safe speed and safe lateral gap. In the simulations, parameters for the algorithm were set as follows: $\psi_{vir} = 30$ [deg], $t_{vir} = 1.5$ [s], $a_{EB} = -5.0$ [m/s²], and the lateral position of target object was set to 1.0 m from the left road boundary.

Figure 4 schematically explains the features of how the safe speed and safe lateral gap are influenced by the object speed and road width. The figure represents three areas corresponding to the conditions (a), (b), and (c). In the area under of condition (a), the safe speed cannot be defined, so the safe speed was stated as 0 km/h, and for the area of condition (c), it is not possible to define the safe lateral gap, therefore, the safe lateral gap is stated as 0 m.

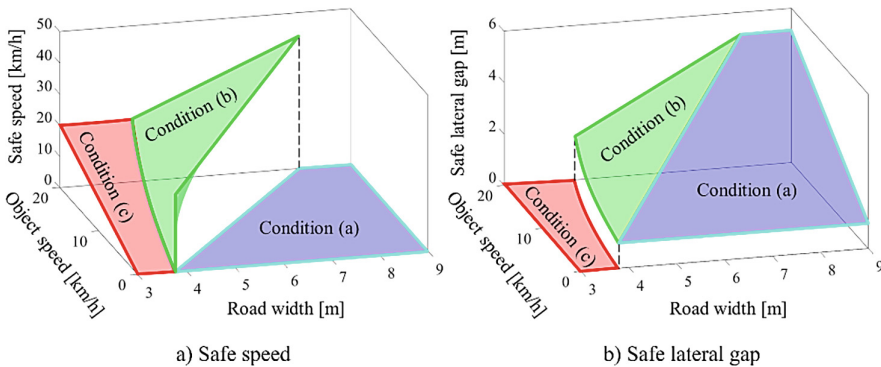


Fig. 4. Characteristics of safe speed and safe lateral gap regarding road width and object speed.

As an example case of the simulation, we set the target object speed v_{obj} to 12.0 km/h and the road width to 6.0 m. From the definitions, the scenario is classified as condition (b), and the safe speed and safe lateral speed were calculated as $v_{safe} = 20.2$ [km/h] and $D_{safe} = 2.9$ [m]. Therefore, the target speed and target positions are defined from Eq. (4).

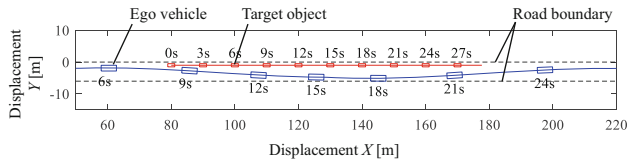


Fig. 5. Path of the autonomous driving vehicle and target object in the simulation.

Figure 5 shows the example simulation of the overtaking scenario. In the simulation, the vehicle model simply decelerates to the safe speed before reaching the target point and reaccelerates after overtaking. For the lateral control, the Triclothoidal path generation was used to maintain the safe lateral gap [9]. From the figure, the method overtook the target with a natural path within the road.

4 Conclusions

This paper proposed a method for autonomous driving system to safely overtake the bicycles. The method can theoretically and geometrically determine the safe speed and safe lateral gap with a low-calculation cost by anticipating the virtual sudden crossing. The method classifies the situation into three conditions related to the drivable space of the road and bicycle speed. The method simply provides the target position and speed that can guarantee collision avoidance with the assumed sudden crossing. Simulations revealed that the method could generate the natural overtaking speed and lateral gap. The advantage of the proposed method is that the method can designate the safe target as a point and speed, therefore, it is compatible with waypoint-based path generation methods. As a future extension of the research, the compatibility of the method and test on the real automated vehicle will be discussed.

References

1. What is a TUAT near-miss database?, SMART MOBILITY RESEARCH CENTER, <https://web.tuat.ac.jp/~smrc/about.html>. (in Japanese). Accessed 31 May 2024
2. A bill for the revision of the road safety act (道路交通法の一部を改正する法律案), Cabinet Legislation Bureau, https://www.clb.go.jp/recent-laws/diet_bill/detail/id=4646. (in Japanese). Accessed 31 May 2024
3. McLeod, K.: Bicycle laws in the united states-past, present, and future. *Fordham Urban Law J.* **42**, 898–903 (2016)
4. Herrera, N., Parr, S.A., Wolshon, B.: Driver compliance and safety effects of three-foot bicycle passing laws. *Transp. Res. Interdisciplinary Perspect.* **6**, 1–6 (2020)
5. Schneegans, J., et al.: Probabilistic VRU trajectory forecasting for model-predictive planning a case study: overtaking cyclists. In: 2021 IEEE Intelligent Vehicles Symposium Workshops, pp. 272–279, Nagoya, Japan (2021)
6. Lin, B.T.W., Bao, S., Gui, H., Chen, S., Chuang, T., Su, H.: A data-driven autonomous driving system for overtaking bicyclists. *Center Connected Autom. Transp.* **73427**, 1–30 (2023)
7. Fujinami, Y., Raksincharoensak, P.: Risk-predictive path planning considering occlusion for urban automated driving. In: 7th International Symposium on Future Active Safety Technology towards zero traffic accidents, pp. 1–5. Kanazawa, Japan (2023)

8. Ota, R., et al.: Risk-predictive path planning considering occlusion for urban automated driving. In: 7th International Symposium on Future Active Safety Technology towards zero traffic accidents, pp. 1–6. Kanazawa, Japan (2023)
9. Fujinami, Y., Raksincharoensak, P.: Experimental validation on intersection turning trajectory prediction method for advanced driver assistance system based on Triclothoidal curve. *Appl. Sci. MDPI* **11**(5900), 1–22 (2021)

Open Access This chapter is licensed under the terms of the Creative Commons Attribution 4.0 International License (<http://creativecommons.org/licenses/by/4.0/>), which permits use, sharing, adaptation, distribution and reproduction in any medium or format, as long as you give appropriate credit to the original author(s) and the source, provide a link to the Creative Commons license and indicate if changes were made.

The images or other third party material in this chapter are included in the chapter's Creative Commons license, unless indicated otherwise in a credit line to the material. If material is not included in the chapter's Creative Commons license and your intended use is not permitted by statutory regulation or exceeds the permitted use, you will need to obtain permission directly from the copyright holder.



Author Index

A

Abe, Masato 178
Adas, Akif 510
Aggarwal, R. K. 57
Ahn, Changsun 721
Ahn, Yoonyong 883
Ahrenhold, Tim 109, 158
Akihito, Akai 890
Akutain, Xabier Carrera 919
Albano, Giovanni 954, 961
Alföldi, Ádám 700
Alirezai, Mohsen 632
Amadini, M. 940
Amano, Masateru 735
Amati, Nicola 826
Amato, Gerardo 597
Andersson, Rickard 315
Ando, Takayuki 777
Anna, Panzer 434
Arai, Norika 137
Arai, Yoshihide 286
Araki, Keizo 897
Arndt, Martin 200
Arrigoni, Stefano 235, 510, 540, 833, 843
Asiabar, Aria Noori 144
Askerdal, Mikael 29
Asperti, Michele 517, 525
Awasthi, Satyesh 510
Awasthi, Satyesh Shanker 540

B

Balachandran, Arvind 151
Ballo, F. 933, 940
Bando, Koki 749
Barbieri, Luca 510
Baslamisli, S. Caglar 440
Bassi, Federico 43
Battlogg, Stefan 533
Baudry, Lucas 597
Becker, Matthias 533
Bertipaglia, Alberto 632
Biffi, A. 933

Bijelic, Mario 833, 843
Birkemeyer, Janick 876
Borkowski, Lukas 876
Borrelli, Francesco 357, 639
Borsboom, Olaf 98
Boscaro, Linda 926
Braghin, Francesco 540, 833, 843
Brandes, Gerrit 207
Broadbent, Nicholas Drake 378
Bruzelius, Fredrik 29, 50, 315, 350, 679, 707
Bukic, Tomislav 975
Burnner, Dominik 975
Bussalai, Giovanni 343

C

Camozzi, Francesco 639
Candela, Andrea 308, 336
Caponio, C. 413
Carbone, Fabio 597
Caresia, Pietro 597
Castellanos Molina, Luis M. 826
Çeliksöz, Dersu 420
Cheli, Federico 235
Chen, Yanbo 164
Cheng, Qian 496
Chindamo, Daniel 308, 336
Choi, Hosik 659
Choi, Jaeho 883
Choi, Seungwon 611
Ciuffo, Biagio 954, 961
Clemente, Maurizio 98
Cole, David 64
Coleman, Sonya 116
Colombo, Francesco 571
Comolli, Francesco 919
Corno, Matteo 8, 43
Cvok, Ivan 804

D

D'Avico, Luca 597
Dahal, Pragyana 833, 843
De Guglielmo, Veronica 926

de Haan, Redmer 214
 dell'Annunziata, Guido Napolitano 22
 Dell'Orto, Gabriele 911
 der Sande, Tom van 214, 221
 Deur, Joško 364
 Deylaghian, Samira 714
 Donà, Riccardo 954, 961
 Drugge, Lars 447, 585
 Du, Xiaolei 474

E

Ebashi, Yusuke 770
 Eberhart, Manuel 200
 Edamoto, Syouma 763
 Edelmann, Johannes 91, 200, 550, 557, 862,
 869
 Els, P. S. 756
 Emvin, Carl 315
 Endo, Ayato 15, 385, 749, 770
 Erdinc, Umur 1, 130

F

Fantin, Davide 578
 Farroni, Flavio 22
 Favelli, Stefano 826
 Feher, Adam Balint 123
 Fényes, Dániel 700, 812
 Fieldhouse, Harry 64
 Fiengo, Giovanni 854
 Flormann, Maximilian 78, 85, 244
 Ford, Richard 329
 Fork, Thomas 357, 639
 Forni, Fabrizio 597
 Fossati, Andrea 926
 Fredriksson, Jonas 29, 130
 Frey, Jonathan 447
 Frigerio, Stefano 293
 Frohn, Christian 564
 Fu, Liting 770
 Fu, Xiao-Yu 639
 Fuchs, Robert 763
 Fujinami, Yohei 137, 982
 Furui, Mitsuaki 749
 Furukawa, Yoshimi 329
 Fusco, Paolo 8

G

Gadola, Marco 308, 336
 Galbiati, Andrea 926

Galvagno, Enrico 36
 Gan, Hanyu 371
 Gao, Haoyu 947
 Gao, Jiaxin 904
 Gao, Richard 763
 Gao, Yangyan 116, 144
 Gáspár, Péter 700, 812
 Ge, Zhaohui 707
 Gelso, Esteban 1
 Gerdes, J. Christian 57, 378
 Giacomel, Filippo 343
 Gim, Juhui 659
 Glomsda, Marvin 301
 Gobbi, Massimiliano 919, 926, 933, 940
 Göçer, İsmail 420, 440
 Gordon, Timothy 116, 144
 Gorsich, David 251
 Gräber, Torben 91, 862, 869
 Grđan, Ivo 364
 Gruber, P. 413
 Gu, Jinyu 461
 Gülsiren, Kerim Arda 420
 Guo, Zijun 228
 Gwak, Jongseong 897

H

Hamersma, H. A. 756
 Han, Lijin 625
 Han, Sangwon 883
 Hankovszki, Z. 413
 Happee, Riender 632
 Harada, Masanori 286
 Haraguchi, Tetsunori 653
 Hartmann, Lukas 207
 Hartwecker, André 791
 Hattori, Yoshikazu 735
 Hayashi, Hideaki 137
 Hegedús, Tamás 812
 Heinze, M. 244
 Heise, Cedric 564
 Henderson, Leon 116, 144
 Hendewerk, Johannes 533
 Hendryk, Lausch 434
 Henze, Roman 78, 85, 109, 158, 207, 244,
 406, 564
 Hiraga, Tojuro 399
 Hirao, Ryusuke 890
 Hjort, Mattias 50
 Hofman, Theo 98
 Homma, Yota 329

Horvath, Hanna Zsofia 123
 Hossain, Ypti 557
 Huh, Kunsoo 272, 611, 883
 Huisman, Mischa 185

I

Iatropoulos, Jannes 109, 564
 Ikami, Daiki 454
 Ikeda, Keigo 15, 385, 749, 770
 Inoue, Masato 672
 Inoue, Shintaro 137
 Ishii, Kyoya 777

J

Jacobson, Bengt 130, 315, 707
 Jannes, Iatropoulos 434
 Jaumann, Florian 91, 862
 Jerrelind, Jenny 447
 Jiang, Beiyan 947
 Jiang, Chenhuan 371
 Jiang, Kun 193, 496
 Jiao, Xinyu 496
 Johannesson, Pär 315
 Jonasson, Mats 130, 604, 714

K

Kageyama, Ichiro 653
 Kaiser, Michael 791
 Kajitani, Koji 329
 Kamimura, Jinnosuke 137
 Kaneko, Satoshi 265
 Kaneko, Tetsuya 653
 Kano, Yoshio 178
 Karyotakis, Ektor 604
 Kati, Maliheh Sadeghi 1, 130
 Kato, Hideaki 15, 385, 749, 770
 Kato, Taro 385, 749, 770
 Katsuyama, Etsuo 258
 Kawasaki, Yoshifumi 890
 Kawasaki, Yosuke 672
 Kerr, Dermot 116
 Kharrazi, Sogol 50
 Khayyat, Michael 540
 Kieu, Mikael 1
 Kim, Byunggun 819
 Kim, Gi-Woo 322
 Kim, Haeyoun 819
 Kim, Jinwoo 171
 Kimura, Kaito 15

Kimura, Shuuji 763
 Kintou, Ri 385
 Klinger, Florian 91, 550
 Klomp, Matthijs 585
 Kobayashi, Ikkei 15, 385, 749, 770
 Komiya, Takumi 178
 Köpeczi-Bócz, Ákos T. 392
 Koutroulis, Georgios 975
 Kracht, Frédéric Etienne 301
 Kranefeld, Ingmar 301
 Krishnakumar, Ajinkya 618
 Kronnie, Nick te 221
 Kubota, Aya 735
 Kuriyagawa, Yukiyo 653
 Kuroda, Jumpei 15, 385, 749, 770

L

Laine, Leo 130, 144
 Lamps, Antoine 343
 Le Gall, Gaetan 798
 Lee, Ho-Jong 322
 Lee, Hongwoo 721
 Lee, Seung-Yong 322
 Lefeber, Erjen 185, 214
 Lenzo, Basilio 22, 279
 Lex, Cornelia 968
 Li, Jialin 481
 Li, Pu 427
 Li, Ruoyao 646
 Li, Shengbo Eben 904, 947
 Li, Zexing 665
 Li, Zihong 427
 Lind Jonsson, Oskar 151
 Liu, Chang 585, 947
 Liu, Hui 625
 Liu, Xiaojun 749
 Lu, Hangyu 693, 742
 Lu, Jianwei 481
 Lyu, Yao 904

M

Ma, Fei 904
 Macaluso, Andrea 343
 Maeda, Kenta 265
 Maglia, Lorenzo 578
 Magri, Paolo 308, 336
 Manca, Raffaele 826
 Mancarella, Alessandro 826
 Mandl, P. 91

Mantovani, Federico 571
 Marelo, Omar 826
 Massaro, Matteo 22
 Mastinu, G. 933, 940
 Mastinu, Giampiero 911, 919
 Mastinu, Gianpiero 926
 Masuda, Makoto 468
 Mattas, Konstantinos 954, 961
 Mavrouidakis, Basileios 343
 Melzi, Stefano 293
 Mentasti, Simone 510
 Metzler, Mathias 557
 Mi, Tian 392
 Miao, Jinyu 193
 Michielan, Luca 571
 Mihalkov, M. 413
 Mihályi, Levente 686
 Milivinti, M. 940
 Montanaro, Umberto 413, 854
 Montini, Edoardo 293
 Moradi, Lee 251
 Mori, Daiki 378
 Morri, Pietro 510
 Mukumoto, Hirotaka 777
 Müller, Steffen 791, 876
 Mun, Seongjae 721
 Muragishi, Yuji 735

N

Naganuma, Ryusei 749
 Nair, Pratheesh Sivaraman 975
 Narita, Takayoshi 15, 385, 749, 770
 Németh, Balázs 812
 Nicoli, Monica 510
 Nie, Shida 625
 Niegl, Matthias 533
 Nielsen, Lars 151
 Niki, Keitaro 137
 Nishio, Minoru 653
 Nogi, Kazunori 137
 Nybacka, Mikael 447

O

Ogawa, Kazuki 15, 385, 749, 770
 Ohms, Leon 207
 Okano, Toshihiko 728
 Okita, Toshinori 137
 Olofsson, Björn 151
 Ono, Ryutaro 15

Orosz, Gábor 371, 392
 Ott, Christoph 550
 Ott, Lorenz 869
 Otto, Lisa Marie 791

P

Paldan, Jesse 251
 Panzani, Giulio 8, 503
 Paparone, Marco 343
 Park, Jinhui 721
 Park, Sungjun 272
 Parthasarathy, Dhasarathy 1
 Peeie, Mohamad Heerwan Bin 770
 Penet, Maxime 798
 Perlo, Pietro 854
 Pethe, C. 244
 Pfeffer, Peter 533
 Piao, Yingxi 947
 Pierini, Matteo 8
 Piiroinen, Petri T. 714
 Pino, Alessandro 343
 Plöchl, Manfred 91, 200, 550, 557, 862, 869
 Poks, Agnes 550
 Pontoglio, Stefano 578
 Prakash, Jai 488
 Previati, Giorgio 926
 Prost, Mattéo 804
 Puščul, Dženana 968

R

Radaelli, Giovanni 919
 Radrizzani, Stefano 503
 Rahman, Shammi 116
 Raksincharoensak, Pongsathorn 78, 85, 137, 406, 454, 982
 Rebesberger, Ron 207
 Reiter, Rudolf 447
 Righetti, Giovanni 22
 Roempke, Jakob 585
 Roman, Henze 434
 Romano, Luigi 315
 Ronchi, Andrea 571

S

Sabbioni, Edoardo 235, 488, 510, 517, 525, 571, 578, 926
 Sago, Takashi 286
 Sakai, Hideki 784
 Salazar, Mauro 98

- Salierno, Marco 293
 Salzwedel, Leon 109, 564
 Sandrini, Giulia 308, 336
 Sasaki, Kensuke 728
 Sathyamangalam Imran, Mohammed Irshadh
 Ismaaeel 540
 Sato, Yu 178
 Savaia, Gianluca 43
 Savaresi, Sergio Matteo 8, 43, 503
 Schabauer, Martin 968
 Schramm, Dieter 301
 Schuster, Tobias 862
 Schyr, Christian 791
 Senofieni, Rodrigo 8, 43
 Seong, Junyeong 272
 Shiiba, Taichi 399, 468
 Shimono, Keisuke 777
 Shingade, Kartik 1
 Shino, Motoki 461
 Shinohara, Naoki 265
 Shyrokau, Barys 632
 Signorini, Maria Gabriella 926
 Silvagni, Mario 826
 Sjöberg, Jonas 350, 604, 679
 Škugor, Branimir 364
 Somma, Antonella 926
 Sonnino, Samuel 571
 Sonoda, Hiroki 265
 Sorniotti, Aldo 413, 854
 Spachtholz, Eva 301
 Stano, Pietro 854
 Stella, Matteo 578
 Stepan, Gabor 481
 Sturm, Axel 78, 85
 Subitoni, Luca 926
 Suda, Yoshihiro 777, 897
 Sugaya, Fumio 137
 Sun, Yiwen 618
 Sung, Jihoon 611, 883
 Suzuki, Takuma 672, 728
- T**
- Takács, Dénes 123, 371, 392, 481, 686
 Takahashi, Masaki 672
 Tamura, Tsutomu 763
 Tan, Vu Van 812
 Tanaka, Yusuke 178
 Tanimoto, Tsutomu 672
 Tavernini, Davide 854
 Tavolo, Gaetano 854
- Thal, S. 158
 Tian, Ziang 71
 Tonoli, Andrea 826
 Tramacere, Eugenio 826
 Trigell, Annika Stensson 447
 Tristano, Mariagrazia 279
 Tufo, Manuela 854
- U**
- Uccello, Lorenzo 926
 Uchino, Daigo 15, 385, 749, 770
 Uechi, Masaaki 137
 Ueno, Ken-taro 178
 Ueyama, Yuki 286
 Unterreiner, Michael 91, 862, 869
 Urakawa, Kazuo 777
- V**
- van Aswegen, J. C. 756
 van Dam, Sander 1
 Vantsevich, Vladimir 251
 Váss, Sandor 954, 961
 Velardocchia, Mauro 36
 Velenis, Efstathios 618, 804
 Vignarca, Daniele 235
 Vignati, Michele 488, 517, 525, 571
 Vörös, Illés 371, 481
- W**
- Wan, Hang 625
 Wang, Wei 406
 Wang, Wenxuan 904
 Wang, Yafei 646, 665
 Wang, Yixiao 350, 679
 Washimi, Yuta 672, 728
 Watanabe, Atsushi 653
 Weber, Trey 378
 Westendorf, M. 158
 Wisell, Lukas 1
 Wu, Mingyu 646, 665
 Wu, Xiaodong 693, 742
 Wu, Zhihao 427
 Wülfing, Ingo 876
- X**
- Xi, Junqiang 71, 164, 228
 Xu, Yong 474

Y

Yamada, Hayato 770
Yamaguchi, Hiroyuki 735
Yamakado, Makoto 178
Yamakaji, Yoshihiro 329
Yan, Liang 693, 742
Yan, Rujun 193
Yang, Derong 50, 447, 604
Yang, Diange 193, 496
Yang, Mengmeng 496
Yang, Mingliang 496
Yang, Sen 947
Yim, Seongjin 171
Yin, Yuming 904

Yoshida, Fumiya 770
Yoshitake, Hiroshi 461
Yu, Huilong 71, 164, 228

Z

Zerbato, Luca 36
Zhang, Bowei 193
Zhang, Jianrun 427
Zhang, Ning 427
Zhang, Wenliang 447
Zhang, Xingguo 137, 454
Zhang, Yichen 646, 665
Zhou, Jian 151
Zivadinovic, Milan 975